Dépôt légal : septembre 2015
COPYMEDIA
Achevé d'imprimer
en septembre 2015 par
www.copy-media.net
CS 20023 - 33693 MÉRIGNAC CEDEX

2015

Electroweak Interactions and Unified Therories

These proceedings are dedicated to the memory of our dear friend
Guido Altarelli

Guido made a very lively contribution to celebrate these
50th Rencontres de Moriond which can be viewed on
`https://webcast.in2p3.fr/videos-the-early-years-of-moriond`

Sponsored by

. CNRS (Centre National de la Recherche Scientifique)
. FNRS (Fond National de la Recherche Scientifique)
. BSP (Belgian Science Policy)

50th Rencontres de Moriond
La Thuile, Aosta Valley, Italy – March 14-21, 2015

2015 Electroweak Interactions and Unified Theories

© Published by ARISF, 2015

ISBN : 978-2-9546400-8-2

web

All rights reserved. This book, or parts thereof, may not be reproduced in any form or by any means, electronic or mechanical, including photocopying, recording or any information storage and retrieval system now known or to be invented, without written permission from the publisher.

Proceedings of the 50th RENCONTRES DE MORIOND

Electroweak Interactions and Unified Theories

La Thuile, Aosta Valley Italy *March 14-21, 2015*

2015

Electroweak Interactions and Unified Theories

edited by

Etienne Augé,

Jacques Dumarchez,

and

Jean Trân Thanh Vân

The 50th Rencontres de Moriond

2015 Electroweak Interactions and Unified Theories

was organized by :

Etienne Augé (LAL, Orsay)
Jacques Dumarchez (LPNHE, Paris)

with the active collaboration of :

A. Abada (LPT, Orsay),
E. Armengaud (IRFU-SPP, Saclay),
J. Conrad (Columbia U)
P. Fayet (ENS, Paris),
J.-M. Frère (Brussels),
P. Hernandez (Valencia),
L. Iconomidou-Fayard (LAL, Orsay),
P. Janot (CERN),
M. Knecht (CPT, Marseille),
J. P. Lees (LAPP, Annecy),
S. Loucatos (IRFU-SPP, CEA, Saclay),
F. Montanet (LPSC, Grenoble),
J. Orloff (LPC, Clermont-Ferrand),
L. Okun (ITEP, Moscow),
A. Pich (Valencia),
S. Pokorski (Warsaw),
V. Tisserand (LAPP, Annecy)
D. Wood (Northeastern Univ.,Boston)

2015 RENCONTRES DE MORIOND

The 50^{th} Rencontres de Moriond were held in La Thuile, Valle d'Aosta, Italy.

The first meeting took place at Moriond in the French Alps in 1966. There, experimental as well as theoretical physicists not only shared their scientific preoccupations, but also the household chores. The participants in the first meeting were mainly french physicists interested in electromagnetic interactions. In subsequent years, a session on high energy strong interactions was added.

The main purpose of these meetings is to discuss recent developments in contemporary physics and also to promote effective collaboration between experimentalists and theorists in the field of elementary particle physics. By bringing together a relatively small number of participants, the meeting helps develop better human relations as well as more thorough and detailed discussion of the contributions.

Our wish to develop and to experiment with new channels of communication and dialogue, which was the driving force behind the original Moriond meetings, led us to organize a parallel meeting of biologists on Cell Differentiation (1980) and to create the Moriond Astrophysics Meeting (1981). In the same spirit, we started a new series on Condensed Matter physics in January 1994. Meetings between biologists, astrophysicists, condensed matter physicists and high energy physicists are organized to study how the progress in one field can lead to new developments in the others. We trust that these conferences and lively discussions will lead to new analytical methods and new mathematical languages.

The 50^{th} Rencontres de Moriond in 2014 comprised three physics sessions:

- March 14 - 21: "Electroweak Interactions and Unified Theories"
- March 21 - 28: "QCD and High Energy Hadronic Interactions"
- March 21 - 28: "Gravitation: 100 years after GR"

We thank the organizers of the 50^{th} Rencontres de Moriond:

- A. Abada, E. Armengaud, J. Conrad, P. Fayet, J.-M. Frère, P. Hernandez, L. Iconomidou-Fayard, P. Janot, M. Knecht, J. P. Lees, S. Loucatos, F. Montanet, L. Okun, J. Orloff, A. Pich, S. Pokorski, V. Tisserand, D. Wood for the "Electroweak Interactions and Unified Theories" session,
- E. Augé, E. Berger, S. Bethke, A. Capella, A. Czarnecki, D. Denegri, N. Glover, B. Klima, M. Krawczyk, L. McLerran, B. Pietrzyk, L. Schoeffel, Chung-I Tan, J. Trân Thanh Vân, U. Wiedemann for the "QCD and High Energy Hadronic Interactions" session,
- P. Binétruy, M.-A. Bizouard, L. Blanchet, L. Cacciapuoti, F. Cavalier, M. Cruise, P. Delva, J. Dumarchez, J.-M. Le Goff, S. Léon-Hirtz, E. Rasel, S. Reynaud, F. Ricci, J.-Y. Vinet for the "Gravitation: 100 years after GR" session

and the conference secretariat and technical staff:

V. de Sá-Varanda and C. Bareille, I. Cossin, G. Dreneau, D. Fliegel, F. Legrand, G. Perrin, N. Ribet, S. Vydelingum.

We are also grateful to Giorgio Palmucci, Francesco Cante, Ida Liseno, Francesco Quinto and the Planibel Hotel staff who contributed through their hospitality and cooperation to the well-being of the participants, enabling them to work in a relaxed atmosphere.

The Rencontres were sponsored by the Centre National de la Recherche Scientifique, the Fonds de la Recherche Scientifique (FRS-FNRS) and the Belgium Science Policy. We would like to express our thanks for their encouraging support.

It is our sincere hope that a fruitful exchange and an efficient collaboration between the physicists and the astrophysicists will arise from these Rencontres as from previous ones.

The 50^{th} edition of these Rencontres offered us the possibility to celebrate with dedicated talks by some of the pillars of Moriond, giving their personnal recollections or panoramic views of the evolution of physics ideas along these 50 Rencontres. We would like to warmly thank D. Treille, G. Altarelli, E. Fischbach, M. Krawczyk, D. Goulianos, and B. Klima. Videos of these moments can be viewd on: `https://webcast.in2p3.fr/events-moriond_2015`, *thanks to the webcast services at CC-IN2P3 and LAL, and particularly to O. Drevon and G. Dreneau. The 50^{th} Rencontres were also the occasion of renewing some long-standing traditions of Moriond, like the slalom: tens of participants of all ages skied down the track in all times and styles to eventually win ... a glass of mulled wine! And delving into the archives we have produced a list of the nearly 10000 participants of these 50 Rencontres, which has been put up as wallpaper along the corridor leading to the bar, resulting in persistant traffic jams!*

E. Augé, J. Dumarchez and J. Trân Thanh Vân

Contents

1. Celebrating the 50th Moriond

50 Years of Moriond	D. Treille	3

2. The Scalar Sector

Scalar Boson: CMS Run 1 final results, prospectives for Run 2 (and HL-LHC)	J. Bendavid	33
Studies of the Higgs Boson and direct searches for new phenomena at the TeVatron	C. Vellidis	41
CMS High mass WW and ZZ Higgs search with the complete LHC Run1 statistics	M. Pelliccioni	47
Beyond the Standard Model Higgs searches at the LHC	P. Meridiani	53
On the search for a second scalar doublet at the LHC	A. Celis	59
BSM Primaries: the Physics of the SM Effective Field Theory	F. Riva	65
Higgs relaxation and the matter-antimatter asymmetry of the universe	A. Kusenko	71
Vacuum stability depends on high energy physics scales	V. Branchina	75
On the Origin of Scales and Inflation	A. Salvio	81

3. Standard Model

Electroweak multi-boson measurements from ATLAS and CMS: Run 1 legacy and Run 2 prospects	L. Perrozzi	89
Recent Electroweak Results from the Tevatron	M. Bauce	95
Prospects for the measurement of m_W at the LHC,	M. Boonekamp	101
Collecting and analysing data at high pile-up with ATLAS and CMS	N. Styles	107
Improving LHC searches for strong EW symmetry breaking resonances	A. Kaminska	113

4. Top Physics

An historical recount of the events leading to the discovery of the top quark in 1995 by the CDF and D0 experiments at the Tevatron	P. Azzi	121
Top Quark Physics at the Tevatron	A. Jung	127
Precision on the top mass	S. Weinzierl	133
ATLAS+CMS top mass: current results and future measurements	M. Voutilainen	141
ATLAS + CMS top production and properties: Run 1 legacy	A. Loginov	149

5. Beyond the Standard Model

ATLAS+CMS: Boosted topologies (Run1 results, Run2 potential)	J. Stupak	161
SUSY: Blind spots at Run 1, perspectives at Run 2 and beyond	G. Polesello	169
ATLAS & CMS Exotics Searches: Run 1 Results and Run 2 Prospects	K. Leney	177
Searching for supersymmetry in compressed scenarios with the CMS experiment	R. Bainbridge	185
Searches for long lived supersymmetric particles with the ATLAS detector	H. Hayward	193
Resonances and unitarity in composite Higgs models	D. Espriu	199
$2h$ production with isotriplet scalars	S. Godunov	205
A bonus complementarity in Simplified Models of Dark Matter	B. Zaldívar	211

6. Neutrino Physics

Status of three-neutrino mixing	E. Lisi
Recent Results from Daya Bay Reactor Neutrino Experiment	B. Hu
Entering the Two-Detector Phase of the Double Chooz Experiment	R. Carr
Uncertainties in Reactor Neutrino Fluxes and in the Anomaly	A. Hayes
Selected results from T2K	J. Myslik
Prospects to determine the neutrino mass hierarchy	S. Choubey
Recent results from Super-Kamiokande	S. Mine
Recent results from Borexino	B. Caccianiga
Recent results from MINERνA	C. Patrick
NA61/SHINE Data for Long Baseline Neutrino Experiments	A. Haesler
Three-Loop Neutrino Mass Models at Colliders	A. Ahriche
Cosmological Constraints on the Seesaw Scale	J. López Pavón
Searches for Exotic Processes in Double Beta Decay with EXO-200	T. Johnson
Neutrinoless double beta decay and nuclear matrix elements	P. Raina
Lepton Number Violation with *and without* Majorana Neutrinos	J. Heeck

7. Heavy Flavours

Latest results on rare decays from LHCb	C. Langenbruch
$B \to K^\star\mu\mu$: theory interpretation or *A hitchiker's guide to* $B \to K^\star\mu\mu$ *optimised observables*	J. Matias
Implications of $b \to s$ measurements	D. Straub
$\boldsymbol{CP}$ Violation in the $\boldsymbol{B^0_{(s)}}$ Meson System at LHCb	J. Wishahi
Lattice inputs to flavor physics	M. Della Morte
Explaining the LHC flavour anomalies	A. Crivellin
Constraining CKM gamma angle at LHCb	A. Vallier
Determination of the quark coupling strength $\mathbf{\lvert V_{ub}\rvert}$ using baryonic decays	W. Sutcliffe
Rare Decays and other Electroweak b-physics - Measurements at ATLAS and CMS	P. Ronchese
Charm mixing and CP violation at LHCb	E. Gersabeck
$K \to \pi\nu\bar{\nu}$ in the Standard Model and Beyond	R. Knegjens
Results from the NA62 2014 Commissioning Run	D. Soldi

8. VHE and Dark Matter

Neutrinos from heaven and hell in IceCube : latest results on astrophysical neutrinos and neutrino oscillations	J.P. Yáñez
The Flavour Composition of the High-Energy IceCube Neutrinos	A. Vincent
Interpretation of the high energy IceCube data	M. Masip
Indirect searches for sterile neutrinos at a high-luminosity Z-factory	V. De Romeri
Recent results from the XENON100 experiment	G. Bruno
Dark matter at the LHC	U. Haisch
Dark matter searches at ATLAS, Run1 results and Run2 potential	C. Doglioni
Direct Dark Matter Search with the CRESST-II Experiment	J. Schieck
First results from darkside-50	D. Franco
3.55 KeV line in minimal decaying Dark Matter	G. Arcadi
Light sterile neutrino limits from cosmology	N. Saviano
Planck 2015 results	S. Henrot-Versillé

9. Young Scientists Forum

Search for a SM-like Higgs boson in the H→ZZ→ $\ell\ell q\bar{q}$ decay channel in CMS	E. Navarro de Martino	479
One-loop effective non-linear Lagrangian with a light H-boson	K. Kanshin	483
Signatures of dynamical scalars	I. Brivio	487
Electroweak production and hadronic activity in Zjj events at CMS	T. Cornelis	491
Limits and Fits from Simplified Models	J. Sonneveld	495
Search for new light gauge bosons in Higgs decays to four-lepton events in pp collisions at $\sqrt{s} = 8$ TeV with the ATLAS detector	D. Paredes Hernández	499
Dark Matter produced in association with top quark pair	D. Pinna	503
Renormalisation of the NMSSM in SloopS	V. Bizouard	507
Higher order proton lifetime estimates in Grand Unified Theories	H. Kolešová	511
Testing left-right symmetric models|	W. Dekens	515
Octant of θ_{23} and precision measurement of atmospheric neutrino oscillations at INO-ICAL detector	D. Kaur	519
Search for a sterile neutrino with the STEREO detector at ILL	S. Zsoldos	523
NEMO-3 analysis of the double-β decay of ^{96}Zr	G. Eurin	527
Study of the decay $B^+ \to K^+\pi^0$ at LHCb	J. Andrews	531
An analysis of $\Lambda_b^0 \to \Lambda\mu^+\mu^-$ decays at the LHCb experiment	L. Pescatore	535
Search for $B^+ \to \ell^+\nu_\ell\gamma$ decays with hadronic tagging using the full Belle data sample	A. Heller	539
Boosted W-Boson Identification at $\sqrt{s} = 8$ TeV with the ATLAS Detector	C. M. Delitzsch	543
Measurement of the distribution of ϕ^*_η in events containing dimuon pairs with masses between 30 and 500 GeV in 10.4 fb^{-1} of $p\bar{p}$ collisions	X. Li	547
Low mass wimp search with EDELWEISS-III: first results	T. Main de Boissière	551
On the use of the escape speed estimates in setting dark matter direct detection limits	S. Magni	555
WIMP Annihilations in the Sun : A search based on the first year of data from the completed IceCube neutrino telescope.	M. Rameez	559

10. Summary

Experimental Summary	T. Wyatt	565
Theory summary	A. Strumia	593

Authors index 609

List of participants 613

1.
Celebrating the 50^{th} Moriond

50 years of Moriond: a personal view

Daniel Treille
CERN
Geneva, Switzerland

50 years of particle physics as seen through the Rencontres de Moriond: are summarized

Introduction

Half a century is a long time and all has changed a lot, for instance the way of skiing, or CERN, which went in 60 years from grass field to the LHC.

The Moriond adventure was decided in 1965 by Jean Tran Thanh Van, from Orsay, helped in this groundbreaking initiative by his wife Kim and, at the start, by five colleagues: Bernard Grossetête, Fernand Renard, Michel Gourdin, Jean Perez Y Jorba and Pierre Lehmann. I did my diploma with Bernard, my thesis with Jean and came to CERN with Pierre. Unfortunately all three have disappeared.

The idea of Moriond is expressed by the word "rencontres", meaning gathering of minds, theorists and experimentalists, young and less young actors, on an equal footing and in an informal atmosphere. In 1966 there were 20 participants. The Rencontres were a success and success calls for an evolution. A biology meeting was added in 1970. Moriond Astrophysics appeared in 1981. Other developments came: rencontres of Vallée d'Aoste, Blois, Vietnam.

But the unique spirit of the Rencontres lived on. J.Cronin, at the 20 years of Moriond, attributed to them a "profound effect on the way we communicate in particle physics". Similar statements came from Ludwik Celnikier at their 40 years. I would also underline the humility of A.Martin in its 67 summary: "je ne vous cacherai pas combien il est embarrassant de tirer les conclusions d'une pareille rencontre".

During decades most of the major actors of the field attended some of the Rencontres and all important events were presented and celebrated.

Table 1 shows what happened in these decades in the domains concerning us. It must be looked at quietly. It indicates the divide line, ante Moriond (AM) and post Moriond (PM). A simplified version of it appears in Table 2, that one can summarize as follows.

Conceptually, a complete change occurred in the end sixties/early seventies, with breakthroughs like the quark model, the EW SM and QCD. Before them, there was no or only poor theoretical guidance. After them, the experimental work became testing and, up to now, validating the SM. Until about the same years, CERN was still in a learning phase, with discoveries mostly coming from elsewhere. Then CERN made its way towards its present leadership at the High Energy

Table 1: The divide line ante Moriond (AM) and post Moriond (PM)

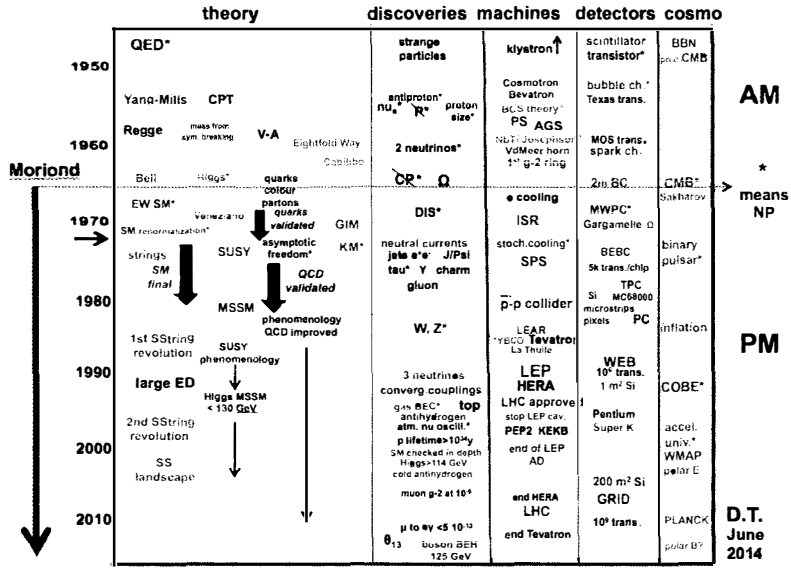

frontier. Of the remarkable sequence of machines, I will focus on only two. I will briefly describe the evolution of experimental techniques, which benefited a lot from the parallel exponential progress of microelectronics and computing means. As for cosmology, it is only with the discovery of the CMB in 1964 that the idea of an expanding universe imposed itself, opening a new point of view on our field, namely re-creation in a microscopic way of the physics, which prevailed at early times of the universe, beyond the curtain of invisibility.

1965 was a good year to start, given the mirabilis year 1964[1,2,3,4,5,6,7,8,9,10] which saw Bell inequalities, CP violation, the CMB discovery, the idea of the BEH boson, the quark model (M.Gell-Mann and G.Zweig, with A.Petermann expressing the same idea) and the discovery of the Ω^-.

Machines

"No klystron, no HEP" was a motto in the early days. Let me simply quote their inventors, the Varian brothers, and a leading figure of the first linacs in Stanford, W.Panofsky.

Focusing on colliders, which look so familiar now, one must realize that one had to wait long before some pioneers dare to consider this possibility: Wideroe 43, and, more precisely, Kerst et al 56, Petoukhov 57 and G.K.O'Neill 56. They considered tangent e^-e^- rings, except the visionary Frascati physicist, B.Touschek, who focused on e^+e^-.

The little ADA e^+e^- ring[11,12,13] (See Figure 1) was built in Frascati and exploited with LAL Orsay linac by a Italian/French team including P.Marin and J.Haissinski, one of the speakers of the very first Moriond in 66. ADA detected interactions and started the long series of such colliders, ACO, VEPP2, ADONE, DCI, CEA, SPEAR, DORIS, DAΦNE, etc, until LEP. In the first Moriond meetings, one heard a lot about e^+e^-, not only concerning the physics prospects (J.Perez y Jorba 76, F.Renard, etc), but also about the machine problems, vacuum, instabilities,

Table 2: A simplified view of particle physics evolution

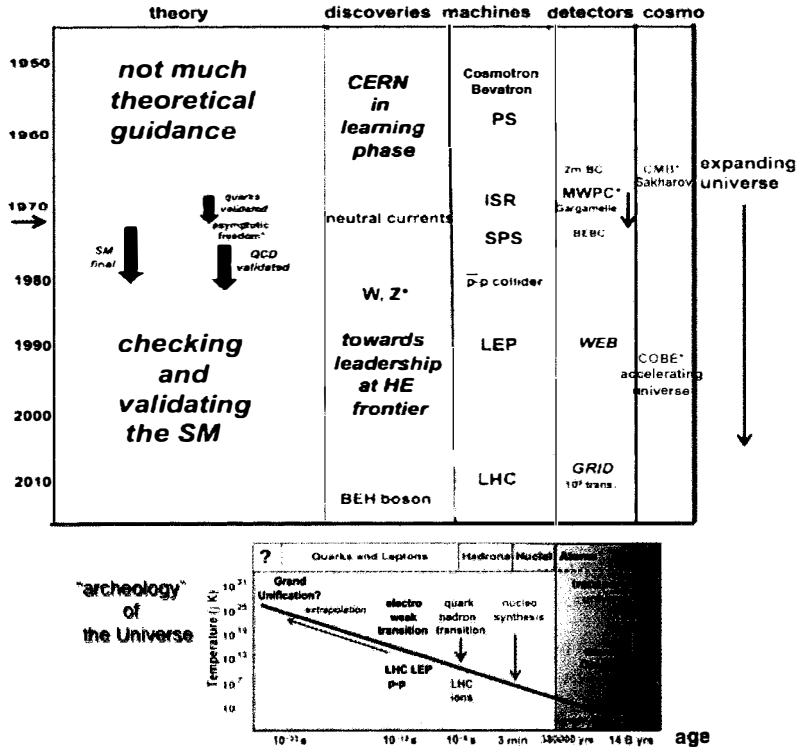

nonlinearities and ways to cure them (e.g.V.Silvestrini 69).

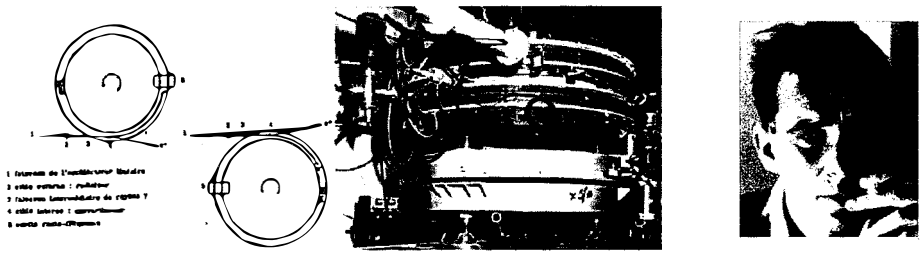

Figure 1 – the ADA ring and B.Touschek (1964)

The second machine I will quote is the first hadron collider, the ISR[14] (1971-1983, $E_b = 31.4\ GeV$), in which, for the first time, stochastic cooling (S.Van der Meer, W.Schnell, etc) was practised (See Figure 2) (and improved in the ICE ring), an excellent ultra vacuum obtained and SC low β quadrupoles used. It was therefore a pioneering machine for all posterior colliders, especially those involving antiprotons (CERN collider, Fermilab Tevatron, LEAR, AD).

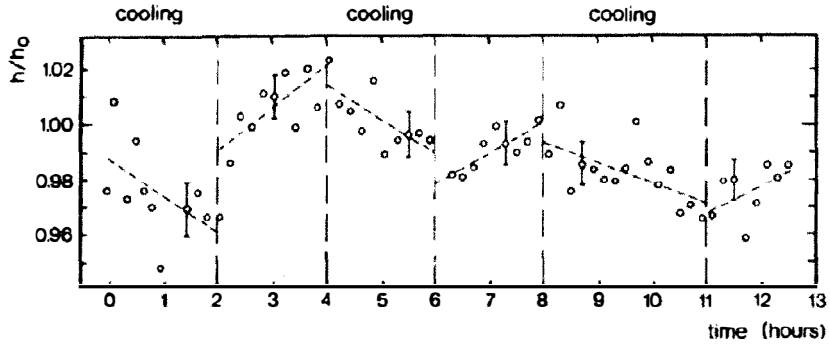

Figure 2 – Stochastic cooling at ISR

Detectors

Concerning detectors, the ancestors were not far away: Wilson chamber 1912, Geiger-Muller counter 1928, scintillators in 1947-50, the Bubble Chamber (BC) in 1953 (Glaser, Nobel 1960).

Our field saw first the reign of BC[15]. This period corresponds to CERN "years of learning", until the success of its big chambers.

Triggered detectors appeared next, with the development of spark chambers (49-59), of their various read out methods, from film to filmless, and of variants as streamer chambers.

The course of HEP changed dramatically with the 68 revolution of G.Charpak (Nobel 1992), his MWPC, followed by drift chambers, multistep devices (F.Sauli) [16]and the TPC (Nygren).

Finally came the progressive rise of Si detectors, from few cm^2 at the SPS to $200m^2$ at LHC[17].

Figure 3 summarizes these mutations. As already said, this evolution benefited a lot from the tremendous one of microelectronics. The transistor is younger than me and modern chips have up to 10 billions of them.

Concerning particle identification, let us mention the RICH technique, from J.Seguinot and T.Ypsilantis (also co-discoverer of the antiproton). Sampling calorimetry saw the progress of scintillator or liquid argon/heavy material devices. Larger and larger arrays of scintillating crystals, more and more radiation hard, were used for electromagnetic calorimetry.

One must underline here the crucial role of permanent and vigorous R&D programs, for instance concerning Si radiation hardness, as well as the important spin off of HEP detectors.

The Quark Story

Strange particles were discovered in 47 - 61, using first cosmic rays and pre-BC techniques. At accelerators and with BC, they were mostly found in US.

Strangeness was introduced as a new quantum number by K.Nishijima and M.Gell-Mann (MGM) in 53, 56.

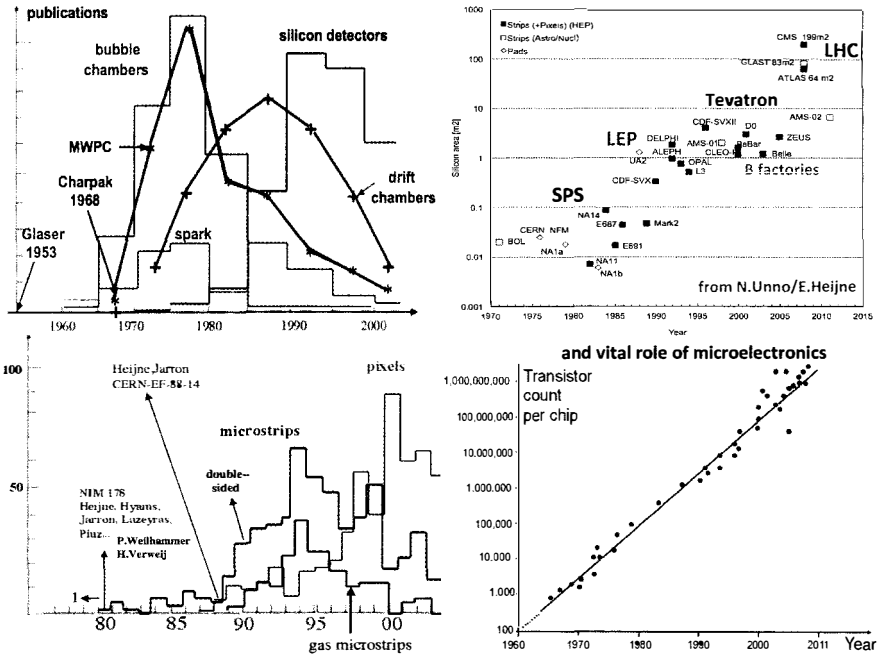

Figure 3 – The evolution of detectors and of microelectronics

In 1960 came the Eightfold way of MGM and Y.Ne'eman, locating the hadronic states at the nodes of diagrams corresponding to representations of flavor SU(3), e.g. the baryon $3/2^+$ decuplet. In 62, the still missing state at the tip of the decuplet (as sss) was predicted at a mass of about 1685 MeV and the corresponding Ω^- was found in 64 in Brookhaven (See Figure 4). Finally MGM and G.Zweig found simpler to focus on the smallest SU(3) representation and proposed a triplet of fractionally charged quarks (or aces). Read MGM to guess what was his deep thinking about them [18,19,20]. Then the well known reduction à la Mendeleev could occur. This is how the story is told.

However at that time a fierce battle was going on between quantum field theory and the S-matrix theory, well accounted for in D.Gross Nobel lecture and H.Pietschmann chronicle [21].

It started with Regge theory, built on the analyticity in angular momentum of scattering amplitudes $A(\cos\vartheta)$. It gives $A(\cos\vartheta) \approx (\cos\vartheta)^{l(s)} \approx s^{l(t)}, where\ l(x) = kx$ is the Regge trajectory function and s, t the usual Mandelstam variables. Among Regge trajectories, the Pomeron was the topic of Moriond 73, summarized by D.Leith. 35 years later, C.Quigg (2008) still calls the Pomeron "a mysterious entity". Then came Dolen, Horn, Schmid duality, telling that s and $t-$channel are two ways to express the same physics, and encoded in Veneziano formula. This approach culminated with the Bootstrap theory of G.Chew, postulating full democracy among particles and that none is fundamental, and the S-matrix axioms kept as only basic principles.

In 65, as a young student in Les Houches summer study, I had as teachers G.Chew, developing his views on Regge theory, bootstrap and the S-matrix, and R.Dalitz, repeating quarks, quarks, quarks, so already deep in this world, and I felt a bit schizophrenic.

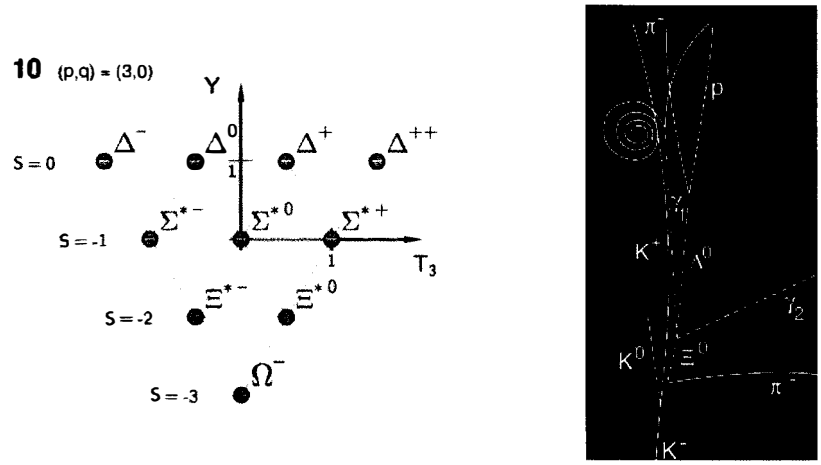

Figure 4 – Prediction and discovery of the Omega minus

From the experimental side, an avalanche of resonances kept pouring in, leading to ≈ 100 strongly interacting particles at the end of the seventies, whose properties were well reviewed in Moriond by L.Montanet, the leading figure of the Rencontres for decades in matter of hadron spectroscopy [22].

On the other hand, in 68, Deep Inelastic electron Scattering (DIS, Friedmann, Kendall, Taylor, Nobel 1990) revealed the existence in the proton of pointlike charged spin 1/2 "partons". With the parton model and Bjorken scaling (Figure 5), the idea of quarks as fundamental objects started to impose itself.

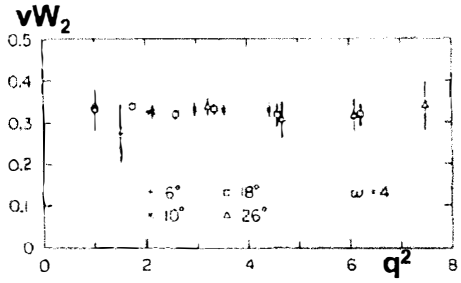

Figure 5 – Bjorken scaling

With the victory of quarks, started the search for free ones, as accounted e.g. in C.Llewellyn Smith 81 summary. Gell-Mann complains: "One atomic spectroscopic friend of mine rings me up, sometimes at midnight, to report his progress in the search for quarks in sea water, ... grinding up oysters and looking for quarks in them".

Distinction was made between constituent and current quarks, leading to current algebra.

In 1973 the ISR discovered large angle hadron scattering, showing that partons are pointlike not only for the electromagnetic, but also for the strong interaction.

Then appeared the Constituent Interchange Model (CIM)[23], a way to bring partons in the game without having to solve the problem of confinement. CIM was much discussed in Moriond by G.Farrar 75 and summary speakers A.Yokosawa 75 and especially R.Blankenbecler 76. The idea is that, in hard hadron scattering, e.g. $AB \to C + X$, parameterized in terms of P_T and $1 - x_T$ (at 90° CM), the exponents of these quantities are related to the number of fundamental constituents involved in the process (Figure 6). At CERN, we were performing elastic hadron scattering at all angles (Lundby 75) and, in the 90° CM angular region, the CIM fitted data very well. This is the way the quark idea became concrete to me.

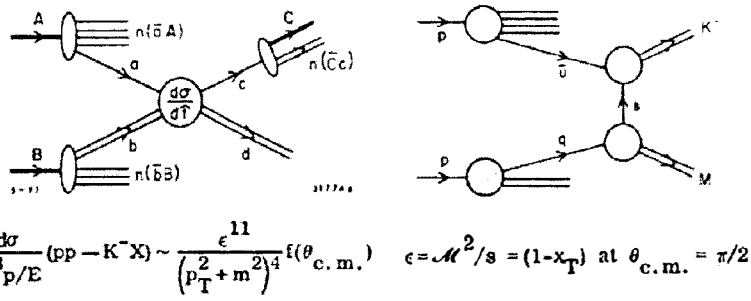

$$\frac{d\sigma}{d^3p/E}(pp \to K^- X) \sim \frac{\epsilon^{11}}{\left(p_T^2 + m^2\right)^4} f(\theta_{c.m.}) \qquad \epsilon = \mathcal{M}^2/s = (1 - x_T) \text{ at } \theta_{c.m.} = \pi/2$$

Figure 6 – The CIM model

J.Cronin has been another major actor of the Rencontres for several reasons (CP violation, hadron hard scattering, later Auger experiment). In 78 came the "Cronin effect", namely the fact that the ratio versus P_T of inclusive yields on two nuclei, weighted by A^{-1}, which should be flat and equal to one, is not flat at all, probably because of re-interaction.

But the systematic exploration of the nucleon with all probes was already on its way.

The Proton, our daily life

The story started in 1957 in Stanford where e^- scattering revealed the finite size of the proton (Hofstadter, NP 1961) and continued in 1968, still in Stanford, where, as just said, harder e^- scattering showed that it contains point-like objects. Then most labs, in particular CERN and Fermilab, invested a lot in the exploration of its structure, using all possible probes.

At CERN, neutrino scattering, providing the weak probe, was performed with powerful SPS neutrino beams. They used van der Meer horn to focus the parent hadrons, and fed the large BC, BEBC and GARGAMELLE, and giant electronic detectors, CDHS 76-84, CHARM, then NOMAD and CHORUS. Similar programs went on in US.

Muon scattering, the electromagnetic (EM) probe, was studied by EMC and NA4, fed by the outstanding CERN muon beam, still in use, and in Fermilab by E203, E665.

Hadron scattering, selecting in the final state a photon or a lepton pair, issued from the hard parton collision, was another fixed target active program, able to measure also the structure functions of the identified incident particles, as did WA11, NA3, WA70, etc.

Finally HERA $e - p$ collider took over this exploration.

From the early days of these programs, one can underline the evidence of scaling violation, i.e.

the fact that the structure found depends on the resolving power of the measurement, as QCD predicts. It was observed first by the large BC (Figure 7), then confirmed by the electronic detectors, with more statistics, but after a long fight against systematic errors. I remember the words of W.Panofsky, referee of one of them, predicting (correctly !) that it would take 10 years to master its systematics.

Hard hadron scattering discovered the so-called K-factor, ratio between experiment and the lowest order theory prediction at the time (Figure 8). This called for more elaborate estimate and, still in 80, J.Peoples, summarizing Moriond, considered "QCD not yet proven".

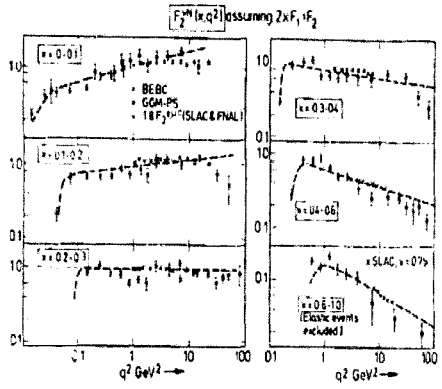

Figure 7 – evidence for scaling violation

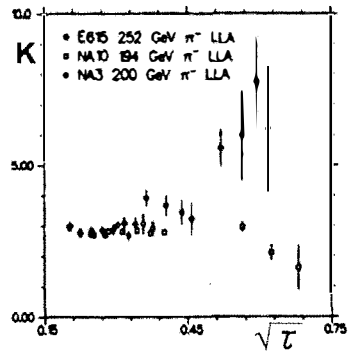

Figure 8 – the K-factor

A question was also the electric charge of quarks, fractional or integer (Han-Nambu, see next).

Muon scattering brought the EMC effect in 83, showing that the nucleon structure depends on the nucleus in which it is immersed, and the spin crisis in 87, indicating that the valence quarks carry only a fraction of the spin of the nucleon.

The road to QCD

I refer here to the talk of Guido Altarelli, a direct actor of the field, and his account in [24]. In brief, the invention of the color quantum number, attributed to Greenberg 64, came first, explaining some mysteries of spin/statistics. The symmetric quark model explained the π^0 lifetime and the R ratio. But, in 65, Han-Nambu used color to propose three sets of quark triplets with integer electric charge. Deciding between Gell-Mann-Zweig and Han-Nambu quarks involved much discussion, as accounted for by C.Llewellyn Smith in his 74 summary. Comparing structure functions from the EM and weak probes, and direct QED Compton scattering, elastic scattering of real photons on quarks (Figure 9), decided in favor of the former.

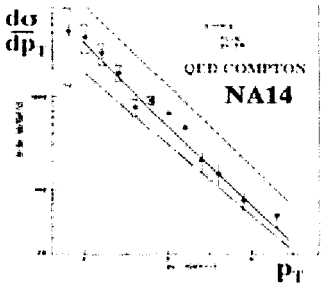

Figure 9 – QED Compton scattering

In 71-72 Fritsch-Gell-Mann gave the outline of the new strong interaction theory and coined the names "gluons", "QCD" [25]. In 72-77 came the DGLAP

evolution equations. In 1973 Asymptotic Freedom was discovered by Gross, Politzer and Wilczek. See G.Altarelli's account of these events [24,25].

J.Ellis in 76 stated that there was no evidence yet of Asymptotic Freedom and explained how to "sniff out glue". L.Hand, summarizing Moriond 79, was still asking "QCD or not?" and calling for the gluon. Evidence for it came from PETRA in DESY in 79 (Figure 10).

Later LEP brought a clear proof of the running of the strong coupling (Figure 11), and, with DIS, contributed to many measurements of the single parameter of QCD, $\alpha_S(M_Z)$.

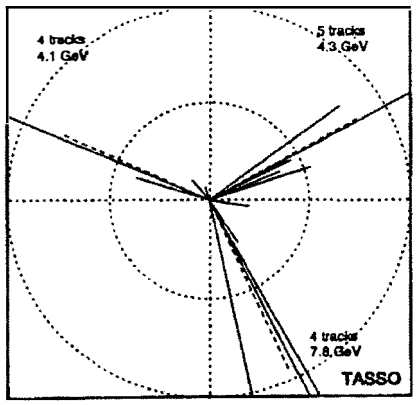

Figure 10 – Evidence for the gluon from PETRA

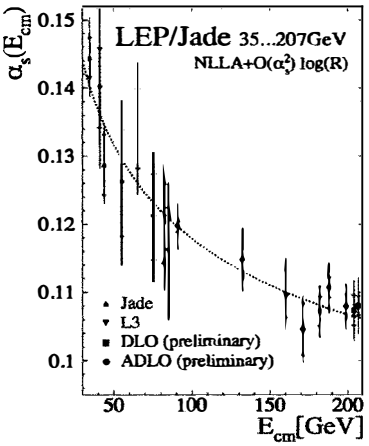

Figure 11 – The running of the strong coupling

Two monumental tasks had still to be accomplished. One was to measure accurately the Structure Functions (SF) of all species of proton constituents, to which HERA brought invaluable contributions. The second, emphasized e.g. by K.Ellis conclusion in 2006, was the computation of higher orders contributions, to go from QCD first principles to a realistic description of its manifestation in HE collisions. Needless to say, both enterprises were absolutely vital for LHC physics.

The QCD session will deal with the physics of heavy collisions, which led CERN to announce in 2000 the observation of a new state of matter.

"The Pandemonium"

Moriond, rather than presenting textbook physics, dealt with "physics being done". This naturally implied that the Rencontres spent a substantial part of their time on topics which finally turned out to be fluctuations, biased analyses, wrong tracks, even plain mistakes [26,27].

Starting by my own one, we thought in 77 having found narrow p-pbar baryonium states, which were not confirmed in subsequent experiments. One can quote also the high y anomaly in 73-78, the A2 splitting in 67, evidence for free quarks in 81, the HERA excess, the long saga of the 17 keV neutrino in tritium beta decay, the evidence for "Achions or Axions" in 2 γ, in Les Arcs 1981, the superluminal neutrinos, etc. J.F.Grivaz, in his 97 conclusions, had to deal, besides HERA excess, with ALEPH evidence for a sum of di-jet mass peak in 4-jet events at LEP130, while DLO, the three other experiments, saw nothing. He rightly called for an exact repetition

of the exposure, and the effect went away. This illustrated the vital need of having more than one experiment at a collider.

Moriond played an extremely important role in such speculative/controversial issues, by providing, as put by A.Franklin, "a forum for those working in the field to meet, present papers, and have both formal and informal discussions and criticism". M.Strovink, in his 98 summary, started with a follow up of the anomalies listed by his predecessor, J.Collins.

The story of three generations

With the muon (1937), its neutrino (1962) and strangeness, it was clear that more than the first generation was existing. In 1963 Cabibbo introduced his angle to account for strangeness production. In 64, Bjorken and Glashow postulated the existence of charm, put on strong grounds by GIM (Glashow, Iliopoulos, Maiani) in 1970, to explain why $K_L \to \mu^+\mu^-$ was unobserved then. Early 74 the R ratio (Figure 12) was a source of perplexity. End 74, the J/Psi, i.e. charmonium, was discovered (Richter, Ting, NP 1976) and charm in 1976. The 2^{nd} generation was there.

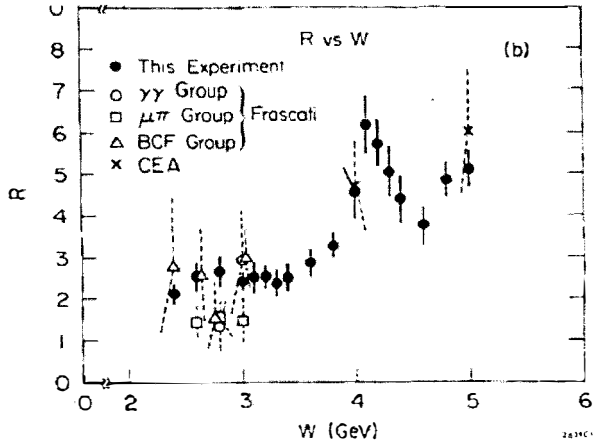

Figure 12 – The R ratio early 1974

Meanwhile Kobayashi-Maskawa (1973, NP 2008) had postulated the existence of a third generation, with good reasons to do so, i.e. the "normal" occurence of CP violation. Beauty was discovered in 1977, after the tau lepton (M.Perl, 1975, NP 1995). For the quark top, see later. LEP finally showed that there were only 3 such generations with a light neutrino. The modern activity, filling the CKM matrix expressing the relationship between quarks, could then start.

All that was stimulating, but generated some frustration at CERN, absent of the major discoveries.

Then a lot of heavy flavor spectroscopy was performed at all machines, SPS, LEP, LHC, Tevatron, etc. For instance, at the SPS, 20 experiments on heavy flavor physics were run. 48 experiments were done in the CERN Omega spectrometer, most dealing with charm and beauty. Charm and beauty tagging started the use of more and more refined silicon detectors.

To this "textbook" version [28,29,30] of the three generations story, let me add some comments.

For sure, charm was anticipated. In April 1974, Glashow[31] said: "There are just three possibilities, (1) charm is not found and I eat my hat (2) charm is found by hadron spectroscopy and we celebrate (3) charm is found by outlanders and you eat your hats". I remember also J.Illiopoulos, telling us when we had doubts: "Look better".

What about charmonium? It was certainly missed in dimuon, because of poor resolution (L.Lederman et al, 1973). Was it anticipated? Not really. Those who came closest to that were M.K.Gaillard, B.Lee and J.Rosner 74[32], postulating a ϕ_c of 2 MeV width, still 20 times the J/Psi width. The discovery of J/Psi caused some trauma at CERN, where we even attempted a desperate charm search at Omega PS... It certainly started the exploration of a new and rich spectroscopy and a lot of speculations on the possible potentials, by e.g. A.Martin.

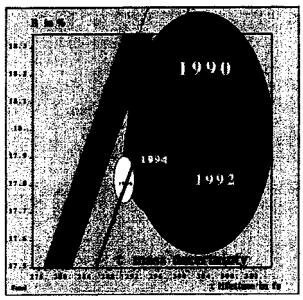

Figure 13 – The tau, summary

The Upsilon appeared first at 6 GeV ('Oops-Leon'), then at 9.5 GeV (1977). The tau came in 1975. Perl and Lederman were both present in Moriond 78. Further Υ studies were performed in PLUTO and DASP at DORIS, in CUSB and CLEO (79 to 2008) at CESR.

Then came the question: are there more than three generations, as discussed e.g. by H.Harari in his 76 conclusions.

E.Paschos, concluding in 89, underlined the "tau controversy", namely some incoherence between the tau properties. Later, by a truly international venture, implying BESS in China, for its nice mass measurement, LEP and CESR for lifetime and branching ratios, all returned to normal, showing that the tau is a mere recurrence of the first leptons (Figure 13[33]). Being normal, the tau could then be used as a precious laboratory for QCD studies and provided experimental input to the $g-2$ of the muon (M.Davier, A.Hoecker).

B^0 mixing was observed by UA1 (1986), then, better, by ARGUS at DORIS2 (1987).

Paschos in 89 put much emphasis on B physics, in particular the role of lattice calculations.

Then PETRA, LEP, the B factories and LHC took the lead in this topic. One can note that, even before the B factories, LEP and others had determined a point in the usual unitary plot, which, assuming that it was the tip of a triangle, showed that this triangle was not flat, indicating CP violation in the B^0 sector (Figure 14).

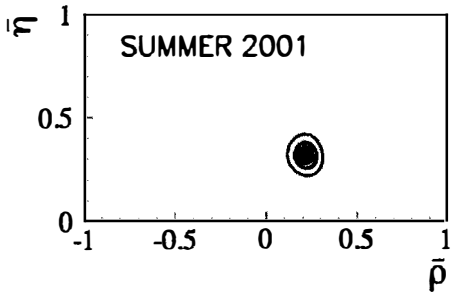

Figure 14 – Tip of the unitary triangle (see figure 20)

Barring some early questions as "Does Bare Bottom Rule Out the Topless E6 Model?" in 83 [34], there was not much doubt concerning the existence of the top quark.

It was searched for with UA1, as reported e.g. by M.Della Negra in les Arcs 89. In 84 UA1 stated that their data were in "agreement with the process $W \to tb$ followed by $t \to bl\nu$, with $30 < m_{top} < 50 GeV/c^2$". In 89 the UA + CDF concluded that m_{top} was heavier than $61 - 77 GeV/c^2$.

However the idea of a light top was still in the minds before LEP and led for instance to consider a possible funny interference between toponium and the Z (Figure 15) [35]. The promise of an eventual subtle toponium spectroscopy led L3 to choose its high resolution BGO calorimetry. Tristan physicists, in the 78 TDR, were hoping to get to the top-antitop threshold.

For various reasons, theorists were advocating a heavier top, as, in 83, Bergström et al and Ginsparg et al, referring to the B lifetime, or, in 92, Ibanez-Ross in the name of EW symmetry breaking in SUSY. But the masses considered stayed modest.

J.Peoples, in his 80 conclusion, said that the toponium was $> 38 GeV$, Paschos in 89 that the top was very likely $> 60 GeV$.

Came next the Tevatron limits, quoted in Moriond by C.Quigg ($91, M_t > 89 GeV$), R.Barbieri ($93, M_t > 108 GeV$).

Then appeared the indirect limits from LEP and other sources: C.Jarlskog ($90, M_t = 143^{+37}_{-44}$ from Langacker et al), F.Dydak ($91, M_t = 131^{+27}_{-32}$+ Higgs), C.Quigg ($94, M_t = 177 \pm 21 GeV$).

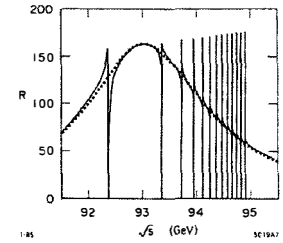

Figure 15 – Z/toponium interference

The top discovery in Fermilab was announced in march 95. In 1996 the direct measurement of Tevatron was $M_t = 172 \pm 6 GeV$. Presently the world average is $M_t = 173.34 \pm 0.27 \pm 0.71 GeV$, while the indirect value is $M_t = 175.8^{+2.7}_{-2.4} GeV$, an outstanding test of the SM. Figure 16, from C.Quigg, summarizes the top saga.

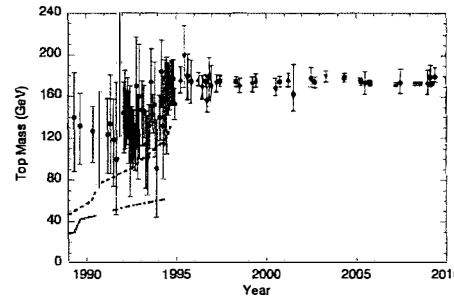

Figure 16 – M_t, direct and indirect

However, as much discussed here, the question is to know what the M_t value exactly means.

About Neutrinos

An interesting pre-Moriond story is the 2-neutrino race, told in particular by D.Haidt [36] and telling how CERN may have missed the discovery, performed in Brookhaven in 62.

Before LEP, the number of generations with a light neutrino, was known to be at least 3, but more was not excluded: $N_\nu \leq 4$ from astrophysics, < 5.5 from W and Z, as quoted by Steigman 86 and Paschos 89.

LEP1 answered to the question, giving, from the Z lineshape, $N_\nu = 2.9835 \pm 0.0083$. This measurement used the one of a cross section and implied thus an excellent absolute normalization. Its accuracy was the result of a great collaboration/competition between theorists and experimentalists, concerning, respectively, the estimate and the measurement of Bhabha scattering, the process used for normalization. The former implied the computation of higher order diagrams, the latter a progressive increase of the accuracy of the luminometers.

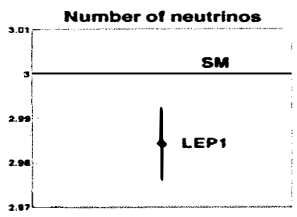

Figure 17 – N_ν at LEP

The number found, slightly below 3 (Figure 17), pleased C.Jarlskog, concluding Moriond 90, since she had deduced that the existence of other, sterile, neutrinos would "steel" from the three active ones. The measurement through the single gamma channel or radiative return gave $N_\nu = 3.00 \pm 0.08$, not competitive at LEP, but which could be quite interesting in a future Giga or Tera-Z factory.

Very briefly, let us quote some highlights of the neutrino saga which occupied Moriond along this half century and is more active than ever. Notorious speakers or concluders were S.P.Rosen 86, F.Vannucci 87, M.Deutsch 88, G.Altarelli 2014, etc. The PS191 experiment of F.Vannucci, J. Dumarchez et al, deserves a special mention for its pioneering aspect.

F.Dydak, concluding in 91, was still fighting with the 17 keV neutrino and already celebrating 20 years of solar ν puzzle.

SuperKamiokande discovered atmospheric neutrino oscillations in 1998. SNO solved the solar neutrino puzzle in 2000. None of these oscillations were in the domain of previous searches at accelerators. This changed when long baselines as Minos, T2K were implemented.

The present activity is to measure the PMNS matrix, with major contributions brought by SNO (2000-04), Kamland, Daya Bay (2012), etc. Figure 18 summarizes the present situation [37,38].

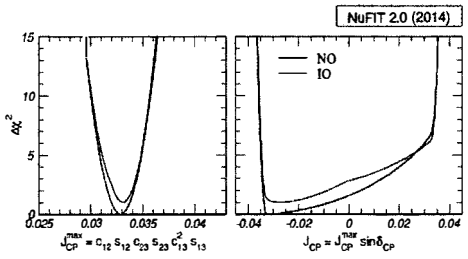

Figure 18 – A neutrino summary

The remaining open problems are well known: hierarchy of neutrino masses? CP violation? Nature of the neutrino, Dirac or Majorana, through neutrinoless double beta decay? Existence or not of sterile ones? in the eV, keV, GeV, etc, domain and their possible roles (Kayser 2003)?

With so many questions and given their importance, neutrino physics will certainly still occupy decades of Moriond.

CP Violation

J.Cronin and V.Fitch got the NP 1980 for the discovery of CP violation in 1964. But J.Cronin himself[39] underlined the role of R.Turlay, then a young actor of their experiment, in the discovery. René, involved in many other CP experiments, was a major figure of Moriond, until his premature disparition.

As a possible explanation of CP violation came the Superweak theory (SW) [40] proposed by Wolfenstein in 64. In Moriond 69, Steinberger and Silvestrini set the "conceptual design" of the procedure to follow, namely to measure the double ratio of K_L and K_S to $\pi^0\pi^0$ and $\pi^+\pi^-$. The accurate measurement of this ratio, expressed as $1 - 6\varepsilon'/\varepsilon$, would tell if $\varrho = \varepsilon'/\varepsilon$ is zero, as in the SW theory, or non-zero, as in Kobayashi-Maskawa (KM) theory, predicting direct CP violation.

R.Schwitters in 82 indicated that experiments were assembled to measure the ratio at 1%. E.Paschos in 89 celebrated the 25th anniversary of CP violation and quoted the first result: $\rho_{CERN} = (33 \pm 11)10^{-4}$, hurting, but not killing, the SW theory. The US E 731 was not yet ready. In R.Barbieri 93 summary appeared $\rho_{731} = (7.4 \pm 5.2 \pm 2.9)10^{-4}$, compatible with a null result, and $\rho_{CERN} = (23 \pm 7)10^{-4}$. Finally J.Ellis, in 99, could quote $\rho_{KTeV} = (28.0 \pm 4.1)10^{-4}$ and the world average became $Re(\varepsilon'/\varepsilon) = (16.3 \pm 2.2)10^{-4}$. Figure 19 is a summary of this adventure.

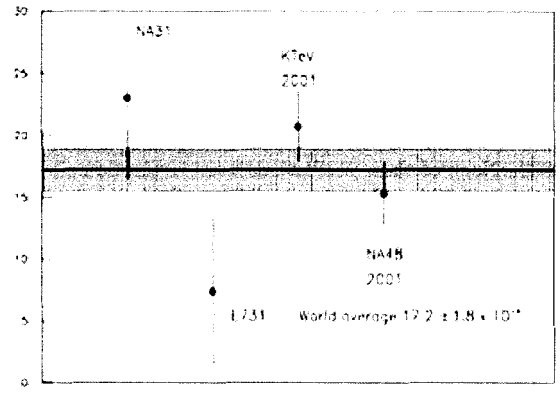

Figure 19 – Towards direct CP violation

It had taken 35 years to answer and falsify the SW theory, at the benefit of the KM theory !

The CERN experiments involved were NA31, followed by NA48, 1986-2001, fed by very clever beam schemes. You can get the full story in various accounts, in particular L.Fayard's talk in "CERN 60 Years" [41,42]. The following experiment, NA62, focuses now on K rare decays.

CP Lear gave the first observation of time reversal violation and confirmed the validity of CPT [43]

fifty times better than before. See also the relevant papers of J.M.Frère on the topic [44].

CP violation in B physics, an objective strongly emphasized by E.Paschos in 89, after preliminary, but assumption dependent, evidence from LEP and others, became the domain of B factories and LHCb, which accomplished an outstanding work, summarized in Figure 20 by the present status of the CKM plot!

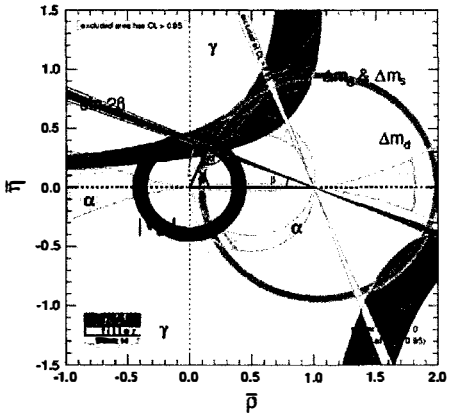

Figure 20 – The unitary triangle

Towards the EW Standard Model

Following Maxwell, and after the quantum revolution, Feynman et al, in 1949, built QED on the grounds of local gauge invariance. In 1954 Yang-Mills extended local gauge invariance to the non-abelian case, i.e. self-interacting vectors of the force. In 1961 Glashow gave the correct algebra of the EW SM model, SU(2) x U(1), but for still massless objects. In 67-68 Salam and Weinberg gave a happy end to the story, by having recourse to the BEH mechanism (Brout, Englert, Higgs), proposed in 64 (Nobel 2013). Glashow, Salam, Weinberg got the 79 Nobel. Finally, in 71, G.t'Hooft showed that the EW SM was a "true" quantum theory and got the 99 Nobel with Veltman.

A clear mission was then defined: to look for W, Z and the BEH boson. In this respect CERN did very well!

However there was some delay in the heads before the SM was fully accepted... Actually even QED was still under check. In 1972 Georgi-Glashow proposed an alternative model [45], with no Z, but a heavy lepton. Some doubts were still expressed. J.Ellis in 76 spoke of Quantum Asthenodynamics "that many people now believe to exist though no-one knows what it is". Bjorken, Sakurai in 80, and others, put forward the Technicolor idea.

There were however early convinced people, as J.Iliopoulos in Moriond 73 (BEH was then called Higgs-Kibble), J.Rosner in 73, "waiting for W, Z, charm, heavy lepton". C.Llewelyn Smith in his 81 conclusion, so after the Neutral Currents, found the "SM healthy", but called for W, Z and the proof of confinement.

In the Weinberg model (76), it was possible, around 1977, to predict $m_W = (78 \pm 3)GeV, m_Z = (89 \pm 3)GeV$, plus $3GeV$ of radiative correction...

Neutral Currents

This was the first major achievement of CERN maturity. The observation of neutrino elastic scattering on electrons and quarks (Figure 21) in the freon of Gargamelle BC brought indirect evidence of the existence of the Z^0 weak boson.

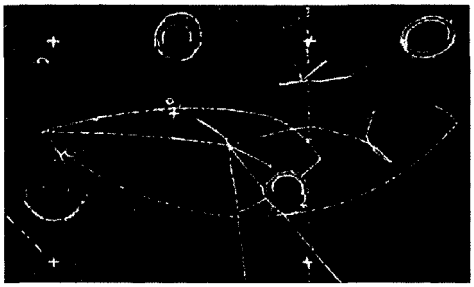

Figure 21 – Hadronic neutral current

Gargamelle, decided end 1965, as Moriond, was built by CEA France and run at CERN. V.Weisskopf and B.Gregory were strong supporters of the project. It was a real odyssey, with much skepticism to fight both on theory and experimental sides. The "alternating currents" of the US competitor, HPWF, did not help. This is an adventure well documented by several chronicles [46,47,48], e.g. of A.Rousset. A.Lagarrigue was the project leader and his premature disparition very likely deprived the NC from a Nobel prize.

Experimentally, the main problem was neutron background. Using the different distribution along the depth of the chamber of neutrons (peaked near the edges) and of neutrinos (flat), J.Fry and D.Haidt, in particular, managed to overcome it.

After the discovery, Gargamelle and subsequent neutrino experiments, measuring the ratio R = NC/CC, got the weak angle, in the Weinberg frame, and, as we said, could predict correctly the boson masses.

With talks by P.Musset 71, 75, A.M. Lutz 73, P.Fayet 74 (where he discussed also Atomic Parity Violation, APV, put forward by A.M. and C.Bouchiat), L.Kluberg 74, V.Brisson 76, Moriond lived the NC saga in real time!

Concerning the weak angle it is worth telling a strange story [49] which happened in 1981 and led to the proton decay fever...Appeared on the market a value of $sin2\theta_W$ about 10% lower than before. Such a value fitted better non-SUSY SU(5) than the SUSY version (Figure 22). GUTs 3: SUSY GUTs 2, said J.Ellis et al. And the former predicted a quite low proton lifetime, of the order of 10^{30} years. Experimentalists were then strongly encouraged to rush to the next cave and look for proton decay. Several did so. The fever calmed down when the weak angle came back to a "normal" value. And in Kamioka mine, the proton decay was not found, but the first neutrinos from a supernova were observed by chance in 1987 and the non-zero mass of neutrinos proved... Ad augusta per angusta.

Another hick up in the determination of the weak angle was the NuTeV anomaly, which however, with a more refined treatment of QCD in particular concerning the strange sea, essentially disappeared [50] (Figure 23).

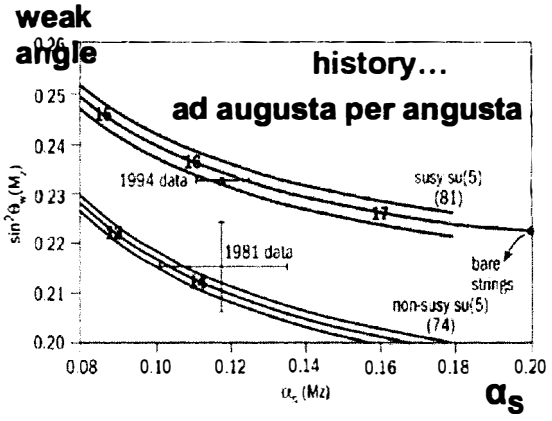

Figure 22 – The 1981 incident

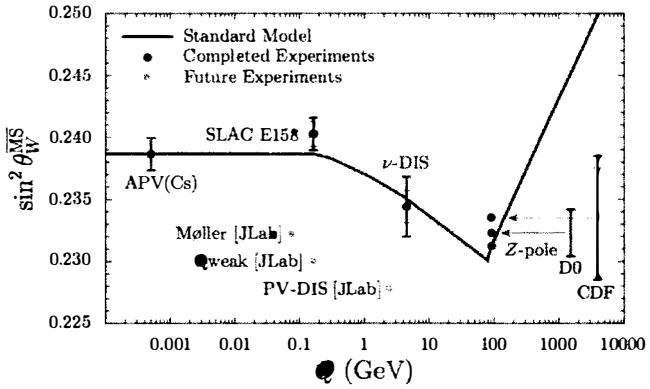

Figure 23 – $sin^2\theta_W$ present situation

ISR Physics

According to M. Jacob [51], ISR physics had "a brilliant start" (71-74), "a somewhat difficult period" (75-77) and "a very active and interesting programme" (78-83).

The highlights included [52]:

- the rising total cross-section (G.Bellettini 76, 86)
- the evidence in 1973 of the production of hadrons at large p_T (Figure 24), showing, as we said, that partons were also point-like relative to the strong interaction
- the discovery in 79 of direct photons, then studied up to the end, an important test of QCD.

The machine was also a great success. Unfortunately J/Psi, charm, beauty, tau, gluon were found elsewhere, while they were potentially in the range accessible to the ISR.

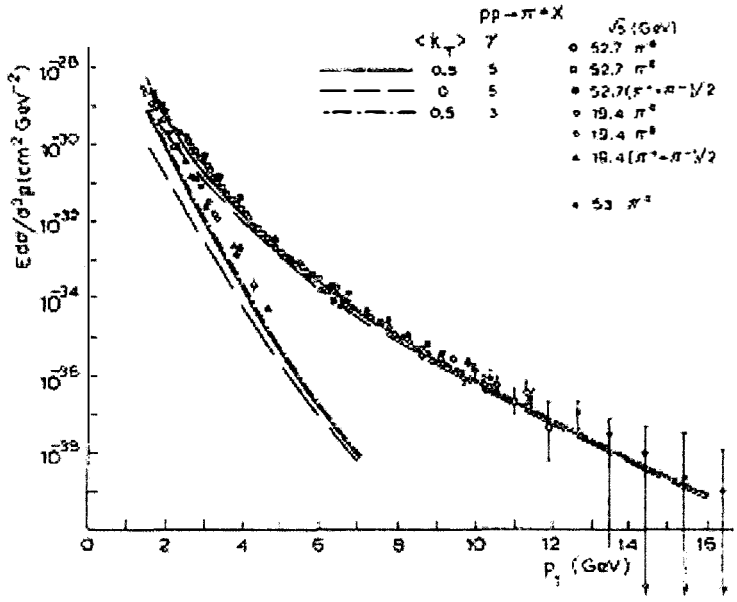

Figure 24 – High p_T hadrons at ISR

This was initially due to inappropriate detectors, focused on the forward region, as the Split Field Magnet, because of a lack of theoretical guidance. When the right ones came, the hadronic rate at large p_T turned out to be a strong background and forced to set high thresholds which prevented the discoveries.

At the End of ISR in 83 M. Jacob said: "I come to bury Caesar not to praise him" (Marc Antony, in Julius Caesar), while V.Weisskopf tried to convince that "it does not matter where discoveries are made". The Pope and the Dalai Lama brought to CERN moral comfort, but the real one came from the success of the proton-antiproton collider.

The proton-antiproton collider

The aim of this machine was clear: to discover W and Z. It did so, and even more.

The most striking was how fast the decisions were taken, only three years between the first paper of C.Rubbia, P.McIntyre and D.Cline (1976) and the approval of the experiments in 79, through the proposal to CERN and Fermilab in 1977, feasibility study and successful tests of stochastic cooling in ICE in 1978. This is largely due to C.Rubbia's determination in a somewhat adverse climate.

The realization was equally fast and led to a great machine and great detectors, offering hermeticity, redundancy, innovating techniques. One can quote in particular the UA1 tracker (Figure 25), in which B.Sadoulet played an important role, and the very good UA2 calorimetry.

As you know, physics was "au rendez vous": hadronic jets, W, Z, etc. In his conclusion of Moriond 83, G. Feldman added the modest jacobian peaks of the two experiments and expressed

Figure 25 – The UA1 tracker

his faith in the discovery of W. C.Rubbia and S.van der Meer got the 1984 Nobel. This history is well documented [53,54] and I will keep brief.

The UA brought important other results: the angular distribution of parton-parton scattering, information on proton structure functions, in particular on the role of gluons at small x, prompt gamma, multijet final states, the p_T distribution of W, beauty mixing, etc.

"L'espoir changea de camp, le combat changea d'âme", said D.Denegri, helped by V.Hugo [55]. Hugo referred to Waterloo, but for true Europeans it does not matter.

SUSY

R.Schwitters, concluding the 82 Moriond quarks, leptons and SUSY "super meeting", where P.Fayet, G.Farrar, J.Ellis had been speaking, said that "even experimentalists cannot fail to be infected by the enthusiasm of the super theorists".

After Russians theorists, the main contributors to SUSY were Wess and Zumino (74 to 76), Fayet (74 to 80), Fayet-Ferrara (75, 76) and, for phenomenology, Farrar-Fayet (78), Witten (78, 82). Haber and Kane produced their "bible" in 84, and G.Kane became a regular visitor of Moriond and an apostle of SUSY.

R.Barbieri, concluding Moriond 93, said: "We were told by G.Kane that there are eight indications that nature is supersymmetric at the EW scale. He agrees that one solid argument would be enough, in fact better that eight vague ones, ...".

Personally, I got a variant of the disease, infected by the SUSY Higgs phenomenology, which, at the difference of the SM, expresses the mass of its lightest boson as a function of the SU(2) and U(1) couplings, $M_h = f(g, g')$. After the computation of radiative corrections (91) and once M_t was known ($172 \pm 6 GeV$ in 96), the prediction for the MSSM SM-like boson was $M_h < 130 GeV$ [56], except by resorting to bizarre twists [57]. It was stated in 1994 that one needed LEP220 to explore fully the domain, and say yes or no about the existence of this boson. Strangely enough, this only crucial prediction of SUSY, fixing a clear objective, was basically left unheard...

At LEP a chargino was excluded below 103 GeV. A limit on the LSP is model dependent. At LHC, there is nothing yet in sight, but no exclusion is valid if $LSP > 500 GeV$. Flavor physics gave no sign of SUSY. Only the $g - 2$ of the muon may offer a hint. Since they are major topics

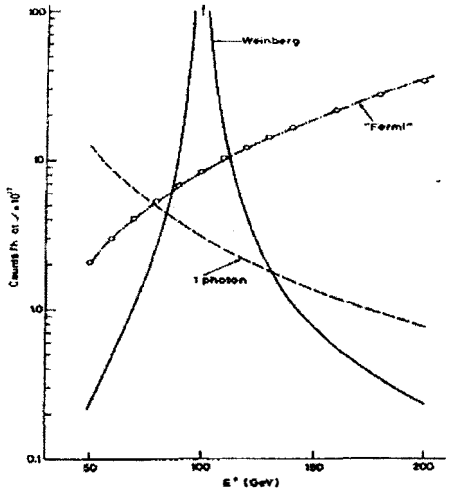

Figure 26 – Anticipating LEP

of the present meeting, I will not deal with "naturalness", "compressed scenarios", variants of the MSSM, as the NMSSM.

Even without any evidence, SUSY will probably never be declared dead. Up to now, with the 125 GeV boson, it passed successfully the only test which could have falsified it. From this mass, a new activity could be to see whether one can predict upper limits on some SUSY partners, e.g. the stop.

A virtue of SUSY was to put a possible name for Dark Matter, the LSP, as a WIMP. This started a vigorous search for WIMPs as relic particles. B.Sadoulet, e.g. in Moriond 91, advocated and pioneered such a quest. In the competition between bolometers and noble liquids, the latter seem to take the lead. Other possibilities for DM were presented in Moriond, in particular the quest for MACHOS through microlensing. The axion as DM was discussed by P.Fayet in 81. I think P.Sikivie[58], presently a major actor of this quest, was in the audience.

LEP era

LEP was a great machine, with 4 good detectors, performing clean and subtle physics, which validated the SM at loop level.

In his seminal paper of 1976 advocating LEP[59], B.Richter prospect, with a Z at 100 GeV, was not far from the truth (Figure 26). At LEP1, 17 millions of Z were collected by ADLO, i.e. the four detectors.

A LC design was not yet ripe[60] and the idea of hosting LHC in the same tunnel was already present. The choice of a circular machine was thus straightforward.

In the LEP Design Report in 1984 the circumference was 26.6 km and the maximum beam energy was 125 GeV, with the prospect of installing RF in the eight straight sections of the machine (a prospect which seems to have been rapidly abandoned).

E.Picasso was LEP project leader. The planning turned out to be quasi perfect. The machine worked beautifully, offering e.g. a luminosity at high E_b 4 times better than foreseen[61,62].

The key of the energy rise was the conception and realization of a park of SC RF cavities (E.Picasso, H.Lengeler, Ph.Bernard, C.Benvenuti). In 99 their accelerating field reached $7.5 MV/m$, a value better than initially foreseen, and LEP2 final useful beam energy was $103 GeV$ (Figure 27).

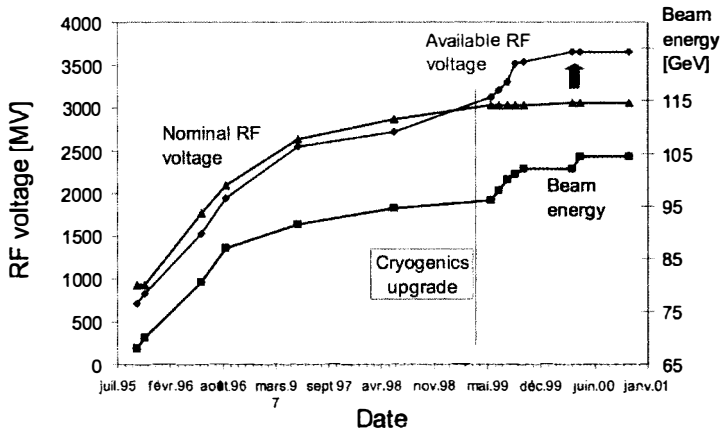

Figure 27 – RF voltage and E_b of LEP

In the field of accurate measurements, LEP did always better, sometimes much better, than expected [63] (tables 3) and took the lead in this domain, with a few exceptions, as the A_{LR} measurement from SLC and the W mass measurement ($\pm 16 MeV$) of Tevatron.

Table 3: Some LEP observables

Quantity	*Expected error*	*Achieved*
m_Z	50 to 20 MeV	**2.1** MeV
m_W	100 MeV	**39** MeV
N_ν	0.3	**0.008**
$A_{FB}^{0,\mu}$	0.0035	**0.0013**
$A_{FB}^{0,b}$	0.0050	**0.0017**
A_τ	0.0110	**0.0043**

LEP got evidence for the role of loops, beyond the running of the coupling α, to up to 13σ from zero. It gave a clear evidence of the IVB self-interaction. It contributed to prove indirectly CP violation in the B sector, before the advent of B factories (Figure 28).

By measuring precisely the couplings of the three forces, it allowed to show their perfect triple convergence at $O(10^{16} GeV)$ in the SUSY scenario.

The only discrepancy with the SM which stayed up to now concerns A_{FB}^b, the forward-backward asymmetry of b quarks (Figure 29). Even if it was still statistically dominated, its QCD corrections are quite involved and one is still at work on these (T.Gehrmann et al).

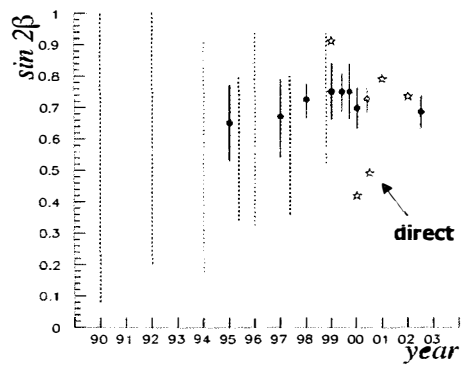

Figure 28 – Indirect and direct measurements of $sin2\beta$

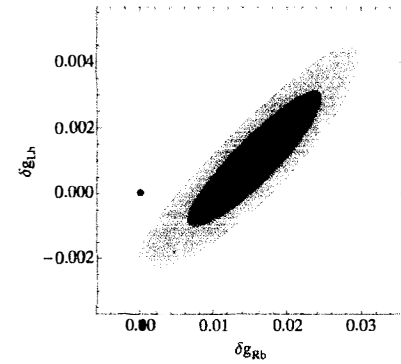

Figure 29 – Couplings needed by LEP A_{FB}^b asymmetry

Similar worries concerning t-tbar asymmetries appeared at Tevatron, but, at present, seem to have faded away.

... and the BEH boson

In 75, J.Ellis, M.K.Gaillard and D.Nanopoulos [64] gave a complete and useful phenomenological profile of the boson, however warning experimentalists that they should "not want to encourage big experimental searches for the Higgs boson".

Concerning LHC, in Lausanne 84, C.Llewelyn Smith [65] said that "discovering a conventional heavy Higgs boson will be difficult even at $20TeV$". Actually, later, the prediction of the top mass went up, favoring the loop production mechanism [66], and, in the 1987 la Thuile meeting [67] (not Moriond), a tenfold increase of the luminosity to $L = 10^{34}$ was suggested and adopted later.

As for LEP, in the Aachen 1986 workshop [68], the Higgs study group concluded that "LEP200 should detect the Higgs if $40 < M_H < 80GeV$, but it will be difficult. It is not at all clear that hadron colliders (of any energy) would be able to detect the Higgs at all".

But B tagging was considered in 1990 and it became clear that, using it, one would be able to "cross" the W and Z barrier. Since the boson is produced at tree level, accompanied by a real Z, the LEP200 mass reach appeared as $2E_b - 100GeV$, a value which, by adding more channels and summing up the four experiments, became rapidly $2E_b - M_Z$.

So it was all a matter of beam energy. K.Hubner [61] says: "the maximum energy of LEP2 was determined by the decision in 1996 to discontinue the industrial production of the superconducting cavities. Whether the potential of LEP should have been better fully exploited up to its reasonable limit of $220GeV$ in CM and whether this would have lead to the discovery of the Higgs boson as a number of models seemed to suggest is a matter of speculation". To be specific, 285 cavities were produced, while 384 could have been installed in the four equipped straight sections of LEP, giving $E_{CM} = 220GeV$.

Before LEP, there was basically no limit on the BEH boson mass. Paschos (89) said that only $2 < M_H < 3.6GeV$ was excluded. LEP1 excluded up to $66GeV$. At LEP200, the mass reach quoted above, $m_h \approx 2E - M_z$, was recognized in 1993 to be attainable, and indeed it was attained at all successive energies of the machine.

In 2000, LEP200 reached $E_{CM} = 206GeV$ as useful energy. But there was no way to increase it more with the available SC RF. Few candidates appeared at $115GeV$ (i.e. at the edge of phase space), mostly in Aleph. Nevertheless LEP was stopped in a great turmoil...For a vivid account of this period, see P.Janot's talks in Moriond 2000 and 2001.

LHC answered in 2012: nothing at $115GeV$, but the boson found at $125GeV$. Since $220 - M_Z = 129GeV$, this gave an answer to the speculation quoted above. SUSY or not, by lack of cavities, LEP200 missed the boson by $10GeV$. See [63] for an history and references.

So the legacy from LEP and Tevatron to the LHC (Figure 30) was clear: the boson should appear above the lower limit of $114.4GeV$, set in 2000 by LEP200, and below the upper limit given by the electroweak fit to all accurate measurements of LEP1 and elsewhere, assuming the validity of the SM. This upper limit was about $200GeV$ in 2000 and went down to $150GeV$ in 2005. In SUSY, the upper limit was $130GeV$, as we said.

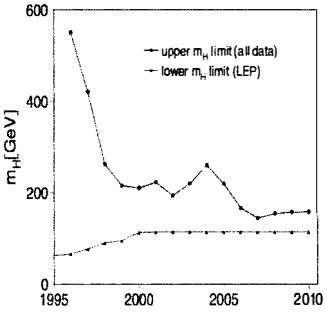

Figure 30 – The LEP legacy for the mass of the BEH boson

It is amusing to plot the innumerable "predictions" of the boson mass made along the years, as in figure 31, drawn from the brave compilation quoted in [69]. Obviously, after 2000 and in the name of SUSY, "predicting" $114 < M_H < 130GeV$ was not very bold...

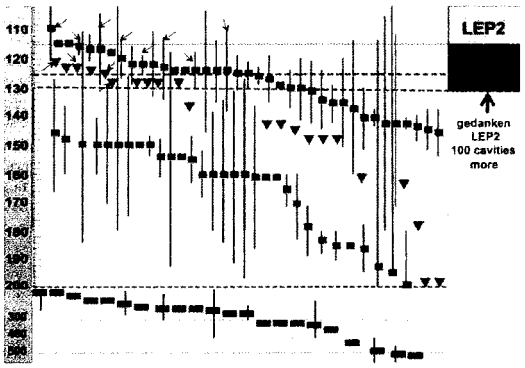

Figure 31 – Predictions of the BEH mass (arrows are for SUSY versions)

As you know, LHC did very well. However at LHC 1 boson to four leptons requires $10^{13}pp$ interactions, while e^+e^- would give one boson (in b-bbar) for a few $10^2 e^+e^-$ annihilations.

The muon $g-2$

"$g-2$ is not an experiment: it is a way of life" said once John Adams (DG of CERN 71-75). Indeed some of the actors of its first version, in 58, were still in the game 40 to 50 years later [70,71,72].

According to Dirac, g should be 2, but loops involving all three forces give a slight deviation from 2. The lowest order correction is $\alpha/2\pi = 0.00116$, giving $g = 2.00232$. But things get rapidly complicated: e.g. there are 12672 five-loops diagrams... A non-zero $g-2$ induces a beat between

the frequency of rotation of the μ and the frequency of precession of its spin, measured by the oscillation of the rate of decay electrons in a given point of the ring.

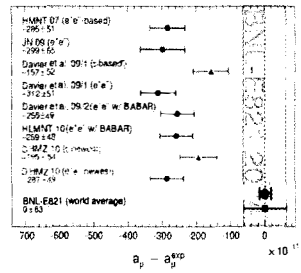

Figure 32 – The $g-2$ discrepancy

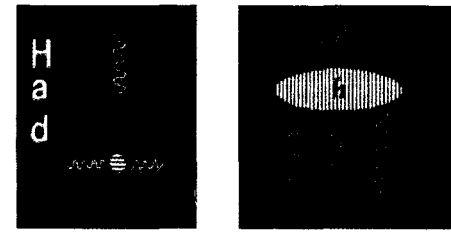

Figure 33 – The problematic diagrams

The program was a superb work, both theoretical and experimental, a "tennis game with well-matched players on either side of the net" (F.Farley).Measurement and prediction agree to 10^{-6} but there subsists a discrepancy of about 3 sigma (Figure 32). Is it new physics? Is it an imperfection in measurement or evaluation? Next experimental information will come after 2017 from Fermilab and J-PARC. On the theory side more work is going on concerning the "photon box" diagram and the hadronic correction (Figure 33) for which new input of low energy e^+e^- hadron production is needed [73].

Conclusions

Let me start with apologies for multiple omissions. It is clear that the high intensity frontier, with searches for rare decays, EDMs, etc, in Brookhaven, PSI, etc, non-accelerator physics, astrophysics were always present in Moriond.

The discovery of the BEH boson, a story that you all know, is a prodigious collective success of our field. There are many key actors to praise, those who played a leading role in the crucial years, and, equally, those by whom all that was made possible, technical coordinators who guided the assembly of the giant detectors, physicists, engineers and technicians whose sharp competences led to the right choices. One can also praise those, like J.Adams, G.Brianti and others, who, long ago, had the vision of the sequence of LEP and LHC in the same tunnel, using the same injectors and infrastructures.

Concerning the future, I have only some personal remarks. I think, hopefully like all of you, that a full exploitation of LHC is mandatory, with a minimum of theoretical biases. It is quite obvious that a discovery would help much for the future. A major one at the energy frontier would give an argument in favor of higher energy p-p collisions, in the same or a new tunnel. If nothing is found, one may be restricted to a study in more detail of what one knows to exist, starting with the BEH boson.

One could dream of a future as described by a slide of Nick Walker in ICHEP 2014, showing all programs which are presently proposed or evoked (Figure 34). A reduced version of it, which is the most often considered, presents the ILC as the next large worldwide project. Such a machine can certainly perform accurate measurements and search for very rare processes. It is unlikely that it may bring the direct discovery of new objects, unless nature has chosen to hide in the blind spots left by LHC, if any. Given the cost and complexity of this machine, it could happen that it is the last one at the high energy frontier.

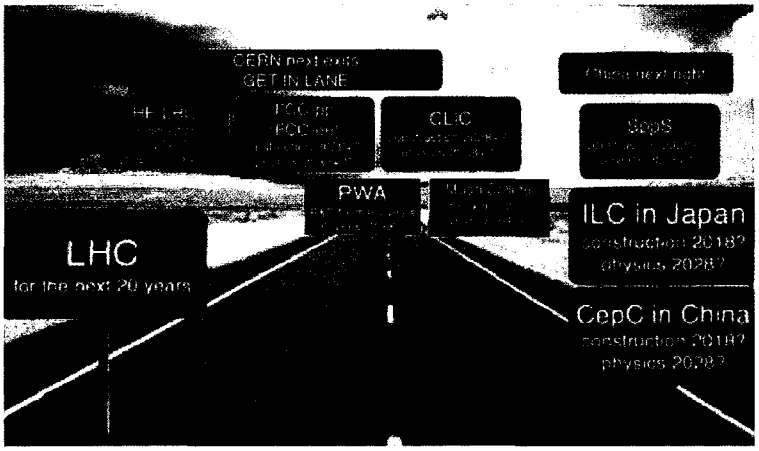

Figure 34 – Future machines under consideration

Still more personal: if and only if no discovery is made at LHC and no large project is launched, maybe the least expensive program would be a LEP3 or super LEP in the existing tunnel. A, Z, W and BEH factory is probably possible. Whether one can reach the top threshold, with a limited luminosity, is an open question. But tunnel, cryogeny, injectors and experiments would be available.

My last words will be to thank and congratulate again Van for having made possible such a beautiful and successful adventure. And I wish him all the best for the future of Moriond and other enterprises.

Acknowledgments

I am very grateful to the organizers for their kind invitation and the stimulating atmosphere of the Rencontres. I thank warmly R.Barate, L.Pape and F.Pauss for their careful reading of the manuscript. My deep gratitude goes also to Vera de Sá-Varanda and Jacques Dumarchez for their invaluable help in preparing the document

References

1. On the Einstein-Podolsky-Rosen paradox. J.S. Bell (Wisconsin U., Madison). Physics **1** 195-200 (1964)
2. Evidence for the 2 pion decay of the K_2^0 meson, Published 27 july 1964, J.H.Christenson, J.W. Cronin, W.L.Fitch and R.Turlay *Phys. Rev. Lett.* **13**, 137 (1964)
3. Broken symmetries, massless particles and gauge fields. Peter W. Higgs (Edinburgh U.). Sep 1964. *Phys. Lett.* B **12**, 132-133 (1964)
4. Broken Symmetries and the Masses of Gauge Bosons. Peter W. Higgs (Edinburgh U.). Oct 1964. *Phys. Rev. Lett.* **13**, 508-509 (1964)
5. Broken Symmetry and the Mass of Gauge Vector Mesons. F. Englert, R. Brout (Brussels U.). 1964. *Phys. Rev. Lett.* **13**, 321-323 (1964)
6. A Measurement of excess antenna temperature at 4080-Mc/s. Arno A. Penzias, Robert Woodrow Wilson (AT-T Bell Labs, Holmdel). Jul 1965. *Astrophys.J.* **142** 419-421 (1965)

7. A Schematic Model of Baryons and Mesons. Murray Gell-Mann (Caltech). *Phys. Lett.* B **8**, 214-215 (1964)
8. G. Zweig (CERN). Jan 17, 1964. CERN-TH-401
9. Concerning the role of A.Petermann, see Who invented quarks? by Álvaro de Rújula, *CERN Courier*, Apr 30, 2014
10. Confirmation of the existence of the Omega- hyperon. V.E. Barnes et al. Sep 1964. *Phys. Lett.* B **12**, 134-136 (1964)
11. From AdA to ACO: Reminiscences of Bruno Touschek. J. Haissinski (Orsay, LAL & Orsay). Dec 1998. In *Frascati 1998, Bruno Touschek and the birth of e^+e^- physics* 17-31
12. Bruno Touschek and the idea of ADA C. Bernardini (Rome U.). 1987. In *Greco, M. (ed.) et al.: Bruno Touschek memorial lectures* 77-79
13. Electron positron storage rings from AdA to LEP. E. Picasso (Pisa, Scuola Normale Superiore). 1998. In *Frascati 1998, Bruno Touschek and the birth of e^+e^- physics* 39-50
14. Experiments with Stochastic Cooling in the ISR. G. Carron, L. Faltin, W. Schnell, L. Thorndahl (CERN). 1977. *IEEE Trans.Nucl.Sci.* **24** 1402-1404 (1977)
15. The legacy of the bubble chamber, *CERN COURIER*, Jun 30, 2003.
16. From bubble chambers to electronic systems: 25 years of evolution in particle detectors at CERN (1979-2004). F. Sauli (CERN). May 2004. *Phys.Rept.***403-404** 471-504 (2004)
17. Development Of Silicon Pixel Detectors: An Introduction. Erik H.M. Heijne, Pierre Jarron (CERN). Oct 1988. *Nucl.Instrum.Meth.* **A275** 467-471(1989)
18. Quarks M. Gell-Mann (CERN). 1981. *Acta Phys.Austriaca Suppl.* **9** 733-761(1972)
19. The story of quarks. Murray Gell-Mann (Santa Fe Inst. & Caltech). 2013. *Int.J.Mod.Phys.* **A28** 1330016 (2013)
20. Present Status of the Fundamental Interactions. Murray Gell-Mann (Princeton, Inst. Advanced Study). 1968. Published in Hadrons and Their Interactions (New York, NY: Academic Press, 1968), pp. 689-701
21. H. Pietschmann, UWThPh-2010-15
22. Hommage à L.Montanet, *CERN COURIER*, Oct 5, 2003
23. Scattering and the Constituent Interchange Model, Richard Blankenbecler (SLAC). Jun 1974. SLAC-PUB-1438
24. G.Altarelli, The Early Days of QCD (as seen from Rome), 1106.3189, Published in *Nuovo Cimento* **C035N1**, 1-8 (2012)
25. The history of QCD, Harald Fritzsch *CERN COURIER*, Sep 27, 2012
26. The rise and fall of the 17-keV neutrino, Douglas R. O. Morrison, *Nature* **366**, 29 - 32 (04 November 1993)
27. The Appearance and Disappearance of the 17-keV Neutrino. Franklin, A. *Rev. of Modern Physics* **67** 457490 (1995)
28. Elementary Particles and SU(4). J.D. Bjorken, S.L. Glashow (Bohr Inst.).*Phys. Lett.* B **11**, 255-257 (1964)
29. The GIM Mechanism: origin, predictions and recent uses. Luciano Maiani (CERN & Rome U.). Mar 25, 2013. Conference: C13-03-02, p.3-16 Proceedings
30. CP Violation in the Renormalizable Theory of Weak Interaction. Makoto Kobayashi, Toshihide Maskawa (Kyoto U.). Feb 1973. *Prog.Theor.Phys.* **49** 652-657 (1973)
31. S.L.Glashow's quotation, in International Conference on Experimental Meson Spectroscopy, 2-27 april 1974, Boston
32. Concerning the anticipation of charmonium, see Search for Charm, Mary K. Gaillard, Benjamin W. Lee (Fermilab), Jonathan L. Rosner (Minnesota U.). Aug 1974. Published in *Rev.Mod.Phys.* 47 277-310 (1975)
33. plot by courtesy of H. Videau
34. For the topless E6 model see U.Sarkar et al, Preprint-83-0355 (Calcutta), 1983
35. For the Z-toponium interference see for instance P.Franzini et al, SLAC-Pub-3541, 1985

36. The neutrino's 50th birthday. D. Haidt (DESY). Feb 2006. Conference: C06-02-07, p.1-21 Proceedings
37. Neutrino summary by M.C. Gonzalez-Garcia et al, 1409.5439
38. On the history of the PMNS Matrix ...with today's perspective, J. Bernabeu, 1312.7451
39. The discovery of CP violation. J.W. Cronin (Chicago U., EFI). 2012. *Eur.Phys.J.* **H36** 487-508 (2012)
40. The superweak theory 35 years later. L. Wolfenstein (Carnegie Mellon U.). Jun 1999. Conference: C99-06-21, p.125-129 Proceedings.
41. CERN, Internal lecture "LEP II era/precision physics" (1994-2004) by L. Fayard, S.Myers and R. Tenchini.
42. CERN COURIER. Oct 27, 2014. CP violation: past, present and future.
43. First direct observation of time-reversal violation. CPLEAR Collaboration (A. Angelopoulos et al.). 2000. *AIP Conf.Proc.* **549** 957-960 (2000)
44. CP violation: From kaons to the universe, J.M. Frère (Paris U., VI-VII). In *Surveys High Energ.Phys.* **9** 203-215 (1996)
45. Unified weak and electromagnetic interactions without neutral currents. Howard Georgi, Sheldon L. Glashow (Harvard U.). 1972. *Phys.Rev.Lett.* **28** 1494 (1972)
46. The weak neutral current - discovery and impact. D. Haidt (DESY), A. Pullia (INFN, Milan & Milan Bicocca U.). 2013. *Riv.Nuovo Cim.* **36** 08, 335-395 (2013)
47. Neutral currents. D. Perkins (Oxford U., Theor. Phys.). 2003. *CERN Cour.* **43N5** S15-19 (2003)
48. The discovery of weak neutral currents. A. Rousset. 1994. *Nucl.Phys.Proc.Suppl.* **36** 339-361(1994)
49. GUTs 3: SUSY GUTs 2. John R. Ellis, Dimitri V. Nanopoulos, Serge Rudaz (CERN). Nov 1981. *Nucl.Phys. B* **202** 43 (1982) CERN-TH-3199
50. Reassessment of the NuTeV determination of the weak mixing angle. W. Bentz et al. Aug 2009. Published in *Phys.Lett. B* **693** 462-466 (2010) , 0908.3198v3
51. History of ISR Physics, M. Jacob (CERN). Jan 1984. CERN-TH-3807
52. The ISR Legacy. Pierre Darriulat (Hanoi U. of Sci.). 2011. *Pontif.Acad.Sci.Scr.Varia* **119** 109-119 (2011)
53. P.Darriulat, The W and Z particles: a personal recollection, CERN COURIER Mar 31, 2004
54. CERN COURIER, Apr 30, 2003, When CERN saw the end of the alphabet.
55. V.HUGO, Les Châtiments, l'Expiation (1853)
56. see for instance Effective potential methods and the Higgs mass spectrum in the MSSM. M. Carena, M. Quiros, C.E.M. Wagner (CERN). Aug 1995. Published in *Nucl.Phys. B* **461** 407-436 (1996)
57. see hep-ph/9707443, figure 11 p 18 and its description p 17.
58. concerning the axion I recall the delicious "The Pool table analogy to axion physics" Pierre Sikivie (Florida U.). Jan 1995. Published in *Phys.Today* **49N12** 22-27 (1996)
59. Very High-Energy Electron-Positron Colliding Beams for the Study of the Weak Interactions. Burton Richter (CERN & SLAC). Apr 1976. *Nucl.Instrum.Meth.* **136** 47 (1976) SLAC-PUB-1738
60. M.Tigner, *Nuovo Cim.* **37** 1228-1231 (1965) and VLEPP, Balakin, Skrinsky, 71, translated from Russian only in 79.
61. Designing and building LEP. K. Hubner (CERN). 2004. *Phys.Rept.* **403-404** 177-188 (2004)
62. A few memories from the days at LEP. Emilio Picasso (CERN). 2012. *Eur.Phys.J.* **H36** 551-562 (2012)
63. LEP/SLC: What did we expect? What did we achieve? A very quick historical review, D. Treille (CERN). 2002. Published in *Nucl.Phys.Proc.Suppl.* **109B** 1-16(2002)
64. A Phenomenological Profile of the Higgs Boson, John R. Ellis (CERN), Mary K. Gaillard

(CERN & Orsay, LPT), Dimitri V. Nanopoulos (CERN). Oct 1975. Published in *Nucl.Phys. B* **106** 292 (1976)

65. CERN-84-10-V-1, ECFA-84-085-V-1. Large Hadron Collider in the LEP tunnel, Lausanne workshop, march 1984.
66. Higgs Bosons from Two Gluon Annihilation in Proton Proton Collisions H.M. Georgi, S.L. Glashow, M.E. Machacek, Dimitri V. Nanopoulos (Harvard U.). Dec 1977. *Phys.Rev.Lett.* **40** 692 (1978)
67. Workshop on physics at future accelerators, La Thuile, Italy, 7-10 Jan 1987: Proceedings. 1. Jun 1987. CERN-87-07-V-1, CERN-YELLOW-87-07-V-1
68. ECFA Workshop: LEP 200, Aachen, FR Germany, Sep 29-Oct 1 1986: Proceedings.1. A. Bohm (ed.), W. Hoogland (ed.) (CERN). Jun 1987. CERN-87-08-V-1, ECFA-87-108, CERN-YELLOW-87-08-V-1
69. Higgs-mass predictions: Thomas Schucker (Provence U. & Sud Toulon Var U.). Aug 2007. arXiv:0708.3344 v1
70. The 47 years of muon g-2. F.J.M. Farley, Y.K. Semertzidis. 2004. *Prog.Part.Nucl.Phys.* **52** 1-83 (2004)
71. The 46 years of muon g-2. F.J.M. Farley (Yale U.). 2004. *Nucl.Phys.Proc.Suppl.* **131** 235-243 (2004)
72. The Muon g-2 experiments. F.J.M. Farley (Yale U.), E. Picasso (CERN). *Adv.Ser.Direct.High Energy Phys.* **7** 479 (1990)
73. Dynamical quark loop light-by-light contribution to muon g-2 within the nonlocal chiral quark model. A.E. Dorokhov (Dubna, JINR), A.E. Radzhabov, A.S. Zhevlakov (RAS, ISDCT). Feb 16, 2015. arXiv:1502.04487

2.
The Scalar Sector

Scalar Boson: CMS Run 1 final results, prospectives for Run 2 (and HL-LHC)

J. Bendavid (CERN)
For the CMS Collaboration

Results are presented for the main standard model Higgs boson channels from the CMS experiment at the LHC. Results in the $\tau\tau$ and $WW \to 2\ell 2\nu$ final states constitute standalone evidences, and results in the $H \to ZZ \to 4\ell$ and $\gamma\gamma$ final states constitute standalone observations. Measured signal strengths are broadly consistent with standard model predictions, as are indirect constraints on the width. Spin/parity tested through angular distributions of decay products strongly favours the Standard Model scalar hypothesis compared to tested alternatives. The Higgs boson mass is measured to be $m_H = 125.02^{+0.26}_{-0.27}(\text{stat.})^{+0.14}_{-0.15}(\text{syst.})$ GeV. Prospects are given for LHC Run 2, as well as projections for HL-LHC.

1 Introduction

One of the main physics goals of the Large Hadron Collider (LHC) is to probe the nature of Electroweak Symmetry breaking. In the standard model (SM), Electroweak symmetry breaking occurs as a result of the Brout-Englert-Higgs mechanism, which predicts an additional scalar field, and an associated scalar boson [1,2] . A Higgs boson was discovered by the ATLAS and CMS experiments in the Summer of 2012, with properties consistent with SM predictions [3,4]. Since then, results in all of the main decay channels have been updated to include the full integrated luminosity available from LHC Run 1, consisting of around 5 fb^{-1} at $\sqrt{s} = 7$ TeV from the 2011 run, and 20 fb^{-1} at $\sqrt{s} = 8$ TeV from the 2012 run. Results presented here include the signal strength (ratio to SM cross section) in the $\tau\tau$, $b\bar{b}$, $WW \to 2\ell 2\nu$,$ZZ \to 4\ell$, and $\gamma\gamma$ decay channels, as well as multilepton final states expected to be enriched in Higgs boson production in association with a $t\bar{t}$ pair, covering a mixture of Higgs decay modes. The mass has also been measured in the $ZZ \to 4\ell$ and $\gamma\gamma$ final states. The spin and parity have been studied through the use of angular distributions in the WW, ZZ, and $\gamma\gamma$ decay modes, and constraints on the width have been derived from off-shell production in the ZZ channel.

2 Run 1 Analyses and Results

2.1 $H \to \tau\tau$

The $H \to \tau\tau$ analysis[5] selects and categorizes events according to leptonic tau decays to electrons and muons, as well as hadronic tau decays. Events are further categorized according to the number of jets, transverse momentum of the tau candidates, or additional leptons in the final state, with sub-channels dominated by gluon fusion, VBF, and W/Z associated production. The signal is extracted from the reconstructed $\tau\tau$ invariant mass distribution across all categories, where the $\tau\tau$ invariant mass is reconstructed using a likelihood estimator taking into account the kinematics of the visible decay products as well as the missing transverse momentum in the event. The dominant irreducible background is $Z/\gamma^* \to \tau\tau$, which is estimated from $Z/\gamma^* \to \mu\mu$ events in data, with the muons replaced with simulated taus. Major reducible backgrounds include W+jets and multijet

events where one or both tau candidates come from a misidentified jet. These are estimated from high transverse mass, and same-sign control regions, respectively.

Although the final results are extracted from a simultaneous likelihood fit to the mass distribution in all of the categories, the $S/(S+B)$-weighted combination of all categories can serve as a visual representation of the result. This distribution is shown in Figure 1 along with a summary of signal strengths grouped in categories enriched in different Higgs boson production mechanisms. The overall signal strength, given as a ratio to the SM expectation is $\sigma/\sigma_{SM} = 0.78 \pm 0.27$. The observed significance of the signal is 3.2σ, with a median expected significance of 3.7σ, corresponding to evidence for the Higgs boson in the $\tau\tau$ channel alone.

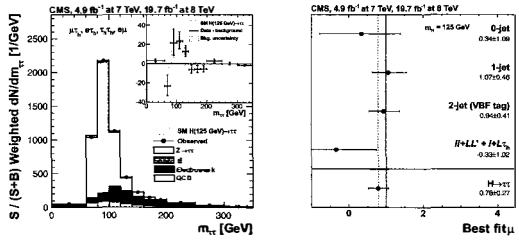

Figure 1 – $S/(S+B)$ weighted sum of $\tau\tau$ invariant mass distribution over all analysis categories (left), with background-subtracted distribution shown in the inset. Fitted signal strengths in groups of categories enhanced in different Higgs boson production mechanisms (right).

2.2 $W/Z + H \to b\bar{b}$

The $H \to b\bar{b}$ channel has a large branching fraction, but overwhelming multijet backgrounds in the inclusive case. The main CMS result for this channel[6] selects events where the Higgs boson is produced in association with a W or Z boson decaying to leptons and/or neutrinos in order to achieve a reasonable signal to background ratio. The analysis requires two b-tagged jets, on which a multivariate energy regression is applied in order to improve the dijet mass resolution. Even after the regression, the dijet mass resolution is only about 10%. The final signal is therefore extracted using an event level multivariate discriminator trained on the kinematics of the b-jets and the recoiling W/Z decay products, as well as the kinematics of additional jets, the b-tag discriminant value (corresponding to b-tag quality) for the two b-tagged jets. Scale factors are derived for Monte Carlo backgrounds using data control regions with inverted b-tagging (for W/Z+light flavour jets), tighter b-tagging plus extra jets (for $t\bar{t}$), and dijet invariant mass sidebands (for irreducible W/Z + heavy flavour jets).

The final BDT discriminant used to extract the signal is shown for the $Z \to \nu\nu + H \to b\bar{b}$ subchannel in Figure 2, along with the $S/(S+B)$ ordered plot for all BDT bins entering the analysis, and a background-subtracted $S/(S+B)$ weighted combination dijet invariant mass distribution from a less sensitive cut-based cross-check analysis. Taken in combination with additional $H \to b\bar{b}$ channels, and taking into account the gluon-induced component of the $Z+H$ production, the fitted signal strength as a ratio to SM prediction is $\sigma/\sigma_{SM} = 0.84 \pm 0.44$, with an observed significance of 2.0σ, where 2.6σ was expected for an SM Higgs boson.

2.3 $H \to WW \to 2\ell 2\nu$

The $H \to WW \to 2\ell 2\nu$ channel has a relatively large branching fraction, but the presence of neutrinos in the final state means that a mass peak cannot be fully reconstructed. The search for the Higgs boson in this channel[7] therefore consists of a search for an excess of events over the SM prediction in the two lepton plus missing transverse momentum final state, with kinematics consistent with the decay of a scalar particle. The analysis is divided into categories for 0, 1, and 2 additional jets, as well as by lepton flavour. In the zero- and one-jet bins for opposite-flavour leptons, the signal is extracted using a two dimensional likelihood fit in dilepton mass and the transverse mass of the dilepton plus missing transverse momentum system. The signal

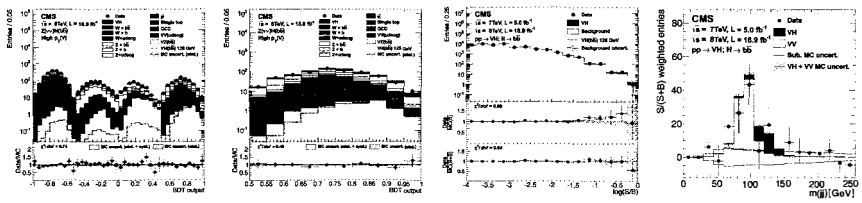

Figure 2 – Distribution of the final BDT discriminant for the $Z \to \nu\nu + H \to b\bar{b}$ sub-channel (far left). The distribution actually arises from a combination of several BDT classifiers used to divide the final distribution into regions enriched in $t\bar{t}$, W/Z+jets, diboson backgrounds, and finally the signal region, which is shown further expanded (center left). This subdivision improves the sensitivity of the analysis by allowing further in-situ constraints on the background scale factors in the final likelihood fit. Distribution of events in all BDT bins entering the final likelihood fit ordered by $S/(S+B)$ (center right). Di-jet invariant mass distribution constructed from an $S/(S+B)$-weighted sum over the categories of a less sensitive cut-based analysis (far right)

in the remaining categories is extracted using a simple counting analysis, including the same-flavour channels where Drell-Yan backgrounds with mismodelled missing transverse momentum are significant, as well as additional categories with extra leptons targeting $W/Z + H$ associated production. The dilepton invariant mass distribution for the selected events are shown for the opposite-flavour zero and one jet categories in Figure 3.

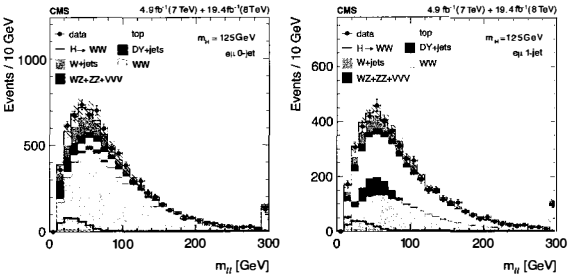

(a) 0-jet (b) 1-jets

Figure 3 – Distribution of dilepton invariant mass for selected events in the opposite flavour 0-jet (left) and 1-jet (right) categories. The dominant background in the 0-jet category is the irreducible continuum SM WW production, whereas the 1-jet category has a significant contribution from $t\bar{t}$, despite the application of b-tagging and soft lepton vetos to reduce this contribution.

Since there is no mass peak, the analysis relies on a careful estimate of the backgrounds using a series of control regions in data. The reducible W+jets background, where one jet is mis-reconstructed as a lepton, is estimated using a lepton + jet control region where the jet passes a loose lepton identification.The $t\bar{t}$ background has been estimated from b-tagged control regions.Background from $W\gamma^*$ where only two leptons are reconstructed have been estimated using a three-lepton control region. Drell-Yan to ee and $\mu\mu$ backgrounds have been estimated using the Z-peak region, which is excluded from the final selection, while the $\tau\tau$ contribution, which also contributes to the opposite-flavour final states, has been estimated using the same embedding technique described in Section 2.1. An additional same-flavour control region is used for further validation of the background estimates.

The two dimensional distributions of dilepton invariant mass and the transverse mass of the dilepton plus missing transverse momentum system are shown for the 0-jet opposite flavour category in Figure 4, and illustrate the discriminating power of the two dimensional likelihood fit, both between a SM Higgs boson and the WW continuum, as well as between an SM Higgs boson and an exotic spin 2 hypothesis. Since the fit is able to constrain the normalization of the WW irreducible background, its normalization is left freely floating and fully determined from the fit.

The combined fitted signal strength corresponds to a ratio to SM prediction $\sigma/\sigma_{SM} = 0.72^{+0.20}_{-0.18}$ with an observed significance of 4.3σ, with 5.8σ expected.

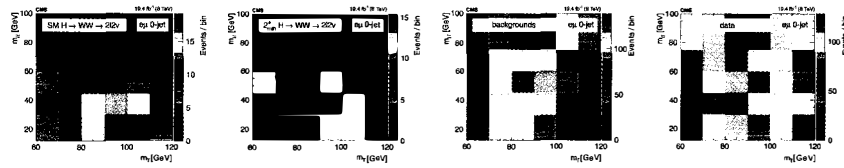

Figure 4 – Two dimensional distributions of dilepton invariant mass and the transverse mass of the dilepton plus missing transverse momentum system in the opposite-flavour 0-jet category for an SM Higgs boson (far left), a spin 2^+ resonance with minimal couplings (center left), the SM backgrounds, dominated in this category by continuum WW production (center right) and the observed distribution in data (far right).

2.4 $H \to ZZ \to 4\ell$

The four lepton final state is characterized by a precise, fully reconstructed mass peak with very small SM backgrounds, consisting mainly of continuum ZZ production. Given the small branching ratio after taking into account the Z boson branching ratio to leptons, it is essential to maintain the largest possible efficiency and acceptance for the leptons. The CMS measurement[8] includes muons down to 5 GeV in p_T and electrons down to 7 GeV, with pseudorapidity coverage out to $|\eta| = 2.4/2.5$. Photons from final state radiation are identified and included in the invariant mass reconstruction as well. The irreducible ZZ continuum background is estimated from simulation, whereas the remaining reducible background, mainly from $Z+b\bar{b}$ is estimated using a combination of Z+same-sign dilepton and Z+jets control regions, with the jets passing a loose lepton selection. The four-lepton invariant mass distribution is shown in Figure 5.

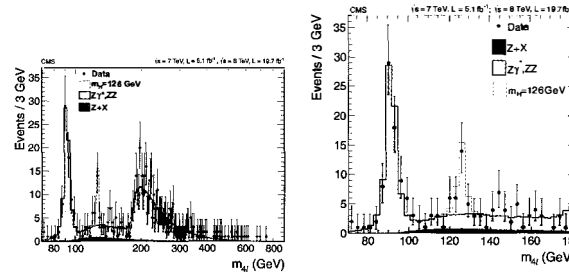

Figure 5 – Four-lepton invariant mass distribution, including the recovered FSR photon where applicable. The full mass range considered in the analysis is shown (left), showing the SM $Z \to 4\ell$ peak, the excess around 125 GeV, and the "shoulder" at high masses corresponding to the kinematic turn-on at twice the Z mass. An expanded view of the low mass region is shown as well (right).

The final results for the cross section are extracted using a three-dimensional unbinned maximum likelihood fit including the four-lepton invariant mass, a matrix element likelihood discriminant exploiting the decay kinematics to further separate the Higgs from the ZZ continuum, and the transverse momentum of the four-lepton system. A dijet category is additionally defined, where the four-lepton transverse momentum is replaced with a kinematic discriminant based on dijet variables to distinguish VBF-like events. The two-dimensional distribution of four-lepton mass vs matrix element discriminant for the 0/1-jet category is shown in Figure 6, along with the four-lepton transverse momentum distribution. The measured signal strength is $\sigma/\sigma_{SM} = 0.93^{+0.26}_{-0.23}(\text{stat.})^{+0.13}_{-0.09}(\text{syst.})$, corresponding to a statistical significance of 6.8σ, with 6.7σ expected. The mass of the Higgs boson is measured using a three-dimensional likelihood of the four-lepton invariant mass, the matrix element kinematic discriminant, and the per-event mass resolution, giving a measured result $m_H = 125.6 \pm 0.4(\text{stat.}) \pm 0.2(\text{syst.})$ GeV.

If the assumption is made that there are no new particles appearing in loops which modify

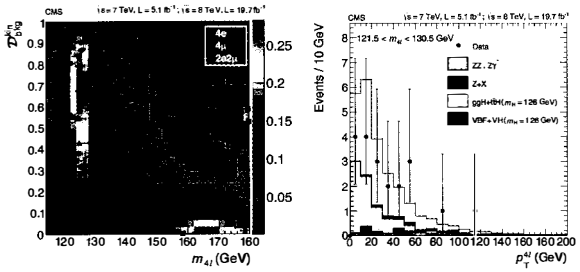

Figure 6 – Two dimensional distribution of four-lepton mass versus matrix element kinematic discriminant in the 0/1-jet category (left), with data points shown overlaid with the expected distribution for an SM Higgs plus backgrounds. Transverse momentum distribution of the four-lepton system (right).

the Higgs boson production, then indirect constraints on the width can be determined with a simultaneous fit to the high mass region, exploiting off-shell production of the Higgs as well as interference with the gluon induced component of the ZZ continuum. Including the combination with the $H \to ZZ \to 2\ell 2\nu$ final state, a limit is set on the Higgs boson width of $\Gamma_H < 22$ MeV (95% C.L.)[9], where the expected SM width is around 4 MeV.

2.5 $H \to \gamma\gamma$

The Higgs boson in the di-photon final state[10] is characterized by a narrow fully reconstructed mass peak on top of a large, smoothly falling background. The selection consists of two isolated, high transverse momentum photons. Multivariate energy corrections are applied to correct for the global and local containment of the electromagnetic shower, as well as residual pileup contamination. These corrections both improve the resolution, and provide a per-event estimate of the per-photon energy resolution with the full granularity of the corrections. Residual energy scale and resolution corrections are derived from $Z \to ee$ events in data, with the same multivariate corrections applied.

Since the CMS electromagnetic calorimeter does not provide any information on the angle of the incident photons, the primary vertex position is needed in order to reconstruct the angle between the two photons and the invariant mass. In a high pileup environment the selection of the primary vertex corresponding to the Higgs boson production is ambiguous. The balancing of the hadronic recoil with the di-photon direction is combined with angular information from reconstructed conversions in the tracker where present to select the correct primary vertex in an expected $\sim 80\%$ of Higgs events.

The main backgrounds are irreducible continuum di-photon production, and reducible photon+jets background, where one jet is mis-reconstructed as a photon. There is a smaller contribution from multijet events where two jets are mis-reconstructed as photons. Since the expected physical width of the Higgs boson is negligible compared to the detector resolution, the effective signal to background ratio scales inversely with the mass resolution, which varies significantly according to the region of the detector where the photons are measured, whether or not the photons converted, and if so, the degree of showering, and the probability that the correct primary vertex was selected. This information is used to construct a per-event mass resolution, which is combined with the kinematics of the photons in a multivariate classifier to distinguish the Higgs from the expected SM backgrounds. This classifier is then used to categorize the events, with the signal extracted from a simultaneous fit to the di-photon invariant mass distribution in all the categories. Further categories are defined with additional leptons, jets, and missing transverse energy in order to select events enriched in VBF, $W/Z + H$, or $t\bar{t} + H$ associated production. The BDT classifier used for event categorization is shown in Figure 7 together with the $S/(S+B)$-weighted sum of di-photon invariant mass distributions across all categories. The overall fitted signal strength corresponds to Overall $\sigma/\sigma_{SM} = 1.14 \pm 0.21(\text{stat.})^{+0.09}_{-0.05}(\text{syst.})^{+0.13}_{-0.09}(\text{th.})$, with a statistical significance of 5.7σ, with 5.2σ expected. The measured mass is $m_H = 124.70 \pm 0.31(\text{stat.}) \pm 0.15(\text{syst.})$ GeV.

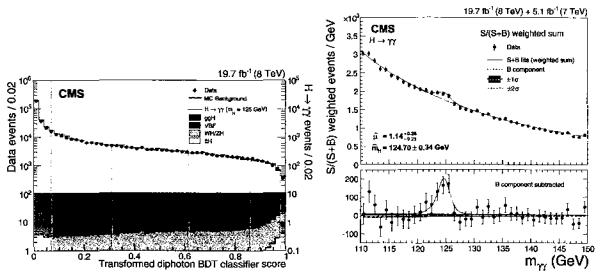

Figure 7 – Distribution of BDT classifier used to categorize untagged events (right), showing all selected data events in the full 100 – 180 GeV di-photon mass range, together with expected distributions for SM Higgs boson and for the combination of SM backgrounds. The output has been transformed such that the distribution for the SM Higgs is uniform. The di-photon invariant mass distribution (right), with the $S/(S+B)$ weighted sum of data distributions and signal+background fit shown, along with the background subtracted distribution.

2.6 Summary and Combination

The signal strengths measured in the various channels are shown in Figure 8, broken down both by decay mode, and by tagged production mode. Results are in good agreement with the SM, with a small excess at the 2σ level compared to SM expectations in the $t\bar{t}+H$ subchannels, driven by the $t\bar{t}+H$ multilepton search[11]. If the results are fit in terms of a combined overall signal strength, the result is $\sigma/\sigma_{SM} = 1.00 \pm 0.14$[12]. The combined mass measurement from $H \to ZZ \to 4\ell$ and $H \to \gamma\gamma$ is $m_H = 125.02^{+0.26}_{-0.27}(\text{stat.})^{+0.14}_{-0.15}(\text{syst.})$ GeV. Using the angular distributions in $H \to ZZ \to 4\ell$, $H \to WW \to 2\ell 2\nu$ and $H \to \gamma\gamma$, the data also strongly favours the SM scalar hypothesis compared to the pseudoscalar hypothesis, as well as a wide range of alternate spin 1 and spin 2 hypotheses.

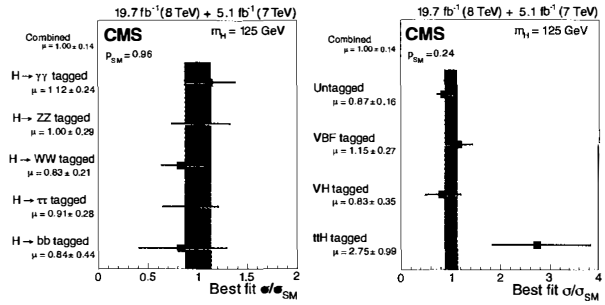

Figure 8 – Measured signal strengths in all channels, broken down by Higgs decay (left) and the main production mechanism in each subchannel (right).

3 Prospects for Run 2 and HL-LHC

After the long shutdown in 2013-2014, the LHC is restarting in spring 2015, marking the beginning of Run 2, at an expected increased center of mass energy of 13 TeV. With an increase in Higgs production cross section of between a factor 2 and 4 depending on the production mode, and up to 3-4 times more integrated luminosity expected compared to Run 1, significant improvements in precision are expected. The legacy Run 1 analyses represent the transition from searches to the first measurements, though the focus has still been on model-dependent cross section ratios compared to the SM expectation in the inclusive phase space. Run 2 is expected to mark a transition to less model-dependent fiducial and differential cross sections, with the latter enabled also by the larger data sample. Challenges include maintaining reconstruction and physics object performance in light of the more difficult pileup conditions associated with the transition from 50ns to 25ns bunch spacing in the LHC, increasing the impact of "out of time" pileup. Ongoing advances in theoretical calculations are also being incorporated into the simulations.

Looking beyond Run 2 to the planned HL-LHC run, simple projections have been made scaling

signal and background yields from preliminary Run 1 analyses to $\sqrt{s} = 14$ TeV and integrated luminosities of 300 and 3000 fb^{-1} [13]. These projections are approximate, neglecting for example analysis improvements, and improvements from detector upgrades on the one hand, and degradation from higher pileup, detector aging on the other. Projected uncertainties on the measured signal strengths in the various Higgs decay channels are shown in Figure 9.

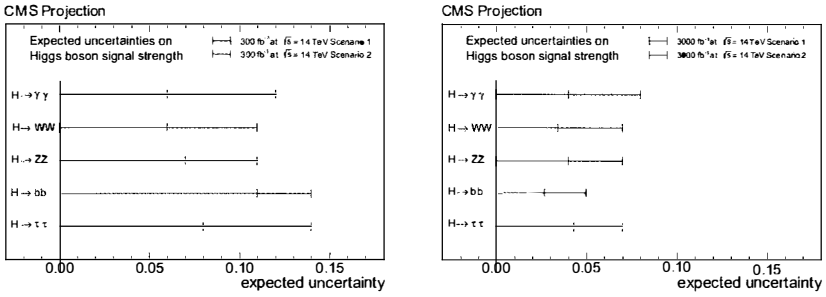

(a) 300 fb^{-1} (b) 3000 fb^{-1}

Figure 9 – Projected uncertainties on the measured signal strengths in the various Higgs decay channels at $\sqrt{s} =$ 14 TeV for 300 fb^{-1} (left) and 3000 fb^{-1} (right). Scenario 1 in green corresponds to a pessimistic projection of the systematic uncertainties in which all systematic uncertainties are left unchanged from Run 1. Scenario 2 in red corresponds to an optimistic projection of the systematic uncertainties in which theoretical uncertainties are reduced by a factor of 2, and all other systematic uncertainties are scaled down with the square root of the integrated luminosity.

References

1. F. Englert and R. Brout. Broken Symmetry and the Mass of Gauge Vector Mesons. *Phys.Rev.Lett.*, 13:321–323, 1964.
2. Peter W. Higgs. Spontaneous Symmetry Breakdown without Massless Bosons. *Phys.Rev.*, 145:1156–1163, 1966.
3. Georges Aad et al. Observation of a new particle in the search for the Standard Model Higgs boson with the ATLAS detector at the LHC. *Phys.Lett.*, B716:1–29, 2012.
4. CMS Collaboration. Observation of a new boson at a mass of 125 GeV with the CMS experiment at the LHC. *Phys.Lett.*, B716:30–61, 2012.
5. CMS Collaboration. Evidence for the 125 GeV Higgs boson decaying to a pair of τ leptons. *JHEP*, 05:104, 2014.
6. CMS Collaboration. Search for the standard model Higgs boson produced in association with a W or a Z boson and decaying to bottom quarks. *Phys.Rev.*, D89(1):012003, 2014.
7. CMS Collaboration. Measurement of Higgs boson production and properties in the WW decay channel with leptonic final states. *JHEP*, 01:096, 2014.
8. CMS Collaboration. Measurement of the properties of a Higgs boson in the four-lepton final state. *Phys.Rev.*, D89(9):092007, 2014.
9. CMS Collaboration. Constraints on the Higgs boson width from off-shell production and decay to Z-boson pairs. *Phys.Lett.*, B736:64, 2014.
10. CMS Collaboration. Observation of the diphoton decay of the Higgs boson and measurement of its properties. *Eur.Phys.J.*, C74(10):3076, 2014.
11. CMS Collaboration. Search for the associated production of the Higgs boson with a top-quark pair. *JHEP*, 09:087, 2014.
12. CMS Collaboration. Precise determination of the mass of the Higgs boson and tests of compatibility of its couplings with the standard model predictions using proton collisions at 7 and 8 TeV. 2014.
13. CMS Collaboration. Projected Performance of an Upgraded CMS Detector at the LHC and HL-LHC: Contribution to the Snowmass Process. 2013.

STUDIES OF THE HIGGS BOSON AND DIRECT SEARCHES FOR NEW PHENOMENA AT THE TEVATRON

COSTAS VELLIDIS
Fermi National Accelerator Laboratory, Kirk Road and Pine Street, Batavia IL 60510, USA

Four years after the cease of operations of the Tevatron $p\bar{p}$ collider at Fermilab, the CDF and D0 experiments keep analyzing the acquired data samples, exploiting the complementarity to the LHC experiments due to different initial state and of lower backgrounds from pile-up and gluon-initiated processes. These advantages of the Tevatron data samples, in certain cases, lead to competitive exclusion limits on new phenomena in the low mass range. Recent results from the Tevatron experiments on Higgs boson studies and searches in the electroweak sector using the full data samples are reported.

1 Tests of the spin and parity state of the Higgs boson

The Higgs boson discovered by the ATLAS [1] and CMS [2] Collaborations in 2012 using data produced in proton-proton collisions at the Large Hadron Collider (LHC) at CERN allows many stringent tests of the electroweak symmetry breaking in the standard model (SM) and extensions to the SM to be performed. To date, measurements of the Higgs boson mass and width, its couplings to other particles, and its spin and parity quantum numbers J and P are consistent with the expectations for the SM Higgs boson [3]. The CDF and D0 Collaborations at the Fermilab Tevatron observed a 3.0 standard deviation (s.d.) excess of events consistent with a Higgs boson signal, largely driven by those channels sensitive to the decay of the Higgs boson to bottom quarks ($H \to b\bar{b}$) [4]. The Tevatron data are also consistent with the predictions for the properties of the SM Higgs boson [4]. The ATLAS and CMS Collaborations recently reported strong evidence for Higgs boson decays to fermions [5], with sensitivity dominated by the $H \to \tau^+\tau^-$ decay mode, though they have not yet performed spin and parity tests using fermionic decays. The particle decaying fermionically for which the Tevatron also found evidence might not be the same as the particle discovered through its bosonic decays at the LHC. Tests of the spin and parity with Tevatron data therefore provide unique information on the identity and properties of the new particle or particles.

It has been proposed [6] to use the Tevatron data to test models for the Higgs boson with exotic spin and parity, using events in which the exotic Higgs boson X is produced in association

with a W or a Z boson and decays to a bottom-antibottom quark pair, $X \to b\bar{b}$. This proposal used two of the spin and parity models, one with a pseudoscalar $J^P = 0^-$ state and the other with a graviton-like $J^P = 2^+$ state. The differential production rates near threshold alter the kinematic distributions of the observable decay products of the vector boson and the exotic boson X relative to those of the vector boson and the Higgs boson H, most notably the invariant mass or the transverse mass of the VX system ($V = W$ or Z). These models predict neither the production rates nor the decay branching fractions of the X particles. The CDF and D0 Collaborations have re-optimized their SM Higgs boson searches to test the exotic Higgs boson models in the $WH \to \ell\nu b\bar{b}$ [7], $ZH \to \ell^+\ell^- b\bar{b}$ [8], and $ZH + WH \to \not{E}_T b\bar{b}$ [9] channels, where $\ell = e$ or μ and $\not{E}_T$ is the missing transverse energy, using multivariate (MVA) discriminants to maximize the sensitivity to the kinematic properties of the exotic VX decays. They recently reported a combination [10] of the CDF [11] and D0 [12] studies of the J^P assignments of the state X, with mass $m_X = 125$ GeV/c^2, in the $X \to b\bar{b}$ decay mode.

The exotic signals are normalized to the SM cross section times branching ratio multiplied by an exotic-signal scaling factor, μ_{exotic}. The scaling factor for the SM Higgs boson signal is denoted by μ_{SM}. Two-dimensional credibility regions, which are the smallest regions containing 68% and 95% of the posterior probabilities, are shown in Fig. 1. The points in the (μ_{SM}, μ_{exotic}) planes that maximize the posterior probability densities are shown as the best-fit values. Upper limits at 95% credibility on the rate of the production of an exotic Higgs boson in the absence of a SM $J^P = 0^+$ signal are set at 0.36 times the SM Higgs production rate for both the $J^P = 0^-$ and the $J^P = 2^+$ hypotheses. If the production rate of the hypothetical exotic particle times its branching ratio to a bottom-antibottom quark pair is the same as that predicted for the SM Higgs boson, then the exotic models are excluded with significances of 5.0 s.d. and 4.9 s.d. for the $J^P = 0^-$ and $J^P = 2^+$ hypotheses, respectively.

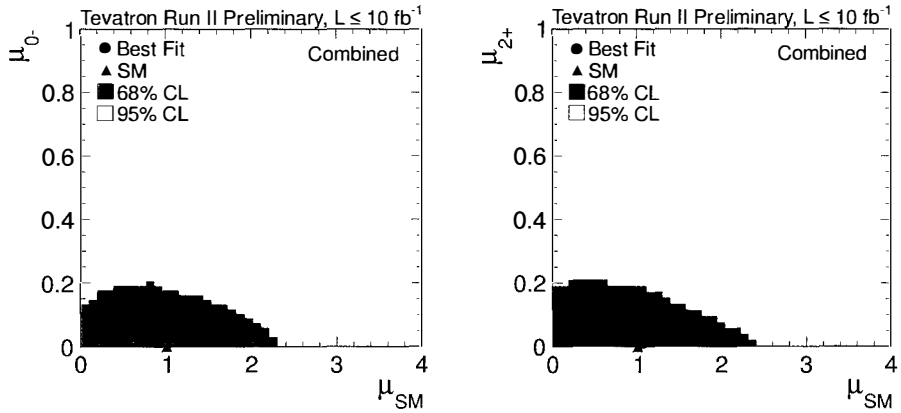

Figure 1 – Two-dimensional credibility regions in the (μ_{SM}, μ_{exotic}) plane, for the combined CDF and D0 searches for the pseudoscalar ($J^P = 0^-$) boson (left) and the graviton-like ($J^P = 2^+$) boson (right).

2 Search for fermiophobic Higgs boson

The LHC experiments discovered a scalar boson in 2012 [1,2,3]. It was recently reported that the new particle actually couples to fermions [5], which is also expected for the SM Higgs boson. The whole picture of the electroweak gauge symmetry breaking (EWSB) is, however, yet to be investigated. Even if the new particle is confirmed to be the SM Higgs boson, it does not mean that, for example, there are no other Higgs bosons. It is thus still necessary to continue testing

various scenarios as long as they are not explicitly excluded. A minimal multiple-Higgs-boson model is the "two Higgs doublet model" (2HDM). The resulting particle spectrum consists of two charged Higgs bosons H^+, H^- and three neutral members h^0, H^0 and A^0. The "fermiophobic" Higgs boson, which signifies very suppressed or zero couplings to the fermions, may arise in a particular version of the 2HDM called type I [13]. In this model, one Higgs doublet of the gauge group couples to all the fermion types, while the other doublet does not. Both couple to the gauge bosons via the kinetic term in the Lagrangian. One vacuum expectation value (VEV) gives masses to all the fermion types f, while the gauge bosons receive their masses from both VEV. Due to the mixing in the neutral Higgs sector, both eigenstates h^0 and H^0 can couple to the fermions. The fermionic coupling of the lightest CP-even Higgs boson h^0 is proportional to $\cos\alpha/\sin\beta$, where α is the mixing angle in the neutral Higgs sector h^0 and H^0 and β is defined by the VEV ratio, $\tan\beta = v_2/v_1$. In the limit $\cos\alpha \to 0$, the $h^0 f\bar{f}$ coupling would vanish, giving rise to fermiophobia, where h^0 is called a fermiophobic Higgs boson (h_f). The main decay mode of h_f in the mass range $m_{h_f} < 100$ GeV/c^2 is into a pair of photons through a W-boson loop.

Experiments at the LEP, Tevatron, and LHC colliders [15] have searched for fermiophobic Higgs bosons in modes such as $e^+e^- \to Z^* \to h_f(\to \gamma\gamma)Z$ and $q\bar{q}' \to V^* \to h_f(\to \gamma\gamma$ or $WW^*)V$ or $q\bar{q}' \to q\bar{q}' \to h_f(\to \gamma\gamma$ or $WW^*)$, with the dominant contribution coming from $V = W^\pm$. The mass range excluded by those searches is $m_{h_f} > 110$ GeV/c^2. All these searches assume that the bosonic h_f couplings are of the same strength as the bosonic couplings of the SM Higgs boson, which in general is not the case for h_f in a realistic model such as the 2HDM (type I). Other production mechanisms are available that allow searching for a light h_f even in the region where the process $q\bar{q}' \to h_f V$ is suppressed and thus h_f could have eluded the previous searches.

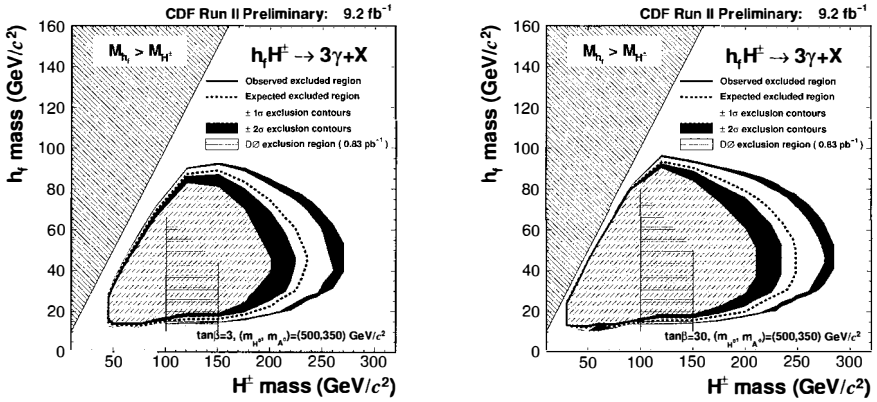

Figure 2 – The expected and observed 95% C.L. excluded mass region of the fermiophobic Higgs boson model for low (left) and high (right) $\tan\beta$.

The CDF Collaboration searched for a fermiophobic Higgs boson [15] in the process $p\bar{p} \to h_f H^\pm \to h_f(h_f W) \to (2\gamma)(2\gamma) + X$ enabled through a timelike W-boson exchange $q\bar{q}' \to W^* \to h_f H^\pm$. The events were selected by requiring 3 central ($|\eta| < 1.1$), calorimeter and track cone-isolated photons, each one with $E_T > 15$ GeV. If more than 3 photons were found in the event, they were sorted in decreasing E_T and the first 3 were used in the analysis. Events with the sum of E_T of the two leading photons greater than 90 GeV were used as the signal region for the search, whereas events with $E_T^{\gamma_1} + E_T^{\gamma_2} \leq 90$ GeV were used as a background control region. The observed number of events is 5, which is consistent with the expected number of 3 ± 1 background events from direct triphoton production, jets faking photons, and radiative leptonic decays of vector bosons. The excluded mass regions are shown in Fig. 2 in comparison with

regions previously excluded by the D0 Collaboration [16]. For $m_{H^\pm} = 90$ GeV/c^2, h_f is excluded in the mass range $15 < m_{h_f} < 75$ GeV/c^2, whereas for $m_{h_f} = 45$ GeV/c^2, $H^\pm$ is excluded in the mass range $50 < m_{H^\pm} < 230$ GeV/c^2.

3 Search for exotic W boson

Several modifications of the SM include massive, short-lived states decaying to pairs of SM leptons or quarks. A resonance decaying to a top and a bottom quark tb can appear in models featuring one or more massive charged vector bosons, generically denoted as W', such as $SU(2)_R$ SM extensions [17], Kaluza-Klein extra-dimensions [18], technicolor [19] or Little Higgs scenarios [20]. Searches for W' bosons in the $W' \to tb$ decay channel are complementary to searches in the leptonic decay channel $W' \to \ell\nu$, and can probe cases where the couplings of the W' to fermions are free parameters. In the recent past, searches in the $W' \to tb$ channel have been performed by the Tevatron [21] and the LHC [22] experiments. For resonance searches at the highest masses, the LHC experiments have superior sensitivity to the Tevatron due to the higher center-of-mass energy. However, in the lower mass region the Tevatron experiments have competitive sensitivity due to the more favorable signal-to-background ratio in searches for particles produced in quark-initiated states, such as the W', with respect to the SM background processes which are mainly gluon-initiated.

A new search for W'-like resonances decaying into tb was performed by the CDF Collaboration [23] in events where $t \to Wb$ and the W decays leptonically. A next-to-leading-order (NLO) left-right symmetric SM extension [24], predicting the existence of W' bosons of unknown mass and universal weak coupling strength to SM fermions, was used as a benchmark model. Since no specific assumptions on the signal model were made throughout the analysis, this search is sensitive to any narrow resonant state decaying to tb. The events were selected with a $\not\!\!E_T$ trigger and optimized into channels containing and not containing a charged lepton (e or μ). The analysis tools were the same as those used for the measurement of the s-channel single-top production cross section [25], based on MVA discriminants. The exclusion limits are shown in Fig. 3 as a function of $M_{W'}$. W' bosons are excluded up to a mass of 860 (880) GeV/c^2 assuming allowed (forbidden) leptonic decays. This search provides the most constraining limits to date for $M_{W'} < 700$ GeV/c^2.

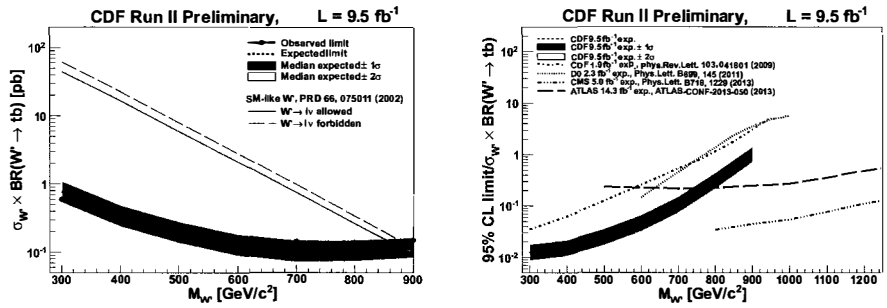

Figure 3 – Left: Observed and expected exclusion limits on $\sigma(p\bar{p} \to W') \times \mathcal{B}(\mathcal{W}' \to \sqcup\lfloor)$. Right: Expected 95% C.L. limits of the W' boson normalized to the theoretical cross section times branching ratio in the case where the leptonic decay mode $W' \to \ell\nu$ is forbidden.

4 Search for Dirac magnetic monopole

The existence of magnetic monopoles would add symmetry to the Maxwell equations without breaking any known physical law. More dramatically, it would make charge quantization a

consequence of angular momentum quantization, as first shown by Dirac [26]. Grand unified theories predict monopole masses of about 10^{17} TeV, so there have been extensive searches for high-mass monopoles produced by cosmic rays [27]. Indirect searches for low-mass monopoles have looked for the effects of virtual monopole/anti-monopole loops added to QED Feynman diagrams[28]. Detector materials exposed to radiation from $p\bar{p}$ collisions at the Tevatron have been examined for trapped monopoles [29]. More recently, the ATLAS experiment excluded monopole production in pp collisions for masses less than 862 GeV/c^2 for spin-1/2 monopoles with Drell-Yan production and provided a model-independent limit for production within their fiducial for monopoles masses between 200 and 1500 GeV/c^2 [30]. MOEDAL, a dedicated monopole search experiment, will start taking data when the LHC resumes operation in 2015 [31].

The CDF experiment searched for Dirac monopoles with mass less than 800 GeV/c^2 [32]. A "Dirac" monopole is a particle bearing no electric charge, having no hadronic interactions, and whose magnetic charge g satisfies the Dirac quantization condition $g/e = n/(2\alpha) \approx 68.5n$, $n = 1, 2, \ldots$. Dirac magnetic monopoles are highly ionizing due to the large value of g. In the CDF detector, they are accelerated in the direction of the solenoidal magnetic field, causing relativistically stretched parabolic trajectories. This is in sharp contrast to ordinary charged particles, which are circular in the plane perpendicular to the magnetic field. Advantage is taken of the large ionization both in the trigger and the offline analysis. A dedicated highly ionizing particle trigger, which requires large light pulses in the time-of-flight (TOF) detector was previously built and used at CDF [33]. The trigger was recalibrated and operated from January until September 2011, with an integrated luminosity corresponding to approximately 1.2 fb^{-1}. A specialized reconstruction isolated monopole candidates by checking for abnormally high ionization within a path that has no curvature in the central outer tracker (COT) in the plane perpendicular to the magnetic field. A benchmark Drell-Yan-like ($q\bar{q} \to e^+e^-$) production model was used for simulations. The exclusion limits are shown in Fig. 4. Monopoles are excluded up to a mass of 476 GeV/c^2 at 95% C.L. The CDF limit is more constraining than the corresponding ATLAS limit for masses below 300 GeV/c^2.

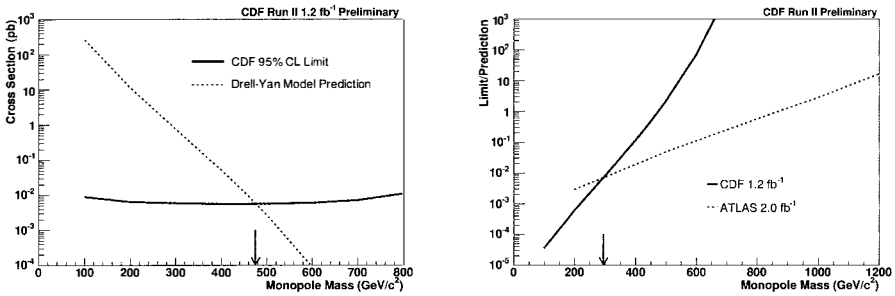

Figure 4 – Observed limits of the magnetic monopole as a function of its mass, on the cross section (left) and on the observation relative to the model prediction (right).

References

1. G. Aad *et al.* (ATLAS Collaboration), *Phys. Lett.* B **716**, 1 (2012).
2. S. Chatrchyan *et al.* (CMS Collaboration), *Phys. Lett.* B **716**, 30 (2012).
3. G. Aad *et al.* (ATLAS Collaboration), *Phys. Rev.* D **90**, 052004 (2014). S. Chatrchyan *et al.* (CMS Collaboration), *Phys. Lett.* B **736**, 64 (2014). G. Aad *et al.* (ATLAS Collaboration), *Phys. Rev.* D **91**, 012006 (2015). S. Chatrchyan *et al.* (CMS Collaboration), *Phys. Rev.* D **89**, 092007 (2015). S. Chatrchyan *et al.* (CMS Collaboration), Eur. Phys.

J. C **74** (2014) 3076. G. Aad *et al.* (ATLAS Collaboration), *Phys. Lett.* B **726**, 120 (2013). S. Chatrchyan *et al.* (CMS Collaboration), J. High Energy Phys. 01 (2014) 096.
4. T. Aaltonen *et al.* (CDF and D0 Collaborations), *Phys. Rev. Lett.* **109**, 071804 (2012). T. Aaltonen *et al.* (CDF and D0 Collaborations), *Phys. Rev.* D **88**, 052014 (2013).
5. S. Chatrchyan *et al.* (CMS Collaboration), *Phys. Rev.* D **89**, 012003 (2014). G. Aad *et al.* (ATLAS Collaboration), J. High Energy Phys. 01 (2015) 069.
6. J. Ellis *et al.*, J. High Energy Phys. 11 (2012) 134.
7. T. Aaltonen *et al.* (CDF Collaboration), *Phys. Rev. Lett.* **109**, 111804 (2012). V. M. Abazov *et al.* (D0 Collaboration), *Phys. Rev.* D **88**, 052008 (2013).
8. T. Aaltonen *et al.* (CDF Collaboration), *Phys. Rev. Lett.* **109**, 111803 (2012). V. M. Abazov *et al.* (D0 Collaboration), *Phys. Rev.* D **88**, 052010 (2013).
9. T. Aaltonen *et al.* (CDF Collaboration), *Phys. Rev.* D **87**, 052008 (2013). V. M. Abazov *et al.* (D0 Collaboration), *Phys. Lett.* B **716**, 285 (2012).
10. T. Aaltonen *et al.* (CDF and D0 Collaborations), *Phys. Rev. Lett.* **114**, 151802 (2015).
11. T. Aaltonen *et al.* (CDF Collaboration), *Phys. Rev. Lett.* **114**, 141802 (2015).
12. V. M. Abazov *et al.* (D0 Collaboration), *Phys. Rev. Lett.* **113**, 161802 (2014).
13. H. E. Haber, G. L. Kane, and T. Sterling, Nucl. Phys. **B161**, 493 (1979).
14. V. Lemaitre for the ALEPH, DELPHI, L3, and OPAL collaborations, "Search for fermiophobic Higgs at LEP", Fundamental Interactions: Proceedings of the 20^{th} Lake Louise Winter Institue, Canada, p199203. The Tevatron New-Phenomena and Higgs Working Group for the CDF and D0 Collaborations, arXiv:1302.1764. G. Aad *et al.* (ATLAS Collaboration), Eur. Phys. J. C **72** (2012) 2157. S. Chatrchyan *et al.* (CMS Collaboration), *Phys. Lett.* B **725**, 36 (2012).
15. CDF conference note 11116.
16. D0 conference note 5067.
17. J. C. Pati and A. Salam, *Phys. Rev.* D **10**, 275 (1974).
18. Y. Mimura and S. Nandi, *Phys. Lett.* B **538**, 406 (2002). G. Burdman, B. A. Dobrecu, and E. Pontoon, *Phys. Rev.* D **74**, 075008 (2006).
19. H. Georgi, E. E. Jenkins, and E. H. Simmons, Nucl. Phys. **B331**, 541 (1990). E. Malkawi, T. M. Tait, and C. Yuan, *Phys. Lett.* B **385**, 304 (1996).
20. M. Perelstein, Prog. Part. Nucl. Phys. **58**, 247 (2007).
21. T. Aaltonen *et al.* (CDF Collaboration), *Phys. Rev. Lett.* **103**, 041801 (2009). V. M. Abazov *et al.* (D0 Collaboration), *Phys. Lett.* B **699**, 145 (2011).
22. G. Aad *et al.* (ATLAS Collaboration), *Phys. Rev. Lett.* **109**, 261803 (2012). S. Chatrchyan *et al.* (CMS Collaboration), *Phys. Lett.* B **718**, 1229 (2013).
23. CDF conference note 11110, submitted to *Phys. Rev. Lett.*
24. Z. Sullivan, *Phys. Rev.* D **66**, 075011 (2002).
25. T. Aaltonen *et al.* (CDF Collaboration), *Phys. Rev. Lett.* **112**, 231805 (2014).
26. P. A. M. Dirac, *Quantized Singularities in the Electromagnetic Field*, Proc. R. Soc. (London), A133 (1931).
27. I. De Mitri, hep2001/213. S. Cecchini *et al.*, Nuovo Cim. 24C:639-644 (2001). S. D. Wick *et al.*, astro-ph/0001233 (2000).
28. I. F. Ginzburg and A. Schiller, *Phys. Rev.* D **57**, 6599 (1998). M. Acciari *et al.*, *Phys. Lett.* B **345**, 609 (1995). L. Gamberg, G. R. Kalbfleisch, and K. A. Milton, hep-ph/9906526.
29. G. R. Kalbfleisch *et al.*, hep-ex/0306045.
30. G. Aad *et al.* (ATLAS Collaboration), *Phys. Rev. Lett.* **109**, 261803 (2012).
31. http://moedal.web.cern.ch.
32. CDF conference note 11102.
33. M. Mullhearn, Ph.D. Thesis, MIT (2003).

CMS High mass WW and ZZ Higgs search with the complete LHC Run1 statistics

M. Pelliccioni
for the CMS collaboration
Istituto Nazionale di Fisica Nucleare, Via P. Giuria 1, 10125 Torino, Italy

A search for the decay of a heavy Higgs boson in the H->ZZ and H->WW channels is reported, analyzing several final states of the H->ZZ and H->WW decays. The search used proton-proton collision data corresponding to an integrated luminosity of up to 5.1 fb^{-1} at $\sqrt{s} = 7$ TeV and up to 19.7 fb^{-1} at $\sqrt{s} = 8$ TeV recorded with the CMS experiment at the CERN LHC. A Higgs boson with Standard Model-like coupling and decays in the mass range of 145 $< m_H <$ 1000 GeV is excluded at 95% confidence level, based on the limit on the product of cross section and branching fraction. An interpretation of the results in the context of an electroweak singlet extension of the standard model is reported.

1 Introduction

In the Standard Model (SM) of electroweak (EW) interactions the existence of the Higgs boson, a scalar particle associated with the field responsible for spontaneous EW symmetry breaking[1,2] is predicted. The ATLAS and CMS experiments reported in 2012 the observation of a new boson with a mass of about 125 GeV[3,4]. We refer to this newly observed Higgs boson as h(125) in this proceedings. While this boson shows SM-like properties, it is possible that it is merely part of a larger EW symmetry breaking sector. This can be accommodated in several extensions of the SM. In particular, we consider the scenario in which the SM Higgs boson mixes with a heavy EW singlet[6]. This scenario is also useful to construct a general modelization of the Higgs sector that allows to interpret the data for several possible Higgs sector configurations.

Both ATLAS and CMS reported several searches for heavy SM-like Higgs bosons. In Ref.[4], ATLAS excludes a SM-like heavy Higgs boson in the mass range of 131 $< m_H <$ 559 GeV at 95% CL. The CMS collaboration excluded an additional SM-like Higgs boson to to masses of 710 GeV at 95% CL[7]. None of the searches by ATLAS and CMS was performed using the full Run-1 LHC statistics collected by the collaborations.

We report on an extension of the CMS search using the full Run-1 dataset. In addition to the previous CMS analysis, we interpreted the data in the scenario of the SM expanded by an additional EW singlet. Both the possible SM-like heavy Higgs boson and the EW singlet are indicated as H. The analysis is performed using the proton-proton collision data recorded by CMS[5], corresponding to integrated luminosities of up to 5.1 fb^{-1} at $\sqrt{s} = 7$ TeV and up to 19.7 fb^{-1} at $\sqrt{s} = 8$ TeV. The search is conducted in the 145 $< m_H <$ 1000 GeV mass range, exploiting both the H -> ZZ and the H -> WW decay channels, which are the most sensitive to high mass Higgs boson decays. The lower boundary of the search is chosen to limit the contamination of h(125). In the H -> ZZ decays, we consider the final states containing four charged leptons (H->ZZ->2l2l'), two leptons and two neutrinos (H->ZZ->2l2ν) and two leptons and two quarks (H->ZZ->2l2q), where l = e, μ and l' = e, μ, and τ. In the H -> WW decays, we consider the fully leptonic (H->WW->lνlν) and semileptonic (H->WW->lνqq) decays.

2 Simulation and Signal Modelization

In order to simulate the signal and the background, we use several Monte Carlo event generators. For the Higgs boson signal, we generate samples for gluon-gluon fusion (ggF) and vector boson fusion (VBF) at next-to-leading order (NLO) using POWHEG 1.0 [8,9] and a dedicated program for angular correlations [10]. Associated production of the Higgs boson with a vector boson (WH and ZH) and ttH are generated using PYTHIA 6.4 at leading order (LO) [11]. Events are weighted at generator level according to the total cross section of pp-→H [12], which includes the ggF next-to-next-to-leading order (NNLO) and next-to-next-to-leading-log (NNLL) contributions, and the VBF NNLO contributions. The diboson invariant mass lineshape for signal is affected by the quantum interference between signal and the SM background. We correct the generated m_H lineshape to obtain the theoretical predictions [13,14,15].

The background from qq-→ WW production is generated with MADGRAPH 5.1 [16]. The background from qq-→ZZ production is simulated with POWHEG at NNLO. The gluon gluon induced vector boson pair background (gg-→VV) is simulated at LO using GG2VV 3.1 [17]. The other background processes considered (WZ, Zγ, Wγ, W+jets and Z+jets) are generated using PYTHIA and MADGRAPH. Backgrounds from tt and tW events are generated with POWHEG at NLO.

PYTHIA is used for parton showering, hadronization and underlying event simulation for all the samples. The detector response is simulated using a detailed description of the CMS apparatus, based on the GEANT4 package [18]. Simulated samples include the presence of multiple proton-proton interactions per bunch crossing (pileup).

We test the presence of both a heavy SM-like Higgs boson and of an EW singlet scalar mixed with h(125). In the EW singlet scenario, the couplings of both states are constrained by unitarity and the coupling of h(125) is therefore lower than in the SM case. Unitarity is enforced by the relation $C^2 + C'^2 = 1$, where C and C' are the scale factors of the couplings of h(125) and the high mass Higgs boson, respectively, with respect to the SM. The production cross section modifier (also known as signal strength) and the width of the high mass Higgs boson are defined as

$$\mu' = C'^2(1 - \mathcal{B}_{new}), \tag{1}$$

$$\Gamma' = \Gamma_{SM}\frac{C'^2}{1 - \mathcal{B}_{new}}, \tag{2}$$

where $\mathcal{B}_{new}$ is the branching fraction of the EW singlet to non-SM decays. The signal strength measured for h(125) [19] can be used to put a 95% CL limit on $C' < 0.28$.

We focus on the case where $C'^2 \leq (1 - \mathcal{B}_{new})$, where the new boson will have a width equal or narrower with respect to the SM Higgs boson. We generate signal samples for different values of the width and scan the C' and $\mathcal{B}_{new}$ parameter space. In order to account for the proper signal and interference lineshape we follow the recommendations of the *LHC Higgs Cross Section Working Group* [12] (HXSWG). The interference between the high mass Higgs boson and the background is assumed to scale with the modified coupling of the Higgs boson. The interference between h(125) and the EW singlet partner is assumed to be small and is covered by a conservative systematic error [20,21].

3 Analyzed channels

The results reported are obtained through the combination of different production and decay modes, as reported in Table 1. All searches are restricted to the invariant mass region above 145 GeV, and for all the final states there are no events overlapping. For the H → WW -→ lνlν decay, the EW singlet model interpretation starts at 200 GeV to avoid contamination from

Table 1: Analyses included in this combination. The column "H production" indicates the production mechanism considered in the analysis. Untagged categories are mostly populated by ggF events. Events with a dijet pair consistent with a VBF topology are referred to as $(jj)_{VBF}$. The category with dijet pairs and single merged jets from a Lorentz-boosted W (Z) are referred to as $(jj)_{W(Z)}$ and $(J)_{W(Z)}$ respectively. Three possible b-tag categories are identified with "0,1,2 b tags".

H decay mode	H production	Exclusive final states	No. of channels	m_H range [GeV]	m_H resolution
$WW \to l\nu l\nu$	untagged	((ee,$\mu\mu$),eμ) + (0 or 1 jets)	4	145–1000	20%
	VBF tag	((ee, $\mu\mu$),eμ) + $(jj)_{VBF}$	2	145–1000	20%
$WW \to l\nu qq$	untagged	(eν, $\mu\nu$) + $(jj)_W$	2	180–600	5–15%
	untagged	(eν, $\mu\nu$) + $(J)_W$ + (0+1-jets)	2	600–1000	5–15%
	VBF tag	(eν, $\mu\nu$) + $(J)_W$ + $(jj)_{VBF}$	1	600–1000	5–15%
$ZZ \to 2l2l'$	untagged	4e, 4μ, 2e2μ	3	145–1000	1–2%
	VBF tag	(4e, 4μ, 2e2μ) + $(jj)_{VBF}$	3	145–1000	1–2%
	untagged	(ee,$\mu\mu$) + ($\tau_h\tau_h$, $\tau_e\tau_h$, $\tau_\mu\tau_h$, $\tau_e\tau_\mu$)	8	200–1000	10–15%
$ZZ \to 2l2\nu$	untagged	(ee,$\mu\mu$) + (0 or $\geq$ 1 jets)	4	200–1000	7%
	VBF tag	(ee,$\mu\mu$) + $(jj)_{VBF}$	2	200–1000	7%
$ZZ \to 2l2q$	untagged	(ee,$\mu\mu$) + $(jj)_Z^{0,1,2\,b\text{ tags}}$	6	230–1000	3%
	untagged	(ee,$\mu\mu$) + $(J)_Z^{0,1,2\,b\text{ tags}}$	6	230–1000	3%
	VBF tag	(ee,$\mu\mu$) + $(jj)_Z^{0,1,2\,b\text{ tags}}$ + $(jj)_{VBF}$	6	230–1000	3%
	VBF tag	(ee,$\mu\mu$) + $(J)_Z^{0,1,2\,b\text{ tags}}$ + $(jj)_{VBF}$	6	230–1000	3%

h(125). The H --> WW --> lνlν, H --> WW --> lνqq (with merged jets) and H --> ZZ --> 2l2q decay channels are analyzed in the $\sqrt{s}$ = 8 TeV sample only. A detailed description of the analysis strategy for all the final states is provided in Khachatryan *et al.* [22].

4 Systematic uncertainties

The main sources of systematic uncertainties arise from the assumptions in the signal model, the objects reconstruction used in the analysis, and several common experimental sources. Theoretical uncertainties on the cross section for the heavy Higgs boson production derive from the uncertainties in the choice of the Parton Distribution Functions and α_s, along with the renormalization and factorization scales. These are typically of the order of 6-7% and 712%, respectively, for ggF production, and 12% and 25%, respectively, for VBF. We also add an uncertainty on the background arising from the off-shell h(125) production, estimated using GG2VV (PHANTOM) for the ggF (VBF) case. This uncertainty is of the order of 3% of the total background for large m_H values. The uncertainties on the lineshape of signal and interference are different depending on the production mode. For ggF, we follow the recommendation of the HXSWG [12]. Since there is no prescription for VF, we assign as systematic uncertainty the renormalization and factorization scale variations in PHANTOM.

A systematic uncertainty common to all decay channels is the luminosity measurement, which is 2.2% (2.6%) for the 7 (8) TeV data. Other uncertainties that are correlated among channels are the muon and electron reconstruction efficiencies, and the jet energy scale and resolution. Lepton fake rate is accounted for in all channels, but it is mostly relevant for the H --> ZZ --> 2l2l' final state, where we consider leptons at lower transverse momentum with respect to the other channels.

5 Interpretation of the results

The statistical combination of the several final states in this analysis was developed within the *LHC Higgs Combination Group* by ATLAS and CMS [23]. To determine the limits on the model

parameters as a function of m_H, a modified frequentist method (best known as CL_s) is used[24]. The uncertainties described in the previous section are introduced as nuisance parameters.

5.1 *Search for a SM-like heavy Higgs boson*

In Figure 1 the combined results for the search of a heavy SM-like Higgs boson are shown. On the left, we show the observed 95% CL limit for each final state entering in the analysis, along with the combination in black. The expected combined limit is shown as a dashed black line, along with the $\pm 2\sigma$ yellow band representing the expected interval of the limit. The plot on the right shows the channel by channel comparison of the expected and observed limit, using the same color legend. The top right plot refers to the WW final states, while the bottom right plot refers to the ZZ final states. While the H -> ZZ -> 4l final state shows good sensitivity across the whole invariant mass spectrum, the H -> WW -> $l\nu l\nu$ channel is more sensitive at lower mass, while in the highest mass region H -> ZZ -> $2l2\nu$ is the most sensitive.

The structures present in the observed limit can be attributed to similar features in the limits of individual channels. The small excess in the combined limit around 280 GeV is present in the H -> ZZ -> 4l and H -> WW -> $l\nu l\nu$ final states. The combined limit on the cross section times the branching ratio excludes at 95% CL the presence of a SM-like Higgs boson across the full range of $145 < m_H < 1000$ GeV.

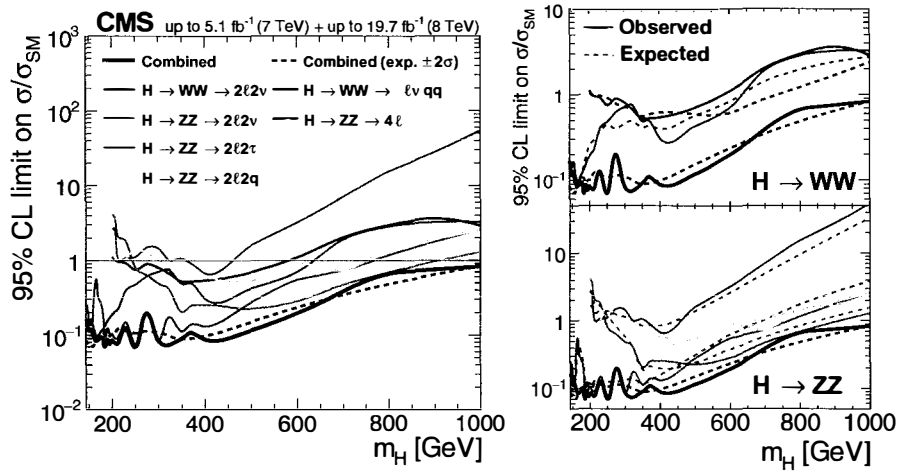

Figure 1 – 95% CL upper limits on a SM-like Higgs boson for all the final states considered and their combination. Observed and expected limits for the individual channels are shown in the right, for WW channels on top and ZZ channels on the bottom.

5.2 *Electroweak Singlet Interpretation*

In the EW singlet model, there are two parameters of interest: C', the coupling scale factor, and $\mathcal{B}_{new}$, the modifier to the total width that parametrizes additional non-SM decays for the heavy Higgs boson. In Figure 2 the observed and expected upper limit on C' as a function of the heavy Higgs mass are shown, for several $\mathcal{B}_{new}$ values. In the same plot, the indirect limit on C' obtained from the measurement of C for h(125) is shown. The upper blue dashed line represents where, for $\mathcal{B}_{new} = 0.5$, the variable width of the heavy Higgs boson reaches the width of a SM-like Higgs boson.

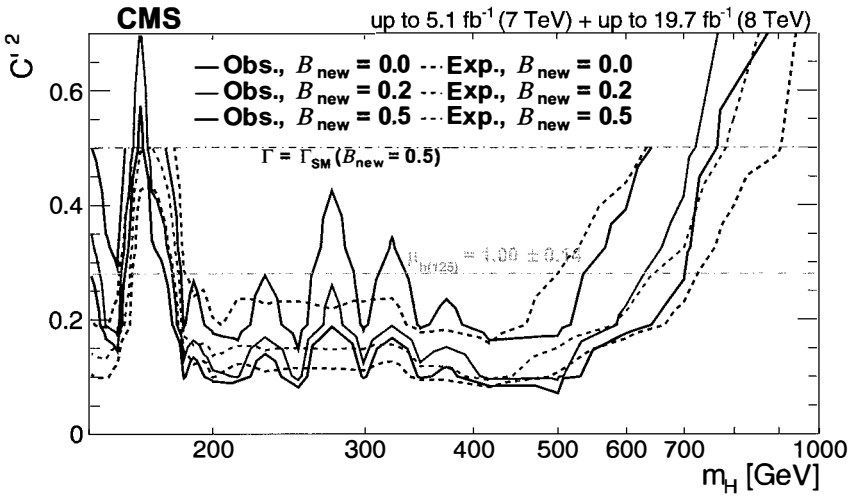

Figure 2 – 95% CL upper limits on C' in the EW singlet scenario, as a function of the heavy Higgs boson mass, for several $\mathcal{B}_{new}$ values. The upper blue dashed line represents where, for $\mathcal{B}_{new} = 0.5$, the variable width of the heavy Higgs boson reaches the width of a SM-like Higgs boson. The lower grey dash-dotted line shows the indirect lower limit on C' obtained from the h(125) signal strength measurement.

6 Conclusions

We present the combination of H → ZZ and H → WW decay searches for a heavy Higgs boson in the $145 < m_H < 1000$ GeV invariant mass range. We interpret our observed data both in a SM-like heavy Higgs scenario, and in the case of a EW singlet in addition to the 125 GeV Higgs boson. We do not observe a significant excess with respect to the expected SM background in either interpretation. In the context of a SM-like heavy Higgs boson, we are able to exclude this hypothesis in the whole mass range considered. For the EW singlet scenario, we are able to set limits on the C' parameter of the theory as a function of the heavy state mass.

References

1. F. Englert and R. Brout, Broken Symmetry and the Mass of Gauge Vector Mesons, *Phys. Rev. Lett.* 13 (1964) 321, doi:10.1103/PhysRevLett.13.321.
2. P. W. Higgs, Broken symmetries, massless particles and gauge fields, *Phys. Lett.* 12 (1964) 132, doi:10.1016/0031-9163(64)91136-9.
3. CMS Collaboration, Observation of a new boson at a mass of 125 GeV with the CMS experiment at the LHC, *Phys. Lett.* B 716 (2012) 30, doi:10.1016/j.physletb.2012.08.021, arXiv:1207.7235.
4. ATLAS Collaboration, Observation of a new particle in the search for the Standard Model Higgs boson with the ATLAS detector at the LHC, *Phys. Lett.* B 716 (2012) 1, doi:10.1016/j.physletb.2012.08.020, arXiv:1207.7214
5. S. Chatrchyan *et al.* [CMS Collaboration], "The CMS experiment at the CERN LHC", JINST **3**, S08004 (2008).
6. V. Barger et al., CERN LHC phenomenology of an extended standard model with a real scalar singlet, *Phys. Rev.* D 77 (2008) 035005, doi:10.1103/PhysRevD.77.035005,

arXiv:0706.4311.
7. CMS Collaboration, Search for a standard-model-like Higgs boson with a mass in the range 145 to 1000 GeV at the LHC, *Eur. Phys. J. C* 73 (2013) 27, doi:10.1140/epjc/s10052-013-2469-8, arXiv:1304.0213.
8. E. Bagnaschi, G. Degrassi, P. Slavich, and A. Vicini, Higgs production via gluon fusion in the POWHEG approach in the SM and in the MSSM, *JHEP* 02 (2012) 088, doi:10.1007/JHEP02(2012)088, arXiv:1111.2854.
9. P. Nason and C. Oleari, NLO Higgs boson production via vector-boson fusion matched with shower in POWHEG, *JHEP* 02 (2010) 037, doi:10.1007/JHEP02(2010)037, arXiv:0911.5299.
10. Y. Gao et al., Spin determination of single-produced resonances at hadron colliders, *Phys. Rev.* D 81 (2010) 075022, doi:10.1103/PhysRevD.81.075022, arXiv:1001.3396.
11. T. Sjostrand, S. Mrenna, and P. Z. Skands, PYTHIA 6.4 physics and manual, *JHEP* 05 (2006) 026, doi:10.1088/1126-6708/2006/05/026, arXiv:hep-ph/0603175.
12. S. Heinemeyer et al., Handbook of LHC Higgs cross sections: 3. Higgs properties, CERN Report CERN-2013-004, 2013. doi:10.5170/CERN-2013-004, arXiv:1307.1347.
13. G. Passarino, C. Sturm, and S. Uccirati, Higgs pseudo-observables, second Riemann sheet and all that, *Nucl. Phys.* B 834 (2010) 77, doi:10.1016/j.nuclphysb.2010.03.013, arXiv:1001.3360.
14. S. Goria, G. Passarino, and D. Rosco, The Higgs-boson lineshape, *Nucl. Phys.* B 864 (2012) 530, doi:10.1016/j.nuclphysb.2012.07.006, arXiv:1112.5517.
15. N. Kauer and G. Passarino, Inadequacy of zero-width approximation for a light Higgs boson signal, *JHEP* 08 (2012) 116, doi:10.1007/JHEP08(2012)116, arXiv:1206.4803.
16. J. Alwall et al., MadGraph/MadEvent v4: the new web generation, *JHEP* 09 (2007) 028, doi:10.1088/1126-6708/2007/09/028, arXiv:0706.2334.
17. T. Binoth, M. Ciccolini, N. Kauer, and M. Kramer, Gluon-induced W-boson pair production at the LHC, *JHEP* 12 (2006) 046, doi:10.1088/1126-6708/2006/12/046, arXiv:hep-ph/0611170.
18. GEANT4 Collaboration, Geant4a simulation toolkit, *Nucl. Instrum. Methods* A 506 (2003) 250, doi:10.1016/S0168-9002(03)01368-8.
19. CMS Collaboration, Precise determination of the mass of the Higgs boson and tests of compatibility of its couplings with the standard model predictions using proton collisions at 7 and 8 TeV, (2015). arXiv:1412.8662. Submitted to *Eur. Phys. J. C.*
20. C. Englert, Y. Soreq, and M. Spannowsky, Off-Shell Higgs Coupling Measurements in BSM scenarios, (2014). arXiv:1410.5440.
21. E. Maina, Interference effects in Heavy Higgs production via gluon fusion in the Singlet Extension of the Standard Model, (2015). arXiv:1501.02139.
22. V. Khachatryan *et al.* [CMS Collaboration], "Search for a Higgs boson in the mass range from 145 to 1000 GeV decaying to a pair of W or Z bosons", arXiv:1504.00936 [hep-ex]. Submitted to *Journal of High Energy Physics*
23. ATLAS and CMS Collaborations, LHC Higgs Combination Group, Procedure for the LHC Higgs boson search combination in Summer 2011, Technical Report ATL-PHYS-PUB 2011-11, CMS NOTE 2011/005, 2011.
24. A. L. Read, Modified frequentist analysis of search results (the CLs method), CERN Report CERN-OPEN-2000-005, 2000.

Beyond the Standard Model Higgs searches at the LHC

P. Meridiani on behalf of the ATLAS and CMS collaborations
Istituto Nazionale di Fisica Nucleare, Roma, P.le Aldo Moro 2, 00185 Roma, Italy

The Run I at the LHC marks the birth of the "Higgs physics", a path which will be followed at its full extent in the future runs of the LHC. Indeed there are two complementary paths to be followed to new physics in the Higgs sector: precision measurements of the Higgs properties (couplings, mass, spin and parity), where new physics can manifest as deviation from the Standard Model, or direct search for processes not foreseen in the Standard Model (Higgs decays not foreseen in the Standard Model, additional scalars which would indicate an extended Higgs sector). The current status of these studies at the LHC is presented, focussing in particular on the direct searches for rare or invisible Higgs decays or for an extended Higgs sector. The results are based on the analysis of the proton-proton collisions at 7 and 8 TeV center-of-mass energy at the LHC by the ATLAS and CMS collaborations.

1 Introduction

The discovery of a Higgs boson by the ATLAS and CMS collaborations with a mass around 125 GeV[1, 2] represents a historical milestone in the understanding of the electro-weak (EW) symmetry breaking mechanism. The hierarchy problem, concerning the naturalness of the Higgs boson mass, the nature of dark matter, and other open questions that the Standard Model (SM) is not able to answer, motivate the possible existence of additional new particles or interactions which could be revealed in the data accumulated by the ATLAS and CMS collaboration during the Run I at the LHC.

LHC data allows to study with increasing precision the Higgs boson couplings to fermions and bosons, and to look for rare or forbidden decays of the discovered Higgs boson. Discrepancy will unveil physics beyond the Standard Model (BSM) and can potentially give new directions to look for new particles. Several BSM theories have been proposed in the last 20-30 years, which are still to be ruled out by the current experimental constraints. Focussing on the Higgs sector, it is still possible that the discovered Higgs boson could be part of an extended Higgs sector, with additional charged or neutral (CP-even or odd) Higgs bosons, or that the Higgs boson is not an elementary particle, representing instead a pseudo-Goldstone boson of a new strong interaction at energies beyond the TeV scale (little or composite Higgs). In these BSM scenarios, the couplings of the Higgs boson are expected to show discrepancies with respect to the SM ones; however the current precision on the measurement of the Higgs scalar couplings[3] (20-30%) still leave ample space for new physics. It is possible to interpret the experimental measurements of the Higgs couplings and its CP properties in the context of BSM scenarios, understanding which is the parameter phase space being excluded by the current experimental precision. Several studies have been performed, either using specific BSM models (MSSM, MCHM, ...) or more generally using an effective lagrangian approach. An example is given in [4], where limits are set within the parameter space of several BSM theories: composite Higgs, Two Higgs Doublet Models (2HDM), additional EW singlet, a simplified Minimal Super-Symmetric Standard Model

(MSSM); another example is given in this recent paper [5], which contain also several references to previous works. More important, with more statistics, such as it will be achieved during Run 2 at the LHC and beyond, the precision of these measurements will improve, moving the Higgs physics into the "precision" era. It will be possible not only to look for scalar deviations of the couplings, but also for kinematic discrepancies as allowed by measuring differential cross-sections for thc different Higgs production modes.

This way to look for new physics in the Higgs sector can be complemented by a direct approach which searches directly new processes not foreseen in the SM. Focussing on the Higgs sector, additional neutral or charged Higgs bosons, at lower or higher masses then the discovered Higgs boson, still represent a viable opportunity; they are foreseen by several extensions of the SM. As we will see, there is also a large window of opportunity to to search for decays of the Higgs boson which are not expected in the SM, which would also represent a direct sign of new physics.

In the rest, we will focus on the current status of the direct searches for BSM physics in the Higgs sector.

2 Rare Higgs decays searches

The observed value of the Higgs mass, 125 GeV, allows to explore several final states for the Higgs boson decays, already with the statistics provided by the LHC Run I data. Intriguingly, as reported in [6] the product of branching ratios of the SM Higgs boson in all decay channels available below the top-antitop threshold is maximum at m_H 125 GeV. As discussed before, no significant discrepancy with the SM expected rates in the different Higgs decay channels explored so far has been reported. In addition, using all the Higgs measured rates in different sub-channels, it is possible to place a limit on undetected or invisible Higgs decays[7, 8], constraining effectively the Higgs total width. This indirect constraint is BR(H-->invisible/undetected)<≈30% at 95% CL, still allowing ample space to look for BSM Higgs decays.

Searches have been performed for decays with very small expected branching ratios in the SM, $H \to \mu^+\mu^-$, $H \to Z(\dashrightarrow l^+l^-)\gamma$, but the current sensitivity is not able to probe yet the SM expected rate of events. Only cross-section limits have been placed [9, 10, 11, 12]. In these channels, you will need the full statistics of next runs at the LHC to start reaching the SM sensitivity.

An excess of events (2.4σ) is reported in the search performed by the CMS collaboration of the lepton flavour violating decay $H \to \mu\tau$ [13]. This search probes directly non-diagonal term of the Yukawa matrix, $|Y_{\mu\tau}|^2 + |Y_{\mu\tau}|^2$, with a sensitivity about 1 order of magnitude higher then looking at exotic τ decays ($\tau \dashrightarrow 3\mu, \tau \dashrightarrow \mu\gamma$). An upper limit $BR(H \to \mu\tau) < 1.57\%$ at 95% CL is placed. The corresponding analysis from ATLAS is not yet public.

Recently the first search for $H \dashrightarrow J/\Psi\gamma$ (and also $H \dashrightarrow \Upsilon\gamma$) and has been made public by the ATLAS collaboration. The search aims at revealing anomalous Higgs couplings to the charm quark (or to the bottom); at the moment, it is able to put a limit on the rate of the process $H \to J/\Psi\gamma$ at about 540 times the SM expected rate at 95% CL, excluding universality in the quark sector, assuming the gluon-fusion production to be driven mostly by the coupling of the Higgs to the top quark. Even at the HL-LHC, however, it will be very difficult that this search will be sensitive to the event rate expected in the SM for this process.

2.1 Invisible Higgs decays searches

An appealing possibility is represented by the the Higgs boson decay into stable or long-lived neutral particles, escaping direct detection, as it is motivated by some BSM theories. This type of decays are currently probed in associate Higgs production with a Z boson or vector boson fusion (VBF); these searches are exploiting the detectable objects in the final state (a lepton pair compatible with the Z mass hypothesis, a pair of forward high pt jets,...) as taggers for the Higgs production. Some attempts are also being made in exploiting boosted gluon fusion events,

signalled by the presence of an unbalanced event with an high pt jet, or associate production with top quarks. ATLAS has released 2 new results in time for this conference [14, 15], improving the sensitivity of the previous searches. In particular, a limit on invisible Higgs decays BR is placed at 29% with 95% CL for a 125 GeV Higgs by the VBF+H(→invisible) search, which represent the most sensitive single search performed to date. It is also possible to interpret these results as searches for dark matter (DM) [17], recasting the BR upper limit into a DM-nucleon scattering cross section upper limit. These interpretations are performed in the "Higgs-portal to DM" [18] scenario, where an effective lagrangian operator couples directly the Higgs field to the DM field; it is possible to assume different nature for the DM candidate (scalar, fermion, vector). Within these assumptions, these results provide competitive cross-section upper limits for low-mass dark matter candidates (indeed assuming an Higgs decay into a pair of DM candidates, only DM candidate masses below half of the mass of the Higgs could be probed).

In addition to completely invisible Higgs decays, the possibility of having one or more additional photons in the final state (quasi-invisible Higgs decays) is considered too. Apart for being experimentally interesting, these searches are motivated, just to give an example, by R-parity conserving super-symmetric scenarios, where Higgs decays into neutralino(NLSP)+LSP, and then the neutralino decays into a photon+LSP (for NLSP masses below half of the Higgs mass, Higgs decays into a NLSP pair is allowed). One or more photons are present in the final state, in addition to transverse missing energy due to the undetected LSP particles. CMS [19] has performed this analysis inclusively, exploiting a low transverse momentum photon trigger, while ATLAS [20] has exploited the VBF production mode. The cross-section limits which are placed by these analysis, are interpreted in a simplified model approach, showing a sensitivity to $BR(H \rightarrow NLSP + \not{L}SP)$ as good as 10%, depending on the NLSP mass, and assuming for the mass of the LSP 1 GeV.

3 Extended Higgs sector searches

A non minimal Higgs sector is required by several BSM theories, most notably the Minimal Supersymmetric Standard Model (MSSM).

The Higgs sector of the MSSM is part of a class of models termed "Two-Higgs-Doublet Models" (2HDM) [21], where two Higgs doublets mix to generate EWSB and fermion masses. Four types of 2HDM models can be derived satisfying flavour changing neutral current constraints, classyfing them according to their couplings to fermions and bosons. 2HDMs predict the existence of five Higgs bosons: two neutral CP-even bosons h and H, one neutral CP-odd boson A, and two charged bosons $H^{\pm}$.

The Next to Minimal Super-Symmetric Standard Model (NMSSM) extends the MSSM by an additional gauge singlet field under a new $U(1)_{PQ}$ symmetry in the Higgs sector of the superpotential [22]. This allows to naturally generate the mass parameter μ term of the MSSM Higgs super potential at the EW scale. With respect to the MSSM, the Higgs sector consists of an additional CP-even boson and an additional CP-odd boson. In the NMSSM it is still possible to have bosons lighter then the discovered Higgs boson, so decays of the Higgs boson into light (pseudo)scalars ($h \rightarrow 2a_1$) represent still an interesting possibility to be looked at. Depending on the a_1 mass, preferential decays in a pair of μ,τ or b are exploited to search for these light scalars.

Other simpler SM extensions can be foreseen too, for example an additional EW singlet. This class of models can also provide a possible dark matter candidate [23]. Mixing of the EW singlet with the Higgs field, leads to modifications of the Higgs couplings, which get reduced by a scale factor, and generate a neutral heavy mass CP-even Higgs boson.

Most of the searches for additional Higgs bosons presented here are performed in a model independent way: interpretation is given in terms of cross-section upper limits for the process which is being probed. No significant attempt is made so far by the ATLAS and CMS collabo-

ration to combine searches in different final states into a single exclusion plots. Some attempts can be found in literature, see for example [24].

3.1 2HDM, MSSM and Heavy Higgs searches

For large tanβ the branching ratio of the heavy neutral MSSM Higgs bosons to tau leptons is enhanced, making the search for $A/H \to \tau\tau$ particularly attractive. ATLAS and CMS have published results [25, 26] based on the full Run I statistics, excluding a large region of heavy scalar masses: tanβ upper limit increases as the neutral heavy Higgs boson hypothesis (almost independently by the MSSM scenario being considered for the exclusion). Model independent upper limits are also given for the gluon-fusion and the b-associated heavy Higgs production.

Charged Higgs bosons searches are particularly sensitive when considering masses of the charged Higgs below the top mass, ($m_{H^\pm} < m_t$), where the decay of the top $t \to bH^+$ can be searched for in the abundant $t\bar{t}$ events. The decay $H^\pm \to \tau\nu$ decay is the preferential decay in the MSSM already from small tanβ values. The most updated results for the $H^\pm \to \tau\nu$ searches reported by ATLAS and CMS [27, 28] are able to exclude $m_{H^\pm} < 160$ GeV independently of the tanβ assumption. Other searches for $H^\pm \to cs$ are performed in the low mass region, while for the high mass region $H^\pm \to tb$ is considered too.

The most difficult region to be covered in the MSSM search is the in the medium (≈ 5) to low tanβ region for $m_A > 200$ GeV. This region can be covered by the searches for $A \to ZH$ and $H \to hh$. Recent results are reported by ATLAS [29] and CMS [30] for $A \to ZH$, which are able to put some constraints in this region.

Heavy scalars are also searched in the WW and ZZ final states. For 2HDM models these searches are sensitive in the medium (≈ 5) to low tanβ region for $m_H > 150$ GeV, but are also motivated by other simpler extensions of the SM, like for example an additional EWK singlet. A narrower state then the SM Higgs hypothesis for the same mass value is expected. The most updated results on these searches by the CMS collaboration are reported in detail in these proceedings [31].

For the region $m_A > 2m_{top}$ at intermediate tanβ the most sensitive analysis is assumed to be the search in the di-top final state. It is possible to re-interpret the current searches done by ATLAS and CMS for di-top resonances in this context, but more dedicated searches are expected to be performed during Run 2.

Searches for neutral heavy scalars are finally performed in the di-photon and $Z\gamma$ final states too [32, 33, 34]. Cross-section upper limits are established.

3.2 Low mass scalar searches

The most updated results are reported by the ATLAS collaboration in the search for $h \to 2a_1 \to 2\mu 2\tau$ final state [35]. This search is able to exclude BR($h \to 2a$) below 10% for mass m_a below 10 GeV and above $2m_\tau$. 4μ final state is also explored [36], while combinations like 4τ and $2\mu 2b$ will be reported in the future.

Associated production of the light pseudo scalar with b is also considered, and will be reported in the future as well.

4 Summary and prospects

The current status of the searches for BSM physics in the Higgs sector is reported. The results are based on the full statistics of the LHC Run I data, some additional analyses are being performed by both collaborations and will be reported in the future. No evidence for BSM physics has been reported so far, but significantly improved precision and sensitivity is expected to be achieved in the future LHC Run II analyses.

References

1. ATLAS Collaboration, Phys. Lett. B 716 (2012) 1-29
2. CMS Collaboration, Phys. Lett. B 716 (2012) 30-61
3. M. Duehrssen, these proceedings
4. ATLAS Collaboration, ATLAS-CONF-2014-010
5. For a recent paper see J. Ellis et al, JHEP 1503 (2015) 157, and references therein
6. D. d'Enterria, arXiv:1208.1993 [hep-ph]
7. ATLAS Collaboration, arXiv:1507.04548 [hep-ex]
8. CMS Collaboration, Eur. Phys. J. C 75 (2015) 212
9. ATLAS Collaboration, Phys. Lett. B 738 (2014) 68
10. CMS Collaboration, Phys. Lett. B 744 (2015) 184
11. ATLAS Collaboration, Phys. Lett. B 732C (2014), pp. 8-27
12. CMS Collaboration, Phys. Lett. B 726 (2013) 587
13. CMS Collaboration, arXiv:1502.07400 [hep-ex]
14. ATLAS Collaboration, ATLAS-CONF-2015-004
15. ATLAS Collaboration, arXiv:1504.04324 [hep-ex]
16. ATLAS Collaboration, ATLAS-CONF-2013-010
17. CMS Collaboration, arXiv:1404.1344 [hep-ex]
18. B. Patt and F. Wilczek, arXiv:0605188 [hep-ph]
19. CMS Collaboration, arXiv:1507.00359 [hep-ex]
20. ATLAS Collaboration, ATLAS-CONF-2015-001
21. T. Lee, Phys. Rev. D. 8 (1973) 1226
22. H. P. Nilles, Phys. Rept. 110 (1984) 1
23. A. Hill and J. van der Bij, Phys. Rev. D36 (1987) 3463
24. A. Djouadi et al., arXiv:1502.05653 [hep-ph]
25. ATLAS Collaboration, JHEP 11 (2014) 056
26. CMS Collaboration, JHEP 10 (2014) 160
27. ATLAS Collaboration, JHEP 03 (2015) 088
28. CMS Collaboration, CMS-HIG-14-020
29. ATLAS Collaboration, Phys. Lett. B 744 (2015) 163
30. CMS Collaboration, Phys. Lett. B 748 (2015) 221
31. M. Pelliccioni, these proceedings
32. ATLAS Collaboration, Phys. Rev. Lett. 113, 171801
33. CMS Collaboration, arXiv:1506.02301 [hep-ex]
34. CMS Collaboration, CMS-PAS-HIG-14-031
35. ATLAS Collaboration, arXiv:1505.01609 [hep-ex]
36. CMS Collaboration, arXiv:1506.00424 [hep-ex]

On the search for a second scalar doublet at the LHC

ALEJANDRO CELIS
Ludwig-Maximilians-Universität München, Fakultät für Physik,
Arnold Sommerfeld Center for Theoretical Physics, 80333 München, Germany

Motivated by the principle of natural flavour conservation, searches for signatures of a second scalar doublet at the LHC are usually limited to models with a very restricted Yukawa structure. Strong correlations between the scalar couplings to fermions are fixed in these models due to the underlying flavour principle, making the results obtained from such analyses highly model dependent. Moreover, constraints derived from flavour experiments also vary radically within the different models considered. The hypothesis of Yukawa alignment provides a suitable framework to perform a more general analysis of 125 GeV boson data and searches for additional scalars at the LHC, allowing for sizable new physics effects to be observed in the scalar sector while accommodating the stringent limits from flavour experiments at the same time. This general setting includes the different models with natural flavour conservation as particular cases.

1 Introduction

This talk is aimed to experimentalists following the spirit of the "Rencontres de Moriond" conference. The discovery of a 125 GeV SM-like scalar boson at the LHC can be interpreted as a confirmation that a complex scalar doublet is responsible for the spontaneous breaking of the electroweak (EW) gauge symmetry. Three degrees of freedom of this doublet give mass to $W^{\pm}$ and Z, the remaining degree of freedom should be the observed 125 GeV boson. Of course, none of the fundamental principles of the SM fix the particle content of the theory and we should search, among other things, for possible signals of additional scalar fields. I am concerned here with a simple extension of the SM by a second complex scalar doublet. Such a simple extension gives rise to a rich phenomenology at flavour factories and collider experiments like the LHC. By extending the SM in such a way, we are not aiming to provide a more fundamental theory of Nature than the SM, the main motivation is to analyze what experimental data is telling us about the EW symmetry breaking sector. On the other hand, an extended scalar sector as the one analyzed here could very well be regarded as a low energy effective theory of a more fundamental theory.

By extending the SM with a second scalar doublet Φ_i $(i = 1, 2)$, we obtain a scalar spectrum composed of three neutral scalars ($\varphi_i^0 = \{h, H, A\}$) and a charged scalar ($H^{\pm}$). One of the neutral scalars of the theory should correspond to the observed 125 GeV state while the additional scalar states would have been missed so far in experimental searches. Searches for signatures of a second scalar doublet at the LHC are strongly influenced by the observed strong suppression of flavour changing neutral currents (FCNCs). A second scalar doublet introduces in general new sources of flavour violation into the theory giving rise to tree-level FCNCs in the scalar sector. FCNCs are strongly constrained by low-energy flavour experiments, motivating the addition of an underlying mechanism which suppresses such dangerous terms. A well known mechanism

to achieve this is the principle of natural flavour conservation (NFC),[1,2] which guarantees the absence of FCNCs at tree-level by assuming that the Lagrangian is invariant under a discrete $\mathcal{Z}_2$ symmetry. The principle of NFC can be realized in different ways, giving rise to 4 different models, known as type I, II, X, Y. Each of these models have different correlations among the scalar couplings to fermions.

The aim of my talk is to discuss the possibility to search for a second scalar doublet in a more general way. Of particular relevance for LHC studies are the scalar couplings to the third generation fermions. We would like to have a framework where the scalar couplings to (t, b, τ) are all independent a priori. If there is actually any relation between these couplings it should be made manifest as a result of the experimental analyses. Keeping the most general Yukawa structure of the model with two scalar doublets is not a good option since it contains too many free parameters, most of which are already strongly constrained by flavour bounds. A convenient framework should incorporate the information obtained from flavour physics experiments while still allow for sizable effects to be observed at the LHC. Based on this premises, it could be argued that a predictive, practical and general model for the search of an additional scalar doublet at the LHC should have the following features:

- It should allow for independent deviations in the scalar couplings to the third generation fermions (t, b, τ).
- Flavour changing neutral currents in the scalar sector should be absent or strongly suppressed.
- It should be possible to implement constraints from flavour physics in a consistent manner without enlarging the number of free parameters in the analysis.
- Models with natural flavour conservation (type I, II, X, Y) should be recovered as particular cases.

The hypothesis of Yukawa alignment provides precisely the desired framework.[3] Flavour constraints on the model still allow sizable effects associated to the scalar sector to be observed at the LHC.[4–13] An additional simplification comes from assuming that CP is conserved in the scalar sector and the only source of CP-violation is the phase of the CKM matrix as in the SM, this assumption can be justified by the non-observation of electric dipole moments. A concise and self-contained description of the main aspects of this framework is given here. In Sec. 2 the extension of the scalar sector of the SM by a second scalar doublet is discussed. Limits of the parameter space in which one of the neutral scalars has SM-like properties are presented in Sec. 3. Finally in Sec. 4 the hypothesis of Yukawa alignment is introduced and it is shown that the different models with NFC correspond to specific cases of this framework.

2 Adding a second scalar doublet

The scalar doublets can be parametrized in full generality by

$$\Phi_1 = \begin{bmatrix} G^+ \\ \frac{1}{\sqrt{2}}\left(v + S_1 + iG^0\right) \end{bmatrix}, \qquad \Phi_2 = \begin{bmatrix} H^+ \\ \frac{1}{\sqrt{2}}\left(S_2 + iS_3\right) \end{bmatrix}. \tag{1}$$

Here we have chosen a scalar basis in which only one of the scalar doublets acquires a non-vanishing vev $v = (\sqrt{2}G_F)^{-1/2} \simeq 246$ GeV. The most general CP-conserving scalar potential compatible with the SM gauge symmetry is

$$\begin{aligned} V &= \mu_1\, \Phi_1^\dagger\Phi_1 + \mu_2\, \Phi_2^\dagger\Phi_2 + \left[\mu_3\, \Phi_1^\dagger\Phi_2 + \text{h.c.}\right] \\ &+ \lambda_1 \left(\Phi_1^\dagger\Phi_1\right)^2 + \lambda_2 \left(\Phi_2^\dagger\Phi_2\right)^2 + \lambda_3 \left(\Phi_1^\dagger\Phi_1\right)\left(\Phi_2^\dagger\Phi_2\right) + \lambda_4 \left(\Phi_1^\dagger\Phi_2\right)\left(\Phi_2^\dagger\Phi_1\right) \\ &+ \left[\left(\lambda_5\, \Phi_1^\dagger\Phi_2 + \lambda_6\, \Phi_1^\dagger\Phi_1 + \lambda_7\, \Phi_2^\dagger\Phi_2\right)\left(\Phi_1^\dagger\Phi_2\right) + \text{h.c.}\right], \end{aligned} \tag{2}$$

with real coefficients $\{\mu_j, \lambda_j\}$. The quartic couplings are expected to be $\lambda_j \sim \mathcal{O}(1)$ and are assumed to be bounded by perturbativity. The following relations are derived from the fact that the minimum of the potential is an extremum point: $\mu_1 = -\lambda_1 v^2$ and $\mu_3 = -\lambda_6 v^2/2$. Introducing a second scalar doublet to the scalar sector of the SM implies the existence of a mass scale in the potential, μ_2, not related a priori to the Fermi constant. The masses of the physical scalars are given in terms of the two available mass scales μ_2 and v, accompanied by quartic couplings. The mass of the charged scalar is

$$M_{H^\pm}^2 = \mu_2 + \frac{1}{2}\lambda_3 v^2 . \tag{3}$$

The neutral scalars are given by

$$\begin{pmatrix} h \\ H \\ A \end{pmatrix} = \begin{bmatrix} \cos\tilde{\alpha} & \sin\tilde{\alpha} & 0 \\ -\sin\tilde{\alpha} & \cos\tilde{\alpha} & 0 \\ 0 & 0 & 1 \end{bmatrix} \begin{pmatrix} S_1 \\ S_2 \\ S_3 \end{pmatrix} , \tag{4}$$

with $M_H \geq M_h$ by convention. The mixing angle is given by

$$\sin\tilde{\alpha} = \left(\frac{2\lambda_1 v^2 - M_h^2}{M_H^2 - M_h^2}\right)^{1/2} , \qquad \sin\tilde{\alpha}\cos\tilde{\alpha} = \frac{-\lambda_6 v^2}{M_H^2 - M_h^2} . \tag{5}$$

We can restrict to $0 \leq \tilde{\alpha} \leq \pi$ since we are free to perform a phase redefinition of the CP-even fields. Furthermore, a global rephasing of the second scalar doublet $\Phi_2 \to -\Phi_2$ is unphysical.[14] We can characterize this two-fold ambiguity in terms of the sign of λ_6, without loss of generality we can then fix the sign of λ_6. By convention we choose $\lambda_6 \leq 0$ which implies $0 \leq \tilde{\alpha} \leq \pi/2$. The masses of the neutral scalars are

$$M_h^2 = \frac{1}{2}(\Sigma - \Delta) , \qquad M_H^2 = \frac{1}{2}(\Sigma + \Delta) , \qquad M_A^2 = M_{H^\pm}^2 + v^2\left(\frac{\lambda_4}{2} - \lambda_5\right) , \tag{6}$$

with

$$\Sigma = M_{H^\pm}^2 + \left(2\lambda_1 + \frac{\lambda_4}{2} + \lambda_5\right)v^2 , \qquad \Delta = \sqrt{\left[M_A^2 + 2(\lambda_5 - \lambda_1)v^2\right]^2 + 4v^4\lambda_6^2} . \tag{7}$$

The scalar potential of the two-doublet model is parametrized in terms of 8 real parameters $\{\mu_2, \lambda_k\}$ $(k = 1, \ldots, 7)$. It is possible to trade some of these parameters for other quantities which are more closely related to physical observables as $\{M_h, M_H, M_A, M_{H^\pm}, \tilde{\alpha}, \lambda_2, \lambda_3, \lambda_7\}$:

$$\begin{aligned} \lambda_1 &= \frac{1}{2v^2}\left[M_h^2\cos^2\tilde{\alpha} + M_H^2\sin^2\tilde{\alpha}\right] , \qquad \lambda_4 = \frac{1}{v^2}\left[M_h^2\sin^2\tilde{\alpha} + M_H^2\cos^2\tilde{\alpha} + M_A^2 - 2M_{H^\pm}^2\right] , \\ \lambda_5 &= \frac{1}{2v^2}\left[M_h^2\sin^2\tilde{\alpha} + M_H^2\cos^2\tilde{\alpha} - M_A^2\right] , \qquad \lambda_6 = -\frac{1}{v^2}(M_H^2 - M_h^2)\cos\tilde{\alpha}\sin\tilde{\alpha} . \end{aligned} \tag{8}$$

The number of free parameters in the scalar potential gets effectively reduced to 7 due to the measurement of the scalar boson mass at the LHC. Since the CP-odd state A does not couple to the massive gauge vector bosons, we know that M_h or M_H should correspond to 125 GeV. The neutral scalar couplings to the massive gauge vector bosons are again determined by the mass generation mechanism up to mixing effects

$$\mathcal{L}_{\varphi V^2} = \frac{2}{v}\left(\cos\tilde{\alpha}\, h - \sin\tilde{\alpha}\, H\right)\left[M_W^2\, W_\mu^\dagger W^\mu + \frac{1}{2}M_Z^2\, Z_\mu Z^\mu\right] . \tag{9}$$

Note that the relation $M_W/(M_Z\cos\theta_W) = 1$ remains valid at tree-level. The interactions of the scalar fields with fermions are not directly correlated anymore to the fermion masses

$$\begin{aligned} \mathcal{L}_Y = &- \sum_{\varphi_i^0, f=u,d,\ell} \varphi_i^0\, \bar{f}\, Y_f^{\varphi_i^0}\, \mathcal{P}_R\, f \\ &- \frac{\sqrt{2}}{v}\, H^+\left\{\bar{u}\left[V_{\mathrm{CKM}}\,\Pi_d\,\mathcal{P}_R - \Pi_u^\dagger\, V_{\mathrm{CKM}}\,\mathcal{P}_L\right] d + \bar{\nu}\,\Pi_\ell\,\mathcal{P}_R\,\ell\right\} + \text{ h.c.} , \end{aligned} \tag{10}$$

with

$$v\,Y_{d,\ell}^{\varphi_i^0} = M_{d,\ell}\,\mathcal{R}_{i1} + \Pi_{d,\ell}\,(\mathcal{R}_{i2} + i\,\mathcal{R}_{i3})\;, \qquad v\,Y_u^{\varphi_i^0} = M_u\,\mathcal{R}_{i1} + \Pi_u\,(\mathcal{R}_{i2} - i\,\mathcal{R}_{i3})\;. \tag{11}$$

Here $\varphi_i^0 = \mathcal{R}_{ij} S_j$ with the mixing matrix $\mathcal{R}$ defined in Eq. 4. The $M_{f=u,d,l}$ are the diagonal fermion mass matrices while the $\Pi_{f=u,d,l}$ represent arbitrary real matrices in flavour space, giving rise to tree-level FCNCs in the scalar sector. The chiral projectors $\mathcal{P}_{L,R} = (1 \mp \gamma_5)/2$ are denoted as usual and $V_{\rm CKM}$ is the CKM matrix.

3 A SM-like scalar boson at 125 GeV

The observation of a SM-like boson at 125 GeV has important implications for the structure of the scalar sector presented previously. The properties of the scalar sector depend strongly on the hierarchy between μ_2 and the EW scale. For $\mu_2 \gg v^2$ and perturbative quartic couplings the second scalar doublet Φ_2 decouples from the theory, leaving a SM-like scalar sector at the EW scale.[15] The scalar masses are given in this limit by

$$M_h^2 \simeq 2\lambda_1 v^2 + \mathcal{O}\left(\frac{v^4}{\mu_2}\right)\;, \qquad M_H^2 \simeq M_A^2 \simeq M_{H^\pm}^2 = \mu_2 + \mathcal{O}(v^2)\,. \tag{12}$$

The mixing between the two scalar doublets is suppressed by the high mass scale, $\tan\tilde{\alpha} \simeq \mathcal{O}(v^2/\mu_2)$, so that the couplings of the light CP-even scalar boson with vector bosons and fermions approach the SM values

$$\cos\tilde{\alpha} = (1 + \tan^2\tilde{\alpha})^{-1/2} \simeq 1 + \mathcal{O}\left(\frac{v^4}{\mu_2^2}\right)\;, \qquad Y_f^h \simeq \frac{M_f}{v} + \mathcal{O}\left(\frac{v^2}{\mu_2}\right)\;. \tag{13}$$

It is said that the approach to the decoupling is faster for the scalar coupling to massive vector bosons than to fermions.[15] In such decoupling scenario, obviously only the lightest CP-even state h could play the role of the 125 GeV boson. In models where the second mass scale μ_2 is absent or is related to the EW scale $\mu_2 \sim v^2$, due to an underlying symmetry for example, there is no decoupling.[15] Even in this scenario it is possible to have a light SM-like scalar boson. This occurs when $\lambda_6 \to 0$ since the mixing between the two scalar doublets vanishes in this limit.[15] In this case the additional scalars should also be around the EW scale assuming perturbativity of the quartic scalar couplings. In this limit any of the CP-even states could play the role of the SM-like 125 GeV boson:

- For $\lambda_6 \to 0$ and $M_A^2 + 2(\lambda_5 - \lambda_1)v^2 > 0$ we get $\cos 2\tilde{\alpha} \simeq 1 + \mathcal{O}(\lambda_6^2)$, so that $\tilde{\alpha} = 0 + 1/2|\arccos\left(\mathcal{O}(\lambda_6^2)\right)|$. The light CP-even state h becomes SM-like ($\cos\tilde{\alpha} \simeq 1$).
- For $\lambda_6 \to 0$ and $M_A^2 + 2(\lambda_5 - \lambda_1)v^2 < 0$ we get $\cos 2\tilde{\alpha} \simeq -1 + \mathcal{O}(\lambda_6^2)$, so that $\tilde{\alpha} = \pi/2 - 1/2|\arccos\left(\mathcal{O}(\lambda_6^2)\right)|$. The heavy CP-even state H becomes SM-like ($\sin\tilde{\alpha} \simeq 1$).

Here we have used the following exact identity

$$\cos 2\tilde{\alpha} = \frac{M_A^2 + 2(\lambda_5 - \lambda_1)v^2}{\sqrt{\left[M_A^2 + 2(\lambda_5 - \lambda_1)v^2\right]^2 + 4v^4\lambda_6^2}}\,. \tag{14}$$

4 A framework for the search of a second scalar doublet at the LHC

From the phenomenological point of view we are interested in a scenario with additional scalar fields accessible at the LHC and with possible deviations from the SM in the 125 GeV boson couplings. The Yukawa alignment hypothesis provides a suitable framework to interpret LHC

data in such scenario. The Yukawa alignment condition is based on the assumption that the Yukawa matrices for each type of fermion are aligned in flavour space, see Eq. 10,[a]

$$\Pi_{d,l} = \varsigma_{d,l} M_{d,l}\,, \qquad \Pi_u = \varsigma_u M_u\,. \tag{15}$$

Here the flavour universal alignment parameters $\varsigma_{f=u,d,l}$ are arbitrary real numbers (assuming CP-conservation). The Yukawa Lagrangian reads

$$\begin{aligned} \mathcal{L}_Y &= -\frac{\sqrt{2}}{v}\, H^+ \left\{ \bar{u}\left[\varsigma_d V_{\rm CKM} M_d \mathcal{P}_R - \varsigma_u M_u V_{\rm CKM} \mathcal{P}_L\right] d + \varsigma_l\, \bar{\nu} M_l \mathcal{P}_R l \right\} \\ &\quad - \frac{1}{v} \sum_{\varphi_i^0, f=u,d,l} y_f^{\varphi_i^0}\, \varphi_i^0 \, \left[\bar{f}\, M_f \mathcal{P}_R f\right] \; + \; \text{h.c.} \end{aligned} \tag{16}$$

The fermionic couplings of the neutral scalar fields are given, in units of the SM scalar couplings by

$$\begin{aligned} y_f^h &= \cos\tilde{\alpha} + \varsigma_f \sin\tilde{\alpha}\,, & y_{d,l}^A &= i\,\varsigma_{d,l}\,, \\ y_f^H &= -\sin\tilde{\alpha} + \varsigma_f \cos\tilde{\alpha}\,, & y_u^A &= -i\,\varsigma_u\,. \end{aligned} \tag{17}$$

The model contains 10 free parameters, 7 coming from the scalar potential as explained in Sec. 2 and 3 from the Yukawa sector $\{\varsigma_u, \varsigma_d, \varsigma_l\}$. This framework satisfies all the conditions spelled in the introduction for the search of a second scalar doublet at the LHC. The first three conditions are manifest in Eqs. 16 and 17. It can also be shown that models with NFC are recovered as particular limits of the Yukawa aligned model.

4.1 Models with natural flavour conservation

NFC models are usually expressed in a scalar basis ϕ_i $(i = 1, 2)$ where both doublets acquire vevs $\langle \phi_i^0 \rangle = v_i/\sqrt{2}$, with $v^2 = v_1^2 + v_2^2$. Such basis is related to the one in Eq. 1 by an orthogonal transformation parametrized by $\tan\beta \equiv v_2/v_1$. The usual convention for models with NFC is to use the rephasing freedom $\Phi_2 \to -\Phi_2$ to fix the sign of $\tan\beta \geq 0$, or equivalently $0 \leq \beta \leq \pi/2$. By doing so, we can no longer fix the sign of λ_6 so that $0 \leq \tilde{\alpha} \leq \pi$.

Table 1: *Models with natural flavour conservation.*

Model	ς_d	ς_u	ς_l
Type I	$\cot\beta$	$\cot\beta$	$\cot\beta$
Type II	$-\tan\beta$	$\cot\beta$	$-\tan\beta$
Type X (lepton-specific)	$\cot\beta$	$\cot\beta$	$-\tan\beta$
Type Y (flipped)	$-\tan\beta$	$\cot\beta$	$\cot\beta$

NFC can be obtained by considering a softly-broken $\mathcal{Z}_2$ symmetry under which ϕ_1 is even and ϕ_2 is odd. Four different NFC models are obtained depending on the assigned fermionic charges (types I, II, X, Y). The presence of such a symmetry in the theory imply correlations among the parameters of the model. In models with NFC all the alignment parameters are given in terms of $\tan\beta$, see Table 1. These relations imply strong correlations between the scalar boson couplings to fermions. For example, taking the type I model we get $|y_u^{\varphi_i^0}| = |y_d^{\varphi_i^0}| = |y_l^{\varphi_i^0}|$ from Eq. 17.

[a] Though the Yukawa alignment condition is not stable under quantum corrections, accidental flavour symmetries in the Lagrangian protect the flavour structure of the model. For the phenomenological purposes we are interested the Yukawa aligned structure can be considered stable.[3,4,16,17,18]

Terms with an odd parity under the $\mathcal{Z}_2$ symmetry are forbidden in the scalar potential, translating into correlations among the parameters of the scalar potential

$$\lambda_6' = (\lambda_1 - \lambda_3 - \lambda_5)\, c_\beta^3 s_\beta + (\lambda_4 + \lambda_5 - \lambda_2)\, c_\beta s_\beta^3 + \lambda_6 (c_\beta^4 - c_\beta^2 s_\beta^2) + 2\lambda_7 c_\beta^2 s_\beta^2 = 0\,,$$
$$\lambda_7' = (\lambda_1 - \lambda_3 - \lambda_4 - \lambda_5)\, c_\beta s_\beta^3 + (\lambda_5 - \lambda_2)\, c_\beta^3 s_\beta + 2\lambda_6\, s_\beta^2 c_\beta^2 + \lambda_7 (c_\beta^4 - s_\beta^2 c_\beta^2) = 0\,. \qquad (18)$$

Here $s_\beta \equiv \sin\beta$ and $c_\beta \equiv \cos\beta$. The parameters $\lambda_{6,7}'$ are the coefficients of $(\phi_1^\dagger\phi_1)(\phi_1^\dagger\phi_2)$ and $(\phi_2^\dagger\phi_2)(\phi_1^\dagger\phi_2)$ in the scalar potential. If the $\mathcal{Z}_2$ symmetry is an exact symmetry of the Lagrangian (it is not softly broken) an additional relation appears between the scalar potential parameters:

$$m_{12}'^2 = (\mu_2 - \mu_1) c_\beta s_\beta - \mu_3 c_{2\beta} = 0\,, \qquad (19)$$

with $m_{12}'^2$ being the coefficient of the term $\phi_1^\dagger\phi_2$ in the scalar potential. Note that there is no decoupling limit in this scenario since the exact $\mathcal{Z}_2$ symmetry relates μ_2 to the EW scale.[15]

5 Conclusions

Signatures of a second scalar doublet could be within the reach of the next runs of LHC. Current analyses of 125 GeV boson data and direct searches for additional scalars at the LHC are being performed by the experimental collaborations within models with natural flavour conservation, which have a very restricted Yukawa structure. Ideally, we should search for signatures of a second scalar doublet in a more general way. The Yukawa aligned model provides a predictive, practical and general framework for this purpose. Allowing for sizable new physics effects associated to the scalar sector to be observed at the LHC while satisfying the stringent flavour limits. Models with natural flavour conservation are recovered as particular cases.

Acknowledgments

I thank the organizers of "The 50th Rencontres de Moriond, Electroweak Session". I am grateful to V. Ilisie and A. Pich for useful comments on this manuscript. A.C. is supported by the Alexander von Humboldt Foundation.

References

1. S. L. Glashow and S. Weinberg, Phys. Rev. D **15** 1958 (1977).
2. E. A. Paschos, Phys. Rev. D **15** 1966 (1977).
3. A. Pich and P. Tuzon, Phys. Rev. D **80** 091702 (2009).
4. M. Jung, A. Pich and P. Tuzon, JHEP **1011** 003 (2010).
5. E. Cervero and J. M. Gerard, Phys. Lett. B **712** 255 (2012).
6. W. Altmannshofer, S. Gori and G. D. Kribs, Phys. Rev. D **86** 115009 (2012).
7. Y. Bai *et al.* Phys. Rev. D **87** 115013 (2013).
8. A. Celis, V. Ilisie and A. Pich, JHEP **1307** 053 (2013).
9. D. Lopez-Val, T. Plehn and M. Rauch, JHEP **1310** 134 (2013).
10. V. Barger *et al.* Phys. Rev. D **88** 11, 115003 (2013).
11. A. Celis, V. Ilisie and A. Pich, JHEP **1312** 095 (2013).
12. L. Wang and X. F. Han, JHEP **1404** 128 (2014).
13. V. Ilisie and A. Pich, JHEP **1409** 089 (2014).
14. S. Davidson and H. E. Haber, Phys. Rev. D **72** 035004 (2005).
15. J. F. Gunion and H. E. Haber, Phys. Rev. D **67** 075019 (2003).
16. C. B. Braeuninger, A. Ibarra and C. Simonetto, Phys. Lett. B **692** 189 (2010).
17. X. Q. Li, J. Lu and A. Pich, JHEP **1406** 022 (2014).
18. G. Abbas, A. Celis, X. Q. Li, J. Lu and A. Pich, arXiv:1503.06423 (2015).

BSM Primaries: the Physics of the SM Effective Field Theory

Francesco Riva
Institut de Théorie des Phénomènes Physiques, EPFL,1015 Lausanne, Switzerland

The phenomenological implications of the Standard Model (SM) are governed by the accidental symmetry structure of the dimension-4 Lagrangian. In this talk I discuss the next order in an expansion in fields and in derivatives, that parametrize the largest effects of heavy physics beyond the SM. The remaining symmetries of this dimension-6 Lagrangian imply relations between experimental observables that should be used to test the consistency of deviations from the SM, to design new physics searches and to make them more sensitive.

1 Motivation

The Higgs bosons discovery marks the culmination of searches for the Standard Model (SM) of particle physics. All of the SM sectors have finally been probed and most of its parameters accessed experimentally, with different levels of precision. At the same time direct searches for physics beyond the SM (BSM) have been unsuccessful, suggesting the existence of a mass gap between the SM states and any possible mass scale characteristic of the new physics sector.

In this situation, where the energy of our experiments seems to be insufficient to produce BSM degrees of freedom on-shell, we can still hope that their virtual exchange induces some visible effects, as modifications of the interactions between SM states. This represents the main motivation to perform SM precision tests.

For these tests to bear any quantitative physical significance and for their results to be readily interpretable in the framework of searches for new physics, an appropriate parametrization of the possible departures from the SM is necessary. This parametrization is naturally provided by an SM effective field theory (EFT), which groups all possible interaction among the SM fields in a series expansion in inverse powers of the scale of new physics Λ: $\mathcal{L}_{\rm eff} = \mathcal{L}_4 + \mathcal{L}_6 + \cdots$, where $\mathcal{L}_4$ is made of dimension-4 operators and defines what we call the SM Lagrangian, while $\mathcal{L}_6$, that contains dimension-6 operators suppressed by Λ^2, gives the leading BSM effects.[a] From a bottom-up perspective, these interactions can be considered necessary and their coefficients (the scales associated with each of them) can be fixed only through experiments, in the same way as one fixes the SM input parameters through precise measurements of the input observables (α, m_Z, G_F,...). From a top-bottom perspective, on the other hand, specific BSM models can be matched straightforwardly to the EFT description, by integrating out the relevant massive particles. This twofold

[a] Assuming lepton and baryon number conservation.

interpretation of the EFT parametrization, makes it a suitable tool to characterize departures from the SM in such a way that precision SM tests can be turned into searching tools and their results compared with other direct or indirect searches.

In this note I review the leading departures from the SM in an EFT description. Interestingly, of the many accidental symmetries and relations that define the SM Lagrangian, some resist at the leading order in the EFT expansion (equivalently: the number of observables affected by the leading EFT effects, is smaller than the number of operators characterizing the leading EFT Lagrangian). For this reason the EFT analysis implies some relations between observables (the analog of, e.g., the SM relation $m_W = m_Z/\cos\theta_W$), that represent an important piece of information about the BSM structure. In fact, these relations can be used the test the assumptions behind the EFT (e.g. a separation of scales or the exactness of the SM symmetries); alternatively, they can be used to identify the directions that have been weakly probed by current and past experiments and understand which observables deserve particular attention.

2 BSM Primaries

There are several possibilities to write $\mathcal{L}_6$. From a top-bottom perspective, different operator bases for $\mathcal{L}_6$ can facilitate the comparison with explicit BSM scenarios. For instance, the SILH basis [1] was constructed to capture the effects of universal theories (where the new physics couples only to bosons), such as SUSY or Composite Higgs[b], while the basis of Ref. [4] makes the matching with theories with (partially) composite fermions more straightforward. From a bottom-up perspective, however, these formulations are all equivalent as one is only interested in complete sets of operators. In fact, from this point of view, we can treat $\mathcal{L}_6$ in exact analogy with the SM Lagrangian $\mathcal{L}_4$: we chose the most precise experiments to fix its parameters (for the SM, $\mathcal{L}_4$, we typically take $\alpha, m_Z, G_F, ...$) and then express all other observables in terms of these *input* parameters (observables in terms of observables). To this end, we must identify a set of well-measured input observables (which are actually affected by the modifications implied in $\mathcal{L}_6$) that allows us to fix the parameters in $\mathcal{L}_6$. This matching between coefficients in $\mathcal{L}_6$ and well-measured observables was performed in Refs. [5,6,7] and named *BSM Primaries* basis, and I summarize it here.

The first important step is to recognize that there is a class of BSM operators, which in the gauge eigenstate basis corresponds to operators of the form $|H|^2 \times \mathcal{L}_{SM}$, which can only be tested in Higgs physics [6,10]. In fact, when these operators are measured in the vacuum $\langle \hat{h} \rangle = v$, they can be absorbed into a redefinition of some SM parameter and they have, therefore, no physical effect. The number of such operators equals the number of SM parameters which, if we limit ourselves to CP conserving quantities and a diagonal flavor structure[c], reduces to eight, which we write as:

$$\Delta\mathcal{L}^h_{\gamma\gamma} = \boldsymbol{\kappa_{\gamma\gamma}} \left(\frac{h}{v} + \frac{h^2}{2v^2}\right) \left[A_{\mu\nu}A^{\mu\nu} + Z_{\mu\nu}Z^{\mu\nu} + 2W^+_{\mu\nu}W^{-\mu\nu}\right], \quad (1)$$

$$\Delta\mathcal{L}^h_{Z\gamma} = \boldsymbol{\kappa_{Z\gamma}} \left(\frac{h}{v} + \frac{h^2}{2v^2}\right) \left[t_{\boldsymbol{\theta_W}} A_{\mu\nu}Z^{\mu\nu} + \frac{c_{2\theta_W}}{2c^2_{\theta_W}} Z_{\mu\nu}Z^{\mu\nu} + W^+_{\mu\nu}W^{-\mu\nu}\right], \quad (2)$$

$$\Delta\mathcal{L}^h_{GG} = \boldsymbol{\kappa_{GG}} \left(\frac{h}{v} + \frac{h^2}{2v^2}\right) G^A_{\mu\nu}G^{A\,\mu\nu}, \quad (3)$$

$$\Delta\mathcal{L}^h_{ff} = \boldsymbol{\delta g^h_{ff}} \left(h\bar{f}_L f_R + \text{h.c.}\right)\left(1 + \frac{3h}{2v} + \frac{h^2}{2v^2}\right), \quad (4)$$

$$\Delta\mathcal{L}_{3h} = \boldsymbol{\delta g_{3h}}\, h^3 \left(1 + \frac{3h}{2v} + \frac{3h^2}{4v^2} + \frac{h^3}{8v^3}\right), \quad (5)$$

$$\Delta\mathcal{L}^h_{VV} = \boldsymbol{\delta g^h_{VV}} \left[h\left(W^{+\mu}W^-_\mu + \frac{Z^\mu Z_\mu}{2c^2_{\theta_W}}\right) + \Delta_h\right], \quad (6)$$

[b] See Refs. [2,3], and references therein, for analysis of the contributions to the EFT of Supersymmetric and Composite Higgs models [7,7]. .

[c] These arguments can be easily extended to higher-order effects in a Minimal Flavor Violation (MFV[11]) expansion[6] or to more complicated flavor structures[12].

where $f = u, d, e$ runs over different types of fermion. Here, I denote $\hat{h} \equiv v + h(x)$ the Higgs field, where h denotes the physical Higgs degree of freedom; Δ_h includes interaction which are irrelevant for experiments in the near future[5] and I define $Z_{\mu\nu} \equiv \hat{Z}_{\mu\nu} - igc_{\theta_W} W^+_{[\mu} W^-_{\nu]}$, $A_{\mu\nu} \equiv \hat{A}_{\mu\nu} - igs_{\theta_W} W^+_{[\mu} W^-_{\nu]}$ and $W^\pm_{\mu\nu} \equiv \hat{W}^\pm_{\mu\nu} \pm igW^\pm_{[\mu}(s_{\theta_W} A + c_{\theta_W} Z)_{\nu]}$. Written in this way, $\mathcal{L}_6$ is automatically ready to incorporate the experimental information from measurements of the Higgs decay and production rates: measurements of the rates $h \to \gamma Z, \gamma\gamma, \bar{f}f$, the production channel $GG \to h$ and the – custodial preserving – $hV_\mu V^\mu$ and h^3 vertices (the latter not yet accessible), allow to fix the parameters $\{\kappa_{\gamma Z}, \kappa_{\gamma\gamma},\ \delta g^h_{uu}, \delta g^h_{dd}, \delta g^h_{ee}, \kappa_{GG}, \delta g^h_{VV}, \delta g_{3h}\}$. Notice that in the above expressions, and throughout this note, I absorb powers of m^2_W/Λ^2_i or v^2/Λ^2 into the coefficients κ_i and δg_i: in this way, for the EFT to make sense, we expect $\kappa_i, \delta g_i \ll 1$. Unfortunately (see e.g. Refs. [8,9,13]) this is not the case for the δg_i couplings at present, implying that the use of the EFT parametrization in this case is not yet justified. However, for the κ_i couplings the constraints are already very stringent: at the 95% C.L.[8,13,6] $\kappa_{\gamma\gamma} \in [-1.3, 1.8] \times 10^{-3}$, $\kappa_{Z\gamma} \in [-2, 4] \times 10^{-2}$, $\kappa_{GG} \in [-1, 1] \times 10^{-2}$. Then, Eqs. (1-6) automatically imply a prediction that the coefficient of structures like $hZ_{\mu\nu}Z^{\mu\nu}$, which modifies the differential distribution of $h \to ZZ^*$ (see below), receives contributions from Eq. (1) and Eq. (2), but this contribution is limited within the range of given above. A second class of BSM effects contained in $\mathcal{L}_6$ can instead be measured both in Higgs physics and in the vacuum. In the language of effective operators, these effects are associated with structures like $H^\dagger \sigma^a H$, which transforms non-trivially under $SU(2)_L$ and implies measurable EWSB effects for $\langle \hat{h} \rangle = v$. In this case, at present, the measurement of these effects is more easily performed in the vacuum[d] and, for this reason, we parametrize this sector of the effective Lagrangian as,

$$\begin{aligned}
\Delta\mathcal{L}^V_{ee} &= \boldsymbol{\delta g^Z_{eR}} \frac{\hat{h}^2}{v^2} Z^\mu \bar{e}_R \gamma_\mu e_R + \boldsymbol{\delta g^Z_{eL}} \frac{\hat{h}^2}{v^2} \left[Z^\mu \bar{e}_L \gamma_\mu e_L - \frac{c_{\theta_W}}{\sqrt{2}} (W^{+\mu} \bar{\nu}_L \gamma_\mu e_L + \text{h.c.}) \right] \\
&\quad + \boldsymbol{\delta g^Z_{\nu L}} \frac{\hat{h}^2}{v^2} \left[Z^\mu \bar{\nu}_L \gamma_\mu \nu_L + \frac{c_{\theta_W}}{\sqrt{2}} (W^{+\mu} \bar{\nu}_L \gamma_\mu e_L + \text{h.c.}) \right], \qquad (7) \\
\Delta\mathcal{L}^V_{qq} &= \boldsymbol{\delta g^Z_{uR}} \frac{\hat{h}^2}{v^2} Z^\mu \bar{u}_R \gamma_\mu u_R + \boldsymbol{\delta g^Z_{dR}} \frac{\hat{h}^2}{v^2} Z^\mu \bar{d}_R \gamma_\mu d_R + \boldsymbol{\delta g^Z_{dL}} \frac{\hat{h}^2}{v^2} \left[Z^\mu \bar{d}_L \gamma_\mu d_L - \frac{c_{\theta_W}}{\sqrt{2}} (W^{+\mu} \bar{u}_L \gamma_\mu d_L + \text{h.c.}) \right] \\
&\quad + \boldsymbol{\delta g^Z_{uL}} \frac{\hat{h}^2}{v^2} \left[Z^\mu \bar{u}_L \gamma_\mu u_L + \frac{c_{\theta_W}}{\sqrt{2}} (W^{+\mu} \bar{u_L} \gamma_\mu d_L + \text{h.c.}) \right] \qquad (8) \\
\Delta\mathcal{L}_{g^Z_1} &= \boldsymbol{\delta g^Z_1} \Big[igc_{\theta_W} \Big(Z^\mu (W^{+\nu} W^-_{\mu\nu} - \text{h.c.}) + Z^{\mu\nu} W^+_\mu W^-_\nu \Big) \\
&\quad - 2gc^2_{\theta_W} \frac{h}{v} \left(W^-_\mu J^\mu_- + \text{h.c.} + \frac{c_{2\theta_W}}{c^3_{\theta_W}} Z_\mu J^\mu_Z + \frac{2s^2_{\theta_W}}{c_{\theta_W}} Z_\mu J^\mu_{em} \right) \left(1 + \frac{h}{2v} \right) \qquad (9) \\
&\quad + \frac{e^2 v}{2c^2_{\theta_W}} h Z_\mu Z^\mu + g^2 c^2_{\theta_W} v\, \Delta_h - g^2 c^2_{\theta_W} \Big(W^+_\mu W^{-\mu} + \frac{c_{2\theta_W}}{2c^4_{\theta_W}} Z_\mu Z^\mu \Big) \Big(\frac{5h^2}{2} + \frac{2h^3}{v} + \frac{h^4}{2v^2} \Big) \Big] \\
\Delta\mathcal{L}_{\kappa_\gamma} &= \frac{\boldsymbol{\delta\kappa_\gamma}}{v^2} \Big[ie\hat{h}^2 (A_{\mu\nu} - t_{\theta_W} Z_{\mu\nu}) W^{+\mu} W^{-\nu} + Z_\nu \partial_\mu \hat{h}^2 (t_{\theta_W} A^{\mu\nu} - t^2_{\theta_W} Z^{\mu\nu}) \\
&\quad + \frac{(\hat{h}^2 - v^2)}{2} \Big(t_{\theta_W} Z_{\mu\nu} A^{\mu\nu} + \frac{c_{2\theta_W}}{2c^2_{\theta_W}} Z_{\mu\nu} Z^{\mu\nu} + W^+_{\mu\nu} W^{-\mu\nu} \Big) \Big], \qquad (10)
\end{aligned}$$

all these effects, in the vacuum, can be measured as modifications of SM couplings (meaning that their contribution interferes with the SM in the amplitude-squared) and from a comparison with LEP1 data, we find[15]

$$\begin{aligned}
\boldsymbol{\delta g^Z_{eL}} = 0.4^{\pm 0.5} \times 10^{-3}, \quad \boldsymbol{\delta g^Z_{eR}} = -0.1^{\pm 0.3} \times 10^{-3}, \quad \boldsymbol{\delta g^Z_{\nu}} = -1.6^{\pm 0.8} \times 10^{-3}, \qquad (11) \\
\boldsymbol{\delta g^Z_{uL}} = -2.6^{\pm 1.6} \times 10^{-3}, \quad \boldsymbol{\delta g^Z_{dL}} = 2.3^{\pm 1} \times 10^{-3}, \\
\boldsymbol{\delta g^Z_{uR}} = -3.6^{\pm 3.5} \times 10^{-3}, \quad \boldsymbol{\delta g^Z_{dR}} = 16.0^{\pm 5.2} \times 10^{-3},
\end{aligned}$$

[d] This is not necessary true for effects that grow with energy and can be measured in VH associated production processes, as discussed in Ref. [14].

with a correlation matrix reported in Ref.[15]; from LEP2 data, on the other hand, we obtain[e] $\delta g_{1,Z} = -0.05^{+0.05}_{-0.07}$ and $\delta\kappa_\gamma = 0.05^{+0.04}_{-0.04}$.

On the other hand, the following effects, which also affect Higgs and EW physics, do not interfere with the SM:

$$\Delta\mathcal{L}_R^W = \boldsymbol{\delta g_R^W} \frac{\hat{h}^2}{v^2} W_\mu^+ \bar{u}_R \gamma^\mu d_R + \text{h.c.}\,, \tag{12}$$

$$\Delta\mathcal{L}^V_{\text{dipole}} = \frac{eY_q\hat{h}}{m_W^2}\Big[\boldsymbol{\delta\kappa_q^G}\frac{g_s}{e}\bar{q}_L T^A \sigma^{\mu\nu} q_R G^A_{\mu\nu} + \boldsymbol{\delta\kappa_q^A}(T_3\bar{q}_L\sigma^{\mu\nu}q_R A_{\mu\nu} + \frac{s_{\theta_W}}{\sqrt{2}}\bar{u}_L\sigma^{\mu\nu}d_R W^+_{\mu\nu}) + \boldsymbol{\delta\kappa_q^Z}(T_3\bar{q}_L\sigma^{\mu\nu}q_R Z_{\mu\nu} + \frac{c_{\theta_W}}{\sqrt{2}}\bar{u}_L\sigma^{\mu\nu}d_R W^+_{\mu\nu}) + \text{h.c.}\Big]\,, \tag{13}$$

for quarks $q = u, d$, where the coefficients are assumed to be real and T_3 denotes weak isospin (and similarly for leptons). Here $\boldsymbol{\delta g_R^W}$ is expected to be suppressed by both the down- and up-type Yukawas in a MFV expansion so that (together with the fact that it doesn't interfere with the SM and its contribution is therefore suppressed in inclusive quantities) it can be neglected. On the other hand the $\boldsymbol{\delta\kappa_q^V}$ can be measured in dipole-type experiments and we omit the result here.

Finally $\mathcal{L}_6$ includes interactions that do not involve the Higgs field. In particular

$$\Delta\mathcal{L}_{\lambda_\gamma} = \frac{i\boldsymbol{\lambda_\gamma}}{m_W^2}\left[(eA^{\mu\nu} + gc_{\theta_W}Z^{\mu\nu})W^-_\nu W^+_{\rho\mu}\right]\,, \quad \Delta\mathcal{L}_{3G} = \frac{\boldsymbol{\kappa_{3G}}}{m_W^2} g_s \epsilon_{ABC} G^{A\,\nu}_\mu G^{B}_{\nu\rho} G^{C\,\rho\mu}\,. \tag{14}$$

and four-fermion interactions, which can be found in [10]. LEP2 data[15] gives $\lambda_\gamma = 0.00^{+0.07}_{-0.07}$, while $\boldsymbol{\kappa_{3G}}$ and four-fermion interactions involving quarks can be constrained using dijet searches at the LHC [17]. Interactions involving leptons and quarks can be constrained at LEP [18] and LHC[6,19].

In summary, Eqs. (1-6) together with Eqs. (7-10), Eqs. (12,13), Eq. (14) and the four-fermion interactions, offer a complete parametrization of all BSM effects accessible at the leading order in an expansion in inverse powers of the new physics scale. They are organized in such a way that experimental (*input*) constraints can be readily implemented and the physical consequences quickly extrapolated, as we show in the next section.

3 Consequences

The main predictions from this analysis are the following[6,5] First of all, from Eqs. (7,8) it is clear that the Wff and Zff vertices are related at the level of $\mathcal{L}_6$, while the W dipole-type interaction for the fermions are related to those of A and Z as can be read from Eq. (13). Furthermore, there are only 3 types of CP-conserving TGC, characterized by[20] δg_1^Z, $\delta\kappa_\gamma$ and λ_γ, while QGC are related to them through

$$\boldsymbol{\delta g_1^Z} = \frac{\delta g^Z}{g^Z_{SM}} = \frac{\delta g^{WW}}{2c^2_{\theta_W} g^{WW}_{SM}} = \frac{\delta g^{ZZ}}{2g^{ZZ}_{SM}} = \frac{\delta g^{\gamma Z}}{g^{\gamma Z}_{SM}} \tag{15}$$

and Eq. (14). Finally, there are only 8 Higgs BSM primary effects (for one family), given in Eqs. (1-6), while all other Higgs interactions can be written as function of the parameters of $\mathcal{L}_6$ discussed so far. An interesting example is the differential distribution of $h \to Vff$[21,22,23,24,25,26,27,28,29], whose amplitude is generically written as

$$\mathcal{M}(h \to VJ_f) = (\sqrt{2}G_F)^{1/2}\epsilon^{*\mu}(q)\, J_f^{V\nu}(p)\left[\, A_f^V\, \eta_{\mu\nu} + B_f^V\, (p\cdot q\, \eta_{\mu\nu} - q_\mu p_\nu)\right]\,, \tag{16}$$

where q and p are respectively the total 4-momentum of V and the fermion pair in the J_f^V current ($J^\mu_{f_{L,R}} = \bar{f}_{L,R}\gamma^\mu f_{L,R}$), ϵ^μ is the polarization 4-vector of V, and I have defined

$$A_f^V = a_f^V + \widehat{a}_f^V \frac{p^2 + M_V^2}{p^2 - M_V^2}\,, \qquad B_f^V = b_f^V \frac{1}{p^2 - M_V^2} + \widehat{b}_f^V \frac{1}{p^2} \qquad (\widehat{b}_f^V = 0 \text{ for } V = W)\,. \tag{17}$$

[e] The extraction of these parameters from data, is complicated by the limited experimental information available, as discussed in Refs. [15,16].

Now, the coefficients a_f^V and b_f^V are associated with Lagrangian structures, such as $hV_{\mu\nu}V^{\mu\nu}$, whose coefficient in $\mathcal{L}_6$ can be readily read from the expressions in the previous section. For the case of $h \to Z\bar{l}l$, we find

$$\frac{\delta a^Z_{l_L}}{a^Z_{l_L}} \in [-0.2, 0.1]\,, \qquad \frac{\delta \widehat{a}^Z_{l_L}}{\widehat{a}^Z_{l_L}} \in [-8, 7] \times 10^{-2}\,, \quad b^Z_{l_L} \in [-2, 5] \times 10^{-2}, \qquad \widehat{b}^Z_{l_L} \in [-2, 5]\,, \times 10^{-2},$$
$$\frac{\delta a^Z_{l_R}}{a^Z_{l_R}} \in [-0.2, 0.3]\,, \qquad \frac{\delta \widehat{a}^Z_{l_R}}{\widehat{a}^Z_{l_R}} \in [-8, 7] \times 10^{-2}, \quad b^Z_{l_R} \in [-3, 2] \times 10^{-2}, \qquad \widehat{b}^Z_{l_R} \in [-2, 5] \times 10^{-2}\,.$$

Although the allowed range in $a^Z_{l_{L,R}}$ is quite large, we notice that their impact on the total amplitude, when summed over lepton chiralities, is much smaller, $2\sum_{l=l_L,l_R} g^l_Z a^Z_l / \sum_{l=l_L,l_R} (g^l_Z)^2 \in [-6, 4] \times 10^{-2}$. This implies that the expected BSM modification in the differential distribution of Higgs decay is already fairly constrained: our analysis sets the goal for future Higgs physics experiments to be competitive.

Interestingly, this differential distribution, although not directly tested by experimental collaborations so far, has been probed by measurements of the custodial parameter λ_{WZ} during LHC Run1. In fact, momentum-dependent deformations of the $hV\bar{f}f$ coupling behave differently when tested in $h \to W\bar{f}f'$ or $h \to Z\bar{f}f$, because of the difference between m_Z and m_W. In some sense, the custodial parameter λ_{WZ} is sensitive to the SM custodial symmetry breaking, through custodial-preserving momentum-dependent interactions. Through our analysis we find

$$\lambda_{WZ} - 1 \;\equiv\; \frac{\Gamma(h \to WW)}{\Gamma^{\rm SM}(h \to WW)} \frac{\Gamma^{\rm SM}(h \to ZZ)}{\Gamma(h \to ZZ)} - 1 \simeq 0.8 g_1^Z - 0.1\kappa_\gamma - 1.6\kappa_{Z\gamma} \in [-5, 6] \times 10^{-2}\,,$$

We see that Eq. (18) puts a bound on λ_{WZ} stronger than the experimental limit [8]: $(\lambda_{WZ} - 1) \in [-0.45, 0.15]$.

4 Conclusions

The SM EFT motivates SM precision tests, providing a framework in which searches for departures from the SM can be interpreted as searches for new physics and can be compared with direct searches of explicit models. In a bottom-up approach, the parameters characterizing the leading BSM piece of this effective Lagrangian, $\mathcal{L}_6$, can be fixed through the most precise SM precision tests. Then, since the parameters in $\mathcal{L}_6$ are less than the observables that are modified by $\mathcal{L}_6$, we can relate different observables and extract concrete, but generic, predictions. This task is facilitated by writing $\mathcal{L}_6$ in the *BSM Primaries* basis, where observables can be written in terms of other observables. Using this procedure, we have provided a quantitative prediction for the expected variation of the differential distribution of $h \to V\bar{f}f$ decays, for the custodial parameter λ_{WZ}, for the W couplings to fermions, for quartic gauge couplings and for dipole-type interactions involving the W-boson. These relations can be used to understand which observables deserve more attention in future experiments and which, instead, are already well measured.

Acknowledgments

I thank the organizers of Moriond 2015 for the invitation and for financial support, and I acknowledge support from the Swiss National Science Foundation, under the Ambizione grant PZ00P2 136932.

References

1. G. F. Giudice, C. Grojean, A. Pomarol and R. Rattazzi, "The Strongly-Interacting Light Higgs," JHEP **0706** (2007) 045 [hep-ph/0703164].

2. R. S. Gupta, M. Montull and F. Riva, "SUSY Faces Its Higgs Couplings," JHEP **1304** (2013) 132 [arXiv:1212.5240 [hep-ph]].
3. M. Montull, F. Riva, E. Salvioni and R. Torre, "Higgs Couplings in Composite Models," Phys. Rev. D **88** (2013) 095006 [arXiv:1308.0559 [hep-ph]].
4. B. Grzadkowski, M. Iskrzynski, M. Misiak and J. Rosiek, "Dimension-Six Terms in the Standard Model Lagrangian," JHEP **1010** (2010) 085 [arXiv:1008.4884 [hep-ph]].
5. R. S. Gupta, A. Pomarol and F. Riva, "Bsm Primary Effects," Phys. Rev. D **91** (2015) 3, 035001 [arXiv:1405.0181 [hep-ph]].
6. A. Pomarol and F. Riva, "Towards the Ultimate Sm Fit to Close in on Higgs Physics," JHEP **1401** (2014) 151 [arXiv:1308.2803 [hep-ph]].
7. E. Masso, "An Effective Guide to Beyond the Standard Model Physics," JHEP **1410** (2014) 128 [arXiv:1406.6376 [hep-ph]].
8. [ATLAS Collaboration], ATLAS-CONF-2013-034.
9. M. Montull and F. Riva, "Higgs Discovery: the Beginning Or the End of Natural Ewsb?," JHEP **1211** (2012) 018 [arXiv:1207.1716 [hep-ph]].
10. J. Elias-Miro, J. R. Espinosa, E. Masso and A. Pomarol, "Higgs Windows to New Physics Through D=6 Operators: Constraints and One-Loop Anomalous Dimensions," JHEP **1311** (2013) 066 [arXiv:1308.1879 [hep-ph]].
11. G. D'Ambrosio, G. F. Giudice, G. Isidori and A. Strumia, Nucl. Phys. B **645** (2002) 155.
12. A. Efrati, A. Falkowski and Y. Soreq, "Electroweak Constraints on Flavorful Effective Theories," arXiv:1503.07872 [hep-ph].
13. A. Falkowski, F. Riva and A. Urbano, "Higgs at Last," JHEP **1311** (2013) 111.
14. A. Biektter, A. Knochel, M. Krmer, D. Liu and F. Riva, "Vices and Virtues of Higgs Effective Field Theories at Large Energy," Phys. Rev. D **91** (2015) 055029.
15. A. Falkowski and F. Riva, "Model-Independent Precision Constraints on Dimension-6 Operators," JHEP **1502** (2015) 039 [arXiv:1411.0669 [hep-ph]].
16. G. Brooijmans, R. Contino, B. Fuks, F. Moortgat, P. Richardson, S. Sekmen, A. Weiler and A. Alloul *et al.*, "Les Houches 2013: Physics at TeV Colliders: New Physics Working Group Report," arXiv:1405.1617 [hep-ph].
17. O. Domenech, A. Pomarol and J. Serra, Phys. Rev. D **85** (2012) 074030.
18. S. Schael *et al.* [ALEPH and DELPHI and L3 and OPAL and LEP Electroweak Collaborations], "Electroweak Measurements in Electron-Positron Collisions at W-Boson-Pair Energies at Lep," Phys. Rept. **532** (2013) 119 [arXiv:1302.3415 [hep-ex]].
19. J. de Blas, M. Chala and J. Santiago, "Global Constraints on Lepton-Quark Contact Interactions," Phys. Rev. D **88** (2013) 095011 [arXiv:1307.5068 [hep-ph]].
20. K. Hagiwara, R. D. Peccei, D. Zeppenfeld and K. Hikasa, Nucl. Phys. B **282** (1987) 253.
21. S. Choi, D. J. Miller, 2, M. M. Muhlleitner, P. M. Zerwas, Phys. Lett. B **553** (2003) 61.
22. Q. -H. Cao, , et al.Phys. Rev. D **81** (2010) 015010.
23. Y. Gao, A. V. Gritsan, Z. Guo, K. Melnikov, M. Schulze and N. V. Tran, Phys. Rev. D **81** (2010) 075022 [arXiv:1001.3396 [hep-ph]].
24. D. Stolarski and R. Vega-Morales, Phys. Rev. D **86** (2012) 117504
25. G. Isidori, A. V. Manohar and M. Trott, arXiv:1305.0663 [hep-ph].
26. G. Isidori and M. Trott, arXiv:1307.4051 [hep-ph].
27. B. Grinstein, C. W. Murphy and D. Pirtskhalava, arXiv:1305.6938 [hep-ph].
28. M. Gonzalez-Alonso, A. Greljo, G. Isidori and D. Marzocca, "Pseudo-Observables in Higgs Decays," Eur. Phys. J. C **75** (2015) 3, 128 [arXiv:1412.6038 [hep-ph]].
29. M. Gonzalez-Alonso, A. Greljo, G. Isidori and D. Marzocca, "Electroweak Bounds on Higgs Pseudo-Observables and $h \to 4\ell$ Decays," arXiv:1504.04018 [hep-ph].

Higgs relaxation and the matter-antimatter asymmetry of the universe

Alexander Kusenko

Department of Physics and Astronomy, University of California, Los Angeles, CA 90095-1547, USA
Kavli Institute for the Physics and Mathematics of the Universe (WPI), University of Tokyo, Kashiwa, Chiba 277-8568, Japan

The recent measurement of the Higgs boson mass implies a relatively slow rise of the Standard Model Higgs potential at large scales, and a possible second minimum at even larger scales. Consequently, the Higgs field may develop a large vacuum expectation value during inflation. The relaxation of the Higgs field from its large postinflationary value to the minimum of the effective potential represents an important stage in the evolution of the universe. During this epoch, the time-dependent Higgs condensate can create an effective chemical potential for the lepton number, leading to a generation of the lepton asymmetry in the presence of some large right-handed Majorana neutrino masses. Electroweak sphalerons redistribute this asymmetry between leptons and baryons. Higgs relaxation leptogenesis can explain the observed matter-antimatter asymmetry of the universe even if the Standard Model is valid up to the scale of inflation, and any new physics is suppressed by that high scale.

1 Introduction

During cosmological inflation, scalar fields, including the Higgs field can deviate from the minimum of the effective potential developing a large vacuum expectation value (VEV).[1] The effect is most pronounced for those fields with flat directions in the effective potentials, or with relatively shallow minima. The recent discovery of the Higgs mass of 125 GeV has allowed extrapolations of the Higgs potential to large scales, leading to the conclusion that, at large VEV, the potential becomes less steep, and that it may, in fact develop an instability.[2] While this instability is probably cured by some new physics at a high scale, there relatively slow rise of the Higgs potential implies that it was likely to have a large VEV at the end of inflation.

Once the inflation is over, the Higgs mass must return to the minimum of the effective potential, and the epoch of Higgs relaxation can have observable consequences, such as the baryon asymmetry of the universe.[3,4] Not only the Higgs relaxation, but also an axion relaxation[5] or a Majoron relaxation[6] can lead to the generation of the matter-antimatter asymmetry of the universe.

2 Higgs relaxation after inflation

During de Sitter expansion, the Higgs field may be trapped in a quasistable second minimum or, alternatively, may develop a stochastic distribution of vacuum expectation values. The two possibilities, arising from different assumptions regarding the new physics at a high scale, are shown in Fig. 1. The initial condition in the case of the false vacuum (IC-1) produces an equal initial value of the field on superhorizon scales. At the end of inflation, reheating leads to a change in the effective potential, which eliminates the barrier, and the field starts rolling down the potential. The other possible initial conditions (IC-2) leads to some stochastic distribution of values for the Higgs field. In this case, some couplings between the Higgs field and the inflaton need to be introduced[3] to equalize the initial field values across superhorizon scales in order to avoid unacceptably large isocurvature perturbations.[7]

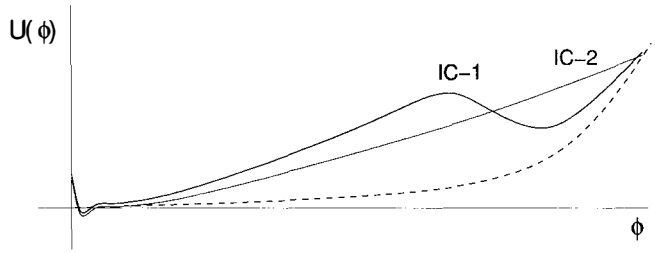

Figure 1 – Two possibilities for the initial conditions, as discussed in the text.

3 Leptogenesis via Higgs relaxation at high temperature

The motion of the Higgs field can generate an effective chemical potential in plasma, if new physics at a scale M_n gives rise to an operator

$$\mathcal{O}_6 = -\frac{1}{M_n^2}(\partial_\mu |\phi|^2)\, j^\mu, \tag{1}$$

where j^μ is the fermion current whose zeroth component is the density of $(B+L)$. This operator has been discussed in connection with spontaneous baryogenesis.[8] It breaks CPT spontaneously, and it generates an effective chemical potential in plasma leading to unequal energy levels between particles and antiparticles.

The amplitude of the oscillations of the Higgs field decreases with time (Fig.2), so that the first large swing dominates various effects of Higgs relaxation on plasma, and, during that time, the derivative $\partial_t \phi^\dagger \phi$ is negative at all points in space. Therefore, the shift in the energy levels of particles and antiparticles has the same sign everywhere.

While the energy levels of particles and antiparticles are biased by the effective chemical potential, any process allowing the violation of baryon or lepton number leads to a particle-antiparticle asymmetry. A heavy right-handed neutrino implied by the seesaw mechanism[9] can mediate such processes at high temperature via the diagrams shown in Fig.3.

A lepton asymmetry produced during the first large swing of the field undergoes partial washout in subsequent oscillations, and also after the oscillations subside. The lepton asymmetry is redistributed between leptons and baryons by the sphaleron transitions, as in thermal leptogenesis.[10] The final baryon asymmetry is consistent with the observed matter-antimatter asymmetry of the universe for some reasonable values of parameters.[10]

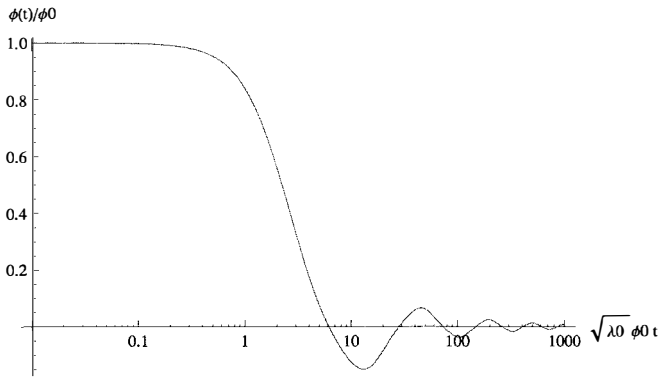

Figure 2 – Time dependence of the Higgs VEV at the end of inflation.

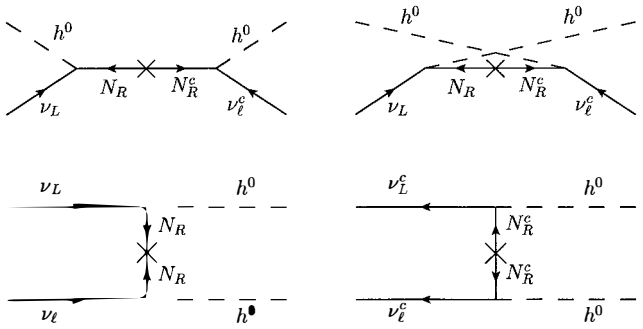

Figure 3 – Lepton number (and $B - L$) violating diagrams with the heavy virtual neutrino exchange.

4 Leptogenesis via Higgs relaxation and particle production

The scenario described above works for a relatively high reheat temperature, and the asymmetry is generated in plasma due to the presence of the effective chemical potential. In a different regime of parameters, the more important effect is the (non-thermal) particle production by the time-dependent, oscillating Higgs field.[4] The asymmetry between particles and antiparticles can still be produced by the $\mathcal{O}_6$ operator, which shifts the energy levels of particles as compared to antiparticles. The production rate is obtained by considering the Bogoliubov transformations for Majorana fermions in the presence of a time-dependent $\mathcal{O}_6$ operator, and a time-dependent effective mass[4].

This form of leptogenesis works particularly well when the Higgs condensate decays rapidly and at low reheat temperature.[4]

5 Conclusion

Higgs relaxation at the end of inflation is a time when the matter-antimatter asymmetry could develop by way of non-thermal leptogenesis.[3,4] Relaxation of an axion[5] or a Majoron[6] field offers an equally good opportunity for leptogenesis. This class of scenarios is different from other models of leptogenesis. In particular, the asymmetry can be generated for reheat temperatures

well below the righthanded neutrino masses. This allows, in particular, for a supersymmetric generalization of the model, in which the problem of gravitino overproduction may not arise. Furthermore, the final asymmetry does not depend on the parameters of the neutrino mass matrix as in thermal leptogenesis, and, therefore, a successful leptogenesis is possible even for the neutrino masses above 0.2 eV, in which case thermal leptogenesis is not possible due to an excessive washout.

6 Acknowledgements

I thank L. Pearce and L. Yang for a fruitful and enjoyable collaboration. This work was supported by the U.S. Department of Energy Grant DE-SC0009937 and by the World Premier International Research Center Initiative (WPI Initiative), MEXT, Japan.

References

1. T. S. Bunch and P. C. W. Davies, Proc. Roy. Soc. Lond. A **360**, 117 (1978); A. D. Linde, Phys. Lett. B **116**, 335 (1982); A. A. Starobinsky and J. Yokoyama, Phys. Rev. D **50**, 6357 (1994) K. Enqvist, T. Meriniemi and S. Nurmi, JCAP **1310**, 057 (2013) [arXiv:1306.4511 [hep-ph]].
2. J. R. Espinosa, G. F. Giudice and A. Riotto, JCAP **0805**, 002 (2008) [arXiv:0710.2484 [hep-ph]]; F. Bezrukov, M. Y. Kalmykov, B. A. Kniehl and M. Shaposhnikov, JHEP **1210**, 140 (2012) [arXiv:1205.2893 [hep-ph]].
3. A. Kusenko, L. Pearce and L. Yang, Phys. Rev. Lett. **114**, no. 6, 061302 (2015) [arXiv:1410.0722 [hep-ph]].
4. L. Pearce, L. Yang, A. Kusenko and M. Peloso, arXiv:1505.02461 [hep-ph].
5. A. Kusenko, K. Schmitz and T. T. Yanagida, arXiv:1412.2043 [hep-ph].
6. M. Ibe and K. Kaneta, arXiv:1504.04125 [hep-ph].
7. P. J. E. Peebles, Nature **327**, 210 (1987); Astrophys. J. Lett. **315**, 73 (1987); K. Enqvist and J. McDonald, Phys. Rev. Lett. **83**, 2510 (1999); Phys. Rev. D **62**, 043502 (2000); K. Harigaya, A. Kamada, M. Kawasaki, K. Mukaida and M. Yamada, Phys. Rev. D **90**, 043510 (2014).
8. A. G. Cohen and D. B. Kaplan, Phys. Lett. B **199**, 251 (1987); M. Dine, P. Huet, R. L. Singleton, Jr and L. Susskind, Phys. Lett. B **257**, 351 (1991).
9. T. Yangida, in Proceedings of the *"Workshop on the Unified Theory and the Baryon Number in the Universe"*, Tsukuba, Japan, Feb. 13-14, 1979, edited by O. Sawada and A. Sugamoto, [KEK report KEK-79-18; Conf. Proc., C70902131] 95-99; T. Yanagida, Prog. Theor. Phys. **64**, 1103 (1980); M. Gell-Mann, P. Ramond and R. Slansky, in *"Supergravity"* (North-Holland, Amsterdam, 1979) *eds.* D. Z. Freedom and P. van Nieuwenhuizen, Print-80-0576 (CERN); see also P. Minkowski, Phys. Lett. B **67**, 421 (1977).
10. M. Fukugita and T. Yanagida, Phys. Lett. B **174**, 45 (1986).

VACUUM STABILITY DEPENDS ON HIGH ENERGY PHYSICS SCALES[a]

VINCENZO BRANCHINA
Department of Physics and Astronomy, University of Catania, and INFN, Sezione di Catania
via S. Sofia, 63, I-95123, Catania, Italy

The stability analysis of the EW vacuum is usually presented with the help of a phase diagram in the $M_H - M_t$ plane. It has been recently shown that new physics interactions, even if they live at very high energy scales, can strongly affect the stability diagram. This result has far reaching theoretical and phenomenological consequences. In particular, despite claims to the contrary, higher precision measurements of the Higgs and top masses, M_H and M_t, will not tell us whether our universe is in a stable or in a metastable vacuum, nor if we live at the "edge of stability". Moreover, the strong sensitivity to new physics casts serious doubts on speculations and models based on the so called "criticality", the observation that the experimental (M_H, M_t) point lies close to the critical line, the line separating the stability from the instability region in the $M_H - M_t$ plane. In fact, new physics can significantly change the position of the critical line, thus making quite unlikely for our universe to live at the edge of stability. Finally, these results also show that candidate UV completions of the SM need to pass a sort of "stability test": only a model where the EW vacuum is stable or metastable, but with a lifetime larger than the age of the universe, can be considered as a viable UV completion of the SM.

1 Stability diagram: the usual analysis.

For our understanding of physics beyond the Standard Model (BSM), the knowledge of the stability condition of the electroweak (EW) vacuum is of the greatest importance. It is well known that due to the loop corrections coming from the quark top, the Higgs potential $V(\phi)$ turns over for values of $\phi > v$, where $v \sim 246$ GeV is the location of the EW minimum, and develops a second minimum at a very large value $\phi^{(2)}_{min}$. When the usual stability analysis is performed, the potential $V(\phi)$ is obtained by considering SM interactions only[5,6,7,8,9,10]. Depending on the values of the Higgs and top masses, M_H and M_t, the second minimum can be higher or lower than (or at the the same height of) the EW minimum.

When $V(\phi^{(2)}_{min}) < V(v)$, the EW vacuum is a metastable state, a *false vacuum*, and we have to consider its lifetime τ, i.e. the tunneling time from the false vacuum (v) to the true vacuum $(\phi^{(2)}_{min})$. At a certain $\phi = \phi_{inst}$, the potential reaches the same value it has at $\phi = v$,

[a]based on work done in collaboration with E. Messina A. Platania, M. Sher [1,2,3,4]

$V(\phi_{inst}) = V(v)$, successively taking lower values: for $\phi > \phi_{inst}$, $V(\phi) < V(v)$. The scale ϕ_{inst} is then the scale where the potential becomes unstable, the *instability scale* for short.

The stability analysis is usually presented with the help of a phase diagram in the $M_H - M_t$ plane. In fig. 1, the stability diagram for the usual analysis is presented. For those values of M_H and M_t such that $V(v) < V(\phi^{(2)}_{min})$, the EW vacuum is the absolute minimum of the potential, and we have the stability region. The instability region is obtained for $V(\phi^{(2)}_{min}) < V(v)$ and $\tau < T_U$, where T_U is the age of the Universe. Finally, the so called metastability region is for $V(\phi^{(2)}_{min}) < V(v)$, but $\tau > T_U$.

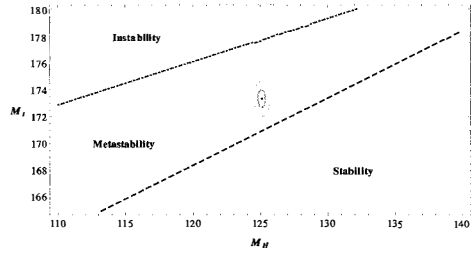

Figure 1 – The stability phase diagram as it results from the usual analysis, i.e. assuming that the presence of new physics interactions at high energy scales can be ignored. The $M_H - M_t$ plane is divided in three sectors, stability, metastability, and instability regions (see text). The dot indicates $M_H \sim 125.09$ GeV and $M_t \sim 173.34$ GeV. The ellipses give the one, two and three sigma errors.

It is worth to know that, for the central experimental values $M_H \sim 125.09$ GeV[11] and $M_t \sim 173.34$ GeV[12], $\phi_{inst} \sim 10^{11}$GeV $>> v$, the second minimum is at $\phi^{(2)}_{min} \sim 10^{30}$ GeV, and τ is much larger than T_U. Naturally, new physics interactions are expected to have an effect long before the scale $\phi^{(2)}_{min} \sim 10^{30}$ GeV is reached. Although we do not know where new physics appears, we certainly expect that, at least at very high energy scales (maybe the Planck scale M_P, if not before) new physics shows up. However, despite the presence of these new interactions, it is believed that τ can be calculated with the potential obtained with SM interactions only[5,6]. It is argued, in fact, that the relevant scale for tunneling is the instability scale $\phi_{inst} \sim 10^{11}$ GeV, and that the contribution to τ coming from very high (Planck) scale physics should be suppressed (decoupling)[6].

Contrary to these expectations, it has been shown that the presence of new physics at very high energy scales can strongly modify the stability condition of the EW vacuum[1,2,3]. The analysis presented in these works, however, is realized by parametrizing new physics interactions in terms of few higher order (non-renormalizable) operators. Some people then considered these results with a certain skepticism, suggesting that when the infinite tower higher dimensional operators of the renormalizable UV completion of the SM is taken into account, this effect should disappear, thus recovering the expected decoupling. Actually, the suspect is that this effect takes place above the physical cutoff, where the control of the theory is lost [13].

The introduction of few higher order operators, however, is just a convenient and efficient way of mimicking the presence of new physics, not a (clearly illegitimate) truncation of the UV completion of the SM[b]. Nevertheless, it is understandable that the parametrization of new physics in terms of higher order operators can be the source of a certain confusion and mislead the reader. The effect has nothing to do with this parametrization.

In the following, we investigate the impact of a *fully renormalizable* (toy) UV completion of the SM on the stability condition of the EW vacuum, when new physics interactions live at scales much higher than the instability scale ϕ_{inst}. According to the usual arguments[5,6], the

[b]Naturally, if we consider the expansion of the potential $V(\phi)$ in powers of ϕ, and we want to use this expansion up to very high energies, we have to take into account the whole tower of terms.

stability diagram should not be altered by this very high energy modification of the SM. In the following we show that this is not the case and discuss the origin and the consequences of this apparently unexpected effect.

2 A renormalizable toy UV completion of the Standard Model

The classical potential for the scalar sector of the SM is:

$$U(\Phi) = m^2 \left(\Phi^\dagger \cdot \Phi\right) + \lambda \left(\Phi^\dagger \cdot \Phi\right)^2 , \tag{1}$$

where Φ is the Higgs doublet

$$\Phi = \frac{1}{\sqrt{2}} \begin{pmatrix} -i(G_1 - iG_2) \\ \phi + iG_3 \end{pmatrix} , \tag{2}$$

ϕ the Higgs field and G_i the Goldstones.

The renormalizable (toy) UV completion of the SM that we use for our analysis is the following. We consider a new scalar field S and a new fermion field ψ that interact in a simple way with Φ, and have masses M_S and M_f well above the instability scale ϕ_{inst}: $M_S, M_f >> \phi_{inst}$. To the SM Lagrangian we add the mass and interaction terms:

$$\Delta\mathcal{L} = \frac{M_S^2}{2} S^2 + \frac{\lambda_S}{4} S^4 + 2g_S \left(\Phi^\dagger \Phi\right) S^2 + M_f \left(\bar{\psi}_L \psi_R + \bar{\psi}_R \psi_L\right) + \sqrt{2} g_f \left(\bar{\Psi}_L \Phi\, \psi_R + \bar{\psi}_R\, \Phi^\dagger \Psi_L\right) \tag{3}$$

(together with the S and ψ kinetic terms), where λ_S is the self-coupling of the new scalar S, g_S the coupling between Φ and S, ψ_L and ψ_R the left and right components of the Dirac field ψ with mass M_f, Ψ_L the left-handed $SU(2)$ fermion doublet $\Psi_L = (0, \psi_L)^T$ (we are not considering additional neutrinos), and g_f the Yukawa coupling between Ψ and the Higgs doublet.

For our purposes, it is useful to write the Lagrangian in Eq. (3) as:

$$\begin{aligned} \Delta\mathcal{L} &= \frac{M_S^2}{2} S^2 + \frac{\lambda_S}{4} S^4 + g_S \varphi^2 S^2 + M_f \bar{\psi}\psi + g_f \varphi \bar{\psi}\psi + g_S \left(G_1^2 + G_2^2 + G_3^2\right) S^2 \\ &+ g_f G_3 \bar{\psi} \left[\left(\frac{1+\gamma_5}{2}\right) + i \left(\frac{1-\gamma_5}{2}\right)\right] \psi . \end{aligned} \tag{4}$$

In fact, as we confine ourselves to consider the impact of these additional terms on the Higgs effective potential only at the one-loop level, in the following we do not need to consider further the second and the third lines in the above equation. The one-loop contribution to $V(\phi)$ from the terms in $\Delta\mathcal{L}$ is:

$$V_1(\phi) = \frac{\left(M_S^2 + 2g_S\phi^2\right)^2}{64\pi^2} \left[\ln\left(\frac{M_S^2 + 2g_S\phi^2}{M_S^2}\right) - \frac{3}{2}\right] - \frac{\left(M_f^2 + g_f^2\phi^2\right)^2}{16\pi^2} \left[\ln\left(\frac{M_f^2 + g_f^2\phi^2}{M_f^2}\right) - \frac{3}{2}\right] \tag{5}$$

According to the decoupling argument[6], these new physics interactions that live at very high energy scales ($M_S, M_f >> \phi_{inst} \sim 10^{11}$ GeV) should have no impact on the stability diagram of fig. 1. We now proceed with the analysis of the SM with the potential modified by the presence of the term (5), so to verify or disprove this expectation.

3 Stability analysis of the UV completed SM

The tunneling rate Γ, inverse lifetime time τ, is given by[14,15] (for the sake of simplicity, we write the formula with the contribution of the scalar sector of the SM only, the inclusion of the other contributions being straightforward. A more complete expression is given in Ref. 3):

$$\Gamma = \frac{1}{\tau} = T_U^3 \frac{S[\phi_b]^2}{4\pi^2} \left|\frac{\det'\left[-\partial^2 + V''(\phi_b)\right]}{\det\left[-\partial^2 + V''(v)\right]}\right|^{-1/2} e^{-S[\phi_b]} \tag{6}$$

where $\phi_b(r)$ is the $O(4)$ bounce solution to the euclidean equation of motion, $r = \sqrt{x_\mu x_\mu}$ is the radial coordinate in four euclidean dimensions, $S[\phi_b]$ is the action for the bounce, and $[-\partial^2 + V''(\phi_b)]$ is the fluctuation operator around the bounce (V'' is the second derivative of V with respect to ϕ). The prime in the det$'$ means that the zero modes are excluded, and $\frac{S[\phi_b]^2}{4\pi^2}$ comes from the translational zero modes.

Before we proceed with the calculation of τ for our UV completed SM, it is worth to consider the corresponding one when the presence of new physics interactions is ignored. For the present central values of M_H and M_t ($M_H = 125.09$ GeV and $M_t = 173.34$ GeV) it gives:

$$\tau \sim 10^{600}\, T_U\,. \tag{7}$$

This result is the basis for the so called metastability scenario. From Eq. (7), in fact, we would conclude that, although the EW minimum is a metastable state (and then a false vacuum), as its lifetime turns out to be much larger than the age of the universe, we may well live in such a state. In fig.1, we have presented the analysis in the whole $M_H - M_t$ plane, performed under the assumption (usually considered in the literature) that new physics interactions at scales $>> \phi_{inst}$ have no impact on the stability condition of the EW vacuum[5,6]. The black dot corresponds to the tunneling time of Eq. (7). The ellipses give the one, two and three sigma errors.

We move now to the computation of the EW vacuum lifetime for our model with new physics at high energy scales, and consider two examples. By starting with taking $M_S = 1.2 \cdot 10^{18}$ GeV, $M_f = 0.6 \cdot 10^{17}$ GeV, $\lambda_S = 0.5$, $g_S = 0.97$, $g_f^2 = 0.48$, $\lambda = \lambda(\mu = M_S) = -0.015$ (where λ is the usual quartic coupling), we find that the Higgs potential $V(\phi)$ develops a new minimum, lower than the EW one, at $\phi_{min}^{(2)} \sim 0.4 \cdot 10^{19}$ GeV. To study the stability condition of the EW vacuum, we have then to calculate the EW vacuum lifetime τ. For the present central experimental values of the Higgs and top masses ($M_H = 125.09$ GeV and $M_t = 173.34$ GeV) we find:

$$\tau \sim 10^{180}\, T_U\,. \tag{8}$$

This result has to be compared with the tunneling time of Eq.(7), obtained by considering the SM potential alone (no new physics included). Although for the example considered here the tunneling time is still much higher than the age of the Universe, Eq. (8) gives a result that is greatly different from the one of Eq.(7).

If we now consider another example, namely we take $M_S = 1.2 \cdot 10^{18}$ GeV, $M_f = 2.4 \cdot 10^{15}$ GeV, $\lambda_S = 0.5$, $g_S = 0.97$, $g_f^2 = 0.48$, and $\lambda = \lambda(\mu = M_S) = -0.015$, by considering the same values for M_H and M_t we find:

$$\tau \sim 10^{-65}\, T_U\,. \tag{9}$$

In this case, the situation is more dramatic than in the previous example: the tunneling time turns out to be much smaller than the age of the Universe. If realistic, the model with these values of the parameters could not be considered as a viable UV completion of the SM.

The lesson from Eqs. (7), (8), and (9) is clear. The expectation that the tunneling time should be insensitive to physics that lives at energies higher than the instability scale, in other words that the result in Eq. (7) should not be modified by the presence of new physics at high energies, is not fulfilled.

The question is then: why the decoupling argument is not operating? The reason is that the decoupling theorem applies when we calculate scattering amplitudes at energies E lower than M_S and M_f. In these cases, the contributions from high energy new physics is suppressed by factors as E/M_S and E/M_f to some appropriate power. In our case, however, we are computing the tunneling time. Tunneling is a non-perturbative phenomenon, and no decoupling applies: in the calculation of τ, no naive suppression factor, ϕ_{inst}/M_S or ϕ_{inst}/M_f, appears. More specifically, the tunneling time τ is essentially given by the exponential $e^{S[\phi_b]}$ (see Eq. (6)). If the Higgs potential is modified by the presence of terms as the one in Eq. (5), the new bounce turns out to be different from the one obtained when this term is absent. The action $S[\phi_b]$ is then modified.

Once exponentiated, it gives rise to a value for τ that can be greatly different from the result obtained when new physics is not considered.

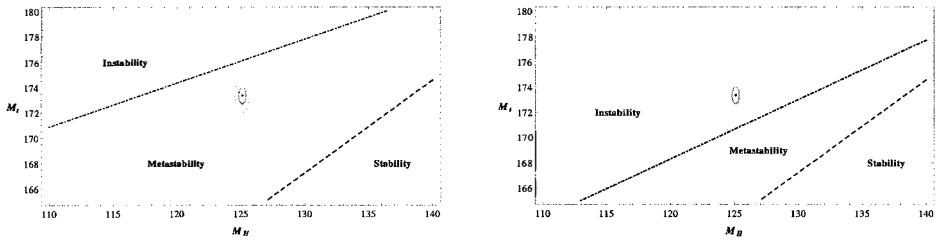

Figure 2 – Left panel: The stability phase diagram for the toy UV completed SM considered in the text and for the following values of the parameters: $M_S = 1.2 \cdot 10^{18}$ GeV, $M_f = 0.6 \cdot 10^{17}$ GeV, $\lambda_S = 0.5$, $g_S = 0.97$, $g_f^2 = 0.48$, $\lambda(\mu = M_S) = -0.015$. As in fig. 1, the $M_H - M_t$ plane is divided in three sectors: stability, metastability, and instability regions. However, compared to the fig. 1 case, the stability and instability lines have moved downwards. Right panel: the same as the left panel, but for different values of the parameters (see text). These two pictures, together with fig. 1, clearly show the main point of the present work, namely that the stability diagram strongly depends on new physics, even when the latter lives at very high energy scales.

We go on now with our analysis. In fig.1 we have shown the stability diagram in the $M_H - M_t$ plane obtained under the assumption that the stability analysis should not depend on new physics that lives at high energy scales. The examples that we have just considered, with the results (7), (8) and (9), indicate that we should on the contrary expect that the stability phase diagram depends on new physics, even if the latter lives at very high energy scales. Still referring to fig.1, we point out that the dashed and the dashed-dotted lines are respectively named the stability line and the instability line. The first one is obtained for those couples of values of M_H and M_t such that the two minima are at the same height, the latter is obtained for the case when $V(\phi^{(2)}_{min}) < V(v)$ and $\tau = T_U$.

Let us repeat this stability analysis when the term (3), i.e. our toy UV completion of the SM, is added to the SM Lagrangian, so that the term (5) is added to the Higgs effective potential. In fig. 2 (left panel), the analysis is performed for the values of the parameters considered in our first example, namely $M_S = 1.2 \cdot 10^{18}$ GeV, $M_f = 0.6 \cdot 10^{17}$ GeV, $\lambda_S = 0.5$, $g_S = 0.97$, $g_f^2 = 0.48$, $\lambda = \lambda(\mu = M_S) = -0.015$.

We first note that the instability line moves downwards. This result had to be expected from the previous results for the tunneling time (see Eqs. (7) and (8)). In fact, we obtained $\tau \sim 10^{180} T_U$ for the UV completed Higgs potential and $\tau \sim 10^{600} T_U$ for the SM Higgs potential. In the case of the UV completed potential, the black dot (experimental point) must be closer to the instability line than in the case of the unmodified potential. The grey lines in fig. 2 are the old instability and stability lines obtained in the case of the unmodified Higgs potential (fig. 1).

Another important result is that even the stability line moves downwards (see fig. 2). When the stability diagram of fig. 1 was thought to be universal (i.e. when it was thought that a decoupling effect assured that new physics at high scales could not modify this diagram), many speculations were triggered by the fact that the experimental point (black dot in the figure), $M_H \sim 125.09$ GeV and $M_t \sim 173.34$ GeV, lies (within 3 sigma) "close" to the stability line. In this respect, it was thought that more refined measurements of M_t and M_H should allow to determine wether the EW vacuum is a stable or a metastable state. Some authors even considered this closeness of the experimental point to the stability line as the most important message from LHC[10], speculating on this closeness and elaborating on it for model building[13].

The results that we have just presented show that the stability condition of the EW vacuum is much more sensitive to high energy new physics than to the values of the Higgs and top masses. Therefore, more refined measurements of M_t and M_H, that are certainly very important for several other reasons, will not allow to determine the stability condition of the EW vacuum.

Speculations and model building based on the so called "criticality condition" seem to be founded on a very unstable result. New physics at high energies actually changes (for the worse) the distance between the experimental point and the critical line, thus greatly weakening (if not excluding) arguments based on this supposed criticality.

In fig. 2 (right panel), the stability diagram for our model with the values of the parameters considered in our second example ($M_S = 1.2 \cdot 10^{18}$ GeV, $M_f = 2.4 \cdot 10^{15}$ GeV, $\lambda_S = 0.5$, $g_S = 0.97$, $g_f^2 = 0.48$, $\lambda = \lambda(\mu = M_S) = -0.015$) is presented. The instability and stability lines move downwards as for the previous case. In this case, however, the tunneling time for the experimental point is much shorter than the age of the Universe, see Eq. (9), and in fact we see that the experimental point is now inside the instability region. This means that the model with these values of the parameters cannot be considered as a viable UV completion of the SM.

This result also contains another important lesson. We have seen that he stability condition of the EW vacuum is strongly sensitive to high energy new physics. Therefore, as we cannot rely on any high energy decoupling, candidate UV completions of the SM models have to pass a sort of stability test: only models with a stable or metastable (but with $\tau > T_U$) EW vacuum can be considered as viable UV completions of the SM.

4 Conclusions

By considering a fully renormalizable (toy) UV completion of the SM, we have definitely shown that new physics interactions, even if they live at very high energy scales, can strongly affect the stability diagram of the SM. This result has far reaching theoretical and phenomenological consequences.

Despite claims to the contrary, it shows that higher precision measurements of M_t and M_H will never tell us whether our universe lives in a stable or in a metastable vacuum, or at the "edge of stability" (near the critical line).

Moreover, as very high energy new physics can significantly modify the position of the critical line, it is quite unlikely that our universe lives at the "edge of stability", i.e. near the critical line. This strongly weakens (if not invalidates) speculations and model building based on this so called "criticality".

Finally, this result shows that candidate UV completions of the SM need to pass a sort of "stability test". Only models with a stable or metastable (but with $\tau > T_U$) vacuum can be considered as viable UV completions of the SM.

References

1. V. Branchina and E. Messina, Phys. Rev. Lett. 111 (2013) 241801.
2. V. Branchina, E. Messina and A. Platania, JHEP 1409 (2014) 182.
3. V. Branchina, E. Messina and M. Sher, Phys.Rev. D91 (2015) 1, 013003.
4. V. Branchina and E. Messina, in preparation.
5. G. Isidori, G. Ridolfi, A. Strumia, Nucl. Phys. B609 (2001) 387.
6. J. R. Espinosa, G. F. Giudice and A. Riotto, JCAP **0805**, 002 (2008).
7. F. Bezrukov, M. Yu. Kalmykov, B. A. Kniehl, M. Shaposhnikov, JHEP 1210 (2012) 140.
8. J. Elias-Miro, J.R. Espinosa, G.F. Giudice, *et al.*, Phys. Lett. B709 (2012) 222.
9. G. Degrassi, S. Di Vita, J. Elias-Miro, *et al.*, JHEP 1208 (2012) 098.
10. D. Buttazzo, G. Degrassi, P. P. Giardino, *et al.*, JHEP 1312 (2013) 089.
11. G. Aad et al. (The ATLAS and CMS Collaborations), Phys.Rev.Lett. 114 (2015) 191803.
12. ATLAS, CDF, CMS, D0 collaborations, arXiv:1403.4427.
13. J. R. Espinosa, G. F. Giudice, E. Morgante, *et al.*, arXiv:1505.04825 [hep-ph].
14. S. Coleman, Phys. Rev. D15 (1977) 2929.
15. C. G. Callan, S. Coleman, Phys. Rev. D16 (1977) 1762.

ON THE ORIGIN OF SCALES AND INFLATION

ALBERTO SALVIO
Departamento de Física Teórica, Universidad Autónoma de Madrid and Instituto de Física Teórica IFT-UAM/CSIC, Madrid, Spain

Report number: IFT-UAM/CSIC-15-033

We give an overview of theories of all interactions (including gravity) in the absence of fundamental scales: *agravity*. All observed masses, such as the Planck and the weak scales, are generated by quantum corrections. The main observational implications for the physics at colliders as well as for cosmology are outlined.

1 Introduction

Two types of motivations for the theories defined in the abstract come to mind.

First, the generation of the Planck and weak scales can be achieved naturally, thereby solving the (fine-tuning) hierarchy problem. As we will see, the mechanism employed to do so differs from standard solutions, such as supersymmetry, where an extra symmetry is introduced to protect the mass M_h of the Standard Model (SM) physical scalar h: within agravity all possible new particles that acquire masses $M \gg M_h$ can have tiny couplings to the SM; this avoids large quantum corrections to M_h.

Second, theories of this sort that remain perturbative at the inflationary scales provide naturally flat inflaton potentials. To explain this point in simple terms let us assume that inflation is driven by a single field I (as we will see this is not necessarily the case). The most general classical action for the self-interactions of I and its couplings to gravity has only two terms:

$$\int d^4x\sqrt{g}\left(-\frac{f(I)}{2}R - V(I)\right), \qquad f(I) = \xi_I I^2, \quad V(I) = \frac{\lambda_I}{4}I^4 \tag{1}$$

where g is the modulus of the determinant of the metric $g_{\mu\nu}$ and R is the Ricci scalar. Notice that the functions f and V are fixed by the no-scale principle. The first term is a non-minimal coupling to gravity, which would make the analysis non-standard, but one can go to a frame where the couplings to gravity are minimal (i.e. Einstein frame), by redefining the metric as $g^E_{\mu\nu} \equiv g_{\mu\nu}f(I)/\bar{M}^2_{\rm Pl}$, where $\bar{M}_{\rm Pl} \simeq 2.4 \times 10^{18}$ GeV is the reduced Planck mass. The potential of I in the Einstein frame is

$$V_E(I) = \frac{\bar{M}^4_{\rm Pl}V(I)}{f(I)^2} = \frac{\bar{M}^4_{\rm Pl}\lambda_I}{4\xi_I^2}, \tag{2}$$

which is flat. Once quantum corrections are included ξ_I and λ_I acquire a dependence on I that is encoded in the renormalization group equations (RGEs). However, perturbativity at the inflationary scales (which we can obtain [1]) ensures that such dependence is small.

This contribution to the proceedings of the 50$^{\rm th}$ Rencontres de Moriond is mainly based on three articles [1,2,3], which I will refer to as I, II and III respectively.

2 Agravity scenario

The *most general* agravity action is

$$S = \int d^4x\sqrt{g}\left(\mathcal{L}_{\rm SM}^{\rm adim} + \mathcal{L}_{\rm BSM}^{\rm adim} + \frac{R^2}{6f_0^2} + \frac{\frac{1}{3}R^2 - R_{\mu\nu}^2}{f_2^2}\right). \tag{3}$$

It consists of two parts.

The first one is the non-gravitational part, described by $\mathcal{L}_{\rm SM}^{\rm adim} + \mathcal{L}_{\rm BSM}^{\rm adim}$. Here $\mathcal{L}_{\rm SM}^{\rm adim}$ is the no-scale SM Lagrangian: namely the SM Lagrangian without the H mass term $m_h^2|H|^2/2$ plus a possible non-minimal coupling $-\xi_H|H|^2R$, where H is the SM doublet; this represents the most general no-scale Lagrangian constructed with only SM fields and their interactions with gravity. $\mathcal{L}_{\rm BSM}^{\rm adim}$ is a beyond the SM (BSM) no-scale Lagrangian, which should account for the observational problems of the SM (e.g. neutrino oscillations, dark matter, baryon asymmetry, the strong CP problem, etc [4]) and generate the scales we see in nature. In order to do so one should include at least one extra real scalar s. Indeed, the possible terms in the Lagrangian $\lambda_{HS}|H|^2s^2/2 - \xi_S s^2R/2$ respectively generate the H mass term and the Planck scale once s acquires a vacuum expectation value (VEV) at quantum level.

The second part of the action is the gravity sector, described by the third and fourth terms in Eq. (3), where $R_{\mu\nu}$ is the Ricci tensor. A remarkable property of this theory is its renormalizability, which allows us to obtain predictions up to infinite energies [a]. However, this comes with a price. By studying the spectrum one finds three states: a massless graviton, which is responsible for the large distance gravitational interactions we are used to, an extra real scalar (graviscalar henceforth) with mass $|f_0|\bar{M}_{\rm Pl}/\sqrt{2}+\ldots$, where the dots are corrections coming from the mixing with other possible scalars, and a massive graviton with mass $M_2 = |f_2|\bar{M}_{\rm Pl}/\sqrt{2}$ and negative norm [5] (i.e. a ghost). Although the energy of the theory is bounded from below there is currently no proof that the latter state can have a sensible physical interpretation. However, a no-go theorem is also not known; thus in the rest of this article we will simply assume that such interpretation exists and discuss the main phenomenological implications.

3 Quantum corrections and generation of scales

The quantum corrections are mostly encoded in the RGEs, which are important to generate the scales we observe and to extract inflationary predictions. For this reason, in Article I we obtained the full set of one-loop RGEs for the most general agravity theory, Eq. (3). This generalizes previous computations [6,7,8] performed without gravity.

3.1 Dynamical generation of the Planck scale

Once the RGEs are known one can study the possible generation of scales, starting from the one we are familiar with, the gravitational constant of Newton's law (i.e. the Planck scale).

Agravity successfully generates $\bar{M}_{\rm Pl}$ if the VEV $\bar{s}$ of the scalar s fulfills the following conditions:

$$\begin{cases} \lambda_S(\bar{s}) \simeq 0 & \leftrightarrow \text{ nearly vanishing cosmological constant (dark energy)} \\ \frac{d\lambda_S}{ds}(\bar{s}) = 0 & \leftrightarrow \text{ minimum condition} \\ \xi_S(\bar{s})\bar{s}^2 = \bar{M}_{\rm Pl}^2 & \leftrightarrow \text{ observed Planck mass} \end{cases}$$

where λ_S is the quartic self-coupling of s and ξ_S is its non-minimal coupling to gravity: in the Lagrangian these couplings appear as $-\lambda_S s^4/4 - \xi_S s^2R/2$.

[a] In fact, even if we do not introduce those terms in the classical Lagrangian, they are generated by quantum corrections.

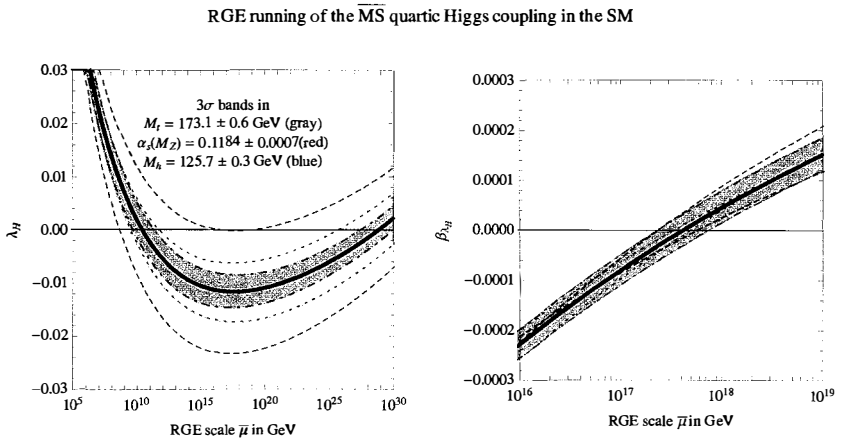

Figure 1 – Running of λ_H (left) and its β-function (right) in the SM [10]: λ_H appears in the potential in a term $\lambda_H|H|^4$, while its β-function is defined by $\beta_{\lambda_H} \equiv d\lambda_H/d\ln\bar{\mu}$. Figure reproduced from Article I.

It is possible to fulfill these conditions: remarkably, this is what happens in the SM for h and top masses around $M_h \approx 125\,\text{GeV}$ and $M_t \approx 171\,\text{GeV}$ (see [b] Fig. 1). Although s and h cannot be identified as their VEVs should differ by several orders of magnitude, this argument clearly shows that we can build concrete models (in fact many models) that generate the Planck scale.

3.2 Observational implications for cosmology

After generating $\bar{M}_{\rm Pl}$ one can study inflation in agravity. How the weak scale is obtained will be discussed later on because M_h is negligible compared to inflationary scales.

Generically inflation in this theory is a multifield process: there are at least three scalar fields (the SM scalar h, the Planckion s and the graviscalar z). By studying the dynamics of h, s and z in the minimal realistic model [2], we found that inflation occurs once an attractor in the plane of s and z is reached [c]. This has two consequences. First, h never dominates inflation: the reason is that the h quartic self-coupling (assumed to be positive) is unavoidably larger than the other scalar couplings, taking into account its RGE running [9,10,11,12]. Second, the presence of an attractor fortunately ensures that the observable predictions do not depend on the chosen initial field values for a given number of e-folds N. Another important parameter is the ratio between $M_0^2 = f_0^2\bar{M}_{\rm Pl}^2(1+6\xi_S)/2$ and $M_s^2 = \partial^2 V/\partial s^2$, where V is the potential of s: when $M_0/M_s \ll 1$ the scalar s becomes very massive and gets frozen to $\bar{s}$; in this case we recover Starobinsky inflation, which gives a small value of the tensor-to-scalar ratio r, of order of 0.001; in the opposite limit it is the other scalar that becomes very massive and we find a sizable value, $r \sim 0.1$. All the intermediate values of r can be obtained for an appropriate M_0/M_s, while the prediction for the scalar spectral index n_s is steadily close to $n_s \approx 0.97$. These findings are in good agreement with a global fit of the most recent studies by PLANCK and BICEP2/KECK [13,14,15,16]. In Fig. 2 there is a more quantitative description of the predictions and the comparison with data. Moreover, in Article II one can see how matching the scalar amplitude P_R with observations requires generically $f_0 > 10^{-5}$.

[b] The RGEs used in this article are defined in the $\overline{\rm MS}$ renormalization scheme and the RGE sliding scale is denoted by $\bar{\mu}$.

[c] See Fig. 4 of Article II.

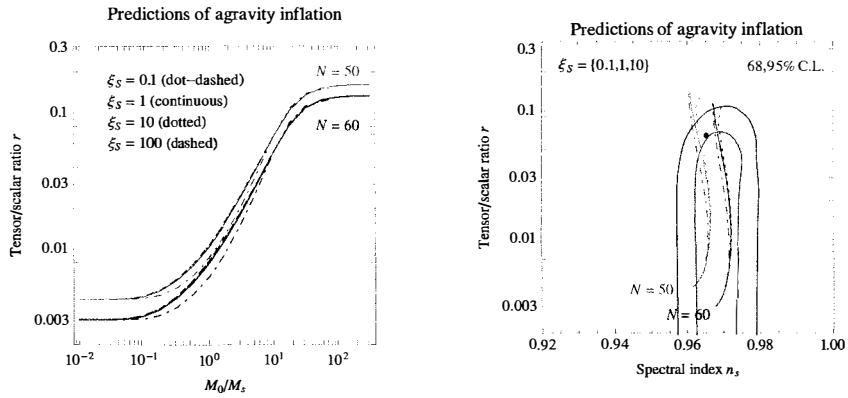

Figure 2 – **Left:** predictions for the tensor-to-scalar ratio r after $N = 50$ or 60 e-folds of inflation for various values of ξ_S as function of M_0/M_s. In the limit where this ratio is large (small) inflation is dominated by the Planckion (the graviscalar). **Right:** predictions for the scalar spectral index n_s and r with the same coding. The green area is favored by a global fit of PLANCK, BICEP2/KECK [13,14,15,16]. Figure reproduced from Article II.

Article II also provided a study of cosmology after inflation. The inflaton decays occur via Planck-suppressed interactions (it couples to a combination of the trace of the energy momentum tensor and of the divergence of the dilatation current) producing a reheating temperature $T_{\rm RH} \sim 10^{7-9}$ GeV. Also, the s-sector must contain fermions that either behave as right-handed neutrinos (if they have no gauge interactions) or are stable. In the latter case, they might be light enough that the inflaton can decay into them, providing the observed Dark Matter abundance with adiabatic primordial inhomogeneities if their mass is around $10 - 200$ TeV.

3.3 Natural dynamical generation of the weak scale

The VEV of s, besides generating the Planck scale, also induces the weak scale. We here describe how these scales can coexist naturally (i.e. avoiding the hierarchy problem). Let us divide the discussion in three energy ranges.

First, focus on $\bar{\mu} < M_{0,2}$. In this case the RGE of m_h is well approximated by the SM one, where m_h is the only mass parameter and therefore one does not see any unnaturally large corrections to m_h.

The situation is more complicated for $M_{0,2} < \bar{\mu} < \bar{M}_{\rm Pl}$, where the RGE for $m_h/\bar{M}_{\rm Pl}$ shows a potentially dangerous term,

$$(4\pi)^2 \frac{d}{d\ln\bar{\mu}} \frac{m_h^2}{\bar{M}_{\rm Pl}^2} = -\xi_H[5f_2^4 + f_0^4(1+6\xi_H)] + \dots , \tag{4}$$

where the dots represent terms that are harmless from the point of view of naturalness [1]. By looking at the RGEs for f_0, f_2 and the ξ couplings, presented in Articles I and II, one finds that a way to obtain the small ratio $m_h/\bar{M}_{\rm Pl} \sim 10^{-16}$ naturally is to impose $f_2 \sim 10^{-8}$ and $1 + 6\xi_H \sim f_2^4/(4\pi f_0)^2$, which can accommodate the value of $f_0 > 10^{-5}$ generically required to match the (inflationary) scalar amplitude.

In the large energy range, $\bar{\mu} > \bar{M}_{\rm Pl}$, the theory is dimensionless and m_h arises from the interaction $\lambda_{HS}|H|^2 s^2/2$, which leads to

$$m_h^2 = \lambda_{HS}\bar{s}^2. \tag{5}$$

Since $\bar{s} \sim \bar{M}_{\rm Pl}$, this requires a tiny value of $\lambda_{HS} \sim 10^{-32}$. The structure of the RGE of λ_{HS} (presented in Article I) are naturally compatible with this small number and the measured scalar amplitude as long as the setting for f_2 and $1 + 6\xi$ discussed in the previous paragraph holds.

Intuitively, Eqs. (4) and (5) tell us that there is a contribution to m_h^2 of the form

$$\delta m_h^2 \sim f^4 M^2, \tag{6}$$

where f is a coupling constant and M is a new mass scale. Therefore, although the difference between m_h and $\bar{M}_{\rm Pl}$ is large, naturalness can be preserved if the smallness of f is compatible with the RGE running. A novel feature here is that a symmetry is not required to protect m_h even if $M \gg m_h$ because some couplings can be small [17]. Possible quadratic divergences with respect to some particular regulator, such as the lattice, are not regarded here as a problem: they do not appear for other regulators, e.g. dimensional regularization [d], and we therefore do not attribute to them a physical meaning.

4 Unification, final theories and experimental consequences at colliders

Agravity provides an alternative solution of the hierarchy problem. Since this problem is most evident in unified models, it is also interesting to ask whether unification can be achieved in this scenario. Here "unification" means embedding the SM into a BSM model without gauge U(1) factors, leading to an explanation for the observed charge quantization. This typically requires new physics with non-negligible couplings to the SM particles. Thus, in practice naturalness tells us that the masses of these new states should not be too far from m_h (see Eq. (6)). Barring symmetries protecting m_h, simple gauge groups, such as SU(5) or SO(10), are not natural as the experimental bounds on proton decay imply large vector boson masses, $M \gg m_h$, that contribute too much to m_h. A possible solution is to use semi-simple gauge groups: the Pati-Salam SU(4)×SU(2)×SU(2) or the trinification SU(3)×SU(3)×SU(3) groups. The new states contained in these theories can be accessible at the LHC or at future colliders.

In the context of agravity there is another reason for unification. The action in (3) is renormalizable and, therefore, can be used to study arbitrarily high energies. A problem in this case, however, is the presence of Landau poles in the SM: e.g. the hypercharge gauge coupling g_Y diverges within perturbation theory at $\sim 10^{42}\,$GeV. A necessary condition to avoid these poles perturbatively is to eliminate any gauge U(1) factor, in other words to have unification. Indeed, in the SM the Landau poles are eliminated only for the unphysical choice [3] $g_Y = 0$ (as well as $M_t = 186\,$GeV, $M_\tau = 0$, $M_h = 163\,$GeV). Realistic theories without Landau poles can be considered as candidate final theories as they describe physics without any energy cut-off. Article III provided a general technique to search for such theories and found examples based on the Pati-Salam group. These examples are, however, affected by a residual little fine-tuning: limits from precision and flavor physics imply [e] that the mass of some vector leptoquarks W'_μ, of charge $\pm 2/3$, corresponding to the broken generators in $SU(4)/SU(3)_c$, is above the TeV scale. An interesting outlook is the quest for other explicit examples where all masses are generated by quantum corrections (as required by the agravity principle).

5 Conclusions

A natural hierarchy between the weak and the Planck scales and a rationale for inflation can be obtained in theories of all interactions (including gravity) in the absence of fundamental scales; we referred to this class of theories as agravity.

Regarding inflation, we found $n_s \approx 0.967$ and $0.003 < r < 0.13$, in agreement with PLANCK and BICEP2/KECK [13,14,15,16]. We observe that a future measurement of r by KECK/BICEP3 would give us more constraints on this scenario.

[d] Divergences of the form $m^2/(d-4)$, where m is a mass and d is the space-time dimension, do not appear simply because there are no masses.

[e] The existence of other examples where this situation is improved is not excluded [3].

The mechanism used here to have naturalness differs from standard solutions, based on symmetries: here a naturally small m_h is obtained by requiring the new physics to be light and/or weakly coupled to h. This is also compatible with unification in the case of Pati-Salam or trinification models, which predict new particles (e.g. W', Z', ...) that are accessible at the LHC or future colliders.

Unification here is also motivated by the requirement to have a consistent theory that is valid up to infinite energies. Indeed, at the perturbative level, such a requirement tells us that the SM should be embedded in a BSM model without Landau poles, which excludes, among other things, any gauge U(1) factor.

Acknowledgments

I thank A. Strumia, K. Kannike, G. Hütsi, L. Pizza, A. Racioppi, M. Raidal, G. F. Giudice, G. Isidori for collaborating with me to realize Articles I, II and III respectively. I thank the organizers of the 50$^{\text{th}}$ Rencontres de Moriond for the invitation to give a talk. This work is supported by the Spanish Ministry of Economy and Competitiveness under grant FPA2012-32828, Consolider-CPAN (CSD2007-00042), the grant SEV-2012-0249 of the "Centro de Excelencia Severo Ochoa" Programme and the grant HEPHACOS-S2009/ESP1473 from the C.A. de Madrid.

References

1. A. Salvio and A. Strumia, JHEP **1406** (2014) 080 [arXiv:1403.4226 [hep-ph]].
2. K. Kannike, G. Hütsi, L. Pizza, A. Racioppi, M. Raidal, A. Salvio and A. Strumia, arXiv:1502.01334 [astro-ph.CO].
3. G. F. Giudice, G. Isidori, A. Salvio and A. Strumia, JHEP **1502** (2015) 137 [arXiv:1412.2769 [hep-ph]].
4. A. Salvio, Phys. Lett. B **743**, 428 (2015) [arXiv:1501.03781 [hep-ph]].
5. K. S. Stelle, Phys. Rev. D **16**, 953 (1977).
6. M. E. Machacek and M. T. Vaughn, Nucl. Phys. B **222**, 83 (1983).
7. M. E. Machacek and M. T. Vaughn, Nucl. Phys. B **236**, 221 (1984).
8. M. E. Machacek and M. T. Vaughn, Nucl. Phys. B **249**, 70 (1985).
9. G. Degrassi, S. Di Vita, J. Elias-Miro, J. R. Espinosa, G. F. Giudice, G. Isidori and A. Strumia, JHEP **1208**, 098 (2012) [arXiv:1205.6497 [hep-ph]].
10. D. Buttazzo, G. Degrassi, P. P. Giardino, G. F. Giudice, F. Sala, A. Salvio and A. Strumia, JHEP **1312**, 089 (2013) [arXiv:1307.3536 [hep-ph]].
11. F. Bezrukov and M. Shaposhnikov, JHEP **0907**, 089 (2009) [arXiv:0904.1537 [hep-ph]].
12. A. Salvio, Phys. Lett. B **727**, 234 (2013) [arXiv:1308.2244 [hep-ph]].
13. P. A. R. Ade *et al.* [BICEP2 and Planck Collaborations], Phys. Rev. Lett. **114**, no. 10, 101301 (2015) [arXiv:1502.00612 [astro-ph.CO]].
14. P. A. R. Ade *et al.* [BICEP2 and Keck Array Collaborations], arXiv:1502.00643 [astro-ph.CO].
15. P. A. R. Ade *et al.* [Planck Collaboration], arXiv:1502.01589 [astro-ph.CO].
16. P. A. R. Ade *et al.* [Planck Collaboration], arXiv:1502.02114 [astro-ph.CO].
17. M. Farina, D. Pappadopulo and A. Strumia, JHEP **1308**, 022 (2013) [arXiv:1303.7244 [hep-ph]].

3.
Standard Model

Electroweak multi-boson measurements from ATLAS and CMS: Run 1 legacy and Run 2 prospects

Luca Perrozzi
Institute for Particle Physics (IPP), ETH Zürich,
Otto-Stern-Weg 5, CH - 8093 Zürich

The talk focuses on Electroweak multi-boson measurements performed by the ATLAS and CMS collaborations. An overview of the Run 1 results is presented together with prospects for Run 2 measurements.

1 Introduction

Measurements of the multi-boson production cross section test the Standard Model (SM) at the TeV scale [1]. They represent a source of irreducible background for Higgs studies and many searches for physics beyond the SM (BSM). Multi-boson production is also capable to probe boson self-interactions, searching for anomalous couplings. In particular, anomalous triple gauge couplings (aTGC) are probed by di-boson production and Electroweak (EW) production of single vector bosons, while anomalous quartic gauge couplings (aQGC) are probed by tri-boson production and EW diboson production.
The following report describes the most recent results from the ATLAS[2] and CMS[3] experiments.

1.1 Signatures and background sources

In multi-boson production processes, the signatures are represented by combinations of γ, W and Z particles, with a production cross sections hierarchy $\sigma(\gamma) > \sigma(W) > \sigma(Z)$. Multi-boson analyses feature high p_T, isolated charged leptons (electrons, muons) and possibly photons. Z bosons can be easily identified by mean of an invariant mass window cut around Z pole. W bosons are selected by requiring large missing transverse energy ($\not{E}_T$) from the undetected neutrino (computed from jets, leptons and calorimeter information), together with a transverse mass selection cut. Photons appear as energy clusters in the electromagnetic calorimeter, with characteristics similar to jets.
Examples of the di-boson, vector boson fusion (VBF), tri-boson and vector boson scattering (VBS) production are reported in figure 1

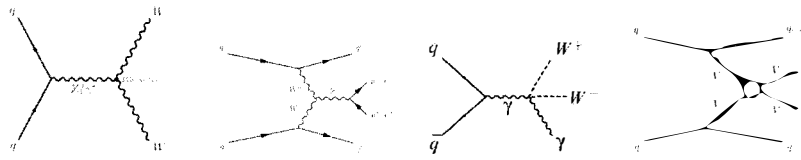

(a) Di-boson (b) VBF (c) Tri-boson (d) VBS

Figure 1 – Examples of Feynman diagrams for di-boson, VBF, tri-boson and VBS production.

1.2 Background sources

The major background sources are represented by events containing vector boson plus jets, with large cross section. In these events the high p_T leptons come from the boson or heavy flavour decays, while the jets are misidentified as charged leptons or photons. The $\not{E}_T$ is instead faked by particles falling outside acceptance. Also $t\bar{t}$ and single top events play a sizeable role, despite their lower cross section, since they naturally contain prompt isolated leptons from W bosons and large $\not{E}_T$. Finally, multi-boson processes act as background sources for each other.
The background contributions can be estimated from MC or with data-driven methods.

2 Effective theory approach to BSM

Most of the CMS and ATLAS anomalous couplings interpretations make use of the Vertex Function[4,5] approach for the neutral triple couplings (ZZZ, $Z\gamma\gamma$, $ZZ\gamma$) and the Effective Lagrangian[5] (though without an operator basis) for charged triple couplings ($WWW, WW\gamma$).
Only recently, a more systematic effective field theory approach (EFT) has been used to parametrize the quartic gauge anomalous couplings ($W^{\pm}W^{\pm}$ EW, $WW\gamma$, $\gamma\gamma \to WW$). In the EFT approach[6], assuming that the new physics scale Λ is separated from the EW scale v ($\Lambda \gg v$), and that the linearly realized $SU(3) \times SU(2) \times U(1)$ local symmetry is spontaneously broken by the vacuum expectation value of the Higgs doublet field, the Lagrangian of the SM can be expanded in operator dimension D:

$$\mathcal{L}_{EFT} = \mathcal{L}_{SM} + \frac{1}{\Lambda}\mathcal{L}^{D=5} + \frac{1}{\Lambda^2}\mathcal{L}^{D=6} + \frac{1}{\Lambda^3}\mathcal{L}^{D=7} + \frac{1}{\Lambda^4}\mathcal{L}^{D=8} + \dots \quad (1)$$

where the terms with $D = 5$ and $D = 7$ can be neglected at the LHC since they are lepton flavor violating, and $D = 8$ is subleading to $D = 6$. For $\mathcal{L}^{D=6}$ several complete non-redundant set of operators, each leading to a completely equivalent physics description, have been proposed in literature and are being used in the context of Higgs physics [7]. Uniformity of approach in the next generation of analyses need to be pursued in order to combine the different result and reach more stringent limits on the BSM parameters.

3 W^+W^- production and aTGC at 8 TeV in CMS

Previous ATLAS[8] and CMS[9] measurements report an excess of the W^+W^- cross section with respect to the next-to-leading order (NLO) SM prediction. A new CMS measurement[10] in the electron and muon channels has been performed, on 19.4 fb^{-1} at 8 TeV. It requires two isolated, opposite sign leptons with $p_T > 20$ GeV and pseudorapidity $|\eta_e| < 2.5$ and $|\eta_\mu| < 2.4$. The projected $\not{E}_T$ is required to be greated than 20 GeV and $p_{T,ll} > 45$ GeV. Several techniques are used to reduce the large background, including an anti b-tagging and jet veto ($N_{jets} < 2$) for $t\bar{t}$, the dilepton boost and Z mass veto for $Z + jet$ events, and a third lepton veto for WZ and ZZ. Multiple control regions are used to estimate the background yields in the signal region.
The systematic uncertainties sum up to 7.9% and are dominated by the jet veto and lepton

efficiency uncertainties. The total measured cross section, after removing the Higgs contribution, is:

$$\sigma_{W^+W^-} = 60.1 \pm 0.9(\text{stat}) \pm 3.2(\text{exp}) \pm 3.1(\text{th}) \pm 1.6(\text{lumi}) \text{ pb} \quad (2)$$

which is in agreement with the NNLO SM theory [11] prediction $\sigma^{NNLO}_{W^+W^-} = 59.8^{+1.3}_{1.1}$ pb.
The W^+W^- unfolded normalized differential cross section is measured as a function of kinematic variables $(p_{T,l}, m_{ll}, p_{T,ll}, \Delta\phi_{ll})$. They are compared to matrix element predictions interfaced to parton shower, and some discrepancies are observed, showing the need for improved accuracy in the calculations. Figure 2 shows the data and MC distributions for the 0−jet category of the p_T of the dilepton system, together with the normalized differential WW cross section as a function of the invariant mass m_{ll}. The latter is compared to predictions from Madgraph, Powheg and MC@NLO.
aTGC are measured in the framework of EFT operators with $D = 6$. No deviations are observed, and limits are set. Figure 2 shows the m_{ll} distribution after full selection with all SM background sources and $c_W/\Lambda^2 = 20/\text{TeV}$, $c_{WWW}/\Lambda^2 = 20/\text{TeV}$ and $c_B/\Lambda^2 = 55/\text{TeV}$.

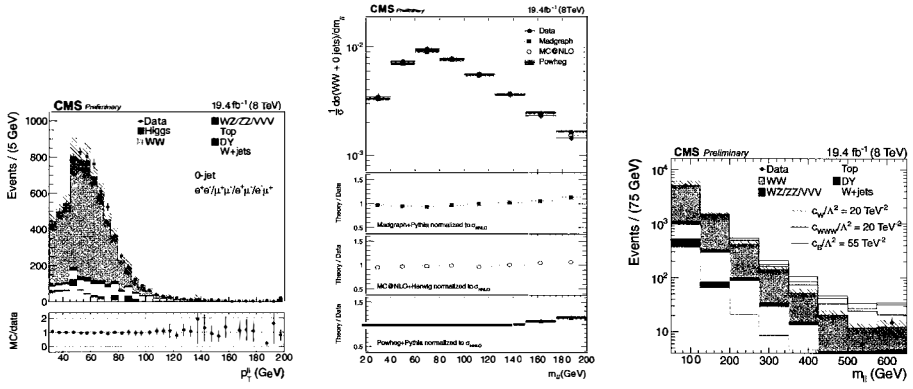

Figure 2 – Left: data and MC distributions for the 0−jet category of the p_T of the dilepton system. Center: normalized differential WW cross section as a function of the invariant mass m_{ll}. Right: m_{ll} distribution after full selection with all SM background sources compared to a given choice of the aTGC parameters.

4 Evidence of $W\gamma\gamma$ production in ATLAS

The production cross section for the $W\gamma\gamma$ process [12] is measured by ATLAS in the muon and electron channels, with 20.3 fb^{-1} at 8 TeV. The analysis is performed in the fiducial phase space for the jet inclusive ($N_{jets} \geq 0$) and exclusive ($N_{jets} = 0$) cases. The systematic uncertainties are dominated by the data-driven background estimate and jet energy scale. In particular, the data-driven fake photon background from $W\gamma j$ and Wjj events is estimated with a 2D template fit to the isolation distributions of the two γ candidates.
The measured cross sections in the inclusive and exclusive case are:

$$\sigma^{N_{jets}\geq 0}_{W\gamma\gamma} = 7.1^{+1.3}_{-1.2}(\text{stat}) \pm 1.5(\text{syst}) \pm 0.2(\text{lumi})$$
$$\sigma^{N_{jets}=0}_{W\gamma\gamma} = 2.9^{+0.8}_{-0.7}(\text{stat})^{+1.0}_{-0.9}(\text{syst}) \pm 0.1(\text{lumi}) \quad (3)$$

The total measured significance is 2.2 σ in the exclusive case and 3.7 σ in the inclusive case, thus representing the first evidence of $W\gamma\gamma$ production. The diphoton invariant mass distribution in the electron and muon channels is shown in figure 3. The fiducial region is defined at particle level, including jet and isolation variables. The fiducial cross section is 1.9 σ higher than the

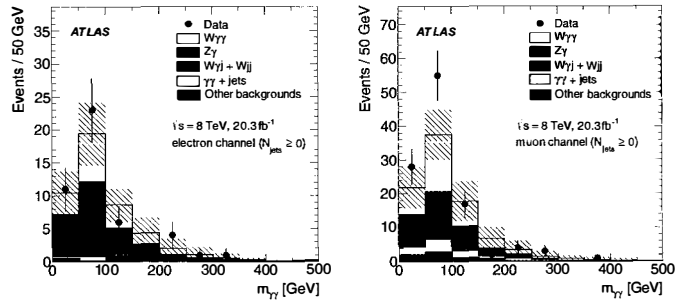

Figure 3 – Diphoton invariant mass distribution in the electron (left) and muon (right) channels. The expected signal based on the SHERPA prediction is shown. The hashed areas show the total systematic and statistical uncertainty on the background sources estimate.

MCFM prediction in the inclusive case, and 1.3 σ higher in the exclusive case.
aQGC are measured in the framework of EFT operators with $D = 8$. Possible deviations from the SM predictions are expected in the high di-photon invariant mass. A search region is therefore defined with $m_{\gamma\gamma} > 300$ GeV. No deviations are observed, and limits are set, improving previous results published by CMS.

5 Updates of preliminary results

5.1 $Z\gamma$ production and aTGC at 8 TeV in CMS

CMS published [13] the measurement of the $Z\gamma$ production cross section in electron and muon channels, with 19.5 fb^{-1} at 8 TeV, whose total inclusive cross section is in agreement with theory predictions. The search for aTGC in the high $E_{T,\gamma}$ spectrum lead to limits on $ZZ\gamma$ and $Z\gamma\gamma$ improves by factor 3 the 7 TeV results.

5.2 Electroweak production of Z+2jets at 7 TeV in CMS

CMS published [14] a measurement of the EW production of Z+2jets at 7 TeV. The analysis uses a quark/gluon discriminator to reduce background, and a BDT to extract signal contribution. The measured cross section is $\sigma = 174 \pm 15(\text{stat}) \pm 40(\text{syst})$ fb and the ratio with the SM prediction is $\sigma/\sigma_{SM} = 0.84 \pm 0.07(\text{stat}) \pm 0.19(\text{syst})$. The analysis precision is limited by the knowledge of large interference effects between production diagrams. A study of the hadronic and jet activity in Z+jet events is included.

5.3 $W^{\pm}W^{\pm}$ VBS production at 8 TeV in ATLAS

ATLAS published [15] the evidence of VBS scattering in $W^{\pm}W^{\pm}$ channel at 8 TeV. The analysis is similar to the search for the Higgs decay in the WW case with VBF topology. It requires two isolate leptons with same charge, featuring a third lepton veto to reduce the WZ background contribution. It also requires two forward jets with high invariant mass and large pseudo-rapidity separation. A cut on the dilepton invariant mass $m_{ll} > 50$ GeV together with $\not{E}_T > 40$ GeV is used to reduce the W+jets and top background sources. The main residual backgrounds arise from $WZ \to 3l\nu$ and non-prompt leptons. The systematic uncertainties are dominated by jet reconstruction and theory uncertainties. In the inclusive region, the measured cross section is $\sigma = 2.1 \pm 0.5(\text{stat}) \pm 0.3(\text{syst})$ fb, corresponding to an observed significance of 4.5σ (when 3.4σ were expected). The measured cross section in the VBS enriched region, requiring $m_{jj} > 500$

GeV, is instead $\sigma = 1.3 \pm 0.4(\text{stat}) \pm 0.2(\text{syst})$ fb, corresponding to 3.6σ observed significance (when 2.8σ were expected).

6 Summary plots

The summary plots for the measured multi-boson cross sections and their ratio with theory predictions are reported in figure 4 for ATLAS and in figure 5 for CMS.

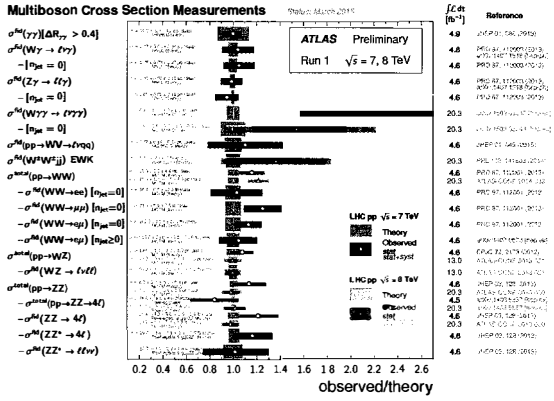

Figure 4 – Summary plots for the measured multi-boson cross sections and their ratio with theory predictions for ATLAS (top) and CMS (bottom).

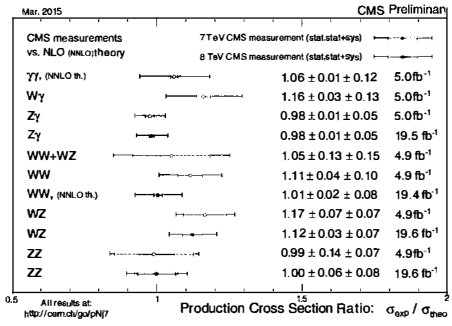

Figure 5 – Summary plots for the measured multi-boson cross sections and their ratio with theory predictions for ATLAS (top) and CMS (bottom).

7 Considerations towards Run 2, and long term projections

A general consideration about the precision of multi-boson measurements in Run 1 of LHC is that they are statistically limited, either in control regions or in signal regions (like high p_T or high mass). Therefore, major improvements are expected during LHC Run 2 at 13 TeV, both due to a large increases of signal cross section and much larger integrated luminosity.
However, further inputs are needed for the next round of analyses. For example, higher order MC calculations are needed to reduce the QCD scale uncertainty on the boson p_T. The NLO

EW corrections are not available in most of the channels, while their contributions becomes sizeable in the search regions, i.e. high p_T or mass. Finally, very limited number of NLO MC tools is available to generate anomalous couplings.
Generally speaking about the anomalous couplings, an unitary approach is needed with other branches, like the measurements performed to characterize the Higgs sector, probing the same physics. This quest for unitary approach is needed both to combine different measurements and take into account correlated effect of BSM physics. A possible answer seems to be provided by the EFT approach, which might become the new standard, superseeding the Vertex Function and Effective Lagrangian proposed during LEP times.
From the experimental point of view, a major effort must be put in providing unfolded spectra. In particular, an important caveat is represented by the definition of the background subtracted "signal", since BSM would coherently affect different signal (and background) channels.

Long term projections on aQGC have been released in 2013 by ATLAS [16] for the VBS $WZ \to 3l\nu$, VBS $ZZ \to 4l$, VBS $W^{\pm}W^{\pm} \to 2l2\nu$, $Z \to 2l2\gamma$, and by CMS [17] for the VBS $WZ \to 3l\nu$. Depending on the new tools available and future analysis developments, however, the performance could be greatly improved.

References

1. K.A. Olive *et al.*, (Particle Data Group), Chin. Phys. C, 38, 090001 u(2014).
2. ATLAS Collaboration, "The ATLAS experiment at the CERN LHC", JINST 3 (2008) S08003.
3. CMS Collaboration, "The CMS experiment at the CERN LHC", JINST 3 (2008) S08004.
4. K. Gaemers and G.Gounaris, *Z. Phys.* C **1**, 259 (1979).
5. K. Hagiwara, *et al.*, *Nucl. Phys.* B **282**, 253 (1987).
6. C. Degrande *et al.*, "Effective Field Theory: A Modern Approach to Anomalous Couplings", (2012). arXiv:1205.4231.
7. R. Gupta *et al.*, "BSM Primary Effects", arXiv:1405.0181.
8. ATLAS collaboration, "Measurement of the W^+W^- production cross section in proton-proton collisions at $\sqrt{s} = 8$ TeV with the ATLAS detector", ATLAS-CONF-2014-033 (2014).
9. CMS collaboration, "Measurement of W^+W^- and ZZ production cross sections in pp collisions at $\sqrt{s} = 8$ TeV", *Phys. Lett.* B **721**, 190 (2013).
10. CMS collaboration, "W^+W^- cross section and anomalous gauge couplings at 8 TeV", CMS-PAS-SMP-14-016.
11. T. Gehrmann *et al.*, "W^+W^- production at hadron colliders in NNLO QCD", *Phys. Rev. Lett.* **113**, 212001 (2014).
12. ATLAS collaboration, "Evidence of $W\gamma\gamma$ production in pp collisions at $\sqrt{s} = 8$ TeV and limits on anomalous quartic gauge couplings with the ATLAS detector", (2015). arXiv:1503.03243, submitted to PRL.
13. CMS collaboration, "Measurement of the $Z\gamma$ production cross section in pp collisions at 8 TeV and search for anomalous triple gauge boson couplings", JHEP **04**, 164 (2015).
14. CMS collaboration, "Measurement of EWK production of two jets in association with a Z boson in pp collisions at $\sqrt{s} = 8$ TeV", EPJC **75**, 66 (2015).
15. ATLAS collaboration, "", *Phys. Rev. Lett.* **113**, 141803 (2014).
16. ATLAS collaboration, "Studies of VBS And Triboson Production with an Upgraded ATLAS Detector at a High-Luminosity LHC", ATL-PHYS-PUB-2013-006 (2013).
17. CMS collaboration, "VBS and aQGC Studies in WZ Production at 14 TeV", CMS-PAS-FTR-13-006 (2013).

Recent Electroweak Results from the Tevatron

MATTEO BAUCE
on behalf of the CDF and D0 collaborations
Sapienza Università di Roma, p.le A. Moro 5, Roma, Italy

In this contribution we present some recent results on the electroweak sector of the Standard Model, carried out by the CDF and D0 experiments. Analyzing the dataset of $p\bar{p}$ collision at a center-of-mass energy of 1.96 delivered by the Tevatron collider it has been possible to perform precise measurement in this peculiar environment. The improvement on the measurement precision for the relevant observables in the electroweak sector allows to tighten indirectly the possible contribution from new physics.

1 Introduction

The unique sample of $p\bar{p}$ collisions produced by the Tevatron at a center of mass energy of 1.96 TeV and collected by the CDF and D0 experiment until the end of september 2011 is still being analyzed to perform precise measurements in the electroweak (EW) sector of the Standard Model (SM). Studying in particular the production of electroweak massive bosons, W and Z, it is possible to extract information on the parton distribution functions (PDF) in a peculiar range of $x = (M/\sqrt{s})e^{\pm y}$, corresponding to $0.002 < x < 1$. The information obtained from these processes is complementary to the study of hadronic jets production at the Tevatron, either in small and large ranges of pseudorapidity. An improved determination of PDF is fundamental for Monte Carlo (MC) simulation of physics processes also at different collision energies, like pp collisions at the Large Hadron Collider (LHC). During the several years of data-taking CDF and D0 greatly improved their measurement accuracy, providing interesting results. We discuss here recent measurements of boson asymmetries, EW parameter determination and diboson production carried out by the CDF and D0 experiments.

2 ϕ^* angular distribution in $Z \to \mu\mu$ events

Analyzing $Z \to \mu\mu$ decays it is possible to investigate the kinematic properties of the produced Z boson with high precision. Considering the muons directions in the beam transverse plane it is useful to define:

$$\phi^* = \tan(\phi_{acop}/2) \cdot \sin\theta^* \qquad \phi_{acop} = \pi - \phi(\mu\mu) \qquad \cos\theta^* = \tanh((\eta_+ - \eta_-)/2) \qquad (1)$$

where $\eta_\pm$ is the pseudorapidity of the positive and negative charged muon respectively. The ϕ^* variable can be considered equivalent to $p_T(\ell\ell)$ since it is proportional to it but the advantage of considering angles is that the experimental resolution on their determination is <1% on $\mathcal{O}$(mrad) angles, better than the one achievable on the lepton momentum determination. D0 carried out a measurement of the ϕ^* distribution considering the full collected dataset of dimuon events in a wide range of the dimuon mass values [3]. Other than the range corresponding to the Z

peak, $70 \leq M_{\mu\mu} \leq 110$ GeV, was considered for the first time also the range below that, $30 \leq M_{\mu\mu} \leq 60$ GeV, and two regions above the Z peak, $160 \leq M_{\mu\mu} \leq 300$ GeV and $300 \leq M_{\mu\mu} \leq 500$ GeV. In the considered mass ranges the ϕ^* distribution in different regions of Z boson rapidity has been compared to ResBos [1] and QCD calculations including the resummation of multiple soft gluon emissions at next-to-next-toleading log accuracy matched to the next-to-leading order MC calculation NNLL+NLO [2], shown in Figures 1 and 2 respectively. The ratio of the ϕ^* distribution in the central and forward region of the detector helps reducing the impact of theoretical uncertainties thanks to some terms cancellations. A good agreement with both predictions has been observed in the aforementioned ratio distribution in the Z peak region. Reasonable agreement with the NNLO+NLO predictions has been observed in the low mass range allowing to constrain small-x region better than from measurements at large detector pseudorapidity. The high mass range, which can help constraining QCD ISR contribution for processes with high resulting mass in the final state, has limited statistic hence a detailed comparison with the theoretical prediction was not available.

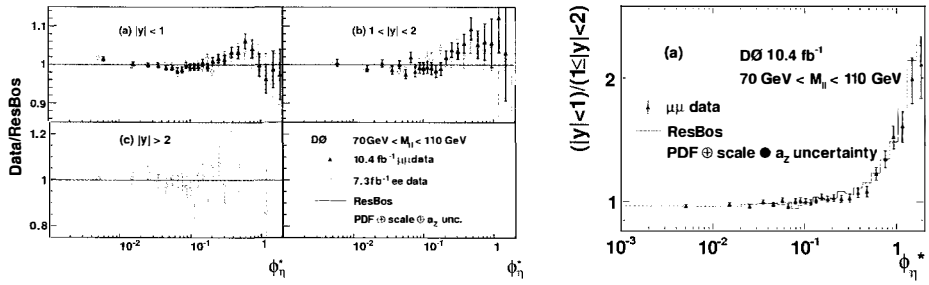

Figure 1 – (left) Ratio of the corrected ϕ^* distribution observed in data to ResBos prediction in the Z peak region for different rapidity regions. (right) The ratio of ϕ^* distribution in the region $|y| < 1$ and $1 \leq |y| \leq 2$ for the data and ResBos predictions.

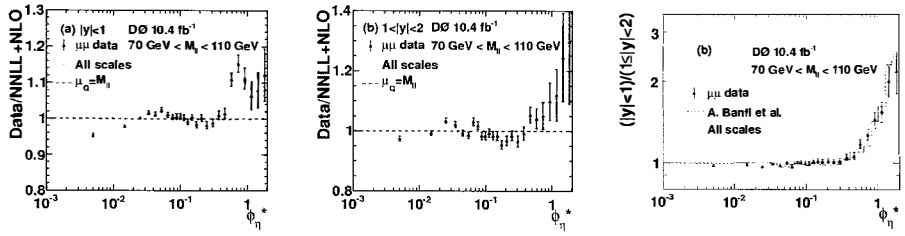

Figure 2 – (left, center) Ratio of the corrected ϕ^* distribution observed in data to NNLO+NLO prediction in the Z peak region for (left) $|y| < 1$ and (center) $1 \leq |y| \leq 2$. (right) The ratio of ϕ^* distribution in the region $|y| < 1$ and $1 \leq |y| \leq 2$ for the data and NNLO+NLO predictions.

3 Electron charge asymmetry in $W^{\pm} \to e^{\pm}\nu$ events

In $p\bar{p}$ collisions $W^{\pm}$ bosons are produced mainly in $u\bar{d}$ and $d\bar{u}$ annihilation hence W^+ and W^- are expected to be produced with a boost in the same direction of the incoming u and $\bar{u}$ quark respectively. It is possible then to define the charge asymmetry, as a function of the boson

rapidity, as

$$A(y_W) = \frac{(d\sigma^+/dy_W) - (d\sigma^-/dy_W)}{(d\sigma^+/dy_W) - (d\sigma^-/dy_W)} = \frac{u(x_p)\bar{d}(x_{\bar{p}}) - d(x_p)\bar{u}(x_{\bar{p}})}{u(x_p)\bar{d}(x_{\bar{p}}) + d(x_p)\bar{u}(x_{\bar{p}})} \quad (2)$$

which is then sensitive to u and d PDFs ($u(x_p)$, $d(x_p)$). The W charge asymmetry was measured by D0 [4] but a more recent result extracted information on the same quantities considering the electron charge asymmetry from $W^{\pm} \to e^{\pm}\nu$ decays [5]. The lepton charge asymmetry is a more straightforward observable since it's easier to determine and there is a strong correlation between the W boson rapidity distribution and the produced electron pseudorapidity, η, distribution. The resulting lepton charge asymmetry is the convolution of the W production asymmetry and its carachteristic $V-A$ subsequent decay. The recent analysis from D0 considers the full collected dataset and improved the lepton energy reconstruction and calibration, for electrons up to $|\eta|=$ 3.2. The observed asymmetries have been corrected for detector effects (*unfolding*), subtracted for the contribution from expected background, and then compared to theoretical predictions obtained using several combinations of generators and PDF sets, in different kinematic regions. Various regions have been defined considering both symmetric and asymmetric requirements on the transverse energy of the electron, E_T^e, and the missing transverse energy from the undetected neutrino, $\not\!\!E_T$. Figure 3 (left) shows the calculated asymmetry distribution obtained requiring $E_T^e \geq 25$ GeV and $\not\!\!E_T \geq 25$ GeV, compared to different predictions, while in Figure 3 (right) is shown, for the same distribution, the difference with respect to the MC@NLO+NNPDF2.3 prediction. While in this case the data are found in good agreement with the aforementioned prediction, in different kinematic regions data are found in agreement with ResBos+CTEQ6.6 prediction, see for example Figure 4 (left), or inconsistent with all the considered predictions, see for example Figure 4 (right). This result represents the most precise lepton charge asymmetry to date and it's contribution to the PDF knowledge in the W production $Q^2 - x$ region will have a strong impact on the upcoming W mass measurement.

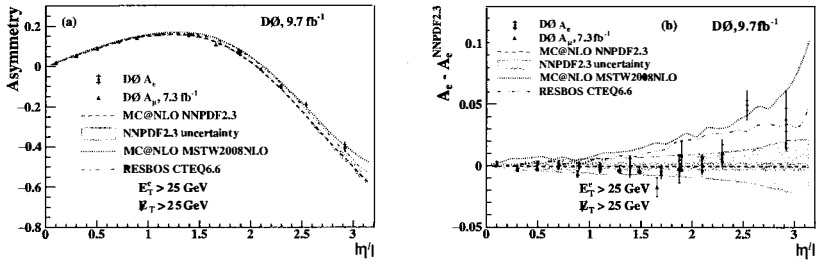

Figure 3 – (left) Electron charge asymmetry observed in data as a function of the lepton pseudorapidity (η^ℓ) for events with $E_T^e \geq 25$ GeV and $\not\!\!E_T \geq 25$ GeV, compared to different theoretical predictions. (right) Asymmetry difference with respect to the MC@NLO+NNPDF2.3 prediction, in events with $E_T^e \geq 25$ GeV and $\not\!\!E_T \geq 25$ GeV.

4 Indirect $\sin^2\theta_W$ measurement from $Z \to ee$ events

In the precise measurement of EW parameters D0 focused also on indirect determination of the effective weak mixing angle, $\sin^2\theta^f_{\rm eff}$. Drell-Yan production, $p\bar{p} \to Z/\gamma^* \to \ell^+\ell^-$, is affected by an axial-vector contributions in the SM lagrangian and is therefore dependent, among other parameters, on $\sin^2\theta_W$. For this an effective value can be defined as $\sin^2\theta^f_{\rm eff}$ taking into account order few percent radiative corrections when considering the decay to a given fermion f. In particular the effective mixing angle can be measured considering the forward-backward charge

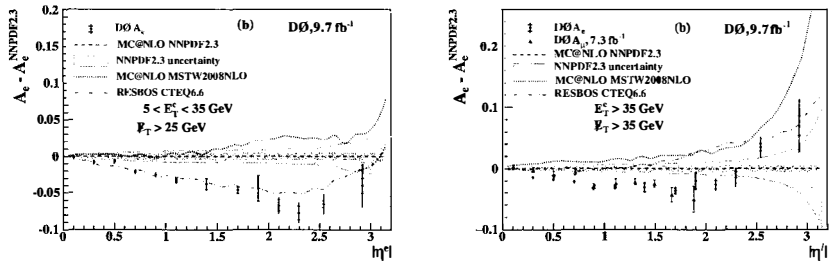

Figure 4 – (left) Asymmetry difference with respect to the MC@NLO+NNPDF2.3 prediction, in events with 25 $\leq E_T^e \leq$ 35 GeV and $\not\!\!E_T \geq$ 25 GeV. (right) Asymmetry difference with respect to the MC@NLO+NNPDF2.3 prediction, in events with $E_T^e \geq$ 35 GeV and $\not\!\!E_T \geq$ 35 GeV.

asymmetry in the lepton emission angle

$$A_{\rm fb} = \frac{\sigma(\cos\theta^* > 0) - \sigma(\cos\theta^* < 0)}{\sigma(\cos\theta^* > 0) + \sigma(\cos\theta^* < 0)} = \frac{N_F - N_B}{N_F + N_B} \tag{3}$$

where θ^* is the polar emission angle of ℓ^+ with respect to the direction of the incoming quark in the Collin-Soper frame, and N_F, N_B are the number of events with ℓ^+ produced in the forward or backward direction respectively. The $A_{\rm fb}$ asymmetry has been recently measured by D0 in di-electron events considering the full collected dataset, improving the electron reconstruction and calibration, and extending the coverage to large pseudorapidity regions. The asymmetry has been evaluated in different M_{ee} bins, for different combinations of electrons reconstructed in the central (CC) or endcap (EC) calorimeters, as shown in Figures 5, and compared to a set of MC samples obtained varying the value of $\sin^2\theta_W$. The effective mixing angle has been obtained minimizing a χ^2 function between the data distributions and the set of simulated templates. The results of the fits are reported in Table 1 for the different sub-channel considered and the corresponding combination, together with the corresponding statistical and systematic uncertainties. The combined result can be translated in SM on-shell renormalization scheme and modified ResBos NLO corrections in terms of the effective weak mixing angle, $\sin^2\theta^\ell_{\rm eff}$ = 0.23147±0.00047, which is the world's best result from Hadron Collider and light quark interactions to date.

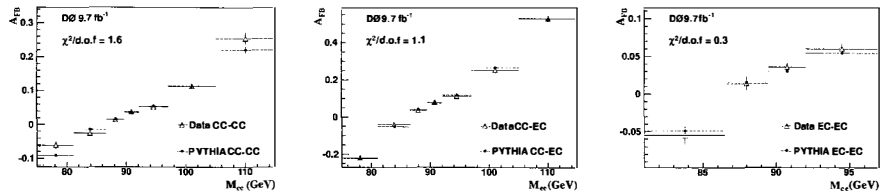

Figure 5 – Forward-Backward asymmetry $A_{\rm fb}$ in di-electron events as a function of M_{ee}, shown for events with (left) two electrons in the central calorimeters, (center) one electron in the central and one in the endcap calorimeter, (right) two electrons in the endcap calorimeters. The distribution observed in data are compared to MC simulation generated using Pythia.

5 WW+jets differential cross sections

CDF and D0 largely investigated diboson production at the Tevatron providing precise inclusive cross section measurements in their different decay modes. CDF focused recently on the WW

Table 1: Measured $\sin^2\theta_W$ value from the fit to data in the considered sub-channels and the corrisponding combination, together with the measurement statistical and systematic uncertainties.

	CC-CC	CC-EC	EC-EC	Combined
$\sin^2\theta_W$	0.23140	0.23142	0.22986	0.23138
Statistical	0.00116	0.00047	0.00276	0.00043
Systematics	0.00009	0.00009	0.00019	0.00008
Energy Calibration	0.00003	0.00001	0.00004	0.00001
Energy Smearing	0.00001	0.00002	0.00013	0.00002
Background	0.00002	0.00001	0.00002	0.00001
Charge Misidentification	0.00002	0.00004	0.00012	0.00003
Electron Identification	0.00008	0.00008	0.00005	0.00007
Total	0.00116	0.00048	0.00277	0.00044

production in association with hadronic jets [7] which can highlight different diboson production mechanisms and is important to investigate Vector Boson Scattering and new physics processes giving similar signatures. $WW \to \ell\nu\ell\nu$ events are selected reconstructing a pair of opposite charged leptons (electrons or muons) associated to a significant amount of missing transverse energy, $\not\!\!E_T$. Such events have been categorized depending on the presence of 0, 1, 2 or more hadronic jets. Events with a single jets have been further divided depending on the energy of such jets, namely considering ranges of E_T^j [15,25] GeV , [25,45] GeV, and above 45 GeV. For each sub-region a different neural network has been trained to isolate the WW signal from the other expected background contributions. The unfolded measurement in each sub-region, which considers jet-bin migration and corrections to hadronic levels, has been obtained with a fit to the neural network output distribution, and is reported in Table 2 and in Figure 6 (left). The measured cross section is homogeneously higher but consistent with the theoretical predictions and is the first differential cross section measurement in massive diboson state.

Table 2: Measured cross section in the different jet multiplicity bins and the corresponding statistical and systematic uncertainties. The last two columns report the corresponding values predicted by two different MC generators.

	σ(pb)	Uncertainty (pb)			σ(pb)	
Jet Bin	Measured	Stat.	Syst.	Lumi.	Alpgen	MC@NLO
Inclusive	14.0	±0.6	$^{+1.6}_{-1.3}$	±0.8	11.3 ± 1.4	11.7 ± 0.9
0 Jets	9.6	±0.4	$^{+1.1}_{-0.9}$	±0.6	8.2 ± 1.0	8.6 ± 0.6
1 Jet Inclusive	3.05	±0.46	$^{+0.48}_{-0.32}$	±0.18	2.43 ± 0.31	2.47 ± 0.18
1 jet, $15 \le E_T \le 25$ GeV	1.47	±0.17	$^{+0.15}_{-0.11}$	±0.09	1.26 ± 0.16	1.18 ± 0.09
1 jet, $25 \le E_T \le 45$ GeV	1.09	±0.18	$^{+0.17}_{-0.12}$	±0.06	0.77 ± 0.10	0.79 ± 0.06
1 jet, $E_T > 45$	0.49	±0.15	$^{+0.20}_{-0.11}$	±0.03	0.40 ± 0.05	0.46 ± 0.03
2 or More jets	1.36	±0.30	$^{+0.46}_{-0.29}$	±0.08	0.64 ± 0.08	0.61 ± 0.05

6 $WW/WZ \to \ell\nu$+heavy flavor jets

CDF exploited the full collected dataset to study the WW and WZ diboson production in final states containing hadronic jets ascribably to heavy-flavor quark decay [8]. Events with one lepton (electron or muon), a significant amount of missing transverse energy ($\not\!\!E_T$), and 2 jets with $E_T \geq$20 GeV have been selected. The dominant background from QCD multijet has been modeled using data in an orthogonal control region and largely rejected using a Support Vector Machine[9]. The analysis aims at the separate measurement of WW and WZ production thanks to the different heavy flavor decay pattern of the corresponding W and Z boson (mainly $W^+ \to c\bar{s}$

while $Z \to b\bar{b}, c\bar{c}$), considering subchannels based on the identification of one or both jets as coming from an heavy-flavor quark (tag). An artificial neural network (NN) has been used to discriminate the flavor of the jet for events with only one tagged jet, aiming at separating b-quarks from c-quarks and light-flavor quarks. The combination of such NN output information with the dijet invariant mass, M_{jj}, allow to discriminate W+c(c) background from W+$b\bar{b}$ background as well as WW from WZ. A 2-dimensional fit of data NN vs. M_{jj} distribution provided a simultaneous measurement of WW and WZ cross sections, shown in Figure 6 (center), and observed being σ^{Obs}_{WW}= 9.4 ± 4.2 pb and $\sigma^{Obs}_{WZ} = 3.7^{+2.5}_{-2.2}$ pb. The fit also measured a total cross section for the diboson production in $\ell\nu$jj final state of σ^{Obs}_{WW+WZ}= 13.9 ± 3.8 pb. These results are consistent with the theoretical predictions.

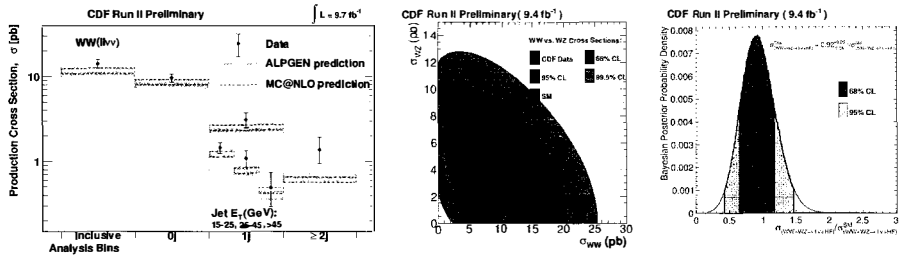

Figure 6 – (left) WW differential cross section measured by CDF compared to two theoretical predictions. (center) Contour plot showing the result of the 2-dimensional fit to the WW and WZ production cross sections in the $\ell\nu$jj final state performed by CDF. (right) Posterior distribution for the total $WW + WZ$ production cross section measured by CDF in the $\ell\nu$jj final state.

7 Conclusions

The CDF and D0 collaboration are producing unique measurements in the electroweak sector thanks to their unique dataset and multi-year improvement of the detector response knowledge. The precise measurement of the EW observables gives a fundamental contribution to the knowledge of PDFs, complementary to similar measurements at the LHC. Other than those just described the two collaborations are finalizing additional measurements and combining the CDF and D0 results to contribute to the Tevatron Legacy.

References

1. M. Guzzi, P. M. Nadolsky and B. Wang, Phys. Rev. D **90** (2014) 1, 014030 [arXiv:1309.1393 [hep-ph]].
2. A. Banfi, M. Dasgupta, S. Marzani and L. Tomlinson, JHEP **1201** (2012) 044 [arXiv:1110.4009 [hep-ph]].
3. V. M. Abazov *et al.* [D0 Collaboration], Phys. Rev. D **91** (2015) 7, 072002 [arXiv:1410.8052 [hep-ex]].
4. V. M. Abazov *et al.* [D0 Collaboration], Phys. Rev. Lett **112** (2015) 151803.
5. V. M. Abazov *et al.* [D0 Collaboration], Phys. Rev. D **91** (2015) 7, 032007.
6. V. M. Abazov *et al.* [D0 Collaboration], arXiv:1408.5016 [hep-ex].
7. CDF Public note 11098 (2014), `http://www-cdf.fnal.gov/physics/ewk/2014/WWjets/cdf11098_WW+jets.pdf`
8. CDF Public note 11157 (2015), `http://www-cdf.fnal.gov/physics/ewk/2015/DibosonHF/pubNote_WWWZ_94fb.pdf`
9. F. Sforza, V. Lippi, *Nucl. Instrum. Methods* A**722** (2013) 11-19.

Prospects for the measurement of m_W at the LHC

M. Boonekamp
CEA / IRFU,
91191 Gif-sur-Yvette, France

I describe the status of the m_W measurement preparations in ATLAS and CMS, with particular focus on the uncertainties induced by the strong interaction.

1 Relevance of the W boson mass and principle of its measurement

The Standard Model (SM) [1,2,3] including radiative corrections [4] provides a predictive theoretical framework in which the fundamental parameters (particle masses and couplings) are interconnected *via* an overconstrained set of relations. This can be exploited to test the validity of the SM. With precisely known Z boson mass (m_Z), Fermi coupling parameter (G_F), electromagnetic and strong coupling constants ($\alpha_{\rm QED}, \alpha_{\rm S}$) and electroweak mixing angle $\sin^2\theta_W$, currently the most interesting set of constraints relates the Higgs boson mass m_H to m_W and to the top quark mass $m_{\rm t}$. The curve correlating m_W and $m_{\rm t}$ is a definite prediction for any given m_H. Comparison with the actual measured values of m_W and $m_{\rm t}$ constitutes a test of this prediction.

This discussion is illustrated in Figure 1, which reports m_W as a function of $m_{\rm t}$ for various Higgs boson mass hypotheses [5]. The central curve corresponds to $m_H = 125.7 \pm 0.4$ GeV. The data point represents the current measured values $m_W = 80.385 \pm 0.015$ GeV and $m_{\rm t} = 173.2 \pm 0.9$ GeV. It can be seen from this figure the uncertainty on m_W currently drives the compatibility of the data with the prediction.

Quantitatively, when testing the validity of the SM, a top quark mass uncertainty of $\delta m_{\rm t} = 0.9$ GeV is matched in sensitivity by $\delta m_W \sim 6$ MeV, *i.e.* a natural obective for the W boson mass accuracy is an improvement by a factor 2.5 to 3 compared to present knowledge. Achieving this goal constitutes a test of the SM by itself; further improvement in $\delta m_{\rm t}$ will become relevant on that timescale.

The measurement relies on the assumption that the kinematic peaks of the W boson decay products (p_T^l, p_T^ν, m_T) can be predicted accurately for a given hypothesis for m_W. To this end, physics generators are used to describe the production and decay process, and realistic distributions are obtained using detector simulation. The detector-level decay product distributions, or template distributions, are then constructed for a set of reasonable m_W hypotheses by varying the mass parameter in the generator. All templates are compared to the data and the best match is determined. Likely the simplest possible measurement from the statistical point of view, the difficulty lies of course in the construction of the templates. These carry physics and experimental uncertainties that need to be evaluated and constrained, as summarized in the next section.

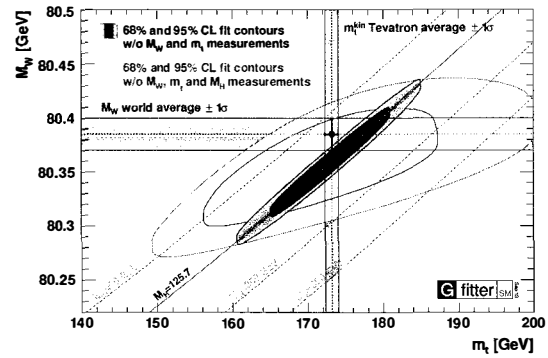

Figure 1 – Comparison of the measured W boson and top quark masses with their predicted values in the Standard Model.

2 Challenges

In contrast to for example the Z boson mass measurement at LEP, or the measurement of $\sin^2\theta_W$ at SLC, where the main requirements were excellent theoretical and experimental control of the initial state, these measurements at hadron colliders almost entirely rely on the understanding of the final state. That is, in the processes

$$pp \to Z + X \to ll + X,$$

$$pp \to W + X \to l\nu + X,$$

the fundamental parameters are extracted from the final state kinematic peaks, as explained in the previous section: the dilepton invariant mass $M(ll)$, the Jacobian peaks of p_T^l, p_T^ν and the transverse mass $m_T = (p_T^l p_T^\nu (1 - \cos\Delta\phi))^{1/2}$, as well as the asymmetries $A_{FB} = (\sigma_F - \sigma_B)/(\sigma_F + \sigma_B)$. The observed distributions of these observables however reflect a combination of experimental and physics effects that need to be disentangled before attempting a physical interpretation. I summarize the main steps below.

The first major goal is a control of the ATLAS and CMS detector energy and momentum scales. These simple final states are dominated by the W or Z decay leptons; the rest of the event, consisting of mostly soft hadronic activity, is considered as a global quantity recoiling against the decaying boson.

In the muon channel, low-mass vector mesons (J/ψ, Υ), W and Z bosons are collected in approximate 10:10:1 proportions, while the relative uncertainties on their masses are $\sim 10^{-6}$, $\sim 10^{-4}$, $\sim 10^{-5}$ respectively. This suggests to use J/ψ and Z events to constrain the momentum scale; the muon calibrations can be applied to the measurement of m_W. In the electron channel, J/ψ events are not collected as efficiently, so that the Z sample constitutes the main handle on the EM calorimeter energy scale. In the case of electrons, a major difficulty is to understand the calorimeter intercalibration, and the passive detector material upstream of it, before the $Z \to ee$ peak position can reliably be interpreted in terms of the calorimeter energy scale and used as a reference applying to W production. The hadronic recoil, input to the calculation of the missing transverse energy $E_T(\nu)$ and m_T, is calibrated exploiting momentum balance in Z events (after lepton calibration).

After the completion of the LHC Run 1, the LHC detectors have finalized their calibrations and published an extensive set of results on electron, muon and recoil performance[6,7,8]. Thanks to the large collected samples, the quality of the modeling of the data by the simulation has been vastly improved compared to initial performance. The J/ψ, υ and Z leptonic decay samples play a particular rôle in this context as the precisely known mass of these particles constrains the absolute scale of the detectors. In addition, since the decay is fully measured, momentum balance in the transverse plane can be exploited to determine the response and resolution of the hadronic recoil. Two example performance plots are are shown in Figure 2. In the following it will be assumed that the understanding of the detector performance is adequate for a measurement of m_W, and these aspects will not be discussed further.

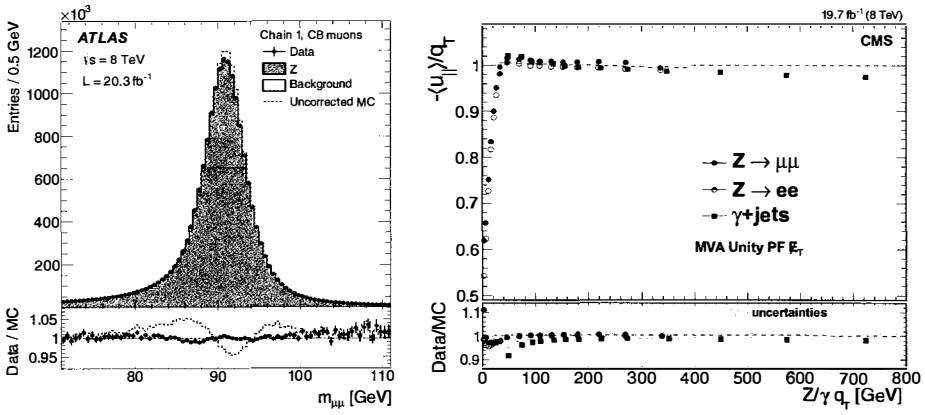

Figure 2 – Left: muon pair invariant mass distribution in the Z peak region, in ATLAS. Right: performance of recoil reconstruction in Z eventsm in CMS.

Complications in the physics modeling of W and Z production originate from strong interaction effects. The proton parton density functions (PDFs) and the initial-state interactions of the colliding partons determine the production distributions, and are partly governed by non-perturbative mechanisms that can not be entirely predicted from first principles.

The W and Z production data themselves are used to specify the models. The most relevant proton PDF constraints are obtained from measurements of the inclusive W^+ , W^- and Z production rates and rapidity distributions. These observables and their ratios allow, together with slightly more complex final states such $W+c$ and $\gamma+c$, a full flavour decomposition of the proton PDFs and a mapping of their Bjorken x dependence.

When colliding, the initial state partons radiate a large number of mostly soft gluons, as a result of their mutual interactions. This initial state "parton shower" contributes to the transverse momentum distribution of the W and Z. The details of this process are not fully predictible and are modeled in a semi-phenomenological way; the Z sample provides the main handle to constrain the model parameters.

In contrast, electroweak corrections to these processes, mostly inherited from the LEP/SLC era, are accurately known, need to be properly taken into account (using appropriate programs) but do not constitute a major source of uncertainty.

3 W boson production and decay

In order to interpret the kinematic peaks of the W decay products as probes of m_W, other effects influencing these distributions must be understood to high accuracy. To be specific: the distribution of $p_T(l)$ reflects, in addition to m_W, the W boson rapidity and transverse momentum distributions and the angular distributions of the decay products, i.e. the W polarization. These in turn largely result from the partonic sub-process, which receives significant contributions from first and second generation quarks. I discuss two specific examples below, to highlight the preparatory role of vector boson production measurements.

W polarization from the valence quark distributions

Consider the decay of a W^+ boson produced at y_W and with $p_T(W) = 0$, so its polarization is purely transverse. The momentum fractions of the partons involved in the process are

$$x_1 = \frac{m_W}{\sqrt{s}} e^{y_W} \quad ; \quad x_2 = \frac{m_W}{\sqrt{s}} e^{-y_W}$$

where $x_1 > x_2$ is assumed, and the parton of highest momentum is oriented towards $z > 0$. Considering first generation quarks only, the relevant sub-process is $u\bar{d} \to W^+$. The cross section receives contributions from u quarks oriented towards $z > 0$ and $z < 0$:

$$\left.\frac{\partial\sigma}{\partial y}\right|_{z>0} \propto u_1 \bar{d}_2 \quad ; \quad \left.\frac{\partial\sigma}{\partial y}\right|_{z<0} \propto u_2 \bar{d}_1$$

where we use the shorthand $u_i \equiv u(x_i)$ and similarly for $\bar{d}$, and $u(x), \bar{d}(x)$ are the up and anti-down quark densities in the proton at momentum fraction x. The first term corresponds to the W being boosted in the direction of the incoming valence quark, and dominates. Introducing θ^*, the angle between the decay lepton and the oriented z axis, the cross section writes

$$\begin{aligned} \frac{\partial^2\sigma}{\partial y \partial \cos\theta^*} &\propto u_1\bar{d}_2(1-\cos\theta^*)^2 + u_2\bar{d}_1(1+\cos\theta^*)^2 \\ &= (u_1\bar{d}_2 + u_2\bar{d}_1)(1+\cos^2\theta^*) - 2(u_1\bar{d}_2 - u_2\bar{d}_1)\cos\theta^* \end{aligned}$$

The first term is even in θ^* and unpolarized. Defining the valence and sea distributions as $u_V(x) = u(x) - \bar{u}(x)$ and $\bar{u}(x) = \bar{d}(x) = q(x)$, the second term becomes

$$(u_1\bar{d}_2 - u_2\bar{d}_1)\cos\theta^* \propto (u_{V1}q_2 - u_{V2}q_1)\cos\theta^* \sim u_{V1}q_2\cos\theta^* \qquad (1)$$

for sufficiently large y_W, since when $x_1 \gg x_2$, $u_{V1} \gg u_{V2}$ and $q_1 \ll q_2$. The overall cross section thus deviates from the unpolarized $(1+\cos^2\theta^*)$ distribution by an amount proportional to the valence distribution. The polarized term disappears when $y_W = 0$, as $x_1 = x_2$ and $(u_{V1}q_2 - u_{V2}q_1) = 0$ whatever the valence distribution. Due to the undetected neutrino, this configuration can however not be isolated in the experiment. The impact of this residual polarization on the $p_T(l)$ distribution is illustrated in Figure 3-a, taken from [9], where the natural distribution is compared to the unpolarized distribution obtained in the hypothetical case where $u_V = 0$. Similar arguments hold for the W^- and involving the d-quark valence, d_V.

The strange density and the charm quark mass

In $cs \to W$ events, the c quark entering the collision has on average higher transverse momentum that the light quarks. This is due to the usual threshold suppression factor present in the $g \to c\bar{c}$ splitting function, at gluon virtuality Q^2, which favours $Q >> 2m_c$, giving more phase space and inducing higher transverse momentum on average compared to light quark splitting functions.

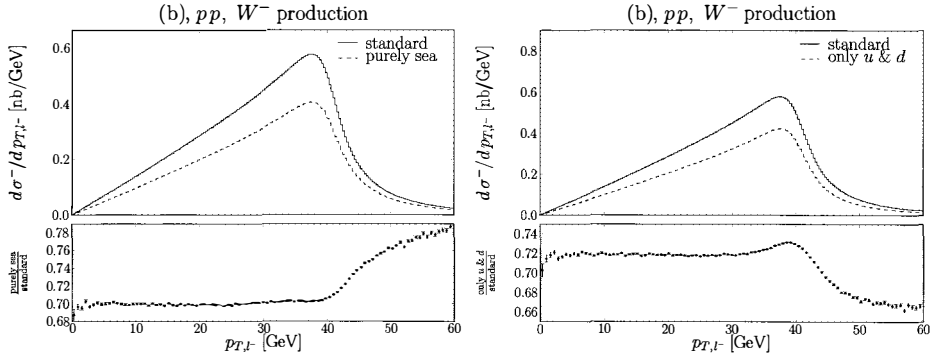

Figure 3 – Left: lepton transverse momentum distributions in W decays, with and without valence contributions. Right: lepton transverse momentum distributions in W decays, with and without contributions from second generation quarks.

As a result, generators predict that $p_T(W)$ is harder in $cs \to W$ events compared to $ud \to W$, by an amount of order m_c. Consequently, the p_T^l distributions differ for these two processes, reflecting a convolution with different underlying $p_T(W)$ distributions. Figure 3-b illustrates the effect, comparing the $p_T(l)$ distributions for the natural mix of sub-processes with that obtained for $ud \to W$ only. A proper modeling of the p_T^l distribution thus relies on our evolving knowledge of the strange density and of the non-perturbative parameters which together determine the p_T^W distribution.

4 Experimental constraints

The LHC experiments have engaged in an extensive measurement program that aims at constraining the QCD parameters describing these effects. Strong experimental constraints on the PDFs come from the W cross sections, measured differentially in lepton pseudorapidity; in particular the eta-dependent W charge asymmetry is specifically sensitive to the u and d valence ratio. These measurements have been pursued by ATLAS and CMS[10]. Z cross section measurements are also performed[11,12]; in conjunction with the W cross section, this provides information on the strange density [13]. The strange density can also be probed directly, via measurements of $W + c$ production [14]. The non-perturbative parameters are most accurately probed through measurements of the Z boson transverse momentum measurements [15], or of the angular correlations of its decay products [16]. Figure 4 illustrates two selected results.

While the existing body of measurements is impressive, the available data are far from fully exploited. In particular, inclusive W production at 8 TeV has not been studied and is important to pursue. Needless to say, the forthcoming Run 2 data, taken at much higher centre-0f-mass energy, will provide extremely useful and complementary information. At $\sqrt{s} \sim 13$ TeV, the typical parton momentum fraction probed is lower than in Run 1, enhancing the influence of the proton sea, and allowing further constraints in this region.

5 Perspectives

The LHC experiments are reaching maturity in terms of detector understanding, and have performed a wide range of measurements aimed at a better understanding of the the proton structure and the strong interaction. A large W sample is also available, sufficient to reach a

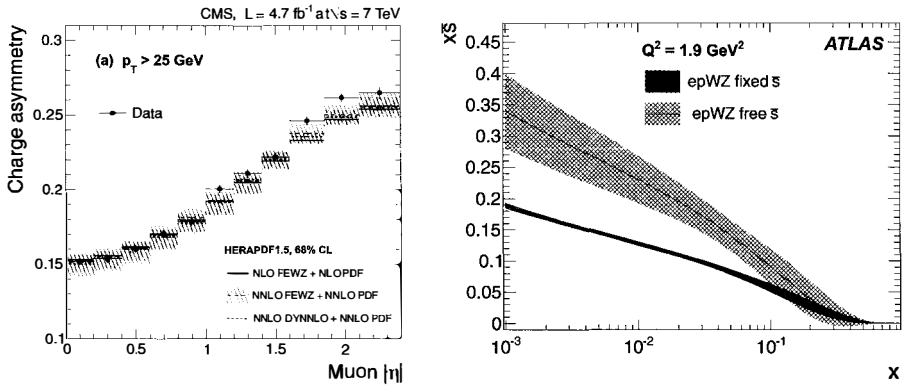

Figure 4 – Left: lepton charge asymmetry at 8 TeV, measured by CMS. Right: strange density determined from the W and Z inclusive cross sections at 7 TeV, from ATLAS.

2 MeV statistical sensitivity on a measurement of m_W.

To complete the first measurements of m_W still requires to combine all the available information in a consistent way. The measured cross sections and rapidity and transverse momentum distributions should be exploited to constrain the proton PDFs and the non-perturbative resummation parameters, properly accounting for the physical correlations between these effects. Such an analysis has not been performed before and is a requirement for a successful measurement of m_W.

References

1. S. L. Glashow, Nucl. Phys. **22**, 579 (1961).
2. A. Salam, Conf. Proc. C **680519** (1968) 367.
3. S. Weinberg, Phys. Rev. Lett. **19**, 1264 (1967).
4. D. Y. Bardin, P. Christova, M. Jack, L. Kalinovskaya, A. Olchevski, S. Riemann, and T. Riemann, *Comput. Phys. Commun.* **133**, 229 (2001).
5. M. Baak, M. Goebel, J. Haller, A. Hoecker, D. Kennedy, R. Kogler, K. Moenig and M. Schott *et al.*, Eur. Phys. J. C **72**, 2205 (2012).
6. G. Aad *et al.* [ATLAS Collaboration], Eur. Phys. J. C **74**, no. 11, 3130 (2014).
7. V. Khachatryan *et al.* [CMS Collaboration], JINST **10**, no. 02, P02006 (2015).
8. G. Aad *et al.* [ATLAS Collaboration], Eur. Phys. J. C **72**, 1844 (2012).
9. M. W. Krasny, F. Dydak, F. Fayette, W. Placzek and A. Siodmok, Eur. Phys. J. C **69**, 379 (2010).
10. S. Chatrchyan *et al.* [CMS Collaboration], Phys. Rev. D **90**, no. 3, 032004 (2014).
11. V. Khachatryan *et al.* [CMS Collaboration], arXiv:1504.03511 [hep-ex].
12. G. Aad *et al.* [ATLAS Collaboration], Phys. Rev. D **85**, 072004 (2012).
13. G. Aad *et al.* [ATLAS Collaboration], Phys. Rev. Lett. **109**, 012001 (2012).
14. S. Chatrchyan *et al.* [CMS Collaboration], JHEP **1402**, 013 (2014).
15. G. Aad *et al.* [ATLAS Collaboration], Phys. Lett. B **738**, 25 (2014).
16. G. Aad *et al.* [ATLAS Collaboration], Phys. Lett. B **720**, 32 (2013).

Collecting and analysing data at high pile-up with ATLAS and CMS

Nicholas Styles, on behalf of the ATLAS and CMS collaborations
Deutsches Elektronen-Synchrotron
Notkestraße 85, 22607 Hamburg

Detector layouts for the Phase 2 upgrades of ATLAS and CMS, designed for operation at the High-Luminosity LHC (HL-LHC) under conditions with pile-up of 140 and beyond, will be presented and discussed. The event reconstruction performance and techniques implied by these detectors and experimental conditions will be demonstrated, and possibilities for further developments will be explored. The physics reach obtainable with the upgraded detectors at HL-LHC will be shown for a selection of possible HL-LHC measurements.

1 Introduction - The High Luminosity LHC

The High Luminosity Large Hadron Collider (HL-LHC) is a planned upgrade to the Large Hadron Collider (LHC) currently in operation at CERN. Foreseen to begin operation in around 2025 following the so-called 'Phase 2' machine upgrade, it will provide $\sqrt{s} = 14$ TeV proton-proton collisions with instantaneous luminosities of between $5-7\times10^{34}$ cm^{-2}s^{-1}. This will allow integrated luminosities of $250-300$ fb^{-1} to be collected every year, resulting a total anticipated dataset of 3 ab^{-1}.

This unprecedentedly large dataset will facilitate a wide spectrum of physics analyses from precision tests of the Standard Model to New Physics searches with significantly enhanced discovery potential. However, in order to make the best use of the available data, the ATLAS and CMS collaborations must make extensive upgrades to detector systems, reconstruction algorithms, and analysis strategies to cope with the challenging experimental environment implied by the high instantaneous luminosities planned.

The experiments anticipate [1] events with an average number of 'pile-up' interactions per bunch crossing $\langle\mu\rangle = 140-200$, and the effects of the resulting high particle multiplicities on the various detector subsystems and algorithms are being thoroughly and carefully investigated using a variety of methods, and designs and optimisations made accordingly in order that the experiments will be able to identify and reconstruct physics processes of interest, maintaining or exceeding the excellent performance obtained by ATLAS and CMS up to now.

2 ATLAS Phase 2 Detector Upgrade

2.1 Inner Tracker Upgrade

As the innermost detector system of ATLAS, the Inner Tracker is the most strongly affected by the increased pile-up at HL-LHC, and so the replacement of the Inner Tracker (ITK) is one of the most crucial aspects of the Phase 2 upgrade [2]. A complete replacement of the tracking system will be undertaken; the gaseous straw-tube based Transition Radiation Tracker (TRT) will be removed due to being rendered inoperational due to the expected occupancies resulting from Phase 2 conditions, and the pixel and microstrip systems will be extended, resulting in a fully silicon based tracking detector.

From the numerous design consideration to be considered when designing a tracking system for working in high pile-up environments, among the most important are: low material budget within tracking acceptance to minimise multiple scattering and generation of secondary particles, high sensor granularity to effectively resolve nearby tracks, and sufficient number of space point measurements per track (including robustness against potential module failures) to combat combinatoric effects. Taking these and other considerations into account, a baseline tracker design was developed which meets the stated goal of maintaining or improving on current levels of performance under Phase 2 conditions, as will be discussed further in Section 4. The baseline

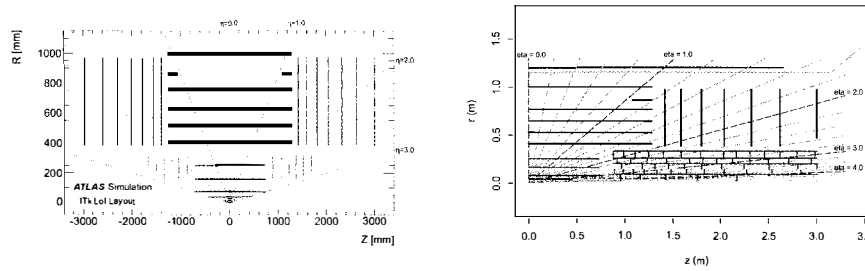

Figure 1 – Baseline ITK design for the ATLAS Phase 2 tracker upgrade (left), and a design showing a potential high-η extension (right). The right-hand figure shows only one quadrant of the detector ($z > 0$), which is symmetric around $z = 0$ and $r = 0$, while the left-hand shows both positive and negative z.

design is currently being used as a benchmark for comparison with further developments to the layout design. One particular development under serious consideration is the so-called 'high-η' extension of the pixel system, which would increase the tracking acceptance of the detector from from $|\eta| < 2.5$ to $|\eta| < 4.0$. Various possibilities for extending the tracking acceptance, as well as other possible layouts, are currently under detailed study. A possible design with high-η extension is shown in Figure 1 alongside the baseline design.

2.2 Upgrades to Other Systems

In addition to the tracker, many other ATLAS systems will undergo significant upgrades ahead of HL-LHC running.

The architecture of the ATLAS trigger system will be comprehensively updated, to move to a 2-level hardware trigger design. At Level 0, calorimeter and muon system information will be used to process events at a rate of 1 MHz and with a latency of 6 μs. Following this, Level 1 will process events at a rate of 300-400 kHz with a latency of 24 μs. Compared to the current ATLAS trigger system, the largest difference is the introduction of 'L1Track' which will bring part of the track reconstruction currently run in the HLT into Level 1. Since running tracking on full events at this stage of the trigger is not feasible, a 'Region Of Interest'-based (RoI) approach will be used, in which only specific $\eta - \phi$ segments of the detector will be processed.

Due to the increased trigger rates and radiation levels at HL-LHC, the electronics of the Tile and Liquid Argon calorimeters will need to be fully replaced. Full replacement of the Forward calorimetry may also be required, depending on the level of degradation observed in the current system in the coming years. Additionally, in the case of a 'high-η' extension, the Forward calorimetry may also be replaced with a higher granularity system to meet physics requirements. Similarly, additional Muon system chambers may be added in this case to make full use of the extended tracking acceptance.

3 CMS Phase 2 Detector Upgrade

3.1 CMS Tracker Upgrade

CMS will also perform a full replacement of their all-silicon tracking system for Phase 2, including replacing the new Pixel system introduced during the 'Phase 1' upgrade [4] around 2020. The design of the CMS baseline Phase 2 tracker [5] fulfils a similar set of requirement to those discussed in Section 2.1; high granularity, low material budget, and sufficient space points on the track. In contrast to the ATLAS design, the CMS baseline already features a pixel system with coverage up to $|\eta|$ =4, as shown in Figure 2 (left).

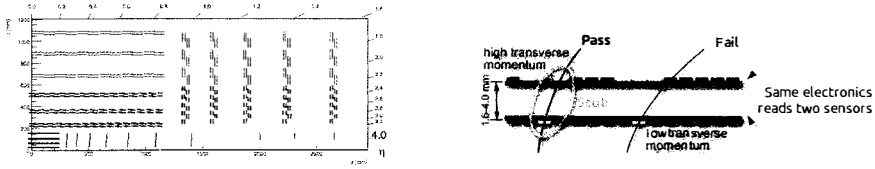

Figure 2 – The CMS basline Phase 2 tracker upgrade design (left) and an illustration of the 'stubs' used in the Silicon Self-Seeded Track Trigger concept (right)

A further significant feature of the CMS design is its use of a so-called 'Silicon Self-Seeded' approach to including track information in its hardware Level 1 trigger. By looking at the relation between pairs of hits on the two sensors of a double-sided module, high p_T track 'stubs' can be identified, as shown in Figure 2 (right). Two types of modules will be used in the 'Outer Tracker' layers according to granularity needs in the region; SS modules comprising two silicon microstrip sensors, and PS modules comprising a pixel sensors and a microstrip sensor. The performance of this system is under study, and very promising results [6] have been obtained in running Level 1 tracking using stub input, as discussed in Section 4. Two different technologies are currently under consideration for this system; FPGAs and associative memory. A latency of around 10 μs is required for processing this track information at Level 1.

3.2 Upgrades to Other Systems

Due to radiation-induced signal loss incurred prior to the Phase 2 upgrade, the CMS forward calorimeter will be replaced [7]. Two concepts are currently under consideration for the upgraded forward calorimeter system. The first is a compact Pb/LYSO Shashlik Forward electromagnetic calorimeter with a scintillator-based hadronic calorimeter. The second is a silicon/lead/copper electromagentic and silicon/brass hadronic calorimeter, with a scintillator/brass backing calorimeter to measure the energy not captured in the hadronic calorimeter.

Several upgrades are planned for the Muon system. The forward region from $1.6 < |\eta| < 2.4$ will use Resistive Plate Chambers (RPCs) and Gas Electron Multipliers (GEMs) to provide higher levels of redundancy, and cope with higher rates. GEMs will also be used to provide a 'Very Forward' extension to the muon system. This extension is planned to cover the region

$2.4 < |\eta| < 3.0$ as a baseline, but this may be extended based on the eventual design of the forward calorimetry.

4 Reconstruction Performance and Pile-up Mitigation

The expected performance of the ATLAS and CMS Phase 2 detectors under HL-LHC pile-up conditions is currently under careful study, and such studies are also being used not only to establish the performance of the layouts, but also to further optimise the detector layouts and the reconstruction techniques used. An important first step is to establish that fundamental reconstruction quantities are well behaved and well understood, such as the tracking efficiency for isolated particles in the presence of pile-up, as shown in Figure 3.

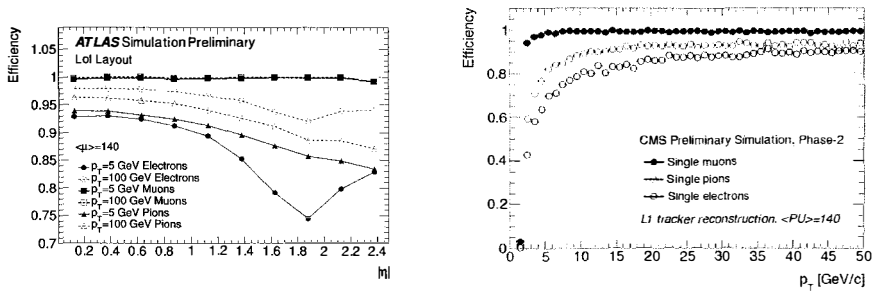

Figure 3 – Tracking efficiency for single particles with $< \mu >= 140$ for ATLAS ITK [3], as a function of η (left), and CMS Phase 2 Upgrade [6] using stub inputs, as a function of p_T (right)

Efficient and accurate reconstruction of primary vertices will be crucial for physics performance under HL-LHC conditions, and CMS have begun the process of optimising the algorithms used for vertexing for Phase 2 performance [8], as shown in Figure 4 (left), where the improved algorithm helps to recover vertex reconstruction efficiency at high pile-up. The vertexing performance achievable will depend on the precise beam spot dimensions provided by the HL-LHC machine, and ATLAS has studied the potential benefits of having a 'Long, Flat' beam spot (up to ± 15 cm in z) rather than a Gaussian beam spot with $\sigma_Z = 5$ cm (right) [9].

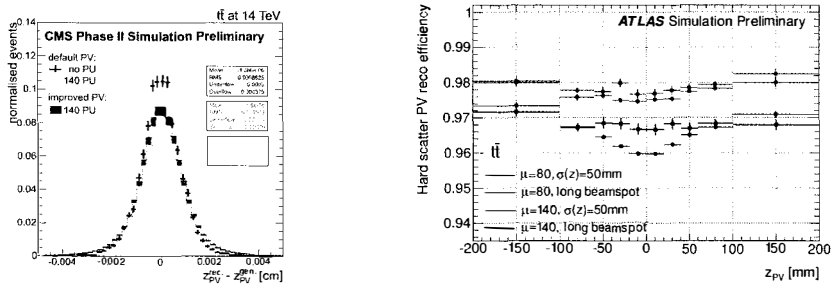

Figure 4 – CMS Primary Vertex reconstruction performance at $\mu = 0$ and $< \mu >= 140$, showing the effect of algorithmic improvements (left), and ATLAS Primary Vertex reconstruction efficiency as a function of vertex z position, for Gaussian and 'long' beamspots at $< \mu >= 80$ and $< \mu >= 140$ (right)

In addition to efficienctly reconstructing physics objects, reliably identifying them will also be crucial for meeting the physics goals of the Phase 2 upgrades. Figure 5 shows the performance

of b-tagging algorithms in distinguishing b-quark jets from light-quark jets, demonstrating the improved b-tagging performance of the upgraded CMS detector even under significantly higher pile-up (left), and the independence of the ATLAS b-tagging Phase 2 b-tagging performance on the beam spot profile, under the assumption that the correct primary vertex can be identified (right).

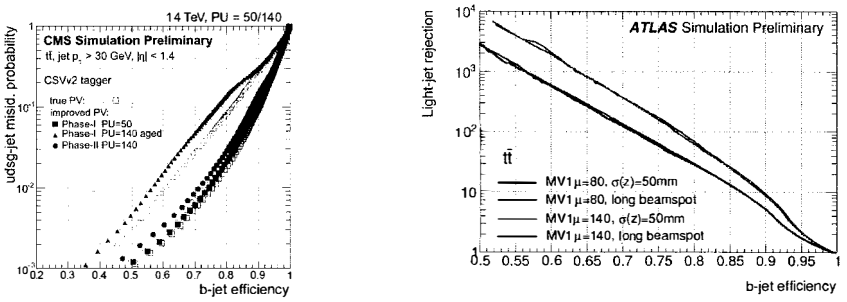

Figure 5 – Light-jet vs b-jet identification performance in simulated $t\bar{t}$ events for the CMS experiment for the Phase 1 and Phase 2 detectors under appropriate pile-up conditions, including detector aging effects and algorithmic improvements (left), and for the ATLAS Phase 2 detector with $< \mu >= 80$ and $< \mu >= 140$, with Gaussian and long beamspots, where the correct hard-scatter vertex has been selected using Monte Carlo Truth information (right)

Specific techniques are also in development for pile-up mitigation, allowing the effective discrimination of objects arising from interactions other than the hard-scatter of interest, which will be crucial for physics analyses of HL-LHC data. Pile-up jets can be effectively suppressed by application of 'Track Matching' criteria, requiring a reconstructed charged track highly compatible with the jet to be present in the event. Applying requirements on the 'Charged Fraction' (ratio of total p_T of associated tracks to the calibrated jet p_T) has also proved effective in reducing the contribution of pile-up jets within events.

Another powerful method for pile-up mitigation is the use of timing information [10], allowing significant improvements in matching photons to jets, tracks to vertices, and identification of merged jets. Effectively using such information would require improved time resolution with respect to the current detectors, with resolutions around $\sim$ 50 ps being considered. Achieving this will require timing-specific detector elements to be included in the detectors, with a number of proposal for how to implement this under consideration [11]; among the possibilities are one or more timing layers embedded in the Electromagnetic calorimeter, a low-mass timing layer in front of the calorimeters, or a pre-shower timing layer.

5 Physics Potential of the Phase 2 Upgrades

In parallel to studies aimed at understanding and optimising detector layouts and event reconstruction, current results and assumptions for Phase 2 performance are being fed into physics analysis studies in order to establish the potential physics reach of the Phase 2 upgrades. Thanks to the huge dataset it will provide, the HL-LHC will allow ATLAS and CMS to reach unprecedented precision in measuring the properties of the Higgs Boson [12 13], such as its couplings to other particles, particularly in the case where significantly improved theoretical uncertainties are available on the same timescale. It will also allow rare Standard Model processes, such as Higgs pair production, which offers a crucial handle for measuring the Higgs self-interaction, to be accessed [14].

The HL-LHC will also offer rich prospects in searches for Beyond the Standard Model physics, significantly increasing the discovery potential in many channels. As examples of a great many

studies performed, that ATLAS has found searches for WIMP Dark Matter [15] using jets and large missing E_T can expect to have a discovery reach up to suppression scales of 2.6 TeV, and CMS has projected for $\chi_1^{\pm}\chi_2^0$ searches in the $W\chi_1^0 H\chi_1^0$ channel with a final state of one lepton, 2 b-tagged jets and missing E_T, the mass reach ($m_{\chi_1^{\pm}} = m_{\chi_2^0}$) can be more than doubled [16].

6 Conclusions

The HL-LHC will provide huge physics potential for the ATLAS and CMS experiments, thanks to the unprecedented integrated luminosity it will provide for study. However, to make best use of this dataset the experiments will require significant upgrades. Both the ATLAS and CMS collaborations have comprehensive plans for upgrades to their detectors and reconstruction techniques, which are already projected to provide excellent performance under Phase 2 conditions. This work will be continued over the coming years to further improve the performance, resulting in an even greater physics reach to be attained.

References

1. The ATLAS and CMS Collaborations, *Expected pile-up values at the HL-LHC*, ATL-UPGRADE-PUB-2013-014, 2013.
2. The ATLAS Collaboration, *Letter of Intent for the Phase-II Upgrade of the ATLAS Experiment*, CERN-LHCC-2012-022, 2012.
3. The ATLAS Collaboration, *Public plots from the ITK Initial Design Review*, PLOT-UPGRADE-2014-001, 2014.
4. A Dominguez et al., *CMS Technical Design Report for the Pixel Detector Upgrade*, CERN-LHCC-2012-016, 2012.
5. A Tricomi, *Upgrade of the CMS tracker*, JINST **9**, C03041 (2014).
6. J Mans, *CMS Phase 2: Upgrade Scope and R and D goals*, ECFA High Luminosity LHC Experiments Workshop, `http://indico.cern.ch/event/315626/`, 2014.
7. B Bilki, *CMS Forward Calorimeters Phase II Upgrade*, J.Phys.:Conf.Ser. **587**, 012014 (2015).
8. P Wells, *Pileup Mitigation at the HL-LHC*, ECFA High Luminosity LHC Experiments Workshop, `http://indico.cern.ch/event/315626/`, 2014.
9. The ATLAS Collaboration, *Primary Vertex and b-Tagging Performance under HL-LHC conditions*, PLOT-UPGRADE-2014-003, 2014.
10. S White, *Experimental Challenges of the European Strategy for Particle Physics*,arXiv:1309.7985 [physics.ins-det], 2013
11. D Del Re, *Timing performance of the CMS electromagnetic calorimeter and prospects for the future*, CMS-CR-2014-074,2014.
12. The CMS Collaboration, *CMS at the High-Energy Frontier. Contribution to the Update of the European Strategy for Particle Physics*, CMS-NOTE-2012-006, 2012.
13. The ATLAS Collaboration, *Projections for measurements of Higgs boson signal strengths and coupling parameters with the ATLAS detector at the HL-LHC*, ATL-PHYS-PUB-2014-016, 2014.
14. The ATLAS Collaboration, *Prospects for measuring Higgs pair production in the channel $H \to \gamma\gamma H \to bb$ using the ATLAS detector at the HL-LHC*, ATL-PHYS-PUB-2014-019, 2014.
15. The ATLAS Collaboration, *Sensitivity to WIMP Dark Matter in the Final States Containing Jets and Missing Transverse Momentum with the ATLAS Detector at 14 TeV LHC*, ATL-PHYS-PUB-2014-007, 2014.
16. The CMS Collaboration, *Supersymmetry discovery potential in future LHC and HL-LHC running with the CMS detector*, CMS-PAS-SUS-14-012, 2014.

Improving LHC searches for strong EW symmetry breaking resonances

Anna Kamińska
PRISMA Cluster of Excellence and Mainz Institute for Theoretical Physics
Johannes Gutenberg University, 55099 Mainz, Germany

Composite Higgs models generically predict the existence of heavy spin-1 resonances with the same quantum numbers as electroweak gauge bosons. The effective lagrangian description of these resonances is presented, pointing out the origin of their interactions with SM matter fields and the resulting LHC phenomenology. Search strategies for spin-1 resonances are discussed, mentioning possible advantages offered by boosted decay products. The impact of interactions between spin-1 resonances and fermion resonances, crucial for the proper interpretation of LHC searches, is pointed out.

1 Introduction

Composite Higgs models invoke electroweak symmetry breaking by new strong dynamics, in analogy with chiral symmetry breaking in QCD, without introducing the hierarchy problem. In order to be consistent with the measured properties of the Higgs boson and the non-observation of new particles beyond the Standard Model, the composite Higgs is a pseudo-Nambu-Goldstone (PNG) boson of some global symmetry of the new strong sector, similar to the pion of QCD. The minimal composite Higgs model (MCHM)[1] is based on $SO(5) \to SO(4) \sim SU(2)_L \times SU(2)_R$ global symmetry breaking, inducing a full pseudo-Goldstone Higgs doublet.

In the effective Lagrangian description, which will be used throughout this note, the PNG bosons $\Pi(x) = \Pi^{\hat{a}}(x) T^{\hat{a}}$ of $SO(5) \to SO(4)$ are parameterized by $U(\Pi) = e^{i\Pi(x)/f}$ transforming as

$$U(\Pi) \to g\, U(\Pi)\, h^{\dagger}(\Pi, g), \qquad g \in SO(5),\ h \in SO(4). \tag{1}$$

The leading order effective Lagrangian term describing self-interactions of these bosons takes the form

$$\mathcal{L}^{\Pi} = \frac{f^2}{4} Tr\{d_\mu d^\mu\} \tag{2}$$

where d_μ is defined by

$$-iU^{\dagger} D_\mu U = d_\mu^{\hat{a}} T^{\hat{a}} + E_\mu^a T^a = d^a + E^a \tag{3}$$

and $T^{\hat{a}}$, T^a are respectively the broken and unbroken generators of $SO(5)$. The covariant derivative takes into account the external gauging and introduces interactions of the composite Higgs doublet with

elektroweak bosons. Whenever the generators corresponding to the electroweak group are "missaligned" with the generators of $SO(4)$, the electroweak symmetry is broken. Such "missalignement" is induced by loop corrections related to $SO(5)$ violating Yukawa and gauge interactions. Naturalness of electroweak symmetry breaking requires that the fermion resonances accompanying SM fermions in the composite Higgs framework have masses not far from the electroweak scale, $m_F \lesssim 1\text{TeV}$[2].

The generically expected experimental signatures of strong electroweak symmetry breaking range from flavor physics, electroweak precision data (S and T parameters), modification of Higgs couplings to the direct observation of new states - fermion resonances and spin-1 resonances. In this note I address the phenomenology of spin-1 resonances in composite Higgs models.

2 Spin-1 resonances in composite Higgs models

In order to speak about direct production and LHC phenomenology of spin-1 resonences, one has to introduce them explicitly into the effective description. There are several formalisms that allow to do that, the CCWZ formalism[3,4] and the "hidden local symmetry"[5] formalism being the most popular ones. At leading order in the effective description, both these formalism lead to equivalent results. The spin-1 resonances related to $\mathcal{G} \to \mathcal{H}$ symmetry breaking are expected to appear in a representation of the unbroken global symmetry of strong dynamics, in the case of MCHM - in representations of $SO(4)$. In the "hidden local symmetry" formalism the effective Lagrangian for vector mesons is constructed by enlarging the symmetry structure to $\mathcal{G} \times \mathcal{H}_{local} \to \mathcal{H}$, where $\mathcal{H}_{local}$ is the "hidden" gauge group (a purely mathematical tool, without physical meaning). The "hidden local symmetry" is broken and its heavy gauge bosons ρ^μ provide degrees of freedom for the effective description of spin-1 resonances. The effective description of a minimal composite Higgs model with a single set of spin-1 resonances has, at the leading-order Lagrangian level, only three free parameters, which can be chosen as

$$m_\rho,\ g_\rho,\ \xi = \frac{v_{EW}^2}{f^2} \tag{4}$$

where m_ρ is the mass of the set of vector resonances, g_ρ is the "hidden" gauge coupling and ξ describes the hierarchy between the weak scale and the energy scale of strong dynamics f. Parameter ξ also scales the departure from SM values of Higgs couplings to electroweak gauge bosons, hence it is restricted to be small $\xi \lesssim 0.1$ by experimental data. The interactions of spin-1 resonances with the Higgs boson are set by the symmetry breaking structure and the PNG-boson nature of the Higgs. The interactions of ρ resonances with SM matter fields are induced by two effects

1. mass mixing between ρ^μ and W^μ, Z^μ fields; this automatically introduces interactions of ρ resonances with electroweak gauge bosons and interactions with SM fermions through mass mixing effects feeding into the covariant derivatives in fermion kinetic terms

2. direct interactions between ρ^μ and fermion resonances, which mass mix with SM fermions (partial compositeness); the description of this effect requires introducing fermion resonances into the effective Lagrangian, which is model dependent.

Naive dimensional analysis (NDA) suggests a connection between the parameters introduced above, $m_\rho \sim g_\rho f$. In order to present a more general picture, I will treat them for the time being as idependent parameters. In the following I consider only a single set of spin-1 resonances transforming in the adjoint representation of $SU(2)_L$, as on grounds of general arguments such resonences are most likely to be most relevant for LHC searches.

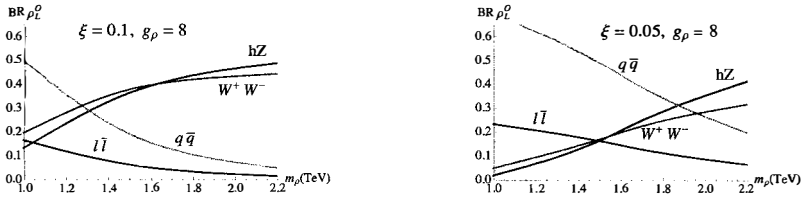

Figure 1 – Branching ratios of ρ resonances from ρ^μ and W^μ, Z^μ mass mixing effect.

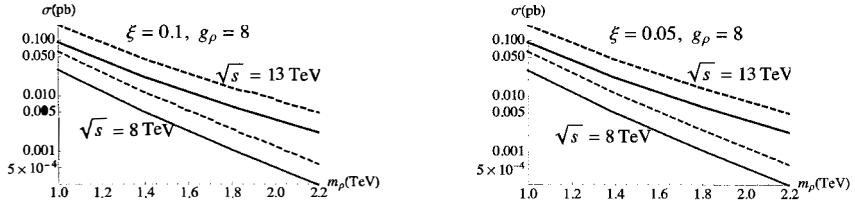

Figure 2 – Production cross-sections of ρ resonances from ρ^μ and W^μ, Z^μ mass mixing effect.

2.1 *ρ properties from mass mixing effects in the electroweak sector*

Let us first consider the effect of mass mixing between ρ^μ and W^μ, Z^μ fields alone. This leads to the following decay widths for spin-1 resonances

$$\begin{aligned}
\Gamma\left(\rho^0 \to W^+W^-\right) &\approx \Gamma\left(\rho^0 \to Zh\right) \approx \frac{m_\rho^5 \xi^2}{192\pi g_\rho^2 v^4}. \\
\Gamma\left(\rho^0 \to e^+e^-\right) &\approx \Gamma\left(\rho^0 \to \mu^+\mu^-\right) \approx \frac{g^4 m_\rho \left(1+\sqrt{1-\xi}\right)^2}{96\ 4\pi g_\rho^2} \\
\Gamma\left(\rho^0 \to q_i\bar{q}_i\right) &\approx \frac{g^4 m_\rho \left(1+\sqrt{1-\xi}\right)^2}{32\ 4\pi g_\rho^2}.
\end{aligned} \tag{5}$$

The mixing angle between ρ^μ and W^μ, Z^μ fields is proportional to g/g_ρ, hence it is not surprising that the deacy widths are suppressed by $1/g_\rho^2$. For sufficiently large values of m_ρ decays into gauge boson pairs and a gauge boson plus a Higgs boson will always dominate. However, for small values of ξ the ρ resonance decays into fermion pairs are non-negligible, especially in the low mass region. This can be seen in figure 1 for a specific value of $g_\rho = 8$ and two values of ξ, $\xi = 0.1$ (left) and $\xi = 0.05$ (right). The LHC production of ρ resonances is dominated by Drell-Yan $q\bar{q} \to \rho$. The production cross-sections for LHC@8TeV and LHC@13TeV are presented in figure 2 as a function of m_ρ, again for a specific value of $g_\rho = 8$ and two values of ξ, $\xi = 0.1$ (left) and $\xi = 0.05$ (right). The dashed lines correspond to the production of charged resonances, while the solid lines are represent the production of neutral resonances.

LHC exclusion limits for the spin-1 resonance mass can be obtained by using the publicly available search results for diboson, dilepton and dijet resonances. Presently the most stringest constraints are given by CMS dilepton resonance searches[6] and are presented in figure 3 (left) in the $g_\rho - m_\rho$ plane for specific values of $\xi = 0.1,\ 0.05$. The right panel of figure 3 shows the predicted range of these exclusion limits for LHC@14TeV. The present day exclusion limits on the mass of spin-1 resonances are slightly below 2TeV, while the predicted future LHC reach goes somewhat above 3TeV.

In order to maximize the LHC potential for the discovery of spin-1 resonances one should also make use of the decay channel $\rho \to Vh$, which becomes dominant in the high ρ mass region together with decays to gauge boson pairs. Together with M.Hoffmann R.Nikolaidou and S.Paganis we have looked at the potential impact of an LHC search for heavy vector mesons decaying to an electroweak gauge boson

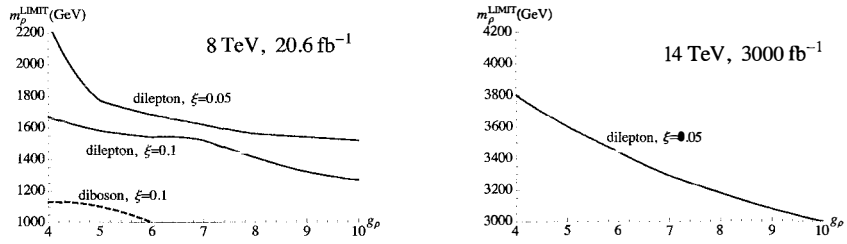

Figure 3 – Exclusion limits for ρ resonances from ρ^μ and W^μ, Z^μ mass mixing effect.

and a Higgs boson, using the fact that the Higgs boson will be highly boosted[7]. Using a $p_\perp \geq 550$ GeV cut on the transverse momentum of the Higgs system in very clean $h \to \gamma\gamma$ and $h \to ZZ^{(*)} \to 4\ell$ (where $\ell = e, \mu$, $V \to jj$) decay channels allows for significant reduction of the SM background. This method can lead to exclusion limits on ρ mass $\sim$ 3TeV at LHC@14TeV.

2.2 *The impact of interactions between ρ resonances and fermion resonances*

As mentioned before, the properties of spin-1 resonances rely not only on the effect of ρ^μ and W^μ, Z^μ mass mixing, but also on the direct coupling between ρ^μ and fermion resonances,

$$-i\bar{\psi} g_\rho \gamma^\mu T^a \rho_\mu^a \psi \tag{6}$$

where T^a are generators of $\mathcal{H}$. The coupling constant is taken to be the same as for the ρ self-interaction which happens to be the case in most effective models.

In the following I will present the approximate prediction of the impact of fermion resonances on the properties of ρ resonances transforming in the adjoint representation of $SU(2)_L$ using a simple toy model. The ρ resonance discussed in the previous section couples to the component of ψ charged under $SU(2)_L$, which I denote by ψ_L. In general ψ mixes through the mass matrix with the SM fermion fields, forming new mass eigenstates. Before electroweak symmetry breaking the SM left-handed quark doublet q_L mixes only with ψ_L. The quark mass matrix is diagonal for the following combinations

$$\begin{aligned} q'_L &= \cos\theta_L q_L - \sin\theta_L \psi_L \\ \psi'_L &= \sin\theta_L q_L + \cos\theta_L \psi_L \end{aligned} \tag{7}$$

where the mixing angle is determined by the Yukawa structure of the specific fermion partner construction. The quark doublet q'_L corresponds to massless fermion eigenstates and plays the role of the SM-like left-handed quark. It has an admixture from the composite fermion sector and following eq. 6 interacts directly with the spin-1 resonance ρ_L through

$$i\bar{q}'_L \gamma^\mu \left(-ig_\rho \sin^2\theta_L T_L^a \rho_{L\,\mu}^a\right) q'_L. \tag{8}$$

Non-zero Higgs VEV generates further mixing effects in the fermion mass matrix. From the point of view of SM-like quark couplings to spin-1 resonances however the leading order effect is given by $\sin\theta_L$ discussed above. In our LHC phenomenology analysis we take into account only this leading order effect.

Fermion resonances exhibit mass mixing terms with SM fermions (partial compositeness), which leads to the modification of spin-1 resonance couplings to SM fermions. This effect is especially important in the top sector, where the degree of partial compositeness is expected to be largest. If the degree of partial compositeness in first two generations of quarks is small, then the effect of direct couplings between ρ resonances and fermion resonances does not affect production cross sections of ρ resonances. However, the coupling of ρ resonances to top quarks becomes modified, leading to the modification of branching ratios and the overall decay width. More importantly, due to the direct coupling between ρ and

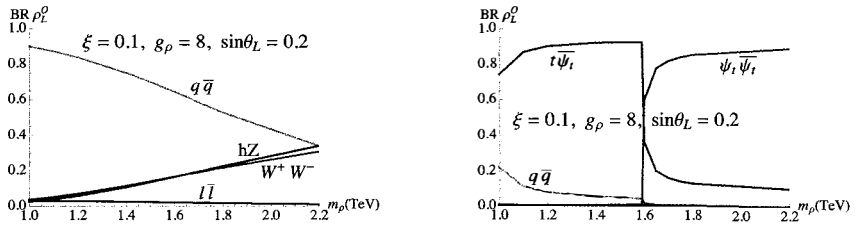

Figure 4 – Branching ratios of ρ resonances including the effect of direct coupling to fermion resonances, for $m_T \gtrsim 2$TeV (left) and $m_T \sim 0.8$TeV (right).

fermion resonances, spin-1 resonances can decay into a pair fermion resonances or a fermion resonance plus a standard model fermion. The mixing in the fermion sector discussed above introduces couplings of a ρ_L resonance to a light and a heavy fermion eigenstate

$$i\bar{q}'_L\gamma^\mu\left(-ig_\rho \sin\theta_L \cos\theta_L T^a_L \rho^a_{L\,\mu}\right)\psi'_L + i\bar{\psi}'_L\gamma^\mu\left(-ig_\rho \sin\theta_L \cos\theta_L T^a_L \rho^a_{L\,\mu}\right)q'_L. \qquad (9)$$

along with a coupling of ρ_L with two heavy fermion eigenstates scaled by $\cos^2\theta_L$. Due to naturalness arguments, top partners are expected to be light, hence the decay of ρ resonances into resonances related to the top sector is highly probable. Such a new decay channel for ρ can have a dramatic effect on LHC phenomenology of these resonances, on search strategies and interpretation of LHC limits. In order to show this effect let us consider two cases

1. heavy top partner $m_T \gtrsim 2$TeV
2. light top partner $m_T \sim 0.8$TeV.

In the first case decays into fermion partners are not kinematically allowed in the ρ resonance mass region probed presently at the LHC. The left panel of figure 4 shows the impact of the modification of ρ couplings with third generation quarks through the coupling with fermion resonances on the branching ratios of ρ, for a specific choice of $\xi = 0.1,\ g_\rho = 8$ and the fermion mixing angle $\sin\theta_L = 0.2$. One can notice that in the low m_ρ region the decays of spin-1 resonances are dominated by decays into quark pairs. Let us now see what happens when the decays into fermion partners become kinematically allowed. The right panel of figure 4 shows the branching ratios of ρ, for a specific choice of $\xi = 0.1,\ g_\rho = 8$ and the fermion mixing angle $\sin\theta_L = 0.2$, in the case when the top partners mass $m_T \sim 0.8$. One can see that the ρ resonance decays become dominated by decays into a SM quark and its composite partner as soon as the decay becomes kinematically allowed. For larger values of m_ρ, when the decay into a pair of fermion resonances becomes possible, this decay channel quickly becomes dominant.

Seeing these results, one immediately suspects that the ρ resonance width is also strongly affected by decays into fermion resonances. This is in fact the case, as one can see in the left panel of figure 5 illustrating the width to mass ratio Γ_ρ/m_ρ as a function of the resonance mass for $\xi = 0.1, \sin\theta_L = 0.2$ and several values of g_ρ. The overall width of ρ explodes as soon as the decay into two fermion resonances becomes possible.

All these effects of the interactions between ρ resonances and fermion partners modifies the interpretation of LHC limits on m_ρ with respect to those presented in the previous section. The limits obtained in both cases discussed above, for $m_T \gtrsim 2$TeV and $m_T \sim 0.8$TeV, are presented in the right panel of figure 5. One can notice that the limits are weaker than previously and no limits can be set when the decays into fermion resonance pairs become kinematically available.

3 Conclusions

Strong electroweak symmetry breaking can be tested at the LHC in many ways - by measuring Higgs boson properties, by constraining flavor observables and by direct searches for fermion and vector resonances. In this note the effective description of spin-1 resonances and the resulting LHC phenomenology

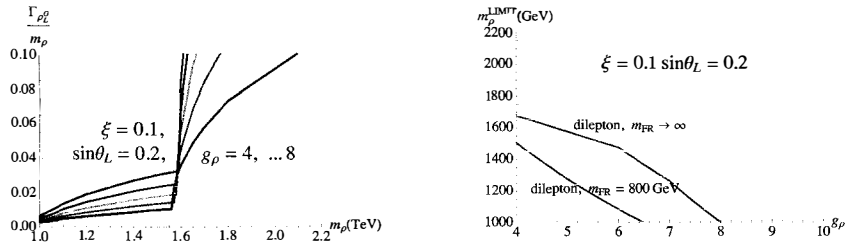

Figure 5 – Branching ratios of ρ resonances including the effect of direct coupling to fermion resonances, for $m_T \gtrsim 2$TeV (left) and $m_T \sim 0.8$TeV (right).

has been discussed. Decays of spin-1 resonances, for moderate values of $m_\rho \sim 1 - 2$ TeV, are often dominated by fermion pair production. Searches for dilepton resonances, due to small backgrounds, are presently sensitive to ρ resonances in this mass range. LHC is already probing the parameter space of vector resonances allowed by electroweak precision data. Searches for heavy vector mesons can be improved by taking advantage of the high $p_\perp$ of their decay products. The decay channel $\rho \to Vh$ (with boosted Higgs) is a promising channel for the search for heavy vector resonances. In order to improve searches for resonances related to strong electroweak symmetry breaking a better understanding of possible interactions between vector and fermion resonances is needed. Such interactions can significantly modify couplings of ρ resonances to SM quarks. Moreover, if ρ decays into fermion resonances are kinematically allowed, they can easily dominate over all other decay channels and magnify significantly the overall decay width, making direct searches for spin-1 resonances at the LHC much more difficult.

References

1. K. Agashe, R. Contino and A. Pomarol, Nucl. Phys. B **719** (2005) 165 [hep-ph/0412089].
2. A. Pomarol and F. Riva, JHEP **1208** (2012) 135 [arXiv:1205.6434 [hep-ph]].
3. S. R. Coleman, J. Wess, B. Zumino, Structure of phenomenological Lagrangians. 1., Phys. Rev. 177 (1969) 2239.
4. C. G. Callan, Jr., S. R. Coleman, J. Wess, B. Zumino, Structure of phenomenological Lagrangians. 2., Phys. Rev. 177 (1969) 2247.
5. M. Bando, T. Kugo, K. Yamawaki, Nonlinear Realization and Hidden Local Symmetries, Phys. Rept. 164 (1988) 217.
6. CMS Collaboration, Search for narrow resonances in dilepton mass spectra in pp collisions at $\sqrt{s} = 7$ TeV, arXiv:1206.1849 [hep-ex] (2013).
7. M. Hoffmann, A. Kaminska, R. Nicolaidou and S. Paganis, Eur. Phys. J. C **74** (2014) 11, 3181 [arXiv:1407.8000 [hep-ex]].

4.
Top Physics

Celebrating 20 years of the discovery of the Top Quark

P. Azzi
CERN & INFN Section of Padova, Via Marzolo 8, 35100 Padova (Italy)

An historical recount of the events leading to the discovery of the top quark in 1995 by the CDF and D0 experiments at the Tevatron.

1 Introduction

This presentation brings us back to the early nineties. It is interesting to picture ourselves without iphone and laptops, working on DEC VAX and having to stay in the office to work because there was no internet at home. The programming language was Fortran and plots were made with PAW. Detectors were becoming bigger and more complex, but no Silicon detector had been tried in a hadron collider yet. To put things in perspective for the LHC physicist of today: the MonteCarlo programs of the time did not differentiate between heavy and light quarks (VECBOS), there were no b-tagging algorithms, it was not clear that a Silicon detector could survive the radiation environement of an hadron collider such as the Tevatron and collecting data took a long time (one year for $20\,\mathrm{pb}^{-1}$). Nonetheless, working at the most powerful accelerator of the time was as exciting as it today.

2 History of particles discoveries

From the sixties onward the story of particle physics went through a phase of reorganization. First the idea that quarks would be the building bricks of mesons and baryons, then the appearance of the fact that quarks and leptons seemed to be organized in some sort of families. Discoveries kept confirming this pattern: quark charm in 1974, tau lepton in 1976 and the bound state of the quark b in 1977. By the year 2000 also the tau neutrino was discovered and only one piece seemed missing, the top quark, companion of the bottom quark with charge 2/3. The historical vision gives the impression of necessity of the existence of this quark but that was not the feeling at the time. On the experimental side the search kept giving null result and mass limits increased.

3 The search in Run0 and the hints from EWK fits

Initially the search was based on the hypotesis that the quark top was so light to be produced in the process of W boson decay, $W \to tb$ followed by $t \to b\ell\nu_\ell$. This was the strategy used during 1988/1989 during the so called Run 0 of the Tevatron, only the CDF experiment was running and did not have a silicon detector yet. A new limit of $M(top) \geq 91$ GeV was established that took out of the game the CERN hadronic machines.

However, once the LEP lepton collider started taking data it became clear that there was a great power in measuring precisely some of the fundamental Electroweak variables so that they could be used to constrain unknown ones, such as the mass of the top quark or the mass of the Higgs boson. As we can see in Fig.1, from the evolution of the value of the top mass as predicted from the result of electroweak fits as a function of time, there is a trend toward high values. A few weeks before the announcement of the CDF evidence for top production, the result of the electroweak fits extrapolation was presented in Moriond EWK 1994 and it corresponded to $M(top) = 174 \pm 11 \pm 18$ GeV.

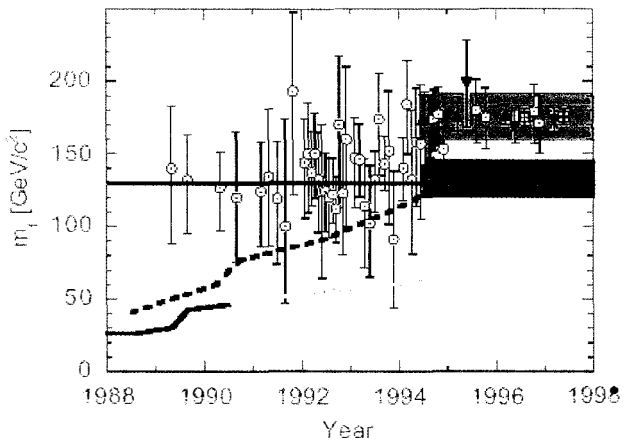

Figure 1 – Top mass from electroweak fits as a function of time

4 The Tevatron and its detectors

The Tevatron was a $p\bar{p}$ collider equipped with superconducting magnets that can provide a centre of mass energy of 1800 GeV. Two general purpose detectors were built around the interaction points: CDF and D0. Each detector a bit complementary to the other: D0 strong in jet and missing energy resolution thanks to its fully hermetic calorimeter, while CDF with better tracking and an innovative vertex silicon detector to identify displaced vertices from b-quark decays.

The top quark would be mainly produced at the Tevatron in pair of t and $\bar{t}$ either initiated by quarks (85% of the time) or by gluons (15% of the time). This is the opposite of what happens at a higher energy collider such as the LHC where the production cross section is dominated by the gluon fusion process. Another interesting comparison is that given the production cross section and the luminosity of the Tevatron there would be about ten $t\bar{t}$ produced per day, while at the LHC at 8 TeV there is about one $t\bar{t}$ event per second. This implies that at the end of Run I the Tevatron produced only about 100 $t\bar{t}$ pairs in each experiment. Not a very large statistic for

discovering a new particle in such a difficult environment.

The top would decay almost 100% in a W boson and a b quark that would hadronize into a jet. The final states of a top pair production can be classified based on the decay of the two W bosons: lepton plus jets (one W to leptons), dileptons (both Ws to leptons) or all-hadronic. Decays with τ leptons are treated separately in case of τ hadronic decays, but enter the (di)lepton cathegory in the other cases.

The Silicon Vertex Detector of CDF

The Silicon Vertex Detector of CDF is the first ever microstrip silicon detector being installed in a hadron collider environment. The initial idea, by a professor from Pisa, Aldo Menzione, was not considered a viable option. However, in 1992 the detector was installed on the beam pipe at the heart of the CDF experiment and started taking data with excellent performance throughout its life. At the time, it was the largest detector of this type, built of two cylinders of four layers of silicon microstrip detectors with 2D reconstruction capability, see Fig.2.

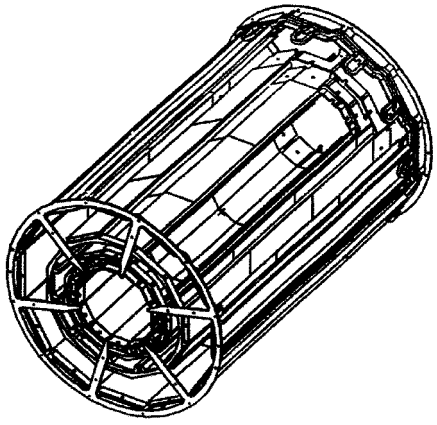

Figure 2 – The CDF Silicon Vertex Detector(SVX) Barrel module

5 The road to discovery

The Tevatron Run I started in 1992 and continued until 1996. During that time the race for the discovery was fierce. Very quickly both experiments were blessed by very spectacular events. For CDF, it was the 1992 "DPF event", a dilepton e-μ event with two jets one of them b-tagged by both SVX and a soft lepton. For D0 it was the "event 417", another dilepton e-μ event consistent with coming from the decay of an object with a mass between 145 and 200 GeV. The analyses strategies for both collaborations were organized in groups following the different final states topologies: dilepton, with the smallest branching ratio but highest signal over background ratio and the lepton plus jets channel, with a larger branching ratio but a higher background from W/Z+jets production, that could be reduced significantly with the identification of a b-jet. However, the initial performance of the Tevatron was disappointing. By the end of 1994 CDF manages to obtain "evidence" for a top signal with a handful of events, dominated by the presence of lepton plus jets events that would all cluster around the mass of 175 GeV.

Things changed during a technical stop of the accelerator, when a misplaced magnet was found, and after that the beam intensities doubled. The competition grew even more. The

concept of "blind analysis" was born: in order to be able to claim a discovery, the experiments decided a set of selection cuts a priori, using the early part of the data, to mantain unchanged until the whole statistics would be collected. A posteriori, since all the optimization was done with the hypotesis of a smaller top mass, the cuts chosen were not so optimal for a heavier object. A fun fact of the period was the fear of leaks of information across the Tevatron ring, the paranoia of the Top Physics groups from both experiments forced people to swear complete secrecy and to hide paper drafts in secret directories. Of course all these effort were useless as the information leaked anyway.

Finally on February 24th 1995 the two collaborations submitted back to back the two discovery papers that are published on April 3rd of the same year[2]. The new particle proved to be indeed very heavy, with a reconstructed mass in the lepton plus jets channel of $M(top) = 176 \pm 13\,\mathrm{GeV}$ for CDF, see Fig.3, and $M(top) = 199 \pm 30\,\mathrm{GeV}$ for D0, see Fig.4.

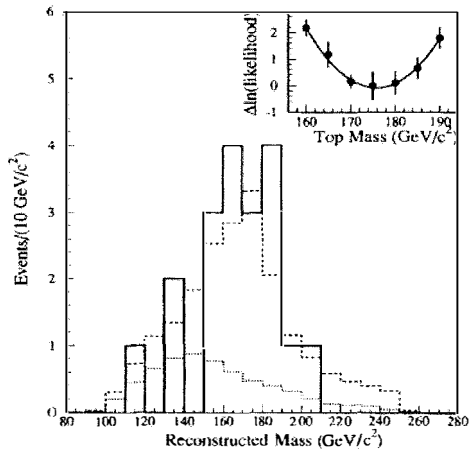

Figure 3 – Reconstructed mass distribution for the b-tagged W+4-jet events (solid). Also shown are the background shape (dotted) and the sum of background plus $t\bar{t}$ Monte Carlo simulations for m_t=175 GeV (dashed), with the background constrained to the calculated value. The inset shows the likelihood fit used to determine the top mass.

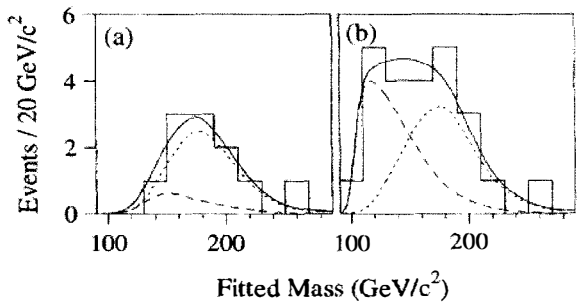

Figure 4 – Fitted mass distribution for candidate events (histogram) with the expected mass distribution for 199 GeV top quark events (dotted curve), background (dashed curve), and the sum of top and background (solid curve) for (a) standard and (b) loose events selection.

Other analyses

As the discovery of the new particle was based only on two final state topologies and very simple analysis strategy, soon enough the experiment were in need of a wider exploration of the properties of the top quark. Two main avenues were pursued, the one of more sophisticated analyses and the extraction of the signal in the remaining final state topologies. Some analyses existed that were indeed able to see a signal during the period before discovery, but using very innovative techniques that could not be fully verified to the satisfaction of the collaboration in the short time available, could finally be published[3]. Some other groups focused first on the more challenging all hadronic final state in order to confirm the expected behaviour of the new particle. For the all jets channels were the signal was submerged by a background several orders of magnitude larger, new ideas for background reduction and estimate were developed that brought to the evidence paper in this final state about one year after the announcement of the discovery[4]. The observation of the remaining decays including hadronic taus followed later on to complete the whole picture.

6 Conclusions

The discovery of the top quark has been one of the major enterprises of particle physics and it was achieved pushing to the extreme the limits of technology and creativity of the particle physics community. After 20 years, the interest in the top quark has not faded as, due to its large mass, it is possibly one of the best handles to find what new physics lies beyond the Standard Model.

References

1. "Evidence for top quark production in $p\bar{p}$ collisions at $\sqrt{s}$=1.8 TeV", CDF Collaboration (Abe, F. et al),*Phys. Rev. Lett.* **73**, 1994 (225-231)
2. "Observation of top quark production in $p\bar{p}$ collisions", CDF Collaboration (Abe, F. et al),*Phys. Rev. Lett.* **74**, 1995 (2626-2631) "Observation of the top quark", D0 Collaboration(Abachi, S. et al.),*Phys. Rev. Lett.* **74**, 1995 (2632-2637)
3. "Kinematic evidence for top quark production in W+multijets events in $p\bar{p}$ collisions at $\sqrt{(s)}$=1.8 TeV", *Phys. Rev.* D **51**, 1995 (4623)
4. "First observation of the all hadronic decay of $t\bar{t}$ pairs", CDF Collaboration (Abe, F. et al.), *Phys. Rev. Lett.* **79**, 1997 (1992-1997)

TOP QUARK PHYSICS AT THE TEVATRON

A.W. Jung
Fermilab, Particle Physics Division, Kirk Rd & Pine St, Batavia, 60510, IL, USA
Preprint: FERMILAB-CONF-15-208-PPD

An overview of recent top quark measurements using the full Run II data set of CDF or D0 at the Tevatron is presented. Results are complementary to the ones at the LHC. Recent measurements of the production cross section of top quarks in strong and electroweak production and of top quark production asymmetries are presented. The latter includes the new measurement of the $t\bar{t}$ production asymmetry by D0 in the dilepton decay channel. Within their uncertainties the results from all these measurements agree with their respective Standard Model expectation. Finally latest updates on measurements of the top quark mass are discussed, which at the time of the conference are the most precise determinations.

1 Introduction

The top quark is the heaviest known elementary particle and was discovered at the Tevatron $p\bar{p}$ collider in 1995 by the CDF and D0 collaboration[1,2] with a mass around 173 GeV. The Tevatron continues to produce complementary and similarly precise results than those at the LHC. At the Tevatron the production is dominated by the $q\bar{q}$ annihilation process, while at the LHC the gluon-gluon fusion process dominates. The top quark has a very short lifetime, which prevents the hadronization process of the top quark. Instead bare quark properties can be observed.
The measurements presented here are performed using either the dilepton ($\ell\ell$) final state or the lepton+jets (ℓ+jets) final state. Within the ℓ+jets final state one of the W bosons (stemming from the decay of the top quarks) decays leptonically, the other W boson decays hadronically. For the dilepton final state both W bosons decay leptonically. The branching fraction for top quarks decaying into Wb is almost 100%. Jets originating from a b-quarks are identified (b-tagged) by means of multi-variate methods employing variables describing the properties of secondary vertices and of tracks with large impact parameters relative to the primary vertex. Details on a typical $t\bar{t}$ event selection, applied requirements to reduce background contributions, and the determination of the sample composition can be found in Ref.[3].

2 Single top quark and top quark pair production

CDF and D0 conclude their measurement program of single top quark production and final results are discussed here. D0 performs a simultaneous measurement of the s- and t-channel electroweak single top-quark production cross sections [4]. Three multivariate analyses are used to separatc the signal from thc background. A two-dimensional discriminant based on the combination of the three methods is used to measure the s-, t- and $s+t$-channel cross sections in one analysis. Integrating over the s-channel or t-channel distribution, the t-channel or s-channel

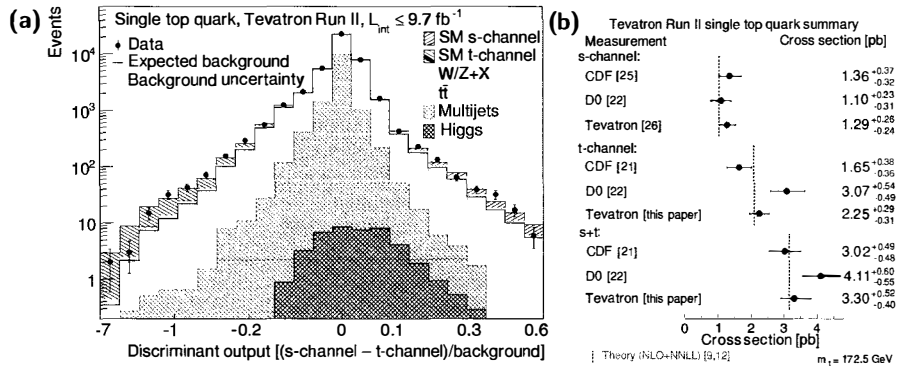

Figure 1 – Measurements of (a) single top quark production cross sections. Distribution of the (b) discriminant output comparing data with signal single top s- and t-channel contributions as well as various background contributions, all normalized to their expected value. Background uncertainties are indicated by the shaded band on top of the sum of the expected background contributions.

cross section is measured, respectively. No assumptions are made on the relative contribution of the s- or t-channel. CDF follows a similar strategy to separate signal and background by employing multivariate analyses in order to measure the individual single top production cross sections in various decay channels [6,7,8,9]. Figure 1(a) shows the combined D0 and CDF discriminant output used to extract the t- and $s+t$-channel cross sections with the signal cross sections and the various background contributions. Earlier D0 and CDF performed a combination of results on s-channel production cross sections, which yields a cross section of $\sigma_{s-\mathrm{ch.}} = 1.29^{+0.26}_{-0.24}$ pb with a significance of 6.3 s.d. corresponding to the first observation of s-channel single top quark production [5]. A summary of single top s-, t- and $s+t$-channel cross section results at D0 and CDF is given in Figure 1(b). All measurements are in good agreement with the latest theoretical calculations. A direct limit on the CKM matrix element $V_{tb} > 0.92$ at 95% confidence level is derived from the combined $s+t$-channel cross section measurement.

2.1 Top quark pair production

D0 uses events in the lepton+jets decay channel [3] to study differential top quark cross sections as a function of p_T (p_T^{top}), the absolute value of the rapidity $|y|$ ($|y^{\mathrm{top}}|$), as well as the invariant mass of the $t\bar{t}$ pair, $m_{t\bar{t}}$. The most direct constraint for contributions of new physics is set by the $m_{t\bar{t}}$ distribution, which is sensitive to the production of resonances decaying into top quarks, like a Z'. To identify the top quarks, a kinematic reconstruction, which takes into account experimental resolutions, is performed. All possible permutations of objects are considered, while preferentially assigning b-tagged jets to b-quarks and the chosen solution is the one with the smallest χ^2. The differential cross section is shown in Figure 2(a) as a function of the invariant mass $m_{t\bar{t}}$ compared to various predictions. Figure 2(b) shows the ratio of the differential cross section as a function of p_T^{top} to the approximate NNLO and various axigluon models [10] that could

alter the production of $t\bar{t}$ events. Data agrees with the SM predictions. Models implementing heavy axigluon masses are already in tension with existing data from the Tevatron and the LHC, but it is especially the low mass region where the Tevatron data adds sensitivity. The low-mass Z' model shows significant tension to the data in all three differential distributions.

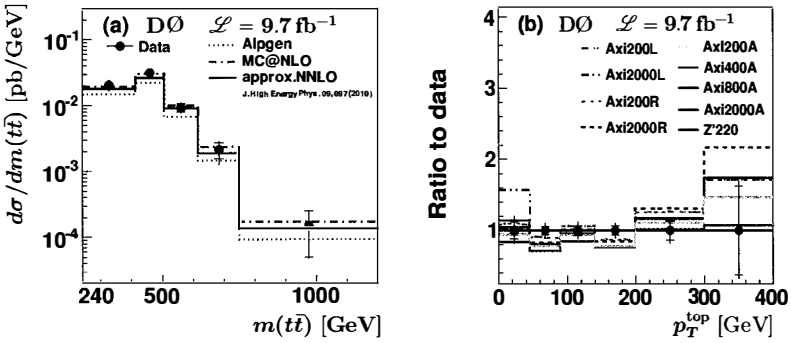

Figure 2 – Differential cross section data as a function of (a) $m_{t\bar{t}}$ compared with expectations from QCD. The inner error bar represents the statistical uncertainty, whereas the outer one is the total uncertainty including systematic uncertainties. Ratio of (b) differential cross section distributions as a function of p_T^{top} to various benchmark models of axigluon contributions to the $t\bar{t}$ production cross section are shown.

3 Top quark production asymmetries

The different initial state makes measurements of angular correlations in $t\bar{t}$ events, such as production asymmetries, complementary between the Tevatron and the LHC. Experimentally,

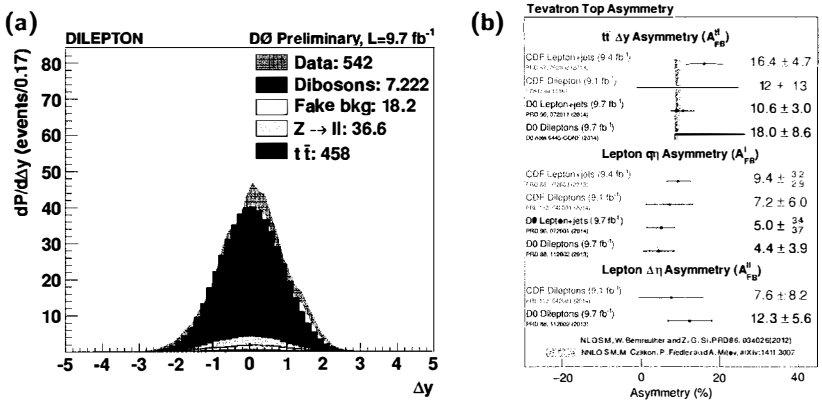

Figure 3 – The (a) Δy distribution for selected events compared to the expectation from MC@NLO and various background contributions. The use of the matrix elements technique reflects in correlated reconstructed Δy values, hence data is indicated by the shaded black band. Summary (b) of $A_{FB}^{t\bar{t}}$ measurements at the Tevatron compared to SM predictions, more details see text.

there are two approaches to measure these asymmetries: Either only a final-state particle, e.g. a lepton ('lepton-based asymmetries') is reconstructed or top quarks are fully reconstructed using

a kinematic reconstruction. The forward-backward asymmetry $A_{FB}^{t\bar{t}}$ at the Tevatron measures $\Delta y = y_t - y_{\bar{t}}$, and employing this quantity the production asymmetry is defined as:

$$A_{\mathrm{FB}}^{t\bar{t}} = \frac{N(\Delta y > 0) - N(\Delta y < 0)}{N(\Delta y > 0) + N(\Delta y < 0)} \tag{1}$$

Calculations at NLO QCD including electroweak corrections [11] predict $A_{FB}^{t\bar{t}} = 0.088 \pm 0.005$ and $A_{\mathrm{FB}}^{\mathrm{lep}} = 0.038 \pm 0.005$. Recently predictions at NNLO+NNLL pQCD including electroweak corrections became available with a predicted value of $A_{FB}^{t\bar{t}} = 0.095 \pm 0.007$ [12]. Latest updates provide a prediction at approximate N^{3}LO pQCD including electroweak corrections with a predicted value of $A_{FB}^{t\bar{t}} = 0.100 \pm 0.006$ [13].

The most recent experimental update is by D0, which presented a measurement of the fully reconstructed top quark asymmetry in the dilepton decay channel [16]. The measurement employs the full Run II data set corresponding to an integrated luminosity of 9.7/fb. Events with at least two jets, two high momentum and isolated electrons or muons or one high momentum isolated electron and muon are selected together with requiring a large missing transverse energy corresponding to the non-detected neutrinos of the leptonic W boson decay. To fully reconstruct the $t\bar{t}$ event a matrix element technique is applied, which calculates a likelihood of all the possible combinations when assigning reconstructed quantities to parton level $t\bar{t}$ quantities.

Figure 3(a) shows the $\Delta y = y_t - y_{\bar{t}}$ distribution for the selected data events compared to the signal expectation from MC@NLO and various background contributions. The measurement is corrected for detector effects to the parton level. If the measurement is interpreted as a test of the SM the measurement yields $A_{FB}^{t\bar{t}} = 0.180 \pm 0.061\,(\mathrm{stat.}) \pm 0.032\,(\mathrm{syst.})$. Due to the unknown top quark polarization an additional model uncertainty of 5.1% applies once the measurement is interpreted as a search for contributions of new physics.

A summary of $A_{FB}^{t\bar{t}}$ and $A_{\mathrm{FB}}^{\mathrm{lep}}$ measurements at the Tevatron is given in Figure 3(b). For measurements of $A_{FB}^{t\bar{t}}$ the deviations from the SM predictions got smaller with the D0 measurement [15] early last year employing the full data set. The recent NNLO+NNLL pQCD calculations are in agreement with the D0 data. CDF results with the full data set are showing deviations at the 1 to 2 s.d. level, especially the differential $A_{FB}^{t\bar{t}}$ measurement [14] shows larger deviations. It should be noted that efforts toward a Tevatron combination of $A_{FB}^{t\bar{t}}$ and $A_{\mathrm{FB}}^{\mathrm{lep}}$ measurements are currently ongoing.

4 Top Quark Mass

A large variety of other measurements of top quark properties at the Tevatron exists to date[18,19] and is not discussed in detail here. Measurements of the top quark mass use different experimental techniques in order to extract the top quark mass. The latest update is a measurement by D0 applying the leading order Matrix Element method based on an event-by-event probability. All top quark mass measurements applying standard methods are dominated by systematic uncertainties. Furthermore there is an additional theoretical uncertainty of about 1 GeV, which originates from the implementation of the quark mass in the MC employed to measure the top quark mass, aka pole vs $\bar{M}S$ mass discussion. Strategies to overcome the limitations in terms of experimental and theoretical uncertainties are already pursued and will become more important for the upcoming run of the LHC.

Currently the single most precise measurement of any experiment is done by D0 in the ℓ+jets decay channel [20] using the full Run II data set. It employs the so-called matrix element method (ME), which calculates an event-by-event probability to match the $t\bar{t}$ final state in the ℓ+jets decay channel to the observed reconstructed objects taking into account detector resolutions.

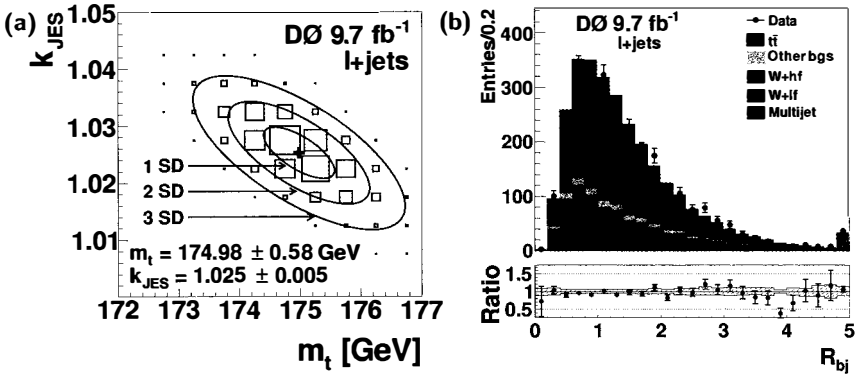

Figure 4 – The (a) two-dimensional likelihood as a function of the top quark mass and the in-situ calibration factor as measured by D0. The (b) ratio of the p_T of b-tagged jets to light quark jets originating from the hadronic W decay. Systematic uncertainties are indicated by the hashed band in the Data to MC ratio at the bottom of the histogram.

The hadronic decay of one of the W bosons allows to constrain the jet energy scale in-situ from data. Figure 4(a) shows the two-dimensional likelihood as a function of the top quark mass and the in-situ calibration factor. It yields a mass of $m_t = 174.98 \pm 0.41\,(\text{stat.}) \pm 0.64\,(\text{sys.} + \text{JES})$ GeV, corresponding to a total relative uncertainty of 0.43%. Figure 4(b) shows the ratio R_{bj} of the p_T of b-tagged jets to light quark jets originating from the hadronic W decay, which is sensitive to the b jet energy scale. Using MC template distributions for various true values of the b jet energy scale a cross check is performed, which yields $R_{\text{bj}} = 1.008 \pm 0.0195\,(\text{stat.})^{+0.037}_{-0.031}\,(\text{syst.})$ in good agreement with the expectation of unity [21].

The latest Tevatron combination of top quark mass measurements [22] by CDF and D0 combines all existing measurements. The combined top quark mass is $m_t = 174.34 \pm 0.64\,(\text{stat.} + \text{sys.} + \text{JES})$ GeV, corresponding to a total relative uncertainty of 0.37%.

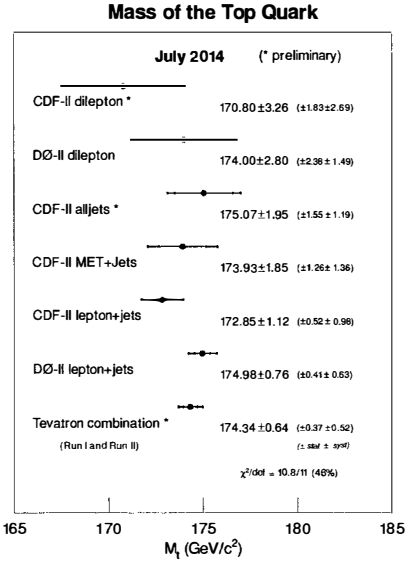

Figure 5 – Most precise input measurements to the latest Tevatron top quark mass combination. Measurements are in good agreement with each other as indicated by the χ^2 value.

Direct measurements of the top quark mass are becoming ever more precise and provide a stringent self-consistency test of the SM by correlating m_t versus m_W. Together with the measurement of the mass of the recently discovered Higgs boson [23,24] this is a strong self-consistency test of the SM [25]. Furthermore the stability of the electroweak vacuum can be studied [26].

5 Conclusions

Various recent measurements of top quark properties at the LHC and at the Tevatron are discussed. CDF and D0 conclude their measurement program of single top quark production and final results were presented at this conference. Pair production cross sections provide stringent tests of the SM calculations and do not show any hint for deviations from the SM. Direct measurements of the top quark mass are becoming ever more precise and provide a stringent self-consistency test of the SM and new insights into the question of the stability of the electroweak vacuum. Unlike in the past the measurements of $A_{FB}^{t\bar{t}}$ and $A_{\rm FB}^{\rm lep}$ basically agree with the latest SM predictions at the 1 to 2 s.d. level. Studies on combinations of $A_{FB}^{t\bar{t}}$ and $A_{\rm FB}^{\rm lep}$ at the Tevatron are currently ongoing. All of the presented results in terms are in good agreement with the Standard Model expectations and do not show any hints for new physics.

Acknowledgments

The author thanks the organizers of the $50^{\rm th}$ Moriond conference for the invitation and for the hospitality of the conference venue.

References

1. F. Abe *et al.* (CDF Collaboration), *Phys. Rev. Lett.* **74**, 2626 (1995).
2. S. Abachi *et al.* (D0 Collaboration), *Phys. Rev. Lett.* **74**, 2632 (1995).
3. V. M. Abazov *et al.* [D0 Collaboration] *Phys. Rev.* D **90**, 092006 (2014).
4. V. M. Abazov *et al.* (D0 Collaboration) *Phys. Lett.* B **726**, 656 (2013).
5. T. Aaltonen *et al.* (CDF & D0 Collaboration) *Phys. Rev. Lett.* **112**, 231803 (2014).
6. T. Aaltonen *et al.* (CDF Collaboration), Conf. Note 11025 [arXiv:1402.0484] (2014).
7. T. Aaltonen *et al.* (CDF Collaboration), Conf. Note 11076 [arXiv:1402.3756] (2014).
8. T. Aaltonen *et al.* (CDF Collaboration), Conf Note 11045 [arXiv:1402.3756] (2014).
9. T. Aaltonen *et al.* (CDF Collaboration), Conf Note 11033 [arXiv:1410.4909] (2014).
10. A. Carmona, M. Chala, A. Falkowski, S. Khatibi, M. M. Najafabadi, G. Perez and J. Santiago, [arXiv:1401.2443], (2014).
11. W. Bernreuther and Z. G. Si *Phys. Rev.* D **86**, 034206 (2012).
12. M. Czakon, P. Fiedler and A. Mitov, [arXiv:1411.3007].
13. N. Kidonakis, [arXiv:1501.01581].
14. T. Aaltonen *et al.* [D0 Collaboration] *Phys. Rev.* D **87**, 092002 (2013).
15. V. M. Abazov *et al.* [D0 Collaboration] *Phys. Rev.* D **90**, 072011 (2014).
16. V. M. Abazov *et al.* [D0 Collaboration] Conference note 6445 (2014).
17. T. Aaltonen *et al.* (CDF Collaboration), *Phys. Rev. Lett.* **113**, 042001 (2014).
18. D0 web page http://www-d0.fnal.gov/Run2Physics/top/
19. CDF web page http://www-cdf.fnal.gov/physics/new/top/top.html
20. V.M. Abazov *et al.* [D0 Collaboration], *Phys. Rev. Lett.* **113**, 032002 (2014).
21. V.M. Abazov *et al.* [D0 Collaboration], Subm. to PRD, [arXiv:1501.07912].
22. T. Aaltonen *et al.* [CDF & D0 Collaboration], [arXiv:1407.2682].
23. G. Aad *et al.* [ATLAS Collaboration], *Phys. Lett.* B **716**, 1 (2012).
24. S. Chatrchyan *et al.* [CMS Collaboration], *Phys. Lett.* B **716**, 30 (2012).
25. M. Baak *et al.* [Gfitter], *Eur. Phys. J.* C **72**, 2205 (2012).
26. D. Buttazzo *et al.*, [arXiv:1307.3536 [hep-ex]] (2013).

Precision on the top mass

Stefan Weinzierl
PRISMA Cluster of Excellence, Institut für Physik, Johannes Gutenberg-Universität Mainz, D - 55099 Mainz, Germany

In this talk I will focus on theoretical issues related to high precision determinations of the top mass. Several mass definitions are reviewed and their respective advantages and disadvantages are discussed. Precision determinations of the top mass will require a short-distance mass definition. I will summarise current work in this direction.

1 Introduction

The top quark mass – or equivalently the top Yukawa coupling – is one of the fundamental parameters of the Standard Model. Precise values for these fundamental parameters encode our current knowledge of the Standard Model and are required for various reasons. Focusing on the top quark mass, the motivations for a precision determination are as follows: First of all, the value of the top mass affects the theory predictions for top quark cross sections. It is therefore relevant in comparing measured top quark cross sections from the Tevatron and the ongoing LHC experiments with theoretical predictions of the Standard Model. Secondly, the value of the top mass affects searches for new particles in beyond the Standard Model (BSM) scenarios. Examples are searches for processes with top background or BSM decays into top quarks. For these first two reasons it is desirable to determine the top quark mass at least to a precision, such that the error originating from the top quark mass is not dominating the final error of the analysis. Currently, this would call for a high precision on the value of the top mass, but not for a very high precision. However, there are also reasons why a very high precision is desirable: The top quark mass is close to the electro-weak symmetry breaking scale $v = 246$ GeV. If there is new physics associated with electro-weak symmetry breaking, top quark physics is a place to look for. New particles with masses above energies accessible with current collider experiments may nevertheless leave their traces in quantum corrections. Therefore the combination of experimental precision measurements and theoretical precision calculations will be sensitive to new physics at higher scales. This is a very strong reason for a high precision determination of the top quark mass. As a final reason let us also mention, that if we assume the Standard Model to be valid to very high scales (possibly as high as the Planck scale), the stability of the electro-weak vacuum crucially depends on the precise numerical value of the top quark mass.

Let me also say from the very beginning that although I used the colloquial phrase "the top quark mass", there is nothing like "the" top quark mass. Like any other parameter in the Lagrangian of the Standard Model, the top quark mass will be subject to renormalisation. Like any other renormalised quantity, the renormalised top quark mass will depend on a chosen renormalisation scheme. As there are several possible renormalisation schemes, there is more than one legitimate definition of a renormalised top quark mass. In this talk I will discuss

subtleties of some popular mass renormalisation schemes and the way they affect experimental measurements.

2 Basic facts about the top quark

The top quark is the heaviest elementary particle known up to today. It has been discovered twenty years ago at the Tevatron [1,2] and it is currently studied at the LHC. The physics of the top quark is governed to a large extent by two essential numbers, the top quark mass and the top quark width. The current values of the top mass and the top width are [3,4]

$$m_t = 173.21 \pm 0.51 \pm 0.71 \text{ GeV}, \qquad \Gamma_t = 2.1 \pm 0.5 \text{ GeV}. \tag{1}$$

With a mass of roughly 173 GeV the top quark is heavier than all other known elementary particles. This large mass sets also a hard scale. From the top quark width one deduces immediately that the top quark lifetime ($\tau_t = \hbar/\Gamma_t$) is shorter than the characteristic hadronisation time scale. This implies that the top quark decays before it can form bound states. Given the facts that the large top quark mass sets a hard scale and that top quarks do not hadronise it follows that top quark physics is an ideal place for the application of perturbative QCD.

On the other hand it should not be forgotten that the top quark is like any other quark a colour-charged particle. Furthermore, the top quark is like any other quark of the second or third generation an unstable particle. These two facts imply that there is no asymptotic free top quark state in quantum field theory. Although top quark physics is described mainly by perturbative QCD, one has to pay attention that non-perturbative effects – originating from the fact that one deals with coloured and/or unstable particles – do not enter from the back door.

A characteristic scale of non-perturbative effects is $\Lambda_{\rm QCD}$. We can see from eq. (1) that the error on the top quark mass is approaching $\mathcal{O}(\Lambda_{\rm QCD})$. This raises immediately the question if the top quark mass can be measured with a precision better than $\mathcal{O}(\Lambda_{\rm QCD})$. Of course, the top quark mass is determined from experimental measurements and it seems at first sight that reducing the error would just imply improving the experimental precision. However, this is not the full story. Up to now there is no "theory-free" experimental determination of the top quark mass. Experimental measurements of the top quark mass rely on theoretical input for example through the template method or the matrix element method. In this way theoretical uncertainties might enter the determination of the top quark mass. There are now two possible scenarios, depending on the chosen mass definition. In the first – and not so favourable – scenario the extraction of the top mass is limited by non-perturbative effects of order $\Lambda_{\rm QCD}$. This means, that the precision on the top mass cannot be improved beyond $\mathcal{O}(\Lambda_{\rm QCD})$ by calculating perturbative higher-order corrections. The pole mass definition is an example for this scenario. In the second – and more favourable – scenario, one is not limited by non-perturbative effects and the precision on the top mass can – at least in principle – be improved below $\mathcal{O}(\Lambda_{\rm QCD})$ by the inclusion of perturbative higher-order corrections. Short-distance mass definitions are examples of the second scenario.

3 Basic facts about a fermion mass

Let us now review the advantages and disadvantages of several mass definitions. The starting point for a theoretical description is the Lagrange density, the relevant part reads

$$\mathcal{L}_{\rm fermion} = \bar{\psi}_{\rm bare} \left(i \not{\partial} - m_{\rm bare} \right) \psi_{\rm bare}. \tag{2}$$

Beyond leading-order in perturbation theory loop diagrams have to be taken into account. One of the simplest loop diagrams, which nevertheless allows us to discuss all relevant features, is

the one-loop fermion self-energy:

$$-i\Sigma \;=\; \text{ 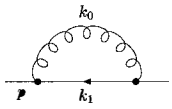 } \;=\; \frac{g^2 C_F}{\mu^{D-4}} \int \frac{d^D k}{(2\pi)^D}\; i\gamma_\rho \,\frac{i}{\not{k}_1 - m_{\rm bare}}\, i\gamma^\rho \,\frac{(-i)}{k_0^2}. \tag{3}$$

In four space-time dimensions the loop integral is divergent. A convenient method of regularisation is the continuation of the number of space-time dimensions to $D = 4 - 2\varepsilon$, the divergences will then show up as poles $1/\varepsilon$. Within dimensional regularisation one introduces in addition an arbitrary scale μ in order to keep the mass dimension of the regulated expression to its four-dimensional value. The loop integral in eq. (3) is easily computed and the result has with respect to the spinor structure the form

$$-i\Sigma \;=\; -i\,(A\not{p} + B m_{\rm bare})\,. \tag{4}$$

Here, A and B are functions of p^2, $m_{\rm bare}^2$, μ^2 and ε. As a function of ε, the quantities A and B have a Laurent series expansion in ε starting with ε^{-1}. Iterations of self-energy insertions may be resummed similar to the resummation of a geometric series:

$$\text{ 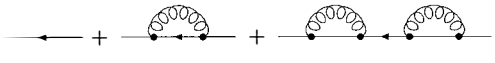 } \;=\; \frac{i}{\not{p} - m_{\rm bare} - \Sigma} \;=\; \frac{i(1+A)}{\not{p} - (1+A+B)m_{\rm bare}} + \mathcal{O}\left(\alpha_s^2\right). \tag{5}$$

Renormalisation relates the bare quantities to the renormalised quantities. We have to consider the quark field renormalisation and the mass renormalisation:

$$\psi_{\rm bare} \;=\; \sqrt{Z_2}\,\psi_{\rm renorm}, \qquad m_{\rm bare} \;=\; Z_m\, m_{\rm renorm}. \tag{6}$$

The quark field renormalisation allows us to absorb the divergences of the expression $(1 + A)$ in the numerator of eq. (5) into Z_2, the mass renormalisation allows us to absorb the divergences of $(1 + A + B)$ in the denominator of eq. (5) into Z_m. It should be stressed that the renormalisation constants and hence the renormalised quantities depend on the renormalisation scheme. In particular, the renormalised mass $m_{\rm renorm}$ depends on the renormalisation scheme. All renormalisation schemes entail that they absorb the ultraviolet divergent terms. Different renormalisation schemes differ in additional non-ultraviolet divergent terms.

4 Implications on the precision for the top quark mass

Let us now review different mass renormalisation schemes and its implications on the determination of the renormalised top quark mass in a given scheme.

4.1 The $\overline{\rm MS}$*-scheme*

The $\overline{\rm MS}$-scheme absorbs by definition only the parts proportional to $\frac{1}{\varepsilon} - \gamma_E + \ln(4\pi)$ and nothing else into the renormalisation constant Z_m. The renormalised and resummed quark propagator of eq. (5) reads then

$$\frac{i}{\not{p} - m_{\overline{\rm MS}} - (A+B)_{\rm fin} m_{\overline{\rm MS}}} \tag{7}$$

The essential properties of the $\overline{\rm MS}$-mass can already be deduced from eq. (7): Although not indicated explicitly, the $\overline{\rm MS}$-mass depends on the scale μ, leading to the concept of a running

mass. This follows from eq. (6): The bare mass m_{bare} is of course scale-independent, while Z_m and in consequence also $m_{\overline{\text{MS}}}$ depend on μ. Secondly, the presence of the finite terms $(A+B)_{\text{fin}} m_{\overline{\text{MS}}}$ in the denominator shows, that the propagator does not have a pole at $p^2 = m^2_{\overline{\text{MS}}}$ and matrix elements do not factor at $p^2 = m^2_{\overline{\text{MS}}}$. Thirdly, the extra terms $(A + B)_{\text{fin}}$ in the denominator are not constant as a function of p^2, they vary with p^2. This implies that the propagator in eq. (7) will not yield a Breit-Wigner shape. These properties should be kept in mind, when performing an analysis based on the $\overline{\text{MS}}$-mass.

The $\overline{\text{MS}}$-mass $m_{\overline{\text{MS}}}$ is an example of a short-distance mass, meaning that the mass definition is not affected by long-distance non-perturbative effects. The $\overline{\text{MS}}$-mass can be extracted from an infrared-safe observable [5,6] for a process like $pp \to l\bar{\nu} j j b\bar{b}$ at high energies by comparing for example σ_{exp} with $\sigma_{\text{theo}}\left(m_{\overline{\text{MS}}}\right)$. It should be stressed that the error of such a measurement is not affected by an $\mathcal{O}(\Lambda_{\text{QCD}})$-barrier. This is related to the fact that $\overline{\text{MS}}$-mass is a short-distance mass. On the theory side, the uncertainty can systematically be improved by the inclusion of higher-order corrections. The current state-of-the-art are NNLO calculations [7] with NNLL resummation [8,9,10,11,12,13] for $pp \to t\bar{t}$ and NLO calculations for the process $pp \to b\bar{b}W^+W^-$ including top decays and non-factorisable corrections [14,15]. At present, the dominant sources for the error on the determination of the $\overline{\text{MS}}$-mass from cross section measurements originates from uncertainties on α_s, the parton distribution functions and experimental uncertainties. None of those are specific to the chosen mass definition. A useful quantity in this context is the sensitivity $\mathcal{S}$ defined by

$$\left|\frac{\delta\sigma}{\sigma}\right| \;=\; \mathcal{S}\left|\frac{\delta m_{\overline{\text{MS}}}}{m_{\overline{\text{MS}}}}\right|. \tag{8}$$

For the determination of the top mass from the total cross section for $t\bar{t}$-production the sensitivity is $\mathcal{S} \approx 5$. The current error on the determination of the $\overline{\text{MS}}$-mass $m_{\overline{\text{MS}}}$ along these lines is about 2 GeV.

As a significant fraction of $t\bar{t}$-events actually are accompanied by additional jets, also the process $pp \to t\bar{t} + \text{jet}$ is of interest. For this process NLO calculations are available [16,17,18,19]. Differential distributions for this process show a sensitivity in the range $\mathcal{S} \approx 10...20$ and have therefore the potential for a more precise extraction of the top mass [20].

4.2 The on-shell-scheme

In the on-shell scheme the mass renormalisation constant Z_m is defined in such a way that the propagator has a pole at m_{pole}, (and m_{pole} is therefore called the pole mass). The renormalised and resummed quark propagator is then by definition

$$\frac{i}{\not{p} - m_{\text{pole}}}. \tag{9}$$

The pole mass m_{pole} includes the width and is therefore a complex quantity. The pole mass has the advantage that matrix elements factor at $p^2 = m^2_{\text{pole}}$ and that the propagator of eq. (9) leads to a Breit-Wigner shape. However, there is a major disadvantage: The pole mass is not a short-distance mass and sensitive to long-distance non-perturbative effects. In the on-shell scheme, the renormalisation constant Z_m contains contributions from all momentum scales, not just the ultraviolet region. It can be shown that in higher order in perturbation theory subsets of diagrams like the one shown in fig. 4.2 are dominated by the infrared region. The renormalised light fermion insertions are given by

$$-\frac{2}{3} N_f \frac{\alpha_s}{4\pi}\left[\ln\left(\frac{-k^2}{\mu^2}\right) - \frac{5}{3}\right], \tag{10}$$

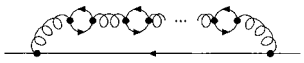

Figure 1 – Self-energy insertions on the gluon line leading to the renormalon ambiguity.

with k being the gluon momentum, which still needs to be integrated over. Due to the logarithm the ultraviolet and the infrared region are enhanced. A power series is Borel-summable if the Borel transform has no singularities on the real positive axis and does not increase too rapidly at positive infinity. With the replacement $\beta_{0,N_f} \to \beta_0$ one finds that the ultraviolet region leads to (non-critical) poles along the negative real axis, while the infrared region leads to poles along the positive real axis. Therefore this subset of diagrams is not Borel-summable and the full perturbative series can only be summed up to an infrared renormalon ambiguity. The renormalon ambiguity is of $\mathcal{O}(\Lambda_{\rm QCD})$ [21,22,23,24]. This ambiguity limits the precision by which the pole mass can be extracted from experiment.

In perturbation theory one can convert between different different renormalisation schemes. We therefore have a relation between the $\overline{\rm MS}$-mass and the pole mass, which with the notation $\bar{m} = m_{\overline{\rm MS}}(\mu = m_{\overline{\rm MS}})$ reads

$$m_{\rm pole} = \bar{m} \times \left[1 + c_1 \frac{\alpha_s(\bar{m})}{\pi} + c_2 \left(\frac{\alpha_s(\bar{m})}{\pi}\right)^2 + c_3 \left(\frac{\alpha_s(\bar{m})}{\pi}\right)^3 + c_4 \left(\frac{\alpha_s(\bar{m})}{\pi}\right)^4 + ...\right]. \quad (11)$$

The coefficients are known to four-loop order, the last coefficient c_4 was computed quite recently [25,26,27]. Numerically, we have for the top quark:

$$m_{\rm pole} = \bar{m} \times [1 + 0.046 + 0.010 + 0.003 + 0.001 + ...]. \quad (12)$$

The perturbative series appearing on the right-hand side of eq. (11) is again only an asymptotic series and has an renormalon ambiguity as well. This is clear from the fact that $\bar{m}$ is free of renormalon ambiguities, while $m_{\rm pole}$ on the left-hand side suffers from a renormalon ambiguity.

Crude estimates of the renormalon ambiguity may be either obtained from renormalon-based calculations [22], yielding

$$\delta m_{\rm pole} \approx C_F \frac{2\pi}{\beta_0} e^{\frac{5}{6}} \Lambda_{\rm QCD} \left(\ln \frac{\bar{m}^2}{\Lambda^2_{\rm QCD}}\right)^{-\frac{\beta_1}{2\beta_0^2}} \approx \mathcal{O}(300\ {\rm MeV}), \quad (13)$$

with $\beta_0 = 11 - 2N_f/3$ and $\beta_1 = 102 - 38N_f/3$, or from the last known term in the conversion formula in eq. (11). The latter gives

$$\delta m_{\rm pole} \approx c_4\, \bar{m} \left(\frac{\alpha_s(\bar{m})}{\pi}\right)^4 \approx \mathcal{O}(200\ {\rm MeV}). \quad (14)$$

Let us stress that both numbers are just crude estimates. Let us also note that the spread of two (or more) ad-hoc non-perturbative models might not reflect the true uncertainty from non-perturbative effects.

Let us finally mention that the top width is not affected by a renormalon ambiguity, when expressed in terms of a short-distance mass [21,24].

4.3 The MSR*-scheme*

We have seen that the pole mass is ambiguous by an amount of order $\mathcal{O}(\Lambda_{\rm QCD})$. But on the other hand the measurement of the peak position of the decay products of the top quark is an experimental observable. This brings us to the question, if one can translate a measurement

Table 1: Summary of the relevant scales, the appropriate effective theories together with the relevant matrix elements. Also indicated is the impact on the peak distribution and the dependence on the top mass.

Scale	Effective theory	Matrix elements	Impact on invariant mass distribution	Top mass dependence
$Q...m_t$	QCD	hard function	norm of the distribution	depends on m_t
$m_t...\Gamma_t$	SCET	jet function	shape and position	depends on m_t
$\Gamma_t...\Lambda_{QCD}$	top-HQET	soft function	shape and position	independent of m_t

of the peak position into a theoretical well defined short-distance mass. As experimentalists can measure many things to high precision (like for example the average number of pions in pp collisions), the question is if and how a measured quantity can be related to a quantity depending only on short-distance physics (the average number of pions is not a short-distance quantity). Before answering this question, let us analyse the problem in more detail. We should first find out, which scales are involved. In a second step we have to address the question on how to define a short-distance mass at a given scale. In the final step we then tackle the issue on how to translate the measurement into a short-distance mass.

Let us start with the involved scales. Effective theories are the appropriate tool to describe the relevant degrees of freedom at a given scale μ. Evolution operators allow us to move from a scale μ_1 to a scale μ_2. The evolution operators sum up large logarithms and avoid in this way large logarithms, which may otherwise spoil a perturbative expansion. Applied to the top mass, this has been analysed in detail for top pair production in electron-positron annihilation [28,29] and similar results are expected to hold for pp-collisions [30]. The relevant scales are the centre-of-mass energy Q, the top mass m_t, the top width Γ_t and $\Lambda_{\rm QCD}$. These scales are ordered as

$$\Lambda_{\rm QCD} < \Gamma_t < m_t < Q. \tag{15}$$

In the range $[m_t, Q]$ physics is described by QCD, while in the range $[\Gamma_t, m_t]$ the appropriate description is in terms of soft-collinear effective theory (SCET). At even lower scales $[\Lambda_{\rm QCD}, \Gamma_t]$ one uses a version of heavy quark effective theory adapted to top quarks (top-HQET). The relevant matrix elements for the various effective theories are the hard function, the jet function and the soft function, respectively. The impact on the invariant mass distribution from the various scales is as follows: Scales in the range $[\Gamma_t, m_t]$ affect mainly the norm of the distribution. The change in normalisation depends on m_t. Scales from the range $[\Gamma_t, m_t]$ have an impact on the shape and the position of the peak and these effects depend again on m_t. For the low scales from the range $[\Lambda_{\rm QCD}, \Gamma_t]$ one finds that these scales influence as well the shape and the position of the peak. However it is important to note that those effects are independent of m_t. The situation is summarised in table 1. Since the effects from the scales $[\Lambda_{\rm QCD}, \Gamma_t]$ are independent of m_t, it follows that we need a short-distance mass definition for scales down to Γ_t. The basic idea for the construction of an appropriate short-distance mass is to remove contributions which would give rise to the renormalon ambiguity. This approach is taken from experience with bottomium physics, where short-distance masses like the potential subtracted mass $m_{\rm PS}$ [31] or the 1S-mass $m_{\rm 1S}$ [32,33] have been considered. For the top quark this will involve apart from the UV-renormalisation scale μ a second scale R. The $\overline{\rm MS}$-mass is an example of a short-distance mass and we have $R = \bar{m}$ in this case. The MSR-mass [34] is a two-scale generalisation with a UV-scale μ and an IR-scale R, such that

$$m_{\rm MSR}(R=0) = m_{\rm pole}, \qquad m_{\rm MSR}(R=\bar{m}) = \bar{m}. \tag{16}$$

We may think of a short-distance mass definition in the same way as we think about an infrared-safe jet definition. A jet is defined by the specification of a jet algorithm (SISCone, k_t-algorithm,

anti-k_t-algorithm, etc.) and by a set of parameters associated to this algorithm (R, f, $n_{\rm pass}$, $y_{\rm cut}$, etc.). In the same way a short-distance mass is defined by the specification of a short-distance renormalisation scheme ($\overline{\rm MS}$-scheme, MSR-scheme, etc.) and by a set of parameters associated to this renormalisation scheme (μ, R, etc.).

As the soft function is independent of the top mass (and information on the soft function may be obtained from massless jet distributions), the peak position of the top invariant mass distribution can be related to a short-distance mass at a scale of Γ_t.

We now discuss how a measurement of the top invariant mass distribution can be translated into a short-distance mass. In the actual extraction of the top mass from experimental measurements theory sneaks in through the use of the template method or the matrix element method. For example, within the template method one generates first from Monte Carlo events for various values of $m_{\rm MC}$ and then determines the best fit to the experimental data. The Monte Carlo mass $m_{\rm MC}$ is only implicitly defined through the program code of the Monte Carlo. However, the factorisation of the effective field theory approach (hard function/jet function/soft function) has an analogy in typical event generators (hard matrix element/parton shower/hadronisation) and the shower cut-off scale is typically of the order of Γ_t (this is a numerical coincidence). Because the shower cut-off provides a strict infrared cut-off for long-distance effects, it can be argued that the Monte Carlo mass $m_{\rm MC}$ is something like a low-scale short-distance mass. Therefore a measurement based on the top invariant mass distribution determines the Monte Carlo mass $m_{\rm MC}$, which is a short-distance mass defined implicitly through the program code of a specific Monte Carlo. In principle we could convert this mass to any other mass definition, but in the case at hand we are hampered by the fact that a precise definition of the Monte Carlo mass is not accessible. Parametrising the ignorance of a precise definition of the Monte Carlo mass, Hoang and Stewart[30] made in a contribution to the Top Quark Physics workshop in 2008 a first estimate for the translation to the MSR-mass:

$$m_{\rm MC} \;=\; m_{\rm MSR}\,(R = 1...9\ {\rm GeV})\,. \tag{17}$$

The uncertainty in the infrared scale R introduces an uncertainty of the order of 1 GeV on the translation from the Monte Carlo mass to the MSR mass. Let us summarise: The Monte Carlo mass is a (not so well specified) short-distance mass and the translation from the Monte Carlo mass to a theoretically well defined short-distance mass at a low scale is currently estimated to be of the order of 1 GeV[30,35].

4.4 Work to do

There are ample opportunities to improve the current state of the art. They can be grouped into three categories.

First of all, the details related to factorisation and the various effective theories have only been worked out for $t\bar{t}$-production in electron-positron annihilation. This remains to be done for pp-collisions. Although it is believed that the general picture will hold in pp-collisions as well, there are some modifications related to initial state partons and phase space cuts imposed by the jet algorithm. These issues were absent in the e^+e^--analysis: There are no initial state partons and the analysis was based on hemisphere masses.

Secondly, it is worth studying the translation from the Monte Carlo mass to a well defined short-distance mass in more detail. In particular, one should firmly establish that the shower cut-off effectively implements some short-distance mass. In addition, the translation and the uncertainty from the Monte Carlo mass to a well defined short-distance mass can be improved.

Thirdly, it is worth a thought to envisage a dedicated event generator, based on a well defined short-distance top mass. This would eliminate the translation from a Monte Carlo mass to a well defined short-distance and the corresponding uncertainties from this part. This might not be impossible. In fact, there are proposals in the literature in a context not specific to top physics to go from effective theories like SCET to exclusive event generators[36,37,38].

5 Conclusions

The precise numerical value of the top mass is essential for many analyses in high-energy precision physics. With the ongoing LHC experiments the error on the top mass is approaching $\mathcal{O}(\Lambda_{\rm QCD})$. At this precision, an adequate short-distance mass definition is mandatory. The pole mass is not a short-distance mass and ambiguous by an amount of $\mathcal{O}(\Lambda_{\rm QCD})$. The $\overline{\rm MS}$-mass is a short-distance mass and can be used at high scales. The MSR-mass is a generalisation of the $\overline{\rm MS}$-mass and can also be used as a short-distance mass at lower scales.

As an outlook towards the future it is expected that a threshold scan at an e^+e^--machine will be able to determine the top quark mass with a precision below 100 MeV. Again, the use of an adequate short-distance mass like the potential subtracted mass or the 1S-mass is mandatory.

References

1. CDF, F. Abe et al., Phys.Rev.Lett. 74 (1995) 2626.
2. D0, S. Abachi et al., Phys.Rev.Lett. 74 (1995) 2632.
3. Particle Data Group, K. Olive et al., Chin.Phys. C38 (2014) 090001.
4. ATLAS, CDF, CMS, D0, (2014), arXiv:1403.4427.
5. U. Langenfeld, S. Moch and P. Uwer, Phys. Rev. D80 (2009) 054009.
6. M. Dowling and S.O. Moch, Eur.Phys.J. C74 (2014) 3167.
7. M. Czakon, P. Fiedler and A. Mitov, Phys.Rev.Lett. 110 (2013) 252004.
8. S. Moch and P. Uwer, Phys. Rev. D78 (2008) 034003.
9. M. Czakon, A. Mitov and G.F. Sterman, Phys. Rev. D80 (2009) 074017.
10. M. Cacciari et al., Phys.Lett. B710 (2012) 612.
11. N. Kidonakis, Phys. Rev. D82 (2010) 114030.
12. V. Ahrens et al., JHEP 09 (2010) 097.
13. M. Beneke et al., Nucl. Phys. B855 (2012) 695.
14. A. Denner et al., Phys. Rev. Lett. 106 (2011) 052001.
15. G. Bevilacqua et al., JHEP 02 (2011) 083.
16. S. Dittmaier, P. Uwer and S. Weinzierl, Phys. Rev. Lett. 98 (2007) 262002.
17. S. Dittmaier, P. Uwer and S. Weinzierl, Eur. Phys. J. C59 (2009) 625.
18. K. Melnikov and M. Schulze, Nucl. Phys. B840 (2010) 129.
19. K. Melnikov, A. Scharf and M. Schulze, Phys.Rev. D85 (2012) 054002.
20. S. Alioli et al., Eur.Phys.J. C73 (2013) 2438.
21. I.I.Y. Bigi et al., Phys. Rev. D50 (1994) 2234.
22. M. Beneke and V.M. Braun, Nucl.Phys. B426 (1994) 301.
23. M. Beneke, Phys. Lett. B344 (1995) 341.
24. M.C. Smith and S.S. Willenbrock, Phys. Rev. Lett. 79 (1997) 3825.
25. K. Chetyrkin and M. Steinhauser, Nucl.Phys. B573 (2000) 617.
26. K. Melnikov and T.v. Ritbergen, Phys.Lett. B482 (2000) 99.
27. P. Marquard et al., Phys.Rev.Lett. 114 (2015) 142002.
28. S. Fleming et al., Phys. Rev. D77 (2008) 074010.
29. S. Fleming et al., Phys.Rev. D77 (2008) 114003.
30. A.H. Hoang and I.W. Stewart, Nucl.Phys.Proc.Suppl. 185 (2008) 220.
31. M. Beneke, Phys.Lett. B434 (1998) 115.
32. A.H. Hoang, Z. Ligeti and A.V. Manohar, Phys.Rev. D59 (1999) 074017.
33. A. Hoang and T. Teubner, Phys.Rev. D60 (1999) 114027.
34. A.H. Hoang et al., Phys.Rev.Lett. 101 (2008) 151602.
35. S. Moch et al., (2014), arXiv:1405.4781.
36. C.W. Bauer and M.D. Schwartz, Phys.Rev. D76 (2007) 074004.
37. C.W. Bauer, F.J. Tackmann and J. Thaler, JHEP 12 (2008) 010.
38. C.W. Bauer, F.J. Tackmann and J. Thaler, JHEP 12 (2008) 011.

ATLAS+CMS TOP MASS: CURRENT RESULTS AND FUTURE MEASUREMENTS

M.A. VOUTILAINEN, FOR THE ATLAS AND CMS COLLABORATIONS
Helsinki Institute of Physics, P.O. Box 64,
FI-00014 University of Helsinki, Finland

The LHC experiments are fast catching up with Tevatron on the accuracy of the top quark mass (m_t) measured using standard methods, with the latest CMS combination reaching an accuracy of 0.66 GeV compared to 0.64 GeV for Tevatron. The future prospects look promising as both ATLAS and CMS have commissioned new methods (3D-R_{bq}, Z+b / Z+jet ratio) to address the leading systematic uncertainty from b-jet energy scale (bJES). At this level of precision the agreement between generator mass m_t^{MC} and the theoretical pole mass m_t^{pole} becomes relevant, and alternative methods are also explored.

1 Introduction

The top quark mass m_t is a fundamental parameter of the standard model, and together with the W boson mass M_W and the Higgs boson mass M_H it provides a strong self-consistency check of the electroweak theory. Using input values of $m_t = 173.34 \pm 0.76$ GeV,[1] $M_W = 80.385 \pm 0.015$ GeV and $m_H = 125.14$ GeV in a global electroweak fit,[2] the three parameters are compatible within 1.5 σ.

The top quark also provides a unique opportunity to directly probe a colored particle that decays before it has time to hadronize, helping to better understand QCD. Top quarks are mostly produced in $t\bar{t}$ pairs, and for almost 100% of the cases, the top and anti-top quark decay into a W boson and a b or $\bar{b}$ quark. The W bosons further decay into a $q\bar{q}'$ pair or a lepton and a neutrino, while the b quark and light quarks form jets. The fast decay of the top quark makes the measurement of the top quark mass theoretically and experimentally challenging. For example, there is a difference between the theoretical top quark pole mass $m_{t,\mathrm{pole}}$ and the definitions $m_{t,\mathrm{MC}}$ used in the MC generators used to calibrate the measurements. The b and anti-b quarks also experience color re-connection that can affect experimental measurements.

The measurement of the top quark mass is done in a very rich hadronic environment, and has multiple spin-offs that can benefit other measurements. The b jets produced in top decays offer a clean sample for studying b quark hadronization, with the m_t and $t\bar{t}$ kinematics offering a reference point for the initial energy at the parton level. The m_W and m_t can also be turned

into constraints on the light quark and b quark jet energy scales, JES and bJES, respectively.

Comparison of the measured top quark and Higgs boson masses to standard model predictions has suggested that we may inhabit a meta-stable vacuum.[3] There is considerable debate about this conclusion, which assumes stability of the SM vacuum up to the Planck scale, an unlikely assumption in itself. There is also some tension between the recent results from the Tevatron[4] and CMS,[5] and uncertainty in the relation between the theoretical pole mass $m_t^{\rm pole}$ used in the stability calculation and the MC generator mass $m_t^{\rm MC}$ measured by the experiments. Nevertheless, the "fate of the universe" implied by vacuum meta-stability has been a fertile ground for discussions.

2 Standard reconstruction

The invariant mass of the top quark can be reconstructed from the decay products of the top quark, which include leptons (μ, e), jets and missing transverse energy $E_{T,\rm miss}$. The top quark mass measurements are traditionally divided by the decay channels of the two W bosons: dilepton events with both W boson decaying into a lepton and a neutrino (5% of all $t\bar{t}$ events), lepton+jets events with one W boson decaying semi-leptonically and the other into $q\bar{q}'$ (30%), and all-jets events (45%) with only hadronic decays of the W bosons.

The so-called standard measurements measure top quark mass relative to the MC generator mass $m_t^{\rm MC}$ by first building an estimator for m_t (*e.g.* invariant mass of the top quark daughters), then parameterizing this estimator versus $m_t^{\rm MC}$ and possibly other variables such as JES and bJES. The single-variable measurement of m_t is typically referred to as 1D, while the combination of m_t and JES is referred to as 2D and m_t, JES and bJES as 3D. The top quark mass is finally extracted by performing a maximum likelihood fit to data. It is also possible to combine multiple estimators per event in the likelihood.

The LHC experiments CMS[6] and ATLAS[7] have collected about 5 fb^{-1} of data at 7 TeV in 2011, corresponding to about 800,000 $t\bar{t}$ pairs, and about 20 fb^{-1} at 8 TeV in 2012, corresponding to about five million $t\bar{t}$ pairs. Measurements are available from CMS in all channels on both data sets,[8,9,10,11,12,13,14] and from ATLAS on the 7 TeV data set.[15,16] In this article we report the most recent 8 TeV resuls from CMS, and the latest 7 TeV results from ATLAS.

2.1 Dilepton events

The signature of the dilepton channel is two b jets, two leptons and $E_{T,\rm miss}$ from two neutrinos. This topology is underconstrained due to the two ν, requiring some external information for solving m_t. The dilepton m_{lb} measurement,[11] which is the first blind m_t measurement from CMS, uses the invariant mass m_{lb} of a lepton and b jet as the estimator for m_t. Another complementary technique called Analytical Matrix Weighting Technique (AMWT)[12] uses the full event kinematics with multiple solutions for m_t. Both measurements have JES (0.4–0.6 GeV) and b fragmentation (0.6–0.7 GeV) among the leading systematic uncertainties. The AMWT is very sensitive to theory scale uncertainty (0.87 GeV), while m_{lb} is less sensitive to theory scale (0.55 GeV), but adds uncertainty from top p_T modeling (0.66 GeV).

The **new** ATLAS dilepton measurement[15] also used the m_{lb} method, with leading systematics from JES (0.75 GeV), bJES (0.68 GeV) and hadronization plus underlying event (0.53 GeV). Compared to the CMS measurement ATLAS has slightly larger JES uncertainty and less events, but benefits from an in-depth study of correlations with the lepton+jet measurement, which reduces the later ATLAS combination uncertainty. The three results are summarized in Table 1.

2.2 Lepton+jets events

The signature of the lepton+jets channel is two b jets, two other jets and $E_{T,\rm miss}$ from a single neutrino. This topology is often referred to as the golden channel as it has very clean event

Table 1: Results from dilepton events.

$m_{t,\mathrm{AMWT}}(\mathrm{CMS})$	=	$172.5 \pm 0.2(\mathrm{stat}) \pm 1.4(\mathrm{syst})$ GeV
$m_{t,m_{lb}}(\mathrm{CMS})$	=	$172.3 \pm 0.3(\mathrm{stat}) \pm 1.3(\mathrm{syst})$ GeV
$m_{t,m_{lb}}(\mathrm{ATLAS})$	=	$173.8 \pm 0.5(\mathrm{stat}) \pm 1.3(\mathrm{syst})$ GeV

kinematics and can be used to constrain the JES in-situ with the hadronic W boson decay using the W boson mass $m_W = 80.4$ GeV as a constraint. ATLAS has developed a novel technique of constraining also the bJES in-situ using the R_{bq} variable, shown in Fig. 1(left), defined approximately as the ratio of the b jet p_T to the W boson p_T.

In the **new** 3D ATLAS lepton+jet measurement at 7 TeV[15] the JSF (JES scale factor) is measured as JSF-1= $+1.9 \pm 2.7\%$(syst + stat) and bJSF (bJES scale factor relative to JES) as bJSF-1= $+0.3 \pm 2.4\%$(syst + stat). The leading systematic uncertainties are 0.67 GeV *statistics-limited* uncertainty for bJES, 0.58 GeV for JES and 0.50 GeV for b tagging, for a total systematic uncertainty of 1.0 GeV. Given the statistical limitations, this measurement is expected to substantially improve in the future.

The CMS 2D lepton+jet measurement[13] at 8 TeV shown in Fig. 1(right) is the most precise LHC result to date, with 0.8 GeV total uncertainty. It measures m_t together with in-situ JSF using the m_W constraint, finding JSF-1= $+0.7 \pm 1.2\%$(syst + stat). The leading systematics are bJES (0.41 GeV) and signal modelling (0.35 GeV), with the rest divided evenly among multiple smaller uncertainties. The measured m_t has been carefully studied versus event kinematics to verify good modelling of the data by the central MadGraph[17]+Pythia 6[18] tune Z2* MC simulation, and by several other MC generators. The studied variables include N_{jet}, ΔR_{xx}, $p_{T,x}$, $|\eta|_x$ *etc.*, where x is q, b, t or W. All variables are found to be in good agreement with simulation. The CMS and ATLAS results are summarized in Table 2.

Table 2: Results from lepton+jets events.

$m_{t,\mathrm{2D}}(\mathrm{CMS})$	=	$172.0 \pm 0.2(\mathrm{stat}) \pm 0.8(\mathrm{syst})$ GeV
$m_{t,\mathrm{3D}}(\mathrm{ATLAS})$	=	$172.3 \pm 0.8(\mathrm{stat}) \pm 1.0(\mathrm{syst})$ GeV

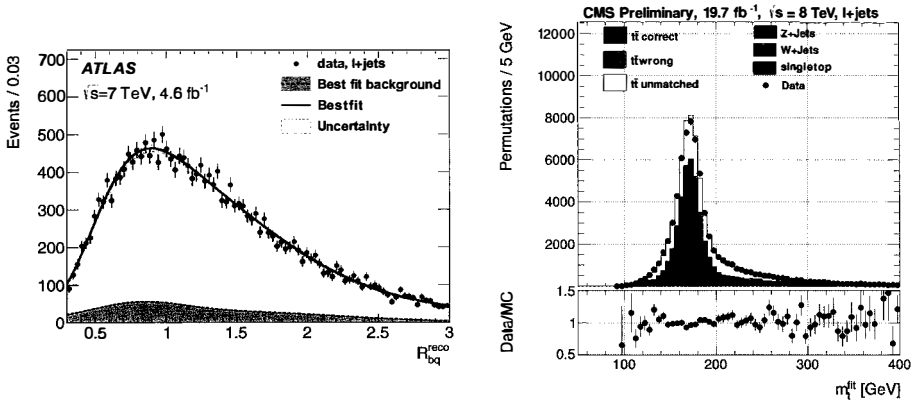

Figure 1 – Lepton+jet measurements at LHC: R_{bq} used for bJSF at ATLAS (left)[15], and fitted top quark mass m_t^{fit} at CMS (right)[13].

2.3 *All-jets events*

The all-jets signature is two b-tagged jets and at least four light jets. The methods employed for the CMS 8 TeV measurement[14] are the same as those used for the lepton+jet measurement, with similar systematics of 0.36 GeV for bJES and 0.29 GeV for signal modelling. The JSF-1= $+0.7 \pm 1.1\%$(syst + stat), in excellent agreement with the lepton+jet measurement. Despite high combinatorial background, the analysis reaches 78% purity with narrow signal peak afer cuts on goodness-of-fit $P_{\rm GOF} > 0.1$ and $\Delta R(b,b) > 2.0$.

The purity before cuts of 16% is very similar to that obtained by the ATLAS 7 TeV measurement[16] (17%), which determines m_t from a template fit to ratio of 3-jet mass to 2-jet mass $R_{3/2}$. This is in essence a 2D measurement as well, without explicit JSF. The leading systematics are 0.62 GeV for bJES, 0.51 GeV for JES and 0.50 GeV for hadronization for a total systematic uncertainty of 1.2 GeV, compared to 0.8 GeV at CMS. The CMS and ATLAS results are summarized in Table 3.

Table 3: Results from all-jets events.

$m_{t,\rm 2D}$(CMS)	=	172.1 ± 0.4(stat) ± 0.8(syst) GeV,
$m_{t,R_{3/2}}$(ATLAS)	=	175.1 ± 1.4(stat) ± 1.2(syst) GeV

2.4 *Run I combinations*

Both CMS and ATLAS have published new combinations of their m_t measurements that are competitive with the the World combination[1] from March 2014 (0.76 GeV uncertainty), or in the case of CMS even exceeding it. The Tevatron experiments have meanwhile released a new combination of their results[4] in July 2014, which currently holds the record precision, but only by a narrow margin (0.64 GeV total uncertainty at Tevatron versus 0.66 GeV at CMS).

The CMS combination uses dilepton and lepton+jets channels from 2010 (7 TeV, 36 pb^{-1}) and all three channels from both 2011 (7 TeV) and 2012 (8 TeV). There is good consistency between individual measurements and channels. The final result is dominated by the 2012 lepton+jets measurement (46.5% constrained BLUE combination coefficient), but with substantial contributions from the 2012 all-hadronic (23.0%), 2011 lepton+jets (14.6%) and other 2011 and 2012 measurements as well.

The **new** optimised ATLAS combination[15] uses only the new 7 TeV lepton+jet and dilepton measurements. The optimised treatment of correlated systematics between these two measurements leads to 28% gain relative to lepton+jet only, and the new measurements improve 36% relative to the previous ATLAS combination and 4% relative to the previous LHC combination (0.91 GeV versus 0.94 GeV). The leading systematics of the ATLAS combination are JES (0.41 GeV), bJES (0.34 GeV), hadronization and UE (0.35 GeV) and b tagging (0.25 GeV).

The Run I combinations from CMS and ATLAS are summarized in Fig. 2. Both experiments measure a value of m_t consistent with the previous world average of 173.34 ± 0.76 GeV, but lower than the new Tevatron combination of 174.34 ± 0.64 GeV,[4] which is dominated by a single new D0 measurement in the lepton+jet channel.[19] The tension between this D0 measurement and the corresponding 8 TeV lepton+jet measurement from CMS[13] is about 3 σ.

3 Alternative methods

The standard methods all share a few common features: (i) $t\bar{t}$ event reconstruction, (ii) mass calibration based on simulation ($m_t^{\rm measured} = m_t^{\rm MC}$), (iii) large sensitivity to JES and bJES uncertainties.

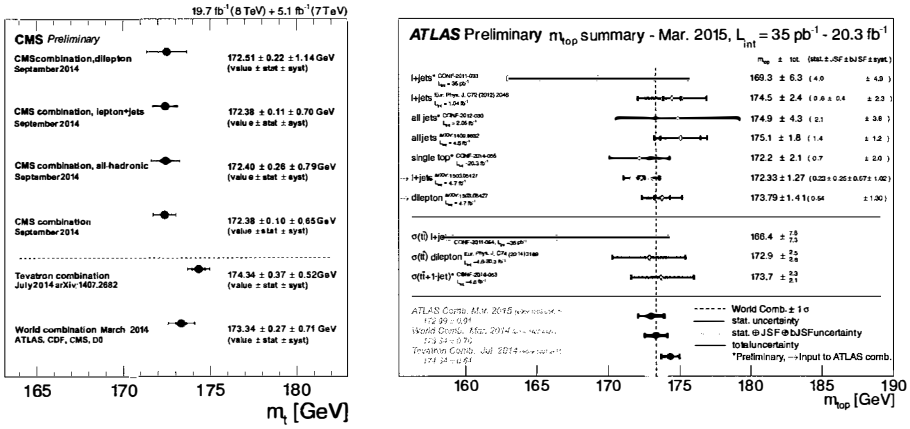

Figure 2 – Run I combinations for m_t from CMS (left)[5] and ATLAS (right) compared to latest world average and Tevatron combination. The ATLAS summary has been updated with the latest results for Moriond 2015.[15]

The alternative methods use observables and/or final states sensitive to different systematic uncertainties, and they often attempt to extract top quark mass in a well-defined renormalisation scheme to avoid dependence on MC generator definition of m_t. Recent alternative analyses include measurements using B-hadron lifetime,[20] kinematic end points,[21] and a propaedeutic study of $b \to J/\Psi$ channel and underlying event.[22] In this article we focus on single-top events in the t-channel[23] and extraction of $m_t^{\rm pole}$ from inclusive $t\bar{t}$ cross section[24,25] and from $t\bar{t}$+jet differential cross section.[26] Although not a m_t measurement, we also discuss the determination of bJES from data.[27]

3.1 Single top in t-channel

The signature of single top in t-channel is one lepton, one b jet, one light jet and $E_{T,\rm miss}$ from a single neutrino. The ATLAS analysis[23] shares many similarities with the dilepton measurement in the $t\bar{t}$ channel, and the mass is also measured using m_{lb} template. The backgrounds are overall larger, but the presence of a single t reduces combinatorial background and having a single ν helps to avoid some issues involved in an underconstrained system. A neural network is used to enrich the t-channel, obtaining an expected purity of about 46%, with another 26% from $t\bar{t}$ and the rest 28% from other non-top quark backgrounds.

The main benefit of the single top is different sensitivity to color reconnection and a different Q^2 scale. The sample is also statistically independent from the $t\bar{t}$ measurements, which helps in m_t combinations. The dominant systematic uncertainties are similar to the dilepton channel in $t\bar{t}$: JES (1.5 GeV), hadronization (0.7 GeV) and backgrounds (0.6 GeV).

3.2 Inclusive $t\bar{t}$ cross section

The $t\bar{t}$ cross section depends on the theoretical pole mass $m_t^{\rm pole}$ in a well-defined way. This allows the cross section $\sigma_{t\bar{t}}$ to be re-interpreted as a measurement of $m_t^{\rm pole}$. The dominant systematic uncertainties in this case are uncertainties from parton distribution functions (PDFs) and the theory scale uncertainty. The biggest challenge is reducing the theory uncertainties to the level where the difference between MC generator masses and pole mass is expected to matter: $\Delta(m_t^{\rm MC}, m_t^{\rm pole}) \leq 1$ GeV.

The pole mass has been measured by ATLAS from combined 7 and 8 TeV data,[25] and by CMS from the 7 TeV data.[24] There is still quite some variability in the results as shown in Fig. 3,

with uncertainties of about 3 GeV on both experiments. The differences in the measured $m_t^{\rm pole}$ between CMS and ATLAS is a direct consequence of the difference in the 7 TeV cross section measurements by the two experiments.

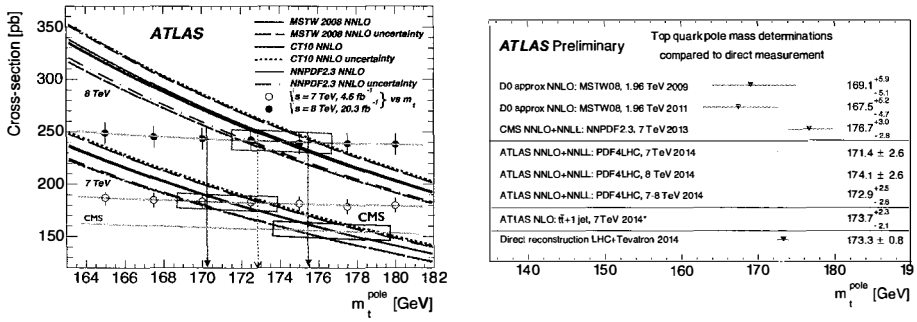

Figure 3 – (Left) Measurement of $m_t^{\rm pole}$ by ATLAS and CMS using inclusive $t\bar{t}$ cross section. The CMS 7 TeV result, cross section boxes and arrows for ATLAS combined result have been overlaid on the original ATLAS plot[25] for direct comparison. (Right) $m_t^{\rm pole}$ determinations compared to direct measurement.[25]

3.3 $t\bar{t}$+jet differential cross section

The most precise determination of $m_t^{\rm pole}$ to date comes from ATLAS,[26] using $t\bar{t}$+jet differential cross section $\sigma_{t\bar{t}+\rm jet}$ to enhance m_t sensitivity with respect to inclusive $\sigma_{t\bar{t}}$. The theoretical calculations have been performed at next-to-leading-order with parton shower (NLO+PS), compared to next-to-next-to-leading order (NNLO) for $\sigma_{t\bar{t}}$. The theory systematic uncertainties come primarily from the scale uncertainty (+0.93, -0.44 GeV). The experimental systematic uncertainties mainly from JES (0.94 GeV) are competitive with standard methods. The measurement is limited by statistical uncertainty (1.5 GeV) so the results will further improve with more data at 8 TeV.

4 Measurement of bJES from data

The bJES uncertainty stands out as a leading systematic in most methods, both standard and alternatives. Even if not directly quoted as bJES uncertainty, even alternatives often rely on the b quark fragmentation $p_{T,\rm B-hadron}/p_{T,\rm b-jet}$ in data. One of the most successful ways to measure bJES in data has been the ATLAS 3D method using $R_{b\ell}$,[15] which effectively reduces the m_t uncertainty from bJES to 0.08(syst.) $\pm$ 0.67(stat.) GeV, altough the final quoted bJSF including additional systematic uncertainties is 1.003 ± 0.008(stat.) $\pm$ 0.023(syst.).

A complementary way to study b-jet scale is to look at b jets produced in association with a Z boson. The Z+b events have kinematics quite similar to the W+b produced in top quark decays, making it possible to measure a single scale factor for bJES. The precision of this approach tested at CMS[27] is on par with the simulation-based bJES uncertainty from comparing Pythia 6[18] and Herwig++[28] at CMS, and with the 3D method used at ATLAS.

To cancel out common systematic uncertainties, the jet response from a b-tagged sample with a purity of about 80% is measured relative to the inclusive Z+jet sample used in determining the central JES. Many of the remaining systematic uncertainties are shared with the b in the W+b from top decays, *e.g.* the neutrinos produced in semileptonic decays, which are the dominant uncertainty (0.32%) for Z+b / Z+jet. The measurement is done with two different methods, missing E_T projection fraction (MPF) and p_T balance (R_{pT}),[29] and by either using a fixed cut

on additional jet activity (face value) or extrapolating the additional activity to zero (fitted). All four approaches give fully consistent results, with the MPF face value having smallest total uncertainty and thus chosen as the central value: bJSF= 0.998 ± 0.004(stat.) ± 0.004(syst.) for b-to-light jet energy scale ratio relative to Pythia 6 tune Z2*.

5 Road to the future

A large drop in the m_t uncertainties is still expected in Run II, given the expected availability of a $t\bar{t}$ data sets of unprecedented size: more than twenty million $t\bar{t}$ pairs for the initial 30 fb^{-1} at 13 TeV.[30] Even though the most precise analyses are already systematics limited, the large data set should enable reducing systematic biases, and therefore uncertainties, that stand out at a level of 2–3 σ.

As shown in Fig. 4, the LHC experiments are well on track with their m_t measurements.[31] CMS has reduced standard method uncertainties with detailed kinematic studies and demonstrated a bJES measurement from Z+b / Z+jet ratio that is still statistics limited and should threfore become more powerful in Run II. ATLAS has shown promising paths for measuring m_t^{pole} from differential $\sigma_{t\bar{t}+\text{jet}}$ and m_t^{MC} with bJES and JES using the 3D method. Both of these analyses are also statistics limited at 7 TeV.

The experiments reached an initial agreement on the common treatment of systematic uncertainties during the LHC and World combinations of m_t in 2014, with the details documented in a public summary.[32] The document also details areas that will need future improvement, putting the LHC top mass combinations on a solid ground in Run II.

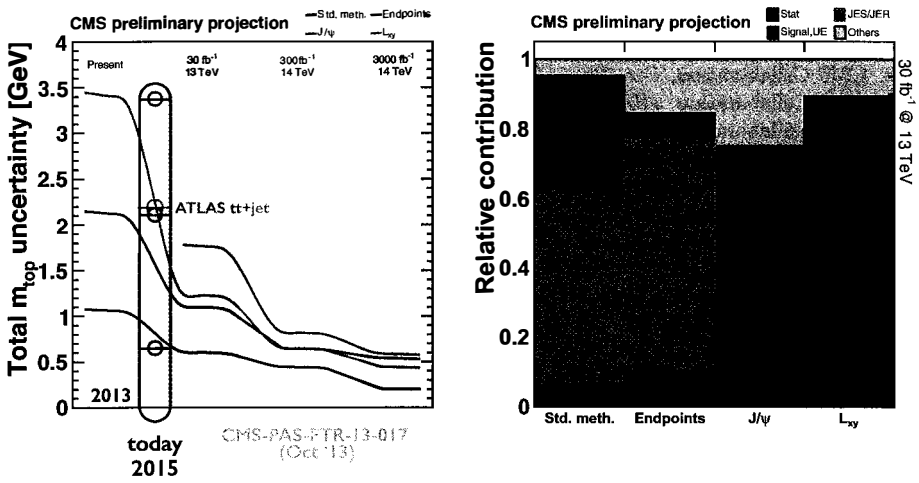

Figure 4 – (Left) Future projections of m_t uncertainties at CMS.[31] The current 2015 results have been overlaid for comparison. (Right) Contributions of various sources of uncertainty to the projected uncertainty in Run II.[31]

6 Conclusions

The past three years have seen rapid improvement in the precision of the top quark mass measurements at the LHC. The precision of the CMS measurements of m_t^{MC} is now on par with the Tevatron measurements: CMS has 0.66 GeV total uncertainty versus 0.64 GeV at the Tevatron. Run II prospects for top quark mass measurements look good with new methods to

constrain the leading systematic uncertainty from bJES with a large number of $t\bar{t}$ and Z+jet events. ATLAS has demonstrated this with the 3D fit using R_{bq}, while CMS has measured bJES using ratio of Z+b and Z+jet events.

All standard measurements are currently systematics limited, but CMS experience with 7 TeV and 8 TeV data sets has shown that more data helps to reduce also the systematic uncertainties. Many alternative measurements are now available, and they complement the standard measurements by changing sensitivity to some of the leading systematic uncertainties. Especially the difference between MC generator mass m_t^{MC} and theoretical pole mass m_t^{pole} can perhaps be addressed in the future using cross-section based measurements of the top quark mass. ATLAS has shown with the differential $t\bar{t}$+jet measurement that it is possible to go beyond inclusive $\sigma_{t\bar{t}}$ in the sensitivity to m_t^{pole}.

The current best measurements of the top quark mass are Tevatron combination[4] of $m_t = 174.34 \pm 0.64$ GeV (July 2014), CMS combination[5] of $m_t = 172.38 \pm 0.66$ GeV (September 2014) and ATLAS combination[15] of $m_t = 172.99 \pm 0.91$ GeV (March 2015). Two of these already exceed the precision of the world combination[1] of $m_t = 173.34 \pm 0.76$ GeV (March 2014) from only a year earlier, boding well for the future.

References

1. ATLAS, CDF, CMS, D0 Collaborations, *arXiv:1403.4427* (2014).
2. M. Baak *et al*, *Eur. Phys. J.* C **74**, 3046 (2014).
3. G. Degrassi *et al*, *JHEP* **08**, 098 (2012).
4. Tevatron Electroweak Working Group, *arXiv:1407.2682* (2014).
5. CMS Collaboration, *CMS-PAS-TOP-14-015* (2014).
6. CMS Collaboration, *JINST* **3**, S08004 (2008).
7. ATLAS Collaboration, *JINST* **3**, S08003 (2008).
8. CMS Collaboration, *Eur. Phys. J.* C **72**, 2202 (2012).
9. CMS Collaboration, *JHEP* **12**, 105 (2012).
10. CMS Collaboration, *Eur. Phys. J.* C **74**, 2758 (2014).
11. CMS Collaboration, *CMS-PAS-TOP-14-014* (2014).
12. CMS Collaboration, *CMS-PAS-TOP-14-010* (2014).
13. CMS Collaboration, *CMS-PAS-TOP-14-001* (2014).
14. CMS Collaboration, *CMS-PAS-TOP-14-002* (2014).
15. ATLAS Collaboration, *arXiv:1503.05427* (2015).
16. ATLAS Collaboration, *Eur. Phys. J.* C **75**, 158 (2015).
17. J. Alwall *et al*, *JHEP* **06**, 128 (2011).
18. T. Sjöstrand *et al*, *JHEP* **05**, 026 (2006).
19. D0 Collaboration, *arXiv:1501.07912* (2015).
20. CMS Collaboration, *CMS-PAS-TOP-12-030* (2013).
21. CMS Collaboration, *Eur. Phys. J.* C **73**, 2494 (2013).
22. CMS Collaboration, *CMS-PAS-TOP-13-007* (2013).
23. ATLAS collaboration, *ATLAS-CONF-2014-055* (2014).
24. CMS Collaboration, *Phys. Lett.* B **728**, 496 (2014); cor. *Phys. Lett.* B **738**, 526 (2014).
25. ATLAS Collaboration, *Eur. Phys. J.* C **74**, 3109 (2014).
26. ATLAS Collaboration, *ATLAS-CONF-2014-053* (2014).
27. CMS Collaboration, *CMS-PAS-JME-13-001* (2014).
28. M. Bähr *et al*, *Eur. Phys. J.* C **58**, 639 (2008).
29. CMS Collaboration, *JINST* **6**, P11002 (2011).
30. M. Cacciari *et al*, *Phys. Lett.* B **710**, 612 (2012).
31. CMS Collaboration, *CMS-PAS-FTR-13-017* (2013).
32. ATLAS and CMS Collabs., *ATL-PHYS-PUB-2014-020 / CMS-PAS-JME-14-003* (2014).

ATLAS + CMS top production and properties: Run 1 legacy

A. Loginov on behalf of the ATLAS and CMS Collaborations
Yale University, Department of Physics, 260 Whitney Avenue, JWG 554
New Haven, CT 06511-8499 USA

The large Run 1 data sample of top-quark events collected at the Large Hadron Collider allows a variety of measurements to analyse the production and properties of the top quark. Measurements of top-quark production cross sections and top-quark properties in proton-proton collisions with the ATLAS and CMS detectors at the LHC are presented.

1 Introduction

To date, in pp collision data at the center-of-mass energies of $\sqrt{s} = 7$ TeV and $\sqrt{s} = 8$ TeV, the CERN Large Hadron Collider (LHC) has successfully delivered a few million top-quark pair ($t\bar{t}$) and single-top-quark events per experiment. The $t\bar{t}$ cross section ($\sigma_{t\bar{t}}$) precision measurements test the Standard Model (SM) [1] theoretical predictions, which nowadays have percent level accuracy [2,3,4,5,6,7]. Differential measurements of $t\bar{t}$ production are especially important for discrimination between different Monte Carlo generators, perturbative Quantum Chromodynamics (QCD) models and parton distribution functions (PDFs). In addition, future top quark studies will become the best way to constrain systematics on b-tagging as well as c/b-jet energy scales. On top of that, inclusive $t\bar{t}$ events are an important background in various Higgs boson analyses as well as beyond the SM searches, and it is therefore crucial to understand this process in detail. New physics [8] can affect both the $t\bar{t}$ and single-top production and decay, modifying the observed cross sections differently in different decay channels and/or affecting differential distributions.

In these proceedings an overview of selected ATLAS [9] and CMS [10] measurements of $t\bar{t}$ production at the LHC at center-of-mass energies of 7 and 8 TeV is presented. Public top physics results for ATLAS and CMS are available at Refs. [11,12], respectively.

2 Inclusive top-pair production

The most precise $t\bar{t}$ cross section measurement to date was performed by ATLAS collaboration in the $e\mu$ channel by counting the numbers of opposite-sign $e\mu$ events with exactly one (N_1) and exactly two (N_2) b-tagged jets [13]. The two event counts are then expressed as $N_1 = L\sigma_{t\bar{t}}\,\epsilon_{e\mu} 2\epsilon_b(1-C_b\epsilon_b)+N_1^{\rm bkg}$ and $N_2 = L\sigma_{t\bar{t}}\,\epsilon_{e\mu} C_b {\epsilon_b}^2 + N_2^{\rm bkg}$, where L is the integrated luminosity of the sample, $\epsilon_{e\mu}$ is the efficiency for a $t\bar{t}$ event to pass the opposite-sign $e\mu$ preselection and C_b is a tagging correlation coefficient close to unity.

To minimise the associated systematic uncertainties, the numbers of events with exactly one and exactly two b-tagged jets are used to simultaneously determine $\sigma_{t\bar{t}}$ and the efficiency to reconstruct and b-tag a jet from a top quark decay. The cross section is measured to be:

$$\sigma_{t\bar{t}} \;=\; 182.9 \pm 3.1 \pm 4.2 \pm 3.6 \pm 3.3\,\text{pb}\ (\sqrt{s} = 7\,\text{TeV}) \text{ and}$$

$$\sigma_{t\bar{t}} \;=\; 242.4 \pm 1.7 \pm 5.5 \pm 7.5 \pm 4.2\,\text{pb}\;(\sqrt{s} = 8\,\text{TeV}),$$

where the four uncertainties arise from data statistics, experimental and theoretical systematic effects, knowledge of the integrated luminosity and of the LHC beam energy. The results are consistent with recent theoretical QCD calculations at next-to-next-to-leading (NNLO) order. This result is compared to other measurements from Tevatron and LHC as shown in Fig. 1.

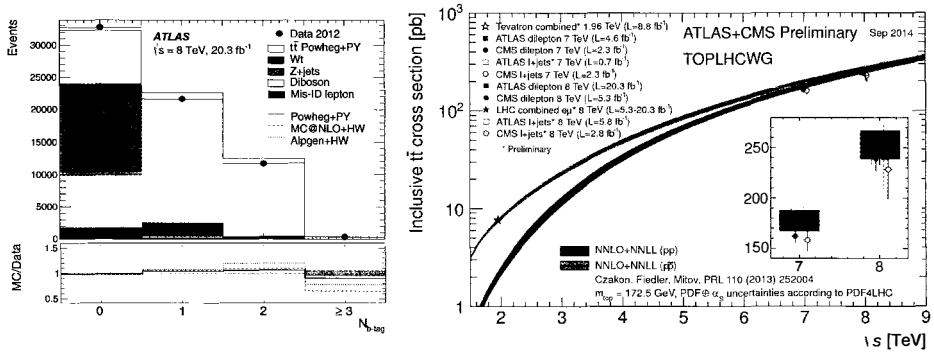

Figure 1 – Left: the number of b-tagged jets in preselected opposite-sign $e\mu$ events in $\sqrt{s} = 8$ TeV ATLAS data compared to the expectation from simulation [13]. The lower part of the figure shows the ratios of simulation to data, using $t\bar{t}$ signal samples generated with POWHEG [14] + PYTHIA6 [15] (PY), MC@NLO [16] + HERWIG [17] (HW) and ALPGEN [18] + HERWIG. The cyan band indicates the statistical uncertainty. Right: summary of LHC and Tevatron measurements [19] of $\sigma_{t\bar{t}}$ as a function of $\sqrt{s}$ compared to the NNLO QCD calculation complemented with NNLL resummation (top++2.0) [6].

The inclusive $\sigma_{t\bar{t}}$ results are used to determine the top-quark pole mass (m_t^{pole}) via the dependence of the theoretically predicted $\sigma_{t\bar{t}}$ on m_t^{pole} giving a result of $m_t^{\text{pole}} = 172.9^{+2.5}_{-2.6}$ GeV.

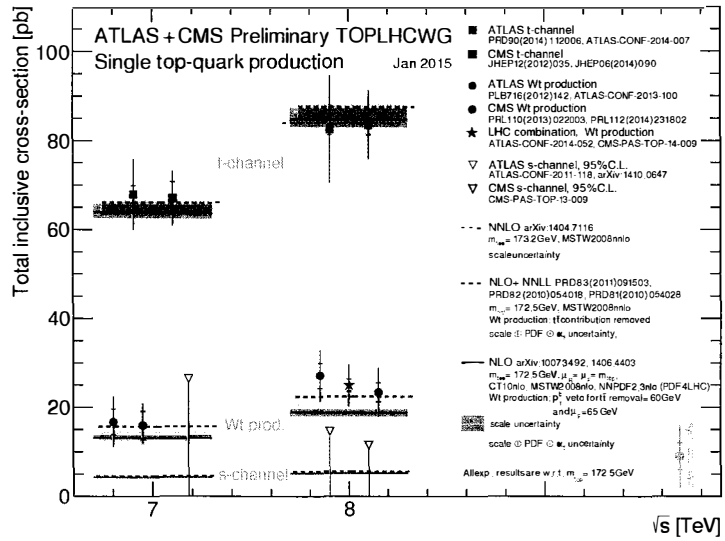

Figure 2 – Summary of ATLAS and CMS measurements [19] of the single top production cross sections $t-$, Wt- and s-channels as a function of $\sqrt{s}$ compared to theoretical calculations.

The preselection efficiency $\epsilon_{e\mu}$ can be written as $\epsilon_{e\mu} = A_{e\mu} G_{e\mu}$, where the acceptance $A_{e\mu}$

represents the fraction of $t\bar{t}$ events which have a true opposite-sign $e\mu$ pair from top-quark (including electrons and muons from tau decays), each with $p_{\mathrm{T}} > 25\,\mathrm{GeV}$ and within $|\eta| < 2.5$, and $G_{e\mu}$ represents the reconstruction efficiency. A fiducial cross section $\sigma_{t\bar{t}}^{\mathrm{fid}}$ is defined as $\sigma_{t\bar{t}}^{\mathrm{fid}} = A_{e\mu}\sigma_{t\bar{t}}$, and measured by replacing $\sigma_{t\bar{t}}\epsilon_{e\mu}$ with $\sigma_{t\bar{t}}^{\mathrm{fid}}G_{e\mu}$. Therefore, measurement of $\sigma_{t\bar{t}}^{\mathrm{fid}}$ avoids the extrapolation from the measured lepton phase space to the full phase space populated by inclusive $t\bar{t}$ production. In the measurement of $\sigma_{t\bar{t}}^{\mathrm{fid}}$ the systematic uncertainties associated with $A_{e\mu}$ come mainly from knowledge of the PDFs and the QCD scale uncertainties. Consequently, the PDF systematic uncertainty is reduced from 1.1% to 0.3%, and the QCD scale uncertainty is reduced from 0.3% to 0.0%.

3 Inclusive single-top production

Different single-top-quark production processes are sensitive to different new physics mechanisms. For instance, the t-channel is sensitive to flavor-changing neutral currents (FCNC) with anomalous vertices with the top quark, gluon and up/charm quark (tcg and tug). The tW-channel is sensitive to new physics that modifies the tWb vertex. Despite a very small cross section, the s-channel is sensitive to various new physics processes. In particular, one can search for new heavy gauge bosons such as the W' by looking for tb resonances in the s-channel. The agreement between experimental results and theoretical predictions is very good as summarized in Fig. 2, except for the s-channel that has not been observed yet.

4 Flavor-changing neutral currents

Flavor Changing Neutral Currents are highly suppressed in the standard model (SM) due to the GIM mechanism [28]. Consequently, the SM predicts very small rates for the branching ratios of top-quark FCNC decays to an up type quark and a neutral gauge or a Higgs boson: $\mathrm{BR}(t \to \gamma/Z/g/H + u/c) < 10^{-10}$. A number of models beyond the SM predict enhancement on the expected rates by introducing new heavy particles which can contribute into the loops. Any observation of these decays would indicate new physics. The most stringent experimental upper bounds obtained in ATLAS and CMS on the top quark FCNC branching ratios are summarized in Table 1. A recent update [29] from CMS experiment focusing on the $t\bar{t} \to Hc + Wb$ process producing a trilepton or same-sign dilepton gives 9.3×10^{-3} 95% confidence limit on the $\mathrm{BR}(t \to Hc)$.

Table 1: The most stringent experimental upper bounds on the top quark FCNC branching ratios (BR) at 95% CL obtained in ATLAS and CMS experiments for different channels.

EXP	$\sqrt{s}$, TeV	$\mathcal{L}$, fb^{-1}	BR(q=u)%	BR(q=c)%	Ref
$t \to q\gamma$					
CMS	8	19.1	0.0161	0.182	20
$t \to qZ$					
CMS	7	4.9	0.51	11.40	21
ATLAS	7	2.1	0.73		22
CMS	7&8	24.7	0.05		23
$t \to qg$					
CMS	7	4.9	0.035	0.34	24
ATLAS	8	14.2	0.0031	0.016	25
$t \to qH$					
ATLAS	7&8	25	0.79		26
CMS	8	19.5	0.56		27

5 Differential top-pair and single-top production cross section measurements

Top-quark measurements have entered a high-precision era for cross sections for both single top-quark and $t\bar{t}$ production. The large numbers of $t\bar{t}$ and single-top events allow measuring precisely their cross sections differentially, providing precision tests of current SM predictions

based on QCD. The measured spectra for various top-quark and $t\bar{t}$ observables are corrected for detector efficiency and resolution effects and are compared to several Monte Carlo simulations and theory calculations.

5.1 Differential top-pair production cross section measurements

ATLAS performed measurements of kinematic distributions of the top quarks in $t\bar{t}$ events in the lepton+jets channel using 4.6 fb^{-1} of 7 TeV data [30]. Normalised differential cross sections have been measured as a function of the top-quark transverse momentum (p_{T}) and as a function of the mass, p_{T}, and rapidity of the $t\bar{t}$ system. In general the Monte Carlo predictions and the QCD calculations agree with data in a wide kinematic region. However, data are softer than all predictions in the tail of the transverse momentum of the hadronically decaying top quark (p_{T}^{t}) spectrum. The p_{T}^{t} distribution shows some preference for HERAPDF1.5 [31] when used in conjunction with a fixed-order NLO QCD calculation.

CMS performed measurements of kinematic distributions of the top quarks in $t\bar{t}$ events in the lepton+jets and dilepton channels (ee, $e\mu$ and $\mu\mu$) using 19.7 fb^{-1} of 8 TeV data [32] as a function of the kinematic properties of the charged leptons, the jets associated to b-quarks, the top quarks, and the $t\bar{t}$ system. The p_{T}^{t} distribution shows some preference for POWHEG+HERWIG and approximate NNLO calculation.

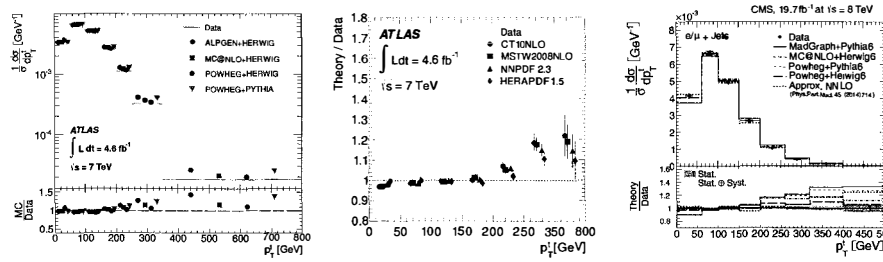

Figure 3 – Left: normalised differential $t\bar{t}$ production cross section ($\sigma_{t\bar{t}}^{\mathrm{diff}}$) for the transverse momentum of the hadronically decaying top quark (p_{T}^{t}) [30]. The lower part of the figure shows the ratio of the generator predictions to ATLAS $\sqrt{s}$ = 7 TeV data. Middle: ratios of the NLO QCD predictions [33] to the measured $\sigma_{t\bar{t}}^{\mathrm{diff}}$ the p_{T}^{t}. The markers are offset in each bin; the gray band indicates the total uncertainty on the ATLAS $\sqrt{s}$ = 7 TeV data in each bin, while the error bars denote the uncertainties in the predictions (PDF set variations and scale uncertainties) [30]. Right: the $\sigma_{t\bar{t}}^{\mathrm{diff}}$ as a function of the p_{T}^{t} using $\sqrt{s} = 8$ TeV CMS data [32]. The inner (outer) error bars indicate the statistical (combined statistical and systematic) uncertainty. This measurement is compared to various MC predictions and to an approximate NNLO calculation [34].

Overall, all these parton-level results are in fair agreement with the predictions in a wide kinematic range. The measurements can also discriminate among different PFD sets. Representative p_{T}^{t} distributions are shown in Fig. 3.

It is a distinctive property of the top quark that it decays before hadronisation. Therefore, extrapolation from the measured (particle-level) observables back to the top-quark (parton-level) is model-dependent. To minimise model dependencies, a new particle-level 'pseudo-top-quark' definition is introduced. Within this approach, pseudo-top and $t\bar{t}$ are built from objects directly related to particle-level observables (leptons, jets, missing transverse energy). This definition has good correspondence to detector-level measurements and reduces model-dependent extrapolations. Monte Carlo generator information at particle-level (after full matrix element, parton shower and hadronisation steps) is used to determine and correct for detector effects.

Both CMS and ATLAS performed analyses in the context of using a unified experimental definition of the particle-level top quark. CMS results in the dilepton channel using 12.2 fb^{-1} of 8 TeV data are summarized in Ref. [35]. ATLAS results using 4.6 fb^{-1} of $\sqrt{s} = 7$ TeV data are

summarized in Ref.[36]. These measurements are currently limited by the systematic uncertainty, the main components being the b-tagging uncertainty, the jet energy measurement uncertainty and the modelling uncertainty. Represenative distributions are shown in Fig. 4. Distributions of the p_{T} of the hadronic pseudo-top-quark show preference to NLO generators (POWHEG and AMC@NLO) and to a lesser extent to the parton shower used.

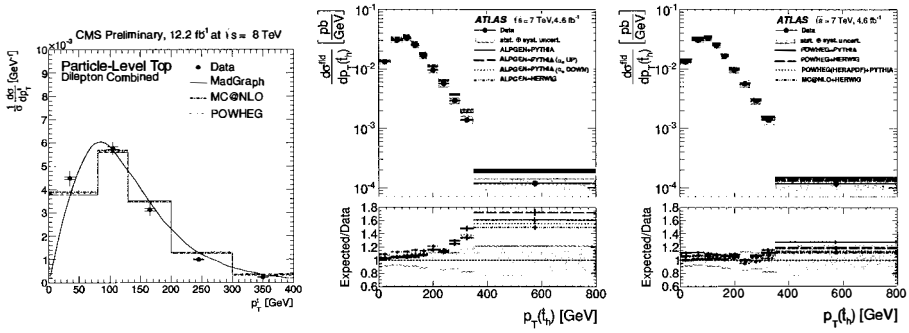

Figure 4 – Left: normalised differential particle-level $t\bar{t}$ production cross section ($\sigma_{t\bar{t}}^{\mathrm{diff}}$) as a function of the p_{T} of the particle-level top quark in CMS $\sqrt{s} = 8$ TeV data[35] compared to predictions from Monte Carlo generators. The inner (outer) error bars indicate the statistical (combined statistical and systematic) uncertainty. Middle and right: the $\sigma_{t\bar{t}}^{\mathrm{diff}}$ as a function of the hadronic particle-level top quark in ATLAS $\sqrt{s} = 7$ TeV data[36]. The data points are shown with a blue band which represents the total uncertainty. The model predictions from ALPGEN[18]+PYTHIA[15] (including variations in the renormalisation scale by factors of 0.5 and 2.0), ALPGEN+HERWIG[17] and several NLO MC generators[14,16] are superimposed.

A precise measurement of the boosted top-quark-pair production provides an improved understanding of $t\bar{t}$ production in the high-p_{T} regime and has a strong potential to reveal a hint of physics beyond the Standard Model.

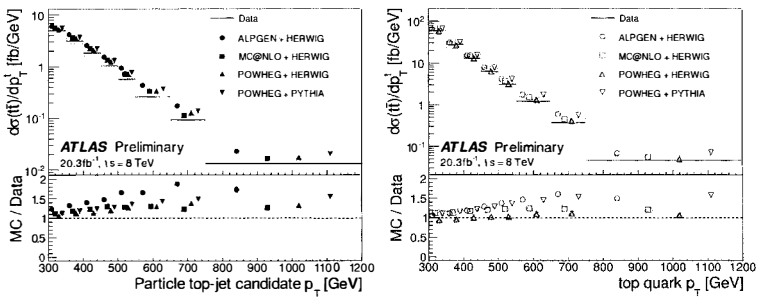

Figure 5 – Left: fiducial particle-level differential cross section ($\sigma_{t\bar{t}}^{\mathrm{diff}}$) as a function of the hadronic top-jet candidate p_{T}[37]. Right: parton-level $\sigma_{t\bar{t}}^{\mathrm{diff}}$ as a function of the top quark p_{T} decaying hadronically[37]. Monte Carlo samples are normalised to the NNLO+NNLL inclusive $t\bar{t}$ cross section of 253^{+13}_{-15} pb[6]. Electroweak corrections are not applied to the POWHEG+PYTHIA prediction. The lower part of the figure shows the ratio between the MC prediction and the data. The shaded area shows the total uncertainty.

ATLAS performed the first measurement[37] of the differential $t\bar{t}$ production cross section as a function of the hadronically decaying top quark p_{T} using 20.3 fb^{-1} of $\sqrt{s} = 8$ TeV data. The measurement is done in the fiducial phase-space particle level and in the full phase-space parton level. Boosted hadronically-decaying top quarks from p_{T} of 300 GeV up to 1200 GeV are reconstructed within large-R jets and identified using jet substructure techniques. A particle-

level cross section is measured in a fiducial region that closely follows the event selection. As shown in Fig. 5, predictions from Monte Carlo generators are above data, increasing with p_T.

5.2 Differential single-top production measurement

The relatively high cross section and purity of the t-channel allows studying single top events in detail. Using 19.7 fb^{-1} of 8 TeV data CMS performed the analysis in the leptonic decay channels of the top quark, with either a muon or an electron in the final state[38]. Artificial neural networks are used to discriminate the signal process from the various background contributions.

The differential single-top cross sections are measured as functions of the transverse momentum and the absolute value of the rapidity of the top quark. The results are found to agree well with predictions from Monte Carlo generators that use different implementations for the modeling of the b-quarks in the initial state of single-top-quark t-channel production as shown in Fig. 6. A similar analysis using 4.59 fb^{-1} of 7 TeV data was performed by ATLAS[39].

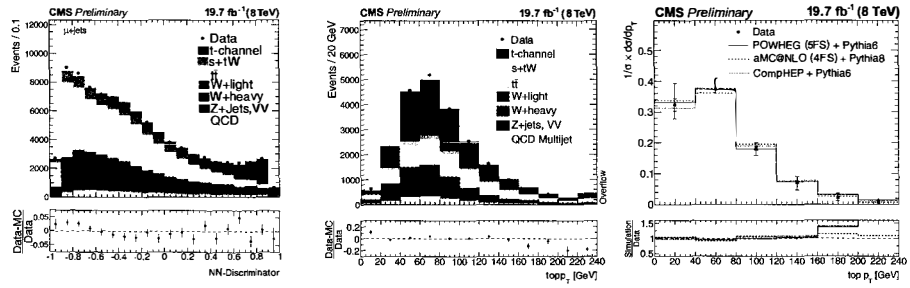

Figure 6 – Left: NN output distributions in the signal region for the muon channel [38]. Middle: distribution of the reconstructed top-quark p_T in the combined (electron and muon) channel with the NN discriminator cuts >0.3 (0.4) applied for the electron (muon) channel[38]. Right: unfolded top-quark p_T in the combined channel compared to Monte Carlo predictions. In the 'five-flavor' scheme (5FS) the b-quark is included in the parton distribution function of the proton, whereas in the 'four-flavor' (4FS) scheme the b-quarks are treated independently [38]. The inner (outer) error bars indicate the statistical (total) uncertainty.

6 Top-pair + W, Z, photon production

The $t\bar{t}V$ (V=W, Z) associate production is a rare process. In addition, the associated $t\bar{t}Z$ production is directly sensitive to $t\bar{t}Z$ couplings. Despite the fact that the top quark was discovered almost two decades ago, its couplings to the Z-boson and the photon have not yet been measured. A measured yield of top-quark pair production in association with a photon ($t\bar{t}\gamma$) is sensitive to top-quark charge and to top-quark-photon couplings. Moreover, it can constrain models of new physics, for example those with composite top quarks[40], or with excited top-quark production, followed by the radiative decay $t^* \to t\gamma$.

CMS performed a measurement of the $t\bar{t}V$ production cross sections ($\sigma_{t\bar{t}V}$) using 19.5 fb^{-1} of 8 TeV data in three independent channels[41]. In the same-sign dilepton channel, sensitive to the $t\bar{t}W$ production, the $\sigma_{t\bar{t}W}$ is measured to be $\sigma_{t\bar{t}W} = 170^{+90}_{-80}(stat) \pm 70(syst)$ fb, corresponding to a significance of 1.6σ over the background-only hypothesis. In the trilepton and four-lepton channels, sensitive to the $t\bar{t}Z$ production, the $t\bar{t}Z$ signal is established with a significance of 2.3σ and 2.2σ, respectively. After combination of these two channels a significance of 3.1σ is obtained and the $\sigma_{t\bar{t}Z}$ is measured to be $\sigma_{t\bar{t}Z} = 200^{+80}_{-70}(\text{stat.})^{+40}_{-30}(\text{syst.})$ fb. Combining all the channels, $\sigma_{t\bar{t}V} = 380^{+100}_{-90}(\text{stat.})^{+80}_{-70}(\text{syst.})$ fb is obtained, corresponding to a combined significance of 3.7σ.

ATLAS performed measurements of $t\bar{t}V$ using 20.3 fb^{-1} of 8 TeV data in final states with two (same-sign and opposite-sign) or three charged leptons[42]. A simultaneous measure-

ment of $t\bar{t}W$ and $t\bar{t}Z$ cross sections yields $\sigma_{t\bar{t}Z} = 150^{+55}_{-50}(\text{stat.}) \pm 21(\text{syst.})$ fb and $\sigma_{t\bar{t}W} = 300^{+120}_{-100}(\text{stat.})^{+70}_{-40}(\text{syst.})$ fb. The observed signal significance from the combined simultaneous fit for the $t\bar{t}Z$ and $t\bar{t}W$ processes individually is 3.1σ each, providing evidence of SM $t\bar{t}Z$ and $t\bar{t}W$ production. The combined $t\bar{t}V$ signal strength is found to be $0.89^{+0.23}_{-0.22}$, corresponding to a 4.9σ excess over the background-only hypothesis.

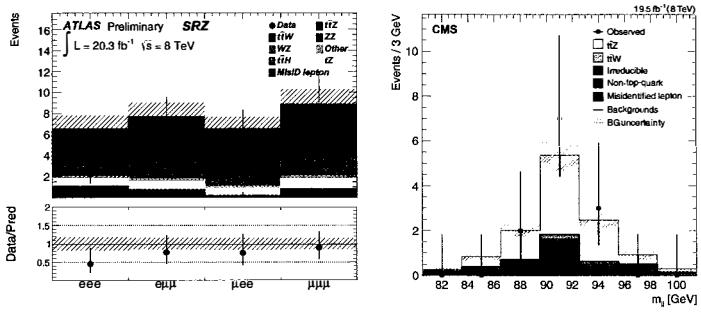

Figure 7 – Left: the lepton flavour combination for events that passed trilepton and same-sign dilepton selections in ATLAS $\sqrt{s} = 8$ TeV data [42]. The shaded bands represent the systematic uncertainties on the expected event counts. Right: Z-boson candidate dilepton mass distribution in CMS $\sqrt{s} = 8$ TeV data [41] after trilepton selection requirements, compared to the expectations. The total uncertainty is denoted by the shaded area.

Both ATLAS and CMS results are compatible within their uncertainties with standard model predictions. Some representative distributions are shown in Fig. 7. However, all presented $t\bar{t}V$ measurements are statistically limited; the measurements will also profit from adding more channels.

ATLAS reported observation of $t\bar{t}\gamma$ production with a significance of 5.3σ away from the null hypothesis [43] using 4.59 fb^{-1} of 7 TeV data. To allow a comparison of the analysis results to theoretical predictions, the cross section measurement is made within a fiducial phase space defined in Monte Carlo simulation for $t\bar{t}\gamma$ decays in the single-lepton (electron or muon) final state. The fiducial $t\bar{t}\gamma$ cross section ($\sigma_{t\bar{t}\gamma}$) is extracted by template fit to the photon track isolation distribution as shown in Fig. 8. The measured value is $\sigma^{\text{fid}}_{t\bar{t}\gamma} \times \text{BR} = 63 \pm 8(\text{stat.})^{+17}_{-13}(\text{syst.}) \pm 1\,(\text{lumi.})\,\text{fb}$ per lepton (electron, muon) flavor, in good agreement with the leading-order (LO) theoretical calculation normalised to the next-to-leading-order (NLO) theoretical prediction of 48 ± 10 fb. In addition, the cross section measurements are performed separately in the electron and muon channels and give $\sigma^{\text{fid}}_{t\bar{t}\gamma} \times \text{BR} = 76^{+16}_{-15}(\text{stat.})^{+22}_{-17}(\text{syst.}) \pm 1(\text{lumi.})\,\text{fb}$ and $\sigma^{\text{fid}}_{t\bar{t}\gamma} \times \text{BR} = 55^{+10}_{-9}(\text{stat.})^{+14}_{-11}(\text{syst.}) \pm 1(\text{lumi.})\,\text{fb}$ respectively.

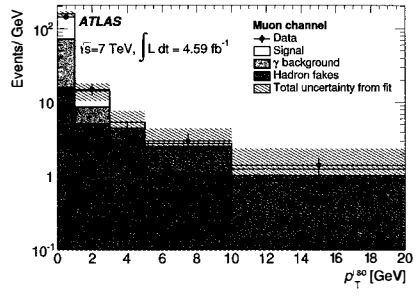

Figure 8 – Results of the combined likelihood fit using the track-isolation ($p_{\text{T}}^{\text{iso}}$) distributions as the discriminating variable for the muon channel [43]. The contribution from $t\bar{t}\gamma$ events is labeled as 'Signal', prompt-photon background is labeled as 'γ backgrounds', the contribution from hadrons misidentified as photons (as estimated by the template fit) is labeled as 'Hadron fakes'.

CMS performed a $\sigma_{t\bar{t}\gamma}$ cross section measurement in the muon channel [44] using 19.7 fb^{-1} of 8 TeV data for $E_{\text{T}}(\gamma) > 20$ GeV and $\Delta R(\gamma, b) > 0.1$. The $\sigma_{t\bar{t}\gamma}$ is measured to be $2.4 \pm 0.2(stat.) \pm 0.6(syst.)$ pb compared to the prediction of 1.8 ± 0.5 pb.

7 Production of top-pair + extra hard jets (including heavy-flavor)

Measurements of $t\bar{t}$ production with additional jets, as a function of the jet p_{T}, is important for constraining models of initial- and final-state radiation at the scale of the top-quark mass. In addition, these measurements provide a test of QCD in the LHC energy regime. If some of the additional jets are b-tagged, a dedicated study of these events is useful to constrain models of heavy-flavor (HF) quark production at the scale of the top-quark mass. In addition, $t\bar{t}$+HF production is the main irreducible background to the largest-yield $t\bar{t}H$ channel with $H \dashrightarrow b\bar{b}$.

CMS measured jet multiplicity distributions in top-quark-pair events using 19.6fb^{-1} of 8 TeV data [45]. Normalised differential cross sections as a function of N_{jets} with different jet p_{T} thresholds are compared to predictions from Monte Carlo generators.

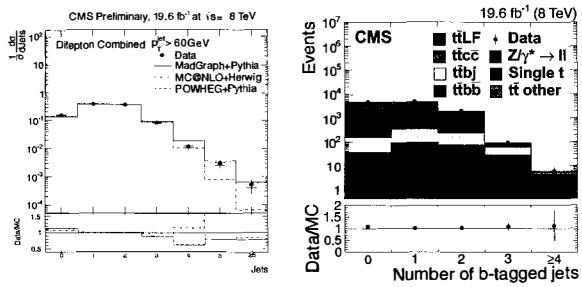

Figure 9 - Left: normalised differential $t\bar{t}$ cross section as a function of jet multiplicity for $p_{\mathrm{T}}^{\mathrm{jet}} > 60$ GeV [45]. The data are compared to Monte Carlo generator predictions. Right: distribution of b-jet multiplicity in data (points) after the four-jet requirement but without the b-tagging requirement compared to Monte Carlo simulation (using results from the fit to data) [46].

Using 19.7 fb^{-1} of 8 TeV data, CMS performed a measurement of the ratio of the $t\bar{t}+b\bar{b}$ production cross section to the $t\bar{t}+$dijet production cross section, $\sigma_{t\bar{t}b\bar{b}}/\sigma_{t\bar{t}jj}$ [46]. The ratio is extracted via fit to the output of the b-tagging algorithm for the third and fourth jets. The measured ratio is $0.022 \pm 0.004(\mathrm{stat.}) \pm 0.005(\mathrm{syst.})$ for b-jet $p_{\mathrm{T}} > 40$ GeV compared to the theoretical NLO calculation of 0.011 ± 0.003. Some representative $t\bar{t}$+jets and $t\bar{t}+b\bar{b}$ distributions are shown in Fig. 9.

ATLAS performed measurement of $R_{\mathrm{HF}} = \sigma_{t\bar{t}+b/c}/\sigma_{t\bar{t}j}$ using 4.7 fb^{-1} of 7 TeV data [47]. To determine the heavy- and light-flavor content of the additional b-tagged jets, a fit to the vertex mass distribution of b-tagged jets in the sample is performed. A value of $R_{\mathrm{HF}} = [6.2 \pm 1.1\,(\mathrm{stat.}) \pm 1.8\,(\mathrm{syst.})]\%$ is extracted. The measurement is consistent with the LO predictions of 3.4% obtained from ALPGEN+HERWIG and 5.2% from a calculation using POWHEG+HERWIG.

8 Summary

In these proceedings selected measurements of single-top-quark and $t\bar{t}$ production cross sections and top-quark properties in proton-proton collisions with the ATLAS and CMS detectors at the LHC are presented. As the LHC keeps providing top quarks in unprecedented quantities, now at 13 TeV, top-quark physics will remain a crucial milestone in the LHC research program in both measuring the properties of the top quark, and in searches for heavy-mass physics beyond the Standard Model. The up-to-date list of public top physics results for ATLAS and CMS is available at Refs. [11,12].

References

1. S.L. Glashow, Nucl. Phys. **22** 588, (1961); S. Weinberg, Phys. Rev. Lett. **19** 1264, (1967); A. Salam, Proc. 8th Nobel Symposium, Stockholm, (1979).
2. M. Cacciari et al., Phys. Lett. B **710**, 612 (2012), arXiv:1111.5869.
3. P. Baernreuther, M. Czakon, and A. Mitov, Phys. Rev. Lett. **109**, 132001 (2012), arXiv:1204.5201.
4. M. Czakon and A. Mitov, J. High Energy Phys. 12, 054 (2012), arXiv:1207.0236.
5. M. Czakon and A. Mitov, J. High Energy Phys. 01, 080 (2013), arXiv:1210.6832.
6. M. Czakon, P. Fiedler, and A. Mitov, Phys. Rev. Lett. **110**, 252004 (2013), arXiv:1303.6254.
7. M. Czakon and A. Mitov, Comput. Phys. Commun. **185**, 2930 (2014), arXiv:1112.5675.
8. J. Silva-Marcos, J. High Energy Phys. **0212**, 036 (2002); S. Sultansoy et al., Acta Phys. Polon. **B37**, 2839 (2006).
9. ATLAS Collaboration, JINST **3**, S08003 (2008).
10. CMS Collaboration, JINST **3**, S08004 (2008).
11. ATLAS Collaboration, https://twiki.cern.ch/twiki/bin/view/AtlasPublic/TopPublicResults.
12. CMS Collaboration, https://twiki.cern.ch/twiki/bin/view/CMSPublic/PhysicsResultsTOP.
13. ATLAS Collaboration, Eur. Phys. J. C **74**, no. 10, 3109 (2014) arXiv:1406.5375.
14. C. Oleari, Nucl. Phys. Proc. Suppl. **205-206**, 36 (2010) arXiv:1007.3893.
15. T. Sjöstrand, S. Mrenna, and P. Skands, J. High Energy Phys. 05, 026 (2006), arXiv:0603175 [hep-ph].
16. S. Frixione, P. Nason, and B. R. Webber, J. High Energy Phys. 08, 007 (2003), arXiv:0305252 [hep-ph].
17. R. Corcella et al., J. High Energy Phys. 01, 010 (2001), arXiv:0011363 [hep-ph].
18. M. L. Mangano et al., J. High Energy Phys. 07, 001 (2003), arXiv:0206293 [hep-ph].
19. TOPLHC W G Summary Plots are available at https://twiki.cern.ch/twiki/bin/view/LHCPhysics/TopLHCWGS
20. CMS Collaboration, CMS-PAS-TOP-14-003.
21. CMS Collaboration, CMS-PAS-TOP-12-021.
22. ATLAS Collaboration, JHEP **1209**, 139 (2012) arXiv:1206.0257.
23. CMS Collaboration, Phys. Rev. Lett. **112**, 171802 (2014) arXiv:1312.4194.
24. CMS Collaboration, CMS-PAS-TOP-14-007.
25. ATLAS Collaboration, ATLAS-CONF-2013-063.
26. ATLAS Collaboration, JHEP **1406**, 008 (2014) arXiv:1403.6293.
27. CMS Collaboration, CMS-PAS-HIG-13-034.
28. S. L. Glashow, J. Iliopoulos and L. Maiani, Phys. Rev. D **2**, 1285 (1970).
29. CMS Collaboration, CMS-PAS-TOP-13-017.
30. ATLAS Collaboration, Phys. Rev. D **90**, no. 7, 072004 (2014) arXiv:1407.0371.
31. H1 and ZEUS Collaboration, F.D. Aaron et al., J. High Energy Phys. 01 (2010) 109, arXiv:0911.0884.
32. CMS Collaboration, arXiv:1505.04480.
33. J. Campbell, K. Ellis, and C. Williams, http://mcfm.fnal.gov/.
34. N. Kidonakis, Phys. Part. Nucl. **45**, no. 4, 714 (2014) arXiv:1210.7813.
35. CMS Collaboration, https://twiki.cern.ch/twiki/bin/view/CMSPublic/PasTop12028AdditionalMaterial.
36. ATLAS Collaboration, JHEP **1506**, 100 (2015) arXiv:1502.05923.
37. ATLAS collaboration, ATLAS-CONF-2014-057.
38. CMS Collaboration, CMS-PAS-TOP-14-004.
39. ATLAS Collaboration, Phys. Rev. D **90**, no. 11, 112006 (2014) arXiv:1406.7844.
40. B. Lillie, J. Shu, and T. M. P. Tait, J. High Energy Phys. 04, 087 (2008), arXiv:0712.3057.
41. CMS Collaboration, Eur. Phys. J. C **74**, no. 9, 3060 (2014) arXiv:1406.7830.
42. ATLAS Collaboration, ATLAS-CONF-2014-038.
43. ATLAS Collaboration, Phys. Rev. D **91**, 072007 (2015) arXiv:1502.00586.
44. CMS Collaboration, CMS-PAS-TOP-13-011.
45. CMS Collaboration, CMS-PAS-TOP-12-041.
46. CMS Collaboration, Phys. Lett. B **746**, 132 (2015) arXiv:1411.5621.
47. ATLAS Collaboration, Phys. Rev. D **89**, no. 7, 072012 (2014) arXiv:1304.6386.

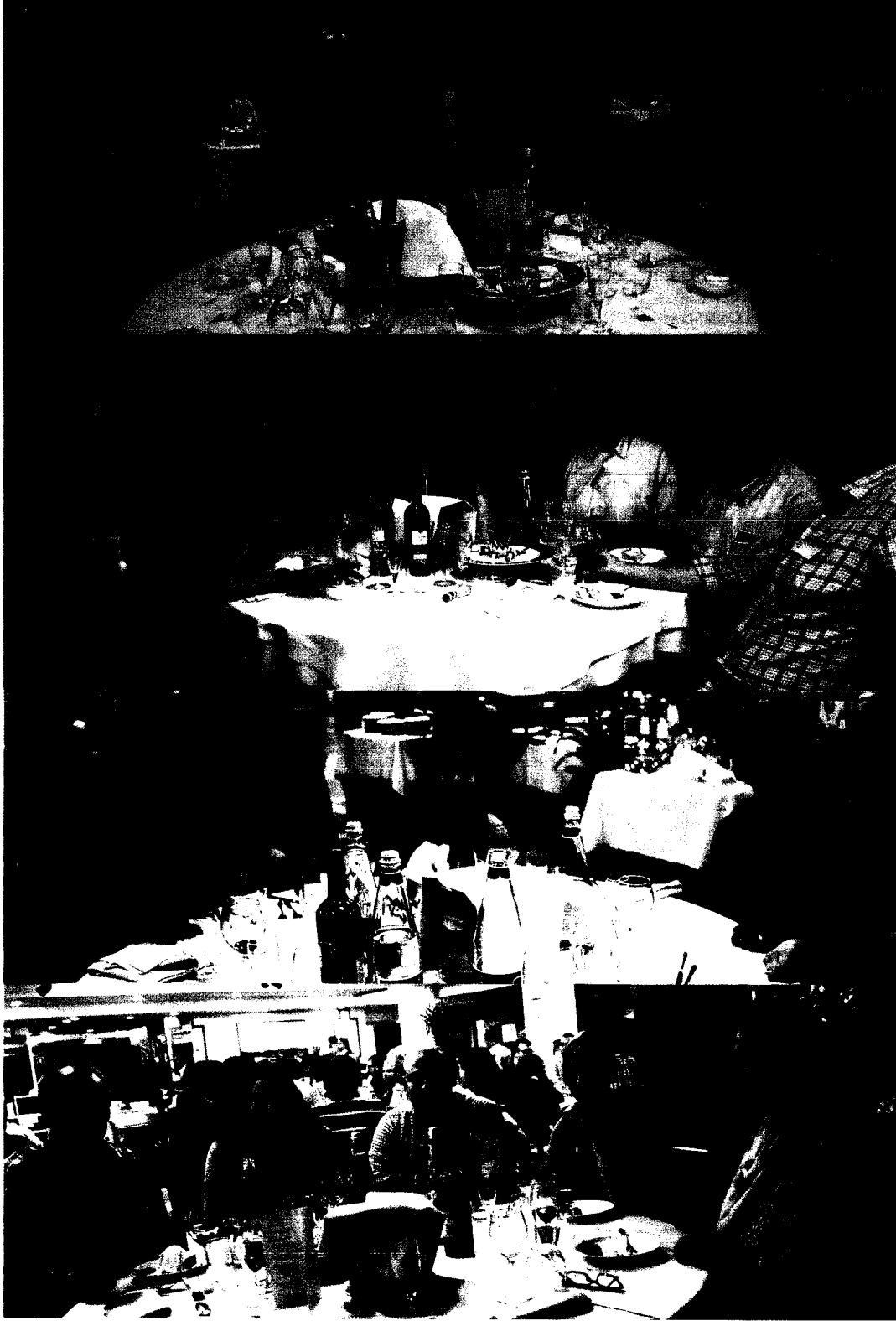

5.
Beyond the Standard Model

ATLAS+CMS: Boosted topologies (Run1 results, Run2 potential)

John Stupak III
on behalf of the ATLAS and CMS collaborations
Purdue University Calumet, Department of Chemistry and Physics,
2200 169th Street, Hammond, IN

As no sign of beyond the Standard Model physics has yet been observed at the LHC, experimental searches continue to probe ever higher mass scales. The decay of new, heavy resonances can produce highly Lorentz boosted particles, such as top quarks and Higgs or vector bosons. The decay products of these boosted particles are very highly collimated, and novel techniques are needed to identify such decays. In this paper, recent analyses from ATLAS and CMS in the boosted regime are reviewed, with an emphasis on jet substructure techniques and their application.

1 Introduction

Many models of beyond the Standard Model (BSM) physics predict the existence of states which decay to top quarks and Higgs or vector bosons. If the mass difference between the mother and daughter particles is sufficient, the daughter particles are produced with significant Lorentz boost and their decay products will be narrowly collimated. In the event the daughter decays hadronically, the resulting shower produces a "fat" jet with a radius of $R \approx 2m/p_T$, where m and p_T are the mass and transverse momentum of the daughter, respectively.

In order to search for such a decay, one must contend with overwhelming background from QCD interactions. Fortunately, a number of techniques have been proposed in the literature to identify the hadronic decays of top quarks and Higgs and vector bosons. The most powerful handle at our disposal to discriminate between jets from heavy particle decays and those from light quarks and gluons ("QCD jets") is the jet mass. Unfortunately, the jet mass is highly sensitive to pileup and underlying event activity. However, a number of grooming algorithms have been proposed (pruning [1], trimming [2], filtering [3], soft drop [4], etc.) to remove soft and wide angle radiation from the jet clustering history, which significantly pushes the mass distribution for light jets towards zero while having only a minimal effect on jets from heavy particles decays. The effect of grooming on the jet mass distribution [5] and the stability with respect to pileup [6] are shown in Figure 1.

In addition to the mass, a number of jet shape observables are useful for discriminating between QCD jets and those from heavy flavor decays. The k_T-splitting scale [7] and mass drop [3] observables exploit the symmetric nature of heavy particle decays. N-subjettiness (τ_N) variables [8] characterize the consistency of a jet with being composed of N or more subjets. Energy correlation functions [9], quark/gluon likelihood [10], jet charge [11], pull angle [12], and Q-jets volatility [13] are useful as well, among others.

Both ATLAS [14] and CMS [15] have developed b-tagging algorithms optimized for the dense environment inside highly-collimated jets. ATLAS performs b-tagging on standard anti-k_T R=0.4 jets and then performs a geometric matching to fat jets to tag them. CMS performs

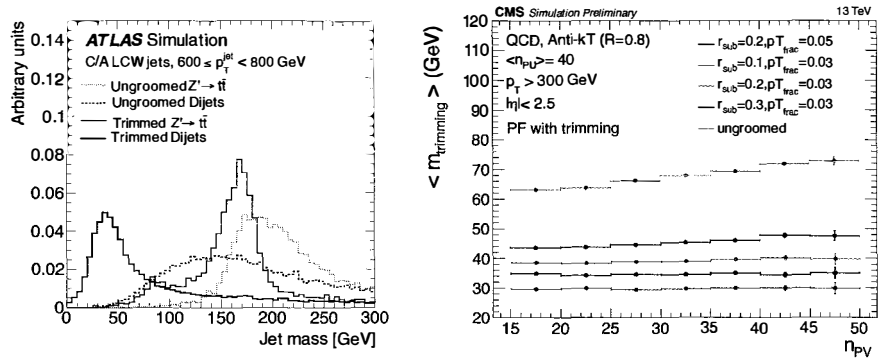

Figure 1 – The jet mass distribution for the leading-p_T jet in simulated $Z' \to t\bar{t}$ and QCD dijet events before and after trimming (left), and the stability of the average jet mass versus pileup for ungroomed and trimmed jets (right).

b-tagging directly on fat jets or subjets, depending on the kinematic regime.

Finally, all of the above techniques can be combined into a dedicated "tagger." This typically involves the application of a groomed mass window requirement along with requirements on the jet substructure. In the case of top and Higgs tagging, b-tagging can also be exploited. The BDRS [3], HEP Top Tagger [16], and CMS Top Tagger [17] are all examples. These top taggers also exploit the presence of a real W boson in the top decay chain, and require a pair of subjets to be compatible with the W mass hypothesis.

2 Analyses in the Boosted Regime

2.1 Searches for Fermion+Fermion Resonances

Both ATLAS and CMS have extensive programs of searches for $Z' \to t\bar{t}$ and $W' \to tb$ resonances. For very high mass resonances with small cross sections, the all-hadronic decay modes with large branching ratios are extremely important. It is also in this regime where jet substructure techniques are most powerful.

CMS has performed a combination of $Z' \to t\bar{t}$ searches in zero, one, and two lepton final states [18]. The all-hadronic channel exhibits a dijet topology. Both high-p_T jets were required to be top-tagged. Separate optimizations were performed in the low and high mass regimes; in the low (high) mass channel, the HEP Top Tagger (CMS Top Tagger) was used, which is based on R=1.5 (R = 0.8) jets. Subjet b-tagging was applied, as well as a requirement on the ratio $\tau_{32} = \tau_3/\tau_2$ in the high mass channel.

The dominant background in the all-hadronic final state is QCD dijet production. This background was modeled using a sophisticated data-driven technique. No excess with respect to the background expectation was observed. Model independent 95% confidence level (CL) cross section upper limits are shown in Figure 2, based on a combination of all channels. These were interpreted in the context of a variety of models to obtain mass exclusions. For a narrow leptophobic topcolor [19] Z' resonance with $\Gamma_{Z'}/m_{Z'} = 1.2\%$, masses below 2.4 TeV are excluded.

ATLAS performed a similar search in the lepton+jets final state [20]. Separate optimizations were performed for the cases where the top quark decay products are merged into a single fat jet, or resolved separately. Events were required to contain a high-p_T lepton, at least 1 b-jet and 1 top-jet, and large missing transverse energy ($\not{E}_T$) and transverse mass. Top tagging was performed on trimmed R=1.0 jets, requiring $m > 100$ GeV and k_T-splitting scale $\sqrt{d_{12}} > 40$ GeV.

The $t\bar{t}$ invariant mass distribution, shown in Figure 2, was used to test for the presence of signal. No significant excess was observed. Like the CMS analysis, 95% CL cross section upper limits were established and interpreted in the context of a variety of models. For a narrow leptophobic topcolor Z' resonance with $\Gamma_{Z'}/m_{Z'} = 1.2\%$, masses below 1.8 TeV are excluded.

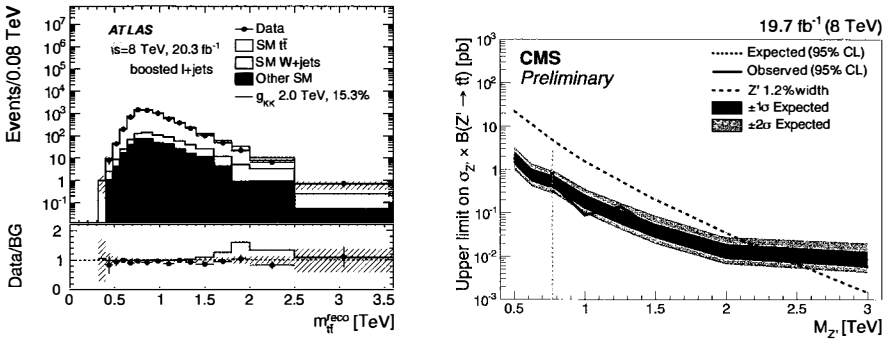

Figure 2 – The ATLAS reconstructed $t\bar{t}$ invariant mass distribution in the boosted channel (left), and the CMS observed 95% CL cross section upper limit (right).

Similar searches have been performed by ATLAS [21] and CMS [22] for $W'\rightarrow$tb resonances.

2.2 Searches for Fermion+Boson Resonances

Many BSM theories predict the existence of fermion+boson resonances; from vector-like quarks in little Higgs models [23; 24], models with extra dimensions [25; 26], and composite Higgs models [25; 26; 27], to excited fermions in composite models [28; 29; 30]. CMS recently performed searches for vector-like top [31] and bottom [32] quark partners, decaying via $T'\rightarrow tH$ and $B'\rightarrow bH$ to all hadronic final states, as well as excited leptons [33] decaying via $\ell^\star \rightarrow \ell\gamma/\ell Z$. The search for $\ell^\star \rightarrow \ell Z$ considered both leptonic and hadronic Z decays; in the latter case, jet substructure techniques were used to reject the overwhelming Z+jets background.

The all hadronic T' and B' searches were very challenging, requiring sophisticated jet substructure techniques to reject the QCD background. The T' analysis was particularly groundbreaking, as it represented the first use of a Higgs tagger combining both substructure information as well as subjet b-tagging, as well as the first vector-like quark search in an all-hadronic final state.

The search was optimized for T' pair-production, where at least one T' decays via tH to the all hadronic $bbbjj$ final state. Events were selected with at least one top-jet and one Higgs-jet. The top-jets were tagged with the HEP Top Tagger, also requiring a subjet b-tag. R=1.5 jets were Higgs-tagged by requiring a double subjet b-tag and trimmed mass $m > 60$ GeV. Events were categorized based on the number of Higgs-tagged jets in the event, and a joint likelihood was constructed based on the scalar sum of the p_T of all reconstructed jets and the mass of the Higgs-tagged jet. No significant deviation from the background prediction was observed in this likelihood distribution. 95% CL cross section upper limits were derived, and interpreted in the triangular branching ratio space of a vector-like top quark partner, shown in Figure 3.

2.3 Searches for Diboson Resonances

A wide variety of diboson resonance searches have been conducted recently by ATLAS [34; 35] and CMS [36; 37; 38; 39] using jet substructure techniques. With the discovery of the

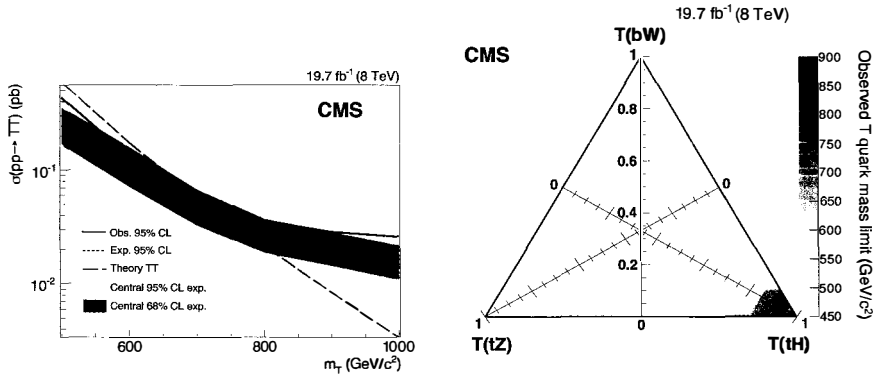

Figure 3 – The 95% CL cross section upper limits for T' pair production (left) and T' mass lower limits (right).

Higgs boson, searches for WH and ZH resonances have become viable and are being pursued vigorously. Initially these searches were focused on the dominant $H \to bb$ decay mode, but in order to maximize search sensitivity recent searches have begun to investigate sub-dominant Higgs decay modes as well.

The first search for a VH resonance in a fully-hadronic final state [36] included channels optimized to select events consistent with $H \to bb$ and $H \to WW \to 4q$ decays of the Higgs boson. This required development of a novel $H \to 4q$ tagger. Pruned R=0.8 jets were used to tag $V \to qq$, $H \to bb$, and $H \to 4q$ decays. In addition to mass window requirements, b-tagging and N-subjettiness information was utilized as well. B-tagging was applied either to the fat jet or the subjets, depending on the geometric separation of the subjets. The $V \to qq$ tagger required the N-subjettiness ratio $\tau_{21} = \tau_2/\tau_1$ to be small, while the $H \to 4q$ tagger instead required the ratio $\tau_{42} = \tau_4/\tau_2$ to be small, owing to the 4-pronged nature of the decay. The t_{42} distribution for the $H \to 4q$ signal and other processes is shown in Figure 4. No significant deviation with respect to the background prediction was observed, and resonance masses below 1.7 TeV were excluded in the Heavy Vector Triplet model [40], as shown in Figure 4.

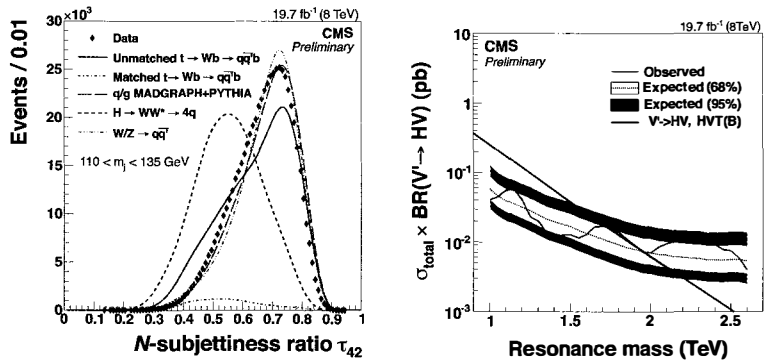

Figure 4 – The τ_{42} distribution for various processes (left) and the 95% CL cross section upper limit for a resonance decaying to VH (right).

Another recent analysis [37], optimized to search for a ZH resonance, developed a novel

$H \to \tau\tau$ tagger. In this analysis, pruned R=0.8 jets were used to tag Z-jets, along with a mass window requirement and a requirement on τ_{21}. The $H \to \tau\tau$ tagger also used pruned R=0.8 jets as a starting point. Jets with a large mass drop $\mu_{1,2} = \max(m_1, m_2)/m_{12}$ were used as inputs to the hadron-plus-strips algorithm [41] with modified isolation requirements. A likelihood-based fit was performed to reconstruct the H candidate from the visible daughters, and a mass window requirement was subsequently applied. Again, no significant deviation from the backrgound prediction was observed.

2.4 Searches for Supersymmetry

Jet substructure techniques have recently found application in high mass stop searches [42; 43]. An ATLAS R-parity violating SUSY search [44] made use of a novel application of jet substructure, so-called "accidental substructure." The analysis was optimized to search for gluon pair production, with cascades containing R-parity violating UDD couplings, ultimately producing 10 or more final state partons.

Figure 5 shows a typical signal event clustered with anti-k$_T$ R=0.4 and R=1.0 jets. When clustered with R=0.4 jets, 17 unique jets are reconstructed, whereas only 5 jets are reconstructed with the larger R parameter. Unlike the jet substructure applications described above, here the goal is not to capture all the decay products from a heavy parent in a single jet; but rather to capture radiation from partons with different parents that "accidentally" fall in the same fat jet, giving rise to large mass. The observable which then discriminates between signal and background is the scalar sum of the masses (after trimming) of the four leading jets m_J^{Σ}. This has the advantage over more traditional analyses which rely on the scalar sum of the jet p_T in that it also exploits the rich angular structure of signal events.

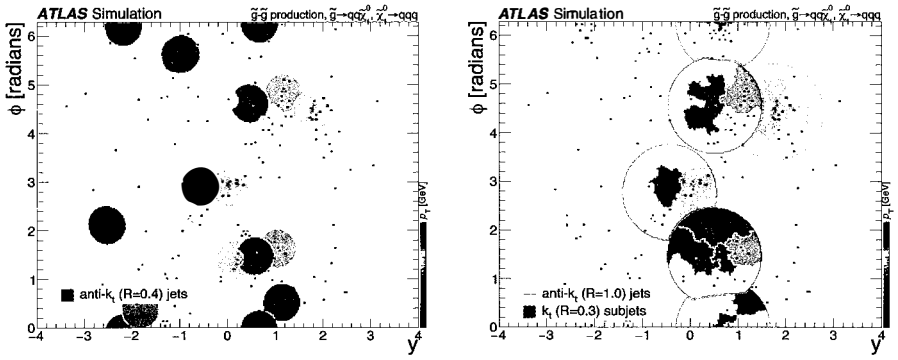

Figure 5 – A signal event clustered with anti-k$_T$ R=0.4 (left) and anti-k$_T$ R=1.0 (right) jets.

In addition to containing at least four R=1.0 jets, selected events were required to have a small separation in η between the two leading jets. Backgrounds were modeled with a data-driven approach. The observed m_J^{Σ} distribution is shown in Figure 6, which agrees well with the background prediction. The resulting 95% CL mass limits in the $m_{\tilde{\chi}_1^0}$ vs. $m_{\tilde{g}}$ plane are shown in Figure 6.

2.5 Standard Model Measurements

The jet substructure techniques outlined above are now sufficiently-well understood for use in precision measurements. As such, they were recently used in a V+jets cross section measurement [45], as well as a $t\bar{t}$ differential cross section measurement [46]. These measurements were able to extend earlier leptonic measurements to a previously inaccessible kinematic regime.

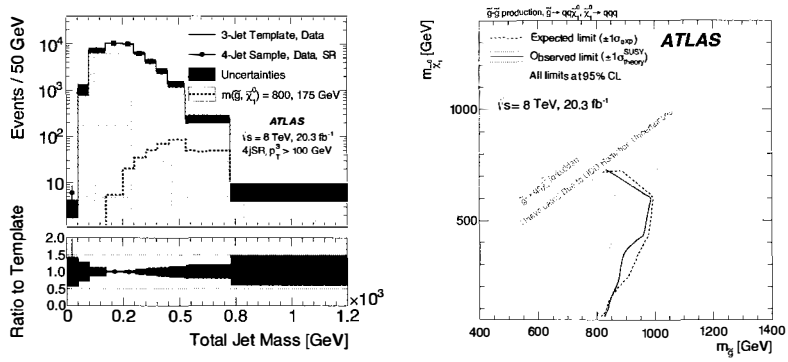

Figure 6 – The predicted and observed m_J^{Σ} distribution for selected events (left) and the expected and observed 95% CL limits in the $m_{\tilde{\chi}_1^0}$ vs. $m_{\tilde{g}}$ plane (right).

Previous V+jets cross section measurements in leptonic decay modes only probed the region of phase space with vector boson $p_T < 300$ GeV. In the recent ATLAS analysis [45] based on hadronic decays, the cross section was measured by selecting events with R=0.6 jets with $p_T > 320$ GeV and $|\eta| < 1.9$. A mass window requirement was applied. A further enhancement of the signal sensitivity was obtained with the use of a likelihood discriminant constructed from jet shape variables in the jet rest frame. The V+jets cross section was obtained from a binned, maximum-likelihood fit to the observed jet mass distribution. A value of 8.5 ± 0.8(stat) $\pm$ 1.5(syst) pb was obtained, in reasonable agreement with the NLO theoretical prediction of 5.1 ± 0.5 pb.

3 Conclusion and Outlook

Novel jet substructure techniques proved extremely useful during Run I of the LHC. The sensitivity of many searches was increased significantly though their use, and precision measurements were extended to extreme kinematic regimes. During Run II, ATLAS and CMS will probe yet higher mass scales in the search for new physics. At these scales, heavy particles will be produced with significant boost, making jet substructure techniques essential in many analyses (if they are not already). New challenges will also be presented. Pileup mitigation will be a serious challenge with higher instantaneous luminosity and 25 ns bunch spacing. It will also be challenging to keep all-hadronic trigger rates at acceptable levels without losing significant signal efficiency. Fortunately, the experimental collaborations, with input form the theory community, are already well on their way to addressing these challenges, and jet substructure techniques will remain a powerful tool during Run II of the LHC.

References

[1] S. D. Ellis, C. K. Vermilion, and J. R. Walsh, "Recombination Algorithms and Jet Substructure: Pruning as a Tool for Heavy Particle Searches," *Phys.Rev.* **D81** (2010) arXiv:0912.0033.

[2] D. Krohn, J. Thaler, and L.-T. Wang, "Jet Trimming," *JHEP* **1002** (2010) arXiv:0912.1342.

[3] J. M. Butterworth, A. R. Davison, M. Rubin, and G. P. Salam, "Jet substructure as a new Higgs search channel at the LHC," *Phys.Rev.Lett.* **100** (2008) arXiv:0802.2470.

[4] A. J. Larkoski, S. Marzani, G. Soyez, and J. Thaler, "Soft Drop," *JHEP* **1405** (2014) arXiv:1402.2657.

[5] ATLAS Collaboration, "Performance of jet substructure techniques for large-R jets in proton-proton collisions at $\sqrt{s} = 7$ TeV using the ATLAS detector," *JHEP* **1309** (2013) arXiv:1306.4945.

[6] CMS Collaboration, "Pileup Removal Algorithms," Tech. Rep. CMS-PAS-JME-14-001, CERN, Geneva, 2014.

[7] S. D. Ellis and D. E. Soper, "Successive combination jet algorithm for hadron collisions," *Phys.Rev.* **D48** (1993) arXiv:hep-ph/9305266.

[8] J. Thaler and K. Van Tilburg, "Identifying Boosted Objects with N-subjettiness," *JHEP* **1103** (2011) arXiv:1011.2268.

[9] A. J. Larkoski, G. P. Salam, and J. Thaler, "Energy Correlation Functions for Jet Substructure," *JHEP* **1306** (2013) arXiv:1305.0007.

[10] CMS Collaboration, "Performance of quark/gluon discrimination in 8 TeV pp data," Tech. Rep. CMS-PAS-JME-13-002, CERN, Geneva, 2013.

[11] D. Krohn, M. D. Schwartz, T. Lin, and W. J. Waalewijn, "Jet Charge at the LHC," *Phys.Rev.Lett.* **110** (2013) arXiv:1209.2421.

[12] J. Gallicchio and M. D. Schwartz, "Seeing in Color: Jet Superstructure," *Phys.Rev.Lett.* **105** (2010) arXiv:1001.5027.

[13] S. D. Ellis, A. Hornig, T. S. Roy, D. Krohn, and M. D. Schwartz, "Qjets: A Non-Deterministic Approach to Tree-Based Jet Substructure," *Phys.Rev.Lett.* **108** (2012) arXiv:1201.1914.

[14] ATLAS Collaboration, "The ATLAS Experiment at the CERN Large Hadron Collider," *JINST* **3** (2008).

[15] CMS Collaboration, "The CMS experiment at the CERN LHC," *Journal of Instrumentation* **3** (2008).

[16] T. Plehn, M. Spannowsky, and M. Takeuchi, "How to Improve Top Tagging," *Phys.Rev.* **D85** (2012) arXiv:1111.5034.

[17] CMS Collaboration, "Boosted Top Jet Tagging at CMS," Tech. Rep. CMS-PAS-JME-13-007, CERN, Geneva, 2014.

[18] CMS Collaboration, "Search for resonant ttbar production in proton-proton collisions at sqrt(s)=8 TeV," arXiv:1506.03062.

[19] R. M. Harris and S. Jain, "Cross Sections for Leptophobic Topcolor Z' Decaying to Top-Antitop," *Eur.Phys.J.* **C72** (2012) arXiv:1112.4928.

[20] ATLAS Collaboration, "A search for $t\bar{t}$ resonances using lepton-plus-jets events in proton-proton collisions at $\sqrt{s} = 8$ TeV with the ATLAS detector," arXiv:1505.07018.

[21] ATLAS Collaboration, "Search for $W' \to tb \to qqbb$ decays in pp collisions at $\sqrt{s} = 8$ TeV with the ATLAS detector," *Eur.Phys.J.* **C75** (2015) arXiv:1408.0886.

[22] CMS Collaboration, "Search for W prime to tbbar in the all-hadronic final state," Tech. Rep. CMS-PAS-B2G-12-009, CERN, Geneva, 2014.

[23] N. Arkani-Hamed, A. G. Cohen, and H. Georgi, "Electroweak symmetry breaking from dimensional deconstruction," *Phys.Lett.* **B513** (2001) arXiv:hep-ph/0105239.

[24] M. Schmaltz and D. Tucker-Smith, "Little Higgs review," *Ann.Rev.Nucl.Part.Sci.* **55** (2005) arXiv:hep-ph/0502182.

[25] I. Antoniadis, K. Benakli, and M. Quiros, "Finite Higgs mass without supersymmetry," *New J.Phys.* **3** (2001) arXiv:hep-th/0108005.

[26] Y. Hosotani, S. Noda, and K. Takenaga, "Dynamical gauge-Higgs unification in the electroweak theory," *Phys.Lett.* **B607** (2005) arXiv:hep-ph/0410193.

[27] K. Agashe, R. Contino, and A. Pomarol, "The Minimal composite Higgs model," *Nucl.Phys.* **B719** (2005) arXiv:hep-ph/0412089.

[28] J. Pati, A. Salam, and J. Strathdee, "Are quarks composite?," *Physics Letters B* **59** (1975).

[29] O. W. Greenberg and C. A. Nelson, "Composite models of leptons," *Phys. Rev. D* **10** Oct (1974).

[30] U. Baur, M. Spira, and P. M. Zerwas, "Excited-quark and -lepton production at hadron colliders," *Phys. Rev. D* **42** Aug (1990).

[31] CMS Collaboration, "Search for vector-like T quarks decaying to top quarks and Higgs bosons in the all-hadronic channel using jet substructure," arXiv:1503.01952.

[32] CMS Collaboration, "Search for pair-produced vector-like quarks of charge -1/3 decaying to bH using boosted Higgs jet-tagging in pp collisions at sqrt(s) = 8 TeV," Tech. Rep. CMS-PAS-B2G-14-001, CERN, Geneva, 2014.

[33] CMS Collaboration, "Search for excited leptons in proton proton collisions at $\sqrt{s}$=8 TeV," Tech. Rep. CMS-PAS-EXO-14-015, CERN, Geneva, 2015.

[34] ATLAS Collaboration, "Search for production of WW/WZ resonances decaying to a lepton, neutrino and jets in pp collisions at $\sqrt{s} = 8$ TeV with the ATLAS detector," *Eur.Phys.J.* **C75** (2015) arXiv:1503.04677.

[35] ATLAS Collaboration, "Search for resonant diboson production in the $\ell\ell q\bar{q}$ final state in pp collisions at $\sqrt{s} = 8$ TeV with the ATLAS detector," *Eur.Phys.J.* **C75** (2015) arXiv:1409.6190.

[36] CMS Collaboration, "Search for a massive resonance decaying into a Higgs boson and a W or Z boson in hadronic final states in proton-proton collisions at sqrt(s) = 8 TeV," Tech. Rep. CMS-PAS-EXO-14-009, CERN, Geneva, 2015.

[37] CMS Collaboration, "Search for narrow high-mass resonances in proton-proton collisions at $\sqrt{s} = 8$ TeV decaying to Z and Higgs bosons," arXiv:1502.04994.

[38] CMS Collaboration, "Search for massive resonances in dijet systems containing jets tagged as W or Z boson decays in pp collisions at $\sqrt{s} = 8$ TeV," *JHEP* **1408** (2014) arXiv:1405.1994.

[39] CMS Collaboration, "Search for massive resonances decaying into pairs of boosted bosons in semi-leptonic final states at $\sqrt{s} = 8$ TeV," *JHEP* **1408** (2014) arXiv:1405.3447.

[40] D. Pappadopulo, A. Thamm, R. Torre, and A. Wulzer, "Heavy Vector Triplets: Bridging Theory and Data," *JHEP* **1409** (2014) arXiv:1402.4431.

[41] CMS Collaboration, "Performance of τ-lepton reconstruction and identification in CMS," *Journal of Instrumentation* **7** (2012).

[42] ATLAS Collaboration, "Search for direct pair production of the top squark in all-hadronic final states in proton-proton collisions at $\sqrt{s} = 8$ TeV with the ATLAS detector," *JHEP* **1409** (2014) arXiv:1406.1122.

[43] ATLAS Collaboration, "Search for top squark pair production in final states with one isolated lepton, jets, and missing transverse momentum in $\sqrt{s}$ =8 TeV pp collisions with the ATLAS detector," *JHEP* **1411** (2014) arXiv:1407.0583.

[44] ATLAS Collaboration, "Search for massive supersymmetric particles decaying to many jets using the ATLAS detector in pp collisions at $\sqrt{s} = 8$ TeV," *Phys.Rev.* **D91** (2015) arXiv:1502.05686.

[45] ATLAS Collaboration, "Measurement of the cross-section of high transverse momentum vector bosons reconstructed as single jets and studies of jet substructure in pp collisions at $\sqrt{s} = 7$ TeV with the ATLAS detector," *New J.Phys.* **16** (2014) arXiv:1407.0800.

[46] ATLAS Collaboration, "Measurement of the differential cross-section of highly boosted top quarks as a function of their transverse momentum using the ATLAS detector in $\sqrt{s}$ = 8 TeV proton-proton collisions," Tech. Rep. ATLAS-CONF-2014-057, CERN, Geneva, Sep 2014.

SUSY: Blind spots at Run 1, perspectives at Run 2 and beyond

G. Polesello
INFN, Sezione di Pavia, Via Bassi 6, 27100 Pavia

On behalf of the ATLAS and CMS Collaborations

The searches for SUSY at LHC with Run 1 data performed by the ATLAS and CMS collaborations are reviewed, focusing on difficult topologies which reduce the experimental sensitivity to low mass particles. Searches for the top squark, the higgsino and the gluino in the mass region suggested by naturalness considerations are examined in detail, and the options for increasing the coverage of future studies are discussed.

1 Introduction

In the course of 2012 the ATLAS [1] and CMS [2] experiments at the LHC have collected proton-proton collisions corresponding to an integrated luminosity of $\sim$20 fb^{-1} for each experiment at a center-of-mass energy of 8 TeV (Run 1). Both experiments have performed extensive searches for new physics in these data, unfortunately with null results. One of the main aims of this activity has been the search for signals from low-mass supersymmetry (SUSY), one of the best motivated theories of physics beyond the standard model (BSM).

Data taking at the LHC is restarting. For Run 2 the LHC will run at a center-of-mass energy of 13 TeV, with a projected integrated luminosity of $\sim$ 100 fb^{-1} within the next three years. It is appropriate at this point to review the results of SUSY searches based on Run 1 data, and try to understand how much of the parameter space of SUSY with particle masses within the kinematic reach of the LHC is still unexplored, why it is so, and what are the perspectives for covering these in the future, both with the LHC and with proposed new high energy accelerators.

SUSY postulates for each standard model (SM) particle a superpartner with the same couplings and spin different by half a unit. The masses of the superpartners are the same as the ones of the corresponding SM partners in unbroken SUSY. Since no SUSY partners are observed in nature, SUSY must be broken, and superpartner masses generated in SUSY breaking. The nature of the breaking is not constrained by theory, and the most generic SUSY breaking brings into the theory $\approx$ 100 free parameters. Searches at the LHC have been aimed at achieving the most general possible coverage of the SUSY parameter space addressing general signatures which appear in many implementations of the model.

For the purposes of this report, it is necessary to restrict the parameter space by imposing constraints on the SUSY models considered. The first constraint is the request that the theory be R-parity conserving. A further restriction is that the invisible lightest supersymmetric particle (LSP) is the lightest neutralino, which is a mixture of the partners of the higgs and of the vector bosons. An additional guidance comes from the request that the corrections to the mass of the Higgs boson from SUSY particles are such as not to induce the need for too precise cancellations to produce the measured Higgs mass of 125 GeV. This requirement defines a minimal set of superpartners that need to be near the TeV scale. This approach is called 'natural SUSY', as

it is meant to ensure that the SUSY spectrum respects the 'naturalness' conditions [3]. In this framework the partner of the Higgs, the higgsino, is required to have a mass below 200-300 GeV, the lighter partner of the top, the stop ($\tilde{t}_1$), to have a mass below ~1 TeV, and the partner of the gluon, the gluino ($\tilde{g}$) below a few TeV. The ATLAS and CMS Collaborations have searched for these particles using Run 1 LHC data, on the basis of simplified models in which each of the particles of interest is directly produced, and all of the superpartners not involved in its decay are assumed to be outside of the observable reach.

The following discussion will concentrate on assessing how near the null results of Run 1 searches have come to excluding Natural SUSY, and what is the sensitivity for covering the non-excluded part of the parameter space with the coming 13/14 TeV LHC runs and possible future facilities.

2 Kinematic considerations

As will become clear in the following, most of the difficult regions for Run 1 SUSY searches are determined by special mass relations among the SUSY and SM particles which spoil the signatures through which the SUSY signal is separated from background, or make the signal completely invisible in the detector.

As an example, consider a heavy particle A decaying into a visible SM particle b and a weakly interacting particle c which escapes the detector unseen, thus providing the $E_{\mathrm{T}}^{\mathrm{miss}}$ signature on which SUSY searches are based. A particular situation happens when $m(A) \sim m(b) + m(c)$. If A is produced at rest b and c are also at rest, so c does not carry any momentum. No missing transverse momentum is observed and the final state is experimentally indistinguishable from the direct production of b. If A is produced boosted, its momentum is shared between b and c proportionally to the respective masses. One has two extreme situations in this case: $m(b) \gg m(c)$, in this case again c is at rest, and no $E_{\mathrm{T}}^{\mathrm{miss}}$ can be observed; $m(c) \gg m(b)$: in this case all of the momentum is carried away by c, and the event is invisible in the detector. The only situation which allows good experimental discrimination of signal and background is A boosted and $m(b) \sim (c)$, yielding a visible signal from b, with $E_{\mathrm{T}}^{\mathrm{miss}}$ from c.

From this discussion, it is clear that the experiments need to concentrate on topologies where the pair of produced SUSY particles are boosted. This happens in two cases. The SUSY system can recoil against hard jets radiated from the incoming partons (ISR), which in case of fully invisible signal also yields a jets plus $E_{\mathrm{T}}^{\mathrm{miss}}$ signature. Otherwise SUSY can be produced in the fusion of two vector bosons radiated by the incoming quarks (VBF). In this case the SUSY signature is supplemented by two typically forward jets which can be used to identify the topology.

3 Stop searches

If simplified models are assumed in which all of the sparticles are set to values outside kinematic reach, except the stop and the lighter ewkinos, the stop decays into two main channels: $\tilde{t}_1 \to t\tilde{\chi}_1^0$, and $\tilde{t}_1 \to b\tilde{\chi}_1^{\pm}$.

If $m(\tilde{\chi}_1^{\pm}) > m(\tilde{t}_1)$, the stop decays with 100% BR into $t\tilde{\chi}_1^0$, as long this is kinematically open. If $m(W) + m(b) < m(\tilde{t}_1) - m(\tilde{\chi}_1^0) < m(t)$, the $\tilde{t}_1$decays into $bW\tilde{\chi}_1^0$. If $m(\tilde{t}_1) - m(\tilde{\chi}_1^0) < m(W) + m(b)$, the $\tilde{t}_1$ decays into $bff'\tilde{\chi}_1^0$ or through a FCNC into $c\tilde{\chi}_1^0$. The ATLAS [6–11] and CMS [12–15] collaborations have performed extensive searches with null results, and the results for this case, are represented as excluded areas in the $(m(\tilde{t}_1), m(\tilde{\chi}_1^0))$ plane in Fig.1.

If $m(\tilde{\chi}_1^{\pm}) < m(\tilde{t}_1)$, the channel $\tilde{t}_1 \to b\tilde{\chi}_1^{\pm}$ will also be open. Extensive searches have also been performed in this channel, under assumption of decay of $\tilde{t}_1$ with 100% branching fracion into it. The kinematics of the signatures depends on the relative values of $m(\tilde{t}_1) - m(\tilde{\chi}_1^{\pm})$

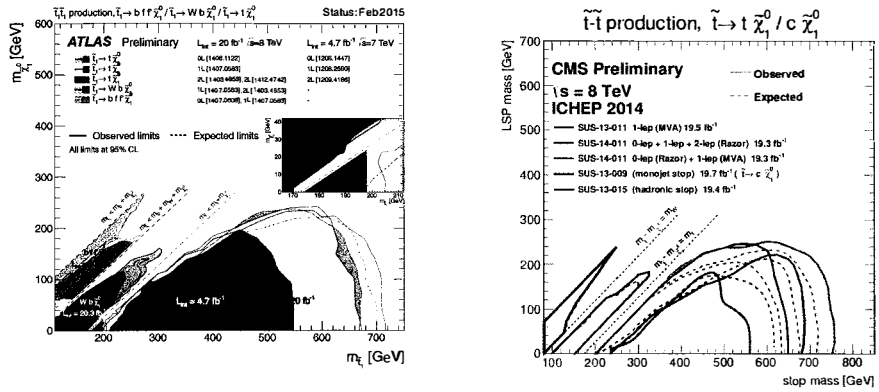

Figure 1 – ATLAS [4] and CMS [5] limits on direct stop production in the plane $(m(\tilde{t}_1), m(\tilde{\chi}_1^0))$, for the decays $\tilde{t}_1 \to t^{(*)}\tilde{\chi}_1^0$ and $\tilde{t}_1 \to c\tilde{\chi}_1^0$.

and $m(\tilde{\chi}_1^{\pm}) - m(\tilde{\chi}_1^0)$, and the results of the searches are presented as excluded areas on the $(m(\tilde{t}_1), m(\tilde{\chi}_1^0))$ or $(m(\tilde{t}_1), m(\tilde{\chi}_1^{\pm}))$ planes with fixed assumptions on the mass of the third sparticle.

While stop masses up to $\sim$ 700 GeV have been excluded for favorable kinematic configurations, a significant parameter space for lower $\tilde{t}_1$ masses is still uncovered. Four main uncovered areas are visible in Fig.1, corresponding to difficult kinematic situations as described in the introduction.

- $m(\tilde{t}_1) - m(\tilde{\chi}_1^0) = m(t)$;
- $m(\tilde{t}_1) - m(\tilde{\chi}_1^0) = m(W) + m(b)$. This area is being targeted by dedicated analyses on Run 1 data, and it is likely it will be excluded by the time this report is published; it will not be discussed further here.
- $m(\tilde{t}_1) < 100$ GeV; the area is outside of the plot in Fig. 1. Most of it is covered by LEP and Tevatron searches. It is, however, necessary to verify that no gap is left;
- $m(\tilde{t}_1) < 200$ GeV, $m(\tilde{\chi}_1^0) < m(t)$. This is the area in the inset on the left plot of Fig.1.

In the area $m(\tilde{t}_1) < 200$ GeV, $m(\tilde{\chi}_1^0) < m(t)$ the $\tilde{t}_1$ production cross-section is very high, approximately 10% of the one for top, and the final state is very similar to SM $t\bar{t}$ production. It should therefore be possible to detect the production of $\tilde{t}_1$ as a discrepancy between the observed $t\bar{t}$ cross-section and the SM predictions [16], which are available at NLLO, with an error assumed to be $\sim$ 7% [17]. The sensitivity of the search can be improved by using the difference in azimuthal angle $\Delta\phi$ of the two charged leptons in the doubly leptonic decay which is sensitive to $t\bar{t}$ spin correlations [18]. The distribution of this variable is shown in the left side of Fig. 2. By combining the information from the cross-section normalisation and $\Delta\phi$, the ATLAS collaboration was able to exclude, at 95% CL, stop masses between the top mass and 191 GeV, assuming a BR of 100% for $\tilde{t}_1 \to t\tilde{\chi}_1^0$ and $m(\tilde{\chi}_1^0) = 1$ GeV. A small slice around $m(\tilde{t}_1) = 200$ GeV is still uncovered. The top cross-section analysis is systematics-limited, and a possible line of improvement would be to use the higher statistics available in Run 2 to select restricted kinematic regions where the systematic uncertainty on $t\bar{t}$ production is lower. An improvement may also come from explicit stop searches in the 1-lepton channel, which, for ATLAS already excludes, at 90% CL, the case $m(\tilde{t}_1) = 200$ GeV, $m(\tilde{\chi}_1^0) = 0$ GeV.

For the region $m(\tilde{t}_1) - m(\tilde{\chi}_1^0) = m(t)$ and $m(\tilde{t}_1) > 300$ GeV, for boosted stop production half of the boost would be carried away by t and half by $\tilde{\chi}_1^0$. A large amount of work on tagging

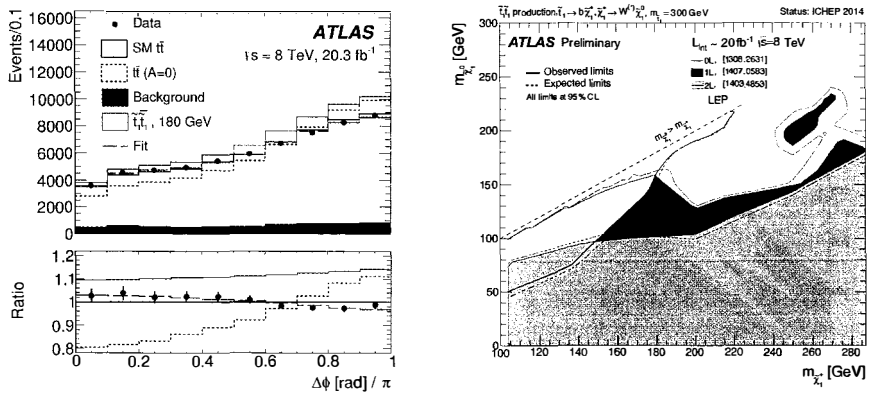

Figure 2 – Left: $\Delta\phi$ distribution of two charged leptons in $t\bar{t}$ events as measured in the ATLAS experiment [11]. Right: excluded areas in the $(m(\tilde{\chi}_1^{\pm}), m(\tilde{\chi}_1^0))$ plane for $m(\tilde{t}_1) = 300$ GeV from the ATLAS experiment [4].

of boosted top quark decays is available in literature. Dedicated signal regions requiring two tagged tops, one additional hard jet and $E_{\mathrm{T}}^{\mathrm{miss}}$ should allow an increase of sensitivity in this area, as shown e.g in [19], which addresses the issue for a 100 TeV collider. An alternative, more model-dependent, approach relies on the search for the $\tilde{t}_2 \to Z(h)\tilde{t}_1$ [20,21].

For $m(\tilde{t}_1) < 100$ GeV, the area corresponding to $m(\tilde{\chi}_1^0) < 10$ GeV can be covered by a precision $t\bar{t}$ cross-section measurement according to [16]. An alternative approach, which would cover the complete area between the LEP limits and the published LHC limits, proposed in [22], relies on adding a b-tagging requirement to the ATLAS monojet analysis [10].

For the decay $\tilde{t}_1 \to b\tilde{\chi}_1^{\pm}$ the 3-dimensional parameter space makes a complete assessment of the difficult regions more complicated. The ATLAS excluded areas in the $(m(\tilde{\chi}_1^{\pm}), m(\tilde{\chi}_1^0))$ plane for a fixed stop mass of 300 GeV are shown in the right side of Fig. 2. The uncovered areas are the ones where $m(\tilde{t}_1) - m(\tilde{\chi}_1^{\pm}) < m(t) - m(W)$ and $m(\tilde{\chi}_1^{\pm}) - m(\tilde{\chi}_1^0) < m(W)$, where the kinematics of visible particles is softer than in $t\bar{t}$. The upper right corner with $m(\tilde{t}_1) \sim m(\tilde{\chi}_1^{\pm}) \sim m(\tilde{\chi}_1^0)$ will be easily covered in Run 2 by monojet analyses which already exclude the same topology up to $m(\tilde{t}_1) \sim 250$ GeV. For the remaining area dedicated searches based on boosted topologies will need to be developed.

4 Higgsino searches

The SUSY partners which do not carry a color charge (ewkinos) are the partner of the higgs, higgsinos, and the partners of the SU(2) and U(1) gauge bosons, respectively the wino and the bino. These particles mix to generate two charged charginos, and two neutral neutralinos. The phenomenology is determined by the parameters entering the mixing matrix, which are μ, the higgsino mass, M_1, the bino mass, M_2, the wino mass, and $\tan\beta$, the ratio of the vacuum expectation values of the two doublets in the theory. It is useful to consider three different hierarchies for these parameters, yielding approximately unmixed neutralino states:

- $\mu \gg M_2 > M_1$: the $\tilde{\chi}_1^0$ is a pure bino, and it is lighter than $\tilde{\chi}_1^{\pm}$ and $\tilde{\chi}_2^0$, which are degenerate;
- $M_1, M_2 \gg \mu$: the $\tilde{\chi}_1^0$, $\tilde{\chi}_2^0$ and $\tilde{\chi}_1^{\pm}$ are pure higgsinos and mass degenerate;
- $\mu \gg M_1 > M_2$: the $\tilde{\chi}_1^0$ and $\tilde{\chi}_1^{\pm}$ are pure winos and are mass degenerate, $\tilde{\chi}_2^0$ is a bino, and is heavier.

In the ewkino sectors degeneracies among particles are not accidental, but are induced by theory.

Both ATLAS and CMS have looked for direct production of charginos and neutralinos in simplified models, paramterised in terms of the $\tilde{\chi}_1^0$ mass and of the $\tilde{\chi}_2^0$ mass, which is assumed degenerate with the $\tilde{\chi}_1^\pm$ mass. The most sensitive channel is associated $\tilde{\chi}_1^\pm$ $\tilde{\chi}_2^0$ production. If sleptons are heavier than ewkinos, the decay happens through WZ, yielding a 3-lepton final state as the 'golden' channel, or through a W and the higgs boson, yielding final states with a lepton from the W and either a pair of photons or a pair of b-jets. Both channels have been investigated, by ATLAS [23, 24] and CMS [25, 26] and the limits are shown in Fig. 3. The limit curves are based on the assumption that $\tilde{\chi}_2^0$ and $\tilde{\chi}_1^\pm$ are both pure gauginos. Two difficult regions

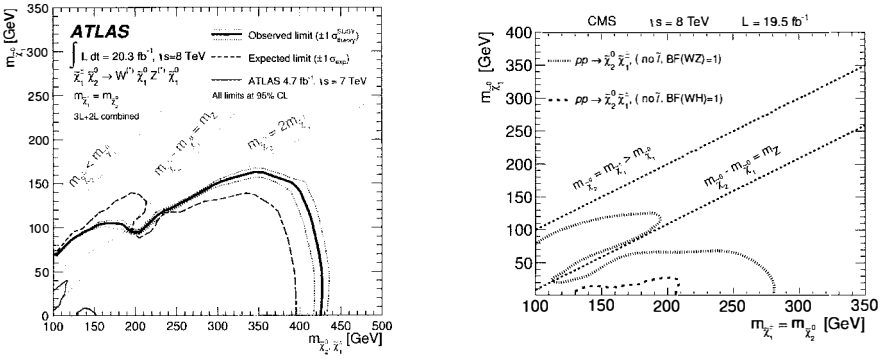

Figure 3 – Limits in the $(m(\tilde{\chi}_2^0), m(\tilde{\chi}_1^0))$ plane for the direct production of $\tilde{\chi}_1^\pm \tilde{\chi}_2^0$ pairs decaying through W,Z and higgs bosons. Left: ATLAS limits [23]; Right: CMS limits [25].

are evident in the $(m(\tilde{\chi}_2^0), m(\tilde{\chi}_1^0))$ plane:

- $m(\tilde{\chi}_1^0) \sim m(\tilde{\chi}_2^0) \sim m(\tilde{\chi}_1^\pm)$, which results only in very soft leptons, and corresponds to the case where the three particles are pure higgsinos.
- $m(\tilde{\chi}_2^0) - m(\tilde{\chi}_1^0) \sim m(Z)$. In this case the final state is very similar to SM WZ production.

Following the naturalness thread, we concentrate, in the following, on the pure higgsino situation.

In that case the critical parameter is Δm, the mass difference $m(\tilde{\chi}_2^0) - m(\tilde{\chi}_1^0)$, which determines the transverse momenta of the leptons in the event. As is visible in Fig. 3, currently the LHC experiments are sensitive to $\Delta m > 25 - 30$ GeV. For $\mu = 200$ GeV, by varying M_1 and M_2, Δm varies between a few tens of GeV, for relatively light M_1 and M_2, to order 100 MeV determined by electroweak radiative corrections, for M_1 and M_2 of the order of a few tens of TeV.

Three different experimental strategies can be considered, depending on the range of Δm:

- If Δm is of order a few hundred MeV or lower, the $\tilde{\chi}_1^\pm$ becomes long-lived, and searches can be performed for tracks stopping inside the inner tracker of the experiment. Searches for this signature have been performed in Run 1, both by ATLAS [27] and CMS [28], and interpreted in the framework of a wino LSP.
- If Δm is of order GeV, then the decay will of $\tilde{\chi}_1^\pm$ will be prompt, and the decay products will be too soft to be detected. The only possibility in this case would be to look for ewkino production recoiling against high p_T QCD radiation, or produced in VBF. Several detailed theoretical studies have been performed on this channel [29–33]. The generic conclusion is that, in order to be sensitive to $\tilde{\chi}_1^\pm/\tilde{\chi}_2^0$ masses of 200 GeV, the SM background, dominated by Z+jets, will have to be known with an error of 1%. The present uncertainty on Run 1

analyses is 3-4%. Reducing this error to the required level is a very serious experimental challenge.

- If Δm is between 10 and 30 GeV, again using ISR or VBF, to boost the ewkino system, leptons from the ewkino decay should have transverse momenta in excess of 5-10 GeV, which would bring them in the range of detectability. The experimental challenge for lepton in this range of transverse momentum is the very high background of fake leptons from misidentified jets. Some dedicated analyses in this direction are being performed on Run 1 data. Theoretical extrapolations [34] claim sensitivity down to Δm=20 GeV when requiring three soft leptons.

Theoretical studies have been performed also for a proton-proton collider with 100 TeV center-of-mass energy [29]. The conclusions are similar, requiring a control of the background at the percent level in order to be able to discover higgsino production. If SUSY does include higgsinos in the 100-300 GeV mass range, the discovery and study of these particles will require a high energy e^+e^- collider over a significant part of the Δm range.

5 Gluino searches

The gluino ($\tilde{g}$) has been searched for in several decay channels, including the one-step decay channel, involving only light quarks and $E_{\mathrm{T}}^{\mathrm{miss}}$, the two-step decay channels through charginos, involving in addition leptons in the final state, and the decay into heavy quarks and $\tilde{\chi}_1^0$, which is dominant in case the stop and sbottom are lighter than the other squarks. The exclusion regions in the $(m(\tilde{g}), m(\tilde{\chi}_1^0))$ plane for two of these channels, from ATLAS [35,36], and CMS [37–39] are shown in Fig. 4 for simplified models where the gluino is assumed to decay with 100% BR into the relevant channel.

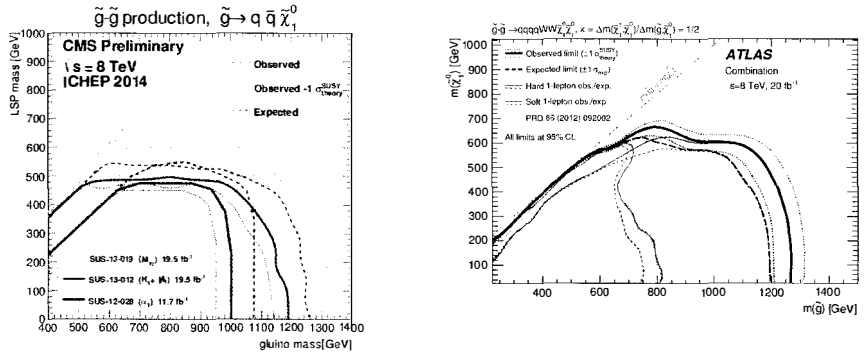

Figure 4 – Excluded areas in the $m(\tilde{g}) - m(\tilde{\chi}_1^0)$ for direct gluino production. Left: CMS limit for the decay $\tilde{g} \to q\bar{q}\tilde{\chi}_1^0$ [5]. Right: ATLAS limit for the decay $\tilde{g} \to qqW\tilde{\chi}_1^0$ [36].

The conclusion from these searches is that gluinos are excluded up to masses of ~1.2-1.3 TeV for massless $\tilde{\chi}_1^0$, but if the $\tilde{\chi}_1^0$ mass is above 500 GeV, there are no limits on the gluino mass, unless the final state involves several b-jets. This is due to the fact that the hard required selections in the $E_{\mathrm{T}}^{\mathrm{miss}}$+jets channel have efficiencies decreasing with the gluino-LSP mass difference. The convolution of decreasing cross-section with growing gluino masses and the efficiency decrease determines the shape of the excluded regions. In Run 2, with the higher center of mass energy, at the high masses under consideration both the signal production cross-section and the signal/background ratio will significantly increase. Simulation studies performed by the ATLAS [40] and CMS [41] Collaborations have shown that already with an integrated luminosity

of 300 fb^{-1} at 14 TeV it will be possible to achieve sensitivities to gluino masses of 2.5 TeV for $\tilde{\chi}_1^0$ massless, and of 1.2 TeV for any mass of $\tilde{\chi}_1^0$.

6 Conclusions

The issue of uncovered SUSY signatures after LHC Run 1 for a 'Natural SUSY' paradigm has been addressed on the basis of the analyses performed by the ATLAS and CMS Collaborations. With the coming LHC Run 2, and the projected high luminosity LHC run, through dedicated searches there is a good chance of covering the difficult regions for stop and gluino production. For higgsino production with a mass difference $m(\tilde{\chi}_2^0) - m(\tilde{\chi}_1^0)$ between a few hundred MeV and$\sim$10 GeV, the discovery at a proton-proton collider would require a systematic control of the main background sources at the percent level.

References

1. ATLAS Collaboration, *The ATLAS Experiment at the CERN Large Hadron Collider*, JINST **3** (2008) S08003.
2. CMS Collaboration, *The CMS experiment at the CERN LHC*, JINST **3** (2008) S08004.
3. M. Papucci, J. T. Ruderman, and A. Weiler, *Natural SUSY Endures*, JHEP **1209** (2012) 035, arXiv:1110.6926 [hep-ph].
4. http://atlas.web.cern.ch/Atlas/GROUPS/PHYSICS/CombinedSummaryPlots/SUSY.
5. http://twiki.cern.ch/twiki/bin/view/CMSPublic/SUSYSMSSummaryPlots8TeV.
6. ATLAS Collaboration, *Search for direct third-generation squark pair production in final states with missing transverse momentum and two b-jets in $\sqrt{s} = 8$ TeV pp collisions with the ATLAS detector*, JHEP **1310** (2013) 189, arXiv:1308.2631 [hep-ex].
7. ATLAS Collaboration, *Search for top squark pair production in final states with one isolated lepton, jets, and missing transverse momentum in $\sqrt{s} = 8$ TeV pp collisions with the ATLAS detector*, JHEP **1411** (2014) 118, arXiv:1407.0583 [hep-ex].
8. ATLAS Collaboration, *Search for direct pair production of the top squark in all-hadronic final states in proton–proton collisions at $\sqrt{s} = 8$ TeV with the ATLAS detector*, JHEP **1409** (2014) 015, arXiv:1406.1122 [hep-ex].
9. ATLAS Collaboration, *Search for direct top-squark pair production in final states with two leptons in pp collisions at $\sqrt{s} = 8$ TeV with the ATLAS detector*, JHEP **1406** (2014) 124, arXiv:1403.4853 [hep-ex].
10. ATLAS Collaboration, *Search for pair-produced third-generation squarks decaying via charm quarks or in compressed supersymmetric scenarios in pp collisions at $\sqrt{s} = 8$ TeV with the ATLAS detector*, Phys. Rev. D **90** (2014) 052008, arXiv:1407.0608 [hep-ex].
11. ATLAS Collaboration, *Measurement of Spin Correlation in Top–Antitop Quark Events and Search for Top Squark Pair Production in pp Collisions at $\sqrt{s} = 8$ TeV Using the ATLAS Detector*, Phys. Rev. Lett. **114** (2015) 142001, arXiv:1412.4742 [hep-ex].
12. CMS Collaboration, *Exclusion limits on gluino and top-squark pair production in natural SUSY scenarios with inclusive razor and exclusive single-lepton searches at 8 TeV.*, CMS-PAS-SUS-13-009, 2014.
13. CMS Collaboration, *Search for top-squark pair production in the single-lepton final state in pp collisions at $\sqrt{s} = 8$ TeV*, Eur. Phys. J. C **73** (2013) 2677, arXiv:1308.1586 [hep-ex].
14. CMS Collaboration, *Search for new physics in the multijet and missing transverse momentum final state in proton-proton collisions at $\sqrt{s} = 8$ TeV*, JHEP **1406** (2014) 055, arXiv:1402.4770 [hep-ex].
15. CMS Collaboration, *Exclusion limits on gluino and top-squark pair production in natural SUSY scenarios with inclusive razor and exclusive single-lepton searches at 8 TeV.*, CMS-PAS-SUS-14-011, 2014.
16. M. Czakon, A. Mitov, M. Papucci, J. T. Ruderman, and A. Weiler, *Closing the stop gap*, Phys.Rev.Lett. **113** no. 20, (2014) 201803, arXiv:1407.1043 [hep-ph].
17. M. Czakon, P. Fiedler, and A. Mitov, *Total Top-Quark Pair-Production Cross Section at Hadron Colliders Through $O(\frac{4}{S})$*, Phys.Rev.Lett. **110** (2013) 252004, arXiv:1303.6254 [hep-ph].
18. G. Mahlon and S. J. Parke, *Spin Correlation Effects in Top Quark Pair Production at the LHC*, Phys.Rev. **D81** (2010) 074024, arXiv:1001.3422 [hep-ph].

19. T. Cohen, R. T. D'Agnolo, M. Hance, H. K. Lou, and J. G. Wacker, *Boosting Stop Searches with a 100 TeV Proton Collider*, JHEP **1411** (2014) 021, arXiv:1406.4512 [hep-ph].
20. ATLAS Collaboration, *Search for direct top squark pair production in events with a Z boson, b-jets and missing transverse momentum in $\sqrt{s} = 8$ TeV pp collisions with the ATLAS detector*, Eur. Phys. J. C **74** (2014) 2883, arXiv:1403.5222 [hep-ex].
21. CMS Collaboration, *Search for top-squark pairs decaying into Higgs or Z bosons in pp collisions at $\sqrt{s} = 8$ TeV*, Phys. Lett. B **736** (2014) 371, arXiv:1405.3886 [hep-ex].
22. G. Ferretti, R. Franceschini, C. Petersson, and R. Torre, *Spot the stop with a b-tag*, arXiv:1502.01721 [hep-ph].
23. ATLAS Collaboration, *Search for direct production of charginos, neutralinos and sleptons in final states with two leptons and missing transverse momentum in pp collisions at $\sqrt{s} = 8$ TeV with the ATLAS detector*, JHEP **1405** (2014) 071, arXiv:1403.5294 [hep-ex].
24. ATLAS Collaboration, *Search for direct pair production of a chargino and a neutralino decaying to the 125 GeV Higgs boson in $\sqrt{s} = 8$ TeV pp collisions with the ATLAS detector*, arXiv:1501.07110 [hep-ex].
25. CMS Collaboration, *Searches for electroweak production of charginos, neutralinos, and sleptons decaying to leptons and W, Z, and Higgs bosons in pp collisions at 8 TeV*, Eur. Phys. J. C **74** (2014) 3036, arXiv:1405.7570 [hep-ex].
26. CMS Collaboration, *Searches for electroweak neutralino and chargino production in channels with Higgs, Z, and W bosons in pp collisions at 8 TeV*, Phys. Rev. D **90** (2014) 092007, arXiv:1409.3168 [hep-ex].
27. ATLAS Collaboration, *Search for charginos nearly mass degenerate with the lightest neutralino based on a disappearing-track signature in pp collisions at $\sqrt{s} = 8$ TeV with the ATLAS detector*, Phys. Rev. D **88** (2013) 112006, arXiv:1310.3675 [hep-ex].
28. CMS Collaboration, *Search for disappearing tracks in proton–proton collisions at $\sqrt{s} = 8$ TeV*, JHEP **1501** (2015) 096, arXiv:1411.6006 [hep-ex].
29. M. Low and L.-T. Wang, *Neutralino dark matter at 14 TeV and 100 TeV*, JHEP **1408** (2014) 161, arXiv:1404.0682 [hep-ph].
30. H. Baer, A. Mustafayev, and X. Tata, *Monojets and mono-photons from light higgsino pair production at LHC14*, Phys.Rev. **D89** no. 5, (2014) 055007, arXiv:1401.1162 [hep-ph].
31. P. Schwaller and J. Zurita, *Compressed electroweakino spectra at the LHC*, JHEP **1403** (2014) 060, arXiv:1312.7350 [hep-ph].
32. T. Han, S. Padhi, and S. Su, *Electroweakinos in the Light of the Higgs Boson*, Phys.Rev. **D88** no. 11, (2013) 115010, arXiv:1309.5966 [hep-ph].
33. C. Han et al., *Probing Light Higgsinos in Natural SUSY from Monojet Signals at the LHC*, JHEP **1402** (2014) 049, arXiv:1310.4274 [hep-ph].
34. S. Gori, S. Jung, and L.-T. Wang, *Cornering electroweakinos at the LHC*, JHEP **1310** (2013) 191, arXiv:1307.5952 [hep-ph].
35. ATLAS Collaboration, *Search for squarks and gluinos with the ATLAS detector in final states with jets and missing transverse momentum using $\sqrt{s} = 8$ TeV proton–proton collision data*, JHEP **1409** (2014) 176, arXiv:1405.7875 [hep-ex].
36. ATLAS Collaboration, *Search for squarks and gluinos in events with isolated leptons, jets and missing transverse momentum at $\sqrt{s} = 8$ TeV with the ATLAS detector*, JHEP **1504** (2011) 116, arXiv:1501.03555 [hep-ex].
37. CMS Collaboration, *Search for new physics in the multijet and missing transverse momentum final state in proton–proton collisions at $\sqrt{s} = 8$ TeV*, JHEP **1406** (2014) 055, arXiv:1402.4770 [hep-ex].
38. CMS Collaboration, *Search for supersymmetry in pp collisions at $\sqrt{s} = 8$ TeV in events with a single lepton, large jet multiplicity, and multiple b jets*, Phys. Lett. B **733** (2014) 328, arXiv:1311.4937 [hep-ex].
39. CMS Collaboration, *Searches for supersymmetry using the M_{T2} variable in hadronic events produced in pp collisions at 8 TeV*, CMS-SUS-13-019, 2015, arXiv:1502.04358 [hep-ex].
40. ATLAS Collaboration, *Search for Supersymmetry at the high luminosity LHC with the ATLAS Detector*, ATL-PHYS-PUB-2014-010, 2014, http://cdsweb.cern.ch/record/1735031.
41. CMS Collaboration, *Supersymmetry discovery potential in future LHC and HL-LHC running with the CMS detector*, CMS-PAS-SUS-14-012, 2015.

ATLAS & CMS Exotics Searches: Run 1 Results and Run 2 Prospects

K. J. C. Leney
on behalf of the ATLAS and CMS Collaborations
University College London, Department of Physics & Astronomy
Gower Street, London, WC1E 6BT, United Kingdom

The latest results of searches for new physics beyond the Standard Model (non-SUSY) from the ATLAS and CMS collaborations are presented and prospects for searches for exotic phenomena during the LHC Run 2 are discussed.

1 Introduction

The Standard Model (SM) of particle physics has been extraordinarily successful at describing the fundamental particles which are responsible for forces and matter. The discovery of the Higgs boson in 2012 by the ATLAS [1] and CMS [2] experiments at the CERN Large Hadron Collider (LHC) has cemented the success of the SM. While the Higgs boson discovery [3,4] has completed the SM, several phenomena, including dark matter, CP violation and gravity, remain unaccounted for. Furthermore, the presence of the Higgs boson introduces a hierarchy problem where radiative corrections to the Higgs mass must be extremely finely tuned to ensure that there is cancellation with the bare mass. The hierarchy problem hints that some solutions may lie at the electroweak symmetry breaking scale and would therefore be accessible at the LHC. The ATLAS and CMS experiments both have a rich program of searches for new exotic phenomena that provide solutions to these, and many more, unsolved questions. The strategy adopted by both experiments is to look for model independent signatures which can then be interpreted in the context of several different models. A complete review of all results is beyond the scope of this document but can be found in [5] (ATLAS) and [6,7] (CMS). The newest results are summarised here, together with an overview of selected searches of personal interest to the author.

2 Searches for New Resonances

Many theories describing physics beyond the SM (BSM) predict narrow resonances at the TeV mass scale, where the resulting signature is a clear excess over a falling background spectrum. Searches for relatively simple di-electron/muon [8,9] or di-jet [10,11] final states are often some of the earliest results published by the experiments, but almost any combination of two SM particles can form a resonance in BSM models. In the case where the daughter particles subsequently decay themselves, this can lead to complex final states. Many new results of searches for new resonances were presented at Moriond EW. These are too numerous to discuss here but are listed in table 1.

Table 1: Recent searches for new heavy resonances from ATLAS and CMS (status as of March 2015).

A search for high-mass resonances decaying to $\tau^+\tau^-$ in pp collisions at $\sqrt{s}$ = 8 TeV with the ATLAS detector	arXiv:1502.07177, submitted to *J. High Energy Phys.*
Search for new physics in final states with a tau and missing transverse energy using pp collisions at $\sqrt{s}$ = 8 TeV (CMS)	CMS-PAS-EXO-12-011
Search for production of WW/WZ resonances decaying to a lepton, neutrino and jets in pp collisions at $\sqrt{s}$ = 8 TeV with the ATLAS detector	arXiv:1503.04677, submitted to *Eur. Phys. J.* C
Search for single production of scalar leptoquarks in pp collisions at $\sqrt{s}$ = 8 TeV with the CMS Detector	CMS-PAS-EXO-12-043
Search for a Heavy Neutral Particle Decaying to $e\mu$, $e\tau$, or $\mu\tau$ in pp Collisions at $\sqrt{s}$ = 8 TeV with the ATLAS Detector	arXiv:1503.04430, submitted to *Phys. Rev. Lett.*
Search for high-mass diphoton resonances in pp collisions at $\sqrt{s}$ = 8 TeV with the ATLAS detector	arXiv:1504.05511, submitted to *Phys. Rev.* D
Search for resonant diboson production in the $\ell\ell qq$ final state in pp collisions at $\sqrt{s}$ = 8 TeV with the ATLAS detector	*Eur. Phys. J.* C 75 (2015) 69
Search for physics beyond the standard model in dilepton mass spectra in proton-proton collisions at $\sqrt{s}$ = 8 TeV (CMS)	*J. High Energy Phys.* **04** (2015) 025
Searches for light- and heavy-flavour three-jet resonances in pp collisions at $\sqrt{s}$ = 8 TeV (CMS)	*Phys. Lett.* B **730**, 193 (2014)
Search for resonances and quantum black holes using dijet mass spectra in proton-proton collisions at $\sqrt{s}$ = 8 TeV (CMS)	*Phys. Rev.* D **91**, 052009 (2015)
Search for excited leptons in proton proton collisions at $\sqrt{s}$ = 8 TeV (CMS)	CMS-PAS-EXO-14-015
A search for ttbar resonances using lepton plus jets events in proton-proton collisions at sqrt(s)=8 TeV with the ATLAS detector	ATLAS-CONF-2015-009

3 Searches for Long-Lived Particles

Several BSM models, including supersymmetry (SUSY), are predicted to give rise to new massive particles with relatively long lifetimes. Such models include:

- Hidden Valley models.
- Minimal B-L extensions of the SM.
- Split SUSY models.
- SUSY with weak R-parity violation.
- Magnetic monopoles.
- Stable charged leptons.

Models with long-lived particles give striking experimental signatures including disappearing tracks, displaced vertices in the tracking detector, displaced muon lepton-jets, and decays in the calorimeter.

Several new searches for long-lived particles were presented at the conference. These are too numerous to discuss here but are listed in table 2. The latest status (as of March 2015) of ATLAS searches in terms of the lifetime of the long-lived particle is summarised in figure 1.

4 The Higgs Boson as a Tool for Discovery

The discovery of the 125 GeV Higgs boson by the ATLAS and CMS experiments in July 2012 was a great success for the SM and provides other avenues for searching for signs of BSM physics. Precise measurements of the Higgs boson properties can be used to set indirect limits on models, and searches for BSM Higgs bosons (e.g. those predicted by SUSY models) abound. The Higgs boson can also be used as an extra handle in searches for exotic models by looking for decays of new particles to the SM (125 GeV) Higgs boson. Several new results were presented at the conference but are too numerous to discuss here in detail. Instead, they are listed in table 3.

Table 2: Recent searches for long-lived particles from ATLAS and CMS (status as of March 2015).

Search for pair-produced long-lived neutral particles decaying in the ATLAS hadronic calorimeter in pp collisions at $\sqrt{s} = 8$ TeV	*Phys. Lett.* B **743**, 15-34 (2015)
Search for long-lived particles that decay into final states containing two electrons or two muons in proton-proton collisions at $\sqrt{s} = 8$ TeV (CMS)	*Phys. Rev.* D **91**, 052012 (2015)
Search for heavy long-lived multi-charged particles in pp collisions at $\sqrt{s} = 8$ TeV using the ATLAS detector	arxiv:1504.04188, submitted to *Eur. Phys. J.* C
Search for Displaced Supersymmetry in Events with an Electron and a Muon with Large Impact Parameters (CMS)	*Phys. Rev. Lett.* **114**, 061801 (2015)
Constraints on the pMSSM, AMSB model and on other models from the search for long-lived charged particles in proton-proton collisions at $\sqrt{s} = 8$ TeV (CMS)	arXiv:1502.02522, submitted to *Eur. Phys. J.* C
Search for long-lived neutral particles decaying into lepton jets in proton-proton collisions at $\sqrt{s} = 8$ TeV with the ATLAS detector	*J. High Energy Phys.* **11** (2014) 088
Search for disappearing tracks in proton-proton collisions at $\sqrt{s} = 8$ TeV (CMS)	*J. High Energy Phys.* **01** (2015) 096
Search for long-lived neutral particles decaying to quark-antiquark pairs in proton-proton collisions at $\sqrt{s} = 8$ TeV (CMS)	*Phys. Rev.* D **91**, 012007 (2015)
Search for long-lived, weakly-interacting particles that decay to displaced hadronic jets in proton-proton collisions at $\sqrt{s} = 8$ TeV with the ATLAS detector	arXiv:1504.03634, submitted to *Phys. Rev.* D

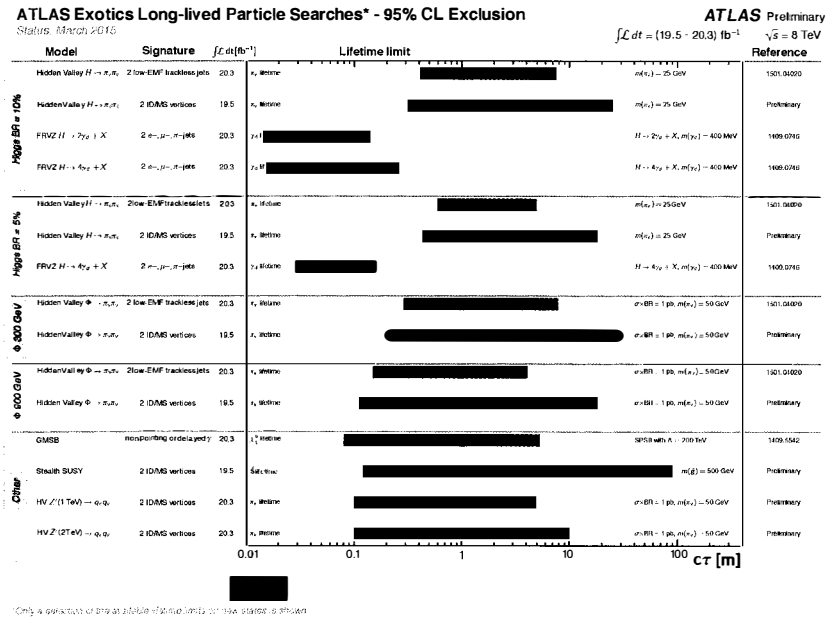

Figure 1: Status (as of March 2015) of ATLAS searches for long-lived particles.

Table 3: Recent searches for new particles decaying to 125 GeV Higgs bosons from ATLAS and CMS (status as of March 2015).

Search for a new resonance decaying to a W or Z boson and a Higgs boson in the $\ell\ell/\ell\nu/\nu\nu + b\bar{b}$ final states with the ATLAS detector	arXiv:1503.04677, submitted to *Eur. Phys. J.* C
Search for new light gauge bosons in Higgs boson decays to four-lepton final states in pp collisions at $\sqrt{s}$ = 8 TeV with the ATLAS detector at the LHC.	ATLAS-CONF-2015-003
Search for Higgs Boson Pair Production in the $\gamma\gamma b\bar{b}$ Final State Using pp Collision Data at $\sqrt{s}$ =8TeV from the ATLAS Detector	*Phys. Rev. Lett.* **114**, 081802 (2015)
Search for resonant HH production in $2\gamma + 2b$ channel (CMS)	CMS-PAS-HIG-13-032
A search for resonant Higgs-pair production in the $b\bar{b}b\bar{b}$ final state in pp collisions at $\sqrt{s}$ = 8 TeV (ATLAS)	ATLAS-CONF-2014-005
Search for resonant pair production of Higgs bosons decaying to two bottom quark-antiquark pairs in proton-proton collisions at 8 TeV (CMS)	arXiv:1503.04114, submitted to *Phys. Lett.* B
Search for narrow high-mass resonances in proton-proton collisions at $\sqrt{s}$ = 8 TeV decaying to Z and Higgs bosons (CMS)	arXiv:1502.04994, submitted to *Phys. Lett.* B
Search for a CP-odd Higgs boson decaying to Zh in pp collisions at $\sqrt{s}$ =8 TeV with the ATLAS detector	*Phys. Lett.* B **744**, 163-183 (2015)

Numerous searches for BSM/non-125 GeV Higgs bosons are undertaken by both collaborations, but are beyond the scope of this document.

5 Other New Search Results

In addition to those already discussed above, searches are performed for a wide variety of other models, including searches for dark matter, heavy majorana neutrinos and Type III seesaw mechanisms. Once again, these are too plentiful to discuss in detail, but are listed in table 4.

6 Overview of ATLAS and CMS Exotics Searches

The current (as of March 2015) status of searches for new physics in terms of the mass reach of various benchmark models is summarised for ATLAS in figure 2, and for CMS in figures 3 and 4.

7 Prospects for Exotics Searches in Run 2

During the LHC Run 2, the LHC will run with a centre-of-mass ($\sqrt{s}$) energy of 13 TeV and is expected to provide ~30 fb^{-1} data per year - a total of 100 fb^{-1}. This increase in $\sqrt{s}$ and larger dataset will enable the experiments to acess processes with smaller cross-sections and/or higher masses. The production cross-sections for all processes will increase. The production cross-section ratios for 13 TeV compared to 8 TeV are shown in figure 5[12]. The ratio increases with the mass of the parent particle, such that a 4 TeV particle produced by gluon-fusion would have a production cross-section ~400 times larger at 13 TeV than at 8 TeV.

An ATLAS study into sensitivity of di-jet resonance searches[13] has shown that only 100 pb^{-1} data with $\sqrt{s}$ = 14 TeV is needed to provide the same experimental sensitivity as was obtained with the full 2012 $\sqrt{s}$ = 8 TeV dataset. The expected mass reach for two benchmark models is shown in figure 6. First collisions at $\sqrt{s}$ = 13 TeV are expected in mid-2015 and the run will continue until 2018 when there will be another long shutdown for detector and machine upgrades and maintenance.

Table 4: Miscellaneous recent searches for exotic models from ATLAS and CMS (status as of March 2015).

Search for low-scale gravity signatures in multi-jet final states with the ATLAS detector at $\sqrt{s} = 8$ TeV	arXiv:1503.08988, submitted to *J. High Energy Phys.*
Search for physics beyond the standard model in final states with a lepton and missing transverse energy in proton-proton collisions at $\sqrt{s} = 8$ TeV (CMS)	arXiv:1408.2745, submitted to *Phys. Rev.* D
Search for new phenomena in monophoton final states in proton-proton collisions at $\sqrt{s} = 8$ TeV (CMS)	arXiv:1410.8812
Search for New Phenomena in Dijet Angular Distributions in Proton-Proton Collisions at $\sqrt{s} = 8$ TeV Measured with the ATLAS Detector	arXiv:1504.00357, accepted by *Phys. Rev. Lett.*
Search for dark matter, extra dimensions, and unparticles in monojet events in proton-proton collisions at $\sqrt{s} = 8$ TeV (CMS)	arXiv:1408.3583, submitted to *Eur. Phys. J.* C
Search for heavy Majorana neutrinos in $\mu^{\pm}\mu^{\pm}$ + jets events in proton-proton collisions at $\sqrt{s} = 8$ TeV (CMS)	arXiv:1501.05566, submitted to *Phys. Lett.* B
Search for heavy lepton partners of neutrinos in pp collisions at 8 TeV, in the context of type III seesaw mechanism (CMS)	CMS-PAS-EXO-14-001
Search for anomalous production of events with same-sign dileptons and b jets in 14.3 fb^{-1} of pp collisions at $\sqrt{s} = 8$ TeV with the ATLAS detector	arXiv:1504.04605, submitted to *J. High Energy Phys.*
Search for production of vector-like quark pairs and of four top quarks in the lepton plus jets final state in pp collisions at $\sqrt{s} = 8$ TeV with the ATLAS detector	ATLAS-CONF-2015-012
Search for new phenomena in final states with an energetic jet and large missing transverse momentum in pp collisions at $\sqrt{s} = 8$ TeV with the ATLAS detector	arxiv:1502.01518, submitted to *Eur. Phys. J.* C

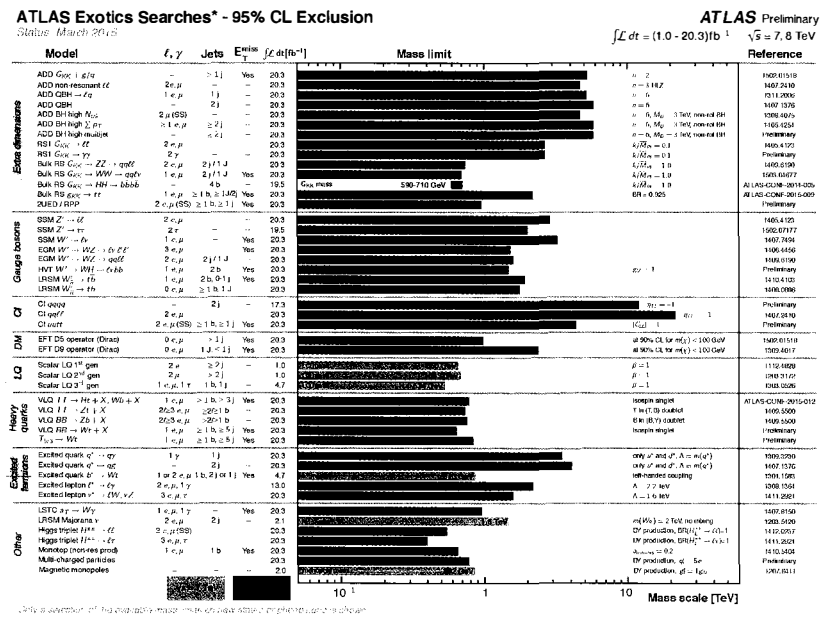

Figure 2: Status (as of March 2015) of ATLAS searches for exotic models [5].

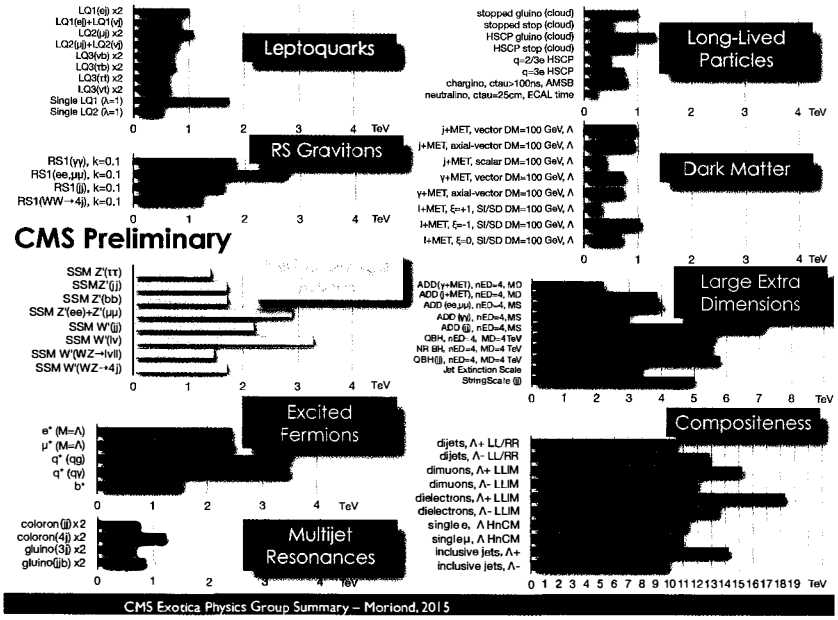

Figure 3: Status (as of March 2015) of CMS searches for exotic models (1) [6].

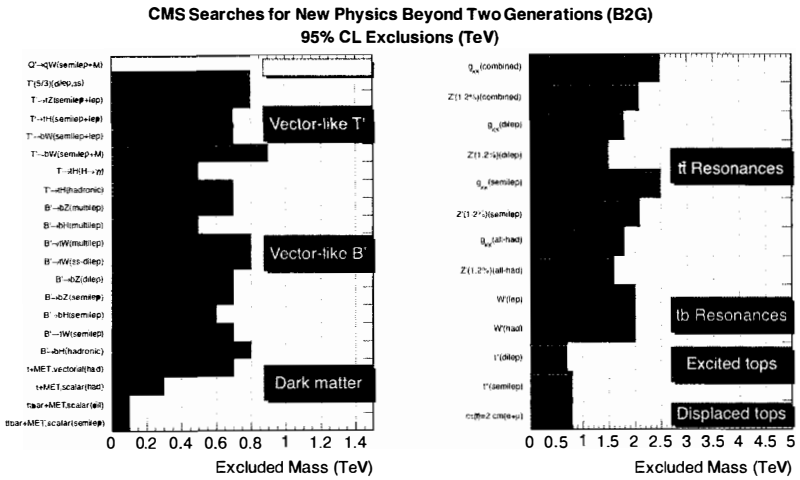

Figure 4: Status (as of March 2015) of CMS searches for exotic models (2) [7].

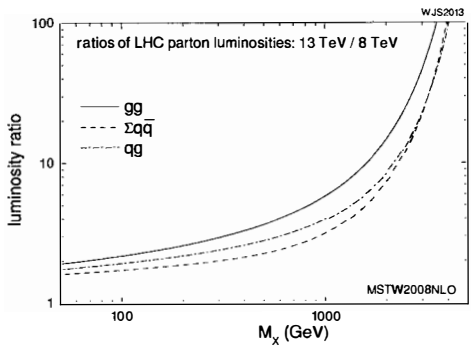

Figure 5: Ratios of LHC parton luminosities at 13 TeV to 8 TeV [12].

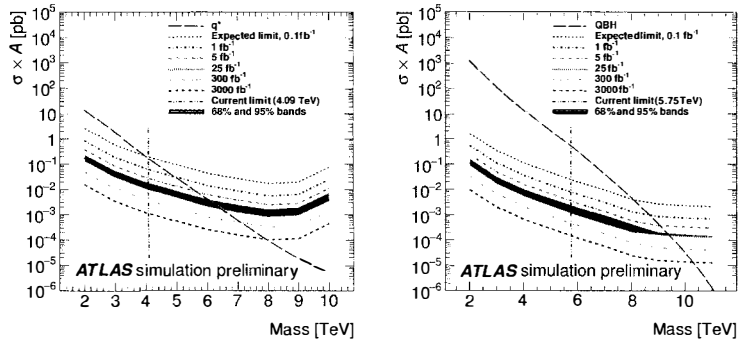

(a) (b)

Figure 6: Expected limits on (a) excited quark ($q*$) and (b) quantum black hole (QBH) models. The dashed vertical lines represent the current limits based on 20.3 fb^{-1} of 8 TeV data: 4.09 TeV for the $q*$ and 5.75 TeV for the QBH [13].

8 Conclusions

The ATLAS and CMS experiments both have a rich program of searches for new physics. A wide range of searches was performed on data from the LHC Run 1 and large regions of phase space for new models have been excluded. The increased centre-of-mass energy and larger dataset expected during LHC Run 2 will provide scope for accessing higher mass objects and rarer processes, thus allowing the experiments to set stronger limits or discover new physics from early data-taking onwards.

References

1. ATLAS Collaboration, *JINST* **3** (2008) S08003
2. CMS Collaboration, *JINST* **3** (2008) S08004
3. ATLAS Collaboration, *Phys. Lett.* B **716**, 1-29 (2012)
4. CMSS Collaboration, *Phys. Lett.* B **716**, 30-61 (2012)
5. `https://twiki.cern.ch/twiki/bin/view/AtlasPublic/ExoticsPublicResults`
6. `https://twiki.cern.ch/twiki/bin/view/CMSPublic/PhysicsResultsEXO`
7. `https://twiki.cern.ch/twiki/bin/view/CMSPublic/PhysicsResultsB2G`
8. ATLAS Collaboration, *Phys. Rev.* D **90**, 052005 (2014)
9. CMS Collaboration, *J. High Energy Phys.* **04** (2015) 025
10. ATLAS Collaboration, *Phys. Rev.* D **91**, 052007 (2015)
11. CMS Collaboration, *Phys. Rev.* D **91**, 052009 (2015)
12. W.J. Stirling, private communication
13. ATLAS Collaboration, ATL-PHYS-PUB-2015-004

Searching for supersymmetry in compressed scenarios with the CMS experiment

R. J. BAINBRIDGE, on behalf of the CMS Collaboration
Blackett Laboratory, Imperial College London, Prince Consort Road, South Kensington, UK

Searches for supersymmetric models with a compressed mass spectrum are presented using data samples collected at a centre-of-mass energy of 8 TeV with the CMS detector at the LHC and corresponding to an integrated luminosity of $19.4 - 19.7\,\mathrm{fb}^{-1}$. This class of model is challenging to detect experimentally, primarily due to low-momentum SM particles arising from decay chains involving SUSY particles of comparable mass. Various searches that are optimised for models involving the production of coloured sparticles or electroweakinos and a compressed mass spectrum are presented.

1 Introduction

A low-energy realisation of supersymmetry (SUSY) with third-generation squarks close in mass to the top quark can provide the mechanism to cancel quadratically divergent loop corrections to the mass of the SM Higgs boson [1,2] without the need for significant fine tuning [3,4,5]. The electroweak sector of R-parity conserving SUSY models is also of relevance, as the lightest supersymmetric particle (LSP), typically assumed to be the $\tilde{\chi}_1^0$, provides a viable dark matter (DM) candidate given its massive yet weakly interacting nature.

The lack of evidence for SUSY so far at the Large Hadron Collider (LHC) has focussed attention on regions of the SUSY parameter space that have relatively weak coverage in the LHC experimental programme. One such class of models is characterised by a compressed mass spectrum, with the LSP close in mass to the parent sparticle produced in the LHC collision. This class of model is difficult to distinguish experimentally from SM backgrounds due to the low levels of leptonic or hadronic activity in the detector. Hence, experimental acceptance to both the coloured and electroweak sectors with a compressed mass spectrum often relies on the sparticles being produced in association with initial state radiation (ISR) or via the vector boson fusion process. The presence of LSPs can result in significant $p_{\mathrm{T}}^{\mathrm{miss}}$ when they are close in mass to their parent sparticles that are boosted against an energetic jet due to ISR. Any low-momentum final-state objects from sparticle decays can also be boosted back into the experimental acceptance.

The ATLAS and CMS collaborations have been able to exclude large regions of the "natural" mass parameter space of the coloured sector during Run 1 of the LHC, with the most constraining

mass limits beyond or near the TeV scale for gluinos and third-generation squarks, respectively, under the assumptions implicit in interpretations with simplified models. However, this coverage weakens significantly for compressed-spectrum models and particularly for top squark production and decay. Strong exclusions also exist for the mass parameter space of the electroweak sector, typically provided by searches in multilepton final states, with chargino/neutralino masses as large as several hundred GeV being excluded. However, the sensitivity of these searches depends on several factors, such as the mass differences between the lightest chargino and neutralino states, the presence or otherwise of light sleptons (which can affect the branching fractions to multilepton final states), and the flavour of the light slepton states (with poor coverage of models assuming light $\tilde{\tau}$-leptons, due to the relatively large misidentification rate for τ-leptons).

Three recent examples of dedicated searches that target these experimentally challenging regions of signal phase space are described below. The analyses are performed using data collected with the CMS detector[6] in proton-proton collisions at a centre of mass energy of $\sqrt{s} = 8$ TeV at the LHC. The data samples correspond to an integrated luminosity of $19.4 - 19.7\,\text{fb}^{-1}$.

2 Search for third-generation squarks in the monojet final state

An analysis of events in the monojet final state[7], which are characterised by a high-p_T jet and significant p_T^miss, is performed in order to provide sensitivity to SUSY models involving strongly produced sparticles and a compressed mass spectrum, i.e. for which the parent sparticle (e.g. $\tilde{\text{t}}$ or $\tilde{\text{b}}$) and LSP are close in mass. The search is based on an optimization of the studies presented in Refs. [8,9,10]. Candidate signal events are recorded by triggers based on the presence of significant missing transverse momentum, $p_\text{T}^\text{miss} > 120\,\text{GeV}$, with a looser requirement ($> 105\,\text{GeV}$) if accompanied by a jet with high transverse momentum ($p_\text{T} > 80\,\text{GeV}$). The baseline set of selection criteria defining a sample of candidate signal events comprises: $p_\text{T}^{j_1} > 110\,\text{GeV}$ and $|\eta| < 2.4$ for the highest-p_T jet in the event; $p_\text{T}^\text{miss} > 250\,\text{GeV}$; a veto requirement for events containing isolated leptons or hadronically-decaying tau leptons; and events containing a second or third jet that satisfies $p_\text{T} > 60\,\text{GeV}$ are considered or rejected, respectively. The raised p_T threshold for additional jets helps to maintain a monojet-like topology in the presence of soft final-state jets originating from the sparticle decays into e.g. charm or bottom quarks, while maintaining rejection power against events from the $\text{t}\bar{\text{t}}$ or QCD multijet processes, the latter of which is suppressed by an additional requirement on the azimuthal angle separating the two highest-p_T jets in the event, $\Delta\phi(\vec{p}_\text{T}^{\,j_1}, \vec{p}_\text{T}^{\,j_2}) < 2.5$. Candidate signal events are finally categorised according to the highest-p_T jet in the event, $p_\text{T}^{j_1} > 250, 300, 350, 400, 450, 500,$ and $550\,\text{GeV}$, in order to define seven inclusive search regions. Figure 1 (Left) shows the transverse momentum of the leading jet in candidate signal events in the monojet search region defined by the aforementioned selection criteria and $p_\text{T}^{j_1} > 250\,\text{GeV}$.

Two SM processes, $\text{Z}(\to \nu\nu)$ + jets and $\text{W}(\to \ell\nu)$ + jets, dominate the background counts in the signal region, the latter of which results from the charged lepton being outside the experimental acceptance or failing the identification criteria. The contributions to the total background counts in the signal region from these processes are estimated from counts in data control samples enriched in $\text{Z}(\to \mu\mu)$ + jets and $\text{W}(\to \mu\nu)$ + jets events and the use of transfer factors derived from simulation. The reconstructed muons are ignored and all kinematic variables are modified accordingly to mimic the kinematic characteristics of the $\text{Z}(\to \nu\nu)$ + jets and $\text{W}(\to \ell\nu)$ + jets processes. The uncertainties in the estimates for the $\text{Z}(\to \nu\nu)$ + jets and $\text{W}(\to \ell\nu)$ + jets backgrounds, at the level of $5 - 19\%$, are dominated by the statistical uncertainties associated with the finite counts in the $\text{Z}(\to \mu\mu)$ + jets and $\text{W}(\to \mu\nu)$ + jets data control samples. Sub-leading contributions from $\text{t}\bar{\text{t}}$, diboson, and QCD multijet events are estimated from samples of simulated events following the application of scale factors determined from data. Residual contributions from single top quark and Drell-Yan processes are estimated directly from simulation.

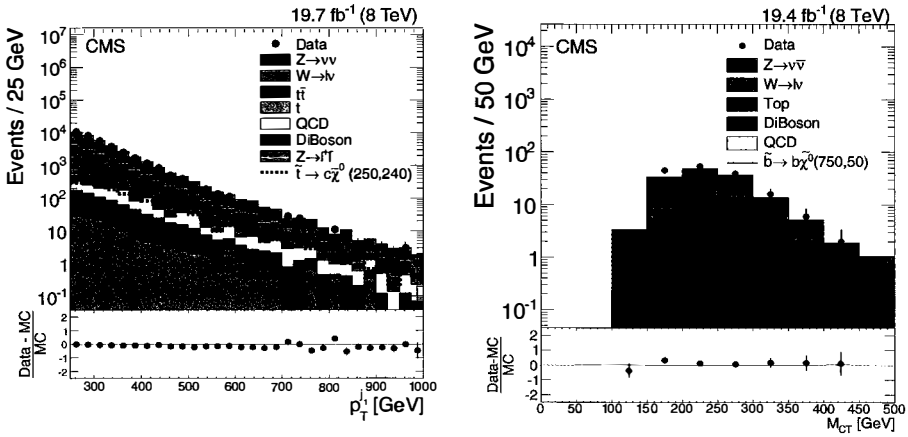

Figure 1 – (Left) Distribution of the leading jet p_{T} in the monojet search region defined by $p_{\mathrm{T}}^{j_1} > 250\,\mathrm{GeV}$ for data and SM backgrounds. SM background distributions are taken from simulation and are normalized to an integrated luminosity of $19.7\,\mathrm{fb}^{-1}$. A representative signal distribution (black dotted line) for $\tilde{\mathrm{t}} \to \mathrm{c}\tilde{\chi}_1^0$ ($m_{\tilde{\mathrm{t}}} = 250, m_{\tilde{\chi}_1^0} = 240\,\mathrm{GeV}$) is also shown. (Right) Distribution of the M_{CT} variable [11,12], described in Sec. 3, for candidate signal events containing exactly two b-tagged jets in the dijet b-tagged search region. The SM background distributions are taken directly from simulation and are normalized to an integrated luminosity of $19.4\,\mathrm{fb}^{-1}$. Also shown (black solid line) is a representative signal distribution for $\tilde{\mathrm{b}} \to \mathrm{b}\tilde{\chi}_1^0$ ($m_{\tilde{\mathrm{b}}} = 750, m_{\tilde{\chi}_1^0} = 50\,\mathrm{GeV}$).

3 Search for third-generation squarks in the dijet final state

The dijet b-tagged analysis [7] is tailored towards a search for the pair production of bottom squarks followed by the decay of each squark to the $\tilde{\chi}_1^0$ LSP and a bottom quark, $\mathrm{pp} \to \tilde{\mathrm{b}}\tilde{\mathrm{b}}, \tilde{\mathrm{b}} \to \mathrm{b}\tilde{\chi}_1^0$. Exactly two central jets are required with $p_{\mathrm{T}} > 70\,\mathrm{GeV}$ and $|\eta| < 2.4$ and one or both of these jets are required to be b-tagged. Events are vetoed if they contain an additional hard jet in the forward region or an isolated muon, electron, or single track (representing unidentified muons, electrons, or single-prong τ-lepton decays), in order to suppress background processes such as $\mathrm{W}(\to \ell\nu) + \mathrm{jets}$ and $\mathrm{t\bar{t}}$ production. Eight exclusive signal regions are defined by categorising events according to the number of b-tagged jets (one or two per event) and four ranges in the boost-corrected contransverse mass variable, M_{CT} [11,12], which assumes the pair production of heavy particles, each of which decays to the same final state that includes an invisible particle such as the LSP, $\tilde{\chi}_1^0$. The M_{CT} distribution is characterised by an endpoint at $(m_{\tilde{\mathrm{b}}}^2 - m_{\tilde{\chi}_1^0}^2)/m_{\tilde{\mathrm{b}}}$ and the four mass ranges that define the signal regions are $M_{\mathrm{CT}} < 250$, 250–350, 350–450, $> 450\,\mathrm{GeV}$. Candidate signal events must also satisfy the following requirements: the scalar p_{T} sum of the two highest-p_{T} jets, $H_{\mathrm{T}}^{j_1 j_2}$, is required to be larger than $250\,\mathrm{GeV}$; $p_{\mathrm{T}}^{\mathrm{miss}} > 175\,\mathrm{GeV}$; the contribution from QCD dijet events is suppressed by the requirement $\Delta\phi(\vec{p}_{\mathrm{T}}^{\,j_1}, \vec{p}_{\mathrm{T}}^{\,j_2}) < 2.5$; and the $\mathrm{W}(\to \ell\nu) + \mathrm{jets}$ and $\mathrm{t\bar{t}}$ backgrounds are suppressed by a requirement on the transverse mass of the lower-p_{T} jet and $p_{\mathrm{T}}^{\mathrm{miss}}$ system, $M_{\mathrm{T}} > 200\,\mathrm{GeV}$. Figure 1 (Right) shows the M_{CT} distribution for candidate signal events containing exactly two b-tagged jets.

Given the definition of the signal regions described above, the acceptance is maximal when the mass difference $\Delta m = m_{\tilde{\mathrm{b}}} - m_{\tilde{\chi}_1^0}$ is large, typically $\Delta m \gg 100\,\mathrm{GeV}$. For smaller mass differences, the p_{T} value of the jet produced in each of the bottom squark decays can fail the jet p_{T} requirement. For this class of model, there is a reliance on ISR to satisfy the trigger and analysis acceptance requirements, through the presence of at least one high-p_{T} jet, and $p_{\mathrm{T}}^{\mathrm{miss}}$ from the recoiling $\tilde{\mathrm{b}}\tilde{\mathrm{b}}$ system. The presence of an additional hard, light-flavour jet is accommodated in the analysis through two additional "ISR" signal regions that categorise events according the

number of b-tagged jets. In addition, the following requirements must be satisfied: a third jet is required with $p_T > 30$ GeV; the two highest-p_T jets must satisfy $p_T > 70$ GeV; the highest-p_T jet must not be b-tagged, while at least one of the other two jets must be b-tagged; the requirements $H_T^{j_1,j_2} > 250$ GeV and $p_T^{miss} > 250$ GeV must be satisfied; no requirement on M_{CT} is imposed; and the azimuthal angle between the p_T^{miss} vector and the p_T vector of any jet, $\Delta\phi(\vec{p}_T^{\,j_i}, \vec{p}_T^{\,miss})$, must be larger than 0.5 radians in order to suppress contributions from QCD multijet events. Finally, the magnitude of the vector sum of transverse momenta of jets that are not b-tagged is required to be larger than 250 GeV in order to select events with a hard ISR component.

The dominant SM backgrounds in each of the ten search regions are events from the $Z(\to \nu\nu)$ + jets, $W(\to \ell\nu)$ + jets, and $t\bar{t}$ processes. The contributions from these SM processes and single-top quark production are determined from data with some reliance on simulation. The $Z(\to \nu\nu)$ + jets background is estimated from data control samples enriched in $W(\to \mu\nu)$ + jets or $Z(\to \mu\mu)$ + jets events, depending on the number of b-tagged jets in the event. Similarly, the $W(\to \ell\nu)$ + jets, $t\bar{t}$ and single top backgrounds are estimated from data control samples enriched in $W(\to \mu\nu)$ + jets or $t\bar{t}$ events, which are disjoint from those used to estimate the $Z(\to \nu\nu)$ + jets background. The contribution of diboson and other rare SM processes (such as $t\bar{t}Z$ production) is less than 3% and is estimated directly from simulation assuming a 50% systematic uncertainty. The contribution from QCD multijet events is expected to be less than a percent of the total background counts from all SM processes in all search regions and is estimated from multijet-enriched data sidebands.

Various sources of systematic uncertainty in the SM background predictions are considered, the most dominant of which include: the limited statistical precision of simulation-based consistency checks on the background estimation methods; uncertainties in the expected contamination from other SM processes, different from the process being estimated, in the various control regions; and uncertainties in the modelling of muon isolation and identification efficiency. The uncertainties in the multijet background predictions are dominated by the statistical uncertainty in the number of observed events in the data control samples. Theoretical uncertainties in higher order QCD and electroweak corrections are accounted for and are sub-dominant with respect to the aforementioned experimental uncertainties.

4 Interpretations of the monojet and dijet searches

The observed counts in the signal regions of the monojet and dijet analyses are in agreement with expectation from SM processes. These results are interpreted in terms of simplified models [13] comprising the pair production of top or bottom squarks and specific decay modes over a broad mass parameter space defined by m_{squark} and $m_{\tilde{\chi}_1^0}$. The following production and decay modes are considered: $pp \to \tilde{b}\tilde{b}, \tilde{b} \to b\tilde{\chi}_1^0$; $pp \to \tilde{t}\tilde{t}, \tilde{t} \to c\tilde{\chi}_1^0$ for $\Delta m = m_{\tilde{t}} - m_{\tilde{\chi}_1^0} \leq 80$ GeV; and $pp \to \tilde{t}\tilde{t}, \tilde{t} \to t\tilde{\chi}_1^0$ for $\Delta m \geq 100$ GeV. For the latter scenario, decays via an intermediate chargino state between the mass of the top squark and LSP are also studied: $\tilde{t} \to b\tilde{\chi}_1^\pm \to bW^\pm\tilde{\chi}_1^0$. The $\tilde{\chi}_1^0$ LSP is assumed to be higgsino-like and near mass-degenerate with the chargino, $\Delta m = m_{\tilde{\chi}_1^\pm} - m_{\tilde{\chi}_1^0} = 5$ GeV, which implies a decay to the $\tilde{\chi}_1^0$ LSP and soft final-state SM particles via an off-shell W boson. Finally, different branching fractions $\mathcal{B}(\tilde{t} \to t\tilde{\chi}_1^0) = 1 - \mathcal{B}(\tilde{t} \to b\tilde{\chi}_1^\pm) = \{0, 0.25, 0.5, 0.75, 1\}$ are considered. Details of the signal sample generation and cross section calculations are provided in Ref [7]. The dominant contribution to the total uncertainty in signal acceptance times efficiency for compressed scenarios is from uncertainties in scale factor corrections applied to simulated event samples to account for the mismodelling of ISR [14] within the MADGRAPH generator code.

Figure 2 (Left) shows the excluded regions of the mass parameter space for the simplified model involving the production and decay mode $pp \to \tilde{b}\tilde{b}, \tilde{b} \to b\tilde{\chi}_1^0$, calculated at 95% confidence level (CL) with the CL_s method [15,16]. The excluded regions as determined from the searches in the monojet (blue lines) and dijet (red lines) final state are shown. For near mass-degenerate

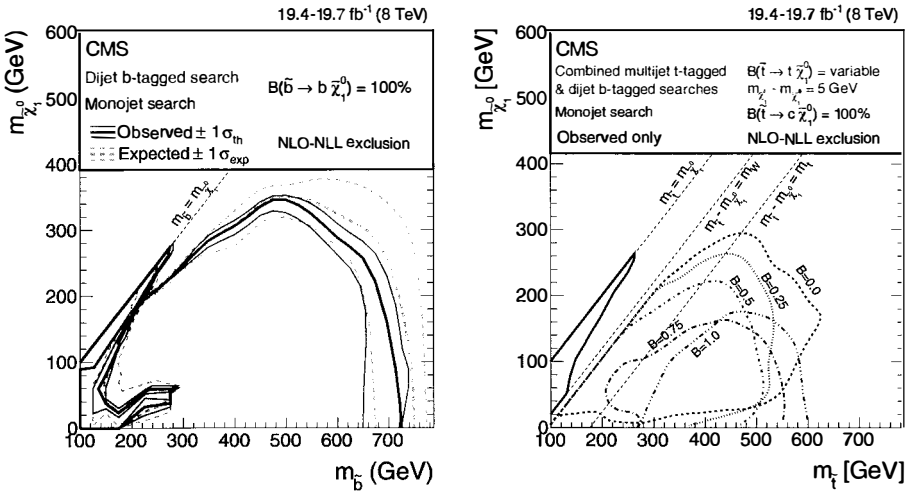

Figure 2 – (Left) Expected (thick dashed line) and observed (thick solid line) excluded regions (95% CL) in the $(m_{\tilde{b}}, m_{\tilde{\chi}_1^0})$ mass plane for bottom-squark pair production assuming $\mathcal{B}(\tilde{b} \to b\tilde{\chi}_1^0) = 1$. The excluded regions assuming $\pm 1\sigma$ variations in the experimental (thin dashed lines) and theoretical (thin solid lines) uncertainties are also shown. The results from the monojet (blue lines) and the dijet (red lines) searches are shown separately. (Right) Various observed excluded regions (95% CL) in the $(m_{\tilde{t}}, m_{\tilde{\chi}_1^0})$ mass parameter space for top-squark pair production assuming various decay modes and branching fractions, in the case of an intermediate chargino state, of the top squarks. The combined results from the dijet and multijet searches (red lines) and the monojet search (blue line) are displayed separately.

scenarios, the monojet search excludes models with bottom squarks as large as 250 GeV, as well as exhibiting a strong dependence on the mass difference $\Delta m = m_{\tilde{b}} - m_{\tilde{\chi}_1^0}$. The figure also shows significant coverage of models with a compressed mass spectrum through the "ISR" search regions of the dijet search. Models defined by Δm as small as ~ 25 GeV are excluded for bottom squark masses as large as 225 GeV, which is a significant improvement in reach with respect to the nominal search regions that are defined by low values of the M_{CT} variable.

Figure 2 (Right) shows the observed excluded regions in the mass parameter space of simplified models assuming the pair production of top squarks and various decay modes. The excluded region determined from the monojet search (blue lines) is shown, which assumes the decay mode $\tilde{t} \to c\tilde{\chi}_1^0$. The excluded region is very similar to that observed for the bottom squark production shown in Figure 2 (Left, blue lines) due to the very similar event topologies that result from the two different models: a high-p_{T} jet, significant $p_{\mathrm{T}}^{\mathrm{miss}}$, and a very low probability of acceptance for the jets resulting from the squark decay.

In addition, Fig. 2 (Right) displays contours (red dashed/dotted lines) that indicate the excluded simplified models involving pair production of top squarks, each of which decays either directly to the top quark and LSP, $\tilde{t} \to t\tilde{\chi}_1^0$, or via an intermediate chargino state, $\tilde{t} \to b\tilde{\chi}_1^{\pm}$. Only models with $\Delta m = m_{\tilde{t}} - m_{\tilde{\chi}_1^0} \geq 100$ GeV are considered. The sensitivity is provided by the dijet analysis, described above, in combination with a search in the multijet final state that employs a variant of the HEPTOPTAGGER algorithm [7]. The multijet search provides sensitivity for mass differences satisfying $\Delta m = m_{\tilde{t}} - m_{\tilde{\chi}_1^0} \gtrsim m_{\mathrm{top}}$ and is not described here. Further details can be found in Ref. [7]. For compressed scenarios satsifying $m_{\mathrm{W}} \lesssim \Delta m \lesssim m_{\mathrm{top}}$, the dijet search provides strong coverage due to the near mass-degeneracy of the $\tilde{\chi}_1^{\pm}$ and $\tilde{\chi}_1^0$ sparticles ($\Delta m = 5$ GeV). As a consequence, the chargino decay results in the LSP $\tilde{\chi}_1^0$ plus low-momentum final-state SM particles that are typically outside the experimental acceptance. Hence, each top

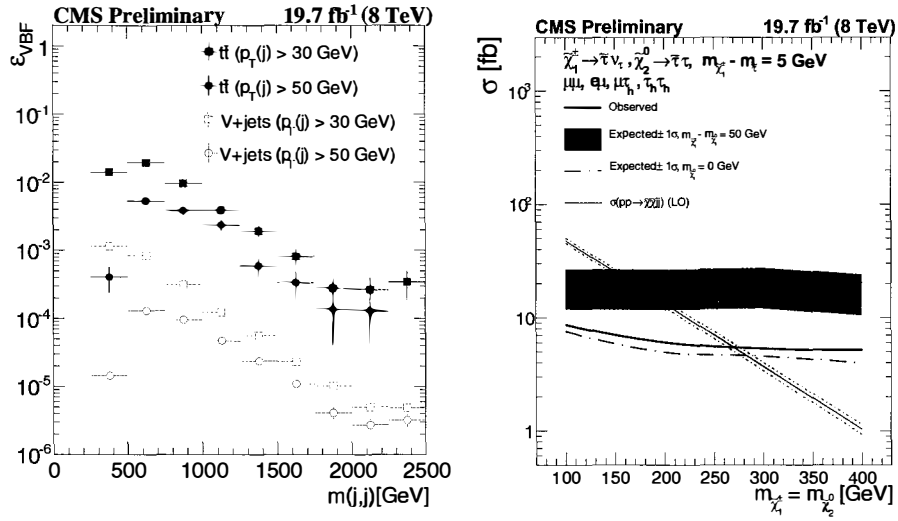

Figure 3 – (Left) Efficiency of the VBF selection criteria, $\varepsilon_{\mathrm{VBF}}$, as a function of the dijet invariant mass, m_{jj}, for the V+jets and $\mathrm{t\bar{t}}$ background processes, shown for jet p_{T} thresholds of 30 and 50 GeV used by the $\mu^{\pm}\mu^{\pm}jj$ and $\mu^{\pm}\mu^{\mp}jj$ signal regions, respectively. (Right) Observed (solid lines) and expected (dashed-dotted lines) upper limits (95% CL) on the chargino/neutralino production cross section as a function of $m_{\tilde{\chi}_1^{\pm}} = m_{\tilde{\chi}_2^0}$. All eight signal regions are considered simultaneously when deriving the upper limit. The model assumes production and decay $\tilde{\chi}_1^{\pm}\tilde{\chi}_2^0 \to \nu\tilde{\tau}\tau\tilde{\tau} \to \nu\tau\tilde{\chi}_1^0\tau\tau\tilde{\chi}_1^0$ with $\tilde{\chi}_1^{\pm} - \tilde{\tau} = 5\,\mathrm{GeV}$ and $m_{\tilde{\chi}_1^0} = 0\,\mathrm{GeV}$ (dashed-dotted line with yellow band) or $m_{\tilde{\chi}_1^{\pm}} - m_{\tilde{\chi}_1^0} = 50\,\mathrm{GeV}$ (dashed-dotted line with green band).

squark decay leads to a final state that is similar to that for $\tilde{\mathrm{b}} \to \mathrm{b}\tilde{\chi}_1^0$. The various contours (red dashed/dotted lines) represents the excluded mass regions when the branching fraction $\mathcal{B}(\tilde{\mathrm{t}} \to \mathrm{t}\tilde{\chi}_1^0) = 1 - \mathcal{B}(\tilde{\mathrm{t}} \to \mathrm{b}\tilde{\chi}_1^{\pm})$ is varied from unity to zero (in steps of 0.25). The dijet search becomes increasingly sensitive as the the branching fraction $\mathcal{B}(\tilde{\mathrm{t}} \to \mathrm{t}\tilde{\chi}_1^0)$ is reduced, with top squark masses as large as $\sim$ 475 GeV ($\sim$ 300 GeV) excluded under the assumptions $\Delta m = m_{\tilde{\mathrm{t}}} - m_{\tilde{\chi}_1^0} = m_{\mathrm{top}}$ (100 GeV) and $\mathcal{B}(\tilde{\mathrm{t}} \to \mathrm{b}\tilde{\chi}_1^{\pm}) = 1$.

5 Search for SUSY electroweak production with the VBF topology

The VBF topology provides coverage of the electroweak sector of SUSY models that is somewhat complementary to multilepton searches that are typically used to probe this class of model. This particular search [17] targets final states exhibiting a topology that is consistent with the VBF process, i.e. containing at least two jets in the forward regions of the detector. In addition, two reconstructed leptons with opposite-sign or like-sign electric charge are required and eight signal regions, defined by independent final states, are considered: $\mu^{\pm}\mu^{\mp}jj$, $\mu^{\pm}\mu^{\pm}jj$, $\mathrm{e}^{\pm}\mu^{\mp}jj$, $\mathrm{e}^{\pm}\mu^{\pm}jj$, $\mu^{\pm}\tau_h^{\mp}jj$, $\mu^{\pm}\tau_h^{\pm}jj$, $\tau_h^{\pm}\tau_h^{\mp}jj$, and $\tau_h^{\pm}\tau_h^{\pm}jj$, where j and τ_h and indicate the presence of a forward jet or the hadronic decay of a τ lepton, reconstructed with the "hadrons plus strips" algorithm [18], respectively.

An inclusive set of baseline "central" selection criteria are then used to define control regions for each of the eight final states considered in the search, which can be summarised as follows: final states involving a muon must satisfy $p_{\mathrm{T}} > 30\,\mathrm{GeV}$ for the muon and the requirement $p_{\mathrm{T}}^{\mathrm{miss}} > 75\,\mathrm{GeV}$; the di-$\tau_h$ final state requires $p_{\mathrm{T}} > 45\,\mathrm{GeV}$ for both τ_h objects and a loose requirement of $p_{\mathrm{T}}^{\mathrm{miss}} > 30\,\mathrm{GeV}$; all leptons must satisfy $|\eta| < 2.1$; all reconstructed leptons and

jets must be well separated in (η,ϕ)-space; the two forward jets in each event must not be b-tagged in order to suppress contributions from $t\bar{t}$. A tighter set of "VBF" selection criteria are used to define the eight signal regions: at least two jets in each event must satisfy $p_T > 50\,\text{GeV}$ ($p_T > 30\,\text{GeV}$ for the like-sign $\mu^{\pm}\mu^{\pm}jj$ final state), $|\eta| < 5$, $\Delta\eta > 4.2$, and $\eta_1 \times \eta_2 < 0$; finally, the dijet invariant mass constructed from the two highest-p_T jets in the event is required to satisfy $m_{jj} > 250\,\text{GeV}$.

The search relies on the potential to identify a broad excess of events above the SM background expectation in the m_{jj} distribution. The dominant SM background sources are the production of W or Z bosons in association with jets, dibosons, $t\bar{t}$, and QCD multijet events. The background composition is primarily dependent on the number of hadronically-decaying τ-leptons in the final state. The $t\bar{t}$ process contributes a significant number of background counts in several channels with opposite- or like-sign charges. The diboson process provides a dominant contribution for like-sign channels. Significant background counts from V + jets production, due to the non-negligible misidentification rate for hadronically-decaying τ-leptons, is expected for final states containing opposite-sign charges and one τ_h. QCD multijet events only provide an appreciable contribution in the $\tau_h\tau_h$ channel. The m_{jj} shape expected from a sum over all relevant SM processes is estimated from multiple control regions. The efficiency of the VBF selection criteria, ϵ_{VBF}, as a function of m_{jj} is measured directly from data when possible and is typically in the range $\approx 10^{-2} - 10^{-4}$ for strongly-produced SM backgrounds, as shown in Fig. 3 (Left).

A wide range of sources for potential bias in the background estimates have been considered. The dominant contributions to the total systematic uncertainty ($1 - 25\%$) in the background estimates are from statistical uncertainties due to finite event counts in the control regions ($3 - 21\%$) and simulation-based closure tests used to validate the methods ($2 - 20\%$). Subdominant contributions from uncertainties in lepton identification efficiencies, lepton energy and momentum scale, p_T^{miss} scale, and trigger efficiencies are also considered. The dominant uncertainty in signal acceptance is due to the modeling of the jet energy scale of forward jets.

Table 1: Observed and predicted SM background yields for the eight signal regions of the search with the VBF topology. Expected yields for two example simplified signal models, defined by the production of neutralino/chargino pairs, their decay via $\tilde{\tau}$-leptons, and the mass parameters ($m_{\tilde{\chi}_1^{\pm}}, m_{\tilde{\tau}}, m_{\tilde{\chi}_1^0}$) [GeV], are also provided. The quoted uncertainties reflect all relevant theory, statistical, and systematic contributions.

Opp. sign	$\mu^{\pm}\mu^{\mp}jj$	$e^{\pm}\mu^{\mp}jj$	$\mu^{\pm}\tau_h^{\mp}jj$	$\tau_h^{\pm}\tau_h^{\mp}jj$
Observed	31	22	41	31
Predicted	32.2 ± 2.4	31.1 ± 4.6	51.8 ± 5.1	22.9 ± 5.1
(200,195,0)	1.7	3.5	4.5	3.8
(100,95,50)	3.3	6.6	4.3	2.1
Like sign	$\mu^{\pm}\mu^{\pm}jj$	$e^{\pm}\mu^{\pm}jj$	$\mu^{\pm}\tau_h^{\pm}jj$	$\tau_h^{\pm}\tau_h^{\pm}jj$
Observed	4	5	14	9
Predicted	5.4 ± 0.3	5.4 ± 3.5	17.6 ± 3.8	8.4 ± 0.9
(200,195,0)	5.4	3.5	4.5	3.8
(100,95,50)	5.7	6.6	4.3	2.1

Table 1 shows the observed event yields in data for each of the eight signal regions, which are compatible with the corresponding estimated SM background counts. These results are intepreted in the context of simplified models that assume the pair production of charginos and neutralinos with two associated jets. A scenario with a bino-like $\tilde{\chi}_1^0$ and wino-like $\tilde{\chi}_1^{\pm}$ and $\tilde{\chi}_2^0$ is considered, in which the $\tilde{\chi}_1^{\pm}$ and $\tilde{\chi}_2^0$ are assumed to be mass-degenerate ($m_{\tilde{\chi}_1^{\pm}} = m_{\tilde{\chi}_2^0}$). An intermediate τ slepton state is also assumed with the mass defined by $m_{\tilde{\chi}_1^{\pm}} - m_{\tilde{\tau}} = 5\,\text{GeV}$. The decays $\tilde{\chi}_1^{\pm} \to \nu\tilde{\tau} \to \nu\tau\tilde{\chi}_1^0$ and $\tilde{\chi}_2^0 \to \tau\tilde{\tau} \to \tau\tau\tilde{\chi}_1^0$ are enforced with a 100% branching fraction. Two scenarios as assumed for the mass of the $\tilde{\chi}_1^0$ LSP: $m_{\tilde{\chi}_1^0} = 0\,\text{GeV}$ that allows potentially large

mass differences and $\Delta m = m_{\tilde{\chi}_1^\pm} - m_{\tilde{\chi}_1^0} = 50\,\text{GeV}$ with a fixed (compressed) mass splitting. The full mass spectrum of the model, $(m_{\tilde{\chi}_1^\pm}, m_{\tilde{\chi}_2^0}, m_{\tilde{\tau}}, m_{\tilde{\chi}_1^0})$, is hence defined by chosing the common mass $m_{\tilde{\chi}_1^\pm} = m_{\tilde{\chi}_2^0}$, for which upper limits (95% CL) on the expected and observed cross sections are derived, as shown in Fig. 3 (Right). Values of the common mass $m_{\tilde{\chi}_1^\pm} = m_{\tilde{\chi}_2^0}$ are excluded up to ~ 260 GeV and ~ 160 GeV for the large and compressed mass splitting scenarios, respectively.

6 Summary

Searches for supersymmetric models characterised by a compressed mass spectrum have been performed with data samples of pp collisions at $\sqrt{s} = 8$ TeV collected by the CMS experiment and corresponding to an integrated luminosity of $19.4 - 19.7\,\text{fb}^{-1}$. Analyses of monojet and di-jet final states with specifically tailored selection criteria provide sensitivity to third-generation squarks with masses only tens of GeV larger than the LSP. Similarly, an analysis of final states containing two forward jets, consisent with the VBF topology, and two additional leptons is used to probe the compressed electroweak sector. By exploiting a range of dedicated search techniques, these analyses are able to probe new regions of signal phase space that is experimentally challenging, through the exploitation of the presence of hard initial state radiation or the VBF topology in order to effectively discriminate between the large SM backgrounds and the potential presence of signal. While these searches have revealed no evidence of new physics during Run 1 of the LHC, this types of dedicated search will be essential during Run 2 of the LHC to provide a complete coverage of the natural SUSY parameter space.

Acknowledgments

The author gratefully acknowledges the support of the HEP group of Imperial College London and the Science and Technology Facilities Council, UK.

References

1. ATLAS collaboration, Phys. Lett. B **716** (2012) 1.
2. CMS collaboration, Phys. Lett. B **716** (2012) 30.
3. E. Witten, Nucl. Phys. B **188** (1981) 513.
4. S. Dimopoulos and H. Georgi, Nucl. Phys. B **193** (1981) 150.
5. R. Barbieri and D. Pappadopulo, JHEP **10** (2009) 061.
6. CMS collaboration, JINST **3** (2008) S08004.
7. CMS collaboration, arXiv:1503.08037, CMS-SUS-14-001, submitted to JHEP.
8. CMS collaboration, CMS-PAS-EXO-12-048, http://cdsweb.cern.ch/record/1525585.
9. CMS collaboration, Phys. Rev. Lett. **107** (2011) 201804.
10. CMS collaboration, JHEP **09** (2012) 094.
11. D. R. Tovey, JHEP **04** (2008) 034.
12. G. Polesello and D. R. Tovey, JHEP **03** (2010) 030.
13. CMS collaboration, Phys. Rev. D **88** (2013) 052017.
14. CMS collaboration, Eur. Phys. J. C **73** (2013) 2677.
15. A. L. Read, J. Phys. G **28** (2002) 2693.
16. T. Junk, Nucl. Instrum. Methods. A **434** (1999) 435.
17. CMS collaboration, CMS-PAS-SUS-14-005, http://cds.cern.ch/record/2002647.
18. CMS collaboration, JINST **7** (2012) P01001.

Searches for long lived supersymmetric particles with the ATLAS detector

H. S. Hayward, On behalf of the ATLAS Collaboration
Oliver Lodge Laboratory, University of Liverpool, Liverpool, L69 3BX UK

Several supersymmetric extensions of the Standard Model predict the existence of new particles whose lifetime can be comparable or longer than the time of flight through a collider detector. The direct detection of these particles, or of their decays inside the detector, requires dedicated experimental techniques. This talk presents recent ATLAS searches, at the LHC, for supersymmetric particles with long lifetimes, performed with 20 fb^{-1} of $\sqrt{s} = 8$ TeV pp data. The results of searches for decays of gluinos, charginos or neutralinos inside the detector, as well as for the direct detection of long lived gluinos, squarks, charginos and sleptons are presented.

1 Introduction

Supersymmetry (SUSY), is a theoretically well-motivated candidate for physics beyond the Standard Model (SM). Long-lived particle signatures arise in SUSY in different ways. In R-parity violating SUSY, if the parameters λ_{ijk}, λ'_{ijk} or λ''_{ijk} in the super-potential [1,2] are small, the lightest SUSY particle (LSP) can have a long lifetime. In R-parity conserving SUSY, if the difference between the mass of the next-to-lightest SUSY particle (NLSP) and the LSP is small, of the order of 100 MeV as predicted by some models of anomaly-mediated SUSY breaking (AMSB) [3], the NLSP can also be long-lived. In Gauge Mediated SUSY Breaking (GMSB) [4,5,6,7,8,9], the NLSP is the $\tilde{\chi}_1^0$ which decays into either a Z boson or a γ and a graviton which is the LSP. If the neutralino is long-lived, and travels before decaying, the signature is either a displaced vertex (in case of Z decay) or a displaced and delayed γ. Within Split SUSY, gluino decay is suppressed by the high scalar mass. Long-lived gluinos then hadronize into heavy R-hadrons that decay at a detectable distance from their production point [10]. Unless otherwise stated, all results here are based on a data sample of 20.3 fb^{-1} collected at $\sqrt{s} = 8$ TeV of pp collisions at the ATLAS detector [11] at the LHC.

2 Search for massive, long-lived particles using multitrack displaced vertices or displaced lepton pairs

If a particle has a lifetime of order a few ns, it can decay inside the tracking detector, producing a vertex at a distance away from the primary vertex. Some of the processes under study include R-parity violating (RPV) scenarios, long-lived neutralinos in General Gauge Mediation (GGM) and a long-lived R-hadron in Split SUSY [12]. Two signatures are considered: a dilepton signature where the vertex is formed from to oppositely charged leptons and multi-track signature where the displaced vertex (DV) contains at least 5 charged-particle tracks [12].

The standard ATLAS tracking is optimised for tracks coming from the primary interaction point, with a requirement that the tracks transverse impact parameter (d_0) is less than 10 mm. In order to increase efficiency for secondary tracks, the silicon-seeded tracking algorithm was

re-run with looser cuts on d_0 using "left-over" hits from the standard tracking. Vertices were discarded if they coincided with regions of dense detector material. This method is able to detect vertices upto 300 mm from the primary interaction point.

The main sources of background for this analysis, for the two signal regions, are low mass DVs that are crossed by an unrelated high-p_T track at a large angle (multi-track signal region) and two unrelated leptons crossing close enough for the vertexing method to combine (di-lepton signal region). These backgrounds are estimated using data driven methods of estimation which involve combining a track from one event with a track or vertex from a second event to calculate the probability of background vertex formation.

With no events observed in any signal region, upper-limits are set on the signal yields and production cross-sections as a function of the proper lifetime $c\tau$ and, for Split SUSY, limits are placed on the gluino mass vs. $c\tau$. These are presented in figure 1.

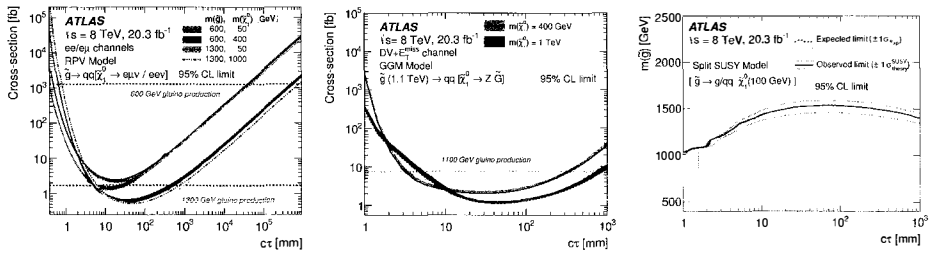

Figure 1 – 95% confidence-level upper limits, obtained from: (left) the dilepton search, on the production cross-section for a pair of gluinos that decay into two quarks and a long-lived $\tilde{\chi}_1^0$ in the RPV scenario with a pure λ_{121} coupling, (middle) the DV+E_T^{miss} on the production cross-section for a pair of gluinos of mass 1.1TeV that decay into two quarks and a long-lived $\tilde{\chi}_1^0$ in the GGM scenario. Right plot: the 95% confidence-level excluded regions that lie below the curves shown in the mass-vs-$c\tau$ plane for the split-SUSY scenarios, with the gluino decaying into a gluon or light quarks, plus a 100 GeV $\tilde{\chi}_1^0$. [12]

3 Search for long-lived, weakly-interacting particles that decay to displaced hadronic jets

A search was performed for the decay of neutral, weakly interacting, long-lived particles (LLP) by searching for events with two displaced vertices in either InnerDetector, Muon Spectrometer or both[13]. Displaced jets appear in a variety of models including Stealth SUSY, Scalar boson and Hidden Valley Z. This analysis studies two separate channels, defined by the trigger used.The first channel, used for the Stealth SUSY and Scalar Boson searches, uses a trigger which identifies clusters of muon region-of-interests that are preceded by little or no activity in the tracking or calorimeter detectors. The second channel, which is used for the Z' search, uses a Jet and missing transverse momentum (E_T^{miss}) trigger. Both channels require good quality vertices, not consistent with material interactions, that are in close proximity to a jet. No significant excess of events above the background expectations is observed and exclusion limits as a function of the proper lifetime of LLP from Higgs boson and scalar boson decays are reported. This paper presents the first upper limits as a function of proper lifetime for Hidden Valley Z' and Stealth SUSY scenarios. The observed 95% CL limits on the branching ration of the Stealth SUSY samples studied is shown in the left plot of figure 2.

4 Search for long-lived heavy charged particles with the ATLAS pixel detector

A search for heavy charged LLP was performed using 18.4 fb^{-1} of data at $\sqrt{s} = 8$ TeV[14]. These particles would have a speed $\beta << 1$ and leave a signature of anomalously large specific energy loss ($\frac{dE}{dx}$) in the pixel detector. Measuring such particles in the vicinity of the interaction vertex

allows sensitivity to metastable particles with lifetimes in the nanosecond range. Additionally, as long as the particle travels at least 45 cm (in radius, r) it can be studied, with little dependence on its subsequent interactions or decay mode.

To select candidate events, an 80 GeV threshold $E_{\mathrm{T}}^{\mathrm{miss}}$ trigger is used with an offline $E_{\mathrm{T}}^{\mathrm{miss}}$ cut of 100 GeV. In order to remove the main source of background, muons from W decays, a transverse mass cut of $m_{\mathrm{T}} > 130$ GeV was employed. Both stable and metastable signal regions were used. For the stable signal region, a veto on the track candidate being matched to a reconstructed muon was applied. Each candidate event is required to have at least one isolated track with transverse momentum $p_{\mathrm{T}} > 80$ GeV and $\frac{dE}{dx} > \sim 1.8$ MeV/g cm^{-2}.

Background is estimated by data driven approach by randomly sampling momentum (p), pseudo-rapidity (η) and $\frac{dE}{dx}$ values from control sample distributions and combining. No significant deviation from background expectations is observed and 95% CL limits are placed on the mass of different types of long lived particles. Stable charginos with mass smaller than 549 GeV are excluded. Also excluded are stable gluino (sbottom, stop) R-hadrons with masses smaller than 1102 (745, 758) GeV respectively. In the metastable case, masses exceeding 1200 GeV are excluded for R-hadrons of 12 ns. This is the first measurement of lifetime dependent mass limit for charged R-hadrons in the 1-10 ns range, with little dependence on their decay mode. Figure 2 shows two example exclusion limits in the LLP lifetime-mass plane for gluino R-hadrons and a chargino decaying to $\chi_1^0 + \pi^{\pm}$.

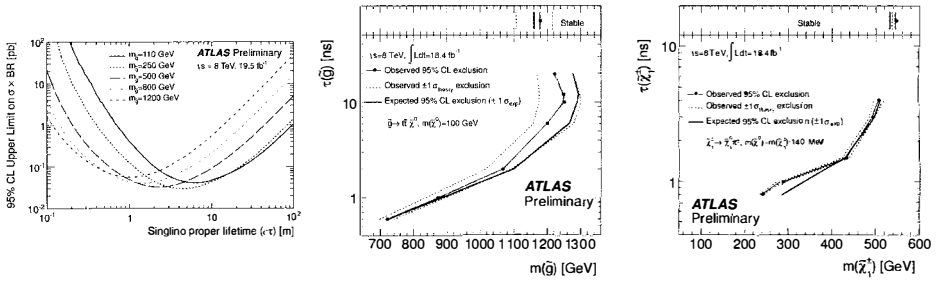

Figure 2 – Left plot: Observed 95% CL limits on $\sigma \times$BR for the Stealth SUSY samples[13], Middle plot: exclusion limits in the τ - m plane for gluino R-hadrons decaying in tt plus a light neutralino of mass $m(\chi_0) = 100$ GeV[14]. Right plot: exclusion limits in the τ - m plane for chargino decaying to $\chi_1^0 + \pi^{\pm}$ [14].

5 Search for charginos nearly mass-degenerate with the lightest neutralino based on a disappearing-track signature

A search was performed for direct chargino production in AMSB scenarios, via: $pp \to \tilde{\chi}_1^{\pm}\tilde{\chi}_1^0 +$ jet and $pp \to \tilde{\chi}_1^+\tilde{\chi}_1^- +$ jet [3]. In AMSB models, the $\tilde{\chi}_1^{\pm}$ and $\tilde{\chi}_1^0$ are almost mass degenerate with the difference in their mass ($\Delta m_{\tilde{\chi}_1}$) being ~160 MeV. The implication of this is that the $\tilde{\chi}_1^{\pm}$ has a lifetime $\mathcal{O}(0.1)$ ns and decays into a $\tilde{\chi}_1^0$ and a low momentum (~100 MeV) $\pi^{\pm}$. This decay leaves a distinctive signature in the detector of a charged track produced at the primary interaction, from the $\tilde{\chi}_1^{\pm}$, which disappears before the outer tracking chambers when it decays into the very soft $\pi^{\pm}$. A search was performed for a high p_{T} "disappearing track" signature together with large $E_{\mathrm{T}}^{\mathrm{miss}}$ and a high p_{T} jet which is required to trigger the event.

In order to suppress backgrounds from W/Z+jets and top-pair production processes, events with electron or muon candidates are discarded. In order to suppress QCD di-jet events, events are required to have at least one jet with $p_{\mathrm{T}} > 90$ GeV, $E_{\mathrm{T}}^{\mathrm{miss}} > 90$ GeV and $\Delta\phi_{\mathrm{min}}^{\mathrm{jet}-E_{\mathrm{T}}^{\mathrm{miss}}} > 1.5$. Candidate "disappearing" tracks are required to be isolated, have $p_{\mathrm{T}} > 15$ GeV, to be of good quality and to have less than 5 hits in the Transition Radiation Tracker. No excess of candidate

tracks is observed and upper limits are placed on the $m_{\tilde{\chi}_1^\pm}$ and $\tau_{\tilde{\chi}_1^\pm}$ at 95% CL . For $\Delta m_{\tilde{\chi}_1} = 160$ MeV, a limit of $m_{\tilde{\chi}_1^\pm} > 245^{+24}_{-30}$ GeV is obtained.

6 Limits on metastable gluinos from ATLAS SUSY searches

If the gluino is just a little long-lived, of the order of 1 ns, standard SUSY searches looking for excesses in events with high-p_T jets and large E_T^{miss} should still apply. As the lifetime of the gluino increases, the efficiency of the search will decrease as: lepton vetoes start to fail impact-parameter cuts, jets start to be identified as b-jets, jets start to fail track cleaning cuts based on the track p_T or the fraction of energy, measured in the calorimeter, which is electromagnetic. The results of SUSY searches designed for promptly decaying $\tilde{q}$ and gluinos, produced at 8 TeV pp collisions, are reinterpreted in the context of metastable gluinos [15]. This is the first explicit re-interpretation of prompt SUSY searches for long-lived gluinos. The left and middle plots of figure 3 show the 95% CL exclusion limits for gluino mass as a function of gluino lifetime for $m_{\tilde{\chi}_1^\pm}$=100 GeV and gluino to $q\bar{q}\,\tilde{\chi}_1^\pm/g\tilde{\chi}_1^\pm$ decays and $m_{\tilde{\chi}_1^\pm}$=100 GeV and gluino to $t\bar{t}\,\tilde{\chi}_1^\pm$ decays.

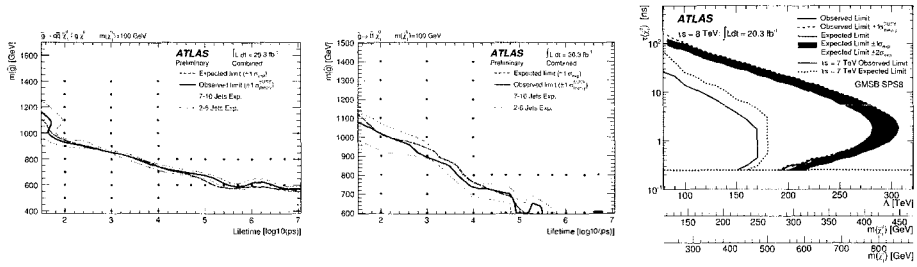

Figure 3 – Left plot: 95% CL excluded gluino mass as a function of gluino lifetime, for $m_{\tilde{\chi}_1^\pm}$=100 GeV and gluino to $q\bar{q}\,\tilde{\chi}_1^\pm/g\tilde{\chi}_1^\pm$ decays[15]. Middle plot: 95% CL excluded gluino mass as a function of gluino lifetime, for $m_{\tilde{\chi}_1^\pm}$=100 GeV and gluino to $t\bar{t}\,\tilde{\chi}_1^\pm$ decays[15]. Right plot: The observed and expected 95% CL limits in the GMSB signal space of $\tilde{\chi}_1^0$ lifetime versus Λ and also versus the $\tilde{\chi}_1^0$ and $\tilde{\chi}_1^\pm$ masses in the SPS8 model[16].

7 Search for nonpointing and delayed photons in the diphoton and missing transverse momentum final state

In GMSB, the NLSP can decay to a γ and a gravitino. If the neutralino is long-lived, the γ may be delayed and non-prompt. This distinct signature arises from finite lifetime (τ) of the NLSP. As GMSB is R-parity conserving, a SUSY-event would contain two SUSY chains with the NLSP ($\tilde{\chi}^0$) decaying to SM particle (γ) and the LSP ($\tilde{G}$). These two γ, would appear as delayed and may not "point-back" to the primary vertex interaction due to the path and β of the $\tilde{\chi}_1^0$.

Events are selected with two photons with $p_T > 50$ GeV (using loose identification criteria due to the wider possible shower shape of the signal photons) and $E_T^{miss} > 75$ GeV due to the 2 gravitinos [16]. Events with low E_T^{miss} are used as control regions to describe the background data. The distributions of the distance between the z co-ordinate of the primary vertex and the apparent origin of the photon, extrapolated from the calorimeter measurements to the z-axis (Δz_γ), and the relative time of the photon measurement with respect to the primary collision as measured by the liquid argon calorimeter (t_γ) are used to perform a 2D search.

A template fit method is used to fit the 386 events in the signal region with template distributions corresponding to background and signal shape distributions. No evidence of non-pointing and delayed photons is found, and the results 95% CL limits exclude values of τ in the range from 0.25 to 100 ns and values of Λ in the range from 80 to about 300 TeV, as shown in the right plot of figure 3.

8 Searches for heavy long-lived charged particles

There are several candidate particles for LLP which are massive. They include long-lived sleptons in GMSB, directly produced $\tilde{\chi}_1^{\pm}$ (with small $\Delta m_{\tilde{\chi}_1}$) and R-hadrons. The common feature between these candidates is that if they are massive, they will be produced with velocities less than the speed of light, $\beta < 1$. In this scenario, their mass (m) can be determined from their measured speed (β) and momentum (p) by the relation $m = p/\beta\gamma$, where γ in this context is the lorentz factor.

Different strategies were used to measure the particles' speed, and $\frac{dE}{dx}$ which is related to $\beta\gamma$ of the particle. The time-of-flight of the particle is measured from timing information from the muon spectrometer and/or the calorimeters and used to determine β. The silicon pixel detectors are used to measure $\frac{dE}{dx}$. The calorimeters and muon detectors are used to provide a time-of-flight measurement.

No excess is observed in any signal region, and 95% CL limits are placed on the mass of LLP in various SUSY models, examples of which are presented in figure 4 [17]. Long-lived $\tilde{\tau}$ in models with GMSB are excluded up to masses between 440 and 385 GeV for tanβ between 10 and 50, with a 290 GeV limit in the case where only direct $\tilde{\tau}$ production is considered. In the context of simplified LeptoSUSY models, where sleptons are stable and have a mass of 300 GeV, $\tilde{q}$ and gluino masses are excluded up to a mass of 1500 and 1360 GeV, respectively. Directly produced $\tilde{\chi}_1^{\pm}$, in simplified models where they are nearly degenerate to the $\tilde{\chi}_1^0$, are excluded up to a mass of 620 GeV. R-hadrons, composites containing a gluino, $\tilde{b}$ or $\tilde{t}$, are excluded up to a mass of 1270, 845 and 900 GeV, respectively, using the full detector; and up to a mass of 1260, 835 and 870 GeV using an approach disregarding information from the muon spectrometer.

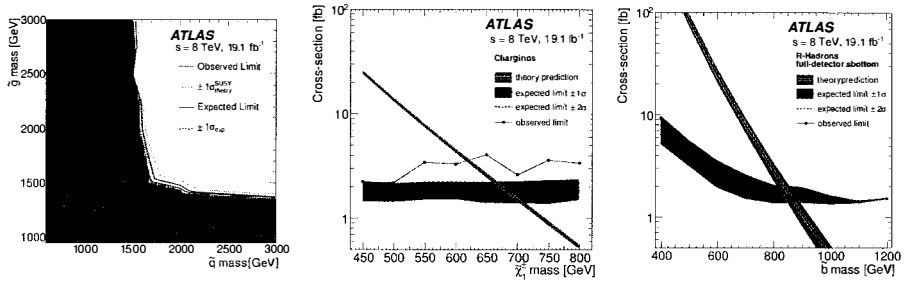

Figure 4 – From left to right: 95% CL excluded regions of squark mass and gluino mass in the LeptoSUSY models; cross-section upper limits for various chargino masses in stable-chargino models; cross-section upper limits as a function of the mass for the sbottom R-Hadron models for the full-detector search. [17]

9 Searches for stopped R-hadrons

A search is performed for $\tilde{g}$, $\tilde{t}$ or $\tilde{b}$ R-hadrons that are produced in a pp collision and have come to rest within the calorimeter, and decay at some later time to hadronic jets and a neutralino, using 5.0 and 22.9 fb^{-1} of pp collisions at 7 and 8 TeV, respectively [18].

Candidate decay events are triggered in selected empty bunch crossings of the LHC to remove pp collision backgrounds. Events are required to have at least one high p_{T} jet, with additional requirements on the jet shape, and no muon candidates. The main background after these selection requirements are events due to beam-halo and cosmic-rays. No excess is observed over the background prediction and limits are set on $\tilde{g}$, $\tilde{t}$, and $\tilde{b}$ masses for different decays, lifetimes, and neutralino masses. With a neutralino of mass 100 GeV, the analysis excludes gluinos with mass below 832 GeV for a gluino lifetime between 10 μs and 1000 s in the generic R-hadron model with equal branching ratios for decays to $q\bar{q} \to \tilde{\chi}^0$ and $g\tilde{\chi}^0$.

10 Summary

With no sign of prompt SUSY decays there has been much speculation that SUSY could be hiding in stable, meta-stable, displaced decays. We are actively addressing this with a number of analyses. Good coverage of different lifetimes is achieved by complementary analyses using different detcctor systcms and novcl techniques. Figure 5 shows the constraints on the gluino mass-vs-lifetime plane for a split-SUSY model with the gluino R-hadron decaying into a gluon or light quarks and a neutralino with mass of 100 GeV from different analyses. The reader is invited to read the detailed papers on each of these analyses.

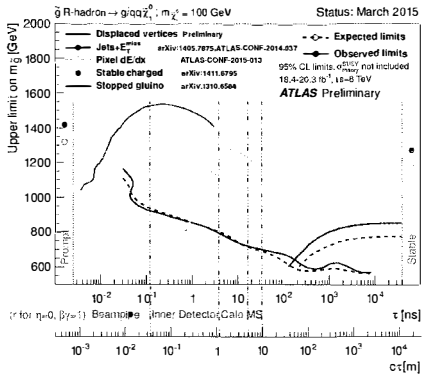

Figure 5 – Constraints on the gluino mass-vs-lifetime plane for a split-SUSY model with the gluino R-hadron decaying into a gluon or light quarks and a neutralino with mass of 100 GeV [19].

References

1. R. Barbier, C. Berat, M. Besancon, M. Chemtob, A. Deandrea, et al. *Phys.Rept.*, 420:1–202, 2005.
2. B. C. Allanach, M. A. Bernhardt, H. K. Dreiner, C. H. Kom, and P. Richardson. *Phys.Rev.*, D75:035002, 2007.
3. ATLAS Collaboration, *Phys.Rev.*, D88(11):112006, 2013.
4. M. Dine and W. Fischler. *Phys. Lett.*, B110:227, 1982.
5. L. Alvarez-Gaume, M. Claudson, and M. B. Wise. *Nucl. Phys.*, B207:96, 1982.
6. C. R. Nappi and B. A. Ovrut. *Phys. Lett.*, B113:175, 1982.
7. M. Dine and A. E. Nelson. *Phys. Rev.*, D48:1277–1287, 1993.
8. M. Dine, A. E. Nelson, and Y. Shirman. *Phys. Rev.*, D51:1362–1370, 1995.
9. M. Dine, A. E. Nelson, Y. Nir, and Y. Shirman. *Phys. Rev.*, D53:2658–2669, 1996.
10. J. L. Hewett, B. Lillie, M. Masip, and T. G. Rizzo. *JHEP*, 0409:070, 2004.
11. ATLAS Collaboration, *JINST* 3 S08003, 2008.
12. ATLAS Collaboration, arXiv:1504.05162 [hep-ex]. 2015.
13. ATLAS Collaboration, arXiv:1504.03634 [hep-ex]. 2015.
14. ATLAS Collaboration. ATLAS-CONF-2015-013. 2015.
15. ATLAS Collaboration. ATLAS-CONF-2014-037. 2014.
16. ATLAS Collaboration, *Phys.Rev.*, D90(11):112005, 2014.
17. ATLAS Collaboration, *JHEP*, 1501:068, 2015.
18. ATLAS Collaboration, *Phys.Rev.*, D88(11):112003, 2013.
19. https://twiki.cern.ch/twiki/bin/view/AtlasPublic/SupersymmetryPublicResults

RESONANCES AND UNITARITY IN COMPOSITE HIGGS MODELS

D. ESPRIU
Institut de Ciències del Cosmos, Universitat de Barcelona,
Martí i Franquès 1, 08028 Barcelona, Spain

The scattering of longitudinally polarized W bosons in extensions of the Standard Model with anomalous Higgs couplings to the gauge sector and higher order $O(p^4)$ operators is considered. The modified couplings should be thought as the low energy remnants of some new dynamics involving the electroweak symmetry breaking sector. By imposing unitarity and causality constraints on $W_L W_L$ scattering amplitudes we relate the possible values of the effective couplings to the presence of new resonances above 300 GeV. We investigate the properties of these new resonances and their experimental detectability.

1 Introduction

We know that in the SM the Higgs boson unitarizes $W_L W_L$ scattering. Consider e.g. the process $W_L^+ W_L^- \to Z_L Z_L$.

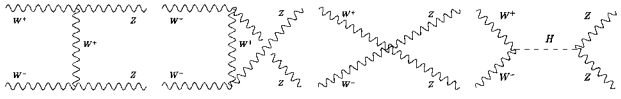

The first 3 diagrams are fixed by gauge invariance, but we can contemplate different Higgs-gauge boson couplings in the last one. If any of these couplings are different from the Standard Model (SM) values, the careful balance necessary for perturbative unitarity is lost. For $s >> M_W^2$ the amplitude in the SM goes as

$$\frac{s}{v^2}\frac{M_H^2}{s - M_H^2} \sim \frac{M_H^2}{v^2}, \tag{1}$$

but on dimensional grounds it should go as

$$\frac{s}{v^2}\frac{s}{s - M_H^2} \sim \frac{s}{v^2}. \tag{2}$$

This is indeed what happens after any modification of the Higgs couplings and produces non-unitary amplitudes. In short the SM value is precisely tuned to preserve unitarity.

Adding new effective operators typically spoils unitarity too

$$\mathcal{L}_{SM} \to \mathcal{L}_{SM} + \sum_i a_i \mathcal{O}_i. \tag{3}$$

New physics may produce either type of modifications. What can the requirement of unitarity in $W_L W_L$ scattering tell us about possible anomalous couplings in the electroweak (EW) sector?

2 Parametrizing composite Higgs physics

A light Higgs boson with mass $M_H \sim 125$ GeV is coupled to the EW bosons according to [1]

$$\begin{aligned}\mathcal{L}_{\text{eff}} \supset & -\frac{1}{2}\text{Tr}W_{\mu\nu}W^{\mu\nu} - \frac{1}{4}\text{Tr}B_{\mu\nu}B^{\mu\nu} + \mathcal{L}_{\text{GF}} + \mathcal{L}_{\text{FP}} + \sum_i a_i \mathcal{O}_i \\ & + \left[1 + 2a\frac{h}{v} + b\frac{h^2}{v}\right]\frac{v^2}{4}\text{Tr}D_\mu U^\dagger D^\mu U - V(h)\end{aligned} \tag{4}$$

$$U = \exp(i\,\omega\cdot\tau/v) \qquad D_\mu U = \partial_\mu U + \frac{1}{2}igW_\mu^i \tau^i U - \frac{1}{2}ig'B_\mu^i U\tau^3 \tag{5}$$

A non-linear realization is used. Setting $a = b = 1$ and a_i=0 exactly reproduces the SM interactions.

The $\mathcal{O}_i$ are a full set of C, P, and $SU(2)_L \times U(1)_Y$ gauge invariant, $d = 4$ operators [2] (of $O(p^4)$ in the chiral language) that along with the couplings a, b parameterize the low-energy effects of an extended high-energy EW symmetry breaking sector (EWSBS) . If we assume that the EWSBS is custodially preserving the relevant operators for $W_L W_L$ scattering are

$$\mathcal{L}_4 = a_4 \left(\text{Tr}\left[V_\mu V_\nu\right]\right)^2, \qquad \mathcal{L}_5 = a_5 \left(\text{Tr}\left[V_\mu V^\mu\right]\right)^2, \qquad V_\mu = \left(D_\mu U\right) U^\dagger. \tag{6}$$

The a_i could be functions of $\frac{h}{v}$. The contribution of these $d = 4$ operators to $W_L^{(\mu)} W_L^{(\nu)} \to Z_L^{(\rho)} Z_L^{(\sigma)}$ scattering is given via the Feynman rule

$$ig^4 \left[a_4 \left(g^{\mu\sigma}g^{\nu\rho} + g^{\mu\rho}g^{\nu\sigma}\right) + 2a_5 g^{\mu\nu}g^{\rho\sigma}\right] \tag{7}$$

Experimentally there are by now solid indications that the Higgs particle couples to the W, Z very similarly to the SM rules. Let us assume for the time being that $a = b = 1$ *exactly*. Then

$$\mathcal{L}_{\text{eff}} \simeq \mathcal{L}_{\text{SM}} + a_4 \left(\text{Tr}\left[V_\mu V_\nu\right]\right)^2 + a_5 \left(\text{Tr}\left[V_\mu V^\mu\right]\right)^2 \tag{8}$$

a_4 and a_5 represent anomalous 4-point couplings of the W bosons due to an extended EWSBS that however does not manifest with $O(p^2)$ couplings being noticeably different to the ones in the SM. These anomalous couplings will lead to violations of perturbative unitarity as they lead to amplitudes that grow [1,2] as s^2.

3 Unitarity and resonances

Violations of unitarity are cured by the appearance of new particles or resonances. We can now use well-understood unitarization techniques to constrain these resonances and the effective couplings $\{a_i\}$. First, let us recapitulate

- The Higgs particle unitarizes amplitudes in the SM, where $a = b = 1, \{a_i\} = 0$.
- The theory is renormalizable without the $\{a_i\}$ if $a = b = 1$.
- If present, the $\{a_i\}$ will then be finite non-running parameters.

We would like to

- Determine how much room is left for the a_i.
- Find possible additional resonances required to restore unitarity.
- Should we have already seen any of these resonances?
- To what extent an extended EWSBS is excluded by current data?

We advance some answers:

- Yes, there may be new resonances with relatively light masses and narrow widths.
- No, we should not have seen them yet. Their signal is too weak.
- Looking for the resonances is an efficient (albeit indirect) way of setting constrains on a nomalous triple and quartic gauge couplings (i.e. the a_i).

Let $t_{IJ}(s)$ be a partial wave derived from the $W_LW_L \to Z_LZ_L$ amplitude. Unitarity requires

$$\begin{array}{rcccc} \mathrm{Im}\, t_{IJ}(s) & = & \sigma(s)|t_{IJ}(s)|^2 & + & \sigma_H(s)|t_{H,IJ}(s)|^2 \\ & & \text{Elastic} & & \text{Inelastic} \\ & & WW \to WW & & WW \dashrightarrow hh \end{array} \tag{9}$$

where σ and σ_H are phase space factors. Given a perturbative expansion

$$\begin{array}{rcccccc} t_{IJ} & \approx & t_{IJ}^{(2)} & + & t_{IJ}^{(4)} & + & \cdots \\ & & \text{tree} & & \text{one-loop} & & \\ & & & & + \ a_i \text{ terms} & & \end{array} \tag{10}$$

we can require unitarity to hold exactly by using the inverse amplitude method (IAM) to define

$$t_{IJ} \approx \frac{t_{IJ}^{(2)}}{1 - t_{IJ}^{(4)}/t_{IJ}^{(2)}} \tag{11}$$

for non-coupled channels.[3] Several analyticity assumptions are implied in the above derivation.

Unitarization of the amplitudes may result in the appearance of new heavy resonances associated with the high-energy theory ($t_{00} \to$ Scalar isoscalar $t_{11} \to$ Vector isovector $t_{20} \to$ Scalar isotensor). We will search for poles in $t_{IJ}(s)$ up to $4\pi v \sim 3$ TeV (domain of applicability of the effective theory). Physical resonances will be required to have the phase shift pass through $+\pi/2$. This method is known to work remarkably well in strong interactions.

Is this unitarization method unique? Certainly not. Many methods exist: IAM, K-matrix approach, N/D expansions, Roy equations,.... While the quantitative results differ slightly, the gross picture does not change. For a detailed discussion of the different procedures see:[3]

4 Calculation and results for $a = b = 1$

Most studies concerning unitarity at high energies are carried out using the Equivalence Theorem (ET). This is understandable as calculations simplify enormously[4]

$$A(W_L^+W_L^- \to Z_LZ_L) \to A(\omega^+\omega^- \dashrightarrow \omega^0\omega^0) + O(M_W/\sqrt{s}) \tag{12}$$

For a light Higgs one needs to include tree-level Higgs exchange as well. Then one could make use of the well known chiral lagrangian techniques to derive the amplitudes and compare with experiment, including the Higgs as an explicit resonance. However for s not too large (which obviously is now an interesting region) the simplest version of the ET may be too crude an approximation and we shall use as much as possible exact amplitudes.

However, a full calculation of the one-loop contribution for the $W_LW_L \to Z_LZ_L$ process, $t_{IJ}^{(4)}$, in particular for arbitrary values of a and b is beyond question. Only one complete calculation

exists due to Denner and Hahn[5] for the SM case and it is available only numerically; not suitable for unitarity analysis. We can take a shortcut. The optical theorem implies the *perturbative* relation

$$\underset{\text{one-loop}}{\text{Im}\, t^{(4)}_{IJ}(s)} = \underset{\text{tree}}{\sigma(s)|t^{(2)}_{IJ}(s)|^2 + \sigma_H(s)|t^{(2)}_{H,IJ}(s)|^2} \tag{13}$$

For the *real part*, note that

$$\begin{aligned} \text{Re}\, t^{(4)}_{IJ} &= a_i\text{-dependent terms} + \text{real part of loop calculation} \\ &\approx a_i\text{-dependent terms} \quad (\text{for large } s,\, a_i) \end{aligned} \tag{14}$$

We approximate the *real part of loop contribution* with one-loop Goldstone boson amplitudes using the ET. The other contributions are computed exactly. See[1] for details.

Are there resonances? To answer this questions we must search for poles in the second Riemann sheet — the phase shift must go through $+\pi/2$ at the resonance. Are there any physically acceptable resonances? This question is answered in the positive. If one looks for resonances with masses below 3 TeV they are present for virtually any value of a_4 and a_5, except for values very close to zero (i.e. very close to the SM).

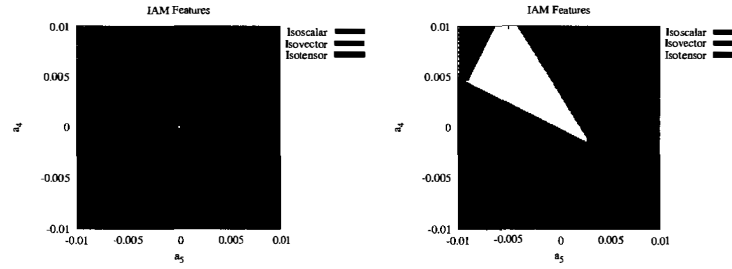

Figure 1 – Left: for $a = b = 1$ regions in $a_4 - a_5$ leading to acceptable resonances. The red (green) region corresponds to acceptable isoscalar (isovector) resonances. The blue-shaded area leads to acausal resonances and the corresponding values for a_4 and a_5 are unphysical — they cannot be realized in any effective theory with a meaningful UV completion. Only a extremely small set of $a_4 - a_5$ parameters (very close to the SM values —zero– nearly invisible in the figure) do not lead to new resonances below 3 TeV. Right: same but now we impose that the resonances should be found below 600 GeV. If not present, the range of values for the anomalous couplings still acceptable (white area) is much enlarged. This could possibly represent the present experimental situation according to the present analysis.

4.1 Properties of the new resonances

In the next figure we show the masses that are obtained in the scalar and vector channels. As we see, by varying the values of $a_4 - a_5$ we obtain masses in the regions $M_S \sim 300 - 3000$ GeV, $M_V \sim 550 - 2300$ GeV. This means that relatively light masses are possible in extended EWSBS leading to appropriate values of the $d = 4$ effective couplings. Observing or excluding these resonances is thus an indirect way of measuring these effective couplings. Note that this analysis is independent of the precise nature of this sector because only general arguments (locality, unitarity,...) have been used. We have similar plots for the widths but we will not present them here due to space reasons. The resonances are generally speaking narrow: $\Gamma_S \sim 5 - 120$ GeV, $\Gamma_V \sim 2 - 24$ GeV.

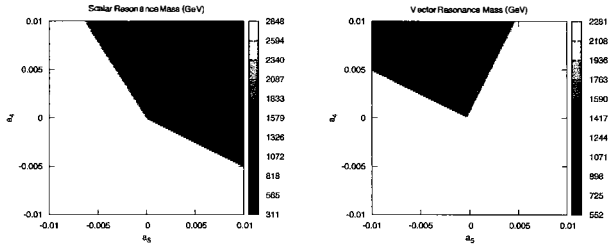

4.2 Visibility of the resonances

The next question is whether these resonances are detectable. The answer is that this is impossible with the present experimental statistics. To see this point clearly we show the signal of two of the resonances predicted by unitarity: one scalar and one vector. They correspond to the values for a_4 and a_5 indicated in the figure. For these values both one scalar and one vector resonances are present (the vector one is heavier). We compare the strength of the signal of the scalar resonance to the one corresponding to a SM Higgs with the same mass. Resonances could still be there, but would give a small signal. This signal is undetectable at present and will necessitate at least 10 times more statistics. In addition this signal would only be present in the $WW \to WW$ or $WW \to ZZ$ channels. The large contribution that the SM Higgs represents leaves little room for additional resonances.

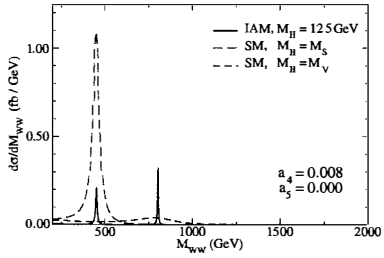

5 Moving away from the SM Higgs couplings

What if the hWW couplings are not exactly the SM ones? Nothing prevents us from carrying out the same programme for arbitraty values of the Higgs-toWW couplings a and b. The resulting effective theory is non-renormalizable and the a_i will be required to absorb the additional divergences[6]

$$\delta a_4 = \Delta_\epsilon \frac{1}{(4\pi)^2}\frac{-1}{12}(1-a^2)^2 \tag{15}$$

$$\delta a_5 = \Delta_\epsilon \frac{1}{(4\pi)^2}\frac{-1}{24}\left[(1-a^2)^2 + \frac{3}{2}((1-a^2)-(1-b))^2\right] \tag{16}$$

We can repeat the same unitarization procedure as for $a = b = 1$ and search for resonances. The results are shown in the following figure.

The characteristics of the resonances tend smoothly to the $a = 1$ case (hWW coupling as in the SM). Resonances tend to be slightly heavier and broader than for $a = 1$. The parameter b is only marginally visible in the widths (not shown). There are constraints on vector masses from S, T, U parameter constraints in some models.[7]

As in the $a = 1$ case the signal is always much lower[1] than the one for a Higgs of the same mass. For $a = 1$ typically $\sigma_{\text{resonance}}/\sigma_{\text{Higgs}} < 0.1$, now $\sigma_{\text{resonance}}/\sigma_{\text{Higgs}} \simeq 0.2$.

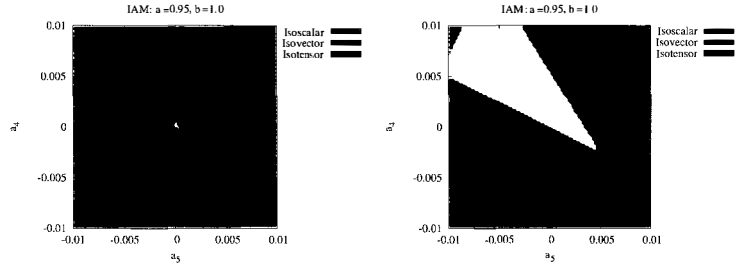

Figure 2 – Exclusion zones and bounds on a_i for $a = 0.95$ ($b = a^2$). Left: in color the excluded region in $a_4 - a_5$ parameter space if no resonance is found < 3 TeV. Right: in color the excluded regions if no resonance exists below $M_R = 600$ GeV. Note that the allowed white areas are slightly larger than in the case $a = b = 1$

To sumarize, the situation for $a < 1$ is not radically different from $a = 1$. Resonances (particularly in the vector channel) are slightly more difficult to appear. They tend to be slightly heavier and broader and they give a slightly larger experimental signal.

This situation changes drastically for $a > 1$. 'Something' happens when $a > 1$. Most of the resonances disappear and in fact most of parameter space is excluded on causality and unitarity grounds. We have no space left to explain the reasons of this radical change of behaviour here and recommend the interested reader to examine our references.[8,1] From a technical point of view, this drastic modification is associated to the change of sign of $t^{(2)}$ when $a > 1$.

Let us summarize our main points. Unitarity is a powerful constraint on scattering amplitudes. The validity is well tested in other physical situations. Even in the presence of a light Higgs, unitarization can help constrain anomalous couplings by helping predict heavier resonances. An extended EWSBS would typically have such resonances even in the presence of a 125 GeV Higgs. However the properties of the resonances are radically different from the 'standard lore'. Limited by statistics, existing LHC searches do not yet probe the IAM resonances.

Acknowledgements

This work is supported by grants FPA2013-46570, 2014-SGR-104 and Consolider grant CSD2007-00042 (CPAN). It is a real pleasure to thank my collaborators B. Yencho and F. Mescia.

References

1. D.Espriu and B. Yencho,*Phys. Rev.* D **87**, 055017 (2013); D.Espriu and F. Mescia, *Phys. Rev.* D **90**, 015035 (2014)
2. A. Dobado, D. Espriu and M.J. Herrero, *Phys. Lett.* B **255**, 405 (1991); D. Espriu and M.J. Herrero, *Nucl. Phys.* B **373**, 117 (1992); M.J. Herrero and E. Ruiz-Morales, *Nucl. Phys.* B **418**, 431 (1994); *Nucl. Phys.* B **437**, 319 (1995)
3. R. Delgado, A. Dobado and F. Llanes, *Jour. High. Ener. Phys.* **1402**, 121 (2014); ibid., arXiv:1502.0484
4. D. Espriu and J Matias, *Phys. Rev.* D **52**, 6530 (1995)
5. A. Denner and T. Hahn, *Nucl. Phys.* B **525**, 27 (1998)
6. D.Espriu, F. Mescia and B. Yencho, *Phys. Rev.* D **88**, 055002 (2013)
7. A. Pich, I. Rosell, J.J. Sanz-Cillero, *Phys. Rev. Lett.* **110**, 181801 (2013); *Jour. High. Ener. Phys.* **1401**, 157 (2014).
8. A. Falkowski, S. Rychkov and A. Urbano, *Jour. High. Ener. Phys.* **1204**, 073 (2012); ;B. Bellazzini, L. Martucci and R. Torre *Jour. High. Ener. Phys.* **1409**, 100 (2014)

$2h$ PRODUCTION WITH ISOTRIPLET SCALARS

S.I. GODUNOV
Institute for Theoretical and Experimental Physics, Moscow, 117218, Russia

The enhancement of double BEH boson production in the extensions of the Standard Model with extra isotriplets is studied. It is found that in the see-saw type II model decays of new heavy scalar H can contribute to the double h production cross section as much as Standard Model channels. In the Georgi–Machacek model the custodial symmetry is preserved and the strongest limitation on triplet parameters is removed so the production cross section can be much larger while $H \to ZZ$ and $H \to WW$ decay channels could be highly suppressed.

1 Introduction

After the discovery of the BEH boson h at the LHC[1] the next steps to check the Standard Model (SM) are the measurement of the coupling constants of the h boson to other SM particles with better accuracy and the measurement of the h self-coupling which determines the shape of the potential. In the SM the triple and quartic couplings are predicted in terms of the known h mass and vacuum expectation value. Deviations from these predictions would mean the existence of New Physics in the h potential. The triple coupling can be measured at the LHC in double h production, in which the gluon fusion dominates: $gg \to hh$. However, the $2h$ production cross section is very small. At $\sqrt{s} = 14$ TeV the cross section $\sigma^{NNLO}(gg \to hh) = 40.2$ fb with $(10 - 15)\,\%$ accuracy[2]. For the final states with the reasonable signal/background ratios double h production will be found and triple coupling will be measured[3] only at the HL-LHC. We are looking for the extensions of the SM scalar sector in which the double h production is enhanced so it can be tested at the LHC in the next couple of years.

One of the well-motivated examples of non-minimal scalar sector is provided by the see-saw type II mechanism of the neutrino mass generation[4]. In this mechanism a scalar isotriplet $(\Delta^{++}, \Delta^{+}, \Delta^{0})$ with hypercharge $Y_\Delta = 2$ is added to the SM. The vacuum expectation value (vev) of the neutral component v_Δ generates Majorana masses of the left-handed neutrinos. In this model we get an additional mechanism of the double h production at the LHC in the mode with intermediate new heavy scalar H. The H production cross section and its decays widths are proportional to v_Δ^2 so to enhance double h production we need v_Δ to be as large as possible.

Since the nonzero value of v_Δ violates the well checked equality of the strength of charged

and neutral currents at tree level, v_Δ should be less than 5 GeV and this value was used for numerical estimates.

The bound $v_\Delta < 5$ GeV is removed in the Georgi-Machacek model [5], in which in addition to $\vec{\Delta}$ a scalar isotriplet with $Y = 0$ is introduced. Bounds on v_Δ come from the measurement of the 125 GeV boson couplings to vector bosons and fermions, which would deviate from their SM values. Since the accuracy of the coupling measurements is poor, v_Δ as large as 50 GeV is allowed and $\sigma(gg \to H)$ can reach 2 pb value which makes it accessible with the integrated luminosity $\int \mathcal{L}dt = 300$ fb^{-1} prior to the HL-LHC run.

The talk is based on results presented in papers [6,7], where more details and references can be found.

2 $2h$ production in the see-saw type II model

In this section we consider see-saw type II model and calculate the double h production cross section. We derive only the necessary formulas (for a detailed description see paper [8]).

In addition to the SM isodoublet field Φ,

$$\Phi \equiv \begin{bmatrix} \Phi^+ \\ \Phi^0 \end{bmatrix} \equiv \begin{bmatrix} \Phi^+ \\ \frac{1}{\sqrt{2}}(v + \varphi + i\chi) \end{bmatrix}, \tag{1}$$

in the see-saw type II an isotriplet is introduced:

$$\Delta \equiv \frac{\vec{\Delta}\vec{\sigma}}{\sqrt{2}} = \begin{bmatrix} \Delta^3/\sqrt{2} & \left(\Delta^1 - i\Delta^2\right)/\sqrt{2} \\ \left(\Delta^1 + i\Delta^2\right)/\sqrt{2} & -\Delta^3/\sqrt{2} \end{bmatrix} \equiv \begin{bmatrix} \delta^+/\sqrt{2} & \delta^{++} \\ \delta^0 & -\delta^+/\sqrt{2} \end{bmatrix},$$
$$\delta^0 = \frac{1}{\sqrt{2}}(v_\Delta + \delta + i\eta). \tag{2}$$

Here $\vec{\sigma}$ are the Pauli matrices.

The scalar sector kinetic terms are

$$\mathcal{L}_{\text{kinetic}} = |D_\mu \Phi|^2 + \text{Tr}\left[(D_\mu \Delta)^\dagger (D_\mu \Delta)\right], \tag{3}$$

where

$$D_\mu \Phi = \partial_\mu \Phi - i\frac{g}{2} A_\mu^a \sigma^a \Phi - i\frac{g'}{2} B_\mu \Phi, \tag{4}$$
$$D_\mu \Delta = \partial_\mu \Delta - i\frac{g}{2}\left[A_\mu^a \sigma^a, \Delta\right] - ig' B_\mu \Delta. \tag{5}$$

Hypercharge $Y_\Phi = 1$ was substituted for isodoublet and $Y_\Delta = 2$ for isotriplet. The terms quadratic in vector boson fields are the following:

$$\mathcal{L}_{V^2} = g^2 \left|\delta^0\right|^2 W^+W^- + \frac{1}{2}g^2 \left|\Phi^0\right|^2 W^+W^- + \bar{g}^2 \left|\delta^0\right|^2 Z^2 + \frac{1}{4}\bar{g}^2 \left|\Phi^0\right|^2 Z^2. \tag{6}$$

For the ratio of vector boson masses neglecting the radiative corrections from isotriplet (not a bad approximation as far as the heavy triplet decouples) we get:

$$\frac{M_W}{M_Z} \approx \left(\frac{M_W}{M_Z}\right)_{\text{SM}} \left(1 - \frac{v_\Delta^2}{v^2}\right). \tag{7}$$

Comparing the result of the SM fit [9] , $M_W^{\text{SM}} = 80.381$ GeV, with the experimental value, $M_W^{\text{exp}} = 80.385(15)$ GeV, at 3σ level we get the upper bound $v_\Delta < 5$ GeV. Since the cross sections we are interested in are proportional to $(v_\Delta)^2$ we will use this bound for numerical estimates.

The scalar potential is:

$$V(\Phi,\Delta)=-\frac{1}{2}m_\Phi^2\left(\Phi^\dagger\Phi\right)+\frac{\lambda}{2}\left(\Phi^\dagger\Phi\right)^2+M_\Delta^2\mathrm{Tr}\left[\Delta^\dagger\Delta\right]+\frac{\mu}{\sqrt{2}}\left(\Phi^T i\sigma^2\Delta^\dagger\Phi+h.c.\right), \tag{8}$$

which is a truncated version of the most general renormalizable potential (see for example eq. (2.6) in paper [10]). The last term in (8) is responsible for generation of v_Δ.

Quadratic in φ, δ terms according to (8) are

$$V(\varphi,\delta)=\frac{1}{2}m_\Phi^2\varphi^2+\frac{1}{2}M_\Delta^2\delta^2-\mu v\varphi\delta. \tag{9}$$

Here and below the terms suppressed as $(v_\Delta/v)^2$ are omitted.

Denoting the states with the definite masses as h and H, we obtain:

$$\begin{bmatrix}\varphi\\ \delta\end{bmatrix}=\begin{bmatrix}\cos\alpha & -\sin\alpha\\ \sin\alpha & \cos\alpha\end{bmatrix}\begin{bmatrix}h\\ H\end{bmatrix},\ \tan 2\alpha=\frac{4v_\Delta}{v}\frac{M_\Delta^2}{M_\Delta^2-m_\Phi^2},\ M_h^2\approx m_\Phi^2,\ M_H^2\approx M_\Delta^2. \tag{10}$$

Since $\tan 2\alpha\approx 4v_\Delta/v\ll 1$, the mass eigenstate h consists mostly of φ and H consists mostly of δ. We suppose that the particle observed by ATLAS and CMS is h, so M_h is about 125 GeV. We do not consider here the mixing and masses of other scalar particles which are present in the see-saw type II model since they are not important for $2h$ production.

Since H has a doublet admixture, the dominant mechanism of H production is the gluon fusion, cross section of which equals that of the SM BEH-scalar production multiplied by $\sin^2\alpha\approx\left[\left(2v_\Delta/v\right)/\left(1-M_h^2/M_H^2\right)\right]^2\approx 2.4\cdot 10^{-3}$. In Table 1 the relevant numbers are presented. All numbers correspond to 14 TeV LHC energy. The subdominant mechanisms of H production are ZZ fusion and associative ZH production and they are negligible [6].

Table 1: The cross sections of H production via gg fusion. Values for the SM h boson are taken from Table 4 in paper [11]. All numbers correspond to 14 TeV LHC energy.

M_h (GeV)	125	300
$\sigma_{gg\to h}$ (pb)	$49.97\pm 10\%$	$11.07\pm 10\%$
M_H (GeV)	X	300
$\sigma_{gg\to H}$ (fb)	X	$25\pm 10\%$

For the decay probabilities we obtain:

$$\Gamma_{H\to hh}=\frac{v_\Delta^2}{v^4}\frac{M_H^3}{8\pi}\left[\frac{1+2\left(\frac{M_h}{M_H}\right)^2}{1-\left(\frac{M_h}{M_H}\right)^2}\right]^2\sqrt{1-4\frac{M_h^2}{M_H^2}}, \tag{11}$$

$$\Gamma_{H\to ZZ}=\frac{v_\Delta^2}{v^4}\frac{M_H^3}{8\pi}\left[\frac{1-2\left(\frac{M_h}{M_H}\right)^2}{1-\left(\frac{M_h}{M_H}\right)^2}\right]^2\left(1-4\frac{M_Z^2}{M_H^2}+12\frac{M_Z^4}{M_H^4}\right)\sqrt{1-4\frac{M_Z^2}{M_H^2}}, \tag{12}$$

$$\Gamma_{H\to WW}=\frac{v_\Delta^2}{v^4}\frac{M_H^3}{4\pi}\left[\frac{M_h^2/M_H^2}{1-\left(\frac{M_h}{M_H}\right)^2}\right]^2\left(1-4\frac{M_W^2}{M_H^2}+12\frac{M_W^4}{M_H^4}\right)\sqrt{1-4\frac{M_W^2}{M_H^2}}, \tag{13}$$

$$\Gamma_{H\to t\bar{t}}=\frac{v_\Delta^2}{v^4}\frac{N_c m_t^2 M_H}{2\pi}\frac{1}{\left(1-M_h^2/M_H^2\right)^2}\left(1-4\frac{m_t^2}{M_H^2}\right)^{3/2}, \tag{14}$$

where $N_c=3$ is the number of colors.

In the see-saw type II model neutrino masses are generated by the Yukawa couplings of isotriplet Δ with lepton doublets. These couplings generate $H \to \nu\nu$ decays as well. As it was noted in paper[12] for $v_\Delta > 10^{-3}$ GeV diboson decays dominate. It happens because the amplitude of diboson decay is proportional to v_Δ, while Yukawa couplings f_i are inversely proportional to it, $f \sim m_\nu / v_\Delta$. That is why for $v_\Delta \gtrsim 1$ GeV leptonic decays are completely negligible. The same holds for decays of charged triplet scalars so direct searches[13] do not lead to new bounds on model parameters (see also paper[14]).

We suppose that 250 GeV $< M_H <$ 350 GeV so the decay $H \to 2h$ is allowed kinematically while $H \to t\bar{t}$ is forbidden so it does not lead to diminishing of Br$(H \to 2h)$. But let us note that even for $M_H > 350$ GeV the branching ratio of $H \to 2h$ decay is also rather large, however H production cross section becomes small due to the large H mass. That is why for numerical estimates we took the value $M_H = 300$ GeV for which $H \to 2h$ and $H \to ZZ$ decays dominate[a] and $\Gamma_{H\to 2h}/\Gamma_{H\to ZZ} \approx 4$, i.e. the branching ratio of $H \to 2h$ decay equals $\approx 80\%$. Thus, decays of H provide ≈ 20 fb of double h production cross section in addition to 40 fb coming from SM. However, unlike SM in which $2h$ invariant mass is spread along rather large interval, in the case of H decays $2h$ invariant mass peaks at M_H which is a distinctive feature of this model (see also[15,16]).

3 $2h$ production enhancement in the Georgi–Machacek model

The amplitudes of H production both via gg fusion and VBF are proportional to the triplet vev v_Δ and due to the upper bound $v_\Delta < 5$ GeV these amplitudes and the corresponding cross sections are severely suppressed.

The triplet vev v_Δ should be small in order to avoid noticeable violation of custodial symmetry which guarantees the degeneracy of W and Z bosons in the SM at tree level in the limit $g' = 0$, $\cos\theta_W = 1$. The vacuum expectation value of the complex isotriplet $\vec{\Delta}$ with hypercharge $Y_\Delta = 2$ violates the custodial symmetry. The custodial symmetry is preserved when two isotriplets (complex $\vec{\Delta}$ and real $\vec{\xi}$ with $Y_\xi = 0$) are added to the SM and when vev's of their neutral components[b] are equal[5]. Thus in the GM variant of the see-saw type II model $M_W/M_Z = \cos\theta_W$, and v_Δ is not bounded by 5 GeV. In this model the bound on v_Δ appears only from measurements of deviations of h couplings to fermions and vector bosons from SM predictions. These deviations in the limit of heavy scalar triplets were studied in the paper[17] (see also paper[18]).

From equations (59) and (61) of paper[17] we get the following estimates for the ratios of the hVV (here $V = W$, Z) and $h\bar{f}f$ coupling constants to that in the SM:

$$\begin{cases} k_V \approx 1 + 3\left(\frac{v_\Delta}{v}\right)^2, \\ k_f \approx 1 - \left(\frac{v_\Delta}{v}\right)^2. \end{cases} \tag{15}$$

Therefore, for the ratios of the cross sections to that in the SM, we get:

$$\mu_i \equiv \frac{\sigma}{\sigma_{SM}} \cdot \frac{\mathrm{Br}}{\mathrm{Br_{SM}}} = 1 + \mathcal{O}\left(\frac{v_\Delta^2}{v^2}\right). \tag{16}$$

Since the accuracy in measuring μ_i is poor, $v_\Delta \approx 50$ GeV is not forbidden. One order of magnitude growth of v_Δ leads to two orders of magnitude growth of H production cross section. Hence 300 GeV heavy scalar boson H can be produced at 14 TeV LHC with 2 pb cross section which should be large enough for it to be discovered prior to the HL-LHC.

[a] The decay $H \to ZZ \to (l^+l^-)\,(l^+l^-)$ provides great opportunity for the discovery of heavy scalar H.

[b] Note that our v_Δ is by $\sqrt{2}$ bigger than what is usually used in the papers devoted to the GM model; our v is also usually denoted by v_Φ, while the value 246 GeV is denoted by v.

Using coupling constants according to papers [17,14], for the partial widths of H decays we get[7]

$$\Gamma_{H\to hh} \approx \frac{v_\Delta^2}{v_\phi^4}\frac{3M_H^3}{16\pi}\left[\frac{1+2\left(\frac{M_h}{M_H}\right)^2}{1-\left(\frac{M_h}{M_H}\right)^2}\right]^2\sqrt{1-4\frac{M_h^2}{M_H^2}}, \tag{17}$$

$$\Gamma_{H\to ZZ} \approx \frac{v_\Delta^2}{v_\phi^4}\frac{M_H^3}{48\pi}\left[\frac{1-4\left(\frac{M_h}{M_H}\right)^2}{1-\left(\frac{M_h}{M_H}\right)^2}\right]^2\left(1-4\frac{M_Z^2}{M_H^2}+12\frac{M_Z^4}{M_H^4}\right)\sqrt{1-4\frac{M_Z^2}{M_H^2}}, \tag{18}$$

$$\Gamma_{H\to WW} \approx \frac{v_\Delta^2}{v_\phi^4}\frac{M_H^3}{24\pi}\left[\frac{1-4\left(\frac{M_h}{M_H}\right)^2}{1-\left(\frac{M_h}{M_H}\right)^2}\right]^2\left(1-4\frac{M_W^2}{M_H^2}+12\frac{M_W^4}{M_H^4}\right)\sqrt{1-4\frac{M_W^2}{M_H^2}}. \tag{19}$$

Deriving these formulae we used the approximation $v_\phi \gg v_\Delta$, i.e. $\sin 2\alpha \approx 2\sin\alpha$.

Using (17), (18), and (19) for $M_H = 300\,\mathrm{GeV}$ we get $\mathrm{Br}\,(H\to hh)\approx 98\%$ while $\mathrm{Br}\,(H\to ZZ)\approx 0.6\%$. It means that in spite of large H production cross section, enhancement in ZZ final state could be negligible so the search for H in this mode at the LHC [19] will not lead to new limits on model parameters.

4 Conclusions

The case of extra isotriplet(s) provides rich scalar sector phenomenology with additional to the SM h boson charged and neutral scalar particles. With the growth of triplet vev, production cross section of new scalar grows and the dominant decays of new particles become decays to gauge and lighter scalar bosons. In the present paper we have discussed the neutral heavy scalar H production at the LHC in which the gluon fusion dominates. $H\to 2h$ decay contributes significantly to the double h production and even may dominate in the GM variant of the see-saw type II model.

It was shown that though in the GM model new heavy neutral scalar H can be produced with large cross section at the LHC, ZZ and WW decay modes can be very suppressed (if $H\to hh$ decays are kinematically allowed and M_H is not significantly larger than 300 GeV) so direct searches for H in these decay modes will not lead to its discovery. This is a peculiar feature of the GM model.

Acknowledgments

The author is grateful to the Organizers for the opportunity to give a talk at the 50th Moriond anniversary and enjoy the atmosphere of this great conference.

The author is partially supported under the grants RFBR No. 14-02-00995, NSh-3830.2014.2, MK-4234.2015.2. In addition, S. G. is supported by Dynasty Foundation and by the Russian Federation Government under grant No. 11.G34.31.0047.

References

1. G. Aad *et al* [ATLAS Collaboration], *Phys. Lett.* B **716**, 1 (2012);
   S. Chatrchyan *et al* [CMS Collaboration], *Phys. Lett.* B **716**, 30 (2012).
2. D. de Florian, J. Mazzitelli, DESY-14-080, LPN-14-073, arXiv:1405.4704.
3. J. Baglio, *PoS DIS2014* 120 (2014), arXiv:1407.1045.
4. J. Schechter, J. W. F. Valle, *Phys. Rev.* D **22**, 2227 (1980);
   T. P. Cheng, L. F. Li, *Phys. Rev.* D **22**, 2860 (1980);

M. Magg, Ch. Wetterich, *Phys. Lett.* B **94**, 61 (1980);
R. N. Mohapatra, G. Senjanovic, *Phys. Rev.* D **23**, 165 (1981).
5. H. Georgi, M. Machacek, *Nucl. Phys.* B **262**, 463 (1985).
6. S.I. Godunov, M.I. Vysotsky, E.V. Zhemchugov, *JETP* **120** (2015) 369-375.
7. S.I. Godunov, M.I. Vysotsky, E.V. Zhemchugov, arXiv:1505.05039.
8. S. Kraml, E. Accomando *et al*, CERN-2006-009, arXiv:hep-ph/0608079.
9. J. Beringer *et al*, *Phys. Rev.* D **86** 010001 (2012).
10. P. S. Bhupal Dev, D. K. Ghosh, N. Okada, I. Saha, *JHEP* **2013**, No. 03, 150 (2013).
11. S. Dittmaier *et al*, CERN-2011-002, arXiv:1101.0593.
12. K. Yagyu, arXiv: 1405.5149;
Sh. Kanemura, K. Yagyu, H. Yokoya, *Phys. Lett.* B **726**, 316 (2013).
13. G. Aad *et al* [ATLAS Collaboration], *Phys. Rev.* D **85**, 032004 (2012);
S. Chatrchyan *et al* [CMS Collaboration], *Eur. Phys. J.* C **72**, 2189 (2012).
14. Ch.-W. Chiang, K. Yagyu, *JHEP* **2013**, No. 01, 026 (2013);
Ch.-W. Chiang, Sh. Kanemura, K. Yagyu, UT-HET-096, arXiv:1407.5053;
Sh. Kanemura, M. Kikuchi, K. Yagyu, H. Yokoya, UT-HET-091, arXiv:1407.6547.
15. M. J. Dolan, C. Englert, and M. Spannowsky, *Phys. Rev.* D **87**, 055002 (2013).
16. V. Barger, L. L. Everett, C.B. Jackson, A. Peterson, G. Shaughnessy, arXiv:1408.0003.
17. K. Hartling, K. Kumar, H. E. Logan, *Phys. Rev.* D **90**, 015007 (2014).
18. C. Englert, E. Re, M. Spannowsky, *Phys. Rev.* D **87**, 095014 (2013).
19. V. Khachatryan *et al.* [CMS Collaboration], arXiv:1504.00936 [hep-ex], CMS-HIG-13-031, CERN-PH-EP-2015-074.

A bonus complementarity in Simplified Models of Dark Matter

Bryan Zaldívar
Service de Physique Théorique, Université Libre de Bruxelles, B-1050 Brussels, Belgium

Nowadays there is an active discussion about the definition of Simplified Models of Dark Matter (SMDM) as a tool for interpreting LHC searches. Here we point out an additional simplified set-up which captures a very well motivated mechanism beyond the Standard Model: the kinetic-mixing of an extra $U'(1)$ gauge symmetry. In addition to that, even if most of the attention has being paid on LHC "mono-signals", here we highlight an unavoidable signature appearing in SMDM with s-channel mediators: dijets or dileptons with no missing energy. We translate these searches into *lower* bounds on the DM couplings to the visible sector, showing the nice complementarity with the previous analyses, such that the parameter space of DM is being reduced from above and from below.

1 Introduction

The searches for Dark Matter (DM) have become one of the most actives lines of research at the LHC in the last few years. Departing from the Supersymmetry framework, the Effective Field Theory (EFT) approach provided a very simple, partially model-independent tool where the different signatures at colliders could be interpreted.[a]

In particular topologies like monojets[4,5], monophotons[6,7], or monoleptons[8,9] (among others) accompanied by large missing transverse energy -which are quoted as "mono-signals" in general- have become the main avenues for DM at the LHC. However, soon after the first analyses were done, it became clear the disadvantages of the EFT, whose validity is limited for events with low momentum transfer [10]. This fact motivated the community to start thinking about simplified -yet more complete- set-ups, where the extra degrees of freedom are not integrated out, thus rendering the event-by-event analysis valid for all the regions of the parameter space.

These Simplified Models of Dark Matter (SMDM) are becoming the next framework within which DM-related searches at the LHC are being interpreted.[b] They consist of very simple (low energy [c]) lagrangians with only 3 or 4 parameters: the DM mass m_χ, the mass of the mediator $M_{\rm med}$, and two couplings, DM-mediator g_χ and mediator-SM g_q, in the case of "portals" (i.e. s-channel processes), or one coupling g_t for the DM-mediator-SM interactions, if considering t-channel processes. Even if popularly used in the context of WIMP searches, other DM alternatives are also analysed in this framework for LHC studies [15].

Although in SMDM implementations it has being usually assumed that the coupling g_q is universal for all quarks -thus simplifying enormously the interpretation of the experimental results-, a priori this may not be the case for the low energy predictions of more fundamental models. Thus it is interesting to ask the question of which are the "ultraviolet" completions of

[a] See [1] and [2] for very early works on the subject, and [3] for a complementarity between the two.

[b] See e.g. refs.[12,13]. See also [14] for a very recent analysis where the DM is studied in a simplified framework, inspired from -but more general than- the neutralino case.

[c] In the sense that they do not attempt to be UV completed theories.

such SMDM realisations and, at the same time, how can such implementations be extended in such a way as to represent other possible theoretically well motivated scenarios. This should be achieved without spoiling their minimality; specifically, without enlarging the number of free parameters which render them feasible for LHC interpretations.

Another aspect concerns the possible signatures at the LHC. The introduction of an explicit mediator between the dark matter and the SM implies that not only processes like SM+SM-→mediator-→DM+DM are possible (leading to monojets+$E^T_{\rm miss}$ for example), but inevitably, the possibility SM+SM-→mediator→SM+SM should also be taken into account (leading to dileptons or dijets with no $E^T_{\rm miss}$). We quantify the complementarity existing between these two kinds of processes, together with the constraints coming from dark matter Direct Detection searches. As we will see, the two strategies constrain the DM parameter space from opposite directions, efficiently excluding large parts of the parameter space of such SMDM set-ups.

In the next sections we will first briefly revise the theoretical motivations for some of the existing SMDM set-ups; specifically focusing in the s-channel configurations and vector mediators. We identify possible alternatives capturing other interesting textures which may be connected to popular UV completions. We then dedicate the rest of the presentation to describe how the complementarity between mono-signals and disignals is achieved.

2 From the UV to Simplified Models

Here we adopt a top-down approach, going from the generic elements of popular complete models to the low energy parametrisations defined by SMDM. We concentrate in "s-channel" set-ups, i.e. those where the dark matter does not have direct interactions with the SM particles but only indirectly via a "portal" which couple to both the dark and the visible sectors. Here we restrict to the case of vector mediators.

Typically the introduction of new vector particles is associated with the postulation of new gauge symmetries. The simplest of these is an abelian $U'(1)$, which is one of the best motivated extensions of the Standard Model. The generic lagrangian for the interaction of a Z' with fermions is:

$$\mathcal{L}_{\rm NC} = g_X J^\mu_{\rm NC} Z'_\mu, \quad J^\mu_{\rm NC} = \sum_i \bar{f}_i \gamma^\mu [g^i_V - g^i_A \gamma^5] f_i, \quad g^i_{V,A} = \frac{Q^i_L \pm Q^i_R}{2} \; ; \tag{1}$$

where $J^\mu_{\rm NC}$ is the associated neutral current, containing every possible fermion f_i. The couplings g_V, g_A are the vector and axial couplings respectively, where $Q^i_{L,R}$ are the left and right charges of every fermion i to Z'. Note from (1) that the gauge coupling g_X is not really a parameter independent of the charges, or viceversa. Let the DM, χ, be on of the above fermions, such that its couplings with the Z' are in general g^χ_V, g^χ_A. To generate the Z' and DM masses can be done in several ways, so one could simply take as working variables the masses themselves $m_\chi, m_{Z'}$, independently on the way they were obtained from the fundamental parameters. From the above arguments we see that we can work in a parametrisation with the following independent variables:

$$m_{Z'}, m_\chi, g^i_V, g^i_A, g^\chi_V, g^\chi_A \; . \tag{2}$$

where i represent every possible SM fermion [d]. All in all there are, a priori, 25 parameters in expr.(2). Most of the (complete) models that can be written regarding a Z' will present the above ingredients. They will differ in the assumptions for the couplings, but also, in the sector

[d] So a priori there are 21 or these g^i's, where RH neutrinos are not counted. However, the requirement for anomaly cancellations may reduce this number, since they constrain the charges to the Z'.

responsible for giving mass to the Z' (like the number of extra scalars acquiring VEVs, or how these scalars are charged under the $U'(1)$ or the SM gauge group). Also, a complete model should take care of the anomalies that are a priori naturally present whenever we have a new gauge sector.

Next we mention some of the most popular models involving Z' bosons [16]:

Sequential Model. In this set up the Z' couplings to the SM fermions are fixed to be equal to those of the Z boson itself. This is just a "reference" realisation, since it says nothing about anomaly cancellations or the origin of the Z' mass. If considered together with DM, this model has only 4 independent, unknown parameters (the two couplings of the DM and the $m_\chi, M_{Z'}$ masses).

$B-L$ Model. By gauging the $B-L$ quantum number, the resulting model is anomaly free with just the matter content of the SM plus RH neutrinos.[e] The associated Z' will have only pure-vector couplings to the SM fermions (i.e. $g_A^i = 0$ in this model).[f] This is one of the simplest Z' realisations. It contains an extra free parameter (w.r.t. the Sequential Model), which may be thought as e.g. the new gauge coupling g_{BL}. We have then 5 independent parameters, since the different g_V^i are determined by anomaly cancellation (modulo this overall multiplicative g_{BL} factor).

E_6 models. This is a realisation motivated from string theory, which is anomaly free thanks to exotic fields that may be decoupled from the low energy phenomenology. It actually consist of two $U'(1)$'s, usually called $U(1)_\chi$ and $U(1)_\psi$, with the corresponding charges of all the fermions to the two gauge bosons. Most studies assume that only one Z', coupling to the linear combination $Q = \cos\theta_{E_6} Q_\chi + \sin\theta_{E_6} Q_\psi$, is relevant at low energies. A priori there are then 3 extra parameters: $\theta_{E_6}, g_\chi, g_\psi$. In one of the realisations, $\theta_{E_6} = \pi/2$, such that only Z_ψ is relevant. Actually in this case all the couplings of the SM fermions to Z_ψ turn out to be purely axial (i.e. $g_V^i = 0$). This latter realisation has, as the previous case, 5 independent parameters; i.e. $g_\psi, M_{Z'}, m_\chi, g_V^\chi$ and g_A^χ.

Kinetic Mixing. This is one of the favourite implementations of an extra $U'(1)$, since many of the existing New Physics models in the literature lead to this kind of set up. Here it is worth commenting a little bit more in detail. For example, Salvioni *et al* [19] have presented a minimal model which is a combination of $B-L$ and hypercharge $U'(1)$, the latter being directly realised by the Kinetic Mixing (KM) set-up. There it is shown how different linear combinations of $B-L$ and KM can generate a whole family of models which predict the existence of Z' particles. In fact, this set up is by now used by the ATLAS collaboration itself [20].

In KM the observation is that a kinetic term like $-\frac{\epsilon}{2} B_{\mu\nu} X^{\mu\nu}$ is actually gauge invariant. Here ϵ is just the kinetic mixing coupling, $B_{\mu\nu}$ the SM stress tensor for $U(1)_Y$, and $X_{\mu\nu}$ the stress tensor of the new gauge group $U'(1)$. Even if at tree level $\epsilon = 0$, it may be generated at loop level if there are particules in the theory coupled to both gauge groups. After redefinition of the gauge fields to render the kinetic terms diagonal, the new fields get mixed once the electroweak symmetry is broken. The resulting mass eigenstates are thus:

$$\begin{aligned} Z'_\mu &= (\cos\theta_W W^3_\mu - \sin\theta_W B_\mu)\sin\alpha + X_\mu \cos\alpha \\ Z_\mu &= (\cos\theta_W W^3_\mu - \sin\theta_W B_\mu)\cos\alpha - X_\mu \sin\alpha \ , \end{aligned} \tag{3}$$

where θ_W is the Weinberg angle and α the mixing, where $\alpha = 0$ for $\epsilon = 0$. The SM fermions, even if not being charged w.r.t. the $U'(1)$, will thus couple to the physical Z' as:

$$\bar{f}_i \gamma^\mu [(g^i_{V,\mathrm{SM}} - g^i_{A,\mathrm{SM}}\gamma^5)\sin\alpha] f_i Z'_\mu \tag{4}$$

[e] See [17] for a recent alternative where a different combination of lepton number is gauged, which is motivated by the recent LHCb anomalies [18].

[f] Except for the neutrinos if they are Majorana.

where $g^i_{(V,A),\mathrm{SM}}$ are the standard couplings of the SM fermions to the Z^{SM}_μ boson. Similarly, even if the DM is not coupled to the SM $U(1)_Y$, the kinetic mixing will induce a coupling of DM to the Z_μ as:

$$\bar{\chi}\gamma^\mu(g_\chi \sin\alpha)\chi Z_\mu \ , \tag{5}$$

where we have assumed that DM couples only with vector-like coupling to the $U'(1)$. The 4 independent parameters of this set-up can be taken to be: the $Z' - Z$ mixing angle $\sin\alpha$, the DM coupling g_χ, and the two masses $m_{Z'}$ and m_χ.

2.1 Towards simplified models

Above we have seen some examples of models where the couplings can be purely vectorial (as for $U(1)_{BL}$), purely axial (as $U(1)_\psi$ in E_6) or a mix of both vector and axial, as the Kinetic Mixing set-up. In the $U(1)_{BL}$ case for example, u and d quarks actually have identical couplings, and the leptons have also identical couplings among themselves. In the $U(1)_\psi$ case, quarks and leptons have all identical axial couplings in fact. The couplings to the 2nd and 3rd fermion generations are identical as the 1st one in all of these cases. [g]

Now we make the connection with the simplified models that has been lately considered in the literature. We see that [12,13]: [h]

$$-\mathcal{L}_V \equiv g_q \sum_q Z'_\mu \bar{q}\gamma^\mu q + g_\chi Z'_\mu \bar{\chi}\gamma^\mu \chi \ , \quad -\mathcal{L}_A \equiv g_q \sum_q Z'_\mu \bar{q}\gamma^\mu\gamma^5 q + g_\chi Z'_\mu \bar{\chi}\gamma^\mu\gamma^5\chi \ , \tag{6}$$

actually correspond to some of the above realisations. Indeed $\mathcal{L}_V$ may be motivated by a $U(1)_{BL}$-type model, where g_q parametrizes the overall multiplicative factor to all quarks. If sticking to this motivation, it should be noted that if we want to extend the $\mathcal{L}_V$ model to the lepton sector, a priori the couplings there would be different w.r.t. the quarks (but identical among themselves). In the same fashion, $\mathcal{L}_A$ may be motivated by some E_6 realisations [i] , $U(1)_\psi$ above, where we have only axial couplings. Thus, for $\mathcal{L}_A$, the lepton sector may have identical couplings as the quarks. On the other hand, none of the above simplified models capture the textures of the KM set-up, where the u_L, u_R, d_L, d_R quarks all have different V, A couplings.

It is then very well motivated to look for a SMDM which capture the KM realisation. To recap, there are only 4 unknown parameters: $m_\chi, m_{Z'}, \sin\alpha, g_\chi$, such that the couplings are:

$$\begin{aligned}
g^i_{(V,A)\mathrm{SM}} \sin\alpha \ &: \quad Z' \text{ couplings to fermions} \\
g^i_{(V,A)\mathrm{SM}} \cos\alpha \ &: \quad Z \text{ couplings to fermions} \\
g_\chi \cos\alpha \ &: \quad Z' \text{ couplings to DM} \\
g_\chi \sin\alpha \ &: \quad Z \text{ couplings to DM} \ .
\end{aligned} \tag{7}$$

Adopting such a simple set-up in addition to the other ones already being considered (6) would definitely spam a large class of scenarios beyond SM where a new Z' interacts with the SM via a kinetic-mixing mechanism.

3 An LHC complementarity for SMDM

Here we focus in an s-channel, vector mediator set-up as the one shown in (6). However the following discussion is equally valid for models with scalar mediators. It is evident that such

[g] See [11] for a recent dark matter model whose Z' portal not only have non-universal couplings, but which also allows for flavour-violating couplings.

[h] Note that couplings to quark are universal in these set-ups.

[i] However, contrary to the $U(1)_{BL}$ case where the breaking scale can be a priori any, in the E_6 case one expects the scale to be very high, order E_{GUT} or lager, since this scenario is motivated by string theory.

model will not only contribute to, for example, monojet signals plus missing energy, but also to signatures with two energetic jets or leptons in the final state, without missing energy. Specifically, the searches for resonances in the dilepton [24] [25] or dijet [26] [27] distributions are among the strongest bounds to New Physics.

The key observation here is that the existence of an invisible Z' branching ratio (provided it can decay to DM) weakens the current LHC limits [21]. Indeed at the partonic level the cross section for $\sigma(pp \to Z' \to \bar{f}f)$, having a Breit-Wigner profile:

$$\sigma(pp \to Z' \to \bar{f}f) \approx \frac{1}{12\pi}(|g_V^q|^2 + |g_A^q|^2)(|g_V^f|^2 + |g_A^f|^2)\frac{s}{(s - m_{Z'}^2)^2 + \Gamma_{Z'}^2 m_{Z'}^2} \tag{8}$$

can be re-expressed as:

$$\begin{aligned} \sigma(pp \to Z' \to \bar{f}f) &\approx \frac{1}{12}(|g_V^q|^2 + |g_A^q|^2)(|g_V^f|^2 + |g_A^f|^2) \\ &\times \frac{m_{Z'}}{\Gamma_{Z'}^v}(1 - Br_\chi)\delta(s - m_{Z'}^2) \end{aligned} \tag{9}$$

after approximating the Breit-Wigner by a Dirac delta. Here Br_χ is the branching ratio of Z' to DM and $\Gamma_{Z'}^v$ the total width of Z' to the visible sector. Thus, for given masses and couplings of Z' to the visible sector, the dilepton (or dijet) production cross section diminishes when Br_χ increases.

However, the invisible branching ratio cannot increase arbitrarily. Upper bounds on it are imposed by the LHC itself with mono-signal searches, but also, by Direction Detection, which in the case of spin-independent (SI) DM-nucleon scatterings are particularly strong. Given a value for the SI cross section $\sigma_{\chi N}^{\rm SI}$, for example, taken from the experimental limit for a given DM mass, one can extract un upper bound on the Br_χ as:

$$Br_\chi = \left[1 + \left(\frac{2\mu_{\chi N}}{m_{Z'}^2}\right)^2 \frac{\tilde{c}_F \alpha_{Z,A}^{\rm SI}}{\pi(1+\alpha^2)\sigma_{\chi N}^{\rm SI,exp}}\right]^{-1} \tag{10}$$

where $\alpha_{Z,A}^{\rm SI} \equiv [g_V^u(1+Z/A) + g_V^d(2-Z/A)]^2$ is a function of the charge number Z and mass number A of the nucleus that contains the nucleon; $\mu_{\chi N}$ is the DM-nucleon reduced mass; $\alpha \equiv g_A^\chi / g_V^\chi$ is the ratio of DM axial to vector coupling to Z' and $\tilde{c}_F \equiv \sum_f c_f(|g_V^f|^2 + |g_A^f|^2)$. Of course the experimental limit $\sigma_{\chi N}^{\rm SI,exp}$ will depend on the DM mass. For example, by applying (10) we find that for $m_{Z'} \sim 3$ TeV and pure vector couplings ($\alpha = 0$), the Br_χ can be even 90% if $m_\chi \sim 6$ GeV, but for $m_\chi \sim 40$ GeV which is around the point of maximum sensitivity for LUX [22], Br_χ is constrained to be below 1%.

For that reason it is motivated to combine the two analysis: by how much we can relax the bounds on $m_{Z'}$ from dijets and dileptons, will depend on LUX, if we allow the Z' to couple to the DM. In fig.1-left) we show the specific case of the interplay between LUX and the dilepton bounds coming from the LHC.[j] By assuming a Sequential Model (see previous section), the ATLAS model prediction [24] (which do not assume any coupling to DM) is shown by the black dot-dashed line. The brazilian exclusion band thus forbids Z' masses below 2.7 TeV or so. Now by adding a coupling to DM (i.e. an invisible branching fraction) such a bound can even go down to ~1 TeV, even for DM mass of 50 GeV which and couples mainly axially to the Z'. This is shown by the blue dashed line. Of course if the coupling is mostly vector-like, the LUX searches are much more sensitive even for a lighter mass, and the dilepton bound can only get down to 1.7 TeV or so (solid red line). However, at $m_\chi = 50$ GeV the LUX bound is so strong, that for pure-vector couplings a Z' of ~ 2.7 TeV or less is not allowed to have an appreciable amount of invisible branching ratio, so the ATLAS bound remain unchanged (solid blue line).

[j] See [23] for an alternative study on dijets instead.

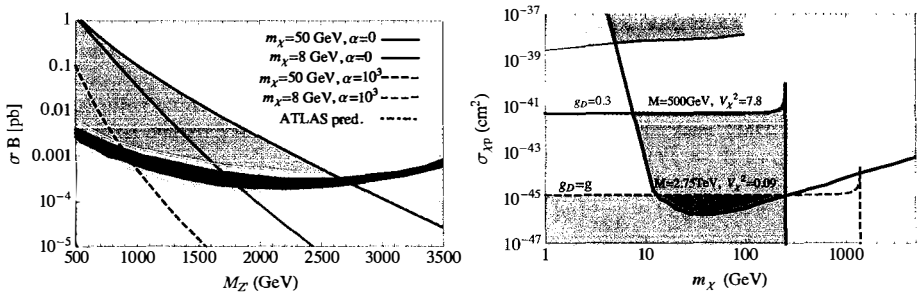

Figure 1 – Left) Dilepton production cross section at the LHC, and limits from resonance searches by ATLAS (brazilian band). The different lines show the bounds on the model for different choices of parameters, according to the LUX experiment. Right) Spin-independent cross section for DM-nucleon scattering. The LUX bound is shown in solid blue, and the monojet bound is shown in red. The black lines correspond to bounds coming from dileptons, for different choices of parameters. In all cases the shaded regions are excluded.

An even more interesting way to see the same effect in shown in fig.1-right. There we put the dilepton searches in the Direct Detection plane, where we compare directly with LUX (blue line) together with the monojet bounds (red). The solid black line corresponds to the exclusion by dilepton, for $m_{Z'} = 500$ GeV and a a dark coupling $g_V^\chi = 0.3 \cdot \sqrt{7.8} = 0.83$. The lower bound comes because for this Z' mass, a smaller Br_χ (leading to a smaller $\sigma_{\chi N}^{\rm SI}$) would render the Z' *too visible* according to the dilepton searches. Of course, for $m_\chi > m_{Z'}/2$ there is no interplay with the dilepton constraint since $Br_\chi = 0$. Also, for a larger Z' mass (as the one in black dashed line) the dilepton constraints are less severe, so the lower limit for $\sigma_{\chi N}^{\rm SI}$ is weaker. See more details at [21].

In any case, it is very interesting to observe how while the monojet and direct detection searches are excluding the parameter space of the model from above, the dilepton searches are excluding it from below. The same remains true for other mono-signals, as compared to dijets, instead of dileptons. The qualitative features of this analysis are also independent of the nature of the mediator, as long as it leads to an s-channel DM-SM portal.

4 Conclusions

We have tried to motivate the implementation of a Simplified Model of Dark Matter which, while being equally "economical" (concerning the number of independent parameters) with respect to the more popular implementations, is able to represent a large class of theoretical scenarios beyond Standard Model which contain an extra $U'(1)$ gauge symmetry, where the corresponding gauge boson kinetically mixes with the SM Z boson.

A posteriori, we have shown that any Simplified Model where the DM communicates to the SM via an s-channel mediator (regardless its nature), will have consequences not only on mono-signal searches, but also di-signal searches, both of them complementing each other. We have illustrated this fact in a particular example where we compare monojets and dileptons searches, together with Direct Detection bounds, in a model where the Z' couples to the Standard Model à la Sequential Model.

This sort of complementarity could be very useful at Run II of the LHC, where the searches for dark matter will play a major role.

Acknowledgments

I thank the organisers of the *Moriond EW 2015* for financial support and the opportunity to present my results, and J. Heeck for useful discussions.

References

1. P. J. Fox, R. Harnik, J. Kopp and Y. Tsai, Phys. Rev. D **84** (2011) 014028 [arXiv:1103.0240 [hep-ph]].
2. M. Buckley, P. Fileviez Perez, D. Hooper and E. Neil, Phys. Lett. B **702** (2011) 256 [arXiv:1104.3145 [hep-ph]].
3. Y. Mambrini and B. Zaldivar, JCAP **1110** (2011) 023 [arXiv:1106.4819 [hep-ph]].
4. G. Aad *et al.* [ATLAS Collaboration], arXiv:1502.01518 [hep-ex].
5. V. Khachatryan *et al.* [CMS Collaboration], arXiv:1408.3583 [hep-ex].
6. G. Aad *et al.* [ATLAS Collaboration], Phys. Rev. D **91** (2015) 1, 012008 [arXiv:1411.1559 [hep-ex]].
7. V. Khachatryan *et al.* [CMS Collaboration], arXiv:1410.8812 [hep-ex].
8. G. Aad *et al.* [ATLAS Collaboration], JHEP **1409** (2014) 037 [arXiv:1407.7494 [hep-ex]].
9. V. Khachatryan *et al.* [CMS Collaboration], arXiv:1408.2745 [hep-ex].
10. G. Busoni, A. De Simone, E. Morgante and A. Riotto, Phys. Lett. B **728** (2014) 412 [arXiv:1307.2253 [hep-ph]].
11. L. Calibbi, A. Crivellin and B. Zaldivar, arXiv:1501.07268 [hep-ph].
12. O. Buchmueller, M. J. Dolan, S. A. Malik and C. McCabe, JHEP **1501** (2015) 037 [arXiv:1407.8257 [hep-ph]].
13. J. Abdallah, A. Ashkenazi, A. Boveia, G. Busoni, A. De Simone, C. Doglioni, A. Efrati and E. Etzion *et al.*, arXiv:1409.2893 [hep-ph].
14. L. Calibbi, A. Mariotti and P. Tziveloglou, arXiv:1505.03867 [hep-ph].
15. N. Daci, I. De Bruyn, S. Lowette, M. H. G. Tytgat and B. Zaldivar, arXiv:1503.05505 [hep-ph].
16. P. Langacker, Rev. Mod. Phys. **81** (2009) 1199 [arXiv:0801.1345 [hep-ph]].
17. A. Crivellin, G. DAmbrosio and J. Heeck, Phys. Rev. Lett. **114** (2015) 151801 [arXiv:1501.00993 [hep-ph]].
18. R. Aaij *et al.* [LHCb Collaboration], Phys. Rev. Lett. **111** (2013) 191801 [arXiv:1308.1707 [hep-ex]].
19. E. Salvioni, G. Villadoro and F. Zwirner, JHEP **0911** (2009) 068 [arXiv:0909.1320 [hep-ph]].
20. G. Aad *et al.* [ATLAS Collaboration], Phys. Rev. D **90** (2014) 5, 052005 [arXiv:1405.4123 [hep-ex]].
21. G. Arcadi, Y. Mambrini, M. H. G. Tytgat and B. Zaldivar, JHEP **1403** (2014) 134 [arXiv:1401.0221 [hep-ph]].
22. D. S. Akerib *et al.* [LUX Collaboration], Phys. Rev. Lett. **112** (2014) 091303 [arXiv:1310.8214 [astro-ph.CO]].
23. A. Alves, S. Profumo and F. S. Queiroz, JHEP **1404** (2014) 063 [arXiv:1312.5281 [hep-ph]].
24. G. Aad *et al.* [ATLAS Collaboration], JHEP **1211** (2012) 138 [arXiv:1209.2535 [hep-ex]].
25. S. Chatrchyan *et al.* [CMS Collaboration], Phys. Lett. B **720** (2013) 63 [arXiv:1212.6175 [hep-ex]].
26. G. Aad *et al.* [ATLAS Collaboration], JHEP **1301** (2013) 029 [arXiv:1210.1718 [hep-ex]].
27. S. Chatrchyan *et al.* [CMS Collaboration], Phys. Rev. D **87** (2013) 11, 114015 [arXiv:1302.4794 [hep-ex]].

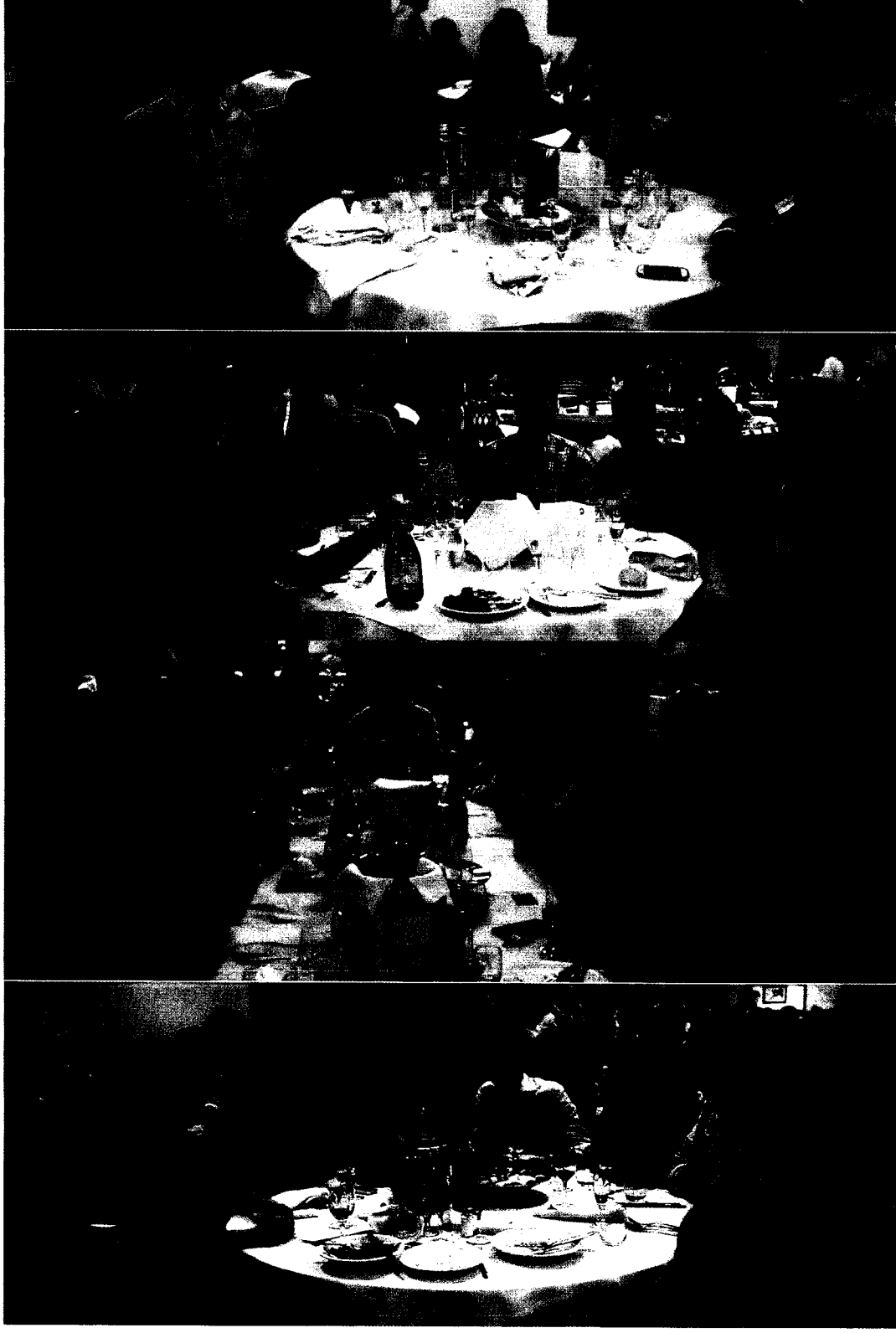

6.
Neutrino Physics

STATUS OF THREE-NEUTRINO MIXING

F. Capozzi[1,2], G.L. Fogli[1,2], E. Lisi[2,a], A. Marrone[1,2], D. Montanino[3,4] and A. Palazzo[5]
[1] *Dipartimento Interateneo di Fisica, Via Amendola 173, 70126 Bari, Italy*
[2] *Istituto Nazionale di Fisica Nucleare, Sezione di Bari, Via Orabona 4, 70126 Bari, Italy*
[3] *Dipartimento di Matematica e Fisica, Via Arnesano, 73100 Lecce, Italy*
[4] *Istituto Nazionale di Fisica Nucleare, Sez. di Lecce, Via Arnesano, 73100 Lecce, Italy*
[5] *Max-Planck-Institut für Physik, Föhringer Ring 6, 80805 München, Germany*

Neutrino oscillation searches using a variety of sources (solar, atmospheric, accelerator and reactor neutrinos) have established a standard three-neutrino (3ν) mass-mixing framework and five of its parameters: the two squared mass gaps (δm^2, Δm^2) and the three mixing angles (θ_{12}, θ_{13}, θ_{23}). At present, a single class of experiments dominates each of these parameters, while only combined analyses of various (eventually all) data sets are needed to constrain the still unknown mass hierarchy [sign(Δm^2)], θ_{23} octant and CP-violating phase δ. We review the status of the known and unknown parameters (as emerging from a global analysis of the oscillation data), investigate the correlations and stability of the such parameters within different combinations of data sets, and discuss the near-term prospects in this field.

1 Prologue

Since the discovery of atmospheric ν oscillations in 1998, a new paradigm — the 3ν mass-mixing framework — has emerged in particle physics [1]. Indeed, the vast majority of ν oscillation data can be explained by assuming that the three known flavor states $\nu_\alpha = (\nu_e, \nu_\mu, \nu_\tau)$ are mixed with three massive states $\nu_i = (\nu_1, \nu_3, \nu_3)$ via three mixing angles $(\theta_{12}, \theta_{13}, \theta_{23})$ and a possible CP-violating phase δ. Oscillations are driven by two independent differences between the squared masses m_i^2, which can be defined as $\delta m^2 = m_2^2 - m_1^2 > 0$ and $\Delta m^2 = m_3^2 - (m_1^2 + m_2^2)/2$, where $\Delta m^2 > 0$ and < 0 correspond to normal (NH) and inverted (IH) hierarchy, respectively [2].

At present, five of the above 3ν oscillation parameters have been measured, with an accuracy largely dominated by a specific class of experiments, namely: θ_{12} by solar data [3], θ_{13} by short-baseline (SBL) reactor data [4], θ_{23} by atmospheric data [1,5], mainly from Super-Kamiokande (SK) [6], δm^2 by long-baseline reactor data from KamLAND (KL) [1], and Δm^2 by long-baseline (LBL) accelerator data [1], mainly from MINOS and T2K [7]. However, the mass hierarchy, the θ_{23} octant, and the CP-violating phase δ are still unknown and will be addresses by future experiments [1,8].

[a] Speaker. Email: eligio.lisi@ba.infn.it

In this context, global neutrino data analyses may be useful to assess the overall consistency and accuracy of the known parameters, as well as to squeeze possible hints about the unknown ones. In the following, we report and discuss the results of a recent global analysis which include data available at the time of this Conference [2]. The reader is referred to Ref. [2] for further details and references not reported herein.

It should be noted that, in the 3ν framework, there are other unknowns not accessible to oscillation experiments, namely: the absolute neutrino mass scale (possibly from cosmology) [9], the Dirac or Majorana nature of the neutrino fields [10,11,12] and, in the latter case, the associated Majorana phases [1]. Current constraints and prospects on these unknowns, which are crucial for theoretical model building [13], will also be briefly commented below. Finally, it should be mentioned that some controversial results (not discussed herein) might indicate possible extensions of the above 3ν framework in terms of one or more additional mass states ν_j ($j \geq 4$), mostly sterile and with mass gaps at the (sub)eV scale. The reader is referred to Refs. [6,14] for up-to-date discussions of the sterile neutrino phenomenology.

2 Methodology of global ν data analysis

In this Section we briefly discuss the various data sets and their combination in global fits.

LBL Acc. + Solar + KL data. The oscillation phenomenology of LBL accelerator experiments is dominated by the oscillation parameters (Δm^2, θ_{23}) in the $\nu_\mu \to \nu_\mu$ disappearance channel, supplemented by θ_{13} in the $\nu_\mu \to \nu_e$ appearance channel. However, the current accuracy of MINOS and T2K data requires that the oscillation probability is precisely calculated in terms of all the input parameters, including matter effects and subdominant terms driven by (δm^2, θ_{12}, δ). Since (δm^2, θ_{12}) are essentially fixed by the Solar and KL experiments, it makes sense to combine these data with LBL accelerator data from the very beginning. We remark that "Solar + KL" data provide a preference for $\sin^2\theta_{13} \sim 0.02$ in our analysis [2], which plays a role in the combination "LBL Acc. + Solar + KL," as discussed below.

Adding SBL reactor data. After the recent T2K observation of electron flavor appearance [7], the combination of LBL Acc. + Solar + KL data can provide a highly significant measurement of θ_{13} which, however, depends on the unknown CP violating phase δ and θ_{23} octant. SBL reactor experiments (Daya Bay, RENO, Double Chooz) provide (δ, θ_{23})-independent and accurate measurements of θ_{13} [4], which play a crucial role in the "LBL Acc. + Solar + KL + SBL Reac." combination.

Adding atmospheric neutrino data. Atmospheric data involve a very rich oscillation phenomenology in both appearance and disappearance modes involving ν_μ and ν_e. In principle, the high-statistics Super-Kamiokande experiment (phases I-IV) is thus sensitive to subleading effects related to the mass hierarchy, the θ_{23} octant and the CP phase δ; however, within the current experimental and theoretical systematic uncertainties, it remains difficult to disentangle and probe such small effects at a level exceeding $\sim 1\sigma$–2σ [8]. Moreover, different and independent analyses of SK data, at comparable levels of refinement, do not necessarily provide similar hints about subleading effects. Therefore, we prefer to add these data only in the final "LBL Acc. + Solar + KL + SBL Reac. + SK Atm." combination, in order to separately gauge their effects on the various 3ν parameters.

Conventions for allowed regions. The data are compared to theoretical expectations via a refined χ^2 function which accounts for all known sources of correlated and uncorrelated uncertainties. In each of the above combined data analyses, the six oscillation parameters (Δm^2, δm^2, θ_{12}, θ_{13}, θ_{23}) are unconstrained in any given hierarchy (normal or inverted). Parameter ranges at N standard deviations are defined as $N\sigma = \sqrt{(\chi^2 - \chi^2_{\rm min})}$. This definition holds also in two-dimensional plots, where it is understood that the previous $N\sigma$ ranges are reproduced by projecting 2D contours over one parameter axis. All undisplayed parameters are marginalized away. Finally, the relative preference of the data for either NH or IH is measured

by the quantity $\Delta\chi^2_{\rm I-N} = \chi^2_{\rm min}({\rm IH}) - \chi^2_{\rm min}({\rm NH})$, with the caveat that it cannot immediately be translated into "$N\sigma$" by taking the square root of its absolute value, because it refers to two discrete hypotheses.

3 Constraints on single parameters

In this Section we graphically report the results of our global analysis of increasingly rich data sets, grouped in accordance to the previous discussion, in terms of single oscillation parameters.

Figures 1, 2 and 3 show the $N\sigma$ curves for the data sets defined in the previous section. In each figure, the solid (dashed) curves refer to NH (IH); the two curves basically coincide for the δm^2 and θ_{12} parameters, since they are determined by Solar+KL data which are largely insensitive to the hierarchy. For each parameter in Figs. 1–3, the more linear and symmetrical are the curves, the more gaussian is the associated probability distribution.

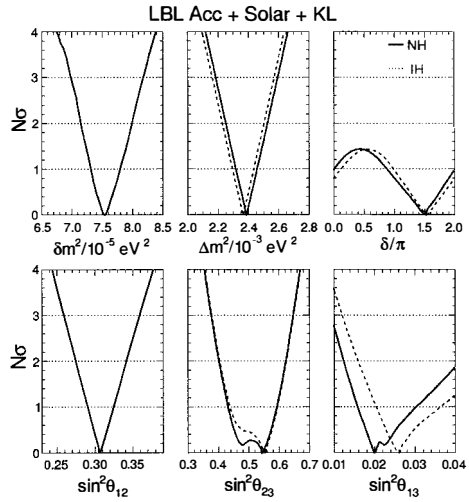

Figure 1 – Combined 3ν analysis of LBL Acc. + Solar + KL data: Bounds on the oscillation parameters in terms of standard deviations $N\sigma$ from the best fit. Solid (dashed) lines refer to NH (IH). The horizontal dotted lines mark the 1σ, 2σ and 3σ levels for each parameter.

Figure 1 refers to the combination LBL Acc. + Solar + KL which, by itself, sets highly significant lower and upper bounds on all the oscillation parameters but δ. In this figure, the relatively strong appearance signal in T2K dominates the lower bound on θ_{13}, and also drives the slight but intriguing preference for $\delta \simeq 1.5\pi$: indeed, for $\sin\delta \sim -1$, the CP-odd term in the $\nu_\mu \to \nu_e$ appearance probability is maximized. It should be noted that current MINOS appearance data generally prefer $\sin\delta > 0$ [2]; however, the stronger T2K appearance signal largely dominates in the global fit. On the other hand, MINOS disappearance data drive the slight preference for nonmaximal θ_{23}, as compared with nearly maximal θ_{23} in T2K[7]. The (even slighter) preference for the second θ_{23} octant is due to the interplay of LBL accelerator and Solar + KL data, as discussed in the next Section.

Figure 2 shows the results obtained by adding the SBL reactor data, which strongly reduce the θ_{13} uncertainty. Further effects of these data include: (*i*) a slightly more pronounced preference for $\delta \simeq 1.5\pi$ and $\sin\delta < 0$, and (*ii*) a swap of the preferred θ_{23} octant with the hierarchy ($\theta_{23} < \pi/4$ in NH and $\theta_{23} > \pi/4$ in IH). These features will be interpreted in terms of parameter covariances in the next Section.

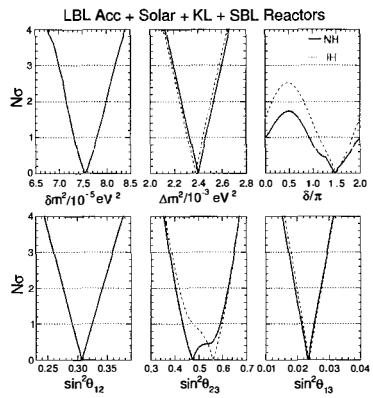

Figure 2 – As in Fig. 1, but adding SBL reactor data in the fit.

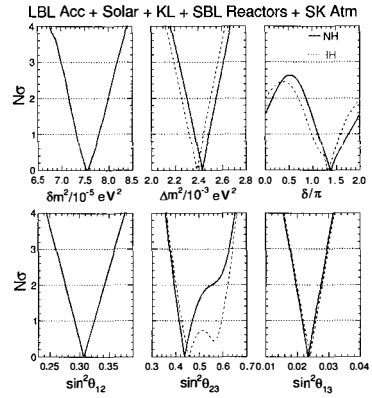

Figure 3 – As in Fig. 2, but adding SK atm. data (global fit to all ν data).

Figure 3 shows the results obtained by adding the SK atmospheric data, thus obtaining the most complete data set. The main differences with respect to Fig. 2 include: (*i*) an even more pronounced preference for $\sin\delta < 0$, with a slightly lower best fit at $\delta \simeq 1.4\pi$; (*ii*) a slight reduction of the errors on Δm^2 and a relatively larger variation of its best-fit value with the hierarchy; (*iii*) a preference for θ_{23} in the first octant for both NH and IH, which is a persisting feature of our analyses. The effects (*ii*) and (*iii*) show that atmospheric neutrino data have the potential to probe subleading hierarchy effects [8], although they do not yet emerge in a stable or significant way.

In Figs. 1–3, an intriguing feature is the increasingly pronounced preference for nonzero CP violation with increasingly rich data sets, although the two CP-conserving cases ($\delta = 0,\ \pi$) remain allowed at $< 2\sigma$ in both NH and IH, even when all data are combined (see Fig. 3). It is worth noticing that the two maximally CP-violating cases ($\sin\delta = \pm 1$) have opposite likelihood: while the range around $\delta \sim 1.5\pi$ ($\sin\delta \sim -1$) is consistently preferred, small ranges around $\delta \sim 0.5\pi$ ($\sin\delta \sim +1$) appear to be disfavored (at $> 2\sigma$ in Fig. 3), In the next few years, the appearance channel in LBL accelerator experiments will provide crucial data to investigate these hints about ν CP violation [2], with relevant implications for models of leptogenesis.

From the comparison of Figs. 1–3 one can also notice a generic preference for nonmaximal mixing ($\theta_{23} \neq 0$), although it appears to be weaker than in our past analyses, essentially because the most recent T2K data prefer nearly maximal mixing, and thus "dilute" the opposite preference coming from MINOS and atmospheric data. Moreover, the indications about the octant appear to be somewhat unstable in different combinations of data. In the present analysis, only atmospheric data consistently prefer the first octant in both hierarchies, but the overall significance remains at the level $\sim 2\sigma$ in NH and is much lower in IH. These fluctuations show how difficult it is to reduce the allowed range of θ_{23}. In this context, the disappearance channel in LBL accelerator experiments will provide crucial data to address the issue of nonmaximal θ_{23} in the next few years.

Finally, we comment on the size of $\Delta\chi^2_{\mathrm{I-N}}$ which, by construction, is not apparent in Figs. 1–3. We find $\Delta\chi^2_{\mathrm{I-N}} = -1.3,\ -1.4,\ +0.3$, for the data sets in Figs. 1, 2, and 3, respectively. Unfortunately, such values are both small and with unstable sign, and do not provide us with any relevant indication about the hierarchy.

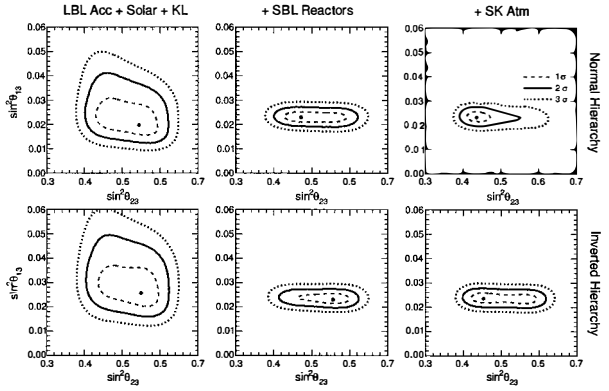

Figure 4 – Results of the analysis in the plane charted by ($\sin^2\theta_{23}$, $\sin^2\theta_{13}$), all other parameters being marginalized away. From left to right, the regions allowed at 1, 2 and 3σ refer to increasingly rich datasets: LBL accelerator + solar + KamLAND data (left panels), plus SBL reactor data (middle panels), plus SK atmospheric data (right panels). Best fits are marked by dots. The three upper (lower) panels refer to normal (inverted) hierarchy.

4 Covariances of pairs of parameters

In this Section we show the allowed regions for selected couples of oscillation parameters, and discuss some interesting correlations.

Figure 4 shows the allowed regions in the plane ($\sin^2\theta_{23}$, $\sin^2\theta_{13}$). From left to right, the panels refer to increasingly rich data sets, while upper and lower panels refer to NH and IH, respectively. In the left panels, a slight negative correlation emerges from LBL appearance data, since the dominant oscillation amplitude contains a factor $\sin^2\theta_{23}\sin^2\theta_{13}$. The contours extend towards relatively large values of θ_{13}, especially in IH, in order to accommodate the relatively strong T2K appearance signal. However, solar + KL data provide independent (although weaker) constraints on θ_{13} and, in particular, prefer $\sin^2\theta_{13} \sim 0.02$ in our analysis. This value is on the "low side" of the allowed regions and is thus responsible for the relatively high value of θ_{23} at best fit, namely, for the second-octant preference in both NH and IH.

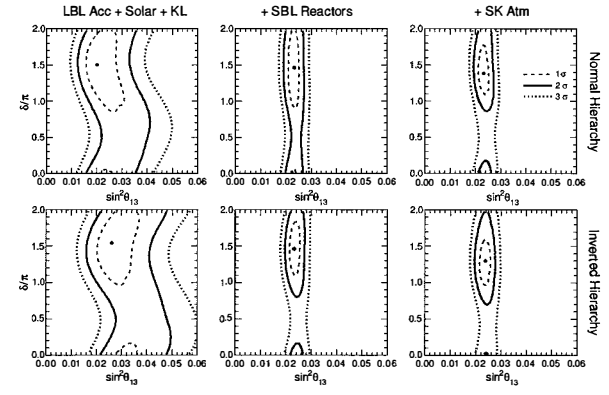

Figure 5 – As in Fig. 4, but in the plane ($\sin^2\theta_{13}$, δ/π).

However, when current SBL reactor data are included in the middle panels, a slightly higher value of θ_{13} ($\sin^2\theta_{13} \simeq 0.023$) is preferred with very small uncertainties: this value is high enough to shift the best-fit of θ_{23} from the second to the first octant in NH, but not in IH. Finally, the inclusion of SK atmospheric data (right panels) provides in our analysis an overall preference for the first octant, which is however quite weak in IH. Unfortunately, as previously mentioned, the current hints about the θ_{23} octant do not appear to be particularly stable or convergent.

Figure 5 shows the allowed regions in the plane ($\sin^2\theta_{13}$, δ/π), which is at the focus of current research in neutrino physics. In the left panels there is a remarkable preference for $\delta \sim 1.5\pi$, where a compromise is reached between the relatively high θ_{13} values preferred by the T2K appearance signal, and the relatively low value preferred by solar + KL data. In the middle panel, SBL reactor data strengthen this trend by reducing the covariance between θ_{13} and δ. Clearly, we can still learn much from the combination of accelerator and reactor data in the next few years. Finally, the inclusion of SK atmospheric data in the right panels also adds some statistical significance to this trend, with a slight lowering of the best-fit value of δ.

5 Absolute mass observables

In general, absolute neutrino masses can be probed via three main methods. The first, classical one is provided by β decay, sensitive to the so-called "effective electron neutrino mass" m_β [1],

$$m_\beta = \left[\sum_i |U_{ei}|^2 m_i^2\right]^{\frac{1}{2}} = \left[c_{13}^2 c_{12}^2 m_1^2 + c_{13}^2 s_{12}^2 m_2^2 + s_{13}^2 m_3^2\right]^{\frac{1}{2}} \ . \tag{1}$$

The second observable — if neutrinos are Majorana spinors — is the effective "Majorana neutrino mass" $m_{\beta\beta}$ in $0\nu\beta\beta$ decay [10,11],

$$m_{\beta\beta} = \left|\sum_i U_{ei}^2 m_i\right| = \left|c_{13}^2 c_{12}^2 m_1 + c_{13}^2 s_{12}^2 m_2 e^{i\phi_2} + s_{13}^2 m_3 e^{i\phi_3}\right| \ , \tag{2}$$

where $\phi_{2,3}$ are additional unknown parameters (Majorana phases). Note that nuclear uncertainties might complicate the interpretation of possible future $0\nu\beta\beta$ signals [12]. The third observable is the sum of neutrino masses in standard cosmology [9]:

$$\Sigma = m_1 + m_2 + m_3 \ . \tag{3}$$

The oscillation constraints reported in the previous Section induce strong correlations among the above three main observables.

Figure 6 shows such correlations in terms of 2σ constraints (bands) in the planes charted by any couple of the absolute mass observables. Note that the bands in the (m_β, Σ) plane of Fig. 6 are quite narrow, due to the high accuracy reached in the determination of all the oscillation parameters. In principle, precise measurements of (m_β, Σ) in the sub-eV range (where the bands for NH and IH branch out) could determine the hierarchy. In the two lower panels of Fig. 6, there remains a large vertical spread in the allowed slanted bands, as a result of the unknown Majorana phases in $m_{\beta\beta}$, which may interfere either constructively (upper part of each band) or destructively (lower part of each band). In principle, precise data in either the ($m_{\beta\beta}$, m_β) plane or the ($m_{\beta\beta}$, Σ) plane might thus provide constraints on the Majorana phases.

At present, there are only safe upper bounds on these absolute mass parameters, at the eV level for m_β [1], and in the sub-eV range for $m_{\beta\beta}$ [10,11] and Σ [9]. A great experimental activity is in progress towards mass sensitivity goals of $O(\sqrt{\Delta m^2})$, at least via $0\nu\beta\beta$ and cosmological probes. Sensitivities of $O(\sqrt{\delta m^2})$ in $0\nu\beta\beta$ decay appear to be extremely challenging at present.

In the most optimistic scenario, the absolute neutrino masses might be all around 0.1–0.2 eV, and thus observable in the next few years through measurements of at least two among

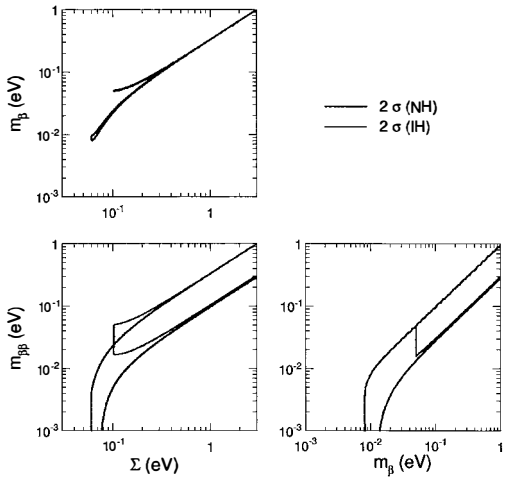

Figure 6 – Constraints induced by oscillation data (at 2σ level) in the planes charted by any two among the absolute mass observables m_β (effective electron neutrino mass), $m_{\beta\beta}$ (effective Majorana mass), and Σ (sum of neutrino masses). Blue (red) bands refer to normal (inverted) hierarchy.

the three (m_β, $m_{\beta\beta}$, Σ) parameters. Then, the concordance of two or three of these observables with the oscillation bands in Fig. 6 woul provide a fundamental cross-check of the standard framework with three massive and mixed neutrinos. If concordance is not achieved (e.g., if strong cosmological limits on Σ are not compatible with possible signals of $m_{\beta\beta} > 0$ within the bands of Fig. 6, or viceversa), the situation would become even more interesting from a phenomenological viewpoint. In this case, data might suggest modifications of the standard framework either in cosmology (e.g., adopting suitable variants of the concordance cosmological model) or in neutrino physics (e.g., exploring nonstandard mechanisms for $0\nu\beta\beta$ decay—a topic witnessing renewed interest). Conversely, the lack of a signal in any of the observables (m_β, $m_{\beta\beta}$, Σ) in the next few years would make the perspectives for the neutrino mass quest extremely challenging.

6 Epilogue

In the light of recent results coming from reactor and accelerator experiments, and of their interplay with solar and atmospheric data, we have updated the estimated $N\sigma$ ranges of the known 3ν parameters (Δm^2, δm^2, θ_{12}, θ_{13}, θ_{23}), and we have revisited the status of the current unknowns [sign(Δm^2), sign($\theta_{23} - \pi/4$), δ]. The results of the global analysis of all data [2] are shown in Fig. 3 in terms of single parameters. One can appreciate the high accuracy reached in the determination of the known oscillation parameters.

We have also discussed in some detail the status of the unknown parameters. Concerning the hierarchy [sign(Δm^2)], we find no significant difference between normal and inverted mass ordering. However, assuming normal hierarchy, we find possible hints about the other two unknowns, namely: a slight preference for the first θ_{23} octant, and possible indications for nonzero CP violation (with $\sin\delta < 0$), although at a level below $\sim 2\sigma$ in both cases. The second hint appears also in inverted hierarchy, but with even lower statistical significance.

In order to understand how the various constraints and hints emerge from the analysis, and to appreciate their (in)stability, we have considered increasingly rich data sets, starting from the combination of LBL accelerator plus solar plus KamLAND data, then adding SBL reactor data, and finally including atmospheric data. We have discussed the fit results both on

single parameters and on selected couples of correlated parameters. It turns out that the hints about the θ_{23} octant appear somewhat unstable at present, while those about δ (despite being statistically weaker) seem to arise from an intriguing convergence of several pieces of data.

Finally, we have discussed the implication of such results for the three observables sensitive to absolute neutrino masses via single- and double-beta decay and cosmology. In general, global analyses of oscillation and non oscillation data appear to provide valuable tools to gauge the overall consistency of the data in a given framework (assumed to be standard 3ν mixing herein). Further experimental data might either confirm the 3ν framework and fix its remaining unknowns (possible CP violation, θ_{23} octant, absolute masses and their ordering, Dirac versus Majorana nature, and Majorana phases in the latter case), or find interesting discrepancies which would require new physics beyond the three known neutrino states and their standard interactions.

In the near or medium term, there are interesting plans to address the hierarchy issue via medium-baseline reactor experiments capable to observe the interference between δm^2 and $\pm\Delta m^2$. Double beta decay searches will also contribute to test the (more favorable) inverted hierarchy range for $m_{\beta\beta}$. Cosmology has, in principle, good chances to test the absolute neutrino mass scale in the near future, if systematics are kept under control. Current long baseline accelerator experiments will probably improve the current indications on the θ_{23} octant and on the favored δ range, but with a significance exceeding $\sim 2\sigma$ only in the most favorable cases. In the far future, more powerful accelerator searches are being planned to get indications at higher confidence levels, especially for CP violation and mass hierarchy; in this context, large-volume atmospheric neutrino detectors may also provide important probes of matter effects, mass hierarchy and θ_{23}. Of course, such expectations and the current planning of near- and far-future projects might be significantly altered by unexpected discoveries, e.g., of new neutrino states or new interactions, which might emerge at any time in this surprising and vibrant field of research.

Acknowledgments

E.L. is grateful to the organizers for their kind invitation and hospitality in La Thuile. This work is supported in part through the Theoretical Astroparticle Physics Research Programs by the Italian Istituto Nucleare di Fisica Nucleare (INFN TAsP Initiative) and Ministero dell'Istruzione, Università e Ricerca (MIUR PRIN Project).

References

1. K.A. Olive et al. (Particle Data Group), Chin. Phys. C **38**, 090001 (2014). See the review therein: "Neutrino mass, mixing and oscillations," by K. Nakamura and S.T. Petcov.
2. F. Capozzi, G. L. Fogli, E. Lisi, A. Marrone, D. Montanino and A. Palazzo, Phys. Rev. D **89**, 093018 (2014).
3. B. Caccianiga, talk at this Conference.
4. R. Carr and B.-Z. Hu, talks at this Conference.
5. J.P. Yanez, talk at this Conference.
6. D.S. Mine, talk at this Conference.
7. J. Myslik, talk at this Conference.
8. S. Choubey, talk at this Conference.
9. S. Henrot-Versille, talk at this Conference.
10. T. Johnson, talk at this Conference.
11. A. Gando, talk at this Conference.
12. P.K. Raina, talk at this Conference.
13. D.A. Ariche, J. Lopez-Pavon, J. Heeck, talks at this Conference.
14. A. Hayes and N. Saviano, talks at this Conference.

Recent Results from Daya Bay Reactor Neutrino Experiment

B. Z. HU
on behalf of the Daya Bay collaboration
Department of Physics, National Taiwan University,
No. 1, Sec. 4, Roosevelt Rd., Taipei 10617, Taiwan

The Daya Bay reactor neutrino experiment announced the discovery of a non-zero value of $\sin^2 2\theta_{13}$ with significance better than 5σ in 2012. The experiment is continuing to improve the precision of $\sin^2 2\theta_{13}$ and explore other physics topics. In this talk, I will show the current oscillation and mass-squared difference results which are based on the combined analysis of the measured rates and energy spectra of antineutrino events, an independent measurement of θ_{13} using IBD events where delayed neutrons are captured on hydrogens, and a search for light sterile neutrinos.

1 Introduction

The neutrino flavor eigenstates are linear combinations of the mass eigenstates, given as

$$|\nu_\alpha\rangle = \sum_{i=1}^{3} U^*_{\alpha,i} |\nu_i\rangle, \tag{1}$$

where α represents the neutrino flavors, e, μ and τ, i represents the mass states, and $U_{\alpha i}$ is the unitary matrix known as the Pontecorvo-Maki-Nakagawa-Sakata (PMNS) mixing matrix,

$$U_{PMNS} = \begin{pmatrix} 1 & 0 & 0 \\ 0 & C_{23} & S_{23} \\ 0 & -S_{23} & C_{23} \end{pmatrix} \begin{pmatrix} C_{13} & 0 & e^{-i\delta} S_{13} \\ 0 & 1 & 0 \\ -e^{i\delta} S_{13} & 0 & C_{13} \end{pmatrix} \begin{pmatrix} C_{12} & S_{12} & 0 \\ -S_{12} & C_{12} & 0 \\ 0 & 0 & 1 \end{pmatrix},$$

where C_{ij} is $\cos\theta_{ij}$, S_{ij} is $\sin\theta_{ij}$ and δ is the CP violating phase. In 2012, the Daya Bay collaboration has published the first non-zero results with a significance of 5.2 standard deviations by using the data from the period with six antineutrino detectors [1, 2].

For electron antineutrinos with energy E traveling a distance L in vacuum, the survival probability is given by

$$P(\overline{\nu}_e \to \overline{\nu}_e) = 1 - \sin^2 2\theta_{13} \sin^2 \left(\frac{\Delta m^2_{ee} L}{4E}\right) - \cos^4 \theta_{13} \sin^2 2\theta_{12} \sin^2 \left(\frac{\Delta m^2_{21} L}{4E}\right), \tag{2}$$

where

$$\sin^2\left(\frac{\Delta m^2_{ee}L}{4E}\right) \equiv \cos^2\theta_{12}\sin^2\left(\frac{\Delta m^2_{31}L}{4E}\right) + \sin^2\theta_{12}\sin^2\left(\frac{\Delta m^2_{32}L}{4E}\right) \quad (3)$$

and

$$\Delta m^2_{ij} \equiv m^2_i - m^2_j. \quad (4)$$

Using $\Delta m^2_{32} = \Delta m^2_{31} = 2.32 \times 10^{-3}\text{eV}^2$, $\Delta m^2_{21} = 7.59 \times 10^{-5}\text{eV}^2$ and $\sin^2 2\theta_{12} = 0.861^{+0.026}_{-0.022}$ [3, 4], the distance L for the first minimum of $P(\bar{\nu}_e \to \bar{\nu}_e)$ for reactor antineutrinos is ~1.6 km. The value of θ_{13} can be determined from the observed deficit of antineutrino flux detected via the inverse beta decay.

To have a precise measurement of θ_{13}, it requires an optimized baseline, high statistics, and low systematic uncertainties and low backgrounds. For the Daya Bay experiment, the far site detectors are near the location of maximum oscillation effect. The Daya Bay power plant has a thermal power of 17.4 GW_{th}, which generate a very high electron antineutrino flux. The target mass for each antineutrino detector is 20 tons in Gd-loaded liquid scintillator region and 20 tons in non-loading liquid scintillator region. The reactor and detector -related systematic errors are reduced by using identically-designed detectors at the near and far sites for a far/near relative measurement.

2 Daya Bay Experiment

The Daya Bay experimental site is located in the southern part of China near Shenzhen city. The Daya Bay nuclear power complex consists of six reactor cores with a total of 17.4 GW_{th} thermal power. There are three underground experimental halls (EHs): two near halls and one far hall. The near-hall detectors measure the neutrino flux from the reactor cores with negligible effect from the mixing angle θ_{13}. The far-hall detectors can measure the neutrino oscillation effect due to θ_{13}. Each near hall contains two antineutrino detectors (ADs) and the far hall contains four ADs [5]. The data taking with 6 ADs started on Dec. 24, 2011, and was paused in the summer of 2012 to install the last two ADs. The data taking has been on-going with 8ADs since October 2012.

2.1 Antineutrino Detector Design

Each of the eight functionally identical antineutrino detectors consists of three zones separated by acrylic vessels. The inner zone is the antineutrino target containing 20 tons of Gadolinium-loaded liquid scintillator (GdLS). The middle zone is the gamma catcher containing 20 tons of liquid scintillator (LS). The outer zone, filled with 40 tons of mineral oil (MO), shields background radiations. There are 192 8" PMTs mounted on eight ladders in each AD. To improve the light collection, there are reflectors on the top and bottom of the outer acrylic vessel. On top of each ACU there are three automatic calibration units (ACUs), each containing three sources, LED, ^{68}Ge and ^{241}Am $-^{13}$ C $+^{60}$ Co. Calibrations are performed once a week.

2.2 Muon Veto System

The muon veto system consists of a water pool instrumented with PMTs as the cherenkov detectors and 4 layers of RPC tracking detectors. The former is composed of the inner water shield (IWS) and outer water shield (OWS), to detect cosmic ray muons and to shield neutrons and gammas from rock. The latter covers the water pool to provide further muon tracking information.

2.3 Detector Response

Many calibration sources (ACU sources, ^{137}Cs, ^{54}Mn, ^{40}K, ^{241}Am $-^{9}$ Be and ^{239}Pu $-^{13}$ C) and environmental sources (^{40}K, ^{208}Tl and n capture on H, C and Fe) were used to measure the energy res-

olution and study the nonlinearity of detector response. The energy resolution is $7.5/\sqrt{E_{vis}/\mathrm{MeV}}$. The nonlinearity of detector response, caused by the liquid scintillator and the readout electroncs characteristics, has a minimal impact on the oscillation angle measurement, but is more relevant for the measurement of the reactor antineutrino mass difference. The energy response model is obtained semi-empirically and is compared with various gamma sources and ^{12}B $\beta-$decay spectrum, as shown in Fig. 1 [6].

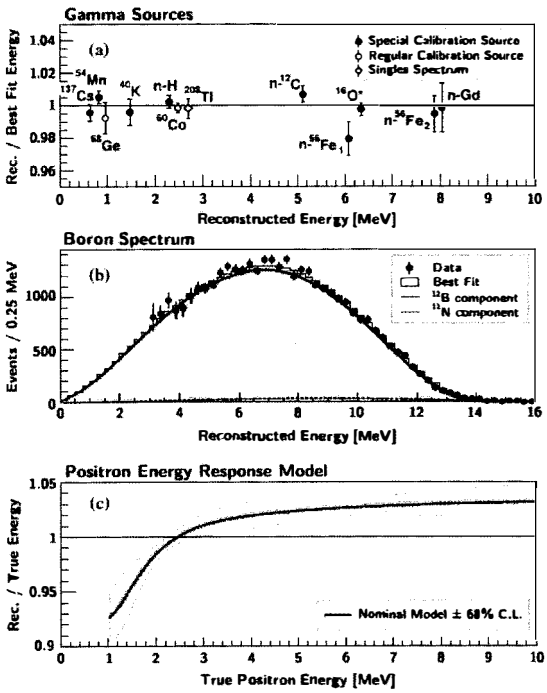

Figure 1 – (a) Ratio of the reconstructed to the best-fit energies of γ lines from calibration source and the singles spectra. (b) Reconstructed energy spectrum (points) compared to the sum (shaded area) of the ^{12}B (solid line) and ^{12}N (dashed line) components of the best-fit energy response model. (c) AD energy response model for positrons.

3 Inverse Beta Decay Event

3.1 Event Selection

Antineutrino events are detected via the inverse beta decay (IBD) process, $\overline{\nu}_e + p \rightarrow e^+ + n$. The positron slows down and annihilates with electron to give a prompt signal. The neutron is thermalized and then captured on Hydrogen (nH) or Gadolinium (nGd) to produce a delayed signal. The delayed signal from the nH capture emits a 2.2 MeV gamma, while the nGd capture produces several gammas with a total energy of ~8 MeV.

The first step for the IBD candidate selection is to remove instrumental background caused by occasional flashing of some PMTs. Muon events are classified into three types, water pool muon (μ_{WP}), AD muon (μ_{AD}) and shower muon (μ_{shower}). The water pool muon events are identified by the number of PMT hits, NHit, in IWS or OWS. If NHits are greater than 12, these events are tagged as water pool muons. Events in AD with energies greater than 20 MeV are classified as AD muons while those with energies greater than 2.5 GeV are classified as shower muons. The non-related events occurring within the time window are rejected. The muon veto time and IBD selection criteria for both nH and nGd analysis are summarized in Table 1.

Table 1: The IBD candidates are selected by the following criteria. For neutron captured on Gadolinium (nGd analysis), $0.7 < E_p < 12.0$ MeV, $6.0 < E_d < 12.0$ MeV, and $1 < \Delta t < 200\mu s$, where E_p (E_d) is the prompt (delayed) energy and $\Delta t = t_d - t_p$ is the time difference between the prompt and delayed signals. For neutron captured on Hydrogen (nH analysis), the prompt energy is between 1.5 and 12.0 MeV, delayed energy is within 3 σ from the peak, and $1 < \Delta t < 400\mu s$. The criteria of distance between prompt and delayed signals, D_{pd}, apply to nH signals.

	nH	nGd
Reject PMT Flashers		
μ_{WP} veto	0.4 μs	0.6 μs
μ_{AD} veto	0.8 μs	1 μs
μ_{shower} veto	1 s	1 s
E_p [MeV]	[1.5, 12]	[0.7,12]
E_d [MeV]	3 σ ($\sigma \sim 0.14$ MeV)	[6,12]
Δt_{pd} [μs]	[1, 400]	[1, 200]
D_{pd} [mm]	500	N/A

3.2 Background Sources

The most important background is accidental background which are from single events and 'accidentally' pass the IBD event selection. The second effective backgrounds are from cosmic ray muons. Muon-induced products, such as fast neutron and ^{9}Li/^{8}He, can mimic IBD as a correlated pair. For the fast neutron case, neutron scattering followed by neutron capture could mimic the IBD event. For the ^{9}Li/^{8}He background, the prompt signals are from the $\beta-$decay and the delayed signals are from neutron capture. The calibration source, AmC, in ACU is another background source.

3.3 Oscillation Parameters from Neutron Captured on Gadolinium Analysis

With 621 days of 6-AD and 8-AD data, 150255 (613813 and 477144) antineutrino candidates with nGd capture were detected in the far site (near sites) detectors. This represents four times higher statistics than previously published results [6].

Current preliminary results have analyzed the spectral information taking into account the nonlinearity correction and various backgrounds discussed earlier. The relative spectral distortion, as shown in Fig. 2 (left), are highly consistent with oscillation interpretation. The best-fit values are $\sin^2 2\theta_{13} = 0.084 \pm 0.005$ and $|\Delta m^2_{ee}| = 2.44^{+0.10}_{-0.11} \times 10^{-3}\text{eV}^2$, as shown in Fig. 2 (right). The precision for θ_{13} is 3 %. Under the assumption of normal (inverted) neutrino mass hierarchy, the results of $|\Delta m^2_{ee}|$ is equivalent to $\Delta m^2_{32} = 2.39^{+0.10}_{-0.11} \times 10^{-3}\text{eV}^2$ ($\Delta m^2_{32} = -2.49^{+0.10}_{-0.11} \times 10^{-3}\text{eV}^2$). These results ate consistent with those from the muon neutrino disappearance experiments [7,8].

4 Recent Results

4.1 Oscillation Parameter from Neutron Captured on Hydrogen Analysis

IBD events can be identified via neutrons captured on Hydrogen signals. In this study, the statistical and the major systematic uncertainties are independent from the previous Gd capture study. Several new techniques were developed to meet the challenges from the higher background and different systematics due to the lower neutron capture energy (2.2 MeV), the longer capture time (200 μs), and the larger energy loss at the detector boundary. With the 217 days of data set from the 6AD period, the rate deficit observed at the far hall is interpreted as $\sin^2 2\theta_{13} = 0.083 \pm 0.018$ with $\chi^2/NDF = 4.6/4$, as shown in Fig. 3. The result has been combined with previous six detectors nGd analysis to give $\sin^2 2\theta_{13} = 0.089 \pm 0.008$ [9]. Current nH analysis with the 8-AD data set is on-going.

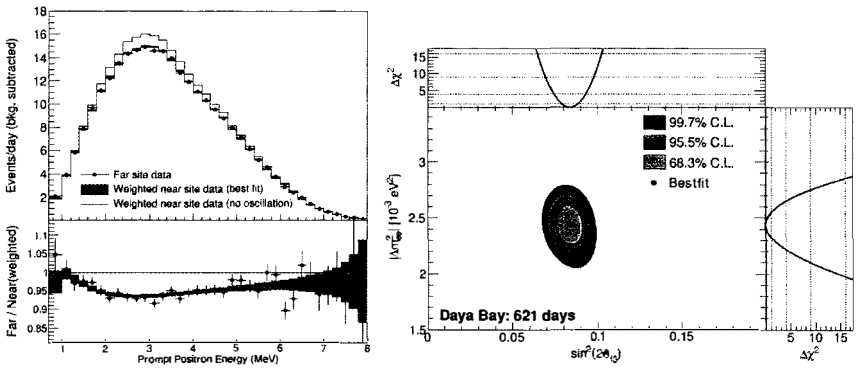

Figure 2 – (Preliminary) Left: the spectrum deficit in the far site. Right: The allowed regions for the neutrino oscillation parameters $\sin^2 2\theta_{13}$ and $|\Delta m^2_{ee}|$ at the 68.3, 95.5 and 99.7% confidence levels. The best estimate of the oscillation parameters are given by the black dot.

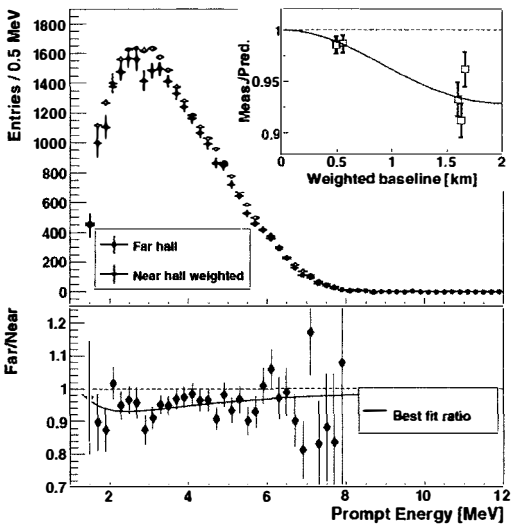

Figure 3 – The detected energy spectrum of the prompt events of the far-hall ADs (blue) and near-hall ADs (open circle) weighted according to baseline. The far-to-near ratio (solid dot) with the best-fit θ_{13} value is shown in the lower plot. In the inset is the ratio of the measured to the predicted rates in each AD vs baseline, in which the AD4 (AD6) baseline was shifted relative to that of AD5 by 30 (-30) m.

4.2 Sterile Neutrino Study

The multiple baselines from six 2.9 GW_{th} nuclear reactors to six antineutrino detectors make it possible to search for light sterile neutrino in the Daya Bay experiment. With the 217 days of data set from the 6AD period, the analysis showed no evidence for sterile neutrino mixing and the most stringent limit was set at $10^{-3}\text{eV}^2 < |\Delta m^2_{41}| < 0.1\text{eV}^2$. Fig. 4 shows the exclusion contours, which were determined using both the Feldman-Cousins method and the CLs method [10].

5 Summary

The Daya Bay experiment has new preliminary measurements with the data set from Dec-24, 2011 to Nov-30, 2013. The results of oscillation parameters from the neutron captured on Gadolinium analysis are $\sin^2 2\theta_{13} = 0.084 \pm 0.005$ and $|\Delta m^2_{ee}| = 2.44^{+0.10}_{-0.11} \times 10^{-3}\text{eV}^2$. This is the most precise measurement of $\sin^2 2\theta_{13}$ to date. The independent neutron captures on Hydrogen rate analysis has measured $\sin^2 2\theta_{13} = 0.083 \pm 0.018$ with $\chi^2/NDF = 4.6/4$. The sterile neutrino search has set

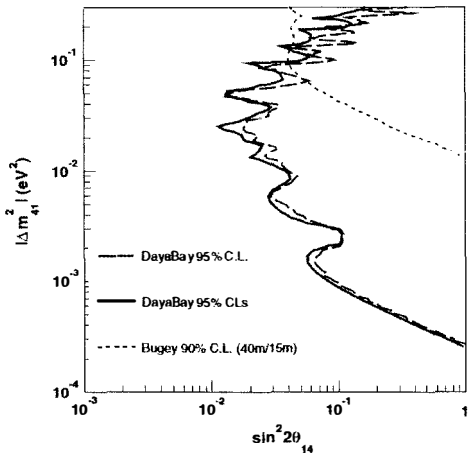

Figure 4 – Exclusion contours for the neutrino oscillation parameters $\sin^2 2\theta_{14}$ and $|\Delta m^2_{41}|$. Normal mass hierarchy is assumed for both $|\Delta m^2_{31}|$ and $|\Delta m^2_{41}|$. The parameter space to the right side of the contours is excluded. The red long-dashed curve represents the 95% C.L. exclusion contour with Feldman-Cousins method. The black solid curve represents the 95% C.L$_s$. exclusion contour. The green dashed curve represents Bugey's 90% C.L. limit on $\bar{\nu}_e$ disappearance.

stringent limits at $10^{-3}\text{eV}^2 < |\Delta m^2_{41}| < 0.1\text{eV}^2$. The data-taking for the Daya Bay experiment is planned to continue to 2017 with eight detectors. The precision of oscillation parameters, $\sin^2 2\theta_{13}$ and $|\Delta m^2_{ee}|$, are expected to reach 3%.

Acknowledgments

Daya Bay is supported in part by the Ministry of Science and Technology of China, the U.S. Department of Energy, the Chinese Academy of Sciences, the National Natural Science Foundation of China, the Guangdong provincial government, the Shenzhen municipal government, the China General Nuclear Power Group, Key Laboratory of Particle Physics and Radiation Imaging (Tsinghua University), the Ministry of Education, Key Laboratory of Particle Physics and Particle Irradiation(Shandong University), the Ministry of Education, Shanghai Laboratory of Particle Physics and Cosmology, the Research Grants Council of the Hong Kong Special Administrative Region of China, the University Development Fund of The University of Hong Kong, the MOE program for Research of Excellence at National Taiwan University, National Chiao-Tung University, and NSC fund support from Taiwan, the U.S. National Science Foundation, the Alfred P. Sloan Foundation, the Ministry of Education, Youth, and Sports of the Czech Republic, the Joint Institute of Nuclear Research in Dubna, Russia, the CNFC-RFBR joint research program, the National Commission of Scientific and Technological Research of Chile, and the Tsinghua University Initiative Scientific Research Program. We acknowledge Yellow River Engineering Consulting Co., Ltd., and China Railway 15th Bureau Group Co., Ltd., for building the underground laboratory. We are grateful for the ongoing cooperation from the China General Nuclear Power Group and China Light and Power Company.

References

1. F. P. An *et al.* [Daya Bay Collaboration], *Phys. Rev. Lett.* **108**, 171803 (2012).
2. F. P. An *et al.* [Daya Bay Collaboration], *Chin. Phys. C* **37**, 011001 (2013).
3. P. Adamson *et al.* [MINOS Collaboration], *Phys. Rev. Lett.* **106**, 181801 (2011).
4. S. Abe *et al.* [KamLAND Collaboration], *Phys. Rev. Lett.* **100**, 221803 (2012).
5. F. P. An *et al.* [Daya Bay Collaboration], *Nucl. Instrum. Methods* A **685**, 78-97 (2012).
6. F. P. An *et al.* [Daya Bay Collaboration], *Phys. Rev. Lett.* **112**, 061801 (2014).
7. P. Adamson *et al.* [MINOS Collaboration], *Phys. Rev. Lett.* **110**, 251801 (2013).
8. K. Abe *et al.* [T2K Collaboration], *Phys. Rev.* D **88**, 032002 (2013)
9. F. P. An *et al.* [Daya Bay Collaboration], *Phys. Rev.* D **90**, 071101 (2014).
10. F. P. An *et al.* [Daya Bay Collaboration], *Phys. Rev. Lett.* **113**, 141802 (2014).

Entering the Two-Detector Phase of the Double Chooz Experiment

Rachel Carr, on behalf of the Double Chooz collaboration
Columbia University; New York, NY 10027, USA

In recent years, observations of electron antineutrino disappearance at nuclear reactor sites have yielded increasingly precise measurements of the neutrino mixing parameter θ_{13}. Two experiments, Daya Bay and RENO, have made such measurements by comparing the antineutrino signal observed approximately 1 km from reactor cores to the essentially unoscillated signal observed in near detectors, a few hundred meters from the cores. Meanwhile, the Double Chooz experiment has produced multiple θ_{13} measurements using only a far detector and reactor flux simulations. Now, as the first months of data are taken with the Double Chooz near detector, the experiment is poised to produce its most precise precise θ_{13} measurements yet. The near detector will also provide rich opportunities to study the reactor antineutrino flux and possible sterile neutrino signatures. This report reviews the latest single-detector analyses from Double Chooz and discusses prospects for the newly inaugurated two-detector phase.

1 Reactor-based measurements of θ_{13}

1.1 Motivation

By 2010, the three-neutrino mixing paradigm had been well established, and many of its parameters had been measured. The magnitudes of the three mass splittings were known, along with two of the three mixing angles. A remaining question was the size third mixing angle, θ_{13}. The CHOOZ experiment indicated this angle was small,[1] but its exact magnitude, including whether it could be distinguished from zero, was not known.

Measuring θ_{13} has important implications for the neutrino sector, and perhaps beyond it. To some extent, the size of this mixing angle sets the difficulty level for determining the neutrino mass hierarchy and measuring the CP-violating phase, δ. More basically, θ_{13} must be nonzero for CP violation to appear in neutrino oscillations. The value of θ_{13} may also provide some insight into the structure of neutrino mixing matrix, which differs dramatically from the analogous CKM matrix in quarks. All of these issues may relate to deeper problems, including the nature of neutrino mass, the baryon asymmetry of the universe, and the origin of flavor.

1.2 Method

The energies and flavor compositions of typical neutrino sources, and the sizes of the relevant mass splittings, present two practical channels for measuring θ_{13}. One is a search for electron neutrino appearance in a muon neutrino beam. The probability of this transition depends on many parameters besides θ_{13}, including both other mixing angles, the sign of Δm^2_{31}, and δ; for sufficiently long baselines, it also involves matter effects. While these dependencies give the $\nu_\mu \to \nu_e$ a broad physics reach, they preclude a straightforward measurement of θ_{13}.

An alternative channel for measuring θ_{13} is the disappearance of electron antineutrinos generated in the beta decays of nuclear fission products. In this context, $\bar{\nu}_e$ survival probability

is a simple expression depending only on θ_{13} and one oscillatory phase. For a $\bar{\nu}_e$ of energy E, traveling a distance L between generation and detection, the survival probability[a] is:

$$P_{\bar{\nu}_e \to \bar{\nu}_e} \approx 1 - \sin^2 2\theta_{13} \sin^2 \left(\frac{\Delta m^2_{31} L}{4E} \right) \quad (1)$$

Given the measured value[2] of $\Delta m^2_{31} \approx 0.0024$ eV^2 and average reactor antineutrino energy of ~ 4 MeV, the first oscillation maximum occurs ~ 2 km from the reactor cores. Therefore, the oscillation probability, and hence $\sin^2 2\theta_{13}$, can be measured by comparing the rate and/or spectral shape of the $\bar{\nu}_e$ signal observed $\sim 1-2$ km from the reactors to the unoscillated flux. The latter may be measured, by observing the $\bar{\nu}_e$ signal a few hundred meters or less from the reactors, or predicted through a reactor simulation. Such simulations depend on semi-empirical calculations of the $\bar{\nu}_e$ emitted by reactors, which have significant normalization and shape uncertainties. Combined with the other uncertainties involved in a reactor flux simulation, these are strong limitations on the precision of single-detector θ_{13} measurements. A near detector, which directly measures the unoscillated reactor antineutrino flux, is required to achieve percent-level precision on $\sin^2 2\theta_{13}$.

2 Double Chooz measurements

2.1 Experiment design

The Double Chooz experiment is located at the Chooz Nuclear Power Plant in the Champagne-Ardenne region of France. The power station hosts two pressurized water reactors, each with a nominal power of 4.25 GW_{th}. The far detector, which began operation in 2011, is located 1050 m from the reactors, in a cavern with 300 m.w.e. overburden. The near detector, which was completed in late 2014, is located 400 m from the reactors, under a 140 m.w.e. overburden.

The detectors were designed to efficiently observe the inverse beta decay (IBD) interaction, $\bar{\nu}_e + p \to e^+ + n$. The positron is detected in liquid scintillator via its ionization track and annihilation, which together deposit $E_{vis} \approx E_\nu - 0.8$ MeV. The neutron is detected when it is absorbed by a nucleus, which then emits at least one gamma ray. The prompt positron signal and delayed neutron capture form a distinct coincidence signature. The detectors are doped with gadolinium to shorten the neutron capture time and increase the energy of the gamma signal, but captures on hydrogen nuclei are also analyzed to enhance statistics.

The near and far detectors are almost identical in design, to maximize cancellation of detector-related uncertainties in a two-detector analysis. Previous Double Chooz publications describe the detector design in detail.[3]

2.2 Single-detector θ_{13} measurements

Double Chooz performed its first oscillation analysis in 2011, becoming the first reactor-based experiment to find evidence for a nonzero value of θ_{13}. Since that time, nearly four times more livetime has been analyzed and many new techniques have been employed. One novel strategy has been searches for IBD interactions followed by neutron captures on hydrogen. The Gd-doped target of the Double Chooz detector has a volume of 10 m^3, while the surrounding vessel of undoped scintillator contains more than twice that volume. Consequently, searching for H signals roughly doubles the potential signal population. Here, we report the most recent Gd- and H-based measurements from the Double Chooz far detector.

The Gd measurement is derived from 467.90 live days, which yield 17,358 IBD candidates. Relative to the previous Gd-based publication,[3] major improvements in this analysis include

[a]This approximation leaves out a θ_{12}-dependent term, which is negligible for reactor antineutrino energies and baselines less than 1 km. In addition, the mass splitting is not exactly Δm^2_{31} but a combination of Δm^2_{31} and Δm^2_{32}.

improved detection efficiency, reduced backgrounds, and a more precise energy scale. Another enhancement is the inclusion of 7.2 live days of data taken when both reactors were shut down. That data helps validate background predictions and serves as a background constraint in oscillation fits.

In this latest Gd analysis, efficiency-related uncertainties contribute a signal normalization uncertainty of 0.6%, while the dominant background, decays of cosmogenic ^{9}Li and ^{8}He, contribute about 1%. The energy scale uncertainty is approximately 0.7%. A signal normalization uncertainty of 1.7%, by far the dominant contribution, comes from reactor flux modeling.

We perform two types of fits to extract $\sin^2 2\theta_{13}$ from the data. The most precise result comes from a rate- and spectrum-shape-based fit which includes the reactor-off data as well as independent background predictions. This Rate+Shape fit yields $\sin^2 2\theta_{13} = 0.090^{+0.032}_{-0.029}$. The second type of fit, which is completely rate-based, exploits the fact that the signal rate scales with reactor power, while the background rate does not. In this fit, data is divided into periods of low reactor power (typically when a single reactor is operating), periods of high reactor power (typically when both are operating), and periods in which both reactors are off. A unique advantage of this Reactor Rate Modulation (RRM) fit is that it does not rely on *a priori* background estimates. For the latest Gd dataset, the RRM fit yields $\sin^2 2\theta_{13} = 0.060 \pm 0.039$. Figures 1 and 2 display the Rate+Shape and RRM fits, respectively. Full details of these analyses have been published.[4]

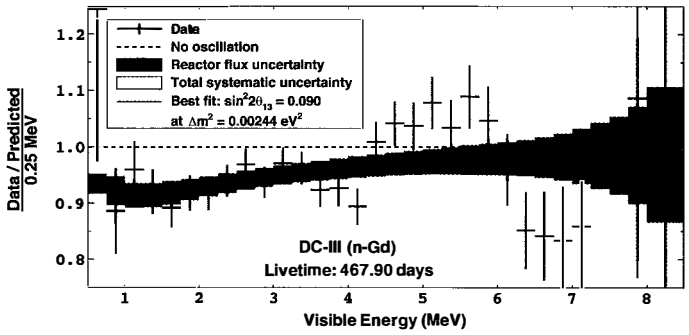

Figure 1 – The ratio of observed, background-subtracted IBD candidates to the no-oscillation prediction (black points with statistical error bars) in the latest Gd-based, Rate+Shape θ_{13} analysis. The red line shows the best fit to the data, with $\sin^2 2\theta_{13} = 0.90$. The dashed blue line shows the ratio expected in the case of no oscillation. The gold band shows the total systematic error in each bin; the green band shows reactor flux uncertainty.

3 Projections for two-detector analyses

An analysis of the H capture channel is underway for the same dataset used in the latest Gd measurement. This new analysis represents a great increase in precision over the first H-based measurement published by Double Chooz.[5] In the previous measurement, a large contamination from accidental coincidences resulted in a signal-to-background ratio of 1:1. A powerful new selection technique, based on an Artifical Neural Network, has increased that ratio by an order of magnitude. Detection efficiency and energy scale systematics have also improved significantly. The results of this analysis, the final single-detector θ_{13} measurement from Double Chooz, will be released in 2015.

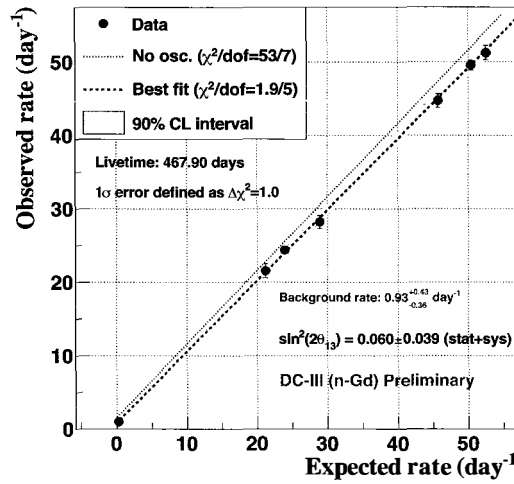

Figure 2 – The rate of observed IBD candidates, as a function of the no-oscillation prediction, for the seven reactor power bins used in the latest Gd-based Reactor Rate Modulation analysis (black points with statistical error bars). The dashed blue line shows the best fit, at $\sin^2 2\theta_{13} = 0.060$, while the gray dashed line corresponds to the no-oscillation hypothesis. The blue region is the 90% CL interval for the fit.

3.1 Additional measurements

In the last year, Double Chooz has also explored physics beyond θ_{13}. One notable result is the event-by-event identification of ortho-Positronium (o-PS) formation.[6] Ortho-Positronium is the singlet bound state of a positron and electron, with a lifetime in liquid scintillator of a few nanoseconds. In some cases, its delayed annihilation can be identified in the PMT pulse profile of positron candidates. This identification allows the collection of a pure positron sample and may have wider applications in liquid scintillator detectors.

Double Chooz also contributed to an unexpected revision in our understanding of the reactor antineutrino flux. In the latest Gd-based oscillation analysis, the spectrum of observed candidates strongly disagreed with expectations in the 4-6 MeV region. This excess is clearly visible in Figure 1. Multiple explanations were tested, including new background contributions, energy scale distortions, and efficiency effects; none of these were compatible with the data. The observation that the excess scaled with reactor power, along with similar distortions in the H-based spectrum and spectrum from the CHOOZ experiment, suggested that a flaw in reactor flux modeling could be the cause.[3] This hypothesis is also supported by observations from Daya Bay and RENO. A resolution, in terms of the underlying reactor or nuclear physics models, is now a subject of interest for researchers in those fields.

3.2 Near detector status

The Double Chooz near detector was completed in December 2014. It began taking data that month. Initial data quality checks show that the spectrum of spallation neutron captures in the near detector is very similar to that in the far detector, demonstrating the near detector's capabilities for IBD detection. The rate of single, uncorrelated events in the near detector is also similar to the far detector rate, indicating the achievement of radiopurity and shielding goals.

3.3 *Two-detector θ_{13} precision*

The near detector will tremendously enhance the θ_{13} precision of the Double Chooz experiment. Figure 3 shows a preliminary projection of future precision. This projection is based on a Rate+Shape fit, assuming the background levels and systematic uncertainties of the Gd-based analysis described in Section 2.2. Further improvements in precision will be possible through the addition of H capture data and continuing reduction of systematic uncertainties.

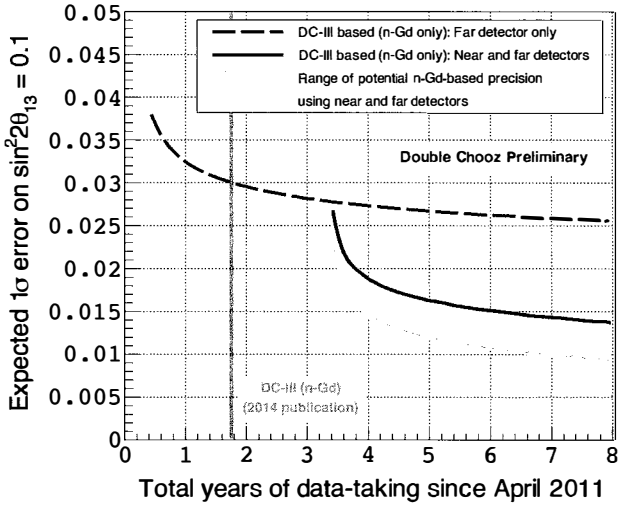

Figure 3 – A projection of the Double Chooz precision in a measurement of $\sin^2 2\theta_{13}$, using only Gd capture data and assuming the same background levels and systematic uncertainties as the latest Gd-based analysis. The vertical axis is the expected 1σ uncertainty on a measurement of $\sin^2 2\theta_{13} = 0.1$. The dashed curve reflects measurements made with only far detector data; the solid curve includes both near and far detector data. The light blue region shows possible improvements in precision which may be achieved by reduction of systematic uncertainties in a Gd-based analysis.

A unique feature of the Double Chooz near detector is its nearly isoflux location. In a perfect isoflux arrangement, the near detector would be located such that it observes precisely the same mixture of events from the two reactors as the far detector. In this case, the near detector would perfectly monitor the flux in the far detector, allowing maximal cancellation of reactor-related uncertainties. Because its site has only two reactors, compared to the six at Daya Bay and RENO, Double Chooz was able to achieve the layout closest to an isoflux geometry. This condition allows simple, model-independent suppression of over 90% of reactor-related uncertainty.

3.4 *Studies of reactor flux and sterile neutrinos*

The near detector provides opportunities for at least two physics measurements beyond θ_{13}. Since it will detector hundreds of IBD interactions each day, the near detector will allow a much more precise study of the reactor spectrum features introduced in Section 3.1. The combination of near and far detector data will also open sensitivity to sterile neutrino oscillations in the range of $\Delta m^2_{41} = 0.001 - 1$ eV^2. A study of sterile neutrino sensitivity is in progress. Both reactor spectrum and sterile neutrino studies will benefit from data taken when only one reactor is operating. During these periods, such as in the first several months of 2015, ambiguity about the neutrino baseline and reactor conditions is eliminated.

4 Conclusions

Double Chooz has produced a number of high-quality measurements in its single-detector phase. Now, as the experiment enters the two-detector phase, it will begin to approach its full potential in measuring θ_{13}. At the same time, near detector data will allow studies of the reactor antineutrino flux and possible sterile neutrino signals.

References

1. M. Apollonio *et al.* Eur. Phys. J. **C27**, 331-374 (2003).
2. P. Adamson *et al.* Phys. Rev. Lett. **110**, 251801 (2013).
3. Y. Abe *et al.* Phys. Rev. **D86**, 052008 (2012).
4. Y. Abe *et al.* JHEP **1410**, 086 (2014).
5. Y. Abe *et al.* Phys. Lett. **B723**, 66 (2013).
6. Y. Abe *et al.* JHEP **1410**, 032 (2014).

Uncertainties in Reactor Neutrino Fluxes and in the Anomaly

A.C. Hayes
[1] *Theoretical Division, Los Alamos National Laboratory, Los Alamos, New Mexico, 87545, USA*

We examine the uncertainties in reactor neutrino fluxes within a nuclear physics framework. These uncertainties enter any analysis of the reactor neutrino anomaly, wherein it is suggested that only about 94% of the emitted antineutrino flux was detected in short baseline experiments. We find that the form of the corrections that lead to the anomaly are very uncertain for the 30% of the flux that arises from forbidden beta decays. Given the present lack of detailed knowledge of the structure of the forbidden transitions, it is difficult to convert the measured aggregate fission beta spectra to antineutrino spectra to the accuracy needed to infer an anomaly. In addition, we analyze the shoulder in the antineutrino spectra observed in current reactor experiments within a nuclear database framework. We find that the ENDF/B-VII.1 database predicts that the antineutrino shoulder arises from an analogous shoulder in the aggregate fission beta spectra. In contrast, the JEFF-3.1.1 database does not predict a shoulder. We consider several possible origins of the shoulder, and find possible explanations. For example, there could be a problem with the measured aggregate beta spectra, or the harder neutron spectrum at a light-water power reactor could affect the distribution of beta-decaying isotopes. In addition to the fissile actinides, we find that ^{238}U could also play a significant role in distorting the total antineutrino spectrum. Distinguishing these and quantifying whether there is an anomaly associated with measured reactor neutrino signals will require new short-baseline experiments, both at thermal reactors and at reactors with a sizable epithermal neutron component.

1 Introduction

There are currently two puzzles associated with measured reactor antineutrino spectra: (1) the magnitude of the spectra measured in all short-baseline experiments is lower than current models, and (2) the shape of the measured spectra deviate from these model predictions. The first of these puzzles is normally termed [1] the "reactor neutrino anomaly", and it generally refers to a 3σ deficit in the number of antineutrinos detected in short-baseline reactor neutrino experiments relative to the number predicted. The second puzzle is that the shape of the antineutrino spectra measured in the near detectors of both Daya Bay [2] and RENO [3] are not consistent with the antineutrino spectrum predictions [4,5] that we refer to as the Huber-Mueller model. Most notably, the measured antineutrino spectra exhibit a significant shoulder relative to the model predictions at antineutrino energies $E_\nu \approx 5-7$ MeV. The spectra measured at Daya Bay [2], RENO [3], and Double Chooz [6] all exhibit this shoulder. We note that the two antineutrino flux puzzles are not necessarily related.

The antineutrino spectrum emitted from a reactor is determined by [7] the reactor thermal power (W_{th}), the energy released in fission by each actinide (e_i), the fractional contribution (f_i/F, $F = \Sigma_i f_i$) of each actinide to the fissions taking place, and the antineutrino spectrum

for each actinide $S_i(E_i)$.

$$S(E_\nu) = \frac{W_{th}}{\Sigma_i (f_i/F) e_i} \Sigma_i (f_i/F) S_i(E_\nu). \quad (1)$$

The thermal power and the fission fractions are both functions of time and are supplied by the reactor operator, while the energy contributing to the thermal power per fission of each actinide (e_i) is normally taken from refs.[8,9]. The Daya Bay near-detector has provided an absolute determination of the reactor antineutrino flux, and this is consistent in magnitude with the previous world average short-baseline reactor neutrino experiments. As such, the measured magnitude is consistent with an anomalous deficit with respect to the most recent estimates[4,5] of the expected reactor antineutrino flux. The spectral distortions and the shape of the shoulder seen in current experiments cannot be produced by any standard L/E dependence required of neutrino oscillations, sterile or otherwise. Thus, there is a need to investigate uncertainties in the antineutrino spectra within a detailed nuclear physics framework.

2 The Corrections to beta-decay that led to the anomaly

There is extensive literature dealing with the reactor anomaly, starting with a seminal paper by Mueller *et al.* [5] that reexamined the reactor antineutrino flux. The latter publication sought to improve the earlier flux estimates based on the ILL on-line measurements[10,11] of the integral beta spectrum of the fission products. The improvements [1,5] on the earlier analyses of ILL integral measurements led to an increased energy of the antineutrino flux, which was subsequently verified in an independent analysis[4].

The beta-decay spectrum S for a single transition in nucleus (Z, A) with end-point energy $E_0 = E_e + E_\nu$ is

$$S(E_e, Z, A) = S_0(E_e) F(E_e, Z, A) C(E_e) (1 + \delta(E_e, Z, A)), \quad (2)$$

where $S_0 = G_F^2 p_e E_e (E_0 - E_e)^2 / 2\pi^3$, $E_e(p_e)$ is the electron total energy (momentum), $F(E_e, Z, A)$ is the Fermi function needed to account for the Coulomb interaction of the outgoing electron with the charge of the daughter nucleus, and $C(E_e)$ is a shape factor[12] for forbidden transitions due to additional lepton momentum terms. For allowed transitions $C(E) = 1$. The term $\delta(E_e, Z, A)$ represents fractional corrections to the spectrum that were the central focus of the original anomaly studies. The primary corrections to beta decay are radiative, finite size, and weak magnetism, or $\delta(E_e, Z, A) = \delta_{\rm rad} + \delta_{\rm FS} + \delta_{\rm WM}$.

Before discussing the details of the corrections $C(E_e)$ and $\delta(E_e)$, we briefly summarize the treatments used in earlier work. The radiative corrections as derived by Sirlin[13] were included in the description of the beta spectra (though not in the antineutrino spectra) in the original analyses of Schreckenbach *et al.* [10,11]. In the later ILL work[11] an approximation for the FS and WM corrections was included by first deducing the antineutrino spectrum from the measured beta spectra without these corrections, and then applying a linear correction to the deduced antineutrino spectrum of the form, $\delta_{\rm FS} + \delta_{\rm WM} = 0.0065(E_\nu - 4\ {\rm MeV})$. In that work no corrections were made for the shape factors $C(E_e)$. In other analyses [5,4,14] an approximation (derived by Vogel[15]) for the FS and WM corrections was applied on a transition-by-transition basis and the shape factor appropriate for unique forbidden transitions was used for all forbidden transitions. In the present work, we derived *ab initio* analytic expressions for the FS and WM corrections for allowed GT transitions, as well as WM and shape factors for first-forbidden GT operators. We used the radiative corrections derived by Sirlin[13].

We now turn to the form of the corrections. The attractive Coulomb interaction *increases* the electron density near the nuclear surface and increases the beta-decay rate, while the finite nuclear size *decreases* the electron density and decreases the rate (relative to the point-nucleus Fermi function). Using first-order perturbation theory in $Z\alpha$, the finite-size correction to the

Table 1: The shape factors and leading-order weak magnetism corrections to allowed and first-forbidden Gamow-Teller beta decays are shown in the top panel. The shape factors for allowed and first-forbidden Fermi beta decays are shown in the bottom panel. All agree with Ref. [20] for $Z = 0$. The weak magnetism correction for $\vec{J}_V$ involves the unknown overlap of very different 1^- matrix elements and is therefore not listed. The nucleon isovector magnetic moment is $\mu_v = 4.7$, M_N is the nucleon mass, g_A is the axial vector coupling constant, and $\beta = p_e/E_e$. No meson currents were used in the magnetic moment operator, and a truncated orbital current led to the factor of "1/2" in $\delta_{\rm WM}$.

Classification	Operator	Shape Factor $C(E_e)$	$\delta_{\rm WM}(E_e)$
Allowed GT	$\Sigma \equiv \sigma\tau$	1	$\frac{2}{3}\left[\frac{\mu_v - 1/2}{M_N g_A}\right](E_e\beta^2 - E_\nu)$
1^{st} For. GT	$[\Sigma, r]^{0-}$	$p_e^2 + E_\nu^2 + 2\beta^2 E_\nu E_e$	0
1^{st} For. ρ_A	$[\Sigma, r]^{0-}$	λE_0^2	0
1^{st} For. GT	$[\Sigma, r]^{1-}$	$p_e^2 + E_\nu^2 - \frac{4}{3}\beta^2 E_\nu E_e$	$\left[\frac{\mu_v - 1/2}{M_N g_A}\right]\left[\frac{(p_e^2+E_\nu^2)(\beta^2 E_e - E\nu) + 2\beta^2 E_e E_\nu (E_\nu - E_e)/3}{(p_e^2+E_\nu^2 - 4\beta^2 E_\nu E_e/3)}\right]$
1^{st} For. GT	$[\Sigma, r]^{2-}$	$p_e^2 + E_\nu^2$	$\frac{3}{5}\left[\frac{\mu_v - 1/2}{M_N g_A}\right]\left[\frac{(p_e^2+E_\nu^2)(\beta^2 E_e - E\nu) + 2\beta^2 E_e E_\nu (E_\nu - E_e)/3}{(p_e^2+E_\nu^2)}\right]$
Allowed F	τ	1	0
1^{st} For. F	$r\tau$	$p_e^2 + E_\nu^2 + \frac{2}{3}\beta^2 E_\nu E_e$	0
1^{st} For. $\vec{J}_V$	$r\tau$	E_0^2	-

Fermi function, $\delta_{\rm FS}$, for allowed GT transitions is [16]

$$\delta_{\rm FS} = -\frac{3}{2}\frac{Z\alpha}{\hbar c}\langle r\rangle_{(2)}\left(E_e - \frac{E_\nu}{27} + \frac{m_e^2 c^4}{3E_e}\right) \quad . \tag{3}$$

The quantity $\langle r\rangle_{(2)} = \int d^3r\, \rho_W(r) \int d^3s\, \rho_{\rm ch}(s)\, |\, \vec{r} - \vec{s}\, |$ is the first moment of the convoluted nuclear weak and charge densities (called a Zemach moment [17]). We assume uniform distributions of radius R for the weak and charge densities, for which [18] $\langle r\rangle_{(2)} = \frac{36}{35}R$.

The WM correction arises from the interference of the magnetic moment distribution of the vector current, $\vec{J}_V = \vec{\nabla} \times \vec{\mu}$, with the spin distribution $\vec{\Sigma}$ of the axial current. We previously derived [16] the WM corrections for allowed and first-forbidden operators. There are four possible operators in the case of first-forbidden GT transitions, and all have well-defined WM corrections, as listed in Table 1. Our [16] FS and WM corrections for allowed GT transitions are identical to those derived by Holstein [19], but differ from the forms used in other work [5,4,14,15]. The first-forbidden shape factors, $C(E_e)$, n Table 1 agree with the forms derived by Millener [20] in the $Z = 0$ limit.

3 The antineutrino spectrum dependence on forbidden transitions

To examine the effect of the forbidden beta-decay transitions on the expected antineutrino spectrum we fitted the Schreckenbach [11] electron spectrum, with and without a treatment for forbidden decays. There is no unique physical prescription for beta-decay operator assignments to the transitions included in the fit. For this reason we examined four prescriptions: (1) all transitions are assumed to be allowed; (2) all end-point energies can be associated with either an allowed or forbidden transition; (3) 30% of the branches are selected to be forbidden at equal energy intervals; (4) 30% of the branches are selected to be forbidden with a bias towards higher energies. In addition, we examine fits in which the operator determining the forbidden decays was taken to be $[\Sigma, r]^{0-}$, $[\Sigma, r]^{1-}$, $[\Sigma, r]^{2-}$ or a combination of these. We found excellent fits to the electron spectrum in all cases. However, different treatments of the forbidden transitions

can lead to antineutrino spectra that differ both in shape and magnitude at about the 4% level. Two examples are shown in Fig.1, where we present the fits obtained when the WM and FS corrections are included. In one case all transitions are assumed to be allowed, while in the second case the best fit results from about 25% forbidden decays. For the assumption of all allowed transitions, we see a systematic increase of about 2.2% in the number of antineutrinos relative to Schreckenbach, while including forbidden transitions leads to no increase relative to Schreckenbach.

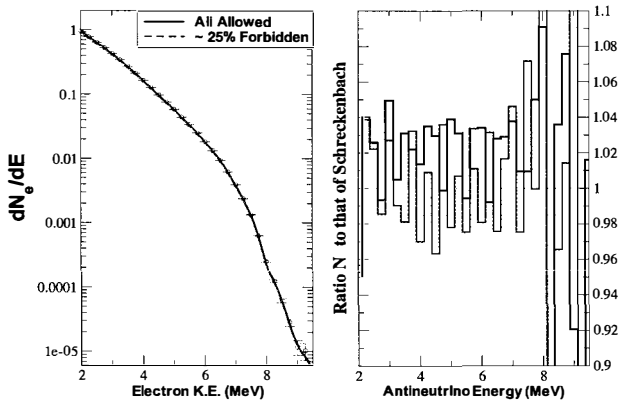

Figure 1 – The fit to the electron spectrum for ^{235}U (left) for two different assumptions on how to treat forbidden transitions, and the ratio of the corresponding antineutrino spectra to that of Schreckenbach (right). The electron spectra are fit assuming (a) all allowed GT branches, or (b) up to 30% forbidden GT transitions. In both cases the WM and FS corrections are included. When folded over the neutrino detection cross section, the case for all allowed (25% forbidden) transitions results in a 2.2% (0.06%) increase in the number of detectable antineutrinos.

4 The Shoulder

We calculated the aggregate beta and antineutrino spectra using both the ENDFB/V-II.1 [21] and JEFF-3.1.1 [22] nuclear data libraries that provide cumulative yields Y_{F_i} for all fission fragments of interest. The updated ENDF/B-VII.1 beta-decay library [23,24] provides spectra for approximately 95% of the nuclei appearing in eq.(2). The remaining 5% of the fission fragments are modeled [25,26] by extension of the Finite-Range Droplet Model plus Quasi-particle Random Phase Approximation (QRPA). Figure (2) shows the database predictions for the shape of the antineutrino spectra for Daya Bay [27] and RENO [28] relative to the Huber-Mueller model [4,5]. The Daya Bay and RENO experiments differ in the linear combination of actinides determining the total fissions. For Daya Bay the ^{235}U: ^{238}U: ^{239}Pu: ^{241}Pu fission split is 0.586: 0.076: 0.288: 0.05. RENO has not published their fission split, but we took 0.62: 0.12: 0.21: 0.05 from Kim [28]. As can be seen in Fig. (2), the ENDF/B-VII.1 fission fragment yields lead to the prediction of a shoulder relative to the Huber-Mueller model, but the JEFF-3.1.1 yields do not. This striking difference arises because the cumulative fission yields for some nuclei that dominate in the shoulder region are different in the two evaluations. Within the ENDF/B-VII.1 analysis, the shoulder in the antineutrino spectrum results from a corresponding shoulder in the aggregate beta spectrum, and involves the decay of several nuclei, as listed in Dwyer and Langford [29]. We next discuss in detail possible origins of the shoulder.

1. Non-fission sources of antineutrinos: We examined the contribution to the antineutrino spec-

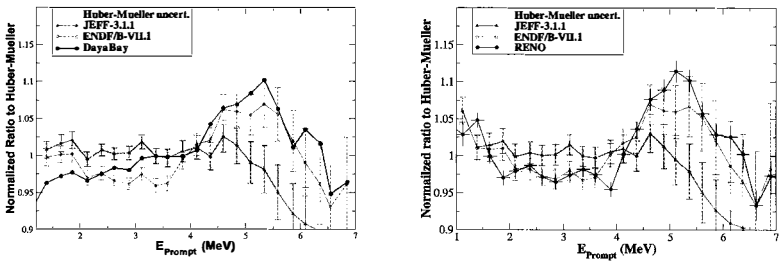

Figure 2 – The ENDF/B-VII.1 and JEFF-3.1.1 predictions for the ratio of the Daya Bay and RENO antineutrino spectra to the Huber-Mueller model. In all cases, the spectra are normalized to the same number of detectable antineutrinos in the energy window $E_\nu = 2-8$ MeV as the Huber-Mueller spectra when folded over the antineutrino detection cross section. The database uncertainties shown are only for the beta-decay branches. The uncertainties arising from the fission-fragment yields are large, as is evident from the difference between the ENDF/B-VII.1 and JEFF-3.1.1 predictions. The large difference between the two database predictions for the shoulder arises entirely from a difference in the evaluated fission fragment yields.

trum from neutron-induced reactions in reactor materials other than the fuel. We used MCNP simulations that are available for all neutron-induced reactions on the coolant, cladding, and structural materials in the NRU CANDU reactor at Chalk River. We then calculated the expected beta-decay spectrum from the unstable nuclei produced by these reactions. We found that all of the antineutrinos from this source are well below the energy of the shoulder. While materials in other reactors may differ in detail from those at the NRU reactor, none is known to produce a significant number of antineutrinos above 2 MeV, and we conclude that non-actinide sources of antineutrinos cannot explain the shoulder.

2. The forbidden nature of transitions: Several of the beta-decay transitions involving ^{96,98}Y, ^{90,92}Rb, and ^{142}Cs that dominate in the shoulder region have a total angular momentum and parity change that generates no weak-magnetism correction [16]. This fact was not taken into account in the analyses of Huber [4], Mueller [5], or Fallot [14]. Above half of the end-point energy in an allowed decay, the weak-magnetism contribution reduces the antineutrino component. This is opposite in sign to the other leading corrections [4,5,16] that suggested the existence of the reactor anomaly [1]. Thus, the lack of a weak-magnetism correction for $0^+ \rightarrow 0^-$ transitions increases the magnitude of the antineutrino flux relative to the Huber-Mueller model. A second issue is that the shape factor, $C(E)$, associated with $0^+ \rightarrow 0^-$ forbidden transitions [16] is quite different from the approximation used by Mueller *et al.* [5], who took the shape factor for all forbidden transitions to be that for a unique forbidden transition. A third issue is the lack of a proper finite-size Coulomb correction to the Fermi function for these transitions [16], where all analyses to-date (including the present one) were forced to use an approximation.

We calculated the antineutrino spectra with and without taking the $\Delta J^{\Delta\pi} = 0^-$ nature of transitions into account. There are two possible shape factors for such transitions [16] that affect the spectrum differently, which introduces an uncertainty in the shape of the aggregate antineutrino spectrum. Using the shape factor that gives the bigger increase in the antineutrino spectrum and setting the weak-magnetism term to zero, we found an increase in the shoulder region of less than 1%. We conclude that a proper treatment of forbidden transitions cannot account for a significant fraction of the shoulder.

3. ^{238}U as a source of the shoulder: RENO reports that ^{238}U is responsible for about 12% of its fissions, while Daya Bay reports only 7.6%. Referring to Fig. (2), relative to their respective experimentally established base lines (rather than with respect to Huber-Muller), the RENO shoulder is more than 50% larger than that observed at Daya Bay. This raises the question

whether ^{238}U, which was not measured in the original ILL experiments [10,11], could be causing the shoulder. Because ^{238}U fissions into isotopes further off the line of stability than ^{235}U, its antineutrino spectrum is both larger and harder in energy, and in the region $E_{\rm prompt} = 4 - 6$ MeV the ^{238}U spectrum is almost twice as large as that of ^{235}U. Thus, ^{238}U contributes about 24% (15%) to the total spectrum in the shoulder region for RENO (Daya Bay). We compared the ENDF/B-VII-1 and JEFF-3.1.1 predictions for ^{238}U to Mueller's prediction [5], and found that both databases predict a significant shoulder for ^{238}U. The magnitude of the JEFF-3.1.1 (ENDF/B-VII.1) shoulder and the percentage contribution to the total antineutrino spectrum suggests that ^{238}U could account for 25% (50%) of the observed shoulder in RENO and Daya Bay. To account for the entire shoulder the ^{238}U yields of the fission products dominating the shoulder region would have to be on average about a factor of four (two) larger than the JEFF-3.1.1 (ENDF/B-VII.1) evaluations. While not ruled out, this is unlikely. Thus, we conclude that ^{238}U could be responsible for a significant fraction of the observed shoulder, but probably not the entire shoulder.

4. The relatively harder PWR Neutron Spectrum: The neutron flux spectra at the PWR reactors used by Daya Bay, RENO and Double Chooz are harder in energy than the thermal spectrum of the ILL reactor, and involve considerably larger epithermal components. This raises the question whether epithermal neutron contributions to the fission of ^{235}U, ^{239}Pu and ^{241}Pu could result in a shoulder in the antineutrino spectrum. Studies [30] of energy-dependent variations in the fission product yields found clear evidence for significant yield changes for nuclei in the valley of the double-humped mass-yield curve. For example, the epithermal yield (relative to thermal) for the relatively unimportant isotope ^{115}Cd varies by a factor of 0.5-3.0, depending on the location of epithermal fission resonances. The effects are much more pronounced in ^{239}Pu than in ^{235}U. Resonance-to-resonance fluctuations cause the *average* effect to be small ($\sim 4\%$) in the energy range $19 < E_n < 61$ eV for ^{235}U, while in ^{239}Pu the prominent and isolated resonance at 0.3 eV produces a change in the ^{115}Cd yield of more than a factor of two. For high-yield fission products, such as ^{96}Y and ^{92}Rb, yield changes are not expected to be as large as for nuclei like ^{115}Cd, both because of theoretical arguments [31] and because the sum of the independent yields is fixed. But changes of the order of 20% are not ruled out. A comparison of the antineutrino spectrum measured at a very thermal reactor with that at a reactor with a sizable epithermal neutron component would be valuable in addressing this issue.

5. A possible error in the ILL beta-decay measurements: As pointed out by Dwyer and Langford [29] the ENDF/B-VII.1 prediction of a shoulder in the antineutrino spectrum in Fig. (2) corresponds to an analogous shoulder in the aggregate beta spectrum. In Fig. (3) we show the absolute ratio of the ENDF/B-VII.1 prediction for the aggregate beta spectrum for ^{235}U to that of Schreckenbach [10,11]. We conclude that the shoulder could be the result of a problem in the measurement or analysis of the beta-spectrum measurements at ILL.

Finally, we comment on whether database analyses of the antineutrino spectra provide any insight on the reactor neutrino anomaly [1]. The most important comment is that the database uncertainties are too large to draw any conclusions. Nonetheless, it is noteworthy that in comparing the two fission-yield evaluations, the prediction of a shoulder (no shoulder) appears to be correlated with the predictions of no anomaly (an anomaly). Daya Bay observes a shoulder and its measured absolute rate is in excellent agreement [27] with the previous world average. The ENDF/B-VII.1 prediction for both the shoulder and the absolute magnitude of the antineutrino spectrum are close to Daya Bay; that is, relative to ENDF/B-VII.1, Daya Bay sees no anomaly. In contrast, the JEFF-3.1.1 predictions are closer to the Huber-Mueller model, which would suggest an anomaly.

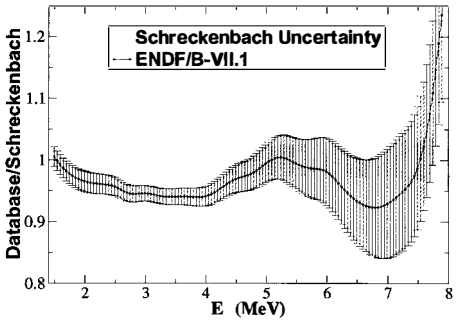

Figure 3 – . The absolute ratio of the ENDF/B-VII.1 aggregate beta spectrum for ^{235}U to that of Schreckenbach. The shoulder in the energy window $E_\beta \approx 4 - 6$ MeV corresponds to the same shoulder in the ENDF/B-VII.1 antineutrino spectrum shown in Fig. (2).

5 The Need for New Experiments

Both the anomaly and the shoulder could be due to (a) a difference in the hardness of the reactor neutron spectrum, or (b) a problem with the original aggregate beta-spectra measurement [10,11] at the ILL. It is also possible that the shoulder and the anomaly are not correlated. Answering these questions is not possible within current theoretical frameworks or from existing data. Consequently a new set of reactor experiments is needed at short baselines. To address the important issue of the anomaly and the possible existence of a 1 eV sterile neutrino, two detectors at different distances viewing the same reactor are needed. To quantify the role of the neutron spectrum on the shape and magnitude of the antineutrino spectrum, one measurement should be carried out at a very thermal reactor and the other at a reactor with a considerably harder neutron spectrum. The use of highly enriched ^{235}U fuel has the advantage of restricting the resulting antineutrino flux to fragments produced by a single actinide. On the other hand, if ^{238}U and/or ^{239}Pu play a significant role in the anomaly or the shoulder, measurements from fuel that is of low enrichment will be needed to reduce these sources of uncertainty.

References

1. G. Mention *et al.*, *Phys. Rev. D* **83** 073006 (2011).
2. F. P. An *et al.*, *Phys. Rev. Lett.* **108**, 171803 (2012).
3. J. K. Ahn *et al.*, *Phys. Rev. Lett.* **108**, 191802 (2012).
4. P. Huber, *Phys. Rev. C* **84**, 024617 (2011).
5. Th. A. Mueller *et al.*, *Phys. Rev. C* **83**, 054615 (2011).
6. Y. Abe *et al.*, *Phys. Rev. Lett.* **108**, 131801 (2012).
7. Jun Cao, *Nucl. Phys. B Proc. Supp.* **229-232**, 205 (2012).
8. M. F. James, *J. Nucl. Energy* **23**, 517 (1969).
9. V. Kopeikin, L. Mikaelyan, and V. Sinev, *Phys. Atom. Nucl.* **67**, 1892 (2004); *Yad. Fiz.* **67** 1916 (2004).
10. K. Schreckenbach, H. R. Faust, F. von Feilitzsch, A. A. Hahn, K. Hawerkamp, and J. L. Vuilleumier, *Phys. Lett.* **99B**, 251 (1981); F. von Feilitzsch, A. A. Hahn, and K. Schreckenbach, *Phys. Lett.* **118B**, 162 (1982).
11. K. Schreckenbach, G. Colvin, W. Gelletly, and F. von Feilitzsch, *Phys. Lett.* **160B** 325

(1985); A. A. Hahn, K. Schreckenbach, W. Gelletly, F. von Feilitzsch, G. Colvin, and B. Krusche, *Phys. Lett.* **B218**, 365 (1989).
12. H. F. Schopper, *Weak Interactions and Nuclear Beta Decay*, North-Holland, Amsterdam, 1966.
13. A. Sirlin, *Phys. Rev.* **164**, 1767 (1967); A. Sirlin, *Phys. Rev. D* **84**, 014021 (2011).
14. M. Fallot, S. Cormon, M. Estienne, A. Algora, V. M. Bui, *et al.*, *Phys. Rev. Lett.* **109**, 202504 (2012).
15. P. Vogel, *Phys. Rev. D* **29**, 1918 (1984) and private communication.
16. A. C. Hayes, J. L. Friar, G. T. Garvey, Gerard Jungman, G. Jonkmans, *Phys. Rev. Lett.* **112**, 202501 (2014).
17. C. Zemach, *Phys. Rev.* **104**, 1771 (1956).
18. J. L. Friar, *Ann. Phys. (N.Y.)* **122**, 151 (1979).
19. B. R. Holstein, *Phys. Rev. C* **9**, 1742 (1974); J. L. Friar and I. Sick, *Phys. Lett.* **B579**, 285 (2004). Equation (2) of the latter allows conversion between the two results.
20. D. J. Millener, D. E. Alburger, E. K. Warburton, and D. H. Wilkinson, *Phys. Rev C* **26**, 1167 (1982).
21. M. B. Chadwick, *Nucl. Data Sheets* **112**, 2887 (2011).
22. M. A. Kellett , O. Bersillon, R. W. Mills, "The JEFF-3.1/-3.1.1 Radioactive Decay Data and Fission Yields Sub-Libraries," JEFF Report 20, NEA Report No. 6287 (2009).
23. A. A. Sonzogni, T. D. Johnson, and E. A. McCutchan, *Phys. Rev. C* **91**, 011301(R) (2015).
24. The beta-decay database used here was kindly provided to us by the Brookhaven Nuclear Data Group, prior to formal release. The updated nuclei relative to ENDF/B-VII-1.1 are ^{82,82}Ge, ^{82}As, $^{88-91}$Br, ^{90}Kr, $^{91-94,96}$Rb, $^{95,97-99}$Y, ^{105}Mo, $^{104-106}$Tc, ^{134,137}Sb, ^{137,138}I, $^{140-142}$Cs, ^{143}Bs, $^{143-145}$La.
25. S. T. Holloway, Toshihiko Kawano, and Peter Möller, *J. Korean Phys. Soc.* **59**, 875 (2011).
26. T. Kawano, P. Moller, and W.B. Wilson, Phys. Rev. C 78, 054601 (2008), and T. Kawano and S. T. Holloway, "CGM: Cascading Gamma-ray and Multiplicity Code Ver. 3," (2010) [unpublished].
27. Weili Zhong (for the Daya Bay collaboration), "Measurement of the Reactor Antineutrino Flux and Spectrum at Daya Bay", Invited talk presented at *ICHEP'14*.
28. Soo-Bong Kim (for the RENO collaboration), "Recent Results from RENO & Future Plan", Talk presented at Fermilab, July 25, 2014, and "Precise Measurement of Reactor Neutrino Spectrum at RENO & Mass Hierarchy at RENO-50", Invited talk presented at workshop *Neutrinos : Recent Developments and Future Challenges*, KIPT, Santa Barbara, November 4, 2014.
29. D. A. Dwyer and T. J. Langford, Phys. Rev. Lett. **114** 012502 (2015).
30. G. A. Cowan, A. Turkevich, C. I. Browne, *Phys. Rev.* **122**, 1286 (1961); G. A. Cowan, B. P. Bayhurst, R. J. Prestwood, *Phys. Rev.* **130**, 2380 (1963); G. A. Cowan, B. P. Bayhurst, R. J. Prestwood, J. S. Gilmore, and G. W. Knobeloch, *Phys. Rev.* **144**, 979 (1966); G. A. Cowan, B. P. Bayhurst, R. J. Prestwood, J. S. Gilmore, and G. W. Knobeloch, *Phys. Rev.* **C2**, 615 (1970).
31. J. A. Wheeler, *Physica* **22**, 1103 (1956).

Selected results from T2K

J. Myslik, for the T2K collaboration
Department of Physics and Astronomy, University of Victoria, 3800 Finnerty Rd, Victoria, BC, V8P 5C2, Canada

The T2K ("Tokai to Kamioka") experiment is a long-baseline neutrino oscillation experiment in Japan. A beam of muon neutrinos or muon anti-neutrinos is produced at the Japan Proton Accelerator Research Complex (J-PARC) in Tokai. The unoscillated neutrino flux is measured by the near detector complex 280 m from the proton target, and the oscillated neutrino flux is measured by the far detector, Super-Kamiokande, 295 km away. The major T2K neutrino oscillation results to date (from neutrino beam run periods) are reviewed, and a first look at the recent anti-neutrino beam run periods is provided.

1 Overview of the T2K experiment

T2K is a long-baseline neutrino oscillation experiment, making use of a neutrino beam, a near detector (ND280), and a far detector (Super-Kamiokande) to explore neutrino oscillation and cross section physics. Full detail on the experimental setup is available elsewhere [1].

1.1 Neutrino beam

At the Japan Proton Accelerator Research Complex (J-PARC) in Tokai, Japan, a 30 GeV beam of protons is collided with a graphite target. This produces a beam of mostly pions, which are focussed by three magnetic horns, and which subsequently decay to produce the neutrino beam. The direction of the current through the horns determines whether π^+ (which decay into neutrinos), or π^- (which decay into anti-neutrinos) are focussed, hence determining whether the beam is in neutrino mode or anti-neutrino mode respectively. This process is simulated using a combination of FLUKA [2,3] and GEANT3 [4] (with GCALOR [5]), and is tuned to external data (e.g. NA61/SHINE). This model also provides the correlations between different flavours and bins of neutrino energy in both beam modes at ND280 and Super-Kamiokande, which allows ND280 measurements to reduce flux uncertainties at Super-Kamiokande. The beam model was recently updated, and now simulates both neutrino and anti-neutrino beam modes, and has reduced uncertainties due to improvements in the hadron production modelling.

1.2 Detectors

Both ND280 and Super-Kamiokande are located 2.5° off-axis from the neutrino beam, which results in an energy spectrum that is peaked at 0.6 GeV, and is much narrower than the on-axis spectrum.

ND280 consists of multiple subdetectors in a 0.2 T magnetic field (provided by the former UA1/NOMAD magnet), situated 280 m from the beam target. For the analysis results discussed here, ND280 measurements were done using the Fine-Grained Detectors (FGDs), which are made

up of scintillator bars which act as an active neutrino target, and the gas-filled Time Projection Chambers (TPCs), which provide momentum measurements and measurement of dE/dx for particle identification. ND280 measures the neutrino beam flux and some neutrino cross section model parameters that are used in the oscillation analyses, thus reducing uncertainties in the oscillation analyses.

Super-Kamiokande is a water Cherenkov detector located 295 km from the beam target. It has a 22.5 kton fiducial mass, and is instrumented with approximately 11000 PMTs. Event selection begins with events that occur within the fiducial volume and are fully contained within the inner detector, called "Fully Contained Fiducial Volume" events, or FCFV. For these events, good discrimination between ν_μ and ν_e is achieved through the shape of the Cherenkov ring. Electrons scatter, undergo bremsstrahlung, and initiate electromagnetic showers, resulting in fuzzy Cherenkov rings, whereas muons, being much heavier, maintain their initial direction, producing sharp Cherenkov rings.

1.3 Neutrino oscillation in a $\nu_\mu/\bar{\nu}_\mu$ beam

An overview of the theory and status of 3 flavour neutrino mixing is given elsewhere [6] in these proceedings. T2K makes use of a beam of muon neutrinos or muon anti-neutrinos, so for the neutrino energy spectrum of T2K muon neutrino disappearance (Eq. 1) and electron neutrino appearance (Eq. 2) are the two relevant channels, where each equation was derived from the PMNS matrix, makes use of the approximation that $|\Delta m^2_{32}| \approx |\Delta m^2_{31}|$, and employs the shorthand of $x \equiv \frac{2\sqrt{2}G_F N_e E}{\Delta m^2_{32}}$ and $D \equiv \frac{\Delta m^2_{32} L}{4E}$. In addition, Eq. 2 is approximated to first order in $\Delta m^2_{21}/\Delta m^2_{31}$, and accounts only for CP-odd terms. A paper [7] is available with more details.

$$P(\nu_\mu \to \nu_\mu) \approx 1 - (\cos^4\theta_{13}\sin^2 2\theta_{23} + \sin^2 2\theta_{13}\sin^2\theta_{23})\sin^2 D \tag{1}$$

$$\begin{aligned} P\left(\overset{(-)}{\nu}_\mu \to \overset{(-)}{\nu}_e\right) \approx \frac{\sin[(1\mp x)D]}{(1\mp x)}\Bigg(&\sin^2 2\theta_{13}\sin^2\theta_{23}\frac{\sin[(1\mp x)D]}{(1\mp x)} \\ &\mp \sin\delta_{CP}\sin 2\theta_{13}\sin 2\theta_{12}\sin 2\theta_{23}\sin D\frac{\sin(xD)}{x}\frac{\Delta m^2_{21}}{\Delta m^2_{32}}\Bigg) \end{aligned} \tag{2}$$

In both Eq. 1 and Eq. 2, the D term provides dependence on the distance the neutrinos travel, their energy, and the mass-squared splitting Δm^2_{32}. For T2K, these values are such that the probabilities of muon neutrino disappearance and electron neutrino appearance are maximal at Super-Kamiokande. From Eq. 2 it is evident that measurements of θ_{13} by measuring $\nu_\mu \to \nu_e$ and $\bar{\nu}_\mu \to \bar{\nu}_e$ depend on the CP violating phase δ_{CP}, and in different ways. Therefore, taking data with ν_μ and $\bar{\nu}_\mu$ beams increases the sensitivity T2K has to δ_{CP}.

1.4 Neutrino interactions at T2K

For the neutrino energy spectrum at T2K, the "Charged Current Quasi-Elastic" (CCQE) neutrino interaction process is dominant. For neutrinos, the process is given by Eq. 3, where ℓ denotes a negative lepton.

$$\nu_\ell + n \to \ell + p \tag{3}$$

CCQE is the T2K signal mode, and has the benefit that the energy of the neutrino can be reconstructed from the momentum and angle of the outgoing lepton, using Eq. 4.

$$E_\nu = \frac{m_p^2 - m_n^2 - m_\ell^2 + 2m_n E_\ell}{2(m_n - E_\ell + p_\ell cos\theta_\ell)} \tag{4}$$

In addition to this signal mode, there are also a number of background modes to consider. If they were mis-identified as CCQE, this would affect the shape of the reconstructed neutrino

energy spectrum, and thus the oscillation analysis results. One such interaction is the multi-nucleon-neutrino interaction, in which a neutrino interacts with multiple correlated nucleons, producing a signal at Super-Kamiokande that is identical to CCQE (since outgoing protons are typically below Cherenkov threshold, and thus not detected). For upcoming T2K analyses, the Nieves multi-nucleon interaction model[8,9] has been implemented as part of the CCQE model. In addition, this CCQE model has been tuned to neutrino and anti-neutrino data from MINERνA and MiniBooNE.

For the neutrino energy spectrum at T2K, the "Charged Current RESonant pion production" (CCRES) interaction process is the dominant background process, and is shown in Eq. 5.

$$\nu_\ell + N \rightarrow \ell + \Delta \rightarrow \ell + \pi + N' \tag{5}$$

If the pion is not detected, this interaction would be mis-identified as a CCQE interaction. One way this pion could be missed is if it were to be absorbed before exiting the nucleus in a "Final State Interaction" (FSI). In addition, the pion could interact outside the nucleus before it is detected, or be below Cherenkov threshold and not otherwise be detected through a Michel electron signal from its decay. The CCRES model has been retuned for upcoming analyses, with new form factors implemented[10], and a re-analysis of the ANL and BNL bubble chamber datasets performed[11].

2 Neutrino beam mode oscillation analyses

2.1 ν_μ disappearance measurement

As per the experimental design, the deficit of muon neutrinos at Super-Kamiokande due to oscillation is quite large, as is shown in Fig. 1 (left). This corresponds to 120 events selected, when 446.0 $\pm$ 22.5 (syst) would be expected without oscillations. The resulting contours for Normal Hierarchy (NH) and Inverted Hierarchy (IH) are shown in Fig. 2. This corresponds to a measurement of $\sin^2\theta_{23} = 0.514^{+0.055}_{-0.056}$ (0.511 ± 0.055) for NH (IH), which is the most precise measurement of this neutrino mixing parameter. There is a paper[12] that describes this study in more detail.

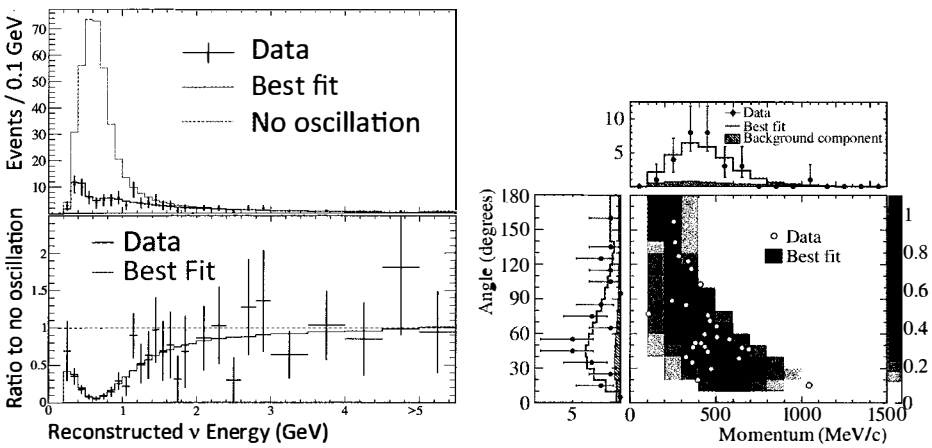

Figure 1 – Reconstructed muon neutrino energy spectrum at Super-Kamiokande, showing data and the best fit Monte Carlo prediction, along with the no oscillation Monte Carlo prediction (left). Momentum and angle of outgoing electron candidate for Super-Kamiokande electron neutrino event selection, showing data and the Monte Carlo best fit and expected background (NH). (right).

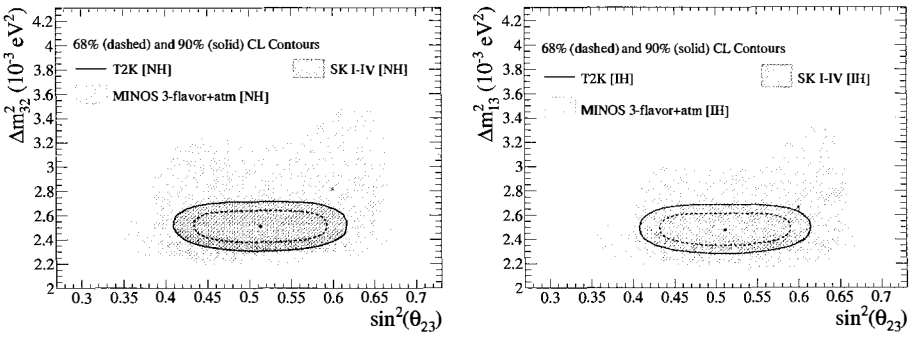

Figure 2 – The 68% and 90% confidence regions for $\sin^2\theta_{23}$ and Δm^2_{32} for NH (left) or Δm^2_{13} for IH (right) from the muon neutrino appearance analysis, with Super-Kamiokande and MINOS 90% confidence regions shown for comparison.

2.2 $\nu_\mu \to \nu_e$ appearance measurement

T2K observed a total of 28 electron neutrino events with an expected background of 4.92 ± 0.55 events. The observed events, the Monte Carlo best fit, and the expected background are shown in Fig. 1 (right). This corresponds to a significance of 7.3σ for the discovery of $\nu_\mu \to \nu_e$ oscillation. The resulting contours for NH and IH are shown in Fig. 3 (left), along with the PDG2012 1σ range coming from reactor neutrino oscillation experiments. More information on this study is available in a paper [13].

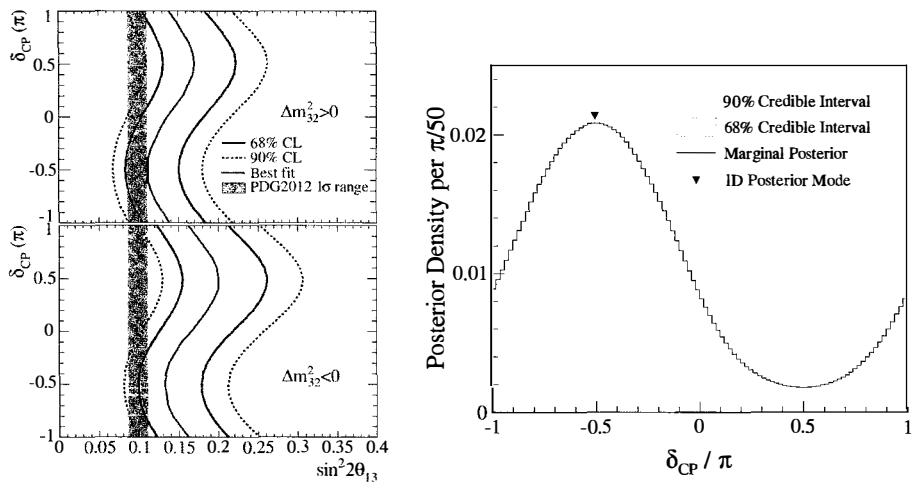

Figure 3 – The 68% and 90% confidence regions for $\sin^2 2\theta_{13}$ and δ_{CP} from the electron neutrino appearance analysis, with the PDG2012 1σ range shown for comparison (left). Posterior density distribution for δ_{CP} from the Bayesian joint analysis with the reactor constraint, where the mass hierarchy has been marginalized over (right).

2.3 Joint $\nu_\mu + \nu_e$ analysis (Bayesian version)

Standalone appearance and disappearance measurements only consider the spectrum of the relevant neutrino flavour at Super-Kamiokande. However, as shown in Eqs. 1 and 2, the relationship

between $P(\nu_\mu \to \nu_\mu)$, $P(\nu_\mu \to \nu_e)$, θ_{23}, θ_{13}, δ_{CP} and Δm^2_{32} is complicated. So, a joint analysis where the ν_μ and ν_e spectra were considered simultaneously was performed. In addition, the constraint from reactor experiments was included. The Bayesian version of this analysis used a Markov Chain Monte Carlo to produce posterior distributions for the oscillation parameters of interest. When including the reactor constraint and marginalizing over the mass hierarchy, the posterior density distribution for δ_{CP} shown in Fig. 3 (right) is produced, which hints towards $\delta_{CP} \approx -\frac{\pi}{2}$. In addition, the T2K and reactor data are found to weakly favour the Normal Hierarchy with a Bayes factor of 2.2, and to weakly favour the upper θ_{23} octant. This analysis and frequentist joint analyses are described in a recently published paper [14].

3 First look at anti-neutrino beam mode

Since the summer of 2014, T2K has been taking data in anti-neutrino beam mode. As of March 5, 2015, 7.001×10^{20} protons had been delivered to the T2K target in neutrino mode, and 2.057×10^{20} protons had been delivered to the T2K target in anti-neutrino mode.

Up to December 22, 2014, 394 FCFV events had been observed at Super-Kamiokande in neutrino mode, and 40 FCFV events had been observed in anti-neutrino mode. An important part of using these events to study neutrino oscillations is to make use of ND280 measurements to reduce systematic uncertainties from the neutrino beam flux and neutrino cross section models. To assist in this effort, two samples were devised to select muon anti-neutrino events in anti-neutrino beam mode. The CC-1Track sample is sensitive to the T2K signal mode, and requires that only one track was reconstructed, and that it is positive and muon-like. For this sample, the momentum of the muon candidate and the cosine of angle it makes with the beam is shown in Fig. 4. The CC-NTracks sample is sensitive to the T2K background modes, and requires that there is more than one track reconstructed, and that the highest momentum positive track is muon-like. For this sample, the momentum of the muon candidate and the cosine of angle it makes with the beam is shown in Fig. 5. Both of these samples will be included as part of the ND280 measurements used in the upcoming T2K anti-neutrino oscillation results.

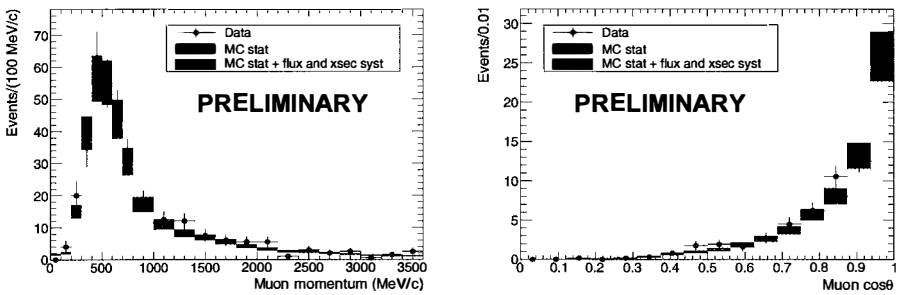

Figure 4 – Momentum (left) and cosine of angle with the neutrino beam (right) of the muon candidate in the ND280 $\bar{\nu}_\mu$ CC-1Track selection. The Monte Carlo prediction includes error bands for the MC statistical error and the prior errors on the flux and interaction models from tuning to external data. ND280 detector systematics are not included, and are expected to be $\approx 4\%$ at the peak.

4 Conclusion and outlook

Using its neutrino beam mode data, T2K has produced some exciting results so far. Through its ν_μ disappearance measurement, T2K has produced the world leading measurement of θ_{23}. By measuring appearance of ν_e, T2K has discovered $\nu_\mu \to \nu_e$ oscillation at 7.3σ. Finally, joint analysis of the ν_μ and ν_e data, combined with the constraint from reactor neutrino experiments,

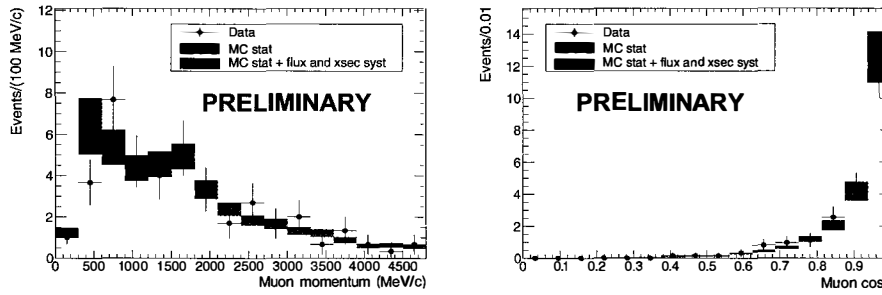

Figure 5 – Momentum (left) and cosine of angle with the neutrino beam (right) of the muon candidate in the ND280 $\bar{\nu}_\mu$ CC-NTracks selection. The Monte Carlo prediction includes error bands for the MC statistical error and the prior errors on the flux and interaction models from tuning to external data. ND280 detector systematics are not included, and are expected to be $\approx 4\%$ at the peak.

hints towards $\delta_{CP} \approx -\frac{\pi}{2}$, and Normal Hierarchy with a Bayes Factor of 2.2. T2K is now taking data in anti-neutrino beam mode, and has recently updated its neutrino beam flux and neutrino cross section models for upcoming analyses. Analysis of this data is well underway, with T2K's first anti-neutrino oscillation results coming in the near future.

References

1. K. Abe et al. The T2K Experiment. *Nucl.Instrum.Meth.*, A659:106–135, 2011.
2. A. Ferrari, P. R. Sala, A. Fasso, and J. Ranft. FLUKA: A multi-particle transport code, Report Nos. CERN-2005-010, SLAC-R-773, INFN-TC-05-11.
3. G. Battistoni, F. Cerutti, A. Fass, A. Ferrari, S. Muraro, J. Ranft, S. Roesler, and P. R. Sala. The FLUKA code: description and benchmarking. *AIP Conference Proceedings*, 896(1), 2007.
4. R. Brun, F. Carminati, and S. Giani. *CERN-W5013*, 1994.
5. P. Dragovitsch, S. L. Linn, and M. Burbank. *Proceedings of the International Conference on Monte Carlo Simulation in High Energy and Nuclear Physics*, page 391, World Scientific, Singapore 1993.
6. E. Lisi. Status of 3 neutrino mixing. *These proceedings*, 2015.
7. Martin Freund. Analytic approximations for three neutrino oscillation parameters and probabilities in matter. *Phys. Rev. D*, 64:053003, Jul 2001.
8. J. Nieves, I. Ruiz Simo, and M. J. Vicente Vacas. Inclusive charged-current neutrino-nucleus reactions. *Phys. Rev. C*, 83:045501, Apr 2011.
9. R. Gran, J. Nieves, F. Sanchez, and M. J. Vicente Vacas. Neutrino-nucleus quasi-elastic and 2p2h interactions up to 10 GeV. *arXiv:hep-ph/13078105*, 2013.
10. Krzysztof M. Graczyk and Jan T. Sobczyk. Form Factors in the Quark Resonance Model. *Phys. Rev.*, D77:053001, 2008.
11. Callum Wilkinson, Philip Rodrigues, Susan Cartwright, Lee Thompson, and Kevin McFarland. Reanalysis of bubble chamber measurements of muon-neutrino induced single pion production. *Phys.Rev.*, D90:112017, 2014.
12. K. Abe et al. Precise Measurement of the Neutrino Mixing Parameter θ_{23} from Muon Neutrino Disappearance in an Off-Axis Beam. *Phys.Rev.Lett.*, 112(18):181801, 2014.
13. K. Abe et al. Observation of Electron Neutrino Appearance in a Muon Neutrino Beam. *Phys.Rev.Lett.*, 112:061802, 2014.
14. K. Abe et al. Measurements of neutrino oscillation in appearance and disappearance channels by the T2K experiment with 6.610^{20} protons on target. *Phys.Rev.*, D91(7):072010, 2015.

Prospects to determine the neutrino mass hierarchy

Sandhya Choubey
Harish-Chandra Research Institute, Chhatnag Road, Jhunsi, Allahabad 211 019, India
Department of Theoretical Physics, School of Engineering Sciences, KTH Royal Institute

We will discuss the prospects of determining the neutrino mass hierarchy in the next generation proposed experiments. In particular, we will look at the expected sensitivity in atmospheric neutrino experiments, near future long baseline experiments and intermediate baseline reactor experiments.

1 Introduction

Remarkable progress has been made in the field of neutrino physics in the last few years. However, a few parameters essential for our complete knowledge of the neutrinos remain to be measured. The neutrino mass hierarchy is one of them. Within the three-generation paradigm, we have two mass squared differences Δm^2_{21} driving the solar neutrino oscillations and Δm^2_{31} driving the atmospheric neutrino oscillations. While the sign of Δm^2_{21} has been determined to be positive to a very high significance from the observation of matter effects in solar neutrino oscillations, the sign of Δm^2_{31} continues to be unknown. In the case where $\Delta m^2_{31} > 0$ the neutrino mass spectrum resembles in ordering to the quark masses and this case is known as normal hierarchy (NH), while in the case where $\Delta m^2_{31} < 0$, we have two heavier mass eigenstates and one light one and this is referred to as inverted hierarchy (IH).

There are various observational consequences of the sign of Δm^2_{31}, which could be used to determine the neutrino mass hierarchy. These include:

- Matter effects in Δm^2_{31}-driven oscillations which will show up in the neutrino channel for $\Delta m^2_{31} > 0$ and in the anti-neutrino channel for $\Delta m^2_{31} < 0$.
- So-called "interference effects" between Δm^2_{31}-driven oscillations and Δm^2_{32}-driven oscillations which depend on the neutrino mass hierarchy.
- Contribution to neutrino-less double beta decay, in case the neutrinos are Majorana particles.
- Contribution to beta decay.

- Contribution to the total energy density of the universe.

In this talk, we will focus only on the determination prospects of the neutrino mass hierarchy through observation of (i) matter effects in Δm^2_{31}-driven oscillations and (ii) interference effects. For the first case we will look at the current status and future prospects at atmospheric neutrino experiments and long baseline experiments. For the second case we will look at the prospects of determining the neutrino mass hierarchy at the proposed reactor experiments JUNO (and RENO-50). We will not discuss the impact of the sign of Δm^2_{31} on neutrino-less double beta decay, beta decay and limits on sum of neutrino masses from cosmology.

2 Prospects at atmospheric neutrino experiments

Atmospheric neutrinos come in ν_e, $\bar{\nu}_e$, ν_μ and $\bar{\nu}_\mu$ flavors. They come from all sides and cover distances between about 15 km to 13000 km depending on whether they come from directly above or from directly below the detector, crossing the Earth. They also come with a very large energy range ranging from MeV to 10^4 GeV and beyond. The Δm^2_{31}-driven oscillations convert the ν_μ and $(\bar{\nu}_\mu)$ predominantly into ν_τ and $(\bar{\nu}_\tau)$ flavors. However, the oscillation probabilities for the neutrinos which cross the Earth acquire a correction due to matter effects. This correction is different between the neutrino and the anti-neutrino channels for a given mass hierarchy and flips when the mass hierarchy is flipped. In particular, in the energy range of $5 - 10$ GeV, one expects strong Earth matter effects. These matter effects show up in both electron and muon channels. However, for the muon channel the Earth matter effects have sharp energy and zenith angle dependence and hence could be easily washed out if the resolutions of the detector are poor. For both channels since Earth matter effects develop only in either the neutrinos or the antineutrinos, they are partially washed out if the detector cannot distinguish one from the other.

Currently the data on atmospheric neutrinos at Super-Kamiokande (SK) detector is unable to give any statistically significant hint for the neutrino mass hierarchy. For 517 degrees of freedom, the total from SK data is $\chi^2 = 559.8$ for NH and 560.7 for IH [1]. The main issues with the SK detector are mainly its relatively smaller size and its inability to distinguish the neutrino from the antineutrino signal. Therefore one needs bigger and better detectors in order to determine the neutrino mass hierarchy from atmospheric neutrino experiments. We show in Fig. 1 the expected $\Delta\chi^2$ or σ for the wrong mass hierarchy as a function of number of years of running of the experiment. The left panel of Fig. 1 shows the sensitivity for Hyper-Kamiokande (HK) [2], middle panel for PINGU [3] and right panel for INO [4].

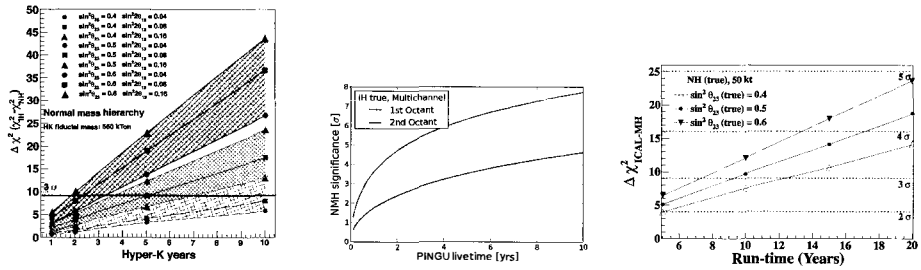

Figure 1 – The expected mass hierarchy sensitivity as a function of the number of years of running of the experiment. The left panel is for HK (taken from [2]), the middle panel is for PINGU (taken from [3]), while the right panel is for INO (taken from [4]).

The proposed megaton scale water Cherenkov detector HK promises better statistics and statistical separation of ν_e from $\bar{\nu}_e$ for about 40-50% of the total sample. This gives HK an

expected median sensitivity of 3σ after 5 years of data-taking. PINGU is the proposed extension of the IceCube detector by increasing the number of optical strings in the DeepCore area to reduce the detector energy threshold. This would give a multi-megaton effective volume and even though PINGU does not have charge identification capability, it is still expected to measure the mass hierarchy to 3σ with only 3 years of running. The ICAL detector at INO will be a 50 kton magnetised iron calorimeter. This detector has very good charge identification capability in addition to its ability to measure the energy (and zenith angle) of the neutrinos better. Therefore, despite is relatively smaller size one expects this experiment to return a sensitivity of 3σ from 10 years of running of the experiment.

Note that the mass hierarchy sensitivity of atmospheric neutrino experiments is hardly affected by our lack of knowledge of the CP phase.

3 Prospects at long baseline experiments

The long baseline experiments can be used to determine the neutrino mass hierarchy. In particular, the long baseline experiments are sensitive to $P_{\mu e}$ oscillation probability which at leading order depends on Earth matter effects and hence mass hierarchy, with the only criteria that the baseline of the experiment should be long enough and the energy in the multi-GeV range.

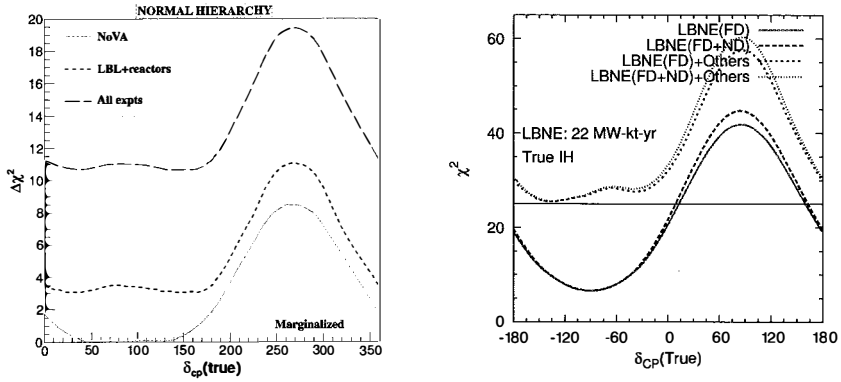

Figure 2 – The left panel shows the $\Delta\chi^2$ for wrong hierarchy as a function of δ_{CP}(true) for NOνA alone and NOνA combined with T2K and reactor data, and with T2K, reactor, and INO data (taken from [5]). The right panel shows the $\Delta\chi^2$ for wrong hierarchy as a function of δ_{CP}(true) for DUNE experiment (marked as LBNE) for different combinations of data set and with and without the near detector (ND) (taken from [6]).

The current data from the T2K experiment [6] gives a best-fit value of θ_{13} which is in mild conflict with the best-fit θ_{13} obtained by the reactor experiments such as Daya Bay [?]. This conflict is less for the NH than for the IH. One could take that as a hint for NH, however this is far from being statistically significant right now. In particular, T2K does not have much Earth matter effects. The NOνA experiment has a longer baseline and hence better sensitivity to the mass hierarchy. In the left panel of Fig. 2 we show the expected $\Delta\chi^2$ as a function of δ_{CP}(true) from NOνA, NOνA combined with T2K and reactor experiments, and NOνA combined with T2K, reactor experiments and INO. We see that once the data from the atmospheric experiment INO is added, one expects more than 3σ sensitivity for mass hierarchy for all values of δ_{CP}(true). In the right panel of Fig. 2 we show the sensitivity to mass hierarchy expected from the proposed LBNE (now called DUNE) experiment. We conclude that 5σ sensitivity is possible for all values of δ_{CP}(true) if one adds the data from T2K, NOνA and INO to the DUNE data. Without the atmospheric neutrino data from INO, one needs an exposure of almost a factor of 2 times more

to get the same sensitivity. DUNE alone will need 95 MW-kton-yr of data to get a 5σ sensitivity on the neutrino mass hierarchy.

4 Prospects at reactor experiments

The neutrino mass hierarchy can be discovered at intermediate baseline reactor experiments through an interesting interplay between Δm^2_{31} and Δm^2_{21} oscillations leading to the so-called interference effects in P_{ee} [8,9]. The expression for the survival probability P_{ee} for NH and IH respectively is given as

$$\begin{aligned} P^{NH}_{ee} &= 1 - 2\sin^2\theta_{13}\cos^2\theta_{13}\left(1 - \cos\frac{\Delta m^2_{31}L}{2E}\right) \\ &- \frac{1}{2}\cos^4\theta_{13}\sin^2 2\theta_{12}\left(1 - \cos\frac{\Delta m^2_{21}L}{2E}\right) \\ &- 2\sin^2\theta_{13}\cos^2\theta_{13}\sin^2\theta_{12}\left(\cos\left(\frac{\Delta m^2_{31}L}{2E} - \frac{\Delta m^2_{21}L}{2E}\right) - \cos\frac{\Delta m^2_{31}L}{2E}\right) \end{aligned}$$

$$\begin{aligned} P^{IH}_{ee} &= 1 - 2\sin^2\theta_{13}\cos^2\theta_{13}\left(1 - \cos\frac{\Delta m^2_{31}L}{2E}\right) \\ &- \frac{1}{2}\cos^4\theta_{13}\sin^2 2\theta_{12}\left(1 - \cos\frac{\Delta m^2_{21}L}{2E}\right) \\ &- 2\sin^2\theta_{13}\cos^2\theta_{13}\cos^2\theta_{12}\left(\cos\left(\frac{\Delta m^2_{31}L}{2E} - \frac{\Delta m^2_{21}L}{2E}\right) - \cos\frac{\Delta m^2_{31}L}{2E}\right) \end{aligned}$$

Note that the only difference between Eqs. (1) and (1) is in the last term where $\sin^2\theta_{12}$ appears for NH while $\cos^2\theta_{12}$ appears from IH. Since we now know at a very high C.L. that the solar mixing angle θ_{12} is not maximal, we expect the survival probability P^{NH}_{ee} to be different from P^{IH}_{ee} and the difference is proportional to $\cos 2\theta_{12}$ [8,9,10,11,12,13,14,15,16].

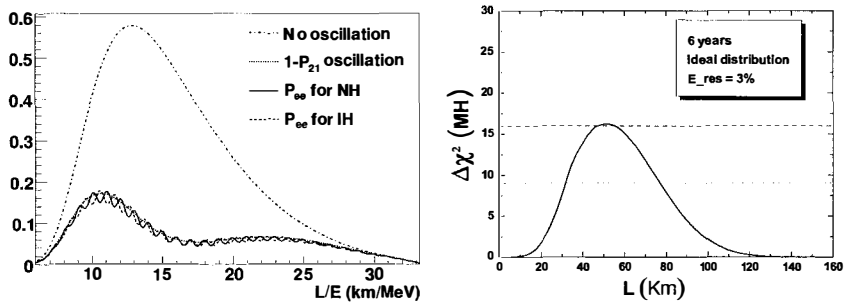

Figure 3 – The right panel shows the survival probability P_{ee} as a function of L/E for NH and IH cases (taken from [10]). The left panel shows the expected $\Delta\chi^2$ for the wrong hierarchy as a function of the baseline, assuming a 3% energy resolution (taken from [12]).

The survival probability for a 50 km baseline in shown in the right panel of Fig. 3. The fine wiggles driven by the faster oscillated are superimposed on the Δm^2_{21} driven oscillations and the difference between the NH and IH can be seen. It is obvious that in order to measure the neutrino mass hierarchy, the detector for this experiment must have extremely good energy resolution. Indeed it has been shown by various groups that the maximum resolution tenable for this kind of experiment is not more than 3%. The left panel of Fig. 3 shows the expected $\Delta\chi^2$ for the wrong hierarchy as a function of the baseline, assuming a 3% energy resolution.

A further washing out of the sensitivity comes from the fact that there are multiple reactors involved and hence the baseline differences, albeit small, leads to blurring out of the interference patterns. The left panel shows that the 50 km baseline yields the best results for mass hierarchy measurement. The proposed JUNO experiment in China and RENO-50 in Korea belong to this class of experiments. JUNO is expected to give 3σ sensitivity in 3 years taking into account all uncertainties into account and with an assumed energy resolution of 3% [13].

Note that the hierarchy measurement in intermediate baseline experiments, even though challenging, is independent of the true value of δ_{CP} as well as θ_{23} as is evident from the expression of the survival probability P_{ee}.

5 Conclusions

To conclude, we have discussed the prospects of determining the neutrino mass hierarchy in the next generation proposed experiments. In particular, we looked at the expected sensitivity in atmospheric neutrino experiments, near future long baseline experiments and reactor experiments. While the atmospheric neutrino and long baseline experiments use Earth matter effects to determine the neutrino mass hierarchy, the intermediate baseline reactor experiments look to disentangle the interference effects between Δm^2_{31} and Δm^2_{21} oscillations between NH and IH, to determine the neutrino mass hierarchy. We stressed that while the mass hierarchy sensitivity of the long baseline experiment suffered from our lack of knowledge of the true value of δ_{CP}, the atmospheric neutrino experiments were independent of any significant δ_{CP} dependence. This lead of useful synergy between the two classes of experiments. However, the hierarchy sensitivity of both class of experiments depends heavily of the true value of θ_{23}. The intermediate baseline reactor neutrino experiments on the other hand are independent of δ_{CP} as well as θ_{23}.

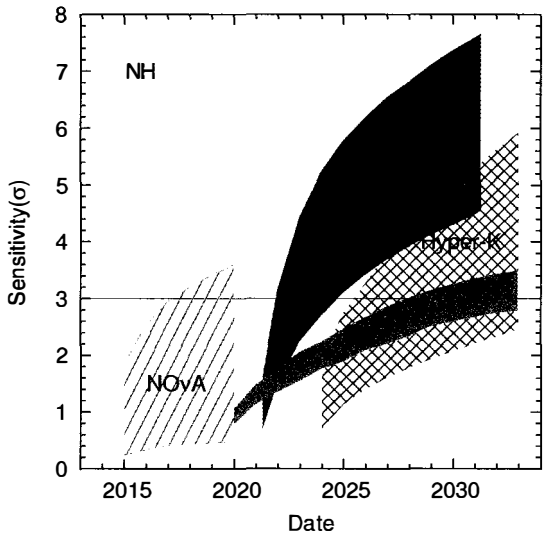

Figure 4 – The median sensitivity to the neutrino mass hierarchy as a function of the date.

We end by showing the projected sensitivity of some of the discussed experiments as a function of time. The figure has been adapted from [17] and is drawn assuming NH to be true. The bands for the atmospheric neutrino experiments come from the uncertainty on true value of θ_{23} while the bands for the long baseline experiments are from uncertainty in δ_{CP}.

References

1. R. Wendell, talk at Neutrino 2014.
2. K. Abe, T. Abe, H. Aihara, Y. Fukuda, Y. Hayato, K. Huang, A. K. Ichikawa and M. Ikeda *et al.*, arXiv:1109.3262 [hep-ex].
3. M. G. Aartsen *et al.* [IceCube PINGU Collaboration], arXiv:1401.2046 [physics.ins-det].
4. M. M. Devi, T. Thakore, S. K. Agarwalla and A. Dighe, JHEP **1410**, 189 (2014) [arXiv:1406.3689 [hep-ph]].
5. T. Thakore, A. Ghosh, S. Choubey and A. Dighe, JHEP **1305**, 058 (2013) [arXiv:1303.2534 [hep-ph]].
6. K. Abe *et al.* [T2K Collaboration], Phys. Rev. D **91**, no. 7, 072010 (2015) [arXiv:1502.01550 [hep-ex]].
7. M. Ghosh, S. Goswami and S. K. Raut, arXiv:1412.1744 [hep-ph].
8. S. T. Petcov and M. Piai, Phys. Lett. B **533**, 94 (2002) [hep-ph/0112074].
9. S. Choubey, S. T. Petcov and M. Piai, Phys. Rev. D **68**, 113006 (2003) [hep-ph/0306017].
10. J. Learned, S. T. Dye, S. Pakvasa and R. C. Svoboda, Phys. Rev. D **78**, 071302 (2008) [hep-ex/0612022].
11. L. Zhan, Y. Wang, J. Cao and L. Wen, Phys. Rev. D **78**, 111103 (2008) [arXiv:0807.3203 [hep-ex]].
12. L. Zhan, Y. Wang, J. Cao and L. Wen, Phys. Rev. D **79**, 073007 (2009) [arXiv:0901.2976 [hep-ex]].
13. Y. F. Li, J. Cao, Y. Wang and L. Zhan, Phys. Rev. D **88**, 013008 (2013) [arXiv:1303.6733 [hep-ex]].
14. P. Ghoshal and S. T. Petcov, JHEP **1103**, 058 (2011) [arXiv:1011.1646 [hep-ph]].
15. S. F. Ge, K. Hagiwara, N. Okamura and Y. Takaesu, JHEP **1305**, 131 (2013) [arXiv:1210.8141 [hep-ph]].
16. F. Capozzi, E. Lisi and A. Marrone, Phys. Rev. D **89**, no. 1, 013001 (2014) [arXiv:1309.1638 [hep-ph]].
17. M. Blennow, P. Coloma, P. Huber and T. Schwetz, JHEP **1403**, 028 (2014) [arXiv:1311.1822 [hep-ph]].

RECENT RESULTS FROM SUPER-KAMIOKANDE

SHUNICHI MINE
Department of Physics and Astronomy, University of California, Irvine, USA

I will summarize the most recent nucleon decay and sterile neutrino results from Super-Kamiokande (SK) experiment.

1 Introduction

SK is the world's largest water Cerenkov detector, located in the Kamioka mine, under ~1 km mountain in Japan. There are four experimental periods SK-I (1996-2001), SK-II (2002-2005), SK-III (2006-2008), and SK-IV (2008-present). The inner detector photo coverage is ~40% in SK-I, SK-III, and SK-IV and ~20% in SK-II. A new front-end electronics module QBEE was implemented from SK-IV. The SK experiment has been running for ~17 years in total. More details about the SK detector as well as its calibration are found in the references[1].

SK has been publishing important physics results in many subjects. For example, in 2014 and 2015 (until Moriond 2015 in March), papers were published on nucleon decay searches[2,3,4,5], atmospheric neutrino oscillation analyses[6,7], solar neutrino oscillation analysis[8], and supernova relic neutrino searches[9]. Among them, I focus on the nucleon decay searches and the sterile neutrino analysis.

2 Nucleon Decay Searches

Grand Unified Theories (GUTs) are very attractive and a strong motivation for experimental nucleon decay searches. If there would be a single symmetry group which involves $SU(3)_{color} \times SU(2)_L \times U(1)_Y$, the number of coupling constants could be unified, the quantization of electric charge could be explained, and so on. Among various GUTs, SO(10) GUTs and Super-Symmetry (SUSY) GUTs are recently popular and related to the recent nucleon decay searches in SK. In the SO(10) GUT, fifteen fermions and a ν_R would fit in a single representation, and very tiny mass of the ν_L could be explained by using the ν_R as a partner in the seesaw mechanism. In SUSY GUT, three coupling constants could meet at $\sim 10^{16}$ GeV and gravity could be included. In all of these cases, GUTs predict nucleon decay.

SK has the world's best sensitivities on the nucleon lifetime thanks to large fiducial volume (22.5 kt corresponding to $\sim$7.5 $\times 10^{33}$ protons), excellent event reconstruction performances, and long stable detector operation. The lifetime limit is proportional to exposure for the background free case but it's not anymore true for non-zero background case. It is important to increase signal efficiency and background rejection and decrease their systematic errors. Many analysis improvements have been done recently especially in the p$\rightarrow \nu K^+$ search and several new searches have been undertaken.

2.1 p$\rightarrow \nu K^+$

p$\rightarrow \nu K^+$ is one of the dominant decay modes in SUSY GUTs and some models predict a lifetime $<\sim 10^{34}$ years which could be probed by SK. In a new data analysis[2], data from SK-II to SK-IV are added, event reconstructions and selections are improved, and Michel electron tagging efficiency is higher in SK-IV thanks to the QBEEs with respect to the previous SK published result[10].

There are three analysis methods. In the first method ("Prompt γ"), the prompt nuclear γ as well as mono-energetic muon from K^+ decay and Michel electron are tagged. Figure 1 (left) shows the number of PMT hits for the prompt γ candidate. The data and atmospheric neutrino (background) MC agree well with each other and no data candidate is seen in the signal region. The same event selections are applied in the second method ("P_μ spec.") except for a relaxed momentum cut and no prompt γ hits. Figure 1 (center) shows the muon momentum distributions and no data excess is seen in the signal region. In the third method ("$\pi^+\pi^0$), both π^+ and π^0 from K^+ decays are used. Figure 1 (right) shows visible energy distributions for the π^+ candidate and no data candidate is seen in the signal region.

Table 1 summarizes the results from all the methods. The numbers in parentheses in SK-I are from the previous SK paper, and the expected background rates are significantly reduced in new analysis. The number of total expected background events (sum of the expected background events from SK-I to SK-IV) are less than 1 in both Prompt γ and $\pi^+\pi^0$ methods.

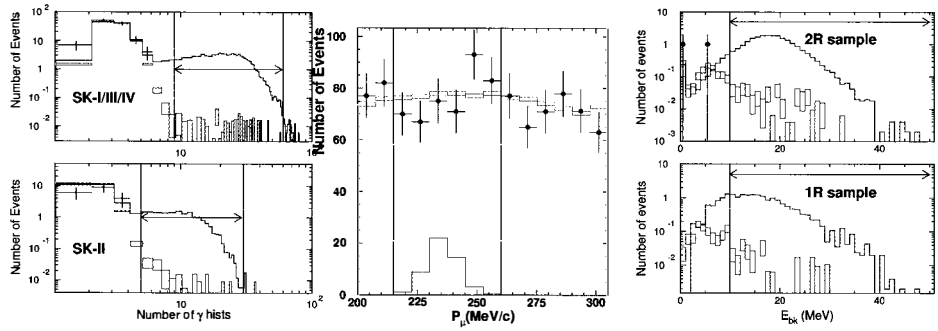

Figure 1 – p$\rightarrow \nu K^+$ search. The number of PMT hits for prompt γ candidate, muon momentum, and visible energy for π^+ candidate are shown from left to right, respectively. p$\rightarrow \nu K^+$ MC, atmospheric neutrino MC, and data are shown in blue, red, and black, respectively.

There is no data excess above the background expectation and the lower limit on the lifetime is set to be $>5.9\times 10^{33}$ years (90% CL). This result is the world's best limit, 2.5 times more stringent than the previous published SK result, and constrains recent SUSY GUT models.

Table 1: Summary of p→ νK^+ search.

		SK-I	SK-II	SK-III	SK-IV
Exposure (kt·yrs)		91.7	49.2	31.9	87.3
Prompt γ	Signal Efficiency (%)	7.9±0.1(8.6)	6.3±0.1	7.7±0.1	9.1±0.1
	Exp. Background	0.08(0.7)	0.14	0.03	0.13
	Data Candidate	0	0	0	0
P_μ spec.	Signal Efficiency (%)	33.9±0.3	30.6±0.3	32.6±0.3	37.6±0.3
	Exp. Background	193	94.3	69.0	223.1
	Data Candidate	177	78	85	226
$\pi^+\pi^0$	Signal Efficiency (%)	7.8±0.1(6.0)	6.7±0.1	7.9±0.1	10.0±0.1
	Exp. Background	0.18(0.6)	0.17	0.09	0.18
	Data Candidate	0	0	0	0

2.2 p→eπ^0

p→eπ^0 is one of the dominant decay modes in non-SUSY GUTs and the most recent result is shown in this report. Detail of the data analysis can be found in the previous published paper[11].

Figure 2 shows total invariant mass and total momentum for p→eπ^0 MC, atmospheric neutrino (background) MC, and real data. The signal efficiency and the number of total expected background events as estimated with the MC are ~40% and ~0.7, respectively. The number of expected background events as well as various kinematics of the final particles used in the background MC was validated with the K2K neutrino beam data[12].

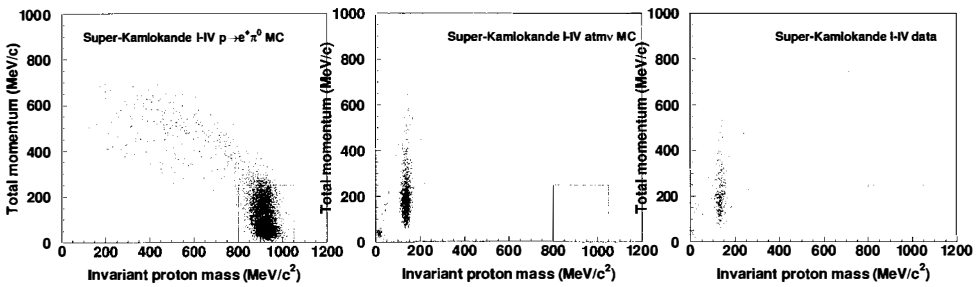

Figure 2 – p→eπ^0 search. Total invariant mass and total momentum are shown for p→eπ^0 MC, atmospheric neutrino MC, and data from left to right, respectively. The signal box is also shown.

There is no data candidate in the signal box, and the data distribution agrees with that of background. The agreement was also confirmed in various basic distributions such as the total mass and the total momentum, respectively, as well as all the parameters used in the event selections. The lifetime lower limit is set to be $>1.4\times10^{34}$ years (90% CL). This is the world's best limit for this mode.

Major on-going improvements being worked on now include neutron tagging in SK-IV, sophisticated event reconstruction algorithm, and reduction of the systematic errors.

2.3 $p \to e\nu\nu$ and $p \to \mu\nu\nu$

As an example of recent nucleon decay searches which had never been done before in SK, $p \to e\nu\nu$ and $p \to \mu\nu\nu$ search results[4] are shown in this report. Some SO(10) models embedded in Pati-Salam's left-right symmetric model predict lifetimes around 10^{30-33} years. Unlike standard nucleon decay channels with $|\Delta(B-L)| = 0$, these decay modes have $|\Delta(B-L)| = 2$.

Figure 3 shows electron and muon momentum distributions in the $p \to e\nu\nu$ and $p \to \mu\nu\nu$ searches, respectively. There is no significant excess in the signal regions in both searches and the

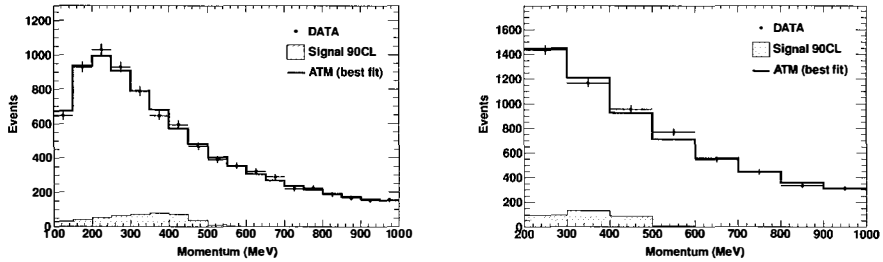

Figure 3 – $p \to e\nu\nu$ and $p \to \mu\nu\nu$ searches. Electron momentum (left) and muon momentum (right) are shown for $p \to e\nu\nu$ and $p \to \mu\nu\nu$ searches, respectively.

lifetime limits are set to be $>1.7\times10^{32}$ years (90% CL) and $>2.2\times10^{32}$ years (90% CL) for $p \to e\nu\nu$ and $p \to \mu\nu\nu$ searches, respectively. They are the world's best limits, an order of magnitude improvement over previous results by other experiments, and provide strong constraints to these models.

3 Sterile Neutrino Analysis

Primary cosmic rays strike air nuclei and decay of the resulting hadrons givcs atmospheric neutrinos. The number of atmospheric neutrinos collected so far in SK is more than 40,000. The travel length (~10-10,000km) and energy (~0.1-10^4GeV) have wide ranges and both neutrino and anti-neutrino exist (~30% for anti-neutrino in the final samples). The atmospheric neutrino is, therefore, an excellent tool for broad studies of neutrino oscillations in SK. In this report, I focus on the sterile neutrino oscillation analysis [6].

The unitary matrix with sterile neutrino is given by:

$$U = \begin{pmatrix} U_{e1} & U_{e2} & U_{e3} & U_{e4} & \cdots \\ U_{\mu1} & U_{\mu2} & U_{\mu3} & U_{\mu4} & \cdots \\ U_{\tau1} & U_{\tau2} & U_{\tau3} & U_{\tau4} & \cdots \\ U_{s1} & U_{s2} & U_{s3} & U_{s4} & \cdots \\ . & . & . & . & . \\ . & . & . & . & . \end{pmatrix} \quad (1)$$

where $|U_{\mu4}|^2$ induces a decrease in event rate of μ-like data of all energies and zenith angles but is not sensitive to δm^2 due to fast oscillations, and $|U_{\tau4}|^2$ causes shape distortion of angular distribution of higher energy μ-like data.

Figure 4 shows zenith angle distribution of the partially contained through-going sample (average energy ~10GeV) for the atmospheric neutrino MC with and without sterile neutrino oscillation overlaid with the data. No evidence of sterile neutrino oscillations is observed and the upper limit on $|U_{\mu4}|^2$ and $|U_{\tau4}|^2$ are set to be <0.054 (90% CL) and <0.23 (90% CL), respectively. Our results as well as other experimental results are summarized in Figure 5.

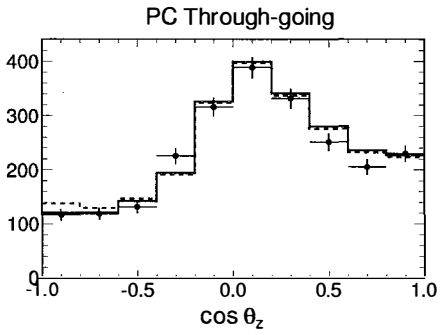

Figure 4 – Sterile neutrino analysis. Zenith angle of partially contained through-going sample for atmospheric neutrino MC without sterile neutrino (black solid), with $|U_{\tau 4}|^2 = 0.31$ (blue dashed), and data (black cross).

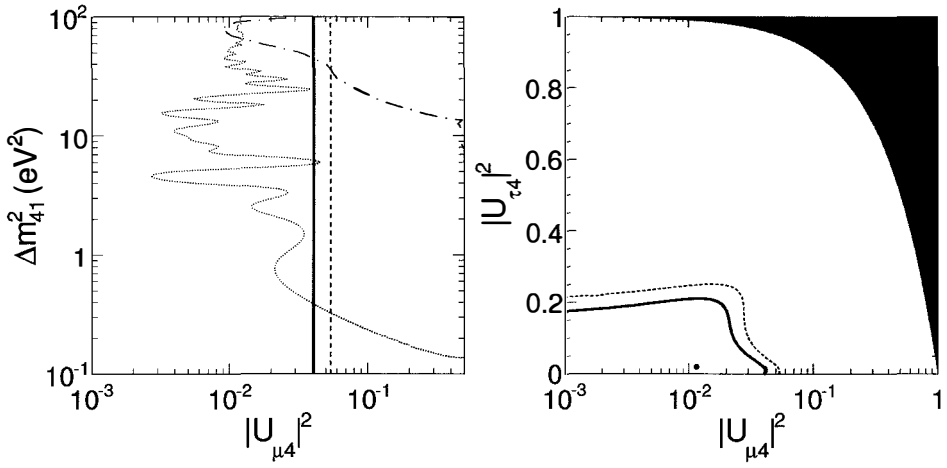

Figure 5 – Sterile neutrino oscillation analysis. The SK 90% CL (99% CL) upper limits are shown as black solid (dashed) lines for $|U_{\mu 4}|^2$ and $|U_{\tau 4}|^2$. Light gray regions are excluded by SK (90% CL). Thin dotted and dot-dashed curves in left are from other experiments. Dark gray region in right is disallowed by unitarity.

4 Summary and Future

No evidence of nucleon decay has been observed so far in SK and we set the most stringent lifetime limits in the world. We are continuing to improve our analyses and increase the data statistics. No indication of non-standard models has been found in the atmospheric neutrino oscillation analyses and we set stringent limits on the relevant parameters.

In all of these analyses, we hope to improve our sensitivity by increasing the sophistication of our reconstruction algorithm, reducing systematic errors, and so on. In the future, the sensitivities would be increased dramatically by building Hyper-Kaimiokande[13,14] (a next generation water Cerenkov detector with a 25 times larger fiducial volume than SK).

References

1. *Nucl. Instrum. Methods* A **737C**, (2014).
2. *Phys. Rev.* D **90**, 072005 (2014).
3. *Phys. Rev. Lett.* **113**, 121802 (2014).
4. *Phys. Rev. Lett.* **113**, 101801 (2014).
5. *Phys. Rev. Lett.* **112**, 131803 (2014).
6. *Phys. Rev.* D **91**, 052019 (2015).
7. *Phys. Rev.* D **91**, 052003 (2015).
8. *Phys. Rev. Lett.* **112**, 091805 (2014).
9. *Astropart. Phys.* 60 (2014) 41-46.
10. *Phys. Rev.* D **72**, 052007 (2005).
11. *Phys. Rev.* D **85**, 112001 (2012).
12. *Phys. Rev.* D **77**, 032003 (2008).
13. arXiv:1109.3262.
14. arXiv:1502.05199.

RECENT RESULTS FROM BOREXINO

B.Caccianiga *, G. Bellini, J. Benziger, D. Bick, G. Bonfini, D. Bravo, F. Calaprice, A. Caminata, P. Cavalcante, A. Chavarria, A. Chepurnov, D. D'Angelo, S. Davini, A. Derbin, A. Empl, A. Etenko, K. Fomenko, D. Franco, F. Gabriele, C. Galbiati, S. Gazzana, C. Ghiano, M. Giammarchi, M. Goeger-Neff, A. Goretti, C. Hagner, E. Hungerford, Aldo Ianni, Andrea Ianni, M. Kaiser, V.V. Kobychev, D. Korablev, G. Korga, D. Kryn, M. Laubenstein, B. Lehnert, T. Lewke, E. Litvinovich, P. Lombardi, F. Lombardi, L. Ludhova, G. Lukyanchenko, I. Machulin, S. Manecki, W. Maneschg, S. Marcocci, Q. Meindl, E. Meroni, M. Meyer, L. Miramonti, M. Montuschi, M. Misiaszek, P. Mosteiro, V. Muratova, L. Oberauer, M. Obolensky, F. Ortica, K. Otis, M. Pallavicini, L. Papp, L. Perasso, A. Pocar, G. Ranucci, A. Razeto, A. Re, A. Romani, N. Rossi, R. Saldanha, C. Salvo, S. Schoenert, H. Simgen, M. Skorokhvatov, O. Smirnov, A. Sotnikov, S. Sukhotin, Y. Suvorov, R. Tartaglia, G. Testera, D. Vignaud, R.B. Vogelaar, F. von Feilitzsch, H. Wang, J. Winter, M. Wojcik, M. Wurm, J. Xu, O. Zaimidoroga, S. Zavatarelli, K. Zuber, G. Zuzel

** Dipartimento di Fisica, Università degli Studi e INFN, Milano 20133, Italy*

The Sun is powered by a chain of nuclear reactions (the so-called "proton-proton cycle") which burn hydrogen and produce Helium. In these reactions also neutrinos are emitted. Unlike photons, which take approximately 100 thousand years to travel from the Sun's core to its surface, neutrinos cross the solar matter in few seconds and reach Earth in 8 minutes, thus providing a real-time picture of the Sun interior. The Borexino experiment has been devoted for over 7 years to the difficult hunt for elusive solar neutrinos. Thanks to the unprecedented radiopurity of the detector and its large mass, Borexino has been able to study most of the components of the solar neutrino spectrum. In this talk I will focus on the latest result published by the experiment, which consists in the first direct observation of the solar neutrinos from the primary reaction $p + p \dashrightarrow d + e^+ + \nu_e$ which is responsible for most of the solar luminosity.

1 Introduction

The Earth is reached every second by a large number of neutrinos coming from the Sun (flux $\sim 10^{10}\,\nu\,\mathrm{cm}^{-2}\mathrm{sec}^{-1}$) which are mainly produced in the so-called "proton-proton cycle" reactions (see Figure 1, left). In spite of their copious flux, detecting solar neutrinos is experimentally challenging due to neutrino elusiveness: it requires large volume detectors and low-background conditions. However, the study of solar neutrinos has been very rewarding: on one hand, it has provided a nice confirmation of the Standard Solar Model; on the other hand, it has proved that neutrinos oscillate (and therefore have mass) and has allowed to determine the oscillation parameters Δm^2_{12} and θ_{12}. In spite of this great success, the study of solar neutrinos is far from being completed. Before Borexino only radiochemical experiments could observe solar neutrinos below 1 MeV, while real-time experiments were sensible only to the very small fraction of the solar neutrino spectrum above ~ 4 MeV. The exceptional radiopurity of Borexino makes it possible to work with a very low energy threshold (down to ~ 150 keV), thus allowing the experiment to perform a complete spectroscopy of solar neutrinos. During the so-called Phase 1 of data-taking (2007-2010), Borexino has reached its original goal of measuring the ^{7}Be flux with high precision (total error below 5%) and its day/night asymmetry [1,2]; it has also achieved

several other important results, including the measurement of the ^{8}B neutrino flux down to the unprecedented threshold of 3 MeV[3], the first observation of neutrinos from the *pep* reaction and the best limit on solar neutrinos from the CNO cycle[4].

In this paper we report about the latest important result of Borexino, namely the first direct observation of the solar neutrinos from the reaction p +p $\rightarrow$ d + e$^-$ + ν_e (the so-called, pp neutrinos)[5]. This reaction, which belongs to the proton-proton cycle, is the keystone process for energy production in the Sun and is responsible for 90% of the solar neutrino flux on Earth. The observation of pp neutrinos is a very difficult task, which was made possible by the excellent performance of the detector as a whole, by the complete knowledge of it response and by the very low levels of background reached after an extensive purification campaign performed in 2010-2011 which improved the already exceptional radiopurity of the Borexino scintillator, especially for what concerns ^{85}Kr.

2 The Borexino detector

Borexino is located deep underground under 3800 meters of water equivalent, in the Laboratori Nazionali del Gran Sasso: at this depth the cosmic muon flux is reduced by a factor $\sim 10^6$. The detector design follows the concept of graded-shielding, in which layers of concentric materials of increasing radiopurity shield the innermost ultra-pure core of the experiment. A schematic view of the Borexino design is depicted in Figure 1 (right). The core of Borexino is 300 tons of ultra-pure liquid scintillator (pseudocumene + 1.5 g/l of PPO) contained in a 4.25 m-radius, 120 μm-thick nylon vessel. The light emitted by the scintillator is detected by 2214 photomultiplier tubes mounted on a 7 m-radius Stainless Steel Sphere (SSS), concentrical with the nylon vessel. The SSS is filled with 1000 tons of ultra-pure buffer liquid (pseudocumene + DMP, a light quencher) which provide shielding against radioactivity from the photomultipliers and the sphere itself. To further increase shielding, the SSS is surrounded by 2000 tons of ultra-pure water contained in a cylindrical dome. The water in the external part of the detector serves also as an active shield to suppress the residual background due to cosmic muons which are able of penetrating underground. In order to do so, 200 photomultiplier tubes are mounted on the external part of the SSS to detect the Cerenkov light emitted by muons which cross the water. The intrinsic radiopurity of the scintillator has been brought to exceptional levels thanks to the successfull purification strategy developed during 15 years of dedicated R&D studies[6]. A detailed description of the Borexino detector can be found in reference[7].

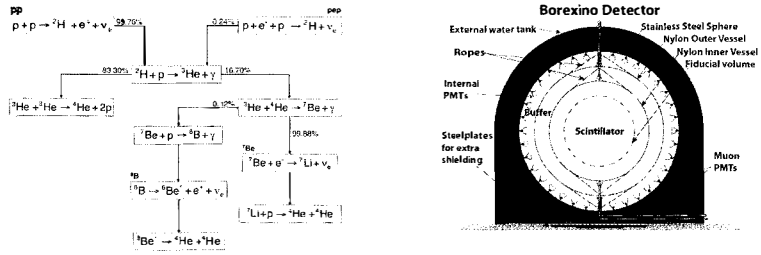

Figure 1 -- Left plot: reactions of the proton-proton cycle, responsible for $\sim$ 99% of the solar luminosity. Right plot: a scheme of the Borexino detector.

3 Analysis

Borexino detects neutrinos by measuring the scintillator light emitted by recoil electrons in the reaction $\nu_x + e^- \rightarrow \nu_x + e^-$. Energy and position of the neutrino-induced events are determined by the number and arrival time of collected photons. The energy scale and detector response throughout the scintillator volume has been determined accurately by means of three calibration campaigns with radioactive sources, combined with a detailed Monte Carlo simulation [8]. Approximately 500 photons are collected for 1 MeV deposited in the Borexino scintillator. The pp-neutrino energy spectrum extends up to 420 keV which corresponds to a maximum recoil energy of the electron of approximately 264 keV. Several backgrounds can mimic the neutrino signal in this energy region, mainly coming from natural radioactivity both native or external to the scintillator. In order to maximize the signal-to-noise ratio, events must satisfy several selection criteria, mainly optimized to reject residual cosmogenic muons, muon-produced isotopes and external background. This last background (due to radioactivity from materials surrounding the core of the detector) is particularly significant and can be very effectively removed by selecting only the innermost part of the scintillator with a fiducial cut(R < 3.021 m and abs(z) < 1.67 m).

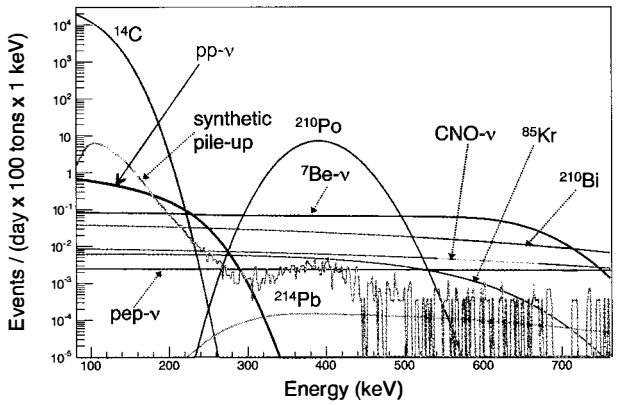

Figure 2 – Expected energy spectra of signal and background. The pp neutrino signal is the thick red curve.

Figure 2 shows the expected relevant contributions to the total energy spectrum after the application of the selection cuts: pp neutrinos (red thick line), other solar neutrinos (^{7}Be, pep and CNO) and residual backgrounds. The pp neutrino spectrum is clearly distinguishable from those of ^{85}Kr, ^{21}Bi, CNO neutrinos and ^{7}Be, which have flat spectral shape in the energy range relevant for this analysis. The most relevant backgrounds which affect the pp analysis are ^{14}C and pile-up (mostly from two ^{14}C events). The ^{14}C contamination is unavoidable in an organic liquid scintillator. It produces a β with an end-point of 156 keV. The total rate of ^{14}C in the Borexino scintillator on the entire energy range is more than four order of magnitude larger than the expected pp neutrino rate. However the ^{14}C and pp neutrino spectral shapes are quite different (see Figure 2): the ^{14}C rate is overwhelming with respect to the pp rate at energies below 150 keV, while the two rates become comparable above 150 keV. Note that because of the finite energy resolution, the effective end-point of ^{14}C is moved to $\sim$264 keV and the pp neutrino spectrum extends up to $\sim$340 keV. In order to disentangle the pp neutrino signal from ^{14}C it is important to precisely know the ^{14}C rate and spectral shape. This was done by looking at a sample of data in which the event causing the trigger is followed by a second event within the acquisition time window of 16 ms. This second event, which is predominantly due to ^{14}C,

does not suffer from hardware trigger-threshold effects. The ^{14}C rate was found to be (40 ± 1) Bq in 100 tons of liquid scintillator.

The second most significant background for the pp neutrino analysis is the pile-up of two events which occur in the same acquisition window. Figure 2 shows that the pile-up spectral shape is very similar to the signal one. Like for ^{14}C, it is therefore important to estimate the pile-up rate and shape indipendently from the main analysis. In order to do so a data-driven method was used in which real triggered events without any selection cuts were artificially overlapped with random data samples ("synthetic pile-up"). The combined synthetic events are then selected and reconstructed using the same procedure applied to the regular data. The total rate of pile-up of ^{14}C-^{14}C events (which dominates over other pile-up combinations) was determined with this method to be (154 ± 10) cpd/100tons.

An alternative method to account for pile-up, the so-called "convolution method", was also used. In this method, pile-up is not treated as a species of its own, but is taken into account by convolving the spectral components of signal and backgrounds used in the fit with the random trigger spectrum. Random triggers are regularly collected during data-taking for monitoring purpose with a frequency of 0.5 Hz.

4 Results

The search for pp neutrinos has been performed on the first part of the Borexino Phase 2 data, namely the period between January 2012 and May 2013 (408 live days). This period features the highest radiopurity, since it follows a successfull purification campaign of the scintillator with water extraction. In particular, ^{85}Kr and ^{210}Bi which are important backrounds for this analysis have been significantly reduced with respect to Phase 1 data. The pp neutrino rate is extracted by fitting the low energy part (between 165 and 590 keV) of the selected energy spectrum with the theoretical spectra of the signal and background components. The energy scale and its linearity is determined from the number of hit PMTs, using a combination of calibrations and a detailed Monte Carlo model [9].

The fit is performed with the spectral-fitter, a multipurpose tool developed in the Borexino collaboration for the ^{7}Be and pep neutrino analyses [9], and adapted for the present work. The free fit parameters are the rates of pp-solar neutrinos, ^{210}Bi, ^{210}Po, and ^{85}Kr. The ^{14}C and the synthetic pile-up are constrained with a penalty to the independently measured rates (see Section 3). The ^{7}Be-neutrino rate is fixed to the measured value [1], while pep and CNO solar neutrino contributions are fixed at the levels of the high-metallicity SSM assuming MSW neutrino oscillations. The ^{214}Pb rate is fixed using the measured rate of ^{214}Bi (β) - ^{214}Po (α) delayed coincidence events. The scintillator light yield and energy resolution are left free to vary in the fit. The energy spectrum and the result of the fit are shown in Figure 3.

In order to estimate the robustness of the analysis procedure, we have performed many fits in slightly different conditions and quoted as systematic error the rms of the distribution of the different fit results. We varied the fit range, the data selection criteria, the energy estimator and the pile-up evaluation method. Our best estimate for the systematic error obtained in this way is 7% . In addition, we include a systematic uncertainty (2%) due to fiducial mass determination which was estimated using calibration data.

We investigated the impact of other potential sources of systematic error: the details of the energy scale definition, the ^{14}C and ^{210}Bi beta-decay shape factors, the dependence of the result on the CNO and pep neutrino rates fixed in the fit. We found all of them to be negligible.

Finally, we verified that the fit performed without the constraint on the ^{14}C rate yields results consistent with the one obtained in the standard fit procedure and that it returns a ^{14}C rate within $1\,\sigma$ of the one determined independently (see Section 3).

In conclusions, our best estimate for the pp neutrino rate in Borexino is

$$(144 \pm 13\,(stat) \pm 10\,(sys))\,\text{cpd/100 tons}$$

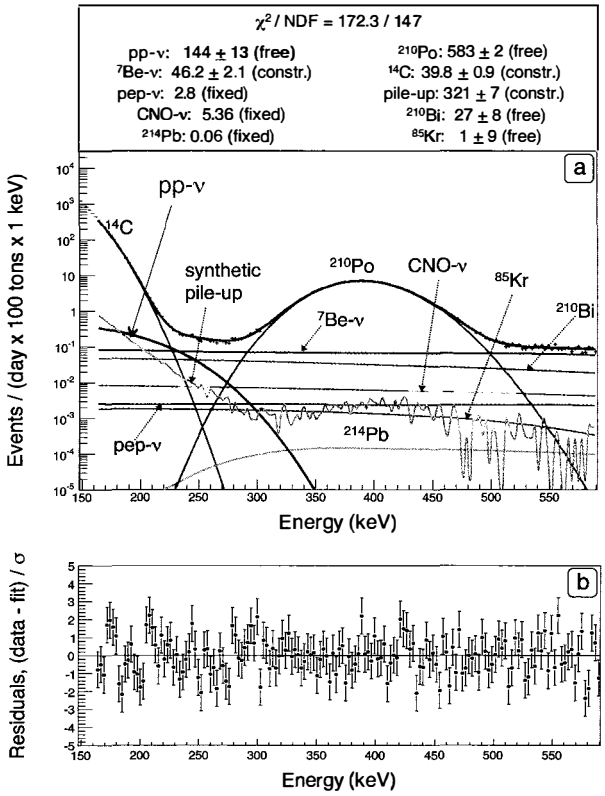

Figure 3 – a) Results of the fit performed on data. b) Residuals of the fit.

From this rate it is possible to extract the pp neutrino flux, once the latest values for the oscillation parameters are properly taken into account. We find $(6.6 \pm 0.7) \times 10^{10}\,\nu\mathrm{sec}^{-1}\mathrm{cm}^{-2}$ which is in good agreement with the Standard Solar Model predictions[10] $(5.98 \pm 0.04) \times 10^{10}\,\nu\,\mathrm{sec}^{-1}\mathrm{cm}^{-2}$. The current result can not help solving the solar metallicity controversy since its uncertainty ($\sim$ 11 %) is too large compared with the small difference ($\sim$1%) in the pp neutrino flux between the high and low metallicity hypothesis.

Conversely, from the the measured pp neutrino rate it is possible to extract the survival probability P_{ee}, once the SSM predictions for the flux are properly taken into account. We find $P_{ee} = 0.64 \pm 0.12$ which is consistent with the expectations from the LMA-MSW values of the oscillation parameters. This result is shown in Figure 4 (red point) together with the other P_{ee} measurements performed by Borexino for the ^{7}Be, pep and ^{8}B neutrinos.

5 Conclusions and outlook

The first direct observation of solar neutrinos from the $p + p \rightarrow d + e^- + \nu_e$ reaction has been presented. This result is a major experimental milestone in solar neutrino physics since it strongly confirms our understanding of the Sun. The pp neutrino flux measured by Borexino shows that neutrino and photon luminosities are equal within errors. However, the experimental uncertainty is still too large to make this comparison significant. Future Borexino-inspired

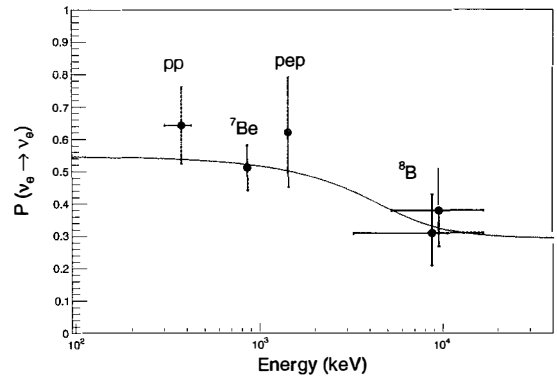

Figure 4 – Survival probability for solar ν_e as a function of energy. The thick purple line is the curve expected for the best-fit values of the oscillation parameters $\Delta\, m^2_{12}$ and θ_{12}. The dots are results from Borexino, including the pp neutrino one (red dot).

experiments could possibly reach a higher enough precision ($\sim 1\,\%$) to investigate finer details of the Sun dynamics.

Borexino has completed the study of solar neutrinos coming from the pp-cycle reactions shown in Figure 1. The most important remaining goal for the Borexino Phase 2 analysis is to attempt the direct observation of solar neutrinos from the CNO-cycle. This group of reactions is expected to contribute less than 1% to the solar luminosity, while it is believed to be the main actor in massive stars. Given their small flux and low energy, CNO neutrinos have never been observed directly: therefore their detection with Borexino would be of exceptional astrophysical interest.

Acknowledgments

The Borexino program is made possible by funding from the INFN (Italy); the NSF (USA); the BMBF, DFG and MPG (Germany); the JINR, RFBR, RSC and NRC Kurchatov Institute (Russia); and the NCN (Poland). We acknowledge the generous support of the Laboratori Nazionali del Gran Sasso (Italy) and that of the Gran Sasso Science Institute.

References

1. G. Bellini et al. (BOREXino), *Phys. Rev. Lett.* **107**, 141302 (2011).
2. G. Bellini et al. (BOREXino), *Phys. Lett.* B **707**, 22 (2012).
3. G. Bellini et al. (BOREXino), *Phys. Rev.* D **82**, 033006 (2010).
4. G. Bellini et al. (BOREXino), *Phys. Rev. Lett.* **108**, 051302 (2012).
5. G. Bellini et al. (BOREXino), *Nature*, **512**, 383 (2014).
6. G. Alimonti et al. (BOREXino), *Nucl. Instrum. Methods* A **609**, 58 (2009).
7. G. Alimonti et al. (BOREXino), *Nucl. Instrum. Methods* A **600**, 568 (2009).
8. H. Back et al. (BOREXino), *JINST*, **7**, P10018 (2012).
9. G. Bellini et al. (BOREXino), *Phys. Rev.* D **89**, 112007 (2014).
10. A. Serenelli et al. *Astrophys. J.*, **743**, 24 (2011).

RECENT RESULTS FROM MINERvA

C.E. PATRICK
Department of Physics and Astronomy, Northwestern University, 2145 Sheridan Road, Evanston, IL, 60208, USA

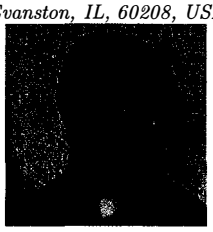

The MINERvA detector is situated in Fermilab's NuMI beam, which provides neutrinos and antineutrinos in the 1-20 GeV range. It is designed to make precision cross-section measurements for scattering processes on various nuclei. These proceedings summarize the differential cross-section distributions measured for several different processes. Comparison of these with various models hints at additional nuclear effects not included in common simulations. These results will help constrain generators' nuclear models and reduce systematic uncertainties on their predictions. An accurate cross-section model, with minimal uncertainties, is vital to oscillation experiments.

1 The MINERvA detector

MINERvA is situated in Fermilab's NuMI muon-neutrino beamline[1]. The results described in this talk were generated from data taken in the low-energy beam configuration between 2010 and 2012, with a peak neutrino energy around 3 GeV. During this period, we collected 3.98×10^{20} protons on target in the neutrino-enhanced configuration, and 1.7×10^{20} in the antineutrino. The detector is now taking data in a medium-energy configuration with a peak energy around 6 GeV.

The MINERvA detector's[2] central tracking region is constructed from 120 planes of parallel triangular strips of plastic (CH) scintillator, arranged almost perpendicular to the beam axis. Each strip contains a wavelength-shifting fiber, which delivers light generated by charged particles to photomultiplier tubes. Planes of these strips are oriented at (0, $\pm 60°$) to enable three-dimensional track reconstruction. Downstream and to the sides of the tracker are a lead electromagnetic calorimeter and a steel hadronic calorimeter, interspersed with scintillator. Upstream of the tracker, scintillator planes are interspersed with planes of nuclear target materials: iron, lead and graphite. A water target is also installed. Directly upstream of the detector is a liquid helium target. The magnetized MINOS[3] near detector, 2m downstream, acts as a muon spectrometer.

MINERvA's energy range of 1-20 GeV allows us to investigate three types[4] of neutrino-nucleon scattering. Quasi-elastic scattering, where a neutrino exchanges a W boson with a single

nucleon, is most prevalent at lower energies. Above 1GeV, we see significant contributions from resonant pion production. Deep inelastic scattering dominates above around 5 GeV.

2 Quasi-elastic scattering

2.1 Quasi-elastic scattering theory

Charged-current quasi-elastic (CCQE) interactions, $\nu_l n \rightarrow l^- p$ and $\bar{\nu}_l p \rightarrow l^+ n$, are important signal processes for oscillation experiments, and have been extensively studied due to their relative simplicity. When a neutrino scatters quasi-elastically from a stationary nucleon, it is possible to reconstruct the neutrino's energy, E_ν, and the four-momentum transfer, Q^2, from final-state lepton's kinematics. For neutrino scattering, Q^2 and E_ν can alternatively be calculated from the kinematics of the final-state proton. The differential cross-section $\frac{d\sigma}{dQ^2}$ can also be calculated [5] using the Llewellyn Smith formalism, as a function of Q^2 and various nucleon form-factors. All but one of these (the axial form-factor F_A) can be measured in electron scattering processes. With F_A modeled as a dipole, this leaves one free parameter, the axial mass, M_A, to be determined from neutrino scattering. Bubble chamber experiments on hydrogen and deuterium [7] [11] give a global average value close to $M_A = 1.0 GeV/c^2$.

In heavy nuclei, however, nucleons are not stationary, and interact with each other; meaning that the Llewellyn Smith cross-section model must be modified to include these effects. The simplest model for this, the Relativistic Fermi Gas (RFG) [6] models the nucleons as independent particles, moving with a Fermi momentum distribution in a field generated by the rest of the nucleus. Additionally, the Pauli exclusion principle requires an ejected nucleon to have a momentum above the Fermi limit. The RFG, however, does not model additional nuclear effects due to nucleon-nucleon correlations [8]. Scattering from correlated pairs of nucleons can not only affect reconstruction, but can also lead to the additional ejection of the correlated partner. [12] Correlations can occur at short, medium, and long range, and can be generated in various ways.

Several models for some or all of these nuclear effects have been implemented. Our nominal Monte Carlo, GENIE 2.6.2 [17], includes the Bodek-Ritchie correction to the RFG [9] [10], which models short-range correlations with a high-momentum tail. An alternative approach is to use a shell model of nuclear energy levels, modifying this spectral function [14] to include energies corresponding to correlated pairs. Amplitudes for Feynman diagrams corresponding to meson exchange currents (which lead to multi-nucleon effects, including correlations) have been calculated [13]. An enhancement found in electron-nucleon scattering, believed to be caused by correlation effects, can be modeled by a modification to the nucleon's magnetic form factor. This is known as the Transverse Enhancement Model [15].

In addition to these initial-state nuclear effects, we must also consider final-state interactions. Hadrons produced by neutrino scattering may re-interact as they propagate through the nucleus. This can affect not only the energy and angle of the final-state particles; it can also alter the number and type of particles in the final state. For example, a proton produced in quasi-elastic scattering may re-scatter and produce a pion; alternatively a pion produced in a resonant process may be absorbed, producing a quasi-elastic-like final state. These processes are particularly important when we rely on hadron kinematics for our reconstruction. GENIE models FSI with the INTRANUKE package [18].

2.2 Quasi-elastic cross-section, calculated from muon kinematics

MINERvA has calculated both the neutrino [21] and the antineutrino [20] differential cross section $\frac{d\sigma}{dQ^2_{QE}}$ in the scintillator tracker, where the four-momentum transfer, Q^2_{QE} and neutrino energy E_ν^{QE} are calculated from the kinematics of the final-state muon.

The MINOS near detector is used to identify correct-sign muons; the price of this is a limited acceptance as only forward going muons (less than 20° to the beam line, depending on

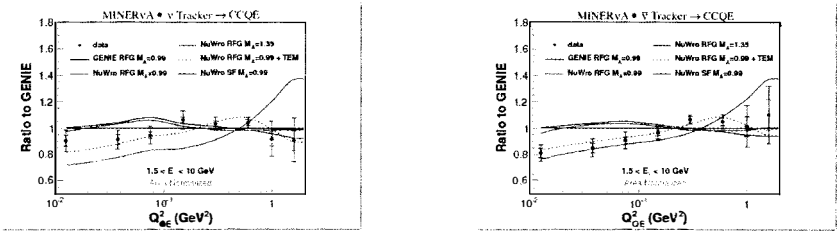

Figure 1 – Neutrino (left) and antineutrino (right) CCQE differential cross-section shapes in data and models, as a ratio to GENIE prediction. Muon kinematics have been used to reconstruct this sample.

the interaction's location) will hit MINOS.

In figure 1, we compare the shape of our measured cross-section distributions with various models. By looking at the shape, as opposed to absolute values, we can substantially reduce systematic uncertainties, particularly due to neutrino flux, which chiefly affects normalization. For clarity, we take a ratio to GENIE's [17] RFG model, with M_A of 0.99 GeV. We also compare to the NuWro [19] generator's RFG models with M_A of 0.99 GeV and 1.35 GeV (consistent with a lower-energy measurement from MiniBooNE [22]), as well as with its modeling of nuclear effects using spectral functions [14] and transverse enhancement (TEM) [15]. In both cases, the data agree most closely with the TEM, hinting at correlation effects.

2.3 Quasi-elastic cross-section, calculated from proton kinematics

In a complementary analysis[23], we reconstruct the event using the kinematics of a stopping proton (note that this requires an incoming neutrino; an antineutrino interaction would produce a neutron, which we cannot track). For this analysis, both a muon and at least one proton track must be identified; however, there is no requirement for the muon to be matched in MINOS. Proton tracks are distinguished from pions by a cut on energy deposition rate dE/dx; we also reject events with Michel electrons from the decay of a pion to a muon, which itself decays at rest. This analysis looks at events with a quasi-elastic-like signature (no pion tracks). In this case, we calculate Q^2 from the kinematics of the most energetic proton. The cross-section results are shown in figure 2. In contrast to figure 1 (which favored TEM), the closest agreement is to the unadorned RFG . However, there are several important differences between the two analyses. The lack of a MINOS match requirement means that the proton-kinematics study has a greater muon-angular acceptance; however, its low Q^2 range is restricted, due to the requirement for a trackable proton, with kinetic energy > 450 MeV. Additionally, FSI modeling becomes important, as the proton used to reconstruct the event may have re-interacted, changing its energy or angle.

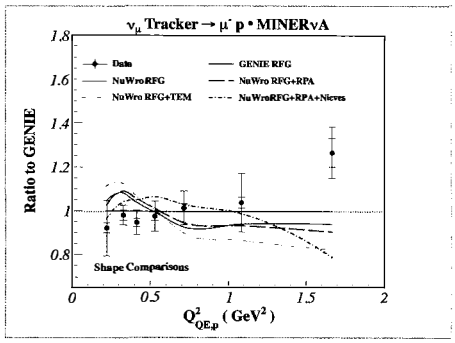

Figure 2 – Neutrino (left) quasi-elastic-like differential cross-section shape in data and models, as a ratio to GENIE. Proton kinematics have been used to reconstruct this sample.

This tension shows that we have not yet tested a theory which is able to accurately reproduce results across the whole phase space, regardless of how they are reconstructed. A complete nuclear quasi-elastic scattering theory should be able to reconcile with the data produced by

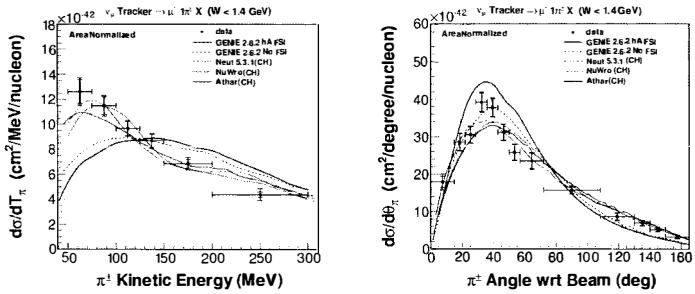

Figure 3 – Differential cross section vs. charged pion kinetic energy (left) and angle (right), in data and various models.

both methods. Further investigation of the quasi-elastic interaction is underway at MINERvA, and double-differential cross-sections (vs. muon parallel and transverse momentum) for both neutrino and antineutrino scattering on scintillator are currently being analyzed.

3 Pion production

3.1 Single charged-pion production form neutrino scattering

MINERvA has calculated the cross section for charged-current processes [27] in which a neutrino scatters from scintillator to produce a muon and a single charged pion ($\nu_\mu A \rightarrow \mu^- \pi^+ A$ or $\nu_\mu A \rightarrow \mu^- \pi^\pm X$ where A is the initial nucleus and X refers to the recoil nucleus (which may not be the same as A), plus any other particles that are not pions). The largest contribution to this comes from resonant processes, where the target nucleon is excited to a resonant state such as $\Delta(1232)$, which decays to a nucleon and pion. To select events with a single pion in the final state, a hadronic invariant mass $W < 1.4$ GeV is required.

Differential cross sections are measured with respect to the outgoing pion's kinetic energy and the angle between the pion and the neutrino beam. As before, we unfold our signal using GENIE [17], which models pion production using the Rein-Sehgal model [24]. We compare the results to GENIE,with and without final-state interactions enabled; to the models used in NuWro [19] and Neut [26], and to a model from Athar et al. [25], which does not include FSI.

The pion energy plot, in particular, shows the data's clear preference for models including FSI effects, highlighting the importance of these processes to pion energy distributions. The results of this study can be used by generators to constrain both the primary interaction rate for these processes and the FSI parameters.

3.2 Neutral pion production from antineutrino scattering

The cross section for charged-current neutral pion production from antineutrinos on scintillator ($\bar{\nu}_\mu A \rightarrow \mu^+ \pi^0 X$, where A and X are as in section 3.1), is not well-studied, and generators' models vary significantly. It is, however, important to oscillation experiments, as its neutral-current analog ($\bar{\nu}_\mu A \rightarrow \bar{\nu}_\mu \pi^0 X$) can mimic a $\bar{\nu}_e$ appearance signature, due to the electromagnetic shower of the $\pi^0 \rightarrow \gamma\gamma$ decay.

Figure 4 shows differential cross sections with respect to the kinetic energy and angle of the neutral pion. The pion is identified by looking for the two photon showers from its decay, and its energy and angle are reconstructed from the calorimetrically measured energy and the positions of these photons with respect to the muon vertex. The plots compare the measured cross section distributions to those predicted by GENIE [17] (with and without FSI), NuWro [19] and Neut [26], appearing to favor Neut's prediction. The generators differ in their FSI modeling methods; FSI

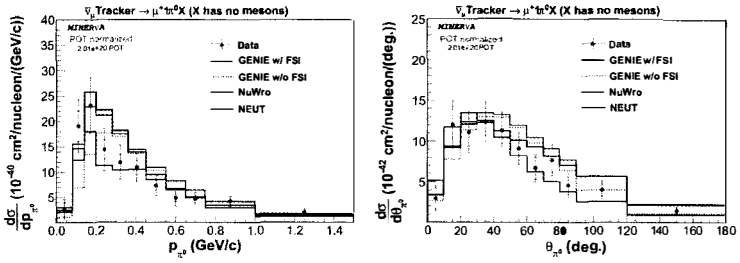

Figure 4 – Differential cross section vs. charged pion kinetic energy (left) and angle (right), in data and various models.

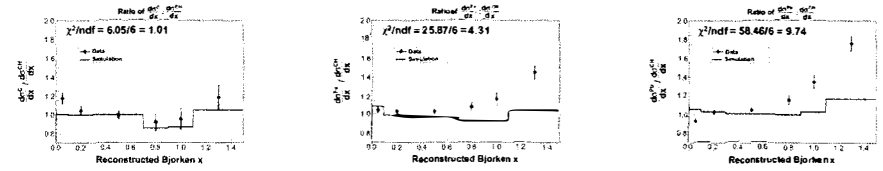

Figure 5 – Charged-current inclusive scattering differential cross section vs Bjorken x, as a ratio to CH scintillator, for increasingly heavy nuclei: carbon (left), iron (middle) and lead (right).

for pions is typically studied in pion beams, and as only charged pion beams are available, π^0 interaction rates must be inferred through isospin relations, leading to significant uncertainties. This measurement will be of use in evaluating the approximations made in generators' models.

4 Charged-current inclusive scattering from nuclear targets

The passive target region of the MINERvA detector allows us to compare scattering cross sections on different nuclei. A charged-current inclusive measurement [29] was made for neutrino scattering on graphite, iron, and lead targets, using events with a reconstructed $2 < E_\nu < 20$ GeV, ($\langle E_\nu \rangle = 8$ GeV). A MINOS-matched μ^- was required to identify charged-current neutrino scattering, limiting the sample to events with a muon angle below 17°.

Figure 5 shows the nucleus-to-scintillator ratio for the differential cross section, $\frac{d\sigma}{dx}$. Also shown is the GENIE [17] prediction. The x axis corresponds to the Bjorken scaling variable $x = \frac{Q^2}{2m\nu}$, which characterizes the type of interaction. Low x corresponds to the region where nuclear shadowing predicts a decreased cross section for heavier nuclei; our data show GENIE is under-predicting this effect. At high x, corresponding mainly to quasi-elastic interactions, GENIE under-predicts the cross section increasingly for heavier nuclei. This may be because GENIE does not include meson-exchange current interactions. In both cases, further study is needed to investigate these effects, and the increased statistics of MINERvA's medium-energy run should provide ample data for further analysis of elastic and deep inelastic scattering distributions in the nuclear targets.

Acknowledgments

This work was supported by the Fermi National Accelerator Laboratory under US Department of Energy contract No. DEAC02-07CH11359 which included the MINERvA construction project. Construction support also was granted by the United States National Science Foundation under Award PHY-0619727 and by the University of Rochester. Support for participating scientists was provided by NSF and DOE (USA) by CAPES and CNPq (Brazil), by CoNaCyT (Mexico), by

CONICYT (Chile), by CONCYTEC, DGI-PUCP and IDI/IGI-UNI (Peru), by Latin American Center for Physics (CLAF), by the Swiss National Science Foundation, and by RAS and the Russian Ministry of Education and Science (Russia). We thank the MINOS Collaboration for use of its near detector data. Finally, we thank the staff of Fermilab for support of the beamline and the detector.

References

1. K. Anderson, B. Bernstein, D. Boehnlein, K. R. Bourkland, S. Childress, et al.,FERMILAB-DESIGN **1998**, 01 (1998)
2. L. Aliaga et al. (The MINERvA Collaboration) *Nucl. Instrum. Methods* **A743**, 130 (2014)
3. D.G. Michael et al. (MINOS Collaboration), *Nucl. Instrum. Methods* **A596**, 190 (2008)
4. J.A. Formaggio and G.P. Zeller, *Rev. Mod. Phys.* **84**, 1307-1341 (2012)
5. C.H. Llewellyn Smith, *Phys. Rept.* **3C**, 261 (1972).
6. R. Smith and E. Moniz, *Nucl. Phys.* B **43**, 605 (1972).
7. A. Bodek, S. Avvakumov, R. Bradford, and H. S. Budd, *J.Phys.Conf.Ser.* **110**, 082004 (2008).
8. O. Lalakulich, U. Mosel, and K. Gallmeister *Phys. Rev. C* **86**, 054606 (2012)
9. A. Bodek, and J. L. Ritchie, *Phys. Rev.* D **23**, 1070 (1980).
10. A. Bodek, and J. L. Ritchie, *Phys. Rev.* D **24**, 1400 (1981).
11. AK. S. Kuzmin, V. V. Lyubushkin, and V. A. Naumov, *Eur. Phys. J.* **C54**, 517 (2008).
12. R. Subedi et al., *Science* **320**, 1476 (2008).
13. J. Nieves, I. Ruiz Simo and M. J. Vicente Vacas, *Phys. Rev. C* **83**, 045501 (2011).
14. O. Benhar, A. Fabrocini, S. Fantoni, and I. Sick, *Nucl.Phys. A* **579**, 493 (1994).
15. A. Bodek, H. Budd, and M. Christy, *Eur. Phys. J.* **C71**, 1726 (2011).
16. J. Carlson et al, *Phys. Rev. C* **65**, 024002 (2002).
17. C. Andreopoulos, et al., *Nucl. Instrum. Methods* **288A**, 87 (2010).
18. S. Dytman, *AIP Conf Proc* **896**, 178-184 (2007)
19. K. M. Graczyk and J. T. Sobczyk, *Eur. Phys. J.* **C31**, 177 (2003).
20. L. Fields, J. Chvojka et al. (The MINERvA Collaboration), *Phys. Rev. Lett.* **111**, 022501 (2013).
21. G.A. Fiorentini, D. Schmitz et al. (The MINERvA Collaboration), *Phys. Rev. Lett.* **111**, 022502 (2013).
22. A. A. Aguilar-Arevalo et al. (MiniBooNE Collaboration), *Phys. Rev. Lett.* **100**, 032301 (2008)
23. T. Walton, M. Betancourt et al. (The MINERvA Collaboration), *Phys. Rev.* D **91**, 071301 (2015).
24. D. Rein and L. M. Sehgal, *Ann. Phys.* **133**, 79 (1981)
25. Athar, M., Chauhan, S., and Singh, S. K., *Eur. Phys. J.* **A43**, 209-227 (2010).
26. Y. Hayato, *Acta Phys.Polon.* **B40**, 2477-2489 (2009).
27. B. Eberly et al. (The MINERvA Collaboration), arXiv:1406.6415 [hep-ex]
28. T. Le et al. (The MINERvA Collaboration), arXiv:1503.02107 [hep-ex]
29. B. Tice et al, (The MINERvA Collaboration), PRL **112**, 231801 (2014)

NA61/SHINE Data for Long Baseline Neutrino Experiments

Alexis Häsler for the NA61/SHINE collaboration
Département de Physique Nucléaire et Corpusculaire - DPNC
University of Geneva, 1205 Geneva, Switzerland

Accelerator based long baseline neutrino experiments require precise neutrino flux predictions to reach their physics goals. These experiments are commonly based on a set of two detectors. At the near detector, cross section measurements are performed and the neutrino flux can be observed before oscillation, while at the far detector the signal for neutrino oscillations is studied. An accurate knowledge on hadron production is mandatory in order to predict the neutrino fluxes. The NA61/SHINE facility at the CERN SPS has proven its ability to deliver high quality measurements of hadron production for the long baseline neutrino experiments. In this paper, the latest results from NA61/SHINE for the neutrino physics programme are reviewed and future plans are presented.

1 Introduction

Conventional neutrino beams at accelerators are generated by impinging high energy protons on a thick target. The prediction of neutrino fluxes depends on the simulation of the interactions of the incident beam protons with the target and the subsequent production of hadrons. Different models can be used to simulate the neutrino fluxes. Specific models can be chosen to match the energy of the incident proton beam. But none of these models is able to accurately reproduce the primary interactions as well as the subsequent re-interactions within the target. It is hence mandatory to have precise hadron production measurements to constrain the models [1] [2]. The T2K long base line neutrino experiment [3] uses the dedicated hadron production measurements taken by NA61/SHINE at CERN.

NA61/SHINE[4] is a fixed target experiment at the CERN SPS. It is a wide acceptance spectrometer built around five TPCs, two of them being embedded into two super-conducting magnets. Most of the components of the detectors were inherited from the NA49 experiment. A forward Time of Flight (ToF) wall, downstream of the spectrometer, was specially built for the hadron production measurements requested by T2K. Data sets were taken with a proton beam set at a momentum of 31 GeV/c to match the primary beam energy of the T2K experiment. Two different targets were used. A thin graphite target ($0.04\lambda_{int}$) and a replica of the T2K target (a graphite cylinder of 90 cm corresponding to 1.9 interaction length and a radius of 1.3 cm).

2 Thin target measurements

Two data sets were recorded with a thin graphite target ($0.04\lambda_{int}$): 0.7 million triggers in 2007 and 5.4 million triggers in 2009. The first NA61/SHINE physics papers were devoted to the measurements of $\pi^{\pm}$ and K^{+} cross sections [5] [6]. Statistical uncertainties were the dominant error contribution in these results. For the 2009 data set, the NA61/SHINE detectors were upgraded

and as a result of the large amount of data recorded, precision measurements of double differential cross-sections for seven particle species could be released, namely $\pi^{\pm}$, $K^{\pm}$, K^0_S, Λ and protons.

Three analysis techniques are used to extract charged hadrons. For negatively charged particles, more than 90% of primary produced hadrons are π^-. Thus, no additional particle identification is required and π^- spectra can be obtain by applying small Monte-Carlo based corrections to the raw hadron spectra. For positively charged hadrons, particle identification is mandatory as K^+, protons and deuterons are also produced. Two different techniques are applied, depending on the energy range of the produced particles. For momenta smaller than 1 GeV/c, particles are outside of the acceptance of the ToF detector. Nevertheless, the identification can be based only on the dE/dx information as all the different species are well separated in the energy loss distribution. For momenta from 1 to 4 GeV/c, the Bethe-Bloch curves overlap and the dE/dx information alone does not allow to separate the type of hadrons. In order to unambiguously distinguish the different particle species, a combined ToF-dE/dx analysis is performed. Figures 1 and 2 show the latest results of the 2009 data set for the π^+ and π^- multiplicities [7]. Figures 3 and 4 present K^+ and K^- multiplicities, while results for protons are displayed in figure 5.

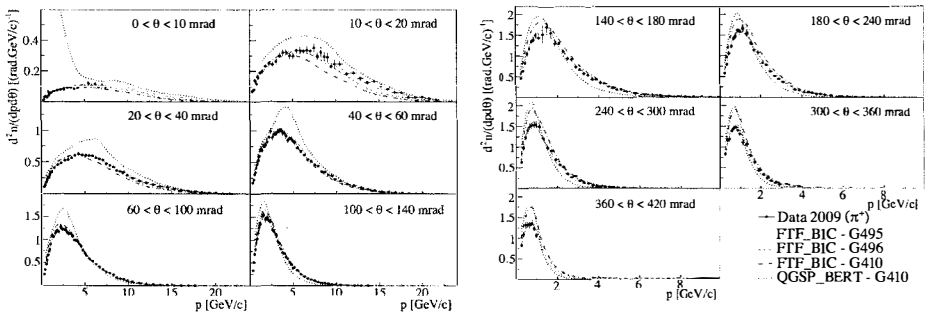

Figure 1 – Comparison of measured π^+ spectra with predictions of some selected GEANT4 physics lists. Distributions are normalized to the mean π^+ multiplicity in all production p+C interactions. The vertical error bars on the data points show the total (stat. and syst.) uncertainty. The horizontal error bars indicate the bin size in momentum.

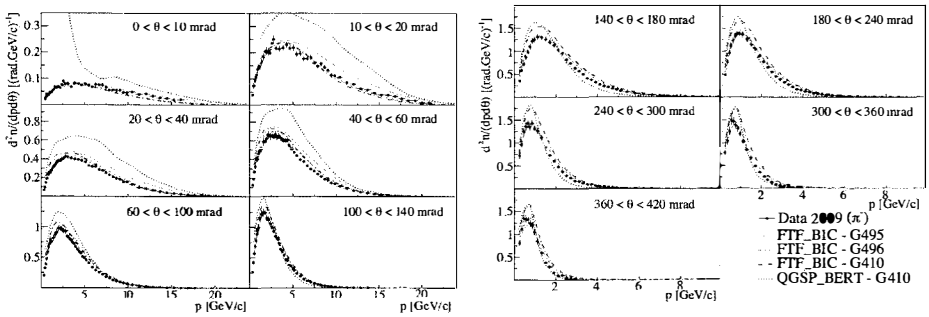

Figure 2 – Comparison of measured π^- spectra with predictions of some selected GEANT4 physics lists. Distributions are normalized to the mean π^- multiplicity in all production p+C interactions. The vertical error bars on the data points show the total (stat. and syst.) uncertainty. The horizontal error bars indicate the bin size in momentum.

The extraction of K^0_S and Λ is done through the reconstruction of so-called V^0, i.e. vertexes

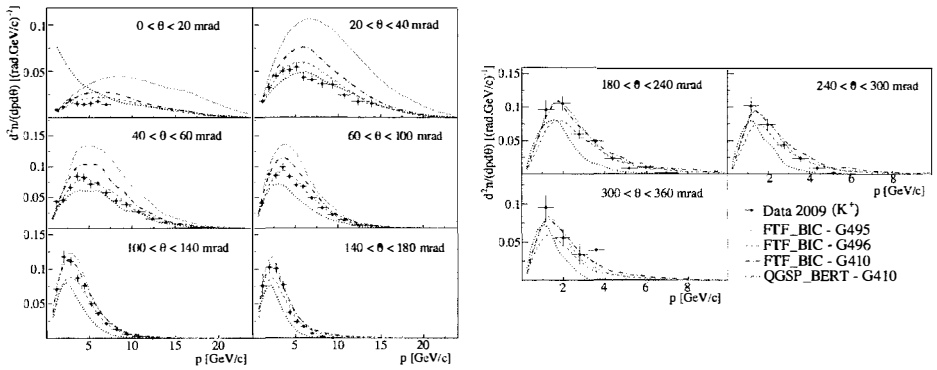

Figure 3 – Comparison of measured K^+ spectra with predictions of some selected GEANT4 physics lists. Distributions are normalized to the mean K^+ multiplicity in all production p+C interactions. The vertical error bars on the data points show the total (stat. and syst.) uncertainty. The horizontal error bars indicate the bin size in momentum.

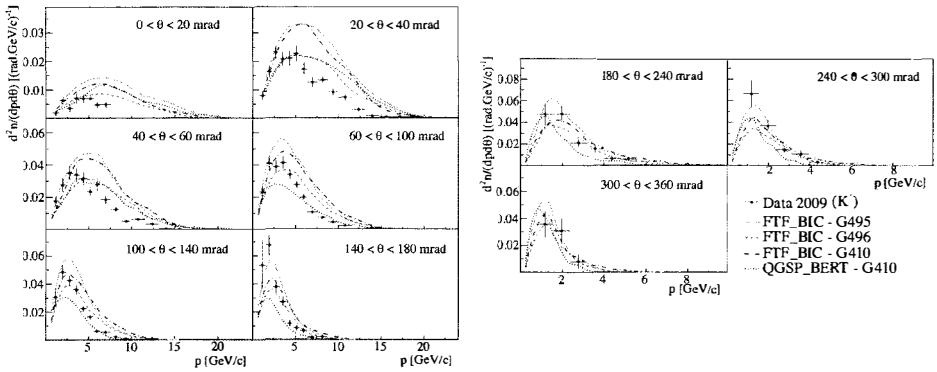

Figure 4 – Comparison of measured K^- spectra with predictions of some selected GEANT4 physics lists. Distributions are normalized to the mean K^- multiplicity in all production p+C interactions. The vertical error bars on the data points show the total (stat. and syst.) uncertainty. The horizontal error bars indicate the bin size in momentum.

from which, two charged particles exit, are reconstructed in the detector and an invariant mass analysis is performed, applying mass spectra hypotheses for the two daughter particles. Figures 6 and 7 present the K^0_S and Λ spectra with comparisons to different models.

The results of the 2007 data sets have already been extensively used within the T2K neutrino flux predictions. They allowed to reduce the uncertainties on the ν_μ flux prediction due to hadronic interactions down to ~12%. The 2009 thin target results have recently been implemented and reduce these uncertainties further down to ~9%. It is due to smaller statistical and systematic uncertainties as well as to a larger coverage of the phase space of interest for T2K (see Figure 8).

3 T2K replica target measurements

Thin target measurements allow to constrain directly primary interactions of the 30 GeV protons in the target. 60% of the T2K ν_μ flux around the beam peak energy is generated via this contribution. The remaining 40% is due to re-interactions inside the target or in the material

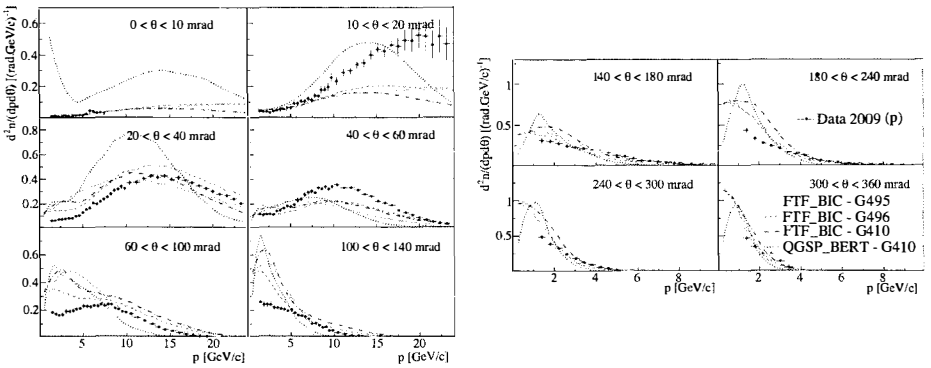

Figure 5 – Comparison of measured Λ spectra with predictions of some selected GEANT4 physics lists. Distributions are normalized to the mean Λ multiplicity in all production p+C interactions. The vertical error bars on the data points show the total (stat. and syst.) uncertainty. The horizontal error bars indicate the bin size in momentum.

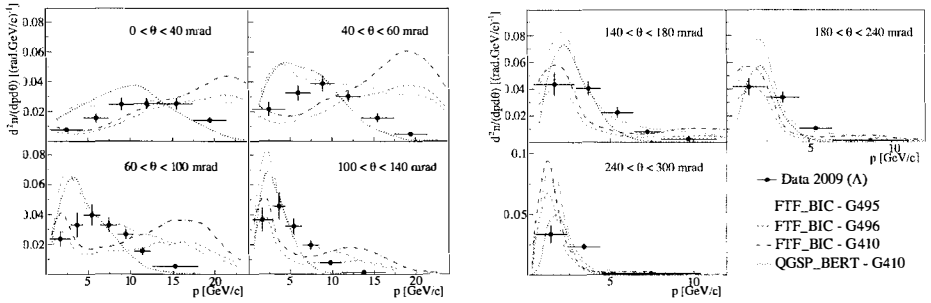

Figure 6 – Comparison of measured proton spectra with predictions of some selected GEANT4 physics lists. Distributions are normalized to the mean proton multiplicity in all production p+C interactions. The vertical error bars on the data points show the total (stat. and syst.) uncertainty. The horizontal error bars indicate the bin size in momentum.

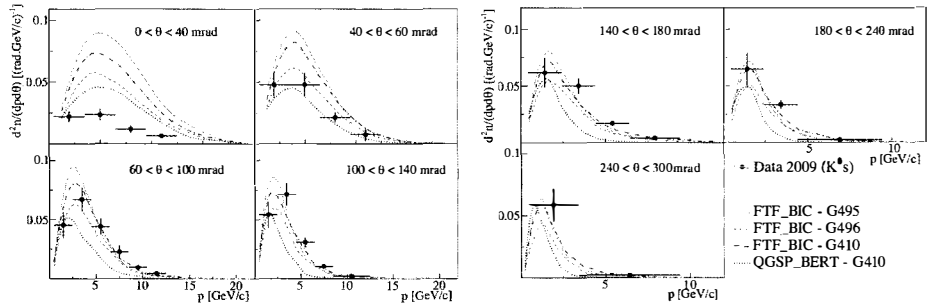

Figure 7 – Comparison of measured K^0_S spectra with predictions of some selected GEANT4 physics lists. Distributions are normalized to the mean K^0_S multiplicity in all production p+C interactions. The vertical error bars on the data points show the total (stat. and syst.) uncertainty. The horizontal error bars indicate the bin size in momentum.

along the beam line. All hadrons exiting from the T2K target surface contribute up to 90% of the ν_μ flux at the far detector. Hence, it is very interesting to measure hadron yields at the

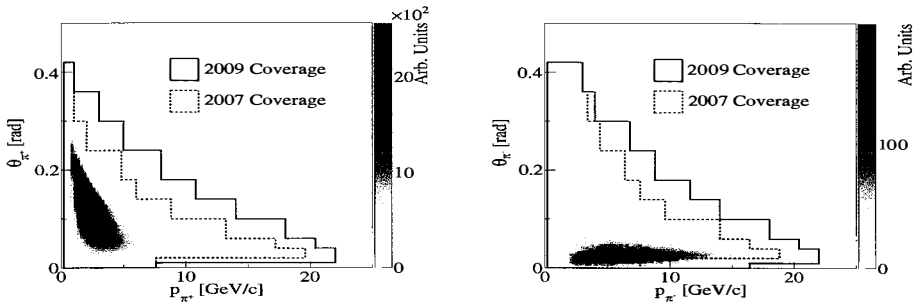

Figure 8 – The phase space of π^+ and π^- contributing to the predicted neutrino flux at SK in the "positive" focusing configuration and the regions covered by the new 2009 data (dashed line) and by the 2007 data set (solid line).

surface of the T2K target. A replica of the T2K target was inserted in the beam line of the NA61/SINE facility and data were performed with a 30 GeV proton beam impinging on the target. In 2007, a first pilot run was recorded and data were analysed. The low statistics of this data set did not allow to improve on the precision of the neutrino flux predictions, but the proof of principle of such measurements and their integration within the T2K beam simulation showed their strong potential. Figure 9 shows the comparisons of the two methods (constraint of hadron production data at primary interactions and on a target surface) and their consistency within the statistical uncertainties. In 2009, 4 million triggers were recorded, and an additional large data set of 10 million triggers in 2010. The analysis of the 2009 data set is now complete. The results are given as multiplicities in polar angle bins θ, as a function of momentum p, and six different longitudinal bins Z for the reconstructed exit position of the particles on the target surface. Figure 10 shows the distribution of the reconstructed exit position along the 90 cm long target and the five longitudinal bins, the sixth bin covering the downstream face of the target.

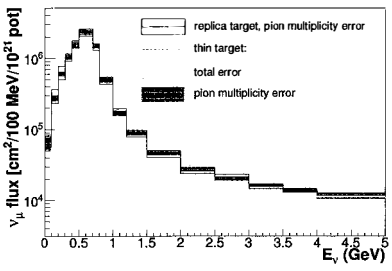

Figure 9 – Re-weighted ν_μ flux predictions at the far detector of T2K based on teh NA61/SHINE thin target and long target data. Error bars correspond to a fully correlated $1-\sigma$ variation of the pion re-weighting factors in both predictions.

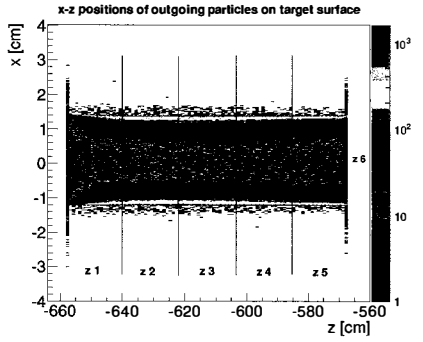

Figure 10 – Distribution of the reconstructed exit point of hadrons with the five Z bins along the target surface, the sixth bin $Z6$ covering the downstream face of the target.

Examples of π^+ spectra for polar angle bins θ between 100 and 180 mrad and the six longitudinal bins Z as a function of momentum p are presented in figure 11.

The statistical error are typically of the order of 5 to 8% while the systematic uncertainties vary between 5% for the central part of the target and up to 12% for the most upstream part of

...

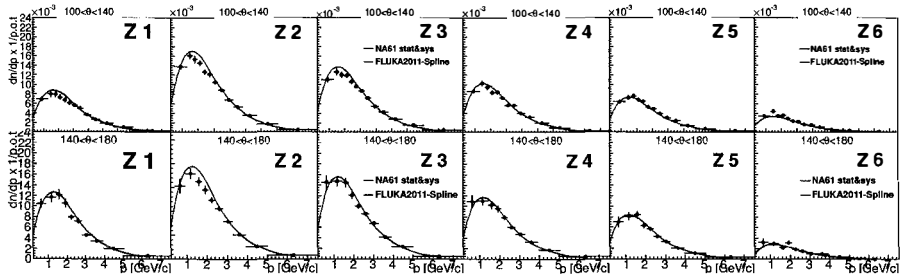

Figure 11 – π^+ multiplicities at the surface of the T2K replica target in two different angular intervals, for the 6 longitudinal bins, as a function of pion momentum. The spectra are normalized to the number of incident protons on target (p.o.t).

the target at small polar angles. The implementation of these data in the T2K flux prediction is under study.

4 Future measurements

Following the accuracy of the measurements taken for T2K, US institutions expressed their interest for taking specific data sets relevant to the NuMI beam line and the related neutrino experiments along this beam line[8]. A pilot run with a 120GeV proton beam on a thin graphite target was conducted in the summer 2012. Larger data taking period are planned for the fall 2015 and the summer 2016 in the context of a new hadron production campaign.

References

1. M. Boncsini, A. Guglielmi , Phys. Rept. **65**, 433 (2006)
2. A. Korzenev, Proceedings of NEUTRINO 2014, arXiv:1409.7887
3. K. Abe *et al.*, *Phys. Rev.* D **87**, 012001 (2013)
4. N. Abgral *et al.*, JINST **9**, P06005 (2014)
5. N. Abgral *et al.*, *Phys. Rev.* C **84**, 034604 (2011)
6. N. Abgral *et al.*, *Phys. Rev.* C **85**, 035210 (2012)
7. A. Korzenev, Proceedings of EPS-HEP 2013, arxiv:1311.5719
8. S. R. Johnson *et al.*, CERN-SPSC-2014-032/SPSC-P-330-ADD-7

Three-Loop Neutrino Mass Models at Colliders

Amine Ahriche [1,2], Kristian L. McDonald [3] & Salah Nasri [4]

[1] *Department of Physics, University of Jijel, PB 98 Ouled Aissa, DZ-18000 Jijel, Algeria*

[2] *The Abdus Salam International Centre for Theoretical Physics, Strada Costiera 11, I-34014, Trieste, Italy*

[3] *ARC Centre of Excellence for Particle Physics at the Terascale, School of Physics, The University of Sydney, NSW 2006, Australia.*

[4] *Physics Department, UAE University, POB 17551, Al Ain, United Arab Emirates*

In this work, we report on recent analyses of a class of models that generate neutrino mass at the three-loop level. We argue that these models offer a viable solution to both the neutrino mass and dark matter problems, without being in conflict with experimental constraints from, e.g. lepton flavor violating processes and the muon anomalous magnetic moment. Furthermore, we describe observable experimental signals predicted by the models and show that they have common signatures that can be probed at both the LHC and ILC.

1 Introduction

The Standard Model has been remarkably successful in describing physics at the weak scale. However, many questions remain, including those relating to the origin of neutrino mass and the reason for its smallness. In this context, models with radiative neutrino mass are of significant experimental interest. These models provide an inherent loop-suppression that allows the new physics responsible for neutrino mass to be lighter than in other scenarios. This loop suppression is more severe as the number of loops increases, making models with three-loop masses particularly interesting, as they generically require new physics near the TeV scale. Such light new particles can be produced and detected within current and near-future experiments by searching for signatures such as lepton flavor violating (LFV) effects.

Here we present a class of models with common features, in which neutrino mass is generated at the three-loop level [1,2,3,4,5], and discuss interesting signatures that can appear at both leptonic and hadronic colliders. We focus primarily on the KNT model [1] and present recent analyses showing that the model satisfies LFV constraints, such as $\mu \to e + \gamma$, and fits the neutrino oscillation data. Furthermore, the model contains a viable candidate for the dark matter (DM) in the universe, in the form of a light right-handed (RH) neutrino. We also show that a strongly first order electroweak phase transition can be achieved with a Higgs mass of $\simeq 125$ GeV, as measured at the LHC [6,7]. The model contains new charged scalars that may lead to significant

modification on the Higgs decay channel $h \to \gamma\gamma$ while $h \to \gamma\gamma$ remains SM-like. We also discuss possible signature of this class of models at the ILC and LHC through possible modifications of the processes $e^-e^+ \to e^-\mu^+ + E_{miss}$ and $pp \to e^-e^+ + E_{miss}$, $\mu^-\mu^+ + E_{miss}$, $e^-\mu^+ + E_{miss}$ respectively.

2 A Class of Three-Loop Models

The class of models we discuss is based on the KNT model [1], which is obtained by extending the SM to include three right-handed (RH) Majorana neutrinos and two electrically charged scalars, $S_1^\pm$ and $S_2^\pm$, all of which are singlets under $SU(2)_L$. In addition, a discrete Z_2 symmetry is imposed, under which $\{S_2, N_i\} \to \{-S_2, -N_i\}$, and all other fields are even. The generalized class of models is obtained by promoting the charged scalar $S_2^\pm$ to a scalar multiplet T, and the three RH neutrinos N_i to three generations of fermionic multiplets E_i, while retaining the same charges under the Z_2 symmetry [a]. This symmetry plays two key roles, preventing a tree-level coupling between N_R (E_i) and the SM Higgs, which would otherwise induce tree-level neutrino masses, and ensuring that the lightest neutral fermion E_i^0 is a stable DM candidate. The general Lagrangian reads as

$$\mathcal{L} = \mathcal{L}_{SM} + \{f_{\alpha\beta} L_\alpha^T C i\tau_2 L_\beta S_1^+ + g_{i\alpha} \bar{E}_i T \ell_{\alpha R} - \frac{1}{2} \bar{E}_i^c M_{ij} E_j + h.c\} - V, \tag{1}$$

where L_α is the left-handed lepton doublet, $f_{\alpha\beta}$ are Yukawa couplings which are antisymmetric in the generation indices α and β, M_{ij} are the fermionic mass matrix elements, C is the charge conjugation matrix, and $V(\Phi, S_1, T)$ is the tree-level scalar potential. Here Φ denotes the SM Higgs doublet.

Using interactions in (1) together with the scalar interaction $V \supset \lambda_s S_1^+ S_1^- T^\dagger T$, the neutrino mass matrix elements can arise from the three-loop diagram in Fig. 1, that are given by [8]

$$(M_\nu)_{\alpha\beta} = \frac{(2n+1)\lambda_s m_{\ell_i} m_{\ell_k}}{(4\pi^2)^3 M_T} f_{\alpha i} f_{\beta k} g_{ij} g_{kj} F\left(M_{E_j}^2/M_T^2, M_{S_1}^2/M_T^2\right), \tag{2}$$

where $\rho, \kappa (= e, \mu, \tau)$ are the charged leptons flavor indices, $i = 1,2,3$ denotes the three E_i multiplets, and the function F is a loop integral which is $\mathcal{O}(1)$ [8]. It is interesting to note that, unlike the conventional seesaw mechanism, the radiatively generated neutrino masses are directly proportional to the charged lepton and RH neutrino masses, as well as being loop-suppressed. Here $n = 0$ corresponds to the KNT model, while $n = 1, 2, 3$ gives generalizations where E_i and T are $SU(2)_L$ triplets, quintuplets and septuplets, respectively (i.e. T and E_i are both assigned to the $(2n+1)$ representation under $SU(2)_L$ and carry two units of hypercharge).

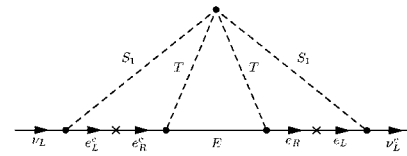

Figure 1 – *The three-loop diagram that generates the neutrino mass.*

The Lagrangian (1) induces flavor violating processes, such as $\ell_\alpha \to \gamma\ell_\beta$ for $m_{\ell_\alpha} > m_{\ell_\beta}$, and an extra contribution to the muon anomalous magnetic moment. Both are generated at one loop via the exchange of the charged scalar $S_1^\pm$, and the members of the multiplets T and E_i. The LFV branching ratios and the muon anomalous magnetic moment are given by

[a] Except for the septuplet case where the global symmetry Z_2 is accidental [4].

$$B(\ell_\alpha \to \gamma \ell_\beta) = \frac{3\alpha_{em} v^4}{36\pi} \left\{ \frac{\left| f_{\kappa\alpha} f^*_{\kappa\beta} \right|^2}{36 M_{S_1}^4} + \frac{(2n+1)^2}{M_T^4} \left| \sum_i g_{i\alpha} g^*_{i\beta} F_2\left(M_{E_i}^2/M_T^2\right) \right|^2 \right\}, \tag{3}$$

$$\delta a_\mu = -\frac{m_\mu^2}{16\pi^2} \left\{ \sum_{\alpha \neq \mu} \frac{|f_{\mu\alpha}|^2}{6 M_{S_1}^2} + n \sum_i \frac{|g_{i\mu}|^2}{M_T^2} F_2(M_{E_i}^2/M_T^2) \right\}, \tag{4}$$

with $\kappa \neq \alpha, \beta$, α_{em} being the fine structure constant and $F_2(x) = (1 - 6x + 3x^2 + 2x^3 - 6x^2 \ln x)/6(1-x)^4$.

In our scan of the parameter space of the model we impose the experimental bounds on $B(\mu \to e\gamma)$ [9], $B(\tau \to \mu\gamma)$ and δa_μ [10], and use the allowed values for the neutrino mixing parameters, $s_{12}^2 = 0.320^{+0.016}_{-0.017}$, $s_{23}^2 = 0.43^{+0.03}_{-0.03}$, $s_{13}^2 = 0.025^{+0.003}_{-0.003}$, and the mass squared differences, $\left|\Delta m_{31}^2\right| = 2.55^{+0.06}_{-0.09} \times 10^{-3}$ eV^2 and $\Delta m_{21}^2 = 7.62^{+0.19}_{-0.19} \times 10^{-5}$eV^2 [11].

3 Dark Matter

An immediate implication of the Z_2 symmetry is that that lightest neutral fermion, E_1^0, is stable, and hence a candidate for dark matter (DM). The E_1^0 number density gets depleted through the process $E_1^0 E_1^0 \to \ell_\alpha \ell_\beta$ via the t- and u-channel exchange of T. In the singlet case ($n = 0$), the non-relativistic limit of the annihilation cross section gives

$$\sigma_{E_1^0 E_1^0} v_r \simeq \sum_{\alpha,\beta} |g_{1\alpha} g^*_{1\beta}|^2 \frac{M_{E_1}^2 \left(M_T^4 + M_{E_1}^4\right)}{48\pi \left(M_T^2 + M_{E_1}^2\right)^4} v_r^2, \tag{5}$$

with v_r is the relative velocity between the annihilation E_1^0's. In cases with nontrivial representations ($n \neq 0$), there exist other annihilation channels, such as $E_1^0 E_1^0 \to WW$, which increase the animation cross section, and therefore the DM candidate should be heavier. The WW annihilation cross section contribution is given by

$$\sigma_{E_1^0 E_1^0 \to WW} v_r = \frac{\pi \alpha_2^2}{M_{E_1}^2} \left(a + b v_r^2\right), \tag{6}$$

with the $SU(2)_L$ structure constant $\alpha_2 = g^2/4\pi$; and $\{a, b\}$=$\{\frac{37}{12}, \frac{17}{48}\}$, $\{\frac{207}{20}, \frac{243}{80}\}$, $\{\frac{174}{7}, \frac{263}{28}\}$ for $n = 1, 2, 3$ respectively.

When combining the relic density together with the neutrino mass and mixing, LFV and muon anomalous magnetic moment bounds, the mass of the charged scalar S_1 should exceed 100 GeV, while the bounds on E_i and T are sensitive to the $SU(2)_L$ quantum numbers. For the KNT case (n=0), we find that $M_{E_1^0} < 225$ GeV while $M_T < 245$ GeV [8]. For the triplet, quintuplet and septuplet cases the DM mass should be in the ranges $M_{E_1^0} = 2.35 \sim 2.75$ TeV [2], $M_{E_1^0} \sim 6$ TeV [3] and $M_{E_1^0} \sim 21$ TeV [4] respectively, with $M_T > M_{E_1^0}$.

4 Electroweak Phase Transition

Although the SM has all the qualitative ingredients for electroweak baryogenesis, the amount of matter-antimatter asymmetry generated is too small. One of the reasons for this smallness is the fact that the electroweak phase transition (EWPT) is not strongly first order, which is necessary to suppress the sphaleron processes in the broken phase. The EWPT strength can be improved if new scalar degrees of freedom around the electroweak scale are coupled to the SM Higgs, which is the case in this class of models.

The investigation of the scalar effective potential reveals that, within the allowed parameter space of the model, the strength of the electroweak phase transition (EWPT) can be first order[8]. We found that if the one-loop corrections to the Higgs mass are sizeable, then the strongly first order EWPT condition, $v(T_c)/T_c > 1$, can be realized while keeping the Higgs mass around 125 GeV. The reason for this being that the extra charged singlets affect the dynamics of the SM scalar field VEV around the critical temperature[12].

The existence of extra fields coupled to SM Higgs doublet will induce one-loop corrections to the triple Higgs coupling, $\lambda^{(3)}_{hhh}$, which is of great interest, especially at leptonic colliders. In Fig. 2-left, we show the plot for $v(T_c)/T_c$ versus the critical temperature. One observes that a strongly first order EWPT is possible while the critical temperature lies around 100 GeV. In Fig. 2-right, we show the ratio $v(T_c)/T_c$ versus the relative enhancement on the triple Higgs coupling due to new physics, $\Delta = \left(\lambda^{(3)}_{hhh} - \lambda^{SM}_{hhh}\right)/\lambda^{SM}_{hhh}$. It is clear that the enhancement is significant when the EWPT is stronger.

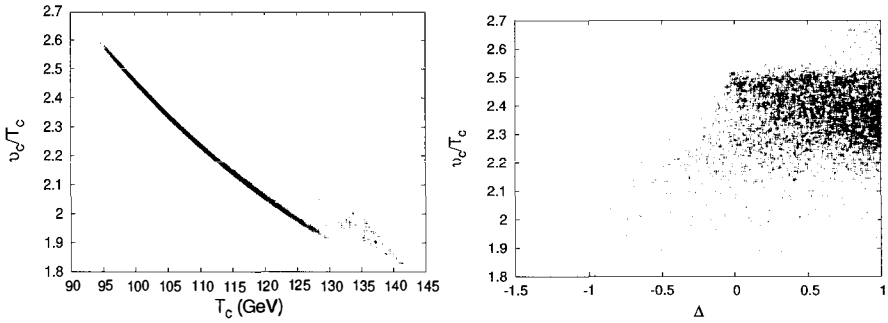

Figure 2 – *Left: the critical temperature is presented versus the quantity* v_c/T_c. *Right: the ratio* v_c/T_c *versus the relative enhancement in the Higgs triple coupling* $\Delta = \left(\lambda^{(3)}_{hhh} - \lambda^{SM}_{hhh}\right)/\lambda^{SM}_{hhh}$.

5 Collider Phenomenology

In these models, there are many common signatures at both the ILC and LHC. Here, we briefly discuss two common signals, one at the ILC and another at the LHC. At the ILC, the process $e^-e^+ \to e^-\mu^+ + E_{miss}$ is modified in this class of models, where $E_{miss} \equiv \nu_\mu\bar{\nu}_e$, $\nu_e\bar{\nu}_\tau$, $\nu_\tau\bar{\nu}_e$, $\nu_\mu\bar{\nu}_\mu$, $\nu_\tau\bar{\nu}_\mu$, $\nu_\tau\bar{\nu}_\tau$, E^0E^0. The first six combinations are mediated by $W^\pm$ or/and $S_1^\pm$ while those of E^0E^0 are mediated by $T^\pm$. Here E^0 could be E_1^0 and possibly $E_{2,3}^0$ if it decays into a charged lepton and $T^\pm$ outside the detector. The background is given by the process $E_{miss} \equiv \nu_\mu\bar{\nu}_e$, which occurs in the SM via 18 Feynamnn diagrams and via 40 diagrams in the present class of models[13]. The total expected cross section and the expected number of events for the processes $e^-e^+ \to e^-\mu^+ + E_{miss}$ are represented by σ^{EX} and $N^{EX} = \mathcal{L}\sigma^{EX}$, with $\mathcal{L}$ being the integrated luminosity. In the SM case we have $N^B = \mathcal{L}\sigma^B$. As an example, we consider the following benchmark for the KNT case (n=0)[13]

$$f_{e\mu} = -(4.97 + i1.41) \times 10^{-2},\ f_{e\tau} = 0.106 + i0.0859,\ f_{\mu\tau} = (3.04 - i4.72) \times 10^{-6},$$
$$g_{i\alpha} = 10^{-2} \times \begin{pmatrix} 0.2249 + i0.3252 & 0.0053 + i0.7789 & 0.4709 + i1.47 \\ 1.099 + i1.511 & -1.365 - i1.003 & 0.6532 - i0.1845 \\ 122.1 + i178.4 & -0.6398 - i0.6656 & -10.56 + i68.56 \end{pmatrix},$$
$$M_{E_i^0} = \{162.2 \text{ GeV},\ 182.1 \text{ GeV},\ 209.8 \text{ GeV}\},\ M_{S_1} = 914.2 \text{ GeV},\ M_T = 239.7 \text{ GeV} \qquad (7)$$

We used CalcHEP [14] to simulate the model and generate the differential cross section and the relevant kinematic variables for different CM energy: E_{CM} =250 , 350, 500 GeV and 1

TeV, initially with unpolarized beams; and then we consider polarized beams with $P(e^-, e^+) = [-0.8, +0.3]$ and/or $P(e^-, e^+) = [+0.8, -0.3]$. After imposing the appropriate cuts in both cases of polarized and unpolarized beams, we summarize the results for the corresponding luminosity values in Table-1.

Table 1: The expected (N_{EX}) and background (N_B) number of events for different CM energy values with/without polarized beams within the cuts given in Table-1.

E_{CM} (GeV)	L (fb^{-1})	$P(e^-, e^+)$	N_B	N_{EX}	N_S
250	250	0,0	16480	16851	371
		−0.8, +03	38498	39775	1277
350	350	0,0	20609	21055	446
		−0.8, +03	47740	48990	1250
500	500	0,0	28280	28815	535
		−0.8, +03	65500	67250	1750
1000	1000	0,0	19.217	469.76	450.54
		+0.8, −03	2.07	727.10	725.03

In Fig. 3, we show the dependance of the significance on the accumulated luminosity with and without polarized beams for the considered CM energies. We clearly see that for a polarized

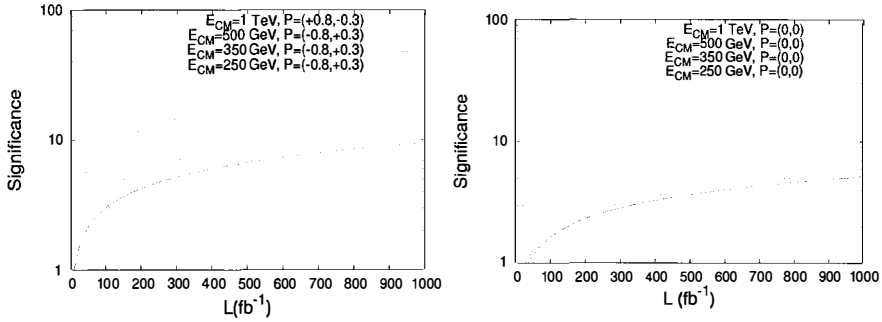

Figure 3 – *The significance versus luminosity at different CM energies within the cuts defined in Table-1; with (left) and without (right) polarized beams. The two horizontal dashed lines represent $\mathcal{S} = 3$ and $\mathcal{S} = 5$, respectively.*

beam, the signal can be observed even with relatively low integrated luminosity. For example, at $E_{CM} = 250$ GeV, the 5σ required luminosity is 150 fb^{-1} for polarized beam as compared to 700 fb^{-1} without polarization.

Turning now to the LHC, the processes $pp \to e^-e^+ + E_{miss}$, $\mu^-\mu^+ + E_{miss}$, $e^-\mu^+ + E_{miss}$ can be modified with respect to the SM, where the missing energy could correspond to any of the combinations mentioned above. We used CalcHEP [14] to generate different distributions for two CM energies $E_{CM} = 8, 14$ TeV. After selecting the cuts, we obtain the results in Fig. 4, which shows the significance versus the charged scalar mass M_{S_1} for the luminosity values $\mathcal{L} = 20.3$ and 100 fb^{-1} that correspond $E_{CM} = 8, 14$ TeV, respectively [15].

From Fig. 4-left, it is clear that the charged scalar mass should be larger than 780 GeV, and from Fig. 4-right, we conclude that this signal can be seen for LHC14.

6 Conclusion

We have shown that a generalized class of three-loop neutrino mass models offers a promising way to experimentally probe the new physics that is responsible for the origin of neutrino mass.

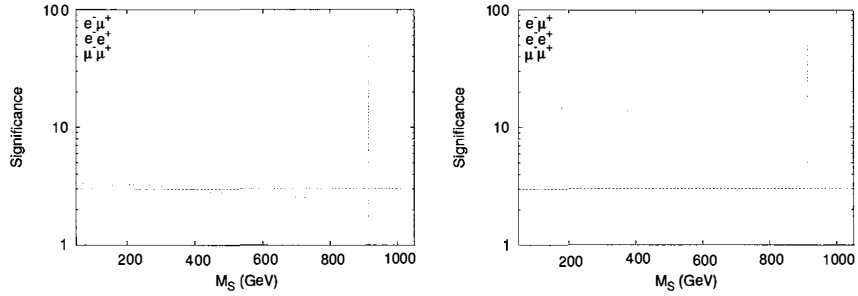

Figure 4 – *The significance versus the charged scalar mass, M_{S_1}, at the CM energy 8 TeV (left) and 14 TeV (right). The two horizontal dashed lines represent $\mathcal{S} = 3$ and $\mathcal{S} = 5$, respectively.*

We showed that the models can solve both the neutrino mass and DM problems without being in conflict with LFV constraints such as the severe bound on $B(\mu \to e\gamma)$ and the muon anomalous magnetic moment. We also investigated possible signatures at both the LHC and ILC through the deviation from the SM in the processes $pp \to e^-e^+ + E_{miss}$, $\mu^-\mu^+ + E_{miss}$, $e^-\mu^+ + E_{miss}$ and $e^-e^+ \to e^-\mu^+ + E_{miss}$ respectively. From the recent results of LHC8, we put a bound on the charged scalar mass $M_{S_1} > 780$ GeV.

Acknowledgments

AA wants to thank the organizers for financial support. The authors thank R. Soualah, C. S. Chen, T. Toma, Ch. Guella and D. Chergui for productive collaborations in this field.

References

1. L. M. Krauss, S. Nasri and M. Trodden, Phys. Rev. D **67**, 085002 (2003).
2. A. Ahriche, C. S. Chen, K. L. McDonald and S. Nasri, Phys. Rev. D **90**, 015024 (2014) [arXiv:1404.2696 [hep-ph]].
3. A. Ahriche, K. L. McDonald and S. Nasri, JHEP **1410**, 167 (2014) [arXiv:1404.5917 [hep-ph]].
4. A. Ahriche, K. L. McDonald, S. Nasri and T. Toma, arXiv:1504.05755 [hep-ph].
5. C. S. Chen, K. L. McDonald and S. Nasri, Phys. Lett. B **734**, 388 (2014) [arXiv:1404.6033 [hep-ph]].
6. G. Aad et al. (ATLAS Collaboration), Phys. Lett. B 716, 1-29 (2012).
7. S. Chatrchyan et al. (CMS Collaboration), Phys. Lett. B 716, 30-61 (2012).
8. A. Ahriche and S. Nasri, JCAP **1307**, 035 (2013).
9. J. Adam *et al.* [MEG Collaboration], Phys. Rev. Lett. **110**, 201801 (2013) [arXiv:1303.0754 [hep-ex]].
10. K.A. Olive et al. (Particle Data Group), Chin. Phys. C, 38, 090001 (2014).
11. D.V. Forero, M. Tortola and J.W.F. Valle, Phys. Rev. D 86, 073012 (2012).
12. A. Ahriche, Phys. Rev. D75, 083522 (2007); A. Ahriche and S. Nasri, Phys. Rev. D 83, 045032 (2011); Phys. Rev. D 85, 093007 (2012);A. Ahriche, G. Faisel, S. Y. Ho, S. Nasri and J. Tandean, arXiv:1501.06605 [hep-ph].
13. A. Ahriche, S. Nasri and R. Soualah, Phys. Rev. D 89, 095010 (2014).
14. A. Belyaev, N. D. Christensen and A. Pukhov, Comput. Phys. Commun. 184 (2013) 1729-1769, arXiv:1207.6082 [hep-ph].
15. C. Guella, et al, 'in progress'.

Cosmological Constraints on the Seesaw Scale

P. Hernández,
M. Kekic
IFIC (CSIC) and Dpto. Física Teórica,
Universidad de Valencia, Edificio Institutos Investigación,
Apt. 22085, E-46071 Valencia, Spain.

J. López-Pavón
SISSA, via Bonomea 265, 34136 Trieste, Italy.
INFN, sezione di Trieste, 34136 Trieste, Italy.

We will analyse the simplest extension of the Standard Model that can account for neutrino masses: the Type-I seesaw with 2 and 3 right-handed neutrinos. The model introduces a New Physics scale, M, which is usually assumed to be much larger than the electroweak scale. However, it is experimentally unconstrained and the light neutrino masses and mixing can be generated for any value of M above $\mathcal{O}$(eV). Paying particular attention to the contribution of the sterile neutrinos to $N_{\rm eff}$ as a function of M, we will show that a large part of the M parameter space (8 orders of magnitude) can be excluded due to cosmological measurements. The phenomenological implications for neutrinoless double beta decay will also be discussed.

The simplest extension of the Standard Model (SM) that can account for the light neutrino masses is the Type-I seesaw model [1] with $N \geq 2$ extra singlet Majorana fermions. We will dub it Minimal Seesaw Model, since it contains the minimum number of extra degrees of freedom required to generate the observed neutrino masses and mixing. The model introduces a New Physics scale, M, associated to the mass of the singlet fermions (sterile neutrinos). The Yukawa couplings are usually assumed to be of the order one because of naturalness arguments, which drives M close to the GUT scale through the seesaw mechanism ($m_\nu \sim Y^2 v^2/M$). The drawback of this assumption is that such a high scale would require an important level of fine tunning in order to stabilize the Higgs mass, since it is quadratically sensitive to M at one loop. In any case, regardless theoretical discussions, M is experimentally unconstrained and the light neutrino masses and mixing can be generated for any value of M above $\mathcal{O}$(eV) [2].

Considering low M scales requires accordingly small Yukawa couplings which can be recognized unnatural. However, low Majorana scales may be also considered technically natural since the Lagrangian gains a $U(1)$ global symmetry in the limit $M \to 0$. In any case, we are going to explore the full parameter space of the model without any theoretical prejudice. The main goal of our analysis is to understand if a general bound on the seesaw scale can be extracted without assuming anything a priori about the parameters of the model. There are important constraints on low-scale models from direct searches and rare processes, but they strongly depend on the sterile-active mixing. Recent results can be found in [3–11].

If lepton number conservation is not imposed, the most general renormalizable Lagrangian when N extra singlet Weyl fermions, ν_R^i, are included is given by

$$\mathcal{L} = \mathcal{L}_{SM} - \sum_{\alpha,i} \bar{L}^{\alpha} Y^{\alpha i} \tilde{\Phi} \nu_R^i - \sum_{i,j=1}^{N} \frac{1}{2} \bar{\nu}_R^{ic} M_N^{ij} \nu_R^j + h.c.,$$

where Y is a $3 \times N$ complex matrix and M_N a diagonal $N \times N$ real matrix. This Lagrangian defines the Type-I seesaw model. We will study the minimal model, which consists in the addition of $N = 2$ singlet Weyl fermions, and the more popular next to minimal model with $N = 3$. The detailed analysis of both models in the context of the cosmological bounds studied here can be found in [12,13] respectively. In both cases, we have considered an extension of the Casas-Ibarra parameterization [14], which is valid at all orders in the seesaw expansion and guaranties the generation of the right pattern of light neutrino masses and mixing [15].

The energy density of the sterile neutrino species, ϵ_s, is usually quantified in terms of $\Delta N_{\rm eff}$ defined by

$$\Delta N_{\rm eff} \equiv \frac{\epsilon_s}{\epsilon_\nu^0}, \tag{1}$$

where ϵ_ν^0 is the energy density of one SM massless neutrino with a thermal distribution. One thermal extra sterile state that freezes out from the thermal bath being relativistic contributes $\Delta N_{\rm eff} \simeq 1$ when it decouples. Indeed, the sterile neutrinos should both achieve thermalization and decouple from the thermal bath when they are still relativistic in order to have any impact on $N_{\rm eff}$. Recall that $N_{\rm eff} = N_{\rm eff}^{SM} + \Delta N_{\rm eff}$, where the contribution of the active neutrinos is $N_{\rm eff}^{SM} = 3.046$ [16,17], and Big Bang Nucleosynthesis (BBN) [18] and Cosmic Microwave Background (CMB) [19] data give us $N_{\rm eff} < 4$ at more than 2σ while $N_{\rm eff} = 5$ is fairly excluded.

If $M_i \lesssim 100$ MeV, the sterile states are always relativistic when they decouple from the thermal bath regardless the value of the free parameters [12]. For $M_i \gtrsim 100$ MeV, no general bound can be extracted on M_i since the sterile neutrinos can become non-relativistic before freezing out and the contribution to $N_{\rm eff}$ would be suppressed by the Boltzmann factor.

The key quantity in order to understand if the sterile neutrinos are thermal is the thermalization ratio $f_{s_j}(T)$:

$$f_{s_j}(T) \equiv \frac{\Gamma_{s_j}(T)}{H(T)}. \tag{2}$$

which measures the sterile production rate of the species s_j in units of the Hubble expansion rate. Γ_{s_j} is the sterile neutrino collision rate [20]:

$$\begin{aligned} \Gamma_{s_j} &\simeq \frac{1}{2} \sum_a \langle P(\nu_a \to \nu_{s_j}) \rangle \times \Gamma_{\nu_\alpha} \\ &\simeq \sum_{\alpha=e,\mu,\tau} \Gamma_{\nu_\alpha} \left(\frac{M_j^2}{2pV_\alpha(T) - M_j^2} \right)^2 |U_{\alpha s_j}|^2 \end{aligned} \tag{3}$$

where $\langle P(\nu_\alpha \to \nu_{s_j}) \rangle$ is the time-averaged probability $\nu_\alpha \to \nu_{s_j}$, Γ_{ν_α} is the active neutrino collision rate, V_α is the effective potential induced by the coherent scattering, and $U_{\alpha s_j}$ is the mixing between the active neutrinos ν_α and the sterile state ν_{s_j}. In [12], we also derived this results from the Boltzmann equations in the assumption of no primordial large lepton asymmetries[a]. In any case, we have numerically solved the Boltzmann equations in order to compute $N_{\rm eff}$ and extract the bounds on M.

$f_{s_j}(T)$ reaches a maximum at the temperature T_{max}, which depends on the free parameters of the model. If it is larger than one, thermalization will be achieved at early times. In the $N = 2$ model, both sterile neutrinos achieve thermalization $f_{s_j}(T_{max}) > 1$ in the full parameter space [12].

[a] The details of the derivation and the expressions for $\Gamma_{\nu_\alpha}(T)$ and $V_\alpha(T)$ can be found in [13].

In Fig. 1 we show the contour plots of the minimum of $f_{s_j}(T_{max})$ (varying the unconstrained parameters of the model in the full range), as a function of m_1 (the lightest neutrino mass) and M_1 in the $N = 3$ model. The three contours correspond to $\mathrm{Min}[f_{s_1}(T_{\mathrm{max}})] = 10^{-1}, 1, 10$. The results are the same in the (M_2, m_1) and (M_3, m_1) planes. As in the $N = 2$ case, the $\mathrm{Min}[f_{s_1}(T_{\mathrm{max}})]$ is roughly independent of the scale M. The figure shows that m_1 ultimately controls the thermalization of the sterile neutrinos. In fact, there is a thermalization threshold at $m_1 \simeq 10^{-3}$ eV. This opens two possible scenarios:

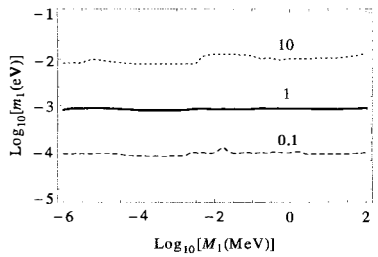

Figure 1 – Contours of $\mathrm{Min}[f_{s_1}(T_{\mathrm{max}})]$=0.1, 1, 10 on the plane (M_1, m_1).

(i) $m_1 \gtrsim 10^{-3}$ eV. The three sterile states achieve thermalization. Therefore, for $M_i \lesssim 100$ MeV, each sterile neutrino will contribute with $\Delta N_{\mathrm{eff}}^{(j)} \backsimeq 1$ when freezing out from the thermal bath. However, there are two possible effects that can modify the contribution to N_{eff} later on and before the active neutrino decoupling, when BBN starts: the entropy dilution and the decay of the sterile states. The effect of the entropy dilution is only relevant for $M_i \gtrsim 10$ KeV[12,13] and sterile states of this range of masses give a contribution to N_{eff} at BBN in agreement with data. However, these sterile neutrinos would give a huge contribution to the energy density when they become non-relativistic later, modifying in a drastic way CMB and structure formation. In fact, CMB measurements close the window all the way down to the $\mathcal{O}(\mathrm{eV})$[21]. The only way to scape from the CMB and BBN bounds is if the sterile neutrinos decay before BBN. Nevertheless, taking into account the bounds on the active-sterile mixing from direct searches, this possibility is excluded for $M_i \lesssim 100$ MeV[22]. In summary, the allowed region of the M parameter space is shown in the upper panel of Fig. 2. The constraints from cosmology essentially exclude the spectra of heavy states in the range 1 eV - 100 MeV.

(ii) $m_1 \lesssim 10^{-3}$ eV. One *and only one* of the sterile neutrinos can never thermalize and it depends on the unknown parameters[13]. In this case, one of the sterile neutrino masses can not be bounded in general. The other two states always thermalize and again the range 1 eV- 100 MeV is severely restricted[13]. If one of the sterile neutrinos never thermalizes, the contribution of the two thermal states reduces to the $N = 2$ case since the other is essentially decoupled from them and the mass generation. The results are qualitatively summarized in the lower panel of Fig. 2, where we show the allowed heavy neutrino spectra in the $m_1 \lesssim 10^{-3}$ eV case.

Finally, the information from cosmology is highly complementary to that coming from neutrino oscillations and neutrinoless double beta decay ($0\nu\beta\beta$ decay). As an example, in Fig. 3 we show the impact of the cosmological bounds when a sterile neutrino in the range 1 eV - 100 MeV is present. The $0\nu\beta\beta$ decay rate is sensitive to the effective mass, $m_{\beta\beta}$, and Fig. 3 shows the separate contribution to $m_{\beta\beta}$ from the active and sterile neutrinos as a function of the lightest neutrino mass m_1. The well-known colored bands correspond to the active neutrino contribution while the maximum contribution of the lightest sterile state is given by the solid ($M_1 = 1$ eV), dashed ($M_1 = 100$ eV) and dotted ($M_1 = 1$ KeV) lines. The other two neutrinos are assumed to be well above 100 MeV. A sterile state with $M_1 \in [1\ \mathrm{eV}, 100\ \mathrm{MeV}]$ gives a long range contribution to the $0\nu\beta\beta$ decay which could in principle be at the reach of the future experiments. However, once the constraints from cosmology are included, it becomes subdomi-

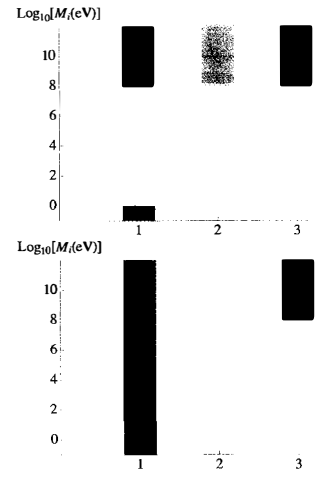

Figure 2 – Allowed spectra of the heavy states M_i for $m_1 \geq 10^{-3}$ eV (upper panel) and $m_1 \leq 10^{-3}$ eV (lower panel).

nant with respect to the active one and well below the future sensitivity $\mathcal{O}(10^{-2}\text{eV})$. Moreover, if $M_1 \in$ [1 eV, 100 MeV], the quasi-degenerate light neutrino spectrum and the region of the parameter space in which a cancellation can occur in the active neutrino contribution would be excluded. This is because in such a case m_1 should be below the thermalization threshold, at $m_1 = 10^{-3}$ eV, in order to make the lightest sterile neutrino non-thermal.

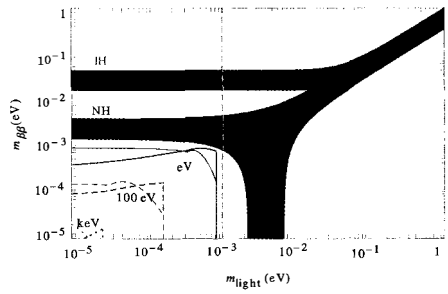

Figure 3 – $m_{\beta\beta}$ as a function of the lightest neutrino mass: contribution from the active neutrinos (red and blue regions) and the maximum contribution of the lightest sterile neutrino, for $M_1 = 1$ eV (solid), 100 eV (dashed), 1 KeV (dotted), for NH (blue) and IH (red) restricting $\Omega_{s_1} h^2 \leq 0.12$ and $f_{s_1}(T_{\max}) \leq 1$, for $M_{2,3} \gg 100$ MeV, as a function of the lightest neutrino mass. The shaded region is ruled out for $M_1 \in$ [1eV-100MeV] by the thermalization bound on the lightest neutrino mass, $m_1 \leq 10^{-3}$eV.

In summary, we have found that the BBN and CMB data essentially excludes the region of the seesaw scale between 1 eV and 100 MeV in both the $N = 2$ and the $N = 3$ models. Only in the $N = 3$ case and provided that $m_1 \lesssim 10^{-3}$ eV, one of the sterile states can be non-thermal and its mass remains unbounded. This has an important impact in the $0\nu\beta\beta$ decay phenomenology.

References

1. P. Minkowski, Phys. Lett. B **67**, 421 (1977); M. Gell-Mann, P. Ramond and R. Slansky, in *Supergravity*, edited by P. van Nieuwenhuizen and D. Freedman (North-Holland, 1979), p. 315; T. Yanagida in *Proceedings of the Workshop on the Unified Theory and the Baryon Number in the Universe*, edited by O. Sawada and A. Sugamoto (KEK Report No. 79-18, Tsukuba, 1979), p. 95; R.N. Mohapatra and G. Senjanovic, Phys. Rev. Lett. **44**, 912 (1980).
2. A. Donini, P. Hernandez, J. Lopez-Pavon and M. Maltoni, JHEP **1107** (2011) 105 [arXiv:1106.0064 [hep-ph]].
3. S. Antusch, C. Biggio, E. Fernandez-Martinez, M. B. Gavela and J. Lopez-Pavon, JHEP **0610** (2006) 084 [hep-ph/0607020].
4. A. Abada, C. Biggio, F. Bonnet, M. B. Gavela and T. Hambye, JHEP **0712** (2007) 061 [arXiv:0707.4058 [hep-ph]].
5. D. Gorbunov and M. Shaposhnikov, JHEP **0710** (2007) 015 [JHEP **1311** (2013) 101] [arXiv:0705.1729 [hep-ph]].
6. S. Antusch, J. P. Baumann and E. Fernandez-Martinez, Nucl. Phys. B **810** (2009) 369 [arXiv:0807.1003 [hep-ph]].
7. A. Atre, T. Han, S. Pascoli and B. Zhang, JHEP **0905** (2009) 030 [arXiv:0901.3589 [hep-ph]].
8. D. N. Dinh, A. Ibarra, E. Molinaro and S. T. Petcov, JHEP **1208** (2012) 125 [JHEP **1309** (2013) 023] [arXiv:1205.4671 [hep-ph]].
9. R. Alonso, M. Dhen, M. B. Gavela and T. Hambye, JHEP **1301** (2013) 118 [arXiv:1209.2679 [hep-ph]].
10. D. N. Dinh and S. T. Petcov, JHEP **1309** (2013) 086 [arXiv:1308.4311 [hep-ph]].
11. M. Drewes and B. Garbrecht, arXiv:1502.00477 [hep-ph].
12. P. Hernandez, M. Kekic and J. Lopez-Pavon, Phys. Rev. D **89** (2014) 7, 073009 [arXiv:1311.2614 [hep-ph]].
13. P. Hernandez, M. Kekic and J. Lopez-Pavon, Phys. Rev. D **90** (2014) 6, 065033 [arXiv:1406.2961 [hep-ph]].
14. J. A. Casas and A. Ibarra, Nucl. Phys. B **618**, 171 (2001).
15. A. Donini, P. Hernandez, J. Lopez-Pavon, M. Maltoni and T. Schwetz, JHEP **1207** (2012) 161 [arXiv:1205.5230 [hep-ph]].
16. G. Mangano, G. Miele, S. Pastor and M. Peloso, Phys. Lett. B **534** (2002) 8 [astro-ph/0111408].
17. G. Mangano, G. Miele, S. Pastor, T. Pinto, O. Pisanti and P. D. Serpico, Nucl. Phys. B **729** (2005) 221 [hep-ph/0506164].
18. R. Cooke, M. Pettini, R. A. Jorgenson, M. T. Murphy and C. C. Steidel, arXiv:1308.3240 [astro-ph.CO].
19. P. A. R. Ade *et al.* [Planck Collaboration], Astron. Astrophys. **571** (2014) A16 [arXiv:1303.5076 [astro-ph.CO]].
20. R. Barbieri and A. Dolgov, Phys. Lett. B **237**, 440 (1990) and Nucl. Phys. B349 (1991) 743. K. Kainulainen, Phys. Lett. B **244**, 191 (1990).
21. E. Di Valentino, A. Melchiorri and O. Mena, JCAP **1311** (2013) 018 [arXiv:1304.5981].
22. O. Ruchayskiy and A. Ivashko, JCAP **1210**, 014 (2012).

Searches for Exotic Processes in Double Beta Decay with EXO-200

T.N. JOHNSON
Indiana University Center for Exploration of Energy and Matter
2401 Milo B. Sampson Lane
Bloomington, IN 47408

EXO-200 is an experiment searching for neutrinoless double beta decay using a time projection chamber with 175 kg of liquid xenon enriched in ^{136}Xe. The observation of this process would indicate that the neutrino is a Majorana fermion and lepton number is not a conserved quantity, and would allow for the calculation of the absolute mass of the neutrino. The low radioactive background and high sensitivity of the experiment also provide a venue to search for other theoretical exotic processes. Majoron modes of double beta decay are processes that would occur if a scalar boson is created in the neutrino self interaction, resulting in an electron sum spectral shape that deviates from the standard two-neutrino double beta decay spectrum. With two years of livetime, an exposure of 99.8 kg·yr to ^{136}Xe was collected, and a stringent limit on the half-life of neutrinoless double beta decay of $T^{0\nu\beta\beta}_{1/2} > 1.1 \cdot 10^{25}$ yrs (90% C.L.) was set. Lower limits on the half-lives of the Majoron-emitting processes are presented, and the future of the experiment is discussed.

1 Why Search for Neutrinoless Double Beta Decay?

Double beta decay is a second-order weak process that only occurs in certain even-even nuclei where single beta decay is energetically forbidden, or forbidden by conservation of angular momentum. Double beta decay has been observed in 11 nuclei, including ^{136}Xe, which undergoes the process $^{136}_{54}\mathrm{Xe} \rightarrow {}^{136}_{56}\mathrm{Ba}^{++} + 2\mathrm{e}^- + 2\bar{\nu}_\mathrm{e}$. The EXO-200 (Enriched Xenon Observatory) experiment has done a precision measurement of the half-life of two-neutrino double beta decay ($2\nu\beta\beta$) in ^{136}Xe, with $\mathrm{T}^{2\nu\beta\beta}_{1/2} = 2.165 \pm 0.016(\mathrm{stat}) \pm 0.059(\mathrm{sys}) \cdot 10^{21}$ years[1].

An isotope that undergoes the process of $2\nu\beta\beta$ is a candidate for the theoretical process of neutrinoless double beta decay ($0\nu\beta\beta$). In the $0\nu\beta\beta$ process, no anti-neutrinos are emitted in the decay ($^{136}_{54}\mathrm{Xe} \rightarrow {}^{136}_{56}\mathrm{Ba}^{++} + 2\mathrm{e}^-$). The observation of $0\nu\beta\beta$ has the potential to answer important lingering questions about neutrinos:

- *Is the neutrino of Dirac or Majorana nature?* Neutrinos are the only observed fundamental particles that have the potential to be of a Majorana nature, fermions with ν and $\bar{\nu}$ differing only by chirality. Neutrinos are candidates because they are observed to be massive [2], are electrically neutral, and all observations have been consistent with ν_L and $\bar{\nu}_R$ handedness [4]. If neutrinos are of a Dirac nature, ν and $\bar{\nu}$ are distinct, following the nature of all other Standard Model fermions. $0\nu\beta\beta$ can only occur in the Majorana case, if one of the anti-neutrinos participating in the double beta decay process undergoes a virtual spin-flip to cancel the other anti-neutrino, as shown in Figure 1.

- *What is the absolute mass of the neutrino?* Neutrinos have been observed to exist in three mass-states, with the square of the mass-state differences measured by neutrino oscillation experiments[5,6]. However, the absolute masses are yet unknown, as is the exact ordering of the masses. Two orderings are possible; they are known as the normal and inverted hierarchies.

Figure 1 – Feynman diagrams of $2\nu\beta\beta$ (left) and $0\nu\beta\beta$ (right)[3].

A measurement of the half-life of $0\nu\beta\beta$ would allow the calculation of an effective Majorona mass from the relation $(T^{0\nu}_{1/2})^{-1} = G^{0\nu}(Q,Z)|M^{0\nu}|^2\langle m_{\beta\beta}\rangle^2$, where $G^{0\nu}(Q,Z)$ is a calculable phase space factor and $|M^{0\nu}|$ is the nuclear matrix element. $\langle m_{\beta\beta}\rangle$ is the effective Majorona mass, which can be used to calculate the value of the lowest mass-state. Depending on the value of $\langle m_{\beta\beta}\rangle$, the mass hierarchy can also be resolved.

- *Is Lepton number a conserved quantity?* In all experiments performed to date, Lepton number (l) has always been conserved (with $l_{e^-} = 1$ and $l_{\bar{\nu}_e} = -1$). The overall process of $0\nu\beta\beta$ violates l by two counts, which would prove that l is not a conserved quantity.

There also exist alternative models of neutrinoless double beta decay in which a new particle (or two) called a Majoron is created in addition to the two betas [7]. The Majoron particle (χ_0) must be a chargeless scalar boson to comply with conservation quantities, with the decay process becoming ${}^{136}_{54}\mathrm{Xe} \rightarrow {}^{136}_{56}\mathrm{Ba}^{++} + 2\mathrm{e}^- + \chi_0(2\chi_0)$. Multiple theories exist for the nature of the particles, whether 1 or 2 χ_0 particles are emitted, if they are Goldstone Bosons, and by what value l is violated. For each of these theories, a spectral index n is defined that governs the spectral shape of the $0\nu\beta\beta\chi_0(\chi_0)$ decay, with $\frac{d\Gamma}{d\epsilon_1 d\epsilon_2} \propto (Q - \epsilon_1 - \epsilon_2)^n$, where $d\Gamma$ is the differential decay rate, ϵ_i is the kinetic energy of the ith electron, and Q is the Q-value of the double beta decay, the energy difference between the mother and daughter isotope.

2 How to search for $0\nu\beta\beta$?

A standard $2\nu\beta\beta$ will share the energy of the Q-value between the two emitted electrons and anti-neutrinos. This energy sharing is what provides the spectrum of summed electron energies emitted in a double beta decay, with the endpoint at the Q-value, shown in green on the left image in Figure 2. If no anti-neutrinos are emitted in the decay, the sum of the emitted electron energies will be exactly the Q-value. An experiment which measures the energy of electrons from double beta decay has the potential to measure this energy peak from a known $2\nu\beta\beta$ isotope. Good energy resolution is required to resolve the $0\nu\beta\beta$ peak (shown in purple in the left plot in Figure 2) from the $2\nu\beta\beta$ spectrum, and an in-depth knowledge of all backgrounds to the experiment is required as the process is expected to be extremely rare.

A Majoron mode decay would emit an extra particle, so there would not be a peak at the standard $2\nu\beta\beta$ endpoint. Instead, the standard $2\nu\beta\beta$ spectral shape would be altered. The raw spectra for each Majoron mode that was searched for in EXO-200 are shown on the right plot in Figure 2.

3 The EXO-200 Experiment

The EXO-200 experiment uses 175 kg of liquid xenon enriched to 80.6% in the isotope ^{136}Xe to search for neutrinoless double beta decay. ^{136}Xe has the advantage of a high Q-value of 2458 keV

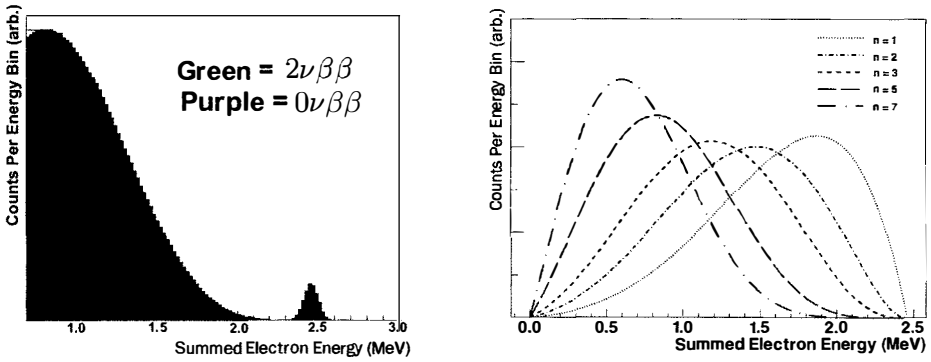

Figure 2 – The left figure shows the electron sum spectrum for $2\nu\beta\beta$ of ^{136}Xe in green, with a peak representing theoretical $0\nu\beta\beta$ in purple. The figure assumes a finite detector energy resolution. A good energy resolution will improve the ability to detect $0\nu\beta\beta$ over the $2\nu\beta\beta$ signal. The right plot shows the raw energy spectrum of each Majoron mode that is searched for with EXO-200. The n=5 mode represents the standard $2\nu\beta\beta$.

[8], above many of the gamma lines from common natural radioactive isotopes. The exceptions, and important radioactive backgrounds to understand, come from the ^{232}Th and ^{238}U decay chains. The xenon is self shielding and attenuates outside gamma radiation, reducing backgrounds and allowing for discrimination of backgrounds based on detector position. There are no long-lived radio-isotopes of xenon, although ^{137}Xe is cosmogenically activated through neutron capture and acts as a background to the experiment. Xenon scintillates at 178 nm through partial recombination of ionization electrons with the ionized xenon. Both ionization and scintillation channels are detected in the experiment.

The detector consists of two back-to-back cylindrical time projection chambers (TPCs) that share a central mesh cathode biased to 8 kV [9]. Each TPC is roughly 20 cm in radius and 22 cm in length. Scintillation light from electron recombination is reflected from teflon tiles surrounding the cylindrical barrel and is collected on a plane of Large-Area Avalanche Photodiodes (APDs) at each TPC end-cap. The free ionization electrons are drifted under the influence of an electric field between the central cathode and anodes at each end-cap. The anode of each TPC is a plane of stretched phosphor-bronze wires held at virtual ground, where the free electrons are collected. Another plane of wires set 6 mm in front of the anode plane and crossed at 60° from the anode plane detects an induction signal as the electrons pass. The combination of the immediate scintillation signal and delayed ionization signals provides a full 3-dimensional event position reconstruction.

The detector is housed under an overburden of 1585 meters water equivalent at the Waste Isolation Pilot Plant near Carlsbad, NM, USA. The module housing the detector is surrounded on four sides by scintillating muon veto panels, which are used to reject events occurring near a muon signal. The TPC is surrounded on all sides by 25 cm of lead, 5 cm of copper, and at least 50 cm of HFE-7000 cryofluid to shield from outside radiation, and all materials placed near the detector have been specially selected for low radioactivity. The xenon is continually circulated through a system that heats it into the gas phase and subjects it to a series of purifiers to remove electronegative impurities.

4 Analysis Techniques

The detector is calibrated with multiple external radioactive sources, with gamma lines covering the full relevant energy spectrum. The main calibration source is ^{228}Th, with a gamma line at 2.6 MeV from ^{208}Tl. This gamma line, close to the ^{136}Xe Q-value, is used to find the optimal combination of ionization and scintillation signals to minimize the energy resolution.

A detailed simulation of the detector setup has been constructed in Geant4 [12], and this is used

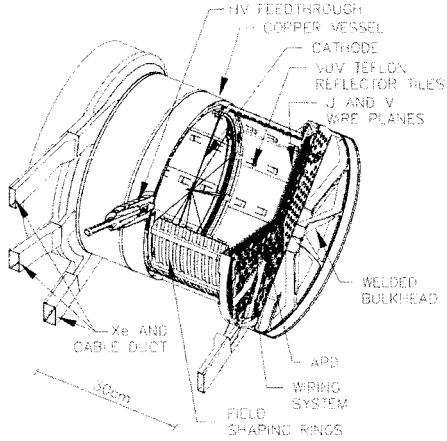

Figure 3 – Cutaway view of the TPC showing the copper vessel, cathode and anodes (u-wire planes), APDs, high voltage feedthrough, teflon reflector, biased rings that shape the electric field, and ducts for LXe and wiring through the mounting legs.

to simulate all signal and backgrounds that are expected to contribute to the data. The output from these simulations are subjected to similar data selection cuts as the data and smeared with the energy resolution determined from source calibration data to make probability distribution functions (PDFs). The PDFs are 2-dimensional, with observables of energy and "stand-off distance," or the distance between a charge signal and the closest detector component. PDFs are fit to histograms of the selected data with a negative log likelihood function to measure the relative contributions of each signal and background component. PDFs are fit to the source calibration data to determine the analysis threshold, data corrections, and various systematic errors.

The data are separated into categories of single-site (SS) and multi-site (MS) depending on whether one or more separate charge deposits are detected in a single event. This provides gamma background discrimination as most beta events are SS, while gamma events tend to Compton scatter, leaving multiple separate charge deposits in the detector. The measured MS events constrain the contributions of different backgrounds to the SS spectrum.

5 Results

Data for these analyses were collected between September 22, 2011 and September 1, 2013. After cuts to data due to quality and muon vetos, the livetime for the analysis is 477.60 ± 0.01 days. Using a hexagonal prism fiducial volume with a apothem of 162 mm in the x-y plane and $10 < |z| < 182$ mm results in an exposure to ^{136}Xe of 99.8 kg·yr.

5.1 $0\nu\beta\beta$ Search

For the search for $0\nu\beta\beta$, a PDF was made for the $0\nu\beta\beta$ mode and fit alongside the various backgrounds. The PDFs in the model were fit to the selected data in both SS and MS channels with a negative log likelihood function (left plot of Figure 4). The best fit value for a profile over the $0\nu\beta\beta$ mode was $\sim$ 10 counts, but this result is consistent with zero at the 90% confidence level (C.L.), so a lower limit of $T_{1/2}^{0\nu\beta\beta} > 1.1 \cdot 10^{25}$ yrs is claimed [13].

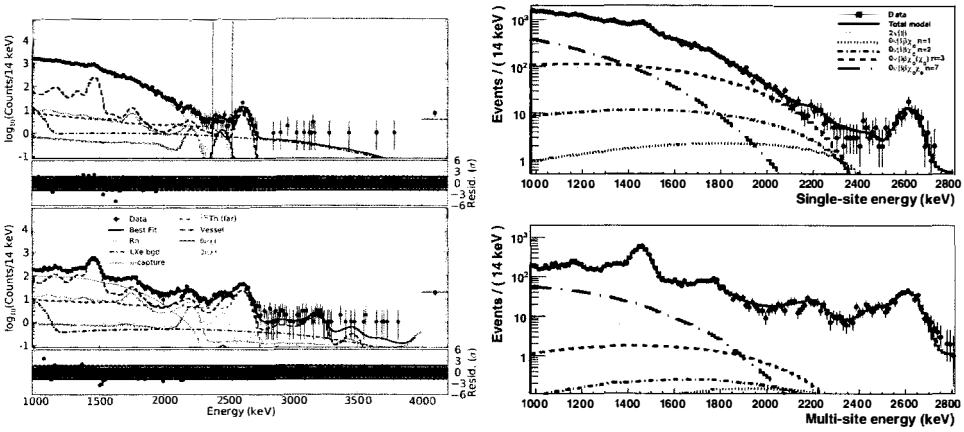

Figure 4 – The left plot shows the SS (upper) and MS (lower) fitted spectra for the $0\nu\beta\beta$ search. The colored lines represent the background groups added to the fit model, and the grey represents the fit to $2\nu\beta\beta$. The $\pm 2\sigma$ region of interest in SS is highlighted in red, showing the best fit PDF for $0\nu\beta\beta$. The right plot shows the best fit model (red line) for the fit to data (black points) with the n=1 Majoron mode included at the 90% C.L. The 90% C.L. fits to each of the other Majoron modes that were searched for are superimposed on the plot to illustrate the magnitude of each mode.

5.2 Majoron Mode Search

Majoron modes for indices 1, 2, 3, and 7 were all searched for separately, assuming no inclusion of the standard $0\nu\beta\beta$ mono-energetic peak. The PDF for each mode was fit alongside the background model, and the number of counts for each mode was profiled over to get the lower half-life limit at the 90% C.L. [14]. These half-life limits were used to set limits on the Majoron-neutrino couplings ($|\langle g_{ee}^{M} \rangle|$) for each mode, shown in Table 1. The right plot in Figure 4 shows the signal + background model fit (red line) over the data (black dots) for the 90% C.L. n=1 Majoron mode search, with the hatched section representing the fit to the $2\nu\beta\beta$. The three other modes that were searched for are superimposed onto the figure to show the magnitudes of the fit to each mode.

Table 1: The half-life lower limits at the 90% C.L. are shown for each Majoron mode that was searched for, along with the limits on the Majoron-neutrino couplings. The spread in the couplings is due to the uncertainty in matrix elements [15,16,17].

Decay Mode	Spectral Index, n	$T_{1/2}$, yr	$\lvert\langle g_{ee}^{M} \rangle\rvert$
$0\nu\beta\beta\chi_0$	1	$> 1.2 \cdot 10^{24}$	$< (0.8 - 1.7) \cdot 10^{-5}$
$0\nu\beta\beta\chi_0$	2	$> 2.5 \cdot 10^{23}$	—
$0\nu\beta\beta\chi_0\chi_0$	3	$> 2.7 \cdot 10^{22}$	$< (0.6 - 5.5)$
$0\nu\beta\beta\chi_0$	3	$> 2.7 \cdot 10^{22}$	< 0.06
$0\nu\beta\beta\chi_0\chi_0$	7	$> 6.1 \cdot 10^{21}$	$< (0.5 - 4.7)$

6 Conclusions and Future Outlook

The EXO-200 detector has proved to be a high sensitivity probe of physics beyond the Standard Model. Stringent limits have been set for the half-lives of both $0\nu\beta\beta$ and Majoron modes with indices 1, 2, 3, and 7. The null results are in agreement with the KamLAND-Zen experiment [10, 11]. The EXO-200 detector is expected to take more data with improved electronics and further background reduction, increasing sensitivity to $0\nu\beta\beta$. As the sensitivity to $0\nu\beta\beta$ is proportional to the source mass and inversely proportional to the background counts and resolution [18], a new

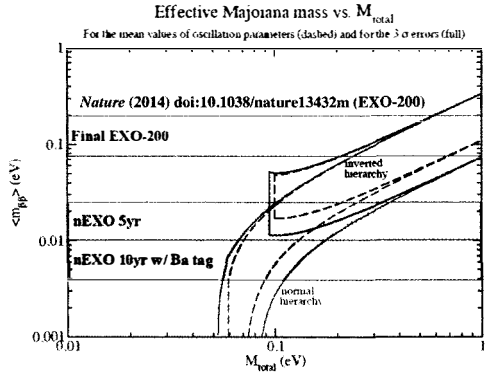

Figure 5 – This plot shows the sensitivity to the effective Majorona mass of the neutrino (calculated from the half-life of $0\nu\beta\beta$) against the sum of neutrino masses. The sensitivity of the nEXO 5-year plan will probe the inverted mass hierarchy, with the band width attributed to the matrix element calculation. The upgrade of nEXO with barium tagging could cover the inverted hierarchy and probe into the normal hierarchy.

detector that uses the knowledge gained through the running of EXO-200 with increased mass could greatly increase the physics reach on a reasonable time scale. A next-generation detector called "nEXO" is being planned that will use approximately 5 tonnes of enriched liquid xenon. The current research and development shows that the nEXO detector will have a sensitivity great enough to probe the inverted mass hierarchy after five years of run-time, and probe into the normal hierarchy after ten years with the upgrade of a barium tagging technique, where the daughter ^{136}Ba ion is positively identified, allowing rejection of nearly all backgrounds.

References

1. J. B. Albert *et al.* [EXO-200 Collaboration], Phys. Rev. C **89**, no. 1, 015502 (2014).
2. Y. Fukuda *et al.* [Super-Kamiokande Collaboration], Phys. Rev. Lett. **81**, 1562 (1998).
3. F.T. Avignone III et al., Double Beta Decay, Majorana Neutrinos, and Neutrino Mass, arxiv:0708.1033v2 [nucl-ex] (2007).
4. Wu, C. S.; Ambler, E.; Hayward, R. W.; Hoppes, D. D.; Hudson, R. P. (1957).
5. T. Araki *et al.* [KamLAND Collaboration], Phys. Rev. Lett. **94**, 081801 (2005).
6. D. G. Michael *et al.* [MINOS Collaboration], Phys. Rev. Lett. **97**, 191801 (2006).
7. P. Bamert, C. P. Burgess and R. N. Mohapatra, Nucl. Phys. B **449**, 25 (1995).
8. M. Redshaw, E. Wingfield, J. McDaniel, and E. G. My- ers, Phys. Rev. Lett., 98, 053003 (2007).
9. M. Auger, D. J. Auty, P. S. Barbeau, L. Bartoszek, E. Baussan, E. Beauchamp, C. Benitez-Medina and M. Breidenbach *et al.*, JINST **7**, P05010 (2012).
10. A. Gando *et al.* [KamLAND-Zen Collaboration], Phys. Rev. Lett. **110**, no. 6, 062502 (2013).
11. A. Gando *et al.* [KamLAND-Zen Collaboration], Phys. Rev. C **86**, 021601 (2012).
12. J. Allison, K. Amako, J. Apostolakis, et al., IEEE Trans. Nucl. Sci., 53, 270 (2006), ISSN 0018-9499.
13. J. B. Albert *et al.* [EXO-200 Collaboration], Nature **510**, 229 (2014).
14. J. B. Albert *et al.* [EXO-200 Collaboration], Phys. Rev. D **90**, no. 9, 092004 (2014).
15. J. Menendez, A. Poves, E. Caurier and F. Nowacki, Nucl. Phys. A **818**, 139 (2009).
16. F. Simkovic, A. Faessler, H. Muther, V. Rodin and M. Stauf, Phys. Rev. C **79**, 055501 (2009).
17. M. Hirsch, H. V. Klapdor-Kleingrothaus, S. G. Kovalenko and H. Pas, Phys. Lett. B **372**, 8 (1996).
18. S. R. Elliott and P. Vogel, Ann. Rev. Nucl. Part. Sci. **52**, 115 (2002)

Neutrinoless double beta decay and nuclear matrix elements

P. K. Raina[a]
Department of Physics, Indian Institute of Technology Ropar
Rupnagar 140001, INDIA

Neutrinoless double beta decay is the only experiment at present promising to settle the Majorana/ Dirac nature of neutrino and is being pursued by a few groups globally. Apart from establishing Majorana character of neutrinos this experiment is also most sensitive to look for the neutrino mass and establish lepton number violation. However, in the process of extraction of neutrino mass from half life measurement one has to use the nuclear transition matrix elements for the nuclei involved. Studies in different models for nuclear matrix elements calculations in general are discussed and the connected uncertainties too are reported.

1 Introduction

Confirmation of neutrino oscillations in different experiments [1] has established the massive character of neutrino and served as a strong evidence to look beyond the well-accepted standard model of particles. Most of the unified theories thus evolved are based on Majorana character of neutrinos. It was realized almost eighty years back that neutrinoless double beta decay (DBD) is one of the best possible experiments to explore the nature of neutrino [2]. Intermittent attempts have been made since then but only after first successful direct experimental observation for ^{82}Se in 1987 the measurements of half lives for two neutrino DBD ware taken up seriously in the decades of 80s and 90s. As a result, now it is known for almost a dozen nuclei in the range of 10^{19} to 10^{22} yrs. In 2004, a controversial HdM measurement [3] on neutrinoless DBD of ^{76}Ge was reported in the order of 10^{25} yrs. Since then quite a few attempts are being made to achieve the expected half lives predicted in this order. Recently [4] some experiments have achieved this range of measurements and have plans to go an order or two higher that would correspond to the mass of neutrino in 10s or 100s of meV ranges. At present neutrinoless DBD is the only experiment promising to disclose the Majorana/ Dirac nature of neutrino and is being pursued rigorously by different groups (reviewed in Refs. [5,6]).

Different theoretical models and approaches used for extraction of nuclear matrix elements (NMEs) play crucial role in arriving at the value of neutrino mass from neutrinoless DBD half life. We have presented brief summary of these models and some of our calculations in deformed HF and projected HFB models in subsequent sections. Physically important considerations to address the variations in NMEs that have been discussed in literature recently are also presented [7]. Calculations of NMEs in general are presented and the connected uncertainties in particular for QRPA and PHFB are reported towards the end. We conclude with the important future considerations to be addressed urgently in near future by theoreticians.

[a]The present work is done in collaboration with P. K. Rath (Univ. of Lucknow, India), S. K. Ghorui (IIT Ropar, India), R. Chandra (BBA Univ., Lucknow, India), K. Chaturvedi (Bundelkhand Univ., Jhansi, India) and J. G. Hirsch (Universidad Nacional Autonona de Mexico)

2 Nuclear Models

A variety of nuclear models is currently employed for the study of double beta decay. Large scale shell model calculations are the most desirable approach [8], but highly limited in the description of medium and heavy mass nuclei. The most popular and successful model is the Quasiparticle Random Phase Approximation (QRPA) and its extensions[9,10]. The inclusion of nuclear deformation has also been carried out in the deformed QRPA [11], the Projected Hartree-Fock-Bogoliubov (PHFB) [12], the Interacting Boson Model (IBM) [13], and the Energy Density Functional (EDF) [14] approaches. The relative applicability and shortcomings of the various models are discussed in more details in Refs. [6,7,9]. Below, we briefly discuss about different models for the completeness.
The Nuclear Shell Model (NSM): The NSM tries to solve the nuclear many-body problem as accurate as possible and correlations are treated exactly. However, only a limited number of orbits close to the Fermi levels are considered. The effective interactions are usually constructed starting from monopole corrected G-matrices or through a renormalization-group treatment.
The Quasiparticle Random Phase Approximation (QRPA): The QRPA and its extensions have emerged as successful model as it include large number of basis space. On the otherhand, all correlations are not included. The particle numbers are not exactly conserved as proton-proton and neutron-neutron pairings are treated in the BCS approximation. The many-body correlations are treated at the RPA level within the quasiboson approximation.
The Projected Hartree-Fock-Bogoliubov Method (PHFB): In the PHFB wave functions of good particle number and angular momentum are obtained by projection on the axially symmetric intrinsic HFB states. In applications to the calculation of the $0\nu\beta\beta$-decay NMEs, the effective Hamiltonian contains terms which are separable in the pairing, quadrupole, and hexadecupole channels.
The Interacting Boson Model (IBM-2): In IBM model the nucleon pair are represented by bosons with angular momentum either L=0 (s boson) or L=2 (d boson). The interacting potential of bosons acts only in pair which is analogous to the Shell Model. The bosons interact through one- and two-body forces giving rise to bosonic wave functions.
The Energy Density Functional (EDF) Method: The EDF method is based on HFB calculations with density dependent Gogny functional. It is an improved method with respect to the PHFB model. The particle number and angular momentum projection for parent and daughter nuclei is performed. Configuration mixing within the generating coordinate method (GCM) is included to take into account beyond mean-field effects. A large single particle basis is considered in the calculations.

3 Results and Discussions

3.1 2ν $\beta\beta$ decay

The nuclear $\beta\beta$ decay is a second order process in weak interaction. The inverse half-life of the 2ν $\beta\beta$ decay for the $0^+ \rightarrow 0^+$ transition can be written as [15]

$$[T^{2\nu}_{1/2}(0^+ \rightarrow 0^+)]^{-1} = G_{2\nu} \left| M_{2\nu} \right|^2 \quad , \tag{1}$$

where $G_{2\nu}$ is the integrated kinematical factor and can be calculated with good accuracy [15,16]. Using the experimental half-life $T^{2\nu}_{1/2}$ and accurately known integrated kinematical factor $G_{2\nu}$, the values of $M_{2\nu}$ can be extracted directly from Eq. (1). It is observed that in all cases of 2ν $\beta^-\beta^-$ decay, the double Gamow-Teller (DGT) transition matrix elements $M_{2\nu}$ are sufficiently quenched. The main motive of all theoretical calculations is to understand the physical mechanism responsible for the observed suppression of $M_{2\nu}$. Hence, the validity of different nuclear models can be tested through the calculation of $M_{2\nu}$.

In Fig. 1, we present a compilation of the magnitude of double beta decay matrix elements calculated within Deformed Hartree-Fock (DHF) model for 0^+(gs) $\rightarrow$ 0^+(gs) transition of the

nuclei studied presently. The purpose of this pictorial representation is for better viewing of the matrix elements calculated within different formalisms and their comparison with the values extracted from average/ recommended experimental half-lives given by Barabash[17] for $g_A = 1.254$ and $g_A = 1.0$. However, these values are updated very recently[18] and we will incorporate them in our future study. From Fig. 1, we see that there is considerably large variation in the $M^{2\nu}$ values calculated within different models. Therefore, it is very difficult to draw a systematic trend for NTMEs.

From the above discussion it is clear that the validity of nuclear models presently employed to calculate two neutrino double beta decay transition matrix elements ($M^{2\nu}$) cannot be uniquely established. It is also to be noted that the value of axial- vector coupling constant g_A plays vital part in the uncertainty of calculated half-lives as the rate of double beta decay varies on $(g_A)^4$. The renormalized or quenched value of $g_A = 1.0$ is taken in order to include the nuclear core (medium) effects such as the spin-isospin correlations. To fine tune the quenching of g_A value, the charge exchange reaction experiments involving the double beta decay nuclei or the nuclei in the vicinity of $\beta\beta$ emitters can play important role.

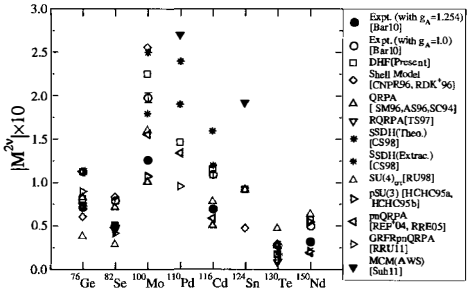

Figure 1 – Comparison of calculated NTMEs with available experimental results for $2\nu\ \beta^-\beta^-$ decay of ^{76}Ge, ^{82}Se, ^{100}Mo, ^{110}Pd, ^{116}Cd, ^{124}Sn, ^{130}Te and ^{150}Nd isotopes for the $0^+(\text{gs}) \rightarrow 0^+(\text{gs})$ transition.

3.2 $0\nu\ \beta\beta$ decay

In the light Majorana neutrino mass mechanism, the half-lives $T^{0\nu}_{1/2}$ for the $0^+ \rightarrow 0^+$ transition are given (in the closure approximation), by[19]

$$\left[T^{0\nu}_{1/2}\left(\beta^-\beta^-\right)\right]^{-1} = G_{01}\left(\beta^-\beta^-\right)\left|\frac{\langle m_\nu\rangle}{m_e}\right|^2 \times \left|\sum_{n,m}\left\langle 0^+_F\left\|\left[-\frac{H_F(r_{nm})}{g_A^2} + \sigma_n\cdot\sigma_m H_{GT}(r_{nm}) + S_{nm}H_T(r_{nm})\right]\tau^+_n\tau^+_m\right\|0^+_I\right\rangle\right|^2 \quad (2)$$

The neutrino potentials associated with Fermi, Gamow-Teller (GT) and tensor operators are given by

$$H_\alpha(r_{nm}) = \frac{2R}{\pi}\int \frac{f_\alpha\left(qr_{nm}\right)}{(q+\bar{A})}\, h_\alpha(q) q dq$$

where $f_\alpha\left(qr_{nm}\right) = j_0\left(qr_{nm}\right)$ and $f_\alpha\left(qr_{nm}\right) = j_2\left(qr_{nm}\right)$ for α =Fermi/GT and tensor potentials, respectively.

The calculation of $M^{(0\nu)}$ in the PHFB model has been discussed in earlier works[12]. The effective Hamiltonian used is given by[12]

$$H = H_{sp} + V(P) + V(QQ) + V(HH) \quad (3)$$

where H_{sp}, $V(P)$, $V(QQ)$ and $V(HH)$ denote the single particle Hamiltonian, the pairing, quadrupole-quadrupole and hexadecapole-hexadecapole part of the effective two-body interaction, respectively.

Short range correlations and radial evolutions of NTMEs

In the literature, the short range correlations (SRC) have been included through the exchange of ω-meson [20], effective transition operator [21], unitary correlation operator method (UCOM) [22], self-consistent CCM [23] and phenomenological Jastrow type of correlations with Miller-Spenser parameterization [24]. Further, Šimkovic *et al.* [23] have shown that in the self-consistent CCM, it is possible to parametrize the effects of Argonne V18 and CD-Bonn nucleon-nucleon (NN) potentials by the Jastrow correlations with Miller-Spenser type of parameterization given by $f(r) = 1 - ce^{-ar^2}(1 - br^2)$. In the present work, the above form is adopted with $a = 1.1\ fm^{-2}$, $1.59\ fm^{-2}$, $1.52\ fm^{-2}$, $b = 0.68\ fm^{-2}$, $1.45\ fm^{-2}$, $1.88\ fm^{-2}$ and $c = 1.0, 0.92, 0.46$ for Miller-Spencer parameterization, Argonne V18 and CD-Bonn NN Potentials, which are denoted as SRC1, SRC2 and SRC3, respectively.

The inclusion of short range correlation (SRC) and finite size of nucleons with dipole form factor (F) induces an extra quenching in the NTMEs $M^{(0\nu)}$, which can range from the order of 18%–23% for SRC1 to negligible for SRC3. The dipole form factor (F) always reduces the NTMEs by 12%–15% in comparision to the point-particle case. Adding SRC (F + SRC) can further reduce the transition matrix elements for SRC1 or slightly enhance them, partially compensating for the effect of the dipole form factor. It is interesting to note that the effect of F+SRC2 is almost negligible, that is, nearly the same as F.

The radial evolution of $M^{(0\nu)}$ can be studied by defining

$$M^{(0\nu)} = \int C^{(0\nu)}(r)\, dr \qquad (4)$$

The radial evolution of $M^{(0\nu)}$ has been studied for four cases, namely F, F+SRC1, F+SRC2 and F+SRC3. To make the effects of finite size and SRC more transparent, we plot them for ^{100}Mo in Fig. 2. In case of finite sized nucleons, the $C^{(0\nu)}$ are peaked at $r \approx 1.25$ fm and with the inclusion of SRC1, SRC2 and SRC3, the position of peak remains unchanged. However, the magnitudes of $C^{(0\nu)}$ change in the latter three cases.

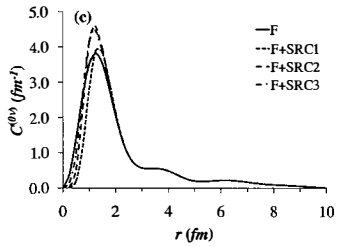

Figure 2 – Radial dependence of $C^{(0\nu)}(r)$ for the $(\beta^-\beta^-)_{0\nu}$ decay of ^{100}Mo isotope.

Table 1: Extracted limits on effective light Majorana neutrino mass $\langle m_\nu \rangle$ and predicted half lives using average NTMEs $\overline{M}^{(0\nu)}$ and uncertainties $\Delta\overline{M}^{(0\nu)}$ for the $(\beta^-\beta^-)_{0\nu}$ decay of ^{96}Zr, ^{100}Mo, ^{128,130}Te and ^{150}Nd isotopes.

$\beta^-\beta^-$ emitters	g_A	$\overline{M}^{(0\nu)}$	ISM [8]	(R)QRPA [23]	IBM [13]	G_{01} (10^{-14}y^{-1})	$T^{0\nu}_{1/2}(yr)$	Ref.	$\langle m_\nu \rangle$	$T^{0\nu}_{1/2}$(y) $< m_\nu >= 50\ meV$
^{100}Mo	1.254	7.22±0.50		2.91–5.56	3.732	4.640	4.6×10^{23}	[25]	$0.48^{+0.04}_{-0.03}$	$4.32^{+0.66}_{-0.54}\times10^{25}$
	1.0	7.94±0.58							$0.69^{+0.05}_{-0.05}$	$8.83^{+1.44}_{-1.15}\times10^{25}$
^{128}Te	1.254	4.22±0.31	2.26	3.21–5.65	4.517	0.1849	1.1×10^{23}	[26]	$8.50^{+0.67}_{-0.58}$	$3.18^{+0.52}_{-0.42}\times10^{27}$
	1.0	4.66±0.34							$12.10^{+0.94}_{-0.81}$	$6.44^{+1.04}_{-0.84}\times10^{27}$
^{130}Te	1.254	4.66±0.43	2.04	2.92–5.04	4.059	4.490	3.0×10^{24}	[27]	$0.30^{+0.03}_{-0.02}$	$1.07^{+0.23}_{-0.17}\times10^{26}$
	1.0	5.15±0.48							$0.42^{+0.04}_{-0.04}$	$2.17^{+0.47}_{-0.35}\times10^{26}$
^{150}Nd	1.254	3.24±0.44			2.321	21.16	1.8×10^{22}	[28]	$2.55^{+0.40}_{-0.31}$	$4.69^{+1.60}_{-1.06}\times10^{25}$
	1.0	3.59±0.50							$3.63^{+0.58}_{-0.44}$	$9.49^{+3.29}_{-2.16}\times10^{25}$

4 Uncertainty in NTMEs

4.1 Statistical uncertainties within PHFB model

In the study of both $(\beta\beta)_{2\nu}$ and $(\beta\beta)_{0\nu}$ decay modes, the renormalized value of axial vector coupling constant g_A is a major source of uncertainty. In the $(\beta\beta)_{0\nu}$ decay, the role of pseudoscalar

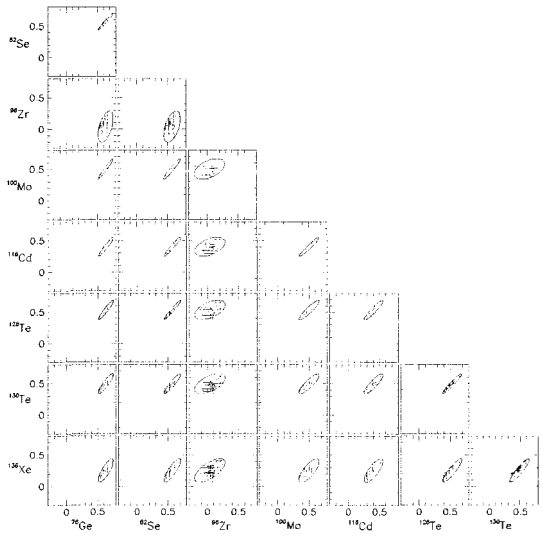

Figure 3 – Scatter plot of estimated QRPA values for logarithms of the $(\beta\beta)_{0\nu}$ matrix element for pairs of decaying nuclei, together with 1σ error ellipses. Reprinted from Ref.[29]; Copyright 2009 by the American Physical Society. Error bars on points indicate uncertainty in the QRPA parameter g_{pp}. Blue points are calculated with the Miller-Spencer treatment of short-range correlation functions and red points with the UCOM treatment.

and weak magnetism terms[19] is crucial, and the finite size of nucleons (FNS) and short range correlations (SRC) play a decisive role vis-a-vis the radial evolution of nuclear transition matrix elements (NTMEs)[8,12].

The uncertainties associated with the NTMEs $M^{(0\nu)}$ and $M^{(0N)}$ for $0\nu\beta\beta$ decay due to the exchange of light and heavy neutrinos, respectively are evaluated by calculating the mean and standard deviation as given by

$$\overline{M}^{(K)} = \frac{\sum_{i=1}^{N} M_i^{(K)}}{N} \quad \text{and} \quad \Delta\overline{M}^{(K)} = \frac{1}{\sqrt{N-1}} \left[\sum_{i=1}^{N} \left(\overline{M}^{(K)} - M_i^{(K)} \right)^2 \right]^{1/2}. \tag{5}$$

In Table 1, we have shown the average NTMEs and uncertainties for light Majorana neutrino mass mechanism. The predicted half-lives are given th Column 8 and compared with the available experimental results. The extracted values of light Majorana-ν mass are tabulated in column 10 of Table 1.

4.2 Statistical uncertainties within QRPA model

Due to large uncertainties in the systematics of nuclear matrix elements calculations, it is difficult to correctly analyze the statistical errors in nuclear matrix elements. However, efforts have been made to study uncertainties in $(\beta\beta)_{0\nu}$ matrix elements for various QRPA-like calculations by varying the value of g_A (1.0 and 1.25), the treatment of short range correlations (via the Miller-Spencer Jastrow function and the UCOM method), the size of the single-particle model space and the g_{pp} parameter (the most important parameter of QRPA model). The log of the nuclear matrix element in one nucleus versus the log of the matrix element in a second, for all possible pairs of nuclei are plotted in Fig. 3 (adopted from Ref.[29]). The error bar on each point representing the uncertainty in g_{pp}. The ellipses in the plot represent 1σ error in the matrix elements.

5 Conclusions

Reduction in uncertainty in NMEs first with in the different versions of a given model has to be reduced by trying to explain all possible systematics of experimental observation of nuclei involved in the DBD including intermediate nuclei. Any important physical processes that might have been ignored in earlier studies or the approximations used in past that might not be desirable for inclusion of short range correlations need to be explored and the effects studied. Finally different models have to include these effects and come to some possible consensus.

Acknowledgments

This work is partially supported by the Council of Scientific and Industrial Research (CSIR), India vide sanction No. 03(1216)/12/EMR-II, Indo-Italian Collaboration DST-MAE project via grant no. INT/Italy/P-7/2012 (ER) and Science and Engineering Research Board (SERB), DST vide sanction no. SB/S2/HEP-007/2013.

References

1. Y. Fukuda, et al., Phys. Rev. Lett. 81, 1562 (1998); Q. R. Ahmed, et al., Phys. Rev. Lett. 89, 011301 (2002); K. Eguchi, et al., Phys. Rev. Lett. 90, 021802 (2003).
2. W. H. Furry, Phys. Rev. 56, 1184 (1939).
3. H. Klapdor-Kleingrothaus et. al., Phys. Lett. B 586, 198 (2004).
4. M. Agostini et al. [GERDA Collaboration] Phys. Rev. Lett. 111, 122503 (2003); The EXO-200 Collaboration, Nature 510, 229 (2014).
5. O. Cremonesi, M. Pavan, Adv. High Eng. Phys. 2014, 951432 (2014).
6. S. M. Bilenky and C. Giunti, Int. J. Mod. Phys. A 30, 1530001 (2015).
7. J. Engel, J. Phys. G: Nucl. Part. Phys. 42, 034017 (2015).
8. E. Caurier, J. Menéndez, F. Nowacki, and A. Poves, Phys. Rev. Lett. **100**, 052503 (2008).
9. J. Suhonen and O. Civitarese, Phys. Rep. **300**, 123 (1998).
10. A. Faessler, and F. Šimkovic, J. Phys. G **24**, 2139 (1998).
11. D. Fang, A. Faessler, V. Rodin and F. Šimkovic, Phys. Rev. C **83**, 034320 (2011); Phys. Rev. C **82**, 051301(R) (2010) (references therein).
12. P. K. Rath et al., Phys. Rev. C. **85**, 014308 (2012); Phys. Rev. C. **88**, 064322 (2013) (references therein).
13. J. Barea and F. Iachello, Phys. Rev. C **79**, 044301 (2009).
14. T. R. Rodríguez and G. Martínez-Pinedo, Phys. Rev. Lett. **105**, 252503 (2010).
15. M. Doi, T. Kotani and E. Takasugi, Prog. Theor. Phys. Supp., **83** 1, (1985)
16. J. Kotila, F. Iachello, Phys. Rev. C 85, 034316 (2012); S. Stoica, M. Mirea, Phys. Rev. C 88, 037303 (2013).
17. A. S. Barabash, Phys. Rev. C 81, 035501 (2010).
18. A. S. Barabash, Nucl. Phys. A 935, 52 (2015).
19. J. D. Vergados, Phys. Rep. **361**, 1 (2002).
20. J. G. Hirsch, O. Castaños, and P. O. Hess, Nucl. Phys. A **582**, 124 (1995).
21. H. F. Wu et. al., Phys. Lett. **B162**, 227 (1985).
22. M. Kortelainen and J. Suhonen, Phys. Rev. C **76**, 024315 (2007); M. Kortelainen, O. Civitarese, J. Suhonen, and J. Toivanen, Phys. Lett. B **647**, 128 (2007).
23. F. Šimkovic et al., Phys. Rev. C **79**, 055501 (2009).
24. G. A. Miller and J. E. Spencer, Ann. Phys. (NY) **100**, 562 (1976).
25. R. Arnold *et al.*, Phys. Rev. Lett. **95**, 182302 (2005).
26. C. Arnaboldi *et al.*, Phys. Lett. **B557**, 167 (2003).
27. C. Arnaboldi *et al.*, Phys. Rev. C **78**, 035502 (2008).
28. J. Argyriades *et al.*, Phys. Rev. C **80**, 032501(R) (2009).
29. A. Faessler et. al., Phys. Rev. **D 79**, 053001 (2009).

Lepton Number Violation with *and without* Majorana Neutrinos [a]

Julian Heeck
Service de Physique Théorique, Université Libre de Bruxelles, B-1050 Brussels, Belgium

We discuss the various incarnations of a gauged $B-L$ symmetry: 1) unbroken, it features Dirac neutrinos, neutrinogenesis to create the baryon asymmetry of our Universe, and a potentially light Z' boson; 2) broken by two units, we obtain the standard case of Majorana neutrinos, seesaw and thermal leptogenesis; 3) broken by four units, we find Dirac neutrinos with lepton-number-violating interactions, which can give rise to a new Dirac leptogenesis mechanism. We review and discuss the signatures distinguishing the three scenarios.

1 Introduction

The observation of a Brout–Englert–Higgs-like scalar boson at the LHC completes the Standard Model (SM). It is however evident that the SM can not be the final description of nature, with

- neutrino masses and mixing,
- dark matter (DM),
- and the baryon asymmetry of the Universe (BAU)

among the most pertinent observations that require new physics. All three problems can be solved by relatively simple SM extensions, but there is no unique or (arguable) even simplest solution, so experimental input and theoretical motivation are required to lead the way. In this talk we will consider baryon (B) and lepton number (L) as guiding principles towards a solution to the three problems above. DM is not the focus here, but we will remark on it parenthetically.

It is well known that the *classical* SM Lagrangian has the accidental global symmetry $U(1)_B \times U(1)_{L_e} \times U(1)_{L_\mu} \times U(1)_{L_\tau}$ due to its particle content/gauge group representations and the requirement for renormalizability. Non-perturbative quantum effects – instantons at zero temperature, sphalerons at $T \neq 0$ – break both B and L by three units each, so $\Delta(B+L) = 6$, while $B-L$ remains conserved: $\Delta(B-L) = 0$. The global symmetry of the *quantum* SM Lagrangian is hence only [1]

$$\mathcal{G}_{\rm sym} = U(1)_{B-L} \times U(1)_{L_e - L_\mu} \times U(1)_{L_\mu - L_\tau}\,, \tag{1}$$

picking a convenient basis in generator space. We know from neutrino oscillations that $U(1)_{L_e-L_\mu} \times U(1)_{L_\mu-L_\tau}$ is a broken symmetry, whereas we have yet to observe a process violating $B-L$. (In fact, no process violating B or L has ever been observed, but we are very confident in the unobservable $\Delta(B+L) = 6$ breaking predicted by theory.)

$\mathcal{G}_{\rm sym}$ is the anomaly-free *global* symmetry of the SM Lagrangian at quantum level, and it is tempting to promote it to a *local* symmetry, i.e. a gauge symmetry alongside $SU(3)_C \times SU(2)_L \times$

[a] Talk presented at the 50th Rencontres de Moriond (EW Session), La Thuile, 15 March 2015.

$U(1)_Y$. This only requires the introduction of three right-handed neutrinos ν_R, uncharged under the SM gauge group, to cancel anomalies – a cheap price to pay for such an enlarged gauge group. Furthermore, the quantum numbers of the ν_R allow us to write down additional couplings

$$\Delta\mathcal{L} = -\overline{\nu}_R y_\nu H^\dagger L + \text{h.c.}, \tag{2}$$

which automatically give rise to a (Dirac) neutrino mass matrix $m_D = y_\nu \langle H \rangle$ after electroweak symmetry breaking. Promoting the global symmetry of the SM to a local symmetry thus requires neutrino masses *for consistency*, which can be taken as a motivation for this approach.

Flavored subgroups of $\mathcal{G}_{\text{sym}}$, such as $U(1)_{B+3(L_e-L_\mu-L_\tau)}$ or $U(1)_{L_\mu-L_\tau}$, make for simple flavor symmetries that can shed light on the leptonic mixing pattern[1] and neutrino hierarchies[2,3] (see also Ref.[4]). Gauged $L_\mu - L_\tau$ in particular has recently received attention as an explanation for some tantalizing hints in $h \to \mu\tau$[5] and lepton-nonuniversal B-meson decays[6,7,8] (see contribution by A. Crivellin in these proceedings).

For simplicity, we will here focus on the unflavored part of $\mathcal{G}_{\text{sym}}$, i.e. consider a gauged $B - L$ symmetry. This still requires three right-handed neutrinos, so the argument regarding automatically massive neutrinos from above applies. In the next sections we will explore the different realizations of a gauged $U(1)_{B-L}$ and their different phenomenology, in particular their very different solutions to the problems of neutrinos mass, the BAU, and DM (parenthetically).

2 Majorana $B - L$

We start with the most popular realization of gauged $U(1)_{B-L}$, in which the symmetry is broken spontaneously by two units, i.e. $\Delta(B - L) = 2$. For this, a new SM-singlet scalar $\phi_{B-L=2}$ is introduced which carries $B - L = 2$ $(= -L)$ and can hence couple to the ν_R via

$$\mathcal{L} \supset -\overline{\nu}_R y_\nu H^\dagger L + \tfrac{1}{2}\overline{\nu}_R K \nu_R^c \, \phi^*_{B-L=2} + \text{h.c.}, \tag{3}$$

which gives rise to a right-handed Majorana mass matrix $\mathcal{M}_R = K\langle\phi_{B-L=2}\rangle$ after $B-L$ breaking and ultimately light Majorana neutrino masses via seesaw:

$$\mathcal{M}_\nu \simeq -m_D^T \mathcal{M}_R^{-1} m_D \sim y_\nu^T K^{-1} y_\nu \left(\frac{10^{14}\,\text{GeV}}{\langle\phi_{B-L=2}\rangle}\right) \text{eV}. \tag{4}$$

For Yukawa couplings of order one, the $B - L$ breaking scale is untestably high and the only signature of "Majorana $B - L$" is neutrinoless double beta decay ($0\nu2\beta$), mediated by the light Majorana neutrinos. While the $0\nu2\beta$ rate is definitely non-zero in this scenario, it could still be unobservably small for normal-hierarchy neutrinos if $(\mathcal{M}_\nu)_{ee} \simeq 0$. Additional signatures arise if the Yukawa couplings are chosen to be small, lowering the right-handed masses below the electroweak scale. In particular, choosing the flavor structure in such a way that one of the right-handed neutrinos, say $\nu_{R,1}$ barely couples to the left-handed neutrinos and has a mass around keV, it can be sufficiently stable to form (warm) DM.[b] The small mixing of $\nu_{R,1}$ then effectively decouples it from the seesaw mechanism, so one of the active neutrinos remains massless.

"Majorana $B - L$" can also explain the BAU by means of leptogenesis, i.e. the out-of-equilibrium decay of the heavy right-handed neutrinos $\nu_R \to LH^*, \overline{L}H$ in the early Universe. CP-violation arises via loops and results in a lepton asymmetry Δ_L, i.e. a different number of leptons and antileptons. Since the sphaleron processes ($\Delta B = \Delta L = 3$) are in equilibrium with the rest of the SM plasma at temperatures $T \gtrsim 100\,\text{GeV}$, the lepton asymmetry will partly be converted to a baryon asymmetry Δ_B.

Breaking $B - L$ by two units can hence solve the three main problems of the SM: neutrinos obtain Majorana masses via seesaw, the BAU is explained by leptogenesis, and one can even

[b] An alternative approach would be to use the remaining $\mathbb{Z}_2^L$ symmetry to stabilize a newly introduced particle with appropriate $B - L$ charge.

make one of the right-handed neutrinos stable enough to form DM. This is however not the only viable realization of a gauged $U(1)_{B-L}$, and we will cover two very different scenarios in the next sections.

3 Unbroken $B-L$

As already stated in the introduction, we have yet to observe a process that violates $B-L$. It is hence tempting to keep $U(1)_{B-L}$ as an unbroken gauge symmetry [9], making $B-L$ a properly conserved quantum number alongside electric charge and color. Neutrinos are then Dirac particles, and one either has to chose the Yukawa couplings very small to obtain the sub-eV required masses, $y_\nu = m_\nu/\langle H\rangle \lesssim 10^{-11}$, or introduce additional new physics that gives a more natural solution.

Surprisingly, even the BAU can be explained in this framework, with a mechanism dubbed neutrinogenesis [10]. For this, new heavy doublet scalars Ψ_j are introduced which decay out of equilibrium in the early Universe. CP violation via loops can give rise to lepton asymmetries in the decays $\Psi_j \to \overline{L}\nu_R, L\overline{\nu}_R$, which take the form $\Delta_{\nu_L} = -\Delta_{\nu_R} \neq 0$. Lepton number is hence not broken in the decays, but merely distributed among left- and right-handed leptons. The crucial observation is now that the Yukawa couplings $y_\nu = m_\nu/\langle H\rangle$ are *too small* to put the ν_R in equilibrium with the rest of the SM plasma, and in particular with the sphalerons. These will therefore only see Δ_{ν_L}, and process it into a baryon asymmetry Δ_B via the usual $\Delta(B+L)=6$ processes, even though the total $B-L$ number of the Universe is zero at all times.

With the BAU and neutrino masses resolved, let us discuss the gauge boson Z' coupled to $B-L$. If massless, the gauge coupling g' is required to be tiny ($g' \lesssim 10^{-24}$) in order to be compatible with tests of the weak equivalence principle. However, since $U(1)_{B-L}$ is abelian, we can actually introduce a Z' mass with the Stückelberg mechanism in a gauge-invariant way without breaking the symmetry. This makes the phenomenology of the Z' much more interesting, because the mass is not coupled to neutrino masses, leptogenesis or the weak scale, and can hence sit at any scale. For low masses, constraints in the $M_{Z'}$–g' plane arise from cosmology, astrophysics (stellar evolution), Big Bang nucleosynthesis and colliders [9]. Unavoidable kinetic mixing results in a Z' coupling to hypercharge and gives rise to additional effects.

As far as DM is concerned, the Z' can be long-lived if the gauge coupling and/or mass are small. The correct abundance can then be obtained by a misalignment mechanism analogous to axions/hidden photons [11]. An alternative way to solve the DM problem in unbroken $B-L$ would be to introduce a new fermion (boson) with even (odd) $B-L$ charge; seeing as all SM fermions (bosons) are odd (even) under $B-L$, the new particle would be stable due to its $U(1)_{B-L}$ charge (similar to the stability of the electron due to the $U(1)_{\rm EM}$). A simple freeze-out mechanism using the Z' interactions is then sufficient to obtain the desired DM abundance.

An unbroken gauged $U(1)_{B-L}$ can hence solve all of the three major problems of the SM: neutrinos obtain simple Dirac masses, the BAU can be obtained by neutrinogenesis, and DM can be obtained either with the Z', or with new particles stabilized by the unbroken $U(1)$.

4 Dirac $B-L$

Let us turn to the third possibility regarding the fate of gauged $U(1)_{B-L}$, where the symmetry is broken – but not by two units. Breaking $B-L$ by any number $\Delta(B-L) \neq 2$ gives Dirac neutrinos, but since $B-L$ is still broken, this framework still allows for lepton number violation [12,13].

Seeing as all SM fermions are odd under $B-L$, only $B-L$ breaking by even numbers can be observable (otherwise spin would be violated), so we focus on the simplest $\Delta(B-L) \neq 2$

case: $\Delta(B-L)=4$. Effective operators can be written down without effort:

$$\mathcal{O}^{d=6} = \overline{\nu}^c_R \nu_R \, \overline{\nu}^c_R \nu_R \,, \qquad \mathcal{O}^{d=8}_1 = |H|^2 \, \overline{\nu}^c_R \nu_R \, \overline{\nu}^c_R \nu_R \,, \tag{5}$$

$$\mathcal{O}^{d=8}_2 = (\overline{L}^c \tilde{H})(H^\dagger L) \, \overline{\nu}^c_R \nu_R \,, \qquad \mathcal{O}^{d=8}_3 = F_Y^{\mu\nu} \overline{\nu}^c_R \sigma_{\mu\nu} \nu_R \, \overline{\nu}^c_R \nu_R \,. \tag{6}$$

At $d=10$, we only give a selection:

$$\mathcal{O}^{d=10}_1 = (\overline{L}^c \tilde{H})(H^\dagger L) \, (\overline{L}^c \tilde{H})(H^\dagger L) \,, \qquad \mathcal{O}^{d=10}_2 = F_Y^{\mu\nu} (\overline{L}^c \tilde{H})(H^\dagger L) \, \overline{\nu}^c_R \sigma_{\mu\nu} \nu_R \,, \tag{7}$$

$$\mathcal{O}^{d=10}_3 = W_a^{\mu\nu} (\overline{L}^c \tilde{H})(H^\dagger \tau^a L) \, \overline{\nu}^c_R \sigma_{\mu\nu} \nu_R \,, \qquad \mathcal{O}^{d=10}_4 = (\overline{u}_R d^c_R)(\overline{d}_R H^\dagger L)(\overline{\nu}^c_R \nu_R) \,, \tag{8}$$

and operators without neutrinos arise at higher dimension still, e.g.

$$\mathcal{O}^{d=20} = \left[(\overline{(D_\mu L)}^c \tilde{H})(H^\dagger D_\nu L) \right]^2 \supset (\overline{e}^c_L W^+_\mu W^+_\nu e_L)^2 \,. \tag{9}$$

Let us present a simple model to show how these effective operators can be obtained and that they are indeed the lowest lepton-number-violating operators, i.e. $\Delta(B-L)=2$ processes do not arise. We introduce a scalar ϕ with $B-L$ charge 4 to break the $U(1)_{B-L}$ spontaneously by four units; in order to connect the symmetry breaking to the fermion sector, a second scalar χ with $B-L$ charge -2 is introduced which serves as a mediator and does not acquire a vacuum expectation value (VEV). The important parts of the Lagrangian are

$$-\mathcal{L} \supset \overline{\nu}_R y_\nu H^\dagger L + \tfrac{1}{2} \overline{\nu}_R K \nu^c_R \chi + \mu \chi^2 \phi + \text{h.c.} \tag{10}$$

One can easily realize a scalar potential with minimum at $\langle \chi \rangle = 0$, $\langle H \rangle \neq 0 \neq \langle \phi \rangle$, which breaks $SU(2)_L \times U(1)_Y \times U(1)_{B-L}$ to $U(1)_{\rm EM} \times \mathbb{Z}_4^L$. An exact $\mathbb{Z}_4^L$ symmetry remains, under which leptons transform as $\ell \to -i\,\ell$ and $\chi \to -\chi$, making the neutrinos Dirac particles but still allowing for $\Delta L = 4$ processes.[c] (The remaining $\mathbb{Z}_4$ symmetry could naturally be used as a stabilizing symmetry for a new DM particle, interacting with the SM via the Z' and the scalars.)

Since χ does not acquire a VEV, the neutrinos will be Dirac particles $\nu = \nu_L + \nu_R$ with mass matrix $m_D = y_\nu \langle H \rangle$, just like in the unbroken $B-L$ case of Sec. 3. The VEV of ϕ splits the masses of the real and imaginary part of χ due to the coupling $\mu \chi^2 \phi$, so we end up with two scalars $\chi_{r,i}$ that couple to $\overline{\nu}_R \nu^c_R$. If these scalars are heavy, we can integrate them out to obtain the $\Delta(B-L)=4$ operator $(\overline{\nu}_R \nu^c_R)^2$ of Eq. (5) (see Fig. 1). Other $\Delta(B-L)=4$ operators can be obtained by attaching SM interactions, or by going to a left–right extension of this simple model (see below). We stress again that neutrinos are Dirac particles here, and that there are no $\Delta(B-L)=2$ processes allowed by the symmetry (such as $0\nu2\beta$).

The $\Delta(B-L)=4$ interactions can give rise to a new leptogenesis mechanism with Dirac neutrinos that differs qualitatively from the neutrinogenesis mechanism described in Sec. 3. For this, we assume several heavy mediator scalars χ_j, which decay out-of-equilibrium in the early Universe. Due to the couplings of Eq. (10), the scalars decay either into $\nu_R \nu_R$ or $\nu^c_R \nu^c_R$, and loop corrections induce a different rate for both channels [13]. After all the scalars have decayed, we thus end up with an asymmetry in the right-handed neutrinos Δ_{ν_R}. This in itself is not helpful, because the right-handed neutrinos are decoupled from the rest of the SM plasma (which was the main trick in neutrinogenesis). In our case, we *need* them to be in equilibrium, so we have to introduce a second scalar doublet to the SM that has stronger couplings to the ν_R than the doublet that generates the neutrino mass. Such a model has already been proposed independently of Dirac $B-L$ in order to explain the smallness of Dirac neutrino masses [15]. In this neutrinophilic two-Higgs-doublet model an additional global symmetry ensures that the second doublet couples only to $\overline{L}\nu_R$, and that it only acquires a tiny VEV (say eV). Because of this, the neutrino masses are small even if the Yukawa couplings to the second scalar doublet are large, solving the issue of small Dirac neutrino masses. Even better, the large Yukawa couplings

[c] Conservation of lepton number modulo $n > 2$ to forbid Majorana masses was also mentioned in Ref. [14].

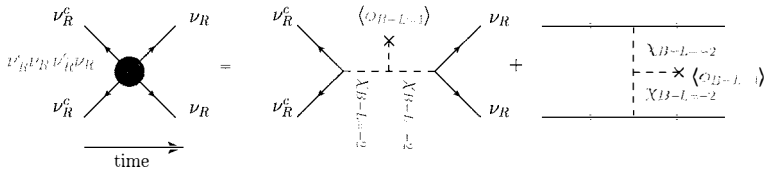

Figure 1 – $\Delta(B-L)=4$ operator $(\overline{\nu^c_R}\nu_R)^2$ realized by exchange of scalars. Arrows show flow of lepton number.

imply that in our leptogenesis scenario the Δ_{ν_R} asymmetry is transferred to an asymmetry in the left-handed leptons by the second doublet, and consequently converted to a baryon asymmetry by the sphalerons. As a consequence of the required thermalization of the ν_R, we expect a contribution to the effective number of neutrinos in the early Universe, namely $N_{\rm eff} \gtrsim 3.14$, to be tested with future Planck-like experiments.

Above we have seen that $\Delta(B-L)=4$ processes can be the lowest-order lepton-number-violating effect if neutrinos are Dirac particles, and also that it can lead to a new kind of Dirac leptogenesis mechanism. Compared to the (already hard to measure) $\Delta L=2$ processes searched for in $0\nu2\beta$ experiments, it is even harder to probe $\Delta L=4$ processes directly, because of the high dimensionality of the underlying effective operators. Sensitive nuclear probes analogous to $0\nu2\beta$ exist – namely the $0\nu4\beta$ decay ${}^{150}_{60}\mathrm{Nd} \to {}^{150}_{64}\mathrm{Gd} + 4e^-$ with energy release $Q_{0\nu4\beta} \simeq 2.08\,\mathrm{MeV}$ testable with existing data from NEMO – but the expected rates in the toy model from above are unmeasurable small[12]. It is hence desirable to construct $\Delta(B-L)=4$ models that can lead to stronger effects, which can be achieved in left–right extensions.

Let us embed the electroweak gauge group $SU(2)_L \times U(1)_Y$ into the left–right symmetry group $SU(2)_L \times SU(2)_R \times U(1)_{B-L}$. Consistency again requires the introduction of right-handed neutrinos (similar to just gauged $B-L$) to complete the right-handed lepton doublet $\Psi_R = (\nu_R,\, e_R)^T \sim (\mathbf{1},\mathbf{2},-1)$, while the scalar H is promoted to a bi-doublet $H \sim (\mathbf{2},\overline{\mathbf{2}},0)$. The most common left–right model corresponds to an extension of "Majorana $B-L$", i.e. features Majorana neutrinos. It is however not difficult to also extend "Dirac $B-L$" to a left–right model, simply by promoting the scalars χ and ϕ from above to

$$\chi_R = \frac{1}{\sqrt{2}}\begin{pmatrix} \chi_R^- & \chi_R^0 & 0 \\ \chi_R^{--} & 0 & \chi_R^0 \\ 0 & \chi_R^{---} & -\chi_R^- \end{pmatrix} \sim (\mathbf{1},\mathbf{3},-2)\,, \tag{11}$$

$$\phi_R = \frac{1}{\sqrt{6}}\begin{pmatrix} \phi_R^{++} & \sqrt{3}\phi_R^{+++} & \sqrt{6}\phi_R^{++++} \\ \sqrt{3}\phi_R^{+} & -2\phi_R^{++} & -\sqrt{3}\phi_R^{+++} \\ \sqrt{6}\phi_R^{0} & -\sqrt{3}\phi_R^{+} & \phi_R^{++} \end{pmatrix} \sim (\mathbf{1},\mathbf{5},4)\,. \tag{12}$$

The couplings analogous of Eq. (10) then take the form (add χ_L and ϕ_L for LR parity)

$$\mathcal{L} \supset y\overline{\Psi}_L H \Psi_R + \kappa\,\overline{\Psi}_R \chi_R \Psi^c_R + \mu\,\mathrm{tr}\,[\chi_R \phi_R \chi_R] + \mathrm{h.c.}, \tag{13}$$

so ϕ_R^0 and χ_R^0 play the same role as ϕ and χ from above. Note that the triplet χ does not acquire a VEV in this model, so the neutrinos are Dirac. $SU(2)_R$ is nevertheless broken above the electroweak scale via $\langle\phi_R\rangle \gg \langle H\rangle$:

$$M^2_{W^\pm_R} \simeq 2g_R^2\langle\phi_R^0\rangle^2\,, \quad M^2_{Z_R} \simeq 8(g_R^2+4g_{B-L}^2)\langle\phi_R^0\rangle^2\,. \tag{14}$$

Compared to the toy model from above, it is now possible to consider processes that do not involve neutrinos, and are in particular not suppressed by small neutrino masses (see Fig. 2). This opens the way towards collider searches for $\Delta L=4$ processes such as $pp \to 4\ell^- + 4W^+$ at the LHC or $e^-e^- \to \ell^+\ell^+ + 4W^-$ at a future like-sign lepton collider[16].

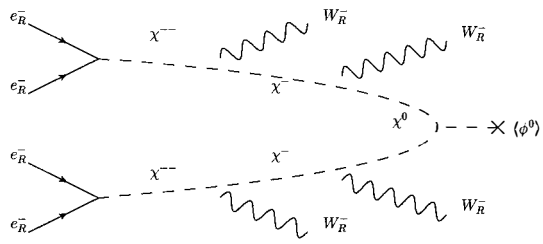

Figure 2 – $\Delta(B-L)=4$ operator $e_R^4 W_R^4$ by exchange of scalars in a left–right model.

5 Conclusion

The incredible success of the Standard Model just deepens the mystery of its anomaly-free global symmetry $U(1)_{B-L}$. Consistently promoting this global symmetry to a local one automatically results in massive neutrinos, amending a major problem of the SM. The matter–antimatter asymmetry of our Universe is also deeply connected to the quantum number $B-L$, and the new particles in the wake of the $U(1)_{B-L}$ are potential candidates for DM. We presented an overview of the three phenomenologically distinct realizations of a gauged $U(1)_{B-L}$: 1) as an unbroken symmetry with a Stückelberg Z', Dirac neutrinos and neutrinogenesis; 2) broken by two units with Majorana neutrinos, seesaw, and leptogenesis; 3) broken by $n \neq 2$ units, e.g. $n=4$, leading to lepton-number-violating Dirac neutrinos and Dirac leptogenesis. Experiments will have to decide the fate of $B-L$ and resolve the mystery surrounding it.

Acknowledgments

I thank Werner Rodejohann for collaboration on some of the work presented here, and the organizers of the *Moriond EW 2015* for financial support and the opportunity to present my results. This work is funded in part by IISN and by Belgian Science Policy (IAP VII/37).

1. T. Araki, J. Heeck and J. Kubo, JHEP **1207** (2012) 083 [arXiv:1203.4951 [hep-ph]].
2. J. Heeck and W. Rodejohann, Phys. Rev. D **84** (2011) 075007 [arXiv:1107.5238 [hep-ph]].
3. J. Heeck and W. Rodejohann, Phys. Rev. D **85** (2012) 113017 [arXiv:1203.3117 [hep-ph]].
4. J. Heeck, Nucl. Phys. Proc. Suppl. **237-238** (2013) 336.
5. J. Heeck, M. Holthausen, W. Rodejohann and Y. Shimizu, arXiv:1412.3671 [hep-ph].
6. W. Altmannshofer, S. Gori, M. Pospelov and I. Yavin, Phys. Rev. D **89** (2014), 095033.
7. A. Crivellin, G. D'Ambrosio and J. Heeck, arXiv:1501.00993 [hep-ph].
8. A. Crivellin, G. D'Ambrosio and J. Heeck, arXiv:1503.03477 [hep-ph].
9. J. Heeck, Phys. Lett. B **739** (2014) 256 [arXiv:1408.6845 [hep-ph]].
10. K. Dick, M. Lindner, M. Ratz and D. Wright, Phys. Rev. Lett. **84** (2000) 4039.
11. A. E. Nelson and J. Scholtz, Phys. Rev. D **84** (2011) 103501 [arXiv:1105.2812 [hep-ph]].
12. J. Heeck and W. Rodejohann, Europhys. Lett. **103** (2013) 32001 [arXiv:1306.0580].
13. J. Heeck, Phys. Rev. D **88** (2013) 076004 [arXiv:1307.2241 [hep-ph]].
14. E. Witten, Nucl. Phys. Proc. Suppl. **91** (2001) 3 [hep-ph/0006332].
15. S. M. Davidson and H. E. Logan, Phys. Rev. D **80** (2009) 095008 [arXiv:0906.3335].
16. J. Heeck, in preparation.

7.
Heavy Flavours

Latest results on rare decays from LHCb

C. Langenbruch on behalf of the LHCb collaboration
University of Warwick, Department of Physics,
Gibbet Hill Road, Coventry CV4 7AL, UK

Rare flavour changing neutral current decays are sensitive indirect probes for new effects beyond the Standard Model (SM). In the SM, these decays are forbidden at tree level and are therefore loop-suppressed. In SM extensions, new, heavy particles can significantly contribute and affect both their branching fractions as well as their angular distributions.
The rare decay $B^0 \to K^{*0}(\to K^+\pi^-)\mu^+\mu^-$ is of particular interest, since it gives access to many angular observables, allowing to model-independently test the operator structure of the decay. A previous analysis of the angular distributions of the final state particles showed interesting tensions with SM predictions using the data sample taken by the LHCb detector during 2011. These proceedings will summarize latest results on rare decays from the LHCb experiment with emphasis on the angular analysis of the decay $B^0 \to K^{*0}\mu^+\mu^-$, using the full Run I data sample of the LHCb experiment.

1 Introduction

Rare flavour changing neutral current (FCNC) decays are, in the Standard Model (SM), forbidden at lowest perturbative order and proceed via loop-order diagrams. New heavy particles in extensions of the SM can appear in competing Feynman diagrams and significantly affect both the branching fractions of rare decays and the angular distributions of the final state particles. Studies of rare decays therefore constitute sensitive searches for effects beyond the SM, and furthermore allow to probe the underlying operator structure via global fits [1,2,3,4].

2 Angular analysis of the rare decay $B^0 \to K^{*0}\mu^+\mu^-$

2.1 *Angular observables in* $B^0 \to K^{*0}\mu^+\mu^-$

The rare decay $B^0 \to K^{*0}\mu^+\mu^-$ is of particular interest since the $K^+\pi^-\mu^+\mu^-$ final state allows access to many angular observables. The final state is fully defined by the three decay angles $\vec{\Omega} = (\cos\theta_l, \cos\theta_K, \phi)$, and q^2, the invariant mass of the dilepton system squared [5]. The *CP*-averaged angular distribution of the decay $B^0 \to K^{*0}\mu^+\mu^-$ in a bin of q^2 is given by

$$\begin{aligned}\frac{1}{\mathrm{d}(\Gamma+\bar{\Gamma})/\mathrm{d}q^2}\frac{\mathrm{d}^3(\Gamma+\bar{\Gamma})}{\mathrm{d}\vec{\Omega}} = \frac{9}{32\pi}\Big[& \frac{3}{4}(1-F_\mathrm{L})\sin^2\theta_K + F_\mathrm{L}\cos^2\theta_K + \frac{1}{4}(1-F_\mathrm{L})\sin^2\theta_K\cos 2\theta_l \\ & - F_\mathrm{L}\cos^2\theta_K\cos 2\theta_l + S_3\sin^2\theta_K\sin^2\theta_l\cos 2\phi \\ & + S_4\sin 2\theta_K\sin 2\theta_l\cos\phi + S_5\sin 2\theta_K\sin\theta_l\cos\phi \\ & + \frac{4}{3}A_\mathrm{FB}\sin^2\theta_K\cos\theta_l + S_7\sin 2\theta_K\sin\theta_l\sin\phi \\ & + S_8\sin 2\theta_K\sin 2\theta_l\sin\phi + S_9\sin^2\theta_K\sin^2\theta_l\sin 2\phi\Big]. \end{aligned} \quad (1)$$

Here, $F_{\rm L}$ denotes the longitudinal polarization fraction of the K^{*0} and $A_{\rm FB}$ the forward-backward asymmetry of the dimuon system. The LHCb collaboration performed two angular analyses [6,7] using angular folding techniques to determine the observables with the data taken during 2011, which corresponds to an integrated luminosity of $1\,{\rm fb}^{-1}$. While all the angular observables in Ref. [6] are found to be in good agreement with SM predictions, the measurement of the less form-factor dependent observable $P_5' = S_5/\sqrt{F_{\rm L}(1-F_{\rm L})}$, that was proposed in Ref. [8], shows a local deviation from the SM prediction, corresponding to 3.7 standard deviations (σ) [7]. Global fits show that the tension can be reduced by a negative shift of the Wilson coefficient $\mathcal{C}_9$ which parametrises the vector coupling strength [1,2,3,4]. New physics (NP) explanations for this shift include the possibility of heavy Z' gauge bosons [9,10,11,12,13] or leptoquarks [14,15,16,17]. However, the significance of the tension could be reduced if hadronic uncertainties are underestimated [18,19,20].

2.2 *Selection of signal candidates*

An update of the angular analysis of $B^0 \to K^{*0}\mu^+\mu^-$ using the full Run I data sample corresponding to $3\,{\rm fb}^{-1}$ was eagerly awaited in the community and preliminary results are presented here for the first time [21]. The selection of $B^0 \to K^{*0}\mu^+\mu^-$ signal candidates is improved compared to Ref. [6,7] with a simplified, yet more efficient, multivariate classifier to reduce combinatorial background events and more stringent vetoes to reject peaking backgrounds. Figure 1 gives the distribution of the invariant mass of the $K^+\pi^-\mu^+\mu^-$ system *vs.* q^2 for signal candidates after the full selection, where the $B^0 \to K^{*0}\mu^+\mu^-$ signal decay is clearly visible as vertical band. The q^2 regions $8.0 < q^2 < 11.0\,{\rm GeV}^2/c^4$ and $12.5 < q^2 < 15.0\,{\rm GeV}^2/c^4$ contain the tree-level decays $B^0 \to J/\psi(\to \mu^+\mu^-)K^{*0}$ and $B^0 \to \psi(2S)(\to \mu^+\mu^-)K^{*0}$ which are used as important control decays but vetoed when selecting $B^0 \to K^{*0}\mu^+\mu^-$ signal candidates. Integrated over q^2, the $B^0 \to K^{*0}\mu^+\mu^-$ signal yield is $2\,398 \pm 57$, as shown in Fig. 1.

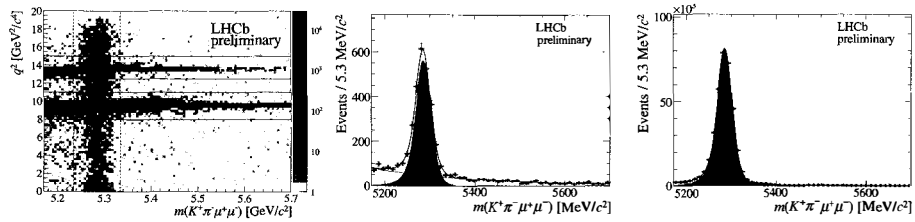

Figure 1 – (Left) Invariant mass of the $K^+\pi^-\mu^+\mu^-$ system *vs.* q^2. The signal decay $B^0 \to K^{*0}\mu^+\mu^-$ is clearly visible as vertical band. (Middle) The signal decay $B^0 \to K^{*0}\mu^+\mu^-$ integrated over q^2. The signal yield is $2\,398 \pm 57$. (Right) The high-statistics control mode $B^0 \to J/\psi\,K^{*0}$.

2.3 *Angular analysis*

The angular observables are determined by performing an unbinned maximum likelihood fit in bins of q^2, using a q^2 binning which is both finer and more regular than the binning used in Refs. [6,7]. The fit uses the invariant mass distribution of the $K^+\pi^-\mu^+\mu^-$ system, the invariant $K^+\pi^-$ mass and the three-decay angles as input distributions without applying angular foldings. This allows to quote the covariance matrices for all eight angular observables which is important for the use of the results in global fits. The invariant $K^+\pi^-$ mass distribution is used to constrain the contribution from events where the $K^+\pi^-$ system is in a spin-0 configuration, the so-called S-wave. The additional six parameters for the description of the S-wave and the interference terms with the K^{*0} P-wave are treated as nuisance parameters and allowed to vary in the fit. The trigger, reconstruction and selection of signal events causes distortions of the distributions of q^2 and the decay angles. This acceptance effect is modelled using a multidimensional combination

of Legendre polynomials. The polynomial coefficients are determined using a moments analysis of a large sample of simulated $B^0 \to K^{*0}\mu^+\mu^-$ events, generated according to a phase-space model. The Feldman-Cousins method [22] is used to guarantee correct coverage for the angular observables even for low signal yields.

2.4 Results

The results for $F_{\rm L}$, $A_{\rm FB}$, S_5 and P_5' are given in Fig. 2, overlaid with SM predictions from Refs.[3,23] and Ref. [24]. The longitudinal polarization fraction $F_{\rm L}$ and the forward-backward asymmetry $A_{\rm FB}$ are found to be in good agreement with SM predictions. Interestingly, for $A_{\rm FB}$, the data points seem to lie systematically below the predictions in the $1.1 < q^2 < 6\,{\rm GeV}^2/c^4$ range. The measurement of the less form-factor dependent observable P_5' is found to be compatible with the previous publication [7] and lies above the SM prediction [24] in the $4.0 < q^2 < 8.0\,{\rm GeV}^2/c^4$ region. The deviation from the SM prediction corresponds to $2.9\,\sigma$ for each of the two q^2 bins in the region $4.0 < q^2 < 6.0\,{\rm GeV}^2/c^4$ and $6.0 < q^2 < 8.0\,{\rm GeV}^2/c^4$. Neglecting correlations between the bins, the χ^2 probability to find a deviation of this size or larger for two degrees of freedom results in a naive significance of $3.7\,\sigma$. The remaining observables S_3, S_4, S_7, S_8 and S_9 are given in Ref. [21] and show good agreement with SM predictions.

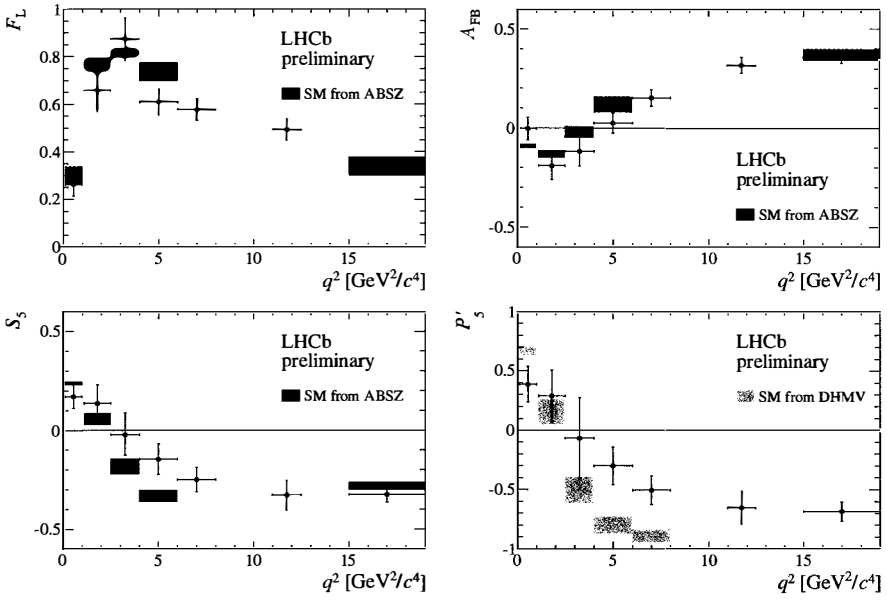

Figure 2 – The angular observables $F_{\rm L}$, $A_{\rm FB}$, S_5 and P_5' overlaid with SM predictions from (purple) Ref.[3,23] and (orange) Ref.[24].

3 Branching fraction measurements of $B \to K^{(*)}\mu^+\mu^-$ and $B_s^0 \to \phi\mu^+\mu^-$ decays

Compared to angular observables, branching fraction measurements of $b \to s\mu^+\mu^-$ processes tend to have larger associated theory uncertainties, since they are directly impacted by the hadronic form-factors. However, the impact of theory uncertainties can be mitigated, by performing measurements of ratios of branching fractions where form-factor uncertainties cancel at leading order. Examples of such quantities are the isospin asymmetry A_I and the CP-asymmetry

$A_{\rm CP}$, defined as

$$A_I = \frac{\Gamma(B^0 \to K^{(*)0}\mu^+\mu^-) - \Gamma(B^+ \to K^{(*)+}\mu^+\mu^-)}{\Gamma(B^0 \to K^{(*)0}\mu^+\mu^-) + \Gamma(B^+ \to K^{(*)+}\mu^+\mu^-)}, \quad (2)$$

$$A_{\rm CP} = \frac{\Gamma(\bar{B} \to \bar{K}^{(*)}\mu^+\mu^-) - \Gamma(B \to K^{(*)}\mu^+\mu^-)}{\Gamma(\bar{B} \to \bar{K}^{(*)}\mu^+\mu^-) + \Gamma(B \to K^{(*)}\mu^+\mu^-)}. \quad (3)$$

In Refs.[28,29], A_I and $A_{\rm CP}$ are found to be compatible with SM predictions[30,5]. The corresponding differential branching fraction measurements for the rare decays $B^+ \to K^+\mu^+\mu^-$, $B^0 \to K^0\mu^+\mu^-$ and $B^+ \to K^{*+}\mu^+\mu^-$ are given in Fig. 3. They are compatible with, but tend to lie below, SM predictions[31,32].

Using $1\,{\rm fb}^{-1}$ of data taken during 2011, LHCb also determines the differential branching fractions for the rare decays $B^0 \to K^{*0}\mu^+\mu^-$ and $B_s^0 \to \phi\mu^+\mu^-$ [6,33]. The differential branching fractions tend to be below SM predictions both at low q^2, where updated light cone sum rule calculations are available[23], and at high q^2, where lattice calculations exist[25,26,27]. For the decay $B_s^0 \to \phi\mu^+\mu^-$ the tension in the region $1 < q^2 < 6\,{\rm GeV}^2/c^4$ corresponds to $3.1\,\sigma$. It is interesting to note, that the deviation of the branching fractions points to a deviation of the $b \to s\mu^+\mu^-$ couplings which is compatible with, but less significant than, what is observed from the angular observables in $B^0 \to K^{*0}\mu^+\mu^-$ at low q^2[23,27]. Updated measurements of $\mathcal{B}(B^0 \to K^{*0}\mu^+\mu^-)$ and $\mathcal{B}(B_s^0 \to \phi\mu^+\mu^-)$ using the full Run I data sample are currently in preparation to clarify the situation.

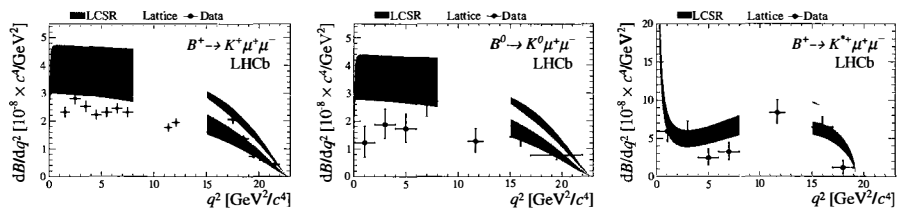

Figure 3 – Differential branching fraction of (left) $B^+ \to K^+\mu^+\mu^-$ (middle) $B^0 \to K^0\mu^+\mu^-$ and (right) $B^+ \to K^{*+}\mu^+\mu^-$, overlaid with SM predictions[31,32].

4 Branching fraction of $B^0_{(s)} \to \pi^+\pi^-\mu^+\mu^-$

The $\pi^+\pi^-\mu^+\mu^-$ final state can be reached from both the decay of a B^0 meson and the decay of a B_s^0 meson. The B^0 decay is expected to be dominated by the $b \to d\mu^+\mu^-$ transition $B^0 \to \rho^0\mu^+\mu^-$, the B_s^0 decay by the $b \to s\mu^+\mu^-$ transition $B_s^0 \to f^0(980)\mu^+\mu^-$. While $b \to d$ decays are expected to be suppressed by the factor $|V_{td}|^2/|V_{ts}|^2 \sim 0.04$ compared to $b \to s$ transitions in the SM, this is not necessarily the case for SM extensions.

The $\pi^+\pi^-\mu^+\mu^-$ final state is studied using the full Run I data sample taken by the LHCb experiment [34], corresponding to an integrated luminosity of $3\,{\rm fb}^{-1}$. The invariant mass of the $\pi^+\pi^-$ system is required to be in the range $0.5 - 1.3\,{\rm GeV}/c^2$ containing both the ρ^0 as well as the $f^0(980)$ resonance. Figure 4 gives the invariant mass distribution of the $\pi^+\pi^-\mu^+\mu^-$ system for the charmonium modes $B^0_{(s)} \to J/\psi\,\pi^+\pi^-$, that are used as control decays for the fit model, as well as the signal decays $B^0_{(s)} \to \pi^+\pi^-\mu^+\mu^-$. The signal yields are found to be $40 \pm 10 \pm 3$ for the $B^0 \to \pi^+\pi^-\mu^+\mu^-$ decay and $55 \pm 10 \pm 5$ for the $B_s^0 \to \pi^+\pi^-\mu^+\mu^-$ decay, resulting in significances of $4.8\,\sigma$ and $7.2\,\sigma$, respectively. The branching fractions are determined with respect to the normalisation mode $B^0 \to J/\psi K^{*0}$. They are found to be

$$\mathcal{B}(B_s^0 \to \pi^+\pi^-\mu^+\mu^-) = (8.6 \pm 1.5_{\rm stat.} \pm 0.7_{\rm syst.} \pm 0.7_{\rm norm.}) \times 10^{-8},$$
$$\mathcal{B}(B^0 \to \pi^+\pi^-\mu^+\mu^-) = (2.11 \pm 0.51_{\rm stat.} \pm 0.15_{\rm syst.} \pm 0.16_{\rm norm.}) \times 10^{-8},$$

when correcting for the q^2 regions removed by the vetoes of the $J/\psi\,\pi^+\pi^-$ and $\psi(2S)\pi^+\pi^-$ decays, in agreement with SM predictions [35,36,37,38].

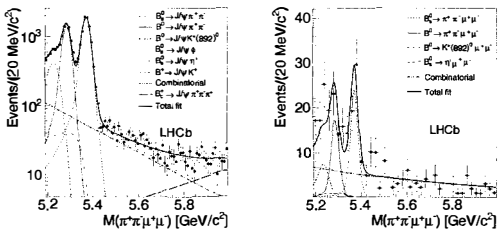

Figure 4 – Invariant mass of the $\pi^+\pi^-\mu^+\mu^-$ final state for (left) tree-level charmonium decays $B^0 \to J/\psi\,\pi^+\pi^-$ and $B_s^0 \to J/\psi\,\pi^+\pi^-$ and (right) the rare decays $B^0 \to \pi^+\pi^-\mu^+\mu^-$ and $B_s^0 \to \pi^+\pi^-\mu^+\mu^-$.

5 The rare baryonic decay $\Lambda_b^0 \to \Lambda\mu^+\mu^-$

The study of the rare Λ_b^0 decay $\Lambda_b^0 \to \Lambda\mu^+\mu^-$ is of particular interest due to the half-integer spin of the Λ_b^0 baryon and the hadronic dynamics involving the heavy b and a light diquark system. Furthermore, the Λ decays weakly into the $p\pi^-$ final state, allowing access to new and complementary information compared to mesonic $b \to s\mu^+\mu^-$ decays [39].

The decay was previously studied in [40,41], where no evidence for signal in the q^2 region below the J/ψ was found. An updated analysis is performed, using the full LHCb Run I data sample [42]. Figure 5 gives the differential branching fraction. Evidence for signal is found below the charmonium resonances at low q^2, the differential branching fraction for the high q^2 range $15 < q^2 < 20\,\mathrm{GeV}^2/c^4$ is determined to be $(1.18^{+0.09}_{-0.08} \pm 0.03 \pm 0.27) \times 10^{-7}\,\mathrm{GeV}^{-2}c^4$ [42]. Angular analyses are performed for the q^2 bins where evidence for signal is found and the angular observables A_{FB}^{ℓ} and A_{FB}^{h}, the forward-backward asymmetries in the dimuon and hadron system, are determined. As shown in Fig. 5, A_{FB}^{ℓ} and A_{FB}^{h} are found to be in good agreement with SM predictions [43,44].

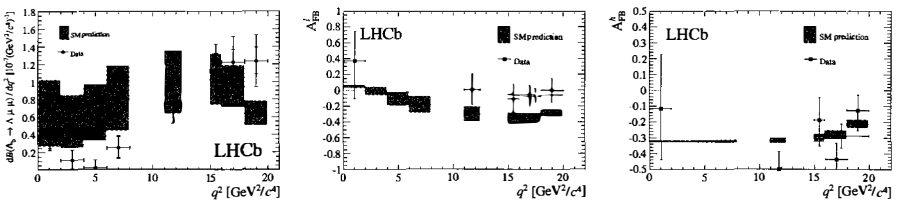

Figure 5 – The (left) differential branching fraction and (middle) leptonic, as well as the (right) hadronic forward-backward asymmetry, overlaid with SM predictions [44,43].

6 A test of lepton universality using the decay $B^+ \to K^+e^+e^-$

The ratio R_K in the q^2 region $[q^2_{\mathrm{min}}, q^2_{\mathrm{max}}]$ is defined as

$$R_K = \frac{\int_{q^2_{\mathrm{min}}}^{q^2_{\mathrm{max}}} \frac{\mathrm{d}\Gamma[B^+ \to K^+\mu^+\mu^-]}{\mathrm{d}q^2}\mathrm{d}q^2}{\int_{q^2_{\mathrm{min}}}^{q^2_{\mathrm{max}}} \frac{\mathrm{d}\Gamma[B^+ \to K^+e^+e^-]}{\mathrm{d}q^2}\mathrm{d}q^2}, \qquad (4)$$

where Γ denotes the q^2 dependent partial width. Due to the universal coupling of γ and Z_0 bosons to leptons, R_K in the region $1 < q^2 < 6\,\mathrm{GeV}^2/c^4$ is predicted to be one with an uncertainty of less than 10^{-3} [45,46]. Small corrections to the ratio arise only from phase-space effects and Higgs penguin contributions.

The measurement is experimentally challenging due to a lower trigger efficiency for electrons compared to muons and the higher emission of Bremsstrahlung which deteriorates the resolution of the invariant mass of the $K^+e^+e^-$ system. In the range $1 < q^2 < 6\,\mathrm{GeV}^2/c^4$, R_K is determined to be

$$R_K = 0.745^{+0.090}_{-0.074}(\mathrm{stat.}) \pm 0.036(\mathrm{syst.}),$$

which corresponds to a deviation of $2.6\,\sigma$ from the SM prediction [47]. Figure 6 shows the decay $B^+ \to J/\psi K^+$, which is used to study the effect of Bremsstrahlung and understand the relative efficiency between reconstructing dimuon and dielectron modes. The signal decay $B^+ \to K^+e^+e^-$ is also given, as well as the LHCb measurement of R_K [47] in comparison with results from the B factories [48,49]. Since R_K is free from hadronic uncertainties, the result received considerable attention from theory [12,13,14,15,17,50,51,52]. Further tests of lepton universality are in preparation, including the measurements of R_{K^*} and R_ϕ.

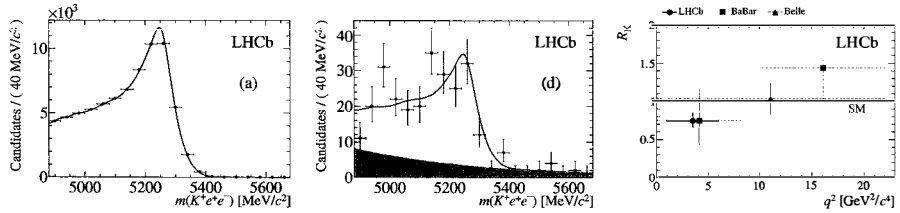

Figure 6 – (Left) $B^+ \to J/\psi K^+$ and (middle) $B^+ \to K^+e^+e^-$ signal candidates, triggered on the electron in the final state. (Right) The ratio R_K as determined by LHCb [47], BaBar [48] and Belle [49] for different q^2 ranges.

7 Angular analysis of $B^0 \to K^{*0}e^+e^-$

The study of rare decays with electrons in the final state allows to perform analyses at very low q^2, due to the tiny electron mass. At low q^2, the contribution from Feynman diagrams in which a virtual photon couples to the lepton pair dominates. This allows to probe the photon polarisation, which is left-handed in the SM.

LHCb performs an angular analysis of the decay $B^0 \to K^{*0}e^+e^-$ in the q^2 range $0.002 < q^2 < 1.120\,\mathrm{GeV}^2/c^4$ [53]. The four angular observables F_L, $A_\mathrm{T}^{(2)}$, A_T^Re and A_T^Im are determined from an unbinned maximum likelihood fit to the decay angles $\cos\theta_l$, $\cos\theta_K$ and ϕ. Of particular interest are the observables $A_\mathrm{T}^{(2)}$ and A_T^Im that are sensitive to the photon polarization. Figure 7 gives the angular fit projections. The measured angular observables are

$$\begin{aligned} F_\mathrm{L} &= +0.16 \pm 0.06 \pm 0.03 \\ A_\mathrm{T}^{(2)} &= -0.23 \pm 0.23 \pm 0.05 \\ A_\mathrm{T}^\mathrm{Re} &= +0.10 \pm 0.18 \pm 0.05 \\ A_\mathrm{T}^\mathrm{Im} &= +0.14 \pm 0.22 \pm 0.05, \end{aligned}$$

which is in good agreement with SM predictions [54,18]. The constraints from $A_\mathrm{T}^{(2)}$, A_T^Im on the contributions from right-handed currents are more precise than those obtained from the average of the time dependent CP-asymmetries in radiative $B^0 \to K^{*0}(\to K^0_\mathrm{S}\pi^0)\gamma$ decays [55,56].

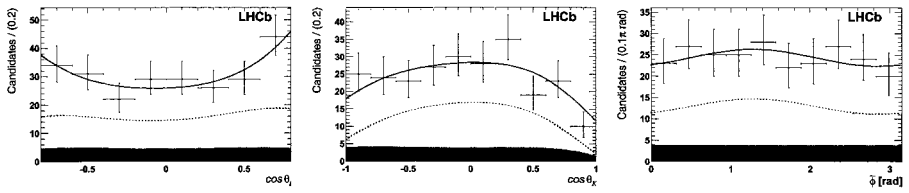

Figure 7 – The three decay angles (left) $\cos\theta_l$ (middle) $\cos\theta_K$ and (right) ϕ of $B^0 \to K^{*0}e^+e^-$ signal candidates, overlaid with the projections of the fitted probability density function.

8 Conclusions

Most of the observables in rare decays are found to be in good agreement with SM predictions. However, three interesting tensions emerge: An update of the angular analysis of the decay $B^0 \to K^{*0}\mu^+\mu^-$ confirms a deviation of the angular observable P_5' in the two q^2 bins $4 < q^2 < 6\,\text{GeV}^2/c^4$ and $6 < q^2 < 8\,\text{GeV}^2/c^4$, with a significance of $2.9\,\sigma$ in each; Furthermore, the branching fraction of the rare decay $B_s^0 \to \phi\mu^+\mu^-$ in the range $1 < q^2 < 6\,\text{GeV}^2/c^4$ is $3.1\,\sigma$ lower than a recently updated theory prediction; Finally, the measurement of R_K shows a tension with lepton universality at 2.6σ.

Consistent NP explanations of all observed tensions in rare decays exist, and first global fits including the updated results on $B^0 \to K^{*0}\mu^+\mu^-$ angular observables prefer the NP solution over the SM by $3.7\,\sigma$ [57]. However, it is too early to speak of clear signs of processes beyond the SM; Unexpectedly large hadronic contributions still can not be excluded. The results clearly motivate future work, both from theory, as well as from experiment, where complementary measurements of rare $b \to (s,d)\ell\ell$ processes will be performed. For the Run I LHCb data, this includes an update of the analysis of the decay $B_s^0 \to \phi\mu^+\mu^-$ and an updated branching fraction measurement of the decay $B^0 \to K^{*0}\mu^+\mu^-$. In addition, further tests of lepton universality and lepton number violation are in preparation. The data sample LHCb will collect during Run II will further improve the experimental sensitivity and allow to probe the operator structure of rare decays with unprecedented precision.

References

1. S. Descotes-Genon *et al.*, Phys. Rev. D **88** (2013) 074002 [arXiv:1307.5683 [hep-ph]].
2. F. Beaujean *et al.*, Eur. Phys. J. C **74** (2014) 2897 [Eur. Phys. J. C **74** (2014) 3179] [arXiv:1310.2478 [hep-ph]].
3. W. Altmannshofer and D. M. Straub, [arXiv:1411.3161 [hep-ph]].
4. T. Hurth and F. Mahmoudi, JHEP **1404** (2014) 097 [arXiv:1312.5267 [hep-ph]].
5. W. Altmannshofer *et al.*, JHEP **0901** (2009) 019 [arXiv:0811.1214 [hep-ph]].
6. R. Aaij *et al.* [LHCb Collaboration], JHEP **1308** (2013) 131 [arXiv:1304.6325 [hep-ex]].
7. R. Aaij *et al.* [LHCb Collaboration], Phys. Rev. Lett. **111** (2013) 191801 [arXiv:1308.1707 [hep-ex]].
8. S. Descotes-Genon *et al.*, JHEP **1305** (2013) 137 [arXiv:1303.5794 [hep-ph]].
9. R. Gauld *et al.*, Phys. Rev. D **89** (2014) 015005 [arXiv:1308.1959 [hep-ph]].
10. A. J. Buras and J. Girrbach, JHEP **1312** (2013) 009 [arXiv:1309.2466 [hep-ph]].
11. W. Altmannshofer *et al.*, Eur. Phys. J. C **73** (2013) 2646 [arXiv:1308.1501 [hep-ph]].
12. S. L. Glashow *et al.*, Phys. Rev. Lett. **114** (2015) 091801 [arXiv:1411.0565 [hep-ph]].
13. A. Crivellin *et al.*, Phys. Rev. Lett. **114** (2015) 151801 [arXiv:1501.00993 [hep-ph]].
14. G. Hiller and M. Schmaltz, Phys. Rev. D **90** (2014) 054014 [arXiv:1408.1627 [hep-ph]].
15. S. Biswas *et al.*, JHEP **1502** (2015) 142 [arXiv:1409.0882 [hep-ph]].
16. A. J. Buras *et al.*, JHEP **1502** (2015) 184 [arXiv:1409.4557 [hep-ph]].

17. B. Gripaios *et al.*, JHEP **1505** (2015) 006 [arXiv:1412.1791 [hep-ph]].
18. S. Jäger and J. Martin Camalich, JHEP **1305** (2013) 043 [arXiv:1212.2263 [hep-ph]].
19. S. Jäger and J. Martin Camalich, arXiv:1412.3183 [hep-ph].
20. J. Lyon and R. Zwicky, arXiv:1406.0566 [hep-ph].
21. R. Aaij *et al.* [LHCb Collaboration], LHCb-CONF-2015-002, cds.cern.ch/record/2002772.
22. G. J. Feldman and R. D. Cousins, Phys. Rev. D **57** (1998) 7
23. A. Bharucha, D. M. Straub and R. Zwicky, [arXiv:1503.05534 [hep-ph]].
24. S. Descotes-Genon *et al.*, JHEP **1412** (2014) 125 [arXiv:1407.8526 [hep-ph]].
25. R. R. Horgan *et al.*, Phys. Rev. D **89** (2014) 9, 094501 [arXiv:1310.3722 [hep-lat]].
26. R. R. Horgan *et al.*, Phys. Rev. Lett. **112** (2014) 212003 [arXiv:1310.3887 [hep-ph]].
27. R. R. Horgan *et al.*, [arXiv:1501.00367 [hep-lat]].
28. R. Aaij *et al.* [LHCb Collaboration], JHEP **1406** (2014) 133 [arXiv:1403.8044 [hep-ex]].
29. R. Aaij *et al.* [LHCb Collaboration], JHEP **1409** (2014) 177 [arXiv:1408.0978 [hep-ex]].
30. J. Lyon and R. Zwicky, Phys. Rev. D **88** (2013) 9, 094004 [arXiv:1305.4797 [hep-ph]].
31. C. Bobeth, G. Hiller and D. van Dyk, JHEP **1107** (2011) 067 [arXiv:1105.0376 [hep-ph]].
32. C. Bobeth *et al.*, JHEP **1201** (2012) 107 [arXiv:1111.2558 [hep-ph]].
33. R. Aaij *et al.* [LHCb Collaboration], JHEP **1307** (2013) 084 [arXiv:1305.2168 [hep-ex]].
34. R. Aaij *et al.* [LHCb Collaboration], Phys. Lett. B **743** (2015) 46 [arXiv:1412.6433 [hep-ex]].
35. F. Kruger *et al.*, Phys. Rev. D **56** (1997) 5452 [Phys. Rev. D **60** (1999) 099905] [hep-ph/9706247].
36. M. Beneke, T. Feldmann and D. Seidel, Eur. Phys. J. C **41** (2005) 173 [hep-ph/0412400].
37. R. H. Li *et al.*, Phys. Rev. D **79** (2009) 014013 [arXiv:0811.2648 [hep-ph]].
38. P. Colangelo *et al.*, Phys. Rev. D **81** (2010) 074001 [arXiv:1002.2880 [hep-ph]].
39. P. Böer, T. Feldmann and D. van Dyk, JHEP **1501** (2015) 155 [arXiv:1410.2115 [hep-ph]].
40. T. Aaltonen *et al.* [CDF Collaboration], Phys. Rev. Lett. **107** (2011) 201802 [arXiv:1107.3753 [hep-ex]].
41. R. Aaij *et al.* [LHCb Collaboration], Phys. Lett. B **725** (2013) 25 [arXiv:1306.2577 [hep-ex]].
42. R. Aaij *et al.* [LHCb Collaboration], [arXiv:1503.07138 [hep-ex]].
43. S. Meinel, PoS LATTICE **2013** (2014) 024 [arXiv:1401.2685 [hep-lat]].
44. W. Detmold *et al.*, Phys. Rev. D **87** (2013) 7, 074502 [arXiv:1212.4827 [hep-lat]].
45. G. Hiller and F. Kruger, Phys. Rev. D **69** (2004) 074020 [hep-ph/0310219].
46. C. Bobeth *et al.*, JHEP **0712** (2007) [arXiv:0709.4174 [hep-ph]].
47. R. Aaij *et al.* [LHCb Collaboration], Phys. Rev. Lett. **113** (2014) 151601 [arXiv:1406.6482 [hep-ex]].
48. J. P. Lees *et al.* [BaBar Collaboration], Phys. Rev. D **86** (2012) 032012 [arXiv:1204.3933 [hep-ex]].
49. J.-T. Wei *et al.* [Belle Collaboration], Phys. Rev. Lett. **103** (2009) 171801 [arXiv:0904.0770 [hep-ex]].
50. S. Sahoo and R. Mohanta, [arXiv:1501.05193 [hep-ph]].
51. D. Ghosh *et al.*, JHEP **1412** (2014) 131 [arXiv:1408.4097 [hep-ph]].
52. T. Hurth *et al.*, JHEP **1412** (2014) 053 [arXiv:1410.4545 [hep-ph]].
53. R. Aaij *et al.* [LHCb Collaboration], JHEP **1504** (2015) 064 [arXiv:1501.03038 [hep-ex]].
54. D. Becirevic and E. Schneider, Nucl. Phys. B **854** (2012) 321 [arXiv:1106.3283 [hep-ph]].
55. B. Aubert *et al.* [BaBar Collaboration], Phys. Rev. D **78** (2008) 071102 [arXiv:0807.3103 [hep-ex]].
56. Y. Ushiroda *et al.* [Belle Collaboration], Phys. Rev. D **74** (2006) 111104 [hep-ex/0608017].
57. W. Altmannshofer and D. M. Straub, arXiv:1503.06199 [hep-ph].

$B \to K^* \mu\mu$: theory interpretation or *A hitchiker's guide to* $B \to K^* \mu\mu$ *optimised observables*[a]

S. Descotes-Genon[1], L. Hofer[2], J. Matias[2] and J. Virto[3]
[1] *Laboratoire de Physique Théorique, CNRS/Univ. Paris-Sud (UMR 8627) 91405 Orsay Cedex, France*
[2] *Universitat Autònoma de Barcelona, 08193 Bellaterra, Barcelona*
[3] *Theoretische Physik 1, Naturwissenschaftlich-Technische Fakultät, Univ. Siegen, 57068, Germany*

We discuss the role and advantages of the different $B \to K^* \mu\mu$ optimised observables, defined to have little sensitivity to hadronic (form factor) input. We focus on the sensitivity of each observable to short-distance Wilson coefficients.

1 Motivation and interest of $B \to K^* \mu\mu$

Flavour-Changing Neutral Currents (FCNC) have been prominent tools in high-energy physics to search for new degrees of freedom, due to their quantum sensitivity to energies much higher than the external particles involved. In the current context where the LHC has discovered a scalar boson completing the Standard Model (SM) picture but no additional particles that would go beyond this framework, FCNC can be instrumental in order to determine in which direction to look for New Physics (NP). One particularly interesting instance of FCNC is provided by $b \to s\ell\ell$ and $b \to s\gamma$ transitions, which can be probed through various decay channels, currently studied in detail at the LHC, in particular at the LHCb and CMS experiments.

Indeed, recent experimental results have shown interesting deviations from the Standard Model. In 2013, the LHCb collaboration announced the measurement of angular observables describing the decay $B \to K^* \mu\mu$ in both regions of low and large-K^* recoils [1]. Two observables, P_2 and P_5', were in significant disagreement with the SM expectations in the large-K^* recoil region [2]. A few months later, an improved measurement of the branching ratio for $B \to K \mu\mu$ at large recoil turned out to be on the low side compared to theoretical expectations [3], as well as the branching ratios of $B \to K^* \mu\mu$ and $B_s \to \phi\mu\mu$ at low recoil [3,4,5]. Another measurement has also raised a lot of attention recently, namely $R_K = Br(B \to K\mu\mu)/Br(B \to Kee)$, measured by LHCb, and showing a significantly lower result than its SM prediction equal to 1 (up to a very good accuracy) [6]. In the Moriond 2015 conference, a new analysis of $B \to K^* \mu\mu$ was presented with an extended data set (3 fb^{-1}), confirming the pattern of deviations observed with a restricted set of data [7].

The presence of very different scales for the external states (at most $O(m_b)$) and the internal degrees of freedom ($O(M_W)$ or above) allows for model-independent analyses relying on the effective Hamiltonian approach. The latter is obtained by focusing on $b \to s$ transitions and integrating out all heavy degrees of freedom, leading to (in the case of the SM):

$$\mathcal{H}^{SM} = -\frac{4G_F}{\sqrt{2}} \left\{ V_{tb}V_{ts}^*[C_1 Q_1^c + C_2 Q_2^c + \sum_{i=3\ldots10} C_i Q_i] + V_{tu}V_{us}^*[C_1(Q_1^c - Q_1^u) + C_2(Q_2^c - Q_2^u)] \right\} \quad (1)$$

[a] Based on talks given by J. Matias at Moriond 2015 Electroweak session and by S. Descotes-Genon at Moriond 2015 QCD session.

up to contributions suppressed by additional powers of m_b/M_W. The Wilson coefficients C_i describe the short-distance physics (function of $m_t, m_W \ldots$ in the SM) whereas the local operators Q_i correspond to long-distance physics involving only light/soft degrees of freedom. In this framework, $b \to s$ transitions are mainly described by $Q_7 = e/(4\pi)^2 \bar{s}\sigma^{\mu\nu}(1+\gamma_5)F_{\mu\nu}\, b$, related to the emission of a real or soft photon, $Q_9 = e^2/(4\pi)^2 \bar{s}\gamma_\mu(1-\gamma_5)b\ \bar{\ell}\gamma_\mu\ell$ involved in $b \to s\mu\mu$ via the emission of a Z boson or a hard photon, and $Q_{10} = e^2/(4\pi)^2 \bar{s}\gamma_\mu(1-\gamma_5)b\ \bar{\ell}\gamma_\mu\gamma_5\ell$ involved in $b \to s\mu\mu$ via the emission of a Z boson. The value of the Wilson coefficients can be obtained by matching the SM at a high-energy scale $\mu_0 = O(m_t)$ and evolving down at $\mu_{\rm ref} = O(m_b)$ (usually 4.8 GeV, with typical values $C_7^{SM} = -0.29$, $C_9^{SM} = 4.1$, $C_{10}^{SM} = -4.3$).

The presence of NP can alter this picture by modifying the value of the Wilson coefficients $C_{7,9,10}$, but also by allowing new long-distance operators Q_i, which would be very suppressed or absent in the SM. This yields the chirally-flipped operators $Q_{7',9',10'}$ (obtained for instance by a heavy spin-1 boson coupling to right-handed fermions), scalar and pseudoscalar operators $Q_{S,S',P,P'}$ (induced, e.g., by the exchange of charged scalar or pseudoscalar Higgs-like bosons) or tensor operators $Q_{T,T'}$ (allowed in principle, but difficult to generate in viable models). These NP contributions are expressed as $C_i = C_i^{SM} + \delta C_i$ at $\mu_{\rm ref}$. An accurate extraction of short-distance physics requires a good understanding of long-distance physics, and in particular QCD effects. In some kinematic configurations (either low or large recoil of the K^* meson), one can use effective theories to separate soft and hard physics, in order to build observables with a limited sensitivity to hadronic uncertainties, or so-called optimised observables[8,9,10,11,12]. Additional studies have been performed in order to assess long-distance effects that could contribute, in particular the charm resonances and loop contributions, the form factors, and the power corrections in the effective-field theory approach [13,14,15]. These elements have been combined in global fits of $b \to s\ell\ell$ Wilson coefficients, with different sets of observables and statistical approaches [16,17,18]. They point towards a large negative contribution to C_9, amounting to 25% of its SM value, leaving open the possibility of large contributions to other Wilson coefficients.

Each optimised observable does play a different role in such fits, pulling the Wilson coefficients in different directions in order to increase the agreement of predictions with LHCb data compared to the SM result. We are going to review their role in this proceeding.

2 $B \to K^*\mu\mu$ observables: Optimised basis

Due to its particularly rich kinematics[19], the $B \to K^*\mu\mu$ decay provides 12 angular coefficients, corresponding to interferences between 8 transversity amplitudes, generally labelled in relation to the polarisation of the K^*-meson and/or the chirality of the dilepton pair ($A_{0,\perp,\parallel}^{L,R}$ and A_t, A_S). However, if lepton masses or scalars are not considered, not all angular coefficients carry independent information: the corresponding redundancies can be worked out thanks to the analysis of symmetries of the transversity amplitudes that leave the angular coefficients invariant[20,21]. In this scenario one can show that only 8 independent observables can be built, out of which 6 optimised observables can be chosen, namely $P_1, P_2, P_3, P_4', P_5', P_6'$. The remaining two observables can be chosen, for instance, to be the (differential) branching ratio and longitudinal polarisation. For a complete phenomenological description, the previous set of P-wave observables should be complemented with a set of S-wave independent observables[22,23,24] associated to $B \to K_0^*\mu^+\mu^-$ where K_0^* is a broad scalar resonance. We will now focus on the optimised observables of the P-wave sector, which exhibit the largest sensitivity to short-distance physics.

2.1 P_1 or A_T^2

The definition in terms of amplitudes is[8]

$$P_1 = A_T^{(2)} = \frac{|A_\perp|^2 - |A_\parallel|^2}{|A_\perp|^2 + |A_\parallel|^2} \tag{2}$$

where in this definition and all the following ones, it should be understood that each term has associated the corresponding CP conjugated term, with the notation $|A_i|^2 = |A_i^L|^2 + |A_i^R|^2 + |\bar{A}_i^L|^2 + |\bar{A}_i^R|^2$. Lepton, scalar and tensor terms are neglected. This observable is particularly suited to detect the presence of right-handed currents. The left-handed structure of the SM implies that the s quark produced in the decay of the b quark will be in a helicity state of $-1/2$ (neglecting the s-quark mass). The combination of the s quark with the spectator quark generates a K^*-meson with helicity -1 or 0, but not $+1$. The suppression of $H_{+1} = (A_\perp + A_\parallel)/\sqrt{2} \simeq 0$ implies $A_\perp \simeq -A_\parallel$ and consequently $P_1^{\rm SM} \simeq 0$. Deviations from this prediction would signal contributions from a new right-handed structure. In Table 1 we present how $\langle P_1 \rangle_{[0.1,0.98]}$, $\langle P_1 \rangle_{[6,8]}$ and $\langle P_1 \rangle_{[15,19]}$ are affected by shifting one Wilson coefficient at a time. Only significant changes are indicated, and shifts improving the agreement with data are indicated in boldface. As expected, changing Wilson coefficients for SM operators (not carrying a right-handed structure) does not induce any sizeable shift. The first bin of P_1 exhibits the largest sensitivity to C_7'. Contrary to most observables, P_1 is also rather sensitive to New Physics at low recoil.

2.2 P_4'

The definition is [11,12]

$$P_4' = \sqrt{2}\frac{\mathrm{Re}(A_0^L A_\parallel^{L*} + A_0^R A_\parallel^{R*})}{\sqrt{|A_0|^2(|A_\perp|^2 + |A_\parallel|^2)}} \tag{3}$$

Together with P_5', this observable establishes bounds on P_1 or enters in consistency relations. In particular, the bound

$$P_5'^2 - 1 \leq P_1 \leq 1 - P_4'^2 \tag{4}$$

works very efficiently in two bins: [6,8] and low-recoil. In the first case, the preference of data for $P_4' \geq 1$ in the [6,8] bin requires $P_1 \leq 0$, in agreement with 2015 data (notice that in 2013 data P_1 was positive in the bin [4.3,8.68]). In the second case, taking the central values of the low-recoil bin as an illustration, one finds that $-0.54 \leq P_1 \leq -0.44$ again in the right ballpark as compared to the measurement $P_1 \simeq -0.50$. Strictly speaking, this is a bound on the unbinned observables, but they can be adapted for binned observables in the case where the observables are slowly varying with q^2, providing important cross-checks among the LHCb measurements.

2.3 P_2

The definition is [12,10]

$$P_2 = \frac{\mathrm{Re}(A_\parallel^L A_\perp^{L*} - A_\parallel^R A_\perp^{R*})}{|A_\perp|^2 + |A_\parallel|^2} \tag{5}$$

This observable is the optimised and clean version of the forward-backward asymmetry, and it was originally [10] called $A_T^e = 2P_2$. It highlights the correlation among A_{FB} and F_L, with a low sensitivity to choices of form factors compared to these observables. Indeed, the prediction for A_{FB} and F_L depends strongly on the parametrisation of form factors used, and the ratio of errors between two commonly used parametrizations, for some bins of A_{FB} or F_L can be as large[25] as a factor 3 or 4. On the contrary, in the case of P_2, besides a shift in central values due to the different central value predictions of the form factors (induced by leading-order power corrections included in our predictions), the ratio of errors is near one showing its robustness and low dependence of this observable on the details of the parametrization.

The observable P_2 contains three relevant elements of information: the position of its zero q_0^2, the position q_1^2 of its maximum, and the value of P_2 at q_1^2. At leading order, assuming no

Table 1: Impact for a given observable of the shift of one of the Wilson coefficients by an amount δC_i (the other Wilson coefficients keeping their SM value). The first row corresponds to the variation due to a positive shift δC_i and the second row to a negative shift by the same amount. The changes improving the agreement of predictions with the 2015 LHCb data are written in boldface. Double "-" means variations below 0.03, only those in $\langle P_2 \rangle_{[2.5,4]}$ are provided explicitly.

$\langle P_1 \rangle_{[0.1,0.98]}$	$\lvert\delta C_7\rvert = 0.1$	$\lvert\delta C_9\rvert = 1$	$\lvert\delta C_{10}\rvert = 1$	$\lvert\delta C_{7'}\rvert = 0.1$	$\lvert\delta C_{9'}\rvert = 1$	$\lvert\delta C_{10'}\rvert = 1$
$+\lvert\delta C_i\rvert$	−−	−−	−−	**− 0.53**	−0.05	−−
$-\lvert\delta C_i\rvert$	−−	−−	−−	+0.52	+0.05	−−
$\langle P_1 \rangle_{[6,8]}$	$\lvert\delta C_7\rvert = 0.1$	$\lvert\delta C_9\rvert = 1$	$\lvert\delta C_{10}\rvert = 1$	$\lvert\delta C_{7'}\rvert = 0.1$	$\lvert\delta C_{9'}\rvert = 1$	$\lvert\delta C_{10'}\rvert = 1$
$+\lvert\delta C_i\rvert$	−−	−−	−−	+0.11	+0.16	**−0.37**
$-\lvert\delta C_i\rvert$	−−	−−	−−	**−0.12**	**−0.16**	+0.37
$\langle P_1 \rangle_{[15,19]}$	$\lvert\delta C_7\rvert = 0.1$	$\lvert\delta C_9\rvert = 1$	$\lvert\delta C_{10}\rvert = 1$	$\lvert\delta C_{7'}\rvert = 0.1$	$\lvert\delta C_{9'}\rvert = 1$	$\lvert\delta C_{10'}\rvert = 1$
$+\lvert\delta C_i\rvert$	−−	−−	−−	**+0.03**	**+0.15**	−0.14
$-\lvert\delta C_i\rvert$	−−	−−	−−	−0.03	−0.11	**+0.19**
$\langle P_4' \rangle_{[6,8]}$	$\lvert\delta C_7\rvert = 0.1$	$\lvert\delta C_9\rvert = 1$	$\lvert\delta C_{10}\rvert = 1$	$\lvert\delta C_{7'}\rvert = 0.1$	$\lvert\delta C_{9'}\rvert = 1$	$\lvert\delta C_{10'}\rvert = 1$
$+\lvert\delta C_i\rvert$	**+0.04**	−−	−−	−0.11	−0.10	**+0.17**
$-\lvert\delta C_i\rvert$	−0.05	−−	−−	**+0.09**	**+0.10**	−0.20
$\langle P_4' \rangle_{[15,19]}$	$\lvert\delta C_7\rvert = 0.1$	$\lvert\delta C_9\rvert = 1$	$\lvert\delta C_{10}\rvert = 1$	$\lvert\delta C_{7'}\rvert = 0.1$	$\lvert\delta C_{9'}\rvert = 1$	$\lvert\delta C_{10'}\rvert = 1$
$+\lvert\delta C_i\rvert$	−−	−−	−−	−−	**−0.06**	+0.05
$-\lvert\delta C_i\rvert$	−−	−−	−−	−−	+0.04	**−0.08**
$\langle P_2 \rangle_{[2.5,4]}$	$\lvert\delta C_7\rvert = 0.1$	$\lvert\delta C_9\rvert = 1$	$\lvert\delta C_{10}\rvert = 1$	$\lvert\delta C_{7'}\rvert = 0.1$	$\lvert\delta C_{9'}\rvert = 1$	$\lvert\delta C_{10'}\rvert = 1$
$+\lvert\delta C_i\rvert$	−0.31	−0.21	**+0.05**	−0.01	−0.01	−0.02
$-\lvert\delta C_i\rvert$	**+0.19**	**+0.15**	−0.04	−0.03	−−	−−
$\langle P_2 \rangle_{[6,8]}$	$\lvert\delta C_7\rvert = 0.1$	$\lvert\delta C_9\rvert = 1$	$\lvert\delta C_{10}\rvert = 1$	$\lvert\delta C_{7'}\rvert = 0.1$	$\lvert\delta C_{9'}\rvert = 1$	$\lvert\delta C_{10'}\rvert = 1$
$+\lvert\delta C_i\rvert$	−0.07	−0.09	−0.06	−−	−−	−−
$-\lvert\delta C_i\rvert$	**+0.11**	**+0.17**	**+0.05**	−−	−−	−−
$\langle P_5' \rangle_{[.1,.98]}$	$\lvert\delta C_7\rvert = 0.1$	$\lvert\delta C_9\rvert = 1$	$\lvert\delta C_{10}\rvert = 1$	$\lvert\delta C_{7'}\rvert = 0.1$	$\lvert\delta C_{9'}\rvert = 1$	$\lvert\delta C_{10'}\rvert = 1$
$+\lvert\delta C_i\rvert$	**−0.07**	**−0.10**	**−0.08**	**−0.23**	+0.08	+0.09
$-\lvert\delta C_i\rvert$	+0.04	+0.11	+0.05	+0.16	**−0.07**	**−0.13**
$\langle P_5' \rangle_{[4,6]}$	$\lvert\delta C_7\rvert = 0.1$	$\lvert\delta C_9\rvert = 1$	$\lvert\delta C_{10}\rvert = 1$	$\lvert\delta C_{7'}\rvert = 0.1$	$\lvert\delta C_{9'}\rvert = 1$	$\lvert\delta C_{10'}\rvert = 1$
$+\lvert\delta C_i\rvert$	−0.11	−0.15	−0.10	−0.11	−0.06	**+0.21**
$-\lvert\delta C_i\rvert$	**+0.16**	**+0.28**	**+0.09**	**+0.15**	**+0.10**	−0.21
$\langle P_5' \rangle_{[6,8]}$	$\lvert\delta C_7\rvert = 0.1$	$\lvert\delta C_9\rvert = 1$	$\lvert\delta C_{10}\rvert = 1$	$\lvert\delta C_{7'}\rvert = 0.1$	$\lvert\delta C_{9'}\rvert = 1$	$\lvert\delta C_{10'}\rvert = 1$
$+\lvert\delta C_i\rvert$	−0.04	−0.07	−0.07	−0.08	−0.08	**+0.19**
$-\lvert\delta C_i\rvert$	**+0.07**	**+0.19**	**+0.09**	**+0.10**	**+0.11**	−0.18
$\langle P_5' \rangle_{[15,19]}$	$\lvert\delta C_7\rvert = 0.1$	$\lvert\delta C_9\rvert = 1$	$\lvert\delta C_{10}\rvert = 1$	$\lvert\delta C_{7'}\rvert = 0.1$	$\lvert\delta C_{9'}\rvert = 1$	$\lvert\delta C_{10'}\rvert = 1$
$+\lvert\delta C_i\rvert$	−−	−−	−−	**−0.03**	**−0.11**	+0.12
$-\lvert\delta C_i\rvert$	−−	+0.06	+0.03	+0.03	+0.10	**−0.14**

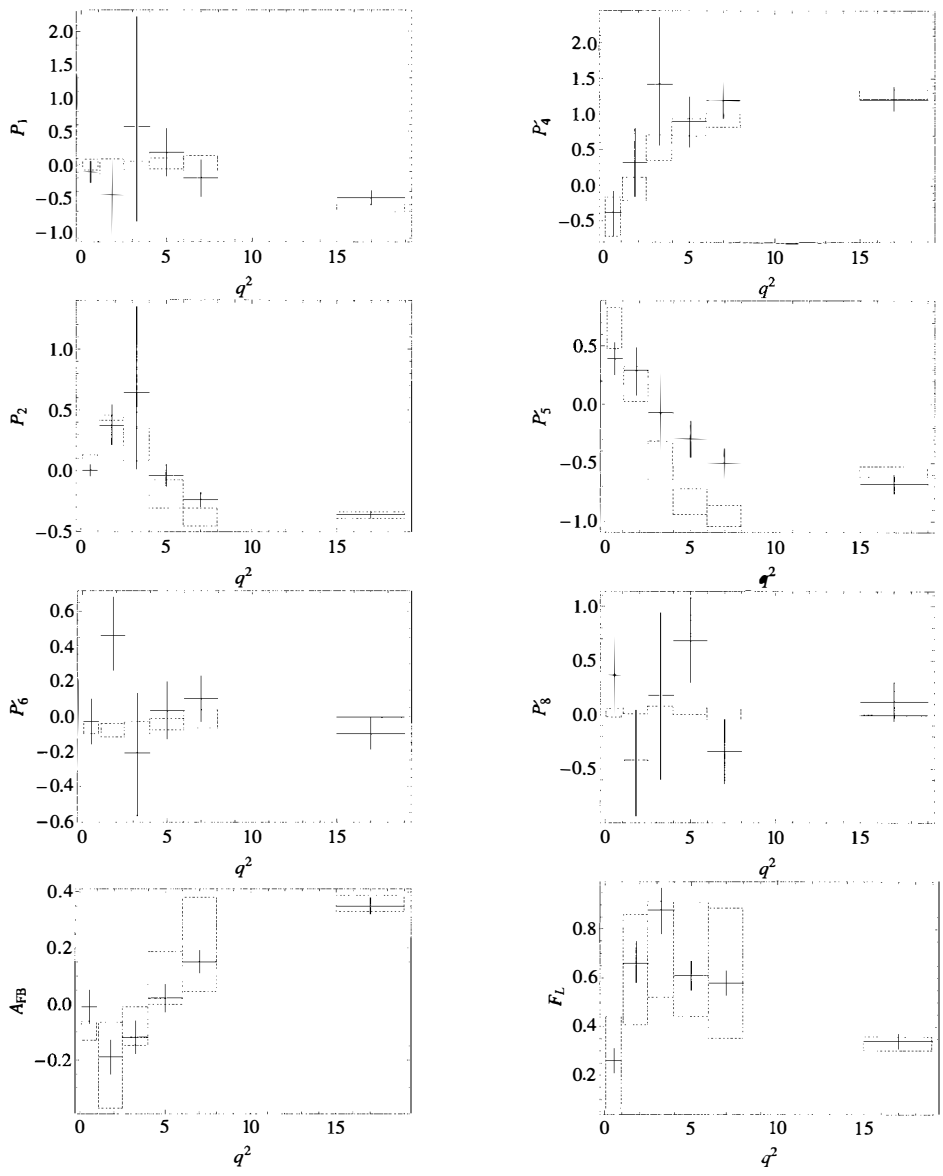

Figure 1 – Set of optimised $B \to K^* \mu\mu$ observables: crosses represent the latest LHCb results and boxes our SM predictions computed using KMPW form factors and including a long-distance charm contribution.

contribution from right-handed currents, i.e., $C_i' = 0$ the first two quantities are given by:

$$q_0^{2\,LO} = -2\frac{m_b M_B C_7^{\rm eff}}{C_9^{\rm eff}(q_0^2)} \quad \text{and} \quad q_1^{2\,LO} = -2\frac{m_b M_B C_7^{\rm eff}}{{\rm Re}C_9^{\rm eff}(q_1^2) - C_{10}} \tag{6}$$

where for the position of the maximum we have neglected a term of $\mathcal{O}({\rm Im}(C_9^{\rm eff})^2)$ following [22]. These expressions illustrate that a NP contribution to C_9 and C_7 would shift both the zero and the maximum of P_2, but with a different magnitude. The position of the maximum can be also shifted via a C_{10} contribution. It was found in [10,22] that a NP contribution to the SM Wilson coefficients $C_{7,9,10}$ can only shift the position of the maximum but not the value of the observable that is fixed at $P_2^{max} = 1/2$. On the contrary, the presence of NP contributions into the chirally flipped operators would reduce the maximum below 1/2, though not by a large amount. Unfortunately, a fluctuation of the $\langle F_L \rangle_{[2.5,4]}$ bin has induced a large experimental error in the corresponding bin of P_2, and the discussion remains inconclusive for the moment.

In Table 1 we show the sensitivity to shifts of Wilson coefficients in the [6,8] bin. The sensitivity of this observable to NP at low recoil is small. At large recoil, one should remark that the same shifts of the Wilson coefficients moving $\langle P_2 \rangle_{[6,8]}$ towards data also improves the agreement of $\langle P_2 \rangle_{[2.5,4]}$ with data (assuming that data is above the SM) except for C_{10} (whose impact is small in any case). On the other hand, chirally flipped coefficients (positive or negative) shift down the value of the observable in this bin (though by a relatively small amount).

Finally, P_2 offers further consistency checks based on the relation [26]

$$P_2 = \frac{1}{2}\left[P_4' P_5' + \sqrt{(-1+P_1+P_4'^2)(-1-P_1+P_5'^2)}\right]. \tag{7}$$

The first check stems from the reality of the square root in the previous equation. If we take a bin where $P_2 = -\epsilon$ (with $\epsilon > 0$), one must have

$$P_5' \leq -2\epsilon/P_4' \tag{8}$$

Considering the [6,8] bin and taking the central values $\langle P_2 \rangle_{[6,8]} \sim -0.24 \equiv -\epsilon$ and $\langle P_4' \rangle_{[6,8]} \sim 1.20$, one obtains $\langle P_5' \rangle_{[6,8]} \leq -0.4$, in fair agreement with the measurement $\langle P_5' \rangle_{[6,8]} \sim -0.5$. More generally, eq. (8) implies a specific order [25] for $\langle P_2 \rangle_{[6,8]}$ and $\langle P_5' \rangle_{[6,8]}$ which is nicely fulfilled by the current data. A similar reasoning holds in the [4,6] bin.

A second check is related to the zero in eq. (7). At the position q_0^2 of the zero of P_2 (or A_{FB}) the following relation should be fulfilled [26]:

$$[P_4'^2 + P_5'^2]_{q_0^2} = 1 - \eta(q_0^2) \tag{9}$$

with $\eta(q_0^2) = [P_1^2 + P_1(P_4'^2 - P_5'^2)]_{q^2=q_0^2}$. If we consider the [4,6] bin, $\langle P_2 \rangle_{[4,6]}$ is close to zero. As an illustration, let us assume that q_0^2 is near the center of the bin, i.e., 5 GeV^2 (this will be measured with precision using the amplitude method analysis [27]). Considering the central values as a raw estimate to test this relation $\langle P_5' \rangle_{[4,6]} \sim -0.30$, $\langle P_4' \rangle_{[4,6]} \sim +0.90$ and $\langle P_1 \rangle_{[4,6]} \sim +0.18$, the left-hand side of eq. (9) yields 0.90 while the right-hand side is 0.84. Even though there is a good agreement, let us remind again that this relation is valid for the unbinned observables and so the binning induces an error, besides the necessary inclusion of the error bars.

2.4 P_5'

The definition is [11,12]

$$P_5' = \sqrt{2}\frac{{\rm Re}(A_0^L A_\perp^{L*} - A_0^R A_\perp^{R*})}{\sqrt{|A_0|^2(|A_\perp|^2 + |A_\parallel|^2)}} \tag{10}$$

In the current data from LHCb, this observable exhibits the largest deviations with respect to the SM prediction in some bins, the so-called "anomaly" [2] illustrated in Fig. 1. Interestingly,

this observable can receive large NP contributions without spoiling the good agreement of P_4' data with SM predictions: in Table 1 the large impact of a variation of C_9 in P_5' corresponds to a negligible effect on P_4' in the [6,8] bin.

Two mechanisms may enforce a larger impact of NP in P_5' with respect to P_4'. The first mechanism consists in weakening the suppression of the right-handed amplitudes with respect to the left-handed amplitudes, in order to profit from the relative minus sign between the two terms in the numerator of P_5' (compared to the plus sign in P_4'). The SM suppression of the right-handed amplitudes is due to the numerical coincidence $C_9^{\rm SM} \sim -C_{10}^{\rm SM}$, which is altered if only one of the two coefficients, say C_9, receives a NP contribution. The second mechanism consists in introducing a NP contribution reducing the size of $A_\perp^L$ in the numerator but keeping the other transversity amplitudes untouched, leading to a significant (minor) change in P_5' (P_4').

In Table 1 we show the sensitivity to shifts of Wilson coefficients for the [4,6], [6,8] and low-recoil bins. One notices the large sensitivity of $\langle P_5' \rangle_{[6,8]}$ to an additional $C_9^{\rm NP}$ as compared to $\langle P_4' \rangle_{[6,8]}$, in agreement with the data. Moreover, all Wilson coefficients have a large impact in this bin as compared to other bins and observables. Similar results are found for $\langle P_5' \rangle_{[4,6]}$. The first large-recoil bin exhibits an interesting sensitivity to C_7', even though lepton mass effects [24,28] affect this first bin (as well as other observables in the same bin). At low recoil, $\langle P_5' \rangle_{[15,19]}$ is more sensitive to NP than other observables in this region, but not as much as at large recoil.

2.5 P_3, P_6' and P_8'

The last optimised observables are defined as [11,12]

$$P_6' = -\sqrt{2}\frac{{\rm Im}(A_0^L A_\parallel^{L*} - A_0^R A_\parallel^{R*})}{\sqrt{|A_0|^2(|A_\perp|^2+|A_\parallel|^2)}} \quad P_8' = -\sqrt{2}\frac{{\rm Im}(A_0^L A_\perp^{L*} + A_0^R A_\perp^{R*})}{\sqrt{|A_0|^2(|A_\perp|^2+|A_\parallel|^2)}} \tag{11}$$

and

$$P_3 = -\frac{{\rm Im}(A_\parallel^{L*} A_\perp^L + A_\perp^R A_\parallel^{R*})}{|A_\perp|^2+|A_\parallel|^2} \tag{12}$$

They are mainly sensitive to phases (strong or weak, SM or beyond). A more direct test of new weak phases is the measurement of the $P_i^{\rm CP}$ observables [12]. Present data is compatible with the SM with large error bars including local fluctuations (up to 2 σ for some of the P_6' measurements) that are expected to disappear with more data. This set of observables also are required to fulfill bounds such as : $P_8'^2 - 1 \leq P_1 \leq 1 - P_6'^2$ (following the same reasoning as the bounds in [26]).

3 Conclusion

Optimised observables for $B \to K^*\mu\mu$ play a prominent role in the search for NP in $b \to s$ transitions. Several analyses have been performed, including some presented at this conference. Our own analysis following our earlier work [2] is under way [28], including experimental and theoretical correlations (they were not included in our results presented at the Moriond 2015 sessions). This study must be performed carefully in order to gauge the impact of correlations for the analysis at different levels (soft form factors, power corrections...).

We will consider the above optimised observables, as well as the branching ratios of $B \to K\mu\mu$, $B_s \to \mu\mu$, $B \to X_s\gamma$, $B \to X_s\mu\mu$, together with observables related to $B \to K^*\gamma$ ($S_{K^*\gamma}$ and A_I). The list of observables to be included is not closed yet: for instance, electronic modes should also be considered [29]. We will take advantage of new determinations of form factors [30] and improved studies of charm effects. This should yield a more complete picture of the Wilson coefficients describing radiative $b \to s$ transitions, and hopefully, this will allow us to disentangle Standard Model and New Physics contributions in these decays.

Acknowledgments

J.M. and L.H. acknowledge support from FPA2011-25948 and the grant 2014 SGR 1450. J.M. is supported in part by the Centro de Excelencia Severo Ochoa SEV- 2012-0234. J.V. is funded by the Deutsche Forschungsgemeinschaft (DFG) within research unit FOR 1873 (QFET).

References

1. R. Aaij *et al.* [LHCb Collaboration], Phys. Rev. Lett. **111** (2013) 191801 [arXiv:1308.1707 [hep-ex]].
2. S. Descotes-Genon, J. Matias and J. Virto, Phys. Rev. D **88** (2013) 074002 [arXiv:1307.5683 [hep-ph]].
3. R. Aaij *et al.* [LHCb Collaboration], JHEP **1406** (2014) 133 [arXiv:1403.8044 [hep-ex]].
4. R. Aaij *et al.* [LHCb Collaboration], JHEP **1307** (2013) 084 [arXiv:1305.2168 [hep-ex]].
5. R. R. Horgan, Z. Liu, S. Meinel and M. Wingate, Phys. Rev. Lett. **112** (2014) 212003 [arXiv:1310.3887 [hep-ph]].
6. R. Aaij *et al.* [LHCb Collaboration], Phys. Rev. Lett. **113** (2014) 151601 [arXiv:1406.6482 [hep-ex]].
7. The LHCb Collaboration [LHCb Collaboration], LHCb-CONF-2015-002, CERN-LHCb-CONF-2015-002; Ch. Langebruch's talk at Moriond 2015 Electroweak session.
8. F. Kruger and J. Matias, Phys. Rev. D **71** (2005) 094009 [hep-ph/0502060].
9. C. Bobeth, G. Hiller and D. van Dyk, JHEP **1007** (2010) 098 [arXiv:1006.5013 [hep-ph]].
10. D. Becirevic and E. Schneider, Nucl. Phys. B **854** (2012) 321 [arXiv:1106.3283 [hep-ph]].
11. S. Descotes-Genon, J. Matias, M. Ramon and J. Virto, JHEP **1301** (2013) 048 [arXiv:1207.2753 [hep-ph]].
12. S. Descotes-Genon, T. Hurth, J. Matias and J. Virto, JHEP **1305** (2013) 137 [arXiv:1303.5794 [hep-ph]].
13. A. Khodjamirian, T. Mannel, A. A. Pivovarov and Y.-M. Wang, JHEP **1009** (2010) 089 [arXiv:1006.4945 [hep-ph]].
14. J. Lyon and R. Zwicky, arXiv:1406.0566 [hep-ph].
15. S. Descotes-Genon, L. Hofer, J. Matias and J. Virto, JHEP **1412** (2014) 125 [arXiv:1407.8526 [hep-ph]] and references within.
16. W. Altmannshofer and D. M. Straub, Eur. Phys. J. C **73** (2013) 2646 [arXiv:1308.1501 [hep-ph]].
17. F. Beaujean, C. Bobeth and D. van Dyk, Eur. Phys. J. C **74** (2014) 2897 [Eur. Phys. J. C **74** (2014) 3179] [arXiv:1310.2478 [hep-ph]].
18. W. Altmannshofer and D. M. Straub, arXiv:1411.3161 [hep-ph]; D. Straub's talk at Moriond 2015 Electroweak session.
19. W. Altmannshofer *et al.* JHEP **0901** (2009) 019 [arXiv:0811.1214 [hep-ph]].
20. U. Egede, T. Hurth, J. Matias, M. Ramon and W. Reece, JHEP **1010** (2010) 056 [arXiv:1005.0571 [hep-ph]].
21. J. Matias, F. Mescia, M. Ramon and J. Virto, JHEP **1204** (2012) 104 [arXiv:1202.4266 [hep-ph]].
22. L. Hofer and J. Matias, arXiv:1502.00920 [hep-ph].
23. D. Becirevic and A. Tayduganov, Nucl. Phys. B **868** (2013) 368 [arXiv:1207.4004 [hep-ph]].
24. J. Matias, Phys. Rev. D **86** (2012) 094024 [arXiv:1209.1525 [hep-ph]].
25. S. Descotes-Genon, L. Hofer, J. Matias and J. Virto, arXiv:1503.03328 [hep-ph].
26. J. Matias and N. Serra, Phys. Rev. D **90** (2014) 3, 034002 [arXiv:1402.6855 [hep-ph]].
27. U. Egede, M. Patel and K. A. Petridis, arXiv:1504.00574 [hep-ph].
28. S. Descotes-Genon, L. Hofer, J. Matias and J. Virto, work in progress.
29. R. Aaij *et al.* [LHCb Collaboration], JHEP **1504** (2015) 064 [arXiv:1501.03038 [hep-ex]].
30. A. Bharucha, D. M. Straub and R. Zwicky, arXiv:1503.05534 [hep-ph].

Implications of $b \to s$ measurements[a]

Wolfgang Altmannshofer[1] and David M. Straub[2,b]
[1] *Perimeter Institute for Theoretical Physics, 31 Caroline St. N, Waterloo, Ontario, Canada N2L 2Y5* [2] *Excellence Cluster Universe, TU München, Boltzmannstr. 2, 85748 Garching, Germany*

The recent updated angular analysis of the $B \to K^*\mu^+\mu^-$ decay by the LHCb collaboration is interpreted by performing a global fit to all relevant measurements probing the flavour-changing neutral current $b \to s\mu^+\mu^-$ transition. A significant tension with Standard Model expectations is found. A solution with new physics modifying the Wilson coefficient C_9 is preferred over the Standard Model by 3.7σ. The tension even increases to 4.2σ including also $b \to se^+e^-$ measurements and assuming new physics to affect the muonic modes only. Other new physics benchmarks are discussed as well. The q^2 dependence of the shift in C_9 is suggested as a means to identify the origin of the tension – new physics or an unexpectedly large hadronic effect.

1 Introduction

Rare B and B_s decays based on the $b \to s$ flavour-changing neutral current transition are sensitive to physics beyond the Standard Model (SM). Recent measurements at the LHC, complementing earlier B-factory results, have hugely increased the available experimental information on these decays. Interestingly, several tensions with SM predictions have shown up in the data, most notably

- several tensions at the 2–3σ level in $B \to K^*\mu^+\mu^-$ angular observables in 1 fb^{-1} of LHCb data taken during 2011 [1];
- a 2.6σ deviation from lepton flavour universality (LFU) in $B^+ \to K^+\ell^+\ell^-$ decays measured by LHCb, including the full 3 fb^{-1} dataset [2].

Several model-independent theoretical analyses [3,4,5,6,7,8,9,10] have shown that both anomalies could be explained by new physics (NP). Today, the LHCb collaboration has released an update of the analyis of $B \to K^*\mu^+\mu^-$ angular observables based on the full 3 fb^{-1} dataset [11], finding a significant tension in particular in the angular observable P_5'. The aim of this talk is to interpret these measurements by performing a global model-independent fit to all available data. The results are updates of an analysis published recently [12] (and building on earlier work [13,14,4]), incorporating the new LHCb measurements. Crucially, the fit makes use of a combined fit [15] to $B \to K^*$ form factors from light-cone sum rules [15] and lattice QCD [16,17] published recently.

2 Model-independent analysis

2.1 Fit methodology

The effective Hamiltonian for $b \to s$ transitions can be written as

$$\mathcal{H}_{\text{eff}} = -\frac{4\,G_F}{\sqrt{2}} V_{tb}V_{ts}^* \frac{e^2}{16\pi^2} \sum_i (C_i O_i + C_i' O_i') + \text{h.c.} \tag{1}$$

[a] Talk presented at the 50th Rencontres de Moriond (Electroweak Session), La Thuile, 20 March 2015.
[b] Speaker.

Considering NP effects in the following set of dimension-6 operators,

$$O_7 = \frac{m_b}{e}(\bar{s}\sigma_{\mu\nu}P_R b)F^{\mu\nu}, \qquad O_7' = \frac{m_b}{e}(\bar{s}\sigma_{\mu\nu}P_L b)F^{\mu\nu}, \tag{2}$$

$$O_9 = (\bar{s}\gamma_\mu P_L b)(\bar{\ell}\gamma^\mu \ell), \qquad O_9' = (\bar{s}\gamma_\mu P_R b)(\bar{\ell}\gamma^\mu \ell), \tag{3}$$

$$O_{10} = (\bar{s}\gamma_\mu P_L b)(\bar{\ell}\gamma^\mu\gamma_5 \ell), \qquad O_{10}' = (\bar{s}\gamma_\mu P_R b)(\bar{\ell}\gamma^\mu\gamma_5 \ell), \tag{4}$$

one can construct a χ^2 function which quantifies, for a given value of the Wilson coefficients, the compatibility of the hypothesis with the experimental data. It reads

$$\chi^2(\vec{C}^{\rm NP}) = \left[\vec{O}_{\rm exp} - \vec{O}_{\rm th}(\vec{C}^{\rm NP})\right]^T \left[\mathcal{C}_{\rm exp} + \mathcal{C}_{\rm th}\right]^{-1} \left[\vec{O}_{\rm exp} - \vec{O}_{\rm th}(\vec{C}^{\rm NP})\right]. \tag{5}$$

where $O_{\rm exp,th}$ and $\mathcal{C}_{\rm exp,th}$ are the experimental and theoretical central values and covariance matrices, respectively. All dependence on NP is encoded in the NP contributions to the Wilson coefficients, $C_i^{\rm NP} = C_i - C_i^{\rm SM}$. The NP dependence of $\mathcal{C}_{\rm th}$ is neglected, but all correlations between theoretical uncertainties are retained. Including the theoretical error correlations and also the experimental ones, which have been provided for the new angular analysis by the LHCb collaboration, the fit is independent of the basis of observables chosen (e.g. P_i' vs. S_i observables). In other words, the "optimization" [18] of observables is automatically built in.

In total, the χ^2 used for the fit contains 88 measurements of 76 different observables by 6 experiments (see the original publication[4] for references). The observables include $B \to K^*\mu^+\mu^-$ angular observables and branching ratios as well as branching ratios of $B \to K\mu^+\mu^-$, $B \to X_s\mu^+\mu^-$, $B_s \to \phi\mu^+\mu^-$, $B \to K^*\gamma$, $B \to X_s\gamma$, and $B_s \to \mu^+\mu^-$.

2.2 *Compatibility of the SM with the data*

Setting the Wilson coefficients to their SM values, we find $\chi^2_{\rm SM} \equiv \chi^2(\vec{0}) = 116.9$ for 88 measurements, corresponding to a p value of 2.1%. Including also $b \to se^+e^-$ observables[c] the χ^2 deteriorates to 125.8 for 91 measurements, corresponding to $p = 0.91\%$. The observables with the biggest individual tensions are listed in table 1. It should be noted that the observables in this table are not independent. For instance, of the set (S_5, F_L, P_5'), only the first two are included in the fit as the last one can be expressed as a function of them[18,d].

Table 1: Observables where a single measurement deviates from the SM by 1.9σ or more (cf. [15] for the $B \to K^*\mu^+\mu^-$ predictions at low q^2).

Decay	obs.	q^2 bin	SM pred.	measurement		pull
$\bar{B}^0 \to \bar{K}^{*0}\mu^+\mu^-$	F_L	$[2, 4.3]$	0.81 ± 0.02	0.26 ± 0.19	ATLAS	$+2.9$
$\bar{B}^0 \to \bar{K}^{*0}\mu^+\mu^-$	F_L	$[4, 6]$	0.74 ± 0.04	0.61 ± 0.06	LHCb	$+1.9$
$\bar{B}^0 \to \bar{K}^{*0}\mu^+\mu^-$	S_5	$[4, 6]$	-0.33 ± 0.03	-0.15 ± 0.08	LHCb	-2.2
$\bar{B}^0 \to \bar{K}^{*0}\mu^+\mu^-$	P_5'	$[1.1, 6]$	-0.44 ± 0.08	-0.05 ± 0.11	LHCb	-2.9
$\bar{B}^0 \to \bar{K}^{*0}\mu^+\mu^-$	P_5'	$[4, 6]$	-0.77 ± 0.06	-0.30 ± 0.16	LHCb	-2.8
$B^- \to K^{*-}\mu^+\mu^-$	$10^7 \frac{dBR}{dq^2}$	$[4, 6]$	0.54 ± 0.08	0.26 ± 0.10	LHCb	$+2.1$
$\bar{B}^0 \to \bar{K}^0\mu^+\mu^-$	$10^8 \frac{dBR}{dq^2}$	$[0.1, 2]$	2.71 ± 0.50	1.26 ± 0.56	LHCb	$+1.9$
$\bar{B}^0 \to \bar{K}^0\mu^+\mu^-$	$10^8 \frac{dBR}{dq^2}$	$[16, 23]$	0.93 ± 0.12	0.37 ± 0.22	CDF	$+2.2$
$B_s \to \phi\mu^+\mu^-$	$10^7 \frac{dBR}{dq^2}$	$[1, 6]$	0.48 ± 0.06	0.23 ± 0.05	LHCb	$+3.1$

[c] We have not yet included the recent measurement [19] of $B \to K^*e^+e^-$ angular observables at very low q^2. Although these observables are not sensitive to the violation of LFU, being dominated by the photon pole, they can provide important constraints on the Wilson coefficients $C_7^{(\prime)}$.

[d] Including the last two instead leads to equivalent results since we include correlations as mentioned above; this has been checked explicitly.

2.3 *Implications for Wilson coefficients*

Next, we have performed fits where a single real Wilson coefficient at a time is allowed to float. The resulting best-fit values, 1 and 2σ ranges, pulls, and p values are shown in table 2. The best fit is obtained for new physics in C_9 only, corresponding to a 3.7σ pull from the SM. A slightly worse fit with a pull of 3.1σ is obtained in the $SU(2)_L$ invariant direction $C_9^{\rm NP} = -C_{10}^{\rm NP}$. This direction corresponds to an operator with left-handed leptons only and is predicted by several NP models. If we include $b \to s e^+ e^-$ observables in the fit and assume NP to only affect the $b \to s\mu^+\mu^-$ modes, the pulls of these two scenarios increase to 4.3σ and 3.9σ, respectively.

Table 2: Constraints on individual Wilson coefficients, assuming them to be real, in the global fit to 88 $b \to s\mu^+\mu^-$ measurements. The p values in the last column should be compared to the p value of the SM, 2.1%.

Coeff.	best fit	1σ	2σ	$\sqrt{\chi^2_{\rm b.f.} - \chi^2_{\rm SM}}$	p [%]
$C_7^{\rm NP}$	-0.04	$[-0.07, -0.01]$	$[-0.10, 0.02]$	1.42	2.4
C_7'	0.01	$[-0.04, 0.07]$	$[-0.10, 0.12]$	0.24	1.8
$C_9^{\rm NP}$	-1.07	$[-1.32, -0.81]$	$[-1.54, -0.53]$	3.70	11.3
C_9'	0.21	$[-0.04, 0.46]$	$[-0.29, 0.70]$	0.84	2.0
$C_{10}^{\rm NP}$	0.50	$[0.24, 0.78]$	$[-0.01, 1.08]$	1.97	3.2
C_{10}'	-0.16	$[-0.34, 0.02]$	$[-0.52, 0.21]$	0.87	2.0
$C_9^{\rm NP} = C_{10}^{\rm NP}$	-0.22	$[-0.44, 0.03]$	$[-0.64, 0.33]$	0.89	2.0
$C_9^{\rm NP} = -C_{10}^{\rm NP}$	-0.53	$[-0.71, -0.35]$	$[-0.91, -0.18]$	3.13	7.1
$C_9' = C_{10}'$	-0.10	$[-0.36, 0.17]$	$[-0.64, 0.43]$	0.36	1.8
$C_9' = -C_{10}'$	0.11	$[-0.01, 0.22]$	$[-0.12, 0.33]$	0.93	2.0

Allowing NP effects in two Wilson coefficients at the same time, one obtains the allowed regions shown in fig. 1 in the C_9-C_{10} plane and the C_9-C_9' plane. Apart from the 1σ and 2σ regions allowed by the global fit shown in blue, these plots also show the allowed regions when taking into account only $B \to K^*\mu^+\mu^-$ angular observables (red) or only branching ratio measurements of all decays considered (green).

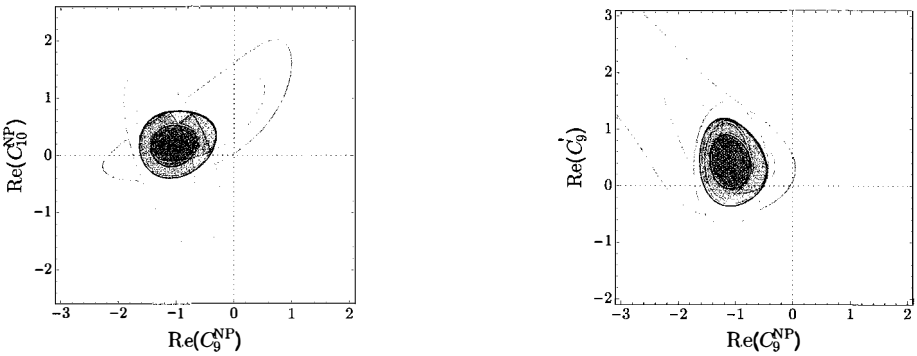

Figure 1 – Allowed regions in the Re($C_9^{\rm NP}$)-Re($C_{10}^{\rm NP}$) plane (left) and the Re($C_9^{\rm NP}$)-Re(C_9') plane (right). The blue contours correspond to the 1 and 2σ best fit regions from the global fit. The green and red contours correspond to the 1 and 2σ regions if only branching ratio data or only data on $B \to K^*\mu^+\mu^-$ angular observables is taken into account.

2.4 *New physics vs. hadronic effects*

The result that the best fit is obtained by modifying the Wilson coefficient C_9 might be worrying as this is the coefficient of an operator with a left-handed quark FCNC and a vector-like coupling to leptons; non-factorizable hadronic effects are mediated by virtual photon exchange and thus also have a vector-like coupling to leptons (and the left-handedness of the FCNC transition is ensured by the SM weak

interactions). It is therefore conceivable that unaccounted for hadronic effects could mimic a new physics effect in C_9. There are at least two ways to test this possibility.

1. The hadronic effect cannot violate LFU, so if the violation of LFU in R_K (or any of the other observables suggested, e.g., in [12]) is confirmed, this hypothesis is refuted;

2. There is no *a priori* reason to expect that a hadronic effect should have the same q^2 dependence as a shift in C_9 induced by NP.

Let us focus on the second point. With the finer binning of the new LHCb $B \to K^*\mu^+\mu^-$ angular analysis, it is possible to determine the preferred range of a hypothetical NP contribution to C_9 in individual bins of q^2. To this end, we have splitted all measurements of $B \to K^*\mu^+\mu^-$ (including braching ratios and non-LHCb measurements) into sets with data below 2.3 GeV^2, between 2 and 4.3 GeV^2, between 4 and 6 GeV^2, and above 15 GeV^2 (the slight overlap of the bins, caused by changing binning conventions over time, is of no concern as correlations are treated consistently). The resulting 1σ regions are shown in fig. 2 (the fit for the region between 6 and 8 GeV^2 is shown for completeness as well but only as a dashed box because we assume non-perturbative charm effects to be out of control in this region and thus do not include this data in our global fit). We make some qualitative observations, noting that these will have to be made more robust by a dedicated numerical analysis.

- The NP hypothesis requires a q^2 independent shift in C_9. At roughly 1σ, this hypothesis seems to be consistent with the data.

- If the tensions with the data were due to errors in the form factor determinations, naively one should expect the deviations to dominate at one end of the kinematical range where one method of form factor calculation (lattice at high q^2 and LCSR at low q^2) dominates. Instead, if at all, the tensions seem to be more prominent at intermediate q^2 values where both complementary methods are near their domain of validity and in fact give consistent predictions[15].

- There does seem to be a systematic increase of the preferred range for C_9 at q^2 below the J/ψ resonance, increasing as this resonance is approached. Qualitatively, this is the behaviour expected from non-factorizable charm loop contributions. However, the central value of this effect would have to be significantly larger than expected on the basis of existing estimates [20,21,22,23,24], as conjectured earlier [23].

Concerning the last point, it is important to note that a charm loop effect does not have to modify the H_- and H_0 helicity amplitudes[e] in the same way (as a shift in C_9 induced by NP would). Repeating the above exercise and allowing a q^2-dependent shift of C_9 only in one of these amplitudes, one finds that the resulting corrections would have to be huge and of the same sign. It thus seems that, if the tensions are due to a charm loop effect, this must contribute to both the H_- and H_0 helicity amplitude with the same sign as a negative NP contribution to C_9.

3 Summary and Outlook

The new LHCb measurement of angular observables in $B \to K^*\mu^+\mu^-$ is in significant tension with SM expectations. An explanation in terms of new physics is consistent with the data. Models with a negative shift of C_9 or with $C_9^{\rm NP} = -C_{10}^{\rm NP} < 0$ give the best fit to the data. These findings are in very good agreement with preliminary results from a similar analysis presented at this conference [25].

Arguments have been given why the tension being caused by underestimated form factor uncertainties, suggested [24] as an explanation of the original $B \to K^*\mu^+\mu^-$ anomaly [1], does not seem to be supported by the data. A detailed numerical analysis of this point, with the help of the new LCSR result [15] (and possibly the relations in the heavy quark limit [22,26,24] as a cross-check) would be interesting.

An important cross-check of the NP hypothesis is the q^2 dependence of the preferred shift in C_9 and it has been argued that also an unexpectedly large charm-loop contribution at low q^2 near the J/ψ resonance could solve, or at least reduce, the observed tensions. A possible experimental strategy to resolve this ambiguity could contain, among others, the following steps.

[e] The modification of the H_+ amplitude is expected to be suppressed [22,24].

- Testing LFU in the $B \to K^* \mu^+ \mu^-$ vs. $B \to K^* e^+ e^-$ branching ratios and angular observables, where spectacular deviations from the SM universality prediction would occur if the R_K anomaly is due to NP [12,27,24], which can be accomodated in various NP models with a Z' boson [28,29,30,31,32,12,33] [f] or leptoquarks [8,38,29,39,40,41];
- Searching for lepton flavour violating B decays like $B \to K^{(*)} e^\pm \mu^\mp$, because in leptoquark models explaining the $B \to K^* \mu^+ \mu^-$ anomaly, either $R_{K^{(*)}}$ deviates from one or lepton flavour is violated [29,41] and also in Z' models these decays could arise [30].
- Measuring the T-odd CP asymmetries [42,43] $A_{7,8,9}$, which could be non-zero in the presence of new sources of CP violation.
- Measuring $\mathrm{BR}(B_s \to \mu^+ \mu^-)$ more precisely as a clean(er) probe of C_{10}.

The first three items are null tests of the SM and could unambiguously prove the presence of new physics not spoiled by hadronic uncertainties; the last one is at least much cleaner than semi-leptonic decays.

On the theory side, the new more precise data could be used, in the spirit of fig. 2, to extract the preferred size, q^2 and helicity dependence of a possible hadronic effect, assuming the SM. Combined with a better understanding of the charm-loop effect and more precise estimates of its possible size, this could shed light on the important question whether the effect observed by LHCb is the first evidence for physics beyond the Standard Model, or our understanding of strong interaction effects in rare semi-leptonic B decays has to be revised. Both possibilities will have important implications.

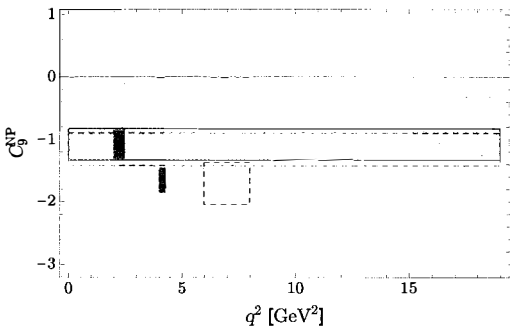

Figure 2 – Purple: ranges preferred at 1σ for a new physics contribution to C_9 from fits to all $B \to K^* \mu^+ \mu^-$ observables in different bins of q^2. Blue: 1σ range for C_9^{NP} from the global fit (cf. tab. 2). Green: 1σ range for C_9^{NP} from a fit to $B \to K^* \mu^+ \mu^-$ observables only. The vertical gray lines indicate the location of the J/ψ and ψ' resonances, respectively.

Acknowledgments

D.S. would like to thank the organizers of the 50th Rencontres de Moriond for the invitation, the members of the LHCb collaboration for sharing unpublished results on the $B \to K^* \mu^+ \mu^-$ angular analysis, and Patrick Koppenburg, Christoph Langenbruch, Guy Wilkinson, and Joaquim Matias for useful discussions. We thank Andreas Crivellin for valuable comments on the manuscript. The research of D.S. is supported by the DFG cluster of excellence "Origin and Structure of the Universe". Research at Perimeter Institute is supported by the Government of Canada through Industry Canada and by the Province of Ontario through the Ministry of Economic Development & Innovation.

References

1. R Aaij et al. Measurement of Form-Factor-Independent Observables in the Decay $B^0 \to K^{*0} \mu^+ \mu^-$. *Phys.Rev.Lett.*, 111(19):191801, 2013.
2. Roel Aaij et al. Test of lepton universality using $B^+ \to K^+ \ell^+ \ell^-$ decays. *Phys.Rev.Lett.*, 113:151601, 2014.
3. Sebastien Descotes-Genon, Joaquim Matias, and Javier Virto. Understanding the $B \to K^* \mu^+ \mu^-$ Anomaly. *Phys.Rev.*, D88(7):074002, 2013.

[f] Some Z' models [34,35,36,37] predict LFU to hold but could still solve the $B \to K^* \mu^+ \mu^-$ anomaly.

4. Wolfgang Altmannshofer and David M. Straub. New physics in $B \to K^* \mu\mu$? *Eur.Phys.J.*, C73:2646, 2013.
5. Frederik Beaujean, Christoph Bobeth, and Danny van Dyk. Comprehensive Bayesian analysis of rare (semi)leptonic and radiative B decays. *Eur.Phys.J.*, C74:2897, 2014.
6. Tobias Hurth and Farvah Mahmoudi. On the LHCb anomaly in B $\to K^* \ell^+ \ell^-$. *JHEP*, 1404:097, 2014.
7. Rodrigo Alonso, Benjamin Grinstein, and Jorge Martin Camalich. $SU(2) \times U(1)$ gauge invariance and the shape of new physics in rare B decays. 2014.
8. Gudrun Hiller and Martin Schmaltz. R_K and future $b \to s\ell\ell$ BSM opportunities. *Phys.Rev.*, D90:054014, 2014.
9. Diptimoy Ghosh, Marco Nardecchia, and S.A. Renner. Hint of Lepton Flavour Non-Universality in B Meson Decays. 2014.
10. T. Hurth, F. Mahmoudi, and S. Neshatpour. Global fits to $b \to sll$ data and signs for lepton non-universality. 2014.
11. LHCb conference note (in preparation). Talk presented by C. Langenbruch at Moriond 2015, Electroweak Session.
12. Wolfgang Altmannshofer and David M. Straub. State of new physics in $b \to s$ transitions. 2014.
13. Wolfgang Altmannshofer, Paride Paradisi, and David M. Straub. Model-Independent Constraints on New Physics in $b \to s$ Transitions. *JHEP*, 1204:008, 2012.
14. Wolfgang Altmannshofer and David M. Straub. Cornering New Physics in $b \to s$ Transitions. *JHEP*, 1208:121, 2012.
15. Aoife Bharucha, David M. Straub, and Roman Zwicky. $B \to V\ell^+\ell^-$ in the Standard Model from Light-Cone Sum Rules. 2015.
16. Ronald R. Horgan, Zhaofeng Liu, Stefan Meinel, and Matthew Wingate. Calculation of $B^0 \to K^{*0}\mu^+\mu^-$ and $B_s^0 \to \phi\mu^+\mu^-$ observables using form factors from lattice QCD. *Phys.Rev.Lett.*, 112:212003, 2014.
17. R.R. Horgan, Z. Liu, S. Meinel, and M. Wingate. Rare B decays using lattice QCD form factors. 2015.
18. Sebastien Descotes-Genon, Tobias Hurth, Joaquim Matias, and Javier Virto. Optimizing the basis of $B \to K^* \ell^+ \ell^-$ observables in the full kinematic range. *JHEP*, 1305:137, 2013.
19. Roel Aaij et al. Angular analysis of the $B^0 \to K^{*0} e^+ e^-$ decay in the low-q^2 region. 2015.
20. Franz Muheim, Yuehong Xie, and Roman Zwicky. Exploiting the width difference in $B_s \to \phi\gamma$. *Phys.Lett.*, B664:174–179, 2008.
21. A. Khodjamirian, Th. Mannel, A.A. Pivovarov, and Y.-M. Wang. Charm-loop effect in $B \to K^{(*)}\ell^+\ell^-$ and $B \to K^*\gamma$. *JHEP*, 1009:089, 2010.
22. S. Jäger and J. Martin Camalich. On $B \to V ll$ at small dilepton invariant mass, power corrections, and new physics. *JHEP*, 1305:043, 2013.
23. James Lyon and Roman Zwicky. Resonances gone topsy turvy - the charm of QCD or new physics in $b \to s\ell^+\ell^-$? 2014.
24. Sebastian Jäger and Jorge Martin Camalich. Reassessing the discovery potential of the $B \to K^* \ell^+ \ell^-$ decays in the large-recoil region: SM challenges and BSM opportunities. 2014.
25. Sebastien Descotes-Genon, Lars Hofer, Joaquim Matias, and Javier Virto. (In preparation). Talk presented by J. Matias at Moriond 2015, Electroweak Session.
26. Sebastien Descotes-Genon, Lars Hofer, Joaquim Matias, and Javier Virto. On the impact of power corrections in the prediction of $B \to K^* \mu^+ \mu^-$ observables. 2014.
27. Gudrun Hiller and Martin Schmaltz. Diagnosing lepton-nonuniversality in $b \to s\ell\ell$. 2014.
28. Wolfgang Altmannshofer, Stefania Gori, Maxim Pospelov, and Itay Yavin. Dressing L_μ - L_τ in Color. *Phys.Rev.*, D89:095033, 2014.
29. Andrzej J. Buras, Jennifer Girrbach-Noe, Christoph Niehoff, and David M. Straub. $B \to K^{(*)}\nu\bar{\nu}$ decays in the Standard Model and beyond. 2014.
30. Sheldon L. Glashow, Diego Guadagnoli, and Kenneth Lane. Lepton Flavor Violation in B Decays? 2014.
31. Bhubanjyoti Bhattacharya, Alakabha Datta, David London, and Shanmuka Shivashankara. Simultaneous Explanation of the R_K and $R(D^{(*)})$ Puzzles. *Phys.Lett.*, B742:370–374, 2015.
32. Andreas Crivellin, Giancarlo D'Ambrosio, and Julian Heeck. Explaining $h \to \mu^\pm\tau^\mp$, $B \to K^*\mu^+\mu^-$ and $B \to K\mu^+\mu^-/B \to Ke^+e^-$ in a two-Higgs-doublet model with gauged $L_\mu - L_\tau$. 2015.
33. Andreas Crivellin, Giancarlo D'Ambrosio, and Julian Heeck. Addressing the LHC flavour anomalies with horizontal gauge symmetries. 2015.
34. Rhorry Gauld, Florian Goertz, and Ulrich Haisch. On minimal Z' explanations of the $B \to K^*\mu^+\mu^-$ anomaly. *Phys.Rev.*, D89:015005, 2014.
35. Andrzej J. Buras and Jennifer Girrbach. Left-handed Z' and Z FCNC quark couplings facing new $b \to s\mu^+\mu^-$ data. *JHEP*, 1312:009, 2013.
36. Rhorry Gauld, Florian Goertz, and Ulrich Haisch. An explicit Z'-boson explanation of the $B \to K^*\mu^+\mu^-$ anomaly. *JHEP*, 1401:069, 2014.
37. Andrzej J. Buras, Fulvia De Fazio, and Jennifer Girrbach. 331 models facing new $b \to s\mu^+\mu^-$ data. *JHEP*, 1402:112, 2014.
38. Sanjoy Biswas, Debtosh Chowdhury, Sangeun Han, and Seung J. Lee. Explaining the Lepton Non-universality at the LHCb and CMS from an Unified Framework. 2014.
39. Ben Gripaios, Marco Nardecchia, and S.A. Renner. Composite leptoquarks and anomalies in B-meson decays. 2014.
40. Suchismita Sahoo and Rukmani Mohanta. Scalar leptoquarks and the rare B meson decays. 2015.
41. Ivo de Medeiros Varzielas and Gudrun Hiller. Clues for flavor from rare lepton and quark decays. 2015.
42. Christoph Bobeth, Gudrun Hiller, and Giorgi Piranishvili. CP Asymmetries in $\bar{B} \to \bar{K}^*(\to \bar{K}\pi)\bar{\ell}\ell$ and Untagged $\bar{B}_s$, $B_s \to \phi(\to K^+K^-)\bar{\ell}\ell$ Decays at NLO. *JHEP*, 0807:106, 2008.
43. Wolfgang Altmannshofer, Patricia Ball, Aoife Bharucha, Andrzej J. Buras, David M. Straub, and Michael Wick. Symmetries and Asymmetries of $B \to K^*\mu^+\mu^-$ Decays in the Standard Model and Beyond. *JHEP*, 0901:019, 2009.

CP Violation in the $B^0_{(s)}$ Meson System at LHCb

Julian Wishahi,
on behalf of the LHCb collaboration
Technische Universität Dortmund, Fakultät Physik,
Otto-Hahn-Str. 4, 44227 Dortmund, Germany

Precision measurements of CP violation in processes involving neutral B^0 and B^0_s mesons allow to probe beyond the boundaries of our current understanding of fundamental interactions as described by the Standard Model of particle physics. We present recent measurements of CP violation in the golden decay modes $B^0_s \to J/\psi K^+K^-$ and $B^0 \to J/\psi K^0_S$ that exploit the full Run I dataset of $3\,\text{fb}^{-1}$ of pp collisions at centre-of-mass energies of 7 and 8 TeV recorded with the LHCb experiment. Furthermore, CP violation measurements in $B^0_s \to J/\psi K^0_S$ and $B^0 \to J/\psi \pi^+\pi^-$ decays are presented, which allow to constrain the effects of higher-order Standard Model processes in the golden modes.

1 Introduction

In the Standard Model of particle physics (SM), CP violation is the result of a single irreducible phase in the Cabibbo-Kobayashi-Maskawa (CKM) quark-mixing matrix [1,2]. The CKM matrix connects observables of various decay modes via its unitarity conditions, hereby allowing for precision tests of the accuracy of the description of CP violation in the SM. Many of these observables are accessible in processes involving oscillation and decay of neutral B mesons [3,4].

In final states f_{CP}, common to both the B^0_q and $\overline{B}{}^0_q$, the interference of the amplitude of the direct decay and the amplitude of the decay after B^0_q–$\overline{B}{}^0_q$ oscillation can lead to a CP asymmetry $\mathcal{A}(t)$ between the decay-time dependent decay rates of $\overline{B}{}^0_q$ and B^0_q. Assuming negligible CP violation in $\overline{B}{}^0_q$–B^0_q mixing, this asymmetry takes the form

$$\mathcal{A}(t) = \frac{\Gamma(\overline{B}{}^0_q(t) \to f_{CP}) - \Gamma(B^0_q(t) \to f_{CP})}{\Gamma(\overline{B}{}^0_q(t) \to f_{CP}) + \Gamma(B^0_q(t) \to f_{CP})} = \frac{S\sin(\Delta m_q t) - C\cos(\Delta m_q t)}{\cosh\left(\frac{\Delta\Gamma_q t}{2}\right) + A_{\Delta\Gamma}\cosh\left(\frac{\Delta\Gamma_q t}{2}\right)}. \quad (1)$$

Here, $\overline{B}{}^0_q(t)$ and $B^0_q(t)$ represent the production flavour and t the decay time. The parameters Δm_q and $\Delta\Gamma_q$ are the mass and the decay width differences between the heavy and the light mass eigenstates of the B^0_q–$\overline{B}{}^0_q$ system, and S, C, and $A_{\Delta\Gamma}$ are CP observables.

The values of S, C, and $A_{\Delta\Gamma}$ depend on the final state f_{CP}. For many of these states, the respective CP observables cannot be interpreted easily in terms of CKM related quantities, as higher order SM effects and hadronic contributions need to be taken into account. Though, for some processes, like B^0_q decays in which the decay amplitudes are dominated by a $b \to c\bar{c}s$ transition, theoretical uncertainties are far below the current experimental uncertainties. These 'golden modes', in particular $B^0 \to J/\psi K^0_S$ in the B^0 and $B^0_s \to J/\psi K^+K^-$ in the B^0_s meson system, are expected to exhibit negligible CP violation in the decay, $C \approx 0$, leaving $S \approx -\eta_{f_{CP}} \sin\phi_q$, where ϕ_q is the phase difference between the direct decay and the decay after oscillation, and $\eta_{f_{CP}}$ is the CP eigenvalue of the final state. In the SM, the phase ϕ_d in $B^0 \to J/\psi K^0_S$ decays can be identified as 2β, and $\phi_s = -2\beta_s$ in $B^0_s \to J/\psi K^+K^-$, where β and β_s are angles of CKM unitarity triangles. Using CKM unitarity conditions and inputs from measurements of other CKM related quantities, the angles β and β_s can be indirectly predicted as [5]

$$\begin{aligned} \beta &= +\arg[-(V_{cd}V_{cb}^*)/(V_{td}V_{tb}^*)] = +0.4402^{+0.0136}_{-0.0310}, \\ \beta_s &= -\arg[-(V_{cs}V_{cb}^*)/(V_{ts}V_{tb}^*)] = -0.0365^{+0.0013}_{-0.0012}. \end{aligned}$$

Comparing these precise values with similarily precise direct measurements of ϕ_d and ϕ_s allows for a stringent test of the CKM sector of the SM.

Despite small theoretical uncertainties in the golden modes, future experimental precision will require an even better understanding of higher-order contributions to the decay amplitudes, in particular to disentangle them from contributions from physics beyond the SM[6]. Experimental input on these higher-order SM contributions can be obtained from decays that are related to the golden modes via $SU(3)_F$ flavour symmetry, as the higher-order contributions are less suppressed in some of these channels [7,8,9].

The most recent LHCb measurements of CP violation in $B^0_s \to J/\psi K^+K^-$ and $B^0 \to J/\psi K^0_S$ are presented, as well as first measurements of CP violation in their respective $SU(3)_F$ related channels, $B^0 \to J/\psi \pi^+\pi^-$ and $B^0_s \to J/\psi K^0_S$. These exploit LHCb's Run I dataset comprising $3\,\text{fb}^{-1}$ of pp collisions at centre-of-mass energies of 7 and 8 TeV. The LHCb detector at CERN is a single-arm forward spectrometer designed for the study of particles containing b and c quarks. Its high-precision tracking and vertexing system, its excellent particle identification system, and the high production cross-section for B mesons at LHC's pp collisions make it perfectly suited for measurements of decay-time dependent CP violation in B mesons. Besides continuing and extending the measurements performed at the B factories, BaBar and Belle, in decays of B^0 and B^+ mesons, it has access to the B^0_s meson system. Due to the large B^0_s oscillation frequency, LHCb's decay time resolution of ≈ 50 fs is a fundamental requirement for precision measurements of decay-time dependent CP violation in the B^0_s meson system. Further details on the LHCb experiment can be found elsewhere [10,11].

2 Measurement of CP violation in $B^0 \to J/\psi K^0_S$

The $J/\psi K^0_S$ final state is (nearly) CP odd, and can be reached by both the B^0 and the $\bar{B}^0$ meson. As $\Delta\Gamma \approx 0$ in the B^0 system, the asymmetry in Eq. 1 simplifies to $\mathcal{A}(t) = S\sin(\Delta m_d t) - C\cos(\Delta m_d t)$. As stated before, $C \approx 0$ and therefore $S = \sin 2\beta$, with $\beta = \arg[-(V_{cd}V_{cb}^*)/(V_{td}V_{tb}^*)]$. An indirect estimate from combining CKM unitarity with measurements of other CKM observables predicts [5] $\sin(2\beta)$ as $0.771^{+0.017}_{-0.041}$, in contrast to the average of direct measurements [13], 0.682 ± 0.019. The latter value is dominated by measurements of CP violation in $B^0 \to J/\psi K^0_S$ decays at the B factories, where the best single measurement [15] by the Belle experiment yields $S = 0.670 \pm 0.029\,(\text{stat}) \pm 0.013\,(\text{syst})$.

In the recent LHCb analysis [12], a total of 114 000 $B^0 \to J/\psi K^0_S$ decays are selected after reconstructing the B^0 decay with subsequent decays of $J/\psi \to \mu^+\mu^-$ and $K^0_S \to \pi^+\pi^-$. The $K^0_S \to \pi^+\pi^-$ candidates are reconstructed in two different categories: *long* K^0_S candidates decay

early enough for the pions to be reconstructed in the vertex detector; *downstream* K^0_S candidates decay later such that track segments of the pions cannot be formed in the vertex detector. As evident from Eq. 1, the distinction between candidates with a B^0 or $\overline{B}^0$ production state, the 'flavour tagging', is indispensable for decay-time dependent *CP* measurements. At LHCb, the flavour tagging[16] exploits the properties of charged particles produced in the fragmentation of the signal B meson (same-side tagging), and the decay products of the b hadron accompanying the production of the signal B meson (opposite-side tagging). A flavour tag can be assigned for 41 560 of the decays, with an effective mistag rate of $(35.62 \pm 0.12)\%$. This corresponds to an effective tagging efficiency of $(3.02 \pm 0.05)\%$, which is a measure of the statistical power of the sample. The measurement of the *CP* parameters is based on a multi-dimensional unbinned maximum

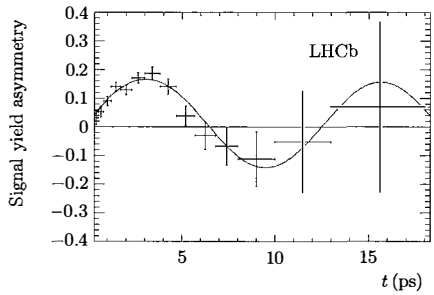

Figure 1 – Signal-yield asymmetry between $B^0 \to J/\psi K^0_S$ decays tagged as $\overline{B}^0$ and as B^0 as a function of their decay time. The data points are obtained after background subtraction, and the solid curve is the projection of the signal PDF.

likelihood fit to the dataset. After a careful evaluation of systematic effects and uncertainties, in particular from the flavour tagging calibration, *CP*-like background asymmetries, and effects from kaon interactions with the detector material, the *CP* parameters are measured as

$$\begin{aligned} S &= 0.731 \pm 0.035\,(\text{stat}) \pm 0.020\,(\text{syst}), \\ C &= -0.038 \pm 0.032\,(\text{stat}) \pm 0.005\,(\text{syst}), \end{aligned}$$

with a statistical correlation coefficient of $\rho(S, C) = 0.483$. A projection of the signal asymmetry is shown in Fig. 1. This result represents the most precise time-dependent *CP* violation measurement at a hadron collider. It has a comparable sensitivity as the results from the B factories, and is in good agreement with both the direct and indirect estimates of $\sin 2\beta$.

3 Controlling Penguin pollution with $B^0_s \to J/\psi K^0_S$

Under U-spin symmetry, i.e. under exchange of s and d quarks, the $B^0 \to J/\psi K^0_S$ decay transforms into $B^0_s \to J/\psi K^0_S$. In contrast to the former channel, the latter exhibits higher-order contributions from penguin topologies that are not Cabibbo suppressed. Thus, $B^0_s \to J/\psi K^0_S$ can be used to constrain the penguin pollution in $B^0 \to J/\psi K^0_S$ by performing a *CP* violation measurement.

A first such measurement in $B^0_s \to J/\psi K^0_S$ has been performed by LHCb[17]. In contrast to the analysis in the $B^0 \to J/\psi K^0_S$ mode, a more stringent selection is required, as the $B^0_s \to J/\psi K^0_S$ decay is Cabibbo suppressed by a factor of ≈ 25 with respect to $B^0 \to J/\psi K^0_S$ and the B^0_s production rate is suppressed by a factor of ≈ 4 with respect to B^0 production. A good background rejection is achieved by using multivariate classifiers, and the resulting mass and decay time distributions are shown in Fig. 2. Using an unbinned maximum likelihood fit to the

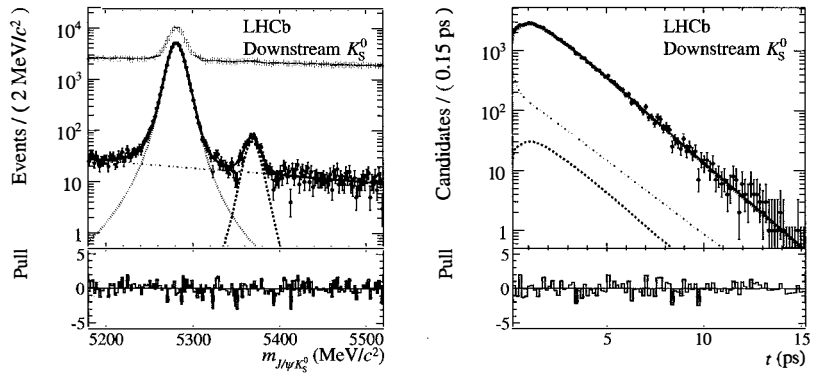

Figure 2 – Mass distribution of $B_s^0 \to J/\psi K_S^0$ candidates at different stages of the event selection (left) and distribution of the decay times after the final selection (right). In both plots, the PDF projections of the $B_s^0 \to J/\psi K_S^0$ (dark blue, dashed), $B^0 \to J/\psi K_S^0$ (red, dotted), and combinatorial background (turqoise, dash-dotted) components are shown.

dataset, the *CP* parameters are measured as

$$\begin{aligned} S &= -0.08 \pm 0.40\,(\text{stat}) \pm 0.08\,(\text{syst}), \\ C &= -0.28 \pm 0.41\,(\text{stat}) \pm 0.08\,(\text{syst}), \\ A_{\Delta\Gamma} &= 0.49 \pm {}^{0.77}_{0.65}\,(\text{stat}) \pm 0.06\,(\text{syst}). \end{aligned}$$

Although being statistically limited, this measurement is the first measurement of *CP* violation in this channel. Additionally, the branching ratio is measured as

$$\frac{\mathcal{B}(B_s^0 \to J/\psi K_S^0)}{\mathcal{B}(B^0 \to J/\psi K_S^0)} = 0.0431 \pm 0.0017\,(\text{stat}) \pm 0.0012\,(\text{syst}) \pm 0.0025\,(f_s/f_d),$$

where the largest uncertainty comes from the imprecise knowledge of f_s/f_d, the ratio of the B_s^0 and the B^0 production fraction.

4 Measurement of *CP* violation in $B_s^0 \to J/\psi K^+K^-$

The recent LHCb measurement [18] of the phase ϕ_s is performed with a dataset of 96 000 $B_s^0 \to J/\psi K^+K^-$ decays. To separate S- and P-wave components, the analysis is performed in 6 bins of the invariant mass of the K^+K^-, as shown in Fig. 3. Furthermore, to disentangle the different *CP*-odd and *CP*-even contributions in the P-wave, the unbinned maximum likelihood fit to the signal weighted data describes the angular distribution of the daughter particles, in addition to the decay time and tagging observables. The projections of the PDF to the angular observables are shown in Fig. 3. The result for the *CP* phase is

$$\phi_s = -0.058 \pm 0.049\,(\text{stat}) \pm 0.006\,(\text{syst}),$$

where the largest systematic uncertainty is related to the limited knowledge of the angular efficiency. In the same analysis, the decay width difference is measured as $\Delta\Gamma_s = 0.0805 \pm 0.0091\,(\text{stat}) \pm 0.0032\,(\text{syst})\ \text{ps}^{-1}$. No evidence for direct *CP* violation is found. The measurement of the phase ϕ_s is the most precise to date, and the results are in agreement with the SM predictions.

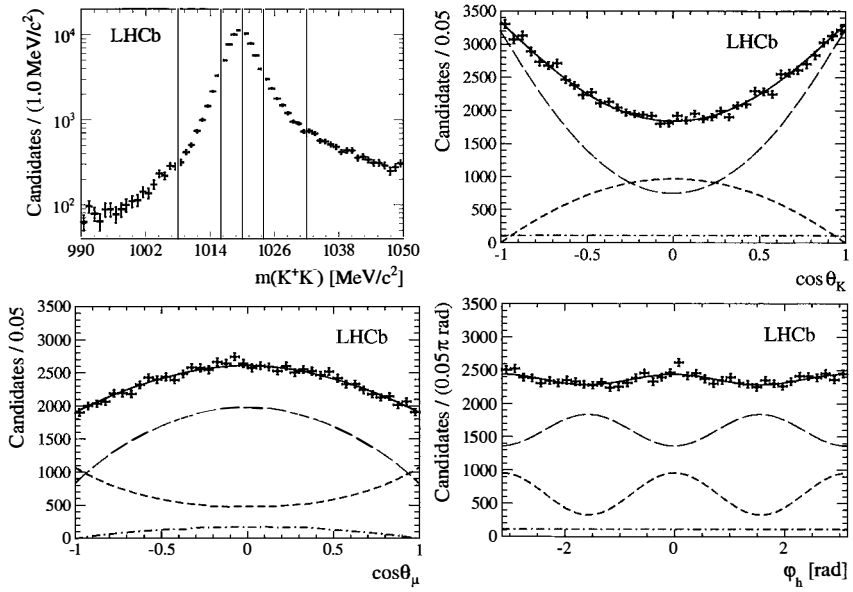

Figure 3 – Background-subtracted (top, left) invariant mass distribution of the K^+K^- system in selected $B_s^0 \to J/\psi K^+K^-$ decays, with vertical red lines indicating the bin boundaries of the six bins used in the analysis. The other three plots show the background-subtracted angle distributions, with the PDF projectiosn of the total signal contribution (blue, solid) and of the CP-even (red, long-dashed). CP-odd (green, short-dashed), and S-wave (purple, dotted-dashed) contributions.

5 Controlling Penguin pollution with $B^0 \to J/\psi\pi^+\pi^-$

A measurement of CP violation in $B^0 \to J/\psi\rho(770)$ allows to constrain possible penguin contributions to ϕ_s in $B_s^0 \to J/\psi K^+K^-$. Using 17500 $B^0 \to J/\psi\pi^+\pi^-$ candidates, the LHCb analysis exploits the distributions of the invariant $\pi^+\pi^-$ mass and the angular distributions to disentangle, amongst others, the $\rho(770) \to \pi^+\pi^-$ resonance, as shown in Fig. 4. In combination with

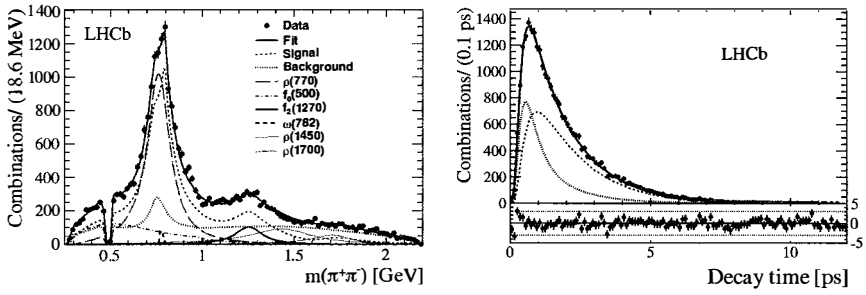

Figure 4 – Distribution of (left) the invariant mass of the $\pi^+\pi^-$ system in $B^0 \to J/\psi\pi^+\pi^-$ decays, showing the different resonant contributions and their fit projections (see the legend for details), and of (right) the decay times. In the latter, the lines represent the projections of the full PDF (blue, solid) and of the signal (red, dashed) and background (black, dotted) contributions.

a tagged, decay-time dependent analysis, the CP observables of the $B^0 \to J/\psi\rho(770)$ mode are

measured as

$$\begin{aligned} S &= -0.66 \ {}^{+0.13}_{-0.12}\,(\text{stat}) \pm {}^{0.09}_{0.03}\,(\text{syst}), \\ C &= -0.063 \pm 0.056\,(\text{stat}) \pm {}^{0.019}_{0.014}\,(\text{syst}). \end{aligned}$$

This measurement is in good agreement with former measurements by the Belle experiment, and constrains the expected shift on ϕ_s to

$$\Delta\phi_s \in [-1.05^\circ, +1.18^\circ] \text{ at } 95\% \text{ CL},$$

which is small compared to the statistical uncertainties on ϕ_s.

6 Conclusion

Analyses of decay-time dependent CP violation in neutral B meson decays with the Run I dataset of LHCb have resulted in precision measurements of CP violation observables, like the mixing-induced phases ϕ_s and ϕ_d. The measurement of ϕ_s in $B_s^0 \to J/\psi K^+K^-$ decays constitutes the current best measurement of this quantity, and can be combined with a ϕ_s measurement in $B_s^0 \to J/\psi\pi^+\pi^-$ decays by LHCb [20]. For ϕ_d, the experimental uncertainty of LHCb has approached the uncertainties of the measurements performed by the B factories, BaBar and Belle. So far, the measurements are statistically limited, and show a good agreement with the SM expectations. Though, a better experimental and theoretical precision is needed to pin down possible contributions from physics beyond the SM.

Acknowledgments

The author has been supported by the German Federal Ministry of Education and Research (BMBF).

References

1. N. Cabibbo, *Phys. Rev. Lett.* **10**, 531 (1963)
2. M. Kobayashi and T. Maskawa, *Prog. Phys.* **49**, no. 2 652 (1973)
3. A. B. Carter and A. I. Sanda, *Phys. Rev.* D **23**, 1567 (1981)
4. I. I. Y. Bigi and A. I. Sanda, *Nucl. Phys.* B **193**, 85 (1981)
5. J. Charles *et al.*, `arXiv:1501.05013`
6. S. Faller, M. Jung, R. Fleischer and T. Mannel, *Phys. Rev.* D **79**, 014030 (2009)
7. M. Jung, `arXiv:1212.4789`
8. K. De Bruyn and R. Fleischer, *JHEP* **1503**, 145 (2015)
9. P. Frings, U. Nierste and M. Wiebusch, `arXiv:1503.00859`
10. LHCb collaboration, A. A. Alves, Jr. *et al.*, *JINST* **3**, S08005 (2008)
11. LHCb collaboration, R. Aaij *et al.*, Int. J. Mod. Phys. A **30**, 1530022 (2015)
12. LHCb collaboration, R. Aaij *et al.*, LHCb-PAPER-2015-004, submitted to PRL
13. Heavy Flavor Averaging Group (HFAG), Y. Amhis *et al.*, `arXiv:1412.7515`, updated results and plots available at: `http://www.slac.stanford.edu/xorg/hfag/`
14. BaBar collaboration, B. Aubert *et al.*, *Phys. Rev.* D **79**, 072009 (2009)
15. Belle collaboration, I. Adachi *et al.*, *Phys. Rev. Lett.* **108**, 171802 (2012)
16. LHCb collaboration, R. Aaij *et al.*, *Eur. Phys. J.* C **72**, 2022 (2012)
17. LHCb collaboration, R. Aaij *et al.*, LHCb-PAPER-2015-005, submitted to JHEP
18. LHCb collaboration, R. Aaij *et al.*, *Phys. Rev. Lett.* **114**, 041801 (2015)
19. LHCb collaboration, R. Aaij *et al.*, *Phys. Lett.* B **742**, 38–49 (2015)
20. LHCb collaboration, R. Aaij *et al.*, *Phys. Lett.* B **736**, 186–195 (2014)

LATTICE INPUTS TO FLAVOR PHYSICS

M. DELLA MORTE
CP³-Origins and Danish IAS, Campusvej 55, 5230 Odense M, Denmark and
IFIC (CSIC), Calle Catedrático José Beltran, 2, 46980 Paterna, Valencia, Spain

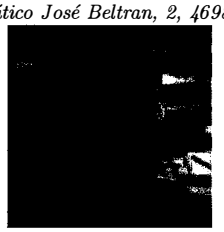

We review recent lattice results for quark masses and low-energy hadronic parameters relevant for flavor physics. We do that by describing the FLAG initiative, with emphasis on its scope and rating criteria. The emerging picture is that while for *light* quantities a large number of computations using different approaches exist, and this increases the overall confidence on the final averages/estimates, in the *heavy-light* case the field is less advanced and, with the exception of decay constants, only a few computations are available.
The precision reached for the *light* quantities is such that electromagnetic (EM) corrections, beyond the point-like approximation, are becoming relevant. We discuss recent computations of the spectrum based on direct simulations of QED+QCD. We also present theoretical developments for including EM effects in leptonic decays.
We conclude describing recent results for the $K \to \pi\pi$ transition amplitudes and prospects for tackling hadronic decays on the lattice.

1 Introduction and FLAG

After its discovery in 2012, the Higgs boson was believed to provide a portal to New Physics. This is even somehow assumed when formulating the hierarchy problem of the Standard Model (SM). However, this far, all measurements of the Higgs boson properties lie within 20% of the SM expectations, as reported by ATLAS [1] and CMS [2]. Instead, there is a number of 2-3 sigmas tensions in rare processes (see for example [3]), with the most prominent examples being in the angular analysis of the $B^0 \to K^{*0}\mu^+\mu^-$ decay [4] and in the enhancement of the $B \to D^{(*)}\tau\bar{\nu}_\tau$ decays[5] . Significances depend on treatment of several non-perturbative effects. Extrapolating to the future, (some of) these rare decays won't be so rare anymore. Belle 2 will report results from about 2018 and coexist with the LHC and High Luminosity (HL)-LHC, after Long Shutdown 3 in 2023-2025. Progress on the theoretical side is needed in many instances, to match the expected experimental accuracy.

There are many different groups, all over the world, using different lattice methods, that calculate hadronic matrix elements relevant for a number of weak decay processes of K, $D_{(s)}$, and $B_{(s)}$ mesons. With so many groups calculating similar matrix elements using different methods, and all providing phenomenologically relevant results with complete error budgets, it is useful to

try to produce global averages/estimates and to review virtues and shortcomings of the different computations in a transparent way, which should be accessible also to the non-experts. This is the goal of the FLAG initiative.

1.1 The FLAG review

The Flavor Lattice Averaging Group started its activity in 2010 focusing on light-quark quantities and providing averages from lattice results with comprehensive error budgets [6]. A second similar initiative was started at around the same time [7], focusing on both heavy- and light-quark quantities. The two groups joined for the second edition of the FLAG-review [8] (FLAG-2). One of the main goals of FLAG is to assess the reliability of systematic error estimates, in particular concerning continuum extrapolations, chiral extrapolations, finite volume effects and renormalization. This is done through quality criteria by assigning to each computation a symbol for each one of the systematics above. For example, the symbols and the criteria adopted for the light-quark quantities in FLAG-2 are:

- Chiral extrapolation:
  - ★ $M_{\pi,\mathrm{min}} < 200$ MeV
  - ○ 200 MeV $\leq M_{\pi,\mathrm{min}} \leq 400$ MeV
  - ■ 400 MeV $< M_{\pi,\mathrm{min}}$

  in addition it is assumed that the chiral extrapolation is done using at least three points.

- Continuum extrapolation:
  - ★ 3 or more lattice spacings, at least 2 points below 0.1 fm
  - ○ 2 or more lattice spacings, at least 1 point below 0.1 fm
  - ■ otherwise

  in addition it is assumed that the action is $O(a)$-improved (i.e. the discretization errors vanish quadratically with the lattice spacing).

- Finite-volume effects:
  - ★ $M_{\pi,\mathrm{min}} L > 4$ or at least 3 volumes
  - ○ $M_{\pi,\mathrm{min}} L > 3$ and at least 2 volumes
  - ■ otherwise.

- Renormalization (where applicable):
  - ★ non-perturbative
  - ○ 1-loop perturbation theory or higher with a reasonable estimate of truncation errors
  - ■ otherwise.

For heavy-light quantities the criteria are similar, with some additional ones concerning discretization effects and treatment of heavy quarks. In general criteria are expected to change in time and possibly become stricter as lattice computations reach new levels of accuracy. In the end, all the *published* (in journals) results with no red symbols enter the final estimates/averages. In some cases, the averaging procedure leads to results which in the opinion of the authors do not cover all uncertainties. In these cases, in order to stay on the conservative side, averages are replaced by estimates (or ranges), which are considered fair assessments of the current knowledge acquired on the lattice. These estimates are based on a critical (and to some extent subjective) analysis of the available information.

In detail, the FLAG-2 collaboration counted 28 members representing the major lattice groups in the world. Different Working Groups were in charge of reviewing different sets of quantities: Quark masses (WG1), V_{us}, V_{ud} (WG2), χPT Low Energy Constants (WG3), B_K (WG4), $f_{B_{(s)}}$, $f_{D_{(s)}}$, B_B (WG5, our group), $B_{(s)}$, D semileptonic and radiative decays (WG6), and finally α_s (WG6). In the following we will focus on the subset of quantities presented during the talk. A more recent update of lattice results concerning heavy-light quantities can be found

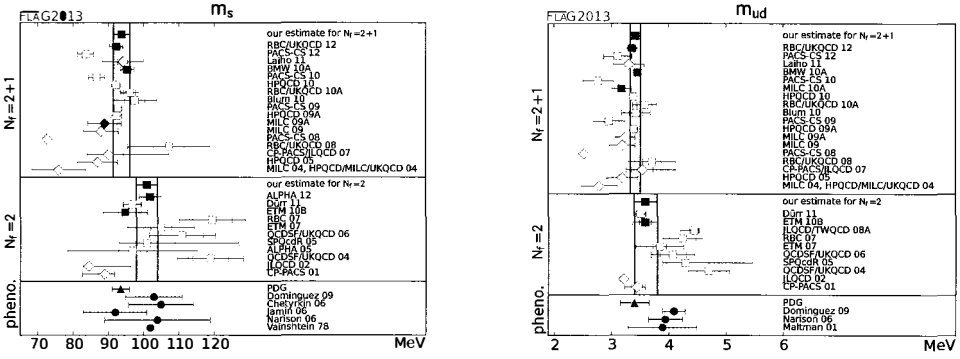

Figure 1 – Lattice results for the strange quark mass m_s and the average up and down quark mass in the $\overline{\text{MS}}$ scheme at the 2 GeV scale. The bottom panels represent non-lattice (and PDG) results. The FLAG-2 final estimates, including filled green points only, are given by the grey bands. Figure from [8].

in[9]. In Fig. 1 we show the results for the strange quark mass and the average up and down quark mass. That also serves the purpose of clarifying the difference between averages and estimates discussed above. Indeed, in the $N_f = 2+1$ case an error has been included in the final estimates accounting for the quenching of the charm quark (see[8] for details).

A second instructive example is taken from the V_{us}, V_{ud} working group. These CKM matrix element can be extracted from leptonic as well as semileptonic decays and therefore the WG2 focuses on kaon and pion decay constants as well as on form-factors relevant for the $K \to \pi\ell\nu$ transition. In particular the form-factor $f_+(0)$ at zero momentum transfer is relevant for phenomenology and for comparisons to χPT. In Fig. 2 we show the summary plots for these quantities from[8]. The results can be used to check the first row unitarity of the CKM matrix in

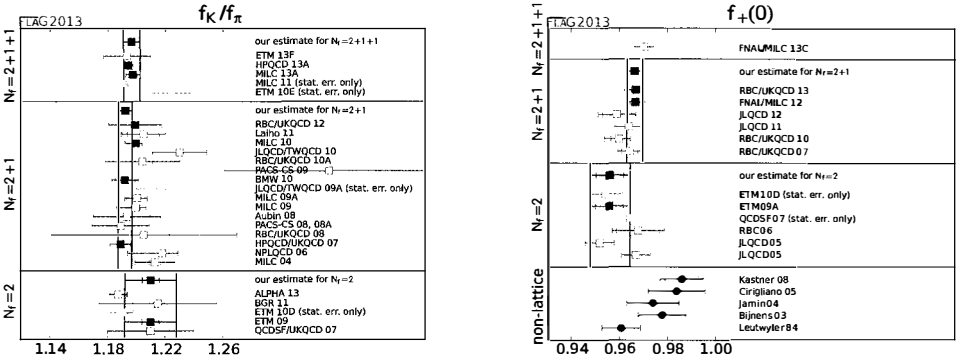

Figure 2 – Lattice results for $f_+(0)$ and the ratio of decay constant f_π/f_k. The FLAG-2 final estimates, including filled green points only, are given by the grey bands. The blue points are non-lattice estimates. Figure from[8].

the SM. Neglecting V_{ub}, the $N_f = 2+1$ estimates give $|V_{ud}|^2 + |V_{us}|^2 = 0.987(10)$. In addition, as discussed in the review, the consistency of leptonic and semi-leptonic determinations of $|V_{us}|$ is a check of the equality of the Fermi constant describing interactions among leptons, and the one describing interactions among leptons and quarks. This gives an important constraint on

possible modifications and extensions of the SM.

As mentioned, the current situation in the heavy-light sector is much less satisfactory. While some quantities like decay constants have been computed by a number of collaborations using a large variety of methods, for more complicated ones like form-factors, even for the "simplest" pseudoscalar to pseudoscalar, tree-level induced, semileptonic transitions, only a few determinations exist. In Fig. 3 we show the FLAG-2 summaries for $f_{B_{(s)}}$ and for the $B \to \pi \ell \nu$ form factor $f_+(q^2)$. For the latter only two computations, based on the same ensembles of configurations (but using different treatments of heavy quarks) exist. The situation is similar for other quantities like the $B_{B_{(s)}}$ mixing parameters (see [8]). Very much like experimental results, the confidence increases when several results from different collaborations/experiments become available. Significant progress in this directions is indeed expected from the lattice community in the next few years and will be visible already in the next FLAG review (expected for 2016).

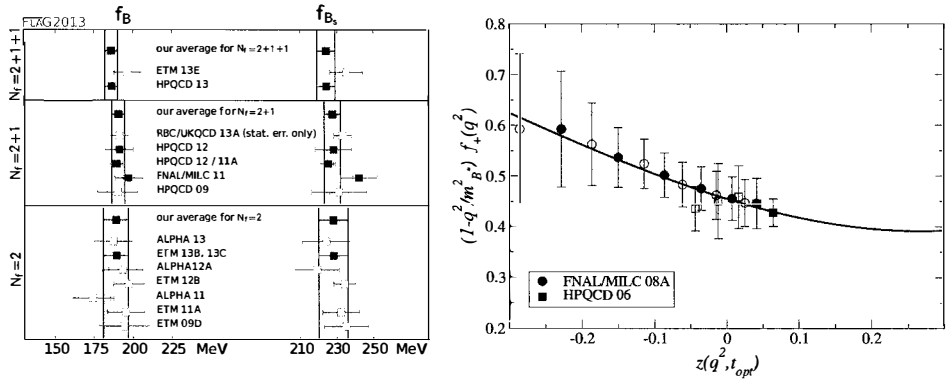

Figure 3 – Lattice results for $f_{B_{(s)}}$ (left) and for the $B \to \pi \ell \nu$ form factor $f_+(q^2)$ (right). The BCL parameterization [9] is used for the latter. The form-factor is expressed as a function of the z variable, obtained from q^2 through a conformal transformation depending on a real parameter t_{opt}. Figure from [8].

2 Inclusion of EM interactions in lattice QCD computations

Most of the lattice calculations concerning the properties of the light mesons are performed in the isospin limit of QCD and neglecting EM interactions. However, at the precision reached (e.g., the FLAG-2 estimates for the pion and kaon decay constants have an error $\leq 1\%$), they cannot be ignored anymore. For example, the EM corrections to the mass of the charged pions are estimated to be 4 - 5 MeV. The current approach mostly relies on χPT for correcting lattice data in order to include both EM and strong isospin breaking effects. Obviously it would be desirable to deal with the corresponding terms directly at the level of the simulations.

The BMW Collaboration reported in [11] about the first direct simulations of QED and QCD with four non-degenerate flavors, in a fully dynamical formulation. The goal is the first-principle computation of the neutron-proton mass difference, a tiny (0.14%) effect, which is crucial in explaining the Universe as we know it. This impressive computation is summarized in Fig. 4, where the results for the contour lines of the neutron-proton mass difference are given in terms of the $m_u - m_d = \delta m$ splitting and the EM coupling α (both normalized to their physical value) [a]. Within the same approach the authors of [11] also compute the mass splittings in the Σ, Ξ, Ξ_{cc} and D channels. They also provide an estimate of the numerical cost for such a

[a] The separation among EM and strong (QCD) isospin breaking effects is ambiguous by $O(\alpha \delta m)$. The prescription adopted in the LO (in isospin breaking) calculation in [11] fixes the EM correction to the mass difference $m_{\Sigma^-} - m_{\Sigma^+}$ to vanish.

computation. Considering the various extrapolations/interpolations in masses and couplings, the poor statistical signal for small values of the electromagnetic constant and the need for very large volumes, such a calculation turned out to be 300 times more expensive then their pure QCD computation of the spectrum of stable hadrons in the theory with two dynamical flavors.

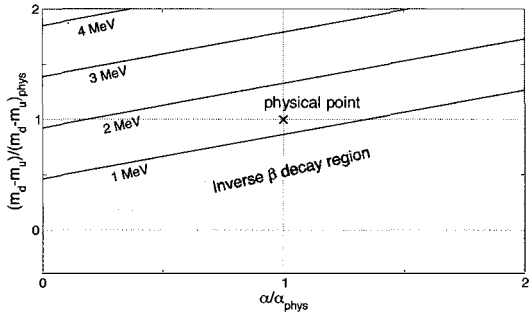

Figure 4 – Contour lines for the neutron-proton mass difference resulting from a direct QED+QCD computation with 1+1+1+1 (i.e., non-degenerate) dynamical flavors. Figure from [11].

Indeed finite volume effects are one of the main issue in simulating QED on a lattice because of the long-range nature of the EM interactions. In particular in a finite volume with periodic boundary conditions (in space) zero modes of the gauge field exist, which can not be eliminated through (standard) gauge-fixing conditions. In [11] the finite-volume zero mode is removed through a non-local constraint. In fact, a rigorous, all-order, proof of the renormalizability of the theory in this setup is still missing. An alternative could be to give a mass to the photon perhaps à la Stueckelberg [12] (and references therein). The massless limit (which would have to be taken numerically) is smooth in this case, at least in the continuum. On a similar line, it may be interesting to reconsider soft covariant gauges, as proposed and studied in [13] for non-Abelian gauge theories.

Additional issues, due to infrared divergences, must be taken into account when trying to include QED corrections into the computation of transition amplitudes. These are already present in the case of the decay constants (or better, the case of leptonic decays), as discussed in [14]. Let us consider the widths describing the $\pi^+ \to \ell^+\nu$ decay at $O(\alpha)$ and label them as Γ_i, with i the number of photons in the final state. It is well known that to obtain physical quantities radiative corrections from virtual and real photons must be combined. Therefore, at this order we are interested in Γ_0 and $\Gamma_1(\Delta E)$, where the energy of the photon in the final state, and in the rest frame of the π^+, is integrated from 0 to ΔE. For the sake of the argument on which the approach in [14] is based, it is sufficient to look at the subset of diagrams shown in Fig. 5, all contributing to Γ_0. The first (from the left) gives the pure QCD contribution and it is factorizable into an hadronic part (encoded in the matrix element of the axial current between the vacuum and a π^+, i.e., the decay constant) and a leptonic one, because a W boson is exchanged in between the two vertices. The second one is again factorizable and could be viewed as an $O(\alpha)$ correction to the decay constant, however it is infrared divergent. These divergences are removed by considering diagrams as the rightmost one and diagrams where a photon is emitted either from a quark line or the lepton line (diagrams contributing to Γ_1). But the third diagram, where a photon is exchanged between a quark and the lepton, is not factorizable, so there is really not much physical sense in "QED corrections to decay constants", rather one should consider corrections to the whole transition process.

In principle, both Γ_0 and $\Gamma_1(\Delta E)$ could be computed on the lattice, however the latter would be computationally very expensive. Instead, the authors of [14] propose to use the pointlike (pt in the following formulae) approximation to calculate $\Gamma_1(\Delta E)$. Values of ΔE around 10 - 20 MeV are experimentally accessible and for such soft photons the coupling to hadrons is conceivably

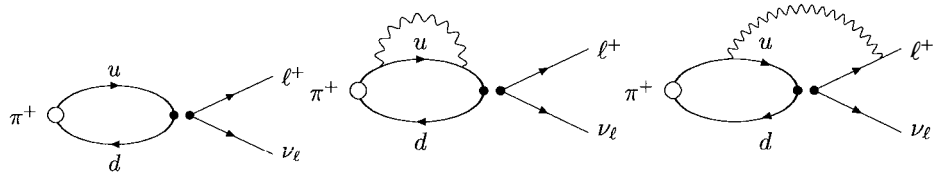

Figure 5 – Pure QCD (left) and examples of factorizable (middle) and non-factorizable (right) contributions to Γ_0 at O(α), see text. Figure from [14].

well described by the pointlike approximation[b]. In order to ensure an accurate cancellation of the infrared divergences, and since Γ_0 is computed on the lattice through numerical simulations, whereas $\Gamma_1(\Delta E)$ is computed in perturbation theory (and in the *pt*-approximation), it is convenient to introduce an intermediate step and re-write

$$\begin{aligned} \Gamma(\Delta E) &\equiv \Gamma_0 + \Gamma_1(\Delta E) = \left\{\Gamma_0 - \Gamma_0^{pt}\right\} + \left\{\Gamma_0^{pt} + \Gamma_1^{pt}(\Delta E)\right\} \\ &= \lim_{L\to\infty}\left\{\Gamma_0(L) - \Gamma_0^{pt}(L)\right\} + \left\{\Gamma_0^{pt} + \Gamma_1^{pt}(\Delta E)\right\}, \end{aligned} \tag{1}$$

where L is the linear extent of the lattice. As pointed out in [14], the small momenta contributions to $\Gamma_0(L)$ and $\Gamma_0^{pt}(L)$ are the same, hence the infrared divergences cancel in the difference. The same is true for the infinite volume combination $\Gamma_0^{pt} + \Gamma_1^{pt}(\Delta E)$, therefore the two terms in the brackets on the r.h.s of eq. 1 are separately infrared finite (and, incidentally, gauge invariant) and have a well defined infinite volume limit.
The correlation functions needed in the lattice computation of $\Gamma_0(L)$ and in particular the three-point functions required for the non-factorizable terms are explicitly constructed in [14]. The implementation of the method is computationally demanding, but seems within reach of present resources, and first studies should soon be performed.

3 Results and perspectives for hadronic decays on the lattice

Many phenomenologically interesting transitions involve hadronic two-body final states and the lattice would be extremely useful in providing first-principle computations which would serve in clarifying existing tensions (e.g., the one mentioned in the angular analysis of $B^0 \to K^{*0}(K\pi)\mu^+\mu^-$ by LHCb), or give an ab-initio explanations of long-standing puzzles such as the $\Delta I = 1/2$ rule and the value of ε'/ε in $K \to \pi\pi$ decays. However, there is no simple relation among Euclidean correlators and the desired Minkowski-space transition matrix elements, a fact which is known as the "Maiani-Testa no-go theorem" [15]. A solution to this problem, for the case where one two-particle state only (say, $\pi\pi$) is kinematically accessible or coupled to the initial state (K), was developed by Lüscher and Lellouch in a series of papers [16,17,18,19]. In a first step a relation is established, in Minkowski-space, between the finite volume dependence of the energy levels of two-particle states ($\pi\pi$) and the infinite-volume S-matrix and phase shifts. Since energy levels are directly computable in Euclidean-space, this allows to measure elements of the S-matrix on the lattice. The kaon is introduced in a second step and it is coupled to the two-pion states through a small, perturbative, Weak-Hamiltonian term H_W. The lattice volume

[b] The Lagrangian describing the interaction of a pointlike meson with the leptons is non-renormalizable by power counting, very much like the chiral Lagrangian, which could indeed have also been used here (although more complicated from the analytical point of view when considered in a finite volume). For the process described, however, these interactions are inserted at tree-level only and therefore there is no need for additional counterterms. The only requirement for the method to work is that the contributions from small momenta are the same in the full theory and in its approximation. Still, for larger values of ΔE some approximations may be more accurate than others.

has to be tuned such that one of the two-pion energy levels gets degenerate with the kaon, that is what is usually called "matching the kinematics". At this point degenerate perturbation theory can be used, and as in the first step, a relation (in terms of "Euclidean" quantities) is established among the perturbative corrections to the two-particle energy levels in finite volume and the perturbative corrections to the infinite-volume S-matrix, which is to say a relation among the finite- and infinite-volume versions of the $\langle \pi\pi | H_W | K \rangle$ matrix element. The latter then gives the $K \to \pi\pi$ transition amplitude.

The approach has been generalized in [20,21,22] to the case of multiple strongly-coupled decay channels into two scalar particles and to the case of external currents injecting arbitrary four-momentum as well as angular momentum. These are first steps towards lattice computations of amplitudes for processes such as $D \to \pi\pi$ and $D \to K\overline{K}$ and towards study of meson decays as $B^0 \to K^{*0}(K\pi)\mu^+\mu^-$.

In the case of the $K \to \pi\pi$ transitions, numerical results became recently available with good control over all the systematics including continuum limit extrapolations. These are outstanding results of many years of efforts and attempts. In [23] the amplitude A_2 for a kaon to decay into two pions with isospin $I = 2$ has been computed on two lattices with resolutions $a = 0.11$ fm and $a = 0.084$ fm respectively. The calculations have been performed using 2+1 flavors of domain wall fermions with pions at the physical mass and $L \approx 5$ fm. The matrix elements of three different operators have to be combined in this case and the final result, extrapolated to the continuum limit, reads

$$\mathrm{Re}A_2 = 1.50(4)_{\mathrm{stat}}(14)_{\mathrm{syst}} \times 10^{-8}\ \mathrm{GeV}\,, \tag{2}$$

$$\mathrm{Im}A_2 = -6.99(20)_{\mathrm{stat}}(84)_{\mathrm{syst}} \times 10^{-13}\ \mathrm{GeV}\,, \tag{3}$$

which is well consistent with both the very accurate (but different) experimental numbers for $\mathrm{Re}A_2$ from charged and neutral kaon decays. The error on the lattice value is dominated by systematics, in particular by the uncertainty in the perturbative evaluation of the Wilson coefficients, currently known at NLO.

The computation of the A_0 amplitude is much more demanding as 10 operators [24], including QCD penguins producing quark disconnected diagrams, need to be considered [c]. However, after the conference, two independent preliminary results [26,27] appeared, both using a single lattice spacing and both reporting on a computation of the $\Delta I = 1/2$ amplitude A_0.

4 Conclusions

Flavor Physics is still playing a prominent role in the indirect search for New Physics. At the same time, and while finalizing the analysis of LHC run I data, new signals from direct searches may emerge (as for example in the search for resonances presented in [28], and interpreted within composite dynamics models in [29]), which will hopefully be confirmed by run II.

The picture provided here is obviously incomplete and the result of our taste and interests, but we hope to have given a flavor of the important role, the main challenges and the exciting future directions and perspectives for lattice gauge theories within Flavor Physics. As the keywords seem to be precise and rare, the lattice community is tackling all subleading effects (e.g., isospin breaking) and theoretical obstructions (e.g. multi-hadron decay channels) to give an indispensable contribution to the quest for New Physics.

Acknowledgments

I thank the organizers of Moriond EW 2015 for the invitation to this very interesting and enjoyable conference. I am grateful to my colleagues in the FLAG collaboration for all their work

[c] Actually 12 operators appear, but Q_{11} and Q_{12} are usually neglected at this level of accuracy since their contributions are suppressed by a factor m_π^2/m_K^2, as discussed in [25].

in completing the corresponding review. In particular I wish to thank the members of the Heavy Quark working groups, Aida X. El-Khadra, Yasumichi Aoki, Enrico Lunghi, Carlos Pena, Junko Shigemitsu and Ruth Van de Water. I thank Tadeusz Janowski, Amarjit Soni, Nazario Tantalo, Uli Haisch and Sebastian Jäger for useful discussions and Francesco Sannino for a critical reading of the manuscript. This work was partially supported by the Spanish Minister of Education and Science, project RyC-2011-08557, and by the Danish National Research Foundation under the grant n. DNRF:90.

References

1. The ATLAS Collaboration, ATLAS-CONF-2015-007, ATLAS-COM-CONF-2015-011, these proceedings.
2. The CMS Collaboration, Eur.Phys.J. C75 (2015) 5, 212, arXiv:1412.8662 [hep-ex].
3. W. Altmannshofer and D. M. Straub, arXiv:1411.3161 [hep-ph].
4. The LHCb Collaboration, LHCb-CONF-2015-002, these proceedings.
5. J. P. Lees *et al.* [BaBar Collaboration], Phys. Rev. Lett. **109** (2012) 101802 [arXiv:1205.5442 [hep-ex]].
6. G. Colangelo, S. Durr, A. Juttner, L. Lellouch, H. Leutwyler, V. Lubicz, S. Necco and C. T. Sachrajda *et al.*, Eur. Phys. J. C **71** (2011) 1695 [arXiv:1011.4408 [hep-lat]].
7. J. Laiho, E. Lunghi and R. S. Van de Water, Phys. Rev. D **81** (2010) 034503 [arXiv:0910.2928 [hep-ph]].
8. S. Aoki, Y. Aoki, C. Bernard, T. Blum, G. Colangelo, M. Della Morte, S. Drr and A. X. El Khadra *et al.*, Eur. Phys. J. C **74** (2014) 2890 [arXiv:1310.8555 [hep-lat]].
9. C. M. Bouchard, PoS LATTICE **2014** (2015) 002 [arXiv:1501.03204 [hep-lat]].
10. C. Bourrely, I. Caprini and L. Lellouch, Phys. Rev. D **79** (2009) 013008 [Phys. Rev. D **82** (2010) 099902] [arXiv:0807.2722 [hep-ph]].
11. S. Borsanyi, S. Durr, Z. Fodor, C. Hoelbling, S. D. Katz, S. Krieg, L. Lellouch and T. Lippert *et al.*, Science **347** (2015) 1452 [arXiv:1406.4088 [hep-lat]].
12. H. Ruegg and M. Ruiz-Altaba, Int. J. Mod. Phys. A **19** (2004) 3265 [hep-th/0304245].
13. D. S. Henty *et al.* [UKQCD Collaboration], Phys. Rev. D **54** (1996) 6923 [hep-lat/9607014].
14. N. Carrasco, V. Lubicz, G. Martinelli, C. T. Sachrajda, N. Tantalo, C. Tarantino and M. Testa, Phys. Rev. D **91** (2015) 7, 074506 [arXiv:1502.00257 [hep-lat]].
15. L. Maiani and M. Testa, Phys. Lett. B **245** (1990) 585.
16. M. Luscher, Commun. Math. Phys. **105** (1986) 153.
17. M. Luscher, Nucl. Phys. B **354** (1991) 531.
18. M. Luscher, Nucl. Phys. B **364** (1991) 237.
19. L. Lellouch and M. Luscher, Commun. Math. Phys. **219** (2001) 31 [hep-lat/0003023].
20. M. T. Hansen and S. R. Sharpe, Phys. Rev. D **86** (2012) 016007
21. R. A. Briceno and Z. Davoudi, Phys. Rev. D **88** (2013) 9, 094507 [arXiv:1204.1110 [hep-lat]].
22. R. A. Briceno, M. T. Hansen and A. Walker-Loud, Phys. Rev. D **91** (2015) 3, 034501 [arXiv:1406.5965 [hep-lat]].
23. T. Blum, P. A. Boyle, N. H. Christ, J. Frison, N. Garron, T. Janowski, C. Jung and C. Kelly *et al.*, Phys. Rev. D **91** (2015) 7, 074502 [arXiv:1502.00263 [hep-lat]].
24. G. Buchalla, A. J. Buras and M. E. Lautenbacher, Rev. Mod. Phys. **68** (1996) 1125 [hep-ph/9512380].
25. S. Bertolini, J. O. Eeg and M. Fabbrichesi, Nucl. Phys. B **449** (1995) 197 [hep-ph/9409437].
26. Z. Bai, T. Blum, P. A. Boyle, N. H. Christ, J. Frison, N. Garron, T. Izubuchi and C. Jung *et al.*, arXiv:1505.07863 [hep-lat].
27. N. Ishizuka, K.-I. Ishikawa, A. Ukawa and T. Yoshi, arXiv:1505.05289 [hep-lat].
28. G. Aad *et al.* [ATLAS Collaboration], arXiv:1506.00962 [hep-ex].
29. D. B. Franzosi, M. T. Frandsen and F. Sannino, arXiv:1506.04392 [hep-ph].

Explaining the LHC flavour anomalies

ANDREAS CRIVELLIN
CERN Theory Division, CH–1211 Geneva 23, Switzerland

The LHC observed deviations from the Standard Model (SM) in the flavour sector: LHCb found a $4.3\,\sigma$ discrepancy compared to the SM in $b \to s\mu\mu$ transitions and CMS reported a non-zero measurement of $h \to \mu\tau$ with a significance of $2.4\,\sigma$. Here we discuss how these deviations from the SM can be explained, focusing on two models with gauged $L_\mu - L_\tau$ symmetry. The first model contains two scalar doublets and vector-like quarks while the second one employs three scalar doublets but does not require vector-like fermions. In both models, interesting correlations between $b \to s\mu\mu$ transitions, $h \to \mu\tau$, and $\tau \to 3\mu$ arise.

1 Introduction

The LHC completed the SM by discovering the Brout–Englert–Higgs particle [1,2]. While no significant direct evidence for physics beyond the SM has been found, the LHC did observe 'hints' for new physics (NP) in the flavor sector, which are sensitive to virtual effects of new particles and can be used as guidelines towards specific NP models: $h \to \mu\tau$, $B \to K^*\mu^+\mu^-$, $B_s \to \phi\mu^+\mu^-$ and $R(K) = B \to K\mu^+\mu^-/B \to Ke^+e^-$. It is therefore interesting to examine if a specific NP model can explain these four anomalies simultaneously. In Refs. [3,4], two variants of such a model were presented, which we want to review here.

LHCb reported deviations from the SM predictions[5,6] (mainly in an angular observable called P_5'[7]) in $B \to K^*\mu^+\mu^-$ [8] with a significance of 2–3 σ. In addition, the measurement of $B_s \to \phi\mu\mu$ disagrees with the SM predictions by about $3\,\sigma$ [9,10]. This discrepancy can be explained in a model independent approach by rather large contributions to the Wilson coefficient C_9 [11,12,9], i.e. an operator $(\bar{s}\gamma_\alpha P_L b)(\bar{\mu}\gamma^\alpha\mu)$, which can be achieved in models with an additional heavy neutral Z' gauge boson [13,14,15,16,17]. Furthermore, LHCb [18] recently found indications for the violation of lepton flavour universality in B meson decays

$$R(K) = \frac{B \to K\mu^+\mu^-}{B \to Ke^+e^-} = 0.745^{+0.090}_{-0.074} \pm 0.036\,, \tag{1}$$

which disagrees from the theoretically rather clean SM prediction $R_K^{\rm SM} = 1.0003 \pm 0.0001$ [19] by $2.6\,\sigma$. A possible explanation is again a NP contributing to $C_9^{\mu\mu}$ involving muons, but not electrons [20,21,22]. Interestingly, the value for C_9 required to explain $R(K)$ is of the same order

as the one required by $B \to K^* \mu^+ \mu^-$ [23,24]. The global fit to the $b \to s\mu\mu$ data presented at this conference gives a $4.3\,\sigma$ better fit to data for the assumption of NP in $C_9^{\mu\mu}$ only, compared to the SM fit [25].

Concerning Higgs decays, CMS measured a lepton-flavour violating (LFV) channel [26] $\mathrm{Br}[h \to \mu\tau] = \left(0.84^{+0.39}_{-0.37}\right)$ which disagrees from the SM (where this decay is forbidden) by about $2.4\,\sigma$. Most attempts to explain this decay rely on models with an extended Higgs sector [27,28,29,30,31]. One particular interesting solution employs a two-Higgs-doublet model (2HDM) with gauged $L_\mu - L_\tau$ [32].

2 The models

Our models under consideration are multi-Higgs-doublet models with a gauged $U(1)_{L_\mu - L_\tau}$ symmetry [32].[a] The $L_\mu - L_\tau$ symmetry with the gauge coupling g' is broken spontaneously by the vacuum expectation value (VEV) of a scalar Φ with $Q^{\Phi}_{L_\mu - L_\tau} = 1$, leading to the Z' mass $m_{Z'} = \sqrt{2} g' \langle \Phi \rangle \equiv g' v_\Phi$ and Majorana masses for the right-handed neutrinos.[b]

In both models at least two Higgs doublets are introduced which break the electroweak symmetry: Ψ_1 with $Q^{\Psi_1}_{L_\mu - L_\tau} = -2$ and Ψ_2 with $Q^{\Psi_2}_{L_\mu - L_\tau} = 0$. Therefore, Ψ_2 gives masses to quarks and leptons while Ψ_1 couples only off-diagonally to $\tau\mu$:

$$\mathcal{L}_Y \supset -\bar{\ell}_f Y^\ell_i \delta_{fi} \Psi_2 e_i - \xi_{\tau\mu} \bar{\ell}_3 \Psi_1 e_2 - \overline{Q}_f Y^u_{fi} \tilde{\Psi}_2 u_i - \overline{Q}_f Y^d_{fi} \Psi_2 d_i + \text{h.c.} \tag{2}$$

Here Q (ℓ) is the left-handed quark (lepton) doublet, u (e) is the right-handed up quark (charged lepton) and d the right-handed down quark while i and f label the three generations. The scalar potential is the one of a $U(1)$-invariant 2HDM [37] with additional couplings to the SM-singlet Φ, which most importantly generate the doublet-mixing term

$$V(\Psi_1, \Psi_2, \Phi) \supset 2\lambda \Phi^2 \Psi_2^\dagger \Psi_1 \to \lambda v_\Phi^2 \Psi_2^\dagger \Psi_1 \equiv m_3^2 \Psi_2^\dagger \Psi_1 \,,$$

that induces a small vacuum expectation value for Ψ_1 [32]. We define $\tan\beta = \langle \Psi_2 \rangle / \langle \Psi_1 \rangle$ and α is the usual mixing angle between the neutral CP-even components of Ψ_1 and Ψ_2 (see for example [37]). We neglect the additional mixing of the CP-even scalars with $\mathrm{Re}[\Phi]$.

Quarks and gauge bosons have standard type-I 2HDM couplings to the scalars. The only deviations are in the lepton sector: while the Yukawa couplings $Y^\ell_i \delta_{fi}$ of Ψ_2 are forced to be diagonal due to the $L_\mu - L_\tau$ symmetry, $\xi_{\tau\mu}$ gives rise to an off-diagonal entry in the lepton mass matrix:

$$m^\ell_{fi} = \frac{v}{\sqrt{2}} \begin{pmatrix} y_e \sin\beta & 0 & 0 \\ 0 & y_\mu \sin\beta & 0 \\ 0 & \xi_{\tau\mu} \cos\beta & y_\tau \sin\beta \end{pmatrix} . \tag{3}$$

It is this τ–μ entry that leads to the LFV couplings of h and Z' of interest to this letter. The lepton mass basis is obtained by simple rotations of (μ_R, τ_R) and (μ_L, τ_L) with the angles θ_R and θ_L, respectively:

$$\sin\theta_R \simeq \frac{v}{\sqrt{2} m_\tau} \xi_{\tau\mu} \cos\beta \,, \qquad \frac{\tan\theta_L}{\tan\theta_R} = \frac{m_\mu}{m_\tau} \ll 1 \,. \tag{4}$$

The angle θ_L is automatically small and will be neglected in the following.[c] A non-vanishing angle θ_R not only gives rise to the LFV decay $h \to \mu\tau$ due to the coupling

$$\frac{m_\tau}{v} \frac{\cos(\alpha - \beta)}{\cos(\beta)\sin(\beta)} \sin(\theta_R)\cos(\theta_R) \bar{\tau} P_R \mu h \equiv \Gamma^h_{\tau\mu} \bar{\tau} P_R \mu h \,, \tag{5}$$

[a] The abelian symmetry $U(1)_{L_\mu - L_\tau}$ is an anomaly-free global symmetry within the SM [33], and also a good zeroth-order approximation for neutrino mixing with a quasi-degenerate mass spectrum, predicting a maximal atmospheric and vanishing reactor neutrino mixing angle [34]. Breaking $L_\mu - L_\tau$ is mandatory for a realistic neutrino sector, and such a breaking can also induce charged LFV processes, such as $\tau \to 3\mu$ [35,36] and $h \to \mu\tau$ [32].

[b] Neutrino masses arise via seesaw with close-to-maximal atmospheric mixing and quasi-degenerate masses [32].

[c] Choosing $Q_{L_\mu - L_\tau} = +2$ for Ψ_2 would essentially exchange $\theta_L \leftrightarrow \theta_R$ [32], with little impact on our study.

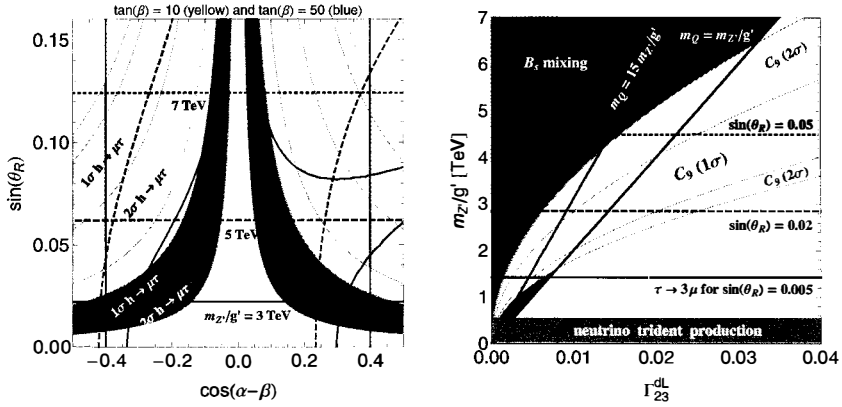

Figure 1 – Left: Allowed regions in the $\cos(\alpha-\beta)$–$\sin(\theta_R)$ plane. The blue (light blue) region corresponds to the 1σ (2σ) region of the CMS measurement of $h \to \mu\tau$ for $\tan\beta = 50$; yellow stands for $\tan\beta = 10$. The (dashed) red contours mark deviations of $h \to \tau\tau$ by 10% compared to the SM for $\tan\beta = 50$ (10). The vertical green lines illustrate the naive LHC limit $|\cos(\alpha-\beta)| \leq 0.4$, horizontal lines denote the 90% C.L. limit on $\tau \to 3\mu$ via Z' exchange. Right: Allowed regions for model 1 in the Γ^{dL}_{23}-$m_{Z'}/g'$ plane from $b \to s\mu^+\mu^-$ data (yellow) and B_s–$\overline{B}_s$ mixing (blue). For B_s–$\overline{B}_s$ mixing, (light) blue corresponds to ($m_Q = 15 m_{Z'}/g'$) $m_Q = m_{Z'}/g'$. The horizontal lines denote the lower bounds on $m_{Z'}/g'$ from $\tau \to 3\mu$ for $\sin(\theta_R) = 0.05,\ 0.02,\ 0.005$. The gray region is excluded by neutrino trident production.

in the Lagrangian, but also leads to off-diagonal Z' couplings to right-handed leptons

$$g' Z'_\nu (\overline{\mu}, \overline{\tau}) \begin{pmatrix} \cos 2\theta_R & \sin 2\theta_R \\ \sin 2\theta_R & -\cos 2\theta_R \end{pmatrix} \gamma^\nu P_R \begin{pmatrix} \mu \\ \tau \end{pmatrix}, \tag{6}$$

while the left-handed couplings are to a good approximation flavour conserving. $m_{Z'}/g'$ needs to be in the TeV range in order to suppress $\tau \to 3\mu$ if we want to explain $h \to \mu\tau$ [32] (see Fig. 1 (left)), which gives stronger bounds than neutrino trident production [15]. In order to explain the observed anomalies in the B meson decays, a coupling of the Z' to quarks is required as well, not inherently part of $L_\mu - L_\tau$ models.

3 Model 1: vector-like quarks

In order to couple the Z' to quarks we follow Ref. [15] and generate effective couplings via heavy vector-like quarks [38] charged under $L_\mu - L_\tau$. As a result, the couplings of the Z' to quarks are in principle free parameters and can be parametrized as:

$$g' \left(\bar{d}_i \gamma^\mu P_L d_j Z'_\mu \Gamma^{dL}_{ij} + \bar{d}_i \gamma^\mu P_R d_j Z'_\mu \Gamma^{dR}_{ij} \right). \tag{7}$$

In the limit of decoupled vector-like quarks with the quantum numbers of right-handed quarks, only C_9 is generated, giving a very good fit to data. The results are shown in the right plot of Fig. 1 depicting that for small values of Γ^L_{sb} and θ_R, $b \to s\mu^+\mu^-$ data can be explained without violating bounds from B_s–$\overline{B}_s$ mixing or $\tau \to 3\mu$. In the left plot of Fig. 2 the correlations of $b \to s\mu^+\mu^-$ and $h \to \mu\tau$ with $\tau \to 3\mu$ are shown, depicting that consistency with $\tau \to 3\mu$ requires large values of $\tan\beta$ (not being in conflict with any data as the decoupling limit is a type I model) and future searches for $\tau \to 3\mu$ are promising to yield positive results. While this model predict tiny branching ratios for lepton-flavour-violating B decays, these branching ratios can be sizable in generic Z' models in the presence of fine tuning in the B_s–$\overline{B}_s$ system [39].

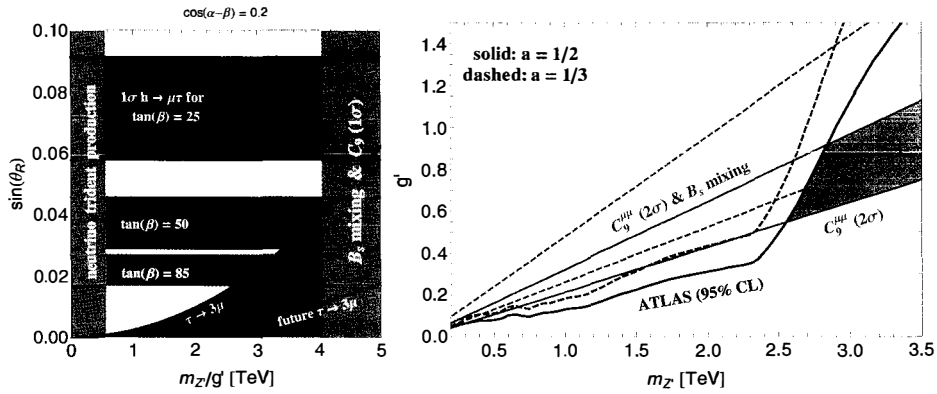

Figure 2 – Left: Allowed regions for model 1 in the $m_{Z'}/g'$–$\sin(\theta_R)$ plane: the horizontal stripes correspond to $h \to \mu\tau$ (1σ) for different $\tan\beta$ and $\cos(\alpha - \beta) = 0.2$, (light) blue stands for (future) $\tau \to 3\mu$ limits at 90% C.L. The gray regions are excluded by neutrino trident production or B_s–$\overline{B}_s$ mixing in combination with the $1\,\sigma$ range for C_9. Right: Limits for model 2 on $q\bar{q} \to Z' \to \mu\bar{\mu}$ from ATLAS (black, allowed region down right) and the $2\,\sigma$ limits on $C_9^{\mu\mu}$ to accommodate $b \to s\mu\mu$ data (allowed regions inside the red cone). Solid (dashed) lines are for $a = 1/2$ ($1/3$). For $a = 1/2$, the green shaded region is allowed (similar for $a = 1/3$ using the dashed bounds).

4 Model 2: horizontal quark charges

In order to avoid the introduction of vector-like quarks, one can assign flavour-dependent charges to baryons as well [4]. Here, the first two generations should have the same charges in order to avoid very large effects in K–$\overline{K}$ or D–$\overline{D}$ mixing, generated otherwise unavoidably due to the breaking of the symmetry necessary to generate the measured Cabibbo angle of the CKM matrix. If we require in addition the absence of anomalies, we arrive at the following charge assignment for baryons $Q'(B) = (-a, -a, 2a)$, while leptons are still assigned $L_\mu - L_\tau$. Here $a \in \mathcal{Q}$ is a free parameter of the model with important phenomenological implications. In this model, one additional Higgs doublet, which breaks the flavour symmetry in the quark sector, is required compared to the model with vector-like quarks. In case the mixing among the doublets is small, the correlations among $h \to \mu\tau$, $b \to s\mu^+\mu^-$ and $\tau \to 3\mu$ are similar as in the model with vector-like quarks discussed in the last subsection (left plot of Fig. 2).

The low-energy phenomenology is rather similar to the one of the model with vector-like quarks (model 1), but the contributions to B_s–$\overline{B}_s$ mixing are directly correlated to B_d–$\overline{B}_d$ and K–$\overline{K}$ mixing, because all flavour violation is due to CKM factors. (These constraints are evaded for $a \leq 1$.) However, the implications concerning direct LHC searches are very different, as the Z' boson couples to quarks of the first generation and can be directly produced on-shell as a resonance in $p\bar{p}$ collisions. The resulting strong bounds are shown in right plot of Fig. 2, where they are compared to the allowed regions from B_s–$\overline{B}_s$ mixing and $b \to s\mu^+\mu^-$ data for different values of a.

5 Conclusions

In these proceedings we reviewed two variants of a model with a gauged $L_\mu - L_\tau$ symmetry which can explain all LHC anomalies in the flavour sector simultaneously: 1) a 2HDM with effective $Z'\bar{s}b$ couplings induced by heavy vector-like quarks, 2) a 3HDM with horizontal charges for baryons. The models can account for the deviations from the SM in $b \to s\mu^+\mu^-$ data and $h \to \mu\tau$ simultaneously, giving also the desired effect in $R(K)$. Due to the small values of the τ–μ mixing angle θ_R, sufficient to account for $h \to \mu\tau$, the Z' contributions to $\tau \to 3\mu$ are not

in conflict with present bounds for large $\tan\beta$ in wide rages of parameter space. Interestingly, $b \to s\mu^+\mu^-$ data combined with B_s–$\overline{B}_s$ put a upper limit on $m_{Z'}/g'$ resulting in a lower limit on $\tau \to 3\mu$ if $\mathrm{Br}[h \to \mu\tau] \neq 0$: for lower values of $\tan\beta$ the current experimental bounds are reached and future sensitivities will allow for a more detailed exploration of the allowed parameter space. The possible range for the $L_\mu - L_\tau$ breaking scale further implies the masses of the Z' and the right-handed neutrinos to be at the TeV scale, potentially testable at the LHC with interesting additional consequences for LFV observables. While the low energy phenomenology of both models is rather similar, the variant with horizontal charges for baryons predicts sizable Z' production rates testable at the next LHC run.

Acknowledgments

We thank the organizers of the invitation to *Moriond EW* and for the opportunity to present these results. A.C. is supported by a Marie Curie Intra-European Fellowship of the European Community's 7th Framework Programme under contract number (PIEF-GA-2012-326948).

References

1. Georges Aad et al. Observation of a new particle in the search for the Standard Model Higgs boson with the ATLAS detector at the LHC. *Phys.Lett.*, B716:1–29, 2012.
2. Serguei Chatrchyan et al. Observation of a new boson at a mass of 125 GeV with the CMS experiment at the LHC. *Phys.Lett.*, B716:30–61, 2012.
3. Andreas Crivellin, Giancarlo D'Ambrosio, and Julian Heeck. Explaining $h \to \mu^\pm\tau^\mp$, $B \to K^*\mu^+\mu^-$ and $B \to K\mu^+\mu^-/B \to Ke^+e^-$ in a two-Higgs-doublet model with gauged $L_\mu - L_\tau$. *Phys.Rev.Lett.*, 114:151801, 2015.
4. Andreas Crivellin, Giancarlo D'Ambrosio, and Julian Heeck. Addressing the LHC flavor anomalies with horizontal gauge symmetries. *Phys.Rev.*, D91:075006, 2015.
5. U. Egede, T. Hurth, J. Matias, M. Ramon, and W. Reece. New observables in the decay mode $B_{(d)} \to K^{*0}\ell^+\ell^-$. *JHEP*, 0811:032, 2008.
6. Wolfgang Altmannshofer, Patricia Ball, Aoife Bharucha, Andrzej J. Buras, David M. Straub, et al. Symmetries and Asymmetries of $B \to K^*\mu^+\mu^-$ Decays in the Standard Model and Beyond. *JHEP*, 0901:019, 2009.
7. Sebastien Descotes-Genon, Tobias Hurth, Joaquim Matias, and Javier Virto. Optimizing the basis of $B \to K^*\ell^+\ell^-$ observables in the full kinematic range. *JHEP*, 1305:137, 2013.
8. R Aaij et al. Measurement of Form-Factor-Independent Observables in the Decay $B^0 \to K^{*0}\mu^+\mu^-$. *Phys.Rev.Lett.*, 111(19):191801, 2013.
9. Ronald R. Horgan, Zhaofeng Liu, Stefan Meinel, and Matthew Wingate. Calculation of $B^0 \to K^{*0}\mu^+\mu^-$ and $B_s^0 \to \phi\mu^+\mu^-$ observables using form factors from lattice QCD. *Phys.Rev.Lett.*, 112:212003, 2014.
10. R.R. Horgan, Z. Liu, S. Meinel, and M. Wingate. Rare B decays using lattice QCD form factors. 2015.
11. Sebastien Descotes-Genon, Joaquim Matias, and Javier Virto. Understanding the $B \to K^*\mu^+\mu^-$ Anomaly. *Phys.Rev.*, D88(7):074002, 2013.
12. Wolfgang Altmannshofer and David M. Straub. New physics in $B \to K^*\mu\mu$? *Eur.Phys.J.*, C73(12):2646, 2013.
13. Rhorry Gauld, Florian Goertz, and Ulrich Haisch. On minimal Z' explanations of the $B \to K^*\mu^+\mu^-$ anomaly. *Phys.Rev.*, D89:015005, 2014.
14. Andrzej J. Buras, Fulvia De Fazio, and Jennifer Girrbach. 331 models facing new $b \to s\mu^+\mu^-$ data. *JHEP*, 1402:112, 2014.
15. Wolfgang Altmannshofer, Stefania Gori, Maxim Pospelov, and Itay Yavin. Quark flavor transitions in $L_\mu - L_\tau$ models. *Phys.Rev.*, D89(9):095033, 2014.

16. Christoph Niehoff, Peter Stangl, and David M. Straub. Violation of lepton flavour universality in composite Higgs models. 2015.
17. Sierra D. Aristizabal, Florian Staub, and Avelino Vicente. Shedding light on the $b \dashrightarrow s$ anomalies with a dark sector. 2015.
18. Roel Aaij et al. Test of lepton universality using $B^+ \dashrightarrow K^+\ell^+\ell^-$ decays. *Phys.Rev.Lett.*, 113(15):151601, 2014.
19. Christoph Bobeth, Gudrun Hiller, and Giorgi Piranishvili. Angular distributions of $B \to K\ell\ell$ decays. *JHEP*, 0712:040, 2007.
20. Rodrigo Alonso, Benjamin Grinstein, and Jorge Martin Camalich. $SU(2) \times U(1)$ gauge invariance and the shape of new physics in rare B decays. *Phys.Rev.Lett.*, 113(24):241802, 2014.
21. Gudrun Hiller and Martin Schmaltz. R_K and future $b \to s\ell\ell$ physics beyond the standard model opportunities. *Phys.Rev.*, D90(5):054014, 2014.
22. Diptimoy Ghosh, Marco Nardecchia, and S.A. Renner. Hint of Lepton Flavour Non-Universality in B Meson Decays. *JHEP*, 1412:131, 2014.
23. T. Hurth, F. Mahmoudi, and S. Neshatpour. Global fits to $b \to s\ell\ell$ data and signs for lepton non-universality. *JHEP*, 1412:053, 2014.
24. Wolfgang Altmannshofer and David M. Straub. State of new physics in $b \dashrightarrow s$ transitions. 2014.
25. Wolfgang Altmannshofer and David M. Straub. Implications of $b \dashrightarrow s$ measurements. 2015.
26. Vardan Khachatryan et al. Search for lepton-flavour-violating decays of the Higgs boson. 2015.
27. Avital Dery, Aielet Efrati, Yosef Nir, Yotam Soreq, and Vasja Susi. Model building for flavor changing Higgs couplings. *Phys.Rev.*, D90:115022, 2014.
28. Miguel D. Campos, A. E. Cárcamo Hernández, Heinrich Päs, and Erik Schumacher. Higgs $\to \mu\tau$ as an indication for S_4 flavor symmetry. 2014.
29. Alejandro Celis, Vincenzo Cirigliano, and Emilie Passemar. Disentangling new physics contributions in lepton flavour violating tau decays. 2014.
30. D. Aristizabal Sierra and A. Vicente. Explaining the CMS Higgs flavor violating decay excess. *Phys.Rev.*, D90:115004, 2014.
31. Chao-Jung Lee and Jusak Tandean. Lepton-Flavored Scalar Dark Matter with Minimal Flavor Violation. *JHEP*, 1504:174, 2015.
32. Julian Heeck, Martin Holthausen, Werner Rodejohann, and Yusuke Shimizu. Higgs $\to \mu\tau$ in Abelian and Non-Abelian Flavor Symmetry Models. *Nucl.Phys.*, B896:281–310, 2015.
33. X.G. He, Girish C. Joshi, H. Lew, and R.R. Volkas. NEW Z-prime PHENOMENOLOGY. *Phys.Rev.*, D43:22–24, 1991.
34. Pierre Binetruy, Stephane Lavignac, Serguey T. Petcov, and Pierre Ramond. Quasidegenerate neutrinos from an Abelian family symmetry. *Nucl.Phys.*, B496:3–23, 1997.
35. Gautam Dutta, Anjan S. Joshipura, and K.B. Vijaykumar. Leptonic flavor violations in the presence of an extra Z. *Phys.Rev.*, D50:2109–2115, 1994.
36. Julian Heeck and Werner Rodejohann. Gauged $L_\mu - L_\tau$ Symmetry at the Electroweak Scale. *Phys.Rev.*, D84:075007, 2011.
37. G.C. Branco, P.M. Ferreira, L. Lavoura, M.N. Rebelo, Marc Sher, et al. Theory and phenomenology of two-Higgs-doublet models. *Phys.Rept.*, 516:1–102, 2012.
38. Paul Langacker. The Physics of Heavy Z' Gauge Bosons. *Rev.Mod.Phys.*, 81:1199–1228, 2009.
39. Andreas Crivellin, Lars Hofer, Joaquim Matias, Ulrich Nierste, Stefan Pokorski, et al. Lepton-flavour violating B decays in generic Z' models. 2015.

CONSTRAINING THE CKM ANGLE γ AT LHCb

ALEXIS VALLIER
On behalf of the LHCb collaboration
Laboratoire de l'Accélérateur Linéaire, Université Paris-Sud 11, CNRS/IN2P3, Orsay, France
avallier@cern.ch

A selection of latest LHCb measurements related to the determination of the CKM angle γ is presented. Included are: the current combination of direct γ measurements, the first observation of the $B_s^0 \to D_s^{\mp\pm} K^\pm$ decay, the first observation and amplitude analysis of the $B^- \to D^+ K^- \pi^-$ decay and the constraint on γ from charmless B decays.

1 Introduction

The CKM angle γ, defined as $\gamma \equiv \arg\left(-V_{ud}V_{ub}^*/V_{cd}V_{cb}^*\right)$, is the only CKM angle measurable from tree only processes. The loop diagrams contribution being negligible, its theoretical uncertainty is below the 10^{-7} order [1]. However γ is still experimentally the least known CKM angle. The B factories measured it with about 15° of precision [2,3], whereas LHCb reaches for now the 10° precision. In contrast, the indirect measurements dominated by loops contributions have better precision. For instance the last result of the CKMfitter group is $\gamma = \left(66.9^{+1.0}_{-3.7}\right)^\circ$ [4]. The result corresponds to a gobal fit of the CKM matrix elements without including direct γ measurements. A significant tension between direct and indirect measurements can be hint of new physics. That is why one of the main goals of the LHCb experiment is to improve the precision on γ, to highlight or discard this potential tension .

The angle γ is measured through the $b \to c\bar{u}s$ and $b \to u\bar{c}s$ interference. Indeed the weak phase between these two transitions is γ. The measurements can be time-independent like with $B^\pm \to DK^\pm$ or $B^0 \to DK^{*0}$ decays [5,6,7,8,9,10] or time-dependent like with $B_s^0 \to D_s^\mp K^\pm$ decay [11,12,13]. These proceedings present the latest lhcb γ combination and the first observations of the $B_s^0 \to D_s^{*\mp} K^\pm$ and $B^- \to D^+ K^- \pi^-$ decays, which can lead to future γ measurements. The determination of γ from charmless B decays is also reported.

2 LHCb γ combination

The latest LHCb γ combination, as of September 2014 [14], includes $\mathcal{CP}$ violation measurements of the $B^\pm \to D(h^+h^-)K^\pm$ [15], $B^\pm \to D(\pi^\pm K^\mp \pi^+ \pi^-)K^\pm$ [16], $B^\pm \to D(K_S^0 h^+ h^-)K^\pm$ [17], $B^\pm \to D(K_S^0 K^+ \pi^-)K^\pm$ [18], $B^0 \to D(h^+h^-)K^{*0}$ [19] and $B_s^0 \to D_s^\mp K^\pm$ [20] decays, where h stands either for a pion or a kaon. All these modes have a limited statistics since they correspond to small branching ratio, typically of the order of 10^{-7}. That is why the γ measurement power comes from the combination of all these measurements. The combination use a Frequentist approach. It takes into account the D^0 mixing and includes some auxiliary inputs for some hadronic parmeters coming from the Heavy Flavor Averaging Group [21] or the CLEO experiment. The result of this combination is at 68% of confidence level $\gamma = \left(73^{+9}_{-10}\right)^\circ$. The corresponding confidence level

curve is shown in Fig. 1. This is the first time that a single experiment reach a 10° precision on γ. A bayesian crosscheck has been also performed and is in good agreement.

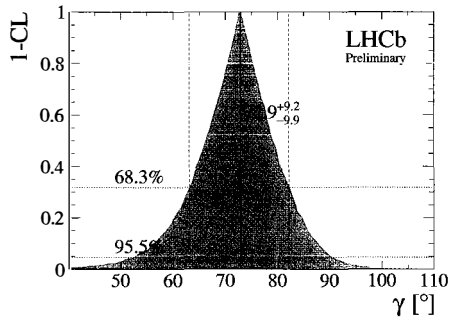

Figure 1 – Confidence level curve for the LHCb γ combination. The dotted lines indicate the 1σ and 2σ bounds.

3 First observation of the $B_s^0 \to D_s^{*\mp} K^\pm$ decay

Similarly to $B_s^0 \to D_s^\mp K^\pm$ already included on the γ combination, the $B_s^0 \to D_s^{*\mp} K^\pm$ decay is sensitive to this CKM angle. This mode has never been observed before and is hard to reconstruct in an hadronic environment such as the one at the LHC. Indeed the excited D_s^* meson is detected with the $D_s^* \to D_s(KK\pi)\gamma$ final state, which includes a photon of very soft momemtum. Hence, as a first step before a $\mathcal{CP}$ violation study, the following branching fraction ratio has been measured

$$\mathcal{R}^* \equiv \frac{\mathcal{B}(B_s^0 \to D_s^{*\mp} K^\pm)}{\mathcal{B}(B_s^0 \to D_s^{*-}\pi^+)}. \quad (1)$$

The full data sample of 3 fb^{-1}, collected by LHCb during the Run 1, is used[20]. A total of 1025±71 $B_s^0 \to D_s^{*\mp} K^\pm$ signal candidates are selected, for 16513 ± 227 candidates of the $B_s^0 \to D_s^{*-}\pi^+$ control mode. The fits to the invariant mass distributions leading to this measurement are shown in Fig. 2. It results in

$$\mathcal{R}^* = 0.068 \pm 0.005\ ^{+0.004}_{-0.003},$$

where the first uncertainty is statistical and the second systematic. The systematic uncertainty is mainly driven by the uncertainty on the combinatorial background. Using the $B_s^0 \to D_s^{*-}\pi^+$ branching fraction measurement from Belle[22], the following value is obtained

$$\mathcal{B}(B_s^0 \to D_s^{*\mp} K^\pm) = (16.3 \pm 1.2\ ^{+1.0}_{-0.7} \pm 4.8) \times 10^{-5}.$$

The first uncertainty is statistical, the second systematic and the third arises from the uncertainty on the Belle branching fraction measurement.

4 First observation and amplitude analysis of the $B^- \to D^+ K^- \pi^-$ decay

The $B^- \to D^+ K^- \pi^-$ decay is interesting for studying the properties of the doubly excited D^{**} mesons and for determining the potential of a γ measurement with the $B^- \to D^{**} K^-$ channel. LHCb observed for the first time this mode with 3 fb^{-1} of data[23]. The reconstructed B invariant mass distribution of the $B^- \to D^+ K^- \pi^-$ signal candidates, with the fit result superimposed, is drawn in Fig. 3. Around 2000 signal events are selected, with a high purity. Using the $B^- \to D^+ \pi^- \pi^-$ control mode, the following branching ratio value is obtained:

$$\mathcal{B}(B^- \to D^+ K^- \pi^-) = (7.92 \pm 0.23 \pm 0.24 \pm 0.42) \times 10^{-5}.$$

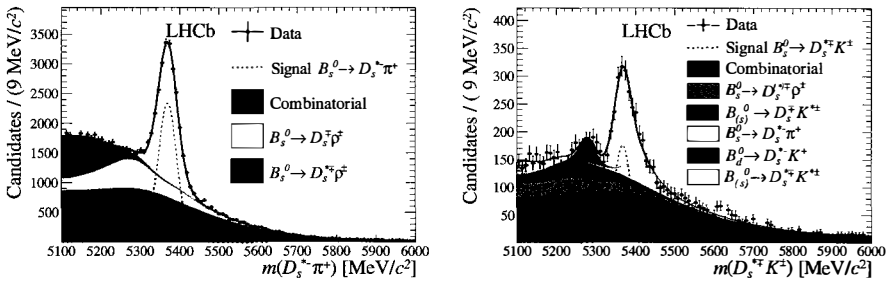

Figure 2 – Invariant mass distributions of $B_s^0 \to D_s^{*-}\pi^+$ (left) and $B_s^0 \to D_s^{*\mp}K^\pm$ (right) candidates with fit results superimposed.

The first uncertainty is statistical, the second systematic and the third comes from the uncertainty on the world average value of the $B^- \to D^+\pi^-\pi^-$ branching fraction.

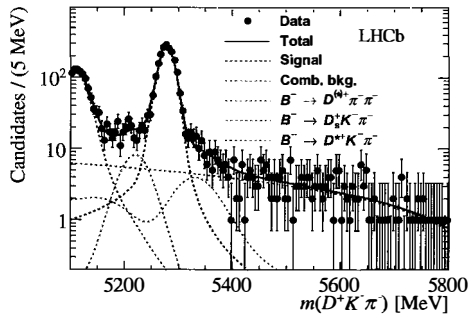

Figure 3 – Result of the fit to the $B^- \to D^+K^-\pi^-$ candidate invariant mass distribution.

Thanks to this sizeable statistics available with a low background level, a Dalitz plot model is determined with an isobar approach. The model uses a coherent sum of the $D_0^*(2400)^0$, $D_2^*(2460)^0$ and $D_1^*(2760)^0$ resonances, with S-wave and P-wave nonresonant amplitudes and with possible contributions from virtual $D_v^*(2007)^0$ and B_v^{*0} resonances. The detailed description of the model can be found in the paper [23]. The projection onto the three Dalitz plane coordinates $m(D\pi)$, $m(DK)$ and $m(K\pi)$ of the data, with the amplitude fit result superimposed, is shown in Fig. 4. This Dalitz plot analysis determines for the first time that the $D_J^*(2760)^0$ resonance is of spin 1.

The masses and the widths of the $D_1^*(2760)^0$ and $D_2^*(2460)^0$ resonances are also reported:

$$\begin{aligned} m(D_2^*(2460)^0) &= (2464.0 \pm 1.4 \pm 0.5 \pm 0.3)\ \text{MeV}, \\ \Gamma(D_2^*(2460)^0) &= (43.8 \pm 2.9 \pm 1.7 \pm 0.6)\ \text{MeV}, \\ m(D_1^*(2760)^0) &= (2781 \pm 18 \pm 11 \pm 6)\ \text{MeV}, \\ \Gamma(D_1^*(2760)^0) &= (177 \pm 32 \pm 20 \pm 7)\ \text{MeV}, \end{aligned}$$

where the three quoted uncertainties are statistical, experimental systematic and arising from the model uncertainty, respectively. The results for the $D_2^*(2460)^0$ are in agreement with the world average values. The mass of the $D_1^*(2760)^0$ is consistent with previous measurements [24,25]. However the measured width is larger than previous measurements, with a deviation of up

to 3 times the combined statistical and systematic uncertainties. This tension will be better understood with an increased statistics.

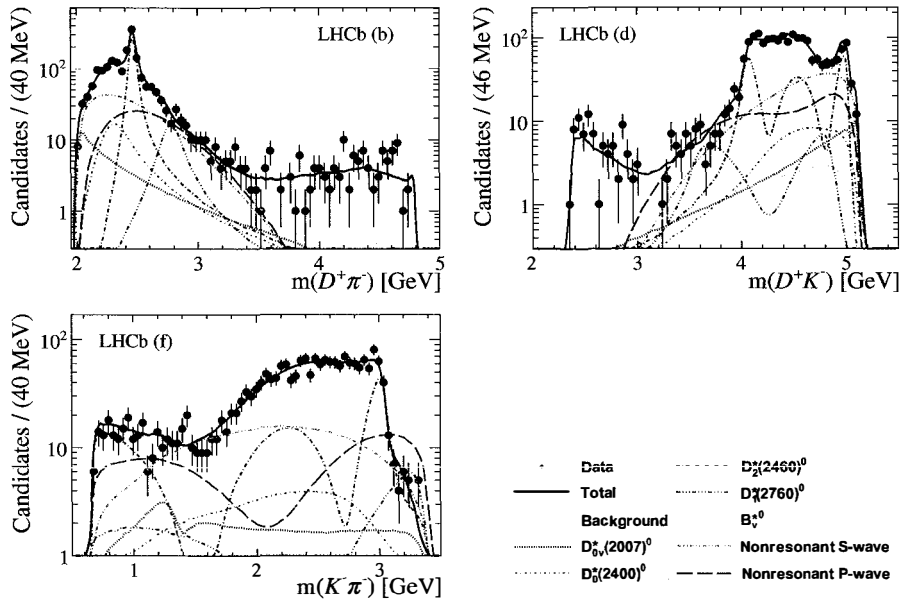

Figure 4 – Projection onto the $m(D\pi)$, $m(DK)$ and $m(K\pi)$ invariant masses of the data with the amplitude fit result superimposed.

The $B^- \to D_2^*(2460)^0 K^-$ decay may in the future lead to an additional measurement of γ. Moreover the improved knowledge on the D^{**} states benefits to other Dalitz analyses, especially to the $B^0 \to DK^+\pi^-$ analysis which is promising for a γ measurement [26].

5 γ from charmless B decays

In addition to the measurements with open-charm final states, γ can be determined from charmless B decays [27]. The sensitivity to γ is obtained by combining $\mathcal{CP}$ violation measurements from $B^0 \to \pi^+\pi^-$, $B_s^0 \to K^+K^-$, $B^0 \to \pi^0\pi^0$ and $B^+ \to \pi^+\pi^0$ decays [28,29,30,31,32]. LHCb contributes to the studies of the two first decays, whereas the others have been studied by BaBar, Belle or CDF. These decays are sensitive to the γ penguin contributions, therefore potentially to New Physics effects, in contrast to the $B \to DK$-like decays. A detailed list of the different inputs used in the combination is available in the paper [27]. To reduce the number of free parameters in the global fit, the combination exploits the isospin and U-spin (exchange of d and s quarks) symmetries.

A Bayesian analysis is performed to determine the probability density function (PDF) of γ, while assuming the world average value of $\sin 2\beta$ compiled by the HFAG collaboration [21]. The dependence of the PDF on U-spin breaking is estimated by letting vary the maximum allowed amount of U-spin breaking. This amount is described with a parameter κ: $\kappa = 0$ corresponds to no U-spin breaking, $\kappa = 1$ corresponds to maximal breaking. The resulting probability intervals of γ as a function of κ is shown in Fig. 5. They depend strongly on the amount of U-spin breaking. If the breaking is assumed to be at most 50%, the global fit provides

$$\gamma = \left(63.5^{+7.2}_{-6.7}\right)^\circ .$$

This measurement is compatible and competitive with the one obtained from tree-level decays (see Sec.2). However, a better theoretical understanding of the U-spin breaking is needed to assess a reliable γ determination from charmless B decays.

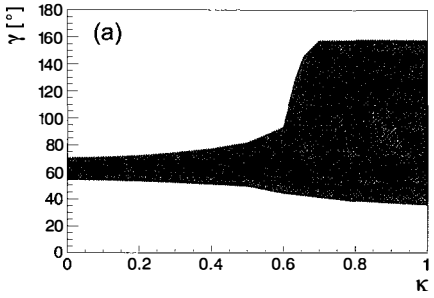

Figure 5 – Dependence of the 68% (hatched area) and 95% (filled area) probability intervals on the allowed amount of non-factorizable U-spin breaking for γ.

Conclusion

In summary, the LHCb experiment performed the best direct measurement of γ to date, with

$$\gamma = \left(73^{+9}_{-10}\right)^{\circ}.$$

Some improvement is still expected with the data collected during the LHC Run 1. A few measurements, already included in the combination, will be updated from 1 fb^{-1} (2011 only data) to 3 fb^{-1} (2011 and 2012 data). And some extra decays channels (with B^0 or neutral particles in the final states) and new Dalitz analyses will be added. With the Run 2 data, the precision should reach 4°.

References

1. Joachim Brod and Jure Zupan. The ultimate theoretical error on γ from $B \to DK$ decays. *JHEP*, 1401:051, 2014.
2. J.P. Lees et al. Observation of direct CP violation in the measurement of the Cabibbo-Kobayashi-Maskawa angle gamma with $B^{\pm} \to D^{(*)}K^{(*)\pm}$ decays. *Phys.Rev.*, D87(5):052015, 2013.
3. K. Trabelsi et al. Study of direct CP in charmed B decays and measurement of the CKM angle gamma at Belle. 2013.
4. J. Charles et al. , *Eur.Phys.J.*, C41:1–131, 2005. updated results and plots available at: http://ckmfitter.in2p3.fr.
5. Michael Gronau and David London. How to determine all the angles of the unitarity triangle from $B^0_d \to DK_S$ and $B^0_s \to D\phi$. *Physics Letters B*, 253(34):483 – 488, 1991.
6. Michael Gronau and Daniel Wyler. On determining a weak phase from charged b decay asymmetries. *Physics Letters B*, 265(12):172 – 176, 1991.
7. David Atwood, Isard Dunietz, and Amarjit Soni. Enhanced CP Violation with $B \to KD^0(\bar{D}^0)$ Modes and Extraction of the Cabibbo-Kobayashi-Maskawa Angle γ. *Phys. Rev. Lett.*, 78:3257–3260, Apr 1997.
8. David Atwood, Isard Dunietz, and Amarjit Soni. Improved methods for observing CP violation in $B^{\pm} \to KD$ and measuring the CKM phase γ. *Phys. Rev. D*, 63:036005, Jan 2001.

9. Anjan Giri, Yuval Grossman, Abner Soffer, and Jure Zupan. Determining γ using $B^{\pm} \to DK^{\pm}$ with multibody D decays. *Phys. Rev. D*, 68:054018, Sep 2003.
10. A. Bondar. In *Proceedings of BINP special analysis meeting on Dalitz, unpublished*, 2002.
11. M. Beneke, G. Buchalla, and I. Dunietz. Mixing induced CP asymmetries in inclusive B decays. *Phys.Lett.*, B393:132–142, 1997.
12. R. Aleksan, I. Dunietz, and B. Kayser. Determining the CP-violating phase γ. *Zeitschrift fur Physik C Particles and Fields*, 54(4):653–659, December 1992.
13. Robert Fleischer. New strategies to obtain insights into CP violation through $B_s \to D_s^{\pm} K^{\mp}, D_s^{*\pm} K^{\mp}$,... and $B_d \to D^{\pm}\pi^{\mp}, D^{*\pm}\pi^{\mp}$,... decays. *Nucl.Phys.*, B671:459–482, 2003.
14. Improved constraints on γ: CKM2014 update, Sep 2014. LHCb-CONF-2014-004.
15. R. Aaij et al. Observation of CP violation in $B^{\pm} \to DK^{\pm}$ decays. *Phys. Lett.*, B712:203, 2012.
16. R. Aaij et al. Observation of the suppressed ADS modes $B^{\pm} \to [\pi^{\pm}K^{\mp}\pi^{+}\pi^{-}]_D K^{\pm}$ and $B^{\pm} \to [\pi^{\pm}K^{\mp}\pi^{+}\pi^{-}]_D \pi^{\pm}$. *Phys. Lett.*, B723:44, 2013.
17. R. Aaij et al. Measurement of the CKM angle γ using $B^{\pm} \to DK^{\pm}$ with $D \to K^0_S\pi^{+}\pi^{-}$, $K^0_S K^{+}K^{-}$ decays. *JHEP*, 10:097, 2014.
18. R. Aaij et al. A study of CP violation in $B^{\pm} \to DK^{\pm}$ and $B^{\pm} \to D\pi^{\pm}$ decays with $D \to K^0_S K^{\pm}\pi^{\mp}$ final states. *Phys. Lett.*, B733:36, 2014.
19. R. Aaij et al. Measurement of CP violation parameters in $B^0 \to DK^{*0}$ decays. *Phys. Rev.*, D90:112002, 2014.
20. R. Aaij et al. Measurement of CP asymmetry in $B^0_s \to D^{\mp}_s K^{\pm}$ decays. *JHEP*, 11:060, 2014.
21. Y. Amhis et al. Averages of b-hadron, c-hadron, and τ-lepton properties as of summer 2014. 2014. updated results and plots available at `http://www.slac.stanford.edu/xorg/hfag/`.
22. R. Louvot et al. Observation of $B^0_s \to D^{*-}_s\pi^{+}, B^0_s \to D^{(*)-}_s \, rho^{+}$ Decays and Measurement of $B^0_s \to D^{*-}_s\rho^{+}$ Polarization. *Phys.Rev.Lett.*, 104:231801, 2010.
23. R. Aaij et al. First observation and amplitude analysis of the $B^{-} \to D^{+}K^{-}\pi^{-}$ decay. 2015. submitted to PRD.
24. P. del Amo Sanchez et al. Observation of new resonances decaying to $D\pi$ and $D^{*}\pi$ in inclusive $e^{+}e^{-}$ collisions near $\sqrt{s}$ =10.58 GeV. *Phys.Rev.*, D82:111101, 2010.
25. R Aaij et al. Study of D_J meson decays to $D^{+}\pi^{-}$, $D^0\pi^{+}$ and $D^{*+}\pi^{-}$ final states in pp collision. *JHEP*, 1309:145, 2013.
26. Tim Gershon and Mike Williams. Prospects for the Measurement of the Unitarity Triangle Angle gamma from $B^0 \to DK^{+}\pi^{-}$ Decays. *Phys.Rev.*, D80:092002, 2009.
27. R. Aaij et al. Determination of γ and $-2\beta_s$ from charmless two-body decays of beauty mesons. *Phys. Lett.*, B739:1, 2014.
28. Robert Fleischer. New strategies to extract Beta and gamma from $B_d \to \pi^{+}\pi^{-}$ and $B_s \to K^{+}K^{-}$. *Phys.Lett.*, B459:306–320, 1999.
29. Robert Fleischer. $B_{s,d} \to \pi\pi, \pi K, KK$: Status and Prospects. *Eur.Phys.J.*, C52:267–281, 2007.
30. Robert Fleischer and Robert Knegjens. In Pursuit of New Physics With $B^0_s \to K^{+}K^{-}$. *Eur.Phys.J.*, C71:1532, 2011.
31. M. Ciuchini, E. Franco, S. Mishima, and L. Silvestrini. Testing the Standard Model and Searching for New Physics with $B_d \to \pi\pi$ and $B_s \to KK$ Decays. *JHEP*, 1210:029, 2012.
32. Michael Gronau and David London. Isospin analysis of CP asymmetries in B decays. *Phys. Rev. Lett.*, 65:3381–3384, Dec 1990.

DETERMINATION OF THE QUARK COUPLING STRENGTH $|V_{ub}|$ USING BARYONIC DECAYS

W. Sutcliffe,
On behalf of the LHCb collaboration
Imperial College London, United Kingdom

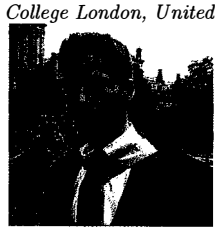

A measurement of the ratio of branching fractions between $\Lambda_b^0 \to p\mu^-\bar{\nu}_\mu$ and $\Lambda_b^0 \to \Lambda_c^+\mu^-\bar{\nu}_\mu$ decays is performed using data corresponding to 2 fb^{-1} of integrated luminosity, collected by the LHCb detector in 2012. This combined with the latest form factor predictions obtained from lattice QCD calculations leads to the first determination of $|V_{ub}|$ at a hadron collider and in a baryon decay, $|V_{ub}| = (3.27 \pm 0.23) \times 10^{-3}$. The measurement is consistent with existing exclusive measurements made using $\bar{B}^0 \to \pi^+\mu^-\bar{\nu}_\mu$, but disagrees with those made inclusively.

1 Context and motivation

In the Standard Model (SM) of particle physics, quark mixing occurs through the weak force according to the 3×3 unitary Cabibbo-Kobayashi-Maskawa (CKM) matrix [1,2]. The unitarity of the CKM matrix results in nine constraints, six of which may be represented as triangles in the complex plane. Constraints from a variety of measurements on the most commonly used triangle are shown in Fig. 1. The uncertainty on the length of this unitarity triangle opposite the angle β is dominated by the uncertainty on $|V_{ub}|$. An inconsistency between this length and the angle β could signify new physics as β is measured in loop level processes which may be affected by new particles in extensions of the Standard Model.

The magnitude of $|V_{ub}|$ is the least known of the CKM matrix elements. The best existing measurements for $|V_{ub}|$ have been made by the e^+e^- collider beauty factory experiments BaBar [3,4] and Belle [5,6] using semi-leptonic exclusive $\bar{B}^0 \dashrightarrow \pi^+\mu^-\bar{\nu}_\mu$ and inclusive $B \dashrightarrow X_u\mu^-\bar{\nu}_\mu$ decays. The world averages for these approaches are respectively $|V_{ub}| = (3.28 \pm 0.29) \times 10^{-3}$ (exclusive) and $|V_{ub}| = (4.41 \pm 0.15^{+0.15}_{-0.17}) \times 10^{-3}$ (inclusive) [7]. In the exclusive scenario, the dominant uncertainty arises in predicting the influence of QCD on the decay. The nature of these interactions can be encompassed within a form factor which is computed using non-perturbative techniques such as lattice QCD (LQCD) or QCD sum rules. In the inclusive case the differential rate for all possible B meson decays containing a $b \dashrightarrow ul^-\bar{\nu}$ quark level transition is measured. In order to suppress the background from $b \dashrightarrow cl^-\bar{\nu}$ decays, the differential rate is measured in a small

region of phase space. This is then extrapolated to the full region using theory, which results in the dominant uncertainty. The discrepency between inclusive and exclusive measurements is approximately three standard deviations and has been a long standing puzzle in flavour physics. A proposed explanation for the discrepency is to introduce a right-handed coupling as an extension to the left-handed W coupling of the SM [8,9,10].

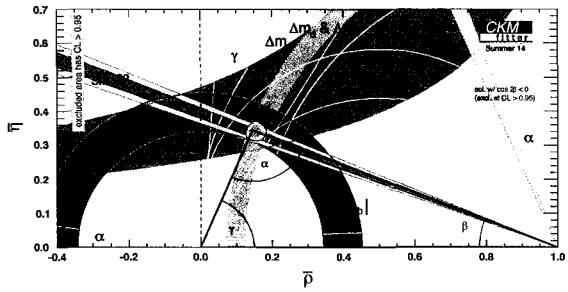

Figure 1 – Global fit for the apex of the unitarity triangle produced by the CKMfitter group [16]. The green circular band shows a constraint on the length of the side opposite the angle β. The uncertainty on this length is dominated by that on the world average of $|V_{ub}|$ made using semi-leptonic exclusive $\bar{B}^0 \to \pi^+\mu^-\bar{\nu}_\mu$ and inclusive $B \to X_u\mu^-\bar{\nu}_\mu$ decays.

The LHCb detector [11,12] is a single-arm forward spectrometer covering the range $2 < \eta < 5$, in which the majority of forward going $b\bar{b}$ pairs are produced. Around 20% of the B hadrons produced in the hadronisation process of b quarks from pp collisions at the LHC are Λ_b^0 (bud) baryons [13]. This allows for the possiblity of an exclusive measurement of $|V_{ub}|$ using the decay $\Lambda_b^0 \to p\mu^-\bar{\nu}_\mu$ [14], which has not been considered previously as Λ_b^0 baryons are not produced at an e^+e^- B-factory. The proton in the final state makes for a distinctive signature given that there are far fewer final state protons than kaons and pions produced from B-hadron decays within the detector. At a hadron collider it is not possible to use the beam energy constraints as employed by e^+e^- colliders. However, the LHCb detector's precision vertexing and excellent particle identification, in conjunction with the large number of Λ_b^0 baryons produced, make this measurement possible.

2 Analysis strategy

A measurement of the ratio of branching fractions of the Λ_b^0 baryon into $p\mu^-\bar{\nu}_\mu$ and $\Lambda_c^+\mu^-\bar{\nu}_\mu$ final states is made at high $\mu\nu$ invariant mass squared, q^2. This is performed using proton-proton collison data from the LHCb detector, corresponding to 2.0 fb^{-1} of integrated luminosity collected at a centre-of-mass energy 8 TeV. This measurement together with recent LQCD calculations [15] allow for the determination of $|V_{ub}|^2/|V_{cb}|^2$ according to

$$\frac{|V_{ub}|^2}{|V_{cb}|^2} = \frac{\mathcal{B}(\Lambda_b^0 \to p\mu^-\bar{\nu}_\mu)_{q^2>15\,\mathrm{GeV}^2/c^4}}{\mathcal{B}(\Lambda_b^0 \to \Lambda_c^+\mu^-\bar{\nu}_\mu)_{q^2>7\,\mathrm{GeV}^2/c^4}} R_{FF} \tag{1}$$

where $\mathcal{B}$ denotes the branching fractions and R_{FF} is a ratio of the relevant form factors, calculated using LQCD. This is then converted into a measurement of $|V_{ub}|$ using the world average for $|V_{cb}|$ from exclusive decays. The choice to measure the branching fractions at high q^2 reflects the fact that lattice QCD predictions for the form factors are most precise in the high q^2 region.

The normalisation to the decay $\Lambda_b^0 \to \Lambda_c^+\mu^-\bar{\nu}_\mu$ is necessary to cancel a number of experimental uncertainties, including the uncertainty on the total production rate of Λ_b^0 baryons. In

order to select this decay, the Λ_c^+ baryon is reconstructed decaying to the final state $pK^-\pi^+$. The required ratio of branching fractions is determined experimentally from

$$\frac{\mathcal{B}(\Lambda_b^0 \to p\mu^-\bar{\nu}_\mu)_{q^2>15\,\mathrm{GeV}^2/c^4}}{\mathcal{B}(\Lambda_b^0 \to \Lambda_c^+\mu^-\bar{\nu}_\mu)_{q^2>7\,\mathrm{GeV}^2/c^4}} = \frac{N(\Lambda_b^0 \to p\mu^-\bar{\nu}_\mu)_{q^2>7\,\mathrm{GeV}^2/c^4}}{N(\Lambda_b^0 \to (\Lambda_c^+ \to pK^-\pi^+)\mu^-\bar{\nu}_\mu)_{q^2>15\,\mathrm{GeV}^2/c^4}} \cdot \frac{\mathcal{B}(\Lambda_c^+ \to pK^-\pi^+)}{\epsilon_{rel}} \tag{2}$$

where $N(\Lambda_b^0 \to p\mu^-\bar{\nu}_\mu)_{q^2>7\,\mathrm{GeV}^2/c^4}$ and $N(\Lambda_b^0 \to (\Lambda_c^+ \to pK^-\pi^+)\mu^-\bar{\nu}_\mu)_{q^2>15\,\mathrm{GeV}^2/c^4}$ are respectively the yields for the decays $\Lambda_b^0 \to p\mu^-\bar{\nu}_\mu$ and $\Lambda_b^0 \to (\Lambda_c^+ \to pK^-\pi^+)\mu^-\bar{\nu}_\mu$. Meanwhile ϵ_{rel} is the relative efficiency for selecting the two modes and $B(\Lambda_c^+ \to pK^-\pi^+)$ is the branching fraction of $\Lambda_c^+ \to pK^-\pi^+$ for which the most recent Belle measurement is used $\mathcal{B}(\Lambda_c^+ \to pK^-\pi^+) = (6.84 \pm 0.24^{+0.21}_{-0.27})\%$ [17]. At the LHC the, number of $\Lambda_b^0 \to p\mu^-\bar{\nu}_\mu$ candidates is large, therefore the event selection is designed to mimimise systematic effects.

3 Selection

In order to select candidates for the decay $\Lambda_b^0 \to p\mu^-\bar{\nu}_\mu$, proton and muon candidates are combined. The proton is distinguished from kaons and pions by information from the detector's two ring-imaging Cherenkov (RICH) detectors, meanwhile, the muon in the decay can be identified by its penetration of the calorimeters to the muon tracking system. A requirement is made that the $p\mu^-$ vertex is displaced from primary proton-proton interaction vertex due to the lifetime of the Λ_b^0 baryon. The associated vertex fit is required to be of good quality which reduces most of the background resulting from $b \to c\mu^-\bar{\nu}_\mu$ decays as the resulting ground state charmed hadrons have a significant lifetime. A tight momentum cut of $P > 15$ GeV/c is placed on the proton as the particle identification performance is most effective for high-momentum protons.

In order to select the decay $\Lambda_b^0 \to (\Lambda_c^+ \to pK^-\pi^+)\mu^-\bar{\nu}_\mu$ an additional two tracks, positively identified as a pion and kaon, are combined with the proton to form a $\Lambda_c^+ \to pK^-\pi^+$ candidate.

There is a large background from b-hadron decays with additional charged tracks in the decay products. To reduce this background, a multivariate classifier (a boosted decision tree, BDT), is used to determine the compatibility of each track in the event to orginate from the same vertex as the signal candidate.

The Λ_b^0 mass is reconstructed using the so-called *corrected mass*

$$m_{corr} = \sqrt{m_{h\mu}^2 + p_\perp^2} + p_\perp \tag{3}$$

where $m_{h\mu}$ is the visible mass of the combined $h\mu$ pair, $p_\perp$ is the momentum of the combined $h\mu$ system perpendicular to the Λ_b^0 flight direction and h is either the p or Λ_c^+ candidate. The flight direction of the Λ_b^0 baryon is determined using the PV and $h\mu$ vertices. An event-by-event uncertainty on the corrected mass associated with the uncertainty on the PV and $h\mu$ vertex positions is determined. Candidates for the $\Lambda_b^0 \to p\mu^-\bar{\nu}_\mu$ decay with an uncertainty of greater than 100 MeV/c^2 are rejected. This significantly increases the seperation in m_{corr} between signal and background as shown in Fig. 2(a).

It is possible to reconstruct the neutrino in the decay and hence q^2 up to a two-fold ambiguity. In order to minimise the influence of the large form factor uncertainty at low q^2 on the $|V_{ub}|$ measurement both solutions are required to exceed 15 GeV$^2/c^4$ for $\Lambda_b^0 \to p\mu^-\bar{\nu}_\mu$ decays and 7 GeV$^2/c^4$ for $\Lambda_b^0 \to (\Lambda_c^+ \to pK^-\pi^+)\mu^-\bar{\nu}_\mu$ decays (see Fig. 2(b)).

4 Signal and normalisation fits

The signal and normalisation yields respectively, $N(\Lambda_b^0 \to p\mu^-\bar{\nu}_\mu)$ and $N(\Lambda_b^0 \to (\Lambda_c^+ \to pK^-\pi^+)\mu^-\bar{\nu}_\mu)$, are determined by binned χ^2 fits to the m_{corr} distributions of $\Lambda_b^0 \to p\mu^-\bar{\nu}_\mu$ and $\Lambda_b^0 \to (\Lambda_c^+ \to pK^-\pi^+)\mu^-\bar{\nu}_\mu$ candidates as shown in Fig. 3.

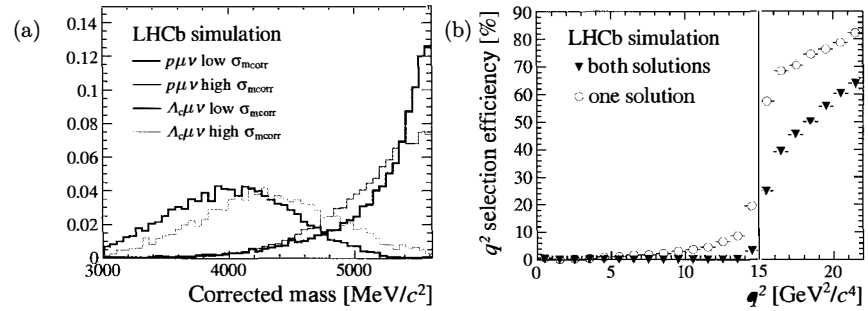

Figure 2 – (a) A comparison of the m_{corr} distributions for simulated signal ($\Lambda_b^0 \to p\mu^-\bar{\nu}_\mu$) and background ($\Lambda_b^0 \to \Lambda_c^+\mu^-\bar{\nu}_\mu$) decays with low and high corrected mass uncertainty. (b) Efficiency of the q^2 selection as a function of q^2 for $\Lambda_b^0 \to p\mu^-\bar{\nu}_\mu$ decays. The choice of requiring both q^2 solutions to be above 15 GeV$^2/c^4$ as opposed to just one solution minimises the efficiency of selecting events with q^2 below 15 GeV$^2/c^4$.

The fit to the m_{corr} distribution for $\Lambda_b^0 \to p\mu^-\bar{\nu}_\mu$ candidates includes a variety of backgrounds. The largest background source is from $\Lambda_b^0 \to \Lambda_c^+\mu^-\bar{\nu}_\mu$ decays in which the decay of the Λ_c^+ contains a proton and additional particles. The majority of the backgrounds are controlled using data-driven techniques except for the background from $\Lambda_b^0 \to N^{*+}\mu^-\bar{\nu}_\mu$ decays, which is given a large freedom in the fit.

For the fit to the $\Lambda_b^0 \to (\Lambda_c^+ \to pK^-\pi^+)\mu^-\bar{\nu}_\mu$ corrected mass, background from combinatorial and $\Lambda_b^0 \to (\Lambda_c^{*+} \to \Lambda_c^+\pi\pi)\mu^-\bar{\nu}_\mu$ decays are considered. The level of combinatorial background is estimated using a fit to the $pK^-\pi^+$ mass.

The observed yields for $\Lambda_b^0 \to p\mu^-\bar{\nu}_\mu$ and $\Lambda_b^0 \to (\Lambda_c^+ \to pK^-\pi^+)\mu^-\bar{\nu}_\mu$ decays are respectively $17,687 \pm 733$ and $34,255 \pm 571$, with this being the first observation of the decay $\Lambda_b^0 \to p\mu^-\bar{\nu}_\mu$.

The relative efficiency, ϵ_{rel}, for reconstruction, trigger and event selection is determined from simulation. A number of corrections are applied to this efficiency to account for differences between data and simulation in the detector response and differences in the kinematic properties of the Λ_b^0 baryon for selected $\Lambda_b^0 \to p\mu^-\bar{\nu}_\mu$ and $\Lambda_b^0 \to (\Lambda_c^+ \to pK^-\pi^+)\mu^-\bar{\nu}_\mu$ candidates. The relative efficiency is determined to be $\epsilon_{rel} = 3.52 \pm 0.20$, where a number of sources of systematic uncertainty are considered.

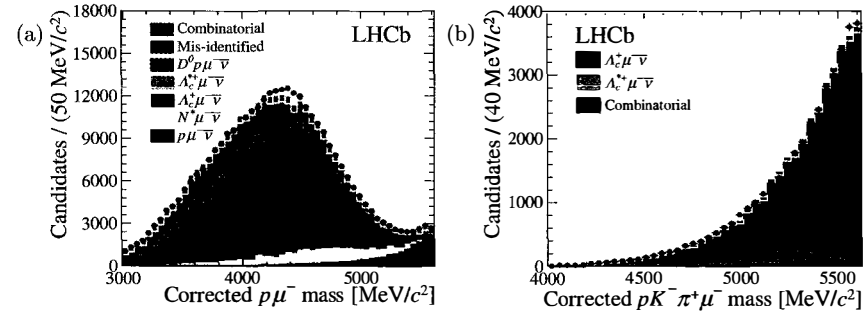

Figure 3 – Fits to the m_{corr} distribution for selected (a) $\Lambda_b^0 \to p\mu^-\bar{\nu}_\mu$ and (b) $\Lambda_b^0 \to (\Lambda_c^+ \to pK^-\pi^+)\mu^-\bar{\nu}_\mu$ candidates.

5 Results

Substituting the relevant yields, relative efficiency and $\mathcal{B}(\Lambda_c^+ \to pK^-\pi^+)$ into equation 2, the ratio of branching fractions between $\Lambda_b^0 \to p\mu^-\bar{\nu}_\mu$ and $\Lambda_b^0 \to \Lambda_c^+\mu^-\bar{\nu}_\mu$ decays in the selected q^2 regions is

$$\frac{\mathcal{B}(\Lambda_b^0 \to p\mu^-\bar{\nu}_\mu)_{q^2>15\,\mathrm{GeV}^2/c^4}}{\mathcal{B}(\Lambda_b^0 \to \Lambda_c^+\mu^-\bar{\nu}_\mu)_{q^2>7\,\mathrm{GeV}^2/c^4}} = (1.00 \pm 0.04 \pm 0.08) \times 10^{-2} \tag{4}$$

where, the first uncertainty is statistical and the second systematic. An overview of the systematic uncertainties considered for the measurement of the ratio of branching ratios of $\Lambda_b^0 \to p\mu^-\bar{\nu}_\mu$ to $\Lambda_b^0 \to \Lambda_c^+\mu^-\bar{\nu}_\mu$ decays is given in the journal article corresponding to the result[14]. The dominant source of systematic uncertainty is due to the uncertainty on $\mathcal{B}(\Lambda_c^+ \to pK^-\pi^+)$.

From the determination of the branching fraction ratio a measurement of $|V_{ub}|/|V_{cb}| = 0.083 \pm 0.004 \pm 0.004$ is made using equation 1 with $R_{FF} = 0.68 \pm 0.07$, as computed using the latest LQCD predictions[15]. The first uncertainty arises from the experimental measurement and the second is due from the LQCD prediction. Finally, using the world average of $|V_{cb}| = (39.5 \pm 0.8) \times 10^{-3}$ measured from exclusive decays, $|V_{ub}|$ is measured as

$$|V_{ub}| = (3.27 \pm 0.15 \pm 0.17 \pm 0.06) \times 10^{-3} \tag{5}$$

where, the first uncertainty is due the experimental measurement, the second uncertainty is associated with LQCD prediction and the final uncertainty results from the uncertainty on $|V_{cb}|$.

In addition a measurement of $\mathcal{B}(\Lambda_b^0 \to p\mu^-\bar{\nu}_\mu) = (3.9 \pm 0.8) \times 10^{-4}$ is made by extrapolating the measured ratio of branching fractions to the full q^2 region. Here the dominant theory uncertainty arises in the $\Lambda_b^0 \to p\mu^-\bar{\nu}_\mu$ form factor predictions at low q^2.

Fig. 4(a) shows a comparison of the measured value $|V_{ub}|$ from $\Lambda_b^0 \to p\mu^-\bar{\nu}_\mu$ decays with existing exclusive and inclusive measurements of $|V_{ub}|$. The measurement is 3.5σ below the inclusive measurement, but agrees with the exclusive measurement from $\bar{B}^0 \to \pi^+\mu^-\bar{\nu}_\mu$ decays.

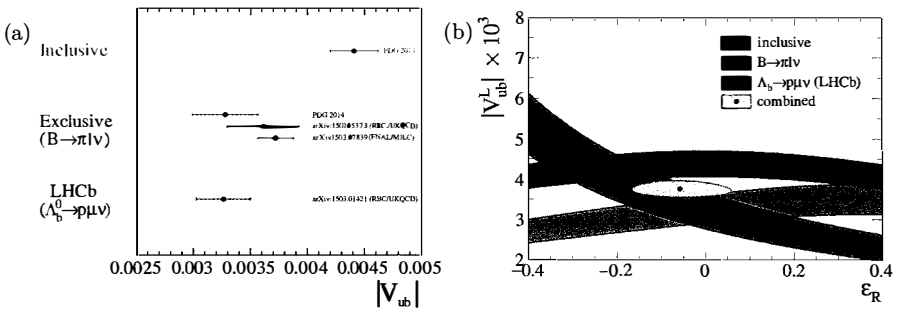

Figure 4 – (a) A comparison of the measurement of $|V_{ub}|$ from $\Lambda_b^0 \to p\mu^-\bar{\nu}_\mu$ decays with existing measurements using exclusive $\bar{B}^0 \to \pi^+\mu^-\bar{\nu}_\mu$ and inclusive $B \to X_u\mu^-\bar{\nu}_\mu$ decays. (b) Experimental constraints on the left-handed coupling, $|V_{ub}^L|$ and a fractional right-handed coupling, ϵ_R.

The value of of $|V_{ub}|$ determined from the measured ratio of branching fractions can be influenced by a right-handed coupling. This is shown in Fig. 4(b), which shows experimental constraints on the left-handing coupling, $|V_{ub}^L|$, against a fractional right-handed coupling ϵ_R. The constraint associated with $|V_{ub}|$ from $\Lambda_b^0 \to p\mu^-\bar{\nu}_\mu$ decays is compared with that from exclusive $\bar{B}^0 \to \pi^+\mu^-\bar{\nu}_\mu$ and inclusive $B \to X_u\mu^-\bar{\nu}_\mu$ decays. The measurement from $\Lambda_b^0 \to p\mu^-\bar{\nu}_\mu$ decays gives a different sensistivity to ϵ_R than that from $\bar{B}^0 \to \pi^+\mu^-\bar{\nu}_\mu$ decays given that the spin of the proton allows for an axial-vector current. The overlap of the bands associated with previous exclusive and inclusive measurements suggests a significant right-handed coupling, however, the inclusion of the $|V_{ub}|$ measurement from $\Lambda_b^0 \to p\mu^-\bar{\nu}_\mu$ decays does not support this.

6 Conclusion

The CKM matrix element $|V_{ub}|$ is an important parameter in constraining global fits to the unitarity of the CKM matrix. The discrepency between exclusive and inclusive measurements of $|V_{ub}|$ has been a long standing puzzle in flavour physics. Whether this is a systematic issue with thc latticc QCD predictions used in the determination of exclusive measurements or an issue with the theoretical issues facing the inclusive measurement is unknown. The puzzle has resulted in a number of proposals which attempt to explain the discrepency with an addition of a right-handed coupling to the SM.

The first determination of $|V_{ub}|$ at a hadron collider and in a baryon decay has been performed using $\Lambda_b^0 \to p\mu^-\bar{\nu}_\mu$ decays, which are observed for the first time. This provides a new avenue for constraining the CKM sector of the SM at the LHC. The measurement is in agreement with the existing exclusive $\bar{B}^0 \to \pi^+\mu^-\bar{\nu}_\mu$ measurement thereby increasing the tension between inclusive and exclusive measurements while at the same time disfavouring a right-handed coupling as an explanation for the discrepency.

Acknowledgments

Many thanks to Stefan Meinel for a productive collaboration regarding form factor predictions of the $\Lambda_b^0 \to p\mu^-\bar{\nu}_\mu$ and $\Lambda_b^0 \to \Lambda_c^+\mu^-\bar{\nu}_\mu$ decays, Winston Roberts for discussions regarding the $\Lambda_b^0 \to N^{*+}\mu^-\bar{\nu}_\mu$ decays and Florian Bernlochner for help in understanding the impact of right-handed currents.

References

1. N. Cabibbo, *Phys. Rev. Lett.* **10**, 531 (1963).
2. M. Kobayashi and T. Maskawa, *Phys. Rev. Lett.* **49**, 652 (1973).
3. BaBar collaboration, P. del Amo Sanchez *et al.*, *Phys. Rev.* D **83**, 032007 (2011).
4. BaBar collaboration, J. P Lees *et al.*, *Phys. Rev.* D **86**, 092004 (2012).
5. Belle collaboration, H. Ha *et al.*, *Phys. Rev.* D **83**, 071101 (2011).
6. Belle collaboration, A. Sibidanov *et al.*, *Phys. Rev.* D **88**, 032005 (2013).
7. Heavy Flavour Averaging Group, Y. Amhis *et al.*, arXiv:1412.7515.
8. C.-H. Chen and S.-h. Nam, *Phys. Lett.* B **666**, 462 (2008)
9. A. Crivellin, *Phys. Rev.* D **81**, 031101 (2010)
10. A. J. Buras, K. Gemmler, and G. Isidori, *Nucl. Phys.* B **843**, 107 (2011)
11. LHCb Collaboration, A. A. Alves Jr. *et al.*, *JINST* **3** (2008)
12. LHCb Collaboration, R. Aaij *et al.*, *Int. J. Mod. Phys.* A **40** 1530022 2015
13. LHCb Collaboration, R. Aaij *et al.*, *Phys. Rev.* D **85**, 032008 (2012)
14. LHCb Collaboration, R. Aaij *et al.*, arXiv:1504.01568
15. W. Detmold, C. Lehner, and S. Meinel, arXiv:1111.2357
16. CKMfitter Group, J. Charles *et al.*, *Eur. Phys. J.* C **41**, 1-131 (2005)
17. Belle Collaboration, A. Zupanc *et al.*, *Phys. Rev. Lett.* **113**, 042002 (2014)

Rare Decays and other Electroweak b-physics Measurements at ATLAS and CMS

P. Ronchese
Università di Padova, Dipartimento di Fisica e Astronomia & INFN, Sezione di Padova
via Marzolo, 8, Padova, Italy
ATLAS and CMS Collaborations

In b quark decay the tree-level process with W exchange is hardly modified by new physics beyond the standard model; the search for new physics hints can be done exploiting the sensitivity of some processes to loop diagrams. Such processes include rare FCNC decays, whose branching ratio or angular distributions could be modified by the presence of new degrees of freedom in the loops. Another process where new physics could show itself is B_s^0 meson mixing, where the CP violation phase is predicted by SM to be very small and the observation of a significant violation would indicate the presence of new processes.

1 Introduction

Among the motivations to study heavy flavour physics at LHC experiments, and specifically CMS and ATLAS, there's the look for indirect evidence, or constraints, of new physics beyond the standard model. In b quark decay the exchange of a W boson at tree level is hardly affected by new physics processes, so the sensitivity to such processes is exploited in loop diagrams. More specifically the branching ratio of decays implying flavour-changing neutral currents can be modified by the presence of new particles circulating in the loops, while angular analysis can probe specific terms in effective lagrangian. While in decays one observes processes with flavour changes of one unit, in B^0 mixing processes with changes of two flavour units are investigated, and new physics contributions to CP violation may appear.

Both ATLAS and CMS experiments collected an integrated luminosity of about 5 fb^{-1} in 2011 at $\sqrt{s} = 7$ TeV and about 20 fb^{-1} in 2012 at $\sqrt{s} = 8$ TeV. All measurements involve dimuons; dedicated triggers requiring the presence of two muons have been developed for the analyses, to achieve a sustainable trigger rate when collecting data at the very high luminosities provided by LHC. Common selections criteria among the analyses include cuts on the dimuon mass, the requirement that the two muons form a displaced vertex and cuts on the pointing angle, that's the angle formed by the dimuon momentum and the flight direction, given by the position of the secondary vertex relative to the primary vertex.

2 Rare decays

2.1 $B^0_{d,s} \to \mu^+\mu^-$ *branching ratio*

The decay $B^0_{d,s} \to \mu^+\mu^-$ is a highly suppressed process in the standard model, because not only it involves a flavour-changing neutral current, but it's also Cabibbo suppressed, it's helicity suppressed and it requires an internal annihilation.

A branching ratio prediction from the standard model including new NLO electroweak corrections and NNLO QCD corrections has been recently published [1]:

$$\mathcal{B}(B_s^0 \to \mu^+\mu^-)_{\rm SM} = (3.65 \pm 0.23) \times 10^{-9}$$
$$\mathcal{B}(B_d^0 \to \mu^+\mu^-)_{\rm SM} = (1.06 \pm 0.09) \times 10^{-10}$$

Significant deviations are predicted by theories beyond the standard model, implying the presence of new degrees of freedom in the loops, as shown in fig.1, both for box and penguin diagrams.

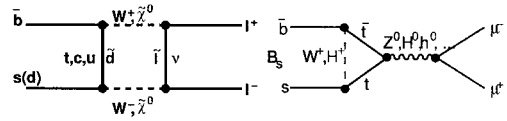

Figure 1 – $B^0_{d,s}$ decay diagrams predicted by SM and new physics models

Enhancements of the branching ratio are predicted by models with non-universal Higgs masses [2], leptoquarks [3] or MSSM with large $\tan\beta$ that can predict branching ratios proportional to $\tan\beta$ up to the $6^{\rm th}$ power [4,5]. On the contrary, other models as supersymmetry with maximum CP violation and minimum flavour violation would predict a suppression [6]. A discrimination among different theories can come from the ratio R of the two branching fractions; for example theories beyond the standard model assuming minimal flavour violation predict a value for R equal as in the standard model itself [7], so a deviation would invalidate them.

Both ATLAS and CMS measured the branching ratio by a comparison with the decay $B^\pm \to J/\psi K^\pm \to \mu^+\mu^- K^\pm$, used for normalization. In this way the uncertainties related to production cross-section and luminosity cancel out. The branching ratio of the $B^0_{d,s}$ was then obtained by the following expression:

$$\mathcal{B}(B^0_{d,s} \to \mu^+\mu^-) = \frac{N_{\rm sig}}{N_{\rm nrm}} \frac{\epsilon_{\rm nrm}}{\epsilon_{\rm sig}} \frac{f_u}{f_{d,s}} \mathcal{B}(B^\pm \to J/\psi K^\pm \to \mu^+\mu^- K^\pm)$$

where $N_{\rm sig}$ and $N_{\rm nrm}$ are the number of events in the signal and normalization samples respectively, $\epsilon_{\rm sig}$ and $\epsilon_{\rm nrm}$ are the selection efficiencies and f_u, $f_{d,s}$ are the B^+ and $B^0_{d,s}$ fragmentation functions; $f_u/f_d = 1$ was assumed while f_s/f_d was taken from LHCb measurements [8,9].

Multivariate analysis was used in the event selection both by ATLAS and CMS.

The most critical point in the measurement of the branching ratio of a decay being so rare is the background evaluation.

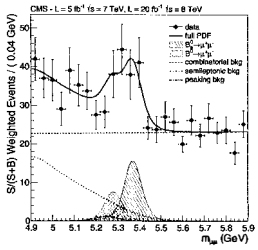

Figure 2 – Combined mass distribution for all BDT categories (CMS). This distribution is for illustrative purposes only and was not used in obtaining the final results.

Combinatorial background, represented by the grey dashed line in fig.2, was estimated using the sidebands. Physical backgrounds have been estimated using the simulations and can be

divided into non-peaking background, shown as a green line in fig.2, composed mainly from semileptonic decays of b hadrons with the final hadron misidentified as a muon, and peaking background, composed by decays of a B hadron to two light hadrons both misidentified as muons.

Fitting the distributions ATLAS set an upper limit [10]:

$$\mathcal{B}(B_s^0 \to \mu^+\mu^-) < 1.5 \times 10^{-8} @\ 95\%\ \text{C.L.}$$

while CMS measured a non zero value [11]:

$$\mathcal{B}(B_s^0 \to \mu^+\mu^-)_{\text{SM}} = (2.8^{+1.0}_{-0.9}) \times 10^{-9}$$
$$\mathcal{B}(B_d^0 \to \mu^+\mu^-)_{\text{SM}} = (4.4^{+2.2}_{-1.9}) \times 10^{-10}$$

This result changed since previously published one [12], to allow a consistent combination with the corresponding one from LHCb. The most important changed quantity is the ratio of the fragmentation functions, taken from latest LHCb measurement [9]. The estimation of the background coming from $\Lambda_b^0 \to p\mu^-\nu$ was also improved; having no measurement for the branching ratio $\mathcal{B}(\Lambda_b^0 \to p\mu^-\nu)$ the latest prediction [13] was used. The new input values, together with previously used ones, are reported in table 1.

Table 1: New input quantities used in $\mathcal{B}(B_{d,s}^0 \to \mu^+\mu^-)$ measurement by CMS. An event by event weighting was applied to $\Lambda_b^0 \to p\mu^-\nu$ simulated events to account for the differences between the simulated and predicted properties of the decay.

Updated quantity	old	new
f_u/f_s	3.91 ± 0.31	3.86 ± 0.22
$\mathcal{B}(\Lambda_b^0 \to p\mu^-\nu)$	$(6.50 \pm 6.50) \times 10^{-4}$	$(4.94 \pm 2.19) \times 10^{-4}$ event by event weights

Another effect considered in the latest CMS analysis is the selection efficiency dependence on the decay time, that's not described by a simple exponential due to the fact that the B_s^0 is a superposition of two different states with different lifetimes, so a time-dependent correction was applied.

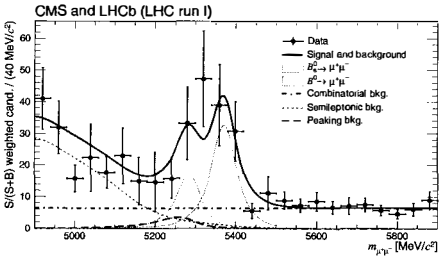

Figure 3 – Mass distribution for combined CMS and LHCb events.

In fig.3 the mass distribution of the combined events of CMS and LHCb is shown; perfoming an unique fit to the global PDF the following results have been obtained:

$$\mathcal{B}(B_s^0 \to \mu^+\mu^-)_{\text{SM}} = (2.8^{+0.7}_{-0.6}) \times 10^{-9}$$
$$\mathcal{B}(B_d^0 \to \mu^+\mu^-)_{\text{SM}} = (3.9^{+1.6}_{-1.4}) \times 10^{-10}$$

In fig.4 the comparison of the results with the standard model expectations is shown.

In the new runs LHC will operate at higher energy, up to $\sqrt{s} = 14$ TeV, that will mean higher cross-sections, and higher luminosity, up to $L = 5 \times 10^{34}$ cm^{-2}s^{-1}, that will mean larger data

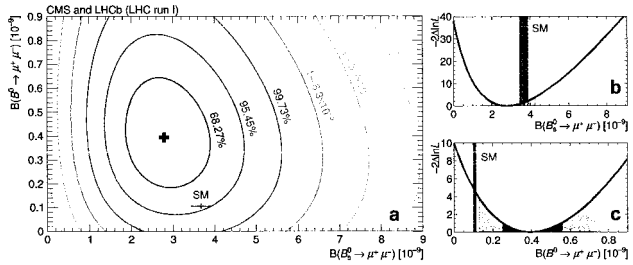

Figure 4 – Likelihood contours in the $\mathcal{B}(B_d^0 \to \mu^+\mu^-)$ versus $\mathcal{B}(B_s^0 \to \mu^+\mu^-)$ plane (a) and variations of the test statistic $-2\Delta \ln L$ for $\mathcal{B}(B_s^0 \to \mu^+\mu^-)$ and $\mathcal{B}(B_d^0 \to \mu^+\mu^-)$ (b,c respectively).

samples but also higher pileup, up to 140 interactions per bunch crossing. CMS will be upgraded to cope with the changing situation: the tracker will be improved after LS2 and for HL-LHC, and the trigger will be improved too. Despite the improvements in the tracking resolution, with high pileup a loss in efficiency can be foreseen due to the higher probability to have an additional primary vertex near the decay point; on the other side the determination of f_s/f_d is expected to improve as well as the background determination. The expected uncertainties[14] in the branching ratios measurements are reported in table 2.

Table 2: Expected uncertainties obtained by CMS in the measurement of the branching fractions $\mathcal{B}(B_s^0 \to \mu^+\mu^-)$, $\mathcal{B}(B_d^0 \to \mu^+\mu^-)$ and their ratio R.

$\mathcal{L}(\text{fb}^{-1})$	$\delta\mathcal{B}/\mathcal{B}(B_s^0 \to \mu^+\mu^-)$	$\delta\mathcal{B}/\mathcal{B}(B_d^0 \to \mu^+\mu^-)$	$\delta\mathcal{R}$
300	13%	48%	50%
3000	11%	18%	21%

2.2 $B^0 \to K^{*0}\mu^+\mu^-$ angular analysis

An angular analysis of the $B^0 \to K^{*0}\mu^+\mu^-$ decay can give hints of effects of physics beyond the standard model[15] through contributions to Wilson coefficients C_7, C_9 and C_{10}. The differential branching ratio can be expressed as a function of 4 kinematic variables, the 3 angles θ_L, θ_K and ϕ, as shown in fig.5, and the q^2, equal to the squared dimuon mass.

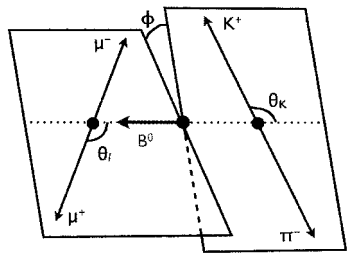

Figure 5 – Decay angles in $B^0 \to K^{*0}\mu^+\mu^-$.

In the analysis performed by ATLAS and CMS the differential decay rate is expressed using the following set of parameters: the forward-backward asymmetry (A_{FB}), the longitudinal polarization of the K^{*0} (F_{L}) and the residual S-wave contribution and interference of the $K^+\pi^-$ system (F_{S} and A_{S}). In the analysis events have been divided in q^2 square bins, the regions

corresponding to the decays $B^0 \to K^{*0}(J/\psi\ ,\psi')$ have been removed and the ϕ angle has been integrated out. Both experiments up to now gave public results only for 2011 data.

ATLAS performed a sequential fit [16]: in the first step signal yields were determined from mass fit, as shown in the fig.6, then asymmetry and polarization were obtained from angles fit, while taking S-wave contributions from BaBar measurements [17].

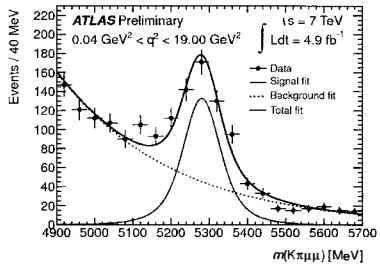

Figure 6 – Invariant mass distribution of $B^0 \to K^{*0}\mu^+\mu^-$ candidates (ATLAS). The solid blue (dark) line denotes the mass likelihood fit with the background component as dotted red line and the signal component as solid green (light) line.

CMS performed a simultaneous fit [18] to the four parameters, constraining the S-wave component to the value obtained fitting the $B^0 \to K^{*0}(J/\psi\ ,\psi')$ regions, and obtained the differential cross section dB/dq^2 by a comparison with the decay $B^0 \to K^{*0}J/\psi$:

$$\frac{d\mathcal{B}(B^0 \to K^{*0}\mu^+\mu^-)}{dq^2} = \frac{\epsilon_N}{\epsilon_S}\frac{\mathcal{B}(B^0 \to K^{*0}J/\psi)}{Y_N}\frac{dY_S}{dq^2}$$

The result of the measurement of dB/dq^2 is shown in fig.7.

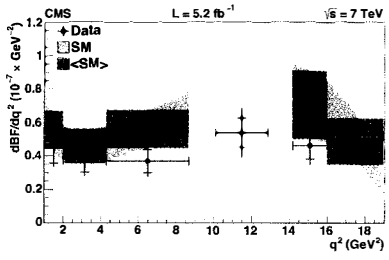

Figure 7 – Results of the measurement of dB/dq^2 versus q^2 (CMS). The statistical uncertainty is shown by inner error bars, while the outer error bars give the total uncertainty.

In fig.8 the results are shown, together with the corresponding ones obtained by previous experiments and the expectations from the standard model both for high and low q^2, while no reliable prediction is available in the mid-q^2 region. Measurements appear to be compatible both among experiments and with the expectations.

3 CP violation

3.1 $B_s^0 \to J/\psi\phi$ lifetime difference and CPV phase

In the $B_s^0 \to J/\psi\phi$ decay the flavoured initial state is an admixture of two mass eigenstates B_L^0 and B_H^0, while the final state is unflavoured, so an interference arises between the direct and mixing-mediated decays. The final state, also, does not have a definite CP, being an

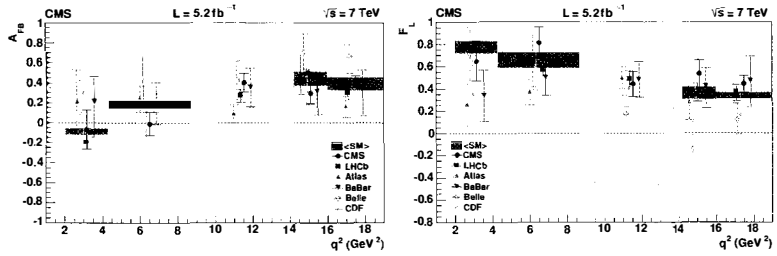

Figure 8 – Comparison of the measurement of $A_{\rm FB}$ (left) and $F_{\rm L}$ (right) versus q^2.

admixture of odd and even CP eigenstates, that must be disentangled performing again an angular analysis. The interference phase in the standard model is predicted to be $\phi_s \simeq -2\beta_s$, where $\beta_s = \arg(-(V_{ts}V_{tb}^*)/(V_{cs}V_{cb}^*)$. The latest prediction[19] for β_s is

$$2\beta_{s(\rm SM)} = 0.0363^{+0.0016}_{-0.0015}\ \text{rad}.$$

Very small deviations from the standard model expectation are also predicted by new physics models with minimal flavour violation, $|\phi_s| < 0.05$, so that any observation of a large CP violation phase would rule out those models[20]. The analysis allows also a determination of the decay width difference predicted by the standard model to be

$$\Delta\Gamma_{s(\rm SM)} = 0.087 \pm 0.021\ \text{ps}^{-1},$$

but this quantity is expected having a reduced sensitivity to new physics processes[21].

The differential decay width is expressed as the sum of 10 functions of the time and the angles:

$$\frac{d^4\Gamma(B_s^0(t))}{d\Theta dt} = f(\Theta,\alpha,ct) \propto \sum_{i=1}^{10} O_i(\alpha,ct)\cdot g_i(\Theta)$$

$$O_i(\alpha,ct) = N_i e^{-t/\tau}\left[a_i\cosh\left(\tfrac{1}{2}\Delta\Gamma_s ct\right) + b_i\sinh\left(\tfrac{1}{2}\Delta\Gamma_s ct\right) \pm c_i\cos\left(\Delta m_s ct\right) \pm d_i\sin\left(\Delta m_s ct\right)\right]$$

i	$g_i(\theta_T,\varphi_T,\psi_T)$	N_i	a_i	b_i	c_i	d_i
1	$2\cos^2\psi_T(1-\sin^2\theta_T\cos^2\varphi_T)$	$\lvert A_0\rvert^2$	1	D	C	$-S$
2	$\sin^2\psi_T(1-\sin^2\theta_T\sin^2\varphi_T)$	$\lvert A_\parallel\rvert^2$	1	D	C	$-S$
3	$\sin^2\psi_T\sin^2\theta_T$	$\lvert A_\perp\rvert^2$	1	$-D$	C	S
4	$-\sin^2\psi_T\sin 2\theta_T\sin\varphi_T$	$\lvert A_0\rvert\lvert A_\perp\rvert$	$C\sin(\delta_\perp-\delta_\parallel)$	$S\cos(\delta_\perp-\delta_\parallel)$	$\sin(\delta_\perp-\delta_\parallel)$	$D\cos(\delta_\perp-\delta_\parallel)$
5	$\frac{1}{\sqrt{2}}\sin 2\psi_T\sin^2\theta_T\sin 2\varphi_T$	$\lvert A_0\rvert\lvert A_\parallel\rvert$	$\cos(\delta_\parallel-\delta_0)$	$D\cos(\delta_\parallel-\delta_0)$	$C\cos(\delta_\parallel-\delta_0)$	$-S\cos(\delta_\parallel-\delta_0)$
6	$\frac{1}{\sqrt{2}}\sin 2\psi_T\sin 2\theta_T\sin\varphi_T$	$\lvert A_0\rvert\lvert A_\perp\rvert$	$C\sin(\delta_\perp-\delta_0)$	$S\cos(\delta_\perp-\delta_0)$	$\sin(\delta_\perp-\delta_0)$	$D\cos(\delta_\perp-\delta_0)$
7	$\frac{2}{3}(1-\sin^2\theta_T\cos^2\varphi_T)$	$\lvert A_S\rvert^2$	1	$-D$	C	S
8	$\frac{1}{3}\sqrt{6}\sin\psi_T\sin^2\theta_T\sin 2\varphi_T$	$\lvert A_S\rvert\lvert A_\parallel\rvert$	$C\cos(\delta_\parallel-\delta_S)$	$S\sin(\delta_\parallel-\delta_S)$	$\cos(\delta_\parallel-\delta_S)$	$D\sin(\delta_\parallel-\delta_S)$
9	$\frac{1}{3}\sqrt{6}\sin\psi_T\sin 2\theta_T\cos\varphi_T$	$\lvert A_S\rvert\lvert A_\perp\rvert$	$\sin(\delta_\perp-\delta_S)$	$-D\sin(\delta_\perp-\delta_S)$	$C\sin(\delta_\perp-\delta_S)$	$S\sin(\delta_\perp-\delta_S)$
10	$\frac{4}{3}\sqrt{3}(1-\sin^2\theta_T\cos^2\varphi_T)$	$\lvert A_S\rvert\lvert A_0\rvert$	$C\cos(\delta_0-\delta_S)$	$S\sin(\delta_0-\delta_S)$	$\cos(\delta_0-\delta_S)$	$D\sin(\delta_0-\delta_S)$

$$C = \frac{1-|\lambda|^2}{1+|\lambda|^2} \qquad S = -\frac{2|\lambda|\sin\phi_s}{1+|\lambda|^2} \qquad D = -\frac{2|\lambda|\cos\phi_s}{1+|\lambda|^2}.$$

The amplitudes $A_\perp$, A_0, $A_\parallel$, $A_{\rm S}$ correspond to the P-wave and S-wave components, with their phases $\delta_\perp$, δ_0, $\delta_\parallel$, δ_S; $|\lambda|$ describes the direct CP violation. In the expression the signs of c_i and d_i coefficients are positive or negative for the decay of an initial B_s^0 or $\bar{B}_s^0$ respectively.

The differential width depends only on the differences among the phases δ, so in the fit $\delta_0 = 0$ was assumed, and the difference $\delta_{S\perp}$ between $\delta_\perp$ and δ_S was fitted as an unique variable to reduce the correlation among the parameters. No direct violation was assumed in the measurement, therefore $|\lambda| = 1$ was fixed.

The discrimination between the positive or negative initial flavour is obtained looking for a second B produced in the event and inferring its flavour looking at the charge of its decay products; of course the charge-flavour correlation is diluted due to the presence of cascade decays and oscillations of the other b hadron itself.

In ATLAS analysis [22] of $\sqrt{s} = 7$ TeV data the flavour was tagged looking at the charge of particles contained in a cone around a muon, assumed to come from the semileptonic decay of a b; if no muon was found the particles in a b-tagged jets were used. A "cone charge" was defined as

$$Q = \frac{\sum_i^{N_{\text{tracks}}} q^i \cdot (p_{T,i})^j}{\sum_i^{N_{\text{tracks}}} (p_{T,i})^j}$$

where $j = 1.1$ and the sum was performed over the reconstructed tracks within a cone size of $\Delta R = 0.5$.

In CMS analysis [23] of $\sqrt{s} = 8$ TeV data only semileptonic decays were used to tag the flavour, looking to both electrons and muons. The performance of the methods were measured with events containing the self-tagging decay $B^+ \to J/\psi K^+$. The efficiency and tagging power of the algorithms are reported in tab.3

Table 3: Performance of flavour tagging algorithm in CMS analysis; errors are statistical only.

	ATLAS	CMS
Tagging efficiency $\epsilon_{\text{tag}}(\%)$	32.1 ± 0.01	7.67 ± 0.04
Mistag fraction $\omega(\%)$	21.3 ± 0.08	32.2 ± 0.3
Tagging power $P_{\text{tag}}(\%)$	1.45 ± 0.05	0.97 ± 0.03

The results of an unbinned maximum likelihood fit, including per-event resolution and tagging probability terms are shown in tab.4 and fig.9.

Table 4: Final results of CP violating phase and decay width difference measurements.

	ATLAS	CMS
ϕ_s[rad]	$0.12 \pm 0.25 \pm 0.05$	$-0.03 \pm 0.11 \pm 0.03$
$\Delta\Gamma_s$[ps^{-1}]	$0.053 \pm 0.021 \pm 0.010$	$0.096 \pm 0.014 \pm 0.007$

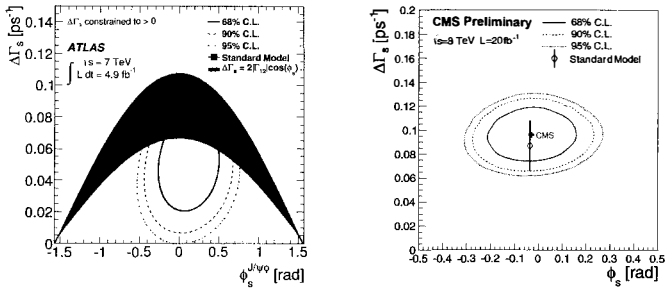

Figure 9 – Likelihood contours in the $\phi_s - \Delta\Gamma_s$ plane in ATLAS (left) and CMS (right) measurements.

Both experiments found a result in agreement with the prediction, but a significant test will require a smaller uncertainty, so further investigations are required.

Again, more data will be available with the new run and increased luminosity, but this will correspond to a more difficult environment. ATLAS will have an improved pixel tracker, with a fourth layer, for Run2, and a new tracker with reduced pixel size for HL-LHC. The need to stay inside a necessarily limited trigger bandwidth will require harder cuts on muon p_T; two possible cuts have been considered, at 6 GeV for Phase-1 and 11 GeV for Phase-2. The upgraded tracker will allow a better vertex reconstruction and an improvement of 30% in proper decay time resolution. In principle this could be affected by the higher pileup, but a dedicated study[24] showed that even in the hypothesis that the number of interaction could reach $N = 200$, no significant effect appears visible, as shown in fig.10.

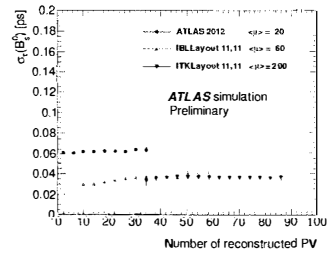

Figure 10 – Proper decay time resolution in ATLAS against the number of reconstructed primary vertices in simulated $B_s^0 \to J/\psi\phi$ events.

Estimating the signal yields applying the harder muon p_T cuts to 2012 data and rescaling with efficiencies and luminosities the results shown in tab.5 are obtained.

Table 5: Estimated ATLAS statistical precisions of ϕ_s measurement for considered LHC periods.

$\mathcal{L}(\text{fb}^{-1})$	$p_{T\mu}$ cut [GeV]	$\sigma(\phi_s)$(stat)[rad]
100	6	0.054
100	11	0.10
250	11	0.064
3000	11	0.022

3.2 $B_s^0 \to J/\psi f_0$ decay

Another channel that can be studied to investigate CP violation is $B_s^0 \to J/\psi f_0$; the f_0 is a scalar and the final state is an almost pure CP-odd eigenstate, so that there's no need to disentangle two components and no angular analysis is required:

$$\Gamma(B_s^0/\bar{B}_s^0 \to J/\psi f_0) = \mathcal{N} e^{-\Gamma_s t} \left\{ e^{\Delta\Gamma_s t/2}(1 + \cos\phi_s) + e^{-\Delta\Gamma_s t/2}(1 - \cos\phi_s) \pm \sin\phi_s \sin(\Delta m_s t) \right\}$$

On the other side the hadronic corrections to apply in predictions depend on the structure of the f_0, that is not completely clear, as it could be a simple quark-antiquark pair, but also a tetraquark or a KK molecule[25]. In the analysis, the initial flavour can be tagged using the same techinque used as for $B_s^0 \to J/\psi\phi$, and the tagging information is to be added to the $\sin\phi_s$ term.

This analysis has not yet been performed, but some propaedeutic study has been done. The branching fraction ratio $\mathcal{B}(B_s^0 \to J/\psi f_0)\mathcal{B}(f_0 \to \pi^+\pi^-)/\mathcal{B}(B_s^0 \to J/\psi\phi)\mathcal{B}(\phi \to K^+K^-)$ has been measured by CMS[26], while the lifetime and CP violation measurements are to come.

This is not only a necessary experimental exercise but is useful to give informations about the hadronic structure of the f_0. Events were selected requiring a dimuon originating from a displaced secondary vertex, to form a J/ψ, and two opposite charged pions to form a f_0 candidate or two kaons to form a ϕ. The $J/\psi\pi^+\pi^-$ invariant mass distribution is shown in fig.11.

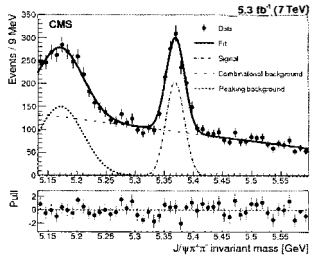

Figure 11 – Invariant mass distribution of the $B_s^0 \to J/\psi f_0$ candidates.

As a ratio is measured, again there's a cancellation of systematic uncertainties; yields were measured using an unbinned maximum likelihood fit and efficiencies were computed from simulation. The final result is

$$R_{f_0/\phi} = \frac{\mathcal{B}(B_s^0 \to J/\psi f_0)\mathcal{B}(f_0 \to \pi^+\pi^-)}{\mathcal{B}(B_s^0 \to J/\psi\phi)\mathcal{B}(\phi \to K^+K^-)} = 0.140 \pm 0.013 \pm 0.018$$

4 Conclusions

ATLAS and CMS have produced significant EW results in HF physics: $\mathcal{B}(B_s^0 \to \mu^+\mu^-)$ have been measured, an angular analysis of $B^0 \to K^{*0}\mu^+\mu^-$ have been performed, the CP violation phase ϕ_s in $B_s^0 \to J/\psi\phi$ decay has been measured and the study of the $B_s^0 \to J/\psi f_0$ decay begun.

All results are, up to now, compatible with SM predictions, but more stringent tests will be obtained with more precise measurement to be done in the future LHC runs.

References

1. C.Bobeth *et al.*, $B_{s,d} \to \ell^+\ell$ in the Standard Model with Reduced Theoretical Uncertainty, *Phys. Lett.* B **112**, 101801 (2014). doi: 10.1103/PhysRevLett.112.101801
2. J.R.Ellis *et al.*, On $B_s^0 \to \mu^+\mu^-$ and cold dark matter scattering in the MSSM with non-universal Higgs, *J. High Energy Phys.* **05**, 063 (2006). doi: 10.1088/1126-6708/2006/05/063
3. S.Davidson and S. Descotes-Genon, "Minimal Flavour Violation" for leptoquarks, *J. High Energy Phys.* **11**, 073 (2010). doi: 10.1007/JHEP11(2010)073
4. S. R. Choudhury *et al.*, SIGNATURES OF NEW PHYSICS IN DILEPTONIC B-DECAYS, *Int. J. Mod. Phys.* A **21**, 2017 (2006). doi: 10.1142/S0217751X06029491
5. J.K.Parry, Lepton flavour violating Higgs boson decays, $\tau \to \mu\gamma$ and $B_s^0 \to \mu^+\mu^-$ in the constrained MSSM + ν_R with large $\tan\beta$, *Nucl. Phys.* B **760**, 38 (2006). doi: 10.1016/j.nuclphysb.2006.10.011
6. J.R.Ellis *et al.*, B-meson observables in the maximally CP-violating MSSM with minimal flavor violation, *Phys. Rev.* D **76**, 115011 (2007). doi: 10.1103/PhysRevD.76.115011
7. G.D'Ambrosio *et al.*, Minimal flavour violation: an effective field theory approach, *Nucl. Phys.* B **645**, 155 (2002). doi: http://dx.doi.org/10.1016/S0550-3213(02)00836-2

8. LHCb Collaboration, Measurement of the fragmentation fraction ratio f_s/f_d and its dependence on B meson kinematics, *J. High Energy Phys.* **04**, 001 (2013) doi: http://dx.doi.org/10.1007/JHEP04(2013)001
9. LHCb Collaboration, Average f_s/f_d b-hadron production fraction ratio for $\sqrt{s} = 7$ TeV collisions, Jul, 2013
10. ATLAS Collaboration, Limit on $\mathcal{B}_s^0 \to \mu^+\mu^-$ branching fraction based on 4.9 fb^{-1} of integrated luminosity, ATLAS-CONF-2013-076. url: http://atlas.web.cern.ch/Atlas/GROUPS/PHYSICS/CONFNOTES/ATLAS-CONF-2013-076
11. CMS and LHCb Collaborations, Observation of the rare $B_s^0 \to \mu^+\mu^-$ decay from the combined analysis of CMS and LHCb data, arXiv:1411.4413. url: http://arxiv.org/pdf/1411.4413v1.pdf
12. CMS Collaboration, Measurement of the $B_s^0 \to \mu^+\mu^-$ Branching Fraction and Search for $B^0 \to \mu^+\mu^-$ with the CMS Experiment, *Phys. Rev. Lett.* **111**, 101804 (2013). doi: 10.1103/PhysRevLett.111.101804
13. A.Khodjamirian *et al.*, Form factors and strong couplings of heavy baryons from QCD light-cone sum rules, *J. High Energy Phys.* **09**, 106 (2011). doi: http://dx.doi.org/10.1007/JHEP09(2011)106
14. CMS Collaboration, Physics Performance for 2nd ECFA workshop. url: https://twiki.cern.ch/twiki/pub/CMSPublic/PhysicsResultsFP/ECFA-CMSPublicResults.pdf
15. W.Altmannshofer *et al.*, Symmetries and asymmetries of $B^0 \to K^{*0}\mu^+\mu^-$ decays in the Standard Modcl and beyond, *J. High Energy Phys.* **01**, 019 (2009). doi: 10.1088/1126-6708/2009/01/019
16. ATLAS Collaboration, Angular analysis of $B^0 \to K^{*0}\mu^+\mu^-$ with the ATLAS Experiment, ATLAS-CONF-2013-038. url: https://atlas.web.cern.ch/Atlas/GROUPS/PHYSICS/CONFNOTES/ATLAS-CONF-2013-038
17. BaBar collaboration, Time-integrated and time-dependent angular analyses of $B \to J/\psi K\pi$: A measurement of $\cos 2\beta$ with no sign ambiguity from strong phases, *Phys. Rev.* D **71**, 032005 (2005). doi: http://dx.doi.org/10.1103/PhysRevD.71.032005
18. CMS Collaboration, Angular analysis and branching fraction measurement of the decay $B^0 \to K^{*0}\mu^+\mu^-$, *Phys. Lett.* B **727**, 77 (2013). doi: 10.1016/j.physletb.2013.10.017
19. J.Charles *et al.*, Predictions of selected flavor observables within the standard model, *Phys. Rev.* D **84**, 033005 (2011). doi: 10.1103/PhysRevD.84.033005
20. G.Isidori, Flavor physics and CP violation, arXiv:1302.0661. url: http://arxiv.org/pdf/1302.0661v1.pdf
21. A.Lenz and U.Nierste, Numerical updates of lifetimes and mixing parameters of B mesons, arXiv:1102.4274. url: http://arxiv.org/pdf/1102.4274v1.pdf
22. ATLAS Collaboration, Flavor tagged time-dependent angular analysis of the $B_s^0 \to J/\psi\phi$ decay and extraction of $\Delta\Gamma_s$ and the weak phase ϕ_s in ATLAS, *Phys. Rev.* D **90**, 052007 (2014). doi: 10.1103/PhysRevD.90.052007
23. CMS Collaboration, Measurement of the CP-violating weak phase ϕ_s and the decay width difference $\Delta\Gamma_s$ using the $B_s^0 \to J/\psi\phi(1020)$ decay channel, CMS-PAS-BPH-13-012. url: http://cds.cern.ch/record/1744869/files/BPH-13-012-pas.pdf
24. ATLAS Collaboration, ATLAS B-physics studies at increased LHC luminosity, potential for CP-violation measurement in the $B_s^0 \to J/\psi\phi$ decay, ATL-PHYS-PUB-2013-010. url: http://cds.cern.ch/record/1604429/files/ATL-PHYS-PUB-2013-010.pdf
25. R.Fleischer *et al.*, Anatomy of $B_s^0 \to J/\psi f_0(980)$, *Eur. Phys. J.* C **71**, 1832 (2011). doi: 10.1140/epjc/s10052-011-1832-x
26. CMS Collaboration, Measurement of the ratio $\mathcal{B}(B_s^0 \to J/\psi f_0)/\mathcal{B}(B_s^0 \to J/\psi\phi(1020))$ in pp collisions at $\sqrt{s} = 7$ TeV, arXiv:1501.06089. url: http://arxiv.org/pdf/1501.06089v1.pdf

Charm mixing and CP violation at LHCb

Evelina Gersabeck on behalf of the LHCb collaboration
Physikalisches Institut, Im Neuenheimer Feld 226, 69120 Heidelberg, Germany

LHCb has collected the world's largest sample of charmed hadrons. This sample is used to search for direct CP violation in the multibody prompt charm decays $D^0 \to \pi^-\pi^+\pi^0$. The search employs an unbinned model independent method known as the energy test. Using the data collected by LHCb at centre-of-mass energy of 8 TeV, the world's best sensitivity to CP violation in this decay is achieved. The data are found to be consistent with the hypothesis of CP symmetry with a p-value of $(2.6 \pm 0.5)\%$. In addition, new measurements of indirect CP violation in muon-tagged D^0 decays to two-body CP even final states are presented. The time dependent CP asymmetries in the decay rates of the singly Cabibbo-suppressed decays $D^0 \to K^-K^+$ and $D^0 \to \pi^-\pi^+$ decays using the full LHCb run 1 data set are determined to be $A_\Gamma(K^-K^+) = (-0.134 \pm 0.077^{+0.026}_{-0.034})\%$ and $A_\Gamma(\pi^-\pi^+) = (-0.092 \pm 0.145^{+0.025}_{-0.033})\%$. These results are compatible with the hypothesis of no indirect CPV and with previous LHCb measurements.

1 Introduction

The excellent performance of the LHC and the LHCb experiment, along with large production $c\bar{c}$ cross sections for pp collisions at $\sqrt{s}$ of 7 and 8 TeV has enabled unprecedentedly large samples of charm decays to be recorded during 2011 and 2012, corresponding to 3 fb^{-1} of integrated luminosity. The data are taken with a regular swap of the polarity of the spectrometer dipole magnet which can compensate for the left-right detector asymmetries to a first order. The large samples of collected and reconstructed charm meson decays allow the study of mixing and CP violation (CPV) effects at a precision not achieved before in charm decays.

The mass eigenstates of the neutral charm mesons are are a linear combination of the flavour eigenstates D^0 and $\bar{D}^0$, $|D_{1,2}\rangle = p\,|D^0\rangle \pm q\left|\bar{D}^0\right\rangle$ where the complex coefficients p, q satisfy $|p|^2 + |q|^2 = 1$. This results in D^0 and $\bar{D}^0$ oscillations. The mixing parameters are defined as $x = (m_1 - m_2)/\Gamma$ and $y = (\Gamma_1 - \Gamma_2)/2\Gamma$, where m_1, m_2, Γ_1 and Γ_2 are the masses and the decay widths for D_1 and D_2, respectively, and $(\Gamma_1 + \Gamma_2)/2 = \Gamma$. The phase convention is chosen such that $CP\,|D^0\rangle = -\left|\bar{D}^0\right\rangle$. The first evidence of D^0 and $\bar{D}^0$ oscillation is reported in 2007 by BaBar [1] and Belle [2]. Now the mixing in the charm sector is well established and it has been measured with a very large significance at the LHCb experiment [3].

The recent results on CP violation searches in charm decays performed by the LHCb experiment are reviewed in these proceedings. Both types of charm decays, originating from the primary vertex, and coming from a parent beauty hadron are exploited at LHCb; this is indicated for each of the presented analyses.

2 Search for CPV in $D^0 \to \pi^-\pi^+\pi^0$ decays with the energy test

Asymmetries in the Dalitz plot substructure can be measured using an amplitude model or using model independent statistical analysis. The latter methods allow the discovery of CP violation without identifying its source. The model independent analysis can be done using binned and unbinned techiques. At LIICb, both types of model independent analyses are widely explored [4, 5, 6].

The energy test [7] is an unbinned model-independent statistical method to search for time-integrated CP violation in $D^0 \to \pi^-\pi^+\pi^0$ decays. The method relies on the comparison of two D^0 and $\bar{D}^0$ flavour samples and is sensitive to CPV localised in the phase-space of the multi body final state. This is the first application of the method for a CPV search.

The final state $\pi^-\pi^+\pi^0$ is a self-conjugate state. The flavour of the prompt D^0 is tagged by the charge of the slow pion, π_s, in the strong decay $D^* \to D^0\pi_s$. The total sample used consists of about 660 thousand $D^0 \to \pi^-\pi^+\pi^0$ decays corresponding to about 2fb^{-1} collected during 2012.

In this analysis two categories of neutral pions are used - resolved, for which the two final photons are reconstructed separately, and merged, which are detected as one merged cluster in the detector. The resolved neutral pions have a lower transverse energy, E_T, while the merged ones have a higher E_T. The decay $D^0 \to \pi^-\pi^+\pi^0$ is dominated by the $\rho(770)$ resonances with the ρ meson decaying into a pair of pions which can be seen in the enhanced event density regions on the Dalitz plot (see Fig. 1). By using both merged and resolved neutral pions for the reconstruction of the D^0 mesons, the coverage of the Dalitz plot is improved.

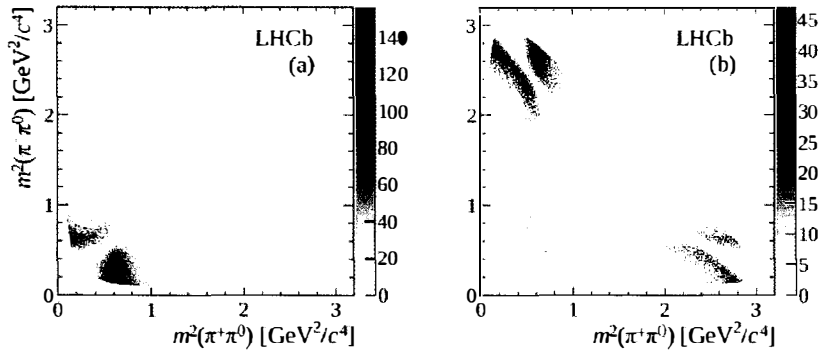

Figure 1 – The Dalitz plot of the $D^0 \to \pi^-\pi^+\pi^0$ decay with merged (a) and resolved (b) neutral pions.

At LHCb, the energy test is used to assign a p-value for a non-zero CPV hypothesis [6]. In this method, a test statistic T is used to compare the average distances based on the metric function ψ. It is defined as

$$T = \sum_{i,j>i}^{n} \frac{\psi_{ij}}{n(n-1)} + \sum_{i,j>i}^{\overline{n}} \frac{\psi_{ij}}{\overline{n}(\overline{n}-1)} - \sum_{i,j}^{n,\overline{n}} \frac{\psi_{ij}}{n\overline{n}}, \tag{1}$$

and the metric function $\psi_{ij} \equiv \psi(d_{ij}) = e^{-d_{ij}^2/2\sigma^2}$ is chosen as a Gaussian function with a tunable parameter σ as it should be a falling function with increasing the distance between events. T compares the average distances of pairs of events belonging to two samples of opposite flavour. The normalisation factor removes the impact of global asymmetries. The distance between two points in phase space is given by $d_{ij} = (m_{12}^{2,j} - m_{12}^{2,i}, m_{23}^{2,j} - m_{23}^{2,i}, m_{13}^{2,j} - m_{13}^{2,i})$, where the $1, 2, 3$

subscripts indicate the final-state particles. For no-CPV, T is expected to be zero, and larger than zero in case of the CPV. This unbinned technique calculates a p-value under the hypothesis of CP symmetry by comparing the nominal T value observed in data to a distribution of T values obtained from permutation samples, where the flavour of the D^0 is randomly reassigned to simulate samples without CP violation. The p-value for the no CPV hypothesis is obtained as the fraction of permutation T values greater than the nominal T value.

LHCb has the best sensitivity to local CPV in this decay (to a few degrees of CPV in the phase, and to a few percent CPV in the amplitude) in general. Only in the case of CPV in the ρ^0 amplitude the LHCb sensitivity is similar to the previous most sensitive study of this decay done by the BaBar collaboration [8]. The sensitivity is examined based on simpli

ed Monte Carlo samples generated using the generator package Laura++ [9].

By counting the fraction of permutations with a T value above the nominal T value in the data, a p-value of $(2.6 \pm 0.5) \times 10^{-2}$ is extracted. This result is based on 1000 permutations. A small phase-space region dominated by the ρ^+ resonance contains candidates with a local positive asymmetry exceeding 1σ significance. The result is consistent with CP conservation at the current level of precision.

The data sample has been split according to various criteria to test the stability of the results. Analyses of sub-samples with opposite magnet polarity, with different trigger configurations, and with fiducial selection requirements removing areas of high local asymmetry of the tagging soft pion from the D^*+ decay all provide consistent results. Various checks have been performed to ensure there are no asymmetries arising form background events or detector related asymmetries. No indication of background or detector related asymmetries is found.

3 Search for indirect CPV in the muon-tagged singly Cabibbo suppressed $D^0 \to h^-h^+$ decays

The indirect CPV is measured through, A_Γ, the asymmetry the effective lifetimes of decays to CP eigenstates

$$A_\Gamma = \frac{\tau(\bar{D^0} \to h^-h^+) - \tau(D^0 \to h^-h^+)}{\tau(\bar{D^0} \to h^-h^+) + \tau(D^0 \to h^-h^+)} \tag{2}$$

A_Γ is equivalent to the indirect CPV asymmetry with a good approximation (neglecting the direct CPV term $A_d\ y\ \cos\phi$)

$$A_\Gamma \approx \frac{1}{2} A_M\ y\ \cos\phi + x\ \sin\phi = -a^{ind}_{CP}. \tag{3}$$

The indirect CPV comprises a non-zero asymmetry in the mixing,

$$A_M = \frac{|q/p|^2 - |p/q|^2}{|q/p|^2 + |p/q|^2}, \tag{4}$$

and CPV through a non-zero phase ϕ. A large value of A_Γ or a final state dependence may indicate new physics.

For this analysis, the flavour of the D^0 mesons at production is determined by the charge of the muon in the semileptonic decays $B \to D^0\mu\nu X$.

To extract A_Γ, the CP asymmetries

$$A_{CP}(t) = \frac{\Gamma(D^0 \to f;t) - \Gamma(\bar{D^0} \to f;t)}{\Gamma(D^0 \to f;t) + \Gamma(\bar{D^0} \to f;t)} \tag{5}$$

in the decay rates of D^0 and $\bar{D^0}$ are measured in 50 bins of the decay times by fits to the D^0 invariant mass. The asymmetry measured in each bin is plotted as a function of the decay time

in Fig. 2. A_Γ is given by the slope of the linear fit of this distribution

$$A_{CP}(t) = A_{CP}^{dir} - A_\Gamma \frac{t}{\tau}. \tag{6}$$

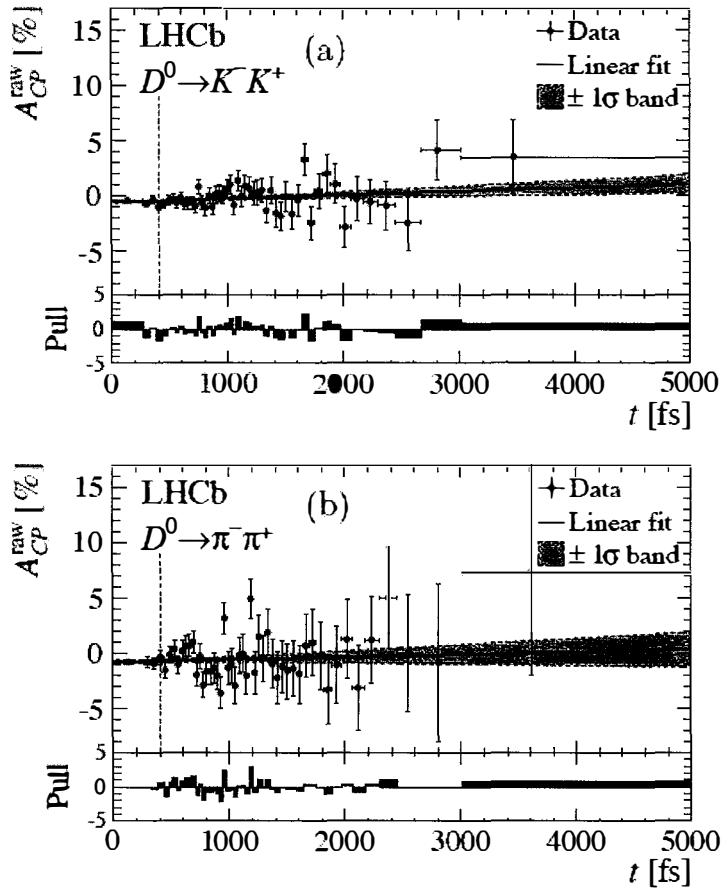

Figure 2 – The asymmetry $A_{CP}(f;t)$ in 50 bins of the decay time for (a) $D^0 \to K^+K^-$ and for (b) $D^0 \to \pi^+\pi^-$ decays.

The results obtained with the full sample of muon-tagged D^0 decays corresponding to 3 fb^{-1} are [10]

$$\begin{aligned} A_\Gamma(K^-K^+) &= (-0.134 \pm 0.077^{+0.026}_{-0.034})\%; \\ A_\Gamma(\pi^-\pi^+) &= (-0.092 \pm 0.145^{+0.025}_{-0.033})\%. \end{aligned} \tag{7}$$

The results for both decay modes are consistent with each other. These measurements are statistically dominated, and the largest systematic contribution arises from the mistag asymmetry. The results are compatible with the Standard model expectations [11, 12] of $A_\Gamma < 10^{-4}$, and they

agree with the current most precise measurements of A_Γ done at LHCb by using the 2011 data sample of the prompt tagged $D^0 \to h^- h^+$ decays[13]

$$A_\Gamma(K^-K^+) = (-0.35 \pm 0.62 \pm 0.12) \times 10^{-3};$$
$$A_\Gamma(\pi^-\pi^+) = (0.33 \pm 1.06 \pm 0.14) \times 10^{-3}. \quad (8)$$

The prompt and the muon-tagged results are uncorrelated, and by studying both, a larger decay time range is covered.

4 Summary of the CP violation searches in charm

The current status of the CPV searches in charm is summarised in Fig. 3[14] combining the most recent A_Γ (including the muon-tagged A_Γ results) and ΔA_{CP} measurements[15], [16]. On the x-axis the indirect CPV asymmetry, a_{CP}^{ind}, is plotted, and on the y-axis the direct CPV asymmetry, Δa_{CP}^{dir}, is shown. The best fit values

$$a_{CP}^{ind} = (0.06 \pm 0.04)\%;$$
$$\Delta a_{CP}^{dir} = (-0.26 \pm 0.10)\%, \quad (9)$$

are compatible with the hypothesis of no-CPV in the charm sector at 1.8% CL.

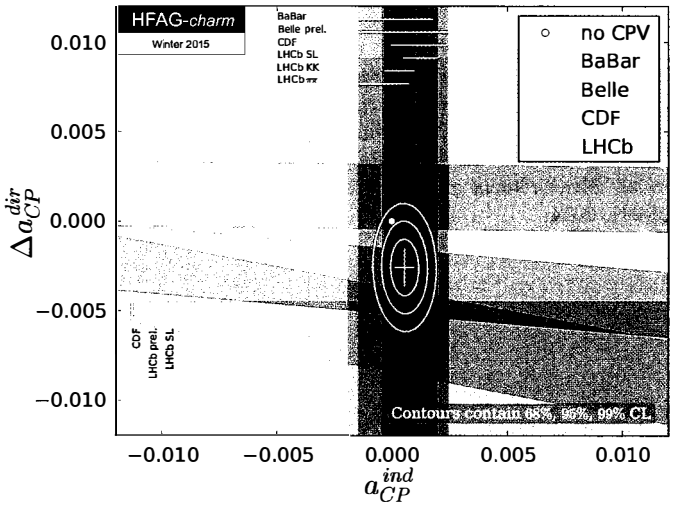

Figure 3 – Direct CP asymmetry versus indirect CPV asymmetry in the charm sector.

5 Conclusions

LHCb has performed world leading measurements in the charm sector. The $D^0 - \bar{D}^0$ mixing is well established. The searches for indirect and direct CPV in two- and multi body decays are consistent with CP conservation, in agreement with the SM at the current level of precision.

References

1. Bernard Aubert et al. Evidence for D^0 -anti-D0 Mixing. *Phys. Rev. Lett.*, 98:211802, 2007.
2. M. Staric et al. Evidence for D^0 - $\bar{D}^0$ Mixing. *Phys. Rev. Lett.*, 98:211803, 2007.
3. R. Aaij et al. Measurement of D^0–$\bar{D}^0$ mixing parameters and search for CP violation using $D^0 \to K^+\pi^-$ decays. *Phys. Rev. Lett.*, 111:251801, 2013.
4. R. Aaij et al. Search for CP violation in the decay $D^+ \to \pi^-\pi^+\pi^+$. *Phys. Lett.*, B728:585, 2014.
5. R. Aaij et al. Model-independent search for CP violation in $D^0 \to K^-K^+\pi^+\pi^-$ and $D^0 \to \pi^-\pi^+\pi^-\pi^+$ decays . *Phys. Lett.*, B726:623, 2013.
6. Roel Aaij et al. Search for CP violation in $D^0 \to \pi^-\pi^+\pi^0$ decays with the energy test. 2014. submitted to PLB.
7. Mike Williams. Observing CP Violation in Many-Body Decays. *Phys. Rev.*, D84:054015, 2011.
8. Bernard Aubert et al. Search for CP Violation in Neutral D Meson Cabibbo-suppressed Three-body Decays. *Phys. Rev.*, D78:051102, 2008.
9. T. Latham et al. Laura++ Dalitz plot Fitting package. http://laura.hepforge.org/.
10. Roel Aaij et al. Measurement of indirect CP asymmetries in $D^0 \to K^-K^+$ and $D^0 \to \pi^-\pi^+$ decays using semileptonic B decays. *JHEP*, 1504:043, 2015.
11. Alexander L. Kagan and Michael D. Sokoloff. On Indirect CP Violation and Implications for D0 - anti-D0 and B(s) - anti-B(s) mixing. *Phys. Rev.*, D80:076008, 2009.
12. Ikaros I. Bigi, Ayan Paul, and Stefan Recksiegel. Conclusions from CDF Results on CP Violation in $D^0 \to \pi^+\pi^-, K^+K^-$ and Future Tasks. *JHEP*, 1106:089, 2011.
13. R. Aaij et al. Measurements of indirect CP asymmetries in $D^0 \to K^-K^+$ and $D^0 \to \pi^-\pi^+$ decays. *Phys. Rev. Lett.*, 112:041801, 2014.
14. Marco Gersabeck. HFAG-charm averages. 2014. updated results and plots available at `http://www.slac.stanford.edu/xorg/hfag/`.
15. LHCb collaboration. A search for time-integrated CP violation in $D^0 \to K^-K^+$ and $D^0 \to \pi^-\pi^+$ decays. *LHCb-CONF-2013-003*, Mar 2013.
16. R. Aaij et al. Measurement of CP asymmetry in $D^0 \to K^-K^+$ and $D^0 \to \pi^-\pi^+$ decays. *JHEP*, 07:041, 2014.

$K \to \pi\nu\bar{\nu}$ in the Standard Model and Beyond

R. Knegjens
TUM Institute for Advanced Study, Lichtenbergstr. 2a,
D-85747 Garching, Germany

The precision expected for the rare $K \to \pi\nu\bar{\nu}$ decays by the NA62 and KOTO experiments in the coming decade will rival their current SM predictions. In preparation for this upcoming opportunity, we review the SM predictions and discuss the sensitivity of these decays to models beyond the Standard Model, considering in particular simplified Z and Z' models as benchmarks. In the latter case we also discuss how these decays could ultimately probe distance scales as small as zeptometers i.e. peek into the Zeptouniverse.

1 Introduction

Since the turn on of the LHC half a decade ago, the high energy physics community has yet to discover a conclusive signal of New Physics (NP), its coveted goal. However, it has narrowed down the search; in particular placing lower mass bounds on several hypothesized NP particles via direct searches. And much progress has also been made on indirect searches, which may be our last hope in the LHC-era should the NP scale prove to be out of reach of direct searches. By indirect searches we refer in particular to flavour changing neutral currents (FCNC) processes, which are necessarily loop suppressed in the Standard Model (SM) due to the GIM mechanism, and further so by the almost diagonal CKM matrix structure. In contrast, FCNCs in models of NP need not be suppressed at all. A prominent example is meson mixing, which is driven by $\Delta F = 2$ FCNC processes that can probe NP scales up to thousands of TeV [1,2] if the NP is unsuppressed, or, equivalently, down to distances smaller than a zeptometer. The catch is that were NP detected through such channels, many details would remain hidden.

This is where rare $\Delta F = 1$ FCNC decays enter, which have the advantage that their operator structure, for example whether they couple left (LH) or right handedly (RH) to quarks or leptons, is exposed by the spin structure of the final state. This would reveal much about the nature of the NP, and it is thereby worth asking what scales could ultimately be reached by such processes. The two famous examples to be discussed in this talk are the rare decays $K^+ \to \pi^+\nu\bar{\nu}$ and $K_L \to \pi^0\nu\bar{\nu}$. These decays are driven by electroweak (EW) loops, in particular Z-penguins with internal top quarks. The two decays differ only by their spectator quarks, though due to its CP-even final state the $K_L \to \pi^0\nu\bar{\nu}$ decay is almost completely CP violating, in contrast to $K^+ \to \pi^+\nu\bar{\nu}$, which also has a CP conserving component. Strikingly, the CKM structure corresponding to the leading $s \to d$ transitions in these decays is two orders of magnitude smaller than for $b \to \{d, s\}$ transitions, making these decays

exceptionally suppressed in the SM. Furthermore, the long-distance physics described by the hadronic matrix elements of these decays, which is typically a troublesome source of uncertainty for meson decays, can be accurately related using chiral perturbation theory to those of charged semileptonic decays [3]. Thus these decays are also exceptionally theoretically clean, and thereby ideal probes of NP.

Experimental progress to date has been modest, with an imprecise branching ratio measurement for $K^+ \to \pi^+\nu\bar{\nu}$ [4], and an upper-bound on $K_L \to \pi^0\nu\bar{\nu}$ [5]. It is therefore exciting that within the next 10 years the NA62 experiment at CERN hopes to measure the former mode with a precision of 10% relative to the SM [6,7], and the KOTO experiment hopes to observe the latter mode [8]. Unfortunately, two experiments planned at Fermilab to measure both to a 5% precision, ORKA [9] and Project X [10], do not look set to continue.

Nonetheless, a lot is possible with the planned precision. In Section 2 we will discuss the status and perspectives of these two decays in the SM. In Section 3 we will discuss how their interplay can discriminate between various models of NP using simplified Z and Z' models as a basis. Furthermore we will briefly discuss what NP scales could ultimately be reached in general for these decays.

2 $K \to \pi\nu\bar{\nu}$ in the Standard Model

In the SM these decays are dominantly driven by so-called Z-penguins. Due to the breaking of the GIM-mechanism by the squared masses of the internal quarks, the heavy top-quark loops dominate, yet charm-loops also remain relevant due to their larger CKM contribution. The branching ratio observables can be expressed as

$$\begin{aligned} \mathrm{BR}(K^+ \to \pi^+\nu\bar{\nu}) &= \tilde{\kappa}_+ \left[\left(\frac{\mathrm{Im}(V_{td}V_{ts}^*)}{\lambda^5} X(x_t) \right)^2 + \left(\frac{\mathrm{Re}(V_{cd}V_{cs}^*)}{\lambda} P_c(X) + \frac{\mathrm{Re}(V_{td}V_{ts}^*)}{\lambda^5} X(x_t) \right)^2 \right] \\ \mathrm{BR}(K_L \to \pi^0\nu\bar{\nu}) &= \kappa_L \left(\frac{\mathrm{Im}(V_{td}V_{ts}^*)}{\lambda^5} X(x_t) \right)^2 \end{aligned} \tag{1}$$

where the accurately determined $\tilde{\kappa}_+$[a] and κ_L include the hadronic matrix elements [3]. The charm loop contributions have been determined with NNLO QCD corrections [12,13] and NLO EW corrections [14]. A numerical update gives [11]

$$P_c(X) = 0.404 \pm 0.024. \tag{2}$$

Similarly, the top loops have been determined with NLO QCD corrections [15,16] and NLO EW corrections [17], for which a numerical update gives [11]

$$X(x_t) = 1.481 \pm 0.005|_{\mathrm{th}} \pm 0.008|_{\mathrm{exp}}. \tag{3}$$

That leaves only the CKM matrix element inputs $V_{td}V_{ts}^*$ and $V_{cd}V_{cs}^*$.

For studies of NP it is preferable to use CKM inputs that are derived from tree-level observables, namely from $|V_{us}|$, $|V_{ub}|$, $|V_{cb}|$ and the unitarity triangle angle γ, as these are not likely to be tainted by NP. However, in doing so we encounter the currently large discrepancies between exclusive and inclusive determinations of the CKM matrix elements $|V_{cb}|$ and $|V_{ub}|$ from semileptonic B decays (see [18]). Specifically, we have $|V_{ub}|_{\mathrm{excl}} = (3.72 \pm 0.14) \times 10^{-3}$ [19] versus $|V_{ub}|_{\mathrm{incl}} = (4.40 \pm 0.25) \times 10^{-3}$ [20] and $|V_{cb}|_{\mathrm{excl}} = (39.36 \pm 0.75) \times 10^{-3}$ [21] versus $|V_{cb}|_{\mathrm{incl}} = (42.21 \pm 0.78) \times 10^{-3}$ [22]. This effect is unlikely to be due to NP [23]. One way to proceed is to assume both determinations are equally correct and take a weighted average, inflating the errors via the PDG method [24], which gives

$$|V_{ub}|_{\mathrm{avg}} = (3.88 \pm 0.29) \times 10^{-3}, \quad |V_{cb}|_{\mathrm{avg}} = (40.7 \pm 1.4) \times 10^{-3}. \tag{4}$$

Using these values together with $|V_{us}| = 0.2252 \pm 0.0009$ and $\gamma = (73.2^{+6.3}_{-7.0})^\circ$ [25] gives the branching ratio predictions

$$\mathrm{BR}(K^+ \to \pi^+\nu\bar{\nu}) = (8.4 \pm 1.0) \times 10^{-11}, \qquad \mathrm{BR}(K_L \to \pi^0\nu\bar{\nu}) = (3.4 \pm 0.6) \times 10^{-11}. \tag{5}$$

[a] The tilde denotes the inclusion of electromagnetic radiative correction.

In Figure 1 we show the corresponding error budgets, where the CKM errors are clearly seen to dominate both predictions. The parametric dependence on the leading CKM input of both decays is given by [11]

$$\mathrm{BR}(K^+ \to \pi^+ \nu\bar{\nu}) = (8.39 \pm 0.30) \times 10^{-11} \left[\frac{|V_{cb}|}{40.7 \times 10^{-3}}\right]^{2.8} \left[\frac{\gamma}{73.2^\circ}\right]^{0.708} \quad (6)$$

$$\mathrm{BR}(K_\mathrm{L} \to \pi^0 \nu\bar{\nu}) = (3.36 \pm 0.05) \times 10^{-11} \left[\frac{|V_{ub}|}{3.88 \times 10^{-3}}\right]^{2} \left[\frac{|V_{cb}|}{40.7 \times 10^{-3}}\right]^{2} \left[\frac{\sin\gamma}{\sin(73.2^\circ)}\right]^{2} \quad (7)$$

Figure 1 – Error budgets for the branching ratio observables $\mathcal{B}(K^+ \to \pi^+\nu\bar{\nu})$ and $\mathcal{B}(K_L \to \pi^0\nu\bar{\nu})$ [11]. The remaining parameters, which each contribute an error of less than 1%, are grouped into the "other" category.

A comparison can be made with the CKM inputs determined purely from the loop-level observables $|\epsilon_K|$, ΔM_d, ΔM_s and $S_{J/\psi K_\mathrm{S}}$, assuming no NP enters these observables [11]. The dominant uncertainty in this case is QCD lattice input, which, using the latest FLAG results [21], results in the more precise predictions

$$\mathrm{BR}(K^+ \to \pi^+ \nu\bar{\nu}) = (9.1 \pm 0.7) \times 10^{-11}, \qquad \mathrm{BR}(K_\mathrm{L} \to \pi^0 \nu\bar{\nu}) = (3.0 \pm 0.3) \times 10^{-11} \quad (8)$$

that are valid only in the SM. In the left panel of Figure 2 a comparison of these results is given with the tree-level averages given above, as well as taking purely inclusive or exclusive values.

It is tempting to construct SM predictions independent of the tree-level $|V_{cb}|$ and $|V_{ub}|$ determinations. To that end we can use that the $B_s \to \mu^+\mu^-$ branching ratio is effectively proportional to $|V_{cb}|^2$ – its dominant uncertainty, followed by the B_s meson decay constant f_{B_s}. Combining this observable with (6) to eliminate $|V_{cb}|$, we then have to a very good accuracy in the SM the prediction [11]

$$\mathrm{BR}(K^+ \to \pi^+ \nu\bar{\nu}) = (65.3 \pm 2.9) \left[\overline{\mathrm{BR}}(B_s \to \mu^+\mu^-)\right]^{1.4} \left[\frac{\gamma}{73.2^\circ}\right]^{0.708} \left[\frac{f_{B_s}}{227\,\mathrm{MeV}}\right]^{-2.8} \quad (9)$$

We show this relation in the right panel of Figure 2 for fixed values of γ, and illustrate the small dependence on the remaining CKM inputs.

3 $K \to \pi\nu\bar{\nu}$ beyond the Standard Model

Due to vanishingly small neutrino masses, Higgs-like scalar couplings to a pair of neutrinos are negligible both in and beyond the SM. As a result NP contributions to $s \to d\nu\bar{\nu}$ transitions in the $K \to \pi\nu\bar{\nu}$ decays are typically mediated by vector bosons. In this case NP generally enters in two ways: via modified Z couplings to quarks, for example in the MSSM involving supersymmetric penguin processes, or via a new heavy Z'-like gauge boson. To illustrate the main features of such models, we will consider simplified Z and Z' models with tree-level FCNC couplings to quarks – for which we denote left and right handed couplings by $\Delta^{sd}_{L,R}(Z^{(\prime)})$ – and diagonal coupling to neutrinos, denoted by $\Delta^{\nu\nu}_{L}(Z^{(\prime)})$. The top-quark loop function in the SM then receives the following NP correction [26]:

$$X(x_t) \to X(x_t)_{\mathrm{SM}} + \frac{\pi^2}{2M_W^2 G_\mathrm{F}^2} \frac{\Delta^{\nu\nu}_L(Z^{(\prime)})}{V_{ts}^* V_{td} M_Z^{(\prime)2}} \left[\Delta^{sd}_L(Z^{(\prime)}) + \Delta^{sd}_R(Z^{(\prime)})\right], \quad (10)$$

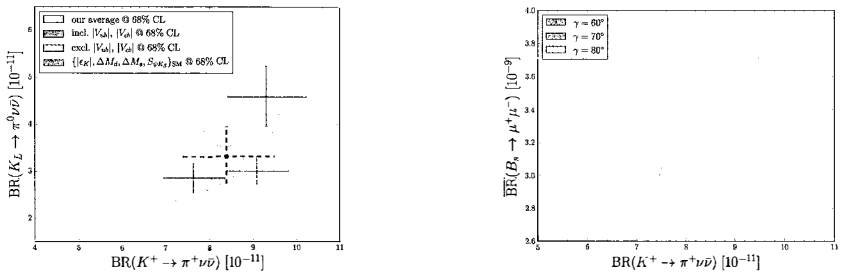

Figure 2 – *Left panel:* comparison of 68% C.L. regions for $\mathcal{B}(K_L \to \pi^0 \nu\bar{\nu})$ and $\overline{\mathcal{B}}(B_s \to \mu^+\mu^-)$ versus $\mathcal{B}(K^+ \to \pi^+ \nu\bar{\nu})$, using different CKM inputs as described in the test [11]. *Right panel:* correlation of $\overline{\mathcal{B}}(B_s \to \mu^+\mu^-)$ versus $\mathcal{B}(K^+ \to \pi^+ \nu\bar{\nu})$ for fixed values of γ: the dashed regions correspond to the 68% C.L. from the uncertainties on all other inputs, while the inner filled regions correspond only to the uncertainties from the remaining CKM inputs [11].

where $M_{Z'}$ is the mass of the heavy new Z' boson. From inspection of (1) we observe that $K^+ \to \pi^+ \nu\bar{\nu}$ is sensitive to both the real and imaginary NP contributions to $X(x_t)$, while $K_{\mathrm{L}} \to \pi^0 \nu\bar{\nu}$ only to the latter. In the left panel of Figure 3 the red region illustrates the general coverage of left and right handed NP with an arbitrary CP violating phases in the $K^+ \to \pi^+ \nu\bar{\nu}$ versus $K_{\mathrm{L}} \to \pi^0 \nu\bar{\nu}$ plane i.e. in general there is no correlation present.

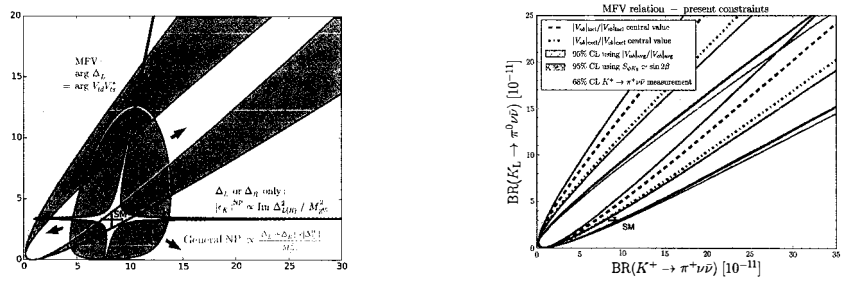

Figure 3 – *Left panel:* illustration of coverage of general LH and RH NP with arbitrary CP phase (red region), compared with correlations occurring in the case of MFV (green region) or purely LH or RH NP subject to kaon mixing constraint (blue region). *Right panel:* the MFV relation between $K^+ \to \pi^+ \nu\bar{\nu}$ and $K_L \to \pi^0 \nu\bar{\nu}$ using $S_{\psi K_S} \simeq \sin 2\beta$ versus using the various tree-level inputs of $|V_{cb}/V_{ub}|$ and γ compatible with current constraints.

Minimal Flavour Violation (MFV) is a mechanism to protect against large FCNCs in models beyond the SM by insisting that FCNCs can only arise from SM Yukawas. For the decays in question this implies the combination $V_{td}V_{ts}^* X(x_t)$ can be modified by NP provided any shifts with respect to $X(x_t)$ are real valued. Translated to our simplified models this means $\arg(\Delta_L^{sd}) = \arg(V_{td}V_{ts}^*)$ and that $\Delta_R^{sd} = 0$ for both Z and Z'. The condition of MFV results in the green band shown in the left panel of Figure 3. The CKM input entering this correlation is to a very good accuracy only the UT angle β, which gives a triple correlation between these two decays and the CP violating observable $S_{J/\psi K_S}$ that is unaffected by NP in MFV [27]. In the right panel of Figure 3 we illustrate the current status of this relation, and compare it to the larger errors obtained from using tree-level CKM inputs.

Correlations between the $K \to \pi\nu\bar{\nu}$ decays also arise from considering the constraints from other kaon observables. Notably NP contributions to CP violation in kaon mixing are proportional to [28]

$$\epsilon_K^{\mathrm{NP}} \propto \frac{1}{M_Z^{(\prime)2}} \mathrm{Im}\left[\Delta_L^{sd}(Z^{(\prime)})^2 + \Delta_R^{sd}(Z^{(\prime)})^2 + 2\kappa_{sd}\,\Delta_L^{sd}(Z^{(\prime)})\Delta_R^{sd}(Z^{(\prime)})\right], \tag{11}$$

where κ_{sd} is the ratio of the corresponding hadronic matrix elements. Thus in the case of purely left or right handed NP, the square of the respective imaginary components are strongly constrained by experiment, which results in the two blue branches illustrated in the left panel of Figure 3. Aside

from its presence in various Z' models with purely left or right handed couplings [29,26], this correlation also appears for instance in Little Higgs models with T-parity [30]. In a Randall-Sundrum model with a custodial symmetry that allows only for large new right-handed FCNC couplings, the correlation is lost due to the kaon mixing constraint being saturated by additional NP [31].

Besides from kaon mixing, also direct CP violation in $K \to \pi\pi$, namely ϵ'/ϵ, can lead to strong constraints for the imaginary parts of $\Delta^{sd}_{L,R}$. In this case the imaginary components are not squared, so that limits on ϵ'/ϵ directly limit the branching ratio of $K_L \to \pi^0\nu\bar{\nu}$. This is in particular the case for a simplified Z model, as in a simplified Z' model the diagonal quark couplings must also be addressed for this constraint to be meaningful. If the coupling of the vector boson driving the $s \to d\nu\bar{\nu}$ transition is related to $s \to d\mu\bar{\mu}$, for example by $SU(2)_L$ symmetry, then also the current upper bound $\mathrm{BR}(K_L \to \mu^+\mu^-)_{SD} < 2.5 \times 10^{-9}$ [33] can constrain NP in $\mathrm{BR}(K^+ \to \pi^+\nu\bar{\nu})$, as its NP contribution is proportional to $\mathrm{Re}(\Delta^{sd}_L - \Delta^{sd}_R)$. The (anti-)correlation of these two branching ratios can also reveal the presence of left-handed (right-handed) NP [34], as for example demonstrated Randall-Sundrum [31] and partially composite models [35].

In models with MFV the corresponding CKM suppression usually implies that the NP effects compatible with present constraints are small. In the MSSM with MFV, for example, it has been shown that NP effects are in general limited to be about 10% [36,37]. In the left panel of Figure 4 we show the applicable constraints in the $K^+ \to \pi^+\nu\bar{\nu}$ versus $K_L \to \pi^0\nu\bar{\nu}$ plane for a simplified Z model with MFV [32]. Similarly, in the right panel we show the constraints for a simplified Z' obeying MFV, with a mass of 5 TeV and the same strength couplings to neutrinos as the Z [32]. We observe that in the case of the lighter Z the $\Delta F = 1$ constraints are the most constraining, while for the Z' the $\Delta F = 2$ constraints are already very constraining.

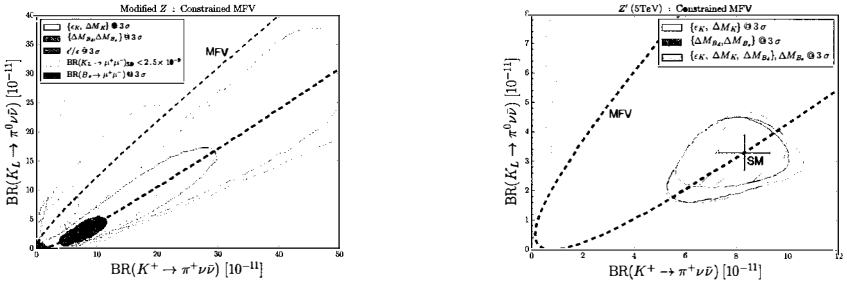

Figure 4 – The 3σ allowed ranges for $\mathcal{B}(K_L \to \pi^0\nu\bar{\nu})$ and $\mathcal{B}(K^+ \to \pi^+\nu\bar{\nu})$ in a simplified model with modified Z couplings (left panel) or a simplified model with a 5 TeV Z' (right panel) obeying CMFV [32]. In the former case $\Delta F = 1$ constraints are most constraining, while in the latter $\Delta F = 2$ are very constraining assuming the Z' has the same coupling to neutrinos as the Z.

Finally let us address what NP scales could ultimately be reached, taking as a benchmark a simplified Z' model with maximum couplings to quarks and leptons consistent with perturbativity. If the Z' couples only left or right handedly to quarks, the constraints from kaon mixing apply, and scales as high as 50 TeV, or equivalently 4 zeptometers can be reached [28]. If both LH and RH couplings are present, then a tuning is possible that cancels the kaon mixing constraint, allowing distances under a zeptometer to be probed. In other words, the $K \to \pi\nu\bar{\nu}$ decays will not only be excellent probes of NP in the coming decade, they could eventually allow the *Zeptouniverse* to be probed by $\Delta F = 1$ rare decays processes.

Acknowledgments

I would like to thank the organizers of the Moriond Electroweak Conference for their organization and hospitality. I am grateful to Andrzej Buras, Dario Buttazzo and Jennifer Girrbach-Noe for their collaboration on topics presented in this talk. This research was completed and financed in the context of the ERC Advanced Grant project "FLAVOUR"(267104) and was partially supported by the DFG cluster of excellence "Origin and Structure of the Universe".

References

1. Jerome Charles, Sebastien Descotes-Genon, Zoltan Ligeti, Stephane Monteil, Michele Papucci, et al. Future sensitivity to new physics in B_d, B_s and K mixings. *Phys.Rev.*, D89:033016, 2014.
2. M. Bona et al. Model-independent constraints on Δ F=2 operators and the scale of new physics. *JHEP*, 0803:049, 2008. Updates available on `http://www.utfit.org`.
3. Federico Mescia and Christopher Smith. Improved estimates of rare K decay matrix-elements from $K_{\ell 3}$ decays. *Phys. Rev.*, D76:034017, 2007.
4. A. V. Artamonov et al. New measurement of the $K^+ \to \pi^+\nu\bar{\nu}$ branching ratio. *Phys. Rev. Lett.*, 101:191802, 2008.
5. J.K. Ahn et al. Experimental study of the decay $K_L^0 \to \pi^0\nu\bar{\nu}$. *Phys.Rev.*, D81:072004, 2010.
6. G. Aglieri Rinella, R. Aliberti, F. Ambrosino, B. Angelucci, A. Antonelli, et al. Prospects for $K^+ \to \pi^+\nu\bar{\nu}$ at CERN in NA62. 2014.
7. Angela Romano. The $K^+ \to \pi^+\nu\bar{\nu}$ decay in the NA62 experiment at CERN. 2014.
8. Koji Shiomi. $K_L^0 \to \pi^0\nu\bar{\nu}$ at KOTO. 2014.
9. E.T. Worcester. ORKA, The Golden Kaon Experiment: Precision measurement of $K^+ \to \pi^+\nu\bar{\nu}$ and other rare processes. *PoS*, KAON13:035, 2013.
10. Andreas S. Kronfeld, Robert S. Tschirhart, Usama Al-Binni, Wolfgang Altmannshofer, Charles Ankenbrandt, et al. Project X: Physics Opportunities. 2013.
11. Andrzej J. Buras, Dario Buttazzo, Jennifer Girrbach-Noe, and Robert Knegjens. $K^+ \to \pi^+\nu\bar{\nu}$ and $K_L \to \pi^0\nu\bar{\nu}$ in the Standard Model: Status and Perspectives. 2015.
12. A. J. Buras, M. Gorbahn, U. Haisch, and U. Nierste. The rare decay $K^+ \to \pi^+\nu\bar{\nu}$ at the next-to-next-to-leading order in QCD. *Phys. Rev. Lett.*, 95:261805, 2005.
13. Andrzej J. Buras, Martin Gorbahn, Ulrich Haisch, and Ulrich Nierste. Charm quark contribution to $K^+ \to \pi^+\nu\bar{\nu}$ at next-to-next-to-leading order. *JHEP*, 11:002, 2006.
14. Joachim Brod and Martin Gorbahn. Electroweak Corrections to the Charm Quark Contribution to $K^+ \to \pi^+\nu\bar{\nu}$. *Phys. Rev.*, D78:034006, 2008.
15. Gerhard Buchalla and Andrzej J. Buras. Qcd corrections to rare k and b decays for arbitrary top quark mass. *Nucl. Phys.*, B400:225–239, 1993.
16. Mikolaj Misiak and Jorg Urban. QCD corrections to FCNC decays mediated by Z penguins and W boxes. *Phys.Lett.*, B451:161–169, 1999.
17. Joachim Brod, Martin Gorbahn, and Emmanuel Stamou. Two-Loop Electroweak Corrections for the $K \to \pi\nu\bar{\nu}$ Decays. *Phys.Rev.*, D83:034030, 2011.
18. Giulia Ricciardi. Status of $|V_{cb}|$ and $|V_{ub}|$ CKM matrix elements. 2014.
19. J.A. Bailey, A. Bazavov, C. Bernard, C. Bouchard, C. DeTar, et al. $B \to \pi\ell\nu$ semileptonic form factors from unquenched lattice QCD and determination of $|V_{ub}|$. 2014.
20. E. Barberio et al. Averages of b–hadron properties at the end of 2006. 2007.
21. Sinya Aoki, Yasumichi Aoki, Claude Bernard, Tom Blum, Gilberto Colangelo, et al. Review of lattice results concerning low-energy particle physics. *Eur.Phys.J.*, C74(9):2890, 2014.
22. Andrea Alberti, Paolo Gambino, Kristopher J. Healey, and Soumitra Nandi. Precision determination of the CKM element Vcb. 2014.
23. Andreas Crivellin and Stefan Pokorski. Can the differences in the determinations of V_{ub} and V_{cb} be explained by New Physics? 2014.
24. J. Beringer et al. Review of Particle Physics (RPP). *Phys.Rev.*, D86:010001, 2012.
25. K. Trabelsi. World average and experimental overview of γ/φ_3; presented at CKM 2014. 2014. http://www.ckmfitter.in2p3.fr.
26. Andrzej J. Buras, Fulvia De Fazio, and Jennifer Girrbach. The Anatomy of Z' and Z with Flavour Changing Neutral Currents in the Flavour Precision Era. *JHEP*, 1302:116, 2013.
27. Andrzej J. Buras and Robert Fleischer. Bounds on the unitarity triangle, $\sin 2\beta$ and $K \to \pi\nu\bar{\nu}$ decays in models with minimal flavor violation. *Phys. Rev.*, D64:115010, 2001.
28. Andrzej J. Buras, Dario Buttazzo, Jennifer Girrbach-Noe, and Robert Knegjens. Can we reach the Zeptouniverse with rare K and $B_{s,d}$ decays? *JHEP*, 1411:121, 2014.
29. Andrzej J. Buras, Fulvia De Fazio, Jennifer Girrbach, and Maria V. Carlucci. The Anatomy of Quark Flavour Observables in 331 Models in the Flavour Precision Era. *JHEP*, 1302:023, 2013.
30. Monika Blanke, Andrzej J. Buras, Bjorn Duling, Stefan Recksiegel, and Cecilia Tarantino. FCNC Processes in the Littlest Higgs Model with T-Parity: a 2009 Look. *Acta Phys.Polon.*, B41:657–683, 2010.
31. Monika Blanke, Andrzej J. Buras, Bjorn Duling, Katrin Gemmler, and Stefania Gori. Rare K and B Decays in a Warped Extra Dimension with Custodial Protection. *JHEP*, 03:108, 2009.
32. Andrzej J. Buras, Dario Buttazzo, and Robert Knegjens. In preparation. 2015.
33. Gino Isidori and Rene Unterdorfer. On the short-distance constraints from $K_{L,S} \to \mu^+\mu^-$. *JHEP*, 01:9, 2004.
34. Andrzej J. Buras and Jennifer Girrbach. Towards the Identification of New Physics through Quark Flavour Violating Processes. *Rept.Prog.Phys.*, 77:086201, 2014.
35. David M. Straub. Anatomy of flavour-changing Z couplings in models with partial compositeness. *JHEP*, 1308:108, 2013.
36. Gino Isidori, Federico Mescia, Paride Paradisi, Christopher Smith, and Stephanie Trine. Exploring the flavour structure of the MSSM with rare K decays. *JHEP*, 08:064, 2006.
37. Christopher Smith. Rare K decays: Challenges and Perspectives. 2014.

Results from the NA62 2014 Commissioning Run

DARIO SOLDI
On Behalf NA62 Collaboration
Universita' degli Studi di Torino, Dipartimento di Fisica,
Via Pietro Giuria 1, Torino

The main purpose of the NA62 experiment is to measure the branching ratio of the (ultra) rare decay $K^+ \to \pi^+\nu\bar{\nu}$ with the precision of 10% collecting $\sim$ 100 events with the Standard Model branching fraction in 3 years of data taking. The commissioning of the experiment after the 2014 pilot run and the prospects for the 2015 run are presented.

1 Introduction

The NA62 experiment is located at the CERN Super Proton Synchrotron accelerator. Its main goal is to measure the branching ratio (BR) of the ultra rare decay [1] $K^+ \to \pi^+\nu\bar{\nu}$, with the precision of $\sim$ 10 %. The Standard Model (SM) prediction is very accurate, taking in account next-to-leading order (NLO) QCD corrections to the top quark contributions, NNLO QCD corrections to the charm contributions, NLO electroweak corrections to both top and charm contributions and extensive calculations of isospin breaking and non-perturbative effects. The best prediction of the branching ratio [2] is $BR(K^+ \to \pi^+\nu\bar{\nu}) = (7.81^{+0.8}_{-0.71} \pm 0.29) \times 10^{-11}$ while the experimental measurement, combining data from E787 and E949 experiments [3] at Brookhaven AGS is $(17.3^{+11.5}_{-10.5}) \times 10^{-11}$. During 2014 the NA62 detector was deployed and commissioned, enabling to accumulate a valuable sample of kaon decays to verify the expected physics sensitivity.

1.1 Experimental strategy

A large number of about 10^{13} kaon decays is needed to reach the expected sensitivity. The experimental principle is the decay-in-flight technique, and the variable used to distinguish the signal from the background is the squared missing mass $m^2_{miss} = (P_{K^+} - P_{\pi^+})^2$ where P are the four momenta of the incoming kaon and outgoing pion. Cuts on the missing mass value allow the rejection of more than 90% of the backgrounds. Figure 1 shows the m^2_{miss} distribution assuming that the charged particle is a pion with momentum lower than 35 GeV. One defines two regions where the signal is not dominated by background, Region I above the $K_{\mu 2}$ but below the $K_{\pi^+\pi^0}$ contribution and Region II above the $K_{\pi^+\pi^0}$ and below the $K_{3\pi}$ contributions. The final rejection relies on a redundant veto system and particle identification.

2 Detector and Beam during the 2014 commissioning run

2.1 Beam

Kaons are produced by the 400 GeV protons from the SPS impinging on a beryllium target. Secondary particles of 75 GeV/c momentum are selected in a non separated beam composed of 71% of pions, 23% of protons and 6% of kaons, with a total rate of $\sim$ 750 MHz. Only about 10% of the

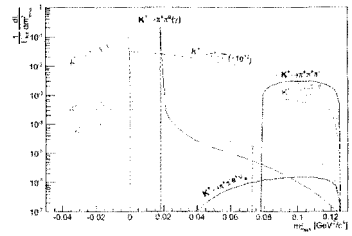

Figure 1 – squared missing mass in the hypothesis of kaon to pion decay

kaon produced decay in the fiducial volume, allowing the detector to collect $\sim 4.5\ 10^{12}$ decays per year.
During the 2014 run the beam optics has been fully commissioned, and the experiment was operating at 5% to 20% of the nominal intensity.

2.2 Kaon Tagging

Kaon tagging is performed by the CEDAR/KTAG detector. CEDAR [4] is a differential Cerenkov counter built for measuring the composition of SPS secondary beams. It has been upgraded to meet the 50 MHz kaon rate requirement: a time resolution better than 100 ps and a tagging efficiency above 95%.
During the 2014 run a preliminary evaluation of the single hit time resolution of ~ 280 ps was was obtained, while the tagging efficiency was above 90%.

2.3 Spectrometers

Both the beam particle and the secondary charged particle must be accurately measured. The beam spectrometer, called GigaTracker [5], consists of three stations of hybrid silicon pixel detectors installed within an achromatic system of four dipole magnets. The constraint of very low material budget has led to the choice of a sensor thickness of 200 μm, read by 10 ASIC 100 μm thick chips bump bonded to the sensor, with a total of 18000 pixels for each station. The time resolution per track should be of the order of 200 ps, while the momentum resolution $\sigma(P)/P$ should be $\sim$0.2%.
During the commissioning run, the three stations have been installed, but only partially read out (10% of the chips). The time resolution measurement is in progress.
The Straw Tracker detector [6] (STRAW) measures the direction and momentum of charged particles from the kaon decay. It is composed of 4 chambers with x,y,u,v views, located in vacuum, before and after a dipole magnet which produces the vertical B-field of 0.36 T.
The detector was fully operational.
Both spectrometers were read out triggerless and the matching with the other detectors was performed offline.

2.4 Photon Vetoes

The photon veto system was designed to suppress the background coming from $K^+ \to \pi^+\pi^0$ ($\pi^0 \to \gamma\gamma$) and radiative decays by identifying photons with an inefficiency less than 10^{-8}. The system provides a hermetic coverage for photon angles up to 50 mrad.
The Large Angle Vetoes (LAV) cover the region between 8.5 and 50 mrad. The LAV consists of 12 stations, made of rings of lead glass blocks recovered from the OPAL electromagnetic calorimeter[7].
All stations have been installed and read out, and the time resolution of tagged photons measured is better than 1 ns.
The other photon veto used in 2014 is the Liquid Krypton calorimeter (LKr), inherited from the

NA48 experiment and equipped with a new readout. It covers photon angle from 1.5 to 8.5 mrad and should guarantee an inefficiency lower than 10^{-5} for photons with energy > 35 GeV.
During the 2014 data taking, the new read out was deeply tested and a calibration of the detector was performed.

2.5 RICH counter

The Ring-Imaging Cherenkov Counter[8] (RICH) is located between the last STRAW chamber and the LKr. It is a 17 m long vessel filled with Neon at atmospheric pressure, and consists of a mosaic of spherical mirrors which reflect the Cherenkov light on to the 2000 photomultiplier array. The RICH provides $\pi - \mu$ separation for charged particles with momentum between 15 and 35 GeV/c leading to an additional muon suppression factor of 10^2. It also measure the pion crossing time with about 100 ps precision.
With the data taken during the 2014 run it is possible to test the ring reconstruction and the matching with the montecarlo expectation.

2.6 Muon Vetoes

The muon veto system (MUV) consists of three different components (MUV1, MUV2 and MUV3) placed after the LKr calorimeter. The MUV3 component is a real muon veto, consisting of an array of 144 scintillator tiles. The two others, MUV2 and MUV3, are hadronic calorimeters (Fe-scintillators), used to measure the deposited energies and shower shapes of incident particles and redundantly distinguish muons from pions.
During the commissioning run MUV2 and MUV3 were installed and read out. In particular MUV3 has been used for muon rejection at the hardware trigger level. The efficiency of MUV2 has been measured to be $\sim 99.9\%$ with a preliminary time resolution of 1.4 ns.

3 Trigger and Data Acquisition

All the acquisition boards were installed for the 2014 run. The electronic boards were deeply tested under the available beam condition (5 to 20% of the nominal intensity).
Two level-0 trigger processors have been developed, one completely based on a FPGA commercial board, while the other[9] makes use of an auxiliary PC to build the trigger logic.
For the 2014 run the first option has been used.

4 First look at the data

During the last days of the 2014 run, data in stable conditions at about 5% of the nominal intensity have been recorded as selected by a Level-0 trigger logic based on fast multiplicity signals from the Charged Hodoscope (CHOD), hadronic energy measured in MUV2 and requiring little or no electromagnetic energy deposited in the scintillating fibre hodoscope embedded in the LKr calorimeter. The analysis of the data sample is in progress[10]. Events with only one charged particle are reconstructed in the STRAW spectrometer. Figure 2 shows the angle between the reconstruction track and the nominal kaon beam direction as a function of momentum. For comparison, the theoretical curves in the angle - momentum plane expected from kaon decays are also displayed. It is possible to see also a 75 GeV/c momentum component, compatible with scattered beam particles reaching the straw spectrometer. Additional cuts are applied to obtain the m^2_{miss} distribution shown in figure 3. The most significant requirements are the presence of a kaon track tagged my CEDAR (a five-fold coincidence in the KTAG), the position of the decay vertex in the fiducial region and the momentum of the decay particle between 15 and 35 GeV/c. The beam spectrometer GTK is not yet used.
The signal region (section 1.1) for $K^+ \to \pi^+\nu\bar{\nu}$ is defined to be $0 < m^2_{miss} < 0.01$ GeV$^2/c^4$ (Region I), and $0.026 < m^2_{miss} < 0.068$ GeV$^2/c^4$ (Region II).

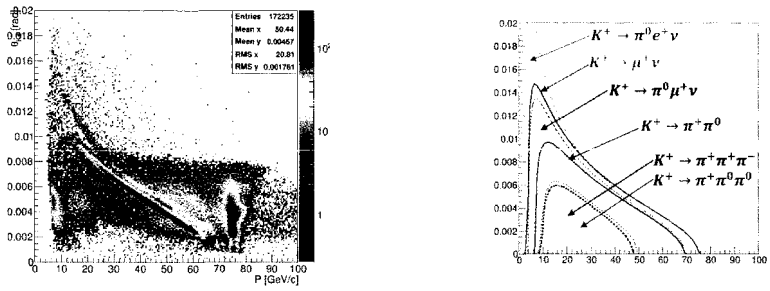

Figure 2 – Distribution of the angle between the decay particle and the kaon beam function of track momentum for data(left) and as expected (right)

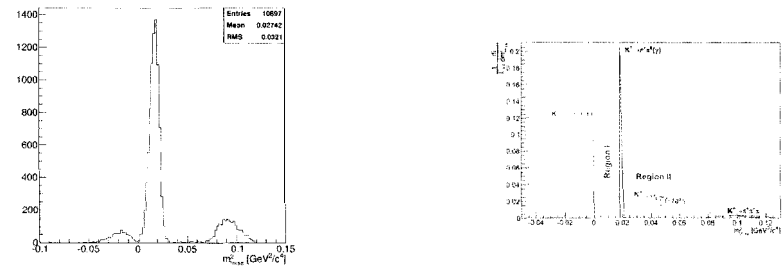

Figure 3 – m^2_{miss} in the hypothesis of kaon to pion decay (left), expected values (right)

Background events enter in Region I due to resolution tails. A factor of four improvement in the resolution is expected after adding the beam spectrometer information. Because photon rejection has not been applied yet in this analysis, decays with photons appear in Region II as well as kaon decays with electrons and resolution tails.

5 Summary

The NA62 experiment has been taken data for two month in 2014. All sub-detectors have been commissioned and successfully operated with good performance. Data analysis is in progress.

References

1. G. Anelli *et al.*, CERN-SPSC-2005-013 (2005).
2. J. Brod, M. Gorbahn, E. Stamou *Phys. Rev.* D **D83**, 034030 (2011).
3. E949 Collaboration, V. Artamonov *et al.*, *Phys. Lett.* B **101**, 191802 (2008).
4. NA62 Collaboration, A. Romano Astroparticle, Particle, Space Physics and Detectors for Physics Applications, World Scientific, 895 (2012).
5. M. Fiorini *et al.*,*Nucl. Instrum. Methods* **A718**, 270 (2013).
6. NA62 Collaboration, H. Danielson, Sci. Symp. Conf. Rec. **2010**, 1914 (2010).
7. OPAL Collaboration, K. Ahmet *et al.*,*Nucl. Instrum. Methods* **A305**, 275 (1991).
8. F. Bucci, G. Collazuol and A. Sergi,*Nucl. Instrum. Methods* **A623**, 327 (2010).
9. M. Pivanti *et al.*, Journal of Physics: Conference Series 513, 012008 (2014).
10. G. Ruggiero, CERN Seminar, http://indico.cern.ch/event/360237/ (2015).

8.
VHE & Dark Matter

NEUTRINOS FROM HEAVEN AND HELL IN ICECUBE
Latest results on astrophysical neutrinos and neutrino oscillations

JUAN PABLO YÁÑEZ for the ICECUBE COLLABORATION[a]
DESY, D-15735 Zeuthen, Germany

The IceCube Neutrino Observatory is a cubic kilometer ice Cherenkov neutrino detector, located at the geographic South Pole, detecting neutrinos of energy above about 100 GeV. In the last couple of years IceCube has established the existence of a high-energy astrophysical neutrino flux in the 100 TeV - PeV range at the level of 10^{-8} GeV cm^{-2} s^{-1} sr^{-1} per flavor with a significance of 5.7σ. DeepCore, a region of denser instrumentation at the lower center of the detector, detects low-energy atmospheric neutrinos (< 100 GeV), which are used to study neutrino oscillations with a precision comparable to that of the leading experiments in the field. The following paper discusses the latest results on both of these topics.

1 Neutrinos from hell

More than a hundred years have passed since the discovery of cosmic rays. During this time multiple experiments have measured them over a wide energy range, including the most energetic particles ever detected, with EeV energies [1]. Despite detailed knowledge of their energy spectrum, the origin of the highest energy component (above PeV energies) remains a mystery [2]. Fermi shock acceleration in extreme environments, such as Active Galactic Nuclei, remains a preferred explanation, although other more exotic scenarios cannot yet be ruled out.

When cosmic rays reach the atmosphere of the Earth, they interact, producing a shower of particles, including charged mesons and eventually neutrinos. In the same way, it is expected that cosmic rays interact either with other matter particles or photon fields near their production site and/or cosmic microwave background photons as they propagate through the Universe. The observation of very high energy cosmic rays thus implies the existence of a similarly high energy astrophysical flux of neutrinos. Such a flux, when found, will cast light on the origin of high energy cosmic rays and will allow us to observe the Universe in a fundamentally new way.

1.1 IceCube: An instrument for neutrino astronomy

IceCube is an ice Cherenkov neutrino detector located at the geographic South Pole, using the Antarctic ice as a detection medium [3]. The detector consists of 5,160 Digital Optical Modules (DOMs), which are glass spheres containing a 10" PMT, together with the electronics necessary for signal digitization and readout [4]. The DOMs are deployed on vertical strings, with a total of 86 of them, each one holding 60 DOMs. The standard IceCube inter-string distance is 125 m, while the typical DOM-to-DOM distance within a string is 17 m. The instrumented volume amounts to a cubic kilometer, located between depths of 1450 m and 2450 m.

The measurement of a flux of astrophysical neutrinos in IceCube is mainly affected by two sources of background: atmospheric muons and atmospheric neutrinos, both produced in cosmic

[a] see http://icecube.wisc.edu/collaboration/authors/current for full author list.

ray interactions in the Earth's atmosphere. Muons can only reach the detector from above ($\cos\theta_z > 0$); they are fully absorbed in the Earth below the detector's horizon ($\cos\theta_z \leq 0$). Atmospheric neutrinos, on the other hand, come from all directions up to PeV energies. Above this energy, absorption of neutrinos as they cross the Earth becomes a sizeable effect.

Two strategies are used to suppress background sources for measuring an astrophysical neutrino flux:

- Focus on high energy neutrinos. The astrophysical neutrino flux is expected to follow an E^{-2} power law [5], which is substantially harder than the $E^{-3.7}$ flux of atmospheric neutrinos from π/K decays [6]. Events above the crossover energy of the fluxes, expected between 10-100 TeV depending on the flavor, are most likely to come from an astrophysical neutrino flux.

- Use the detector itself as veto. Atmospheric muons produce Cherenkov light as they enter the instrumented volume of the detector. By using edge layers of the detector as veto and looking exclusively for events that start inside the fiducial region, a significant part of the background can be reduced. This approach also reduces the background of high energy atmospheric neutrinos from above the detector, as they have a large probability of being accompanied by a TeV muon [7]. Figure 1 shows how the veto scales with the number of photons observed for one of the studies presented next.

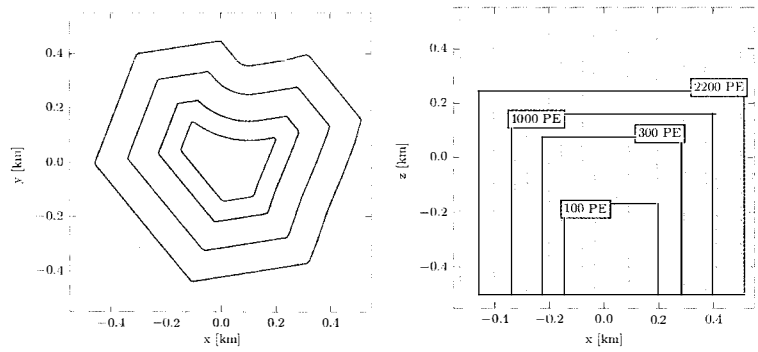

Figure 1 – Fiducial volume scaling evaluated at four different photo-electron counts. Left: Overhead view, showing the positions of the IceCube strings and the boundaries of the fiducial volume for events with a given total photon count. Right: Side view, showing the modules along strings.

1.2 Analysis of diffuse neutrino signals

The first evidence of astrophysical neutrinos came from a search which made use of both of the strategies described above with two years of detector live time [8], and has been updated to include three years of data [9]. A complementary study has also been performed using a dynamic veto to extend the analysis to lower neutrino energies [10]. Reducing the analysis threshold makes the overall contribution of background higher than for the original search, but it results in a more precise fit of the contributions of muon background and atmospheric neutrinos.

A total of 283 cascade-like and 105 track-like events were found in the first two years of the extended search. Figure 2 shows how the events are distributed as a function of deposited energy in the detector separated into the northern and southern sky. The simulation describes the data accurately, and events with energies around the transition between background and

signal regions can be clearly observed for the southern sky. Above 50 TeV of reconstructed energy there is large overlap with the sample that gave first evidence of an astrophysical flux.

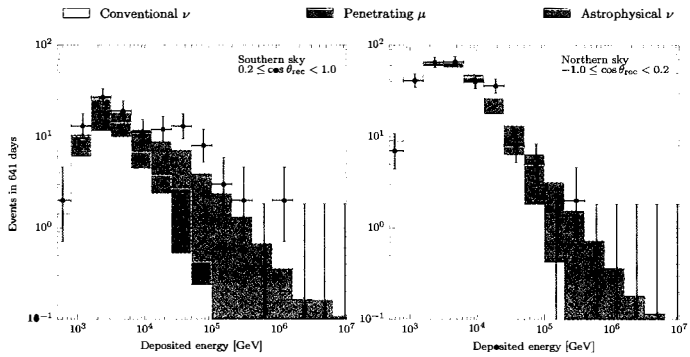

Figure 2 – Deposited-energy spectra from the northern and southern skies with the best-fit combination of atmospheric and astrophysical contributions. Below 3 TeV, the events observed from the northern sky are adequately explained by conventional atmospheric neutrinos. In the same energy range in the southern sky, penetrating atmospheric muons account for the remaining events. Above 10 TeV, an extra component is required to account for the observed high-energy events, especially those in the southern sky. Since atmospheric neutrinos are often vetoed by accompanying muons, the excess is best explained by astrophysical neutrinos.

Diffuse searches which target muon tracks from ν_μ interactions have also been performed. The arrival direction of muons can be reconstructed with sub-degree accuracy, thus it is possible to forgo using the outer layers of the detector as a veto and rely on the Earth absorbing the atmospheric muon background. Following this strategy produces a sample with higher statistics, although it is restricted to "up-going" events. In the latest search of this kind an excess of data over the expectation from atmospheric neutrinos, with a significance of 3.7 standard deviations, was found. The excess, shown in Fig. 3, is both consistent with an isotropic astrophysical neutrino flux and with the searches described above.

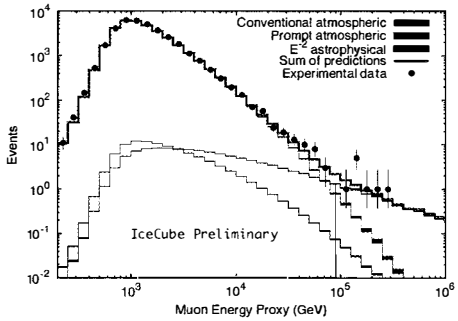

Figure 3 – The distribution of reconstructed muon energies of events in the final sample, compared to the expected distributions for the best fit model parameters. Only statistical errors are shown.

A joint likelihood analysis of the three diffuse searches mentioned, plus three separate studies previously published [11,12,13], has been performed. In the fit, the data is assumed to be explained by four components: an astrophysical flux, atmospheric muons, atmospheric neutrinos from π/K decays, and atmospheric neutrinos from the decay of charmed mesons [b]. The flux

[b] Charmed mesons decay before losing energy so neutrinos from these decays have a harder spectrum than those from π/K decays.

normalization and spectral index of the different components are fit to the data.

Figure 4a shows the best fit to the data, which corresponds to a single unbroken power law, with a flux normalization of $6.7^{+1.1}_{-1.2} \times 10^{-18}\,(\mathrm{GeV\,s\,sr\,cm^2})^{-1}$ at 100 TeV, and a spectral index of -2.50 ± 0.09, which is significantly different from the $\gamma = -2$ typically assumed. The flux quoted is valid in the range between 25 TeV and 2.8 PeV. No evidence is found for more complicated spectral shapes (e.g. cut-off, broken power law).

Taking the event topology into account allows us to perform a fit of the neutrino flavor composition observed at Earth. A 30% probability for the classifier to identify events with a muon track as cascades is included in the fit. Figure 4b shows the result of this study, which corresponds to an equal contribution of ν_μ and ν_e, and no contribution from ν_τ. The canonical scenario of having equal contributions of all flavors is compatible with the one-sigma error of the result. A previous result, which relied on a more limited data sample, yielded compatible results with a stronger degeneracy between electron and tau neutrino flavors [14] .

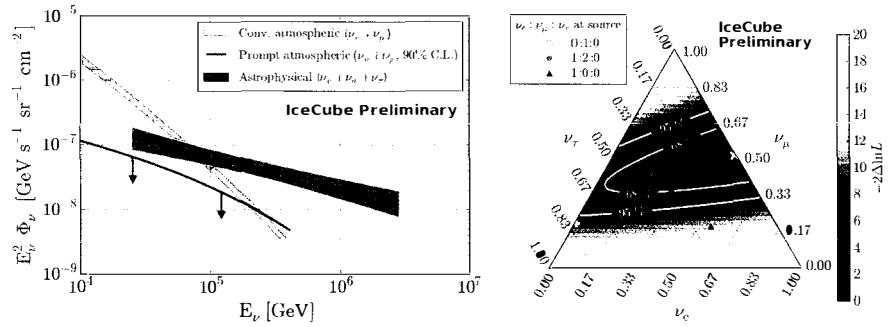

(a) (b)

Figure 4 – Results from the global fit of diffuse analyses. In (a): Best fit neutrino spectra for the single power law model. The blue and red shaded areas correspond to 68% C.L. allowed regions for the conventional atmospheric and astrophysical neutrino flux, respectively. The flux of atmospheric neutrinos from charmed mesons is fitted to zero, its 90% C.L. upper limit is shown in green. In (b): Profile likelihood scan of the flavor composition at Earth. The best fit composition is marked with x, 68% and 95% confidence regions are indicated. Ratios corresponding to three flavor composition scenarios at the sources of the neutrinos are also shown

1.3 Origin of the astrophysical neutrino flux

The incoming direction of the neutrino candidates above a reconstructed energy of 50 TeV which start in the detector was tested for clustering. Cascade events have a typical angular resolution of 10°, while tracks can attain sub-degree angular resolutions. The result of a point source analysis returns no significant deviation from the background-only expectation [9].

A strategy which bridges diffuse from point-source searches is the study of the neutrino flux from a population of astrophysical objects. This approach, known as "stacking", has been used for Gamma Ray Bursts [15] and recently for the Blazars identified in the Fermi catalogue. Since no significant deviation from background has been observed from any of these classes of objects, a limit on the upper limit on the contribution to the diffuse flux of astrophysical neutrinos was derived. The upper limit contribution of the Blazars from the Fermi catalogue is between 8% and 17%, depending on the correlation assumed between the gamma-ray flux and the neutrino flux [16].

2 Neutrinos from heaven

Atmospheric neutrinos, a source of background in the search for neutrinos from hell, are used to study the phenomenon of neutrino oscillations with IceCube. Because neutrinos are massive particles with mixed flavor and mass eigenstates, the probability for one to be emitted with flavor α and to interact as a different flavor β is nonzero and depends on its energy E and the distance it has traveled L. For atmospheric neutrinos above a few GeV, which travel from a few kilometers to the entire diameter of the Earth ($\sim 12700\,\mathrm{km}$), the dominant effect of oscillations is ν_μ disappearance, which can be approximated as

$$P(\nu_\mu \to \nu_\mu) \simeq 1 - \sin^2(2\theta_{23}) \sin^2\left(1.27\,\Delta m^2_{32}\,L/E\right). \quad (1)$$

Here, the large mass splitting $\Delta m^2_{32} \simeq \Delta m^2_{31}$ and the mixing angle θ_{23} are the fundamental parameters of the phenomenon. Maximal disappearance of ν_μ is reached at $E_\nu \simeq 25\,\mathrm{GeV}$ for neutrinos that cross the entire Earth, moving to shorter baselines for lower energies. This disappearance effect is the target of oscillation measurements with neutrino telescopes [17].

2.1 IceCube DeepCore: An instrument for particle physics

The central lower part of IceCube houses a region with denser instrumentation known as DeepCore. In this region, eight irregularly spaced strings were deployed, with a reduced spacing from 125 m to 40-70 m. These strings hold DOMs with 30% higher efficiency than the standard IceCube DOMs. The DOMs on a string are separated by 7 m, instead of the 17 m spacing in the standard IceCube strings [18]. Their instrumentation begins at a depth of 2 km and it goes until the bottom of the detector. The first 10 DOMs of the dedicated DeepCore strings are situated above the naturally occuring dust layer which divides the detector (see Fig. 1) and are used to veto atmospheric muons. The fiducial volume used for analysis starts below the dust layer. The volume has a height of 350 m, and has a radius of approximately 150 m. The fiducial volume encloses about 500 DOMs with reduced spacing, which results in a threshold for detection and reconstruction of neutrinos of 10 GeV, where atmospheric neutrino oscillations can be measured.

2.2 Neutrino oscillation analysis in DeepCore

The study of neutrino oscillations in DeepCore presented here is a measurement of the disappearance pattern of ν_μ [19]. Muon neutrinos undergoing charged current interactions constitute the signal. The main source of background are single atmospheric muons, which trigger the detector at a rate 10^5 higher than the signal, and can mimic the light pattern produced by a neutrino interaction. Neutral current interactions of all flavors and charged current interactions of ν_e and ν_τ constitute a secondary source of background, and add up to about a third of the total signal rate.

DeepCore data selection

Neutrinos are separated from muons using a similar strategy as for the high energy analyses, i.e. vetoing events when there are hints that a particle is entering the fiducial volume. Events starting within the detector are most likely to be neutrinos. For this study the veto is independent of the charge observed by the detector, and it is defined as the region surrounding the fiducial volume, described above.

Different cut variables are defined based on the light deposited before the time at which the event triggers the detector. In their current implementation, which aim for a muon contamination smaller than 5%, genuine starting events have a large probability of being rejected due to noise. Figure 5 demonstrates how the background is reduced at three different stages of the

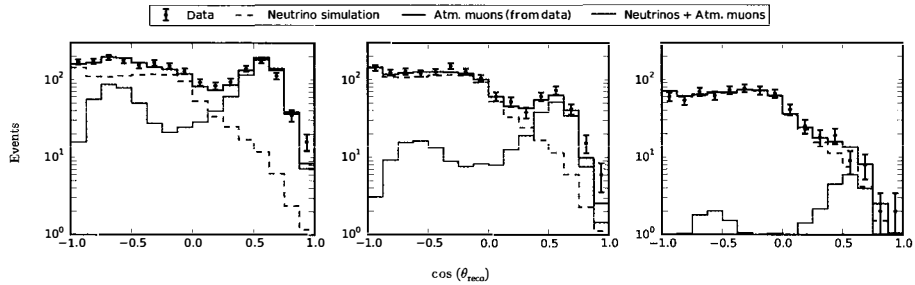

Figure 5 – Zenith angle distributions of neutrino simulation and atmospheric muons derived from data for three subsequent steps in the event selection with increasing veto cuts. A comparison is also made to a 10 % control sample of the 953 days of detector live time analyzed.

event selection. In the final step the atmospheric muon contamination of the "up-going" part of the sample is less than 2%.

The neutrino events selected for analysis are those interactions which produce photons that did not suffer strongly from scattering before detection. A delay of 20 ns from the geometric arrival time is allowed. The events which fulfil this condition can be reconstructed with little dependence on the properties of the South Pole ice, which vary as a function of depth. Figure 6a shows how direct hits align with the expectation from a muon track emitting Cherenkov light.

Two reconstructions are applied to the direct hits of every event, which differ by having one or no muons in the final state particles. Neutrino interactions with a muon track are most likely to come from ν_μ scattering and thus are favored in the selection. Events which fulfil these criteria are reconstructed with a precision of 10° in zenith angle, and 25% in energy at 20 GeV. Figure 6b shows the energy distribution of the events selected to study oscillations. Muon neutrinos dominate the sample, and a strong disappearance effect is present below 50 GeV.

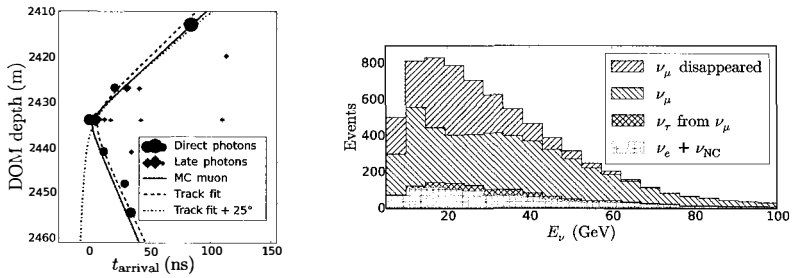

(a) Light pattern of a muon track.

(b) Energy distribution of neutrinos.

Figure 6 – Selection of events for the study of neutrino oscillations. In (a): Light pattern produced by an 8 GeV muon (42 m range) in DeepCore. The DOM depth as a function of the arrival time of photons at the string with most light collected is shown. Marker sizes scale with charge. The expected hyperbolae from simulation, a track fit and the same fit altered by 25° are also shown. In (b): True energy distribution of simulated neutrino events in the final sample, with hatched areas representing each component. The missing ν_μ component is also shown.

Data analysis and results

The data is analyzed by comparing data and simulation in a two-dimensional 8×8 histogram in reconstructed energy and zenith angle. Only events that pass through the Earth ($\cos\theta_{\text{reco}} \leq 0$) and have been reconstructed with an energy between $\log_{10}(E/\text{GeV}) = [0.8, 1.75]$ are consid-

ered. In 953 days of detector live time, a total of 5174 neutrino candidates were selected. The oscillation parameters that fit the data best are, assuming a normal mass ordering, $\Delta m^2_{32} = 2.72^{+0.19}_{-0.20} \times 10^{-3}\,\mathrm{eV}^2$ and $\sin^2\theta_{23} = 0.53^{+0.09}_{-0.12}$. There is no significant preference found for the mass ordering. The total error of the measurement has an equal contribution from statistics and systematic effects. The level of contamination from atmospheric muons, obtained by fitting tagged muons from data to the final sample, is 1%, consistent with the expectation from simulation.

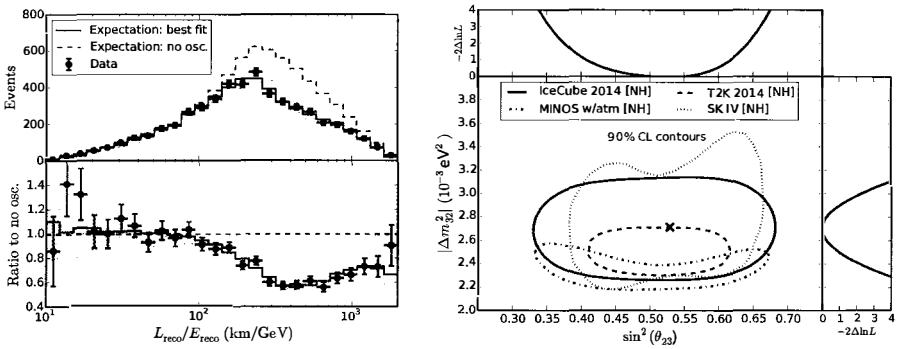

(a) (b)

Figure 7 – Neutrino oscillations results. In (a): Distribution of events as a function of reconstructed L/E. Data are compared to the best fit and assuming no oscillations on top. The ratio of data and best fit to the case without oscillations at the bottom. Bands indicate estimated systematic uncertainties. In (b): 90% confidence contours of the result in comparison with other experiments. The log-likelihood profiles for individual oscillation parameters are also shown (right and top). A normal mass ordering is assumed.

Data and simulation are in very good agreement, with a $\chi^2/\mathrm{d.o.f.} = 54.9/56$ for the full two-dimensional histogram analyzed. The L/E distribution, shown in Fig. 7a, also demonstrates the agreement but now in a variable which does not enter the analysis directly. The 90% confidence contours on the oscillation parameters are shown in Fig. 7b, together with those of the experiments leading the field. This is the first time that a very large volume neutrino telescope has measured neutrino oscillations with a precision comparable to dedicated experiments [20,21,22].

3 Summary and conclusions from heaven and hell

The last five years have been an exciting time for neutrino astronomy. Data taken by the IceCube neutrino telescope have demonstrated the existence of a high energy astrophysical diffuse neutrino flux, now observed as tracks and cascades, both starting in and crossing the detector. The different searches give compatible results, and a global study of them allows us to measure the flux precisely and is giving first hints on the flavor composition at Earth. While the sources of these neutrinos remain unknown, the lack of association with Gamma Ray Bursts and Blazars from the Fermi catalogue discards both object classes as the main source of the observed flux.

At drastically different energies, below a 100 GeV, data acquired with the DeepCore subarray have been used to study atmospheric neutrino oscillations. Systematic uncertainties, a big concern for such a sparsely instrumented detector, have been kept under control, and do not dominate the result yet. The errors obtained are, for the first time for a very large volume neutrino telescope, of the same order of magnitude as those of the leading experiments in the field. Improvements will come soon from refinements in the event selection and particle reconstruction, as well as from including neutrinos which do not produce a muon in the fit.

A possible way to resolve the sources of astrophysical neutrinos, and improve the precision of oscillation studies and determine the ordering of the neutrino masses, is the IceCube Gen2 + PINGU proposal [23,24]. On the high-energy front, the baseline proposal involves the deployment of 120 new strings surrounding IceCube, with an increased spacing of up to 300 m. On the low-energy side, 40 additional strings with 60-90 DOMs each would be placed inside the current DeepCore volume, reducing the energy threshold to less than 10 GeV and significantly increasing the light collected per event.

References

1. D.J. Bird et al. Fly's Eye Collaboration. 1994, arXiv:astro-ph/9410067.
2. Thomas K. Gaisser, Todor Stanev, and Serap Tilav. *Front. Phys. China*, 8:748–758, 2013, arXiv:1303.3565. doi:10.1007/s11467-013-0319-7.
3. A. Achterberg et al. IceCube Collaboration. *Astropart. Phys.*, 26:155–173, 2006, arXiv:astro-ph/0604450. doi:10.1016/j.astropartphys.2006.06.007.
4. R. Abbasi et al. IceCube Collaboration. *Nucl. Instrum. Meth.*, A601:294–316, 2009, arXiv:0810.4930. doi:10.1016/j.nima.2009.01.001.
5. Julia K. Becker. *Phys. Rept.*, 458:173–246, 2008, arXiv:0710.1557. doi:10.1016/j.physrep.2007.10.006.
6. M. Honda, T. Kajita, K. Kasahara, and S. Midorikawa. *Phys. Rev.*, D83:123001, 2011, arXiv:1102.2688. doi:10.1103/PhysRevD.83.123001.
7. Stefan Schonert, Thomas K. Gaisser, Elisa Resconi, and Olaf Schulz. *Phys. Rev.*, D79:043009, 2009, arXiv:0812.4308. doi:10.1103/PhysRevD.79.043009.
8. M.G. Aartsen et al. IceCube Collaboration. *Science*, 342:1242856, 2013, arXiv:1311.5238. doi:10.1126/science.1242856.
9. M.G. Aartsen et al. IceCube Collaboration. *Phys. Rev. Lett.*, 113:101101, 2014, arXiv:1405.5303. doi:10.1103/PhysRevLett.113.101101.
10. M.G. Aartsen et al. IceCube Collaboration. *Phys. Rev.*, D91(2):022001, 2015, arXiv:1410.1749. doi:10.1103/PhysRevD.91.022001.
11. M.G. Aartsen et al. IceCube Collaboration. *Phys. Rev.*, D89(10):102001, 2014, arXiv:1312.0104. doi:10.1103/PhysRevD.89.102001.
12. M.G. Aartsen et al. IceCube Collaboration. *Phys. Rev.*, D89(6):062007, 2014, arXiv:1311.7048. doi:10.1103/PhysRevD.89.062007.
13. Schonwald et al. In *Proc. 33rd Int. Cosmic Ray Conf.*, page 0662, 2013, arXiv:1309.7003.
14. M.G. Aartsen et al. IceCube Collaboration. *Phys. Rev. Lett.*, 114(17):171102, 2015, arXiv:1502.03376. doi:10.1103/PhysRevLett.114.171102.
15. R. Abbasi et al. *Nature*, 484:351–354, 2012, arXiv:1204.4219. doi:10.1038/nature11068.
16. T. Glusenkamp. IceCube Collaboration. 2015, arXiv:1502.03104.
17. Jrgen Brunner. *Adv. High Energy Phys.*, 2013:782538, 2013. doi:10.1155/2013/782538.
18. R. Abbasi et al. IceCube Collaboration. *Astropart. Phys.*, 35:615–624, 2012, arXiv:1109.6096. doi:10.1016/j.astropartphys.2012.01.004.
19. M.G. Aartsen et al. IceCube Collaboration. *Phys. Rev.*, D91(7):072004, 2015, arXiv:1410.7227. doi:10.1103/PhysRevD.91.072004.
20. K. Abe et al. T2K Collaboration. *Phys. Rev. Lett.*, 112(18):181801, 2014, arXiv:1403.1532. doi:10.1103/PhysRevLett.112.181801.
21. P. Adamson et al. MINOS Collaboration. *Phys. Rev. Lett.*, 110:251801, 2013, arXiv:1304.6335. doi:10.1103/PhysRevLett.110.251801.
22. A. Himmel. Super-Kamiokande Collaboration. In *7th International Conference on Interconnection between Particle Physics and Cosmology (PPC 2013)*, 2013, arXiv:1310.6677.
23. M.G. Aartsen et al. IceCube Collaboration. 2014, arXiv:1412.5106.
24. M.G. Aartsen et al. IceCube-PINGU Collaboration. 2014, arXiv:1401.2046.

The Flavour Composition of the High-Energy IceCube Neutrinos

Aaron C. Vincent
Institute for Particle Physics Phenomenology (IPPP), Department of Physics, Durham University, Durham DH1 3LE, UK.

Sergio Palomares Ruiz, Olga Mena
Instituto de Física Corpuscular (IFIC), CSIC-Universitat de València, Apartado de Correos 22085, E-46071 Valencia, Spain

We present an in-depth analysis of the flavour and spectral composition of the 36 high-energy neutrino events observed after three years of observation by the IceCube neutrino telescope. While known astrophysical sources of HE neutrinos are expected to produce a nearly $(1:1:1)$ flavour ratio (electron : muon : tau) of neutrinos at earth, we show that the best fits based on the events detected above $E_\nu \geq 28$ TeV do not necessarily support this hypothesis. Crucially, the energy range that is considered when analysing the HE neutrino data can have a profound impact on the conclusions. We highlight two intriguing puzzles: an apparent deficit of muon neutrinos, seen via a deficit of track-like events; and an absence of $\bar{\nu}_e$'s at high energy, seen as an absence of events near the Glashow resonance. We discuss possible explanations, including the misidentification of tracks as showers, and a broken power law, in analogy to the observed HE cosmic ray spectrum.

1 Introduction

The detection of 37 high-energy events consistent with an astrophysical origin at the IceCube neutrino detector at the South Pole[1,2,3] has signalled the beginning of the era of high-energy neutrino astronomy. Neutrinos are a powerful, complementary tool in observations of the extragalactic sky: unlike protons and other cosmic rays, they are not affected by magnetic fields in the intergalactic medium and thus point directly back towards their source; their low interaction cross-section means that they are not attenuated during their propagation to earth. In principle they allow us to peer *inside* sources. Finally, they carry an additional quantum number, *flavour*, which can yield information about source properties, propagation and detection, and has long been known to be an important observable for both astro and particle physics[4,5,6,7,8,9].

The flavour composition is determined by the production mechanism and by oscillation during propagation. The canonical astrophysical neutrino production scenario is via the disintegration of charged pions produced by proton-proton and photon-proton collisions in cosmic ray sources. This yields a flavour composition at the source $(\alpha_e : \alpha_\mu : \alpha_\tau) = (1:2:0)$. Other scenarios can affect this expectation: rapid muon energy loss can suppress the production of ν_e's at the same energy scale, giving $(0:1:0)$, while the the same phenomenon at higher energies gives the complementary ratio $(1:1:0)$. Finally, neutron decay-dominated sources yield only electron (anti) neutrinos, giving $(1:0:0)$. Following production, neutrino oscillation averages the flavour composition over the large uncorrelated distances to Earth. The $(1:2:0)$ canonical expectation averages to a ratio very close to $(1:1:1)$ at Earth; other source compositions must lie inside a small triangle around this point (shown in blue in our figures below). A mea-

sured flavour composition at Earth outside of this triangle would indicate either of exotic new physics during propagation, a non-astrophysical origin, or a systematic problem in the flavour reconstruction, e.g. due to a misidentification of event topologies.

The search for astrophysical neutrinos is complicated by the large production rate of atmospheric neutrinos, originating from the pions and kaons produced when cosmic rays strike the Earth's atmosphere. These are detected in IceCube at a rate of ~ 3000 per second, dwarfing the expected astrophysical signal by orders of magnitude. Atmospheric neutrinos are characterized by a high coincidence rate with muons and other neutrinos, anisotropies due to the projected atmospheric column density, as well as characteristic flavour and spectral information. By establishing a strict veto protocol, the IceCube collaboration was able to isolate 37 events in 3 years of data, consistent with neutrinos from a non-atmospheric origin, with energies between 28 TeV and 2 PeV. These events follow the expected shallower spectral shape, and are so far consistent with an isotropic distribution in the sky.

In this study [10,11,12], we focused on the flavour composition of the observed high-energy neutrinos. Our first study has spurred wide interest both from the IceCube collaboration [13,14] as well as independent authors [15,16,17]. TeV–PeV energy neutrinos are seen in IceCube via one of two morphologies: 1) showers (cascades), caused by neutral current (NC) interactions with nuclei, and charged current (CC) interactions of electron and tau neutrinos in the ice; and 2) muon tracks, which trace the propagation of a high-energy muon produced by the CC interaction of a muon neutrino, or by tau lepton production followed by decay to muon. Out of three years of data collection, IceCube expects 8.4 track-producing atmospheric muons and 6.6 atmospheric neutrinos. However, only 8 out of the 36[a] observed events are muon tracks. From these numbers alone, there is a hint of a possible deficit in astrophysical muon neutrinos.

In this work, we use both the topological and spectral information available for the 36 high-energy neutrinos seen at IceCube to test the available parameter space of flavours, spectra and total contribution of astrophysical and atmospheric neutrinos and muons to observations.

We begin with an overview of the high energy neutrino event rate calculation is Sec. 2, followed in Section 3 by our likelihood analysis. We conclude with a short discussion of the physical implications and of other flavour studies that have appeared in the recent literature.

2 Spectral analysis of the IceCube events

The spectrum of true deposited energies $dN^c/dE_{\rm true}$ – the electromagnetic energy that is deposited in the ice – as a function of incident neutrinos of energy E_ν, flavour $\ell = \{e, \mu, \tau\}$ and origin f (astrophysical or atmospheric), is a function of the exposure T, the whole-sky averaged attenuation $Att^f_{\nu_\ell}(E_\nu)$, the effective mass $M_{\rm eff}(E_{\rm true})$ of the detector and the differential neutrino flux $d\phi^f_{\nu_\ell}(E_\nu)/dE_\nu$. It follows a general form:

$$\frac{dN^c}{dE_{\rm true}} = T\, N_A \int_0^\infty Att^f_{\nu_\ell}(E_\nu)\, M_{\rm eff}(E_{\rm true})\, \frac{d\phi^f_{\nu_\ell}(E_\nu)}{dE_\nu}\, \frac{d\sigma^c_{\nu_\ell}(E_\nu, E_{\rm true})}{dE_{\rm true}}\, dE_\nu \ . \qquad (1)$$

The cross section $d\sigma^c_{\nu_\ell}(E_\nu, E_{\rm true})/dE_{\rm true}$ depends on the neutrino flavour and the interaction channel c. If the cascade is electronic, all of the energy is effectively deposited in the detector; if it is hadronic, then the energy-dependent deposition efficiency must be included in the calculation of (1). The specific form of the cross sections and differential spectra in (1) is given in the appendices of our detailed study [12]. In the case of CC muon neutrino events, the energy deposited by the muon track must be added to the associated cascade. We model this by computing the average energy deposited by a muon with a random point of origin and orientation in the detector. At relevant energies, this is equal to 0.119 times its initial energy. We account for the escape of tau leptons from the fiducial volume before decay in a similar manner.

[a] We discard event 32 because its energy could not be reconstructed and was coincident with a pair of background atmospheric muons.

We also include interactions between antielectron neutrinos and electrons in the ice, although this only becomes important around the Glashow resonance at 6.3 PeV, where the centre of mass energy is equal to the W boson mass.

The effective detector mass as a function of $E_{\rm true}$ is obtained by deconvolving the effective masses provided by IceCube[1] as a function of the neutrino energy E_ν. The flux in terms of deposited energy in the detector is then evaluated as a function of the "true" electromagnetic energy deposited in the ice via a convolution with a resolution function $R(E_{true}, E_{dep}, \sigma(E_{true}))$:

$$\frac{dN^c}{dE_{{\rm dep},i}} = \int_0^\infty \frac{dN^c}{dE_{\rm true}} R(E_{\rm true}, E_{{\rm dep},i}, \sigma(E_{\rm true}))\, dE_{\rm true} \ . \tag{2}$$

We model R as a gaussian distribution around $E_{\rm dep}$ with an asymmetric standard deviation, fitted to the errors given for each event [3].

Atmospheric differential event rates are modelled in the same way, using recent computations of the atmospheric fluxes[18]. These are then averaged over the whole sky, and a suppression due to IceCube's veto is included. Attenuation of all flavours and regeneration of tau neutrinos in the passage through Earth is included for astrophysical and atmospheric events.

3 Results

We turn to our main results. The reader interested in more detailed results – including tabulated best fits and exclusions, as well as results concerning a prompt (charm) atmospheric component, is referred to the complete paper [12].

We start by restricting ourselves to a study of the topological information in the 36 observed events [10,11]. The likelihood $\mathcal{L}$ of the observed event topology composition as a function of the flavour composition, is presented in the left panel of Fig. 1. We have fixed the background atmospheric muon and neutrino fluxes to the expected values (8.4 and 6.6, respectively), and the astrophysical neutrino spectrum to $\phi_\nu \propto E_\nu^{-2}$. The black line is the 68% CL exclusion line; cyan represents 95% CL. The best fit occurs at $(1:0:0)$, and the canonical $(1:1:1)$ is disfavoured at 92% CL. Assuming a slightly steeper spectrum somewhat softens this constraint. This strong constraint is due to the low track-to-shower ratio $(8:28)$ which is taken up entirely by the expected atmospheric muon background.

In order to include spectral information, we introduce the expected flux (1) into the following PDF, as a function of the flavour composition $\{\alpha_\ell\}$, for each event i of topology k and caused by each type f of incoming particle (astrophysical, atmospheric muon or atmospheric neutrino):

$$\mathcal{P}_i^f(\{\alpha\},\gamma) = \frac{1}{\sum_{\ell,j} \alpha_\ell \int_{E_{\rm min}}^{E_{\rm max}} dE_{\rm dep} \frac{dN_\ell^{j,f}}{dE_{\rm dep}}} \sum_\ell \alpha_\ell \frac{dN_\ell^f}{dE_{{\rm dep},i}} \ . \tag{3}$$

From the partial likelihood $\mathcal{L}_i = \sum_f N_f \mathcal{P}_i^f$, the total likelihood is then:

$$\mathcal{L} = e^{-N_a - N_\nu - N_\mu} \prod_{i=1}^{N_{\rm obs}} \mathcal{L}_i \ . \tag{4}$$

The right panel of Fig. 1 shows the effect of including spectral information. The best fit is still close to $(1:0:0)$, but constraints are weaker: this is an indication that while the low number of tracks is entirely consistent with a complete atmospheric origin, their spectrum is not.

This can be tested by freeing the atmospheric flux N_μ and N_ν. We also allow the astrophysical flux's spectral index γ to vary freely. Results are shown in the left panel of Fig. 2. In this case a wider range of flavour ratios may be accommodated: the spectral index is best fit by $\gamma = 2.96$, and $N_\mu = 4.7$, $N_\nu = 4.8$. If the energy range is cut at $E_{\rm min} = 60$ TeV, most of the atmospheric background is removed, leaving only 20 events and a cleaner astrophysical

signal. Interestingly, in this case the best fit returns to $(1:0:0)$. This is shown in the right panel of Fig. 2. One recovers $\gamma = 2.34$, very near IceCube's best fit ($\gamma = 2.3$), and atmospheric neutrinos should account for 6.5 events, while the best fit for atmospheric muons is consistent with expectations, with $N_\mu = 0.1$.

There is no a priori reason to cut the energy range at $E_{\rm max} = 2$ PeV. In fact, at 6.3 PeV a larger flux is expected from the Glashow resonance. We show the effect of increasing the energy range to 10 PeV in the left panel of Fig. 3. The best fit in the 60 TeV – 10 PeV range is near $(0:0:1)$: an indication of a deficit in muon neutrinos (from the topological information) and in electron antineutrinos (from the lack of events at the Glashow resonance). In this case $\gamma = 2.48$, $N_\nu = 1.5$ and $N_\mu = 2.2$.

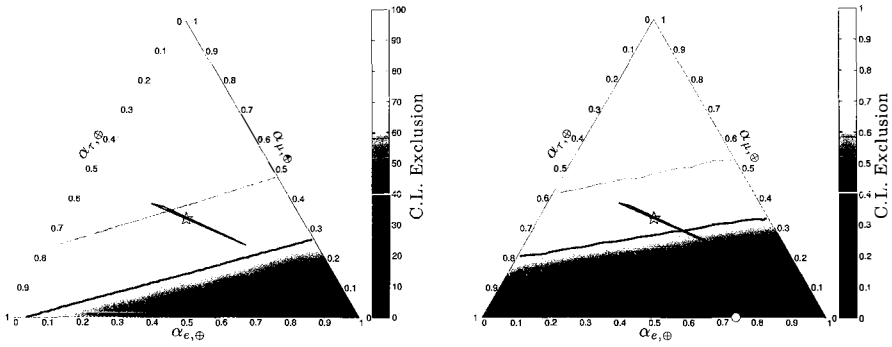

Figure 1 – Left: the exclusion confidence limits on possible flavour compositions for the 36 high-energy events observed at IceCube in the 28 TeV - 2 PeV range, using event topology information alone, fixing the atmospheric muon and neutrino rates to their expected values, and fixing the spectral index to $\gamma = 2$. The flavour composition and number of astrophysical neutrinos N_α is allowed to vary. Right: same as left panel, but including spectral information as in (3-4). In every case the thin blue triangle indicates the space to which astrophysical neutrinos may oscillate, the white star indicates $(1:1:1)$ and the best fit is denoted by a white circle.

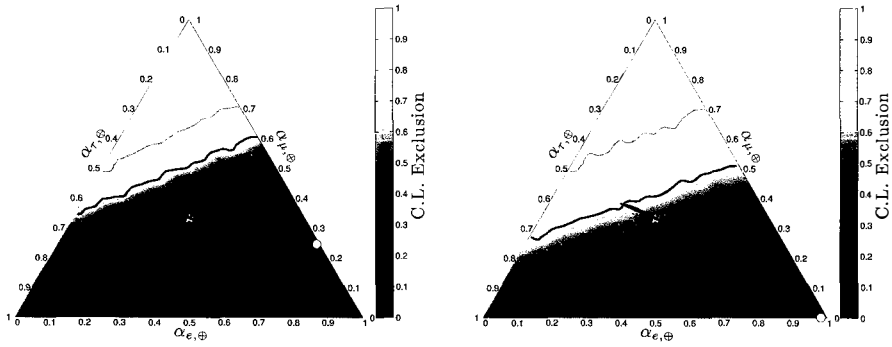

Figure 2 – As in Fig. 1, but allowing the atmospheric muon N_μ and neutrino fluxes N_ν, the astrophysical spectral index γ to vary, in addition to the flavour composition and astrophysical flux N_α. Right panel: same, but only considering the 20 events observed above 60 TeV.

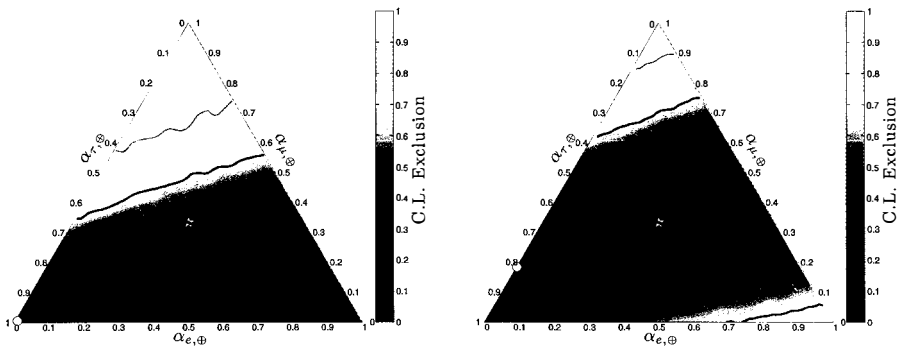

Figure 3 – As in Fig. 2, but extending the energy range to 60 TeV – 10 PeV. Left: the absence of events near the Glashow resonance leads to a best fit that is mostly composed of tau neutrinos. Right panel: the effect of assuming a 30% rate of misidentification of muon tracks as showers.

4 Discussion

From the results presented in Figs. 1–3, we are left with two potential puzzles, assuming future IceCube events follow the trends seen here. The first is a paucity of muon tracks, indicating a lack of muon neutrinos in the astrophysical flux. The second is a deficit of electron antineutrinos around the Glashow resonance. The latter can be solved for example by a break in the power law, in analogy with the cosmic ray spectrum. The former can lead to more interesting effects. If the best fit ends up away from $(1 : 1 : 1)$, it could mean that a non-standard source is responsible for the bulk of the astrophysical neutrino flux, e.g. neutron decay[15]. If the best fit lies outside the thin blue region, indicating a flavour composition that cannot be achieved by known oscillation physics, this could be an indication a non-astrophysical origin, or of new phenomena such as neutrino decay[19], extra dimensions[20], modifications of gravity[21] or other new effects during propagation. The explanation could be much more mundane, however. A misidentification of muon tracks as showers could easily account for the ν_μ deficit[10,12,13]. We show the effect of a 30% misidentification rate in the right panel of Fig. 3. In this case, compatibility with $(1 : 1 : 1)$ is much more plausible.

We have shown that the assumptions that go into the reconstruction of the flavour and spectral composition of the 36 high energy neutrino events observed at IceCube are crucial when it comes to drawing conclusions about their origin. Other studies of the flavour composition ostensibly agree with the results presented here[12]. A recent study by IceCube[13] agreed with our early conclusions after repeating our single-energy bin analysis[10,11]. After adding 101 lower-energy events, they found a preference for a tau-dominated flux when including spectral information and extending the analysis to 10 PeV. They attribute the lack of ν_μ's to a 30% misclassification rate of tracks as showers, in agreement with our findings in Fig. 3, and with our initial conclusions[10]. In a separate study, the inclusion of a larger number of low-energy events consistent with an astrophysical component gives a similar picture, but flipped so that the best fit lies along the $\nu_e - \nu_\mu$ axis, rather than the $\nu_\tau - \nu_\mu$ axis[14]. This is unsurprising, since adding several hundred events below 100 TeV removes any statistical power from the Glashow resonance region.

Nonetheless, the significance of the results presented here and in other analyses remain low – even when through-going muons are included[17] – for the simple reason of low statistics. While IceCube expects a few dozen more events in the next years, future experiments such as KM3Net and Gen-2 IceCube will be crucial in the next step of the new exciting field of neutrino astronomy.

Acknowledgments

S. P. R. is supported by a Ramón y Cajal contract, by the Spanish MINECO under Grant No. FPA2011-23596, by the Generalitat Valenciana under Grant PROMETEOII/2014/049, and by the Portuguese FCT through CERN/FP/123580/2011 and PTDC/FIS-NUC/0548/2012, partially funded through POCTI (FEDER). O. M. is supported by the Consolider Ingenio Project CSD2007-00060 and by Grant FPA2011–29678 of the Spanish MINECO, and by PROMETEO/2009/116. The authors are also partially supported by PITN-GA-2011-289442-INVISIBLES.

References

1. IceCube Collaboration: M. G. Aartsen *et. al.*, *First observation of PeV-energy neutrinos with IceCube*, *Phys.Rev.Lett.* **111** (2013) 021103.
2. IceCube: M. G. Aartsen *et. al.*, *Evidence for High-Energy Extraterrestrial Neutrinos at the IceCube Detector*, *Science* **342** (2013) 1242856.
3. IceCube Collaboration: M. G. Aartsen *et. al.*, *Observation of High-Energy Astrophysical Neutrinos in Three Years of IceCube Data*, *Phys.Rev.Lett.* **113** (2014) 101101.
4. H. Athar, M. Jezabek, and O. Yasuda, *Effects of neutrino mixing on high-energy cosmic neutrino flux*, *Phys.Rev.* **D62** (2000) 103007.
5. J. F. Beacom, N. F. Bell, D. Hooper, S. Pakvasa, and T. J. Weiler, *Measuring flavor ratios of high-energy astrophysical neutrinos*, *Phys.Rev.* **D68** (2003) 093005.
6. T. Kashti and E. Waxman, *Flavoring astrophysical neutrinos: Flavor ratios depend on energy*, *Phys.Rev.Lett.* **95** (2005) 181101.
7. W. Rodejohann, *Neutrino Mixing and Neutrino Telescopes*, *JCAP* **0701** (2007) 029.
8. P. Lipari, M. Lusignoli, and D. Meloni, *Flavor Composition and Energy Spectrum of Astrophysical Neutrinos*, *Phys.Rev.* **D75** (2007) 123005.
9. S. Pakvasa, W. Rodejohann, and T. J. Weiler, *Flavor Ratios of Astrophysical Neutrinos: Implications for Precision Measurements*, *JHEP* **0802** (2008) 005.
10. O. Mena, S. Palomares-Ruiz, and A. C. Vincent, *On the flavor composition of the high-energy neutrino events in IceCube*, *Phys.Rev.Lett.* **113** (2014) 091103.
11. S. Palomares-Ruiz, O. Mena, and A. C. Vincent, *On the flavor composition of the high-energy neutrinos in IceCube*, `arXiv:1411.2998`.
12. S. Palomares-Ruiz, A. C. Vincent, and O. Mena, *Spectral analysis of the high-energy IceCube neutrinos*, `arXiv:1502.0264`.
13. IceCube: M. Aartsen *et. al.*, *Flavor Ratio of Astrophysical Neutrinos above 35 TeV in IceCube*, *Phys.Rev.Lett.* **114** (2015) 171102.
14. J. P. Yáñez, *Neutrinos from heaven and hell in IceCube*, *Proceedings of the 50th Rencontres de Moriond Electroweak Session, La Thuile, Italy* (2015).
15. L. A. Anchordoqui, *Neutron β-decay as the origin of IceCube's PeV (anti)neutrinos*, *Phys.Rev.* **D91** (2015) 027301.
16. A. Watanabe, *A flavored model of astrophysical neutrinos in IceCube*, `arXiv:1412.8264`.
17. A. Palladino, G. Pagliaroli, F. Villante, and F. Vissani, *Which is the flavor of cosmic neutrinos seen by IceCube?*, *Phys.Rev.Lett.* **114** (2015) 171101.
18. T. Sinegovskaya, A. Morozova, and S. Sinegovsky, *High-energy neutrino fluxes and flavor ratio in the Earths atmosphere*, *Phys.Rev.* **D91** (2015) 063011.
19. J. F. Beacom, N. F. Bell, D. Hooper, S. Pakvasa, and T. J. Weiler, *Decay of high-energy astrophysical neutrinos*, *Phys.Rev.Lett.* **90** (2003) 181301.
20. E. Aeikens, H. Päs, S. Pakvasa, and P. Sicking, *Flavor ratios of extragalactical neutrinos and neutrino shortcuts in extra dimensions*, `arXiv:1410.0408`.
21. J. I. Illana, M. Masip, and D. Meloni, *A new physics interpretation of the IceCube data*, *Astropart.Phys.* **65** (2014) 64–68.

INTERPRETATION OF THE HIGH ENERGY ICECUBE DATA

J.I. ILLANA[a], M. MASIP[a], D. MELONI[b]

[a] *CAFPE and Departamento de Física Teórica y del Cosmos*
Universidad de Granada, E-18071 Granada, Spain

[b] *Dipartimento di Matematica e Fisica*
Università di Roma Tre, I-00146 Rome, Italy

IceCube has recently published the observation of 37 events of TeV-PeV energies. We show that the angular distribution, the spectrum and the muon to shower ratio of these events can not be explained by atmospheric neutrinos. We obtain an excellent fit, however, if cosmogenic neutrinos of ultrahigh energy experience new neutral current interactions that are very soft, with only a small fraction of energy being transferred to the target nucleon. We describe models that may provide cross sections with the precise features required to fit the data and discuss the implications of our hypothesis on future observations.

1 High energy events at IceCube

IceCube can measure large energy depositions in the ice. In particular, we will be interested in recent data that they have published in Science [1] and Physical Review Letters [2] where the minimum energy is set at 30 TeV. It is apparent that the only thing that can get there, 2 km under the ice, and deposit energy are muons and neutrinos. IceCube can see, for example, a neutrino coming from any direction and having a neutral current (NC) interaction or a charged current (CC) interaction with no muon in the final state. In these *shower events* the hadronic or electromagnetic energy is absorbed within a few meters of ice, and the direction of the primary can be distinguished with an uncertainty of 15 degrees. Since in the two analyses IceCube targets non-atmospheric neutrinos, they discard events with simultaneous activity in IceTop, as most likely these neutrinos come from mesons produced in extensive air showers. IceCube can also see CC interactions of muon neutrinos, with an initial energy deposition and then a muon track crossing the detector. They select these *track events* if, in addition to a subthreshold activity in Icetop, the track does not start in the detector boundary.

After cuts IceCube selects 37 events. Despite their efforts to eliminate atmospheric muons, IceCube estimate that 8.4 ± 4.2 events could still be muons entering the detector from outside,

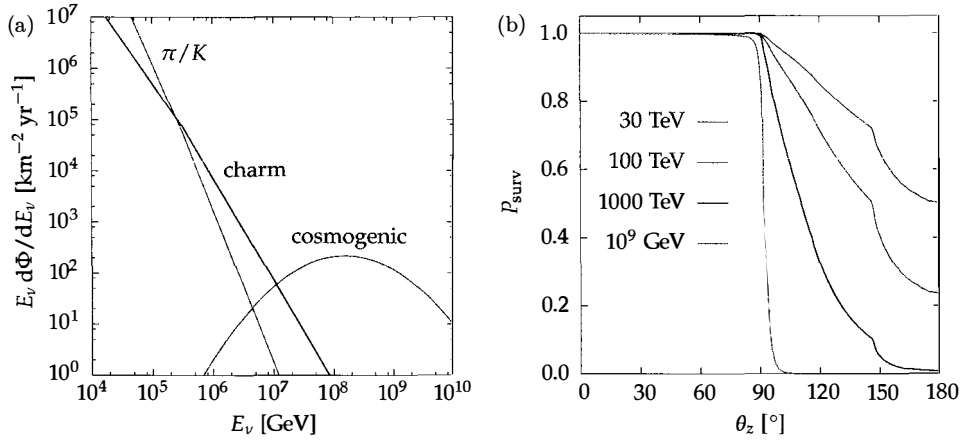

Figure 1 – (a) Atmospheric and cosmogenic neutrino fluxes integrated over all directions and including all flavors. (b) Probability $P_{\rm surv}$ that a neutrino reaches IceCube from a zenith angle θ_z for several energies E_ν.

which seems consistent with the 5 events (one of them containing two coincident muons from unrelated air showers) where the track starts near the detector boundary. We will in principle exclude these 5 downgoing events (which could be done imposing harder cuts) and assume that we are left with 32 genuine neutrino events.

To understand the data, it is essential to estimate the atmospheric ν flux and the attenuation of this flux when neutrinos propagate from the Earth surface to the detector.

Most atmospheric neutrinos come from pion and kaon decays. However, above 50 GeV the spectrum of these neutrinos (in Fig. 1a) is very steep, as the parent meson tends to collide in the air and lose energy before it can decay. At energies around $10^{5.5}$ GeV one expects [3] that the flux becomes dominated by νs from D mesons, which are less abundant in the atmosphere but shorter lived. The π/K component has a strong dependence on the zenith angle (it is larger from horizontal directions, where these mesons find a thinner air) and is dominated by the ν_μ flavor. The charm component is isotropic and contains ν_μ and ν_e with the same frequency, together with 2% of ν_τ. In Fig. 1a we also plot the cosmogenic neutrino flux [4], a few hundred neutrinos per km^2 and year that should dominate over the atmospheric flux one decade above the energies observed at IceCube. As for the attenuation of these fluxes, in Fig. 1b we plot the probability that a neutrino gets to the detector from different zenith angles. We see that at IceCube energies the absorption by the Earth is only important from $\theta_z \geq 110^o$ (*i.e.*, more than 20^o below the horizon). In particular, a 100 TeV (1 PeV) neutrino has in average a 50% (20%) probability to reach IceCube from $110^o < \theta_z < 180^o$. Cosmogenic neutrinos are almost completely suppresed at inclinations below the horizon.

The previous arguments motivate an analysis [5] that includes three direction bins of similar angular size: *downgoing*, with declinations $-90° \leq \delta < -20°$ ($\delta = \theta_z - 90°$), *near-horizontal* ($-20° \leq \delta < +20°$) and *upgoing* ($+20° \leq \delta < +90°$). It is important to distinguish the near-horizontal bin because it includes the largest atmospheric ν_μ flux and also because, unlike upgoing directions, horizontal directions are not affected by attenuation. A two bin analysis (just up and downgoing events) would *average* and erase these crucial features in the neutrino flux, whereas a larger number of bins is not adequate to the still thin statistics.

Our simulation of the atmospheric background provides the results in the second column of Table 1.

We have included two energy bins and have distinguished between the two event topologies. An inspection of the data (summarized in the first column) reveals two clear results: *(i)* The

Table 1: Data, atmospheric background, excess from a E^{-2} diffuse flux, and excess from eikonal collisions of cosmogenic neutrinos ($M_5 = 1.7$ TeV, $m_c = 1$ GeV) in 988 days.

	Data	Atm	E^{-2}	NP	Data	Atm	E^{-2}	NP	
Tracks	2	0.8	0.6	0.0	0	0.0	0.1	0.0	UPGOING
Showers	5	2.7	3.6	0.0	0	0.0	0.7	0.0	$(+20° < \delta < +90°)$
Tracks	2	3.5	1.5	0.0	0	0.0	0.5	0.0	NEAR HORIZONTAL
Showers	8	5.9	6.4	4.2	1	0.2	2.6	1.9	$(-20° < \delta < +20°)$
Tracks	0	0.2	1.6	0.0	0	0.0	0.6	0.0	DOWNGOING
Showers	11	0.6	6.5	8.0	3	0.0	2.9	3.5	$(-90° < \delta < -20°)$
	30 – 300 TeV				300 – 3000 TeV				

number and distribution of tracks is well explained by atmospheric neutrinos, as IceCube see 4 tracks for an expected background of 4.3. If we added the 5 downgoing tracks excluded in our analysis together with the 8.4 ± 4.2 muon background, we would expect a total of 12.9 track events and find only 9 in the data. *(ü)* There is an excess of showers that is especially significant from downgoing directions. At lower energies we find 11 events for 0.6 expected, whereas in the 300–3000 TeV bin they observe 3 showers for a 0.04 background. If we include near-horizontal directions we obtain a total of 23 events for just 6.7 expected.

IceCube then proposes a fit using a diffuse flux of astrophysical neutrinos with a E^{-2} spectrum (third column in Table 1). This hypothesis that has two generic implications. First, it gives around 4.5 showers per track. The data, however shows an excess of 18.6 showers (28 observed, 9.4 expected) while there is no need for extra tracks. Second, it implies a very similar number of downgoing and near-horizontal events, but we see an excess of 13.2 downgoing events and just 1.4 extra events from near-horizontal directions. Therefore, although the statistical significance of these deviations is not conclusive yet, it is apparent that other possibilities may give a better fit. In particular, we will define a new physics framework that only introduces near-horizontal and downgoing showers (in a 1:2 ratio) with no new muon tracks from any directions.

2 Very soft collisions mediated by TeV gravity

We intend to introduce new NC interactions at very high energies, so that only cosmogenic neutrinos (with $E_\nu \approx 10^9$ GeV) experience them. TeV gravity provides an ideal ground: it becomes strong at transplanckian energies ($\sqrt{s} > M_5 \approx 1$ TeV) and it reaches long distances (it is mediated by light gravitons) that imply very large cross sections. It turns out that a modification of the usual RS framework [6] does the work. The model has two free parameters, M_5 and the 5-dim curvature k (the length of the extra dimension is used to fit M_P). The second parameter defines the mass $m_n \approx \left(n + \frac{1}{4}\right) k\pi$ of the KK gravitons, and a value $k \leq 50$ MeV will imply large cross sections at ultrahigh energies while avoiding cosmological [7] and astrophysical bounds.

We have shown [5] that, at distances between $1/m_c$ and $1/M_5$, this set up gives the same gravitational potential as an ADD model [8] with just one flat extra dimension.

The processes relevant at IceCube will be scatterings with large impact parameter: longer than the typical ones to form a black hole (and thus with a larger cross section) but still shorter than $1/m_c$, so that gravity is still purely 5-dimensional. In these processes [9,10] the incident neutrino interacts with a parton in the target nucleon, transfers a very small fraction $y = (E_\nu - E'_\nu)/E_\nu$ of its energy and keeps going with almost the same energy. Using the eikonal approximation the amplitude can be calculated in impact parameter space as a sum of ladder and cross-ladder diagrams. In Fig. 2 we can see that at low energies the new physics is negligible and neutrinos interact with matter only through W and Z exchange. Above an energy threshold

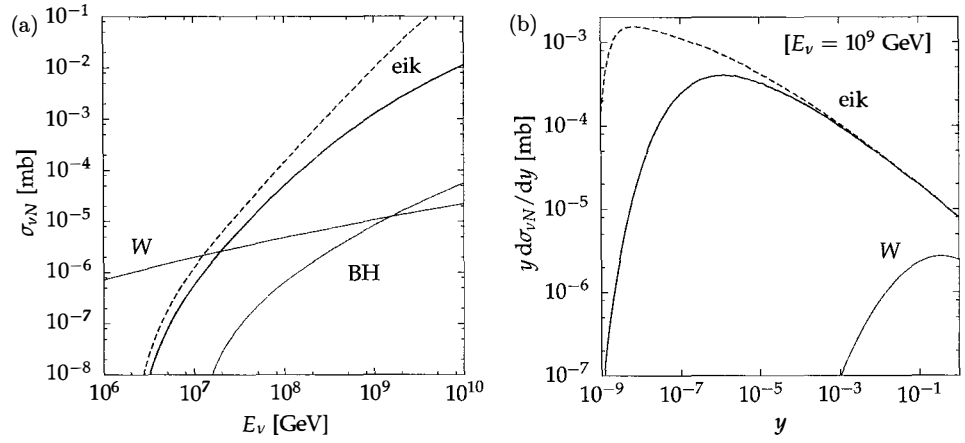

Figure 2 – (a) νN cross sections for proceses mediated by TeV-gravity and by W exchange. (b) Differential cross sections $y\,\mathrm{d}\sigma/\mathrm{d}y$ for $E_\nu = 10^9$ GeV. In both panels $M_5 = 1.7$ TeV and $m_c = 5$ GeV (solid), 50 MeV (dashed).

$E_\nu = M_5^2/(2m_N) \approx 10^6$ GeV the gravitational cross section grows fast and becomes much larger than the standard one at $E_\nu \approx 10^8$ GeV. This large cross section, however, is very soft: the neutrino mean free path in ice becomes short (≈ 10 km at 10^9 GeV) but the fraction of energy deposited in each interaction is small ($\langle y \rangle \approx 10^{-5}$).

3 Fit of the IceCube events

Our model will explain the IceCube data using soft collisions of cosmogenic neutrinos. Three observations are here in order. *(i)* The new physics only adds neutral current interactions: new showers but no new muon tracks. *(ii)* At cosmogenic energies neutrinos can reach the detector only from downgoing and horizontal directions: no new upgoing events. *(iii)* Notice that these eikonal interactions do not stop the neutrino, it can interact in the ice several times before reaching the detector.

In the fourth column of Table 1 we give the contribution of these eikonal interactions to the different bins. The new physics introduces showers in the downgoing and near horizontal bins in a 2 to 1 ratio. After adding the atmospheric background, it provides the most accurate fit of the data. In particular, the likelihood ratio [11] λ

$$-2\ln\lambda = \sum_i^N 2\left(E_i - X_i + X_i \ln\frac{X_i}{E_i}\right) \tag{1}$$

gives a significant difference between our hypothesis and IceCubes's:

$$-2\ln\lambda^{NP} = 5.9\,, \qquad -2\ln\lambda^{E^{-2}} = 15.4\,. \tag{2}$$

If the 5 ambiguous tracks were included in the analysis, we would obtain similar values:

$$-2\ln\lambda^{NP} = 7.3\,, \qquad -2\ln\lambda^{E^{-2}} = 15.1\,. \tag{3}$$

4 Summary and discussion

The observation by IceCube of 37 events with energy above 30 TeV is a very interesting result. The interpretation of these events in terms of an astrophysical neutrino flux with E^{-2} spectrum gives an acceptable fit, but it introduces some tension with the data in the following regards:

- In the data there is no excess of muon tracks, which can be explained with atmospheric neutrinos. However, an astrophysical neutrino flux favors equipartition between the three flavors, which implies 1 track per each 4.5 extra showers.
- IceCube's fit prefers an astrophysical flux dominated by ν_e and ν_τ. The electron flavor, however, introduces events at the Glashow resonance ($E_\nu = 6.4$ PeV) that have not been seen yet. Moreover, in their analysis the neutrino flux from charm decay (that should dominate the atmospheric flux at $10^{5.5}$ GeV) is left as a free parameter end then fitted to zero.
- IceCube's hypothesis implies the same number of events in the downgoing and the near-horizontal bins, whereas the data shows a clear preference for the former bin.

We have proposed a different interpretation that implies a better fit: cosmogenic neutrinos, with a flux correlated with the ultrahigh energy cosmic ray flux, experience new NC interactions of very soft nature where they deposit a small fraction of energy. Our hypothesis introduces only shower events, it does not *see* the Glashow resonance, and it predicts a 2:1 ratio for the number of events in the downgoing and near-horizontal direction bins. We have shown that models of TeV gravity provide cross sections with the required features.

An increased statistics could then distinguish between both hypotheses. In addition, a larger detection volume in IceCube (a possibility that is currently under study) would introduce another clear difference between both scenarios. The cosmogenic neutrino flux is very low, so our interpretation requires a large cross section with matter at ultrahigh energies. As a consequence, an increased volume would necesarily imply double-bang events inside the detector, a topology that could not be explained with standard physics.

Acknowledgments

This work has been supported by MICINN of Spain (FPA2013-47836, and Consolider-Ingenio **Multidark** CSD2009-00064), by Junta de Andalucía (FQM101,3048,6552), and by MIUR of Italy under the program Futuro in Ricerca 2010 (RBFR10O36O).

References

1. M. G. Aartsen *et al.* [IceCube Collaboration], *Science* **342** (2013) 1242856.
2. M. G. Aartsen *et al.* [IceCube Collaboration], *Phys. Rev. Lett.* **113** (2014) 101101.
3. J. I. Illana, P. Lipari, M. Masip and D. Meloni, *Astropart. Phys.* **34**, 663 (2011).
4. K. Kotera, D. Allard and A. V. Olinto, *JCAP* **1010** (2010) 013.
5. J. I. Illana, M. Masip and D. Meloni, *Astropart. Phys.* **65**, 64 (2015).
6. G. F. Giudice, T. Plehn and A. Strumia, *Nucl. Phys.* B **706** (2005) 455.
7. S. Hannestad, *Phys. Rev.* D **64** (2001) 023515.
8. N. Arkani-Hamed, S. Dimopoulos and G. R. Dvali, *Phys. Lett.* B **429** (1998) 263.
9. R. Emparan, M. Masip and R. Rattazzi, *Phys. Rev.* D **65** (2002) 064023.
10. J. I. Illana, M. Masip and D. Meloni, *Phys. Rev.* D **72** (2005) 024003.
11. K. A. Olive *et al.* [Particle Data Group Collaboration], *Chin. Phys.* C **38** (2014) 090001.

INDIRECT SEARCHES FOR STERILE NEUTRINOS AT A HIGH-LUMINOSITY Z-FACTORY

VALENTINA DE ROMERI [a]
Laboratoire de Physique Corpusculaire, CNRS/IN2P3 – UMR 6533,
Campus des Cézeaux, 24 Av. des Landais, F-63177 Aubière Cedex, France

A future high-luminosity Z-factory has the potential to investigate lepton flavour violation. Rare decays such as $Z \to \ell_1^\mp \ell_2^\pm$ are potentially complementary to low-energy (high-intensity) observables of lepton flavour violation. Here we consider two extensions of the Standard Model which add to its particle content one or more sterile neutrinos. We address the impact of the sterile fermions on lepton flavour violating Z decays, focusing on potential searches at FCC-ee (TLEP), and taking into account experimental and observational constraints. We show that sterile neutrinos can give rise to contributions to BR($Z \to \ell_1^\mp \ell_2^\pm$) within reach of the FCC-ee. We discuss the complementarity between a high-luminosity Z-factory and low-energy charged lepton flavour violation facilities.

1 Introduction

Despite the recent experimental advances, the neutrino physics picture is still incomplete. Among the missing ingredients are the CP-violating phase(s), the mass ordering (normal (NH) or inverted (IH) hierarchy) and the absolute mass scale. Moreover, it remains to clarify whether neutrinos are Majorana or Dirac particles, and to understand what is the underlying mechanism responsible for the generation of their masses. Several frameworks which account for neutrino masses and mixings are extensions of the Standard Model (SM) which introduce sterile neutrinos. These models are further motivated by anomalous experimental results (see [1] and references therein), as well as by certain indications from large scale structure formation [1, 2].
The existence of sterile neutrinos may be investigated at colliders: for instance, the case for a high luminosity circular e^+e^- collider (called FCC-ee), operating at centre-of-mass energies ranging from the Z pole up to the top quark pair threshold is being actively studied [3]. Its characteristics should allow to obtain a typical peak luminosity at the Z pole of $\sim 10^{36}\text{cm}^{-2}\text{s}^{-1}$. A year of operation at the Z pole centre-of-mass energy would then yield $\sim 10^{12}$ Z boson decays to be recorded. Motivated by the design study for such a powerful machine, we have investigated the prospects for indirect searches for sterile neutrinos by means of rare *charged* lepton flavour violating (cLFV) Z decays [4].

[a] based on a work done in collaboration with A. ABADA, S. MONTEIL, J. ORLOFF and A. M. TEIXEIRA

2 Leptonic Z decays in the presence of sterile neutrinos

Lepton-flavour changing Z decays are forbidden in the SM due to the GIM mechanism [5], and their rates remain extremely small ($\sim 10^{-54} - 10^{-60}$) even when lepton mixing is introduced. The observation of such a rare decay would therefore serve as an indisputable evidence of new physics [6–13]. We consider here two extensions of the SM which introduce sterile fermions. The mixing in the neutral lepton sector induced by these Majorana states also opens the possibility for flavour violation in $Z\nu_i\nu_j$ interactions (flavour-changing neutral currents), coupling both the left- and right- handed components of the neutral fermions to the Z boson. Together with the charged-current LFV couplings, these interactions will induce an effective cLFV vertex $Z\ell_1^{\mp}\ell_2^{\pm}$.

3 Extensions of the SM by sterile neutrinos

The effective "3+1 toy model" A simple approach to address the impact of sterile fermions on rare cLFV Z decays consists in considering a minimal model where only one sterile Majorana state is added to the three light active neutrinos of the SM. This allows for a first, generic, evaluation of the impact of the sterile fermions for these processes. In this simple toy model, no assumption is made on the underlying mechanism of neutrino mass generation. The addition of an extra neutral fermion to the particle content translates into extra degrees of freedom: the mass of the new sterile state, m_4, three active-sterile mixing angles θ_{i4}, two new (Dirac) CP phases and one extra Majorana phase. This leads to the definition of a 4×4 mixing matrix U_{ij}, whose 3×4 sub-matrix $\mathbf{U}_{lj}$ appears in the SM charged-currents Lagrangian (see Eq. (4) below).
In our analysis, and for both NH and IH light neutrino spectra, we scan over the following range for the sterile neutrino mass: 10^{-9} GeV $\lesssim m_4 \lesssim 10^6$ GeV, while the active-sterile mixing angles are randomly varied in the interval $[0, 2\pi]$ [b]. All CP phases are also taken into account, and likewise randomly varied between 0 and 2π.

The Inverse Seesaw framework The Inverse Seesaw (ISS) mechanism [14] is an example of (type I) low-scale seesaw realisation which in full generality calls upon the introduction of at least two generations of SM singlets. Here, we consider the addition of three generations of right-handed neutrinos ν_R and of extra $SU(2)$ singlets fermions X to the SM particle content. Both ν_R and X carry lepton number $L = +1$ [14]. The SM Lagrangian is thus extended as $\mathcal{L}_{\rm ISS} = \mathcal{L}_{\rm SM} - Y^{\nu}_{ij}\,\bar{\nu}_{Ri}\,\tilde{H}^{\dagger}\,L_j - M_{Rij}\,\bar{\nu}_{Ri}\,X_j - \frac{1}{2}\mu_{Xij}\,\bar{X}^c_i\,X_j + \text{h.c.}$, where $i, j = 1, 2, 3$ are generation indices and $\tilde{H} = i\sigma_2 H^*$. Lepton number $U(1)_L$ is broken only by the non-zero Majorana mass term μ_X, while the Dirac-type RH neutrino mass term M_R does conserve lepton number. In the $(\nu_L, \nu^c_R, X)^T$ basis, and after EW symmetry breaking, the (symmetric) 9×9 neutrino mass matrix $\mathcal{M}$ is given by

$$\mathcal{M} \;=\; \begin{pmatrix} 0 & m_D^T & 0 \\ m_D & 0 & M_R \\ 0 & M_R^T & \mu_X \end{pmatrix}, \tag{1}$$

with $m_D = Y^{\nu} v$ the Dirac mass term, v being the vacuum expectation value of the SM Higgs boson. Under the assumption that $\mu_X \ll m_D \ll M_R$, the diagonalization of $\mathcal{M}$ leads to an effective Majorana mass matrix for the active (light) neutrinos [15],

$$m_{\nu} \simeq m_D^T\, M_R^{T-1}\, \mu_X\, M_R^{-1}\, m_D\,. \tag{2}$$

The remaining six (mostly) sterile states form nearly degenerate pseudo-Dirac pairs, with masses

$$m_{S_{\pm}} = \pm\sqrt{M_R^2 + m_D^2} + \frac{M_R^2\,\mu_X}{2\,(m_D^2 + M_R^2)}\,. \tag{3}$$

[b] We always ensure that the the perturbative unitary bound on the sterile masses and their couplings to the active states is respected.

In the ISS, the full neutrino mass matrix is diagonalised by a 9×9 unitary mixing matrix U as $\mathrm{U}^T \mathcal{M} \mathrm{U} = \mathrm{diag}(\mathrm{m_i})$. In the basis where the charged lepton mass matrix is diagonal, the leptonic mixing matrix $\mathbf{U}$ (see Eq. (4) below) is given by the rectangular 3×9 sub-matrix corresponding to the first three columns of U. This framework is phenomenologically appealing because it allows to accommodate neutrino data with natural values of the Yukawa couplings, while at the same time comparatively light sterile neutrino masses are possible. The possibility of having sizeable mixings between the active and sterile states, will have a non-negligible impact for several observables.

4 Constraints on sterile neutrino extensions of the SM

The introduction of sterile fermion states, which have a non-vanishing mixing to the active neutrinos, leads to a modification of the leptonic charged current Lagrangian:

$$-\mathcal{L}_{\mathrm{cc}} = \frac{g}{\sqrt{2}} \mathbf{U}^{ji} \bar{\ell}_j \gamma^\mu P_L \nu_i W_\mu^- + \mathrm{c.c.}\,, \tag{4}$$

where $\mathbf{U}$ is the leptonic mixing matrix, $i = 1, \ldots, n_\nu$ denotes the physical neutrino states and $j = 1, \ldots, 3$ the flavour of the charged leptons. In the standard case of three neutrino generations, $\mathbf{U}$ corresponds to the unitary matrix U_{PMNS}. For $n_\nu > 3$, the mixing between the left-handed leptons, which we denote by $\tilde{U}_{\mathrm{PMNS}}$, corresponds to a 3×3 sub-block of $\mathbf{U}$, which can show some deviations from unitarity. One can parametrise [16] the $\tilde{U}_{\mathrm{PMNS}}$ mixing matrix as $U_{\mathrm{PMNS}} \to \tilde{U}_{\mathrm{PMNS}} = (\mathbb{1} - \boldsymbol{\eta})\, U_{\mathrm{PMNS}}$, where the matrix $\boldsymbol{\eta}$ encodes the deviation of the $\tilde{U}_{\mathrm{PMNS}}$ from unitarity [17,18], due to the presence of extra neutral fermion states. One can also introduce the invariant quantity $\tilde{\boldsymbol{\eta}}$, defined as

$$\tilde{\boldsymbol{\eta}} = 1 - |\mathrm{Det}(\tilde{U}_{\mathrm{PMNS}})|\,, \tag{5}$$

particularly useful to illustrate the effect of the new active-sterile mixings (corresponding to a deviation from unitarity of the $\tilde{U}_{\mathrm{PMNS}}$) on several observables.
The deviation from unitarity of $\mathbf{U}$ will induce a departure from the SM expected values of several observables. In turn, this is translated into a vast array of constraints which we will apply to our analysis (see details and references in [4]):

- **Neutrino oscillation data** The most important constraint on any model of massive neutrinos is to comply with ν-oscillation data. We impose neutrino oscillation parameters from [19], for both NH and IH of the light neutrino spectrum.

- **Perturbativity** Although no upper limit on the mass of the heavy neutrinos exists, the decay of the (mostly) sterile heavy states should comply with the perturbative unitary condition $\frac{\Gamma_{\nu_i}}{m_{\nu_i}} < \frac{1}{2} \quad (i \geq 4)$, which translates into a bound on sterile neutrino masses.

- **Unitarity constraints** Non-standard neutrino interactions with matter can be generated by the introduction of fermionic sterile states. We consider the constraints on the non-unitarity matrix η from [20,21], for sterile neutrino masses in the range GeV $\lesssim m_\nu \lesssim \Lambda_{\mathrm{EW}}$, being Λ_{EW} the electroweak scale.

- **Electroweak precision data** The addition of sterile states to the SM, with a sizeable active-sterile mixing, may have an impact on electroweak precision observables either at tree-level (charged currents) or at higher order. We apply these bounds to our analysis and we further require that the new contributions to the cLFV Z decay width do not exceed the present uncertainty on the total Z width.

- **LHC constraints** LHC data constrain parts of the parameter space where the sterile neutrinos are lighter than the Higgs boson, through searches for Higgs decays to an active neutrino and a heavier (mostly) sterile one.

- **Leptonic and semileptonic meson decays** Further constraints arise from leptonic and semileptonic decays of pseudoscalar mesons, as for example K, D, D_s, B.

- **Laboratory searches** Negative searches for monochromatic lines in the spectrum of muons from $\pi^{\pm} \to \mu^{\pm}\nu$ decays also impose robust bounds on sterile neutrino masses in the MeV-GeV range.

- **Neutrinoless double beta decay** The introduction of Majorana sterile neutrinos allows for processes which violate lepton number, such as $0\nu2\beta$ decay. The sensitivities of current experiments put a limit on the effective neutrino Majorana mass - to which the amplitude of $0\nu2\beta$ process is proportional - in the range $|m_{ee}| \lesssim 140$ meV $- 700$ meV.

- **Lepton flavour violation** The sterile fermions will contribute to several charged lepton flavour violating processes such as $\ell \to \ell'\gamma$, $\ell \to \ell_1\ell_1\ell_2$ and $\mu - e$ conversion in muonic atoms, the rates depending on their masses and mixings with the active neutrinos. In our analysis we compute the contribution of the sterile states to all these observables, imposing compatibility with current experimental bounds and considering the impact of future experimental sensitivities.

- **Cosmological bounds** Several cosmological observations (CMB, Lyman-α, X-rays, clusters, etc...) put severe constraints on sterile neutrinos with a mass below the TeV. However, these bounds are derived assuming a standard cosmology; the possibility of a non-standard cosmology could allow to evade some of the above bounds. Aiming at conservativity, we will allow for the violation of these cosmological bounds in some scenarios.

5 Results

We proceed to discuss the impact of the additional sterile states on cLFV Z decays for the two scenarios discussed in Section 3.

cLFV Z decays in the "3+1 model"
This minimal extension of the SM by one sterile neutrino can account for values of $\mathrm{BR}(Z \to \ell_1^{\mp}\ell_2^{\pm})$ within the sensitivity of a high luminosity Z-factory, such as the FCC-ee. Nevertheless, the largest cLFV Z decay branching fractions (as large as $\mathcal{O}(10^{-6})$) cannot be reconciled with current bounds on low-energy cLFV processes. Indeed, sterile neutrinos also contribute via Z penguin diagrams to cLFV 3-body decays and $\mu - e$ conversion in nuclei, which severely constrain the flavour violating $Z\ell_1^{\mp}\ell_2^{\pm}$ vertex (sce also [10–12]). Moreover, the recent MEG result on $\mu \to e\gamma$ also excludes important regions of the parameter space. These constraints are especially manifest in the case of $Z \to e\mu$ decays, since the severe limits from $\mathrm{BR}(\mu \to 3e)$ and $\mathrm{CR}(\mu - e, \mathrm{Au})$ typically preclude $\mathrm{BR}(Z \to e\mu) \gtrsim 10^{-13}$.
In Fig. 1 we illustrate the complementary rôle of a high-luminosity Z-factory with respect to low-energy (high-intensity) cLFV dedicated experiments. We display the sterile neutrino contributions to $\mathrm{BR}(Z \to \ell_1^{\mp}\ell_2^{\pm})$ versus two different low-energy cLFV observables: $\mathrm{CR}(\mu - e, \mathrm{Al})$ and $\mathrm{BR}(\tau \to \mu\gamma)$. In the plots, we identify as grey points the solutions which fail to comply with (at least) one of the constraints listed in Section 4. We depict in red the points that survive all other bounds but are typically disfavoured from standard cosmology arguments. Finally, blue points are in agreement with *all* imposed constraints. We further highlight in dark yellow solutions which allow for a third complementary observable within future sensitivity, which is the effective neutrino mass in $0\nu2\beta$ decays. As can be inferred from Fig. 1, low-energy cLFV dedicated facilities offer much better prospects to probe lepton flavour violation in the $\mu - e$ sector of the "3+1 model" than a high-luminosity Z-factory. In particular, Mu3e (PSI) [22] and COMET (J-PARC) [23] will be sensitive to regions in parameter space associated with $\mathrm{BR}(Z \to e\mu) \sim 10^{-17 \div -13}$, beyond the reach of FCC-ee. Interestingly, the situation is reversed for the case of the $\mu - \tau$ sector. Moreover, a non negligible subset of the parameter space is testable at a third type of facilities, through

$0\nu2\beta$ decay searches (especially in the case of an IH light neutrino spectrum, although we have not displayed it here).

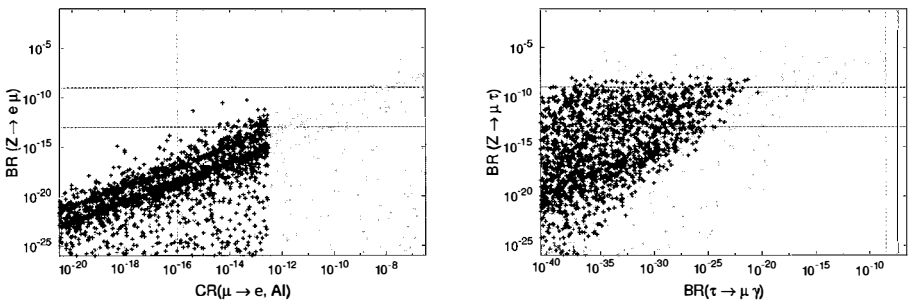

Figure 1 – The "3+1 model": on the left, BR($Z \to e\mu$) versus CR($\mu - e$, Al), and BR($Z \to \mu\tau$) vs BR($\tau \to \mu\gamma$) on the right, for a NH light neutrino spectrum (IH leads to similar results). See text for the description of the color code. When present, the additional green vertical lines denote the current bounds (solid) and future sensitivity (dashed), and dark-yellow points denote an associated $|m_{ee}|$ within experimental reach.

cLFV Z decays in the ISS

We show the results for this well motivated framework of neutrino mass generation in Fig. 2. On the left, we show the BR($Z \to \mu\tau$) as a function of the average of the absolute masses of the mostly sterile states, $\langle m_{4-9}\rangle = \sum_{i=4...9} \frac{1}{6}|m_i|$ (same color code as in Fig. 1). These results indicate that this ISS realisation can account for sizeable values of cLFV Z-decay branching ratios, at least for the second and third generations of leptons. This in general requires sterile states with a mass $\gtrsim \Lambda_{\rm EW}$, and can occur even for very mild deviations from unitarity of the $\tilde{U}_{\rm PMNS}$. Other cLFV decays, $Z \to e\mu$ and $Z \to e\tau$ have BRs $\lesssim \mathcal{O}(10^{-11})$, but still within experimental sensitivity. The prospects for the observation of cLFV Z decays in this framework are summarised in the right plot of Fig. 1 by considering the values of BR($Z \to \ell_1^{\mp}\ell_2^{\pm}$) in the $(\tilde{\eta}, \langle m_{4-9}\rangle)$ parameter space of this specific realisation and for a NH light neutrino spectrum. We denote the values of the BRs from larger (dark blue) to smaller (orange); cyan denotes values of the branching fractions below 10^{-18}. As to the complementarity of low-energy cLFV observables and cLFV Z decays at a high-luminosity Z factory, the results (which are not shown here) are in agreement with the findings for the "3+1 model". Low-energy experiments - as COMET looking for $\mu - e$ conversion in Al nuclei - are better probes of cLFV in the $\mu - e$ sector of this ISS realisation; on the other hand, a future high-luminosity Z factory has a stronger power to probe lepton flavour violation in the $\mu - \tau$ sector via Z decays.

6 Conclusions

We have considered two extensions of the SM which add to its particle content one or more sterile neutrinos. We have explored indirect searches for these sterile states at a future circular collider like FCC-ee, running close to the Z mass threshold. We have considered the contribution of the sterile states to rare cLFV Z decays in these two classes of models and discussed them taking into account a number of experimental and theoretical constraints. Among these, low-energy LFV observables like cLFV 3-body decays and $\mu - e$ conversion in nuclei impose strong constraints on the sterile neutrino induced BR($Z \to \ell_1^{\mp}\ell_2^{\pm}$). Our analysis emphasises the underlying synergy between a high-luminosity Z factory and dedicated low-energy facilities: regions of the parameter space of both models can be probed via LFV Z decays at FCC-ee, at low-energy cLFV dedicated facilities and also via searches for $0\nu2\beta$. Notably, FCC-ee could better probe LFV in the $\mu - \tau$ sector, in complementarity to the reach of low-energy experiments like COMET.

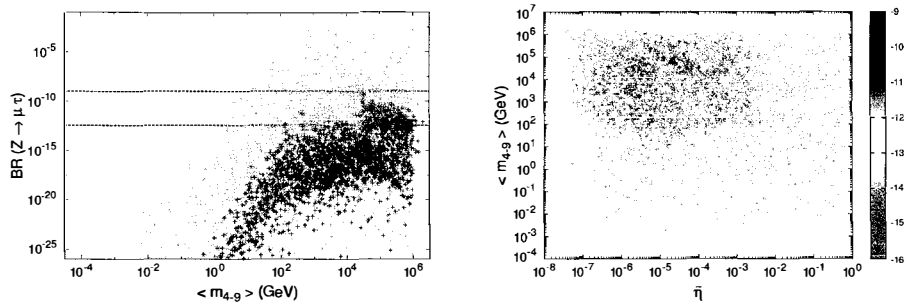

Figure 2 – ISS realisation: BR($Z \to \mu\tau$) as a function of the average value of the mostly sterile state masses (right), $\langle m_{4-9} \rangle$, for a NH light neutrino spectrum (left); maximal values (in log scale) of BR($Z \to \ell_1^{\mp} \ell_2^{\pm}$) on the ($\bar{\eta}$, $\langle m_{4-9} \rangle$) parameter space (right) for a NH light neutrino spectrum, from larger (dark blue) to smaller (orange) values. Cyan denotes values of the branching fractions below 10^{-18}.

Acknowledgments

VDR is grateful to the organisers of the Moriond 2015 EW session for the invitation and for the financial support. The research of VDR is supported by the European Union FP7 ITN INVISIBLES (Marie Curie Actions, PITN-GA-2011-289442).

References

1. K. N. Abazajian *et al.*, arXiv:1204.5379 [hep-ph].
2. A. Kusenko, Phys. Rept. **481** (2009) 1 [arXiv:0906.2968 [hep-ph]].
3. M. Bicer *et al.*, JHEP **1401** (2014) 164 [arXiv:1308.6176 [hep-ex]].
4. A. Abada, V. De Romeri, S. Monteil, J. Orloff and A. M. Teixeira, JHEP **1504** (2015) 051 [arXiv:1412.6322 [hep-ph]].
5. S. L. Glashow *et al.*, Phys. Rev. D **2** (1970) 1285.
6. G. Mann and T. Riemann, Annalen Phys. **40** (1984) 334.
7. J. I. Illana *et al.*, in *2nd ECFA/DESY Study 1998-2001*, 490-524 [hep-ph/0001273].
8. J. I. Illana and T. Riemann, Phys. Rev. D **63** (2001) 053004 [hep-ph/0010193].
9. A. Ilakovac and A. Pilaftsis, Nucl. Phys. B **437** (1995) 491 [hep-ph/9403398].
10. M. A. Perez *et al.*, Int. J. Mod. Phys. A **19** (2004) 159 [hep-ph/0305227].
11. A. Flores-Tlalpa *et al.*, Phys. Rev. D **65** (2002) 073010 [hep-ph/0112065].
12. D. Delepine and F. Vissani, Phys. Lett. B **522** (2001) 95 [hep-ph/0106287].
13. S. Davidson, S. Lacroix and P. Verdier, JHEP **1209** (2012) 092 [arXiv:1207.4894 [hep-ph]].
14. R. N. Mohapatra and J. W. F. Valle, Phys. Rev. D **34** (1986) 1642.
15. M. C. Gonzalez-Garcia and J. W. F. Valle, Phys. Lett. B **216** (1989) 360.
16. E. Fernandez-Martinez *et al.*, Phys. Lett. B **649** (2007) 427 [hep-ph/0703098].
17. J. Schechter and J. W. F. Valle, Phys. Rev. D **22** (1980) 2227.
18. M. Gronau, C. N. Leung and J. L. Rosner, Phys. Rev. D **29** (1984) 2539.
19. D. V. Forero, M. Tortola and J. W. F. Valle, Phys. Rev. D **90** (2014) 093006 [arXiv:1405.7540 [hep-ph]].
20. S. Antusch, J. P. Baumann and E. Fernandez-Martinez, Nucl. Phys. B **810** (2009) 369 [arXiv:0807.1003 [hep-ph]].
21. S. Antusch and O. Fischer, JHEP **1410** (2014) 94 [arXiv:1407.6607 [hep-ph]].
22. A. Blondel *et al.*, arXiv:1301.6113 [physics.ins-det].
23. Y. Kuno [COMET Collaboration], PTEP **2013** (2013) 022C01.

Recent results from the XENON100 experiment

G. Bruno (on behalf of the XENON collaboration)
Institut für Kernphysik, Wilhelms-Universität Münster, 48149 Münster, Germany

A direct approach to the dark matter detection is to measure the nuclear recoils produced in the scattering of DM particles off the nuclei of target materials in detectors placed deep underground.
The XENON100 experiment is the second phase of the XENON program, it consists of a double phase xenon-filled time projection chamber deployed at the Laboratori Nazionali del Gran Sasso.
The experiment set one of the most stringent limits on the WIMP-nucleon spin-independent cross section (2×10^{-45} cm^2 for a 55 Gev/c^2 WIMP mass at 90% CL). The experiment also demonstrated so far the best upper limit on the spin dependent WIMP-nucleon cross section for WIMP masses above 6 GeV, with a minimum cross section of 3.5×10^{-40} cm^2 for a 45 Gev/c^2 WIMP mass at 90% CL.
XENON100 also excludes, at 90% CL, solar axion coupling to electrons at $g_{Ae} > 7.7 \times 10^{-12}$ for a mass of $m_{Axion} < 1$ keV/c^2 and axion-like particles couplings by $g_{Ae} > 1 \times 10^{-12}$ in the $m_{Axion} = 5 - 10$ keV/c^2 mass range.
Here the results from 225 live days of data taken from March 2011 to April 2012 will be presented. We also report on the status of XENON1T, the first tonne-scale direct WIMP search experiment. XENON1T, currently under commissioning, is expected to start collecting a first science data in late 2015.

1 Introduction

One of the most remarkable cosmological puzzle is that we still don't know what the primary constituent of the Universe is. An increasing number of astronomical and astrophysical observations unambiguously indicate that the Universe is composed of more than 96% of invisible matter and energy, pointing to the existence of an unknown form of matter. Some of the most popular theories suggest that it should be non luminous, non baryonic and non relativistic (i.e. cold), therefore called Cold Dark Matter (CDM) [1].
Among the most plausible candidates for CDM there are Weakly Interaction Massive Particles (WIMPs). They are stable particles in thermal equilibrium in the early Universe, resulted from the extension of the standard model of electroweak interaction in the Supersymmetry theory (SUSY), in which each standard particle has a super-partner with the same quantum numbers except for the spin, which differs by 1/2 from its partner particle.

In SUSY, one favorite WIMP candidate is the neutralino, the lightest supersymmetric particle. Dark matter (DM) doesn't interact electromagnetycally or strongly, however it is a quite well motivated assumption that has, in addition to gravity, also weak interaction with normal matter. If this is the case, DM particles can be detected directly by experiment using existing technologies. If WIMPs exist, they are also the dominant mass in our own [2] Milky Way, and though they only very rarely interact with conventional matter, they should nonethless be detectable by sufficiently sensitive detectors on the Earth. In XENON100, one attempts to observe the nuclear recoils (NRs) produced by WIMP scattering off xenon nucleons.

2 The XENON100 experiment

XENON100 was built to search for WIMPs and is installed underground at the Laboratori Nazionali del Gran Sasso (LNGS), Italy, below an average 3600 m water equivalent rock overburden, which reduces the muon flux by a factor $\sim 10^6$. The XENON100 detector is filled with a total of 161 kg of ultra pure liquid xenon (LXe), divided in two optically separated volumes[3]. The inner target volume is a dual phase time-projection chamber (TPC) of 30.5 cm height and 15.3 cm radius containing 62 kg of xenon, the outer volume is operated as an active veto for an efficient suppression of external radioactive background.
The whole volume is viewed by a total of 242 squared (1" $\times$ 1") low radioactivity photomultiplier tubes (PMTs) Hamamatsu R8520-06-Al, especially developed to be operational at the LXe temperature for the characteristic xenon scintillation wavelength (λ=178 nm).
The electric field required for the operation of the TPC is provided by a cathode mesh on the bottom and by a gate and an anode mesh on the top. Forty field shaping rings, regularly spaced along the TPC wall, ensure the homogeneity of the field.
Both TPC and veto are mounted in a double-walled stainless-stell cryostat, enclosed by a multilayer passive shield. Moreover the shield is continuously purged with boil-off N_2 gas in order to suppress radon background.
A particle interaction in the LXe target creates both excited and ionized atoms. De-excitation leads to a prompt scintillation signal (S1), which is recorded by PMTs placed below the target in the LXe and above in the gas phase. Due to the presence of an electric field of 0.53 kV/cm, a large fraction of the ionization electrons is drifted away from the interaction and extracted from the liquid into the gas phase by a strong extraction field of $\sim$12 kV/cm, generating a light signal (S2) by proportional scintillation in the gas. Since the electron drift velocity in LXe is constant for a given field ($\sim$1.74 mm/μs at 0.53 kV/cm), the time distance between S1 and S2 gives the information of the position of the interaction vertex in the vertical axis. The hit pattern on the PMTs in the gas phase is used to reconstruct the position in the horizontal plane. Three different methods are used to reconstruct the XY position, based on χ^2 minimization, neural network and support vector machine algorithms. In this way a 3-dimensional event position is available. This property allows the definition of an ultra-low-background fiducial volume inside the target. Moreover, the ratio S2/S1 is different for electronic recoil events from interaction with the atomic electrons (from γ and β), and for interactions with the nucleus itself (from WIMPs or neutrons), and is it used to further discriminate the signal against background.

3 The analysis

The XENON100 data presented here, includes 224.6 live days and 34 kg fiducial mass, collected between March 2011 and April 2012. Compared to the previous data set, this science run has a longer exposure, a significantly lower intrinsic ^{85}Kr contamination, a reduced electronic noise and a lower trigger threshold. Calibrations were done regularly during the science run with various radioactive sources. ^{137}Cs is used to estimate the electron lifetime[3] in liquid xenon. The electronic recoil (ER) background is determined from the ^{232}Th and ^{60}Co sources. A neutron

source (^{241}AmBe) is used to determine the nuclear recoil (NR) response of the detector [4].
A profile likelihood (PL) approach is used to test the background-only and signal hypothesis[5]. The systematic uncertainties in the energy scale and in the background expectation are profiled out and represented in the limit. Poisson fluctuations in the number of photoelectrons (PEs) dominate the S1 energy resolution and are also taken into account along with the single PE energy resolution of the PMTs.

3.1 WIMPs search

For the signal model, we assume an isothermal halo with a local density of 0.3 GeV/cm^3, a local circular velocity of 220 km/s, and a Galactic escape velocity of 544 km/s. WIMPs interactions can be described in terms of scalar (spin-independent, SI) and axial-vector (spin-dependent, SD) couplings. If the WIMP is a spin-1/2 or a spin-1 field, the contributions to the WIMP-nucleus scattering arise from couplings of the WIMP field to the quark axial current and will couple to the total angular momentum of a nucleus. Only nuclei with an odd number of protons or/and neutrons will yield a significant sensitivity to this channel. Natural xenon contains two nonzero spin isotopes, ^{129}Xe (spin-1/2) and ^{131}Xe (spin-3/2), with an abundance of 26.4% and 21.2%, respectively.
The 90% CL exclusion on spin-independent WIMP-nucleon cross section can be seen in Fig. 1 [24]. The constraints on the SD WIMP-nucleon cross section were derived as shown in Fig.2 [25].

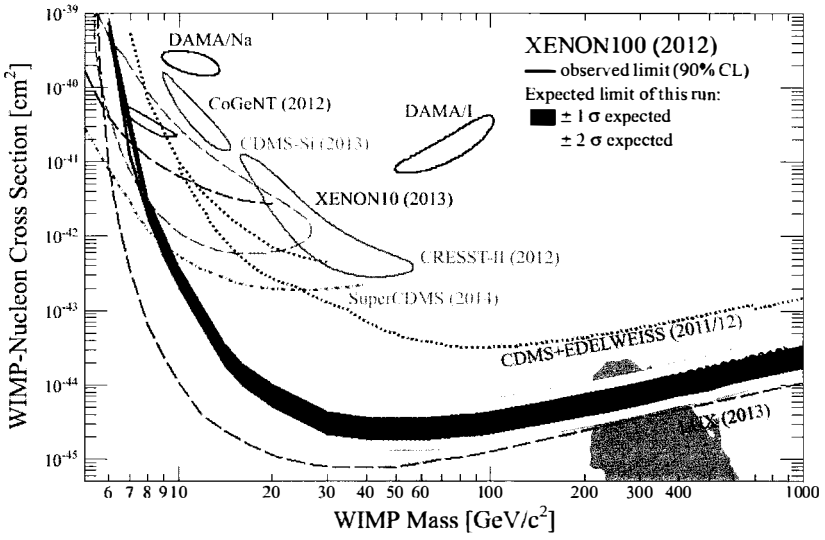

Figure 1 – Results on spin-independent WIMP-nucleon scattering from XENON100. The measured limit is shown by the solid blue line. Other experimental limits and detection claims are also shown for comparison[24].

XENON100 was able to exclude WIMP-neutron cross section down to 3.5 $\times$ 10^{-40} cm^2 for a WIMP mass of 45 GeV/c^2 setting the most stringent limit to date on the WIMP-neutron SD couplings for WIMP masses above 6 GeV/c^2.

3.2 Solar axions and ALPs

Axions were introduced by Peccei and Quinn to solve the strong CP problem as pseudo-Nambu-Goldstone bosons emerging from the breaking of a global U(1) symmetry [6,7,8]. Altough this original model has been ruled out, "invisible" axions arising from higher symmetry-breaking

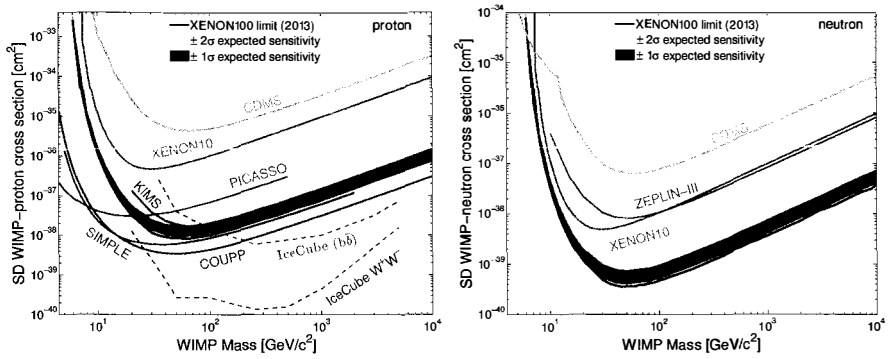

Figure 2 – XENON100 90% CL upper limits on the WIMP SD cross section on proton (left panel) and neutron (right panel). Other experimental limits are also shown for comparison[25].

energy scale are still allowed, as described, for example, in the DFSZ and KSVZ models[9,10,11,12]. In addition to QCD axions, axion-like-particles (ALPs) are pseudoscalars that do not necessarily solve the strong CP problem, but that were introduced by many extensions of the Standard Model of particle physics.

Solar axions are postulated to be produced in the Sun via Bremsstrahlung, Compton scattering, atomic recombination and atomic de-excitation.

Axions and ALPs are another class of well motivated cold dark matter candidates [13] which interact predominantly with atomic electrons in the medium and can couple to photons, electrons and nuclei. The coupling to electrons, g_{Ae}, can be tested through the axio-electric effect, which is analogous to the photoelectric effect, but with an axion/ALP playing the role of the photon: the axion ionizes an atom and it is absorbed, extracting an electron. Therefore axions and ALPs can scatter off electrons of the LXe target, and so they can be searched for in XENON100 by looking at the ER events.

The first axion searches performed with the XENON100 experiment are reported in [14].

The expected interaction rate is obtained by the convolution of the flux and the axio-electric cross section. The latter is given, both for QCD axions and ALPs, by [15,16,17,18,19]:

$$\sigma_{Ae} = \sigma_{pe}(E_A)\frac{g_{Ae}^2}{\beta_A}\frac{3E_A^2}{16\pi\alpha_{em}m_e^2}\left(1-\frac{\beta_A^{2/3}}{3}\right)$$

where σ_{pe} is the photoelectric cross section for LXe[20], E_A is the axion energy, α_{em} is the fine structure constant, m_e is the electron mass, and β_A is the axion velocity over the speed of light, c.

For solar axions, both flux (taken from [21]) and cross section depend upon g_{Ae}^2, thus the interaction rate scales with the fourth power of the coupling. For the ALPs, assuming that they constitute the whole dark matter halo density ($\rho_{DM} \sim 0.3\ GeV/cm^3$ [22]), the total flux is given by $\phi_{ALP} = c\beta_A \times \rho_{DM}/m_A$, where m_A is the ALP mass. The interaction rate for these ALPs depends on g_{Ae}^2, as the flux is independent from the axion coupling. As $\beta_A \approx 10^{-3}$ in the non-relativistic regime, the velocities cancel out in the convolution between σ_{Ae} and the flux. Thus the expected recoil spectrum is indpendent from the particle speed and a monoenergetic peak at the axion mass is expected.

The expected S1 spectrum for solar axions, lighter than 1 keV/c^2, is shown in fig. 3, left panel, as a blue dashed line for $g_{Ae} = 2 \times 10^{-11}$, which is the best limit so far, reported by the EDELWEISS-II collaboration [23]. Also shown in fig. 3, right panel, is the expected signal for different ALP masses, assuming a coupling constant of $g_{Ae} = 4 \times 10^{-12}$ and that ALPs constitute

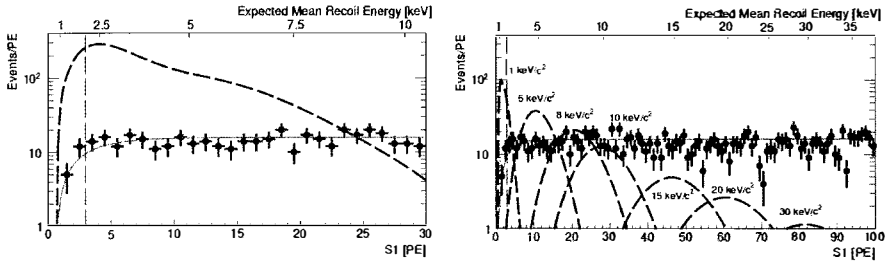

Figure 3 – Left panel: event distribution of the data (black dots), and background model (grey) of the solar axion search. The expected signal for solar axions with m_A <1 keV/c^2 is shown by the dashed blue line. Right panel: black dots represent the event distribution in the galactic ALPs search region between 3 and 100 PE. The grey line shows the background model used for the profile likelihood function.The expected signal in XENON100 for various ALP masses, assuming $g_{Ae} = 4 \times 10^{-12}$, is shown as blue lines[14].

all of the galactic dark matter. For both the solar axion search and the ALPs search, the data

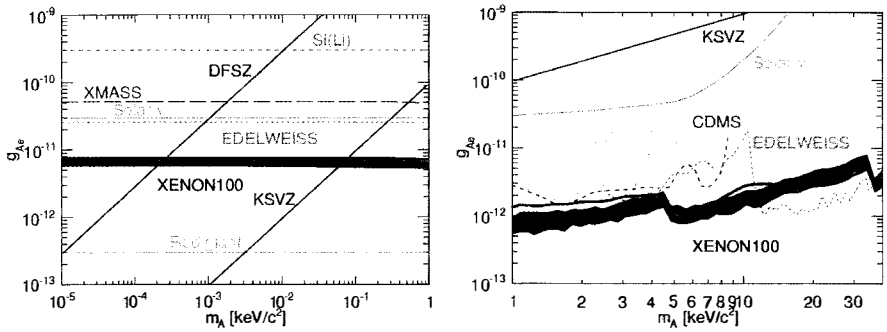

Figure 4 – The XENON100 90% limit on the solar axions and on galactic ALPs are shown in the left and right panel, respectively. Other experimental constraints, astrophysical bounds and theoretical benchmark models are also represented[14].

is compatible with the background model, and no excess is observed for the background-only hypothesis.

The left panel of fig. 4 shows the new XENON100 90% exclusion limit on the solar axions coupling to electrons, at 90% CL. The sensitivity is shown by the green/yellow band ($1\sigma/2\sigma$). For comparison, we also present recent experimental constraints. Astrophysical bounds and theoretical benchmark models are also shown. For solar axions with masses below 1 keV/c^2, XENON100 is able to set the strongest constraint on the coupling to electrons, excluding values of g_{Ae} larger than 7.7×10^{-12} (90% CL).

The right panel of fig. 4 shows the XENON100 90% CL exclusion limit on ALP coupling to electrons as a function of the mass. In the 5-10 keV/c^2 mass range, XENON100 sets the best upper limit, excluding an axio-electron coupling $g_{Ae} > 1 \times 10^{-12}$ at the 90% CL, assuming that ALPs constitute all of the galactic dark matter.

4 XENON1T

The XENON1T detector is a scaled-up design of the succesful XENON100 one: it is a dual-phase LXe TPC of about 1 m height and about 1 m diameter, containing 3.3 tons (~2.2 tons

active volume) of high-purity liquid xenon, instrumented from both above and below with low-radioactivity PMTs and kept under a uniform electric field of about 1.0 kV/cm.
The goal is to reduce the background by a factor of ~100 compared to the one of XENON100. This will be achieved by using a Čerenkov muon-veto, an improved material screening and selection and by reducing the intrinsic ^{85}Kr and radon using dedicated devices. XENON1T detector will be instrumente with 248 3" Hamamatsu model R11410-21 PMTs made of extremely low radioactivity materials.
With realistic assumptions on the detector performance and anlysis efficiency, the maximal sensitivity to spin-independent WIMP-nucleon cross sections will be reached by 2017 and is expected to be 2×10^{-47} cm^2 at a WIMP mass around 40 Gev/c^2.

5 Beyond XENON1T

While XENON100 is still running, the XENON1T detector, installed in the Hall B of the LNGS, is currently under commissioning.
With a design sensitivity two orders of magnitude better than XENON100, over a broad range of WIMP masses and interaction types, this first LXe TPC experiment at the tonne-scale will have significant discovery potential. In designing the experiment, we have foreseen the possibility for a scale-up by a factor of ~2 of the target mass, changing the inner vessel and the TPC, but re-using most of the other subsystems and infrastructures built for XENON1T. The goal is another factor 10 improvement in sensitivity by 2020.

References

1. G. Jungman, M. Kamionkowski, and K. Gries, *Phys. Rep.* **267**, 195 (1996)
2. M.R. Merriefield, *Astronom. J.* **103**, 1552 (1992)
3. E. Aprile *et al.* (XENON100 Collaboration), *Astropart. Phys* **35**, 573 (2012)
4. E. Aprile *et al.* (XENON100 Collaboration), *Phys. Rev. D* **88**, 012006 (2013)
5. E. Aprile *et al.* (XENON100 Collaboration), *Astropart. Phys* **54**, 11-24 (2014)
6. R.D. Peccei and H.R. Quinn, *Phys. Rev. Lett.* **38**, 1440 (1977)
7. S. Weinberg, *Phys. Rev. Lett.* **40**, 223 (1978)
8. F. Wilczeck, *Phys. Rev. Lett.* **40**, 279 (1978)
9. M. Dine, W. Fischeler, and M. Srednicki, *Phys. Lett. B* **104**, 199 (1981)
10. A.R. Zhitnitsky, *Sov. J. Nucl. Phys.* **31**, 260 (1980)
11. J.E. Kin, *Phys. Rev. Lett.* **43**, 103 (1979)
12. M.A. Shifman, A.I. Vainshtein and V.I. Zakharov, *Nucl. Phys. B* **166**, 493 (1980)
13. L. Abbott and P. Sikivie, *Phys. Lett. B* **120**, 133 (1983)
14. E. Aprile *et al* (XENON100 Collaboration), *Phys. Rev. D* **90**, 062009 (2014)
15. F.T. Avignone *et al.*, *Phys. Rev. D* **35**, 2752 (1987)
16. M. Pospelov, A. Ritz, and M. Voloshin, *Phys. Rev. D* **78**, 115012 (2008)
17. A. Derevianko *et al.*, *Phys. Rev. D* **82**, 065006 (2010)
18. K. Ariska *et al.*, *Astropart. Phys.* **44**, 59 (2013)
19. F. Alessandria *et al.* (CUORE Collaboration), *JCAP* **1305**, 007 (2013)
20. NIST, URL `http://physics.nist.gov/PhysRefData/Xcom/html/xcom1.html`
21. J. Redondo, *JCAP* **1312** (2013) 008
22. A. M. Green, *Mod. Phys. Lett.* **A27**, 1230004 (2012)
23. E. Armengaud *et al.* (EDELWEISS-II Coll.), *JCAP* **1311**, 067 (2013)
24. E. Aprile *et al.* (XENON100 Collaboration), *Phys. Rev. Lett.* **109**, 181301 (2012)
25. E. Aprile *et al.* (XENON100 Collaboration), *Phys. Rev. Lett.* **111**, 021301 (2013)

Dark matter at the LHC

Ulrich Haisch
Department of Physics, Theoretical Physics, 1 Keble Road, Oxford OX1 3NP, England

I briefly discuss recent theoretical advances in the description of mono-X signals at the LHC.

1 Introduction

The existence of dark matter (DM) provides the strongest evidence for physics beyond the standard model (SM). DM has been probed using particle colliders, direct detection underground experiments and indirect detection in space telescopes. Despite these intensive searches it has so far proven elusive. We thus must be thorough and creative as we continue the important mission to search for DM. In the coming years, direct and indirect detection experiments will reach new sensitivities, and the LHC will begin operation at 13 TeV after a very successful (7) 8 TeV run. Taken together these strategies will provide crucial tests of our ideas about the dark sector, and have great potential to revolutionise our understanding of the nature of DM.

2 Precision mono-jet predictions

The minimal experimental signature of DM production at the LHC would be an excess of events with a single final-state object X recoiling against large amounts of missing transverse momentum or energy ($E_{T,\text{miss}}$). In Run I of the LHC, the ATLAS and CMS collaborations have examined a variety of such mono-X signatures involving jets of hadrons, gauge bosons, top and bottom quarks as well as the Higgs boson in the final state.[1,2] Unfortunately, the SM backgrounds in these searches are large and the $E_{T,\text{miss}}$ spectrum of the signal is essentially featureless although it is slightly harder than that of the SM background. This feature is illustrated on the left in Fig. 1. Systematical uncertainties were already a limiting factor at Run I, and will become even more relevant at Run II. A combination of experimental and theoretical efforts is therefore needed to improve the reach of future searches.

From the theoretical side, this requires calculating both background and signal predictions accurately. In the case of mono-jet searches, the dominant backgrounds, resulting from the production of SM vector bosons in association with a jet, have been known to next-to-leading order (NLO) for a long time.[3,4] More recently, attention has been paid to the importance of NLO corrections for the signal process.[5] These calculations have been implemented into the Monte Carlo program `MCFM`.[6] Ideally, the LHC collaborations should be able to use an NLO implementation of the expected DM signal in order to optimise their cuts in such a way that backgrounds are reduced and uncertainties are minimised. For this purpose, a parton-level implementation is insufficient, because a full event simulation including showering and hadronisation is required. This can be achieved using a NLOPS method, i.e. an approach that allows

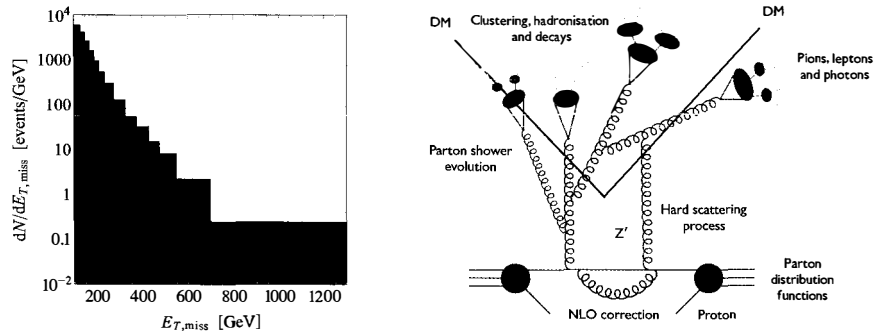

Figure 1 – Left: Comparison between the $E_{T,\mathrm{miss}}$ spectrum of a mono-jet signal arising from DM-pair production (green) and the leading SM background due to $pp \to j + Z(\to \nu\bar{\nu})$ (red). Separating the small numbers of signal events from the background requires to perform "tail surgery" at large values of $E_{T,\mathrm{miss}}$. Right: Schematic diagram of all the ingredients that enter a NLOPS mono-jet prediction. The propagator labelled Z' indicates a spin-1 resonance that mediates the interactions between the SM quarks and DM.

to match consistently a NLO computation with a parton shower (PS). Utilising the POWHEG method,[7,8] a NLOPS calculation, which permits the automatic generation of mono-jet events in spin-0 and spin-1 simplified models with s-channel exchange, has been performed and is now publicly available.[9] A pictorial representation of all the ingredients needed to achieve NLOPS accuracy is shown on the right-hand side in Fig. 1.

For the cuts used by ATLAS[11] and CMS[10] in their latest analyses, one finds that the mono-jet cross sections at NLOPS are always very similar to the leading order plus PS (LOPS) cross sections,[9] which have been used in Run I to set bounds on the couplings of DM to quarks and gluons. In the case of a vector mediator this feature is illustrated in the left panel of Fig. 2. To understand the smallness of higher-order QCD effects, we show on the right-hand side of the same figure the fraction of events of the total jets + $E_{T,\mathrm{miss}}$ cross section with exactly 1, 2, 3 and 4 or more jets, employing CMS cuts.[10] One observes that — in spite of the name "mono-jet search" — only 35% of the events contain a single jet, while 65% of the cross section is due to events with 2 or more jets. The large importance of secondary jets, which are not vetoed in all recent LHC mono-jet analyses, reduces the impact of the fixed-order NLO corrections to the $j + E_{T,\mathrm{miss}}$ channel. In turn, the resulting NLOPS bounds are not significantly stronger than those obtained at LOPS, but more reliable, since the NLO corrections reduce the factorisation and renormalisation scale uncertainties of the signal prediction.[5,9]

3 Spin-0 s-channel DM models

As we have seen, for spin-1 interactions between DM and the SM, loop corrections do not play an important role, and one may ask if this is a generic feature. The answer is no, because in simplified spin-0 s-channel models with Higgs-like couplings, the tree-level $j + E_{T,\mathrm{miss}}$ cross section is small as the heavy-quark luminosities are tiny and the contributions from light quarks are strongly Yukawa suppressed. At the 1-loop level top-quark loops start to contribute to the mono-jet cross section and are expected to lift the Yukawa suppression. A relevant diagram is shown on the right in Fig. 3. In fact, including loop contributions in the spin-0 case, increases the cross section for mono-jet production compared to the tree-level prediction by a factor of around 500 (900) for scalar (pseudoscalar) interactions.[12] It is straightforward to translate the constraints arising from mono-jet searches into bounds on the elastic DM-nucleon scattering cross

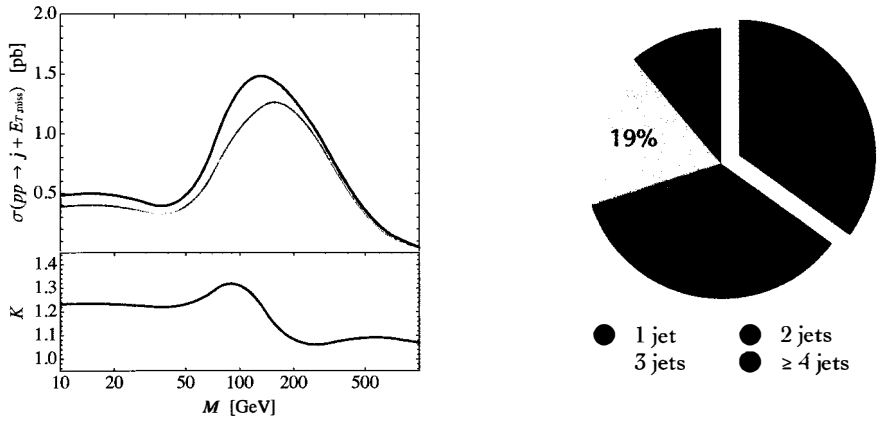

Figure 2 – Left: NLOPS (purple curve and band) and LOPS (orange curve and band) mono-jet cross sections as a function of the vector mediator mass M employing CMS cuts.[10] The resulting K factor, i.e. the ratio between the NLOPS and LOPS cross section, is also given. The shown predictions assume a Dirac DM mass $m_\chi = 50\,\mathrm{GeV}$ and a total decay width $\Gamma_V = M/3$ of the mediator. Right: Fractions of events with exactly 1, 2, 3 and 4 or more jets relative to the total jets + $E_{T,\mathrm{miss}}$ cross section. All numbers correspond to vector interactions, CMS cuts and $m_\chi = 10\,\mathrm{GeV}$.

section. For scalar interactions and Dirac DM, the outcome of such an exercise is presented in the left panel of Fig. 3. From the figure it is evident that for large DM masses, direct detection experiments give stronger bounds than the mono-jet searches. For $m_\chi \simeq 10\,\mathrm{GeV}$ however, the constraints become comparable, while below this value the bounds from LHC searches are superior. One also sees that the inclusion of 1-loop corrections gives a pertinent improvement of the mono-jet limits, because it excludes the possibility that the DAMA modulation[13] or the CoGeNT excess[14] arise from the interactions of a heavy scalar mediator.

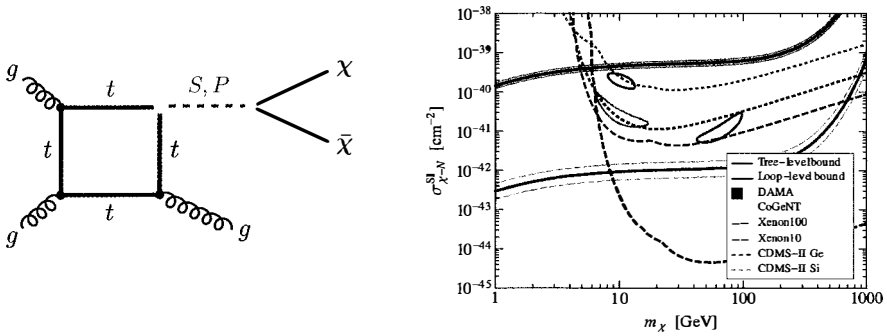

Figure 3 – Left: A typical loop-level diagram with virtual top-quark exchange that leads to mono-jet events. The mediator can be both a scalar (S) or pseudoscalar (P) resonance. Right: LHC mono-jet bounds on the spin-independent (SI) DM-nucleon cross section $\sigma^{\mathrm{SI}}_{\chi-N}$ as a function of the DM mass m_χ for scalar interactions. While the tree-level mono-jet bound (red curve and band) is too weak to constrain the parameter regions favoured by DAMA and CoGeNT, the loop-level bound (green curve and band) clearly excludes these regions.

A second way to probe spin-0 interactions between DM and top quarks relies on detecting the top-quark decay products that arise from the tree-level reaction $t\bar{t} + E_{T,\mathrm{miss}}$.[2,15,16,17,18,19,20,21,22] Since the channels $j + E_{T,\mathrm{miss}}$ and $t\bar{t} + E_{T,\mathrm{miss}}$ test the same interactions, an obvious question

to ask is, which search sets stronger constraints after Run I, and to compare their reach at future stages of LHC operation. By scanning the full 4-dimensional parameter space of the simplified spin-0 models, it has been shown that for both the scalar and the pseudoscalar case the current ATLAS and CMS searches cannot exclude parameters arising from purely weakly-coupled theories.[23] The scan in addition revealed that the $j + E_{T,\text{miss}}$ searches in general exclude more parameter space than the $t\bar{t} + E_{T,\text{miss}}$ searches. These features are illustrated in the two panels of Fig. 4. At the 14 TeV LHC, one finds that the shapes of the exclusion contours remain qualitatively the same, but that the bounds that one should be able to set will improve notable compared to the limits obtained at 8 TeV. Still in the initial stages of data taking only model realisations in which the mediators have masses not too far above the weak scale ($M_{S,P} < 1$ TeV) and couple strong enough to the SM ($g^{S,P}_{\text{SM}} > 1$) can be explored.[23] Since for realistic cuts the fiducial $pp \to \bar{t}t\,(\to jbl\nu) + E_{T,\text{miss}}$ cross section is much smaller than that of $pp \to j + E_{T,\text{miss}}$, the $t\bar{t} + E_{T,\text{miss}}$ channel will only become competitive to the mono-jet signature at the phase-1 and phase-2 LHC upgrades. Realising that the existing $t\bar{t} + E_{T,\text{miss}}$ analyses are all recasts of top-squark searches, the LHC reach might however be improved further by trying to optimise these searches to the specific topology of the $t\bar{t} + E_{T,\text{miss}}$ signature arising in simplified scalar and pseudoscalar models.

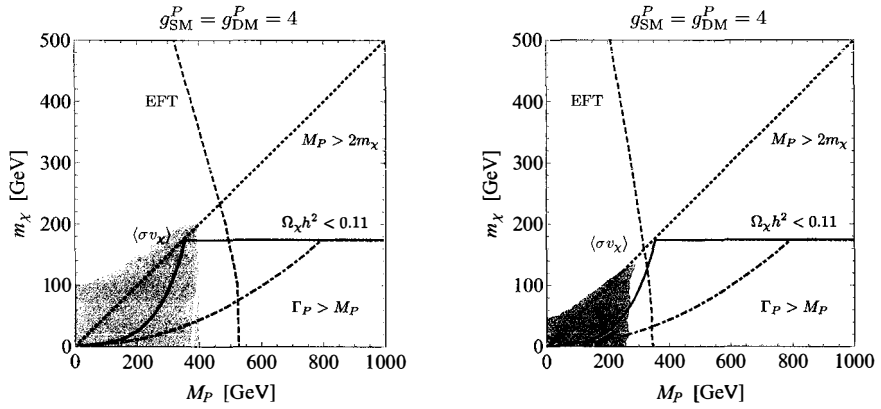

Figure 4 – Exclusion contours at 95% confidence level (CL) for pseudoscalar mediators following from Run I data on $j + E_{T,\text{miss}}$ (red region in left panel) and $t\bar{t}\,(\to jbl\nu) + E_{T,\text{miss}}$ (green region in right panel). The couplings have been fixed to $g^P_{\text{SM}} = g^P_{\text{DM}} = 4$. The regions with $\Gamma_P > M_P$ (brown contours), the parameter spaces with $\Omega_\chi h^2 < 0.11$ (dot-dashed purple curves), the effective field theory (EFT) limits (dashed red and green curve) and the regions with $M_P > 2m_\chi$ (dotted black lines) are also shown. The present Fermi-LAT 95% CL limit[24] on the total velocity-averaged DM annihilation cross section $\langle\sigma v_\chi\rangle$ is indicated by the solid blue curves.

4 Angular correlations in DM production

While the existing $E_{T,\text{miss}}$ searches are well suited to discover DM, they are unlike to provide enough information to determine further DM properties. For instance, with the existing cut-and-count $j + E_{T,\text{miss}}$ searches it is impossible to distinguish a $E_{T,\text{miss}}$ signal associated to spin-1 vector (V) mediator production from one where a axialvector (A) resonance furnishes the DM-SM portal by comparing the $E_{T,\text{miss}}$ spectrum of the two different interactions. In fact, from the left panel of Fig. 5, one sees that within theoretical uncertainties the predictions for $pp \to j + V\,(\to \chi\bar{\chi})$ and $pp \to j + A\,(\to \chi\bar{\chi})$ cannot be told apart.

Some of these limitations can however be overcome by studying two-particle (or multi-particle) correlations in processes involving $E_{T,\text{miss}}$.[25,26,27] In the case of a mono-jet signal, a

sensitive probe of the Lorentz structure of the DM-SM interactions is provided by the jet-jet azimuthal angle difference $\Delta\phi_{j_1 j_2}$ in $2j+E_{T,\text{miss}}$ events.[26] The same observable can be used to test the structure of couplings between pairs of DM particles and gauge bosons.[25,27] To demonstrate the power of angular correlations in characterising the portal couplings, the normalised $\Delta\phi_{j_1 j_2}$ spectra for two dimension-7 operators with different CP properties is depicted on the right-hand side in Fig. 5. The sine-like (cosine-like) behaviour of the modulation in the azimuthal angle distribution corresponding to $\bar{\chi}\chi W^i_{\mu\nu} W^{i,\mu\nu}$ ($\bar{\chi}\chi W^i_{\mu\nu}\tilde{W}^{i,\mu\nu}$) — with $W^i_{\mu\nu}$ the $SU(2)_L$ field strength tensor and $\tilde{W}^i_{\mu\nu}$ its dual — is clearly visible in the figure. The SM background is instead close to flat in the angle $\Delta\phi_{j_1 j_2}$. Last but not least, in the case of $t\bar{t}+E_{T,\text{miss}}$ production the pseudorapidity difference $\Delta\eta_{b_1 b_2}$ ($\Delta\eta_{l^+l^-}$) between the two bottom-quark jets (charged leptons) that result from the top-quark decays may be used to disentangle scalar from pseudoscalar interactions.[28] These three examples show that studies of the correlations of the SM final state particles in $E_{T,\text{miss}}$ events offer unique opportunities to probe the DM-SM interactions, making any dedicated effort at LHC Run II in this direction more than welcome.

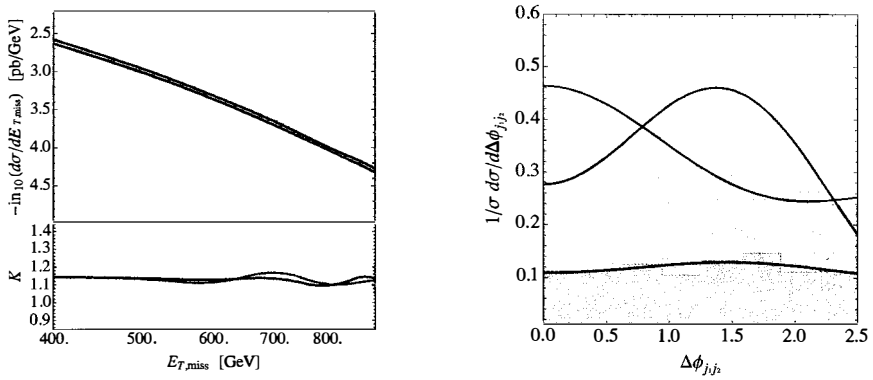

Figure 5 – Left: Comparison of the $E_{T,\text{miss}}$ spectra of a mono-jet signal resulting from vector and axialvector interactions. Overlaid are the LO (blue curves and bands) and NLO (red curves and bands) predictions and the K factor is also shown. Taking into account scale variations the results are clearly indistinguishable. Right: Normalised $\Delta\phi_{j_1 j_2}$ distributions for $300\,\text{fb}^{-1}$ of 14 TeV LHC data, assuming $m_\chi = 100\,\text{GeV}$. The red (blue) histogram shows the signal plus background prediction for the operator $\bar{\chi}\chi W^i_{\mu\nu} W^{i,\mu\nu}$ ($\bar{\chi}\chi W^i_{\mu\nu}\tilde{W}^{i,\mu\nu}$). The grey bar chart represents the expected SM background, which for better visibility, has been rescaled by a factor of 1/3. The solid curves indicate the best fits of the form $a_0 + a_1 \cos\Delta\phi_{j_1 j_2} + a_2 \cos(2\Delta\phi_{j_1 j_2})$.

5 Conclusions

With the start of LHC Run II, collider searches for $E_{T,\text{miss}}$ signatures are soon to explore new territory, and the large statistics expected at the phase-1 and phase-2 upgrades at 14 TeV have the potential to radically change our understanding of DM. New theoretical developments that allow for a better description of both signals and backgrounds have to go along with the experimental advances in order to exploit the full physics potential of the LHC. Harnessing the ideas discussed here may play a key role in this effort.

Acknowledgments

I thank Andreas Crivellin, Anthony Hibbs, Felix Kahlhoefer, Emanuele Re and James Unwin for collaborations on various aspects of DM physics. I am furthermore grateful to the organisers of Moriond Electroweak 2015 for the invitation to a great and very enjoyable conference. The warm hospitality and support of the CERN theory division is also acknowledged.

References

1. C. Dolglioni on behalf of the ATLAS and CMS Collaboration, talk at Moriond Electroweak 2015, https://indico.in2p3.fr/event/10819/session/1/contribution/92/material/slides/0.pdf
2. D. Pinna on behalf of the CMS Collaboration, talk at Moriond Electroweak 2015, arXiv:1505.04100 [hep-ex].
3. W. T. Giele and E. W. N. Glover, Phys. Rev. D **46**, 1980 (1992).
4. U. Baur, T. Han and J. Ohnemus, Phys. Rev. D **57**, 2823 (1998) [hep-ph/9710416].
5. P. J. Fox and C. Williams, Phys. Rev. D **87**, 054030 (2013) [arXiv:1211.6390 [hep-ph]].
6. J. M. Campbell, R. K. Ellis, and C. Williams, http://mcfm.fnal.gov
7. P. Nason, JHEP **0411**, 040 (2004) [hep-ph/0409146].
8. S. Frixione, P. Nason and C. Oleari, JHEP **0711**, 070 (2007) [arXiv:0709.2092 [hep-ph]].
9. U. Haisch, F. Kahlhoefer and E. Re, JHEP **1312**, 007 (2013) [arXiv:1310.4491 [hep-ph]].
10. V. Khachatryan *et al.* [CMS Collaboration], arXiv:1408.3583 [hep-ex].
11. G. Aad *et al.* [ATLAS Collaboration], arXiv:1502.01518 [hep-ex].
12. U. Haisch, F. Kahlhoefer and J. Unwin, JHEP **1307**, 125 (2013) [arXiv:1208.4605 [hep-ph]].
13. R. Bernabei *et al.* [DAMA and LIBRA Collaborations], Eur. Phys. J. C **67**, 39 (2010) [arXiv:1002.1028 [astro-ph.GA]].
14. C. E. Aalseth, P. S. Barbeau, J. Colaresi, J. I. Collar, J. Diaz Leon, J. E. Fast, N. Fields and T. W. Hossbach *et al.*, Phys. Rev. Lett. **107**, 141301 (2011) [arXiv:1106.0650 [astro-ph.CO]].
15. K. Cheung, K. Mawatari, E. Senaha, P. Y. Tseng and T. C. Yuan, JHEP **1010**, 081 (2010) [arXiv:1009.0618 [hep-ph]].
16. T. Lin, E. W. Kolb and L. T. Wang, Phys. Rev. D **88**, 063510 (2013) [arXiv:1303.6638 [hep-ph]].
17. G. Artoni, T. Lin, B. Penning, G. Sciolla and A. Venturini, arXiv:1307.7834 [hep-ex].
18. M. R. Buckley, D. Feld and D. Goncalves, Phys. Rev. D **91**, no. 1, 015017 (2015) [arXiv:1410.6497 [hep-ph]].
19. CMS Collaboration, http://cds.cern.ch/record/1697173/files/B2G-13-004-pas.pdf
20. CMS Collaboration, http://cds.cern.ch/record/1749153/files/B2G-14-004-pas.pdf
21. G. Aad *et al.* [ATLAS Collaboration], Eur. Phys. J. C **75**, no. 2, 92 (2015) [arXiv:1410.4031 [hep-ex]].
22. V. Khachatryan *et al.* [CMS Collaboration], arXiv:1504.03198 [hep-ex].
23. U. Haisch and E. Re, arXiv:1503.00691 [hep-ph].
24. M. Ackermann *et al.* [Fermi-LAT Collaboration], Phys. Rev. D **89**, 042001 (2014) [arXiv:1310.0828 [astro-ph.HE]].
25. R. C. Cotta, J. L. Hewett, M. P. Le and T. G. Rizzo, Phys. Rev. D **88**, 116009 (2013) [arXiv:1210.0525 [hep-ph]].
26. U. Haisch, A. Hibbs and E. Re, Phys. Rev. D **89**, 034009 (2014) [arXiv:1311.7131 [hep-ph]].
27. A. Crivellin, U. Haisch and A. Hibbs, Phys. Rev. D **91**, no. 7, 074028 (2015) [arXiv:1501.00907 [hep-ph]].
28. U. Haisch, talk at DM @ LHC 2014, http://indico.cern.ch/event/312657/session/1/contribution/40/material/slides/0.pdf

DARK MATTER SEARCHES AT ATLAS AND CMS: RUN 1 RESULTS AND RUN 2 POTENTIAL

Caterina Doglioni
Lund University
On behalf of the ATLAS and CMS Collaborations

Despite the recent discovery of the Higgs boson contributing to the success of the Standard Model, the large excess of Dark Matter with respect to ordinary matter in the universe remains one of the outstanding questions in science. This excess cannot be explained by Standard Model particles; a compelling hypothesis is that Dark Matter is comprised of particles that can be produced at the LHC, called Weakly Interacting Massive Particles (WIMPs). This talk presents a number of ATLAS and CMS searches for WIMP Dark Matter, outlining the main theoretical benchmarks and issues in terms of complementarity with Direct and Indirect Detection experiments, and describes the studies on Dark Matter searches for the upcoming LHC run.

1 Introduction

Experimental data from particle colliders is so far consistent with the Standard Model (SM). Despite its success, the Standard Model is neither a complete nor a sufficient description of our universe. Experimental evidence points to a number of shortcomings of the SM, such as the lack of ordinary matter necessary to explain the mass detected through gravitational effects. The missing matter is called Dark Matter.

A wide range of theoretical models attempt to incorporate Dark Matter. Many of these models postulate the presence of a new massive subatomic particle, with only weak interactions with Standard Model particles as a Dark Matter candidate. The presence of these Weakly Interacting Massive Particles (WIMPs) could be inferred by a variety of experimental observations [1] [2].

Direct Detection (DD) experiments rely on the interaction between an incoming Dark Matter particle and target nuclei within the detector; Indirect Detection (ID) experiments detect the fluxes of SM particles that are produced from the annihilation of DM particles. The ATLAS [3] and CMS [4] experiments at the LHC search for the production of pairs of DM particles from proton-proton collisions. All these searches are strongly motivated by the consistency of the thermal relic density and the annihilation rates of WIMP candidates with masses in the GeV-TeV range, detectable by these experiments [1]. DD, ID and LHC searches are complementary, as they probe different kinds of WIMP-SM interactions and WIMP mass ranges. A graphical

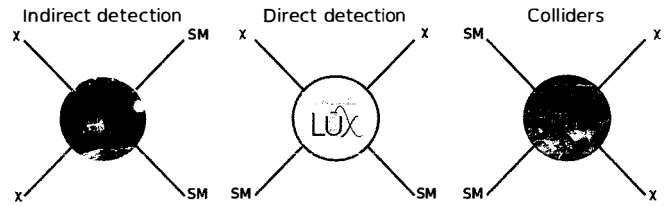

Figure 1 – A pictorial view of the complementarity between Direct Detection, Indirect Detection and Collider searches for DM.

view of this complementarity is shown in Fig. 1.

This contribution describes a series of searches for DM particles at the LHC performed by the ATLAS and CMS collaborations, using proton-proton collision data collected during the $\sqrt{s} = 8$ TeV LHC run. It also outlines the preparation and prospects for the upcoming $\sqrt{s} = 13$ TeV run, with a focus on the theoretical benchmark models that are necessary to fully exploit the complementarity among different experiments.

2 Details of searches for Dark Matter at the LHC

Most searches for Dark Matter at the LHC and at the Tevatron exploit the recoil of undetected pair-produced WIMPs against an object, radiated by one of the initial-state quarks or gluons. This leads to a distinctive signature of a high p_{T} object X in association with large missing transverse energy ($\not{E}_{\mathrm{T}}$), see Fig. 2 for a sketch. This signature is common to many other new physics signals.

Figure 2 – Sketch of typical DM benchmark models and their signatures at the LHC - left, contact interaction (commonly called Effective Field Theory) leading to a $\not{E}_{\mathrm{T}}$ + X signature, where X is the recoil object; right, simplified model with an $s-$channel mediator of mass M_{med} decaying in two DM particles.

The main set of Dark Matter benchmarks adopted for Run-1 represents the DM-SM interaction as a four-point vertex, as sketched in the left side of Fig. 2[5]. Commonly termed Effective Field Theory (EFT) operators, these benchmark models are characterized by the type of interaction between DM and SM, by the Dark Matter particle mass and the energy scale at which the new interaction would occur (cut-off scale, called either Λ or M_*). EFT operators are therefore an attractive tool to encapsulate the relevant degrees of freedom for Dark Matter without introducing the complexity of a full theory, aiding in the design of more model-independent searches. However, the EFT is only an approximation of a more complete theory, only valid for sufficiently low energies. The EFT approach is invalid if the momentum transfer of the collision approaches the mass of the particle mediating the interaction between the SM and the Dark Matter particles. Therefore, the reliability of the EFT framework in the high-energy collisions of the LHC is not always guaranteed. Models with an explicit mediator (see right-hand sketch in Fig. 2) overcoming this issue will be detailed in Section 3.

2.1 *Searches for Dark Matter in jet+$\not{E}_T$ and dijet final states*

Gluons are the most common objects produced as initial state radiation: the jet+$\not{E}_T$ signature is the most sensitive for most Dark Matter benchmark models considered. Events included in this search are required to have a *monojet* signature: at least one jet with p_T > 120 (110) GeV for the ATLAS [6] (CMS [7]) analysis, at least 150 (250) GeV of $\not{E}_T$ and no leptons. The backgrounds, dominated by $Z \to \nu\nu + jet$, are estimated by normalizing the simulated SM processes to data using control regions with vector bosons decaying into leptons. No deviations from the SM prediction are observed by either experiment in the signal regions, in a counting experiment for different values of $\not{E}_T$, as shown for the CMS case in Fig. 3.

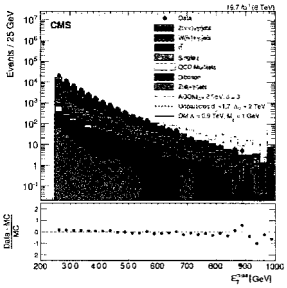

Figure 3 – $\not{E}_T$ distribution for the CMS monojet search.

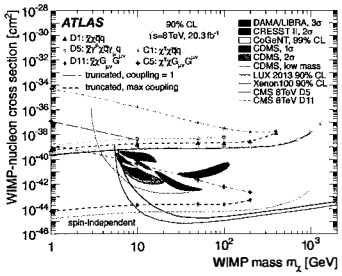

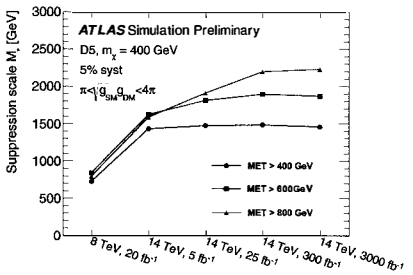

Figure 4 – Left: Inferred 90% CL limits on the spin-independent WIMP–nucleon scattering cross section as a function of DM mass m_χ for different operators. Results from direct-detection experiments for the spin-independent and spin-dependent cross section, and the CMS (untruncated) results are shown for comparison. Right: The 95% CL lower limits on the suppression scale M_* on simulated data at $\sqrt{s}$=8 TeV and 14 TeV for different luminosity values and for three signal regions defined by $\not{E}_T$>400, 600 and 800 GeV, assuming a DM mass of 400 GeV and 5% total background systematic uncertainty.

Lower limits on the suppression scale can be translated into constraints on the DM-nucleon cross section and compared to DD experiments, as shown in the left side of Fig. 4. In this comparison, the limitations of the EFT at LHC energies are a concern: for this reason, the ATLAS results include more conservative constraints where invalid events are removed from the search [8,9].

The sensitivity of the upcoming LHC datasets to one of the untruncated EFT operators is tested, using simulated data at 14 TeV [10]. The right side of Fig. 4 shows that the reach in M_* for the upcoming dataset will quickly surpass previous results, and it will be improved further when considering the full expected dataset from the High-Luminosity LHC [a]

As described in [11], the search for deviations in the dijet angular distribution is complementary to the search in the jet+$\not{E}_T$ final state, to constrain EFT operators. ATLAS [12] and CMS [13] both constrain contact interactions with the 8 TeV dataset, but no interpretation of the most recent results in terms of Dark Matter operators is available to date.

[a] Additional signal regions with a higher $\not{E}_T$ cut than those considered in this note could be considered for the highest luminosity dataset, further enhancing the reach of the search with respect to what shown in Fig. 4.

2.2 *Searches for Dark Matter with electroweak bosons*

Even though the jet+$\not{E}_{\mathrm{T}}$ signature is the most powerful for DM searches given the large statistics at high $\not{E}_{\mathrm{T}}$, signatures with an electroweak boson in the final state are still worth investigating due to their lower backgrounds and sensitivity to different benchmark models. ATLAS and CMS search for DM in the photon+$\not{E}_{\mathrm{T}}$ final state [14,15], as well as in the W and Z boson+$\not{E}_{\mathrm{T}}$ final states in their hadronic [16] and leptonic decay channels [17,18,19]. While searches with photons and leptons enjoy lower backgrounds, the larger background of the all-hadronic final states can be overcome using jet substructure techniques allowing the identification of jets from boson decays and selecting those compatible with the W and Z mass, as shown in Fig. 5. Benchmark models with EFT operators coupling two electroweak bosons and DM particles yield a mono-boson signature, are also tested in these searches.

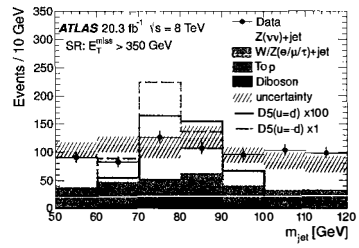

Figure 5 – Distribution of the jet mass in the data and for the predicted background in the signal regions (SR) with $\not{E}_{\mathrm{T}} > 350$ GeV (top). Also shown are the combined mono-W- and mono-Z-boson signal distributions with DM mass=1 GeV and M_*=1 TeV, for the scaled D5 operator in the case of destructive and constructive interference.

2.3 *Searches for Dark Matter in association with heavy quarks*

Models with DM that couples preferentially to heavy flavor quarks are sought in final states with a pair of top or b quarks in association with $\not{E}_{\mathrm{T}}$. Operators with scalar and pseudo-scalar interactions between DM and SM have a cross-section dependence on the quark mass, privileging final states with heavy flavor quarks with respect to light-quark monojet signatures. ATLAS [20] and CMS [21,22] searches in the all-hadronic, semileptonic and leptonic channels have observed no excesses on top of the SM background, estimated through simulation and data-driven techniques, as shown in the ATLAS case in the left-hand side of Fig. 6. Limits are set on the suppression scale assuming validity of the EFT framework, and compared to direct detection experiments, in the right-hand side of Fig. 6 for the CMS search.

3 Simplified models and DM benchmarks for the upcoming LHC run

The question of validity of the contact interaction approach employed as benchmark models for the first LHC run leads to consideration of a different set of Run 2 benchmark models. Simplified models [23,24], where a mediator particle is defined explicitly rather than integrated out, overcome the issue of EFT validity and provide a more faithful representation of the kinematics of the new phenomena where a truncation would only discard invalid events and lose information. Simplified models are an appealing benchmark for first LHC DM searches, thanks to limited number of parameters (mediator mass and couplings, in addition to the Dark Matter mass) that encapsulate the relevant features of a full Dark Matter theory. Moreover, given the unique sensitivity of the LHC to the mediator particles themselves, it is possible to consider signatures beyond the $\not{E}_{\mathrm{T}}$+X ones in order to constrain Dark Matter in the simplified model framework.

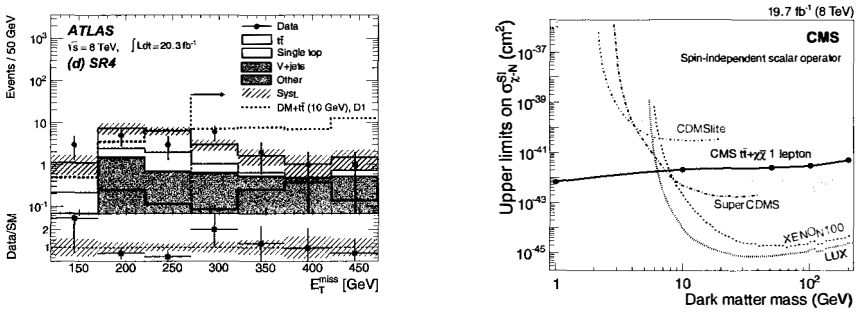

Figure 6 – Left: Comparison between data and expected SM background for the $\not{E}_{\mathrm{T}}$ distribution for one of the signal regions in the ATLAS heavy flavor quark + $\not{E}_{\mathrm{T}}$ all-hadronic search, with signal superimposed. The final selection requirement is denoted with an arrow. Error bars on the SM prediction represent the statistical uncertainty, while the dashed area corresponds to systematic uncertainties. Right: The 90% CL upper limits on the DM-nucleon spin-independent scattering cross sections as a function of the DM particle mass for the scalar operator considered in the CMS single-lepton search, shown with the 90% CL limits from various direct DM search experiments.

A possible simplified model benchmark for Dark Matter includes a color neutral vector boson mediator coupling to quarks and to Dark Matter, exchanged in the $s-$channel [25 26]. This model has been considered in 8 TeV jet and photon+$\not{E}_{\mathrm{T}}$ searches by both ATLAS and CMS in 8 TeV searches.

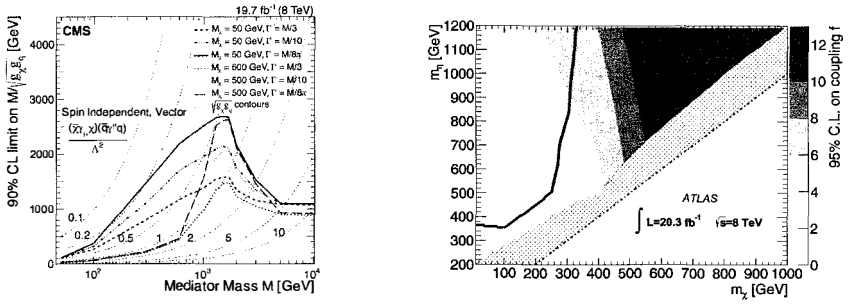

Figure 7 – Left: Observed limits from the CMS jet+$\not{E}_{\mathrm{T}}$ search on the mediator mass divided by coupling, as a function of the mass of the mediator, M, assuming vector interactions and a dark matter mass of 50 GeV (blue, filled) and 500 GeV (red, hatched), varying the mediator width. Right: Observed 95% C.L. upper limits on the product of the coupling constants of the scalar-mediator theory as a function of DM and mediator mass, for the ATLAS Z+$\not{E}_{\mathrm{T}}$ search. The cross-hatching shows the theoretically accessible region outside the range covered by this analysis, while the white region indicates phase space beyond the model's validity. The region in the upper left-hand corner is excluded by the lower limit on the couplings based on the DM relic density calculations.

The left side of Fig. 7 shows the limit on the mediator mass divided by the square root of the couplings of the mediator to quarks and DM ($M_{med}/\sqrt{g_\chi g_q}$, equivalent to the new physics scale M_*) as a function of the mediator mass. It can be seen from this figure that the limits converge to those obtained within the EFT framework at large mediator mass [7], strengthen when the mediator is on-shell and the production cross-section is resonantly enhanced, and weaken at low mediator mass. A t-channel colored scalar mediator has been considered as a benchmark model in the ATLAS Z+$\not{E}_{\mathrm{T}}$ search: limits on the coupling constant between the mediator, the quark and the DM particle are shown in the right-hand side of Fig. 7. A simplified model that has been constructed as a possible explanation for the galactic center excess observed by the

Fermi-LAT collaboration [27] is considered in the ATLAS heavy flavor + $\not{E}_T$ search [20].

The single top + $\not{E}_T$ final state is a search signature that is well-suited to simplified models. Resonant and non-resonant production of new invisibly-decaying particles in association with a top quark can encapsulate the characteristics of various full theories with a limited set of parameters. The ATLAS [28] and CMS [29] searches show no excess above the SM backgrounds; a background-enriched $\not{E}_T$ distribution from the CMS search and the limits on one of these models from the ATLAS search are shown in Fig. 8.

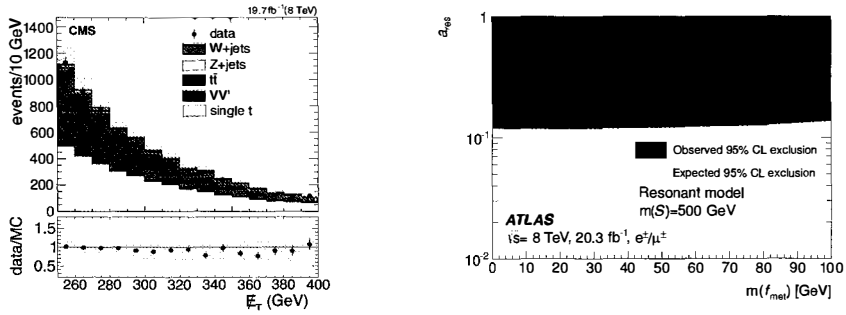

Figure 8 – Left: Distribution of $\not{E}_T$ in events after the signal selection for the CMS monotop search, modified to as to enrich the sample with the V+jets events. The shaded area represents the quadratic sum of the systematic uncertainties related to the renormalization and factorization scales for the $t\bar{t}$ and V+jets backgrounds, showing a good understanding of the main backgrounds for this search. Right: Observed and expected excluded coupling strengths for the resonant model with a new particle mass of 500 GeV, as a function of the mass of the new invisible fermion f_{met}, for the ATLAS search.

The Higgs boson can also be considered a mediator between SM and DM in Higgs Portal models [30]. Decays of the Higgs into DM particles would have observable bearing on Higgs properties: direct searches for invisibly decaying Higgs, and a combined fit to the Higgs couplings can constrain these models.

In preparation for the upcoming 13 TeV LHC run, where searches for DM and mediator particles will benefit from the increase in the center of mass energy and dataset size, the ATLAS and CMS collaborations have established a Forum to agree on the benchmark models and assumptions that will be considered for early Run-2 Dark Matter searches. The ATLAS/CMS Dark Matter Forum concludes its works at the end of May 2015, with a publicly available summary document and model repository.

Conclusions

Searches for DM particles in a wide range of final states have been undertaken by the ATLAS and CMS Collaborations during the first LHC run. No DM candidates have been observed, and stringent limits have been set on different benchmark models, highlighting the complementary of collider searches to direct and indirect detection experiments at low DM masses. The Run-1 LHC searches paved the way to the recognition of the limitations of the current benchmark models based on contact interaction (EFT) operators, and the potential of simplified models for Run-2 searches. Collider experiments not only can search for the invisible Dark Matter particles, but they can also directly probe the interaction between Standard Model and Dark Matter by searching for the particles that mediate it: this will be reflected in the choice of benchmark models for Run-2, agreed by the two collaborations within the ATLAS/CMS Dark Matter Forum.

References

[1] G. Bertone et al., *Particle DM: Evidence, candidates and constraints*, *Phys.Rept.* **405** (2005) 279–390, [hep-ph/0404175].

[2] D. Bauer et al., *DM in the Coming Decade: Complementary Paths to Discovery and Beyond*, 1305.1605.

[3] **ATLAS** Collaboration, *The ATLAS Experiment at the CERN Large Hadron Collider*, *JINST* **3** (2008) S08003.

[4] **CMS** Collaboration, *The CMS experiment at the CERN LHC*, *JINST* **3** (2008) S08004.

[5] J. Goodman et al., *Constraints on Dark Matter from Colliders*, *Phys.Rev.* **D82** (2010) 116010, [1008.1783].

[6] **ATLAS** Collaboration, *Search for new phenomena in final states with an energetic jet and large missing transverse momentum in pp collisions at* $\sqrt{s} = 8$ *TeV with the ATLAS detector*, 1502.01518.

[7] **CMS** Collaboration, *Search for dark matter, extra dimensions, and unparticles in monojet events in proton-proton collisions at* $\sqrt{s} = 8$ *TeV*, 1408.3583.

[8] G. Busoni, A. De Simone, E. Morgante, and A. Riotto, *On the Validity of the Effective Field Theory for Dark Matter Searches at the LHC*, *Phys.Lett.* **B728** (2014) 412–421, [1307.2253].

[9] G. Busoni, A. De Simone, J. Gramling, E. Morgante, and A. Riotto, *On the Validity of the Effective Field Theory for Dark Matter Searches at the LHC, Part II: Complete Analysis for the s-channel*, *JCAP* **1406** (2014) 060, [1402.1275].

[10] **ATLAS** Collaboration, *Sensitivity to WIMP Dark Matter in the Final States Containing Jets and Missing Transverse Momentum with the ATLAS Detector at 14 TeV LHC*, . ATL-PHYS-PUB-2014-007.

[11] H. Dreiner, D. Schmeier, and J. Tattersall, *Contact Interactions Probe Effective Dark Matter Models at the LHC*, *Europhys.Lett.* **102** (2013) 51001, [1303.3348].

[12] **ATLAS** Collaboration, *Search for New Phenomena in Dijet Angular Distributions in Proton-Proton Collisions at* $\sqrt{s} = 8$ *TeV Measured with the ATLAS Detector*, 1504.00357.

[13] **CMS** Collaboration, *Search for quark contact interactions and extra spatial dimensions using dijet angular distributions in proton-proton collisions at sqrt(s) = 8 TeV*, 1411.2646.

[14] **CMS** Collaboration, *Search for new phenomena in monophoton final states in proton-proton collisions at* $\sqrt{s} = 8$ *TeV*, 1410.8812.

[15] **ATLAS** Collaboration, *Search for new phenomena in events with a photon and missing transverse momentum in pp collisions at* $\sqrt{s} = 8$ *TeV with the ATLAS detector*, *Phys.Rev.* **D91** (2015), no. 1 012008, [1411.1559].

[16] **ATLAS** Collaboration, *Search for dark matter in events with a hadronically decaying W or Z boson and missing transverse momentum in pp collisions at* $\sqrt{s} = 8$ *TeV with the ATLAS detector*, *Phys.Rev.Lett.* **112** (2014), no. 4 041802, [1309.4017].

[17] **ATLAS** Collaboration, *Search for dark matter in events with a Z boson and missing transverse momentum in pp collisions at $\sqrt{s}$=8 TeV with the ATLAS detector*, *Phys.Rev.* **D90** (2014), no. 1 012004, [1404.0051].

[18] **CMS** Collaboration, *Search for physics beyond the standard model in final states with a lepton and missing transverse energy in proton-proton collisions at $\sqrt{s}$ − 8 TeV*, 1408.2745.

[19] **ATLAS** Collaboration, *Search for new particles in events with one lepton and missing transverse momentum in pp collisions at $\sqrt{s}$ = 8 TeV with the ATLAS detector*, *JHEP* **1409** (2014) 037, [1407.7494].

[20] **ATLAS** Collaboration, *Search for dark matter in events with heavy quarks and missing transverse momentum in pp collisions with the ATLAS detector*, *Eur.Phys.J.* **C75** (2015), no. 2 92, [1410.4031].

[21] **CMS** Collaboration, *Search for the Production of Dark Matter in Association with Top Quark Pairs in the Di-lepton Final State in pp collisions at $\sqrt{s} = 8$ TeV*, . CMS-PAS-B2G-13-004.

[22] **CMS** Collaboration, *Search for the production of dark matter in association with top-quark pairs in the single-lepton final state in proton-proton collisions at sqrt(s) = 8 TeV*, 1504.03198.

[23] J. Abdallah et al., *Simplified Models for Dark Matter and Missing Energy Searches at the LHC*, 1409.2893.

[24] S. Malik, C. McCabe, H. Araujo, A. Belyaev, C. Boehm, et al., *Interplay and Characterization of Dark Matter Searches at Colliders and in Direct Detection Experiments*, 1409.4075.

[25] M. T. Frandsen et al., *LHC and Tevatron Bounds on the DM Direct Detection Cross-Section for Vector Mediators*, *JHEP* **1207** (2012) 123, [1204.3839].

[26] H. An et al., *Light DM and Z′ Dark Force at Colliders*, *JHEP* **1207** (2012) 182, [1202.2894].

[27] P. Agrawal, B. Batell, D. Hooper, and T. Lin, *Flavored Dark Matter and the Galactic Center Gamma-Ray Excess*, *Phys.Rev.* **D90** (2014), no. 6 063512, [1404.1373].

[28] **ATLAS** Collaboration, *Search for invisible particles produced in association with single-top-quarks in proton-proton collisions at $\sqrt{s}$ = 8 TeV with the ATLAS detector*, *Eur.Phys.J.* **C75** (2015), no. 2 79, [1410.5404].

[29] **CMS** Collaboration, *Search for Monotop Signatures in Proton-Proton Collisions at $\sqrt{s}$ = 8 TeV*, *Phys.Rev.Lett.* **114** (2015), no. 10 101801, [1410.1149].

[30] A. Djouadi, A. Falkowski, Y. Mambrini, and J. Quevillon, *Direct Detection of Higgs-Portal Dark Matter at the LHC*, *Eur.Phys.J.* **C73** (2013), no. 6 2455, [1205.3169].

Direct Dark Matter Search with the CRESST-II Experiment

J. Schieck
for the CRESST collaboration
Institute of High Energy Physics, Nikolsdorfer Gasse 18, 1050 Wien, Austria and
University of Technology, Institute of Atomic and Subatomic Physics, Stadionallee 2, 1020 Wien, Austria

The quest for the particle nature of dark matter is one of the big open questions of modern physics. The CRESST-II experiment, located at the Gran Sasso laboratory in Italy, is optimised for the detection of the elastic scattering of dark matter particles with ordinary matter. We present the result obtained with an improved detector setup with increased radiopurity and enhanced background rejection. The limit obtained in the so-called low mass region between one and three GeV/c^2 is at the present among the best limits obtained for direct dark matter experiments. In addition we give an outlook of the future potential for direct dark matter detection using further improved CRESST $CaWO_4$ cryogenic detectors.

1 Introduction

Understanding the origin of dark matter is one of the scientific key questions at the beginning of the 21st century. The existence of dark matter at galactic and cosmological scales is undisputed. Several uncorrelated measurements indicate that about 25% of the overall energy-matter density of the universe consists of Dark Matter [1]. The underlying character of dark matter is still not understood. Assigning particle character to dark matter is one of the most promising approaches for solving this open topic. However, none of the known particles of the Standard Model of particle physics can act as a candidate for Dark Matter. The new particle cannot be charged or baryonic, it must be cold, traveling much more slow than the speed of light, and its decaytime must be below the age of the universe. The abundance of the dark matter particles should match the dark matter relic density. The interaction of a hypothetic dark matter particle with known Standard Model particles is unknown. All dark matter observations are based on gravity, however, a weak interaction between the unknown dark matter particle and known particles is expected.
One of the best studied particle candidates for dark matter is the so-called WIMP, a weakly interacting massive particle. WIMPs are thermally produced during the evolution of the universe. A WIMP dark matter candidate with a mass at the electroweak mass scale ($\mathcal{O}$(100GeV/c^2))and a cross section similar to the electroweak scale ($\mathcal{O}$(pb)) could match the observed relic dark matter density. However, thermally produced WIMPs with a mass below 5-10 GeV/c^2 would lead to an over-closure of the universe and are therefore excluded. The best exclusion limits for WIMPs are obtained with direct dark matter detection experiments based on liquid noble gases.
Asymmetric dark matter models predict particle candidates below the mass regime expected from standard WIMP based models [2]. The underlying model links two big unsolved riddles of modern physics: dark matter and the baryon asymmetry. A baryon violating process leads to a small imbalance between matter and antimatter and during the evolution of the universe the remaining antimatter completely annihilates with the matter, leading to the observed matter dominated environment. The observed dark matter and baryon density in the universe is of similar magnitude, motivating the assumption that the process leading to the observed matter-anti-matter imbalance

also controls the dark matter density. Asymmetric dark matter models predict anti-dark Matter and matter being initially equally produced. The same process leading to the observed baryon asymmetry is expected to produce a small excess of dark matter over anti-dark Matter, succeeded by the annihilation of the anti-dark Matter component. Following this idea, we expect that the mass of the hypothetical dark matter particle is about five times larger than the typical mass scale of ordinary matter, which is dominated by the proton mass. Asymmetric dark matter models predict Dark Matter candidates around 5 GeV/c^2, below the mass scale expected for WIMPs. This article summarises the results previously published in [3].

1.1 Search for low mass dark matter candidates

Most direct dark matter detection experiments aim for the identification of dark matter candidates by elastic scatters with a target nucleus. The nuclear recoil deposits energy in the experiment and the amount of the energy is a measure of the mass of the dark matter candidate. The expected differential recoil energy spectrum dR/dE_R, with R being the event rate and E_R the deposited recoil energy, falls exponentially. The dR/dE_R spectrum falls steeper for low mass dark matter candidates compared to heavy candidates. For an increased sensitivity for low mass dark matter particles a experiment needs to extend the recoil energy detection threshold towards lower values.

1.2 Results from the previous CRESST-II Data taking Period

In 2011 the CRESST collaboration reported an excess of events over the expected number of background events [4]. One background source originated from polonium decays, $^{210}Po \rightarrow ^{206}Pb + \alpha$. The lead nuclei from the polonium decay can deposit energy in the target crystal with the generated signal being similar to the signal of a dark matter candidate. Interpreting the surplus of events in the region of interest as dark matter elastic scattering resulted in two distinguished solutions, M1 and M2, in the mass versus cross section plane, with a significance of more than 4 σ. The analysis energy threshold for nuclear recoils was above 10 keV, leading to a steep decrease in sensitivity for dark matter candidates below 10 GeV.

2 The CRESST-II Experiment

Two main facts drive the design of a direct detection dark matter experiment: Dark matter particle - nucleus elastic scattering leads to a nuclear recoil with an energy deposition of a few keV at most. Second, dark matter candidates are expected to interact only weakly with the nucleus, resulting in an extremely low interaction rate. For this reason a successful dark matter experiment needs to be sensitive to very low energy depositions of a few keV or less, and an effective background rejection or suppression is needed for a good signal to background ratio.
To suppress background events originating from cosmic rays, the CRESST-II experiment is located at the Gran Sasso underground laboratory in Italy. In addition, the experiment contains active and passive background shielding to repress background events. The result presented here is based on data taken in the year 2013.

2.1 Cryogenic Detectors

In CRESST-II the target material for the dark matter particle nucleus elastic scattering is $CaWO_4$, a scintillating crystal operated at a temperature of about 10 mK. This very low operating temperature results in a small heat capacity. A small energy deposition of about few keV returns a measurable temperature change of several μK. The crystal is thermally coupled to a heat bath. This temperature increase, emerging as phonons, is detected in a bolometric mode by superconducting thermometers being operated at their phase transition between the normal and the superconducting state. Almost the complete deposited energy is carried away by the phonons allowing for an unbiased measurement of the full deposited energy. A small fraction of the energy

is transformed into scintillation light. The scintillation light is detected by a light detector made of silicon-on-saphire, read out again by a superconductor operated at its phase transition. An impression of the scintillation light being emitted by a $CaWO_4$-crystal is visualised in Fig. 1 (left). The light emitted strongly depends on the type of radiation and the type of recoiling target. The so-called light yield, the energy deposited in the light channel normalised to the energy in the phonon channel, differs for an electron or gamma compared to nuclear recoils. The light yield of an electron or gamma is calibrated to one at 122 keV and a nuclear recoil returns a significantly reduced value of almost zero. A cut on the light yield therefore allows an efficient discrimination of background events originating from electrons or gammas. For an improved background rejection the crystal is located in a scintillating housing. Additional light from the alpha impinging on the housing veto events from surface alpha decays originated from the inner surfaces of the module. As discussed above (see section 1.2) alpha-decays from polonium close to the crystal surface could mimic a signal event. During the previous data taking period the coverage was not hermetic and due to the missing scintillating light some ^{210}Po related decays may not have been identified as background events. For the data taking period described here the module design was adjusted, leading to a complete coverage. In addition the mounting was performed in a radon free environment leading to a decreased ^{210}Po contamination of the surfaces. A sketch of the module design is shown in Fig.1 (right).

The $CaWO_4$ crystal used for data taking is produced at the Technische Universität München.

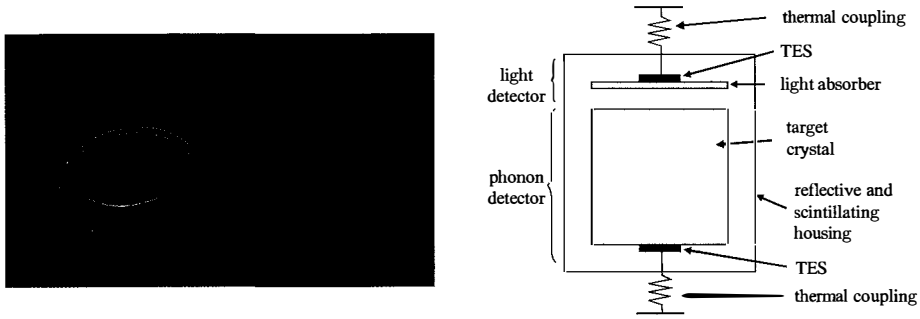

Figure 1 – Left: Light emission from two scintillating $CaWO_4$-crystals. Right: Sketch of a CRESST detector modul with the target crystal being read out by a transition edge superconductor (TES) to detect the phonons and a light absorber combined with another TES to measure the scintillation light. The whole crystal is thermally coupled to a heat bath and operated within a reflective scintillating housing[4].

Special care is taken in selecting radiopure material and in the various production steps to achieve a very high intrinsic radiopurity. As a result the electron / gamma background in the region of interest could be improved up to a factor of ten with respect to commercially available crystals. The low-energy spectrum of a single module (TUM-40) with an exposure of 29.4 kg days is shown in Fig. 2. The threshold energy for a 50% trigger efficiency is determined to be about 600 eV, with a resolution of about 100 eV. Various quality cuts are applied to the recorded events. Events are required to be collected during stable detector operation and are not to be in coincidence with cosmic muon events or with an event in any other detector module. The fit to determine the energy from the measured signal pulse needs to fulfil certain quality criteria and the signal shape must be consistent with the energy being deposited in the crystal and not in any other part of the detector module. These cuts lead to an overall efficiency just above 70% for energies above 3 keV.

3 Results

The distribution of events after the event selection criteria being applied is shown in Fig. 3. Background electron / gamma events with a light yield being consistent with one are clearly

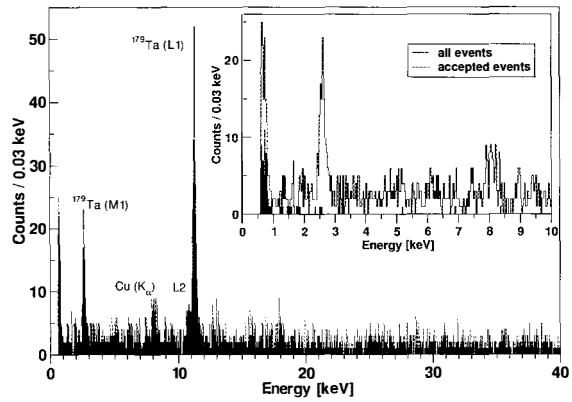

Figure 2 – The energy distribution of all selected events. The indicated lines mainly originate from cosmogenic activation. The insert is a zoom into the energy region below 10 keV energy with blue being all events and red indicating the events in the region of interest [3].

visible. Towards smaller energies the emitted scintillating light output is reduced and the noise of the light detector dominates the width of the light yield distribution. At energies below about 10 keV electron / gamma events leak into the signal region, representing the only background contribution.

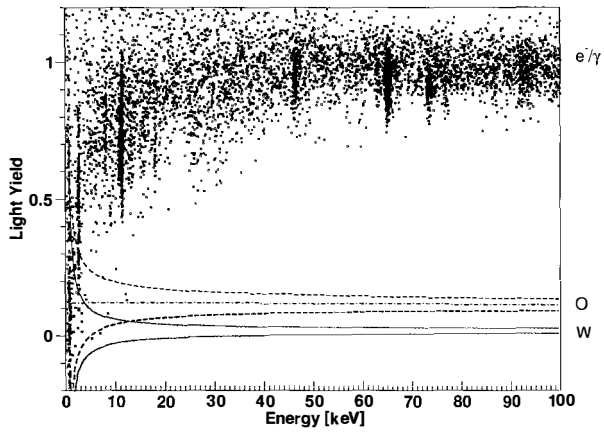

Figure 3 – Light yield versus energy for events after the selection being applied. The dashed grey line indicates the expected light yield for dark matter particle oxygen nucleus elastic scattering events (oxygen band) and the red line indicates the light yield for dark matter particle tungsten nucleus scattering events (tungsten band). The region of interest is defined for nuclear recoils between 0.6 keV and 40 keV and a light yield below the center of the oxygen band (yellow box) [3].

The number of events observed in the region of interest (Fig. 3) is consistent with the expected number of events originating from a leakage of electron / gamma events. All events are considered as signal events and a limit of dark matter particle nucleon cross-section is set. The spectrum of expected signal events is estimated using standard astrophysical assumptions for the dark matter distribution within the vicinity of the earth. The upper limit for the cross section as a function of

the dark matter particle mass is calculated with Yellin's optimum interval method[5]. The exclusion limit for masses between one and 30 GeV/c^2 is summarised in Fig. 4. The result previously obtained and if being interpreted as a possible WIMP signal[4] indicated with M2 in Fig. 3 is excluded and the point M1 is disfavoured.

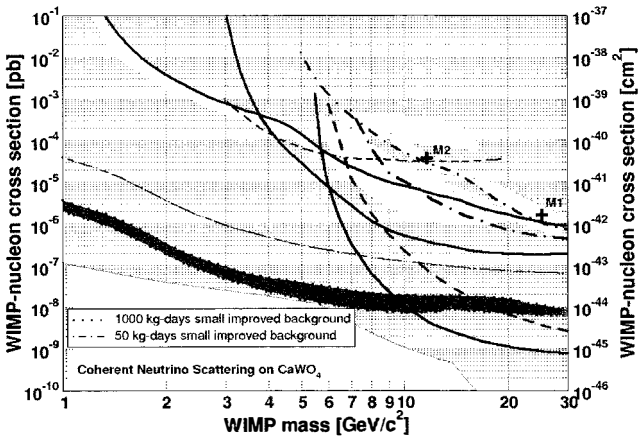

Figure 4 – The exclusion limit for the dark matter nucleon cross section as a function of the dark matter mass is shown here. The red line represents the limit obtained with data taken taken by the CRESST-II experiment in 2013. The dotted and dash-dotted lines indicate the limits expected for future data taking using an improved CRESST-II detector module design and reduced intrinsic radioactive background. The other lines correspond to limits obtained with other dark matter experiments, for a complete description of the other results see[3,6].

4 Outlook

The limit reached by the CRESST-II experiment is among the best limits obtained for direct detection of dark matter particles in the mass region between one and three GeV/c^2. Further improvements in the module design will lead to a reduced detection threshold, additionally improving the limit for low mass dark matter particles[6]. Together with a reduction of the intrinsic radioactive contamination the sensitivity almost reaches the level of coherent solar neutrino nucleus scattering on $CaWO_4$. The expected sensitivity is summarised in Fig. 4.

5 Historical Interlude

The achieved sensitivity for low mass dark matter particle candidates is mainly due to the very low detection threshold and the high intrinsic radiopurity. Limits obtained with the predecessor experiment, the CRESST experiment[7], achieved a similar sensitivity in the low mass region (see Fig. 5). The CRESST experiment also used a cryogenic setup, however with Al_2O_3-crystals as target material. Al_2O_3 is not scintillating and therefore the background discrimination is hindered, leading to a reduced sensitivity in the higher mass region. With the current technology CRESST-II has the foremost limit in the mass region of low-mass dark matter particles, while still reaching a reasonable sensitivity for medium-mass dark matter particles. Increasing the exposure would allow a further improvement in sensitivity by up to four orders of magnitude in the medium- and high-mass region.

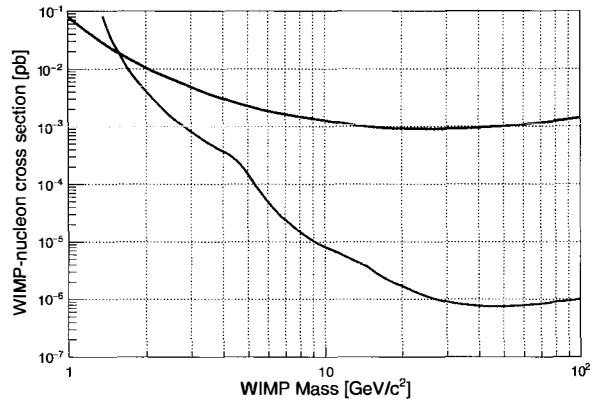

Figure 5 – Limits for low mass dark matter particles obtained with the CRESST (blue) [7] and the CRESST-II experiment (red) [3].

6 Summary

CRESST-II is a cryogenic experiment searching for a dark matter particle elastically scattering from a nucleus of a $CaWO_4$ crystal. A new data taking campaign using an improved module design and increased radiopurity could not confirm the excess above background events previously observed by CRESST-II. The significantly reduced detection threshold is about 600 eV, leading to high sensitivity for the detection of low-mass dark matter particles. Currently CRESST-II is among the direct dark matter detection experiments with the best limit in the low mass region. Future upgrades of the experiment are expected to increase the sensitivity in this mass region by three to four orders of magnitude.

References

1. A. Del Popolo, Int. J. Mod. Phys. D **23**, 1430005 (2014) [arXiv:1305.0456 [astro-ph.CO]].
2. K. M. Zurek, Phys. Rept. **537**, 91 (2014) [arXiv:1308.0338 [hep-ph]].
3. G. Angloher *et al.*,Eur. Phys. J. C **74**, no. 12, 3184 (2014) [arXiv:1407.3146 [astro-ph.CO]].
4. G. Angloher *et al.*,Eur. Phys. J. C **72**, 1971 (2012) [arXiv:1109.0702 [astro-ph.CO]].
5. S. Yellin, Phys. Rev. D **66**, 032005 (2002) [physics/0203002].
6. G. Angloher *et al.*,arXiv:1503.08065 [astro-ph.IM].
7. G. Angloher *et al.*,Astropart. Phys. **18**, 43 (2002).

FIRST RESULTS FROM DARKSIDE-50

D. FRANCO FOR THE DARKSIDE COLLABORATION
APC, Univ. Paris Diderot, CNRS/IN2P3, CEA/Irfu, Obs. de Paris, Sorbonne Paris Cité, 75205 Paris, France

P. Agnes, T. Alexander, A. Alton, K. Arisaka, H. O. Back, B. Baldin, K. Biery, G. Bonfini, M. Bossa, A. Brigatti, J. Brodsky, F. Budano, L. Cadonati, F. Calaprice, N. Canci, A. Candela, H. Cao, M. Cariello, P. Cavalcante, A. Chavarria, A. Chepurnov, A. G. Cocco, L. Crippa, D. D'Angelo, M. D'Incecco, S. Davini, M. De Deo, A. Derbin, A. Devoto, F. Di Eusanio, G. Di Pietro, E. Edkins, A. Empl, A. Fan, G. Fiorillo, K. Fomenko, G. Forster, F. Gabriele, C. Galbiati, A. Goretti, L. Grandi, M. Gromov, M. Y. Guan, Y. Guardincerri, B. Hackett, K. Herner, P. Humble, E. V. Hungerford, Al. Ianni, An. Ianni, C. Jollet, K. Keeter, C. Kendziora, S. Kidner, V. Kobychev, G. Koh, D. Korablev, G. Korga, A. Kurlej, P. X. Li, B. Loer, P. Lombardi, C. Love, L. Ludhova, S. Luitz, Y. Q. Ma, I. Machulin, A. Mandarano, S. Mari, J. Maricic, L. Marini, C. J. Martoff, A. Meregaglia, E. Meroni, P. D. Meyers, R. Milincic, D. Montanari, M. Montuschi, M. E. Monzani, P. Mosteiro, B. Mount, V. Muratova, P.Musico, A. Nelson, S. Odrowski, M. Okounkova, M. Orsini, F. Ortica, L. Pagani, M. Pallavicini, E. Pantic, L. Papp, S. Parmeggiano, R. Parsells, K. Pelczar, N. Pelliccia, S. Perasso, A. Pocar, S. Pordes, D.Pugachev, H. Qian, K. Randle, G. Ranucci, A. Razeto, B. Reinhold, A. Renshaw, A. Romani, B. Rossi, N. Rossi, S. D. Rountree, D. Sablone, P. Saggese, R. Saldanha, W. Sands, S. Sangiorgio, E. Segreto, D. Semenov, E. Shields, M. Skorokhvatov, O. Smirnov, A. Sotnikov, C.Stanford, Y. Suvorov, R. Tartaglia, J. Tatarowicz, G. Testera, A. Tonazzo, E. Unzhakov, R.B. Vogelaar, M. Wada, S. Walker, H. Wang, Y. Wang, A. Watson, S. Westerdale, M. Wojcik, A. Wright, X. Xiang, J. Xu, C. G. Yang, J. Yoo, S. Zavatarelli, A. Zec, C. Zhu, G. Zuzel

DarkSide-50 is dual-phase liquid argon time projection chamber, designed for direct WIMP search. The detector, consisting of 50 kg of liquid argon and shielded by active neutron and muon vetoes, is installed at Gran Sasso underground laboratory. DarkSide-50 is taking data since November 2013, collecting more than 10^7 events with atmospheric argon, naturally contaminated with cosmogenic ^{39}Ar beta decay. This contamination is equivalent to ~20 years of data taking with underground argon, depleted in ^{39}Ar by a factor larger than 150. Thanks to the excellent nuclear-electron recoil discrimination power of liquid argon and to the high efficiencies of the vetoes, no event has been observed in the WIMP region of interest in 47.1 days of data taking. We present the detector design and performance and the results from the atmospheric argon run.

1 Introduction

In the last two decades several observations have provided a wide range of astronomical evidences for the existence of Dark Matter, even if its nature is still a deep mystery. Among the different explanations, the Weakly Interacting Massive Particle (WIMP) represents one of the leading candidates. Several experiments are exploring new avenues to increase the sensitivity to the WIMPs trough their scattering with target nuclei.

Liquid argon (LAr) based detectors offers at the same time the advantage of a scalable target, and the unique add-on key feature of the excellent pulse shape discrimination (PSD) power to disentangle WIMP signal from electron-like background. This in fact relies on the singlet (6

ns) and triplet ($\sim$1.5 μs) excimer states, responsible of the emission of the 128 nm scintillation photons. The probability to excite singlet and triplet states depends on the interacting particle stopping power: nuclear recoils, from WIMP or neutron scattering, populate more singlet states than electron recoils, from β/γ radiation. The net effect is a faster scintillation component in the nuclear recoil signals, which represent a clean signature to efficiently discriminate electron recoil events.

In addition, the long-standing issue of the ^{39}Ar contamination in natural argon was recently solved by the DarkSide collaboration. ^{39}Ar is a cosmogenic beta-decay with a Q-value of 565 keV, produced by the interaction of cosmic rays with natural argon. Liquid argon is commonly extracted from the atmosphere, which is naturally exposed to cosmic ray radiation and hence largely contaminated in ^{39}Ar. The DarkSide collaboration identified in the argon extracted from deep underground the solution to this issue. Underground argon (UAr) is in fact naturally shielded against cosmic rays, and hence depleted in ^{39}Ar. Measurements of ^{39}Ar in UAr determined a depletion factor larger than 150 [2].

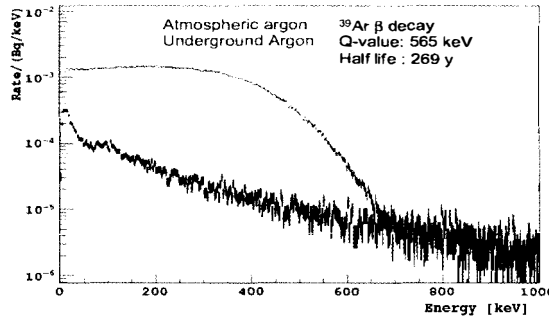

Figure 1 – Comparison between the atmospheric Argon (green) and the underground Argon (blue) spectra, as measured at the KURF underground laboratory .

DarkSide-50 is a direct dark matter search detector based on the double-phase LAr time projection chamber (TPC) technique, with $\sim$50 kg target mass, located in Hall C of LNGS at a depth of 3800 m.w.e.. DarkSide-50 is running since October 2013 with atmospheric argon, and it was recently filled (February 2015) with UAr. We report here the results obtained with the atmospheric argon run.

2 The DarkSide-50 detector

The DarkSide-50 TPC is designed to simultaneous detect the prompt scintillation light pulse (S1) and ionization electrons produced by the WIMP interaction in LAr. Ionization electrons are drifted toward the top of the TPC and extracted in the argon gaseous phase, producing a secondary light pulse (S2) by electroluminescence. Two arrays of 19 3" PMTs, placed at the top and the bottom of the TPC, observe the light pulses. The drift field is 200 V/cm and the maximum drift time, corresponding to the height of the TPC (35.6 cm), is $\sim$375 μs. The low drift field provides a double advantage: a high precision determination of the z-position of the particle interaction, by looking the time delay between S1 and S2, and the enhancement of the electron-ion recombination effect, which contributes to the increasing of the S1 light yield. The extraction field is set to 2.8 kV/cm. A sketch of the TPC is shown in figure 2.

The TPC is placed at the center of the Liquid Scintillator Veto (LSV), designed to shield the TPC against radiogenic and cosmogenic neutrons, gammas and cosmic muons. The anti-

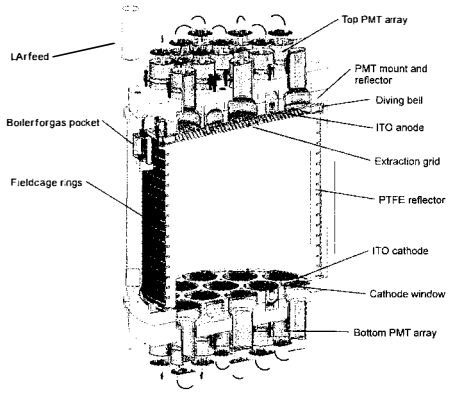

Figure 2 – The DarkSide-50 Liquid Argon Time Projection Chamber.

coincidence between LSV and TPC is particularly effective in rejecting neutrons, originating in the detector materials, interacting in the LAr target, and escaping the TPC. The 30 t of borated scintillator surrounding the TPC allows to detect and reject ~98% of neutrons with a single scattering in LAr, thanks to the neutron-capture reaction $^{10}B(n,\alpha)^{7}Li$. Single scattering neutrons represent the most dangerous source of background, being able to perfectly mimic the WIMP signal. The LSV is a 4.0 m-diameter stainless steel sphere and equipped with an array of 110 Hamamatsu R5912 8" PMTs, with low-radioactivity glass bulbs and high-quantum-efficiency photocathodes.

The LSV is in turn located inside the Water Cherenkov Detector (WCD), serving as shielding and as anti-coincidence for cosmic muons. The WCD is an 11 m-diameter, 10 m-high cylindrical tank filled with high purity water. An array of 80 ETL 9351 8" PMTs, mounted on the side and bottom of the water tank, detects Cherenkov photons produced by muons or other relativistic particles traversing the water.

A scale sketch of the of the entire detector system is shown in figure 3.

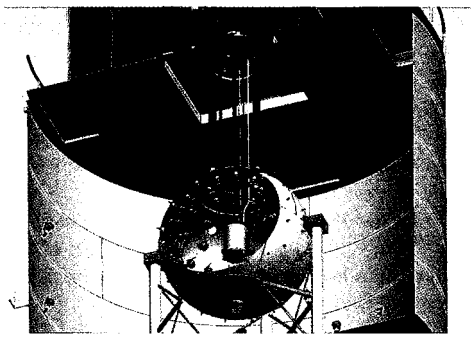

Figure 3 – Scale sketch of the three DarkSide detectors.

3 Analysis of the atmospheric Argon data set

The detector was calibrated with a ^{83m}Kr source, diffused inside LAr with the circulation loop. The ^{83m}Kr decays with τ=2.64 h to the ground state in two sequential electromagnetic transitions of 32.1 keV and 9.4 keV energy. The short intermediate mean life of about 222 ns cannot be resolved in the TPC because of the slow scintillation component. The two decays are then observed as a single deposition of 41.5 keV. The so-measured light yield resulted in 7.9 $\pm$ 0.4 pe/keV in absence of electric field, and $\sim$7.0 pe/keV at 200 V/cm. Figure 4 shows the combined fit of the ^{39}Ar spectrum and of the ^{83m}Kr peak in the field-on configuration.

Thanks to the ^{83m}Kr calibration, the high purity of the LAr target was also established: the electron lifetime was measured to be larger than 5 ms, with respect to the maximum electron drift time of 375 μs (drift velocity $\sim$ 0.93 mm/μs). In addition, the large statistics of ^{39}Ar events and the ^{83m}Kr calibration itself, allowed to accurately constrain the TPC non-uniformity of the light collection efficiency.

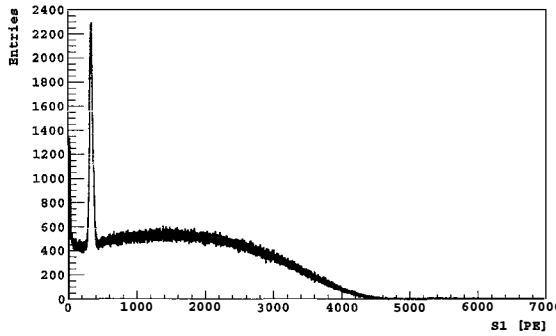

Figure 4 – Combined fit of the ^{83m}Kr peak and of the ^{39}Ar spectrum with DarkSide-50.

The WIMP acceptance band is defined in DarkSide-50 as the portion of the f90–S1 parameter space, containing 90% of the nuclear recoil interactions. The f90 variable is an estimator of the PSD, defined as the fraction of photons detected in the first 90 ns, with respect to the entire acquisition gate ($\sim$7 μs). The WIMP search energy range is defined from 60 to 460 pe, corresponding to 40 to 200 keVnr (8 to 40 keVee).

The WIMP acceptance band was determined by exploiting the results of the SCENE detector, a small scale TPC exposed to a low energy pulsed narrowband neutron beam produced at the Notre Dame Institute for Structure and Nuclear Astrophysics [3]. The limited size of the SCENE detector strongly reduced the probability of multiple scattering neutrons. Measuring the angles of the single scattered neutrons with respect to the source-TPC direction by means of neutron detectors, SCENE was able to select, by kinematical constraints, samples of nuclear recoils at different energies and with different drift fields. The SCENE results were then "scaled" to DarkSide-50 to define the nuclear acceptance band, taking into account the systematics induced by the differences of the two detectors. A direct DarkSide-50 calibrations with neutron (AmBe) and gamma (^{57}Co, ^{133}Ba, ^{137}Cs) sources, deployed in the LSV next to the cryostat, was run afterward the publication of the here presented results. These calibrations indeed confirmed our procedure for translating the Scene results to DarkSide-50.

The atmospheric argon data campaign lasted 47.2 days of live-time, along which $\sim$1.5$\times$10^7 of ^{39}Ar events falling in the WIMP energy range were acquired. The very high statistical sample of electron recoil events and the stringent requirement of the maximum electron recoil leakage of 0.01 events / 5 pe in the nuclear band, reduced the acceptance of the WIMP interactions, as

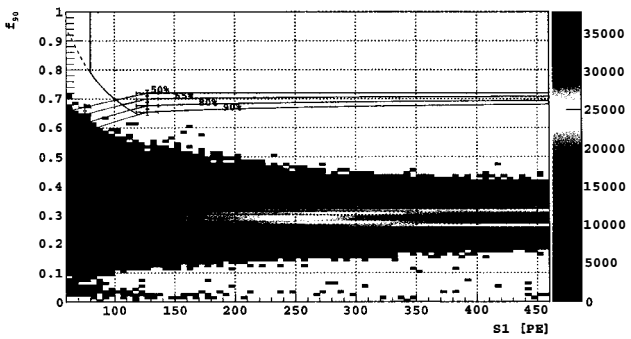

Figure 5 – Distribution of the events in the scatter plot of S1 vs. f90 after all quality and physics cuts. Shaded blue with solid blue outline: Dark Matter search box in the f90 vs. S1 plane. Percentages label the f90 acceptance contours for nuclear recoils drawn connecting points (shown with error bars) determined from the corresponding SCENE measurements.

shown in figure 5. The electron recoil leakage was obtained by fitting the F90 distributions for fixed energies, with the Hinkley model [4], as shown in figure 6.

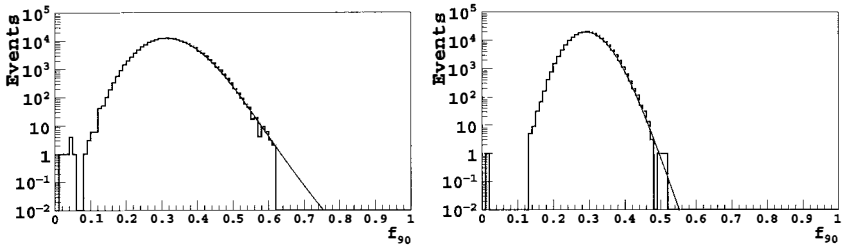

Figure 6 – Fits of f90 experimental distributions using the Hinckley model in the [80-85] (left) and [180-185] (right) pe WIMP search regions.

The nuclear recoil background, as already mentioned, is mostly due to cosmogenic and radiogenic neutrons. The fraction of cosmogenic neutrons, not detected by the double veto and falling in the WIMP search energy region, is negligible. For what concerns the radiogenic component, the dominant source of neutrons are the PMTs, and the subdominants are the cryostat and the fused silica windows, serving as anode and cathode in the TPC. The total expected neutron emission yield was evaluated with the TALYS package [5] in ~100 n/y. Geant4 based simulations evaluated in 5×10^{-4} the fraction of neutrons interacting once in the TPC and escaping the NV without any detectable signal (<30 pe). The large error associated to this fraction (20%) is mostly due to the uncertainty on the liquid scintillator α–quenching factor. The residual neutron background is rejected with ~98% efficiency by the LSV (this comparatively low efficiency of the LSV has since been improved to an anticipated 99.5%. [7]).

A fiducialization of the active volume is applied only in the vertical coordinate (measured by electron drift time) and no radial cut is applied. The fiducial cut vetoes about 3.6 cm of the LAr mass below the extraction grid and above the cathode. This reduced the total active volume to (36.9 ± 0.6) kg.

The last background component expected in DarkSide-50 are the α's emanated from the TPB-coated cylindrical reflector (TPB is the wavelength shifter), with a rate <10/m^2/day. In this case, an additional light contribution is expected from the TPB's own scintillation. No α

event was observed in the analyzed data set and preliminary studies exploiting the reconstructed x-y event position suggest that the radial fiducialization will suppress any surface background that may become evident in longer running.

4 Results and perspectives

The DarkSide-50 detector successfully concluded the atmospheric argon run, collecting a statistics corresponding to an an exposure of 1422 ± 67 kg days. No event was observed in the WIMP search region. The amount of collected ^{39}Ar events corresponds to a data taking of 215,000 kg days with UAr, assuming an ^{39}Ar depletion factor of 150. Further, the preliminary results from the UAr run suggests an even larger depletion factor (>300[6]), enhancing the final sensitivity of DarkSide-50.

The 0-event observation in the WIMP region in the atmospheric argon run was translated in a 90% WIMP mass-nucleon cross section, shown in figure 7. The limit at 100 GeV WIMP mass is equal to 6.1×10^{-44} cm^2, the most stringent ever obtained with a LAr target.

The excellent PSD power, in association with the preliminary results from the UAr run and the performances of the LSV in rejecting neutrons, are paving the way toward the next DarkSide phase, a dual-phase LAr detector with a fiducial mass of 20 ton, with the ambition to reach a sensitivity of $\sim 10^{-47}$ cm^2 at 1 TeV WIMP mass.

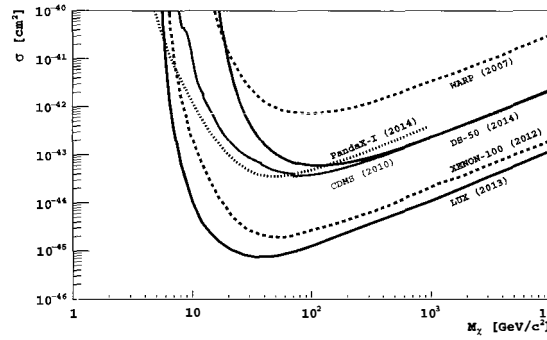

Figure 7 – 90% C.L. exclusion limits in the spin-independent WIMP nucleon cross section - mass parameter space.

Acknowledgments

We acknowledge the financial support from the UnivEarthS Labex program of Sorbonne Paris Cité (ANR-10-LABX-0023 and ANR-11-IDEX-0005-02) with the JE2 grant.

References

1. P. Agnes et al. (DarkSide Collaboration), *Phys. Lett.* B **743**, 456 (2015).
2. J. Xu et al., Astropart. Phys. **66** 53 (2015).
3. T. Alexander et al. (SCENE Collaboration), *Phys. Rev.* D **88**, 092006 (2013).
4. W. H. Lippincott et al., *Phys. Rev.* D **78**, 035801 (2008).
5. TALYS package: http://www.talys.eu/
6. C. Galbiati presentation at LNGS Scientific Committee meeting, April 2015, https://agenda.infn.it/conferenceDisplay.py?confId=9608
7. S. Davini presentation at LNGS Scientific Committee meeting, April 2015, https://agenda.infn.it/conferenceDisplay.py?confId=9608

3.55 KeV line in minimal decaying Dark Matter

Giorgio Arcadi
Laboratoire de Physique Théorique Université Paris-Sud, F-91405 Orsay, France

We present a simple model aimed at correlating the recently reported X-ray line with searches of new physics at LHC. The Standard Model is extended with a Majorana fermion DM, with mass set to 7 KeV, and a scalar field charged under the SM gauge group and capable of being pair produced at the LHC. The combined requirements of a DM lifetime in agreement with the line detection and the correct relic density, through the freeze-in mechanism, determine the typical decaying lenght and main decay channels at collider of the scalar field. It results promply decaying into two SM fermions. This kind of channel is already probed by LHC searches. The decay channel into DM, responsible for the generation of its relic density, has instead a too low branching ratio to be observable.

1 Introduction

Although conventional paradigms rely on stable dark matter (DM) candidates, whose stability is enforced by a symmetry of the underlying particle sector, decaying dark matter candidates, with lifetimes largely exceeding the age of the Universe, are not a priori fordidden. This kind of scenarios feature interesting prospects of Indirect Detection (ID), in cosmic rays, of DM decay processes occuring at present times. Among the possible signals, the most spectacular are probably narrow lines originating from decays of the DM into photons. A signal of this kind has been recently identified in the combined spectrum of a large set of galaxy clusters [1] as well as the combined observation of the Perseus Cluster and the M31 Galaxy [2]. This line has an energy of approximately 3.55 KeV and can be interpreted as the decay into photons of a DM particle with mass $m_{\rm DM} = 2E_\gamma \simeq 7\,{\rm KeV}$ (see anyway [3]). We remark anyway that this DM interpretation is still controversial [4] and most probably new data are needed to confirm (or disprove) it.
In this document we will discuss the interesting possibility of correlating this hypothetical Indirect Detection with searches of New Physics at LHC.
In order to investigate this possible interplay we will consider the very simple extension of the Standard Model (SM), presented in [5,6]. A SM singlet Majorana DM candidate is coupled with a scalar field, charged under the SM gauge group, and with the SM fermions. In the case of very light DM, namely below $\sim 1\,{\rm GeV}$, the only kinematically allowed DM decay is a two body processes, induced at one loop, with the scalar field and SM fermions running inside it, into a photon and a neutrino, thus reproducing the X-ray line for a DM mass of approximately 7

KeV. In addition, the scalar field sets the DM relic density through the freeze-in mechanism. Combining the requirements of reproducing the detected line and the correct DM relic density it is possible to infer the relevant couplings of the model. These determine the typical decay lenght of the scalar field, possibly pair produced at the LHC, and its dominant decay channels, thus determining the most suitable search strategies and the prospects of detection.
The document is organized as follows. In section 2 we will briefly describe the minimal decaying Dark Matter model. Section 3 is devoted to a brief review of the freeze-in mechanims. In section 4 we will then investigate the impact on the parameter space of the combined requirement of the agreement with the X-ray signal and of the correct DM relic density and infer the possible relevant LHC phenomenology of our scenario. We will then state our conclusions in section 5.

2 The model

As mentioned above we will consider a simple extension of the SM with two extra fields: a Majorana fermion ψ, the DM candidate, singlet with respect to the SM gauge group, and a scalar field Σ_f, with non trivial quantum numbers with respect to at least some components of the SM gauge symmetry group. This new state can couple to a SM fermion through a Yukawa type interaction of the form:

$$L_{\Sigma\psi f} = \lambda \bar{\psi} f \, \Sigma_f^{\dagger} + h.c. \tag{1}$$

where f is a quark or a lepton according the assignment of the quantum numbers of Σ_f. In absence of additional symmetries a similar interaction between the scalar field and only SM fermions:

$$L_{\Sigma f f} = \lambda^{'} \bar{f} f \, \Sigma_f^{\dagger} + h.c. \tag{2}$$

is also allowed by gauge symmetry. In its simplest realization, our scenario can be described by just four free parameters: the two couplings λ and $\lambda^{'}$ and the masses m_{ψ} and m_{Σ_f} of the two new states. The interactions above induce a tree-level three-body decay of the DM into SM fermions mediated by the scalar field. A photon line can be produced by the two body decay of DM into a photon and a neutrino, originating at the loop level as shown in fig. (1). This last decay channel can be dominant only if the three-level one is kinematically forbidden. This requirement is easily fullfilled by imposing, by kinematics, $E_{\gamma} = \frac{m_{\psi}}{2}$, thus setting $m_{\psi} \simeq 7\,\mathrm{KeV}$. From now on, unless differently stated, we will assume the DM mass fixed to this value, thus leaving three free parameters.
The scalar field Σ_f features also ordinary gauge interactions, strong and/or electroweak, which allow its efficient pair production at the LHC, in particular in the case of a color charged field. It can then decay through two possible kind of channels, DM and SM fermion or two SM fermions, with the corresponding rates proportional to, respectively, λ and $\lambda^{'}$. As will shown below, it is possible to infer from DM phenomenology the values of these two couplings and then the prospects of probing the production of the scalar field at the LHC. Indeed the DM lifetime is sensitive to the product $\lambda\lambda^{'}$ while the requirement of the correct relic density will allow an individual determination of the coupling λ, as function of the mass of the scalar field. Combining these two informations it is thus possible to infer the values of both the relevant couplings of the model. This allows to predict the typical collider decay lenght of the scalar field, thus determining whether it decays promptly, through displaced vertices or might even result detector stable, and its main decay channels. In such a way it is possible to determine the most suitable collider search strategy and the prospects for a future LHC detection.

3 Freeze-in mechanism

A very simple and economical mechanism for the DM production in our scenario is the so called freeze-in [7,8,9]. The DM is produced by the decays of scalar field while this is still in thermal equilibrium with the primordial thermal bath, as guaranteed by its gauge interactions. On

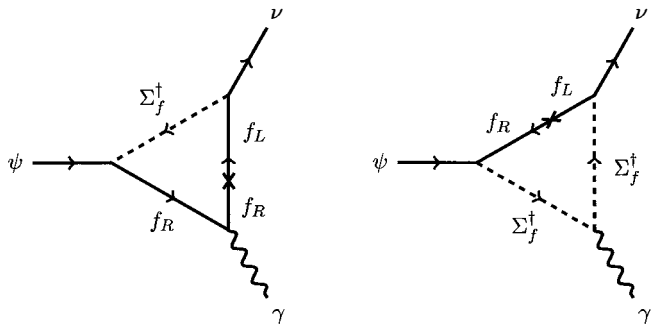

Figure 1: DM 2-body decay into γ and ν with the loop induced by Σ_d.

the contrary the DM should, instead, not be coupled to the thermal bath and have negligible abundance in the Early Universe. This condition can be fullfilled by imposing, as rule of thumb, that $\Gamma\left(\Gamma_f \to \psi + SM\right) < \mathcal{H}$, where $\mathcal{H} \approx 1.66 g_*(T) \frac{T^2}{M_{\rm Pl}}$ is the Hubble expansion parameter, g_* represent the number of relativistic degrees of freedom at the temperature T, and the relation is computed at $T = m_{\Sigma_f}$. Taking $\Gamma\left(\Gamma_f \to \psi + SM\right) = \frac{\lambda^2 m_{\Sigma_f}}{8\pi}$ it is possible to obtain the upper limit $\lambda < O\left(10^{-7}\right)$. If this limit is exceeded the DM would be in thermal equilibrium at early stages of the history of the Universe and decouple at temperatures of the order of the mass of the scalar field, while still relativistic, thus overclosing the Universe.
The relic density associated to the freeze-in mechanism is given by[a]:

$$\Omega_{\rm DM} h^2 \approx 1.09 \times 10^{27} \frac{g_{\Sigma_f}}{g_*^{3/2}} \frac{m_\psi}{m_{\Sigma_f}} \frac{\Gamma\left(\Sigma_f \to f\psi\right)}{m_{\Sigma_f}} \tag{3}$$

and is thus proportional to the decay rate of the scalar field into DM. Requiring the correct amount of DM abundance it is then possible to obtain, from eq. (3), a condition on the coupling λ. Combining this requirement with the one of reproducing the DM lifetime accounting for the X-ray line it is possible, as we will see in the next section, to determine the two relevant couplings λ and λ' as function of the DM mass (already set to a definite value) and the mass of the scalar field, which can be constrained through collider phenomenology.

4 DM lifetime and impact on collider searches

The decay process reported in fig. (1) occurs only for a limited set of operators, with respect to the ones allowed by gauge invariance, and only for some definite assignments of the quantum numbers of the field Σ_f:

$$\begin{aligned}
L_{\rm eff} &= \lambda' \bar{d}_R l_L \Sigma_q + h.c. && \Sigma_q = (3,2,1/3) \\
L_{\rm eff} &= \lambda' \bar{l}^c_R q_L \Sigma_d^\dagger + h.c. && \Sigma_d = (3,1,-2/3) \\
L_{\rm eff} &= \lambda' \bar{l}^c_R l_L \Sigma_e^\dagger + h.c. && \Sigma_\ell = (1,2,-1) \\
L_{\rm eff} &= \lambda' \bar{e}_R l_L \Sigma_l + h.c. && \Sigma_e = (1,1,-2)
\end{aligned} \tag{4}$$

[a] On general grounds a contribution from out-of-equilibrium (i.e. after chemical freeze-out) decays of the scalar fiels is expected as well. It is determined by the branching ratio of decay of the scalar field into DM and by its abundace at chemical freeze-out. The latter is however very low, because of the efficient gauge interactions, and thus its contribution to the DM relic density is negligible [5].

The decay rate of the DM into a neutrino and a photon is given by [10]:

$$\Gamma(\psi \to \gamma\nu) = \frac{g^2_{\psi\gamma\nu}}{8\pi} m_\psi, \quad g_{\psi\gamma\nu} = -\frac{e m_\psi}{16\pi^2} \sum_i \frac{m_i}{m^2_{\Sigma_f}} \lambda'_i \lambda_i f_1 \left(\frac{m_i^2}{m^2_{\Sigma_f}}\right)$$
$$f_1(x) = \frac{1}{1-x}\left[1 + \frac{1}{1-x}\ln x\right] \tag{5}$$

where the sum runs over the fermions flowing into the loop. We notice that the decay rate depends on the mass of the SM fermion in the loop since a chirality flip in the internal fermion line is required. The DM decay rate is thus mostly sensitive to the couplings of the scalar field with third generation fermions. The maximal value of the rate is achieved in the case of a bottom quark running in the loop, since, due to the SM neutrino quantum numbers, it is not possible to construct a loop with an intermediate top quark. Taking $m_b = 4$ GeV, the lifetime of the DM in this case can be estimated as:

$$\tau(\psi \to \gamma\nu) \approx 5.6 \times 10^6\,\mathrm{s}\left(\frac{m_\psi}{7\,\mathrm{keV}}\right)^{-3}\left(\frac{m_{\Sigma_f}}{1\,\mathrm{TeV}}\right)^4\left(\lambda\lambda'\right)^{-2} \tag{6}$$

By requiring a value of the lifetime of the order 10^{28} s, as expected for the detected photon line, we obtain the condition:

$$\lambda\lambda' \approx 2.4 \times 10^{-11}\left(\frac{m_\psi}{7\,\mathrm{keV}}\right)^{-3/2}\left(\frac{m_{\Sigma_f}}{1\,\mathrm{TeV}}\right)^2\left(\frac{\tau(\psi \to \gamma\nu)}{10^{28}\,\mathrm{s}}\right)^{-1/2} \tag{7}$$

Combining (7) with the requirement of the correct relic density which, from eq. (3), gives:

$$\lambda \simeq 0.8 \times 10^{-8}\left(\frac{m_\psi}{7\,\mathrm{keV}}\right)^{-1/2}\left(\frac{m_{\Sigma_f}}{1\,\mathrm{TeV}}\right)^{1/2}\left(\frac{g_*}{100}\right)^{3/4}\left(\frac{\Omega h^2}{0.11}\right)^{1/2}, \tag{8}$$

we obtain the following prediction for the coupling λ':

$$\lambda' \approx 3 \times 10^{-3}\left(\frac{m_\psi}{7\,\mathrm{keV}}\right)^{-1}\left(\frac{m_{\Sigma_f}}{1\,\mathrm{TeV}}\right)^{3/2}\left(\frac{\tau(\psi \to \gamma\nu)}{10^{28}\,\mathrm{s}}\right)^{-1/2}. \tag{9}$$

We notice that there is a strong hierarchy between the couplings λ' and λ. We thus expect that a pair produced scalar field at LHC would mostly decay into only SM fermions with typical decay lenght:

$$l_{\Sigma_f} \approx 5.6 \times 10^{-11}\,\mathrm{cm}\left(\frac{m_\psi}{7\,\mathrm{keV}}\right)^2\left(\frac{m_{\Sigma_f}}{1\,\mathrm{TeV}}\right)^{-4}\left(\frac{\tau(\psi \to \gamma\nu)}{10^{28}\,\mathrm{s}}\right) \tag{10}$$

This very small decay lenght implies prompt decays of the scalar field at the LHC. We remark that, due to the dependence of eq. (5) on the internal fermion mass, the value of λ' reported in (9) is the minimal achievable. The conclusion above hence is valid for all the realizations given in (4). For this reason we will focus from now on, for definiteness, our analysis to the case of a Σ_d-type (i.e. quantum numbers of a right-handed d-quark) field.

This scenario can be probed at LHC by searches of Leptoquarks. Assuming that the scalar field is only coupled to third generation quarks (given the dependence on the quark masses of the DM decay rate this is the only coupling accessible to our analysis), LHC searches already exclude masses of the scalar field below 740 GeV [11].

The interplay between LHC searches and DM phenomenology is summarized in fig. (2) in the plane (m_{Σ_f}, λ'). The red line represents the value of λ' given by eq. (9). The blue line represents the value of λ' which is obtained by combining eq. (7) with the condition $\Gamma(\Sigma_d \to b\psi) = \mathcal{H}$, giving:

$$\lambda = 0.6 \times 10^{-7}\left(\frac{m_{\Sigma_f}}{1\,\mathrm{TeV}}\right)^{1/2} \tag{11}$$

The light blue region below this last curve corresponds to a DM in thermal equilibrium in the Early Universe and, hence, largely overabundant if its mass is set to 7 KeV. The requirement of not overclosure of the Universe further enforces the prediction of a scalar field promptly decaying at the LHC[b]. Interestingly this prediction would be valid even for similar line signals, with respect to the one considered, for a rather broad range of masses, given the rather weak dependence of eq. (3) on the DM mass. In order to have a scalar field decay lenght compatible with displaced decays (purple dashed line) one needs to require $\lambda\lambda^{'} \lesssim 10^{-14}$, leading to unobservable DM decays in present and next future experiments. The gray region finally represents current exclusion from LHC searches of Leptoquarks.

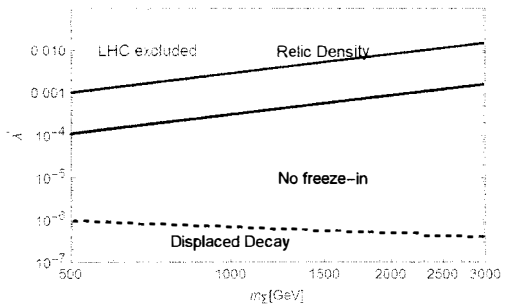

Figure 2: Summary plot in the $\left(m_{\Sigma_f}, \lambda^{'}\right)$ plane. The red line corresponds to a DM lifetime compatible with the detection of the X-ray line and of the correct DM relic density through the freeze-in mechanism. The gray region is excluded by current LHC limits while in the blue region the DM is in thermal equilibrium in the early cosmological epochs and would overclose the Universe.

We just comment that the result obtained is sensitively different with respect to the case $m_\psi \gtrsim O(\text{GeV})$. In this case, by requiring an hypothetical signal from, for example, the tree-level decay $\psi \to \bar{b}b\nu$ (in this case one might observe a signal in antiprotons rather than a photon line), corresponding to a DM lifetime of $\tau \sim 10^{-(27\div 28)}$s (approximately corresponding to current experimental limits in this mass range), on would get $\lambda\lambda^{'} \sim 10^{-20}$, leading to a long-lived scalar field, with respect to LHC detector scales, giving displaced vertices and/or disappearing tracks as possible signals[6].

As evident in the discussion, the requirement of a viable KeV DM reproducing the X-ray signal allows a rather clear prediction of the parameters of the model and definite prospects for LHC searches. On the other hand a reconstruction of these from an hypothetical LHC signal would be rather challenging. In particular it would be hard to discriminate our scenario from other models. Indeed the most peculiar signature, i.e. the presence of two different, namely DM+SM and only SM, decay modes of the scalar field, is not accessible to detection. In particular a direct test of the freeze-in paradigm is not possible because of the negligible branching fraction of the decay channel into DM. On the other hand, in case of LHC determination of the mass and lifetime of the scalar field, the combination with the Indirect DM signal would allow to infer the parameters of the model.

5 Conclusions

We have considered the possibility of reproducing the observation of X-ray signal through a minimal extension of the SM with a 7 KeV DM and a TeV scale DM. It has been possible to enforce a correlation between DM ID and searches at LHC of the scalar field. The requirement of viable DM is translated into the prediction of a scalar field promptly decaying into SM fermions

[b]Notice that this argument is strictly valid only assuming a standard cosmological history.

which can be probed by current searches of leptoquarks in case the scalar field carries color charge. It is however not possible to test the freeze-in hypothesis since the decay channel into DM has a suppressed branching ratio.

References

1. E. Bulbul, M. Markevitch, A. Foster, R. K. Smith, M. Loewenstein and S. W. Randall, *Astrophys.* J **789**, 13 (2014).
2. A. Boyarsky, O. Ruchayskiy, D. Iakubovskyi and J. Franse, *Phys. Rev. Lett.* **113**, 251301 (2014).
3. A. Falkowski, Y. Hochberg and J. T. Ruderman, *JHEP* **1411**, 140 (2014)
4. T. E. Jeltema and S. Profumo, arXiv:1408.1699
5. G. Arcadi and L. Covi, *JCAP* **1308**, 005 (2013).
6. G. Arcadi, L. Covi and F. Dradi, *JCAP* **1410**, 063 (2014)
7. T. Asaka, K. Ishiwata and T. Moroi, *Phys. Rev.* D **73**, 051301 (2006)
8. A. Kusenko, *Phys. Rev. Lett.* **97**, 241301 (2006)
9. L. J. Hall, K. Jedamzik, J. March-Russell and S. M. West, *JHEP* **1003**, 080 (2010)
10. M. Garny, A. Ibarra and S. Vogl, *JCAP* **1204**, 033 (2012)
11. V. Khachatryan *et al.* [CMS Collaboration], *Phys. Lett.* B **739**, 229 (2014)

LIGHT STERILE NEUTRINO LIMITS FROM COSMOLOGY

NINETTA SAVIANO
Institute for Particle Physics Phenomenology, Department of Physics, Durham University, Durham DH1 3LE, United Kingdom

The Early Universe represents an important environment to test the neutrino proprieties. Indeed Big Bang Nucleosynthesis, Cosmic Microwave Background radiation, Large Scale Structure formation could be essentially influenced by the presence of neutrinos, in particular by their number and their mass. In recent years a renewed attention has been devoted to low-mass sterile neutrinos ($m \sim$1 eV), after intriguing but controversial hints coming from laboratory oscillation experiments. Given the doubtful situation, is necessary to study the physical conditions under which the sterile production occurs and to investigate the consequences on the cosmological observables.

1 Introduction

The 3-ν standard scenario explains with success most the results coming from neutrino oscillation experiments. However there are some data, called *anomaly*, that cannot be explained in this framework. If interpreted as oscillation signals, they point towards the possible existence of 1 or more sterile neutrinos with mass square difference $\Delta m^2 \sim O(1\ \mathrm{eV}^2)$. Many analyses have been performed to explain the anomalies and scenarios with one ("3 + 1") or two ("3 + 2") sterile neutrinos have been suggested in order to fit different data [1,2]. The search for sterile neutrinos in laboratory experiments is presently open. Indeed, since each experimental measurement has its own systematic uncertainties, it is important to use as many observations as possible to probe sterile neutrinos. In this context, cosmological observations represent a valid complementary tool to probe these scenarios, being sensitive to the number of neutrinos and to their masses. It is commonly assumed that sterile neutrinos are produced in the primordial plasma via mixing with the active neutrinos and in presence of collisions. They participate, if sufficiently light, to the radiation content (parametrized in terms of the effective number of relativistic degrees of freedom N_{eff}) in addition to photons and ordinary neutrinos, leaving possible traces on different cosmological observables. Moreover, once sterile neutrinos become non-relativistic, they contribute to the matter density producing a peculiar imprint on structure formation. In order to evaluate the abundance of sterile neutrinos and their impact on the cosmological observables, is necessary to solve the kinetic equations for the flavour evolution of an active-sterile system, involving non-linear refractive effects and neutrino scatterings.

2 Effective number of neutrino species N_{eff}

For temperature of the universe $T < m_e$, after the $e^+ - e^-$ annihilation, the remaining relativistic degrees of freedom are photons, the three light active neutrinos and other particles if they exist. The non-elctromagnetic energy density of the universe is then expressed in terms of the *effective number of neutrino species* N_{eff}:

$$\epsilon_R = \epsilon_\gamma \left(1 + \frac{7}{8}\left(\frac{4}{11}\right)^{4/3} N_{\rm eff}\right) = \epsilon_\gamma \left(1 + \frac{7}{8}\left(\frac{4}{11}\right)^{4/3} (N_{\rm eff}^{\rm SM} + \Delta N)\right) \quad (1)$$

The Standard Model expectation (plus active neutrino oscillations) for this parameter is $N_{\rm eff}^{\rm SM} = 3.046$ [3], where the slightly excess with respect to 3 is to due to the non instantaneous neutrino decoupling thanks to which neutrinos share a small part of the entropy release after the $e^+ - e^-$ annihilation.

Concerning the extra radiation, it may be accounted for by different particles, such as sterile neutrinos totally or partially thermalised, axions and axion-like particles, hidden sector photons, majorons, or even gravitons. Among them we consider the presence of light sterile neutrinos ($\Delta m_s^2 \leq 1$ eV^2) oscillating with the active ones.

3 Impact of sterile neutrinos on the cosmological obeservations

3.1 Big Bang Nucleosynthesis

Big Bang Nucleosynthesis (BBN) is the epoch of the Early Universe when the primordial abundances of light elements were produced, in particular ^{2}H, ^{3}He, ^{4}He and ^{7}Li. Soon after neutrinos decouple by primordial plasma (at temperature $T_d \sim$(1 MeV)), charged-current weak neutron-proton interconversions also become too slow to guarantee the $n - p$ chemical equilibrium. For temperatures below $T_d \sim 0.7$ MeV, the n/p density ratio departs from its equilibrium value and freezes out at the asymptotic value

$$\frac{n_n}{n_p} = \frac{n}{p} = e^{-\frac{\Delta m}{T_d}} \sim \frac{1}{6} \quad (2)$$

with $\Delta m = 1.29$ MeV the neutron-proton mass difference. The n/p ration is very important since it fixes the primordial yields, especially the helium abundance characterised by the "helium mass fraction" $Y_P = (2n/p)/(1 + n/p)$.

Sterile neutrinos can influence the production of the primordial light elements in two ways:

- Cosmological neutrinos of each flavor contribute to the radiation energy density that governs the expansion rate of the Universe before and during BBN epoch. In particular, if the additional sterile states are produced before the active-neutrino decoupling T_d , they would acquire quasi-thermal distributions (depending on their temperature) and behave as extra degrees of freedom at the time of primordial nucleosynthesis. This would anticipate the weak interaction decoupling altering the n/p ratio at the onset of BBN and hence the light element abundances.

- Furthermore, sterile neutrinos, oscillating with the active species, can distort the momentum spectra of ν_e and $\bar{\nu}_e$ which directly participate in the charged current weak interactions ruling the neutron/proton chemical equilibrium. Any change in the neutrino momentum distributions can alter the n/p ratio and then modify the primordial abundances.

3.2 Cosmic Microwave background and Structure Formation

Unlike BBN, the later time observables CMB anisotropies and LSS distributions are not sensitive to the flavor content of the neutrino sector, but only to $N_{\rm eff}$ and to the mass of the neutrino species.

If additional degrees of freedom are still relativistic at the time of CMB formation, they impact the CMB anisotropies spectrum at both large and small scales, and so it is possible to obtain important information on $N_{\rm eff}$ especially if the CMB data are combined with other cosmological probes. One of the main effect of increasing the radiation density is the delay of the

epoch of matter-radiation equality, with consequences on the width of the first peak and also on the peaks locations. Concerning the power spectrum of the structure formation, it is suppressed at small scale in presence of free-streaming massive neutrinos for at least two reasons: by the absence of neutrino perturbations in the total matter power spectrum and by a slower growth rate of CDM/baryon perturbations at late times [4].

3.3 Cosmological bounds on extra species

Starting with the BBN, given the impact of extra radiation on the abundance of the primordial light nuclei, we can obtain from them robust constraints on $N_{\rm eff}$. In according to several and independent investigations, one extra thermalised sterile neutrino specie is marginally allowed, while two extra degrees of freedom are completely excluded [5,6]: $N_{\rm eff} < 4$.

Concerning the CMB data combined with other cosmological information, we consider the 95% C.L. upper bounds from the combined analysis of $N_{\rm eff}$ and the effective mass for sterile neutrino $m_{\rm st}^{\rm eff}$ (defined as the physical mass weighted by the sterile abundance) performed by the Planck collaboration using the last cosmological data [7], including Planck temperature power spectrum, lensing data and baryonic acoustic oscillations:

$$N_{\rm eff} < 3.7 \quad \text{and} \quad m_{\rm st}^{\rm eff} < 0.52 \text{ eV}, \tag{3}$$

$$N_{\rm eff} < 3.7 \quad \text{and} \quad m_{\rm st}^{\rm eff} < 0.38 \text{ eV}. \tag{4}$$

The former set is computed in presence of the prior cutoff of $m_{\rm s}^{\rm ph} < 10$ eV, while the latter restricting to the region where $m_{\rm s}^{\rm ph} < 2$ eV.

Moreover a possible non-zero sterile neutrino mass has been claimed in order to relieve the discrepancy between the CMB measurements and other observations, like current expansion rate H_0, the galaxy shear power spectrum and counts of galaxy clusters, providing a value $m_{\rm st}^{\rm eff} \simeq 0.7$ eV at 2σ [8,9,10,11] or an upper bound of $m_{\rm st}^{\rm eff} < 0.6$ eV [12]. Stronger bounds have also be quoted in [11,12].

4 Flavour evolution for the active-sterile system

A proper characterization of the evolution of a neutrino ensemble, simultaneously mixing and scattering in the Early Universe, requires the use of the density matrix formalism. According to it, the neutrino (antineutrino) ensemble for the (3+1) scenario is expressed in terms of 4×4 density matrices ϱ ($\bar{\varrho}$):

$$\rho(p) = \begin{pmatrix} \rho_{ee} & \rho_{e\mu} & \rho_{e\tau} & \rho_{es} \\ \rho_{\mu e} & \rho_{\mu\mu} & \rho_{\mu\tau} & \rho_{\mu s} \\ \rho_{\tau e} & \rho_{\tau\mu} & \rho_{\tau\tau} & \rho_{\tau s} \\ \rho_{se} & \rho_{s\mu} & \rho_{s\tau} & \rho_{ss} \end{pmatrix} , \tag{5}$$

The evolution equation for the ρ is the following:

$$\mathrm{i}\,\frac{d\rho}{dt} = [\Omega, \rho] + C[\rho]\,, \tag{6}$$

and a similar expression holds for the antineutrino matrix $\bar{\rho}$. The first term on the right side of the equation (6) describes the flavour conversions,

$$\Omega = \frac{\mathsf{M}^2}{2}\frac{1}{p} + \sqrt{2}\,G_{\rm F}\left[-\frac{8p}{3}\left(\frac{\mathsf{E}_\ell}{m_{\rm W}^2} + \frac{\mathsf{E}_\nu}{m_{\rm Z}^2}\right)\right] . \tag{7}$$

where we identify different contributions: $\mathsf{M}^2 = \mathcal{U}^\dagger \mathcal{M}^2 \mathcal{U}$ denotes the mass matrix, while the terms proportional to the Fermi constant G_F represent the matter effects. In particular, the term E_ℓ is linked to the energy density of the pairs $e^\pm$, instead E_ν to the energy density of ν e $\bar{\nu}$. The last term of the right side of the equation (6) is the collisional one which takes into account the processes proportional to G_F^2.

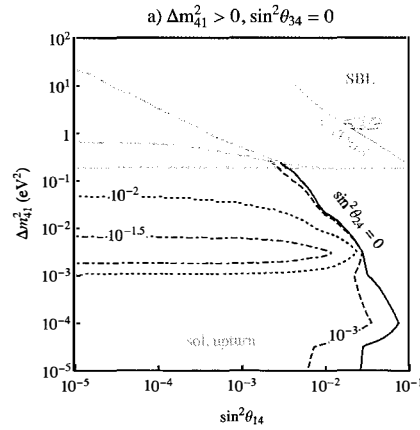

Figure 1 – Exclusion plots for the active-sterile neutrino mixing parameter space from N_{eff} (black curves) and $\Omega_\nu h^2$ (red curves) at 95 % C.L. The contours refer to different values of $\sin^2\theta_{24}$: $\sin^2\theta_{24} = 0$ (continuous curves), $\sin^2\theta_{24} = 10^{-2}$ (dotted curves), $\sin^2\theta_{24} = 10^{-1.5}$ (dot-dashed curves).

Sterile neutrino constraints

Given the recent data release of the Planck experiment for the radiation content $N_{\rm eff}$ and for the neutrino mass bound, is interesting to update the scan of the sterile neutrino parameter space in a 3+1 model, with sterile mass splitting $\Delta m^2_{\rm st}$ in the range $(10^{-5} - 10^2)\,{\rm eV}^2$, considering, for the first time, two non-vanishing active-sterile mixing angles. We fix the values of the three active mixing angles to the current best-fit from global analysis of the different active neutrino oscillation data [13]. Concerning the active-sterile mixing angles we choose as representative range $10^{-5} \leq \sin^2\theta_{i4} \leq 10^{-1}$ (i=1,2,3). The 4ν mass spectrum is parameterized as $\mathcal{M}^2 = {\rm diag}\,(m_1^2, m_1^2 + \Delta m^2_{21}\,, m_1^2 + \Delta m^2_{31}\,, m_1^2 + \Delta m^2_{41})$. We consider a hierarchical mass spectrum, obtained setting $m_1 = 0$. This is consistent with the scenario adopted by the Planck collaboration to obtain the constraint on the sterile neutrino mass.

The solar and the atmospheric mass-square differences are given by $\Delta m^2_{21} = m_2^2 - m_1^2 = 7.54 \times 10^{-5}\ {\rm eV}^2$ and $|\Delta m^2_{31}| = |m_3^2 - m_1^2| = 2.43 \times 10^{-3}\ {\rm eV}^2$, respectively [13], with the *normal* mass hierarchy considered for both the active sector (NH, $\Delta m^2_{31} > 0$) and the sterile one (SNH, $\Delta m^2_{41} > 0$).

The first quantity we are exploiting to constrain the sterile neutrino parameter space is the overall non electromagnetic radiation content, parametrized via $N_{\rm eff}$,

$$N_{\rm eff} = \frac{1}{2}{\rm Tr}(\rho + \bar{\rho}). \tag{8}$$

The bounds are given comparing this number with the one measured by Planck experiment, $N_{\rm eff} < 3.80$ at 95 % C.L. Given the current limit on the sum of the neutrino masses, we comment that the constraints on $N_{\rm eff}$ are valid for sterile mass $m_4 < 0.5$ eV considering a fully thermalised extra neutrino species. Indeed, larger values of the sterile neutrino mass would be not relativistic anymore at the CMB decoupling and therefore we cannot use radiation constraints. However, mass bounds become very important through the neutrino contribution to the energy density in the Universe. Assuming the existence of a thermalized massive sterile neutrino together with two massless active neutrinos and a massive one with mass fixed by the atmospheric mass-splitting (i.e. m$\sim$0.06 eV), the second quantity is

$$\Omega_\nu h^2 = \frac{1}{2}\frac{\sqrt{\Delta m^2_{41}}\cdot(\rho_{ss}+\bar{\rho}_{ss})}{94.1\ \text{eV}} \quad . \tag{9}$$

The constraint on the neutrino energy density is $\Omega_\nu h^2 \leq 0,005$ at 95 % C.L., coming from the Planck+ BAO bound on the effective sterile mass.

In Fig. 1 we present the exclusion plots in the planes $(\Delta m^2_{41}, \sin^2\theta_{14})$ for different values of the other mixing angle $\sin^2\theta_{24}$. In according to the analysis for the laboratory anomalies, $\sin^2\theta_{34}$ is fixed to zero. The excluded regions from N_{eff} are those on the right or at the exterior of the black contours, while the ones from $\Omega_\nu h^2$ are above the red contours. For comparison, we show at 95 % C.L. the slice at $\sin^2\theta_{24} = 10^{-2}$, for the allowed region obtained from the global analysis of short-baseline oscillation data [14] (blue filled region in the up right part of the plot denoted by SBL). We observe that it is completely ruled out by the cosmological bound from $\Omega_\nu h^2$, [15]. This is due to the fact that, for the mass and mixing parameters preferred by laboratory data, sterile neutrinos are copiously produced by oscillation until they reach one extra d.o.f, (i.e. the sterile abundance ρ_{ss}=1), see Fig. 2.

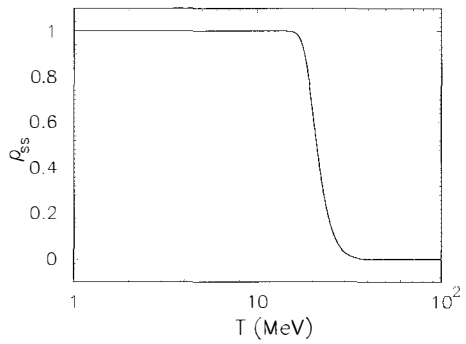

Figure 2 – Sterile neutrinos abundance in function of the temperature for the mass and mixing parameters preferred by laboratory .

5 Possible solution for the eV sterile neutrino problem

From the results of analysis shown before, we conclude that the sterile neutrino parameter space is severely constrained and the (3+1) scenario with sterile mass $m \sim \mathcal{O}(1\ \text{eV})$ is strongly disfavoured [15], producing a tension among the thremalized sterile neutrino hints from short-baseline experiments and the cosmological bounds. Living a part the possibility of a different cosmological model (as for example considered in [16]), this tension could be overcome if the production of sterile neutrinos is suppressed. Several mechanisms have been proposed in order to achieve this suppression. The first one is represented by the introduction of a large primordial neutrino-antineutrino asymmetry term ($L \geq 10^{-2}$)[17,18,19] in the equations for the flavor evolution. However, in presence of this large asymmetry, the flavor conversions occur at lower temperature (few MeV), around the neutrino decoupling time, leading to distortions in the active neutrino spectra and so to a non trivial implication for the BBN [18,19]. Recently, a different model has been proposed by several authors [20,21] in order to achieve an analogous suppression of the flavor evolution. This model is based on new secret interactions among only sterile neutrinos, mediated by a new gauge boson. In presence of the new interactions, flavor conversions are shifted at lower temperature and sterile neutrinos are resonantly and collisional produced. BBN and mass bounds strongly constrain the model, disfavoring values of the mass of the new gauge boson

$M_X > 1$ MeV [22,23]. Finally, if the new interactions are mediated by a very light (or massless) pseudoscalar might represent an escape route to the cosmological mass bounds [24].

Acknowledgments

N.S. acknowledges support from the European Union FP7 ITN INVISIBLES (Marie Curie Actions, PITN- GA-2011-289442).

References

1. C. Giunti, M. Laveder, Y. F. Li and H. W. Long, Phys. Rev. D **88**, (2013) 073008.
2. J. Kopp, P. A. N. Machado, M. Maltoni and T. Schwetz,
3. G. Mangano, G. Miele, S. Pastor, T. Pinto, O. Pisanti and P. D. Serpico, Nucl. Phys. B **729**, 221 (2005).
4. J. Lesgourgues and S. Pastor, New J. Phys. **16** (2014) 065002.
5. G. Mangano and P. D. Serpico, Phys. Lett. B **701**, 296 (2011).
6. R. Cooke, M. Pettini, R. A. Jorgenson, M. T. Murphy and C. C. Steidel, The Astrophysical Journal **781**, Issue 1, article id. 31 (2014).
7. P. A. R. Ade *et al.* [Planck Collaboration], arXiv:1502.01589 [astro-ph.CO].
8. M. Wyman, D. H. Rudd, R. A. Vanderveld and W. Hu, Phys. Rev. Lett. **112** (2014) 5, 051302.
9. J. Hamann and J. Hasenkamp, JCAP **1310**, 044 (2013).
10. R. A. Battye and A. Moss, Phys. Rev. Lett. **112** (2014) 5, 051303.
11. M. Archidiacono, N. Fornengo, S. Gariazzo, C. Giunti, S. Hannestad and M. Laveder, JCAP **1406**, 031 (2014).
12. B. Leistedt, H. V. Peiris and L. Verde, Phys. Rev. Lett. **113**, 041301 (2014).
13. G. L. Fogli, E. Lisi, A. Marrone, D. Montanino, A. Palazzo and A. M. Rotunno, Phys. Rev. D **86**, 013012 (2012).
14. C. Giunti, M. Laveder, Y. F. Li, Q. Y. Liu and H. W. Long, Phys. Rev. D **86**, 113014 (2012).
15. A. Mirizzi, G. Mangano, N. Saviano, E. Borriello, C. Giunti, G. Miele and O. Pisanti, Phys. Lett. B **726** (2013) 8.
16. S. Gariazzo, C. Giunti and M. Laveder, JCAP **1504** (2015) 04, 023.
17. S. Hannestad, I. Tamborra and T. Tram, JCAP **1207**, 025 (2012).
18. A. Mirizzi, N. Saviano, G. Miele and P. D. Serpico, Phys. Rev. D **86**, 053009 (2012).
19. N. Saviano, A. Mirizzi, O. Pisanti, P. D. Serpico, G. Mangano and G. Miele, Phys. Rev. D 87, **073006** (2013).
20. S. Hannestad, R. S. Hansen and T. Tram, *How Self-Interactions can Reconcile Sterile Neutrinos with Cosmology*, Phys. Rev. Lett. **112** (2014) 3, 031802.
21. B. Dasgupta and J. Kopp, *Cosmologically Safe eV-Scale Sterile Neutrinos and Improved Dark Matter Structure*, Phys. Rev. Lett. **112** (2014) 3, 031803.
22. N. Saviano, O. Pisanti, G. Mangano and A. Mirizzi, *Unveiling secret interactions among sterile neutrinos with big-bang nucleosynthesis*, Phys. Rev. D **90** (2014) 11, 113009.
23. A. Mirizzi, G. Mangano, O. Pisanti and N. Saviano, *Collisional production of sterile neutrinos via secret interactions and cosmological implications*, Phys. Rev. D **91** (2015) 025019.
24. M. Archidiacono, S. Hannestad, R. S. Hansen and T. Tram, *Cosmology with self-interacting sterile neutrinos and dark matter - A pseudoscalar model*, arXiv:1404.5915 [astro-ph.CO].

PLANCK 2015 RESULTS

S. HENROT-VERSILLE on behalf of the Planck collaboration
Laboratoire de l'Accélérateur Linéaire IN2P3-CNRS and Université de Paris-Sud XI, bat. 200 Centre scientique d'Orsay, F-91898 Orsay Cedex

The Planck 2015 cosmogical results are discussed with an emphasis on the improvements compared to the last data release, and on the methodology used to extract the parameters, both for the likelihood building and for the statistical method. As far as the base ΛCDM model is concerned, the implications of the cold dark matter density measurement in SUSY scenarios is illustrated. For the results on the extensions of ΛCDM, they are given for the neutrinos sector: the CMB being sensitive to the sum of the neutrino masses and to the effective number of relativistic degrees of freedom. Finally on the primordial gravitational waves side: implications in the strings parameters space derived from a limit set of the gravitational wave energy density is shown, as well as the limit on the tension over scalar ratio, r, coming from a combined analysis with BICEP.

1 Improvements, methodology and base ΛCDM results

The Planck mission has been launched in 2009 with the main objectives of measuring with an unprecedented accuracy the Cosmic Microwave Background (CMB) in an all-sky survey both in temperature and in polarisation. The satellite is composed of a 1.5m off-axis telescope at the focal plane of which are installed two instruments: the Low Frequency Instrument (LFI) measuring the CMB with HEMT in three frequency bands (30, 44 and 70 GHz), and the High Frequency Instrument (HFI) aiming at the measurement at higher frequencies (100, 143, 217, 353, 545 ad 857 GHz) with bolometers. Both instruments are sensitive to the polarisation: E-modes of the CMB are generated by Thomson scattering, while the B-modes are produced through two processes: the primordial tensor modes (i.e. primordial gravitational waves) and the lensing of the E-modes. While Planck was not designed to measure the B modes of the CMB, it does provide very important informations on the BB spectrum of the polarised dust (see section 2.2). A first round of results has been published in 2013 based on the first 14 months of the survey with the temperature data[1 2 3].

1.1 Improvements and spectra

The 2015 results[4] are based on the full Planck mission, including a first analysis of the polarisation data. Improvements have been made in the understanding of a remaining systematic effect due to the 4K cooler. The calibration discrepancy with the WMAP power spectra has been solved thanks to a better calibration procedure, and additionnal accuracy has been obtained in the beams characterisation. The main impact of these improvements is a reduction of both the statistical and systematical errors. In addition, while for the 2013 release, Planck did need the WMAP polarisation data at low multipole to constrain the cosmological parameters (mainly τ), the 2015 results are now fully based on Planck-only data (LFI+HFI). The resulting TT, TE and EE spectra are shown on figure 1, where the red line corresponds to the best fit cosmological

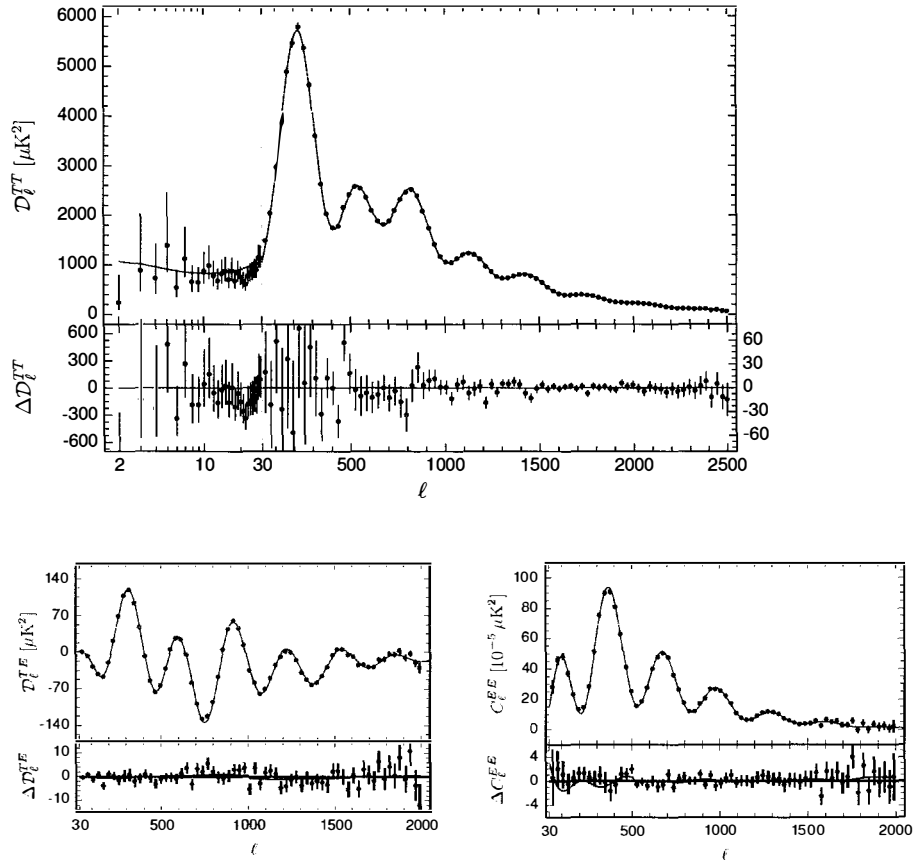

Figure 1 – Upper plot: temperature power spectrum, Lower plots: frequency averaged TE and EE spectra. The red lines correspond to the theoretical model for TT (upper), TE and EE (lower plots) computed using the Planck TT+lowP best fit corresponding to the upper plot.The error bars show $\pm 1\sigma$ errors.

parameters obtained with the temperature only data, showing that the polarisation spectra are already very well constrained by the cosmological information extracted from the temperature data.

1.2 Likelihood Building

To extract the cosmological parameters values from the Planck data, three likelihoods are used: a pixel-based one for the low multipoles (up to $\simeq 29$) that is built from low resolution maps of LFI (which is denoted lowP in the following), and a hybrid HFI likelihood using both a pixel based (for intermediate ℓ) and a spectra-based approach (for $\ell \geq 50$). This splitting is due to the expected statistical distribution of the C_ℓ which are assumed to be Gaussian for small angular scales, while the low ℓ regimes is driven by the cosmic variance. The high-ℓ likelihood

can therefore be written under the form:

$$-2\ln\mathcal{L} = \sum_{\substack{X,Y=T,E\\X',Y'=T,E}} \sum_{\substack{i,j=100..i\leq j\\ i',j'=100,i'\leq j'}}^{217} \sum_{\ell=\ell_{\min}^{X_iY_j}}^{\ell_{\max}^{X_iY_j}} \sum_{\ell'=\ell_{\min}^{X'_{i'}Y'_{j'}}}^{\ell_{\max}^{X'_{i'}Y'_{j'}}} \mathcal{R}_\ell^{X_iY_j} \left[\Sigma_{\ell\ell'}^{X_iY_j,X'_{i'}Y'_{j'}}\right]^{-1} \mathcal{R}_{\ell'}^{X'_{i'}Y'_{j'}}; \qquad (1)$$

where the first sum is over the temperature/polarisation components while the second sum deals with the frequencies, $\mathcal{R} = C_\ell - \hat{C}_\ell$ denotes the residual of the estimated cross-power spectrum (C_ℓ) with respect to the model ($\hat{C}_\ell$) and Σ is the full covariance matrix. In $\mathcal{R}$ is incorporated the theoretical expected distribution of the anisotropies of the CMB, that is computed using a Boltzman code (see section 1.3), but also a parameterisation of the foregrounds (dust, synchrotron, point sources, cosmic infrared background ...). This is a matrix which size is of the order of 26000x26000 elements.

1.3 Statistical method and base ΛCDM results

The base ΛCDM model is described by 6 parameters: the baryon density of the Universe $\Omega_b h^2$, the Cold Dark Matter (CDM) density $\Omega_{cdm} h^2$, the characteristic angular size of the CMB fluctuations (θ_{MC}), the optical depth to reionization (τ) and the amplitude and spectral index of the primordial spectrum ($\ln(10^{10}A_s)$ and n_s). The sum of the neutrino masses is fixed and assumed to be 0.06eV. Two approaches can be followed to extract their values from the likelihood: using Monte Carlo Markov Chains followed by a Bayesian analysis or performing a profile likelihood analysis. Both methods have been tested, using a different Boltzman code for the evolution of the Universe, giving a completely independent cross-checks of the obtained results: for instance the profile method makes use of the CLASS software [5]. They both give similar results as it is shown on the first two columns of table 1: the small descrepancy observed for the characteristic size of the CMB fluctuations coming from a slightly different definition in the Boltzman codes.

Table 1: Mean values and errors obtained for the cosmological parameters within the ΛCDM scenario for the Planck temperature and LowP likelihood using the MCMC analysis (first column), and the profile likelihood method (second column). The third column gives the results for the combination of temperature and polarized Planck data with lensing[6] and external datasets (see text for details).

Parameter	PlanckTT+LowP (MCMC)	PlanckTT+LowP (Profiles)	TT,TE,EE+lowP +lensing+ext (MCMC)
$\Omega_b h^2$	0.02222 ± 0.00023	0.02227 ± 0.00023	0.02230 ± 0.00014
$\Omega_{cdm} h^2$	0.1197 ± 0.022	0.1198 ± 0.0022	0.1188 ± 0.0010
$100\theta_{MC}$ or $100\theta_0$	1.04085 ± 0.00047	1.04184 ± 0.00044	1.04093 ± 0.00030
τ	0.078 ± 0.019	0.082 ± 0.020	0.066 ± 0.012
$\ln(10^{10}A_s)$	3.089 ± 0.036	3.098 ± 0.037	3.064 ± 0.023
n_s	0.9655 ± 0.0062	0.9663 ± 0.0063	0.9667 ± 0.0040

The parameters values and their errors are given in the last column of table 1 when the Planck likelihood described previously is combined with the lensing information and external datasets: the Baryon Acoustic Oscillations measurements [7], the Type Ia supernovae from the Joint Light curve Analysis [8], and the Hubble constant measurement as explained in [4].

1.4 CDM and SUSY

As an illustration of the implications of the CDM density measurement of Planck, figure 2 shows the favored area (the reddish, the more favored is the region) in the (M_2, M_1) and (μ, M_1) parameters spaces of a TeV-scale 13 parameters MSSM (Minimal SuperSymmetric Model)

SUSY model, where the minimum value of all squarks (except the stop) masses has been set to 2 TeV in order to be above the LHC present limits, M_3 is fixed to 2 TeV and $A_b = 0$. This SFitter[9] analysis[10] has been performed using a combination of cosmological and particle physics measurements (namely $\Omega_{cdm}h^2$ from Planck[3], the Higgs boson mass[11], the branching ratios of rare B decay[12], the top mass[13] and the anomalous moment of the muon[14] and the Xenon limit[15]). The pattern of the favored regions is mainly driven by the Higgs mass and the CDM measurement through the dark matter annihilations channels. Given the theoretical error on $\Omega_{cdm}h^2$ due to the extrapolation of the SUSY branching ratios which is of the order of 0.012 (to be compared to the statistical error from table 1), those analyses are already limited by the theory error.

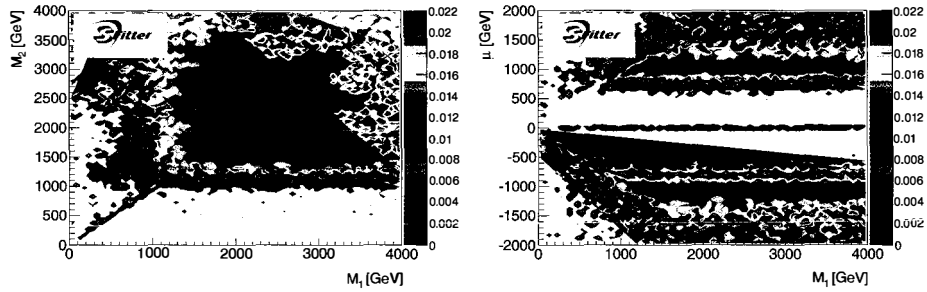

Figure 2 – Profile likelihood projection onto the (M_1, M_2) plane (left) and the (M_1, μ) plane (right).

2 ΛCDM extensions

A very complete set of ΛCDM extensions has been explored by the Planck collaboration[4]. This talk concentrates on the neutrino and the primordial gravitational wave (GW) background sectors.

2.1 The neutrino sector

The CMB is sensitive to the sum of the neutrino masses, impacting the first acoustic peak and the shape of the spectrum on small scales. The combined temperature information with LowP, the Planck lensing, and the external dataset, the obtained limit reaches $\sum(m_\nu) < 0.23$ eV at 95% CL. Combining those measurements with to-come oscillations results will probably allow to test the hierarchy in the near future.

CMB can also constrain the effective number of relativistic degrees of freedom $N_{\rm eff}$. Under the assumption that only the photons and the standard light neutrinos contribute to the radiation, this parameter is the effective number of neutrinos and is expected to be 3.046[16]. Any deviation from this value can be attributed to either sterile neutrino, axions[17,18], decay of non-relativistic matter[19], extra dimensions[20,21,22], early dark energy[23], asymmetric dark matter[24], or leptonic asymmetry[25], or even primordial gravitational waves[26]. The results are summarized in table 2 for temperature and polarisation, with and without BAO data. Within the obtained error, one cannot conclude of a convincing evidence for any extra relativistic component.

2.2 The primordial gravitational waves

Inflation predicts the existence of a background of gravitational waves (GW) or tensor modes fluctuations[27,28,29,30]. From the observations of the CMB, since those GW contribute to the

Table 2: N_{eff} limit at 95%CL obtained for different combinations of likelihoods including the Planck 2015 temperature (TT), and low multipoles polarisation (lowP). Illustrations of the impact of the use of high multipoles polarisation data (TE and EE) and BAO are also given.

3.13 ± 0.32	Planck TT +lowP
3.15 ± 0.23	Planck TT +lowP +BAO
2.99 ± 0.20	Planck TT,TE,EE +lowP
3.04 ± 0.18	Planck TT,TE,EE +lowP +BAO

anisotropies (both in temperature and linear polarisation), one can deduce constraints on related parameters such as their energy density, $\Omega_{GW}h^2$, and the tensor to scalar ratio, r .

from N_{eff}

Using the N_{eff} results, one can set a limit on the gravitational wave energy density through the relation [31,16]:

$$\Omega_{GW}h^2 \leq \frac{7}{8}(\frac{4}{11})^{4/3}(N_{eff} - 3.046)\Omega_\gamma \ , \qquad (2)$$

for which an analysis has been performed using profile likelihoods [32] with the 2013 Planck data (combined with the Wmap data at low ℓ, the BAO and the Lensing) and leads to $\Omega_{GW}h^2 < 3.8\ 10^{-6}$. Assuming the GW can be attributed to a network of cosmic strings, this result can be interpreted as exclusions limits in the strings parameters space as shown in figure 3 where is shown the new limit obtained for the small loop regime (with $p = 10^{-3}$) in the loop size vs. string tension space, pushing further the previous constraints. If the size of the loops is determined by gravitational back-reaction, string tension values greater than $\sim 4 \times 10^{-9}$ are excluded for a reconnection probability of 10^{-3}.

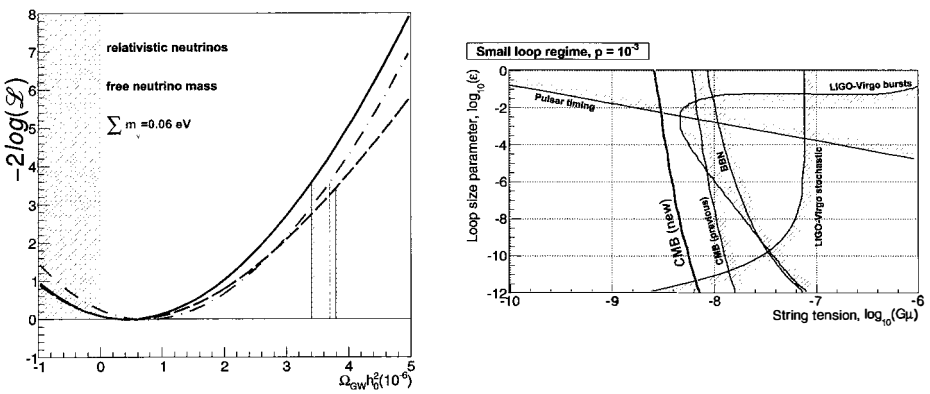

Figure 3 – Left hand side: $\Omega_{GW}h^2$ profile likelihood obtained with the full Planck+WP+highL+BAO+Lensing 2013 data set in three neutrino models: when they are considered to be massless (in black full lines), when $\sum m_\nu = 0.03$ eV (in red dashed and dotted lines) and when the neutrino mass is free to vary in the fit (blue dashed lines). Right hand side: constraints on cosmic string parameters $(G\mu, \epsilon)$ assuming the loops are small and fixing $p = 10^{-3}$. The new constraints are compared to previous ones [26].

from B modes

With the 2013 release, Planck published the best limit on the tensor modes using CMB alone[3] with $r < 0.11$ at 95%CL. In 2014, BICEP2, a low angular resolution experiment operating at the South Pole from 2010 and 2012, published[33] a B-mode excess measurement above the $r = 0$ lensed ΛCDM expectation for $0 \leq \ell \leq 150$. In 2014, Planck released two papers: one on the structure of the dust polarisation[34] and one on the frequency dependence[35] of this emission relevant to CMB studies. Consequently, a joint analysis[36] of both datasets has been performed showing that no significant evidence for primordial gravitational waves was found. An upper limit on the tension over scalar ratio has been deduced and gives $r < 0.12$ at 95%CL.

3 Conclusions

The Planck 2014 release includes a first release of all sky polarisation data from LFI (30, 44, 70 GHz) and HFI (353 GHz). The high quality data (CMB and Lensing) confirm the ΛCDM base model with an unprecedented accuracy and permit to test its extensions. The next Planck challenge is the release of cleaned HFI polarised data at 100, 143, and 217 GHz.

References

1. P. A. R. Ade *et al.* [Planck Collaboration], Astron. Astrophys. **571**, A15 (2014)
2. P. A. R. Ade *et al.* [Planck Collaboration], Astron. Astrophys. **571**, A17 (2014)
3. P. A. R. Ade *et al.* [Planck Collaboration], Astron. Astrophys. **571**, A16 (2014)
4. P. A. R. Ade *et al.* [Planck Collaboration], arXiv:1502.01589 [astro-ph.CO].
5. Lesgourgues, J. 2011, arXiv:1104.2932
6. P. A. R. Ade *et al.* [Planck Collaboration], arXiv:1502.01591 [astro-ph.CO].
7. Beutler, F., Blake, C., Colless, M., et al. 2011, Mon. Not. Roy. Astron. Soc. 416, 3017
   Anderson, L., Aubourg, E., Bailey, S., et al. 2012, Mon. Not. Roy. Astron. Soc. 427, 3435
   A. J. Ross, L. Samushia, C. Howlett, W. J. Percival, A. Burden and M. Manera, Mon. Not. Roy. Astron. Soc. **449**, 835 (2015)
8. Betoule, M., Marriner, J., Regnault, N., et al. 2013, Astronomy and Astrophysics, 552, A124
9. R. Lafaye, T. Plehn and D. Zerwas, arXiv:hep-ph/0404282;
   R. Lafaye, T. Plehn, M. Rauch and D. Zerwas, Eur. Phys. J. C **54**, 617 (2008).
10. S. Henrot-Versillé, R. Lafaye, T. Plehn, M. Rauch, D. Zerwas, S. Plaszczynski, B. Rouill d'Orfeuil and M. Spinelli, Phys. Rev. D **89**, no. 5, 055017 (2014)
11. ATLAS Collaboration, Science **338**, 1576 (2012).
12. R. Aaij *et al.* [LHCb Collaboration], Phys. Rev. Lett. **110**, 021801 (2013), CMS Collaboration, Phys. Rev. Lett. **111**, 101804 (2013), Particle Data Group `http://pdg.lbl.gov/2012/reviews/rpp2012-rev-b-meson-prod-decay.pdf`
13. Particle Data Group:
    `http://pdg.lbl.gov/2012/reviews/rpp2012-rev-standard-model.pdf`
14. Particle Data Group:
    `http://pdg.lbl.gov/2012/reviews/rpp2012-rev-g-2-muon-anom-mag-moment.pdf`
15. E. Aprile *et al.* [XENON100 Collaboration], Phys. Rev. Lett. **107**, 131302 (2011);
    E. Aprile *et al.* [XENON100 Collaboration], Phys. Rev. Lett. **109**, 181301 (2012)
16. Mangano G, Miele G, Pastor S, Pinto T, Pisanti O *et al.* 2005 *Nucl.Phys.* **B729** 221–234
17. Melchiorri A, Mena O and Slosar A 2007 *Phys.Rev.* **D76** 041303
18. Hannestad S, Mirizzi A, Raffelt G G and Wong Y Y 2010 *JCAP* **1008** 001
19. Fischler W and Meyers J 2011 *Phys.Rev.* **D83** 063520
20. Binetruy P, Deffayet C, Ellwanger U and Langlois D 2000 *Phys.Lett.* **B477** 285–291
21. Shiromizu T, Maeda K i and Sasaki M 2000 *Phys.Rev.* **D62** 024012

22. Flambaum V and Shuryak E 2006 *Europhys.Lett.* **74** 813–816
23. Calabrese E, Huterer D, Linder E V, Melchiorri A and Pagano L 2011 *Phys.Rev.* **D83** 123504
24. Blennow M, Fernandez-Martinez E, Mena O, Redondo J and Serra P 2012 *JCAP* **1207** 022
25. Caramete A and Popa L 2014 *JCAP* **1402** 012
26. Smith T L, Pierpaoli E and Kamionkowski M 2006 *Phys.Rev.Lett.* **97** 021301
Sendra I and Smith T L 2012 *Phys.Rev.* **D85** 123002
27. Grishchuk L 1975 *Sov. Phys. JETP* **40** 409–415
28. Starobinski A 1979 *JETP Lett.* **30** 682–686
29. Bar-Kana R 1994 *Phys.Rev.* **D50** 1157–1160 (*Preprint*
30. Easther R, Giblin John T J and Lim E A 2007 *Phys.Rev.Lett.* **99** 221301 (*Preprint*
31. Maggiore M 2000 *Phys.Rept.* **331** 283–367
32. Henrot-Versillé, S., Robinet, F., Leroy, N., et al. 2015, Classical and Quantum Gravity, 32, 045003
33. P. A. R. Ade *et al.* [BICEP2 Collaboration], Astrophys. J. **792**, 62 (2014) [arXiv:1403.4302 [astro-ph.CO]].
34. Planck Collaboration, Ade, P. A. R., Aghanim, N., et al. 2015, Astronomy and Astrophysics, 576, A104
35. Planck Collaboration, Ade, P. A. R., Alves, M. I. R., et al. 2015, Astronomy and Astrophysics,, 576, A107
36. P. A. R. Ade *et al.* [BICEP2 and Planck Collaborations], Phys. Rev. Lett. **114**, no. 10, 101301 (2015) [arXiv:1502.00612 [astro-ph.CO]].

LA THUILE
30
24
25
12
22
35
2
15
16
9
14

9.
Young Scientists Forum

SEARCH FOR A SM-LIKE HIGGS BOSON IN THE H-→ZZ-→ $\ell\ell q\bar{q}$ DECAY CHANNEL IN CMS

E. NAVARRO DE MARTINO
Dpto. de Investigación Básica, Av. Complutense, 40,
CIEMAT, Madrid, Spain

A search for a high mass standard-model-like Higgs boson decaying into two Z bosons with subsequent decay into two leptons and two quarks performed at CMS is presented. The analysis is based on 19.7 fb^{-1} of proton-proton collisions produced in LHC at $\sqrt{s} = 8$ TeV. Different categories are exploited in order to isolate hypothetical Higgs boson-like signals in the mass range up to 1 TeV. The data are interpreted in terms of a standard-model-like Higgs boson as well as an electroweak singlet, visible through the interference with the 125 GeV Higgs boson. No evidence of a signal is found and upper limits are set on the production cross section and other model parameters.

1 Introduction

The recent discovery of a scalar particle in the CMS and ATLAS experiments, h(125), with properties compatible with those predicted for the SM Higgs boson, opens the possibility of the existence of additional particles belonging to an enlarged scalar sector. In this context, CMS has exploited the decay channels of a heavy Higgs boson, H, decaying into a pair of gauge bosons, H-→ZZ and H-→WW. This work reports the search for such a heavy Higgs boson in the decay mode H-→ZZ-→ $\ell\ell q\bar{q}$ [1]. The analysis uses data from proton-proton collisions at $\sqrt{s} = 8$ TeV, collected by CMS during 2012, corresponding to an integrated luminosity of 19.7 fb^{-1}.

The process H-→ZZ-→ $\ell\ell q\bar{q}$ shows a clear signature in CMS, consisting of two high-momentum leptons and two high-momentum hadronic jets. The analysis suppresses the overwhelming background contribution, which has a cross section larger than 10^3 times that of the H boson. The dominant background is the production of a Z boson in association with one or more jets, Z+jets. Other relevant backgrounds stem from top quark pairs, decaying into two leptons, two b-quarks and 2 neutrinos, and the direct production of gauge boson pairs (ZZ, WW and WZ).

The mass of the two reconstructed leptons and the two hadronic jets, $m_{\ell\ell q\bar{q}}$, is used as the main discriminant between signal and background. This observable is completely reconstructed since all products are detected in CMS, allowing for a powerful discrimination. For masses above 200 GeV, the $m_{\ell\ell q\bar{q}}$ distribution has an exponentially falling shape, while a high mass Higgs boson signal would present the form of a resonance, centered in the H mass, m_H. The two main production mechanisms are considered in this work, gluon fusion (ggH) and vector boson fusion (VBF).

2 Data analysis

To reconstruct a heavy Higgs boson decaying into H-→ZZ-→ $\ell\ell q\bar{q}$, events with two opposite-sign same-flavor leptons and two hadronic jets are selected. They are recorded in CMS using

triggers requiring two high-momentum leptons, with transverse momentum p_T >17(8) GeV for the first(second) lepton.

Isolated leptons (electrons or muons), ℓ, are used to build leptonic Z boson candidates, Z-→ $\ell^+\ell^-$. To ensure high efficiency and good momentum determination the leading (subleading) lepton is required to have p_T >40(20) GeV. Muons inside the pseudorapidity range $|\eta| < 2.4$ are considered for analysis, while electrons are selected in the $|\eta| < 2.5$ range, excluding the transition region between the barrel and the endcap, $1.44 < |\eta| < 1.57$. Each Z→ $\ell^+\ell^-$ candidate is restricted to the dilepton mass range 76 GeV< $m_{\ell\ell}$ <106 GeV in order to reduce backgrounds not containing a real leptonic Z, such as the top quark pair production.

Hadronic jets, j, are reconstructed by clustering particles with the anti-k_T algorithm [2], with radius parameter R=0.5 (AK5 jets). To avoid double counting, AK5 jets overlapping with a reconstructed lepton are removed from the event. Each pair of jets is considered as a hadronic Z boson. The energy of the jet is corrected to account for the non-linear response of the calorimeter and detector noise. To ensure good momentum determination, AK5 jets are selected for analysis if they have p_T >30 GeV, after energy corrections. For high resonance masses, above 600 GeV, both quarks emerging from the collision are highly boosted. Therefore, the two jets originating from the quarks overlap. In this case, the requirement of having two distinct jets in the event leads to a drastically lost of efficiency. To recover the events with boosted jets, two leptons and a single merged jet, J, are required in the events. The merged jet is reconstructed using the Cambridge-Aachen algorithm [2] with radius parameter 0.8 (CA8 jets). Events with $p_T(\ell^+\ell^-)$ > 200 GeV and a CA8 jet with $p_T(J)$ >100 GeV are considered as boosted candidates. To improve the mass resolution a jet pruning algorithm is performed on the CA8 jets [3]. Additionally, the boosted candidates are required to have n-subjettiness ratio [3] of $\tau_{21} < 0.5$, in order to reject background from the hadronization of single quarks and gluons.

The dijet mass is restricted to the 71 GeV< m_{jj} <111 GeV region, largely reducing the Z+jets background. Additionally, a sideband region is defined for control purposes and background determination, requiring events with m_{jj} in the $[60, 71] \cup [111, 130]$ GeV region.

Since the Higgs boson is a scalar particle that carries no spin, five angles fully describe the decay kinematics[4]. A single angular discriminant is built from the probability ratio of the signal and background angular distributions. This discriminant is weakly correlated with the ZZ, $\ell\ell$ and $q\bar{q}$ masses, and provides a good discrimination power between background and signal.

Jets from the hadronic Z decay have higher b-quark content than jets coming from the Z+jets background. Thus, the parton flavor identification of the jets (b-tagging) is exploited to enhance the sensitivity to the signal. To identify jets coming from the b-quark hadronization, the Jet Probability algorithm [5] is used, either on both AK5 jets or on the subjets identified from the CA8 merged jet.

The $t\bar{t}$ background is especially relevant in events with two b-tagged jets, characterised by a significant amount of missing transverse energy, $\not{E}_T$. Signal events are, however, typically well-balanced. The $\not{E}_T$ significance [1], λ, is defined as the likelihood that the observed $\not{E}_T$ in an event comes from true $\not{E}_T$ and not from detector-related limitations. The loose requirement $\lambda < 10$ largely reduces the $t\bar{t}$ contamination.

The hadronic and leptonic reconstructed Z bosons are used to reconstruct Higgs boson candidates. To obtain the best sensitivity to the signal, the H candidates are classified into 14 exclusive categories, according to the following criteria. First, the event is separated by its production mechanism. If the event contains two forward AK5 jets ($|\eta| < 4.7$) with a pseudorapidity difference $\Delta\eta > 3.5$ and high invariant mass, $m_{jj} > 500$ GeV, it is identified as a VBF-like event. Otherwise, it is considered as a ggH-like event. The event sample is also split into the dielectron and dimuon categories. Events are further classified by the hadronic Z decay: if the event contains a suitable CA8 jet passing the $p_T > 100$ GeV and $\tau_{21} < 0.5$ criteria, it is categorized as a merged jet event. The remaining events constitute the dijet category. The ggH-like events are additionally split into three categories, according to the number of b-tagged

(sub)jets: the 0, 1, 2 btag categories.

3 Background and signal modeling

The main background of the analysis is Z+jets. Its shape is extracted from large simulated samples, generated using MadGraph. The sideband control region mentioned in Sec. 2 is used to constrain its relative normalization. The control sample is also used to correct small discrepancies in the transverse momenta spectrum of the ZZ system, using an event-by-event weight computed from data over simulation in the sideband [1].

In ggH-like events, the $t\bar{t}$ background is estimated from data using $e^{\pm}\mu^{\mp}$ events passing the selection described above, which are dominated by top quark pair production events. The validity of this data-driven method is confirmed using a top-enriched sample, requiring events outside the dilepton mass window and with high $\not\!\!E_T$ ($\lambda > 8$). In VBF-like events, the $t\bar{t}$ production plays a minor role and it is estimated using a simulated sample generated using PYTHIA.

The diboson production is a small contribution to the total background. It is estimated using simulated samples, generated using Pythia.

The signal is extracted from POWHEG simulated events. The signal simulation is modified to take into account the correct H lineshape, using the Complex-Pole Scheme approximation [6], important for Higgs bosons with masses above 400 GeV. Moreover, the effect of the interference with the gg-→ZZ [7] process is also included in the ggH simulation.

4 Results

Several systematic uncertainties, affecting both the shape and normalization of the signal and background, are included in the result. The most important systematic effects from lepton reconstruction are the muon momentum scale, electron energy scale and efficiency on lepton identification, isolation and triggering. From jet reconstruction the main uncertainties are: the jet energy scale, pile up, jet flavor tagging and boosted Z tagging. The following theoretical systematics are also considered: H production mechanism, signal cross section and branching fraction uncertainties. The background determination methods have the following uncertainties associated: Z+jets p_T(ZZ) correction uncertainty, the limited statistics in the $e^{\pm}\mu^{\mp}$ events and the diboson cross section uncertainty.

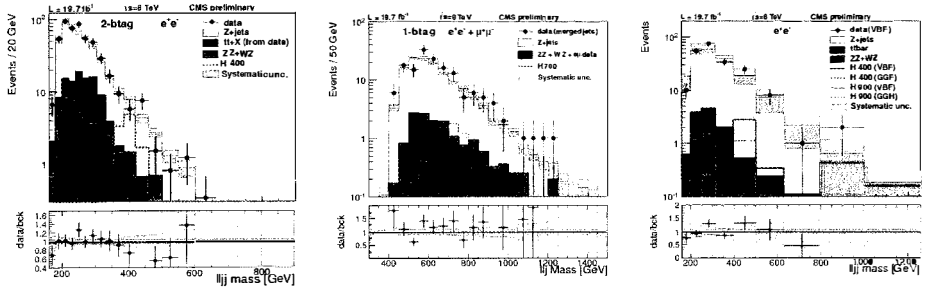

Figure 1 – $m_{\ell\ell qq}$ distribution for three categories of the analysis: dielectron dijet 2-btag (left), merged-jet 1-btag (center) and dielectron VBF (right).

The $m_{\ell\ell q\bar{q}}$ distribution is studied for the 14 categories separately. As an example, three of these spectra are shown in Fig. 1, which show an overall good agreement between data and expectation. The data are compared to the signal-plus-background and background-only distributions for 16 heavy SM-like Higgs boson mass hypothesis, ranging from 230 to 1000 GeV.

There is no significant deviation of data with respect to the background expectations. Based on $m_{\ell\ell q\bar{q}}$ distributions, a statistical maximum likelihood fit is performed simultaneously in the 14 categories of the analysis, using the modified frequentist CL_s approach[8], treating systematic uncertainties as nuisance parameters. As no significant deviation of data with respect to the background is observed, exclusion limits on the signal strength, $\mu = \sigma/\sigma_{SM}$, are calculated (Fig. 2, left). This analysis excludes the existence of a SM-like Higgs boson in the mass range between 305 and 744 GeV.

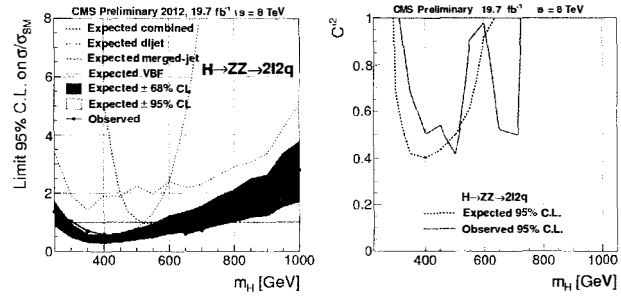

Figure 2 – (Left) 95% C.L. upper limits on the signal strength for the SM-like Higgs boson as a function of its mass. (Right) Observed and expected 95% C.L. exclusion limits on the C'^2 parameter of the electroweak singlet model as a function of the H mass, under the $B_{new} = 0$ hypothesis.

Additionally, the results are interpreted in a model with an additional electroweak singlet mixed with the SM Higgs boson. The couplings of the SM Higgs boson and the electroweak singlet are modified by the scale factors C and C' [1]. The unitarity is preserved by imposing the condition $C^2 + C'^2 = 1$. The signal strength μ' and width Γ' of the electroweak singlet are modified with respect to the SM predictions by:

$$\begin{aligned} \mu' &= C'^2 \cdot (1 - B_{new}) \\ \Gamma' &= \Gamma_{SM} \cdot \frac{C'^2}{1-B_{new}}, \end{aligned}$$

where B_{new} is the branching fraction of the electroweak singlet to decay modes not predicted by the SM. The analysis is performed similarly to the SM-like Higgs boson interpretation, but weighting the simulated samples to match the width and signal strength defined above. The expected and observed excluded region in the C'^2-m_H plane is shown in Fig. 2 (right), for the $B_{new} = 0$ case.

The results presented in this work are included in the CMS combination of H→ZZ and H→WW channels [9], which excludes the presence of a SM-like Higgs boson up to m_H =1 TeV and provides a strong constraint in the C'^2-B_{new} parameter space of the electroweak singlet interpretation.

References

1. CMS Collaboration, HIG-14-007, Geneva, 2014.
2. M. Cacciari *et al*, *JHEP* **04**, 005 (2008).
3. CMS Collaboration, *JHEP* **12**, 017 (2014).
4. Y. Gao *et al*, *Phys. Rev.* D **81**, 075022 (2010).
5. CMS Collaboration, *JINST* **8**, P04013 (2013).
6. S. Goria *et al*, *Nucl. Phys.* B **864**, 530-579 (2012).
7. G. Passarino, *JHEP* **08**, 146 (2012).
8. CMS Collaboration, *Phys. Lett.* B **710**, 26 (2012)
9. CMS Collaboration, Submitted to *JHEP* (2015) [arXiv:1504.00936].

ONE LOOP EFFECTIVE NONLINEAR LAGRANGIAN WITH A LIGHT H-BOSON

K. KANSHIN
Dipartimento di Fisica e Astronomia "G. Galilei", Università di Padova and INFN, Sezione di Padova, Via Marzolo 8, I-35131 Padua, Italy

We study one loop structure of the scalar sector of non-linear electroweak chiral Lagrangian (EWChL) with a light (composite) H-boson up to four derivatives. First, we introduce relevant Lagrangian terms in general parametrization of would-be Goldstone modes, taking into account potential and finite mass of the scalar. Then we compute 1-, 2-, 3- and 4-point functions and perform complete off-shell renormalization of the processes considered. On the way we found new divergencies involving also the H-boson which cannot be absorbed by the parameters of chiral invariant Lagrangian. We have demonstrated explicitly how these divergencies can be removed by field redefinition, and therefore proved that they are non-physical and give no contribution to the on-shell amplitudes. As a physical result renormalization group equations are derived to be used for future H-boson data analyses.

1 Introduction

As far as discovery of H-boson has not been accompanied by appearance of further light states one seeks for the solution of so-called hierarchy problem, or in simple words why is it so light? Possible solution, H-boson as pseudo-goldstone boson was proposed long time ago [1,2] and nowadays received further development [3,4]. EWChL is a model-independent way to describe the nonlinearly realized electroweak symmetry breaking enjoyed by those models. The present work is aimed to clarify the issues of consistency and completeness of the effective Lagrangian at loop level. It also prompts the expected size of coefficients of BSM effective operators.

2 The Lagrangian

We consider the scalar sector of the EWChL invariant under global $SU(2)_L \times SU(2)_R$ chiral transformation. It has been previously studied [5,6,7,8,9] and fully derived in [10,11]. In this work the notations of the last reference are adopted. The building blocks are the scalar field h and $\mathbf{V}_\mu = (D_\mu \mathbf{U})\mathbf{U}^\dagger$ with $\mathbf{U}(\boldsymbol{\pi})$ being the Goldstone bosons matrix corresponding to the $SU(2)_{EW} \times U(1)_Y \to U(1)_{em}$ symmetry breaking. Fields $\boldsymbol{\pi}$ denote triplet of "pions" – longitudinal components of the gauge bosons. In the scalar sector the Lagrangian can be sorted

according to the number of derivatives. In present work we go up to four derivatives:

$$\mathcal{L} = \mathcal{L}_0 + \mathcal{L}_2 + \mathcal{L}_4\,, \tag{1}$$

$$-\mathcal{L}_0 = V(h) = \mu_1^3\, h + \frac{1}{2} m_h^2 h^2 + \frac{\mu_3}{3!} h^3 + \frac{\lambda}{4!} h^4\,, \tag{2}$$

$$\mathcal{L}_2 = \frac{1}{2}\partial_\mu h \partial^\mu h\ \mathcal{F}_H(h) - \frac{v^2}{4}\mathrm{Tr}[\mathbf{V}_\mu \mathbf{V}^\mu]\ \mathcal{F}_C(h)\,, \tag{3}$$

$$\mathcal{L}_4 = \sum_i c_i \mathcal{P}_i\,, \tag{4}$$

where functions $\mathcal{F}_i(h) = 1 + 2a_i h/v + b_i h^2/v^2$ have to be treated as generic polynomials in h, coefficients a_i, b_i encode deviation of H-boson from the doublet structure; μ_1 is kept to cancel the tadpole divergence and set to zero after the renormalization. For explicit form of $\mathcal{P}_i$ – terms with four derivatives and their expansions in terms of $\boldsymbol{\pi}$ we refer to the original paper [12].

$\mathcal{L}_0, \mathcal{L}_2$ are used to derive both Feynman rules for the one loop calculation and correspondent counterterms, while $\mathcal{L}_4$ serves as a source of counterterms only.

Custodial symmetry breaking term with two derivatives has been omitted, since its coefficient is constrained to be small. Consequently for consistency at one loop level we do not need to take into account custodial breaking counterterms in $\mathcal{L}_4$ as we do not consider neither Yukawa terms nor gauge fields. Therefore all the Lagrangian terms preserve custodial symmetry.

When relations between bare and renormalized parameters are set, counterterm Lagrangian is derived straightforwardly.

2.1 General U–matrix parametrization

Requirement of $\mathbf{U}(\boldsymbol{\pi})$ having proper transformation properties under chiral symmetry group does not fix completely the functional dependence on $\boldsymbol{\pi}$ field [13]. We consider expansion of $\mathbf{U}$ up to $\boldsymbol{\pi}^4$, since higher order terms do not contribute at one loop. In this case it can be shown that the most general parametrization has the form:

$$\mathbf{U} = 1 - \frac{\boldsymbol{\pi}^2}{2v^2} - \left(\eta + \frac{1}{8}\right)\frac{\boldsymbol{\pi}^4}{v^4} + \frac{i(\boldsymbol{\pi}\boldsymbol{\tau})}{v}\left(1 + \eta\frac{\boldsymbol{\pi}^2}{v^2}\right) + O(\boldsymbol{\pi}^5), \tag{5}$$

where η is unphysical "parametrization parameter". All the physical results will be independent of η, therefore general parametrization is a useful tool for the sanity check of the expressions obtained.

Some particular choices of the parameter up to $O(\pi^5)$ correspond to the parametrizations widely used in literature: $\eta = 0$ gives the square root parametrization $\mathbf{U} = \sqrt{1 - \boldsymbol{\pi}^2/v^2} + i(\boldsymbol{\pi}\boldsymbol{\tau})/v$; $\eta = -1/6$ corresponds to the exponential one: $\mathbf{U} = \exp(i\boldsymbol{\pi}\cdot\tau/v)$.

3 Loops and divergencies

We performed explicit computation of divergent parts and renormalization of all possible 1-, 2-, 3- and 4-point one loop Green functions involving h and/or $\boldsymbol{\pi}$ off-shell external legs and found full agreement with previously known literature where only $\boldsymbol{\pi}$ legs and/or on-shell Green functions were considered [14,15,16,17]. We adopted dimensional regularization and off-shell minimal subtraction scheme as renormalization procedure.

By the off-shell renormalization we mean the matching of momenta structures with divergent coefficients generated by loops on the one hand with the momenta structures of the counterterms on the other. This procedure reveals the importance of some operators in $\mathcal{L}_4$ which are often disregarded in the literature. In our set up none of them can be disregarded or traded by equations of motion (EOM) unless full basis, including terms with fermions and gauge bosons is taken into account.

Finally, the divergent structures which cannot be matched with the any chiral invariant counterterms have been found, meaning this we call them non-invariant divergences (NIDs). However those divergencies do not vanish individually as the external legs are put on-shell, all the physical amplitudes, i.e. the combinations of all relevant Green functions giving divergent contribution to the process are NID free. The problem of NID in nonlinear σ model has been discussed long ago [18,19,20,21,22,14]. Generalizing the approach of [14] to the case of the light scalar in the spectrum we make pion field redefinition to remove NIDs from the final off-shell answer.

3.1 Field redefinition

It has been proved some time ago that Lagrangians related by local field redefinitions, even including ones with space-time derivatives are physically equivalent [23,24,25,26]. In other words if redefinition $\boldsymbol{\pi} \to \boldsymbol{\pi} f(\boldsymbol{\pi}, h, \partial_\mu)$ with $f(0) = 1$ changes Lagrangian according to $\mathcal{L} \to \mathcal{L} + \delta\mathcal{L}$, then $\delta\mathcal{L}$ piece is unphyscial. Our goal is to find a proper f to remove all NIDs. The minimal redefinition is:

$$\pi_i \to \pi_i \left(1 + \frac{\alpha_1}{2v^4}\boldsymbol{\pi}\Box\boldsymbol{\pi} + \frac{\alpha_2}{2v^4}\partial_\mu\boldsymbol{\pi}\partial^\mu\boldsymbol{\pi} + \frac{\beta}{2v^3}\Box h + \frac{\tilde{\gamma}_1}{2v^4}h\Box h + \frac{\gamma_2}{2v^4}\partial_\mu h\partial^\mu h\right) + \\ + \frac{\alpha_3}{2v^4}\Box\pi_i(\boldsymbol{\pi}\boldsymbol{\pi}) + \frac{\alpha_4}{2v^4}\partial_\mu\pi_i(\boldsymbol{\pi}\partial^\mu\boldsymbol{\pi}). \tag{6}$$

Treating $\delta\mathcal{L}$ as counterterm and matching it with NIDs we have obtained (Δ_ε is divergence):

$$\begin{aligned} \alpha_1 &= \left(9\eta^2 + 5\eta + \tfrac{3}{4}\right)\Delta_\varepsilon, & \beta &= -\left(\tfrac{3}{2} + 5\eta\right)a_C\Delta_\varepsilon, \\ \alpha_2 &= \left[1 + 4\eta + \left(\tfrac{1}{2} + \eta\right)a_C^2\right]\Delta_\varepsilon, & \gamma_1 &= \left(\tfrac{3}{2} + 5\eta\right)\left(2a_C^2 - b_C\right)\Delta_\varepsilon, \\ \alpha_3 &= 2\eta^2\Delta_\varepsilon, & \gamma_2 &= \left(\tfrac{3}{2} + 5\eta\right)\left(a_C^2 - b_C\right)\Delta_\varepsilon. \\ \alpha_4 &= 2\eta\left(a_C^2 - 1\right)\Delta_\varepsilon \end{aligned} \tag{7}$$

Note that choice of $\eta = -3/10$ set all mixed $\boldsymbol{\pi} - h$ terms to zero. To our knowledge this does not correspond to any parametrization considered in the literature before.

Thus we determined field redefinition which removes all the NIDs.

3.2 Renormalization Group Equations

After counterterms have been explicitly calculated it is straightforward to derive RGEs. For the resulting expressions we refer to the original paper [12]. It is worth mentioning that some of the terms in RGEs are weighted by large numerical factors, therefore even the couplings which are small at low energies can be enhanced to the large values by running to the high scales.

Acknowledgements

The work is supported by an ESR contract of the European Union network FP7 ITN INVISIBLES (Marie Curie Actions, PITN-GA-2011-289442), of MICINN, through the project FPA2012-31880. I also would like to thank the organizers of Rencontres de Moriond meeting for the great organization of the event.

References

1. D. B. Kaplan and H. Georgi, Phys. Lett. B **136** (1984) 183.
2. H. Georgi and D. B. Kaplan, Phys. Lett. B **145** (1984) 216.
3. K. Agashe, R. Contino and A. Pomarol, Nucl. Phys. B **719** (2005) 165 [hep-ph/0412089].
4. R. Contino, L. Da Rold and A. Pomarol, Phys. Rev. D **75** (2007) 055014 [hep-ph/0612048].
5. B. Grinstein and M. Trott, Phys. Rev. D **76** (2007) 073002 [arXiv:0704.1505 [hep-ph]].

6. R. Contino, C. Grojean, M. Moretti, F. Piccinini and R. Rattazzi, JHEP **1005** (2010) 089 [arXiv:1002.1011 [hep-ph]].
7. A. Azatov, R. Contino and J. Galloway, JHEP **1204** (2012) 127 [JHEP **1304** (2013) 140] [arXiv:1202.3415 [hep-ph]].
8. A. Azatov and J. Galloway, Int. J. Mod. Phys. A **28** (2013) 1330004 [arXiv:1212.1380].
9. I. Brivio, T. Corbett, O. J. P. boli, M. B. Gavela, J. Gonzalez-Fraile, M. C. Gonzalez-Garcia, L. Merlo and S. Rigolin, JHEP **1403** (2014) 024 [arXiv:1311.1823 [hep-ph]].
10. G. Buchalla, O. Cat and C. Krause, Nucl. Phys. B **880** (2014) 552 [arXiv:1307.5017 [hep-ph]].
11. R. Alonso, M. B. Gavela, L. Merlo, S. Rigolin and J. Yepes, Phys. Lett. B **722** (2013) 330 [Phys. Lett. B **726** (2013) 926] [arXiv:1212.3305 [hep-ph]].
12. M. B. Gavela, K. Kanshin, P. A. N. Machado and S. Saa, JHEP **1503** (2015) 043 [arXiv:1409.1571 [hep-ph]].
13. S. Weinberg, Phys. Rev. **166** (1968) 1568.
14. T. Appelquist and C. W. Bernard, Phys. Rev. D **23** (1981) 425.
15. R. L. Delgado, A. Dobado and F. J. Llanes-Estrada, JHEP **1402** (2014) 121 [arXiv:1311.5993 [hep-ph]].
16. D. Espriu, F. Mescia and B. Yencho, Phys. Rev. D **88** (2013) 055002 [arXiv:1307.2400 [hep-ph]].
17. R. L. Delgado, A. Dobado, M. J. Herrero and J. J. Sanz-Cillero, JHEP **1407** (2014) 149 [arXiv:1404.2866 [hep-ph]].
18. J. M. Charap, Phys. Rev. D **2** (1970) 1554.
19. D. I. Kazakov, V. N. Pervushin and S. V. Pushkin, Teor. Mat. Fiz. **31** (1977) 169.
20. D. I. Kazakov, V. N. Pervushin and S. V. Pushkin, Theor. Math. Phys. **31** (1977) 389 [J. Phys. A **11** (1978) 2093].
21. B. de Wit and M. T. Grisaru, Phys. Rev. D **20** (1979) 2082.
22. J. Honerkamp, Nucl. Phys. B **36** (1972) 130.
23. M. Ostrogradsky, Mémoire sur les équations différentielles relatives an probléme des isopérimétres,1850
24. C. Grosse-Knetter, Phys. Rev. D **49** (1994) 6709 [hep-ph/9306321].
25. S. Scherer and H. W. Fearing, Phys. Rev. D **52** (1995) 6445 [hep-ph/9408298].
26. C. Arzt, Phys. Lett. B **342** (1995) 189 [hep-ph/9304230].

SIGNATURES OF DYNAMICAL SCALARS

I. BRIVIO
Instituto de Física Teórica UAM/CSIC and Departamento de Física Teórica, Universidad Autónoma de Madrid, Cantoblanco, 28049 Madrid, Spain

Effective Lagrangians represent an important, model independent tool for studying physics beyond the Standard Model, via its impact on electroweak scale observables. In particular, two different effective descriptions may be appropriate, depending on how the electroweak symmetry breaking is realized at high energies: a linear effective Lagrangian is best suited in presence of linear dynamics, while a non-linear -chiral- one is more pertinent for scenarios featuring a non-linear realization. In this talk I will present a few examples of low-energy signals that differentiate the phenomenology of the two descriptions, thus providing a powerful insight into the nature of the Higgs boson.

1 Motivation

The discovery [1,2] at the LHC of a scalar resonance compatible with the Brout-Englert-Higgs boson (from here on just "Higgs boson", for brevity) represents the ultimate experimental proof supporting the Standard Model (SM) of fundamental interactions. At the same time, new physics is still expected to exist around the TeV scale in order to cure the theoretical inconsistencies that affect the SM and especially its scalar sector. From this point of view, the observation of the Higgs boson provides a new, unequaled window to shed light on the dynamics of spontaneous electroweak (EW) symmetry breaking (EWSB).

In particular, the viable UV completions of the SM can be classified into two main categories, depending on whether they rely on a linear or on a non-linear implementation of EWSB. In the former scenario the Higgs typically appears as an elementary particle, while in the latter framework it arises naturally as a "dynamical" -composite- state.

At energies around the EW scale, the impact of beyond-Standard Model (BSM) physics of either class can be described in a model-independent way by means of a Lorentz and gauge-invariant effective Lagrangian. More specifically, a linear effective Lagrangian is pertinent in scenarios with linearly realized EWSB, such as supersymmetric models, where the Higgs particle belongs to an $SU(2)_L$ doublet Φ and the new physics scale is $\Lambda \gg v$, being v the EW vacuum expectation value (vev). The linear effective expansion contains operators weighted by inverse powers of the cutoff scale Λ and the leading corrections to the SM Lagrangian have then canonical mass dimension $d = 6$ [13–16]. In dynamical Higgs scenarios, on the other hand, the Higgs particle is a composite field which happens to be a pseudo-goldstone boson (GB) of a spontaneously broken global symmetry. As a consequence, the most suitable effective Lagrangian for this scenario is a non-linear [17] or "chiral" one: a derivative expansion as befits the Goldstone boson dynamics. A typical example of this scenario are composite Higgs models [3–12].

The effective linear and chiral Lagrangians with a light Higgs are in general different: the latter is indeed more general, and contains the former as a special limit which can only be obtained imposing specific constraints by hand [18] or assuming peculiar dynamics at high

energies [19]. In this talk I present a few examples of signals that differentiate the two scenarios and that can thus provide powerful insights to the origin of the EWSB mechanism.

2 The effective non-linear Lagrangian for a light Higgs

The effective low-energy chiral Lagrangian for a light Higgs is written in terms of the SM fermions and gauge bosons and of two scalar fields: the SM GBs are described by a dimensionless unitary matrix [20–24] $\mathbf{U}(x) = e^{i\sigma_a \pi^a(x)/v}$, $\mathbf{U}(x) \to L\,\mathbf{U}(x)R^\dagger$, with L, R denoting respectively the $SU(2)_{L,R}$ global transformations of the scalar potential. The Higgs boson is represented by the singlet field h and its couplings are encoded in generic functions

$$\mathcal{F}_i(h) = 1 + 2a_i\frac{h}{v} + b_i\frac{h^2}{v^2} + \dots \tag{1}$$

that lack any $SU(2)_L$ structure: as often pointed out (e.g. refs. [25,26]), the resulting effective Lagrangian can describe many setups including that for a light SM singlet isoscalar.

In a phenomenological approach, the effective non-linear Lagrangian for a light Higgs can be written as $\mathscr{L}_{\text{chiral}} = \mathscr{L}_0 + \Delta\mathscr{L}$, where the leading order $\mathscr{L}_0$ is the SM Lagrangian and $\Delta\mathscr{L}$ describes any deviation from the SM due to the presence of strong-interacting new physics above the EW scale. The former term reads then

$$\begin{aligned}\mathscr{L}_0 =& \frac{1}{2}(\partial_\mu h)(\partial^\mu h) - \frac{1}{4}W^a_{\mu\nu}W^{a\mu\nu} - \frac{1}{4}B_{\mu\nu}B^{\mu\nu} - \frac{1}{4}G^a_{\mu\nu}G^{a\mu\nu} - V(h)\\ &- \frac{(v+h)^2}{4}\,\mathrm{Tr}[\mathbf{V}_\mu\mathbf{V}^\mu] + i\bar{Q}\not{D}Q + i\bar{L}\not{D}L\\ &- \frac{v+h}{\sqrt{2}}\left(\bar{Q}_L\mathbf{U}\mathbf{Y}_Q Q_R + \text{h.c.}\right) - \frac{v+h}{\sqrt{2}}\left(\bar{L}_L\mathbf{U}\mathbf{Y}_L L_R + \text{h.c.}\right)\,,\end{aligned} \tag{2}$$

where $\mathbf{V}_\mu \equiv (D_\mu\mathbf{U})\,\mathbf{U}^\dagger$ ($\mathbf{T} \equiv \mathbf{U}\sigma_3\mathbf{U}^\dagger$) is the vector (scalar) chiral field transforming in the adjoint of $SU(2)_L$. The covariant derivative is

$$D_\mu\mathbf{U}(x) \equiv \partial_\mu\mathbf{U}(x) + igW_\mu(x)\mathbf{U}(x) - \frac{ig'}{2}B_\mu(x)\mathbf{U}(x)\sigma_3\,, \tag{3}$$

with $W_\mu \equiv W^a_\mu(x)\sigma_a/2$ and B_μ denoting the $SU(2)_L$ and $U(1)_Y$ gauge bosons, respectively. In eq. (2), the first line describes the h and gauge boson kinetic terms, and the effective scalar potential $V(h)$. The second line describes the W and Z masses and their interactions with h, as well as the kinetic terms for GBs and fermions. Finally, the third line corresponds to the Yukawa-like interactions written in the fermionic mass eigenstate basis. A compact notation for the right-handed fields has been adopted, gathering them into doublets Q_R and L_R. $\mathbf{Y}_Q \equiv \mathrm{diag}\,(Y_U, Y_D)$ and $\mathbf{Y}_L \equiv \mathrm{diag}\,(Y_\nu, Y_L)$ are two 6×6 block-diagonal matrices containing the usual Yukawa couplings.

The term $\Delta\mathscr{L}$ includes all the effective operators with up to four derivatives allowed by Lorentz and gauge symmetries. In the bosonic (pure gauge, pure Higgs and gauge-h operators), CP even sector, to which we restrict in this talk[a], it can be decomposed as

$$\begin{aligned}\Delta\mathscr{L} =& c_B\mathcal{P}_B(h) + c_W\mathcal{P}_W(h) + c_G\mathcal{P}_G(h) + c_C\mathcal{P}_C(h) + c_T\mathcal{P}_T(h) + c_H\mathcal{P}_H(h) +\\ &+ c_{\Box H}\mathcal{P}_{\Box H}(h) + \sum_{i=1}^{26} c_i\mathcal{P}_i(h)\end{aligned} \tag{4}$$

where c_i are model-dependent coefficients, and the explicit form of the operators $\mathcal{P}_i(h)$ can be read from ref. [18].

[a] The bosonic CP odd sector is analyzed in [27], while a complete basis comprehensive of both bosonic and fermionic operators has been proposed in [28].

3 Phenomenology: signatures of non-linearity

In order to identify the phenomenological signatures that differentiate the linear form the non-linear EFTs, it is useful to compare the chiral set of operators (eq.(4)) with a complete basis of dimension six, bosonic, CP even linear operators. Here we choose the so-called HISZ linear basis [29,30] and we report the main results of the exhaustive analysis performed in refs. [18,31].

Exploiting the correspondence $\Phi = (v+h)/\sqrt{2}\mathbf{U}\,(0\ 1)^T$, it is possible to identify two main categories of discriminating effects:

1. Some couplings are predicted to be correlated in the linear parameterization, but receive contributions from independent operators in the non-linear description. For example, the linear term $\mathcal{O}_B = (ig'/2)B_{\mu\nu}D^\mu\Phi^\dagger D^\nu\Phi$ is set in correspondence with the combination of two non-linear terms:

$$\mathcal{O}_B \to \frac{ig'v^2}{16}B_{\mu\nu}\big[\mathrm{Tr}(\mathbf{T}[\mathbf{V}^\mu,\mathbf{V}^\nu])\mathcal{F}_2(h) + 2\,\mathrm{Tr}(\mathbf{T}\mathbf{V}^\mu)\partial^\nu\mathcal{F}_4(h)\big] = \frac{v^2}{16}\big[\mathcal{P}_2(h) + 2\mathcal{P}_4(h)\big]\,, \qquad (5)$$

   where $\mathcal{P}_2(h)$ contributes to the TGCs usually dubbed κ_Z and κ_γ, while $\mathcal{P}_4(h)$ introduces the anomalous HVV vertices $A_{\mu\nu}Z^\mu\partial^\nu h$ and $Z_{\mu\nu}Z^\mu\partial^\nu h$.

   In a linear scenario any departure of one of these couplings from its SM value is expected to be correlated with effects in the other three, since they all receive a contribution from $\mathcal{O}_B$ (obviating for the time being all the other possible operators). Moreover, the relative magnitude of such contributions is fixed by the structure of the covariant derivative $D_\mu\Phi$. In the most general non-linear framework, instead, no such correlation is present: deviations in $\{\kappa_Z, \kappa_\gamma\}$ are parameterized in terms of the coefficient c_2, while those in the two anomalous HVV vertices are proportional to c_4. This effect is due to the different gauge representation chosen in the two theories for the Higgs field: in the chiral formalism the Higgs particle h is treated as a gauge singlet, independent of the three SM GBs. As a consequence, this framework lacks the strong link between the couplings of the Higgs and those of the longitudinal gauge bosons, which in the linear realization is imposed by the doublet structure of the field Φ. A completely analogous analysis holds for another linear operator, $\mathcal{O}_W = (ig/2)\,D^\mu\Phi^\dagger W_{\mu\nu}D^\nu\Phi$, that contributes to the same TGV and HVV vertices as $\mathcal{P}_2(h)$, $\mathcal{P}_4(h)$ and corresponds to the chiral operators $\mathcal{P}_3(h)$ and $\mathcal{P}_5(h)$:

$$\mathcal{O}_W \to \frac{igv^2}{8}\big[\mathrm{Tr}(W_{\mu\nu}[\mathbf{V}^\mu,\mathbf{V}^\nu])\mathcal{F}_3(h) - 2\,\mathrm{Tr}(W_{\mu\nu}\mathbf{V}^\mu)\partial^\nu\mathcal{F}_5(h)\big] = \frac{v^2}{8}\big[\mathcal{P}_3(h) - 2\mathcal{P}_5(h)\big]\,. \qquad (6)$$

   In the event of some anomalous observation in either of the couplings mentioned above, the presence or absence of correlations would allow for direct testing of the nature of the Higgs boson. A preliminary global-fit analysis on the four parameters c_{2-5} was presented in ref. [18]. Analogous (de)correlation effects between couplings with different number of Higgs legs have been discussed in refs. [32, 33]. Finally, a more complex example, that involves the six chiral operators $\mathcal{P}_{\Box h}$, $\mathcal{P}_{6-10}$ is analyzed in ref. [31].

2. Some couplings appear only at higher order in the linear expansion, i.e. in linear operators of dimension $d \geq 8$, but are allowed as first-order corrections to the SM (i.e. at the four-derivatives level) in the non-linear description. This kind of signal arises as a consequence of the adimensionality of the $\mathbf{U}(x)$ matrix, which ensures that the GB contributions do not exhibit any scale suppression. This is in contrast with the linear description, where the light h and the three SM GBs are encoded into the scalar doublet Φ, with mass dimension one: in that case any insertion of Φ pays the price of a suppression factor $1/\Lambda$.

   As an example, the operator $\mathcal{P}_{14}(h) = g\varepsilon^{\mu\nu\rho\lambda}\,\mathrm{Tr}(\mathbf{T}\mathbf{V}_\mu)\,\mathrm{Tr}(\mathbf{V}_\nu W_{\rho\lambda})\mathcal{F}_{14}(h)$ contains the anomalous TGC $\varepsilon^{\mu\nu\rho\lambda}\partial_\mu W^+_\nu W^-_\rho Z_\lambda$, called g_5^Z in the parameterization of [34]. This coupling appears only at dimension 8 in the linear expansion. Therefore, if found to be

non-zero and comparable in size to other leading corrections to the SM, this effect would represent a smoking gun of non-linearity in the EWSB sector. Current limits on g_5^Z are derived from LEP data; however, the LHC has the potential to improve these bounds: the study presented in [18], based on the kinematical analysis of the process $pp \to W^{\pm}Z \to \ell'^{\pm}\ell^+\ell^-\not{E}_T$, shows that with a luminosity of 300 fb^{-1} at a c.o.m. energy of 14 TeV it is possible to measure g_5^Z at a level of precision comparable to that of the current constraints on dimension 6 linear operators.

Acknowledgments

My work is supported by an ESR contract of the European Union network FP7 ITN INVISIBLES (Marie Curie Actions, PITN-GA-2011-289442). I also acknowledge partial support of the Spanish MINECOs Centro de Excelencia Severo Ochoa Programme under grant SEV-2012-0249. and I thank the organizers of the Moriond conference for the kind invitation and for their efforts in organizing this enjoyable meeting.

References

1. G. Aad et al., *Phys. Lett.* B **716**, 1 (2012)
2. S. Chatrchyan *et al*, *Phys. Lett.* B **716**, 30 (2012)
3. D. B. Kaplan and H. Georgi, *Phys. Lett.* B **136**, 183 (1984)
4. D. B. Kaplan, H. Georgi, and S. Dimopoulos, *Phys. Lett.* B **136**, 187 (1984)
5. T. Banks, *Nucl. Phys.* B **243**, 125 (1984)
6. H. Georgi, D. B. Kaplan, and P. Galison, *Phys. Lett.* B **143**, 152 (1984)
7. H. Georgi and D. B. Kaplan, *Phys. Lett.* B **145**, 216 (1984)
8. M. J. Dugan, H. Georgi, and D. B. Kaplan, *Phys. Lett.* B **254**, 299 (1985)
9. K. Agashe, R. Contino, and A. Pomarol, *Nucl. Phys.* B **719**, 165 (2005)
10. R. Contino, L. Da Rold, and A. Pomarol, *Phys. Rev.* D **75**, 055014 (2007)
11. B. Gripaios, A. Pomarol, F. Riva, and J. Serra, *JHEP* **0904**, 070 (2009)
12. D. Marzocca, M. Serone, and J. Shu, *JHEP* **1208**, 013 (2012)
13. W. Buchmuller and D. Wyler, *Nucl. Phys.* B **268**, 621 (1986) *Nucl.Phys.*, B268:621, 1986.
14. B. Grzadkowski, M. Iskrzynski, M. Misiak, and J. Rosiek, *JHEP* **1010**, 085 (2010)
15. G.F. Giudice, C. Grojean, A. Pomarol, and R. Rattazzi, *JHEP* **0706**, 045 (2007)
16. I. Low, R. Rattazzi, and A. Vichi, *JHEP* **1004**, 126 (2010)
17. C. G. Callan, S. Coleman, J. Wess, and B. Zumino, *Phys. Rev.* **177**, 2247 (1969)
18. I. Brivio, T. Corbett, O.J.P. Éboli, M.B. Gavela *et al*, *JHEP* **1403**, 024 (2014)
19. R. Alonso, I. Brivio, B. Gavela, L. Merlo, and S. Rigolin, *JHEP* **1412**, 034 (2014)
20. T. Appelquist and C. W. Bernard, *Phys. Rev.* D **22**, 200 (1980)
21. A. C. Longhitano, *Phys. Rev.* D **22**, 1166 (1980)
22. A. C. Longhitano, *Nucl. Phys.* B **188**, 118 (1981)
23. F. Feruglio, *Int.J.Mod.Phys.* A **8**, 4937 (1993)
24. T. Appelquist and G.-H. Wu, *Phys. Rev.* D **48**, 3235 (1993)
25. B. Grinstein and M. Trott, *Phys. Rev.* D **76**, 073002 (2007)
26. R. Contino, C. Grojean, M. Moretti, F. Piccinini, and R. Rattazzi, *JHEP* **1005**, 089 (2010)
27. M.B. Gavela, J. Gonzalez-Fraile, M.C. Gonzalez-Garcia *et al*, *JHEP* **1410**, 44 (2014)
28. G. Buchalla, O. Catà, and C. Krause, *Nucl. Phys.* B **8800**, 552 (2014)
29. K. Hagiwara, S. Ishihara, R. Szalapski, and D. Zeppenfeld, *Phys. Rev.* D **48**, 2182 (1993)
30. K. Hagiwara, T. Hatsukano, S. Ishihara and R. Szalapski, *Nucl. Phys.* B **496**, 66 (1997)
31. I. Brivio, O.J.P. Éboli, M.B. Gavela, M.C. Gonzalez-Garcia, *et al*, *JHEP* **1412**, 004 (2014)
32. A. Azatov, R. Contino, and J. Galloway, *JHEP* **1204**, 127 (2012)
33. Gino Isidori and M. Trott, *JHEP* **1402**, 082 (2014)
34. K. Hagiwara, R.D. Peccei, D. Zeppenfeld, and K. Hikasa, *Nucl. Phys.* B **282**, 253 (1987)

Electroweak production and hadronic activity in Zjj events at CMS

Tom Cornelis
Department of Elementary Particle Physics
Universiteit Antwerpen, 2020 Antwerp, Belgium

The measurement of the electroweak production cross section of a Z boson in association with two jets in proton-proton collisions at $\sqrt{s} = 8$ TeV is presented. The results are based on a data sample recorded by the CMS experiment with an integrated luminosity of 19.7 fb^{-1}. The hadronic activity in these events is also studied, in particular in the rapidity interval between the two jets.

1 Introduction

In proton-proton collisions at the LHC, Vector Boson Fusion (VBF) happens when two electroweak vector bosons, radiated from a quark in each of the two colliding protons, interact with each other. The two quarks are typically scattered away from the beam line and inside the detector acceptance, where they reveal as hadronic jets. The distinctive feature of VBF processes is therefore the presence of two energetic forward-backward jets, separated by a large pseudorapidity interval $\Delta\eta_{jj}$, and a large dijet invariant mass M_{jj}. In this analysis, we aim to study the production of a Z-boson through the VBF process, with the Z decaying to a di-electron or dimuon pair. There are, however, other pure electroweak diagrams which result in the same final $lljj$ state: the Z-strahlung diagram and the multi-peripheral diagram in which a neutrino is exchanged between the two vector bosons. Those diagrams have similar features as the VBF diagram, and large negative interference effects occur between them. We therefore consider them as one signal process and refer to them as EW Zjj production, rather than VBF production. Diboson production is not considered as part of the signal, as those events have small dijet invariant mass and are therefore negligible in this analysis. The background is dominated by the Drell-Yan production of Zjj, through mixed electroweak and strong interactions, as shown in Figure 1. Another particular feature of the EW Zjj process, and more general VBF processes, is the absence of color exchange between the two tagging quarks. This leads to the expectation of low hadronic activity in the central part of the detector. This analysis is an important benchmark to cross-check and validate Higgs VBF measurements, but also serves as a probe for triple-gauge couplings, for searches beyond the standard model, and as a precursor to the measurement of elastic vector boson pair scattering.

2 Event selection and Drell-Yan background model

Events are selected by requiring a muon or electron pair with opposite charge, in which both leptons satisfy standard CMS quality and isolation criteria, a transverse momentum of at least 20 GeV and $|\eta| < 2.4$. The reconstructed dilepton mass is required to be within the 15 GeV of the nominal Z boson mass. The two leading particle-flow jets within $|\eta| < 4.7$ are selected as

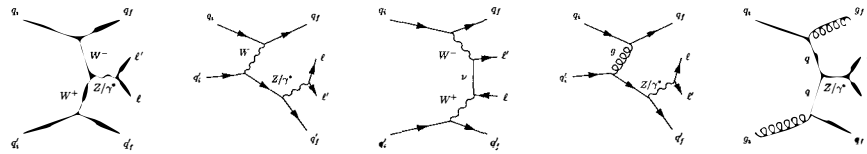

Figure 1 – Representative Feynman diagrams for $lljj$ production in proton-proton collisions. The signal comprise electroweak contributions: vector boson fusion (far left), Z-strahlung (center-left) and multi-peripheral production (center). The background is given by mixed electroweak and strong contributions (center-right and far-right).

the VBF jet candidates. Events with $p_T^{j_1,j_2} > 50, 30$ GeV and a dijet invariant mass exceeding 200 GeV are kept for further analysis. Both a simulation-based and data-driven model for the DY Zjj background are explored. The data-driven analysis makes use of γjj data to model the properties of the VBF jets, which are expected to be the similar for γjj and DY Zjj. The p_T of the photon is reweighted to the Z boson p_T in order to mitigate the differences induced by the specific Z or γ sample. The requirement $p_T(Z/\gamma) > 50$ GeV is applied to ensure a good photon purity. The data-driven analysis uses events with $M_{jj} > 450$ GeV.

3 Cross section measurement

Boosted decision trees (BDT) are constructed to acquire the best separation of signal and background. The BDTs make mostly use of dijet kinematics, including a quark-gluon discriminator for both signal jets which originate from quark jets as opposed to the background where both gluon and quark initiated jets are present. The simulation-based analysis also uses the kinematics of the Z boson. The electroweak $lljj$ cross section is extracted after fitting the data with the expected BDT output distributions for signal and background, shown in Figure 2. The obtained signal strength for the simulation based analysis is 0.84 ± 0.07 (stat) ± 0.19 (syst). This corresponds to a measured signal cross section, after extrapolation to the kinematic region $M_{ll} > 50$ GeV, $M_{jj} > 120$ GeV, $p_T^j > 25$ GeV and $|\eta_j| < 5$, of

$$\sigma(\mathrm{EW}lljj) = 174 \pm 15\ (\mathrm{stat}) \pm 40\ (\mathrm{syst})\ \mathrm{fb} \tag{1}$$

with the background-only hypothesis excluded with a significance greater than 5 σ. The signal strength is in good agreement with the 0.88 ± 0.16 (stat) ± 0.18 (syst) obtained by the data-driven analysis.

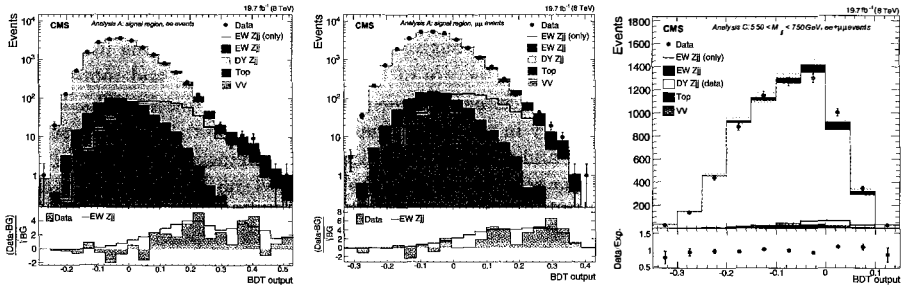

Figure 2 – Output for BDT distributions used for the signal cross section extraction: dielectron (left) and dimuon (center) events in the simulation based analysis, and dilepton events with $M_{jj} > 750$ GeV in the data driven analysis (right). The bottom panels show the difference of the data with respect to the background, as well as the expected signal contribution with respect to the background.

4 Hadronic activity in the pseudorapidity interval between the two tagging jets

A first study of the central hadronic activity bewteen the two tagging jets is done using soft track-jets. Soft track-jets are constructed using high purity tracks ($p_T > 300$ MeV), associated with the main interaction primary vertex and not associated with either of the two leptons or the two jets, which are clustered by the anti-k_T algorithm with distance parameter 0.5. The soft H_T variable represents the scalar sum of the p_T of the three leading-p_T soft track-jets in the pseudorapidity interval between the two leading jets. The dependence of the H_T as a function of M_{jj} and $\Delta\eta_{jj}$ is shown in Figure 3 and good agreement is observed between data and simulation.

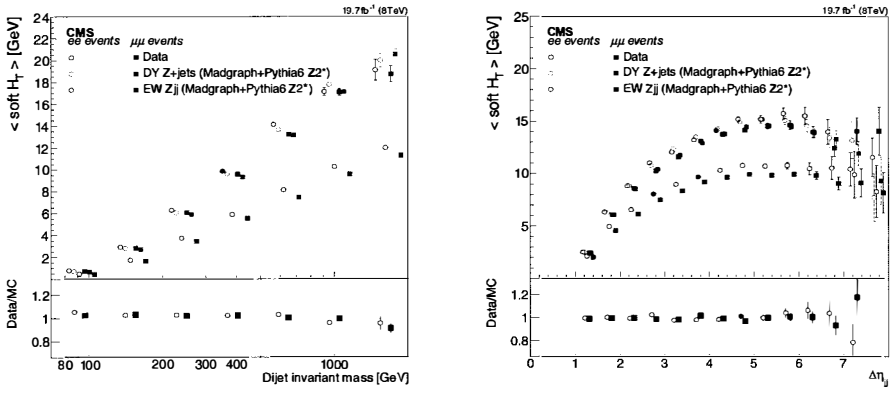

Figure 3 – Average soft H_T computed using the three leading soft-track jets reconstructed in the pseudorapidity interval $\Delta\eta_{jj}$ between the leading jets. The soft H_T is shown as a function of M_jj (left) and $\Delta\eta_{jj}$ for both the dielectron and dimuon channels. The ratios of data to expectation are given in the bottom panels. The expectations for the electroweak production of Zjj is shown separately.

The central hadronic activity is also studied in a high purity signal region ($M_{jj} > 1250$ GeV), with the use of additional jets ($p_T > 15$ GeV) found in the pseudorapidity interval between the two leading jets. Figure 4 shows the additional jet multiplicity and the scalar sum H_T of the p_T of these jets. The data, in agreement with the simulation, indicates the presence of the EW $lljj$ signal with suppressed emission of additional jets compared with the background.

Also excellent data-simulation agreement is found for the transverse momentum of the leading additional jet, which could be used to compute the efficiency of a central jet veto as shown in Figure 5. The gap fraction corresponds to the fraction of events for which the tested variable does not exceed a given threshold and is calculated for data, simulation and the data-driven prediction. Also the η_3^* variable, which is the pseudorapidity for the leading additional jet relative to the average of the tagging jets, is shown in Figure 5. The leading additional jet seems to be slightly more central in data, but poor statistical and other uncertainties prevents us from drawing further conclusions.

References

1. CMS Collaboration, *Eur. Phys. J.* C **75**, 66 (2015)

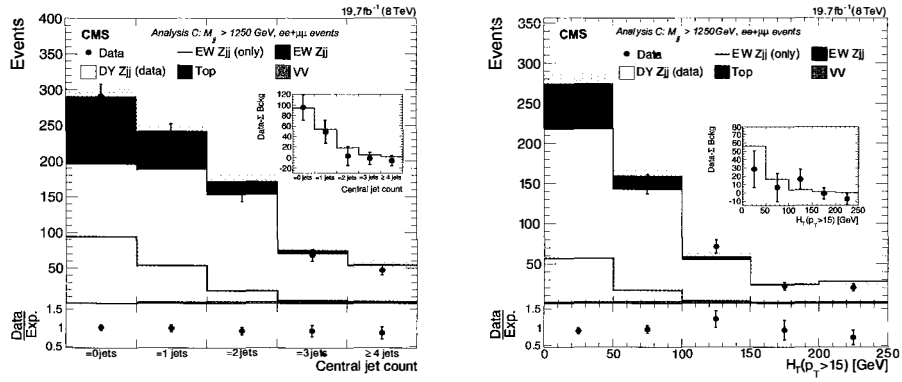

Figure 4 – Additional jet multiplicity (left) and corresponding H_T (right) within the pseudorapidity interval $\Delta\eta_{jj}$ between the leading jets in events with $M_{jj} > 1250$ GeV. The expected contributions of signal and backgrounds are shown stacked in the main panel, and are compared to the observed data. The inset shows the signal-only contribution which is compared to the residual data after subtraction of the backgrounds. The bottom panels show the ratio of data to expectation, including the uncertainties represented by the shaded bands.

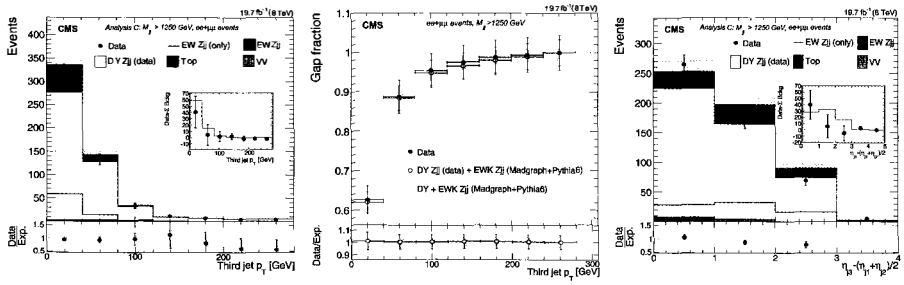

Figure 5 – The transverse momentum p_T (left) and η_3^* (right) of the leading additional jet within the pseudorapidity interval $\Delta\eta_{jj}$ between the leading jets in events with $M_{jj} > 1250$ GeV. The p_T of the leading additional jet is used to compute the gap fraction (center), shown for data and two different signal plus background predictions where DY Zjj is modelled either from γjj data or from simulation. The bottom panels show the ratio between the observed data and different predictions.

LIMITS AND FITS FROM SIMPLIFIED MODELS [a]

JORY SONNEVELD
Institute for Theoretical Particle Physics and Cosmology, RWTH Aachen, Sommerfeldstraße 16, 52074 Aachen, Germany

An important tool for interpreting LHC searches for new physics are simplified models. They are characterized by a small number of parameters and thus often rely on a simplified description of particle production and decay dynamics. We compare the interpretation of current LHC searches for hadronic jets plus missing energy signatures within simplified models with the interpretation within complete supersymmetric and same-spin models of quark partners. We found that the differences between the mass limits derived from a simplified model and from the complete models are moderate given the current LHC sensitivity. We conclude that simplified models provide a reliable tool to interpret the current hadronic jets plus missing energy searches at the LHC in a more model-independent way.

1 Introduction

In order to cover a broad part of BSM theories' parameter space, current searches for new physics at the LHC use simplified models motivated by supersymmetry to quantify their results [1,2,3,4,5]. Several recently developed tools [6,7,8,9] use simplified model results to enable one to test BSM theories against LHC results. It is thereby assumed that upper limits calculated from signal efficiencies for simplified models are mostly unchanged compared to more realistic, more complicated models that include more particles or even have particles with a different spin.

One simplified SUSY model for squarks called T2, shown in figure 1, includes light-flavor squarks, where squarks decay to a quark and a lightest supersymmetric stable particle (LSP). Gluinos (as all other supersymmetric particles except the LSP) are decoupled, and it is assumed that the quark partners produced in this simplified model are scalar particles.

We investigated the effects of adding a finite-mass gluino to the simplified model of squarks used by the experimental collaborations, as well as the influence on mass limits upon changing the spin assumption.

2 Production of squarks at the LHC

In the simplified model of squark production T2, since only light-flavor squarks are present, the blob in figure 1 is represented by the diagrams for squark-antisquark production shown in figure 3. Squark-antisquark production occurs also through the exchange of a gluino in the t-channel when a finite-mass gluino is present, as shown in figure 2. With the presence of this diagram, squark pair production and mixtures of left- and right-handed squark production occur as well. That is, instead of only $\tilde{q}_L\tilde{q}_L^*$ production, in the case of finite $m_{\tilde{g}}$ we also have $\tilde{q}_L\tilde{q}_L$, $\tilde{q}_L\tilde{q}_R$ and $\tilde{q}_L\tilde{q}_R^*$ production (as well as $R \leftrightarrow L$, with equal cross sections for mass-degenerate squarks).

[a] Talk presented at the 50th Rencontres de Moriond (EW session), La Thuile, March 18th 2015.

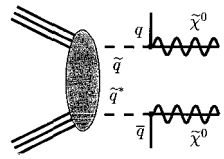

Figure 1 – The simplified model T2 for squark production at the LHC as used by the experimental collaborations. The gluino is decoupled.

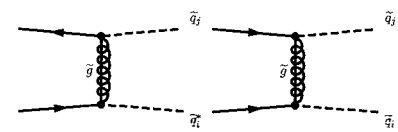

Figure 2 – The t-channel gluino diagrams that contribute only when finite-mass gluinos are present.

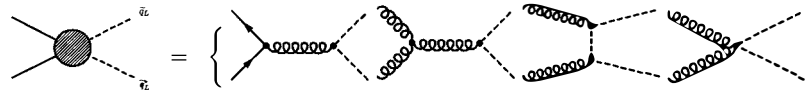

Figure 3 – The diagrams contributing to squark-antisquark production in the T2 supersymmetric simplified model.

3 Limits for MSSM-like squarks and LSPs

Adding a finite-mass gluino to the simplified model T2, we obtain what we named MSSM-like squark production. To investigate the differences in limits obtained from efficiencies of this model versus limits from efficiencies for the T2 model in the $m_{\tilde{q}}$-$m_{\tilde{\chi}_1^0}$ mass plane, we used two strongly excluding[6,9,10] SUSY analyses CMS-SUS-13-012[11] and CMS-SUS-12-028[12], which we named according to their main cut variables MHT and α_T, respectively.

Using a simulation of the 8 TeV LHC with `MadGraph 5`[13], `Pythia 6`[14], and `Delphes 3`[15,16] and our own implementations of the MHT and α_T analyses, we obtained efficiencies from which we calculated upper limits with `RooStatS`[21]. Upon comparing these upper limits with the NLO prediction for the cross section of the MSSM-like squark production that was calculated with `Prospino`[17], we obtained the red solid lines in figure 4[18].

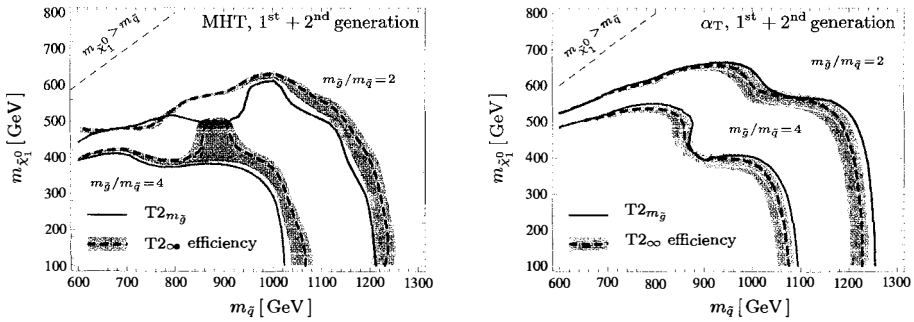

Figure 4 – 95% C.L. exclusion limits at the 8 TeV LHC derived from the full finite-mass gluino $T2_{m_{\tilde{g}}}$ model (red solid curves) and from the efficiencies for the T2, or $T2_\infty$ simplified model (blue dashed curves). The shaded regions around the curves denote the uncertainties due to scale variation ($\mu = m_{\tilde{q}}/2, 2m_{\tilde{q}}$).

Repeating the process for calculating limits from efficiencies for the T2 model, and again comparing with the NLO prediction for the cross section of the MSSM-like squark production, we obtained the blue dashed lines in figure figure 4. The blue and red exclusion lines are within the error for the theoretical prediction of the cross section of the full model exclusions.

Note that the limits shown are from our own simulations and for the most sensitive bin only that was calculated with a pure background hypothesis. CMS, on the contrary, combines bins; this procedure can be expected to yield stronger exclusion limits.

4 Production of same-spin quark partners at the LHC

When one assumes that in the T2 model same-spin instead of scalar quark partners are produced, the exclusion limits from the original scalar quark partner T2 model may change. In this case of same-spin KK quark production, the blob in figure 1 is for UED-like quark production represented by the three diagrams shown in figure 5.

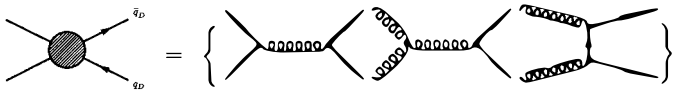

Figure 5 – The diagrams contributing to KK quark pair production for the UED equivalent of the T2 simplified model. D stands for doublet, as q_D is an SU(2) doublet quark.

As before for MSSM-like squark production, when the gluon partner mass is finite, an additional t-channel diagram appears, yielding not only KK quark-antiquark production $q_D\bar{q}_D$ (where D, S stand for SU(2) doublet and singlet, respectively), but also KK quark pair and mixed doublet and singlet production q_Dq_D, q_Dq_S and $q_D\bar{q}_S$ (and D $\leftrightarrow$ S with equal cross sections).

5 Limits for UED-like quarks and LKPs

We investigated the difference in limits obtained for a model of UED-like quark production from the full model, containing spin-1/2 quark partners and a finite gluon partner mass, as opposed to limits for this model from the SUSY-T2 model containing scalar quark partners and no gluon partner. Following the same procedure as described in the previous section, with now MadGraph 5 LO cross section predictions of UED-like quark production, we again find that the limit curves in the quark partner and LKP mass plane are close [19], as shown in figure 6. The α_T analysis slightly underestimates, whereas the MHT analysis overestimates the limits.

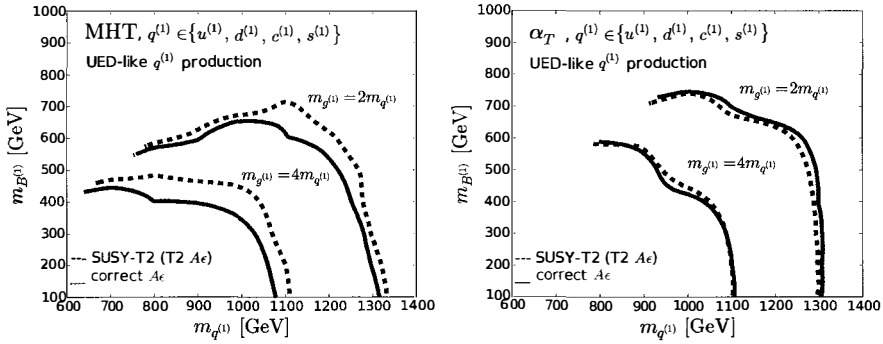

Figure 6 – Limits for a model of UED-like quark production at the 8 TeV LHC from the simplified SUSY-T2 model (blue dashed line) and from a simulation of the full model (red solid line). Same-spin quark partners are denoted $q^{(1)}$; the lightest KK particle is denoted $B^{(1)}$.

Note that for this model, the limits are up to 1300 GeV quark partner masses. Most experimental results up to now, however, present limits up to 1 TeV squark masses. This means that when a BSM model with higher cross sections than a simplified SUSY model is tested against those results, a tool like SModelS would not contain and hence not yield any results in these higher mass regions.

6 Conclusion

We conclude that simplified models are a good approximation for (1) more general models of supersymmetry and (2) same-spin models that are not originally described by these models[18,19].

Since recasting simplified model results is faster than a complete analysis of a specific model or calculating efficiencies for that model, they are ideal for performing global fits using e.g. a combination of `SModelS`[6,9] and `Fittino`[20].

Acknowledgments

I thank the organizers of the 50th Rencontres de Moriond for giving me the opportunity to present these results. I thank Lisa Edelhäuser, Michael Krämer, Jan Heisig, and Lennart Oymanns for collaboration on this work. I also thank Christian Autermann and Wolfgang Waltenberger for useful discussions and suggestions, as well as the Institute of High Energy Physics (HEPHY) for their hospitality. The work described here was supported by the Deutsche Forschungsgemeinschaft through the graduate school "Particle and Astroparticle Physics in the Light of the LHC".

References

1. N. Arkani-Hamed *et al.*, hep-ph/0703088 [HEP-PH].
2. J. Alwall, P. Schuster and N. Toro, Phys. Rev. D **79**, 075020 (2009) [arXiv:0810.3921 [hep-ph]].
3. D. Alves *et al.* [LHC New Physics Working Group], J. Phys. G **39**, 105005 (2012) [arXiv:1105.2838 [hep-ph]].
4. D. S. M. Alves, E. Izaguirre and J. G. Wacker, JHEP **1110**, 012 (2011) [arXiv:1102.5338 [hep-ph]].
5. S. Chatrchyan *et al.* [CMS Collaboration], Phys. Rev. D **88**, no. 5, 052017 (2013) [arXiv:1301.2175 [hep-ex]].
6. S. Kraml *et al.*, Eur. Phys. J. C **74**, 2868 (2014) [arXiv:1312.4175 [hep-ph]].
7. M. Drees *et al.*, Comput. Phys. Commun. **187**, 227 (2014) [arXiv:1312.2591 [hep-ph]].
8. M. Papucci, K. Sakurai, A. Weiler and L. Zeune, Eur. Phys. J. C **74**, no. 11, 3163 (2014) [arXiv:1402.0492 [hep-ph]].
9. S. Kraml *et al.*, arXiv:1412.1745 [hep-ph].
10. W. Beenakker, R. Hopker, M. Spira and P. M. Zerwas, Nucl. Phys. B **492**, 51 (1997) [hep-ph/9610490].
11. S. Chatrchyan *et al.* [CMS Collaboration], JHEP **1406**, 055 (2014) [arXiv:1402.4770 [hep-ex]].
12. S. Chatrchyan *et al.* [CMS Collaboration], Eur. Phys. J. C **73**, no. 9, 2568 (2013) [arXiv:1303.2985 [hep-ex]].
13. J. Alwall *et al.*, JHEP **1407**, 079 (2014) [arXiv:1405.0301 [hep-ph]].
14. T. Sjostrand, S. Mrenna and P. Z. Skands, JHEP **0605**, 026 (2006) [hep-ph/0603175].
15. J. de Favereau *et al.*, JHEP **1402**, 057 (2014) [arXiv:1307.6346 [hep-ex]].
16. M. Cacciari, G. P. Salam and G. Soyez, Eur. Phys. J. C **72**, 1896 (2012) [arXiv:1111.6097 [hep-ph]].
17. W. Beenakker, R. Hopker and M. Spira, hep-ph/9611232.
18. L. Edelhäuser, J. Heisig, M. Krämer, L. Oymanns and J. Sonneveld, JHEP **1412**, 022 (2014) [arXiv:1410.0965 [hep-ph]].
19. L. Edelhäuser, M. Krämer and J. Sonneveld, JHEP **1504** 146 (2015) [arXiv:1501.03942 [hep-ph]].
20. P. Bechtle *et al.*, PoS EPS **-HEP2013**, 313 (2013) [arXiv:1310.3045 [hep-ph]].
21. G. Schott for the RooStats Team, (2012) [arXiv:1203.1547 [physics.data-an]].

SEARCH FOR NEW LIGHT GAUGE BOSONS IN HIGGS DECAYS TO FOUR-LEPTON EVENTS AT $\sqrt{s} = 8$ TEV WITH THE ATLAS DETECTOR

DANIELA K. PAREDES HERNANDEZ
On behalf of the ATLAS Collaboration

Laboratory of Nuclear and Particle Physics, Aristotle University of Thessaloniki, 54124 Thessaloniki, Greece

This study presents a search for Higgs bosons decaying to four leptons via one or two light exotic gauge bosons Z_d, $H \to ZZ_d \to 4\ell$ and $H \to Z_dZ_d \to 4\ell$. The search uses the data taken in pp collisions with the ATLAS detector at the LHC at $\sqrt{s} = 8$ TeV. The observed data are well described by the Standard Model prediction. Upper bounds on the branching ratios of $H \to ZZ_d \to 4\ell$ and $H \to Z_dZ_d \to 4\ell$, relative to the branching ratio of $H \to 4\ell$ and to the Standard Model branching ratio of $H \to ZZ^* \to 4\ell$ respectively, are set as a function of the mass of the exotic vector boson at 95% confidence level.

1 Introduction

Some models Beyond the Standard Model (BSM) include dark sector states that use the Higgs boson as a portal to look for New Physics [1,2,3]. These kinds of models add a $U(1)_d$ gauge symmetry which introduces a new gauge field Z_d with kinetic mixing ϵ with the hypercharge gauge boson and an additional Higgs boson with mass mixing κ leading to a new Higgs doublet. This dark sector can be inferred either from deviations from the Standard Model (SM) predicted rates or decays through exotic intermediate states. This opens the possibility of processes such as Higgs decays to dark vector bosons in four-leptons events, $H \to ZZ_d \to 4\ell$ and $H \to Z_dZ_d \to 4\ell$ (see Fig. 1), where Z_d is a BSM light gauge boson, and whose existence is motivated by Dark Matter candidate searches.

This study presents a search for Higgs bosons decaying to four leptons via one or two Z_d bosons using the data taken in pp collisions with the ATLAS experiment [4] at the CERN LHC at $\sqrt{s} = 8$ TeV. The search uses a dataset corresponding to around 20 fb^{-1}. Same-flavor decays of the Z and Z_d bosons to electron and muon pairs are considered, giving the final states of $4e$, $2e2\mu$, $2\mu2e$ and 4μ. The search is restricted to the mass range where the Z_d from the decay of the Higgs boson is on-shell, i.e. 15 GeV $< m_{Z_d} < m_H/2$, where $m_H = 125$ GeV. Detailed descriptions of the searches of $H \to ZZ_d \to 4\ell$ and $H \to Z_dZ_d \to 4\ell$ are given in Section 2 and Section 3, respectively. Finally, the conclusions are presented in Section 4.

2 $H \to ZZ_d \to 4\ell$

2.1 Search strategy

The $H \to ZZ_d \to 4\ell$ search uses the same sample of 4ℓ events as used in Ref.[5]. This collection of events is referred to as the 4ℓ sample. The invariant mass of the same-flavor opposite-sign (SFOS) pair closest to the value of Z-boson mass of 91.2 GeV is denoted as m_{12}. The invariant

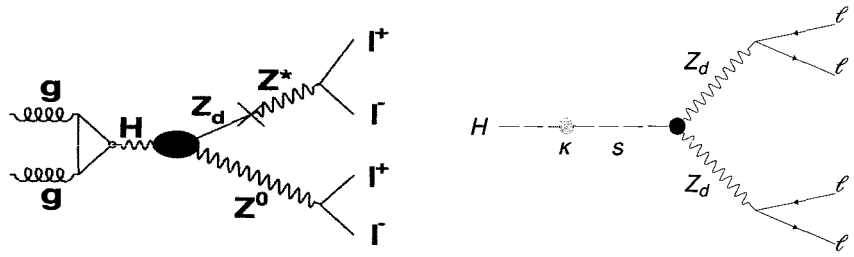

Figure 1 – Left: Higgs decay into an SM Z boson and a hidden or dark sector Z_d boson, where the Z_d is kinetically mixed with an (off-shell) Z^*. Subsequently the SM Z and Z^* bosons decay to two leptons each. Right: Exotic Higgs decay to four leptons induced by intermediate dark vector bosons via mixing between the SM Higgs boson H and the dark sector Higgs boson S (Higgs portal)[8].

mass of the remaining dilepton pair is defined as m_{34}. The $H \to 4\ell$ yield is determined by subtracting the relevant backgrounds from the 4ℓ sample as shown in Eq. 1:

$$n(H \to 4\ell) = n(4\ell) - n(ZZ^*) - n(t\bar{t}) - n(Z + \text{jets}) \equiv N \tag{1}$$

Backgrounds from WW, WZ, ZJ/ψ and $Z\Upsilon$ are negligible and not considered.

The search is performed by inspecting the m_{34} mass spectrum, looking for a local excess consistent with the decay of a narrow Z_d resonance. This is done through a template fit of the m_{34} distribution, using histogram-based templates of the $H \to ZZ_d \to 4\ell$ signal and background. The pre-fit signal and the $H \to ZZ^* \to 4\ell$ background event yields, are set equal to the $H \to 4\ell$ observed yield given by Eq. 1. In the absence of a significant observed excess (signal), the search is used to constrain the relative branching ratio R_B, defined as:

$$R_B = \frac{BR(H \to ZZ_d \to 4\ell)}{BR(H \to 4\ell)} = \frac{BR(H \to ZZ_d \to 4\ell)}{BR(H \to ZZ_d \to 4\ell) + BR(H \to ZZ^* \to 4\ell)}. \tag{2}$$

A measurement of R_B can be obtained from a likelihood function ($\mathcal{L}$), defined as a product of Poisson probability densities ($\mathcal{P}$) in each bin (i) of the m_{34} distribution:

$$\mathcal{L}(\rho, \mu_H, \nu) = \prod_{i=0}^{N\text{bins}-1} \mathcal{P}(n_i^{\text{obs}} | n_i^{\text{exp}}) = \prod_{i=0}^{N\text{bins}-1} \mathcal{P}(n_i^{\text{obs}} | \mu_H \times (n_i^{Z^*} + \rho \times n_i^{Z_d}) + b_i(\nu)), \tag{3}$$

where μ_H is the normalization of the $H \to ZZ^* \to 4\ell$ background, ρ the parameter of interest related to the $H \to ZZ_d \to 4\ell$ normalization and $\rho \times \mu_H$ the normalization of the $H \to ZZ_d \to 4\ell$ signal. ν represents the systematic uncertainties on the background estimates that are treated as nuisance parameters, and Nbins the total number of bins of the m_{34} distribution. The upper bound on ρ is obtained from the binned likelihood fit to the data, and used in Eq. 2 to obtain R_B, taking into account the relative detector acceptances ($\mathcal{A}$) and reconstruction efficiencies (ε) of the $H \to ZZ_d \to 4\ell$ to $H \to ZZ^* \to 4\ell$ events, defined by the parameter $C = \frac{\mathcal{A}_{ZZ_d} \times \varepsilon_{ZZ_d}}{\mathcal{A}_{ZZ^*} \times \varepsilon_{ZZ^*}}$. Thus,

$$R_B = \frac{\rho \times \mu_H \times N}{\rho \times \mu_H \times N + C \times \mu_H \times N} = \frac{\rho}{\rho + C}. \tag{4}$$

2.2 Event selection

Events are selected by requiring two pairs of SFOS leptons. The value of m_{12} is required to be between 50 GeV and 106 GeV. The value of m_{34} is required to be in the range 12 GeV $\leq m_{34} \leq$ 115 GeV. The four-lepton invariant mass, $m_{4\ell}$, is required to be in the range 115 $< m_{4\ell} <$ 130 GeV. The events are grouped into four channels based on the flavors of the reconstructed leptons: $4e$, 4μ, $2e2\mu$ and $2\mu2e$.

2.3 Results

The consistency of the data with the signal-plus-background and background-only hypotheses is tested with a profile-likelihood test statistic with the CL_s modified frequentist formalism [6,7]. Separate fits are performed for different m_{Z_d} hypotheses, and no significant deviation from SM expectations is observed.

The asymptotic approximation [7] is used to estimate the exclusion limits on ρ. The relative branching ratio R_B as a function of the m_{Z_d} is extracted using Eqs. 2 and 4. The 95% CL upper limit on R_B is shown in Fig. 2 for the combination of all four final states.

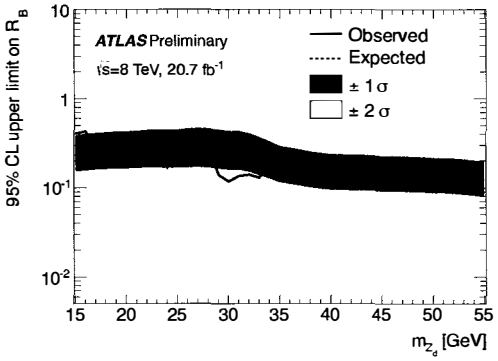

Figure 2 – The 95% CL upper limits on the relative branching ratio, R_B, as a function of m_{Z_d} [8].

3 $H \to Z_d Z_d \to 4\ell$

3.1 Search strategy

The search assumes that both Z_d particles coming from the Higgs decay have exactly the same mass. The small mass difference between the two SFOS pairs of the selected quadruplet is exploited in order to perform a counting experiment. In the absence of a significant observed excess, upper bounds on the signal strength parameter μ_d, defined as:

$$\mu_d = \frac{\sigma \times BR(H \to Z_d Z_d \to 4\ell)}{[\sigma \times BR(H \to ZZ^* \to 4\ell)]_{\rm SM}}, \tag{5}$$

are set, as a function of the mass of the dark vector boson.

3.2 Event selection

Events with at least four selected leptons are kept. All possible combinations of four leptons containing two SFOS pairs are formed. Among all the different quadruplets, only one is selected which minimizes the mass difference $\Delta m = |m_{12} - m_{34}|$, where m_{12} and m_{34} are the invariant masses of the first and second pairs, respectively. The mass difference Δm is expected to be minimal for the signal since the two dilepton systems should have invariant masses consistent with the same m_{Z_d}. The events are grouped into three channels: $4e$, 4μ, $2e2\mu$. The signal region (SR) is defined by three final requirements:

1. $115 < m_{4\ell} < 130$ GeV, where $m_{4\ell}$ is the invariant mass of the four leptons;
2. Z, J/ψ and Υ-vetos on all SFOS pair associations in the selected quadruplet.
3. $|m_{Z_d} - m_{2\ell}| < \delta m$, with $\delta m = 5/3/4.5$ GeV for the $4e/4\mu/2e2\mu$ final states respectively.

3.3 Results

After the event selection, no significant excess of events has been found. Therefore, upper bounds on the signal strength parameter μ_d are set as a function of the hypothesized m_{Z_d}. A maximum likelihood fit to the number of data and expected signal and background events is used to compute the limits, following the CL_s modified frequentist formalism [6] with the profile likelihood test statistic [7]. The 95% CL upper limits on μ_d are shown in Fig. 3 for the combination of the three different final states.

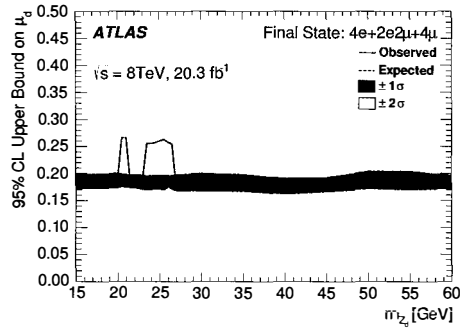

Figure 3 – The 95% CL upper bound on the signal strength μ_d parameter as a function of m_{Z_d} [8].

4 Conclusions

Two searches with the ATLAS detector in the 4-lepton channel for an exotic gauge boson, Z_d, that couples to the discovered Higgs boson (at a mass around 125 GeV), have been presented.

For the $H \to ZZ_d \to 4\ell$ search, exclusion limits on R_B have been estimated for the combination of all the final states. For $R_B > 0.4$ (observed), the entire mass range of $15 < m_{Z_d} < 55$ GeV is excluded with the current luminosity, at 95% CL.

For the $H \to Z_d Z_d \to 4\ell$ search, one data event is observed in the $4e$ channel passing the SR selection, consistent with $m_{Z_d} \sim 25$ GeV and with a significance of 1.70 σ. Another data event is observed in the 4μ channel, consistent with $m_{Z_d} \sim 20$ GeV and with a significance of 1.65 σ. No significant excess of events has been observed. Therefore, upper bounds on μ_d have been set for the mass range of $15 < m_{Z_d} < 60$ GeV using the combination of all final states.

Acknowledgements

This research has been co-financed by the European Union (European Social Fund ESF) and Greek national funds through the Operational Program "Education and Lifelong Learning" of the National Strategic Reference Framework (NSRF) - Research Funding Program: Aristeia. Investing in knowledge society through the European Social Fund.

References

1. D. Curtin *et al*, *JHEP* **2**, 157 (2015).
2. D. Curtin *et al*, *Phys. Rev.* D **90**, 075004 (2014).
3. H. Davoudiasl *et al*, *Phys. Rev.* D **85**, 115019 (2012).
4. ATLAS Collaboration, *JINST* **3**, S08003 (2008)
5. ATLAS Collaboration, *Phys. Lett.* B **726**, 88-119 (2013).
6. A. L. Read, *J. Phys. G* **28**, 2693-2704 (2002).
7. G. Cowan *et al*, *Eur. Phys. J. C* **71**, 1554 (2011).
8. ATLAS Collaboration, ATLAS-CONF-2015-003, https://cds.cern.ch/record/2002118/.

DARK MATTER PRODUCED IN ASSOCIATION WITH TOP QUARK PAIR

D. PINNA
on behalf of the CMS Collaboration
Department of Physics, University of Zurich, 190 Winterthurerstrasse, 8057 Zurich, Switzerland

A search for dark matter produced in association with a top quark pair is presented. The search is performed using 19.7fb^{-1} of proton-proton collisions recorded at a center of mass energy of 8 TeV with the CMS detector at the LHC. The signature investigated is top quark pairs in the semi-leptonic final state plus missing transverse energy. This work focuses in particular on dark matter production through scalar interaction where a proportionality to the quark mass is expected.

1 Introduction

Astrophysical studies provide precise information about the presence of dark matter (DM) in our universe and its abundance [1]. These observations cannot be included into the standard model (SM), which is able to describe only the visible matter, which makes up 4% of the mass of the universe. Dark matter instead accounts for about 24% of the mass of the universe, but so far no information about its nature nor non-gravitational interactions is available.
In DM searches, a common assumption is to interpret DM as a weakly interacting massive particles, which interacts with SM particles. Under this hypothesis DM particles can be detected through dedicated experiments [2,3], and it could be produced in proton-proton collisions at LHC. Collider data provides access to a different range of possible interactions between SM and DM particles with respect to current dedicated experiments, allowing an important interplay and complementarity among experiments to discover DM.
Many specific models provide a DM particle candidate in agreement with astrophysical observations [4,5], making essential a model-independent DM searches. A possible approach is given by an effective field theory, where the interaction between DM and SM particles is parameterized by effective operators.

1.1 Effective field theory and scalar operator

Effective field theory (EFT) approach is valid only when the energy of the interaction is such that the details of the mediators are not resolved [6]. To avoid this limitation the particle that

mediates the interaction of the DM particles with the particles of the SM can be assumed to be somewhat heavier than the DM particle itself. Under this assumption, the interaction can be seen as between the DM and the SM particles directly and parameterized by effective operators[7]. Assuming a scalar interaction between the DM and the SM particles, the strength of the interaction is proportional to a Yukawa term. For example, assuming that the DM particle is a Dirac fermion χ, the effective scalar operator can be expressed as[8]:

$$L_{int} = \frac{m_q}{M_*^3} q\bar{q}\chi\bar{\chi} \tag{1}$$

where m_q is the mass of the quark q that interacts with the DM particle and $M_\star$ is the interaction scale.

As a consequence, couplings to light quarks are suppressed and the sensitivity to the scalar interaction can be improved by searching for DM particles in final states with third-generation quarks[9]. This motivates the search for the production of DM particles in association with a pair of top quarks through a scalar interaction. In this work such study is done using the data collected by the CMS experiment[10] at LHC[12].

The dominant associated Feynman diagrams for this process is given by the interaction of gluons from the protons, a top quark pair together with two DM particles, as shown in Fig. 1. The top quark decays into a W boson and a b quark and the semileptonic final state, where one W boson decays leptonically and the other one hadronically, is studied in the analysis performed at $\sqrt{s} = 8$ TeV. The advantages of this final state are coming from the high branching ratio combined with a clean signature.

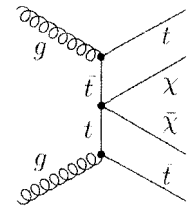

Figure 1 – Dominant diagram contributing to the production of DM particles in association with top quarks at the LHC.

2 Analysis strategy

Signal events will be expected to contain large missing transverse energy (MET) in their final state, as well as one lepton (electron or muon) and four jets, two of which originate from b quarks. The optimal selection for the signal topology is obtained requiring one lepton and at least three jets of which at least one coming from a b quark. SM processes, referred as background processes, can provide the same signature. Relevant backgrounds for this search include $t\bar{t}$, single top and W + jets, Di-bosons, and Drell-Yan events. To improve the sensitivity of the analysis it is essential to reject background events and precisely determine the remaining contributions.

Background contaminations can be reduced using kinematical differences with the signal. Using simulation, the DM signal shows a larger MET than the backgrounds because of the two DM particles escaping the detector.

After a minimal requirement on the MET, the main background contributions originate from W + jets and $t\bar{t}$ events containing a single leptonically decaying W boson. The transverse mass $M_T = \sqrt{2p_{lep}E_{miss}(1\cos(\Delta\phi))}$, where p_l is the transverse momentum of the lepton and $\Delta\phi$ is the opening angle in azimuth between the lepton and MET vector, is constrained kinematically

to $M_T < M_W$ for the on-shell W boson decay in the $t\bar{t}$ and W + jets events.
The two leading jets (j_1 and j_2) and the MET tend to be more separated in ϕ in signal events than in $t\bar{t}$ events, therefore a selection on this variable helps to further enhance the signal sensitivity.
The most challenging background for this analysis comes from $t\bar{t}$ events where one of the leptons is unobserved, leading to high values of MET. To distinguish signal from background events, the mass of the particle from which the MET originates can be estimated using kinematical constraints. This is achieved using the M_{T2}^W variable [11], which is constrained to the top quark mass for $t\bar{t}$ events and it will have higher values for signal events.
The selections found to be optimal to define the signal region (SR) for this analysis are: MET> 320 GeV, $M_T > 160$ GeV, $min\Delta\phi(j_{1,2}, MET) > 1.2$, and $M_{T2}^W > 200$ GeV.

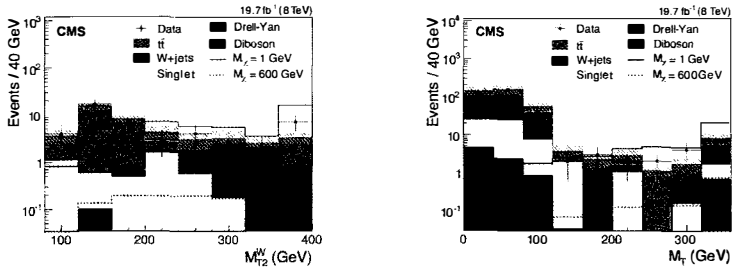

Figure 2 – Distributions of MT (left) and M_{T2}^W (right), each plotted after applying all other selections, showing the discriminating power between signal and background. Two simulated DM signals with mass M_χ of 1 and 600 GeV and an interaction scale M_* of 100 GeV are included for comparison. The hatched region represents the total uncertainty in the background prediction.

The normalization for the $t\bar{t}$ and W + jets simulated distributions is determined from data to achieve higher precision estimates. The other remaining SM processes contribute around 20% to the total backgrounds and are taken directly from simulation.
The normalization estimation from data consists in evaluating the background yields in a control region (CR). The predicted background yields and their uncertainties are then extrapolated from the CR to the SR using the shape of the distributions from simulation. In this analysis, two CRs have been used, one enriched in W + jets events and another enriched in $t\bar{t}$ events [12]. This technique helps to further improve the precision of the background estimation, constraining the systematic uncertainties affecting the shape and the normalization. A total background uncertainty of about 13% is obtained.

3 Results

The number of events observed in the SR are presented in Table 1, as well as the expected number of background and signal events for a DM particle with mass of $M_\chi = 1$ GeV and an interaction scale $M_* = 100$ GeV. No excess of events in the SR is observed and 90% confidence level (CL) upper limits can be set on the production cross section of DM particles in association with a pair of top quarks, as shown in Fig. 3.

Assuming a DM particle with a mass of 100 GeV, interaction scales at 90% CL below 118 GeV can be excluded. This represents the best limit up to date on the scalar interaction between SM and DM particles performed at CMS.
In this analysis, DM production is modeled by an EFT. The couplings g between the mediator and the DM-SM particles should be below the perturbative regime for the EFT to be valid and the momentum transfer Q_{tr} in the event has to be small compared to the mediator mass [6]. The region of parameter space in Fig. 3 that does not meet the perturbative condition is indicated

Table 1: Expected number of background events in the SR, expected number of signal events for a DM particle with the mass $M_\chi = 1$ GeV, assuming an interaction scale $M_* = 100$ GeV, and observed data. The statistical and systematic uncertainties are given on the expected yields.

Source	Yield ($\pm$stat $\pm$syst)
$t\bar{t}$	$8.2 \pm 0.6 \pm 1.9$
W	$5.2 \pm 1.8 \pm 2.1$
Single top	$2.3 \pm 1.1 \pm 1.1$
Diboson	$0.5 \pm 0.2 \pm 0.2$
Drell–Yan	$0.3 \pm 0.3 \pm 0.1$
Total Bkg	$16.4 \pm 2.2 \pm 2.9$
Signal	$38.3 \pm 0.7 \pm 2.1$
Data	18

by the grey-dashed area. The momentum transfer requirements is considered showing the lower limits on the results for the cases were a fraction R of 50% and 80% of the events satisfies the momentum transfer conditions for $g = 4\pi$ and $g = 2\pi$.

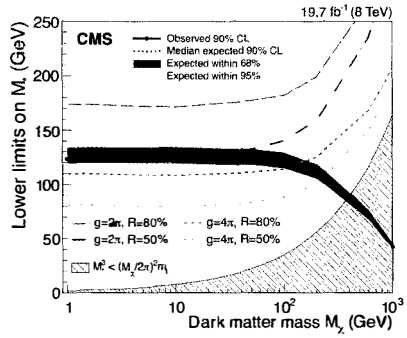

Figure 3 – Observed and expected lower limits at 90% CL on scalar interactions. A lower bound on the validity of the EFT is given the grey-hatched area. The four curves correspond to lower limits on the results for the situations were a fraction R of 50% and 80% of the events satisfies the momentum transfer conditions for $g = 4\pi$ and $g = 2\pi$.

References

1. E. Komatsu *et al*, *Astrophys. J. Suppl.* **192**, 18 (2011)
2. XENON100 Collaboration, *Phys. Rev. Lett.* **105**, 131302 (2010)
3. PAMELA Collaboration, *Phys. Rev. Lett.* **111**, 081102 (2013)
4. L. Bergstrom, *Annalen Phys.* **524**, 479-496 (2010)
5. J. L. Feng, *Ann. Rev. Astron. Astrophys.* **48**, 495-545 (2010)
6. G. Busoni *et al*, *JCAP* **1406**, 060 (2014)
7. J. Goodman *et al*, *Phys. Rev.* D **82**, 116010 (2010)
8. M. Beltran *et al*, *JHEP* **09**, 037 (2010)
9. T. Lin *et al*, *Phys. Rev.* D **88**, 063510 (2013)
10. CMS Collaboration, *J. Instrum.* **3**, S08004 (2008)
11. Y. Bai *et al*, *JHEP* **1207**, 110 (2012)
12. CMS Collaboration, arXiv **1504.03198**, hep-ex (2015), (submitted to *JHEP)*

RENORMALISATION OF THE NMSSM IN SLOOPS

V. BIZOUARD
LAPTh, 9 Chemin de Bellevue,
74940 Annecy-le-Vieux, France

The renormalisation of the chargino and neutralino sector of the NMSSM as implemented in SloopS is presented together with a few numerical examples.

1 Introduction

The Standard Model (SM) of particle physics is a successful theory that predicts with a very high precision most of measured observables. Even if no significant deviations from the SM have been observed so far, several theoretical arguments as well as cosmological and astrophysics observations indicate that it cannot be complete. In particular, the hierarchy problem, dark matter as well as neutrino masses cannot be explained in this model. This motivates the need to go beyond the Standard Model (BSM). One of the best motivated and studied theory is supersymmetry (SUSY). Its minimal incarnation, the Minimal Supersymmetric Standard Model (MSSM) presents some problems such as the so-called μ problem or the difficulty to get a 125 GeV Higgs boson without fine-tuning radiative corrections. Adding a new singlet Higgs chiral superfield to the MSSM, called then the Next to Minimal Supersymmetric extension of the SM (NMSSM), will solve these problems [1].

1.1 The NMSSM

In the MSSM, two Higgs superfields $\hat{H}_u$ and $\hat{H}_d$, which are weak doublets are necessary to generate quarks and gauge-boson masses via the usual Higgs mechanism and also to avoid gauge anomaly. These two superfields are linked in the superpotential :

$$W_{\text{Higgs}}^{\text{MSSM}} = \mu \hat{H}_u . \hat{H}_d, \tag{1}$$

The μ parameter has the dimension of a mass and is a free parameter. In this sense, its mass scale can vary *a priori* between 0 and the Planck mass. However, μ is related to other observables, such as the Z-boson mass,

$$M_Z^2 \simeq -2\mu^2 + 2\frac{m_{H_d}^2 - t_\beta^2 m_{H_u}^2}{t_\beta - 1}, \tag{2}$$

where m_{H_u} and m_{H_d} are the soft mass terms for $\hat{H}_u$ and $\hat{H}_d$, and t_β is defined via their vacuum expectation values (vev), $t_\beta = \frac{v_u}{v_d}$. Therefore, μ has to be of the order of the electroweak or SUSY breaking scale, even if, in the MSSM, it has no reason to be so. This is called the μ-problem.

In the NMSSM, the addition of a new gauge singlet Higgs superfield $\hat{S}$ will modify the Higgs superpotential, Eq. 1, as,

$$W_{\text{Higgs}}^{\text{NMSSM}} = \lambda \hat{S} \hat{H}_u . \hat{H}_d + \frac{\kappa}{3} \hat{S}^3, \tag{3}$$

where λ and κ are now dimensionless couplings. The scalar (and neutral) part of $\hat{S}$ gets a vev s, generated by soft mass terms, of the order of the SUSY breaking scale. This will generate a new effective μ term, $\mu_{eff} = \lambda s$, at the desired scale, thus solving the μ-problem.

Another challenge for the MSSM is the Higgs mass, the upper bound is given by :

$$m_{h,\text{MSSM}}^2 = m_Z^2 \cos(2\beta) + \frac{3}{(4\pi)^2} \frac{m_t^4}{v^2} \left[\ln \frac{m_{\tilde{t}}^2}{m_t^2} + \frac{X_t^2}{m_{\tilde{t}}^2} \left(1 - \frac{X_t^2}{12 m_Z^2} \right) \right], \tag{4}$$

where m_Z is the Z-boson mass, m_t the top mass, $m_{\tilde{t}}^2 = m_{\tilde{t}_1} m_{\tilde{t}_2}$ the product of both stop masses, $X_t = A_t - \frac{\mu}{t_\beta}$ the off-diagonal term in the stop mass matrix and $v^2 = v_u^2 + v_d^2$. In Eq. 4, the first term is the tree level mass term, whose value is bounded by the Z-boson mass. To get a 125 GeV Higgs boson, one then has to fine tune the second term, which is the dominant top sector contribution to the radiative corrections of the Higgs mass. Consequently, the MSSM is strongly constrained by the Higgs sector.

In the NMSSM, this is not the case anymore. Indeed, the modification of the Higgs superpotential, Eq. 3, will add a new tree-level mass term to the upper bound shown in Eq. 4 :

$$m_{h,\text{NMSSM}}^2 = m_{h,\text{MSSM}}^2 + \lambda^2 v^2 \sin^2(2\beta). \tag{5}$$

With this new contribution, it is possible to reach already at tree-level a Higgs boson mass of 125 GeV thus relaxing the fine-tuning of radiative corrections. This feature renders the NMSSM more natural than the MSSM.

The NMSSM features an extended Higgs sector with tree CP-even Higgs bosons that are mixture of the two doublets and the singlet Higgs gauge eigenstates. The lightest or the second lightest ones could correspond to the Higgs observed at the LHC. Indeed, if the lightest one is dominantly singlet, all its couplings to other particles, except to the other Higgses, are suppressed and it could escape detection. Moreover, the singlino, the fermionic content of the superfield $\hat{S}$, mixes with the higgsinos, bino and neutral wino to give five neutralinos rather than four in the MSSM. The phenomenology of neutralinos, especially for Dark Matter searches, is then broadened.

2 Renormalisation of charginos-neutralinos

Precise predictions for observables require to be able to compute radiative corrections, for this the renormalisation of the model is required. We will describe here the renormalisation of the chargino/neutralino sectors of the NMSSM.

The non standard fermionic particles of the NMSSM are the 2 charginos, combination of charged winos and Higgsinos, and the 5 neutralinos, combinations of bino, wino, neutral higgsinos and the pure NMSSM singlino :

$$\psi_c^R = \begin{pmatrix} -i\tilde{W}^- \\ \tilde{H}_d^- \end{pmatrix}, \quad \psi_c^L = \begin{pmatrix} -i\tilde{W}^+ \\ \tilde{H}_u^+ \end{pmatrix}, \quad \psi_n^R = \psi_n^L = \psi^0 = \begin{pmatrix} -i\tilde{B}^0 \\ -i\tilde{W}_3^0 \\ \tilde{H}_d^0 \\ \tilde{H}_u^0 \\ \tilde{S}^0 \end{pmatrix} \tag{6}$$

The mass matrix for the charginos (X) are the same as in the MSSM while the mass matrix for neutralinos reads

$$Y = \begin{pmatrix} M_1 & 0 & -M_Z s_W c_\beta & M_Z s_W s_\beta & 0 \\ 0 & M_2 & M_Z c_W c_\beta & -M_Z c_W s_\beta & 0 \\ -M_Z s_W c_\beta & M_Z c_W c_\beta & 0 & -\mu & -\lambda v_u \\ M_Z s_W s_\beta & -M_Z c_W s_\beta & -\mu & 0 & -\lambda v_d \\ 0 & 0 & -\lambda v_u & -\lambda v_d & 2\kappa s \end{pmatrix}, \tag{7}$$

where M_1 and M_2 are the U(1) and SU(2) gaugino masses, λ the coupling between the three Higgs superfields in the NMSSM, κ the trilinear coupling of the singlet Higgs superfield with itself. There is also a dependence on s and t_β. All these parameters have to be renormalised to be able to compute radiative corrections. We also recall that $\mu = \lambda s$, which means that we need to extract the counterterms for only 2 of these 3 parameters.

The transition to mass eigenstates is realized with unitary matrices (U, V, and N),

$$\chi^R = U\psi_c^R, \quad \chi^L = V\psi_c^L, \quad \chi^0 = N\psi^0 \quad . \tag{8}$$

and the mass eigenstates read

$$\tilde{X} = U^* X V^\dagger = diag(m_{\tilde{\chi}_1^+}, m_{\tilde{\chi}_2^+}), \quad \tilde{Y} = N^* Y N^\dagger = diag(m_{\tilde{\chi}_1^0}, m_{\tilde{\chi}_2^0}, m_{\tilde{\chi}_3^0}, m_{\tilde{\chi}_4^0}, m_{\tilde{\chi}_5^0}). \tag{9}$$

In the code `SloopS`, presented below, we choose to not renormalize the rotation matrices, which then remain the same at one-loop order. Therefore only the shifts of the mass matrices and wave functions are needed to specify the counterterms :

$$M_0 = M + \delta M, \tag{10}$$

$$\chi_{i_0}^{R,L} = \left(\delta_{ij} + \frac{1}{2}\delta Z_{ij}^{R,L}\right)\chi_j^{R,L}. \tag{11}$$

For charginos, which are Dirac fermions, the left and right-handed parts are not shifted in the same manner, Eq. 11. The renormalised self-energies are then given by (P_L and P_R are the left and right projection operator) :

$$\begin{aligned}\hat{\Sigma}_{ij}(q) = \Sigma_{ij}(q) - P_L\delta m_{ij} - P_R\delta m_{ji}^* + \frac{1}{2}(\not{q} - m_{\tilde{\chi}_i})\left[\delta Z_{ij}^L P_L + \delta Z_{ij}^{R*}\right] \\ + \frac{1}{2}\left[\delta Z_{ji}^{L*} P_R + \delta Z_{ji}^R P_L\right](\not{q} - m_{\tilde{\chi}_j})\end{aligned} \tag{12}$$

To fix the wave function and mass counterterms and then extract the counterterms for parameters, we use on-shell renormalisation conditions. Requiring that the masses of particles chosen as input do not receive any one-loop corrections, is equivalent to imposing the following condition on the renormalised self energies : $Re\hat{\Sigma}_{ii}(m_{\chi_i}^2) = 0$. This gives the mass counterterms. We also demand that the propagators of all charginos and neutralinos are properly normalised with a residue equal to 1 at the pole mass, $Re\hat{\Sigma}'_{ii}(m_{\chi_i}^2) = 0$. From this we extract the diagonal wave function renormalisation constants. Finally, we require no mixing between fields when on-shell, $Re\hat{\Sigma}_{ij}(m_{\chi_i}^2) = 0$. This gives the non diagonal wave function renormalisation constants and completes the renormalisation of the chargino-neutralino sector.

3 SloopS

`SloopS` is a code developed at LAPTh to compute cross-sections and other observables at one-loop in SUSY. The full renormalisation of the MSSM was done some years ago [2,3]. In this code, the complete spectrum and set of vertices are generated at the tree-level through the LanHEP package [4]. The complete set of Feynman rules is then derived automatically and passed to

the bundle FeynArts/FormCalc/LoopTools [5,6,7]. A powerful feature of SloopS is the ability to check not only the UV finiteness , but also IR convergence and gauge independence of the results through a generalized gauge fixing Lagrangian. Here we present the renormalisation of the NMSSM, whose implementation is still in progress in SloopS.

4 Numerical results

In the chargino-neutralino sector, one needs to renormalize six parameters. In an on-shell scheme, this means that the masses of six particles should be chosen as input. Different schemes are implemented and compared, for example we can take choose both charginos and four neutralinos as input. A look at the mass matrices, Eq. 7, shows that the charginos will basically reconstruct $\delta\mu$ and δM_2 and the neutralinos δM_1, $\delta\kappa$, δs and δt_β. Since there are five neutralinos, we apparently have the freedom to choose any set of four neutralinos as input. In practice, some choices lead to numerical instability. In fact, to reconstruct δM_1, it is essential to take the dominantly bino neutralino as input. Indeed, we have to invert a system of six equations to get the counterterms of the six parameters. If the bino-like neutralino is not in input, this will imply division by small elements of the mixing matrix and yield a bad reconstruction. The same argument shows that the dominantly singlino and at least one of the two higgisnos should be used as input. For each point of the parameter space, a procedure to choose the best scheme must be implemented. To illustrate the scheme dependence, we compare two schemes, one with the four lightest neutralinos as input (OS_{1234}) and one with the four heaviest ones (OS_{2345}) for three points with different neutralino hierarchy and compute the corrected mass of the remaining neutralino. The results are presented in table 1.

Table 1: (Left) Hierachy of neutralinos for three benchmark points, only the dominant part for each neutralino is listed. (Right) Corrected mass of the remaining neutralino in both schemes

	χ_1^0	χ_2^0	χ_3^0	χ_4^0	χ_5^0
Point 1	W_3^0	$\tilde{H}^0$	$\tilde{H}^0$	$\tilde{S}^0$	$\tilde{B}^0$
Point 2	$\tilde{S}^0$	$\tilde{B}^0$	$\tilde{H}^0$	$\tilde{H}^0$	W_3^0
Point 3	W_3^0	$\tilde{S}^0$	B^0	H^0	$\tilde{H}^0$

,

Scheme	Masses	point 1	Point 2	Point 3
OS_{1234}	$m_{\tilde{\chi}_5}^{tree}$	1002.17	614.78	573.89
	$m_{\tilde{\chi}_5}^{1-loop}$	710.69	614.82	574.92
OS_{2345}	$m_{\tilde{\chi}_1}^{tree}$	125.68	123.51	139.40
	$m_{\tilde{\chi}_1}^{1-loop}$	125.55	-114.38	139.43

Following the discussions above, we expect OS_{1234} to be a good scheme for point 2 and 3, but not for point 1 where the bino is not in input while OS_{2345} should be a good scheme only for points 1 and 3. Indeed, for a good choice of scheme, the corrected mass of the neutralino not chosen as input receives only a small correction neutralino, below 0.1%, but is wrong otherwise.

These few results illustrate the importance of the choice of renormalisation scheme to obtain reliable results. The procedure described here allows to compute automatically radiative corrections for physical observables such as decay widths and cross sections in the NMSSM. More complete results will be presented in an upcoming paper we well as the renormalisation of the sfermion and Higgs sectors.

References

1. Ulrich Ellwanger, Cyril Hugonie, and Ana M. Teixeira. *Phys.Rept.*, 496:1–77, 2010.
2. N. Baro, F. Boudjema, and A. Semenov. *Phys.Rev.*, D78:115003, 2008.
3. N. Baro and F. Boudjema. *Phys.Rev.*, D80:076010, 2009.
4. A.V. Semenov. *Nucl.Instrum.Meth.*, A389:293–294, 1997.
5. T. Hahn and M. Perez-Victoria. *Comput.Phys.Commun.*, 118:153–165, 1999.
6. Thomas Hahn. *Comput.Phys.Commun.*, 140:418–431, 2001.
7. Thomas Hahn. *Nucl.Phys.Proc.Suppl.*, 135:333–337, 2004.

HIGHER ORDER PROTON LIFETIME ESTIMATES IN GRAND UNIFIED THEORIES

H. KOLEŠOVÁ
Faculty of Nuclear Sciences and Physical Engineering, Czech Technical University in Prague, Břehová 7, Prague 114 19, Czech Republic

Since the main experimentally testable prediction of grand unified theories is the instability of the proton, precise determination of the proton lifetime for each particular model is desirable. Unfortunately, the corresponding computation usually involves theoretical uncertainties coming e.g. from ignorance of the mass spectrum or from the Planck-suppressed higher-dimensional operators, which may result in errors in the proton lifetime estimates stretching up to several orders of magnitude. On the other hand, we present a model based on SO(10) gauge group which is subsequently broken by a scalar adjoint representation, where the leading Planck-suppressed operator is absent, hence the two-loop precision may be achieved.

1 Introduction

Baryon number violation as a smoking gun of the grand unified theories (GUTs) is searched for by number of experiments. Let us concentrate for simplicity on the $p \to e^+\pi^0$ decay which has a clean signature in the water Cherenkov detectors and which is usually predicted by non-SUSY GUT models. For this channel the recent bound on the proton lifetime is set by the Super-Kamiokande experiment[1] to $\tau_p \geq 1.4 \times 10^{34}$ y, whereas the future Hyper-Kamiokande experiment assumes to reach the bound of $\tau_p \geq 10^{35}$ y after 10 years of data taking[1]. If this progress on experimental side should distinguish between different GUT models, the uncertainties in the theorists' computations of proton lifetime can not exceed one order of magnitude and a next-to-leading order computation is necessary.

The aim of this text is twofold. First, we would like to explain in Section 2 what are the ingredients for such a higher order computation of the proton lifetime. Second, we would like to present a particular GUT model based on SO(10) gauge group which was analyzed at next-to-leading order and interesting correlations between the proton lifetime and particle spectrum were found (see Section 3).

2 Error estimates for proton lifetime computation in GUTs

In non-SUSY GUTs the proton decay is predominantly mediated by vector bosons with large masses M_X and if the the contributions of the scalar fields are neglected, M_X is also the scale above that the β-functions for the SM couplings coincide. For this reason, we assume in the first approximation that the scale M_G where the SM couplings intersect is equal to M_X, hence determines the proton lifetime τ_p. The errors in the position of M_G then lead to errors in τ_p, let us examine what are their sources.

1. *Finite order of perturbation theory.* Defining the variable $t = \frac{1}{2\pi}\log\frac{\mu}{M_Z}$, the renormalization group equation for the gauge couplings may be rewritten in the form

$$\frac{\mathrm{d}}{\mathrm{d}t}\alpha_i^{-1} = -a_i - \frac{b_{ij}}{4\pi}\alpha_j - \frac{c_{ijk}}{16\pi^2}\alpha_j\alpha_k + \dots \tag{1}$$

where $\alpha_i \equiv g_i^2/4\pi$, a, b and c are $\mathcal{O}(1)$ coefficients corresponding to one-, two- and three-loop contributions, and the dots correspond to higher order contributions. Consequently, one can estimate that if working at one-loop level, the error coming from neglecting the two-loop effects at the GUT scale $M_G \sim 10^{16}\,\mathrm{GeV}$ is of the order of

$$\Delta\alpha_i^{-1}(M_G)_{1-\mathrm{loop}} \sim \frac{\mathcal{O}(1)}{16\pi^2}(t_G - t_Z) \sim 0.03 \times \mathcal{O}(1). \tag{2}$$

Similarly, the error of the two-loop calculation reads

$$\Delta\alpha_i^{-1}(M_G)_{2-\mathrm{loop}} \sim \frac{\mathcal{O}(1)}{(16\pi^2)^2}(t_G - t_Z) \sim 0.0002 \times \mathcal{O}(1)\,. \tag{3}$$

2. *Measurement of α_S at the EW scale.* Taking into account the experimental value for the strong coupling $\alpha_S(M_Z) = 0.1185 \pm 0.0006$, 1σ uncertainty in α_S^{-1} reads

$$\Delta\alpha_S^{-1}(M_G)_{1\sigma} \approx \Delta\alpha_S^{-1}(M_Z)_{1\sigma} = 0.04 \tag{4}$$

(strictly speaking, the uncertainty is reproduced at the GUT scale without any change only in case of one-loop running which is linear). Typically, the $\mathcal{O}(1)$ factor in Eq. 2 makes the one-loop error more significant than the error in Eq. 4, however, it is obvious that switching to the three-loop calculation is meaningless with today's precision in α_S measurement.

3. *Threshold effects.* In real models the masses of the heavy fields are not equal and so called matching[2] of the couplings at the GUT scale has to be performed. If a simple gauge group G is spontaneously broken into a direct product of subgroups G_i (with at most one abelian factor) at the scale μ, then at the one-loop formula reads[3]

$$\begin{aligned} \alpha_i^{-1}(\mu) &= \alpha_G^{-1}(\mu) - 4\pi\lambda_i(\mu) \qquad (5)\\ \lambda_i(\mu) &= \frac{S_2(V_i)}{48\pi^2} + \frac{1}{8\pi^2}\left[-\frac{11}{3}S_2(V_i)\log\frac{M_V}{\mu} + \frac{4}{3}\kappa_F S_2(F_i)\log\frac{M_F}{\mu} + \frac{1}{3}\eta_S S_2(S_i)\log\frac{M_S}{\mu}\right]. \end{aligned}$$

(V, F and S denote the heavy vector bosons, fermions and scalars integrated out at the scale μ). As a rule, all the heavy masses are products of the scalar couplings and the vacuum expectation value of the scalar field responsible for the breaking of the group G, and the matching scale μ is chosen close to the barycenter of these masses. Consequently, the heavy masses M should lie close to μ and comparing Eqs. 5 and 2 one obtains

$$\Delta\alpha_i^{-1}(M_G)_{\mathrm{matching}} \sim \Delta\alpha_i^{-1}(M_G)_{1-\mathrm{loop}}.$$

if $\left|\log\frac{M}{\mu}\right| \sim \frac{1}{16\pi^2}\log\frac{M_G}{M_Z}$. However, the threshold effects may be even more significant for larger splitting of the heavy spectrum. Therefore, if one would like to work at two-loop precision level, the (one-loop) threshold effects have to be taken into account.

4. *Gravity induced operators.* Since the unification scale is typically rather close to the (reduced) Planck scale $M_{\mathrm{Pl}} = 2.43 \times 10^{18}$, one has to take into account also the effective operators such as[4]

$$\frac{k}{M_{\mathrm{Pl}}}\mathrm{Tr}\,(G_{\mu\nu}G^{\mu\nu}H) \tag{6}$$

where $G_{\mu\nu}$ is the GUT field strength, H is a scalar multiplet and k is an $\mathcal{O}(1)$ constant. Let us suppose that the vacuum expectation value (VEV) $\langle H \rangle \equiv V_G$ breaks the gauge group G to the SM. Then $V_G \sim M_G$ and Eq. 6 contains the contributions to the SM kinetic terms $\epsilon_i \mathrm{Tr}\left(F^i_{\mu\nu} F^{i\mu\nu}\right)$ with $\epsilon_i \sim \mathcal{O}(10^{-2})$. In order to maintain the canonical normalization of the kinetic terms, one has to redefine $A^i_\mu \to (1+\epsilon_i)^{1/2} A^i_\mu$, $g_i \to (1+\epsilon_i)^{-1/2} g_i$. It is this redefined coupling which is measured at the EW scale, however, the unification condition holds for the original couplings: $\alpha_G = (1+\epsilon_i)\alpha_i(M_G)$ for all $i = 1,2,3$. Naturally, this induces the uncertainty

$$\Delta\alpha_i^{-1}(M_G)_{\mathrm{Pl}} \sim \mathcal{O}(10^{-2})$$

which is comparable to the one-loop error, let alone the fact that in case of large number of fields in the theory, the effective Planck scale may be lowered by as much as one order of magnitude[4] and then the "gravity smearing" effects are even more pronounced.

To demonstrate the effect of the uncertainties in α_i^{-1} on the proton lifetime prediction, let us consider a toy model where only the SM fields are present up to the unification scale M_G which is determined by the intersection of the $SU(2)_L$ and strong couplings (this could be the case e.g. in the simplest flipped SU(5) models). Assuming $M_X = M_G$ let us evaluate the proton lifetime using the naive formula[a] $\tau_p \approx \frac{M_G^4}{g^4 m_p^5}$. If the uncertainties $\Delta\alpha_i(M_G)^{-1}$ are applied, the corresponding errors in M_G are found to be rather large due to the small angle between the two curves describing the running. On the l.h.s of Figure 1 we show an example of the effect of $\Delta\alpha_i^{-1}(M_G)_{1-\mathrm{loop}}$ on the determination of M_G (assuming the $\mathcal{O}(1)$ factor in Eq. 2 to acquire values between -5 and 5), the corresponding errors in the proton lifetime are then shown in the first column of the plot on the r.h.s. The second column in the same plot corresponds to the proton lifetime computed using the two-loop β-function with the error-bars depicting the 1σ uncertainty in $\alpha_S(M_Z)$. Finally, the third column shows the error coming from the Planck-suppressed operators where we assumed $k \in (0, 0.5)$, $\epsilon_L > 0$ and $\epsilon_S < 0$ which leads to a shift to lower M_G and hence only one-sided error bar in τ_p. For M_G shifted to higher values, the gravity smearing effects get completely out of control and the two couplings may not even intersect.

Finally, let us add that the 30-40% error in the lattice computation of the hadronic matrix elements[5] introduces also an uncertainty in τ_p, which, however, does not exceed one order of magnitude. On the other hand, the ignorance of the superpartner spectrum in case of the SUSY GUTs may lead to an error stretching up to several orders of magnitude.

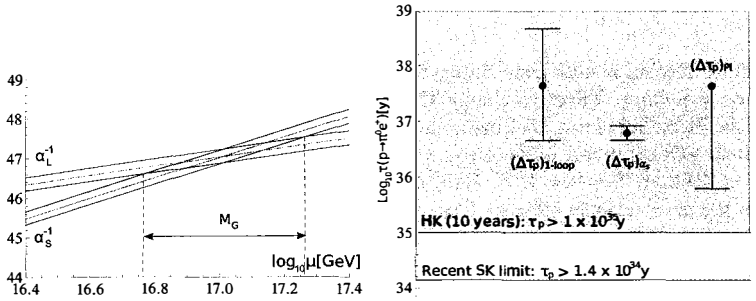

Figure 1 – On the l.h.s., the effect of $\Delta\alpha_i^{-1}(M_G)_{1-\mathrm{loop}}$ on the determination of M_G is shown whereas the errors in the proton lifetime due to $\Delta\alpha_i^{-1}(M_G)_{1-\mathrm{loop}}$, $\Delta\alpha_S^{-1}(M_G)_{1\sigma}$, and $\Delta\alpha_i^{-1}(M_G)_{\mathrm{Pl}}$ are depicted on the r.h.s.

[a] We are aware of the fact that in the precise calculation the proper formula[5] has to be used, however, we believe that this simplification is enough for estimating the errors which are mostly driven by the fact that $\tau_p \propto M_G^4$

3 Minimal SO(10)

Fortunately, the gravity smearing effects are absent in some of the unification models such as the one based on SO(10) gauge group broken by the VEV of a scalar adjoint representation 45_H since $\mathrm{Tr}\,(G_{\mu\nu}45_H G^{\mu\nu}) = 0$, and the next-to-leading order analysis is possible.

Although this model was abandoned for a long time due to the presence of tachyonic instabilities in the tree-level spectrum, it was found[7] that this problem is cured at the quantum level. Subsequently, the SO(10) unification with scalar sector composed of 10-, 45- and 126-dimensional representations was studied in depth and it was observedthat the exact unification and also the seesaw scale $\sigma \equiv \langle 126 \rangle$ in the ballpark of $10^{13} - 10^{14}\,\mathrm{GeV}$ may be achieved, if the scalar fields with SM quantum numbers $(8, 2, +1/2)$ or $(6, 3, 1/3)$ are accidentally light. In both cases the scalar spectrum was computed, hence the two-loop analysis including the one-loop matching was performed[3,8] and an interesting feature of the parameter space compatible with the unification and all the other constraints was found: Either the proton decay will be seen in the Hyper-Kamiokande experiment or only the light octet scenario is viable and this scalar is within the reach of LHC[8].

4 Conclusions

Some of the obstacles to the precise determination of the proton lifetime in the GUTs were mentioned in this text. Namely, we show that the recent error in the measurement of the strong coupling does not allow the computation beyond the two-loop precision level. Moreover, the Planck-suppressed operators or ignorance of the mass spectrum may introduce an uncertainty comparable with the one-loop error. In this case even the two-loop precision can not be reached and using a toy model we show that the error in the proton lifetime estimate considerably exceeds one order of magnitude, the size of the improvement of the planned experiments with respect to the recent bounds. On the other hand, we presented an SO(10) model where the Planck-suppressed operators are absent because of the group-theory structure, hence the two-loop precision may be achieved.

Acknowledgements

The work of H.K. is supported by Grant Agency of the Czech Technical University in Prague, grant No. SGS13/217/OHK4/3T/14.

References

1. S. Mine. Recent results from Super-K. Talk at Moriond 2015.
2. Steven Weinberg. Effective Gauge Theories. *Phys.Lett.*, B91:51, 1980.
3. Stefano Bertolini, Luca Di Luzio, and Michal Malinsky. Light color octet scalars in the minimal SO(10) grand unification. *Phys.Rev.*, D87:085020, 2013.
4. Xavier Calmet, Stephen D.H. Hsu, and David Reeb. Grand unification and enhanced quantum gravitational effects. *Phys.Rev.Lett.*, 101:171802, 2008.
5. P. Nath and P.F. Pérez. Proton stability in grand unified theories, in strings and in branes. *Physics Reports*, 441:191–317, 2007.
6. Y. Aoki, E. Shintani, and A. Soni. Proton decay matrix elements on the lattice. *Phys.Rev.*, D89(1):014505, 2014.
7. Stefano Bertolini, Luca Di Luzio, and Michal Malinsky. On the vacuum of the minimal nonsupersymmetric SO(10) unification. *Phys. Rev.*, D81:035015, 2010.
8. Helena Kolešová and Michal Malinský. Proton lifetime in the minimal SO(10) GUT and its implications for the LHC. *Phys.Rev.*, D90(11):115001, 2014.

Testing left-right symmetric models[a]

W. Dekens
Van Swinderen Institute for Particle Physics and Gravity,
University of Groningen, Nijenborgh 4,
9747 AG Groningen, The Netherlands

The difference between left- and right-handed particles is perhaps one of the most puzzling aspects of the Standard Model (SM). In left-right models (LRMs) the symmetry between left- and right-handed particles can be restored at high energy. Due to this symmetry these models are quite predictive with regards to experimental observables, making them interesting beyond the SM candidates. Here we discuss the more symmetric LRMs, the experimental constraints, and the fine-tuning present in the Higgs sector.

1 Introduction

Left-right (LR) models [1,2,3,4,5] extend the SM gauge-group to $SU(3)_c \times SU(2)_L \times SU(2)_R \times U(1)_{B-L}$. These models allow one to interpret the $U(1)$ generator in terms of baryon and lepton number and naturally incorporate the see-saw mechanism for neutrino masses [6,7]. Furthermore, in some grand unified theories (GUTs), such as $SO(10)$ and E_6, the gauge group of the LRM can appear as an intermediate step [8]. Perhaps the most attractive feature of LRMs is the possibility of a symmetry between left- and right-handed particles at high energies. Such LR symmetric models are invariant under parity (P) and/or charge conjugation (C) at high energies. Thus, P- (C-)symmetric LRMs account for the asymmetry between left and right in the SM by spontaneous breaking of P (C).

Here we focus on the more symmetric LRMs which might be the most attractive from a theoretical standpoint. We introduce the *minimal* LRM and present the most general Higgs potential in the next section. Experimental constraints, especially those from B- and K-meson mixing, and the fine-tuning in the Higgs sector are discussed in section 3.

2 Minimal left-right models

The gauge group of left-right models is given by $SU(2)_L \times SU(2)_R \times U(1)_{B-L}$. The fermions are assigned to representations of this gauge group as follows,

$$\begin{aligned} Q_L &= \begin{pmatrix} u_L \\ d_L \end{pmatrix} \in (2,1,1/3), \qquad Q_R = \begin{pmatrix} u_R \\ d_R \end{pmatrix} \in (1,2,1/3), \\ L_L &= \begin{pmatrix} \nu_L \\ l_L \end{pmatrix} \in (2,1,-1), \qquad L_R = \begin{pmatrix} \nu_R \\ l_R \end{pmatrix} \in (1,2,-1). \end{aligned} \tag{1}$$

Given the above representations, a scalar bidoublet, $\phi \in (2,2^*,0)$, is required in order to allow for fermion mass terms. In addition, the *minimal* LRM (mLRM) [6,9,5,10] introduces two scalar

[a] Talk presented at the 50th Recontres de Moriond (EW session), La Thuile, March 20, 2015.

triplets $\Delta_{L,R}$ assigned to $(3,1,2)$ and $(1,3,2)$, respectively

$$\phi = \begin{pmatrix} \phi_1^0 & \phi_1^+ \\ \phi_2^- & \phi_2^0 \end{pmatrix}, \qquad \Delta_{L,R} = \begin{pmatrix} \delta_{L,R}^+/\sqrt{2} & \delta_{L,R}^{++} \\ \delta_{L,R}^0 & -\delta_{L,R}^+/\sqrt{2} \end{pmatrix}. \tag{2}$$

These scalar fields acquire the following vacuum expectation values (vevs)

$$\langle \Delta_R \rangle = \sqrt{1/2} \begin{pmatrix} 0 & 0 \\ v_R & 0 \end{pmatrix}, \qquad \langle \phi \rangle = \sqrt{1/2} \begin{pmatrix} \kappa & 0 \\ 0 & \kappa' e^{i\alpha} \end{pmatrix}, \qquad \langle \Delta_L \rangle = \sqrt{1/2} \begin{pmatrix} 0 & 0 \\ v_L e^{i\theta_L} & 0 \end{pmatrix}. \tag{3}$$

The vev of the right-handed triplet field, v_R, defines the high scale of the LRM and breaks its gauge group down to that of the SM. Instead, κ and κ' are responsible for electroweak symmetry breaking, $\sqrt{\kappa^2 + \kappa'^2} = v \simeq 246\,\text{GeV}$. Finally, the vev of the left-handed triplet contributes to the Majorana masses of the neutrinos, such that one would expect it not to exceed the neutrino-mass scale by much, $v_L \lesssim 1\,\text{eV}$. These vevs are determined by the conditions for a minimum of the Higgs potential, the most general form of this potential is

$$\begin{aligned} V_H \;=\; & -\mu_1^2\,\mathrm{Tr}(\phi^\dagger\phi) - \mu_2^2\mathrm{Tr}(\tilde{\phi}^\dagger\phi) - \mu_2^{*2}\mathrm{Tr}(\phi^\dagger\tilde{\phi}) - \mu_{3L}^2\mathrm{Tr}(\Delta_L\Delta_L^\dagger) - \mu_{3R}^2\mathrm{Tr}(\Delta_R\Delta_R^\dagger) \\ & + \lambda_1\left[\mathrm{Tr}(\phi^\dagger\phi)\right]^2 + \left[\lambda_2\mathrm{Tr}(\tilde{\phi}^\dagger\phi)\right]^2 + \lambda_2^*\left[\mathrm{Tr}(\phi^\dagger\tilde{\phi})\right]^2 + \lambda_3\,\mathrm{Tr}(\tilde{\phi}^\dagger\phi)\,\mathrm{Tr}(\phi^\dagger\tilde{\phi}) \\ & + \mathrm{Tr}(\phi^\dagger\phi)\left[\lambda_4\mathrm{Tr}(\tilde{\phi}^\dagger\phi) + \lambda_4^*\mathrm{Tr}(\phi^\dagger\tilde{\phi})\right] + \rho_{1L}\left[\mathrm{Tr}(\Delta_L\Delta_L^\dagger)\right]^2 + \rho_{1R}\left[\mathrm{Tr}(\Delta_R\Delta_R^\dagger)\right]^2 \\ & + \rho_{2L}\mathrm{Tr}(\Delta_L\Delta_L)\mathrm{Tr}(\Delta_L^\dagger\Delta_L^\dagger) + \rho_{2R}\mathrm{Tr}(\Delta_R\Delta_R)\mathrm{Tr}(\Delta_R^\dagger\Delta_R^\dagger) + \rho_3\mathrm{Tr}(\Delta_L\Delta_L^\dagger)\mathrm{Tr}(\Delta_R\Delta_R^\dagger) \\ & + \rho_{4L}\mathrm{Tr}(\Delta_L\Delta_L)\mathrm{Tr}(\Delta_R^\dagger\Delta_R^\dagger) + \rho_{4R}\mathrm{Tr}(\Delta_R\Delta_R)\mathrm{Tr}(\Delta_L^\dagger\Delta_L^\dagger) \\ & + \mathrm{Tr}(\phi^\dagger\phi)\left[\alpha_{1L}\mathrm{Tr}(\Delta_L\Delta_L^\dagger) + \alpha_{1R}\mathrm{Tr}(\Delta_R\Delta_R^\dagger)\right] \\ & + \left(\mathrm{Tr}(\tilde{\phi}^\dagger\phi)\left[\alpha_{2R}\mathrm{Tr}(\Delta_R\Delta_R^\dagger) + \alpha_{2L}\mathrm{Tr}(\Delta_L\Delta_L^\dagger)\right] + \text{h.c.}\right) \\ & + \alpha_{3L}\mathrm{Tr}(\phi\phi^\dagger\Delta_L\Delta_L^\dagger) + \alpha_{3R}\mathrm{Tr}(\phi^\dagger\phi\Delta_R\Delta_R^\dagger) + \beta_1\,\mathrm{Tr}(\phi\Delta_R\phi^\dagger\Delta_L^\dagger) + \beta_1^*\mathrm{Tr}(\phi^\dagger\Delta_L\phi\Delta_R^\dagger) \\ & + \beta_2\mathrm{Tr}(\tilde{\phi}\Delta_R\phi^\dagger\Delta_L^\dagger) + \beta_2^*\mathrm{Tr}(\tilde{\phi}^\dagger\Delta_L\phi\Delta_R^\dagger) + \beta_3\mathrm{Tr}(\phi\Delta_R\tilde{\phi}^\dagger\Delta_L^\dagger) + \beta_3^*\mathrm{Tr}(\phi^\dagger\Delta_L\tilde{\phi}\Delta_R^\dagger), \end{aligned} \tag{4}$$

where all parameters apart from μ_2, $\lambda_{2,4}$, $\alpha_{2L,2R}$, and β_i are real. Large amounts of fine-tuning result from the fact that the minimum conditions relate the different vevs, and thereby widely varying scales, to one another. We will expand on this point in section 3.

One of the most characteristic ways in which LR models affect the observables we will consider, is through the interactions of the right-handed $W_R^\pm$ boson. The charged-current interactions involving the quarks, in the quark-mass basis, are given by

$$\mathcal{L}^{\text{CC}} = \frac{g_L}{\sqrt{2}}\overline{U}_L\gamma^\mu V_L D_L W_{L\mu}^+ + \frac{g_R}{\sqrt{2}}\overline{U}_R\gamma^\mu V_R D_R W_{R\mu}^+ + \text{h.c.}\,, \tag{5}$$

where V_L and V_R are the SM CKM matrix and its right-handed equivalent, and $g_{L,R}$ are the coupling constants of $SU(2)_{L,R}$. The right-handed current gives rise to additional contributions to $\bar{K}$-K and $\bar{B}_{d,s}$-$B_{d,s}$ mixing observables, which for symmetric mLRMs are currently the best probes of the LR scale. These additional contributions depend on V_R, which, in turn, depends on the choice of LR symmetry. As a rcsult, the constraints on LRSMs depend on the LR symmetry that is imposed. There are two possible transformations which qualify as symmetries between left and right

$$\begin{aligned} P: &\qquad Q_L \longleftrightarrow Q_R, \qquad \phi \longleftrightarrow \phi^\dagger, \qquad \Delta_L \longleftrightarrow \Delta_R, \\ C: &\qquad Q_L \longleftrightarrow (Q_R)^c, \qquad \phi \longleftrightarrow \phi^T, \qquad \Delta_L \longleftrightarrow \Delta_R^*, \end{aligned} \tag{6}$$

where the superscript c indicates charge conjugation. It turns out that the most symmetric option, *C and P* invariance, is already excluded. There are multiple ways to implement both symmetries[11,12], but none of the possible models can simultaneously reproduce the observed CP violation in K mixing and the Belle and LHCb measurements of CP violation in B mixing (ϕ_d), and give rise to a realistic Higgs spectrum[13,14,15,16]. This conclusion also holds for the minimal *pseudomanisfest*[17,18] LRM, whose P-symmetric and real Yukawa couplings coincide with one of the C- and P-symmetric models.

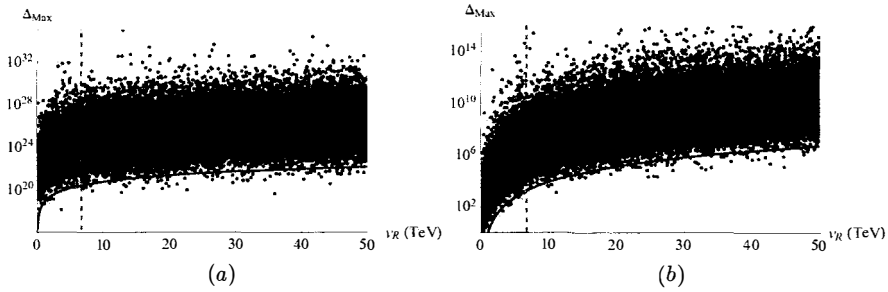

Figure 1 – The figure shows the fine-tuning measure $\Delta_{\rm Max}$ as a function of v_R in TeV for a P-symmetric V_H. The blue points are randomly generated points and the red line is chosen such that 0.1% of the points are found below it. Figure 1a shows $\Delta_{\rm Max}$ in the case where β_i and v_L are nonzero, while in Fig. 1b we set $\beta_i = v_L = 0$.

3 The *P- or C*-symmetric LRMs

In the P-invariant case the elements of the right-handed CKM matrix can be solved in terms of quark masses and V_L, such that it contains no free parameters. The exact solution was recently derived [19,20], which is approximately given by [10,21] $V_L^{ij} \simeq \pm V_R^{ij}$. Instead, in the C-symmetric case we have the relation, $V_R = K_u V_L^* K_d$, where $K_{u,d} = \mathrm{diag}(e^{i\theta_{u,d}}, e^{i\theta_{c,s}}, e^{i\theta_{t,b}})$ are diagonal matrices of phases. Although in the C-symmetric case V_R contains additional free parameters, in both the C- and P-symmetric cases the combination of B- and K-mixing constraints result in a lower limit on the LR scale of roughly $M_{W_R} \gtrsim 3\,\mathrm{TeV}$ [22]. In the often considered case of the minimal *manifest* [23,18] LRM, which has P-symmetric Yukawa couplings and $\alpha = 0$, the lower bound is extended to $M_{W_R} \gtrsim 20\,\mathrm{TeV}$ [24] [b]. This limit places the manifest scenario beyond the reach of future direct searches at the LHC or foreseen LHCb limits. Although the current limits for the C- and P-symmetric cases are similar, $M_{W_R} \gtrsim 3\,\mathrm{TeV}$ in each case, in principle, B- and K-mixing observables could distinguish between the two possibilities, as the two scenarios lead to different right-handed CKM matrices.

In contrast to the CKM matrices the C- and P-invariant Higgs potentials are rather similar [26]. As a result, the fine-tuning that is required is very similar in either case and we focus on the P-invariant case here. We study this issue by solving the minimum equations for as many parameters, which we will denote by p_i, as there are equations. We then consider the dependence of these p_i on the remaining parameters, p_j, through the fine-tuning measure, Δ, often employed for supersymmetric models [27,28],

$$\Delta_i = \mathrm{Max}_j \left| \frac{d \ln p_i}{d \ln p_j} \right|. \tag{7}$$

We calculate this fine-tuning measure for randomly generated points in parameter space, the results for the P-symmetric case are shown in Fig. 1, where we plot the maximum value of $\Delta_{\rm Max} \equiv \mathrm{Max}\,\Delta_i$ against v_R. The huge amount of fine-tuning, $\sim v_R^2/v_L^2$, in Fig. 1a arises from the so-called 'vev see-saw' relation [5], $2\rho_1 - \rho_3 \sim \beta_i\, \kappa\kappa'/v_L v_R$. This minimum condition calls for precise cancellations on the right-hand side if the ρ_i parameters are to be $\mathcal{O}(1)$. As has been noted [5] and can be seen from Fig. 1b, the fine-tuning may be considerably decreased by setting $v_L = \beta_i = 0$, see e.g. [10]. In this case, however, still a fine-tuning of order $\Delta = \mathcal{O}(v_R^4/\kappa_+^4) \gtrsim 100$ remains. We note that setting only v_L to zero leads to the same reduction in the amount of fine-tuning [26]. It remains to be seen whether these special cases can be justified or not [5,16,29].

[b] This limit also holds in the P-symmetric case if one does not incorporate a mechanism to set the QCD $\bar{\theta}$-term to zero. The neutron EDM limit then stringently constrains α, effectively resulting in the manifest LRM [24]. In LRMs with a mechanism to enforce $\bar{\theta} = 0$ the constraint on α is less severe, however, in this case the LRM predicts a relation between the EDMs of light nuclei [25], allowing for an experimental test of the model.

4 Conclusions

In summary, LRMs with a LR symmetry are arguably the most attractive of the possible LRMs, but also the most constrained. The most symmetric models, invariant under P and C, are already excluded by B- and K-mixing data. The LR scale of LRSMs with a P or a C symmetry is currently constrained by B- and K-mixing observables to be in the TeV range, $M_{W_R} \gtrsim 3\,\text{TeV}$, while future B-factory and LHCb data is expected to probe this scale up to roughly $8\,\text{TeV}$ [22]. In the Higgs sector the potentials of the P-symmetric and C-symmetric LRSMs turn out to be quite similar, and both require a huge amount of fine-tuning, except in the case $v_L = 0$.

Acknowledgments

I thank Daniël Boer for collaboration on this work and reading of the manuscript. I thank the organizers of Moriond EW 2015 for financial support and the opportunity to present this work.

References

1. J. C. Pati and A. Salam, Phys. Rev. D **10**, 275 (1974).
2. R. N. Mohapatra and J. C. Pati, Phys. Rev. D **11**, 566 (1975).
3. G. Senjanović and R. N. Mohapatra, Phys. Rev. D **12**, 1502 (1975).
4. G. Senjanović, Nucl. Phys. B **153**, 334 (1979).
5. N. G. Deshpande, J. F. Gunion, B. Kayser, and F. I. Olness, Phys. Rev. D **44**, 837 (1991).
6. R. N. Mohapatra and G. Senjanović, Phys. Rev. Lett. **44**, 912 (1980).
7. R. N. Mohapatra and G. Senjanović, Phys. Rev. D **23**, 165 (1981).
8. T. G. Rizzo and G. Senjanović, Phys. Rev. Lett. **46**, 1315 (1981).
9. P. Duka, J. Gluza, and M. Zralek, Ann. Phys. **280**, 336 (2000).
10. Y. Zhang, H. An, X. Ji, and R. N. Mohapatra, Nucl. Phys. B **802**, 247 (2008).
11. G. Ecker, W. Grimus, and H. Neufeld, Nucl. Phys. B **247**, 70 (1984).
12. G. Ecker and W. Grimus, Nucl. Phys. B **258**, 328 (1985).
13. J. M. Frère *et al.*, Phys. Rev. D **46**, 337 (1992).
14. P. Ball, J. M. Frère, and J. Matias, Nucl. Phys. B **572**, 3 (2000).
15. P. Ball and R. Fleischer, Phys. Lett. B **475**, 111 (2000).
16. G. Barenboim, M. Gorbahn, U. Nierste, and M. Raidal, Phys. Rev. D **65**, 095003 (2002).
17. H. Harari and M. Leurer, Nucl. Phys. B **233**, 221 (1984).
18. P. Langacker and S. U. Sankar, Phys. Rev. D **40**, 1569 (1989).
19. G. Senjanović and V. Tello, Phys. Rev. Lett. **114**, 071801 (2015).
20. G. Senjanović and V. Tello, (2015), arXiv:1502.05704.
21. Y. Zhang, H. An, X. Ji, and R. Mohapatra, Phys. Rev. D **76**, 091301 (2007).
22. S. Bertolini, A. Maiezza, and F. Nesti, Phys. Rev. D **89**, 095028 (2014).
23. M. A. B. Beg, R. V. Budny, R. N. Mohapatra, and A. Sirlin, Phys. Rev. Lett. **38**, 1252 (1977).
24. A. Maiezza and M. Nemevšek, Phys. Rev. D **90**, 095002 (2014).
25. W. Dekens *et al.*, JHEP **1407**, 069 (2014).
26. W. Dekens and D. Boer, Nucl. Phys. B **889**, 727 (2014).
27. J. R. Ellis, K. Enqvist, D. V. Nanopoulos, and F. Zwirner, Mod. Phys. Lett. A **1**, 57 (1986).
28. R. Barbieri and G. F. Giudice, Nucl. Phys. B **306**, 63 (1988).
29. K. Kiers, M. Assis, and A. A. Petrov, Phys. Rev. D **71**, 115015 (2005).

Octant of θ_{23} and precision measurement of atmospheric neutrino oscillations at INO-ICAL detector

Daljeet Kaur, Md. Naimuddin, Sanjeev Kumar
Department of Physics and Astrophysics, University of Delhi, Delhi, India

We present the sensitivity of the iron calorimeter detector at India-based neutrino obsevatory for the determination of octant of θ_{23} and the precision measurement of oscillation parameters with the atmospheric muon neutrino events, generated through Monte Carlo NUANCE event generator. The analysis has been performed using neutrino energy and muon direction as the observables. The iron calorimeter detector will be able to detect muons tracks and hadron showers produced by neutrino events. The detector capability has been estimated with realistic detector resolutions and efficiencies using neutrino energy and muon angle observables based on a marginalised χ^2 analysis for 10 years of exposure.

1 Introduction

Neutrino oscillations and their masses are now confirmed with various compelling evidences provided by several experiments but measurement of correct neutrino mass hierarchy, octant of θ_{23} and determination of value CP violating phase δ_{CP} are still unknown puzzles. Atmospheric neutrino experiments have potential to explain these unknown mysteries through their wide coverage of baseline and with energies in the range from MeV to TeV. The India-based Neutrino Observatory (INO)[1] is an approved project which will host a 50 kt magnetized Iron CALorimeter (ICAL) detector to study these atmospheric neutrinos through the earth matter effects. The ICAL detector consists of total three modules, each of dimension 16 m x 16 m x 14.5 m. Total detector will be a stack of 151 horizontal layers of 5.6 cm thick iron slab interleaved within 4 cm gap for the Resisitve Plate Chambers (RPC) which are active detector elements. RPC detectors are known to have good efficiency, time and spatial resolutions[2]. The main goals of INO experiment is to measure the correct neutrino mass hierarchy, θ_{23} octant determination and the precise measurement of neutrino mixing parameters through the observation of atmospheric ν_μ and $\bar{\nu}_\mu$ events. The unique feature of ICAL is to separate the atmospheric ν_μ and $\bar{\nu}_\mu$ with its excellent charge identification capabilities provided by the magentic field of strength 1.5 Tesla.

In this paper, we show the ICAL physics potentials using atmospheric muon neutrino (anti-neutrinos) oscillation events, generated through Monte Carlo NUANCE[3] event generator. We show the ICAL sensitivity for the atmospheric neutrino mixing parameters ($\sin^2\theta_{23}$ and $|\Delta m^2_{32}|$) and also for the determination of octant of θ_{23} based on marginalised χ^2 analysis, where neutrino energy and muon zenith angle are considered as observables.

2 Ananlysis

For the analysis, we simulate 1000 year unoscillated NUANCE data (ν_μ and $\bar{\nu}_\mu$ events) generated using Honda et al. 3D flux[4] with the ICAL detector specifications. The implementation of

oscillation effects to these unoscillated data have been done using a well known re-weighting algorithm as presented in Ref. [5]. Further, these ν_μ and $\bar{\nu}_\mu$ interactions are normalised for 10 years of exposure to keep Monte Carlo fluctuations under control. We use the fixed values of solar mixing parameters $\sin^2(2\theta_{12}) = 0.86$, $\Delta m^2_{21} = 7.6 \times 10^{-5} eV^2$ and $\delta_{cp} = 0$, whereas the atmospheric mixing parameters are marginalised within their 3σ range with the best fit values $\sin^2(\theta_{23}) = 0.5$ and $\Delta m^2_{32} = 2.4 \times 10^{-3} eV^2$. We use $\sin^2(\theta_{13}) = 0.03$ with 3σ marginalisation range. Here, we assume normal hierarchy is true.

Interaction of atmospheric neutrinos with the detector produce associative lepton and hadrons through Quasi-Elastic (QE), Single pion production (Resonance) and Deep Inelastic scattering (DIS) processes. Muons are produced due to Charged Current interactions of muon neutrinos ant anti-neutrinos while single pion along with one lepton produced due to resonance interactions. Hadrons are produced due to deep inelastic scattering (DIS) at high energies. Muons create a long track on their passage through detector and their charge and momenta can be identified through the track bending and curvature in presence of magnetic field whereas hadrons produce bunch of hits in form of shower. Reconstruction of the neutrino energy required the measurement of muon as well as hadron energy. The energy of muons has been reconstructed using a track fitting algorithm whereas total energy deposited by the hadron shower ($E'_{had} = E_\nu - E_\mu$) has been used to calibrate the detector response. The details of INO resolution analysis can be found in Refs. [6,7]. We used the muon and hadron energy resolutions as a function of true energy E_{true} and direction $\cos\theta_{true}$ as obtained by the INO collaboration. Finally, reconstructed neutrino energy is taken as the sum of reconstructed muon and hadron energy. We have also taken care of muon's reconstruction and charge identification efficiencies as provided by INO collaboration in the present work.

2.1 χ^2 Analysis

The oscillation parameters determining the atmospheric neutrinos are extracted by χ^2 analysis. The re-weighted events with detector resolutions and efficiencies folded in, are binned into reconstructed neutrino energy and muon direction for the estimation of χ^2. The data has been divided into total 10 equal neutrino energy bins in the range of 0.8 - 10.8 GeV with bin width of 1 GeV. A total of 20 $\cos\theta_\mu$ direction bins in the range of -1 to 1, with equal bin width has been chosen. The above mentioned binning scheme is applied for both ν_μ and $\bar{\nu}_\mu$ events. We have implemented five systematic errors in analysis; a 20% error on atmospheric neutrino flux normalisation, 10% error on neutrino cross-section, an overall 5% statistical error, a 5% uncertainty due to zenith angle dependence of the fluxes and an energy dependent tilt error as applied in earlier ICAL analyses [5] using the method of "pulls" as mentioned in Ref. [8]. Further, we used the poissonian definition of χ^2 given as:

$$\chi^2(\nu_\mu) = min \sum_{i,j} \left(2(N^{th'}_{ij}(\nu_\mu) - N^{ex}_{i,j}(\nu_\mu)) + 2N^{ex}_{i,j}(\nu_\mu)(\ln \frac{N^{ex}_{i,j}(\nu_\mu)}{N^{th'}_{i,j}(\nu_\mu)}) \right) + \sum_k \zeta_k^2, \tag{1}$$

where

$$N^{th'}_{ij}(\nu_\mu) = N^{th}_{i,j}(\nu_\mu) \left(1 + \sum_k \pi^k_{ij} \zeta_k \right). \tag{2}$$

In Eq. (1), N^{ex}_{ij} are the observed number of reconstructed μ^- events generated using true values of the oscillation parameters in i^{th} neutrino energy bin and $j^{th}\cos\theta_\mu$ bin. In Eq. (2), N^{th}_{ij} are the number of theoretically predicted events generated by varying oscillation parameters, $N^{th'}_{ij}$ shows modified events spectrum due to different systematic errors, π^k_{ij} is the systematic shift in the events of i^{th} neutrino energy bin and $j^{th}\cos\theta_\mu$ bin due to k^{th} systematic error. ζ_k is the univariate pull variable corresponding to the π^k_{ij} uncertainty. The similar expression for $\chi^2(\bar{\nu}_\mu)$ can be obtained using reconstructed μ^+ event samples. We have calculated $\chi^2(\nu_\mu)$ and $\chi^2(\bar{\nu}_\mu)$

separately and then these two are added to get total χ^2_{total}. Since the value of θ_{13} is now known to several Gaussian standard deviations (σ), so we use a 10% prior to marginalise over $\sin^2\theta_{13}$. Finally, we minimise the χ^2_{total} function by varying oscillation parameters within their allowed ranges over all systematic uncertainties.

The octant sensitivity for ICAL has been estimated using neutrino-like events considering Normal hierarchy. The significance of ruling out the wrong octant is given by

$$\Delta\chi^2 = \chi^2(false\ octant) - \chi^2(true\ octant), \tag{3}$$

where χ^2 (true octant) has been obtained by considering both the predicted and observed event spectrum in the true octant while the χ^2 (false octant) has been obtained by assuming predicted events with the true octant and observed events with the false octant. For this study we kept all the oscillation parameters fixed and the analysis has been performed for different true values of $\sin^2\theta_{23}$.

3 Results & Conclusions

The two dimensional confidence region of the oscillation parameters ($|\Delta m^2_{eff}|$, $\sin^2\theta_{23}$) are determined from $\Delta\chi^2_{total}$ around the best fit. The resultant region is shown in Fig.1. The precision on the oscillation parameters can be defined as:

$$Precision = \frac{P_{max} - P_{min}}{P_{max} + P_{min}}, \tag{4}$$

where P_{max} and P_{min} are the maximum and minimum values of the concerned oscillation parameters at the given confidence level. The current study shows that ICAL is capable of measuring the atmospheric mixing angle $\sin^2\theta_{23}$ with a precision of 13% and $|\Delta m^2_{eff}|$ with a precision of 4% at 1σ confidence levels respectively.

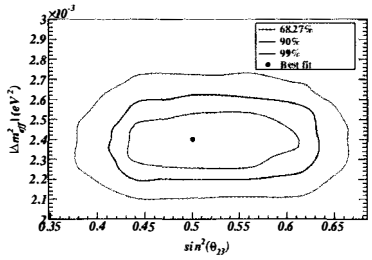

Figure 1 – Contour plots for $\sin^2(\theta_{23})$ and $|\Delta m^2_{eff}|$ measurements at 68%, 90% and 99% confidence level for 10 years exposure of ICAL detector.

Fig. 2 show the χ^2 plot for the identification of octant sensitivity for different true values of $\sin^2\theta_{23}$ assuming Normal hierarchy. The two-dimensional contour plots for the same in the $\sin^2\theta_{23}$ and Δm^2_{32} plane provides the significance levels for the octant sensitivity assuming the true lower octant value ($\sin^2\theta_{23} = 0.4$) and true higher octant value ($\sin^2\theta_{23} = 0.65$) and is shown in Fig. 3. It can be seen from Fig. 3 that the ICAL is able to determine the deviation of θ_{23} from the maximal mixing upto 2σ confidence level in 10 years of running. Further details on these studies can be found in Ref. [9].

We find an average 20% improvement of precision measurement of $\sin^2\theta_{23}$ and $|\Delta m^2_{eff}|$ parameters respectively using neutrino energy, muon angle observables over ICAL analysis with muon energy and muon angle observables [5]. These results can further be improved using improved resolutions of ICAL and with fine energy and direction binning. This study shows that the inclusion of hadron information impoves the physics potential of ICAL experiment.

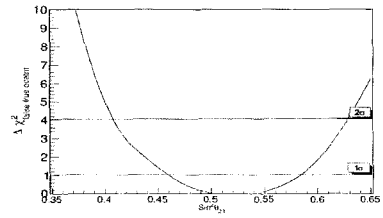

Figure 2 – $\Delta\chi^2_{false-true\ octant}$ for different input values of $\sin^2\theta_{23}$.

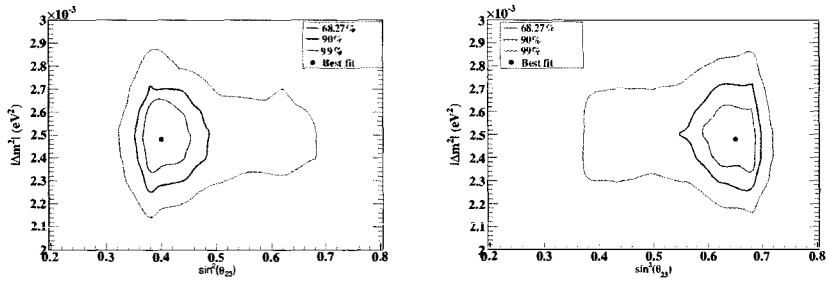

(a) (b)

Figure 3 – Contour plots indicating 68%, 90% and 99% CL (a) at true $\sin^2\theta_{23} = 0.4$ and (b) at true $\sin^2\theta_{23} = 0.65$ assuming NH is true for 10 year of ICAL exposure.

4 Acknowledgment

We would like to thank the INO physics analysis group for their important comments and suggestions. We also thank Council of Scientific Research (CSIR) & Department of Science and Technology (DST), Government of India, for supporting thiswork.

References

1. The Technical Design Report of INO-ICAL Detector.
2. D. Kaur *et al.,* Nucl. Instrum. Methods *A* **774**, *74-81 (2015).*
3. *D. Casper, Nucl.Phys. Proc.Suppl.* ***112****, 161 [arXiv:0208030][hep-ph](2002).*
4. *M. Honda et al.,* Phys. Rev. *D* **70**, *(2004).*
5. *T. Thakore et al.* JHEP **05**, 058 (2013).
6. A. Chatterjee *et al.,* JINST **9** P007001 (2014).
7. M. M. Devi *et al.,* JINST **8** P11003 (2013).
8. Maltoni *et al., [arXiv:0404085v1][hep-ph].*
9. *D. Kaur et al.,* Euro. Phys. J. C, **75:156** (2015).

Search for a sterile neutrino with the STEREO detector at ILL

S. ZSOLDOS
Laboratoire de Physique Subatomique et Cosmologie (LPSC), 53 Avenue des Martyrs, 38026 Grenoble Cedex, France

In 2011, a re-evaluation of the antineutrino spectrum emitted by nuclear reactors revealed a 6% deficit between the observed flux and the expected one. This anomaly is significant at 2.9σ and can be explained by a new oscillation at short range due to a light sterile neutrino, with parameter Δm^2 = 0.1-1 eV. The STEREO detector in construction at ILL will be the first ever to measure with precision the antineutrino spectrum and flux at very short distance (9-11m) from a compact reactor core and it will be able to confirm or reject the existence of this light sterile neutrino. In the following we introduce the relevant parameter to study the neutrino oscillation, then the STEREO detector and its discovery potential.

1 Status of neutrino mixing and anomalies

1.1 Introduction

Since the sixties and shortly after the neutrino was discovered, several experiments reported anomalous values of the flux from different sources of neutrinos (so-called *solar*, *atmospheric* and *reactor*), which were smaller than expected.

Convincing evidence was finally smeared out in 1998 by the Super-Kamiokande Collaboration [1], which was looking at neutrinos created in the atmosphere. From then on, many other experiments validated this observation and accurately probed the solar (SNO, GALLEX, SAGE, Super-K) and the reactor (KamLAND, CHOOZ, Palo Verde, Daya Bay, Reno, Double CHOOZ) sectors as well. Moreover, other experiments (LSND, miniBOONE) measured the apparition of electronic neutrino in a pure muonic neutrino beam produced by an accelerator source.

These results are interpreted within the framework of oscillation and comfort the hypothesis of a non-vanishing mass for neutrinos. To produce oscillation in the Standard Model, we assume that mass eigenstates, which are the ones who propagates through Shrodinger equation, differ from interaction eigenstates. We can therefore define a change-of-basis matrix U by :

$$\underset{\alpha=e,\mu,\tau}{|\nu_\alpha\rangle} = \sum_{i=1}^{3} U_{\alpha i}|\nu_i\rangle \Longleftrightarrow \underbrace{\begin{pmatrix}\nu_e\\ \nu_\mu\\ \nu_\tau\end{pmatrix}}_{\text{flavor}} = \begin{pmatrix}U_{e1} & U_{e2} & U_{e3}\\ U_{\mu 1} & U_{\mu 2} & U_{\mu 3}\\ U_{\tau 1} & U_{\tau 2} & U_{\tau 3}\end{pmatrix} \underbrace{\begin{pmatrix}\nu_1\\ \nu_2\\ \nu_3\end{pmatrix}}_{\text{mass}} \tag{1}$$

The transition probability between two flavors states is given by computing the squared amplitude

of the wave function :

$$P(\alpha \to \beta) = \|A(\alpha \to \beta)\|^2 = \sum_i \sum_j U_{\alpha i} U_{\beta i}^{-1} \overline{U_{\alpha j} U_{\beta j}^{-1}} \exp\left(-i\Delta m_{ij}^2 \frac{L}{2E}\right) \quad (2)$$

From Eq. 2, a non-zero mass for neutrinos has to be assumed in order to observe the oscillation mechanism. The measured values of the squared neutrino mass eigenstate difference are $\Delta m_{12}^2 = 7.54 \pm 0.26 \times 10^{-5}$ eV^2 and $\Delta m_{13}^2 \simeq \Delta m_{23}^2 = 2.43 \pm 0.06 \times 10^{-3}$ eV^2.

The matrix U is unitary, and so can be parametrized by three euler angles. This framework corresponds to the Pontecorvo-Maki-Nakagawa-Sakata matrix, and is given by :

$$U_{\text{PMNS}} = \begin{pmatrix} 1 & 0 & 0 \\ 0 & \cos\theta_{23} & \sin\theta_{23} \\ 0 & -\sin\theta_{23} & \cos\theta_{23} \end{pmatrix} \times \begin{pmatrix} \cos\theta_{13} & 0 & \sin\theta_{13} \\ 0 & 1 & 0 \\ -\sin\theta_{13} & 0 & \cos\theta_{13} \end{pmatrix} \times \begin{pmatrix} \cos\theta_{12} & \sin\theta_{12} & 0 \\ -\sin\theta_{12} & \cos\theta_{12} & 0 \\ 0 & 0 & 1 \end{pmatrix} \quad (3)$$

Historically, we define the mixing angle with respect to the region were the oscillation is driven, and the corresponding angle between mass states are $\theta_{23} = 41.4^{\circ}{}^{+1.9}_{-1.3}$: *athmospheric* (1998), $\theta_{12} = 33.7^{\circ}{}^{+1.1}_{-1.1}$: *solar* (2001), $\theta_{13} = 8.80^{\circ}{}^{+0.37}_{-0.38}$: *reactor* (2012). So far, this three neutrinos mixing scheme gives a very good fit to most of measurements [2] except for some anomalies among which the reactor antineutrino anomaly that is discussed below is found.

1.2 Recent results

In 2011, a reevaluation of the electron anti-neutrino flux from nuclear reactor suggested an increase of the expected flux with respect to previous estimations [3]. This study led to a reanalysis of previous experiments [4] and showed a deficit of 2.9σ from the expected flux. When combined with previous *Gallium anomaly* [5] (where a deficit of neutrinos was observed during the calibration of Ga detectors - typically for solar experiments), the effect becomes significant to 3.6σ. This deviation is shown on Fig. 1.

One possible explanation for this observation could be the existence of a new neutrino state, which oscillates with the other ones. This state has to be *sterile*, because of the Z decay width measurement at LEP, which constraints the number of states interacting with the Z boson to 2.9840 ± 0.0082 [6]. The best fit parameters for this new oscillation are $\sin^2(2\theta_{new}) = 0.17 \pm 0.04(1\sigma)$ and $\Delta m_{new}^2 = 2.3 \pm 0.1(1\sigma)$.

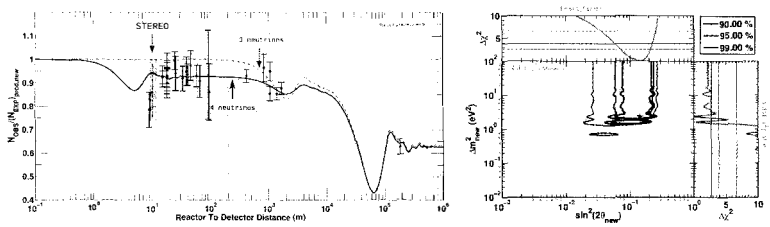

Figure 1 – Left : Reevaluation of the reactor antineutrinos experiment with the 3 neutrinos fit (dashed) and with an additional sterile state (solid). Right : Allowed regions of $\sin^2(2\theta_{new})$ and Δm_{new}^2 by the reactor antineutrino anomaly

Due to the high value of Δm_{new}^2, of the order of one eV, one of the best way to search for this sterile state is by looking at the disappearance of reactor antineutrinos at very short distance from their source, where the probability of oscillation is maximum. Note that all of the previous very short baseline experiments measured the antineutrino flux at some distance and compared it to the expected calculated flux. These "flux only" measurements are subjected to uncertainties on the energy spectrum of the emitted antineutrinos by reactors [7]. To work around this problem and to sign unequivocally the oscillating character of the propagation, we are proposing instead to observe the deformation of the interacting neutrino energy spectrum as a function of the distance from the source.

2 The STEREO detector

The STEREO experiment aims at measuring the rate and energy spectrum of antineutrinos emitted by the ILL reactor in Grenoble, France, at 6 different positions between 9m and 11m from the core. Antineutrinos are detected through their inverse beta decay reaction (IBD) : $\bar{\nu}_e + p \rightarrow e^+ + n$. The experimental signature is based on a delayed coincidence between the positron annihilation and the neutron capture.

The detector consist of a 6 cells target volume of $40 \times 40 \times 90$ cm^3, each filled with a liquid scintillator doped with gadolinium, to enhance the neutron capture. The positron deposits almost instantanously its energy, which constitutes the *prompt* signal. This prompt visible energy in the detector is defined as the kinetic energy from the positron plus its anihilation with an electron :

$$E_{\text{vis}} = E_{\bar{\nu}_e} + m_p - m_n + m_e = E_{\bar{\nu}_e} - 0.782\text{MeV} \tag{4}$$

The neutron created by the IBD process with a few 10 keV energy will rapidly thermalize in the liquid scintillator and then it will diffuse for few μs until being captured on a nucleus. Doping the liquid with gadolinium allows to reduce the diffusion time and to sign the neutron capture by a 8 MeV γ-cascade well above the natural background.

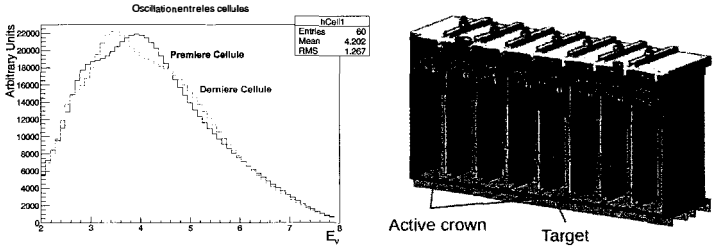

Figure 2 – Left : Antineutrinos energy spectrum deformation between the first cell and the last one, in case of a new oscillation at the best fit parameters. Right : Scheme of the STEREO detector, where the 6 targets and γ-catcher are represented. Photomultipliers are placed above the cells and separated by a acrylic buffer to enhance the signal. The top is covered by the water-cherenkov muon veto

The target volume is placed between two cells filled with liquid scintillator only, called the γ-catcher. It aims at collecting the energy deposited by events happening at the edge of the target : they might create gamma rays which will escape the target volume, and this would bias the energy reconstruction of the event if missed.

On the top of the cells, a thick acrylic buffer separates the liquid scintillator from the photomultipliers. Its aim is twofold : optimizing the detection efficiency and increasing background rejection and shielding.

Covering the whole surface of the target volume and γ-catcher, a water-cerenkov detector aimed at detecting cosmic muons will work as a veto for the acquisition.

3 Sensitivity and discovery potential

The challenge raised by measuring the energy spectrum of antineutrinos close to a reactor core is mostly to control multiple sources of background. They are divided into two categories : the accidental background, where two random processes emit light in the detector in a time window of a few μs, and the correlated background, where only one process mimick the IBD signal.

3.1 Accidental background

The main sources of accidental background come from thermal neutrons and γ produced in the surroundings of the detector. Campaigns of measurements have been performed to characterize the

sources and the energies of those backgrounds. Heavy shieldings of lead (against γ) and polytehylene (against neutrons) have been designed and are being placed all around the detector. The expected rate of accidental events is defined as :

$$R_{\text{accidental}} = \Phi_{\text{n}} \times \Phi_{\gamma} \times T_{\text{window}} \tag{5}$$

Thanks to our heavy shielding, we expect to drop thermal neutrons and γ rate to $\Phi_{\text{n}} \simeq 1\text{Hz}$ and $\Phi_{\gamma} \simeq 350\text{Hz}$. With $T_{\text{window}} \simeq 10\mu\text{s}$, we expect less than 1mHz of accidental backgrounds.

3.2 Correlated background

Essentially all of the correlated background comes from fast neutrons interacting in the detector. They hit protons whose recoil induces a scintillation light (mimick the prompt signal), and they are captured shortly afterwards (mimick the delayed signal). Sources of fast neutrons are the reactor core and cosmic muons. A high-energy muon can interact with a high-Z material and create fast neutrons by spallation. Additional polyethylene shielding is used to moderate fast neutrons from the reactor and the veto above the detector allows to tag muons events. Thanks to these additional shielding, the expected rate of fast neutrons inside the detectors is expected to be of the order of $\simeq$ 1mHz.

3.3 Sensitivity

The expected sensitivity of the experiment is shown in Fig. 3. The STEREO detector will be able to cover all the reactor antineutrino anomaly in 2 years of data taking with a 95% CL. Detection and reconstruction of systematics are included, as well as systematics of the antineutrino spectrum.

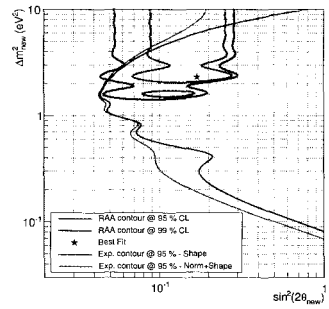

Uncorrelated	
Fission Spectrum	$0.7 \rightarrow 4.0\%$
Correlated	
Weak Magnetism	$(E - 1.0) * 1.0\%/MeV$
Energy scale	2.0%
Normalization	
Np	0.5%
Spill in spill out	1.0%
Detection efficiency	2.0%
Thermal power	2.0%
Fission spectrum	1.8%
Total normalization	3.5%

Figure 3 – Sensitivity of the STEREO experiment. Area at the right of the blue and pink contours are the region explored by the detector after 300 days of data taking at 95% CL, respectively with the energy shape distorsion analysis only and with the shape + norm analysis. The red and green contours are the region allowed by the reactor antineutrino anomaly at 95% CL and 99% CL respectively, and the star shows the best fit parameters. On the right, the table summing the uncertainties effect taken in account

References

1. Y Fukuda *et al* "Evidence for oscillation of atmospheric neutrinos", *Phys. Rev. Lett.* **81**, 1562 (1998)
2. E Lisi "Status of three neutrino mixing", *Moriond Electroweak Proceeding*, 2015
3. P Mueller *et al* "Improved predictions of reactor antineutrino spectra", *Phys. Rev.* C **83**, 054615 (2011)
4. G Mention *et al* "The Reactor Antineutrino Anomaly", *Phys. Rev.* D **83**, 073006 (2011)
5. C Giunti, M Laveder "Statistical Significance of the Gallium Anomaly", *Phys. Rev.* C **83**, 065504 (2010)
6. The ALEPH, DELPHI, L3, OPAL, SLD Collaboration "Precision Electroweak Measurements on the Z Resonance", *Phys. Rept.* **427**, 257-454 (2006)
7. A Hayes "Systematic Uncertainties in Reactor Antineutrino Fluxes and Anomaly", *Moriond Electroweak Proceeding*, 2015

NEMO-3 analysis of the double-β decay of ^{96}Zr

G. Eurin on behalf of the NEMO-3 collaboration
LAL, Univ Paris-Sud, CNRS/IN2P3, F-91405 Orsay, France
UCL, London WC1E 6BT, United Kingdom

The NEMO-3 detector was searching for neutrinoless double-β decay. A dedicated study on the double-β processes of ^{96}Zr to ^{96}Mo has been performed using an exposure of 49 g·y. ^{96}Zr is a very promising isotope for neutrinoless double-β decay searches thanks to its high $Q_{\beta\beta}$ value of 3.35 MeV. Analysis techniques and status of two-neutrino process half-life measurements to ground state and excited states with the entire NEMO-3 statistics are exposed.

1 The NEMO-3 detector

NEMO-3 was a tracker-calorimeter detector designed to search for neutrinoless double-β decay ($0\nu\beta\beta$). Data taking started on February 14th 2003 and stopped on January 11th 2011.

The full kinematic reconstruction of the two-electron events is one of the crucial and unique assets of the NEMO technique. A double-β event is identified by two electrons arriving in time from the same vertex in the source foil. Three-dimensional tracks are reconstructed combining information from different cell layers in the tracking device. The magnetic field inside the tracker allows electrons to be distinguished from positrons via the track curvature. The e^- energies (individual and total) and their times of arrival are measured in the segmented calorimeter.

The detector is able to discriminate events with γ, α, e^+, e^- and $\mu^\pm$. e^+ and e^- produce long tracks with a curvature due to the magnetic field and γ-particles a hit in the calorimeter without any associated track (see Figure 1).

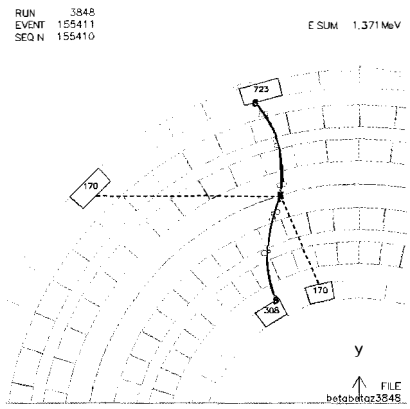

Figure 1 – *Event display from NEMO-3 data with two electrons and two γ-particles.*

2 NEMO-3 analysis of ^{96}Zr

Control samples can be defined thanks to the tracking and calorimetry assets of the NEMO-3 detector. Data and Monte-Carlo simulations are compared in individual analysis channels, enabling independent background measurements and double-β decay searches.

2.1 Two-neutrino double-β decay to ground state

Due to its high $Q_{\beta\beta}$ value, only few background components exist for the $0\nu\beta\beta$ decay of ^{96}Zr. Several measurements of the half-life of the two-neutrino double-β decay ($2\nu\beta\beta$) of ^{96}Zr to the ground state have already been performed . The current best measurement obtained with a shorter dataset of NEMO-3 provided [1]:

$$T_{1/2}^{2\nu\beta\beta}(^{96}Zr \rightarrow^{96} Mo) = 2.35 \pm 0.14\ (stat.) \pm 0.16\ (syst.) \times 10^{19}\ y \quad (1)$$

A new study has been carried out with the full statistics. In order to optimise the signal to background ratio, an elliptic selection in energy has been done as displayed on Figure 2. Indeed, ^{40}K appeared to be the dominant background as visible on Figure 3 (left). The kinematics of the decays provided by the detector enabled this two-dimensional study on Monte-Carlo simulations. The two variables were the maximal electron energy as a function of the minimal electron energy, different due to the two electrons production mechanisms. This has the effect of rejecting ^{40}K decays, the main background contribution in the two electron analysis channel. 96 % of ^{40}K events were rejected while keeping 79 % of the signal events.

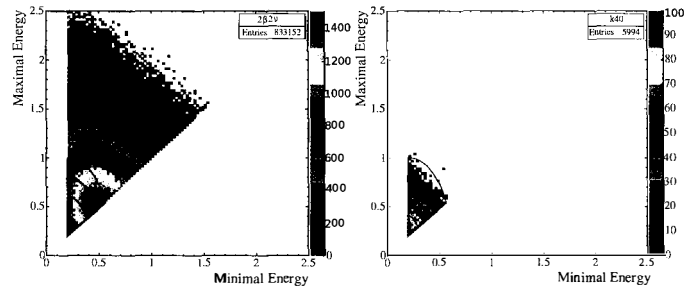

Figure 2 – *Distribution of the maximal energy as a function of the minimal energy in the 2 electrons channel from Monte-Carlo simulations. The signal from two-neutrino double-β decay is on the left and ^{40}K is on the right. Events inside the bold red ellipse are rejected.*

After this selection, the total energy has been fitted with simulations (see Figure 3, right).

After approval by the collaboration, this $2\nu\beta\beta$ half-life measurement should be the most precise obtained with NEMO-3 and by any other experiment. Compared to the previous result, the signal over background should be improved by a factor of 3-4 and the exposure by 30 %.

2.2 Two-neutrino double-β decay to excited states

^{96}Zr is one of the double-β decay isotopes that can undergo a double-β decay to an excited state. The energy levels of ^{96}Mo, daughter nucleus of ^{96}Zr, are displayed on Figure 4.

The decay to excited states is expected to be strongly suppressed compared to $2\nu\beta\beta$ to the ground state. Two energy levels exist, 0_1^+ and 2_1^+, but the 2_1^+ level is theoretically more suppressed. Therefore, the study was performed assuming no contribution from the 2_1^+ level. Given the decay scheme of ^{96}Zr to the 0_1^+ excited state of ^{96}Mo, a cascade of two γ's is expected

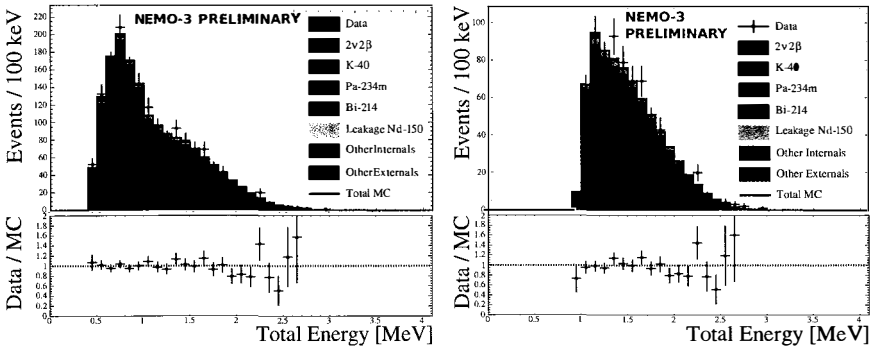

Figure 3 – *Comparison between data and Monte-Carlo simulations for the total energy in the 2 electrons channel before (left) and after (right)* ^{40}K *rejection.*

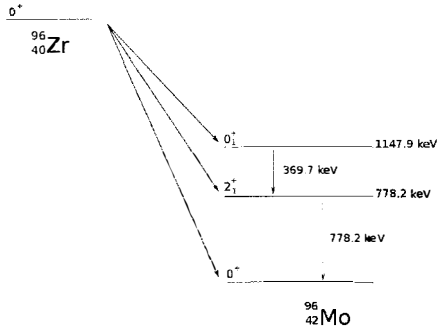

Figure 4 – *Energy scheme for the double-*β *decay of* ^{96}Zr *to* ^{96}Mo *to ground and excited states.*

to be detected along with the two electrons. NEMO-3 is very powerful when considering electron detection. However, the efficiency to detect γ's is approximately of 50 %. It is compensated with a more distinctive event topology and lower background.

A selection optimising signal over background is again realised based on Monte-Carlo simulations for each of the main contributions. The energy of the unique γ-particle or the sum of the energies of the two γ's is compared to the sum of the energies of the electrons. Elliptic selections of events are performed in the plane constituted by these two kinematic variables. The position of the ellipse in the plane (ΣE_γ, ΣE_e) on Figure 5 illustrates the cut performed to optimise the signal over background ratio. In order to strongly reduce the background, this cut selects 17 % of the total number of $2\beta2\nu$ to excited state events. This allows to reject 93.5 % of ^{214}Bi, 97.1 % of ^{208}Tl and 96.1 % of the contribution from $2\nu\beta\beta$ to ground state.

A comparison between data and simulations for the total energy is performed (see Figure 6). Data and simulations are compatible within a 2 σ background fluctuation hypothesis, estimated from a Poisson probability.

The dotted red line is the distribution of the decay to the 0_1^+ excited state. It illustrates the number of events that would be observed assuming a half-life equal to the current best limit from another experiment [2]. Careful cross-check of background systematics are currently ongoing.

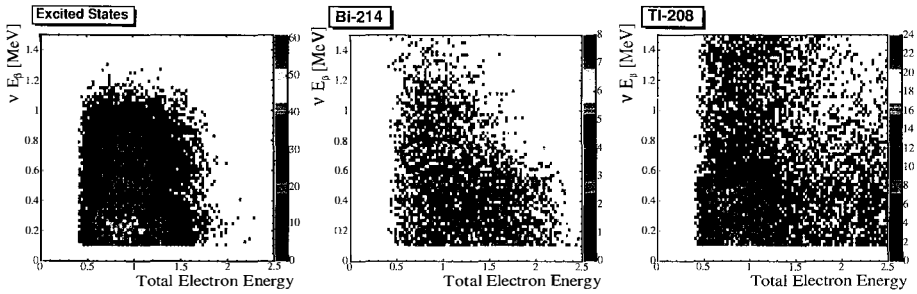

Figure 5 – *Display of the dominant backgrounds and the result of the optimisation of the signal over background for the decay to the 0_1^+ excited state of ^{96}Mo.*

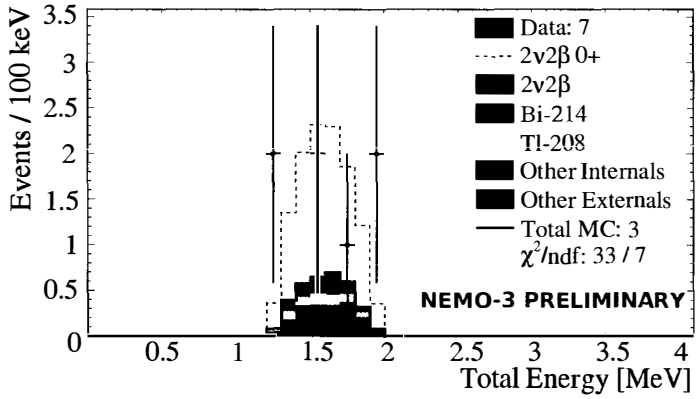

Figure 6 – *Distribution of the total energy in the 2 electrons and N γ-particle channel after strict selection cuts.*

3 Summary

A measurement of the half-life of $2\nu\beta\beta$ of ^{96}Zr to the ground state has been performed with the entire data available from NEMO-3. The half-life measurement is consistent with previously published values. A first search for $2\nu\beta\beta$ of ^{96}Zr to the 0_1^+ state with NEMO-3 data has been carried out. A limit on the half-life of this process should be set close to the current best limit.

Acknowledgments

The collaboration would like to thank the Modane Underground Laboratory staff for their technical assistance in running the experiment.

References

1. J. Argyriades et al. Measurement of the two neutrino double beta decay half-life of Zr-96 with the NEMO-3 detector. *Nuclear Physics A*, 847:168–179, 2010.
2. A. S. Barabash et al. Investigation of the $\beta\beta$ decay of ^{96}Zr to excited states in ^{96}Mo. *Journal of Physics G: Nuclear and Particle Physics*, 22(4):487–496, 1996.

Study of the decay $B^+ \to K^+\pi^0$ at LHCb

J.E. Andrews
On behalf of the LHCb collaboration
University of Maryland, College Park, Maryland, USA

This analysis investigates the capability of LHCb to study the decay mode $B^+ \to K^+\pi^0$. The proton-proton collision data set collected in 2011–2012, corresponding to 3.0 fb^{-1} of integrated luminosity, is studied. An analysis strategy is developed to mitigate the effects of low trigger efficiency and large combinatorial background leading to the reconstruction of 72 ± 26 signal events with a statistical significance of 3.7σ. Based on the findings of this study, a dedicated software trigger is being developed for use in the next data-taking period scheduled for later this year, when the LHC centre-of-mass energy will be increased.

1 Motivation

Rare decays of heavy-flavoured hadrons that primarily proceed through hadronic or radiative penguin (loop) diagrams are amongst the most powerful probes for the effects of new physics beyond the Standard Model (SM). The polarisation of the photon in decays such as $B^0 \to K^0_S\pi^0\gamma$, $B^0_s \to \phi\gamma$, and $\Lambda^0_b \to \Lambda^0\gamma$ can provide strong bounds on the effects of new physics. The family of $B \to K\pi$ decays, dominated by hadronic penguin amplitudes in the SM, can be influenced by the presence of additional amplitudes due to new physics. Measurements[1] in the $B \to K\pi$ decays at CDF, the B factories, and LHCb, have revealed significant deviations from the expected pattern of CP-violating asymmetries in these channels, the so-called "$K\pi$ puzzle". While LHCb has already improved the measurements in the $B^0 \to K^+\pi^-$ decay[2], a resolution of the puzzle requires a comprehensive study of the entire decay family, including improved measurements of final states containing π^0 mesons.

The LHCb collaboration has published measurements of several processes involving the π^0 meson, such as the $D^0 \to \pi^-\pi^+\pi^0$ decay[3] and the $B^0_s \to J/\psi\eta$ decays where the η meson decays to the $\pi^+\pi^-\pi^0$ final state[4]. However, the decay topologies considered in this work, $B \to h\pi^0$, where h denotes a charged or neutral hadron, present additional challenges in the LHCb environment. They suffer from a low π^0 meson reconstruction efficiency, which in the case of the $B^+ \to K^+\pi^0$ decay, results in an overall reconstruction efficiency of about 11%. Due to the lifetime of the h hadron, the decays considered lack a secondary vertex, a signature typically required by LHCb hadronic triggers. Altogether, these aspects result in low overall signal efficiencies and high combinatorial backgrounds.

A strategy for extracting $B^+ \to K^+\pi^0$ decays from the current LHCb data, along with techniques applicable to analyses of modes with similar topologies is presented. This analysis also provides a basis for the development of a dedicated inclusive software trigger for the next data-taking period, which can be used in future analyses of these channels. The study is performed with the 3.0 fb^{-1} data set recorded by the LHCb detector at centre-of-mass energies of 7 TeV and 8 TeV in 2011 and 2012, respectively.

2 The LHCb trigger

The LHCb trigger [5] consists of a hardware stage, based on information from the calorimeter and muon systems, followed by a software stage, which applies a full event reconstruction. The software trigger consists of many different algorithms (trigger lines) which run independently. Some trigger lines are inclusive, and serve a large range of the LHCb physics programme, while others are designed to trigger exclusively on specific decay modes. Events are said to be triggered on-signal (TOS) with respect to a particular trigger line when the constituents of a reconstructed signal candidate are sufficient to satisfy the requirements of that trigger[6].

With the exception of single-muon triggers, every software trigger line used during the 2011–2012 data-taking requires a reconstructed secondary vertex, hence $B^+ \to K^+\pi^0$ signal events cannot be TOS with respect to the software trigger. The presence of another secondary vertex in the event, independent of the signal, is then required for signal events to pass through this stage of the trigger. The trigger efficiencies are consequently very low, as this typically requires the presence of a second b hadron with enough transverse momentum and reconstructible daughters to satisfy the requirements of one of the trigger lines. In simulation, the overall trigger efficiencies are found to range from 5% to 11% over different data-taking periods and reconstruction strategies. These efficiencies are calculated as the fractions of triggered events in the total sample of simulated events that pass the cut-based selection described in Sect. 3. The dedicated software trigger line that is being developed is intended to recover a significant fraction of signal events which would otherwise be ignored at the data-taking stage.

3 Event selection

Reconstructed charged particles with a $p_{\rm T}$ greater than 250 MeV/c are used as K^+ candidates. They are required to be significantly displaced from the primary vertex (PV), and are distinguished from other charged particles using information from the RICH and calorimeter systems. candidate π^0 mesons are required to have $p_{\rm T}$ greater than 2.6 GeV/c, p greater than 10 GeV/c, and a reconstructed mass within the range $79.6 < m < 199.6\,{\rm MeV}/c^2$.

The four-momenta of the K^+ and π^0 candidates are added to form B^+ candidates. Each B^+ candidate is required to have a $p_{\rm T}$ greater than 1.5 GeV/c, and a reconstructed mass within the range $4.0 < m < 6.0\,{\rm GeV}/c^2$. A trajectory is made from the PV closest to the daughter K^+ candidate, along the direction of the reconstructed B^+ candidate momentum. The variable called mother-trajectory distance-of-closest-approach (MT-DOCA) is the DOCA between the K^+ candidate and this trajectory. This variable is motivated by the significant displacement of the signal B^+ from its PV, and is designed to provide some quantitative measure of the decay position in the absence of a reconstructed decay vertex. For well-reconstructed signal events, the MT-DOCA is small, whereas the distribution of random combinations of final-state particles has a tail at large values. A χ^2 for the MT-DOCA is constructed using the covariance matrix of the reconstructed PV. The $\chi^2_{\text{MT-DOCA}}$ is required to be less than 10 for B^+ candidates reconstructed from 2011 data, and less than 9 for those reconstructed from 2012 data.

Variables characterizing how well-isolated a candidate is from other tracks in the event are also calculated. Vertex isolation variables are calculated by combining another track in the event with the K^+ candidate to form a two-track secondary vertex. This procedure is performed for all tracks in the event. The multiplicity of two-track secondary vertices with $\chi^2_{\rm vtx} < 9$ is recorded as the variable $V_{\rm Mult.}$, where $\chi^2_{\rm vtx}$ is the χ^2 of the vertex fit. Candidates reconstructed from 2011 data are required to have a $V_{\rm Mult.}$ fewer than 8, and those reconstructed from 2012 data are required to have a $V_{\rm Mult.}$ fewer than 6.

The $p_{\rm T}$ asymmetry of the reconstructed B^+ candidate is defined as

$$\mathcal{A}(p_{\rm T}) = \frac{p_{{\rm T}B} - p_{\rm Tcone}}{p_{{\rm T}B} + p_{\rm Tcone}}, \tag{1}$$

where $p_{{\rm T}B}$ is the transverse momentum of the reconstructed B^+ signal candidate, and $p_{\rm Tcone}$ is

the magnitude of the vector sum of the transverse momenta of the charged particles near the reconstructed B^+ candidate. It is used to isolate the reconstructed candidate from nearby tracks. To determine whether a track is "near" the signal candidate, the quantity $\Delta R = \sqrt{(\Delta\phi)^2 + (\Delta\eta)^2}$ is required not to exceed 1.2, where $\Delta\phi$ is the difference between the azimuthal angle of the momentum of the reconstructed candidate and the track, and $\Delta\eta$ is the difference between their pseudorapidities. The cone size, $\Delta R = 1.2$, is optimised using simulated data for the signal, and a subsample of experimental data for the background.

In order to maximise the sensitivity, a multivariate analysis is developed using a boosted decision tree (BDT) [8,9] classifier. Several kinematic variables are used as event classification variables, as well as the isolation variables described above. The multivariate classifier is trained and tested using experimental data to represent the background, and simulated $B^+ \to K^+\pi^0$ data that are corrected using the event weights. The optimal cut value of the classifier response variable is found for the data set by maximising the figure of merit $N_S/\sqrt{N_S + N_B}$, where N_S is the number of signal events and N_B is the number of background events. While optimal, this requirement has a very low signal efficiency, roughly 7%, as a consequence of the low trigger efficiency and enormous combinatorial background. The total efficiency, accounting for all geometric acceptance, trigger, and selection requirements is of the order 3×10^{-5}.

4 Results

The mass distribution of reconstructed candidates, after all selection requirements, is shown in Fig. 1. To extract the number of signal events, we fit a model to this distribution which consists of an exponential function for the combinatorial background; the tail of a Gaussian function for additional background in the low-mass region; and the sum of two Crystal Ball functions [7] for the signal, to account for the tails on both sides of the signal peak. The Crystal Ball functions share a common mean and width, and their tail shapes are taken from simulation. The background remaining in the final selection consists primarily of partially reconstructed $B \to K^+\pi^0 X$ decays, or B^+ candidates reconstructed with misidentified π^0 candidates. Several exclusive decay modes, including $B \to K^*\pi^0$, $B \to K^+\rho$, and $B \to K^*\gamma$ are also considered and are found to make negligible contributions in the signal region. The shape of the combinatorial background is determined from a fit to the upper sideband. Normalisations of the individual components are allowed to float in the fit, as well as the means and widths of the signal and low-mass background shapes.

A signal yield of 72 ± 26 candidates is found. The statistical significance of the signal is determined from the change in the fit likelihood, with and without a signal component, to be 3.7σ. The signal width of 99 ± 38 MeV is consistent with the expected resolution from simulation, which is estimated to be 95 ± 4 MeV. Several variations of the fit are performed with different shapes modelling the low-mass background. Variations are also performed with and without the signal width fixed from simulation, and with the signal mean fixed to the known value of the B^+ mass. All variations are found to be compatible with the fit shown here, and a systematic uncertainty of the signal yield due to the choice of fit model is estimated to be 10 events.

5 Prospects for 2015 and beyond

A rough estimate of the prospects for this channel in the next data-taking period is made by taking into account expected improvements due to a dedicated software trigger line (×3–5), the increased $b\bar{b}$ cross section at 13 TeV(×2), and the potentially increased overall offline analysis efficiency (×5). The software stage of the trigger that would be improved by a dedicated trigger line is estimated from simulation to be about 16% efficient during the 2011–2012 data-taking, after offline reconstruction. This efficiency is typically above 75% for b-hadron decays to two charged particles [5], so an improvement of at least a factor of 3 is not unrealistic. In order to assess possible improvements in the offline analysis efficiency due to the enhanced yield as a result of the improved trigger, an estimate of the expected combinatorial background level during the next data-taking period is required. The background is assumed to be dominated by generic $b\bar{b}$ events, the cross section for

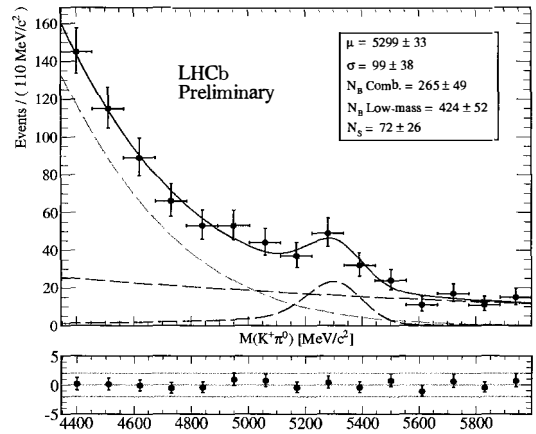

Figure 1 – Mass distribution of the reconstructed candidates, selected from the entire data set. The data are drawn as black points. The fit to the B^+ reconstructed mass is drawn as a solid blue line. The signal component is drawn in dashed blue, the combinatorial background is drawn in dashed purple, and the low-mass background is drawn in dashed magenta.

which scales linearly with centre-of-mass energy. This assumption is supported by the absence of significant contributions from exclusive partially reconstructed modes whose rate could potentially increase with the future dedicated trigge. A data sample representing the expected effect on the background level of a factor 5 increase in the total offline efficiency is selected from the 2011–2012 data by loosening the requirement on the multivariate classifier. This, together with appropriately scaled simulated signal events, is used to estimate the possible signal significance with this modified selection. We estimate a signal yield of 700–1100 events in $1\,\text{fb}^{-1}$ of integrated luminosity gathered in the next data-taking period, with an uncertainty of about 100 events, dominated by the background yield. This neglects other sources of improvements such as increased identification and reconstruction efficiencies of π^0 mesons, and a reoptimised and retrained multivariate classifier.

6 Conclusions

A study of the decay $B^+ \to K^+\pi^0$ is performed with the LHCb 2011–2012 data set. Despite a low trigger efficiency, and a very low selection efficiency after suppressing the combinatorial background, evidence for a signal is found for the first time at a hadron collider. With a dedicated software trigger line in place, measurements in this decay channel will be possible at an estimated level of 10% precision with $1\,\text{fb}^{-1}$ of data. Motivated by the results of this study, an exclusive software trigger line is being developed for use in the next data-taking period of the LHCb experiment.

References

1. Heavy Flavor Averaging Group, Y. Amhis *et al.*, arXiv:1207.1158.
2. LHCb collaboration, R. Aaij *et al.*, *Phys. Rev. Lett.* **108**, 201601 (2012)
3. LHCb collaboration, R. Aaij *et al.*, *Phys. Lett.* B **B740**, 158 (2015)
4. LHCb collaboration, R. Aaij *et al.*, *J. High Energy Phys.* 01.024 2015.
5. LHCb collaboration, R. Aaij *et al.*, *JINST* 8.P04022 2012.
6. Puig. Albert, CERN-LHCb-PUB-2014-046.
7. Skwarnicki, Tomasz, *Institute of Nuclear Physics, Krakow*, DESY-F31-86-02, 1986.
8. Breiman, L. and Friedman, J. H. and Olshen, R. A. and Stone, C. J., Wadsworth international group, Belmont, California, USA. 1984.
9. Schapire, Robert E. and Freund, Yoav, *Jour. Comp. and Syst. Sc.*, 55.119 1997.

An analysis of $\Lambda_b^0 \to \Lambda\mu^+\mu^-$ decays at the LHCb experiment

L. Pescatore*,
on behalf of the LHCb collaboration
*University of Birmingham, United Kingdom

The branching fraction of the rare decay $\Lambda_b^0 \to \Lambda\mu^+\mu^-$ is measured as a function of q^2, the square of the dimuon invariant mass. The analysis is performed using proton-proton collision data, corresponding to an integrated luminosity of 3.0 fb^{-1}, collected by the LHCb experiment. Evidence of signal is found for the first time in the q^2 region below the square of the J/ψ mass. In the q^2 intervals where the signal is observed, angular distributions are studied and two forward-backward asymmetries, in the dimuon and hadronic systems, are measured for the first time.

1 Rare decays and Λ_b^0

The $\Lambda_b^0 \to \Lambda\mu^+\mu^-$ decay is a rare ($b \to s$) flavour changing transition, which is forbidden at tree level in the Standard Model (SM) but can happen through loop level electroweak processes [1]. Since the branching ratio of this type of decays is small, typically $\sim 10^{-6}$ or less, they are very sensitive to contributions from physics beyond the SM. The study of Λ_b^0 decays is of particular interest for severals reasons. First of all, the Λ_b^0 baryon has non-zero spin, which allows to extract additional information about the helicity structure of the underlying theory. Secondly, the Λ_b^0 baryon can be considered as a heavy quark plus a light di-quark system, and therefore the hadronic physics differs significantly from similar B meson decays. Finally, a further motivation specific to the $\Lambda_b^0 \to \Lambda\mu^+\mu^-$ decay is that the Λ baryon decays weakly and its polarisation is preserved which gives access to complementary information to that available from meson decays [2]. In this work the differential branching ratio and angular observables are measured as a function of the square of the dimuon mass, q^2, since theoretically different treatments of form factors are used depending on the considered q^2 region [2]. Previous observations of the decay [3 4] $\Lambda_b^0 \to \Lambda\mu^+\mu^-$ found evidence for signal only in q^2 intervals above the square of the mass of the J/ψ resonance. These proceedings are based on an analysis [5] using pp collision data, corresponding to an integrated luminosity of 3.0 fb^{-1}, collected during 2011 and 2012 by the LHCb detector [6] at centre-of-mass energies of 7 and 8 TeV, respectively.

2 Differential branching fraction

In order to measure their differential branching fraction, candidate $\Lambda_b^0 \to \Lambda\mu^+\mu^-$ decays are reconstructed from a dimuon and a Λ candidate, where the Λ baryon is reconstructed through its $p\pi^-$

decay mode. The rates are normalised with respect to the tree level $b \to c\bar{c}s$ decay $\Lambda_b^0 \to J/\psi\Lambda$, where the J/ψ meson decays into a $\mu^+\mu^-$ pair, as this mode has the same final state particles as the signal channel.

The selection is based on a neural network classifier[7]. The signal sample used to train the neural network consists of simulated $\Lambda_b^0 \to \Lambda\mu^+\mu^-$ events, while the background is taken from data in the upper sideband of the Λ_b^0 candidate mass spectrum. The variable that provides the greatest discrimination is the χ^2 from a kinematic fit of the complete decay chain in which the proton and pion are constrained such that the $p\pi^-$ invariant mass corresponds to the known Λ baryon mass, and the Λ and dimuon systems are constrained to originate from their respective vertices. Other variables that contribute significantly are: the transverse momentum of the Λ candidate; the particle identification information for the muons, a likelihood variable built using information from LHCb's muon system and ring imaging Cherenkov detectors[6]; the separation of the muons, the pion and the Λ candidate from the pp interaction vertex; and the distance between the Λ_b^0 and Λ decay vertices.

Since the Λ baryon is long-lived, its decay has a topology with a displaced secondary vertex. This leads to little background from other decays: the only relevant contribution comes B^0 decays into K_S^0 and muons, where $K_S^0 \to \pi^+\pi^-$ and one pion is misidentified as a proton. This background, especially significant for the normalisation channel, is modelled in the fit.

In Fig. 1 the invariant mass distribution of the $\Lambda\mu^+\mu^-$ system is reported in the q^2 interval $15 < q^2 < 20$ GeV$^2/c^4$ together with the fit function used to extract the yield. The signal is modelled using the sum of two Crystal Ball functions and the combinatorial background with an exponential. The background from K_S^0 decays is very small in the rare decay sample and is not visible on Fig. 1.

The absolute branching fraction of the $\Lambda_b^0 \to \Lambda\mu^+\mu^-$ decay is obtained by multiplying the relative branching fraction by the absolute branching fraction of the normalisation channel[8], $\mathcal{B}(\Lambda_b^0 \to J/\psi\Lambda) = (6.3 \pm 1.3) \times 10^{-4}$. Measured values are given in Fig. 1 as a function of q^2 together with SM predictions[9]. The uncertainty on these values is dominated by the precision of the branching fraction for the normalisation channel, while the uncertainty on the relative branching fraction is dominated by the size of the data sample available.

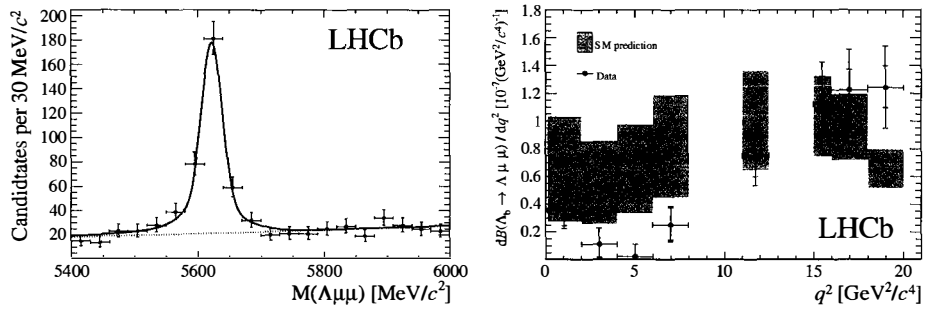

Figure 1 – (left) Invariant mass of the $\Lambda\mu^+\mu^-$ system in the $15 < q^2 < 20$ GeV$^2/c^4$ interval with the fit function overlaid. (right) Measured differential branching fraction of the rare $\Lambda_b^0 \to \Lambda\mu^+\mu^-$ decay as a function of q^2 with the SM prediction[9] superimposed. The inner error bar on data points represents the total uncertainty on the relative branching fraction (statistical and systematic); the outer error bar also includes the uncertainties from the branching fraction of the normalisation mode.

3 Angular analysis

The $\Lambda_b^0 \to \Lambda\mu^+\mu^-$ decay has a non-trivial angular structure which, in the case of unpolarised Λ_b^0 production, is described by the helicity angles of the muon (θ_ℓ) and proton (θ_h), the angle between the planes defined by the Λ decay products and the two muons, and the square of the dimuon invariant mass, q^2. The angle θ_ℓ is defined as the angle between the positive (negative) muon and the dimuon system directions and θ_h as the angle between the proton and the Λ baryon directions, both in the

Λ_b^0 ($\bar{\Lambda}_b^0$) rest frame.

In this work two forward-backward asymmetries, in the dimuon ($A_{\rm FB}^{\ell}$) and $p\pi^-$ ($A_{\rm FB}^{h}$) systems, are measured. The observables are determined from one-dimensional angular distributions as a function of $\cos\theta_\ell$ and $\cos\theta_h$. The differential rate as a function of $\cos\theta_\ell$ is described by the function

$$\frac{{\rm d}^2\Gamma(\Lambda_b \to \Lambda\,\ell^+\ell^-)}{{\rm d}q^2\,{\rm d}\cos\theta_\ell} = \frac{{\rm d}\Gamma}{{\rm d}q^2}\left[\frac{3}{8}\left(1+\cos^2\theta_\ell\right)(1-f_{\rm L}) + A_{\rm FB}^{\ell}\cos\theta_\ell + \frac{3}{4}f_{\rm L}\sin^2\theta_\ell\right], \quad (1)$$

where $f_{\rm L}$ is the fraction of longitudinally polarised dimuons. The rate as a function of $\cos\theta_h$ has the form

$$\frac{{\rm d}^2\Gamma(\Lambda_b \to \Lambda(\to p\pi^-)\ell^+\ell^-)}{{\rm d}q^2\,{\rm d}\cos\theta_h} = \mathcal{B}(\Lambda \to p\pi^-)\frac{{\rm d}\Gamma(\Lambda_b \to \Lambda\,\ell^+\ell^-)}{{\rm d}q^2}\frac{1}{2}\left(1+2A_{\rm FB}^{h}\cos\theta_h\right). \quad (2)$$

These expressions assume that Λ_b^0 baryons are produced unpolarised, which is in agreement with the Λ_b^0 production polarisation recently measured at LHCb [10].

The observables are measured using unbinned maximum likelihood fits. The signal PDF consists of a theoretical shape, given by Eqs. 1 and 2, multiplied by a function modelling the angular efficiency. Selection requirements on the minimum momentum of the muons generate distortions in the $\cos\theta_\ell$ distribution by removing candidates with extreme values of $\cos\theta_\ell$. Similarly, impact parameter requirements remove events with large $|\cos\theta_h|$, since very forward hadrons tend to have smaller impact parameter values. The angular efficiency is parametrised using a second-order polynomial and determined by fitting simulated events.

To limit systematic uncertainties related to the background parametrisation, a narrow interval around the mass peak, dominated by the signal, is used in the angular analysis and a polynomial component is added to the fit to account for the residual background.

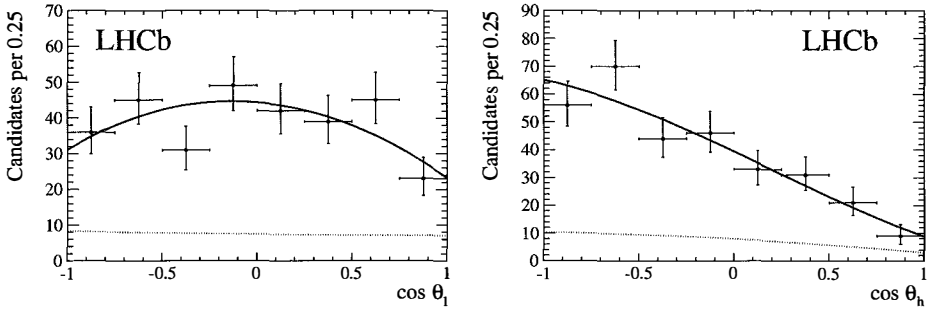

Figure 2 – Distributions of the (left) $\cos\theta_\ell$ and (right) $\cos\theta_h$ angles in data in the $15 < q^2 < 20$ GeV$^2/c^4$ interval with overlaid the total fit function, solid (blue) line, and the background component, dashed (red) line.

Figure 2 shows the $\cos\theta_\ell$ and $\cos\theta_h$ distributions in the $15 < q^2 < 20$ GeV$^2/c^4$ interval with the fit functions overlaid. Measured values of the leptonic and hadronic forward-backward asymmetries, $A_{\rm FB}^{\ell}$ and $A_{\rm FB}^{h}$, are shown in Fig. 3 together with SM predictions [9]. The statistical uncertainties are obtained using the likelihood-ratio ordering method [11] and nuisance parameters are accounted for using the plug-in method [12]. One dimensional 68% Confidence Level (CL) intervals are obtained by varying one parameter at a time and treating the others as nuisance parameters. In the analysis [5] the statistical uncertainties on $A_{\rm FB}^{\ell}$ and $f_{\rm L}$ are also reported in the form of two-dimensional 68% CL regions, where the likelihood-ratio ordering method is applied by varying both observables at the same time and therefore taking correlations into account.

4 Conclusions

A measurement of the differential branching fraction of the rare $\Lambda_b^0 \to \Lambda\mu^+\mu^-$ decay is performed using data recorded by the LHCb detector at centre-of-mass energies of 7 and 8 TeV and corresponding to an integrated luminosity of 3.0 fb^{-1}. Evidence for the signal is found for the first time in the

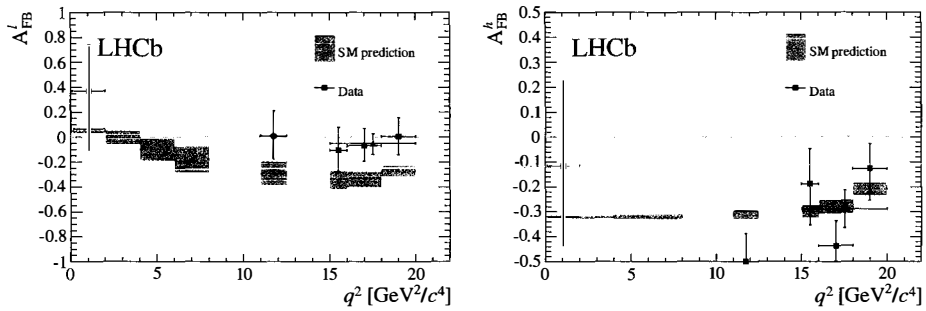

Figure 3 – Forward-backward asymmetries as a function of q^2 in the dimuon system (left) and $p\pi^-$ system (right) with the SM prediction[9] overlaid.

q^2 region below the square of the J/ψ mass, and in particular in the $0.1 < q^2 < 2.0$ GeV$^2/c^4$ interval, where an enhanced yield is expected due to the proximity of the photon pole. The uncertainties of the measurements in the $15 < q^2 < 20$ GeV$^2/c^4$ interval are reduced by a factor of approximately three relative to the previous LHCb measurement[3]. This improvement is due to a larger data sample and a better control of systematic uncertainties. The branching fraction measurements are compatible with SM predictions in the high-q^2 region, above the square of the J/ψ mass, and lie below the predictions in the low-q^2 region. Furthermore, the first measurement of angular observables for this decay is reported. Two forward-backward asymmetries, in the dimuon and $p\pi^-$ systems, are measured. The measurements of the $A_{\rm FB}^{h}$ observable are in good agreement with the SM predictions while for the $A_{\rm FB}^{\ell}$ observable measuremcnts are consistently above the predictions.

References

1. T. Gutsche *et al.*, *Rare baryon decays* $\Lambda_b^0 \to \Lambda\ell^+\ell(\ell = e, \mu, \tau)$ *and* $\Lambda_b^0 \to \Lambda\gamma$*: differential and total rates, lepton- and hadron-side forward-backward asymmetries*, *Phys. Rev.* D **87**, 074031 (2013).
2. P. Ber, T. Feldmann, and D. van Dyk, *Angular analysis of the decay* $\Lambda_b \to \Lambda(\to N\pi)\ell^+\ell^-$, *JHEP* **01**, 155 (2015).
3. LHCb collaboration, R. Aaij *et al.*, *Measurement of the differential branching fraction of the decay* $\Lambda_b^0 \to \Lambda^0\mu^+\mu^-$, *Phys. Lett.* B **725**, 25 (2013).
4. CDF collaboration, T. Aaltonen *et al.*, *Observation of the baryonic flavor-changing neutral current decay* $\Lambda_b^0 \to \Lambda^0\mu^+\mu^-$, *Phys. Rev. Lett.* **107**, 201802 (2011).
5. LHCb collaboration, R. Aaij *et al.*, *Differential branching fraction and angular analysis of* $\Lambda_b^0 \to \Lambda^0\mu^+\mu^-$ *decays*, arXiv:1503.07138.
6. LHCb collaboration, A. A. Alves Jr. *et al.*, *The LHCb detector at the LHC*, *JINST* **3**, S08005 (2008).
7. M. Feindt and U. Kerzel, *The NeuroBayes neural network package*, *Nucl. Instrum. Methods* A **559**, 190 (2006).
8. Particle Data Group, K. A. Olive *et al.*, *Review of particle physics*, *Chin. Phys.* C **38**, 090001 (2014).
9. S. Meinel, *Flavor physics with* Λ_b^0 *baryons*, PoS **LATTICE2013**, 024 (2014).
10. LHCb collaboration, R. Aaij *et al.*, *Measurements of the* $\Lambda_b^0 \to J/\psi\Lambda^0$ *decay amplitudes and the* Λ_b^0 *polarisation in pp collisions at* $\sqrt{s} = 7$ *TeV*, *Phys. Lett.* B **724**, 27 (2013).
11. G. J. Feldman and R. D. Cousins, *Unified approach to the classical statistical analysis of small signals*, *Phys. Rev.* D **57**, 3873 (1998).
12. B. Sen, M. Walker, and M. Woodroofe, *On the unified method with nuisance parameters*, *Statistica Sinica* **19**, 301 (2009).

Search for $B^+ \to \ell^+\nu_\ell\gamma$ decays with hadronic tagging using the full Belle data sample

A. HELLER

Karlsruhe Institute of Technology,
Institut für Experimentelle Kernphysik,
Wolfgang-Gaede-Str. 1,
76131 Karlsruhe, Germany

The semileptonic decay $B^+ \to \ell^+\nu_\ell\gamma$ with $\ell^+ = e^+, \mu^+$ allows for the measurement of the first inverse moment of the B meson distribution amplitude λ_B. This parameter is needed for the calculation of charmless hadronic B decays in the QCD factorization scheme. We search for the decay $B^+ \to \ell^+\nu_\ell\gamma$ with $\ell^+ = e^+$ or μ^+ using the full Belle data set of $772 \times 10^6 B\bar{B}$ pairs. We observe no significant signal within the phase space of $E_\gamma^{\rm sig} > 1$ GeV and obtain upper limits of $\mathcal{B}(B^+ \to e^+\nu_e\gamma) < 6.1 \times 10^{-6}$, $\mathcal{B}(B^+ \to \mu^+\nu_\mu\gamma) < 3.4 \times 10^{-6}$, and $\mathcal{B}(B^+ \to \ell^+\nu_\ell\gamma) < 3.5 \times 10^{-6}$ at 90% credibility level [1].

1 Introduction

The semileptonic decay $B^+ \to \ell^+\nu_\ell\gamma$ [2] proceeds via a $\bar{b}u$ annihilation into a W^+ boson that decays into a lepton-neutrino pair. This is accompanied by a photon emission from one of the participating charged particles, with emission from the up quark being the dominant contribution. The resulting decay amplitude depends on the first inverse moment $\lambda_B^{-1} = \int_0^\infty d\omega \Phi_{B^+}(\omega)/\omega$, where $\Phi_{B^+}(\omega)$ is the B meson light-cone distribution amplitude in the high energy limit. This parameter is an important input to the QCD factorization scheme used in charmless non-leptonic B decay amplitudes [3]. It cannot be calculated reliably by theory and therefore a tighter experimental limit on—or measurement of λ_B would improve the predictions for all of these processes.

The decay $B^+ \to \ell^+\nu_\ell\gamma$ allows for the determination of λ_B with relatively small uncertainty, since the decay width is otherwise proportional to a set of well known parameters in leading order: $\Gamma(B^+ \to \ell^+\nu_\ell\gamma) \propto \frac{\alpha_{\rm em}(|V_{ub}|G_F m_B f_B)^2}{\lambda_B^2} + \mathcal{O}\left(\frac{1}{m_b}\right)$. Here $\alpha_{\rm em}$ is the electromagnetic coupling constant, V_{ub} is the CKM matrix element, G_F is the Fermi coupling constant, m_B is the B meson mass, and f_B is the decay constant of the B meson. The calculation is performed in Heavy Quark Effective Theory [4] which is valid for a high energetic photon emission above the QCD scale of $E_\gamma \gg \Lambda_{QCD}$. The largest theoretical uncertainty, originating from a soft sub-leading order contribution of the light quark, has been calculated to higher precision [5].

The most stringent limits for the decay process have been reported by the BaBar collaboration [6] at the 90% confidence level, with $\mathcal{B}(B^+ \to e^+\nu_e\gamma) < 17 \times 10^{-6}$, $\mathcal{B}(B^+ \to \mu^+\nu_\mu\gamma) < 26 \times 10^{-6}$, $\mathcal{B}(B^+ \to \ell^+\nu_\ell\gamma) < 15.6 \times 10^{-6}$, and a partial branching fraction $\Delta\mathcal{B}(B^+ \to \ell^+\nu_\ell\gamma) < 14 \times 10^{-6}$ for photons with energies higher than 1 GeV. For a preferred value of $\lambda_B \approx 200$ MeV, a Standard Model branching fraction of $\mathcal{B}(B^+ \to \ell^+\nu_\ell\gamma) \approx \mathcal{O}(10^{-6})$ is expected [4].

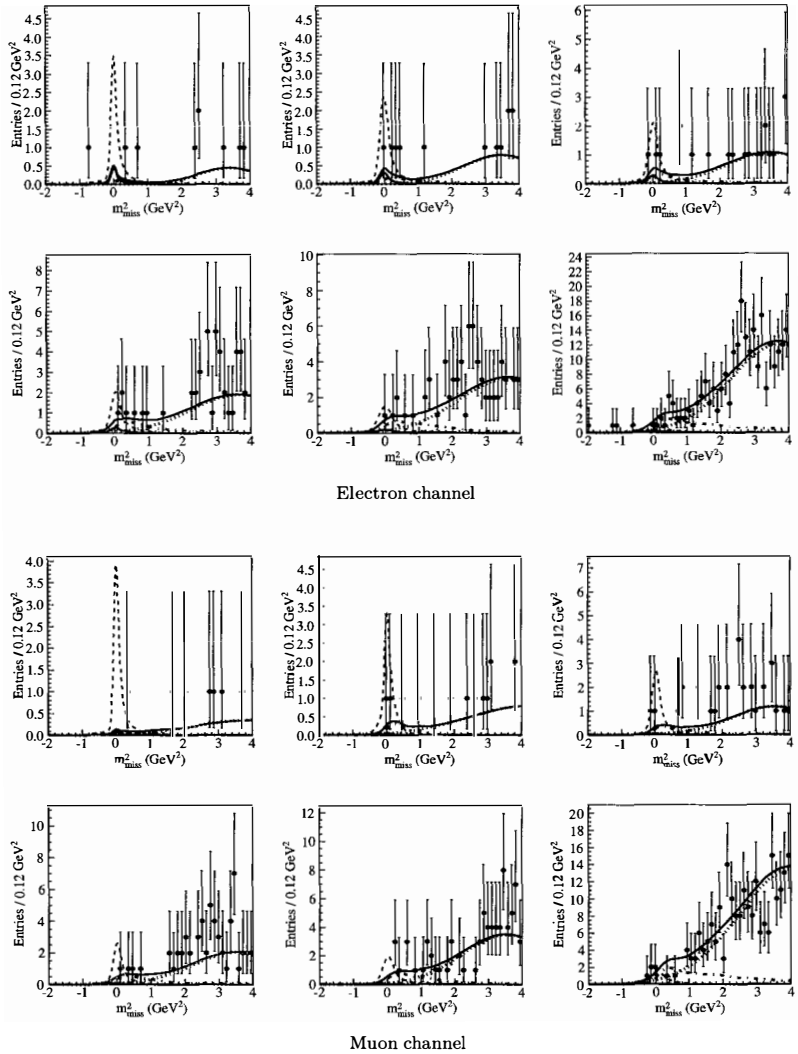

Figure 1 – Distributions of $m^2_{\rm miss}$ on data (points with error bars) in bins of the network output. The PDFs are for signal (solid blue), enhanced signal (dashed violet), fixed $B \to X_u \ell^+ \nu_\ell$ backgrounds (dash-dotted green), fitted backgrounds (dotted red), and the sum (solid black). The enhanced signal function, which has the same normalization for each bin, corresponds to a branching fraction of 30×10^{-6}. The most signal-like bin is found in the upper left panel and the most background-like bin in the lower right panel.

2 Analysis procedure

Our measurement is performed on the full Belle data sample of $(771.6 \pm 10.6) \times 10^6 B\bar{B}$ pairs recorded by the Belle detector [7] which were collected at the KEKB asymmetric-energy e^+e^- collider [8] running at the $\Upsilon(4S)$ resonance. The analysis procedure is determined using Monte Carlo (MC) samples where for the background study, $B\bar{B}$ processes with $e^+e^- \to \Upsilon(4S) \to B\bar{B}$

and $e^+e^- \to q\bar{q}(q = u, d, s, c)$ continuum processes are used. For the signal MC the model from Ref. [4] is implemented.

As the neutrino of the signal decay cannot be detected, the full reconstruction technique is used to put strong constraints on the kinematics of the signal decay. One of the B mesons ($B_{\rm tag}$) is reconstructed in many hadronic decay channels, where a hierarchical reconstruction scheme with neural network (NN) based estimators for each decay channel is used [9]. The algorithm provides an NN output which corresponds to the probability of the $B_{\rm tag}$ being correctly reconstructed. This network also contains event-shape variables which distinguish between continuum processes and $B\bar{B}$ events. The hadronic reconstruction has an efficiency of about 0.6% for our signal process.

With the $B_{\rm tag}$ candidate three-momentum $\vec{p}_{B_{\rm tag}}$, the four-momentum of the signal-side $B_{\rm sig}$ meson in the CMS is given by $p_{B_{\rm sig}} = (E_{\rm beam}/c, -\vec{p}_{B_{\rm tag}})$; here the meson energy is identified with the beam energy. This approach makes use of the two-body decay kinematics of the $\Upsilon(4S)$ and the measured CMS boost of the $B\bar{B}$ system. The $B_{\rm sig}$ four-momentum is used to compute the squared missing mass, which is the strongest discriminator between signal and background. The variable is defined as $m^2_{\rm miss} = (p_{B_{\rm sig}} - p_\ell - p_\gamma)^2/c^4$, where the four-momenta of the daughter lepton and photon are subtracted from that of the $B_{\rm sig}$ meson. For correctly reconstructed signal events, the variable corresponds to the neutrino mass and therefore peaks around zero. For the signal extraction, the region with $m^2_{\rm miss} \in (-2.0, 4.0)\mathrm{GeV}^2/\mathrm{c}^4$ around the signal peak is used. According to the theoretical recommendation [4], the analysis is performed for signal photon energies above 1 GeV in the $B_{\rm sig}$ rest frame.

2.1 Signal selection

After hadronic tag-side reconstruction, one charged track and one high-energy photon are expected in the detector. This simple decay signature allows for a very efficient signal selection. No additional charged-tracks beyond the signal's lepton daughter are permitted. The charged-track candidate is required to be of opposite charge of the $B_{\rm tag}$. Its impact parameters have to lie within $dr < 2\,\mathrm{cm}$ and $|dz| < 4\,\mathrm{cm}$, where $|dz|$ and dr are the distances of closest approach of the track to the interaction point along the beam axis and in the transverse plane, respectively. Electrons and muons are identified by likelihood variables combining information from several detector parts. A high-momentum neutrino is selected by requiring the missing momentum in the event to be above $800\,\mathrm{MeV/c}$ in the $B_{\rm sig}$ rest frame. Further selections are made on the angles between signal particles to veto events in which bremsstrahlung of the signal electron is mis-reconstructed as the signal photon, and to veto badly modeled continuum processes. The remaining energy in the electromagnetic calorimeter ($E_{\rm ECL}$) is the summed energy of clusters not associated with signal or tag-side particles and it is required to be below 900 MeV. To suppress the main background of $B^+ \to \ell^+\nu_\ell\pi^0$ decays, a π^0 veto is constructed that combines the signal photon candidate with all remaining photons in the ECL above an energy of 100 MeV to compute the invariant mass, where only the candidate closest to the nominal π^0 mass is kept. A window of $30\,\mathrm{MeV/c^2}$ around the nominal π^0 mass is vetoed. For the tag-side, the beam-energy-constrained mass $M_{\rm bc} = \sqrt{E^2_{\rm beam} - \vec{p}^{\,2}_{B_{\rm tag}}}\,/c^2$ is required to be greater than $5.27\,\mathrm{GeV/c^2}$. The NN output of the $B_{\rm tag}$ meson is chosen to have a probability above 2×10^{-4} of being correctly reconstructed. The overall signal selection efficiency after full reconstruction is 47% (45%) for the muon (electron) channel.

2.2 Network training and fit

For the final signal selection another NN is formed where the $E_{\rm ECL}$ and the angles between the signal particles are used as input. To further separate the main background processes of

$B^+ \to \ell^+\nu_\ell\pi^0$ and $B^+ \to \ell^+\nu_\ell\eta$, where the π^0 and η decay into two photons and one of the photons is misidentified as the signal photon, meson-veto variables are added to the network. These are computed in the same way as for the signal selection above but with different energy thresholds on the remaining photons in the ECL.

The signal yield is extracted in an extended unbinned maximum likelihood fit to the $m^2_{\rm miss}$ distribution in six bins of the NN output. The fit model consists of three components: $B^+ \to \ell^+\nu_\ell\gamma$ signal; measured $b \to u\ell^+\nu_\ell$ decays referred to hereinafter as the $B \to X_u\ell^+\nu_\ell$ component; and a component denoted as "fitted background" that includes unmeasured $b \to u\ell^+\nu_\ell$ contributions, resonant $b \to c$ decays and non-resonant $q\bar{q}$ processes. In the fit to data, the expected yield of the $B \to X_u\ell^+\nu_\ell$ component containing mainly the known decay modes with $X_u = \pi^0, \eta$, and ω is fixed according to the world average values. The shapes of the three components are determined from MC in each network output bin separately and fixed in the fit to data together with the relative normalizations among the bins. Each bin contains the same number of expected signal events, and the bin number is chosen to maximize the expected significance of the signal. The number of signal and fitted background events are the two free parameters of the fit model. The two signal channels $B^+ \to e^+\nu_e\gamma$ and $B^+ \to \mu^+\nu_\mu\gamma$ are measured in separate fits. Additionally, the $B^+ \to \ell^+\nu_\ell\gamma$ branching fraction is measured in a simultaneous fit to both channels, where the branching fractions of both channels are fixed to the same value.

3 Measurement

The fit results are listed in Table 1 and the $m^2_{\rm miss}$ distributions are shown in Fig. 1 for both signal channels. No significant signal is found in any of the fits and the fitted background yields are in agreement with the MC prediction. The limits are given by the 90% quantile of the likelihood function, where systematic uncertainties are included by convolving the likelihood with a Gaussian function whose width is equal to the systematic error. From the $B^+ \to \ell^+\nu_\ell\gamma$ limit, a central value $\lambda_B > 238\,\text{MeV}$ is obtained at 90% credibility level. The limit changes within a range of $\lambda_B > (172, 410)\text{MeV}$ by varying external input parameters. Consistent results are obtained for a secondary analysis with a relaxed signal photon energy threshold of 400 MeV.

Table 1: Measured signal yields on data, where the first error is statistical and the second error systematic. The significances and 90% credibility levels contain systematic errors.

Mode	Signal yield	$\mathcal{B}$ (10^{-6})	Significance (σ)	$\mathcal{B}$ limit (10^{-6})
$B^+ \to e^+\nu_e\gamma$	$6.1^{+4.9\,+1.0}_{-3.9\,-1.3}$	$3.8^{+3.0\,+0.7}_{-2.4\,-0.9}$	1.7	< 6.1
$B^+ \to \mu^+\nu_\mu\gamma$	$0.9^{+3.6\,+1.0}_{-2.6\,-1.5}$	$0.6^{+2.1\,+0.7}_{-1.5\,-1.1}$	0.4	< 3.4
$B^+ \to \ell^+\nu_\ell\gamma$	$6.6^{+5.7\,+1.6}_{-4.7\,-2.2}$	$2.0^{+1.7+0.6}_{-1.4-0.7}$	1.4	< 3.5

References

1. In common HEP usage, Bayesian intervals or credibility levels have been reported as "confidence intervals" or "confidence levels", which is a frequentist-statistics term.
2. Throughout the text, the inclusion of the charge-conjugate decay mode is implied.
3. M. Beneke *et al.*, Nucl. Phys. B **591**, 313 (2000).
4. M. Beneke and J. Rohrwild, Eur. Phys. J. C **71**, 1818 (2011).
5. V. M. Braun and A. Khodjamirian, Phys. Lett. B **718**, 1014 (2013).
6. B. Aubert *et al.* (BaBar Collaboration), Phys. Rev. D **80**, 111105 (2009).
7. Detector section in J. Brodzicka *et al.*, Prog. Theor. Exp. Phys. **2012**, 04D001 (2012).
8. T. Abe *et al.*, Prog. Theor. Exp. Phys. **2013**, 03A001 (2013).
9. M. Feindt *et al.*, Nucl. Instr. and Meth. A **654**, 432 (2011).

Boosted W-Boson Identification at $\sqrt{s} = 8$ TeV with the ATLAS Detector

Chris Malena Delitzsch
on behalf of the ATLAS Collaboration
Département de Physique Nucléaire et Corpusculaire, Quai Ernest-Ansermet 24, 1211 Geneva, Switzerland

The performance of boosted hadronic W-boson identification has been studied with the data collected in 2012 with the ATLAS detector at the Large Hadron Collider and is presented here. Different jet grooming algorithms have been tested in simulated events to estimate the discrimination of signal jets coming from the decay of W-bosons with respect to light-quark and gluon jets. The performance of W-boson tagging based on the jet mass and different jet substructure variables is compared. Tagging variables with a high background rejection are compared in data and simulation using a pure sample of W-boson jets in top-quark pair events. Good agreement has been observed for all the variables considered.

1 Introduction

The high center-of-mass energy of the pp collisions at the LHC enables searches for new particles with masses at the TeV scale. These heavy resonances can decay to final states with high p_{T} W- and Z-bosons. The hadronic decay modes of these bosons hold the potential for increased sensitivity via use of jet substructure techniques. However the cross-section of background events originating from light-quark and gluon jets is orders of magnitude higher than the production of W/Z-bosons. At large transverse momentum p_{T}, the decay products of the boson are collimated into one individual large-radius jet. Due to the high-luminosity conditions, soft particles unrelated to the hard scattering can contaminate these jets resulting in a diminished mass resolution. To enhance the sensitivity to new physics processes and to mitigate the influence of pile-up, jet grooming algorithms such as trimming [1] and mass-drop filtering [2] (BDRS) have been designed. In addition, substructure techniques are used to distinguish a two-body decay of a boson from a jet originating from gluons or light-quarks. Within the ATLAS Collaboration [3] the combinations of these techniques have been extensively studied [4] to identify boosted W-bosons. The same techniques could be in principle used to identify boosted Z-bosons.

2 Samples and Event Selection

Simulations of Kaluza-Klein gravitons [5] G $\dashrightarrow WW \dashrightarrow \ell\nu jj$ with masses between 400 and 2000 GeV are used to provide a pure sample of jets from hadronically decaying W-bosons. For the background, jets produced in association with a $W(\dashrightarrow \ell\nu)$ and $Z(\dashrightarrow \ell\ell)$-boson are used. Jets originating from light-quarks and gluons are in the following referred to as "QCD jets".
To make an unbiased comparison of the different grooming techniques and jet clustering algorithms, the leading calorimeter jet has to be matched to the same C/A $R = 1.2$ ungroomed truth jet with $p_{\mathrm{T}} > 100$ GeV which is then used to divide the sample in different p_{T} bins.

3 Jet Algorithm and Grooming Algorithms

Jets used in the following studies are reconstructed either with the anti-k_t [6] or the Cambridge-Aachen (C/A) [7,8] algorithms. To uncover the hard substructure of signal jets in dense pile-up conditions, several grooming algorithms have been studied but only the best performing are presented: trimming and the BDRS algorithm.

For the trimming algorithm, subjets of $R = 0.3$ are removed if they carry less than 5% of the parent anti-k_t $R = 1.0$ jet p_T.

The BRDS algorithm decomposes a C/A jet with $R = 1.2$ (J) into two subjets j_1, j_2 ($m_{j_1} > m_{j_2}$) by undoing its last clustering step. If there is a significant mass drop $\mu_{12} = m_{j_1}/m_J < \frac{2}{3}$ and the subjets are balanced in momentum $\sqrt{y_f} = \frac{\min(p_T^{j1}, p_T^{j2})}{m_J} \times \Delta R_{12} > 0.3$, the jet J is presumed to have an underlying hard structure and is kept. Otherwise the procedure is repeated with $J \rightarrow j_1$.

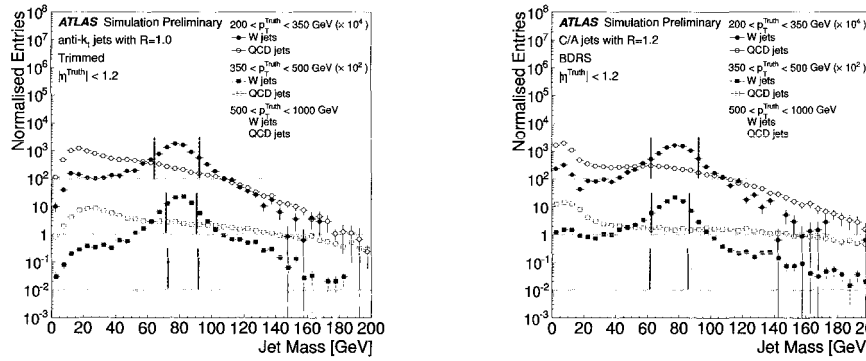

Figure 1 – Reconstructed mass distribution for anti-k_t $R = 1.0$ trimmed jets (left) and C/A $R = 1.2$ BDRS jets (right). Shown are the jet mass distributions in signal (W-jets) and background (QCD-jets) for three different p_T bins. The smallest mass window containing 68% of the signal events is indicated by the blue vertical lines [4].

4 Grooming Algorithm Performance

The jet mass distributions are used to compare the performance of the different jet grooming algorithms and are shown in Fig. 1 for anti-k_t $R = 1.0$ trimmed jets and C/A $R = 1.2$ BDRS jets in signal and background. A good grooming algorithm is required to have the most probable value close to the mass of the W-bosons, and a minimal background efficiency within a mass window containing 68% of the signal events. Furthermore, a good signal mass resolution is required. The fraction of QCD jets within the 68% mass window is smaller for the BDRS algorithm than the trimmed algorithm at high p_T as shown in Table 1.

Table 1: Background efficiency in the smallest mass window containing 68% of the signal events for anti-k_t $R = 1.0$ trimmed jets and C/A $R = 1.2$ BDRS jets in different p_T bins.

p_T bin	anti-k_t $R = 1.0$ trimmed	C/A $R = 1.2$ BDRS
$200 < p_T^{truth} < 350$ GeV	13.6 ± 0.1 %	14.8 ± 0.1 %
$350 < p_T^{truth} < 500$ GeV	9.9 ± 0.2 %	7.8 ± 0.2 %
$500 < p_T^{truth} < 1000$ GeV	8.4 ± 0.5 %	6.7 ± 0.5 %

5 Tagging Variable Performance

In addition to the jet mass, the background rejection can be further increased by considering variables that classify whether a jet is more likely to come from the hadronic W-boson decay or from light-quarks and gluons. Examples for these variables are the splitting scales $\sqrt{d_{12}}$ [9], the momentum balance and the N-subjettiness τ_N [10]. The splitting scale $\sqrt{d_{12}}$ distinguishes whether the energy distribution of a jet is symmetric (W-boson) or asymmetric (QCD jet). The N-subjettiness describes to what degree the substructure of a given jet is compatible with the hypothesis of the jet to consist of N or fewer subjets. To discriminate a jet containing N subjets, the ratio τ_N/τ_{N-1} is used. Hence for the two-body W-boson decay, the ratio is τ_2/τ_1. The discriminating power of $\sqrt{d_{12}}$, $\sqrt{y_f}$ and τ_{21} are shown in Fig. 2 for anti-k$_t$ trimmed and C/A BDRS jets.

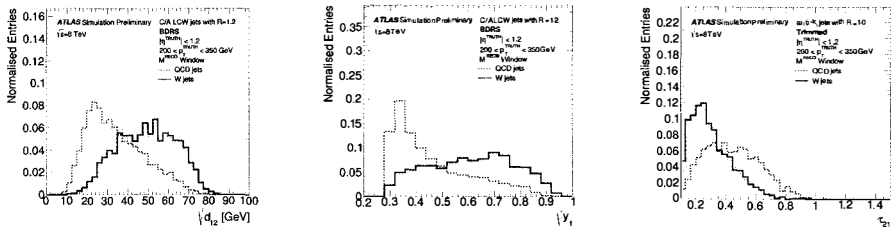

Figure 2 – Distributions of the jet splitting scale $\sqrt{d_{12}}$ (left) and momentum balance $\sqrt{y_f}$ (middle) for C/A $R = 1.2$ BDRS jets and the two-subjettiness τ_{21} (right) for anti-k$_t$ $R = 1.0$ trimmed jets. Shown are the distributions for signal (solid) and background (dashed) jets with $200 < p_{\mathrm{T}}^{\mathrm{Truth}} < 350$ GeV [4].

Within the 68% mass window, the signal efficiency against the background rejection (1 – background efficiency) is shown in Fig. 3, for each substructure variable considered. Only the grooming algorithm with the highest background rejection at a fixed signal efficiency of 50% is shown. The left side of Fig. 3 shows only the effect of the substructure tagging variable whereas the right side shows the combined effect of the mass window cut ($\epsilon_{\mathrm{W\ Jets}}^{\mathrm{Groom}} = 68\%$) and the tagging variable (ϵ^{Tag}). At low signal efficiencies, a high background rejection can be achieved with the BDRS algorithm and $\sqrt{y_f}$ as tagging variable whereas for high signal efficiencies, $\sqrt{d_{12}}$ has a higher background rejection.

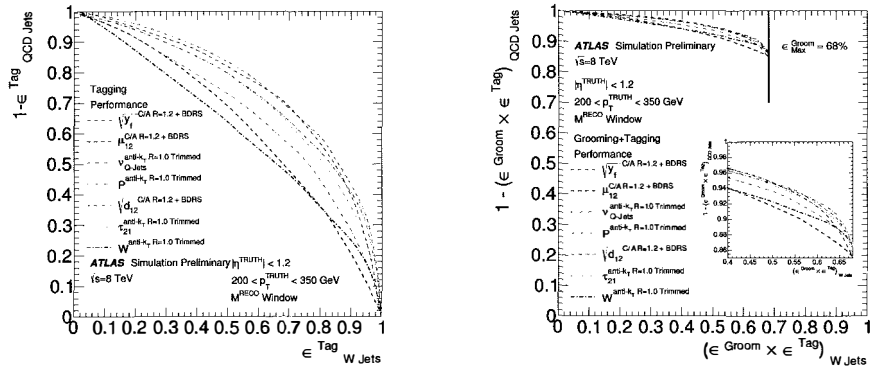

Figure 3 – Comparison of the background rejection ($1-\epsilon_{\mathrm{QCD\ Jets}}^{\mathrm{Tag}}$) as a function of the signal efficiency $\epsilon_{\mathrm{W\ Jets}}^{\mathrm{Tag}}$ for different substructure variables. For each variable only the jet algorithm with the highest background rejection is shown. The tagger performance (left) where the optimal mass window selection is applied in both the numerator and denominator is compared to the tagger+groomer performance (right) using the mass window cut only in the numerator. The grooming efficiency for signal jets $\epsilon_{\mathrm{W\ Jets}}^{\mathrm{Groom}}$ is 68% [4].

6 Substructure Variable Comparison in Data and Simulation

The modelling in the simulation of the variables employed in the tagging algorithms is as important as being able to achieve a large background rejection. In order to compare the distributions in simulation and data, the HEPTopTagger [11,12] algorithm is used to select hadronic boosted W-bosons from lepton+jcts $t\bar{t}$ events. The dataset used for these studies corresponds to an integrated luminosity of $\mathcal{L} = 20.3$ fb^{-1} collected at a center-of-mass-energy of $\sqrt{s} = 8$ TeV. Fig. 4 depicts the jet mass, splitting scale $\sqrt{d_{12}}$ and two-subjettiness τ_{21} for anti-k$_t$ $R = 1.0$ trimmed jets in data and simulation. In addition, a Kolmogorov-Smirnov test is performed to test the compatibility between data and simulation. Overall good agreement is observed for the jet mass and the substructure variables.

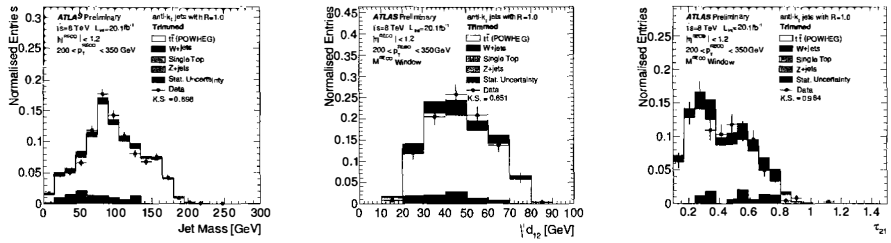

Figure 4 – Leading groomed jet mass (left), splitting scale $\sqrt{d_{12}}$ (middle) and two-subjettiness τ_{21} (right) distribution for anti-k$_t$ $R = 1.0$ trimmed jets in data and MC simulation events passing the HEPTopTagger selection [4].

7 Conclusions

The identification of hadronic W-bosons has been performed with the ATLAS data recorded in 2012 at a center-of-mass energy of $\sqrt{s} = 8$ TeV. To enhance the signal W-bosons over the QCD background (which is many orders of magnitude larger), different jet grooming algorithms and tagging variables have been explored and their combined performance has been studied. The full 2012 dataset corresponding to an integrated luminosity of $\mathcal{L} = 20.3$ fb^{-1} has been used to compare the tagging variables in data and simulation in top-quark pair events which provide a pure sample of hadronic W-bosons. Good agreement was observed for all the variables.

References

1. D. Krohn, J.Thaler, and L.-T. Wang *JHEP* **02**, 084 (2010)
2. J.M Butterworth et al., *Phys. Rev. Lett.* **100**, 242001 (2008)
3. ATLAS Collaboration, JINST **3**, S08003 (2008)
4. The ATLAS Collaboration, ATL-PHYS-PUB-2014-004 (2014)
5. K. Agashe, H. Davoudiasl, G. Perez, and A. Soni, *Phys. Rev.* D **76**, 036006 (2007)
6. M. Cacciari, G.P. Salam and G. Soyez *JHEP* **04**, 063 (2008)
7. Y. L. Dokshitzer, G. D. Leder, S. Moretti and B. R. Webber, *JHEP* **08**, 001 (1997)
8. M. Wobisch and T. Wengler, arXiv:hep-ph/9907280 (1999)
9. J.M Butterworth, B.E. Cox, and J.R. Forshaw, *Phys. Rev.* D **65**, 096014 (2002)
10. J.Tahler and K. Van Tilburg, *JHEP* **03**, 015 (2011)
11. T. Plehn, G.P. Salam, and M. Spannowsky, *Phys. Rev. Lett.* **104**, 111801 (2010)
12. T. Plehn et. al *JHEP* **10**, 078 (2010)

Measurement of the distribution of ϕ^*_η in events containing dimuon pairs with masses between 30 and 500 GeV in 10.4 fb^{-1} of $p\bar{p}$ collisions

Xingguo Li
on behalf of D0 Collaboration
School of Physics and Astronomy,University of Manchester, Manchester M13 9PL, UK

We present a measurement of the distribution of the variable ϕ^*_η in dimuon pairs with masses between 30 and 500 GeV, using the complete Run II data collected by the D0 detector at the Fermilab Tevatron proton-antiproton collider. The integrated luminosity corresponds to 10.4 fb^{-1} at $\sqrt{s}$ = 1.96 TeV. The variable ϕ^*_η probes the same physics as the Z/γ^* boson transverse momentum, but is less sensitive to the effects of experimental resolution and efficiency. The data, having been corrected for detector effects, are presented in bins of dimuon mass and rapidity and compared to QCD predictions based on the resummation of multiple soft gluons.

1 Introduction

In hadron colliders Drell-Yan dilepton pair decays of Z/γ^* may be produced with a non-zero momentum in the plane transverse to the beam direction, $p_T^{\ell\ell}$, due to recoils of gluons or quarks radiated from the incoming partons. The precise study of Drell-Yan $p_T^{\ell\ell}$ distribution provides an ideal ground for testing and improving initial state QCD radiation models because of the relatively low background and absence of color flow between initial state and final state. Understanding the performance of such models has important implications in W mass measurement and Higgs production as well as new physics searches at hadron colliders.

In the low region of $p_T^{\ell\ell}$ spectrum, the precision is limited by uncertainties for correcting effects of experimental resolution and efficiency. An alternative variable ϕ^*_η [1], with better experimental resolution and low susceptibility to detector effects, has been introduced to probe the low-$p_T^{\ell\ell}$ domain of Z/γ^* production. The ϕ^*_η variable is defined as:

$$\phi^*_\eta \equiv \tan\left(\phi_{\rm acop}/2\right) \sin\theta^*_\eta, \tag{1}$$

where $\phi_{\rm acop}$ is the acoplanarity angle, given by: $\phi_{\rm acop} = \pi - \Delta\phi^{\ell\ell}$, and $\Delta\phi^{\ell\ell}$ is azimuthal opening angle between the leptons.

Figure 1 presents a schematic diagram of relevant variables in the plane transverse to the beam direction [2]. The variable θ^*_η is a measure of the scattering angle of the leptons with respect to the proton beam direction in the rest frame of the dilepton system. It is defined by:

$\cos(\theta^*_\eta) = \tanh\left[(\eta^- - \eta^+)/2\right]$, where η^- and η^+ are the pseudorapidities of the negatively and positively charged lepton, respectively. Thus ϕ^*_η depends exclusively on the track directions of the two leptons, which is experimentally better measured than quantities relying on the momenta of the leptons, such as $p^{\ell\ell}_T$. It is highly correlated with $p^{\ell\ell}_T/m_{ll}$, where m_{ll} is the invariant mass of the dilepton pair.

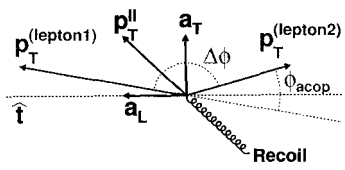

Figure 1 – Illustration in the plane transverse to the beam direction of the variables defined in the text and used to analyse the dilepton transverse momentum[2]. The variables a_T and a_L [3] correspond to the decomposition of $p^{\ell\ell}_T$ into two orthogonal components as illustrated.

In this proceeding we present a short description of the updated measurements [4] in the dimuon final state of the normalized ϕ^*_η distribution, $(1/\sigma) \times (d\sigma/d\phi^*_\eta)$, in bins of dimuon rapidity, $|y|$, in $p\bar{p}$ collisions at $\sqrt{s} = 1.96$ TeV. In addition to the measurements updated for $70 < m_{\ell\ell} < 110$ GeV to the complete 10.4 fb^{-1} data set collected by the D0 detector, we extend the measurements to "off-peak" samples of dimuon events and consider ranges of $m_{\ell\ell}$ between 30 and 500 GeV. These are the first measurements at any collider of the ϕ^*_η distributions away from the Z peak.

2 Event selection and analysis mythology

Simulation samples are used to model Drell-Yan dimuon signal and background processes from $Z/\gamma^* \to \tau^-\tau^+$, $W \to \ell\nu$ (+jets), and $WW \to \ell\nu\ell\nu$. Background from multijet events is estimated using data-driven techniques.

Candidate dimuon events are required to pass the single-muon trigger and required to be matched to a pair of oppositely–charged particle tracks reconstructed in the central tracking detectors with momentum transverse to the beam direction of $p_T > 15$ GeV and $|\eta| < 2$. Candidate muons are required to pass identification and isolation criteria to reject misidentified hadrons or in-flight decay of hadrons. Contamination from cosmic ray muons is eliminated by requirements on the primary vertex impact parameters, times-of-flight and rejecting events in which the two muon candidates are back to back in η.

In the off-peak region, additional selection criteria are imposed to select well-measured Drell-Yan dimuon events with acceptable levels of background. An important source of background in all the off-peak samples of dimuon events arises from Drell-Yan dimuon events that originate close to the Z peak, but are reconstructed with a value of $m_{\ell\ell}$ away from the Z peak due to final state photon radiation (FSR) or the mis-measurement of the p_T of one of the muon candidates. Optimized cuts based on the momentum balance of the two leptons have been developed in the off-peak region to reject such migration background in $m_{\ell\ell}$.

For $70 < m_{\ell\ell} < 110$ GeV a total of 645k dimuon events is selected with a total background fraction of 0.2%, mainly arising from multijet background. A total of 74k dimuon events is selected for $30 < m_{\ell\ell} < 60$ GeV, where the selection criteria are relaxed to requiring $p_T > 10$ GeV for both muons, with one muon required to satisfy $p_T > 15$ GeV to increase selection efficiency in this low-mass region and to reduce any bias on the distribution of ϕ^*_η. After event selection in the low-mass region, $Z/\gamma^* \to \tau^-\tau^+$accounts for 5% of the total background and the fraction of migration in $m_{\ell\ell}$ is 1.3%, with the remaining background amount to 1.8% mainly from multijet background. For the mass ranges $160 < m_{\ell\ell} < 300$ GeV and $300 < m_{\ell\ell} < 500$ GeV, respectively, the numbers of selected events are 1744 and 207, and the fractions of the selected event samples arising from migration background are 24% and 44%, respectively.

3 Differential cross-section measurement and systematic uncertainties

The observed ϕ^*_η distributions are corrected for background, and for experimental efficiency and resolution. When evaluating the correction factors, the same kinematic selection criteria on $m_{\ell\ell}$ and muon p_T and pseudorapidity used in data is applied at the MC particle level as

specified above. For this purpose, MC particle level muons are defined after QED final state radiation, which mimics the measurement of muon momentum in the tracking detector. Since the experimental resolution in ϕ^*_η is narrower than the chosen bin widths, simple bin-by-bin corrections of the ϕ^*_η distribution are sufficient.

In almost all ϕ^*_η bins the total systematic uncertainty is substantially smaller than the statistical uncertainty. Dominant systematic uncertainties arise from variations of the muon identification and trigger efficiencies at the detector module boundaries throughout the dimuon mass spectrum of interest. Modeling of $Z/\gamma^* \to \tau^-\tau^+$ background is the main systematic uncertainty in the below Z peak region and uncertainties due to migration in $m_{\ell\ell}$ is the largest in the above Z peak region.

4 Comparison to QCD predictions

The corrected dimuon data are compared to the predictions from RESBOS[5,6] and from a calculation[7] with QCD corrections at the next-to-leading-order (NLO) and next-to-next-to-leading-log (NNLL) accuracy.

Figure 2 shows for $70 < m_{\ell\ell} < 110$ GeV the ratio of the corrected ϕ^*_η distributions to the RESBOS predictions. In addition to the dimuon data from the present analysis, the dielectron data from Ref.[2] are shown. Given that the experimental acceptance corrections are very different between dimuon and dielectron channels, this consistency represents a powerful cross check of the corrected distributions.

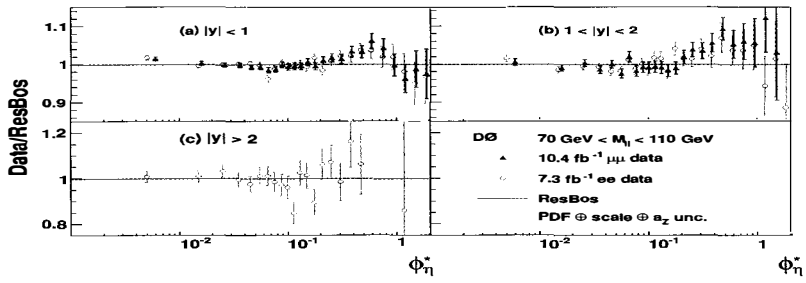

Figure 2 – Ratio of the corrected distributions of $(1/\sigma) \times (d\sigma/d\phi^*_\eta)$ in dielectron and dimuon data to the predictions of RESBOS for $70 < m_{\ell\ell} < 110$ GeV: (a) $|y| < 1$ and (b) $1 < |y| < 2$. The error bars on the data points represent statistical and systematic uncertainties combined in quadrature. The yellow band around the RESBOS prediction represents the quadrature sum of uncertainty due to PDFs, QCD scales and non-perturbative parameter a_Z.

Figure 3 shows for $30 < m_{\ell\ell} < 60$ GeV the ratio of the corrected ϕ^*_η distributions to the the NNLL+NLO predictions of Ref.[7,8]. The prediction describes the corrected data well within the assigned theoretical uncertainties.

Figure 4 shows for $160 < m_{\ell\ell} < 300$ GeV and and $300 < m_{\ell\ell} < 500$ GeV the ratio of the corrected ϕ^*_η distributions to the RESBOS predictions. Within the fairly large statistical uncertainties, the predictions are in reasonable agreement with the corrected data.

5 Conclusion

Using 10.4 fb^{-1} of $p\bar{p}$ collisions we have measured the normalized ϕ^*_η distribution, $(1/\sigma) \times (d\sigma/d\phi^*_\eta)$, in two bins of dimuon rapidity and in four bins of dimuon mass. Relative to the results presented in Ref.[2], these measurements in the dimuon channel represent an extension to the full D0 data set and also to regions of dimuon mass away from the Z peak. The data are reasonably well

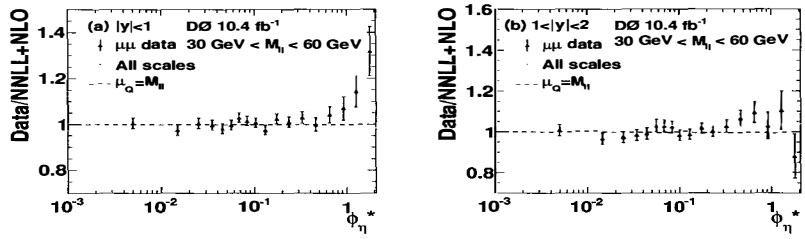

Figure 3 – Ratio of the corrected distributions of $(1/\sigma) \times (d\sigma/d\phi_\eta^*)$ to the NNLL+NLO predictions of Ref. [7,8] for $30 < m_{\ell\ell} < 60$ GeV: (a) $|y| < 1$ and (b) $1 < |y| < 2$. Statistical and systematic uncertainties are combined in quadrature. The yellow band around the NNLL+NLO prediction represents the uncertainty due to variations in the QCD scales.

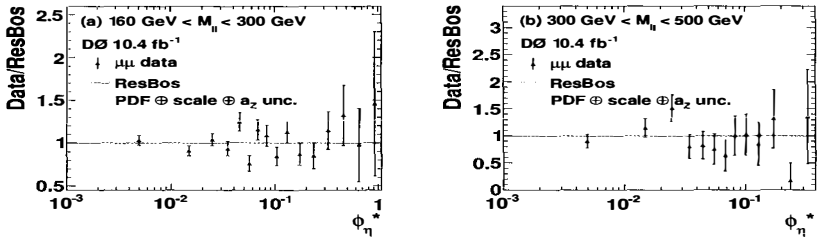

Figure 4 – Ratio of the corrected distributions of $(1/\sigma) \times (d\sigma/d\phi_\eta^*)$ to RESBOS for (a) $160 < m_{\ell\ell} < 300$ GeV and (b) $300 < m_{\ell\ell} < 500$ GeV. Statistical and systematic uncertainties are combined in quadrature. The yellow band around the RESBOS prediction represents the quadrature sum of uncertainty due to PDFs, QCD scales and non-perturbative parameter a_Z.

described within the theoretical uncertainties by the RESBOS predictions and by the predictions at NNLL+NLO accuracy of Ref. [7,8].

References

1. A. Banfi, S. Redford, M. Vesterinen, P. Waller, T. R. Wyatt, Eur. Phys. J. **C 71**) 1600 (2011).
2. DØ Collaboration, V. M. Abazov *et al.*, Phys. Rev. Lett. **106** 122001 (2011).
3. M. Vesterinen and T. R. Wyatt, Nucl. Instr. and Meth. **A602** (2009) 432.
4. DØ Collaboration, V. M. Abazov *et al.*, Phys. Rev. D **91**, 072002 (2015)
5. C. Balazs, C. P. Yuan, Phys. Rev. D **56**, 5558 (1997).
6. M. Guzzi, P.M. Nadolsky and B. Wang, arXiv: 1309.1393v1(2013).
7. A. Banfi, M. Dasgupta, S. Marzani, L. Tomlinson, J. High Energy Phys. **1201**, 044 (2011).
8. L. Tomlinson, private communication.

LOW MASS WIMP SEARCH WITH EDELWEISS-III: FIRST RESULTS

Thibault DE BOISSIÈRE[a] (for the EDELWEISS collaboration)
CEA, Centre d'Études Saclay, IRFU, 91191 Gif-Sur-Yvette Cedex, France

We present the first search for low mass WIMPs using the Germanium bolometers of the EDELWEISS-III experiment. Upgrades to the detectors and the electronics enhance the background discrimination and the low energy sensitivity with respect to EDELWEISS-II. A multivariate analysis is implemented to fully exploit the detector's potential, reaching a sensitivity of 7.5 $\times 10^{-6}$ pb for a WIMP mass of 7 GeV/c^2 with a fraction of the data set, unblinded for background modeling and analysis tuning.

1 The EDELWEISS experiment

A variety of observations (see [1] for a review) point to the existence of cold, non baryonic dark matter which would make up to 27% of the content of the universe [2]. After decades of experimentations, its nature remains poorly constrained. One well-motivated candidate (referred to as a Weakly Interacting Massive Particle or WIMP) arises from Beyond Standard Model theories like SUSY. Its mass and weak cross section naturally provide the observed relic density. If WIMPs exist, they should be found in the galactic halo and are expected to scatter off nuclei on Earth. This motivates direct detection experiments which search for nuclear recoils in massive detectors. The experimental challenge (background rejection at $\sim$ keV energies) requires the use of extremely pure materials in clean environments.

The EDELWEISS experiment operates germanium bolometers at very low temperatures (18 mK) in the Underground Laboratory of Modane. The detectors are protected from external radioactivity by lead and polyethylene (PE) shields. An active veto monitors cosmic muons in order to reject muon-induced neutrons, which can mimic the WIMP signal. Each detector is equipped with a set of interleaved electrodes and thermometers. These sensors measure the ionization and phonon signals triggered by incoming particles. The comparison of the two signals allows a separation of nuclear recoils from electron recoils induced for instance by β and γ radioactivity. The interleaved design modifies the field lines near the surface (see Fig. 1). This allows us to define a fiducial volume for each detector and to reject near-surface interactions using the information on the veto electrode.
The current setup includes some notable improvements over the previous phase of the experiment. A new PE shielding has been inserted between the bolometers and the electronics, while the copper used in the thermal shields has been replaced by much purer NOSV copper. The cryogenics have been upgraded as well: thermal machines are now placed outside the shields, allowing microphonics reduction. By replacing the feedback resistances with mechanical relays, the ionisation read-out was improved, yielding a 30% better baseline resolution. The detector design has evolved as well: detectors now carry interleaved electrodes on the lateral surfaces.

[a] thibault.main-de-boissiere@cea.fr

This increases the share of the fiducial volume to 75%, up from 40% and allows better rejection. The detectors are also more massive: 800 g up from 400 g.

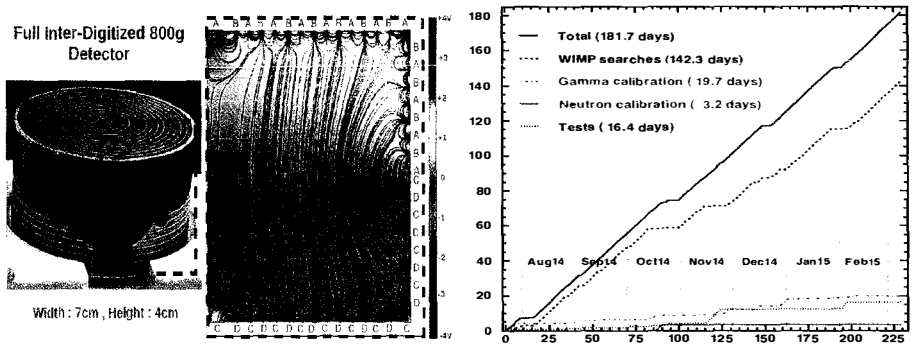

Figure 1 – **Left:** EDELWEISS-III Fully Inter-Digitized (FID) detector. The black lines show the electric field within the detector. **Right:** EDELWEISS-III data acquisition progress since summer 2014.

2 Low mass WIMPs

Recent excesses of events have been reported by collaborations such as CDMS [3] and CoGeNT [4], as well as from gamma ray surveys in the galactic center [5]. These excesses can be interpreted in terms of low mass WIMPs (5 - 30 GeV/c^2). These findings have renewed interests for light dark matter. Low mass WIMPs are particularly hard to identify in direct detection experiments because they generate extremely low energy recoils. This means a large part of the signal can be hidden by threshold effects. Event discrimination is also more difficult near the threshold because the different populations tend to overlap.

2.1 Data selection

In the analysis shown here, we used only a small fraction of the whole data set shown in Fig. 1. We unblinded a single, standard detector (called FID837) to tune the analysis and build background models. The analysis threshold was fixed at 3.6 keVnr (nuclear recoil energy scale). This is a conservative value, chosen such that the online trigger efficiency is 100% and that threshold effects can safely be neglected.
The data shown in this paper was first passed through gencral sclection cuts. These include a period selection based on the online trigger level: periods where the online trigger is higher than 2.4 keVnr were rejected. We also discarded time periods with noisy ionization or heat signals in order to ensure that the data set remains homogeneous. We also include quality cuts to remove noisy or poorly reconstructed events. Since we do not expect WIMP multiple scatters, multiple events are rejected. We further discard pile-up events which can lead to erroneous interpretations. Taking into account the efficiency of all these cuts, the fiducial volume and the deadtime correction leads to a final, effective exposure of 35 kg.d.
Then, we defined a loose "WIMP-box" cut in order to shrink the parameter space to the region with the highest likclihood of finding WIMPs. That is why we set the analysis range to 3.6 keVnr - 30 keVnr and imposed a lax cut on the veto electrodes (require less than 5 standard deviation on the veto electrodes). This cut has the advantage of facilitating the work of multivariate methods (which need to scan less parameter space) while leading to negligible efficiency loss.

2.2 Background and Signal models

All background models in this analysis were data driven. We have used sideband (i.e. region without signal) data to feed a generative model for well-known backgrounds (gamma, beta, lead recoils). Surface event models were cross checked against calibration data and were found to be in good agreement with a Kolmogorov Smirnov test. The so-called heat-only background required a more careful study. As can be seen from Fig. 2, this is the dominant background for this analysis. It is made of events for which only the heat signal is clearly identified. These events chart an irregular rate over time and are likely due to mechanical vibrations. Fortunately, above the analysis threshold, heat-only events can be fully characterised in a sideband.

The WIMP signal was generated using the well known theoretical formula for nuclear elastic scattering [6]. The parameterisation for the nuclear quenching factor is that of the EDELWEISS experiment, verified by many neutron calibrations: $Q(E) = 0.16 \times E^{0.18}$.

2.3 Results

We used TMVA's [8] Boosted Decision Trees (BDT) for the event discrimination. This is a multivariate method which combines several inputs into a single discriminating variable. The BDT first undergoes a training phase where it learns to separate background from signal. The feature space is spanned by the 4 ionisation and 2 heat channels of the EDELWEISS experiment. The training sample is generated with the background and signal models outlined in the previous section. Given that this work is essentially a validation study for future analyses, we decided to report an upper limit on the WIMP cross section. This was done by defining an optimal cut value on the BDT output and quoting the upper limit corresponding to the number of observed events after cut. The optimal cut value was derived from further simulations by maximising the signal over noise ratio, effectively rejecting all backgrounds (< 1 background event expected). A BDT was trained for each WIMP mass. The resulting limit is shown in Fig. 2 (right), showing competitive results in spite of the small exposure and relatively high threshold. Fig. 2 (left) shows that a clear separation between signal and background events can be achieved. This is a tribute to the new FID detector design which allows for remarkable surface event rejection. This clearly demonstrates the potential of EDELWEISS bolometers for low mass WIMP searches.

3 Conclusions

We analyzed the first data from the EDELWEISS-III experiment in a low mass WIMP search. The results are very promising for future searches: improvements in the baseline resolution (and hence the experimental threshold) allow a single detector (35 kg.d of exposure) to beat the published EDELWEISS-II low mass limit [7] (113 kg.d.) The experimental sensitivity will further increase by pushing the analysis in two directions: we are going to increase the available statistics by combining several detectors and we plan to decrease the analysis threshold in order to improve the sensitivity to very low mass WIMPs (< 5 GeV/c^2).

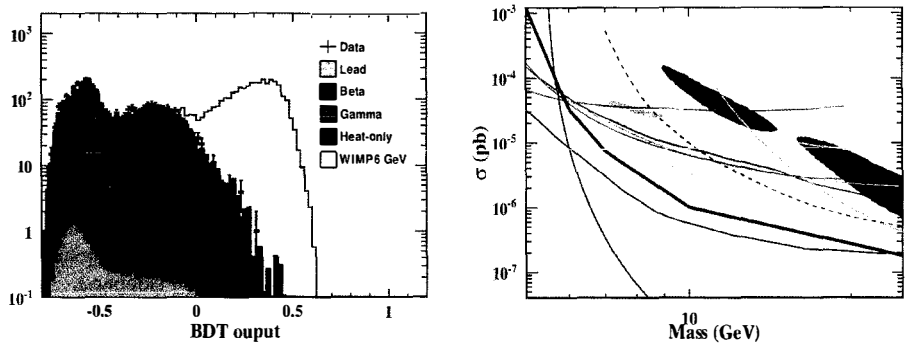

Figure 2 – **Left:** Boosted Decision Trees' discriminating variable. The colored histograms show the background contributions, the grey histogram shows the expected WIMP signal from a 6 GeV WIMP and the black dots are the data. **Right:** Limit on the WIMP cross section, given the WIMP masses. Color code: SCDMS (*blue*), CDMS-Si contour (*light blue*), CDMSlite (*purple*), DAMA (*salmon*), CRESST limit and contours (*green*), SIMPLE (*yellow*), COUPP (*gray*), PICO (*teal*), Xenon10 (*brown*), LUX (*black*), CoGeNT (*orange*), EDELWEISS-II (*dashed red*) and EDELWEISS-III 35 kg.d in (*red*) (this work).

4 Acknowledgements

The help of the technical staff of the Laboratoire Souterrain de Modane and the participant laboratories is gratefully acknowledged. The EDELWEISS project is supported in part by the German ministry of science and education (BMBF Verbundforschung ATP Proj.-Nr. 05A14VKA), by the Helmholtz Alliance for Astroparticle Phyics (HAP), by the French Agence Nationale pour la Recherche and the Labex Lyon Institute of Origins (ANR-10-LABX-0066) of the Universit de Lyon within the program "Investissement d'Avenir" (ANR-11-IDEX-00007), by Science and Technology Facilities Council (UK) and the Russian Foundation for Basic Research (grant No. 07-02-00355-a).

References

1. G. Bertone, D. Hooper, J. Silk, Particle Dark Matter: Evidence, Candidates and Constraints *Phys. Rept.*, 405:279-390
2. The Planck collaboration, Planck 2013 results. XVI. Cosmological parameters *A & A* 571 (2014)
3. R. Agnese et al. [CDMS Collaboration], *Phys. Rev. Lett.* 111 (2013) 251301
4. C. E. Aalseth et al. [CoGeNT Collaboration], *Phys. Rev.* **D** 88 (2013) 1, 012002.
5. D. Hooper and T. Linden, *Phys. Rev.* **D** 84 (2011) 123005.
6. J. D. Lewin and P. F. Smith. Review of mathematics, numerical factors, and corrections for dark matter experiments based on elastic nuclear recoil. *Astropart.Phys.*,6:87112, 1996.
7. E. Armengaud et al. Search for low-mass wimps with edelweiss-ii heat-and-ionization detectors. *Phys.Rev.* **D**, 86, 2012.
8. A. Hoecker, P. Speckmayer, J. Stelzer, J. Therhaag, E. von Toerne, and H. Voss, "TMVA: Toolkit for Multivariate Data Analysis," PoS A CAT 040 (2007) [physics/0703039].

ON THE USE OF THE ESCAPE SPEED ESTIMATES IN SETTING DARK MATTER DIRECT DETECTION LIMITS

S. MAGNI
Laboratoire Univers et Particules de Montpellier, Montpellier, France

J. LAVALLE
Laboratoire Univers et Particules de Montpellier, Montpellier, France

The knowledge of the high velocity tail of the WIMP velocity distribution has a strong impact on the way direct detection (DD) may constrain or discover light WIMPs in the GeV mass range. Recently, there have been important observational efforts to estimate the so-called Galactic escape speed at the position of the Earth, for instance the analysis published in early 2014 by the RAVE Collaboration [1], which is of interest in the perspective of reducing the astrophysical uncertainties in DD. Nevertheless, these new estimates cannot be used blindly as they rely on assumptions in the dark halo modeling, which induce tight correlations between the escape speed and other local astrophysical parameters (e.g. the local circular speed and dark matter density). We make a self-consistent study of the implications of the RAVE results on DD assuming isotropic DM velocity distributions, both Maxwellian and ergodic. Taking as reference the experimental sensitivities currently achieved by LUX, CRESST2, and SuperCDMS, we show that the DD constraints on WIMPs (and associated uncertainties) are slightly stronger (moderate).

1 Introduction

DD aims at detecting WIMPs via their scattering off nuclei. A careful investigation of the physics affecting the low WIMP mass region of the parameter space for the spin-independent interpretation of this scattering is fundamental, because at around 10 GeV signal-like events reported by some experiments (e.g. DAMA), are at odds with limits. Different effects impact DD limits at low WIMP masses, particularly relevant are the local escape speed from the Milky Way (MW) and the local circular speed, as the sum of both defines the maximum speed in the observer's frame. While the latter has been studied in depth by many authors, this is not the case for the former. A method to measure it is to use nearby high-velocity stars, that are supposed to trace the high velocity tail of the stars speed distribution, which should vanish at the escape speed. Following this approach, the RAVE collaboration published in 2014 the latest estimate of this quantity [1] (P14). Directly using those results to compute DD limits is straightforward, but this would lead to inconsistent results because neglecting the hypotheses these estimates rely upon. In our work [2] we analyzed these assumptions and derived a self-consistent model for the local phase-space of the DM, which consistently takes into account the correlations between the astrophysical parameters. We computed the corresponding exclusion curves, with associated uncertainties, for the most constraining experiments at the moment of writing.

2 Milky Way Mass Model from Rave analysis

P14 analysis is based on a sample of $\sim$ 100 stars mostly from the RAVE catalog. The escape speed for a star in $\vec{r}$ is defined as $v_{\rm esc}(\vec{r}) \doteq \sqrt{2\,|\Phi(\vec{r})|}$, $\Phi(\vec{r})$ being the gravitational potential GP of the MW. To derive observational constraints on $v_{\rm esc}$ from stellar velocities P14 needed to make an assumption on the shape of the high velocity tail of the stars speed distribution, namely $f_\star(v) \propto (v_{\rm esc} - v)^k$, with k calibrated from cosmological simulations. To estimate $v_{\rm esc}$ at the position of the Sun, P14 rescaled the $v_{\rm esc}$ of the observed stars using the GP of the MW, for which a particular MW mass model (MWM) had to be assumed and where only the DM halo parameters were left free. They thus transformed the line of sight velocity $v_{||}(\vec{r})$ of each star according to $v'_{||}(\vec{r}) = v_{||}(\vec{r}) \times \sqrt{|\Phi(\vec{r}_\odot)/\Phi(\vec{r})|}$ ($\vec{r}_\odot$ being the position of the Sun) before performing a likelihood analysis. This introduces a dependence on the MWM and thus correlations in the astrophysical parameters relevant to DD, that one must take into account when using P14 results.

P14 fixed the Sun's distance from the Galactic center $r_\odot = 8.28$ kpc [3], the peculiar motion of the Sun [4], and repeated the analysis for 3 cases: $v_{\rm c} = 220$ km/s, $v_{\rm c} = 240$ km/s and $v_{\rm c}$ free. Their MWM is based on a fixed baryonic model (disk and bulge), and on an NFW profile for the dark halo, the parameters of which were left free (the scale density ρ_s and radius r_s).

The speed of a body which is on a circular orbit on the Galactic plane can be computed from the GP of the MW as $v_{\rm c}^2(R,0) = R\frac{d\Phi(R,z)}{dR}\big|_{z=0}$ (here in cylindrical coordinates). The escape speed is set by the kinetic energy an object needs to get unbound, i.e. to reach a certain $R_{\rm max}$, it is thus defined as: $v_{\rm esc}(r_\odot) \doteq \sqrt{2\,|\Phi(r_\odot) - \Phi(R_{\rm max})|}$. To take into account the presence of nearby galaxies, the above distance is chosen to be $R_{\rm max} = 3R_{340}$ (where R_{340} is the radius at which the average DM density is 340 times the critical one). Since the assumed MWM has only two free parameters, a pair of ρ_s, r_s (or equivalently a pair of M_{340}, c_{340}) converts into a pair of $v_{\rm c}$, $v_{\rm esc}$. P14 results for the 3 cases mentioned above (prior or not on $v_{\rm c}$) can thus be converted in that plane, more relevant to DD; this is shown in Fig.1. It is clear from this figure that, because of the assumed MWM, the results of P14 induces strong correlations among $v_{\rm c}$, $v_{\rm esc}$ and the local DM density $\rho_\odot \doteq \rho_{DM}(r_\odot)$.

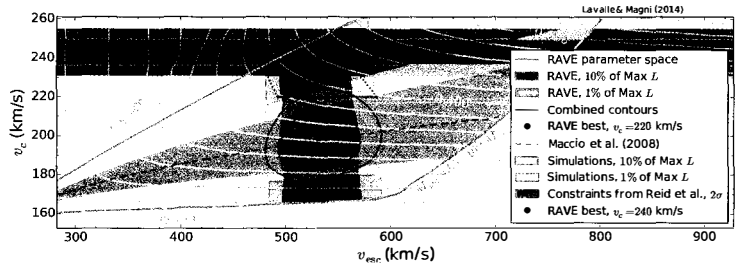

Figure 1 – P14 parameter space (yellow contours), with the regions where their likelihood for free $v_{\rm c}$ decreases down to the 10% (blue) and 1% (cyan) of its maximum, the best-fit P14 results for fixed $v_{\rm c} = 220$ km/s and $v_{\rm c} = 240$ km/s (with 90% C.L. error bars) and the curves of constant $\rho_\odot$ (in GeV/cm^3, in gray).

3 DD limits from P14 results and related astrophysical uncertainties

We translated the P14 estimates into DD limits, focusing on the spin-independent interpretation of the elastic scattering of a WIMP (mass m_χ) off a nucleus (atomic number A, mass m_A), and no isospin violation. The differential event rate per atomic target mass in an experiment is:

$$\frac{dR}{dE_r}(E_r) = \frac{\rho_\odot \sigma_{pSI} A^2}{2 m_\chi \mu_{\rm p}^2} F^2(E_r) \int_{|\vec{v}|>v_{min}(E_r)} d^3\vec{v} \frac{f_\oplus(\vec{v},t)}{|\vec{v}|}\ , \qquad (1)$$

with $\mu_{\rm p}$ the WIMP-proton reduced mass, E_r the recoil energy, σ_p the WIMP-nucleon cross section, $F\left(E_{\rm r}\right)$ the nuclear form factor (assumed of the Helm type), and $v_{min} = \sqrt{m_A E_r/(2\mu_{\rm p})}$ the minimal velocity that a WIMP needs to transfer to a nucleus the recoil energy E_r. $f_{\oplus}\left(\vec{v},t\right)$ is the DM velocity distribution in the Earth reference frame. In addition, we take into account the experimental efficiency, energy resolution of the detector, fractions of atomic targets, isotopic compositions for each target element, and we take the time average of Eq. 1.

Usually, DD limits are computed by means of the Standard Halo Model (SHM), a set of assumptions in which the WIMP velocity distribution is a truncated Maxwell-Boltzmann (MB), $f\left(\vec{v}\right) \doteq \left[\exp(-\left|\vec{v}\right|^2/v_{\rm c}^2) - \exp(-v_{\rm esc}^2/v_{\rm c}^2)\right] \bullet \left(v_{\rm esc} - \left|\vec{v}\right|\right) / \left(N_{\rm esc}\pi^{3/2}v_{\rm c}^3\right)$, where $N_{\rm esc}$ is the normalization and $\bullet$ the Heaviside step function. The SHM also fixes $\rho_{\odot}^{SHM} = 0.3$ GeV/cm^3, $v_{\rm c}^{SHM} = 220$ km/s and $v_{\rm esc}^{SHM} = 544$ km/s. Because of the by-hand cutoff at the escape speed, the MB distribution is no more a solution of the Jeans equation, so it is not even self-consistent.

In order to build a self-consistent velocity distribution, we are going to consider functions of integrals of motion, which automatically satisfy the Jeans equation. Assuming spherical symmetry and velocity isotropy, the phase-space distribution becomes a function of the total energy $E = m\Phi + \frac{1}{2}mv^2$ only, which is an integral of motion. Such systems are called ergodic [5]. Under these assumptions we can use the Eddington equation [6], which allows to compute the phase-space distribution for the DM directly from the assumed GP of the Milky Way Φ and the DM density profile ρ. This equation reads:

$$f\left(\epsilon\right) = \frac{1}{\sqrt{8}\pi^2}\left[\int_0^{\epsilon}\frac{d^2\rho}{d\Psi^2}\frac{d\Psi}{\sqrt{\epsilon-\Psi}} + \frac{1}{\sqrt{\epsilon}}\left(\frac{d\rho}{d\Psi}\right)_{\Psi=0}\right] , \qquad (2)$$

where $\Psi = -\Phi + \Phi_0$ is the relative GP of the MW, $\epsilon = -E/m + \Phi_0$ the relative energy per unit mass and Φ_0 a constant. The local velocity distribution for the DM is given by $f_{\rm erg}\left(v, r_{\odot}\right) = f\left(\epsilon\right)/\rho\left(r\right)$. This procedure can be applied only to spherically symmetric systems, and the assumed MWM is not, because of the disk, but since this does not dominate it can be shown that we can force spherical symmetry while not affecting the circular velocity at the Sun position.

4 Results and discussion

We converted P14 results and used them to derive DD limits, focusing on LUX [7] (Xe), SuperCDMS [8] (Ge) and CRESST II [9] (multi-target). The changes with respect to the SHM are both in the WIMP velocity distribution and in $\rho_{\odot}$. Eq. 1 tells us how the astrophysical parameters affect the exclusion curves. The sum $v_{\rm esc} + v_{\rm c}$ impacts on the position of the asymptote of the limit at low WIMP mass and $v_{\rm c}$ on the position of the maximum of sensitivity of the experiment on the m_{χ} axis, while $\rho_{\odot}$ produces a linear vertical translation of the entire curve.

We considered the best-fit point with prior $v_{\rm c} = 240$ km/s, likely the most motivated given recent estimates (e.g. [10]). Fig.2 shows the exclusion curves with associated 90% C.L. uncertainties for this configuration. Comparing our results with those obtained for the SHM, we find that the former are more constraining by $\sim 40\%$ in a wide range of high WIMP masses, due to the P14-inferred value of $\rho_{\odot} = 0.43 \pm 0.05$ GeV/cm^3, higher than the SHM one. We also show the effect of using a MB velocity distribution (instead of a more consistent ergodic one). This impacts especially at low WIMP masses, because of significant differences between the high-velocity tail of the two distributions. The uncertainties saturate at $\sim \pm 10\%$ at high WIMP masses, value set by the allowed range in $\rho_{\odot}$, and they degrade toward very low WIMP masses, where the maximum possible recoil energy approaches the threshold energy. Some of the bumps in Fig.2 in the case of CRESST2 come from the presence of more than one target nucleus (the others from applying the Maximum Gap Method). This shows that employing different target nuclei in a detector helps to reduce the astrophysical uncertainties (as well as combining different experiments).

We consider also the v_c free analysis of P14. We do not use the same prior on the concentration of the DM halo of P14 (pink in Fig.1) but instead we combine the region provided by the v_c free analysis of RAVE in the plane of Fig.1, with the constraint on v_c published in [10], independent on any MWM. That work obtained $v_c = 243 \pm 12$ km/s at 2σ (the green band in Fig.1). In the above region the allowed values of the local DM density reach up to $\rho_\odot = 0.57$ GeV/cm^3, i.e. they are higher than those of the SHM, but in agreement with those found in recent studies [11]. These results, translated into DD limits, have a behavior qualitatively similar to the one already described for the $v_c = 240$ km/s, but with uncertainties that saturates at values of $\pm 20\%$, due to the allowed range of $\rho_\odot \in [0.37, 0.57]$ GeV/cm^3.

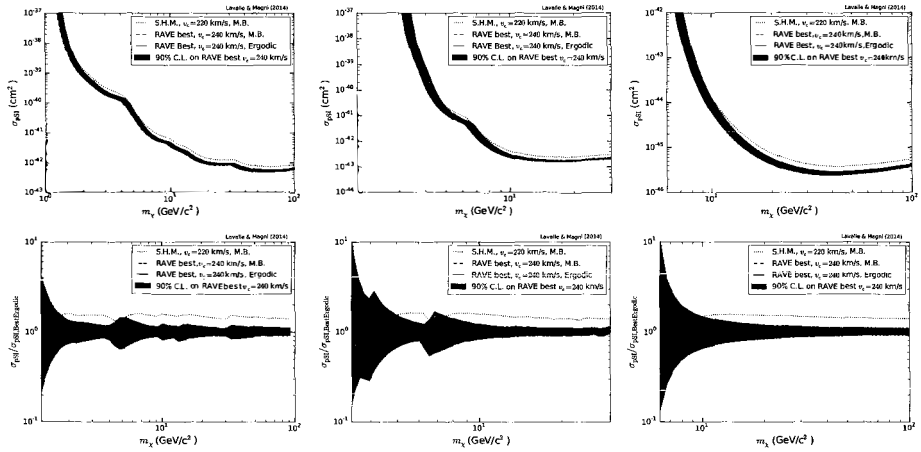

Figure 2 – Experimental 90% C.L. exclusion curves, calculated using the P14 result for the $v_c = 240$ km/s analysis (upper: absolute, lower: relative). From left to right: CRESST2, SuperCDMS, LUX.

5 Conclusions

We presented a method to use the local escape speed estimates of P14 in deriving DD limits. A naive use of these estimates would neglect the underlying assumptions, and thus the correlations they induce among the astrophysical parameters and the DM velocity distribution. We found that a consistent use of these estimates implies large values for $\rho_\odot$, so more constraining exclusion curves, and evaluated the associated uncertainties. We are generalizing this work to anisotropic velocity distributions and testing our methods on cosmological simulations.

References

1. T. Piffl et al., Astronomy & Astrophysics, Volume 562 (2014),
2. J. Lavalle and S. Magni, Phys. Rev. D 91, 023510 (2015)
3. S. Gillessen et al., Astrophys.J. 692 (2009) 1075-1109
4. R. Schönrich et al., Mon. Not R. Astron. Soc. 000,1-5 (2009)
5. J. Binney and S. Tremaine, Second Edition (2008) Princeton University Press
6. P. Ullio and M. Kamionkowski, JHEP 0103:049 (2001)
7. C.H. Faham et al. (LUX Collaboration), Proceedings for the 2014 Rencontres de Moriond (Cosmology Session), La Thuile, Italy
8. R. Agnese et al. (SuperCDMS Collaboration), Phys.Rev.Lett. 112 (2014) 24, 241302
9. G.Angloher et al., Eur.Phys.J. C74 (2014) 12, 3184
10. M. J. Reid et al., Astrophysical J., Volume 700, Issue 1 (2009)
11. O. Bienaymé et al., Astronomy & Astrophysics, Volume 571 (2014)

WIMP ANNIHILATIONS IN THE SUN : A SEARCH BASED ON THE FIRST YEAR OF DATA FROM THE COMPLETED ICECUBE NEUTRINO TELESCOPE

M. RAMEEZ for the IceCube Collaboration[a]
Département de physique nucléaire et corpusculaire, Université de Genève, 24 Quai Ernest Ansermet, 1211 Genève, Switzerland

Weakly Interacting Massive Particles, which are favored candidates for Dark Matter, may be captured gravitationally in the Sun and pair-annihilate to produce standard model particles, including neutrinos. The resulting neutrino flux from the Sun might be detected by terrestrial neutrino telescopes such as IceCube. In these proceedings we present the preliminary results from the analysis of 341 days of operation of IceCube-DeepCore, between May 2011 and May 2012, in the completed 86 string configuration. In addition to the standard analysis using upward going neutrino-induced events during austral winter, improved veto techniques have been used to reduce the atmospheric muon background and improve sensitivity during the austral summer. Overall sensitivity has also benefited from better analysis methods and reconstructions and improved with respect to all previous analyses.

1 Introduction

Astrophysical observations provide strong hints about Dark Matter(DM). However the nature of it is entirely unknown. An exciting and experimentally accessible candidate is the so called 'Weakly Interacting Massive Particle (WIMP)'(see [1] for a comprehensive review). If the DM content of the universe consists of WIMPs, they can scatter off nuclei in massive bodies such as the Sun and be captured gravitationally[2], where they may pair-annihilate into standard model particles, including neutrinos at an enhanced rate. Given enough time, the capture and annihilation processes would reach equilibrium [3] and on average only as many WIMPs annihilate as are captured in any unit time. This DM-induced neutrino flux may be detected at terrestrial neutrino detectors such as IceCube. As the region at the centre of the Sun where most of the annihilations will occur is very small, the search is equivalent to looking for a point-like source of neutrinos. However, neutrinos above 1 TeV have interaction lengths significantly smaller than the radius of the Sun, and as a result all the signal is expected in the range of a few GeVs to ~1 TeV, making this a very low energy point-source search by the standards of IceCube.

2 The Detector and Event Selection

IceCube is a cubic-kilometer-sized detector embedded in the ice at the geographic South Pole [6]. A more detailed description of the detector is presented in [7]. Neutrino flux predictions at Earth from WIMP annihilations in the Sun have been widely studied, for example in Ref [4]. We use the flux predictions from DarkSuSy and WimpSim [4] to simulate signals for the IceCube detector according to specific annihilation scenarios.

The energy range of the expected signal (a few TeV at maximum) and the properties of IceCube at these energies dictate the event selection strategies. While the principal IceCube array has an energy threshold of ~100 GeV, the more densely instrumented DeepCore infill array has an energy threshold of

[a] see `http://icecube.wisc.edu/collaboration/authors/current` for full author list.

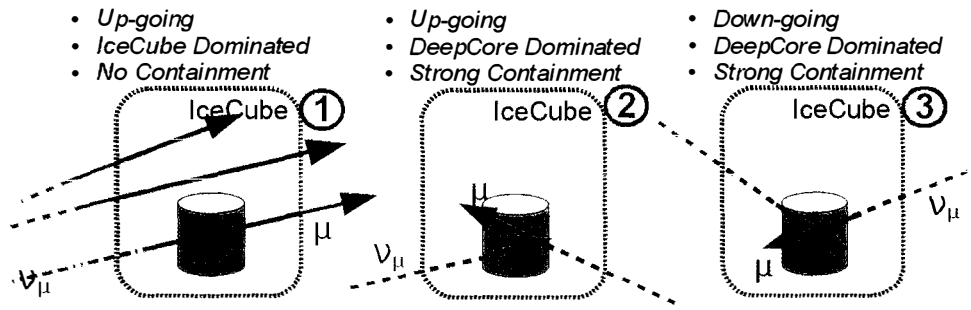

Figure 1 – The three event selection strategies for the solar WIMP analysis. Most of the sensitivity for neutrino signals below 100 GeV comes from the DeepCore (DC) dominated low energy samples. During the austral summer (when the Sun is a source of downgoing neutrinos), the overwhelming muon background forces us to use the outer detector as a Veto (see Fig. 2) and consequently there is only a DeepCore dominated - low energy sample.

~10 GeV. This means that for WIMP masses < 200 GeV, which produce signal neutrinos mostly with energies below the IceCube threshold, only DeepCore[5] will contribute significantly towards the effective volume. However, for higher WIMP masses where a significant fraction of the resultant neutrinos are above the IceCube threshold, the full effective volume of IceCube comes into play. For optimizing the event selections for the analysis and setting upper limits, we consider two scenarios: WIMPs annihilating completely into W^+W^-, a 'hard' channel with emission peaked at neutrino energies close to the WIMP mass, and WIMPs annihilating completely into $b\bar{b}$, a 'soft' channel with emission peaked at neutrino energies of a few GeV. Since IceCube acceptance is very energy dependent, cuts have to be optimized for the spectral composition of the expected signal flux. For WIMP masses below 80.4 GeV, we also consider a WIMP annihilating into $\tau\bar{\tau}$, since annihilations to W^+W^- are no longer kinematically allowed.

Within IceCube, a standard set of filters are used to pre-select signal-like muon events and reduce the rate of the dominant atmospheric background. This analysis starts with a stream of data from three of these filters, a low-energy DeepCore filter and two filters selecting muon-like events that point upwards. After these filters the data rate is ~ 100 Hz. From this point onwards, data are treated differently depending upon whether they fall in the austral winter or summer.

During the austral winter, when the Sun is below the horizon, the signal consists of upgoing neutrinos. The background is dominantly made up of downgoing atmospheric muons falsely reconstructed as upgoing. Reconstructed event properties quantifying topology, track length, reconstruction quality etc are used to reject background such as very high energy events or vertical events which obviously cannot come from the Sun and reduce the data to ~ 2 Hz. At this point, a likelihood reconstruction with a prior based on the zenith distribution, which takes into account that the majority of the tracks are downgoing atmospheric muons, is performed to identify and remove falsely reconstructed downgoing events. Depending upon the location of the majority of detected Cherenkov photons (whether within IceCube (1) or within DeepCore (2)), events are split into two streams (see Fig 1). Subsequently, separate instances of a multivariate classification algorithm, known as Boosted Decision Tree (BDT), are used to select signal-like events from both these streams. The BDT of the IceCube dominated sample (1) is optimized for events from a 1 TeV WIMP annihilating into the hard W^+W^- channel while the DeepCore dominated sample (2) is optimized for events from 100 GeV and 50 GeV Wimps annihilating into W^+W^-, $b\bar{b}$ and $\tau^+\tau^-$ channels. After the selection based on the BDT classifier, event rates of the two samples are ~ 2.9 and ~ 0.34 mHz, respectively, consistent with expectations from a background that is dominated by atmospheric neutrinos.

During the austral summer (23rd September 2011 to 16th March 2012), the signal (downgoing) is overwhelmed by a background of downgoing atmospheric muons (~ 10^6 times higher in rate) in addition to the atmospheric neutrinos. A sample of DeepCore dominated downgoing tracks (3) can be isolated by using the outer laters of IceCube as a veto (see Fig. 2). This sample is again optimized using a BDT algorithm to select events expected from 100 GeV and 50 GeV Wimps annihilating into

W^+W^-, $b\bar{b}$ and $\tau^+\tau^-$ channels. After the BDT-based event selection the even rate is ~ 0.24 mHz, consistent with the expected residual atmospheric neutrino and muon background.

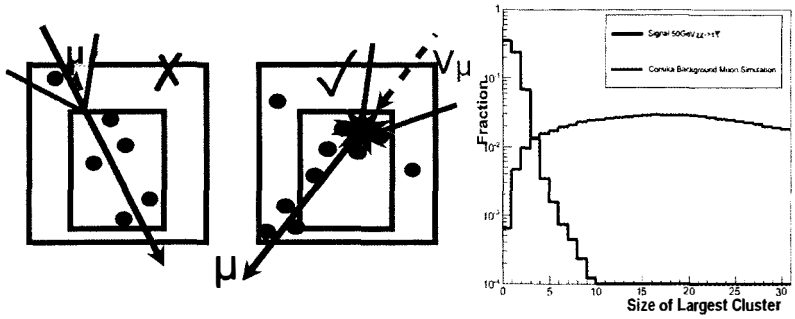

Figure 2 – On the left and center: A schematic representation of the veto concept to reject atmospheric muon background and retain neutrinos during austral summer. Only events with their reconstructed vertex near DeepCore are selected. Subsequently, the number of hits within a cone of 40° half-angle at the vertex and aligned along the muon track that are within a specific 'Radius + Time (RT)' radius of each other are counted. The size of the largest of these clusters of hits is reported. On the right: size of this cluster for signal (green) and background (red). Selecting events with cluster sizes ≤ 3 will keep more than 90% of signal while rejecting more than 90% of background of atmospheric muons.

Fig. 3 summarizes final effective areas and angular resolutions of the two samples.

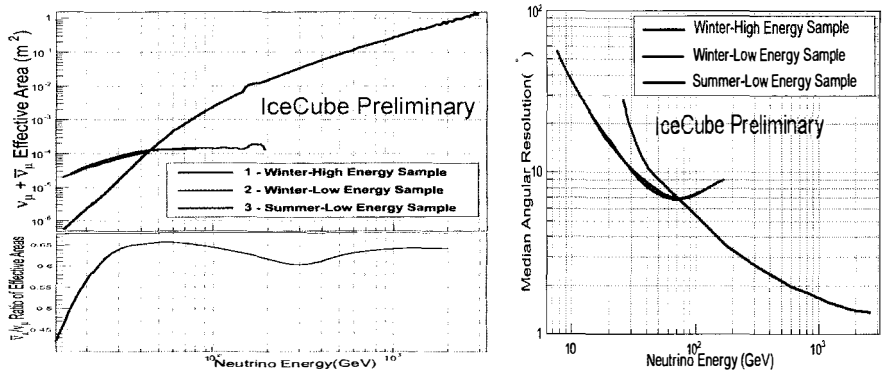

Figure 3 – Top Left: $\nu_\mu + \bar{\nu}_\mu$ effective areas for the three different event selections. Bottom Left : Ratio of the $\bar{\nu}_\mu$ and ν_μ effective areas. Right: The angular resolutions of the three samples at different energies, defined as the median of the angular separation between the incoming neutrino and the reconstructed muon.

3 Analysis method

The significance of a cluster of events in the direction of the Sun can be estimated using a modified version of the unbinned maximum likelihood ratio method described in Ref. [8]. Due to the very large point spread function of IceCube at these low neutrino energies, we model the spatial signal p.d.f of Ref. [8] as a Fisher-Bingham distribution from directional statistics [9].

For the fully contained events of the DeepCore dominated samples (2) and (3), the energy of the neutrino can be estimated by summing the energy of the muon (obtained by reconstructing the starting and stopping vertex of the muon) and the hadronic cascade from the charged current interaction. Signal and background p.d.f.s are constructed from the signal simulation and datasets randomized in azimuth respectively. Energy weighting is added to the likelihood to enhance sensitivity. Thus the signal p.d.f. is given by:

$$S_i(|\vec{x}_i - \vec{x}_{sun}(t_i)|, E_i, m_\chi, c_{ann}) = \mathcal{K}(|\vec{x}_i - \vec{x}_{sun}(t_i)|, \sigma_i) \times \mathcal{E}_{m_\chi, c_{ann}}(E_i), \quad (1)$$

where $\mathcal{K}$ stands for the spatial and $\mathcal{E}$ for the spectral parts of the p.d.f. and m_χ and c_{ann} stand for the mass and annihilation channel of the WIMP respectively. The best estimate for the number of signal events in the sample is obtained by maximizing the likelihood ratio as defined in Ref. [8]. The significance of the observation can be estimated without depending on Monte Carlo simulations by repeating the process on datasets scrambled in right ascension. As the three separate event selections have no events in common, they can be combined statistically using the method described in [10]. Confidence intervals on the number of signal events present within the sample are constructed using the method of Feldman and Cousins[11].

4 Results and discussion

No significant excess was found in the direction of the Sun, allowing us to set stringent limits on the neutrino flux from the Sun in the GeV-TeV range. This limit can also be interpreted as a limit on the WIMP-nucleon scattering cross section. For the spin dependent case, IceCube limits are the most competitive in the region above $\sim$ 20 GeV (Fig. 4). Limits have improved by a factor of $\sim$30% to 60% w.r.t. the previous IceCube analysis.

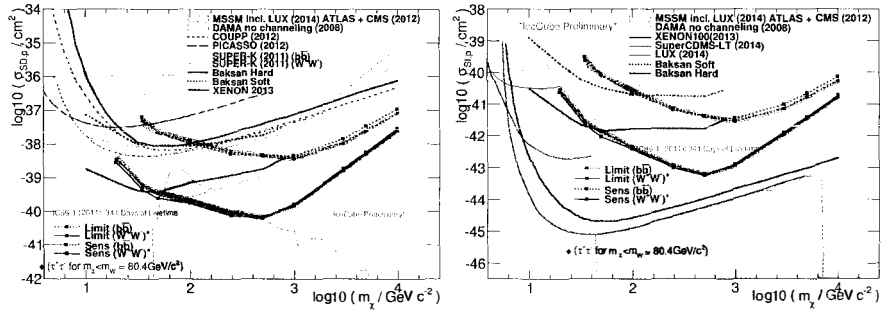

Figure 4 – Limits on the spin dependent (left) and spin independent (right) WIMP-Nucleon scattering cross section as a function of the WIMP mass, derived from this analysis and compared to other experiments' limits from [12,13,14,16,15,17,18,19]. The assumed local DM density is 0.3 GeV/cm^3 and a standard Maxwellian halo velocity distribution.

References

1. G. Bertone *et al* Phys Rep., 405 (2005) p.279
2. A. Gould *et al* 1987 ApJ, vol. 321, Oct. 1, 1987, p. 571-585.
3. G. Jungman *et al* Phys.Rept. 267 (1996) 195-373
4. J. Edsjö, http://www.fysik.su.se/edsjo/wimpsim/
5. R. Abbasi *et al.*, [IceCube Coll.] Astropart. Phys. **35** (2012).
6. A. Achterberg *et al.*, [IceCube Coll.] Astropart. Phys. **26** (2006) 155.
7. 'Latest results from IceCube on astrophysical neutrinos and neutrino oscillations', Proceedings of the 50th Rencontres de Moriond, La Thuile, Italy.
8. J. Braun *et al* Astropart.Phys. **29**, 299-305 (2008).
9. J.T. Kent, J. Royal. Stat. Soc., 44:71-80.
10. M. G. Aartsen *et al.* [IceCube Coll.] ApJ **796** (2014) 109.
11. G. Feldman and J. Cousins Phys.Rev.D57:3873-3889,1998.
12. M. M. Boliev *et al.* arXiv:1301.1138 [astro-ph.HE] .
13. D. S. Akerib *et al.* [LUX Coll.] Phys. Rev. Lett. 112, 091303 (2013).
14. R. Agnese *et al.* [SuperCDMS Coll.] Phys. Rev. Lett. 112, 241302 (2014).
15. E. Aprile *et al.* [XENON Coll.] Phys. Rev. Lett, 109, 181301 (2012).
16. R. Bernabei *et al.* Eur. Phys. J. C. 53 (2008), 205.
17. H. Silverwood et al., arXiv:1210.0844v1 (2012).
18. The ATLAS Collaboration, ATLAS-CONF-2012-033 (2012).
19. The CMS Collaboration, arXiv:1207.1798 (2012).

10.
Summary

Experimental Conference Summary

Terry Wyatt
School of Physics and Astronomy, University of Manchester, Manchester M139PL, England

I review the experimental talks presented at the 50th Rencontres de Moriond: Electroweak Interactions and Unified Theories.

0 Introduction and Overview

In this summary I have given emphasis to recent experimental results presented at the conference. Unfortunately, I have very little time to cover the specifics of individual detectors, or to dwell too much on the presentations of future prospects. It is a great honour to review the many excellent talks at this special 50th Moriond meeting. Especial credit goes to the speakers at the Young Scientist Forums — from the quality of their talks and of the science presented therein we can be confident that the future of our field is in good hands.

This summary is structured in sections that are numbered as follows:

1. Neutrinos
2. Dark matter searches
3. Higgs
4. Electroweak
5. Top
6. Exotica
7. Heavy Flavour

1 Neutrinos

Mixing in the 3-neutrino model [1] is illustrated in Figure 1. The mass eigenstates ν_1, ν_2, ν_3 are illustrated by the horizontal bars and their decomposition in terms of the flavour eigenstates ν_e, ν_μ, ν_τ is indicated by the three shades of grey.

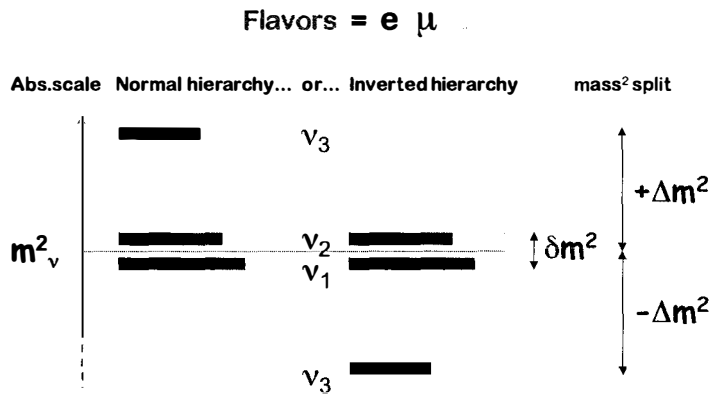

Figure 1 – Graphical overview of mixing in the 3-neutrino model [1].

$$U_{\alpha i} = \begin{bmatrix} 1 & 0 & 0 \\ 0 & c_{23} & s_{23} \\ 0 & -s_{23} & c_{23} \end{bmatrix} \begin{bmatrix} c_{13} & 0 & s_{13}e^{-i\delta} \\ 0 & 1 & 0 \\ -s_{13}e^{i\delta} & 0 & c_{13} \end{bmatrix} \begin{bmatrix} c_{12} & s_{12} & 0 \\ -s_{12} & c_{12} & 0 \\ 0 & 0 & 1 \end{bmatrix} \begin{bmatrix} 1 & 0 & 0 \\ 0 & e^{i\alpha/2} & 0 \\ 0 & 0 & e^{i\beta/2} \end{bmatrix}$$

[only if Majorana]

Figure 2 – The Pontecorvo-Maki-Nakagawa-Sakata (PMNS) matrix that describes mixing and CP violation in the 3-neutrino model [1].

The mixing angles $\theta_{12}, \theta_{13}, \theta_{23}$ are defined by the Pontecorvo-Maki-Nakagawa-Sakata (PMNS) matrix, as illustrated in Figure 2. The values of the mixing angles and mass splittings have already been measured and could therefore be considered as *Terra Cognita* in Figure 3.

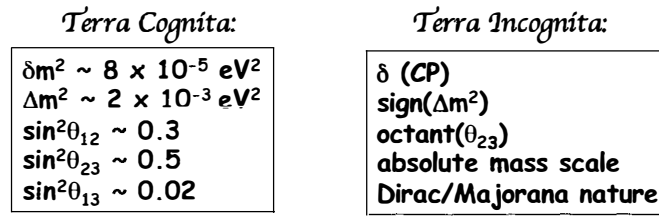

Figure 3 – Neutrino physics parameters to be measured [1].

Some unanswered questions are listed [1] as *Terra Incognita* in Figure 3. The PMNS matrix includes a complex phase angle δ which, if non-zero, could be associated with CP violation in the neutrino sector. As illustrated in Figure 1, the sign of the larger of the two mass splittings is unknown; that is, we do not know whether the two closely separated states ν_1, ν_2 lie above or below in mass relative to ν_3. The measured value of θ_{23} is close to $\pi/4$. However since nothing

of great significance depends on when its value crosses $\pi/4$ the question of *octant*(θ_{23}) is perhaps not as interesting as the others. So far only the mass splittings have been measured, but not the absolute masses.

If one accepts the 3-neutrino picture then, in some sense, one could argue that these are all rather obvious questions and so might be thought of as *Terra Incognita Cognita*[2]. Getting much closer to the territory of *Terra Incognita Incognita*[2] would be the question of whether or not neutrinos might be their own antiparticles and gain a Majorana mass. Other items of *Terra Incognita Incognita* might be whether or not there are additional low mass (sterile) or high mass (weakly interacting) neutrino states still to be discovered.

Detectors for low energy neutrinos and searches for dark matter share a number of common features, which are driven by the need to fight background:

1. Deep underground.
2. Active/passive shielding around active volume.
3. Fiducial volume to select fully contained events.
4. Extremely high radiopurity.
5. Require systematic calibration and monitoring.
6. Require coincidence between more than one detection technique for signal: e.g., ionization, scintillation light, Cerenkov light, phonons producing a temperature rise, prompt + delayed signal, etc.

Figure 4 shows an overview of the three main reactor-based neutrino facilities. This figure demonstrates some of the advantages of the Daya Bay facility in terms of overburden, reactor power, detector mass, and location of the far detector relative to the minimum in the $\overline{\nu}_e$ survival probability[3].

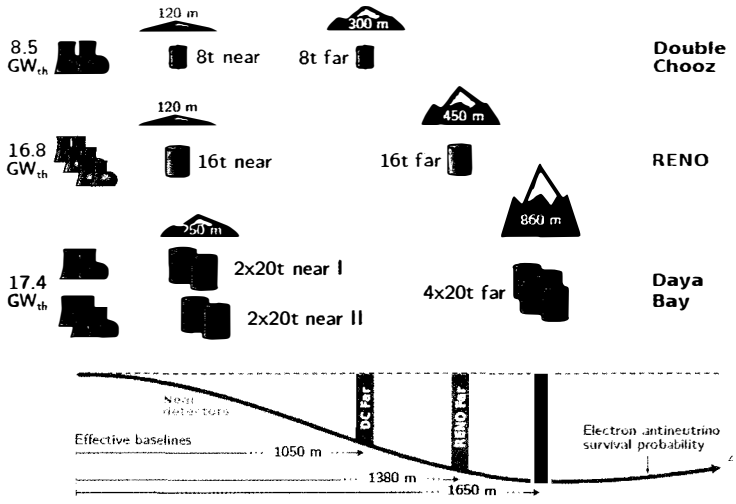

Figure 4 – Overview of the three main reactor-based neutrino facilities[3].

The upper part of Figure 5 shows the inverse beta decay process, by which $\overline{\nu}_e$ produced in reactors are observed. In addition to the prompt signal produced by the positron, a delayed

signal is produced by the capture of the neutron on hydrogen or the gadolinium dopant. The lower part of Figure 5 shows the correlation plot of the energies of prompt and delayed signals observed by Daya Bay.

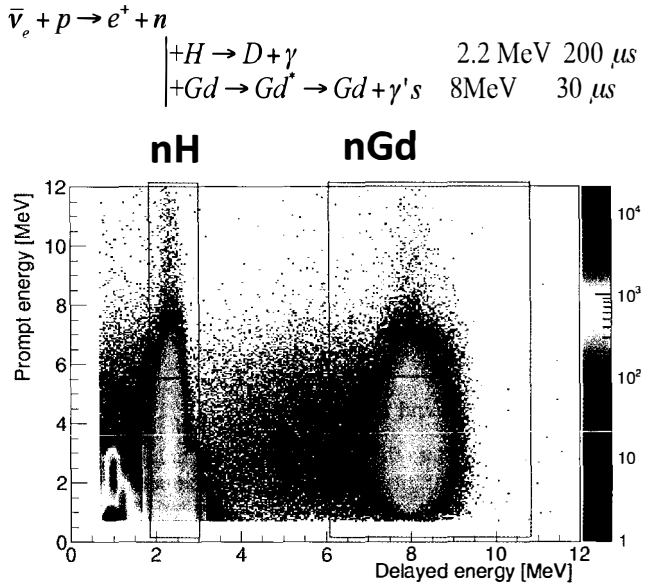

Figure 5 – The inverse beta decay process, by which $\bar{\nu}_e$ produced in reactors are observed (above) and the correlation between the energies of prompt and delayed signals observed by Daya Bay (below) [3].

Figure 6 shows results from the Daya Bay experiment presented for the first time at this conference. This represents a factor four increase in the previously published gadolinium data set, with over 10^6 signal events. Figure 6 (left) shows as a function of weighted distance from the Daya Bay reactors, the ratio between the number of observed neutrino reactions and the number expected in the hypothesis of no mixing. The red line shows the best fit mixing result. Figure 6 (right) shows the energy spectrum of neutrinos observed at the far detector, compared to two expections based on the rate seen at the near detector. The blue line corresponds to no oscillations and the red band corresponds to the best fit mixing result.

Figure 7 shows the updated Daya Bay measurements of $\sin^2 2\theta_{13}$ and Δm^2. This is the most precise determination of $\sin^2 2\theta_{13}$ and is already around a factor two more precise than will be achievable with Double Chooz in 5 years' time [4].

The term 'reactor anitneutrino anomaly' has been used to refer to an apparent deficit in the flux of $\bar{\nu}_e$ detected in short baseline reactor experiments by a factor of around 0.94 relative to predictions [5]. This is illustrated in Figure 8. Figure 9 shows for Daya Bay and Reno that the deficit in the observed flux of $\bar{\nu}_e$ has a strong energy dependence. A significance of around 3 standard deviations has been claimed for this effect and it has been interpreted as possible evidence for 'sterile' neutrinos. Such sterile neutrinos could influence neutrino mixing measurements, but would not undergo weak interactions mediated by the W and Z bosons (and would thus not be directly detected in experiments and would not contribute to the invisible decay width of the Z boson).

However, it has been pointed out [5] that there are significant model dependencies in predictions of $\bar{\nu}_e$ fluxes from reactors. For example, Figure 10 shows predictions of kinetic energy

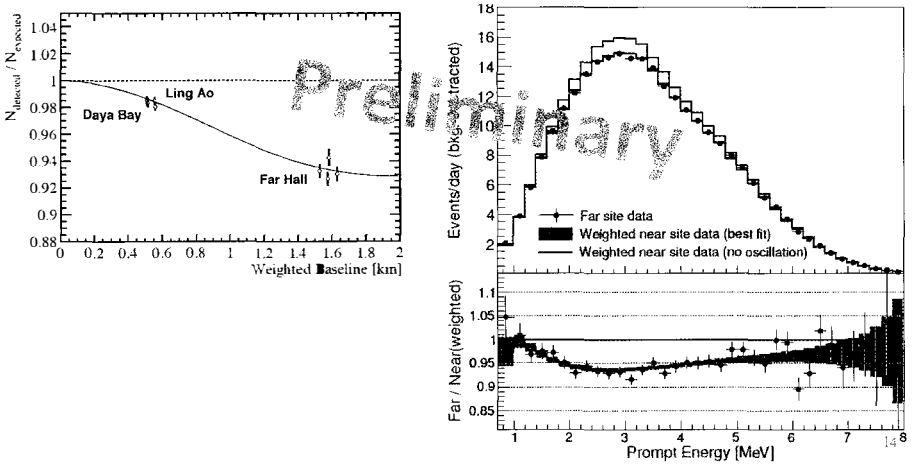

Figure 6 – As a function of weighted distance from the Daya Bay reactors, the ratio between the number of observed neutrino reactions and the number expected in the hypothesis of no mixing. (left). Energy spectrum of neutrinos observed at the far detector, compared to two expections based on the rate seen at the near detector. The blue line corresponds to no oscillations and the red band corresponds to the best fit mixing result (right)[3].

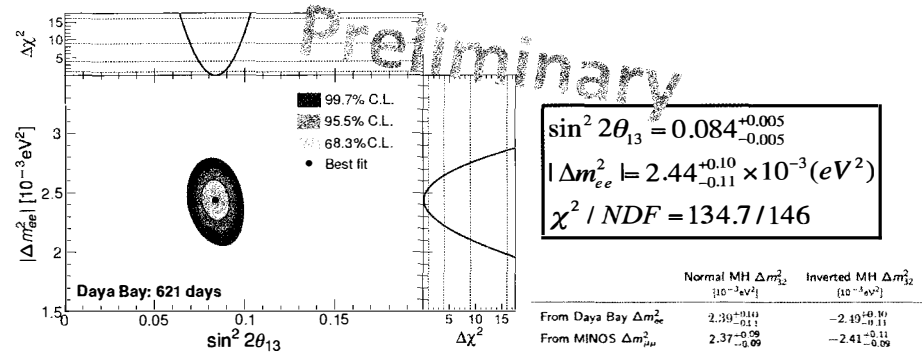

Figure 7 – Updated Daya Bay measurements of $\sin^2 2\theta_{13}$ and Δm^2 [3].

spectra of electrons and $\overline{\nu}_e$ from two different theoretical models. When these theoretical uncertainties are properly taken into account the reactor anitneutrino deficit cannot be considered to be significant [5]. New experiments such as PROSPECT, SOLID, NUCIFER, STEREO are required in order to provide the experimental input that is necessary to constrain these theoretical uncertainties.

In addition to reactor experiments, the value of $\sin^2 2\theta_{13}$ can be measured in ν_e appearance in ν_μ beams in long baseline experiments [6]. Figure 11 shows the angular and energy distributions of ν_e interactions observed by the T2K experiment. This represents 7.3 σ significant observation of ν_e appearance in a ν_μ beam.

Figure 12 shows the extracted value of the PMNS parameter δ as a function of $\sin^2 2\theta_{13}$ for the two mass hierarchies. It can be seen that no statistically significant deviation from $\delta = 0$ can be claimed at the present.

Measurements of ν_μ disapperance are summarised in Figure 13, which shows contours in

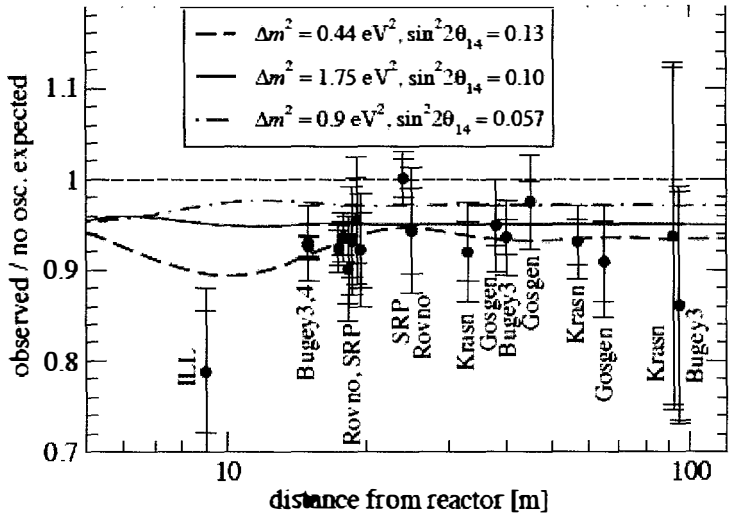

Figure 8 – The reactor anitneutrino anomaly: an apparent deficit by a factor of around 0.94 in the detected flux of $\overline{\nu}_e$ from short baseline reactor experiments[5].

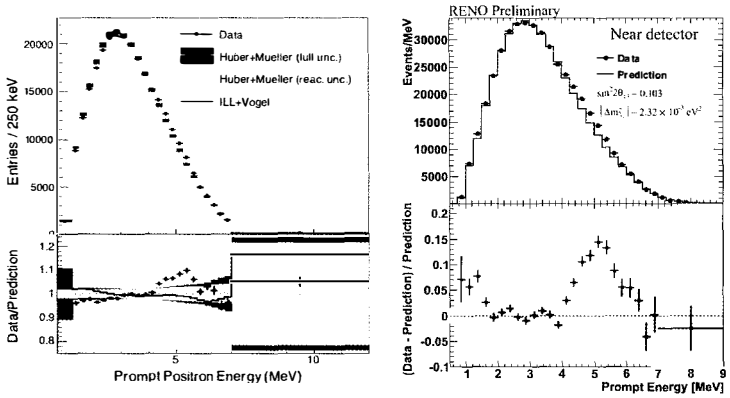

Figure 9 – The reactor anitneutrino anomaly: for Daya Bay (left) and Reno (right) the observed deficit in flux of $\overline{\nu}_e$ has a strong energy dependence[5].

Δm^2_{32} vs. $\sin^2 2\theta_{13}$. It is interesting to note that for the first time the results of IceCube fit onto a plot that shows the results of the long baseline experiments[7].

The primary aim of the IceCube experiment[7] is to measure the fluxes of ultra-high energy neutrinos from astrophysical sources. Cerenkov light produced by the passage of charged particles in ice of Anarctica is detected within a 1 km^3 active volume that is situated 1.52.5 km under the surface. The detection threshold is at a neutrino energy of around 200 GeV.

Figure 14 illustrates the main sources of signals seen in IceCube. In addition to the neutrinos from astrophysical sources, there are also atmospheric neutrinos (which yield the results on mixing included in Figure 13) and also cosmic ray muons that traverse the active area and are vetoed.

Figure 15 shows the energy spectrum of high energy neutrino interactions observed in Ice-

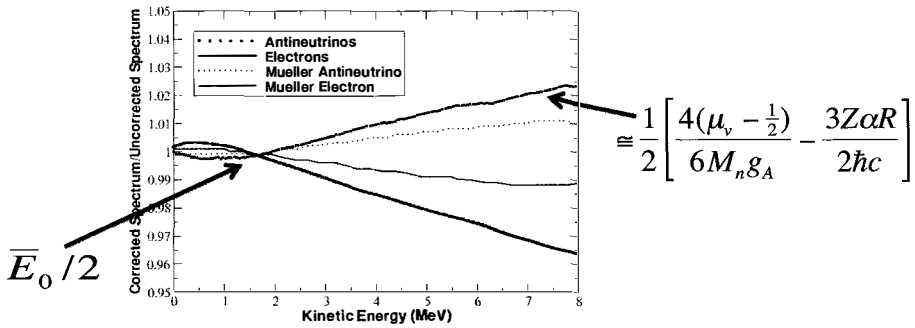

Figure 10 – Predictions of kinetic energy spectra of electrons and $\bar{\nu}_e$ from two different theoretical models[5].

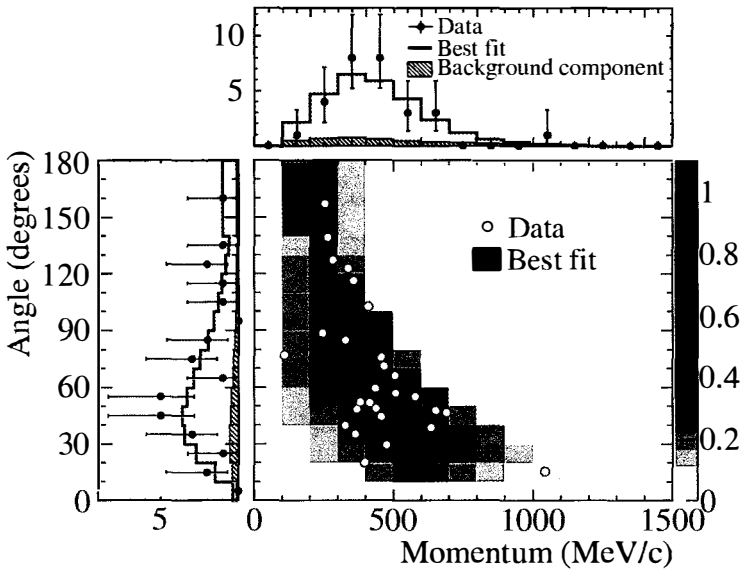

Figure 11 – The angular and energy distributions of ν_e interactions observed by the T2K experiment[6].

Cube, separately for downward-going and upward-going events. The region of low energy shows good understanding of atmospheric neutrino and cosmic muon backgrounds. In the high energy region above the dashed lines shown in Figure 15 there are 37 candidates and the data show a clear signal for astrophysical neutrinos, with a significance of 5.7 σ above the backgrounds.

By studying the topology of the observed events, IceCube has some sensitivity to the flavour of the observed neutrinos. The result is shown in Figure 16. A flavour composition of $(\nu_e : \nu_\mu : \nu_\tau) = (1 : 1 : 0)$ is preferred (shown by the white cross). However, as shown by the contours drawn at 68% and 95% CL, at present the data have rather limited statistical precision and are compatible with a wide range of values, including $(\nu_e : \nu_\mu : \nu_\tau) = (1 : 1 : 1)$. The coloured symbols show the expected values at the detector corresponding to various initial neutrino flavour compositions at the source.

As shown in Figure 17 IceCube sees no statistically significant evidence for clustering in the

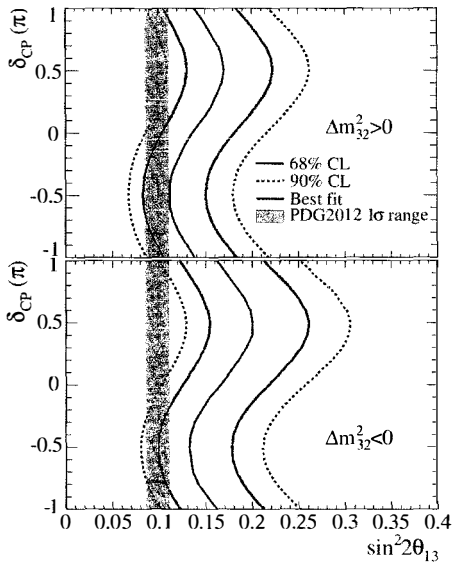

Figure 12 – The extracted value of δ as a function of $\sin^2 2\theta_{13}$ for the two mass hierarchies [6].

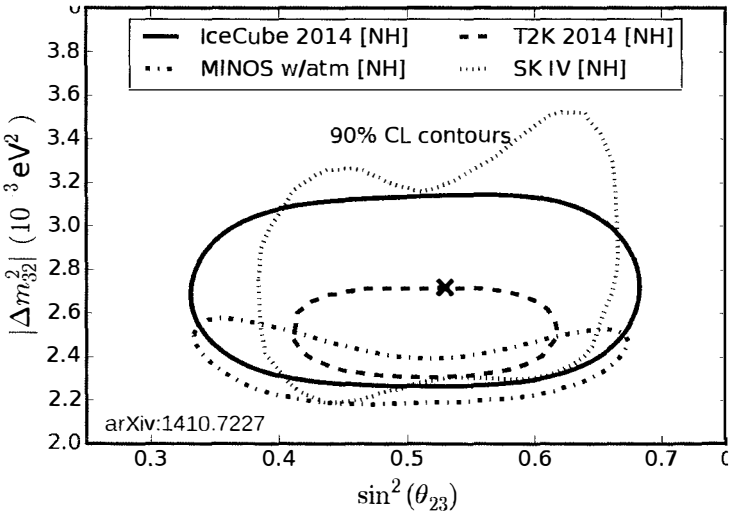

Figure 13 – Contours in Δm^2_{32} vs. $\sin^2 2\theta_{13}$ [7].

direction from which the astrophysical neutrinos arrive.

Figure 18 gives an overview of the nuclear processes in the sun and the resulting energy spectrum of the produced neutrinos. The Borexino dectector, which consists of 300 tons of liquid scintillator, provides no directional information and is looking for relatively low energy neutrinos. Therefore, extremely high radiopurity required.

Figure 19 shows the neutrino energy spectrum observed by Borexino, together with a fit to

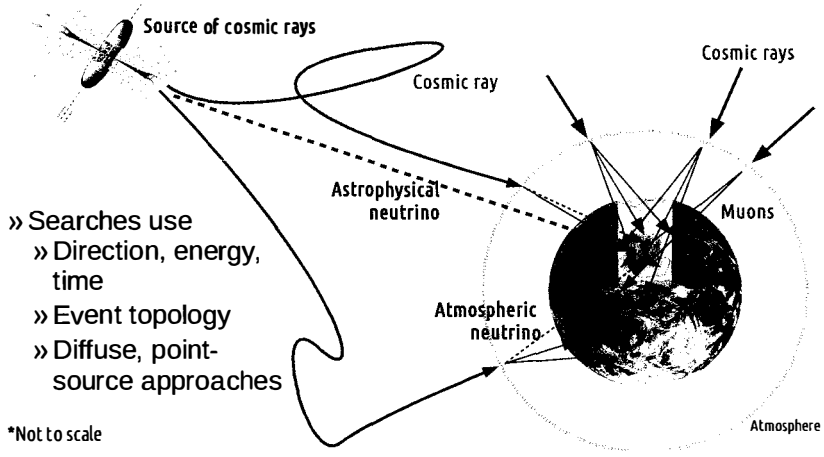

Figure 14 – Illustration of the main sources of signals seen in IceCube [7].

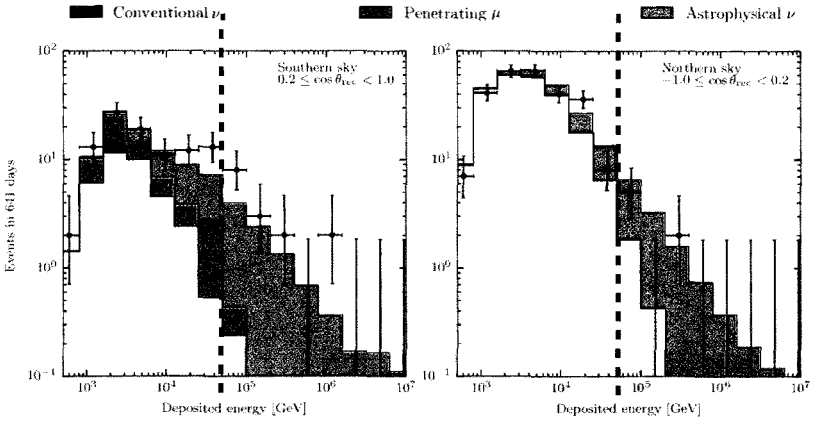

Figure 15 – The energy spectrum of high energy neutrino interactions observed in IceCube, separately for downward-going (left) and upward-going events (right) [7].

determine the composition. The residuals show that the data are well described by the fitted model. One of the main backgrounds arises from ^{14}C, which is an unavoidable component of the scintillator. Good control of the rate for this background is essential in order to observe the low energy neutrinos produced by the *pp* process (shown as the red curve in Figure 19). The fitted number of *pp* ν counts per day per 100 tons is 144 ± 13 (stat.) $\pm$ 10 (syst.). This rate is consistent with expectations from the observed photon luminosity of the sun, and therefore provides useful information on solar stability.

The EXO-200 collaboration searches for evidence of neutrinoless double beta decay using a detector of 200 kg of liquid xenon enriched to the level of 80% in the isotope ^{136}Xe. The fiducial volume is 76.3 kg. Results from an exposure of 100 kg.years have been presented [9].

The experiment produces coincident signals in scintillation light and ionization. As shown for calibration data with a ^{228}Th source in in Figure 20, an anti-correlation between the magnitudes of the scintillation and ionization signals is exploited to optimise the energy resolution and

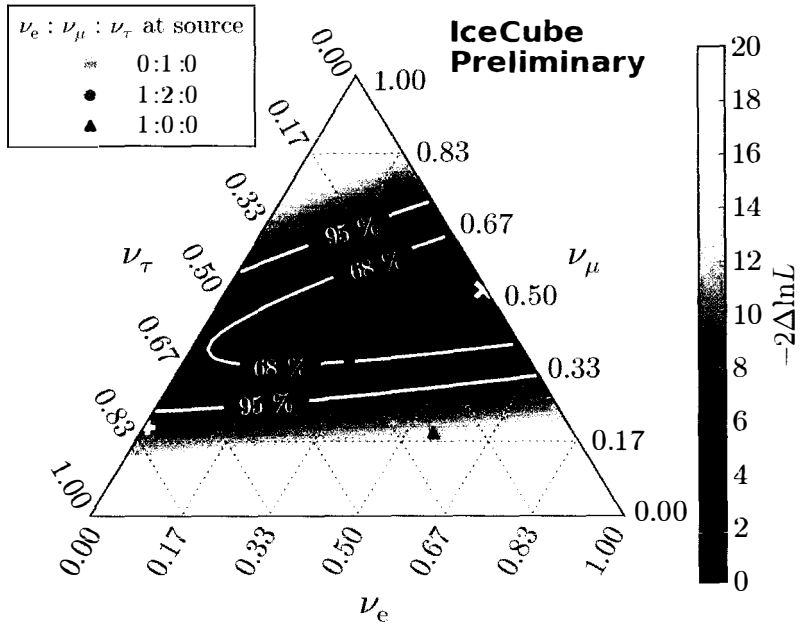

Figure 16 – Neutrino flavour of the interactions observed by IceCube[7]. The white cross shows the central value of $(\nu_e : \nu_\mu : \nu_\tau) = (1 : 1 : 0)$ preferred by the data. Contours are drawn at 68% and 95% CL. The coloured symbols show the expected values at the detector corresponding to various initial neutrino flavour compositions at the source.

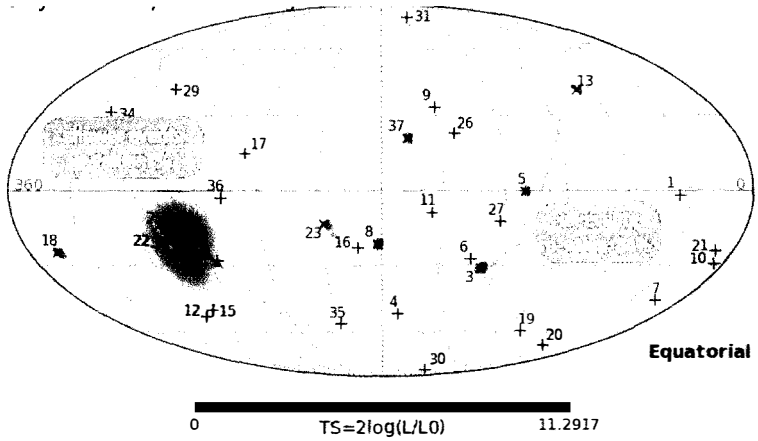

Figure 17 – The direction from which the astrophysical neutrinos are observed to arrive in IceCube[7].

improve the discrimination against background.

As illustrated on the left-hand picture in Figure 21, events are characterised by their topology as either 'single site' or 'multi-site' depending on the spatial separation of the observed ionization signals. Figure 21 (right) shows the observed energy spectra for the two classes of event. The

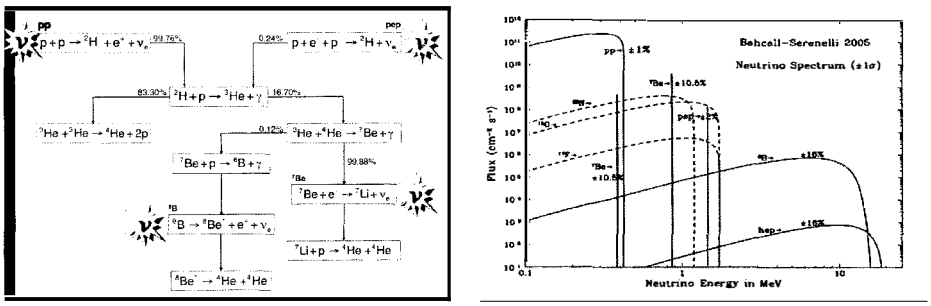

Figure 18 – Overview of the nuclear processes in the sun (left) and the resulting energy spectrum of the produced neutrinos (right) [8].

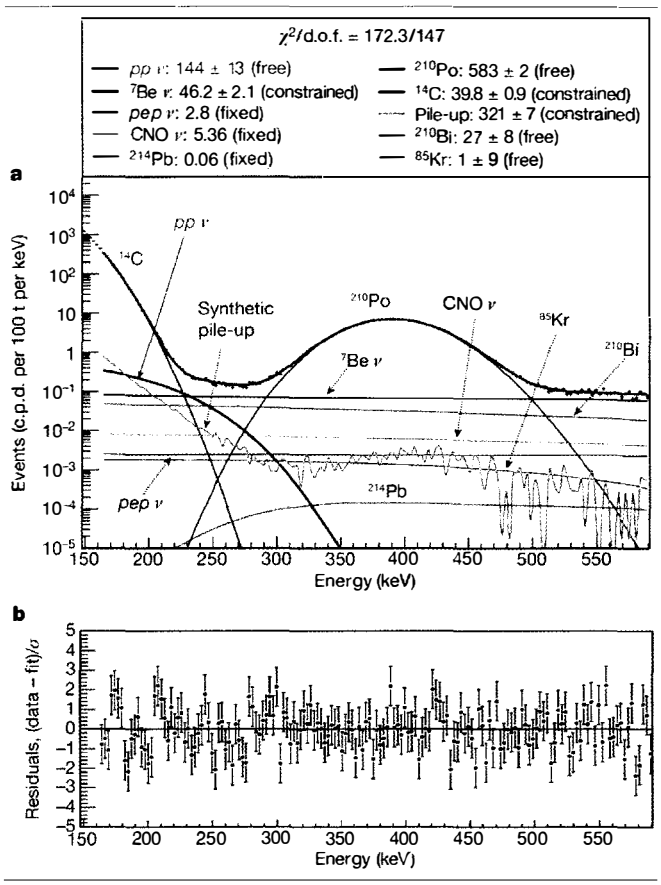

Figure 19 – Fit to Borexino neutrino energy spectrum [8].

fitted contribution for a potential signal from neutrinoless double beta decay is indicated in the magenta curves. There is no significant signal observed and a lower limit on the half-life for neutrinoless double beta decay of ^{136}Xe is set at $\tau_{1/2}0\nu\beta\beta > 1.1 \times 10^{25}$ years at 90% CL.

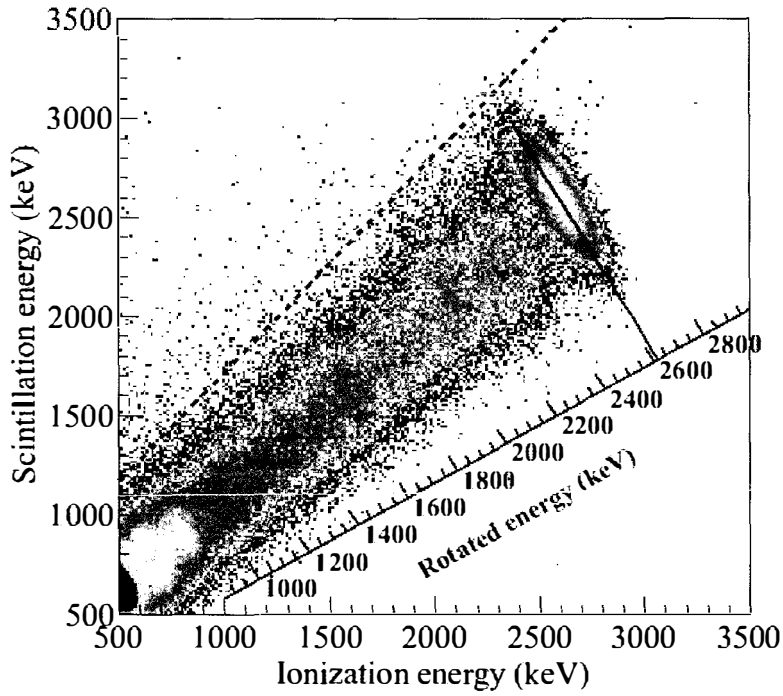

Figure 20 – Magnitudes of the scintillation and ionization signals observed by the EXO-200 experiment in calibration data with a ^{228}Th source. [9].

2 Dark matter searches

Strong evidence for the existence of dark matter comes from a number of sources such as: rotation curves of galaxies, gravitational lensing, structure formation in the early universe. In order not to have been directly observed, such matter would have to have no electromagnetic or QCD interactions. It might or might not have weak interactions mediated by the W and Z bosons and it is similarly not clear whether or not it would couple to the Higgs field. Dark matter particles would have to be stable or at least have lifetimes large compared to the age of the universe. Particle masses might be around a GeV or be at the TeV scale. The standard model of particle physics (SM) does not contain any such particles, and so this is the most direct evidence we have for physics beyond the SM (BSM).

Weakly interacting dark matter particles (WIMPs) can be searched for in a number of different ways. Figure 22 illustrates the complementary strategies that are employed:

- direct searches for the scattering of dark matter particles with SM particles in an underground detector;
- indirect searches for the SM particles produced in the annihilation or decay of dark matter particles;
- searches at colliders for dark matter particles produced in the scattering of SM particles.

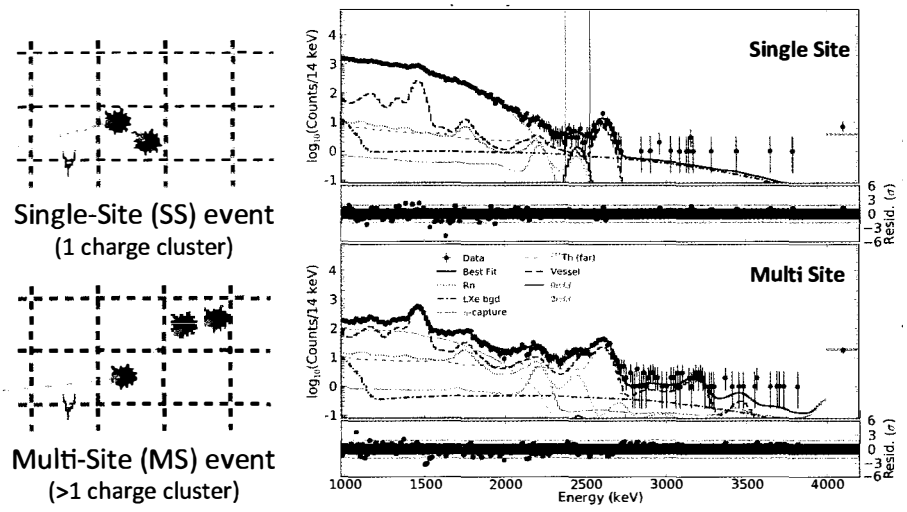

Figure 21 – Events in EXO-200 are characterised by their topology as either 'single site' or 'multi-site' depending on the spatial separation of the observed ionization signals (left). Energy spectra for the two classes of event (right) [9].

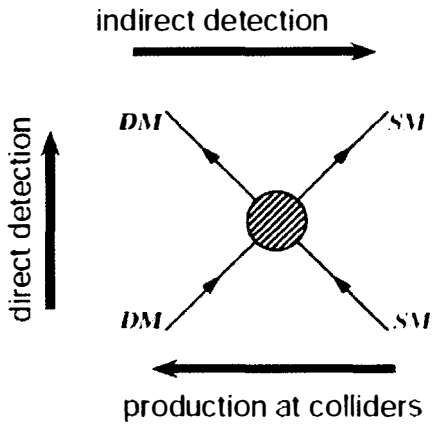

Figure 22 – Complementary strategies that are employed to search for dark matter.

At colliders dark matter particles may also be produced in the decay of other BSM particles.

XENON100 is a direct detection experiment that looks for coincident scintillation light and ionization in a 62 kg liquid Xe detector, with a 34 kg fiducial region [10]. The results of a search for axions are shown in Figure 23. The left-hand plot shows the observed detector signal (also expressed in terms of the mean recoil energy) compared with the additional number of events expected as a function of BSM particle mass, if these were to make up the entire dark matter needed to explain galactic halo observations. The right-hand plot shows the XENON100 observed and expected limits on mass and couplings compared to limits from other experiments.

CRESST II is a direct detection experiment that looks for coincident scintillation light and

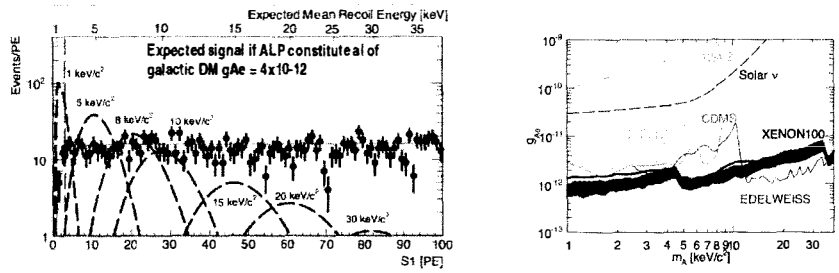

Figure 23 – XENON100 axion search. The observed detector signal (also expressed in terms of the mean recoil energy) compared with the additional number of events expected as a function of BSM particle mass, if these were to make up the entire dark matter needed to explain galactic halo observations (left). The XENON100 observed and expected limits on mass and couplings compared to limits from other experiments (right) [10].

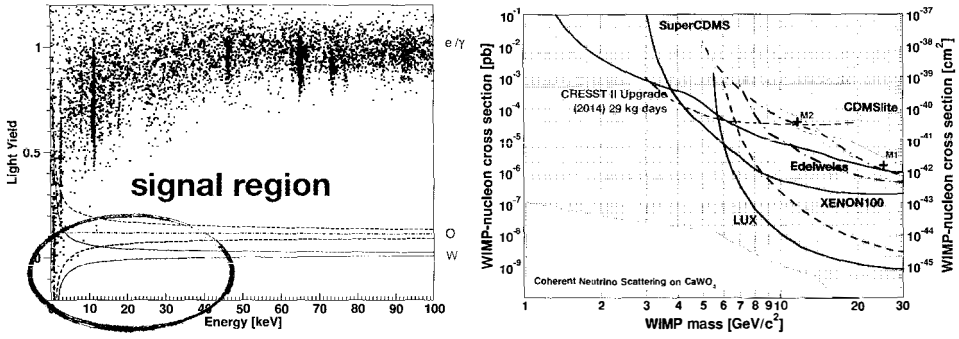

Figure 24 – CRESST II WIMP search. The correlation between the scintillation light yield and phonon energy (left). CRESST II limits on the WIMP-nucleon cross section and WIMP mass compared to limits from other experiments (right) [11].

temperature rise from phonons [11]. CRESST II uses $CaWO_4$ crystals operated at around 15 mK in the Gran Sasso laboratory in Italy. The left-hand plot in Figure 24 shows the correlation between the scintillation light yield and phonon energy. A clear separation is seen between the background from electron recoils and the signal from nuclear recoils. The right-hand plot shows the CRESST II limits on the WIMP-nucleon cross section and WIMP mass compared to limits from other experiments. It can be seen that CRESST II has sensitivity in the very low mass region (below 4 GeV) that is inaccessible to any other experiment.

HESS is an example of an indirect detection experiment [12]. It is looking for DM annihilation to SM particles. It consists of four 12 m and one 28 m telescopes and has an energy threshold of order 30 GeV. The search is performed in regions where large DM accumulations might be expected such as dwarf galaxies and the inner galactic halo. Example limits from HESS as a function of DM particle mass are shown in Figure 25.

At the LHC the signature of DM production is missing transverse momentum E_T^{miss}, from the non-interacting DM particles, produced in association with observed SM particles (see Figure 26 (left) [13]). There are large SM backgrounds to such signatures. For example, Figure 26 (right) shows a plot of E_T^{miss} in events containing jets from the CMS experiment. The dominant background arises from $Z \to \nu\nu$ events.

The results [?] presented by the Plank satelite for 2015 show a number of improvements in: data calibration; better control of systematics; full mission data: increase of statistics; inclusion of polarization results. When combined with data from other facilities, the highlights include

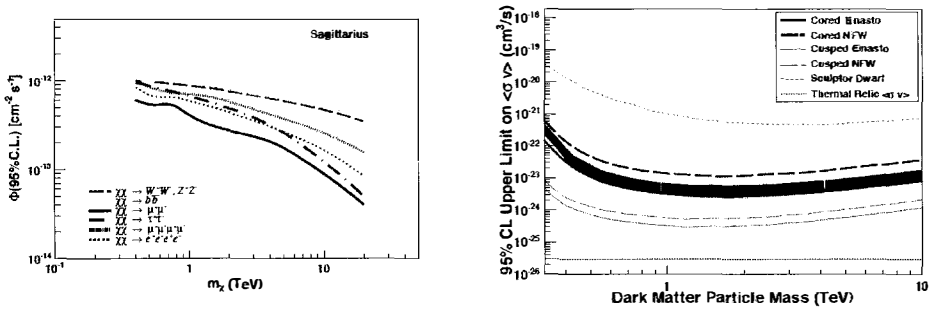

Figure 25 – HESS DM search [12]. Limits on neutralino flux in dwarf galaxies from $\chi\chi$ annihilation into various final states (left) as function of neutralino mass. Limits from the inner galactic halo on the DM particle $< \sigma v >$ [12] as a function of mass.

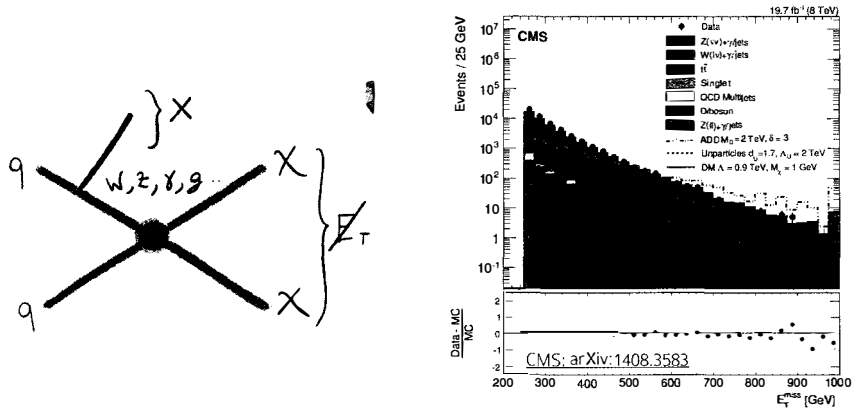

Figure 26 – Schematic Feynman diagram for the production of DM particles at the LHC [13] (left). A pair of neutralinos are produced in association with an observable SM system, denoted by 'X'. Plot of E_T^{miss} in events containing jets from the CMS experiment (right). The dominant background arises from $Z \to \nu\nu$ events.

an upper limit on the sum of the masses of light neutrinos of 0.23 eV at 95% CL. The effective number of relativistic degrees of freedom is found to be 3.04 ± 0.18, which can be compared with the expectation of 3.046 if only photons and the standard three flavours of light neutrinos contribute to the radiation.

3 Higgs

Figure 27 shows a summary [15] of the individual measurements of the Higgs mass in the two precise channels $H \to \gamma\gamma$ and $H \to ZZ \to 4-$leptons, from the two experiments. Figure 28 shows a summary [15] of the combined Higgs mass from the two experiments. The precision has reached 0.19% already.

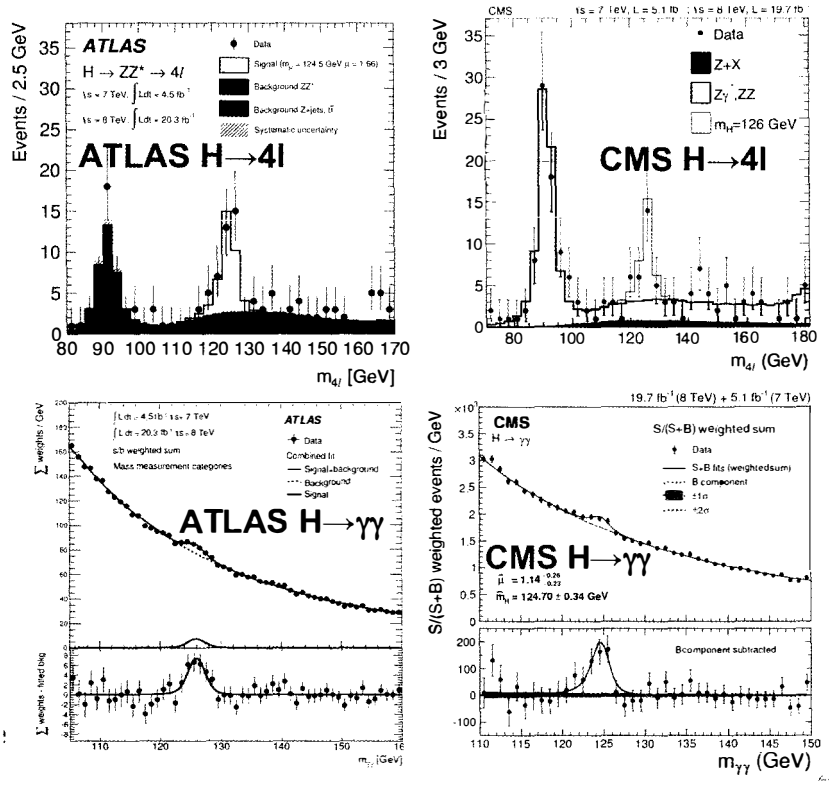

Figure 27 - A summary of the individual measurements of the Higgs mass in the two precise channels from the two experiments [15].

The rates at which Higgs production and decay are measured are usually expressed in terms of a *Signal Strength*, defined by $\mu = \sigma_{\text{observed}}/\sigma_{\text{SM}}$. The signal strengths for different decay modes are shown in Figure 29. The signal strengths for different production modes are shown in Figure 30. There are many possible ways of re-expressing these signal strength measurements to focus on particular combinations or ratios. For example, both experiments have 3-4σ evidence for the VBF production mode. However, the essential message remains the same: the data are consistent with the expectations for a SM Higgs boson. Searches for rare Higgs decays (such as $H \to \mu\mu$), exotic decays (such as decays to invisible particles), as well as searches for additional

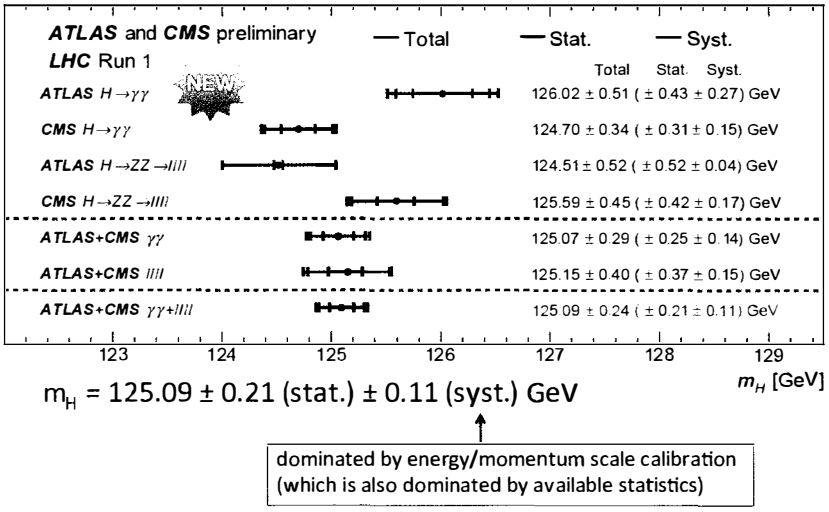

Figure 28 – A summary of the combined Higgs mass from the two experiments [15].

high mass Higgs states, have not thus far yielded any hints of deviations from SM expectations.

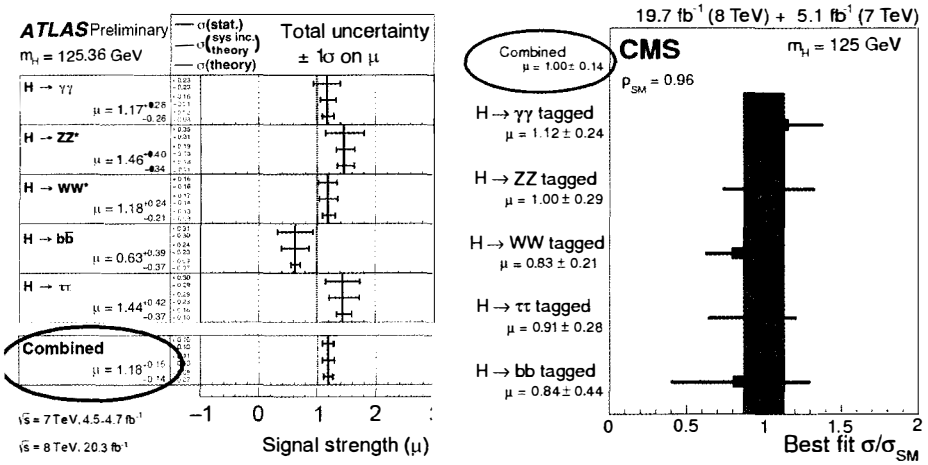

Figure 29 – The Higgs boson signal strengths for different decay modes [15].

Measurements of the production and decay kinematics provide sensitivity to the spin and parity of the observed boson. Spin 1 and 2 variants are ruled out at better than 95% CL and limits have been presented on possible admixtures of 0^- or other BSM Higgs contributions.

As is illustrated in Figure 31, indirect sensitivity to the decay width of the Higgs boson is provided by interference effects in the high mass tail in the 4-lepton decay modes. This analysis requires some assumptions, but achieves very interesting sensitivity to a quantity that is so small in the SM that it cannot be measured directly except at a muon collider. At 95% CL the limits obtained are: $\Gamma_H/\Gamma_{\rm SM} < 4$ (CMS) and $\Gamma_H/\Gamma_{\rm SM} < 5.5$ (ATLAS).

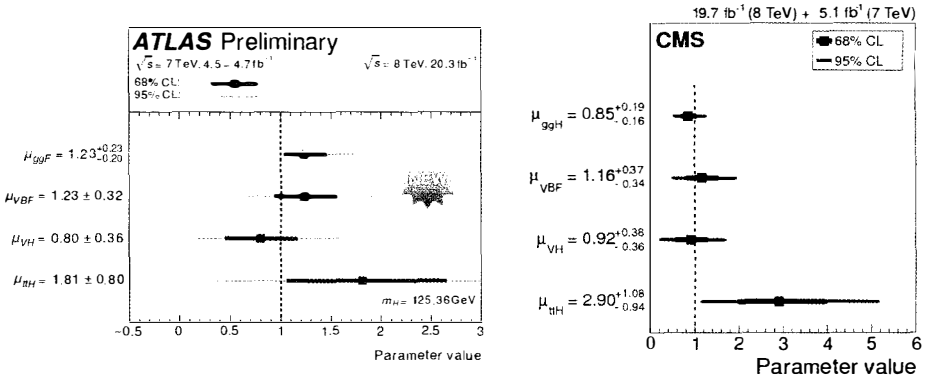

Figure 30 – The Higgs boson signal strengths for different production modes [15].

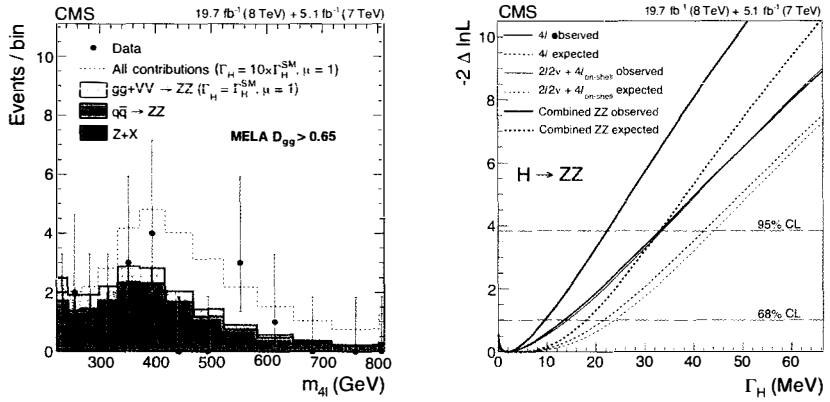

Figure 31 – Measurement of the 4-lepton mass in the high mass region by CMS [15] (left) and the resulting indirect limits on the Higgs boson decay width (right).

It is worth remembering just how little data, and at such low energy (25 fb^{-1}, 7-8 TeV) these amazing results have been obtained with. Even just observing the Higgs boson with this data set was a surprise! To be able to make such precise measurements is astounding. It is also worth noting that even with todays tiny dataset the precision of some of the experimental measurements is within a factor of two of the theoretical uncertainty. A huge theoretical effort will be needed in the years to come to reduce the theoretical uncertainties to an adequate level.

4 Electroweak

The global fit to precision electroweak data [16] now includes corrections calculated to 2-loop EW precision. Mixed EW-QCD terms are included only at order $\alpha\alpha_s$. The fit now includes a theoretical uncertainty on the mass of the top quark of 0.5 GeV to reflect the ambiguity in relating the directly measured mass at the Tevatron and LHC to the pole mass used in the EW fits. The overall result of the EW fit is illustrated in Figure 32. There is a consistent fit to all the data with $\chi^2 = 17.8$ for 14 d.o.f. Improving the precision of the direct measuremens of the mass of the W boson is clearly a high priority given the precision of $\Delta M_W = 15$ MeV

from direct measurements (shown as a point with error bars), which can be compared with the indirect determination with a precision of $\Delta M_W = 8$ MeV from the fit.

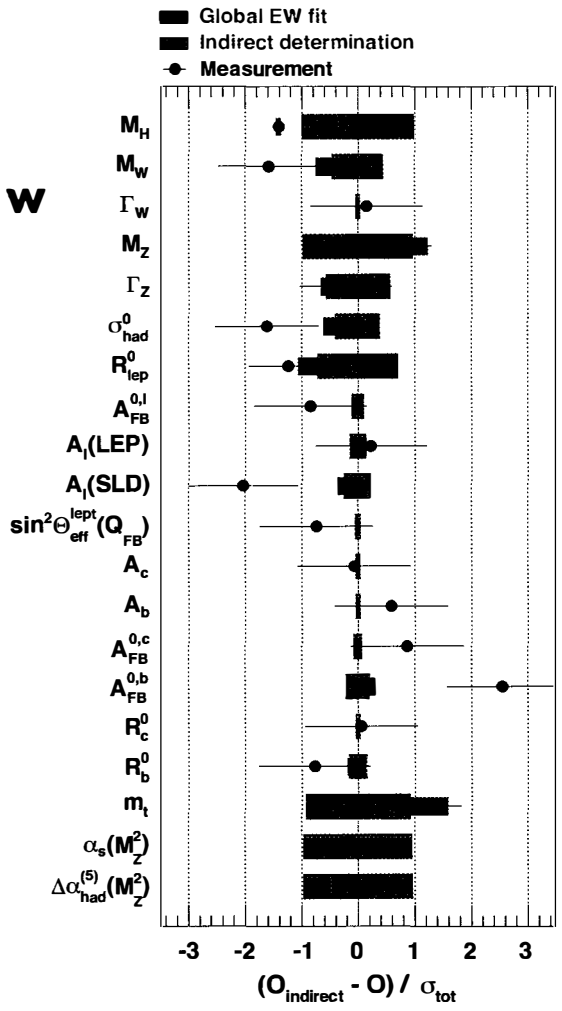

Figure 32 – The overall result of the global fit to precision electroweak data [16].

A number of interesting measurements of final states involving multiple EW bosons were presented. These are of interest because they yield sensitivity to potential anomalous couplings between the EW bosons in addition to allowing searches for resonances decaying to multiple EW bosons. First evidence (at 3.7σ significance) for the production of a tri-boson final state: $W\gamma\gamma \to \ell\nu\gamma\gamma$ was presented by ATLAS [17]. Figure 33 shows a clear excess in the invariant mass of the di-photon system consistent with the expectation from $W\gamma\gamma$.

Several precise EW measurements were shown from the Tevatron [18], including a determination of $\sin^2\theta_W$ from the electron pair forward-backward asymmetry by DØ. This measurement is sensitive to light (u,d) quark couplings. As shown in Figure 34, it is competitive in precision with the LEP combined measurements of leptonic forward-backward asymmetry or τ polarisation.

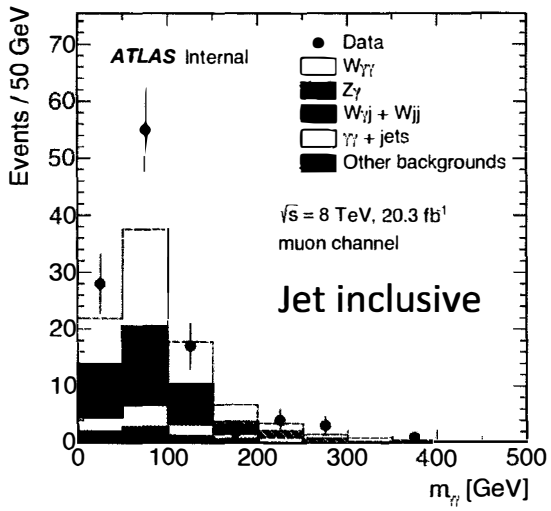

Figure 33 – The invariant mass of the di-photon system in the search for $W\gamma\gamma$ production [17].

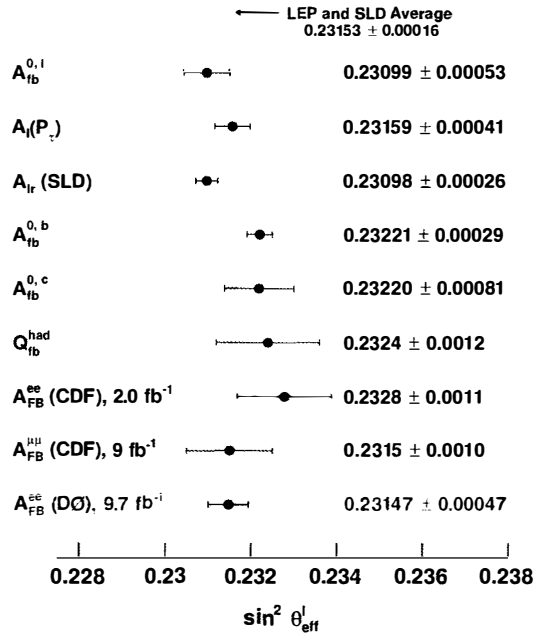

Figure 34 – $\sin^2\theta_W$ determinations from LEP, SLC and the Tevatron [18].

5 Top

A special celebration was presented [19] of the discovery of the top quark, twenty years ago at the Tevatron by the CDF and DØ collaborations. The progress from the handful of top quark events

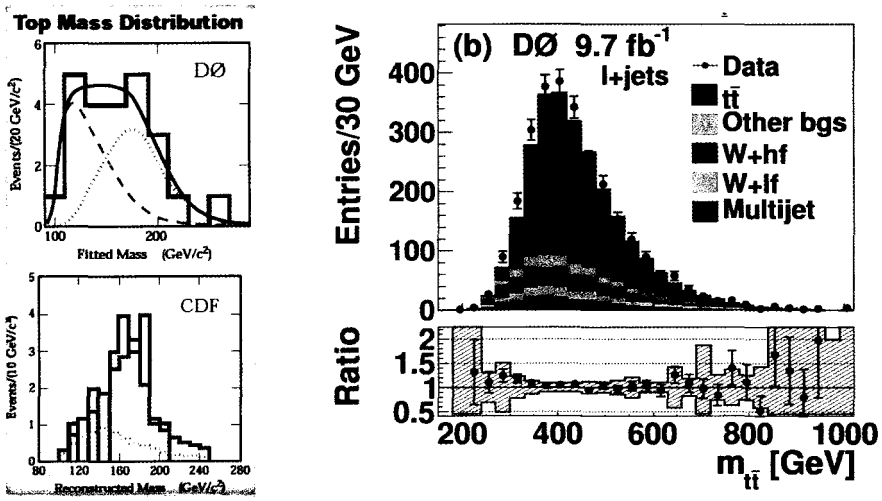

Figure 35 – The top mass distributions at the time of the discovery (left) [19]. The $t\bar{t}$ mass distribution in the full dataset of the DØ experiment (right) [20].

in the discovery plots Figure 35 (left) to the very precise measurements of top quark production and decay properties of the Tevatron (see, e.g., Figure 35 right) and LHC experiments today is enormous. The top quark mass is now measured to a precision of 0.64 GeV at the Tevatron and at a similar precision at the LHC.

As summarised in Figure 36 there has been great progress in the study of the electroweak production of single top quarks at the LHC (top) and Tevatron (bottom).

Top quark asymmetries at the Tevatron no longer show any great discrepancy between data and theory, with movement of both in the direction to wash out the previous hints.

6 Exotica

Many ingenious searches for direct evidence for new phenomena have been carried out at the LHC and elsewhere, but unfortunately there are no definite signals at the moment. I provide here just a couple of examples of searches that I found particularly interesting.

The pair producion of stop quarks followd by the decay to a top quark and a neutralino (χ^0) is illustrated [22] in Figure 37. In the case that the neutralino is stable a search for this process can be performed in top pair events that have an anomalously large missing transverse momentum $E_T^{\rm miss}$ (from the unobserved χ^0s). However, if the mass of the stop is very close to that of the top quark the $E_T^{\rm miss}$ distribution in the stop pair signal events becomes very similar to that of SM top pair events. However, in the SM production of top quark pairs there are correlations between the spins of the two top quarks, which are observable in the angular correlations between their decay products. This is illustrated in Figure 38, which shows the azimuthal angle between the two charged leptons in di-leptonic top pair candidate events in ATLAS. The solid black line, which agrees well with the data, shows the SM expected distribution (with spin correlations). The dashed line shows the expectation for top quark pair production at the SM cross section, but without spin correlations. The solid green line shows the SM expected distribution (with spin correlations) with the addition of stop pairs with a mass of 180 GeV (in which there are no spin correlations). The data clearly rule out the stop pair hypothesis. This is a nice example of a technique developed in the context of precision measurements providing sensitivity to the direct production of BSM physics.

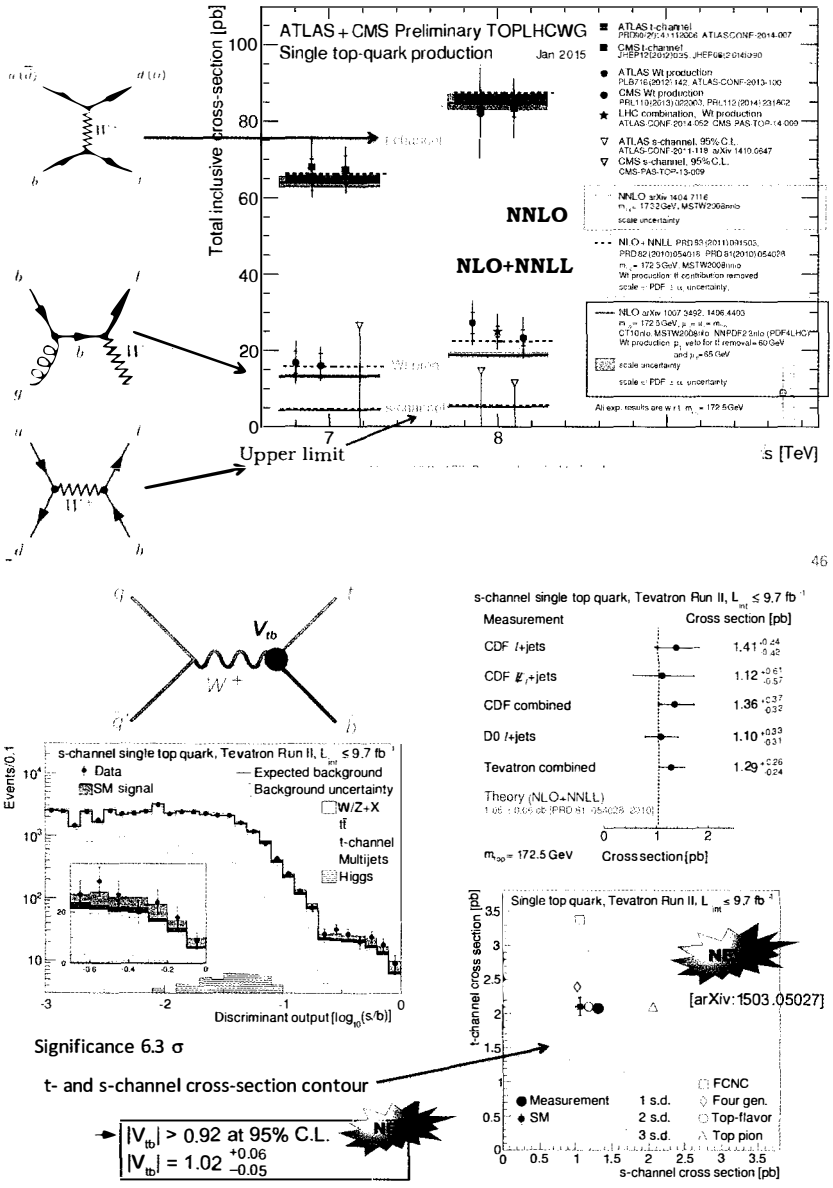

Figure 36 – Summary of single top production at the LHC [21] (top). Observation of single top production in the s-channel at the Tevatron [20] (bottom).

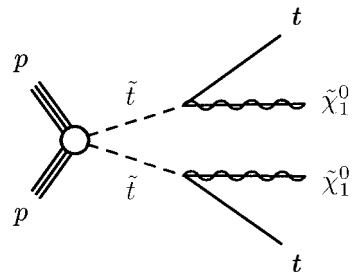

Figure 37 – The pair producion of stop quarks followed by the decay to a top quark and a neutralino[22].

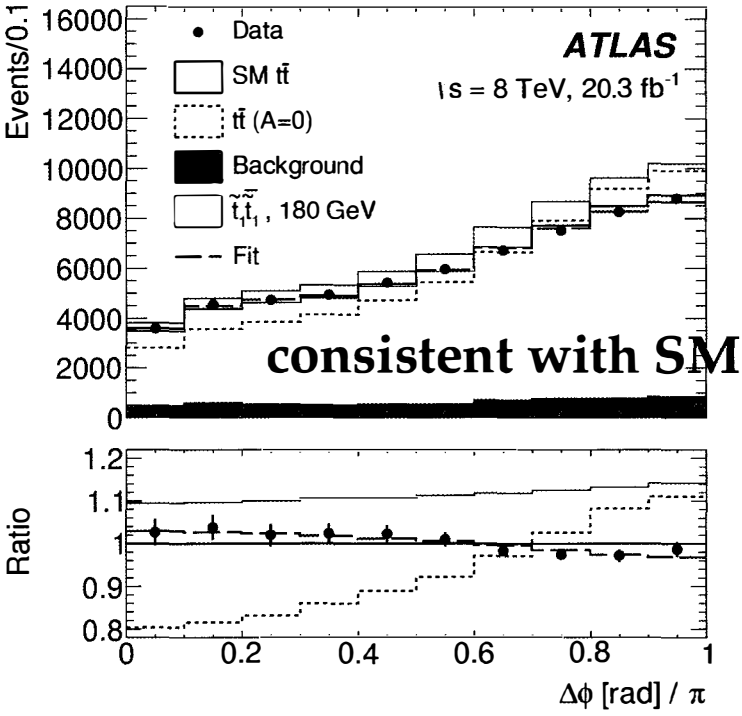

Figure 38 – The azimuthal angle between the two charged leptons in di-leptonic top pair candidate events in ATLAS. The solid black line shows the SM expected distribution (with spin correlations). The dashed line shows the expectation for top quark pair production at the SM cross section, but without spin correlations. The solid green line shows the SM expected distribution (with spin correlations) with the addition of stop pairs with a mass of 180 GeV (in which there are no spin correlations). The lower plot shows the ratios to the SM expected distribution. [22].

A heavy resonance decaying to top quark pairs, as illustrated in Figure 39, could lead to a peak in the observed mass distribution of top quark pair events. However, at very high mass of the hypothetical resonance the decay products of the top quark will be highly boosted and be reconstructed as a single 'fat' jet. Special techniques have been developed to reconstruct top quark candidates in such circumstances[23]. Figure 40 shows the invariant mass of top pair systems

reconstructed by CMS using such techniques. The data are consistent with the expectations from SM top pair production and show no evidence for any BSM contributions. Figure 41 shows the p_T distribution of hadronically decaying top quarks in top pair events reconstructed by ATLAS. Using 'boosted top' techniques has allowed the measurement to be extended to higher values of top quark p_T than were previously accessible. This is a nice example of a technique developed in the context of BSM searches being used to improve precision measurements.

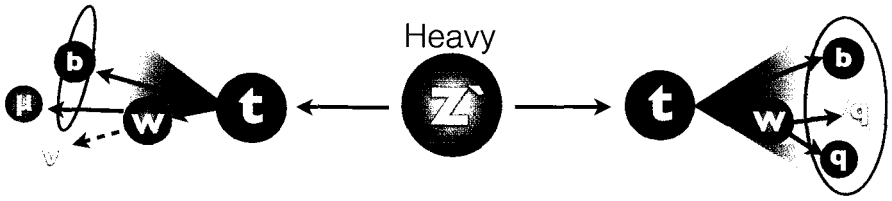

Figure 39 – The pair producion of top quarks from the decay to a top quark and a neutralino [23].

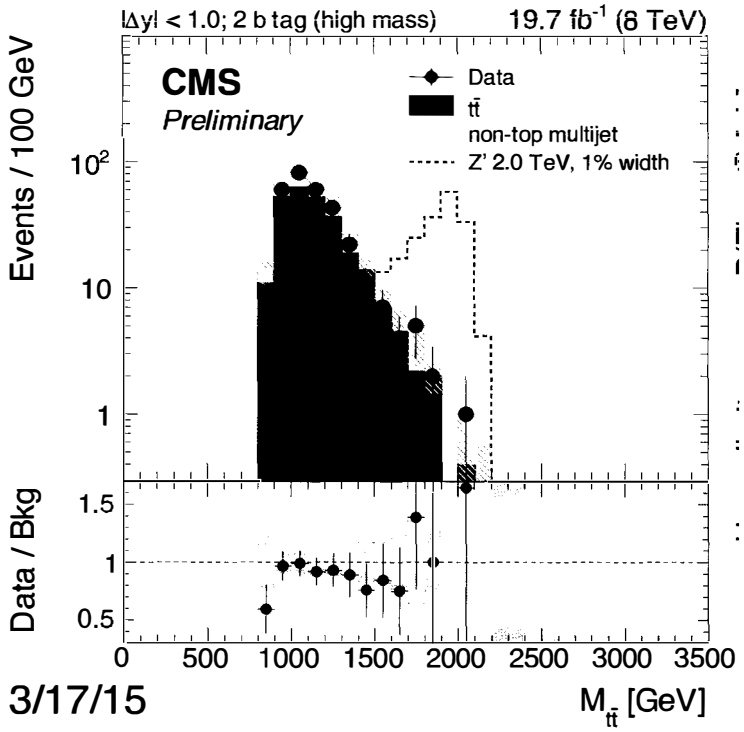

Figure 40 – The invariant mass of top pair systems reconstructed by CMS using 'boosted top' techniques [23].

Run 2 of the LHC at 13–14 TeV will take place between 2015–2018. The large in increase in centre of mass energy and integrated luminosity holds great promise for the direct discovery of BSM physics.

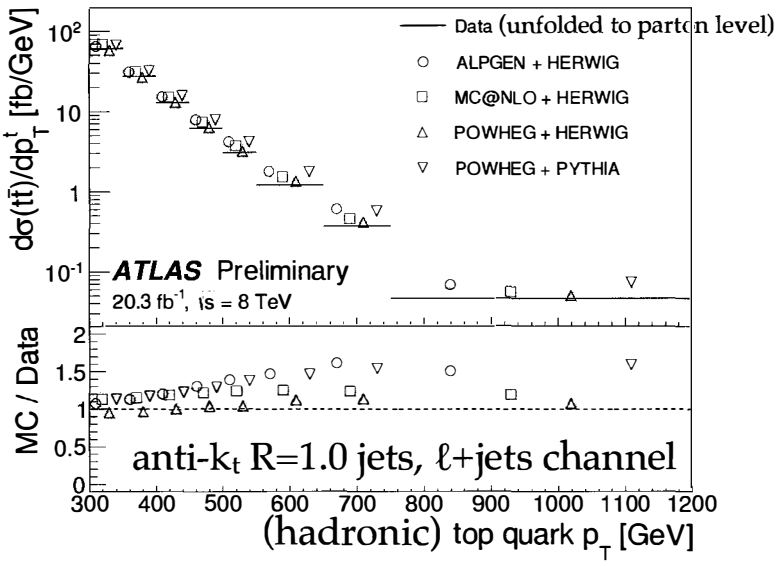

Figure 41 – The p_T distribution of hadronically decaying top quarks in top pair events reconstructed by ATLAS using 'boosted top' techniques [23].

7 Heavy Flavour

One of the most exciting measurements presented at the conference was the updated measurement [24] by LHCb using the full 3 fb^{-1} data set of $B^0 \to K^{*0}\mu^+\mu^-$. Figure 42 shows the two dimensional distribution in muon pair mass vs. mass of the muon pair plus K^{*0} system, in whicha clear signal is seen at the B^0 mass. The bands in muon pair mass corresponding to the J/ψ and $\psi(2s)$ are vetoed. A number of angular observables are studied and show good agreement with expectations except for P_5, which is a combination of the fitted angular coefficients for which hadronic form factor uncertainty is expected to be small.

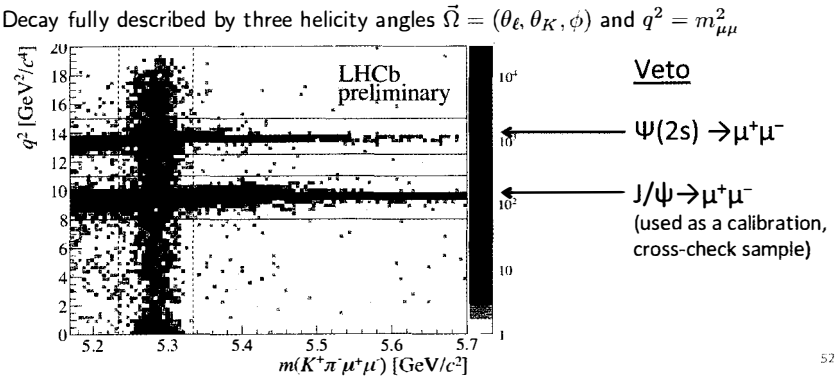

Figure 42 – The $B^0 \to K^{*0}\mu^+\mu^-$ analysis: two dimensional distribution in muon pair mass vs. mass of the muon pair plus K^{*0} system [24].

The naive significance of the discrepancy in the two q^2 bins from 4-8 GeV^2 is 3.7σ. The results with 3 fb^{-1} are compatible with and more precise than those presented previously with 1 fb^{-1}.

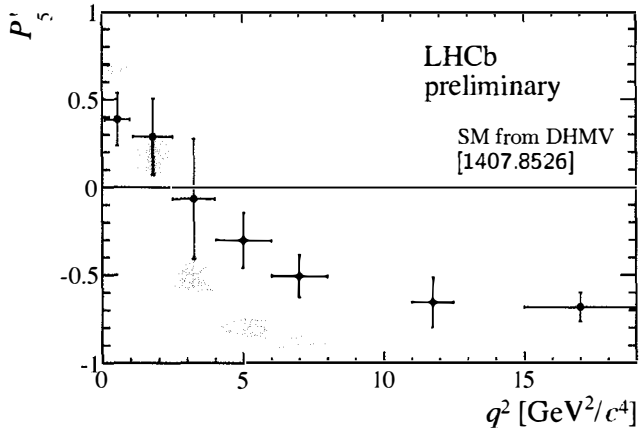

Figure 43 – The $B^0 \to K^{*0}\mu^+\mu^-$ analysis: P_5, which is a combination of the fitted angular coefficients for which hadronic form factor uncertainty is expected to be small plotted as a function of the muon pair mass [24].

Many other very interesting measurements were presented by LHCb, such as those on CP violation in B_s, where the world average is totally dominated by LHCb. In the direct measurement of CKM Angle γ there is still a long way to go before direct measurements will match the precision of indirect determinations through the CKM fits.

A first observation [25] of the exclusive decay $\Lambda_b \to p\mu^-\overline{\nu}_\mu$ was shown LHCb and used to determine the value of $|V_{ub}|$. Figure 44 displays the corrected $p\mu^-$ mass distribution, showing a very clear signal for the exclusive decay $\Lambda_b \to p\mu^-\overline{\nu}_\mu$.

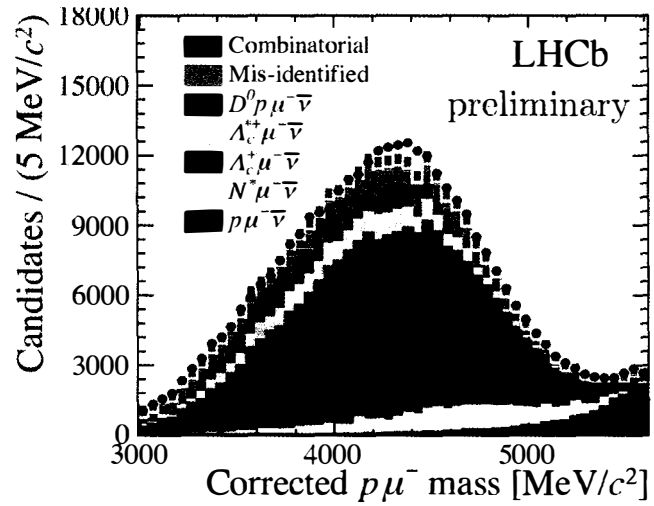

Figure 44 – Corrected $p\mu^-$ mass distribution, showing a very clear signal for the exclusive decay $\Lambda_b \to p\mu^-\overline{\nu}_\mu$ [25].

8 Moriond: the 50th edition

Two great talks by Guido Altarelli[26] and Daniel Treille[27] celebrated the contribution that the Moriond series of conferences has made to bringing experimentalists and theorists together to discuss the advances in our field and the most urgent current problems. Long may Moriond continue to serve our community in this way as we re-enter the era of 'not much theoretical guidance'! (See Figure 45.)

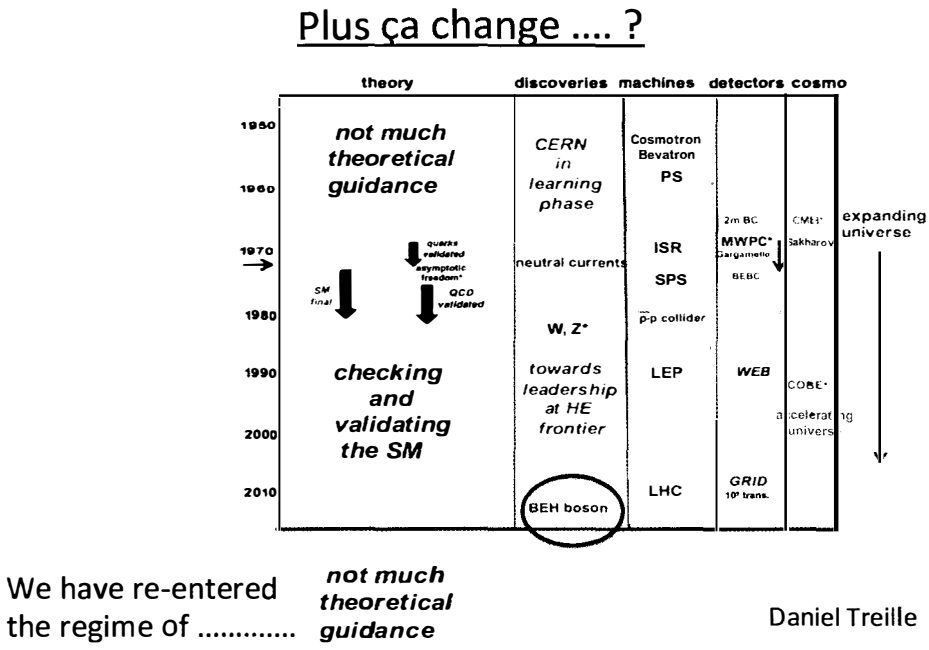

Figure 45 – Fifty years of Moriond: my slight additions to a slide by Daniel Treille[27].

Acknowledgments

I am very grateful to many of the speakers and other participants at th 50th Recontres de Moriond for illuminating discussions.

References

1. Eligio Lisi, 'Status of three-neutrino mixing' and the references contained therein (these proceedings).
2. Dondald Rumsfeld, imaginary communication.
3. Bei-Zhen Hu, 'Recent results from Daya Bay reactor neutrino experiment', and the references contained therein (these proceedings).
4. Rachel Carr, 'Entering the two-detector phase of the Double Chooz experiment', and the references contained therein (these proceedings).
5. Anna Hayes, 'Systematic uncertainties in reactor antineutrino fluxes and anomaly', and the references contained therein (these proceedings).

6. Jordan Myslik, 'Selected results from T2K', and the references contained therein (these proceedings).
7. Juan Pablo Yanez, 'Latest results from IceCube on astrophysical neutrinos and neutrino oscillations', and the references contained therein (these proceedings).
8. Barbara Caccianiga , 'Recent results from Borexino', and the references contained therein (these proceedings).
9. Tessa Johnson, 'Searches for beyond the standard model physics in double beta decay with EXO-200', and the references contained therein (these proceedings).
10. Gianmarco Bruno, 'Recent results from the XENON100 experiment', and the references contained therein (these proceedings).
11. Jochen Schieck, 'Direct dark matter search with CRESST', and the references contained therein (these proceedings).
12. Emmanuel Moulin, 'Recent results from H.E.S.S.', and the references contained therein (these proceedings).
13. Caterina Doglioni, 'Dark matter searches at ATLAS and CMS: Run 1 results and Run 2 potential', and the references contained therein (these proceedings).
14. S. Henrot-Versillé, 'Planck 2015 results', and the references contained therein (these proceedings).
15. Michael Duehrssen, 'Higgs combination' (these proceedings). See also a number of other talks in these proceedings, in which the individual results were presented in more detail.
16. Roman Kogler, 'The global Electroweak fit', and the references contained therein (these proceedings).
17. Luca Perrozzi, 'EWK measurements from ATLAS and CMS', and the references contained therein (these proceedings).
18. M. Bauce, 'Recent Electroweak results from the Tevatron', and the references contained therein (these proceedings).
19. Patrizia Azzi, 'Celebrating 20 years of the discovery of the Top quark', and the references contained therein (these proceedings).
20. Andreas Jung, 'Top quark physics at the Tevatron', and the references contained therein (these proceedings).
21. Andrey Loginov, 'ATLAS+CMS top production and properties', and the references contained therein (these proceedings).
22. Stephanie Majewski, 'Top quarks in ATLAS: bridging measurements and searches', and the references contained therein (these proceedings).
23. John Stupak III , 'Boosted Topologies: ATLAS and CMS', and the references contained therein (these proceedings).
24. C. Langenbruch, 'Latest results on rare decays from LHCb', and the references contained therein (these proceedings).
25. William Sutcliffe, '$|V_{ub}|$ using $\Lambda_b \dashrightarrow p\mu^-\overline{\nu}_\mu$ at LHCb', and the references contained therein (these proceedings).
26. Guido Altarelli, 'The Early Years of Moriond' (these proceedings).
27. Daniel Treille, '50 years of Moriond' (these proceedings).

THEORY SUMMARY OF MORIOND ELECTRO-WEAK 2015

ALESSANDRO STRUMIA
Dipartimento di Fisica, Univ. di Pisa and INFN and NICPB

I summarise the theoretical talks at Moriond 2015, with emphasis on naturalness.

The theoretical talks at the electro-weak session of the 50th edition of the Moriond conference touched many hot topics: neutrinos (section 1), dark matter (section 2), the Higgs (section 3), the bottom (section 4), the top (section 5), and finally new physics — or better how the lack of new physics is challenging our ideas about naturalness of the Higgs mass (section 6).

1 Neutrinos

1.1 $\nu_e \leftrightarrow \nu_\mu \leftrightarrow \nu_\tau$ oscillations

E. Lisi[1] reviewed how a lot of data are non-trivially explained by 3ν oscillations. This fascinating field started as astro-physics and so far gave us 5 new fundamental parameters:

$$\begin{gathered}\Delta m^2_{12} = 7.50 \pm 0.20\ 10^{-5}\,\mathrm{eV}^2, \qquad |\Delta m^2_{23}| = 2.45 \pm 0.10\ 10^{-3}\,\mathrm{eV}^2 \\ \tan^2\theta_{12} = 0.452 \pm 0.035, \qquad \sin^2 2\theta_{13} = 0.087 \pm 0.0045, \qquad \sin^2 2\theta_{23} = 1.02 \pm 0.04\end{gathered} \tag{1}$$

Some years ago, Lisi and others claimed that global fits of solar and atmospheric data favoured at $\sim 1.5\sigma$ level a non vanishing θ_{13}:

$$\sin^2 2\theta_{13} = \begin{cases} 0.05 \pm 0.05 & \text{CHOOZ and atmospheric} \\ 0.07 \pm 0.04 & \text{KamLAND and solar} \\ 0.05 \pm 0.03 & \nu_\mu \to \nu_e \text{ at MINOS, normal hierarchy} \\ 0.084 \pm 0.005 & \bar\nu_e \to \bar\nu_e \text{ at DayaBay} \\ 0.113 \pm 0.023 & \bar\nu_e \to \bar\nu_e \text{ at RENO} \\ 0.090 \pm 0.032 & \bar\nu_e \to \bar\nu_e \text{ at Double CHOOZ} \\ 0.140 \pm 0.035 & \nu_\mu \to \nu_e \text{ at T2K for } \delta_{\rm CP} = 0, \text{ normal hierarchy.} \end{cases} \tag{2}$$

In 2012 the reactor experiments DayaBay and others confirmed this hint, finding a clear evidence for θ_{13}. With the most recent data we start to have an indication for a 6th parameter:

a non-vanishing CP-violating phase $\delta_{\rm CP}$. Indeed, as shown in fig. 1, θ_{13} is measured by reactor experiments, and a combination of θ_{13} and of $\delta_{\rm CP}$ is measured by the T2K long-baseline experiment. The two determinations are in better agreement if

$$\delta_{\rm CP} \sim -\pi/2. \tag{3}$$

So far all observed CP-violating phenomena have the same source: the CKM phase. The observation of CP violation in neutrino oscillations would double the observed CP-violating parameters. We have no idea of why CP is violated in nature. Do complex phases appear everywhere with order one size?

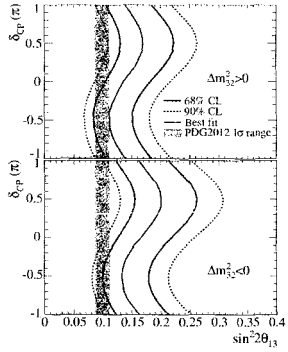

Figure 1 – Measurements of θ_{13} from reactors (red vertical band) and from T2K (black/blue bands).

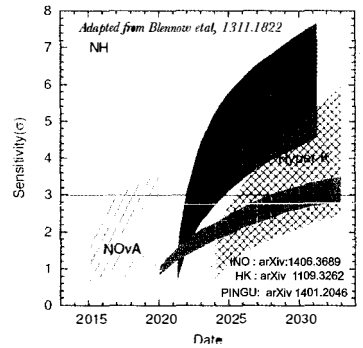

Figure 2 – Future prospects for determining the neutrino mass hierarchy: normal or inverted?

Furthermore, the sign of Δm^2_{23} is unknown. S. Choubey[1] reviewed how the neutrino mass hierarchy can be determined with

a) matter effects in future long-baseline experiments;

b) matter effects in future atmospheric ν experiments;

c) interference between solar and atmospheric oscillations in future dedicated reactor experiments.

Future prospects are summarised in figure 2.

1.2 (What) are we learning?

Observing a 3×3 chessboard might be not enough to reconstruct the laws that rule chess. We observed $3+3$ mixing angles and $3+3+3+2$ fermion masses. With this, we fail to identify the laws that rule flavour. Unlike in the case of Balmer lines, data show no clean pattern.

Nevertheless, the observed semi-ordered flavour pattern somehow resembles SU(5) unification with some flavour symmetry acting only on 10_i fermions, such that

$$\lambda_D \sim \lambda_E \propto \epsilon, \qquad \lambda_U \propto \epsilon^2, \qquad \lambda_N \propto \epsilon^0, \qquad \theta_{\rm CKM} \sim \epsilon, \qquad \theta_{\rm MNS} \sim 1. \tag{4}$$

But this does not give rise to any sharp prediction. Only low-level theories (such as texture zeroes or numerology) give precise predictions. It is maybe interesting to point out that

$$V_{\rm PMNS} = R_{12}(\theta_C) \cdot R_{23}(\pi/4) \cdot R_{12}(\pi/4)$$

(where θ_C is either the Cabibbo angle or the Golden angle $\theta_{\text{Golden}} \equiv \text{arccot}\,\varphi^3$) predicts neutrino mixings

$$\theta_{23} = 44.2^\circ, \qquad \theta_{12} = 35.5^\circ \qquad \theta_{13} = 9.3^\circ \tag{5}$$

in agreement with measurments. When searching if this was already known, I first found chinese authors who studied a similar ansatz, but with $R_{12}(\theta_C)$ on the wrong side. Later I found that other chinese authors put $R_{12}(\theta_C)$ on both sides, obtaining another wrong prediction. Finally, I found that more chinese authors who basically got the same prediction [2].

What is the lesson? Fig. 3 shows a compilation of predictions for θ_{13}: there are so many of them that any measured value would have agreed with some prediction.

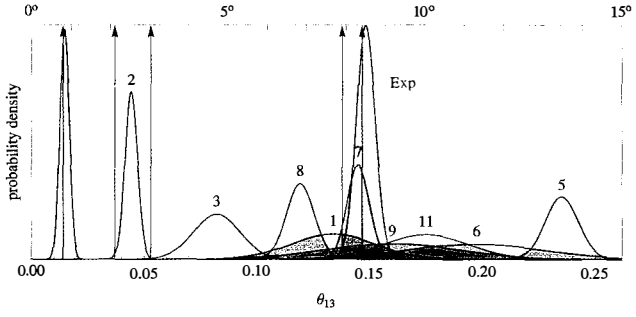

Figure 3 – Compilation of predictions for θ_{13}: the bells show the central value and (when possible) the uncertainty of each prediction. The green bell is the observed value of θ_{13}.

1.3 The rector $\bar{\nu}_e$ anomaly

A re-computation of $\bar{\nu}_e$ fluxes emitted by fission reactors claims that measured rates are $\sim 5\%$ lower than predicted unoscillated rates and that the theoretical uncertainty is at the $1 - 2\%$ level.

The deficit could be due oscillations into extra sterile neutrinos ν_s. S. Zsoldos[1] presented STEREO: a new reactor experiment with short base-line $L \sim 10\,\text{m}$ to search for sterile oscillations with $\Delta m^2 \sim \text{eV}^2$. Indeed, present null results push $m_{\nu_s} \gtrsim \text{eV}$. However, such a large sterile neutrino mass is already disfavoured by standard cosmology, as discussed by N. Saviano[1].

Furthermore, the measured $\bar{\nu}_e$ reactor spectra differ also from the predicted spectra at the same level, showing a 'bump' that cannot be due to oscillations. A. Hayes[1] reviewed the issue: nuclear theory and data seem to be not solid enough to allow the claim that there is an anomaly. Modern reactor experiments bypass these uncertainties by observing oscillations as differences between the energy spectra measured in a near detector and a far detector.

1.4 Neutrino-less double-beta decay

If neutrino masses are of Majorana type, neutrino-less double-beta decay is the only realistic way of observing lepton-number violation in the electron sector: the amplitude is proportional to m_{ee}, the ee entry of the Majorana neutrino mass matrix.

Oscillation experiments imply a detectable $0\nu2\beta$ rate if neutrinos have inverted mass hierarchy. However the computation of $0\nu2\beta$ rates involves difficult and uncertain nuclear physics. P.K. Raina[1] reviewed the issue of nuclear matrix elements. The $0\nu2\beta$ rate is computed as

$$\Gamma_{0\nu2\beta} = G\ |\mathcal{M} m_{ee}/m_e|^2 \tag{6}$$

where G is known phase space factor and $\mathcal{M}$ is the nuclear matrix element. We heard that "NTEM QRPA, PHFB, DHF, EDF, IBM, SSDH, OEM", which, in the language of nuclear physics, means "there are various approaches, but no agreement". Even worse, some experts think that the axial nucleon coupling g_A, measured in vacuum to be $g_A \approx 1.25$, can acquire inside nuclei a smaller value, $g_A \approx 1.25 A^{-0.15}$. In the worst case, such nuclear quenching of g_A could reduce $0\nu2\beta$ rates by up to $6 - 50$, making all experiments much less sensitive than what initially thought[3].

Table 1: Summary of $0\nu2\beta$ parameters and experimental data and bounds.

nucleus	^{76}Ge	^{82}Se	^{100}Mo	^{130}Te	^{136}Xe	^{150}Nd
Q in keV	2039	2995	3034	2529	2476	3367
$T^{2\nu2\beta}_{1/2}$ in 10^{20} yr	15 ± 1	0.92 ± 0.07	$.071 \pm .004$	9 ± 1	23 ± 1	$.082 \pm .009$
G in 10^{-14}/yr	0.63	2.73	11.3	4.14	4.37	19.4
$\mathcal{M}$ [IBM-2 2015]	4.68	4.37	3.7	4.03	3.33	2.32
$\mathcal{M}$[ŠFRVE 2007]	$3.3 \div 5.7$	$2.8 \div 5.1$	$2.2 \div 4.6$	$2.3 \div 4.3$	$1.2 \div 2.8$	
$\mathcal{M}$ [CS 2009]	$4.0 \div 6.6$	$2.8 \div 4.6$	$2.7 \div 4.8$	$3.0 \div 5.4$	$2.1 \div 3.7$	
$\mathcal{M}$ [MPCN 2008]	2.3	2.2		2.1	1.8	
$\mathcal{M}$ [BI 2009]	5.5	4.4	3.7	4.1		2.3
$\mathcal{M}_0$ [SMK 1990]	4.2	4.0	1.3	3.6	1.7	0.6
90%CL bound on $T^{0\nu2\beta}_{1/2}$ in 10^{23} yr	190,160,210 HM, IGEX,GERDA	4.4 NEMO-3	5.8 NEMO-3	30 CUORICINO	260 KL-Zen, EXO	0.036 NEMO-3
Bound on m_{ee}/h	0.35, 0.38, 0.33eV	1.2eV	1.5eV	0.40eV	0.29eV	31eV

1.5 High-energy neutrinos

A. Vincent[1] discussed flavour reconstruction of neutrino-induced events observed at ICECUBE: after taking into account track mis-identification, all oscillated neutrino production mechanisms (π decays, μ decays, n decays) can fit the data.

M. Masip[1] argued that the excess over the neutrino atmospheric background observed by ICECUBE seems to be showers, rather than tracks. In theoretical language, this means Neutral Current events, rather than Charged Current events. Consequently he proposed that the claimed excess can be fitted by new physics that increases the NC cross sections of ordinary atmospheric neutrinos; in particular models with extra dimensions predict double-bang events.

J. Heeck[1] reviewed gauged $U(1)_{B-L}$. If broken by 4 units, by an ν_R^4 operator, one would obtain $pp \to 4\ell$ signals; Dirac leptogenesis would be allowed, giving an excess of neutrinos in the Cosmic Microwave Background, $N_{\rm eff} \approx 3.14$. J. Lopez Pavon[1] discussed type-I see-saw in the full range of possible right-handed neutrino masses, finding that $1\,{\rm eV} < m_{\nu_R} < 100\,{\rm MeV}$ is excluded by cosmology because ν_R would thermalise. V. de Romeri[1] discussed type-I see-saw signal at a future circular e^+e^- collider, finding that a $Z \to \mu\tau$ rate could be produced at an observable level, while an observable $Z \to e\mu$ is already excluded by $\mu \to e\gamma$ and related measurements.

2 Dark Matter

In the past century we understood matter. Cosmology and astrophysics tell that there is more matter left to be understood, called Dark Matter.

For some time 'neutralino' was used as a synonymous of 'Dark Matter', but theoretical progress showed that the DM mass can be in the wider range $M_{\rm DM} = 100\,{\rm GeV} \times 10^{\pm 40}$. This means that DM could be macroscopical objects to be studied as astrophysics (although cosmology disfavours this possibility), DM could be an unobservable Planck-scale particle (to be studied by string theorists); DM could be a weak scale particle (to be studied by particle physicists), DM could be lighter (in the energy range of nuclear physics down to chemistry), DM could be an axion-like ultra-light scalar (to be studied as classical field theory, searching for modulations at $\omega = 1/M_{\rm DM}$), demanding a variety of experimental approaches.

Let us summarise what is known.

So far we observed Dark Matter gravity. We only have upper bounds on any other DM interaction with matter and among itself. In cosmology, this lack of interactions is what allows DM to cluster forming galaxies, while normal matter is still interacting with non-clustering photons. Cosmological data are reproduced if DM has a primordial inhomogeneity of adiabatic type: a single dominant primordial perturbation equal for all components of the universe. Loosely speaking, this suggests some connection with matter. The assumption that DM is a thermal relic favours $M_{\rm DM} \lesssim 100\,{\rm TeV}$: then DM could be discovered in direct, indirect, collider searches around 2010 or maybe later. We passed the golden moment where PAMELA, FERMI, AMS, CDMS, XENON, LHC started to produce data: backgrounds are starting to become a limitation.

2.1 Dark Matter searches are reaching the backgrounds

Direct searches for DM with electro-weak mass improved by 3 orders of magnitude in the past decade and are now 3-4 orders of magnitude above the irreducible ν background, as shown in fig. 4. This was discussed by J. Billard[1] who proposed how, in case of no signal above the background, we might survive to the crash on the ground, relying on seasonal variations (DM rates are maximal in June, while solar ν rates are maximal in January), multiple experiments, directionality of scattered particles. Various authors explore how to improve searches for sub-GeV DM particles: present bounds are still far from the irreducible ν backgrounds.

Indirect searches aim at detecting in cosmic rays an excess of e^+, $\bar{p}$, γ possibly produced by DM annihilations or decays. In the past years such cosmic rays have been observed at weak scale energies, and no undisputable evidence of a DM excess above the astrophysical fluxes was found. The uncertain uncertainties on such backgrounds to DM searches are now the limiting factor: it will be difficult to clarify the tentative claims and to improve the searches. Once all data will be available, it will maybe possible to better understand galactic astro-particle physics, improving DM searches.

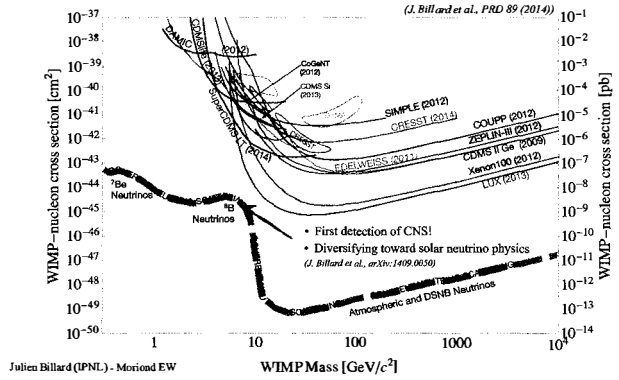

Figure 4 – The neutrino background to direct DM searches.

Searches at colliders mostly rely on the classical DM signal

$$\text{missing energy} + \text{something to tag the event (a jet, a } \gamma, \ldots). \tag{7}$$

At a hadron collider, this signal can be easily seen if DM is produced with QCD-like cross section, like in supersymmetric models. On the other hand, the same signal can be easily missed below

the backgrounds, if instead the cross section for DM production is (loosely speaking) below the electro-weak neutrino cross section.

Furthermore, DM can easily be too heavy for LHC. This is for example the case of Minimal DM models, where DM only has electro-weak gauge interactions: assuming that the cosmological DM abundance is reproduced as thermal relic, one predicts a TeV-scale DM mass.

The TeVatron and LHC experimental collaborations searched for the signals in eq. (7) without finding new physics. Various bounds have been presented in the context of effective contact operators between DM and quarks, suppressed by a scale Λ: this is appreciated as a general framework that allows collider experimentalists to present results in the same $(M_{\rm DM}, \sigma_{\rm SI/SD})$ plane used in direct DM searches. However:

1. The effective operator approximation fails at LHC.

   Effective operators are a valid approximation at energies below Λ. For any collider the sensitivity to Λ will be much below the collider energy, because tagging the invisible signal needs extra j or γ, implying a small cross section.

2. Effective operators could mislead to miss the missing energy signal.

   The assumed growth of $\sigma \sim E^2/\Lambda^4$ with energy is crucial in making high-energy colliders competitive with direct searches. But in models where $1/\Lambda^2 \approx g^2_{\rm mediator}/M^2_{\rm mediator}$, such growth stops at the mediator mass: the signal is no longer at the highest energy.

3. What LHC would first see is the heavy mediator particle, not missing energy.

   Even using "simplified models" the casistics of possible mediators is tedious. The basic possibilities are a colored mediator in t-channel (that would be pair produced with a large QCD cross section) or a neutral mediator in s-channel (that would also give a peak in the $pp \to jj$ cross section). In both cases the mediator gives much cleaner signals than Dark Matter.

This was described by many recent works, and there is presently interest in systematizing "simplified models" that capture a minimal and sufficient amount of new physics. This approach was described by B. Zaldivar[1,4]. U. Hash[1] emphasised how higher order corrections for DM search at LHC can be relevant.

2.2 Models for DM

Building models for DM that satisfy the present theoretical and experimental restrictions is not particularly difficult. At the Moriond 2015 conference A. Ahrice[1,5] and D.R. Lamprea[1] presented models that simultaneously can account for observed DM and for observed neutrino mass.

Furthermore, G. Arcadi[1] proposed a model of decaying DM, containing the Yukawa couplings

$$y \text{ matter DM scalar} + y' \text{ matter matter scalar}.$$

y gets predicted by assuming that the cosmological DM abundance is reproduced through the freeze-in mechanism, implying a scalar long lived compared to collider time-scales.

3 The Higgs

R. Kogler[1] summarized global fits of electroweak precision data. The summary of the summary is: 'SM ok'.

Various authors presented general aspects of composite Higgs models. Since I never worked on this subject, the theoretical summary in fig. 5 has been obtained by processing the slides with a computer code that identifies the key words. Below, I would like to explain my doubts about the field of composite Higgs models.

Figure 5 – Theoretical summary of talks about Composite Higgs. D. Espriu[1] discussed how unitarity can constrain resonances. K. Kanshin[1] discussed operators with arbitrarily high dimensions characteristic of non-linearities assuming a chiral Lagrangian for the Higgs. I. Brivio[1,6] discussed typical effects of such nonlinearities. A. Kaminska[1,7] considers techni-ρ in (partially)composite Higgs models. F. Riva[1] reviewed new physics signals as dimension 6 operators: there are 79 of them (2499 with flavour). Given present experiments, NRO are mostly equivalent to simpler κ modifications of h and Z SM couplings.

3.1 Is the Higgs composite?

Now that the SM scalar boson was found and that its properties started to be measured, this question is obviously a hot topic for experimentalists. A. David[1] emphasised that future data will allow to go beyond overall rates, where new physics effects are parameterized by overall κ factors. Already at LHC run I experimentalists measured angular correlations and transverse momentum distributions that confirm that the resonance at 125 GeV is really the scalar Higgs, rather than some impostor that fakes the same total rates. Given the possibility that some new physics might cancel out in the total rate, it would be useful to identify extra useful pseudo-observables, that describe how the rates depend on kinematics.

Since decades, naturalness motivates a significant theoretical activity on composite Higgs models of a special type: models where the Higgs is *composite at the weak scale and made of fermions.*

However LEP precisely measured 3 components of the Higgs doublet H (those eaten by the Z and by the $W^{\pm}$), setting a strong bound $\Lambda \gtrsim 10\,\text{TeV}$ on the compositeness scale that suppresses the $|H^{\dagger}D_{\mu}H|^2$ effective operator that violates the custodial symmetry, accidentally present in the SM. LHC finally discovered the last component of H, the physical Higgs h, allowing to set weaker constraints on a wider set of effective operators. As a consequence composite Higgs models need some fine-tuning to achive electroweak-symmetry breaking compatibly with data.

More importantly, the Higgs does much more than breaking the electroweak symmetry. The SM elementary Higgs also has a set of Yukawa couplings that non-trivially reproduce the observed pattern of lepton and quark masses and of flavour-violating processes. It looks impossible to find a theory at the weak scale that dynamically generates all this flavor structure, while at the same time giving no new physics effects in flavour observables.

In this situation, theory of composite Higgs degenerated in 'cosettology'. While the $SU(3)_L \otimes SU(3)_R \to SU(3)_V$ dynamical symmetry breaking pattern of QCD is understood as the result of having 3 light quarks, composite Higgs theories postulate ad-hoc properties of the unknown extra strong dynamics in order to recover the custodial symmetry (this looks plausible), to satisfy flavour bounds (partial compositeness is invoked), etc. All of this gets described in a formal way using general techniques (chiral effective Lagrangians, AdS/CFT, approximations to QCD...). In absence of a fundamental theory with the structure needed to accomodate all null results, it is not clear how much the deep words in fig. 5 really go beyond a purely phenomenological approach, useful when data are coming.

As far as I know, one could make real theories of composite Higgs by giving up on naturalness:

a) One possibility is accepting a very large compositeness scale (for example 10^{10} GeV such that axion-Higgs unification becomes possible).

b) Another possibility is making TeV-scale theories using elementary techni-scalars $\mathcal{H}$ and techni-fermions $\mathcal{Q}$ with techni-Yukawas $y_{ij}\,\psi_i \mathcal{H}_j \mathcal{Q}$ to SM fermons ψ, realising partial compositeness.

3.2 More Higgs

A. Celis[1,14] studied models with 2 Higgs doublets and Yukawa matrices proportional to each other (at least at tree level) in order to avoid unobserved flavor-violating effects. S.I. Godunov[1] considered Higgs triplets present in type-II see-saw models, discussing signals where the triplet decays into hh; furthermore he pointed out how higher rates can be obtained with an ad-hoc fine tuning proposed by Georgi and Machacek. V. Bizouard[1] performed one-loop computation of the system of 3 scalar Higgses present in the NMSSM. This was the first talk about supersymmetry.

M. Neubert[1] presented predictions for rare Z, W decays into exclusive channels, that can be precisely computed using factorisation and measured with high luminosity LHC:

Decay mode	Branching ratio	
$Z^0 \to \pi^0\gamma$	$(9.80^{+0.09}_{-0.14\,\mu} \pm 0.03_f \pm 0.61_{a_2} \pm 0.82_{a_4}) \cdot 10^{-12}$	
$Z^0 \to \rho^0\gamma$	$(4.19^{+0.04}_{-0.06\,\mu} \pm 0.16_f \pm 0.24_{a_2} \pm 0.37_{a_4}) \cdot 10^{-9}$	
$Z^0 \to \omega\gamma$	$(2.89^{+0.03}_{-0.05\,\mu} \pm 0.15_f \pm 0.29_{a_2} \pm 0.25_{a_4}) \cdot 10^{-8}$	ATLAS analysis:
$Z^0 \to \phi\gamma$	$(8.63^{+0.08}_{-0.13\,\mu} \pm 0.41_f \pm 0.55_{a_2} \pm 0.74_{a_4}) \cdot 10^{-9}$	arXiv:1501.03276
$Z^0 \to J/\psi\,\gamma$	$(8.02^{+0.14}_{-0.15\,\mu} \pm 0.20_{f\,-0.36\,\sigma}^{+0.39}) \cdot 10^{-8}$	$< 2.6 \cdot 10^{-6}$
$Z^0 \to \Upsilon(1S)\,\gamma$	$(5.39^{+0.10}_{-0.10\,\mu} \pm 0.08_{f\,-0.08\,\sigma}^{+0.11}) \cdot 10^{-8}$	$< 3.4 \cdot 10^{-6}$
$Z^0 \to \Upsilon(4S)\,\gamma$	$(1.22^{+0.02}_{-0.02\,\mu} \pm 0.13_{f\,-0.02\,\sigma}^{+0.02}) \cdot 10^{-8}$	
$Z^0 \to \Upsilon(nS)\,\gamma$	$(9.96^{+0.18}_{-0.19\,\mu} \pm 0.09_{f\,-0.15\,\sigma}^{+0.20}) \cdot 10^{-8}$	

Furthermore, Neubert discussed how searches for $h \to J/\psi\,\gamma$ and $h \to \Phi\gamma$ could somehow constrain the small Higgs couplings to the charm quark and maybe the even smaller coupling to the strange quark.

4 Bottom quark

4.1 The $B \to K^*\mu^+\mu^-$ anomaly

This is the topic that attracted most attention, given that the LHC-B collaboration[1] presented, for the first time, the full LHC run I data about angular distributions in $B \to K^*\mu^+\mu^-$ decays. The anomaly found in the previous partial data release persists: the central values got closer to present SM predictions, with smaller experimental uncertainties.

In order to understand what goes on, one needs to perform a global analyses of this data together with data about related $B \to K\ell^+\ell^-$ and other total decay rates. Luckily, J. Matias[1,8] and D. Straub[1,9] obtained the LHC-B data, disappeared from coffee breaks and ski slopes, and, on the final day of the conference, reappeared to present the results of their analyses, that favour new physics beyond the Standard Model at $\approx 4\sigma$ confidence level. This caused more panic than the solar eclipse that took place during their talks.

Their two independent analyses agree on this result, and on the claim that the needed new physics can be the following effective operator

$$\frac{(\bar{b}\gamma_\mu s)_L(\bar{\mu}\gamma_\mu\mu)_{L \text{ or } V}}{(20 - 30\,\text{TeV})^2}. \tag{8}$$

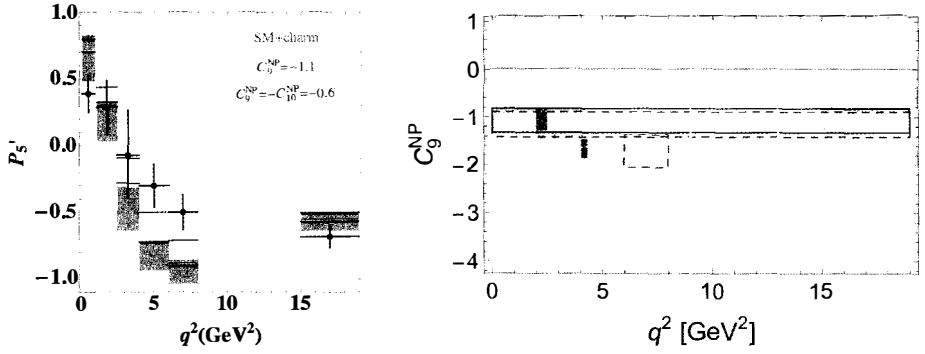

Figure 6 – Left: data from the LHC-B collaboration about some angular distribution parameter in $B \to K^*\mu^+\mu^-$ compared to SM predictions, and to fits with new physics beyond the SM (thanks to J. Matias). Right: q^2-dependence of the anomaly in $B \to K^*\mu^+\mu^-$ decays (thanks to D. Straub).

Fig. 6a shows the LHC-B data, the SM prediction, and how this operator can improve the agreement with data. According to the analysis by Matias, reasonable fits are obtained also if the quark current is right-handed. A. Crivellin[1,10] discussed how this kind of operator can be mediated at tree level by lepto-quarks or by a Z' vector coupled to $L_\mu - L_\tau$.

The big question is if QCD uncertainties, possibly related to some unknown non-perturbative non-factorizable charm quark loop effect, have been under-estimated and could bring the SM prediction in agreement with data. The charm loop would give a left-handed quark current (due to the coupling to the W) and a vectorial lepton current (due to the coupling to the photon). This kind of structure is compatible with data, see eq. (8). Furthermore, fig. 6b shows how the anomaly depends on the transferred momentum q^2: the effective operator of eq. (8) would give a constant; while the charm could give some unknown q^2-dependent effect. Both possibilities are compatible with data. Finally, the charm loop would give an effect equal in $\mu^+\mu^-$ and in e^+e^-, while new physics could violate lepton universality e.g. in

$$R_K = \frac{\mathrm{BR}\,(B^+ \to K^+\mu^+\mu^-)}{\mathrm{BR}\,(B^+ \to K^+e^+e^-)} = 0.745 \pm 0.09_{\mathrm{stat}} \pm 0.036_{\mathrm{syst}}. \tag{9}$$

New physics could even violate lepton flavour giving $B \to K^{(*)}\mu e$ decays. So far data about rates favour an effect present only in muons; but from an experimental point of view measuring electrons is more difficult.

In conclusion, it seems that future data can clarify the situation.

4.2 More flavour

M. della Morte[1] reviewed lattice predictions for flavour physics. R. Knegjens[1] reviewed the SM predictions for $K^+ \to \pi^+\nu\bar{\nu}$ and $K_L \to \pi\nu\bar{\nu}$, and how these decays (with experimental results coming soon) are golden channels for probing new physics. W. Dekens reviewed left-right symmetric extensions of the Standard Model and their signals in B and K mixing.

5 The top quark

A precise measurement of the top quark mass (or better, of the top quark Yukawa coupling y_t, which is the fundamental parameter, well defined at loop level even including weak corrections)

is important because y_t is the biggest coupling of the Higgs, relevant for naturalness; for stability bounds on the SM Higgs potential; for MSSM predictions of the Higgs mass...

Concerning this latter issue, the use of effective field theory techniques, that apply if the SUSY scales is above about 1 TeV, allowed to decrease the theoretical uncertainty on M_h from $\pm 3\,\text{GeV}$ down to about $\pm 1\,\text{GeV}$. The predicted M_h is a few GeV below the output of codes based on the diagrammatical approach: consequently the SUSY scale needed to reproduce the observed M_h becomes heavier and is in the multi-TeV region, as shown in fig. 7.[11] The dominant uncertainty on the M_h prediction is now the uncertainty on M_t.

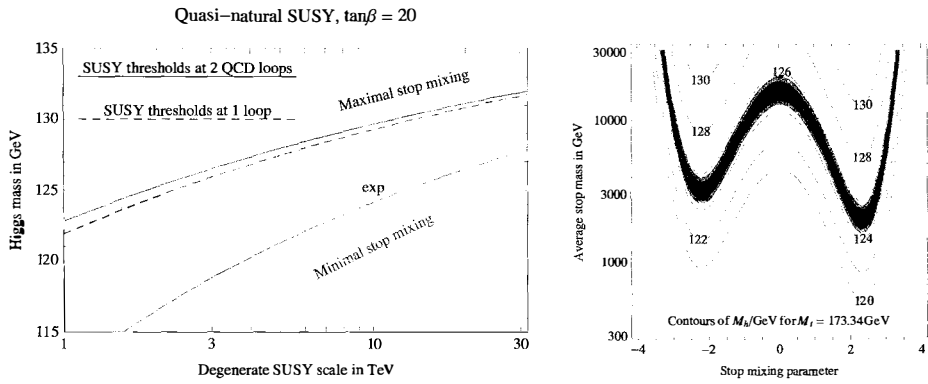

Figure 7 – Precise MSSM prediction for the Higgs mass in the limit of degenerate sparticles.

R. Kogler[1] presented the indirect determination of M_t from precision data:

$$M_t = 177 \pm 0.5_{\text{th}} \pm 2.4_{\text{exp}} \qquad \text{with uncertainty dominated by } M_W, \sin^2\theta. \tag{10}$$

Similarly, a global fit of flavour data gives[a]

$$M_t = 171.5 \pm 7\,\text{GeV}. \tag{11}$$

All these measurements agree with the more precise direct measurement of the top pole mass performed at TeVatron and LHC:

$$M_t = 173.34 \pm 0.76\,\text{GeV}. \tag{12}$$

However, the top pole mass is only defined up to a non-perturbative QCD uncertainty of about $\pm\Lambda_{\text{QCD}} \approx 0.3\,\text{GeV}$. Furthermore, this measurement of the peak in the invariant mass of final state particles produced by top decays needs a significant amount of reverse engineering: one sums over visible products, but MonteCarlo simulations are needed to rescale the result, adding invisible neutrinos and removing initial state radiation. Basically, this means employing a formula of the type: $M_{\text{pig}} = K_{\text{MC}} \sum M_{\text{sausages}}$. Data are now rich enough that the kinematical features predicted by MonteCarlo simulations can be validated by observations.

But still it's better if sausage-making is discussed among experts behind closed doors. Two workshops discussed how to reduce the estimated theorethical uncertainty of about $\pm 0.3\,\text{GeV}$. The result was an increase in the estimated theoretical uncertainty up to $\pm 1\,\text{GeV}$. S. Weinzierl[1] reported that QCD experts now know what to do to improve the situation with short-distance definitions of M_t (somewhat analogously to what done in the past decade for defining jets).

[a] Thanks to Pierini, Silvestrini, Paradisi.

6 The quest for physics Beyond the Standard Model

The question asked by Dirac — why $F_{\text{gravity}} \sim 10^{-40} F_{\text{electric}}$? — becomes in the Standard Model a deeper naturalness question about its only dimensionful parameter: why $M_h^2 \sim 10^{-35} M_{\text{Pl}}^2$? According to standard lore "the Higgs mass receives power divergent quantum corrections

$$\delta M_h^2 \sim g_{\text{SM}}^2 \Lambda_{\text{UV}}^2 \lesssim M_h. \tag{13}$$

New-physics must realise the cut-off Λ_{UV} at the weak-scale such that M_h is naturally smaller than the Planck scale".

G. Altarelli[1] recalled early Moriond conferences: we heard that supersymmetry as a solution to the naturalness problem started to be a major topic since 1982. A review by H.P. Nilles already appeared in 1984, telling that *"experiments within the next 5-10 years will enable us to decide whether supersymmetry, as a solution to the naturalness problem of the weak interaction is a myth or reality"*[12].

5-10 years later LEP measured the SM gauge couplings, finding values in agreement with SU(5) unification in presence of supersymmetry at the weak scale.

25 years later the theoretical community worried about the LHC Inverse Problem: naturalness of the Higgs mass needs so much new sparticles at the electroweak scale that we will be inundated by new physics and data might not be enough to unambiguously understand what it is. LHC started, and the problem got solved: the new sparticles predicted by supersymmetry missed to show up at their appointment with history.

Even if they will come later, they might be too heavy for satisfying the naturalness requirement of eq. (13).

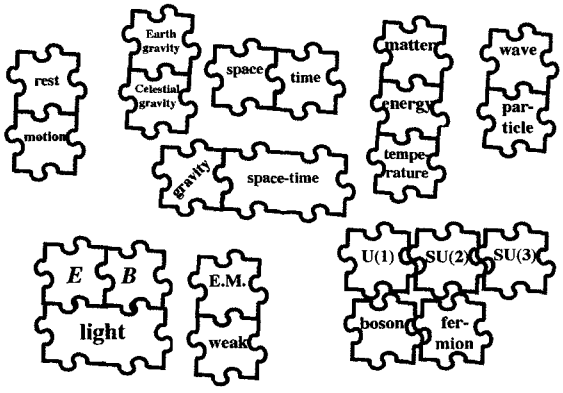

Figure 8 – Super-symmetry would continue the path towards unification in physics.

6.1 Is nature natural?

Super-symmetry is by far the best proposed natural theory, as it would continue the path towards unification in physics (see fig. 8): supersymmetry allows for SU(5), SO(10), E_6 unification of gauge couplings; supersymmetry unifies bosons with fermions; local supersymmetry is the gauge symmetry needed for a consistent theory of spin 3/2 particles, supersymmetry avoids tachyon instabilities of strings...

These unification ideas can be tested experimentally: gauge unification implies proton decay, and weak-scale supersymmetry gives observable signals at colliders.

That have not been observed.

The probability that a numerical accident made sparticles too heavy is roughly given by the inverse of the fine-tuning. Generic models where the Higgs mass is comparable to other soft-breaking SUSY parameters (such as the Constrained MSSM) started to be fine-tuned after LEP. Before LHC, this issue was seen as a motivation to search for special natural models where the Higgs mass is a loop factor lighter than other sparticles. After LHC run I even these special models start to be fine-tuned. Furthermore, within the MSSM, the measurement of the Higgs mass $M_h \approx 125\,\text{GeV}$ points to even heavier sparticles. Theorists specialised in naturalness model-building propose ways to reduce the fine-tuned *S*trangeness but at the price of delivering ultra-special models with increased *B*aroqueness, without reducing the *BS* product.[b]

From a theoretical point of view, it is difficult to believe that supersymmetry could be the wrong path: one it tempted to hammer together the pieces of the puzzle, beliving that supersymmetry will be discovered and that the quotation by Nilles can be fixed by just removing the dash between 5 and 10. A. Soni[1] emphasised that we must be sure before abandoning naturalness: exploring the 10-100 TeV range with flavour and collider experiments would allow to reach fine-tunings up to about 10^{4-5}. But colliders can no longer be bureaucratically justified by the warranty that some missing piece of the Standard Model will be discovered. While the unnaturalness of the Higgs would be more interesting than the Higgs itself, in the minds of funding agencies the exchange rate between Fine Tuning and Swiss Franc could not be good enough.

*6.2 Ant**pic selection in a multiverse*

In the past, similar naturalness arguments correctly anticipated new physics that keeps the electron mass naturally small (the positron), that keeps the mass difference between charged and neutral pions naturally small (QCD compositeness), that keeps flavor-violating effects naturally small (the charm). In condensed matter systems, the mass of higgs-like scalars that describe collective excitations is naturally close to their ultimate cut-off (the Lorentz-breaking atomic lattice).

So, it is surprising that in particle physics naturalness might not apply to the dimensionful parameters that today seem fundamental: the Higgs mass, the Planck mass, the cosmological constant.

The observed cosmological constant, $V_{\text{min}} \approx 10^{-123} M_{\text{Pl}}^4$, poses another naturalness hierarchy problem that neither supersymmetry nor any other known theory can explain. Then, anthropic selection in a multiverse of $> 10^{120}$ vacua are invoked to justify the unnaturalness: one of these vacua could accidentally have acosmological constant small enough that galaxies can there form. Then, observers can form and understand why the cosmological constant is so small that it starts to dominate just now.

The Higgs mass naturalness problem could also have an anthropic interpretation. In the SM the hundreds of nuclei needed to develop a complex chemistry come out from a numerical accident: the charged proton is the lightest baryon (despite not being the most neutral baryon nor the baryon made of lighter quarks) because these two competing effects are comparable:

$$(y_d - y_u)v \approx \alpha_{\text{em}} \Lambda_{\text{QCD}}. \tag{14}$$

From a fundamental point of view, the two contributions to the mass splitting could have differed by orders of magnitude. If v gets increased or reduced by more than about one order of magnitude, the proton ceases to be the lightest baryon and complex chemistry disappears. Then, many authors think that $M_h \ll M_{\text{Pl}}$ is just another anthropic fine tuning.

[b] The *BS* plane was first introduced by A. Falkowski.

Nobody talked about antrhopics at Moriond 2015. This has an anthropic interpretation: Moriond is not in California. Clearly, social factors are playing a role, as always when experiments cannot set the issue. On one side, 'having discovered the multiverse' is physically indistinguishable from 'having pursued a failed unification program', but sounds much better. On the other side, future physicists could consider us as crazy for not having immediately accepted anthropic arguments.

In my opinion, *anthropic selection in a multiverse does not explain an unnaturally small Higgs mass.* The reason is that, even accepting that we live in some random vacuum in a multiverse, there is no need for a fine-tuning as unlikely as $v^2/M_{\rm Pl}^2$. The most likely outcome should have been:

- one of the existing natural theories, like weak-scale supersymmetry;
- or an anthropically acceptable alternative to the SM that does not involve an unnaturally light Higgs scalar;
- or, even within the Standard Model, more natural values of its parameters: smaller $M_{\rm Pl}$ and bigger v (compensated in eq. (14) by reduced Yukawa couplings $y_{u,d}$).

6.3 Subtle is the Lord...

Today we are confused about naturalness: theory and experiment are pointing in apparently contradictory directions. But nature is surely following some logic. Suppose you get lost while traveling and encounter this apparently contradictory signpost:

What does it mean? Unfortunately it's not clear. Fortunately there are theorists who start to think. The smartest theorist immediately proposes a beautiful natural interpretation: there is some fundamental symmetry such that

$$\text{Napoli} = \text{Salerno}. \tag{15}$$

However, after a bit of traveling, one starts to worry that this identification might not be supported by geographical data.

Then, another theorist proposes an alternative anthropic interpretation:

it's just mafia selling signposts.

Plausible, but how can it be confirmed? After a debate about Popperian falsifiability and circular reasoning, a prediction emerges: if there is mafia, then, probably, we are in Italy. Correct, but probably you already knew it.

To understand the real meaning one needs to think different — in this case like the bureaucrats who place signposts. Then, one can deduce where the photo was taken. This is left as an exercise.

6.4 *Data speaks and is telling SM, SM, SM*

Summarizing: the smallness of the Higgs mass seems unnatural (section 6.1), it does not seem antrhopic (section 6.2), so we should search for its hidden logic (section 6.3).

After the measurement of the Higgs mass we finally have all the SM parameters. We can now try to assume that the SM is valid up to unnaturally large energies and see where this leads us to:

Fact 1: the SM can be extrapolated at least up to $M_{\rm Pl}$;

Fact 2: in the SM, $M_h \approx 130\,\text{GeV}$ corresponds to $\lambda(M_{\rm Pl}) \approx 0$;

Fact 3: in the SM, $\beta(\lambda) = d\lambda/d\ln E$ vanishes around $M_{\rm Pl}$.

For sure, these could be just accidents with no meaning; new physics can change these properties, by a bit or by a lot. The goal of this discussion is not proofing anything, but searching for possible messages in the data that we have now. If this is the message from nature, it is incompatible with our ideas of naturalness.

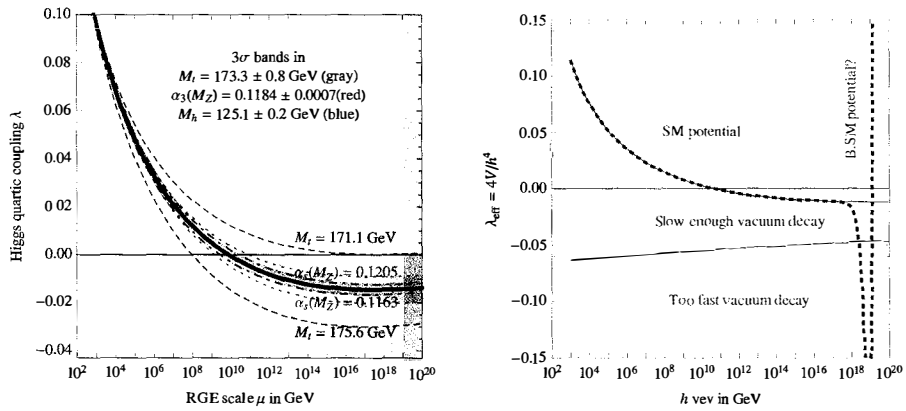

Figure 9 – Running of the Higgs quartic in the SM (left) and in the BranchinaSM (right).

Looking more precisely at the SM, one notices that if $M_t \gtrsim 171\,\text{GeV}$ and if the SM holds up to large energy, the Higgs potential $V_{\rm SM} = \lambda_{\rm eff}(h)h^4/4$ is unstable, falling down at field values $h > h_{\rm max}$. For present central values of the SM parameters, the critical higgs field value is $h_{\rm max} \sim 10^{11}\,\text{GeV}$, but uncertainties on M_t can largely change it, see fig. 9a. This instability behind by a potential barrier leads to vacuum decay, with a rate proportional to $\exp(-8\pi^2/3|\lambda_{\rm eff}|)$, which is too fast if $\lambda_{\rm eff} < -0.05$. The vacuum decay rate is safely small because $\lambda_{\rm eff}$ gets negative but remains small.

V. Branchina[1] showed that the vacuum decay rate can be much faster (possibly as fast as the rate at which he emphasises such statement) in BSM models where $V_{\rm SM}$ is stabilised at $h \lesssim M_{\rm Pl}$ in this peculiar way:

$$V_{\rm BSM} = V_{\rm SM} - \frac{h^6}{M_{\rm Pl}^6} + \frac{h^8}{M_{\rm Pl}^8} + \cdots$$

plotted in fig. 9b. In my opinion, searching for possible implications of data, it is better to focus on subtle possibilities, rather than on malicious ones.

The instability of the SM potential raises cosmological issues: can cosmological evolution end up in the electroweak vacuum, despite that it is much smaller in field space than the Planck-scale vacuum? The answer is: yes, if the top mass lies in the special range $171\,\text{GeV} \lesssim M_t \lesssim 175\,\text{GeV}$. Indeed, during inflation with Hubble constant $H = 2.5\ 10^{14}\,\text{GeV}\sqrt{r}$ (where $r \lesssim 0.1$ as found by the Planck collaboration[1]) the Higgs h can fluctuate acquiring a large random vev, $h \sim H$. Provided that $\langle h^2 \rangle$ is not too large, during the thermal phase after inflation the Higgs acquires a thermal mass $\approx T$, such that its vacuum expectation value returns to zero, finally landing in the SM minimum. $M_t \lesssim 175\,\text{GeV}$ is needed to guarantee the happy end: otherwise thermal tunneling can be too fast.

A. Kusenko[1] showed how this out-of-equilibrium phase could provide baryogengesis (altought extra ad-hoc model building is needed to avoid iso-curvature perturbations, which are disfavoured by cosmological observations).

6.5 Crazy alternative ideas about naturalness

Usual naturalness, as formulated in eq. (13), attributes physical meaning to regulators and to power divergences. However these are unphysical computational tools. Maybe we are over-interpreting quantum field theory, analogously to what happened a century ago, when theorists over-interpreted Maxwell wave equations as implying the existence of a medium where light propagates. Experimentalists failed to find such æther, opening the road to crazy alternative ideas.

Maybe naturalness only demands that physical (potentially observable) quantum corrections to the Higgs mass are naturally small. Then the SM alone would be natural, for its observed values of the parameters. New physics can also be natural provided that

$$\delta M_h \sim g_{\text{BSM}} M_{\text{BSM}} \lesssim M_h. \tag{16}$$

This naturalness condition differs from the usual one, eq. (13), because g_{SM} (the SM couplings of the Higgs boson, such as the top Yukawa coupling) is replaced by couplings g_{BSM} to new heavy particles, and the cut-off Λ_{UV} by M_{BSM}, the mass of extra particles. For example, SU(5) gauge unification needs heavy vectors, not compatible with eq. (16).

My collaborator A. Salvio[1] argued that power divergences must vanish if nature is described, at fundamental level, by a theory with no dimensionful parameters. Quantum corrections break classical scale invariance giving a renormalization group running for the dimensionless couplings, allowing to dynamically generate mass scales. He showed how the dimensionless extension of Einstein gravity, agravity, is renormalizable and allows to dynamically generate the Planck mass, provided that a scalar quartic runs in such a way that it and its β functions simultaneously vanish around the Planck scale. This is similar to how the SM Higgs quartic runs if $M_t \approx 171.1\,\text{GeV}$, see fig. 9a. In agravity the usual gravitational coupling $g_{\text{gravity}} \sim E^2/M_{\text{Pl}}$ gets substituted at large energy $E \gtrsim M$ by dimensionless couplings: naturalness, as redefined by eq. (16), is satisfied provided that M is low enough $M \lesssim \sqrt{M_{\text{Pl}} M_h} \sim 10^{12}\,\text{GeV}$. The new physics with mass M involves a ghost-like particle, that might or might not receive a sensible quantum interpretation. Salvio also discussed inflationary predictions ($n_s \approx 0.96$ and $0.003 < r < 0.13$) and attempts of finding natural extensions of the SM that can hold up to infinite energy, avoiding any Landau pole.

Furthermore, a recent paper claims to have, for the first time, a conventionally natural model that does not need new physics at the weak scale, thanks to a cosmological evolution that selects a small Higgs mass[13].

7 Conclusions

Not today. LHC run II is starting now, and results presented at Moriond 2016 could bring us much closer to the conclusion.

Acknowledgments

I thank the organisers for creating a unique environment for interchange of ideas, and all participants for a multitude of new insights.

References

1. Proceedings of Moriond 2015.
2. Y. Y. Zheng and B. Q. Ma, Eur. Phys. J. Plus 127, 7 (2012) [arXiv:1106.4040].
3. J. Barea, J. Kotila and F. Iachello, Phys. Rev. C91, 034304 (2015).
4. B. Zaldivar, arXiv:1505.04579.
5. A. Ahrice et al., arXiv:1505.04320.
6. I. Brivio, arXiv:1505.04541.
7. A. Kaminska, arXiv:1505.04645.
8. S. Descotes-Genon, L. Hofer, J. Matias and J. Virto, arXiv:1503.03328.
9. W. Altmannshofer and D. M. Straub, arXiv:1503.06199.
10. A. Crivellin, G. D'Ambrosio, J. Heeck, arXiv:1505.02026.
11. E. Bagnaschi, G. F. Giudice, P. Slavich and A. Strumia, JHEP 1409, 092 (2014) [arXiv:1407.4081]. J. Pardo Vega, G. Villadoro, arXiv:1504.05200.
12. H. P. Nilles, Phys. Rept. 110, 1 (1984).
13. P. W. Graham, D. E. Kaplan and S. Rajendran, arXiv:1504.07551.
14. A. Celis, arXiv:1505.00537.

Authors index

Ahriche, A.	Three-Loop Neutrino Mass Models at Colliders	285
Altmannsfofer, W.	Implications of $b \to s$ measurements	333
Andrews, J.	Study of the decay $B^+ \to K^+\pi^0$ at LHCb	531
Arcadi, G.	3.55 KeV line in minimal decaying Dark Matter	457
Azzi, P.	An historical recount of the events leading to the discovery of the top quark in 1995 by the CDF and D0 experiments at the Tevatron	121
Bainbridge, R.	Searching for supersymmetry in compressed scenarios with the CMS experiment	185
Bauce, M.	Recent Electroweak Results from the Tevatron	95
Bendavid, J.	Scalar Boson: CMS Run 1 final results, prospectives for Run 2 (and HL-LHC)	33
Bizouard, V.	Renormalisation of the NMSSM in SloopS	507
Boonekamp, M.	Prospects for the measurement of m_W at the LHC,	101
Branchina, V.	Vacuum stability depends on high energy physics scales	75
Brivio, I.	Signatures of dynamical scalars	487
Bruno, G.	Recent results from the XENON100 experiment	425
Caccianiga, B.	Recent results from Borexino	267
Carr, R.	Entering the Two-Detector Phase of the Double Chooz Experiment	235
Celis, A.	On the search for a second scalar doublet at the LHC	59
Choubey, S.	Prospects to determine the neutrino mass hierarchy	255
Cornelis, T.	Electroweak production and hadronic activity in Zjj events at CMS	491
Crivellin, A.	Explaining the LHC flavour anomalies	353
De Romeri, V.	Indirect searches for sterile neutrinos at a high-luminosity Z-factory	419
Dekens, W.	Testing left-right symmetric modelsl	515
Delitzsch, C. M.	Boosted W-Boson Identification at $\sqrt{s} = 8$ TeV with the ATLAS Detector	543
Della Morte, M.	Lattice inputs to flavor physics	345
Descotes-Genon, S.	$B \to K^\star\mu\mu$: theory interpretation or *A hitchiker's guide to* $B \to K^\star\mu\mu$ *optimised observables*	325
Doglioni, C.	Dark matter searches at ATLAS, Run1 results and Run2 potential	437
Espriu, D.	Resonances and unitarity in composite Higgs models	199
Eurin, G.	NEMO-3 analysis of the double-β decay of ^{96}Zr	527
Franco, D.	First results from darkside-50	451
Gersabeck, E.	Charm mixing and CP violation at LHCb	381
Godunov, S.	$2h$ production with isotriplet scalars	205
Haesler, A.	NA61/SHINE Data for Long Baseline Neutrino Experiments	279
Haisch, U.	Dark matter at the LHC	431
Hayes, A.	Uncertainties in Reactor Neutrino Fluxes and in the Anomaly	241
Hayward, H.	Searches for long lived supersymmetric particles with the ATLAS detector	193
Heeck, J.	Lepton Number Violation with *and without* Majorana Neutrinos	309
Heller, A.	Search for $B^+ \to \ell^+\nu_\ell\gamma$ decays with hadronic tagging using the full Belle data sample	539
Henrot-Versillé, S.	Planck 2015 results	469
Hernández, P.	Cosmological Constraints on the Seesaw Scale	291
Hofer, L.	$B \to K^\star\mu\mu$: theory interpretation or *A hitchiker's guide to* $B \to K^\star\mu\mu$ *optimised observables*	325
Hu, B.	Recent Results from Daya Bay Reactor Neutrino Experiment	229
Illana, J.	Interpretation of the high energy IceCube data	413
Johnson, T.	Searches for Exotic Processes in Double Beta Decay with EXO-200	297
Jung, A.	Top Quark Physics at the Tevatron	127
Kaminska, A.	Improving LHC searches for strong EW symmetry breaking resonances	113
Kanshin, K.	One-loop effective non-linear Lagrangian with a light H-boson	483
Kaur, D.	Octant of θ_{23} and precision measurement of atmospheric neutrino oscillations at INO-ICAL detector	519
Kekic, M.	Cosmological Constraints on the Seesaw Scale	291
Knegjens, R.	$K \to \pi\nu\bar{\nu}$ in the Standard Model and Beyond	387
Kolešová, H.	Higher order proton lifetime estimates in Grand Unified Theories	511
Kumar, S.	Octant of θ_{23} and precision measurement of atmospheric neutrino oscillations at INO-ICAL detector	519
Kusenko, A.	Higgs relaxation and the matter-antimatter asymmetry of the universe	71
Langenbruch, C.	Latest results on rare decays from LHCb	317
Lavalle, J.	On the use of the escape speed estimates in setting dark matter direct detection limits	555

Leney, K.	ATLAS & CMS Exotics Searches: Run 1 Results and Run 2 Prospects
Li, X.	Measurement of the distribution of ϕ^*_η in events containing dimuon pairs with masses between 30 and 500 GeV in 10.4 fb^{-1} of $p\bar{p}$ collisions
Lisi, E.	Status of three-neutrino mixing
Loginov, A.	ATLAS + CMS top production and properties: Run 1 legacy
López Pavón, J.	Cosmological Constraints on the Seesaw Scale
Magni, S.	On the use of the escape speed estimates in setting dark matter direct detection limits
Main de Boissière, T.	Low mass wimp search with EDELWEISS-III: first results
Masip, M.	Interpretation of the high energy IceCube data
Matias, J.	$B \dashrightarrow K^\star\mu\mu$: theory interpretation or *A hitchiker's guide to* $B \to K^\star\mu\mu$ *optimised observables*
McDonald, K.	Three-Loop Neutrino Mass Models at Colliders
Meloni, D.	Interpretation of the high energy IceCube data
Mona, O.	The Flavour Composition of the High-Energy IceCube Neutrinos
Meridiani, P.	Beyond the Standard Model Higgs searches at the LHC
Mine, S.	Recent results from Super-Kamiokande
Myslik, J.	Selected results from T2K
Naimuddin, M.	Octant of θ_{23} and precision measurement of atmospheric neutrino oscillations at INO-ICAL detector
Nasri, S.	Three-Loop Neutrino Mass Models at Colliders
Navarro de Martino, E.	Search for a SM-like Higgs boson in the H-->ZZ--> $\ell\ell q\bar{q}$ decay channel in CMS
Palomares Ruiz, S.	The Flavour Composition of the High-Energy IceCube Neutrinos
Paredes Hernández, D.	Search for new light gauge bosons in Higgs decays to four-lepton events in pp collisions at $\sqrt{s} = 8$ TeV with the ATLAS detector
Patrick, C.	Recent results from MINERνA
Pelliccioni, M.	CMS High mass WW and ZZ Higgs search with the complete LHC Run1 statistics
Perrozzi, L.	Electroweak multi-boson measurements from ATLAS and CMS: Run 1 legacy and Run 2 prospects
Pescatore, L.	An analysis of $\Lambda_b^0 \to \Lambda\mu^+\mu^-$ decays at the LHCb experiment
Pinna, D.	Dark Matter produced in association with top quark pair
Polesello, G.	SUSY: Blind spots at Run 1, perspectives at Run 2 and beyond
Raina, P.	Neutrinoless double beta decay and nuclear matrix elements
Rameez, M.	WIMP Annihilations in the Sun : A search based on the first year of data from the completed IceCube neutrino telescope.
Riva, F.	BSM Primaries: the Physics of the SM Effective Field Theory
Ronchese, P.	Rare Decays and other Electroweak b-physics - Measurements at ATLAS and CMS
Salvio, A.	On the Origin of Scales and Inflation
Saviano, N.	Light sterile neutrino limits from cosmology
Schieck, J.	Direct Dark Matter Search with the CRESST-II Experiment
Soldi, D.	Results from the NA62 2014 Commissioning Run
Sonneveld, J.	Limits and Fits from Simplified Models
Straub, D.	Implications of $b \to s$ measurements
Strumia , A.	Theory summary
Stupak, J.	ATLAS+CMS: Boosted topologies (Run1 results, Run2 potential)
Styles, N.	Collecting and analysing data at high pile-up with ATLAS and CMS
Sutcliffe, W.	Determination of the quark coupling strength $\|\mathbf{V_{ub}}\|$ using baryonic decays
Treille, D.	50 Years of Moriond
Vallier, A.	Constraining CKM gamma angle at LHCb
Vellidis, C.	Studies of the Higgs Boson and direct searches for new phenomena at the TeVatron
Vincent, A.	The Flavour Composition of the High-Energy IceCube Neutrinos
Virto, J.	$B \to K^\star\mu\mu$: theory interpretation or *A hitchiker's guide to* $B \dashrightarrow K^\star\mu\mu$ *optimised observables*
Voutilainen, M.	ATLAS+CMS top mass: current results and future measurements
Weinzierl, S.	Precision on the top mass
Wyatt , T.	Experimental Summary
Yáñez, J.P.	Neutrinos from heaven and hell in IceCube : latest results on astrophysical neutrinos and neutrino oscillations
Zaldívar , B.	A bonus complementarity in Simplified Models of Dark Matter
Zsoldos, S.	Search for a sterile neutrino with the STEREO detector at ILL

List of Participants

Family name	First name	Institution logo	Country	Email address
Ahriche	Amine	University of Jijel	Algeria	aahriche@gmail.com
Allanach	Benjamin	University of Cambridge	UK	B.C.Allanach@damtp.cam.ac.uk
Altarelli	Guido	Università Roma III	Italy	guido.altarelli@cern.ch
Andrews	Jason	University of Maryland	USA	jea@umd.edu
Arcadi	Giorgio	LPT	France	arcadi.giorgio@gmail.com
Azzi	Patrizia	INFN - CERN	Italy	patrizia.azzi@cern.ch
Bachtis	Michail	CERN	Switzerland	bachtis@cern.ch
Bainbridge	Robert	Imperial College	UK	robert.bainbridge@cern.ch
Bassler	Ursula	IN2P3	France	ursula.bassler@admin.in2p3.fr
Bauce	Matteo	Università La Sapienza	Italy	matteo.bauce@roma1.infn.it
Ben-Haim	Eli	LPNHE	France	benhaim@in2p3.fr
Bendavid	Josh	CERN	Switzerland	Josh.Bendavid@cern.ch
Bernardi	Gregorio	LPNHE	France	gregorio@fnal.gov
Billard	Julien	IPN Lyon	France	j.billard@ipnl.in2p3.fr
Bizouard	Vincent	LAPTh	France	vincent.bizouard@lapth.cnrs.fr
Boonekamp	Maarten	CEA Saclaym - IRFU/SPP	France	maarten.boonekamp@cern.ch
Bozek	Krzysztof	King's College	UK	krzysztof.bozek@kcl.ac.uk
Branchina	Vincenzo	Università di Catania	Italy	branchina@ct.infn.it
Brivio	Ilaria	UAM	Spain	ilaria.brivio@uam.es
Bruno	Gianmarco	Universität Münster	Germany	bruno@lngs.infn.it
Caccianiga	Barbara	INFN	Italy	barbara.caccianiga@mi.infn.it
Carr	Rachel	Nevis Labs - Columbia University	USA	rec2126@columbia.edu
Celis	Alejandro	Ludwig Maximilian Universität	Germany	alejandro.celis@ific.uv.es
Choubey	Sandhya	Harish-Chandra research Institute	India	sandhya@hri.res.in
Clerbaux	Barbara	ULB	Belgium	bclerbau@ulb.ac.be
Cornelis	Tom	University of Antwerp	Belgium	tom.cornelis@uantwerpen.be
Crivellin	Andreas	CERN	Switzerland	andreas.crivellin@cern.ch
David	André	CERN	Switzerland	andre.david@cern.ch
De Cecco	Sandro	LPNHE	France	sandro.dececco@lpnhe.in2p3.fr
De Romeri	Valentina	LPC Clermont	France	deromeri@clermont.in2p3.fr
Dekens	Wouter	Van Swinderen Institute	The Netherlands	w.g.dekens@rug.nl
Delgove	David	LAL	France	delgove@lal.in2p3.fr
Delitzsch	Chris Malena	Université de Genève	Switzerland	chris.malena.delitzsch@cern.ch
Della Morte	Michele	CP3-Origins	Denmark	dellamor@cp3-origins.net
Doglioni	Caterina	Université de Genève	Switzerland	caterina.doglioni@cern.ch
Duehrssen	Michael	CERN	Switzerland	michael.duehrssen@cern.ch
Espriu	Domenec	Universitat de Barcelona - ICCUB	Spain	espriu@icc.ub.edu
Eurin	Guillaume	LAL	France	eurin@lal.in2p3.fr
Fayard	Louis	LAL	France	lfayard@in2p3.fr
Fong	Chee Sheng	Universidade de São Paulo	Brazil	fong@if.usp.br
Franco	Davide	APC	France	dfranco@in2p3.fr
Frère	Jean-Marie	ULB - Physique Théorique	Belgium	frere@ulb.ac.be
Gando	Azusa	Tohoku University - RCNS	Japan	azusa@awa.tohoku.ac.jp
Gersabeck	Evelina	Physikalisches Institüt	Germany	evelina.gersabeck@cern.ch
Godunov	Sergey	ITEP	Russia	sgodunov@itep.ru
Golutvin	Andrey	Imperial College	UK	andrey.goloutvin@cern.ch
Grivaz	Jean-François	LAL	France	grivaz@lal.in2p3.fr
Haesler	Alexis	Université de Genève	Switzerland	alexis.haesler@unige.ch
Haisch	Uli	Oxford University	UK	u.haisch1@physics.ox.ac.uk
Hayes-Sterbenz	Anna	Los Alamos National Lab.	USA	anna_hayes@lanl.gov
Hayward	Helen	University of Liverpool	UK	helen.hayward@cern.ch
Heeck	Julian	ULB	Belgium	julian.heeck@ulb.ac.be
Heller	Andreas	KIT	Germany	andreas.heller@kit.edu

Henrot-Versillé	Sophie	LAL	France	versille@lal.in2p3.fr
Hoecker	Andreas	CERN	Switzerland	andreas.hoecker@cern.ch
Hu	Bei-Zhen	National Taiwan University	Taiwan	ptbei1985@gmail.com
Iconomidou-Fayard	Lydia	LAL	France	lyfayard@in2p3.fr
Janot	Patrick	CERN	Switzerland	Patrick.Janot@cern.ch
Johnson	Tessa	Indiana University	USA	tesjohns@imail.iu.edu
Jung	Andreas	Fermilab	USA	ajung@fnal.gov
Kaminska	Anna	Johannes Gutenberg University	Germany	akaminsk@uni-mainz.de
Kannike	Kristjan	NICPB	Estonia	Kristjan.Kannike@cern.ch
Kanshin	Kirill	INFN	Italy	k.kanshin@gmail.com
Kaur	Daljeet	University of Delhi	India	daljeet.kaur97@gmail.com
Kim	Yeong Gyun	Gwanjiu National Univ. of Education	Korea	ygkim@gnue.ac.kr
Knegjens	Robert	TU München - IAS	Germany	robert.knegjens@tum.de
Kogler	Roman	University of Hamburg	Germany	roman.kogler@uni-hamburg.de
Kolesova	Helena	Czech Technical University	Czech Republic	helena.kolesova@fjfi.cvut.cz
Koppenburg	Patrick	NIKHEF	The Netherlands	patrick.koppenburg@cern.ch
Kotlarski	Wojciech	University of Warsaw	Poland	Wojciech.Kotlarski@fuw.edu.pl
Kozanecki	Witold	CEA Saclay - DSM/IRFU/SPP	France	witold.kozanecki@cern.ch
Kusenko	Alexander	UCLA	USA	kusenko@ucla.edu
Lamont	Mike	CERN	Switzerland	Mike.Lamont@cern.ch
Lamprea	David R.	Institüt für Theoretische Physik	Germany	david.lamprea@uni-muenster.de
Langenbruch	Christoph	Warwick University	UK	christoph.langenbruch@cern.ch
Lazutkina	Anastasya	Moscow State University	Russia	19_Nastenka@mail.ru
Lee	Kang Young	Gyeongsang National University	South Korea	kylee.phys@gnu.ac.kr
Leney	Katharine	University College	UK	katharine.leney@cern.ch
Leonardo	Nuno	LIP	Portugal	nuno.leonardo@cern.ch
Li	Xingguo	University of Manchester	UK	xingguo.li@cern.ch
Lisi	Eligio	INFN	Italy	eligio.lisi@ba.infn.it
Loginov	Andrey	Yale University	USA	andrey.loginov@yale.edu
Lopez Pavon	Jacobo	SISSA	Italy	jlpavon@sissa.it
Loucatos	Sotiris	APC	France	s.loucatos@cea.fr
Magni	Stefano	LUPM	France	stefano.magni@univ-montp2.fr
Main de Boissière	Thibault	CEA Saclay - DSM/IRFU/SPP	France	thibault.main-de-boissiere@cea.f
Majewski	Stephanie	University of Oregon	USA	smajewsk@uoregon.edu
Malgeri	Luca	CERN	Switzerland	Luca.Malgeri@cern.ch
Mansoulié	Bruno	CEA Saclay - IRFU/SPP	France	bruno.mansoulie@cea.fr
Marzocca	David	Universität Zürich	Switzerland	marzocca@physik.uzh.ch
Masip	Manuel	Universidad de Granada	Spain	masip@ugr.es
Matias	Joaquim	Universitat Autonòma de Barcelona	Spain	matias@ifae.es
Meridiani	Paolo	INFN - Università Roma I	Italy	paolo.meridiani@cern.ch
Meyer	Andreas	DESY	Germany	andreas.meyer@cern.ch
Mine	Shunichi	University of California	USA	smine@uci.edu
Montanet	François	LPSC	France	montanet@in2p3.fr
Moulin	Emmanuel	CEA Saclay - IRFU/SPP	France	emmanuel.moulin@cea.fr
Murray	William	University of Warwick	UK	bill.murray@cern.ch
Myslik	Jordan	University of Victoria	Canada	myslik@uvic.ca
Navarro Martino	Eduardo	CIEMAT	Spain	eduardo.navarro@ciemat.es
Neubert	Matthias	Johannes Gutenberg Univ.	Germany	neubertm@uni-mainz.de
Onofre	Antonio	LIP - Universidade do Minho	Portugal	antonio.onofre@cern.ch
Orloff	Jean	LPC Clermont	France	orloff@in2p3.fr
Ortona	Giacomo	Lab. Leprince-Ringuet	France	ortona@llr.in2p3.fr
Paredes	Daniela	Aristotle University	Greece	daniela.paredes.hernandez@cerr
Parolini	Alberto	KAIST	SouthKorea	parolini@kaist.ac.kr
Patrick	Cheryl	Northwestern University	USA	cheryl.e.patrick@gmail.com

Pelliccioni Mario	INFN	Italy	mario.pellic@gmail.com
Pepe Altarelli Monica	CERN	Switzerland	monica.pepe.altarelli@cern.ch
Perrozzi Luca	RETH	Switzerland	perrozzi@cern.ch
Pescatore Luca	University of Birmingham	UK	luca.pescatore@cern.ch
Piacquadio Giacinto	SLAC	USA	giacinto.piacquadio@cern.ch
Pinna Deborah	Universität Zürich	Switzerland	deborah.pinna@cern.ch
Polesello Giacomo	INFN	Italy	giacomo.polesello@cern.ch
Raina Prabhu K.	Indian Institute of Technology	India	pkraina@iitrpr.ac.in
Rameez Mohamed	Université de Genève - DPNC	Switzerland	Mohamed.Rameez@cern.ch
Riva Francesco	EPFL	Switzerland	francesco.riva@cern.ch
Rolandi Gigi	CERN	Switzerland	Gigi.Rolandi@cern.ch
Ronchese Paolo	Dpt. Fisica e Astronomia	Italy	paolo.ronchese@pd.infn.it
Salvio Alberto	UAM - Inst. Física Teórica	Spain	alberto.salvio@uam.es
chez-Hernandez Alberto	CINVESTAV	Mexico	asanchez@fnal.gov
Saviano Ninetta	IPPP	UK	ninetta.saviano@durham.ac.uk
Schieck Jochen	Inst. High Energy Physics	Austria	Jochen.Schieck@oeaw.ac.at
chwanenberger Christian	University of Manchester - Particle Ph.	UK	schwanen@fnal.gov
Sliwa Krzysztof	Tufts University	USA	krzysztof.sliwa@cern.ch
Soldi Dario	INFN	Italy	dario.soldi@to.infn.it
Soni Amarjit	BNL	USA	adlersoni@gmail.com
Sonneveld Jory	RWTH	Germany	sonneveld@physik.rwth-aachen.de
Stoll Yannick	LAPTh	France	stoll@lapth.cnrs.fr
Straub David	TU München	Germany	david.straub@tum.de
Strumia Alessandro	INFN / Università di Pisa - NICPB	Italy	astrumia@cern.ch
Stupak John	Purdue University Calumet	USA	jstupak@fnal.gov
Styles Nicholas	DESY	Germany	nicholas.styles@desy.de
Sutcliffe William	Imperial College	UK	william.lawrence.sutcliffe@cern.ch
Tinyakov Peter	ULB	Belgium	petr.tiniakov@ulb.ac.be
Tisserand Vincent	LAPP - Univ. Savoie-Mont Blanc	France	tisserav@lapp.in2p3.fr
Treille Daniel	CERN	Switzerland	daniel.treille@cern.ch
Tuna Alexander	University of Pennsylvania	USA	tuna@cern.ch
Ulmer Keith	Texas A&M University	USA	ulmer@tamu.edu
Unal Guillaume	CERN	Switzerland	Guillaume.Unal@cern.ch
Vagnoni Vincenzo M.	INFN	Italy	Vincenzo.Vagnoni@bo.infn.it
Vallier Alexis	LAL	France	vallier@lal.in2p3.fr
Vellidis Costas	Fermilab	USA	vellidis@fnal.gov
Vincent Aaron	IPPP - Durham University	UK	aaron.vincent@durham.ac.uk
Voutilainen Mikko	Helsinki Institute of Physics	Finland	mikko.voutilainen@cern.ch
Weinzierl Stefan	Universität Mainz	Germany	stefanw@thep.physik.uni-mainz.de
Wengler Thorsten	CERN - PH Division	Switzerland	Thorsten.Wengler@cern.ch
Wilkinson Guy	CERN & Oxford University	Switzerland	guy.wilkinson@cern.ch
Wishahi Julian	TU Dortmund	Germany	julian.wishahi@tu-dortmund.de
Wyatt Terry	University of Manchester	UK	twyatt@fnal.gov
Yanez Juan Pablo	DESY	Germany	juan.pablo.yanez@desy.de
Zaldivar Bryan	ULB	Belgium	bryan.zaldivar@ulb.ac.be
Zsoldos Stéphane	LPSC	France	zsoldos@lpsc.in2p3.fr